Tribikram Kundu *Editor*

Nonlinear Ultrasonic and Vibro-Acoustical Techniques for Nondestructive Evaluation

ASA PRESS

Springer

Nonlinear Ultrasonic and Vibro-Acoustical Techniques for Nondestructive Evaluation

Tribikram Kundu
Editor

Nonlinear Ultrasonic and Vibro-Acoustical Techniques for Nondestructive Evaluation

ASA PRESS

Springer

Editor
Tribikram Kundu
Department of Civil Engineering
and Engineering Mechanics
Aerospace and Mechanical Engineering
University of Arizona
Tucson, AZ, USA

ISBN 978-3-319-94474-6 ISBN 978-3-319-94476-0 (eBook)
https://doi.org/10.1007/978-3-319-94476-0

Library of Congress Control Number: 2018956564

This Springer imprint is published by the registered company Springer Nature Switzerland AG
The registered company address is: Gewerbestrasse 11, 6330 Cham, Switzerland

The ASA Press

The ASA Press imprint represents a collaboration between the Acoustical Society of America and Springer dedicated to encouraging the publication of important new books in acoustics. Published titles are intended to reflect the full range of research in acoustics. ASA Press books can include all types of books published by Springer and may appear in any appropriate Springer book series.

The Acoustical Society of America

On 27 December 1928 a group of scientists and engineers met at Bell Telephone Laboratories in New York City to discuss organizing a society dedicated to the field of acoustics. Plans developed rapidly and the Acoustical Society of America (ASA) held its first meeting on 10-11 May 1929 with a charter membership of about 450. Today ASA has a worldwide membership of 7000.

The scope of this new society incorporated a broad range of technical areas that continues to be reflected in ASA's present-day endeavors. Today, ASA serves the interests of its members and the acoustics community in all branches of acoustics, both theoretical and applied. To achieve this goal, ASA has established technical committees charged with keeping abreast of the developments and needs of membership in specialized fields as well as identifying new ones as they develop.

The Technical Committees include acoustical oceanography, animal bioacoustics, architectural acoustics, biomedical acoustics, engineering acoustics, musical acoustics, noise, physical acoustics, psychological and physiological acoustics, signal processing in acoustics, speech communication, structural acoustics and vibration, and underwater acoustics. This diversity is one of the Society's unique and strongest assets since it so strongly fosters and encourages cross-disciplinary learning, collaboration, and interactions.

ASA publications and meetings incorporate the diversity of these Technical Committees. In particular, publications play a major role in the Society. The Journal of the Acoustical Society of America (JASA) includes contributed papers and patent reviews. JASA Express Letters (JASA-EL) and Proceedings of Meetings on Acoustics (POMA) are online, open-access publications, offering rapid publication. Acoustics Today, published quarterly, is a popular open-access magazine. Other key features of ASA's publishing program include books, reprints of classic acoustics texts, and videos.

ASA's biannual meetings offer opportunities for attendees to share information, with strong support throughout the career continuum, from students to retirees. Meetings incorporate many opportunities for professional and social interactions and attendees find the personal contacts a rewarding experience. These experiences result in building a robust network of fellow scientists and engineers, many of whom became lifelong friends and colleagues.

From the Society's inception, members recognized the importance of developing acoustical standards with a focus on terminology, measurement procedures, and criteria for determining the effects of noise and vibration. TheASAStandards Program serves as the Secretariat for four American National Standards Institute Committees and provides administrative support for several international standards committees.

Throughout its history to present day, ASA's strength resides in attracting the interest and commitment of scholars devoted to promoting the knowledge and practical applications of acoustics.The unselfish activity of these individuals in the development of the Society is largely responsible for ASA's growth and present stature.

I would like to dedicate this book to my wife Nupur whose continuous inspiration, support, and sacrifice made this project possible.

Contents

Contributors

V. V. Aleshin National Center for Scientific Research, Joint International Laboratory LICS-LEMAC, Institute of Electronics, Microelectronics and Nanotechnologies, Villeneuve d'Ascq, France

Brian E. Anderson Department of Physics and Astronomy, Brigham Young University, Provo, UT, USA

Francesco Aymerich Department of Mechanical, Chemical and Materials Engineering, University of Cagliari, Cagliari, Italy

Sourav Banerjee Integrated Material Assessment and Predictive Simulation Laboratory (i-MAPS), Department of Mechanical Engineering, University of South Carolina, Columbia, SC, USA

H. Berjamin Aix Marseille Univ, CNRS, Centrale Marseille, LMA, Marseille, France

Shiro Biwa Department of Aeronautics and Astronautics, Graduate School of Engineering, Kyoto University, Kyoto, Japan

O. Bou Matar Ecole Centrale de Lille, Joint International Laboratory LICS-LEMAC, Institute of Electronics, Microelectronics and Nanotechnologies, Villeneuve d'Ascq, France

G. Chiavassa Aix Marseille Univ, CNRS, Centrale Marseille, M2P2, Marseille, France

S. Delrue Department of Physics, Wave Propagation and Signal Processing Research Group, KU Leuven Kulak, Kortrijk, Belgium

Kajetan Dziedziech Department of Robotics and Mechatronics, AGH University of Science and Technology, Kraków, Poland

Jesús N. Eiras Aix Marseille Univ, CNRS, Centrale Marseille, LMA, Marseille, France

N. Favrie Aix Marseille Univ, CNRS, IUSTI, Marseille, France

Julian Grill ASI Analog Speed Instruments GmbH, Koenigstein im Taunus, Burgweg, Germany

Wolfgang Grill ASI Analog Speed Instruments GmbH, Koenigstein im Taunus, Burgweg, Germany

Sylvain Haupert Laboratoire d'Imagerie Biomédicale – INSERM – CNRS – Sorbonne Université, Paris, France

Ming Hong Department of Mechanical Engineering, The Hong Kong Polytechnic University, Kowloon, Hong Kong SAR

L. Jacobs Georgia Institute of Technology, Atlanta, GA, USA

Paul A. Johnson Geophysics Group, Earth and Environmental Sciences, Los Alamos National Laboratory, Los Alamos, NM, USA

J.-Y. Kim Georgia Institute of Technology, Atlanta, GA, USA

Andrzej Klepka Department of Robotics and Mechatronics, AGH University of Science and Technology, Kraków, Poland

Tribikram Kundu Department of Civil Engineering and Engineering Mechanics, Aerospace and Mechanical Engineering, University of Arizona, Tucson, AZ, USA

Francesco Lanza di Scalea Department of Structural Engineering, University of California San Diego, La Jolla, CA, USA

Michael J. Leamy School of Mechanical Engineering, Georgia Institute of Technology, Atlanta, GA, USA

Pierre-Yves Le Bas Detonation Science and Technology Group (Q-6), Los Alamos National Laboratory, Los Alamos, NM, USA

Weibin Li School of Aerospace Engineering, Xiamen University, Xiamen, Fujian, China

Hyung Jin Lim Department of Civil and Environmental Engineering, KAIST, Daejeon, Republic of Korea

Peipei Liu Department of Civil and Environmental Engineering, KAIST, Daejeon, Republic of Korea

B. Lombard Aix Marseille Univ, CNRS, Centrale Marseille, LMA, Marseille, France

Tsuyoshi Mihara Tohoku University, Sendai, Japan

Claudio Nucera Barclays Investment Bank, London, UK

Yoshikazuf Ohara Tohoku University, Sendai, Japan

Byeongjin Park Korea Institute of Materials Science, Changwon, Gyeongsangnam-do, Republic of Korea

Pawel Packo Department of Robotics and Mechatronics, AGH University of Science and Technology, Kraków, Poland

Subir Patra Integrated Material Assessment and Predictive Simulation Laboratory (i-MAPS), Department of Mechanical Engineering, University of South Carolina, Columbia, SC, USA

Jordi Payá Instituto de Ciencia y Tecnología del Hormigón (ICITECH), Universitat Politècnica de València, Valencia, Spain

C. Payan Aix Marseille Univ, CNRS, Centrale Marseille, LMA, Marseille, France

Lukasz Pieczonka Department of Robotics and Mechatronics, AGH University of Science and Technology, Kraków, Poland

J. S. Popovics Department of Civil and Environmental Engineering, University of Illinois at Urbana-Champaign, Urbana, IL, USA

J. Qu Tufts University, Medford, MA, USA

Rafal Radecki Department of Robotics and Mechatronics, AGH University of Science and Technology, Kraków, Poland

Marcel C. Remillieux Geophysics Group (EES-17), Los Alamos National Laboratory, Los Alamos, NM, USA

Guillaume Renaud Laboratoire d'Imagerie Biomédicale – INSERM – CNRS – Sorbonne Université, Paris, France

Jacques Rivière Department of Engineering Science and Mechanics, Pennsylvania State University, University Park, PA, USA

Parisa Shokouhi Department of Engineering Science and Mechanics, Pennsylvania State University, University Park, PA, USA

Hoon Sohn Department of Civil and Environmental Engineering, KAIST, Daejeon, Republic of Korea

Igor Solodov IKT, University of Stuttgart, Stuttgart, Germany

Ankit Srivastava Illinois Institute of Technology, Chicago, IL, USA

Wieslaw J. Staszewski Department of Robotics and Mechatronics, AGH University of Science and Technology, Kraków, Poland

Zhongqing Su Department of Mechanical Engineering, The Hong Kong Polytechnic University, Kowloon, Hong Kong SAR

James A. TenCate Geophysics Group, Earth and Environmental Sciences, Los Alamos National Laboratory, Los Alamos, NM, USA

Tadeusz Uhl Department of Robotics and Mechatronics, AGH University of Science and Technology, Kraków, Poland

T. J. Ulrich Detonation Science and Technology Group (Q-6), Los Alamos National Laboratory, Los Alamos, NM, USA

K. Van Den Abeele Department of Physics, Wave Propagation and Signal Processing Research Group, KU Leuven Kulak, Kortrijk, Belgium

Kazushi Yamanaka Tohoku University, Sendai, Japan

Chapter 1
Fundamentals of Nonlinear Acoustical Techniques and Sideband Peak Count

Tribikram Kundu, Jesús N. Eiras, Weibin Li, Peipei Liu, Hoon Sohn, and Jordi Payá

1.1 Introduction

Nonlinear acoustical techniques are useful for detecting very small defects that often remain hidden to linear techniques. If the nonlinear acoustical techniques use acoustic signals in the ultrasonic range (above 20 kHz), then these techniques are called *nonlinear ultrasonic techniques*. Therefore, nonlinear ultrasonic techniques can be considered as a subset of nonlinear acoustical techniques. Before discussing nonlinear techniques let us first briefly talk about the conventional linear acoustical techniques.

For many years the integrity of a specimen has been checked by striking the specimen with a hammer and listening to the sound it generates. Since undamaged and damaged specimens have different natural frequencies they produce different sounds from their vibrations. The attenuation pattern of the generated sound has also been used for inspecting a specimen. Damaged specimens show

T. Kundu (✉)
Department of Civil Engineering and Engineering Mechanics, Aerospace and Mechanical Engineering, University of Arizona, Tucson, AZ, USA
e-mail: tkundu@email.arizona.edu

J. N. Eiras
Aix Marseille Univ, CNRS, Centrale Marseille, LMA, Marseille, France

W. Li
School of Aerospace Engineering, Xiamen University, Xiamen, Fujian, China

P. Liu · H. Sohn
Department of Civil and Environmental Engineering, KAIST, Daejeon, Republic of Korea

J. Payá
Instituto de Ciencia y Tecnología del Hormigón (ICITECH), Universitat Politècnica de València, Valencia, Spain

T. Kundu (ed.), *Nonlinear Ultrasonic and Vibro-Acoustical Techniques for Nondestructive Evaluation*, https://doi.org/10.1007/978-3-319-94476-0_1

different sound absorption characteristics than pristine specimens. These two acoustic parameters—*resonance frequency* and *attenuation coefficient* or *quality factor* (inverse of attenuation)— are the two most popular linear acoustic parameters that have been used for damage detection in materials. Linear acoustic analysis is sufficient for relating the resonance frequency and attenuation coefficient of an object to its elastic constants (stiffness) and damping coefficient. For this reason, resonance frequency and quality factor are called linear acoustic parameters. Large defects in a specimen significantly affect these linear parameters and therefore, relatively large defects can be detected by monitoring the change in these linear parameters. However, very small defects may not affect the linear parameters. Later it will be shown that nonlinear acoustic parameters are affected significantly more by very small defects and therefore the nonlinear parameters should be considered to detect those defects.

Since dominant resonance frequencies of most specimens are generally well below the ultrasonic range the resonance frequency and attenuation coefficients obtained from the vibrational analysis are called acoustic parameters instead of ultrasonic parameters. Two common ultrasonic parameters that are used for internal defect detection are *ultrasonic wave speed* and its *attenuation*. Ultrasonic waves are reflected and scattered by internal cracks. Reflection, refraction, and scattering of ultrasonic waves by internal cracks can be analyzed from the linear analysis of the interaction between the material defects and the propagating elastic waves. Internal damage can affect the velocity and attenuation of elastic waves in the material. Thus by monitoring the ultrasonic wave speed and its attenuation, and/or analyzing the scattering pattern of the propagating ultrasonic waves, internal damages can be detected and characterized. Since the linear analysis is sufficient for relating the crack geometry to the wave scattering pattern and wave velocity or attenuation this is also called linear acoustical technique (or linear ultrasonic technique if the frequency is greater than 20 kHz). Similar to the vibration-based linear acoustical techniques the wave propagation-based linear ultrasonic techniques also fail to detect very small defects. It will be shown in this chapter as well as in subsequent chapters that nonlinear acoustical/ultrasonic techniques can detect very small defects, such as micro-cracks at the grain boundaries that are much smaller than the wavelength of the interrogating ultrasonic signal.

Nonlinear acoustical techniques assume nonlinear stress–strain relation while linear techniques are based on linear stress–strain relation. Nonlinearity in stress–strain relation can be due to many reasons—one popular belief is that as waves propagate through the damaged material crack surfaces near the crack tips open and close causing variations in stiffness of the material in that region.

When waves of two different frequency propagate through a linear material their frequencies do not change. However, if the material is nonlinear, then the interaction between these two waves having frequencies f_1 and f_2 produces waves of many other frequencies ($mf_1 \pm nf_2$) where m and n are integer values. Waves having these new frequency values can be analyzed for detecting very small defects. This technique is known as the *Nonlinear Wave Modulation Spectroscopy* (NWMS) technique. Even when a wave of single frequency propagates through a nonlinear material

new waves of higher and lower frequency can be generated in the material. Higher frequency waves must have frequencies that are integer multipliers of the input wave frequency, these waves are known as *higher harmonics*. Under certain conditions the generated wave frequency can be half of the input wave frequency which is called *subharmonics*. Higher harmonic, subharmonic, and modulated waves can be effectively used for detecting very small defects. Various nonlinear ultrasonic techniques have been developed for internal defect detection by efficiently using these new waves commonly known as higher harmonic, subharmonic, and modulated waves.

Similar to the wave propagation-based techniques the vibration-based nonlinear techniques are also more sensitive to small defects than linear acoustical techniques. Linear acoustical techniques measure the resonance frequency and attenuation. In a linear system this resonance frequency and attenuation coefficient do not change with the intensity of excitation. However, in a nonlinear system both resonance frequency and attenuation coefficient change with the vibration amplitude. The nonlinear acoustical technique monitors this change with the intensity of excitation. This technique is known as the Nonlinear Impact Resonant Acoustic Spectroscopy or NIRAS. It has been shown by different investigators that NIRAS and its several variations are much more effective in detecting small defects in comparison to the linear parameters like resonance frequency and attenuation coefficient.

In summary, it can be stated that the linear acoustic parameters (or features) are not sensitive enough for the evaluation of the degradation of material properties and detection of microscopic defects. However, even tiny discontinuities in a material can produce detectable acoustic nonlinearity that is orders of magnitude higher than the intrinsic nonlinearity of the intact material. Thus, micro-defects that are too small to be detected by linear ultrasonic techniques are ideal candidates for inspection by nonlinear acoustical techniques. The use of nonlinear acoustics has been shown to be one of the most promising techniques for nondestructive evaluation (NDE) needed to assess the damage at its early stage in many structural components. It should be noted that the linear ultrasonic NDE techniques only deal with the frequencies of the input signals, while the nonlinear ultrasonic NDE techniques are interested in detecting and measuring acoustic signals whose frequencies are different from those of the input signals.

The experimental evidence of nonlinear behavior due to micro-cracks in damaged materials can be found in static stress–strain behavior and dynamic nonlinear wave interaction. Due to material nonlinearity a wave can distort creating accompanying harmonics and interaction of waves of different frequency. Nonlinearity causes changes in resonance frequency as a function of excitation amplitude. The level of nonlinearity in materials containing structural damage is generally far greater than in materials with no structural damage.

There are several approaches for damage detection by nonlinear acoustical and ultrasonic techniques. These techniques are briefly introduced in this chapter and then discussed in detail in subsequent chapters. The fundamental mechanics behind the nonlinear acoustic/ultrasonic behavior is presented first. A newly developed nonlinear technique based on the sideband peak counts (SPCs) is also discussed in this chapter. The authors of other chapters describe in detail their developed techniques.

1.2 Mechanics of Higher Harmonic Generation for Bulk Waves

Ultrasonic wave of one frequency when propagates through a nonlinear material generates ultrasonic waves of higher frequency that are n times the original frequency (where $n = 2, 3, 4, \ldots$.) due to the material nonlinearity. These are commonly known as higher harmonics. This acoustic nonlinear response which is caused by the material nonlinearity can be characterized by a nonlinear parameter β. The parameter β determines the degree of distortion of the ultrasonic waveform as it travels through the material. Analytical expression for β in terms of the amplitudes of the original monochromatic wave of frequency f and the second harmonic or the generated wave of frequency $2f$ is derived in the following section. By measuring the changes in β, the degree of nonlinearity which is related to the damage accumulation can be estimated.

1.2.1 Nonlinear Wave Equations

We start with some of the fundamental equations of elasticity in elastostatics and elastodynamics. Interested readers are referred to Kundu [1] for derivations of these equations. In any orthogonal coordinate system the traction–stress relation is given by

$$T_i = \sigma_{ji} n_j = \sigma_{ij} n_j \tag{1.1}$$

where σ_{ij} is the stress tensor, n_j is the unit vector in the direction of the normal to the surface on which the traction vector is defined. Index notation (also known as tensorial notation) is used in Eq. (1.1) and in subsequent equations. Free index i can take values 1, 2, and 3 to define traction components in x_1, x_2, and x_3 directions, respectively, in Cartesian coordinate system (or in r, θ, ϕ directions in spherical coordinate system, or in r, θ, z directions in cylindrical coordinate system). Repeated index j is called dummy index and must be summed as shown below.

$$T_i = \sigma_{i1} n_1 + \sigma_{i2} n_2 + \sigma_{i3} n_3 \tag{1.2}$$

Using the above traction–stress relation and applying Newton's first and second laws on an elemental volume the following equilibrium equation (Eq. 1.3) for the elastostatic case and governing equation of motion (Eq. 1.4) for the elastodynamic case can be obtained [1]:

$$\frac{\partial \sigma_{ij}}{\partial x_j} + f_i = \sigma_{ij,j} + f_i = 0 \tag{1.3}$$

$$\frac{\partial \sigma_{ij}}{\partial x_j} + f_i = \sigma_{ij,j} + f_i = \rho \ddot{u}_i \tag{1.4}$$

where the body force f_i is defined as the force per unit volume. In index notation the comma (,) followed by index j denotes the derivative with respect to x_j while double dots (..) above u_i denotes double derivative of u_i with respect to time.

Ignoring the body force, in the Lagrangian coordinate system the equation of motion (Eq. 1.4), which is also known as the linear momentum equation, can be written as

$$\rho \frac{\partial^2 u}{\partial t^2} = \nabla P = \nabla \sigma \tag{1.5}$$

where P is the Lagrangian stress tensor, same as σ used in Eqs. (1.1) through (1.4). For convenience both symbols P and σ are used to represent stress. Displacement gradients $u_{i,j}$ include higher-order elastic constants in a nonlinear isotropic solid. These expressions can be derived from the strain energy function as given by Landau and Lifschitz [2] in the following form:

$$W = \frac{1}{2}\lambda I_E^2 + \mu II_E + \frac{1}{3}AIII_E + BI_E II_E + \frac{1}{3}CI_E^3 \tag{1.6}$$

where I_E, II_E, and III_E are three strain invariants: $I_E = \varepsilon_{ii}$, $II_E = \varepsilon_{ij}\varepsilon_{ji}$, and $III_E = \varepsilon_{ij}\varepsilon_{jk}\varepsilon_{ki}$. λ and μ are Lame's constants which are second-order elastic constants. A, B, and C are third-order elastic constants (Murnaghan constants). The Lagrangian strain tensor is given by

$$\varepsilon_{ij} = \frac{1}{2}\left(u_{i,j} + u_{j,i} + u_{i,k}u_{k,j}\right) \tag{1.7}$$

$$\sigma_{ij}^L = \frac{\partial W}{\partial u_{i,j}} \tag{1.8}$$

$$\sigma_{ij} = \sigma_{ij}^L + \sigma_{ij}^{NL} \tag{1.9a}$$

where σ_{ij}^L is the linear term $\sigma_{ij}^L = \lambda\delta_{ij}\varepsilon_{kk} + 2\mu\varepsilon_{ij}$ and σ_{ij}^{NL} is the nonlinear term, it can be expressed as:

$$\begin{aligned}\sigma_{ij}^{NL} = &\left(\mu + \frac{A}{4}\right)\left\{u_{l,i}u_{l,j} + u_{j,l}u_{i,l} + u_{l,j}u_{i,l}\right\} \\ &+ \frac{1}{2}(\lambda - \mu + B)\left\{u_{l,m}u_{l,m}\delta_{ij} + 2u_{i,j}u_{l,l}\right\} \\ &+ \frac{A}{4}u_{j,l}u_{l,i} + \frac{B}{2}\left\{u_{l,m}u_{m,l}\delta_{ij} + 2u_{j,i}u_{l,l}\right\} + Cu_{l,l}u_{k,k}\delta_{ij}\end{aligned} \tag{1.9b}$$

From Eqs. (1.5) through (1.9a and 1.9b), we get the nonlinear wave equation:

$$(\lambda+\mu)\,u_{j,ji}+\mu u_{i,jj}-\rho_0\frac{\partial^2 u_i}{\partial t^2}=f_i, \tag{1.10}$$

where f is the nonlinear term given by,

$$\begin{aligned} f_i = & \left(\mu+\frac{A}{4}\right)\left(u_{l.i}u_{l.jj}+2u_{l.j}u_{i.lj}+u_{l.jj}u_{i.l}\right) \\ & +\left(\lambda+\frac{1}{4}A+B\right)\left(u_{l.ij}u_{l.j}+u_{j.jl}u_{i.l}\right)+(\lambda-\mu+B)\,u_{i.jj}u_{l.l} \\ & +\left(\frac{A}{4}+B\right)\left(u_{j.lj}u_{l.i}+u_{l.ij}u_{j.l}\right)+(B+2C)\,u_{j.ji}u_{l.l} \end{aligned} \tag{1.11}$$

Let us now consider one-dimensional nonlinear wave propagation in x_1 direction. For simplicity, coordinate directions x_1, x_2, and x_3 are replaced by x, y, and z, respectively, while u, v, and w denote three displacement components u_1, u_2, and u_3, respectively. For one-dimensional wave propagation analysis, the displacements are functions of x and t; then, the nonlinear plane wave equations are simplified to [3, 4]

$$\begin{aligned} u_{tt} &= c_l^2 u_{xx}+\left(3c_l^2+C_{111}/\rho\right)u_x u_{xx}+\left(c_l^2+C_{166}/\rho\right)(v_x v_{xx}+w_x w_{xx}) \\ v_{tt} &= c_t^2 v_{xx}+\left(c_l^2+C_{166}/\rho\right)(u_x v_{xx}+v_x u_{xx}) \\ w_{tt} &= c_t^2 w_{xx}+\left(c_l^2+C_{166}/\rho\right)(u_x w_{xx}+w_x u_{xx}) \end{aligned} \tag{1.12}$$

where $C_{111}=2A+6B+2C$, $C_{166}=\frac{1}{2}A+B$, ρ is the density. x is the wave propagation direction, derivatives of u with respect to t and x are denoted as, $u_{tt}=\frac{\partial^2 u}{\partial t^2}$, $u_x=\frac{\partial u}{\partial x}$, and $u_{xx}=\frac{\partial^2 u}{\partial x^2}$; similar notations are used for derivatives of v and w with respect to x and t.$c_l$and c_t are the propagation speeds of linear longitudinal and transverse waves, respectively:

$$c_l=\sqrt{\frac{\lambda+2\mu}{\rho}},\quad c_t=\sqrt{\frac{\mu}{\rho}} \tag{1.13}$$

Perturbation method can be used to solve these nonlinear wave equations. First, we expand the solution of the nonlinear wave equations to second order as given below:

$$\begin{aligned} u &= u^{(1)}+u^{(2)} \\ v &= v^{(1)}+v^{(2)} \\ w &= w^{(1)}+w^{(2)} \end{aligned} \quad \text{where} \quad \begin{aligned} u^{(1)} &>> u^{(2)} \\ v^{(1)} &>> v^{(2)} \\ w^{(1)} &>> w^{(2)} \end{aligned} \tag{1.14}$$

where $u^{(1)}$, $v^{(1)}$, and $w^{(1)}$ are the first-order primary wave solutions, while $u^{(2)}$, $v^{(2)}$, and $w^{(2)}$ are the second-order solutions. Equation (1.12) can be expanded as:

$$\begin{aligned} {u^{(1)}}_{tt} - c_l^2 {u^{(1)}}_{xx} &= 0 \\ {v^{(1)}}_{tt} - c_t^2 {v^{(1)}}_{xx} &= 0 \\ {w^{(1)}}_{tt} - c_t^2 {w^{(1)}}_{xx} &= 0 \end{aligned} \tag{1.15}$$

and

$$\begin{aligned} {u^{(2)}}_{tt} - c_l^2 {u^{(2)}}_{xx} &= \left(3c_l^2 + C_{111}/\rho\right) {u^{(1)}}_x {u^{(1)}}_{xx} \\ &\quad + \left(c_l^2 + C_{166}/\rho\right)\left({v^{(1)}}_x {v^{(1)}}_{xx} + {w^{(1)}}_x {w^{(1)}}_{xx}\right) \\ {v^{(2)}}_{tt} - c_t^2 {v^{(2)}}_{xx} &= \left(c_l^2 + C_{166}/\rho\right)\left({u^{(1)}}_x {v^{(1)}}_{xx} + {v^{(1)}}_x {u^{(1)}}_{xx}\right) \\ {w^{(2)}}_{tt} - c_t^2 {w^{(2)}}_{xx} &= \left(c_l^2 + C_{166}/\rho\right)\left({u^{(1)}}_x {w^{(1)}}_{xx} + {w^{(1)}}_x {u^{(1)}}_{xx}\right) \end{aligned} \tag{1.16}$$

1.2.2 Acoustic Nonlinear Parameters for Longitudinal Waves

For the case when there is only one purely longitudinal wave mode propagating in the solid having weak nonlinearity, so that only longitudinal displacement exists in Eq. (1.12), then this equation is reduced to,

$$u_{tt} = c_l^2 u_{xx} + \left(3c_l^2 + C_{111}/\rho\right) u_x u_{xx} \tag{1.17}$$

In Eq. (1.13) one can see that the longitudinal wave speed is a function of Lame's constants and density for an elastic medium. Substituting Eq. (1.13) into Eq. (1.17) one gets,

$$\rho u_{tt} = (\lambda + 2\mu)\, u_{xx} + (3\,(\lambda + 2\mu) + C_{111})\, u_x u_{xx} \tag{1.18}$$

The above one-dimensional equations (1.17 and 1.18) can be transformed into nonlinear longitudinal wave equation by introducing the coefficient of nonlinearity,

$$\beta_l = -\left(3 + \frac{C_{111}}{\rho c_l^2}\right) \tag{1.19}$$

Substituting Eq. (1.19) into Eq. (1.17) we get,

$$u_{tt} = c_l^2 u_{xx} - \beta_l c_l^2 u_x u_{xx} \tag{1.20}$$

Since the amplitude of the second harmonic wave is much less than that of the fundamental primary wave, the perturbation method can be applied to solve this nonlinear governing equation. The displacement u is assumed to have the following form:

$$u = u_1 + u_2 \tag{1.21}$$

The nonlinear wave Eq. (1.20) can be decomposed into two linear wave equations,

$$\frac{\partial^2 u_1}{\partial t^2} = c_l^2 \frac{\partial^2 u_1}{\partial x^2} \tag{1.22}$$

and

$$\frac{\partial^2 u_2}{\partial t^2} = c_l^2 \frac{\partial^2 u_2}{\partial x^2} - c_l^2 \beta_l \frac{\partial u_1}{\partial x} \frac{\partial^2 u_1}{\partial x^2} \tag{1.23}$$

where u_1 is the primary wave with fundamental frequency, while u_2 is the second harmonic wave with double frequency. The general solution for u_1 of the wave Eq. (1.22) can be expressed as,

$$u_1 = A_1 \sin(kx - \omega t) \tag{1.24}$$

Thus, Eq. (1.23) can be represented as

$$\frac{\partial^2 u_2}{\partial t^2} = c_l^2 \frac{\partial^2 u_2}{\partial x^2} + \frac{1}{2} c_l^2 \beta_l k^3 \sin(2kx - 2\omega t) \tag{1.25}$$

Assume $u_2 = xg\left(\frac{x}{c_l} - t\right)$, and substitute it into Eq. (1.25). Thus, u_2 can be solved as,

$$u_2 = \frac{1}{8} A_1^2 k^2 \beta_l x \cos 2(kx - \omega t) \tag{1.26}$$

Therefore, the amplitude of the propagating second harmonic wave whose frequency is twice the frequency of the fundamental wave is given by,

$$A_2 = A_1^2 k^2 \beta_l x / 8 \tag{1.27}$$

where A_1 is the amplitude of the fundamental wave, and A_2 is the amplitude of the second harmonic. In Eq. (1.27) k is the wave number. The material nonlinearity can be quantified by the acoustic nonlinear parameter β, which is related to the amplitude of the second harmonic and the square of the fundamental wave amplitude,

$$\beta_l = \frac{8A_2}{{A_1}^2 k^2 x} \tag{1.28}$$

Thus, the material nonlinearity can be evaluated by measuring the fundamental wave amplitude and the second harmonic wave amplitude from an ultrasonic test.

Another interesting property of the nonlinear parameter β for the longitudinal wave is that, for a given specimen, if the frequency of the wave is kept constant then

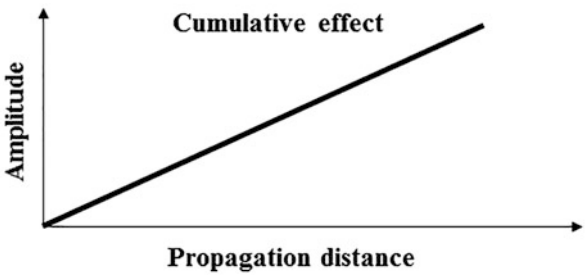

Fig. 1.1 Variation of the second harmonic wave amplitude [A_2] for constant amplitude of the monochromatic exciting wave [A_1], or in other words variation of $A_2/(A_1)^2$ with transmitter–receiver distance

the measured second harmonic amplitude linearly increases with x. This is known as the accumulative or cumulative effect of the second harmonic. The cumulative effect of the second harmonic amplitude has a major advantage for experimental measurement of the nonlinear effect. It can improve the signal-to-noise ratio simply by letting the wave propagate a longer distance as evident from Eq. (1.29).

From Eq. (1.28),

$$\frac{A_2}{A_1^2} \propto \beta_l x \tag{1.29}$$

Thus, the material nonlinearity can be evaluated by measuring the ratio of the second harmonic wave amplitude to the square of the fundamental wave amplitude as a function of the distance between the transmitter and the receiver, as shown in Fig. 1.1.

1.2.3 Acoustic Nonlinear Parameter for Transverse Waves

For the case of a purely transverse wave propagating in the x direction in a solid with weak nonlinearity, only transverse displacement exists in Eqs. (1.15) and (1.16), and therefore, they can be simplified to,

$$\frac{\partial^2 v_1}{\partial t^2} = c_t^2 \frac{\partial^2 v_1}{\partial x^2} \tag{1.30}$$

$$\frac{\partial^2 u_2}{\partial t^2} = c_l^2 \frac{\partial^2 u_2}{\partial x^2} + \left(c_l^2 + C_{166}/\rho\right) \frac{\partial v_1}{\partial x} \frac{\partial^2 v_1}{\partial x^2} \tag{1.31}$$

where v_1 and u_2 are linear (or first order) transverse displacement and nonlinear (or second order) longitudinal displacement components, respectively. It shows that the first-order transverse wave component generates second-order longitudinal wave components, and wave mixing occurs. Solution of Eqs. (1.30) and (1.31) by perturbation methods shows that a first-order transverse component generates no

second-order transverse component. The nonlinear parameter for one-dimensional transverse wave propagation can be defined as,

$$\beta_t = -\left(1 + \frac{C_{166}}{\rho c_l^2}\right) \tag{1.32}$$

Then Eq. (1.31) is simplified to

$$\frac{\partial^2 u_2}{\partial t^2} = c_l^2 \frac{\partial^2 u_2}{\partial x^2} - c_l^2 \beta_t \frac{\partial v_1}{\partial x} \frac{\partial^2 v_1}{\partial x^2} \tag{1.33}$$

where v_1 is the primary wave with fundamental frequency, while u_2 is the second harmonic wave with double frequency. The general solution for v_1 shown in Eq. (1.30) is given by,

$$v_1 = A_1 \exp[i\,(k_t x - \omega t)] \tag{1.34}$$

Substituting Eq. (1.34) into Eq. (1.33) gives rise to,

$$\frac{\partial^2 u_2}{\partial t^2} = c_l^2 \frac{\partial^2 u_2}{\partial x^2} + i c_l^2 \beta_t k_t^3 {A_1}^2 \exp[i2\,(k_t x - \omega t)] \tag{1.35}$$

The solution of this linear non-homogenous partial differential equation can be expressed as the sum of particular integral and homogenous solution,

$$u_2 = u_2^p + u_2^h \tag{1.36}$$

where u_2^p, u_2^h are particular integral and homogenous solution, respectively. It can be assumed that the particular solution of this equation is,

$$u_2^p = M \exp i2\,(k_t x - \omega t) \tag{1.37}$$

Substituting the particular solution into Eq. (1.35) we obtain,

$$u_2^p = \frac{-i\beta_t k_t^3 {A_1}^2}{4\left(k_t^2 - k_l^2\right)} \exp[i2\,(k_t x - \omega t)] \tag{1.38}$$

where $k_l = \frac{\omega}{c_l}, \quad k_t = \frac{\omega}{c_t}$.

The homogenous solution can be expressed as,

$$u_2^h = N \exp[i2\,(k_l x - \omega t)] \tag{1.39}$$

For pure shear wave excitation at $x = 0$ only the transverse motion exists; therefore, the boundary condition on u_2 is $u_2 = 0$ at $x = 0$. Substituting the homogenous solution in the total solution and taking into consideration the boundary condition, the final homogeneous solution is obtained as,

$$u_2^h = \frac{i\beta_t k_t^3 {A_1}^2}{4\left(k_t^2 - k_l^2\right)} \exp[i2\left(k_l x - \omega t\right)] \tag{1.40}$$

Thus, the complete solution of Eq. (1.35) can be written as

$$u_2 = \frac{-\beta_t k_t^3 {A_1}^2}{2\left(k_t^2 - k_l^2\right)} \sin\left[\left(k_t - k_l\right) x\right] \exp[i\left[\left(k_l + k_t\right) x - 2\omega t\right]] \tag{1.41}$$

Therefore, the amplitude of the second-order solution is

$$A_2 = \frac{-\beta_t k_t^3 {A_1}^2}{2\left(k_t^2 - k_l^2\right)} \sin\left[\left(k_t - k_l\right) x\right] \tag{1.42}$$

From Eq. (1.42) the material nonlinearity can be expressed as the acoustic nonlinear parameter, which is related to the amplitudes of the second harmonic and the square of the fundamental wave amplitude as,

$$\beta_t = \frac{A_2}{{A_1}^2} \frac{-2\left(k_t^2 - k_l^2\right)}{k_t^3 \sin\left[\left(k_t - k_l\right) x\right]} \tag{1.43}$$

As shown in Fig. 1.2, the amplitude of the second harmonic wave becomes zero at certain propagation distances. Since the amplitude of the second harmonic waves does not grow with propagation distance one can say that the second-order longitudinal component generated by the primary transverse wave does not have the cumulative effect.

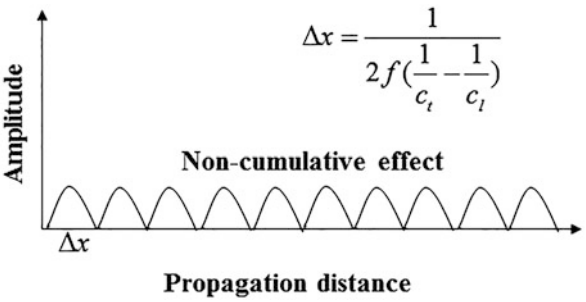

Fig. 1.2 Non-cumulative effect of the second harmonic longitudinal wave amplitude generated by the transverse wave

1.2.4 Use of Nonlinear Bulk Waves for Nondestructive Evaluation

As mentioned above, the cumulative effect on the amplitude of the second harmonic for longitudinal wave propagation in a nonlinear material is important for experimental detection of material nonlinearity with improved signal-to-noise ratio. Therefore, the second harmonic generated by propagating longitudinal waves is widely used to evaluate material nonlinearity. In this section, an example of the use of nonlinear longitudinal ultrasonic waves for nondestructive evaluation of material microstructural change is provided.

It has been reported in the literature [5–9] that microscopic defects such as lattice deformation or dislocations are the main sources of material nonlinearity. Material properties are highly dependent on the material microstructure. The microstructure can be changed through heat treatment process. Generally, slip homogenization and restriction of localized plastic deformation parallel to the boundaries caused by heat treatment gives better material properties. The objective of the investigation reported here is to study the correlation between heat treatment and material nonlinearity and evaluate the material nonlinearity change with improved material properties using nonlinear ultrasonic technique. The proposed procedure can be used to evaluate the heat treatment effects nondestructively, and to optimize the heat treatment parameters.

1.2.4.1 Nonlinear Acoustic Parameter Measurement

The material nonlinearity is monitored through generation and measurements of higher harmonics. The measurement of higher harmonic amplitude is needed for determining the value of the nonlinear acoustic parameter β. From Eq. (1.28) one can see that the nonlinear parameter is related to the amplitudes of the fundamental wave and the second harmonic in the following manner:

$$\beta = \frac{8A_2}{{A_1}^2 k^2 x} \tag{1.44}$$

where A_1 is the amplitude of fundamental wave, A_2 is that of the second harmonic wave, k is the wave number, and x is the wave propagation distance. During experiments, the value of $\widehat{\beta}$ is calculated from the following relation:

$$\widehat{\beta} = \frac{A_2}{A_1^2} \propto \beta \tag{1.45}$$

This ratio can be obtained experimentally. Thus, the material nonlinearity can be evaluated from the amplitudes of the fundamental and the second harmonic waves.

Table 1.1 Percentage of chemical components of Inconel X-750

Al	C	Cr	Copper	Iron	Mn	Ni	Nm	Si	Sr	Ti
0.4–1	0.08 Max	14–17	0.5 Max	5–9	1 Max	–	0.7–1.2	0.5 Max	0.01 Min	2.25–2.5

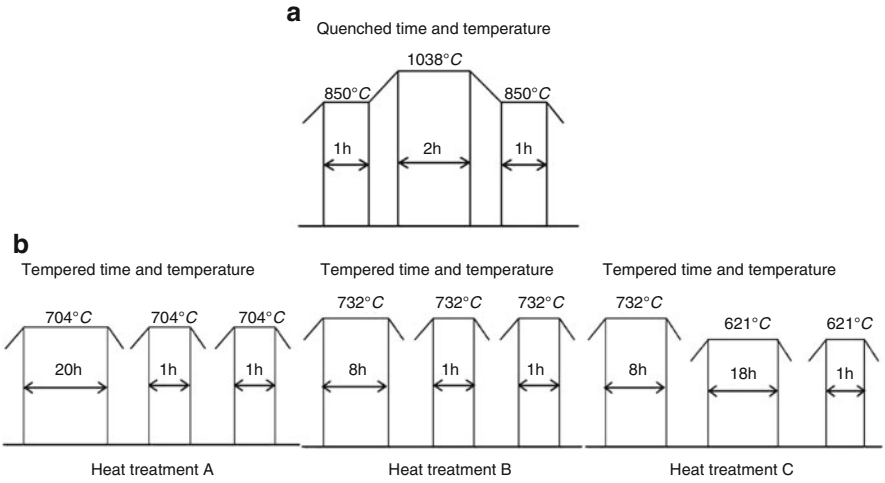

Fig. 1.3 Heat treatment process details: (**a**) Same quenching stage but (**b**) different tempering stages for the three specimens (from [10])

1.2.4.2 Specimens and Experimental Setup

The specimens considered for this investigation are rectangular plates [8, 9]. The dimensions of the specimens are 30 × 200 × 5 mm. The chemical compositions of the tested specimens are given in Table 1.1. One of these specimens is kept as the original untreated specimen, while the other three went through various levels of heat treatment. The heat treatment processes included quenching and tempering at various stages. Tempering involves reheating the quenched alloy to a temperature below the eutectoid temperature and then cooling it. The temperatures and times are the same during the quenching stage but different in the tempering stage, as shown in Fig. 1.3. During this process, the alloy is heated to dissolve and distribute alloying elements uniformly.

A piezoelectric transducer (made of PZT—lead-zirconate-titanate crystal) with central frequency of 5 MHz was used to generate the signal. The transducer generated signal first went through an attenuator to lower the noise level. The center frequency of the receiving transducer was set at 10 MHz for detecting primarily the second harmonic waves generated by the 5 MHz transducer. An amplifier was employed to increase the amplitude of the received second harmonic waves. Two transducers were placed carefully on opposite sides of the specimen as shown in Fig. 1.4a with holders designed to ensure uniform coupling condition. Before the signal processing, a Hanning window was used to modulate the received signal.

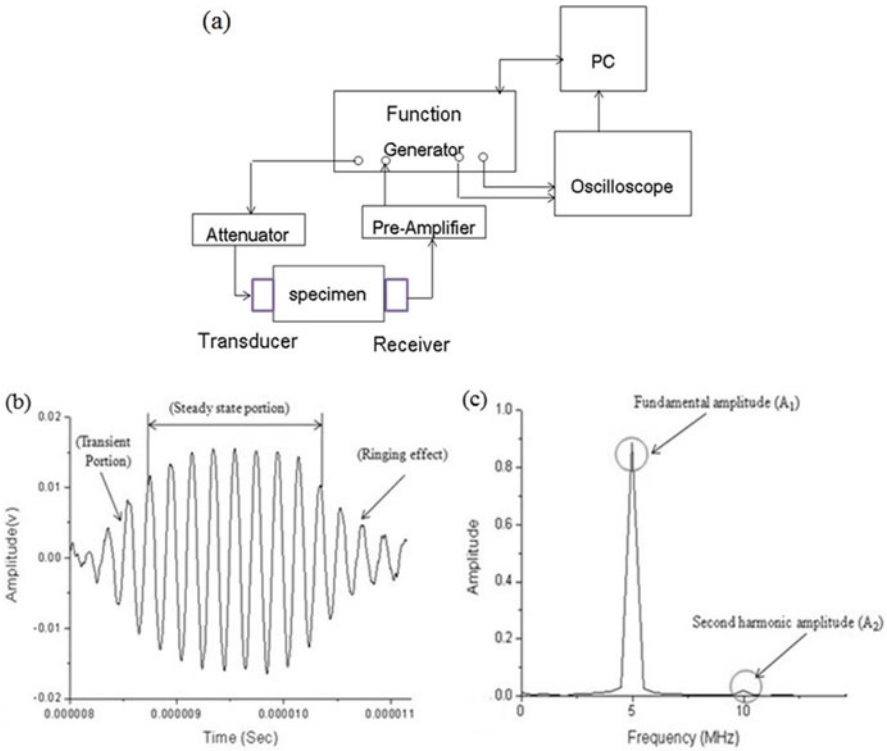

Fig. 1.4 (**a**) Ultrasonic nonlinearity measurement system, (**b**) time-domain signal, and (**c**) frequency spectrum (FFT) of the signal (from [10])

Fast Fourier transform (FFT) was then applied to the modulated signal to obtain amplitude A_1 of the fundamental frequency and A_2 of the second harmonic (double frequency). Figure 1.4b, c shows a typical time history and its FFT plot after the ultrasonic signal has propagated through the specimen.

One can see from Eq. (1.45) that the nonlinear parameter for the longitudinal wave propagation can be expressed as the ratio of the second harmonic amplitude (A_2) and the square of the fundamental wave amplitude $\left(A_1^2\right)$ for a fixed wave number and propagation distance. This value helps us to correlate the acoustic nonlinearity with the material nonlinearity of the specimens for different heat treatment conditions. The measured parameters are normalized with respect to their initial values to show relative changes.

The variation of the nonlinear acoustic parameter for the specimens with different heat treatment conditions is shown in Fig. 1.5. Compared to the pristine specimen that did not go through any heat treatment, the three heat treated specimens showed distinctly lower nonlinear acoustic parameter value. Figure 1.3b illustrates the heat treatment conditions A, B, and C.

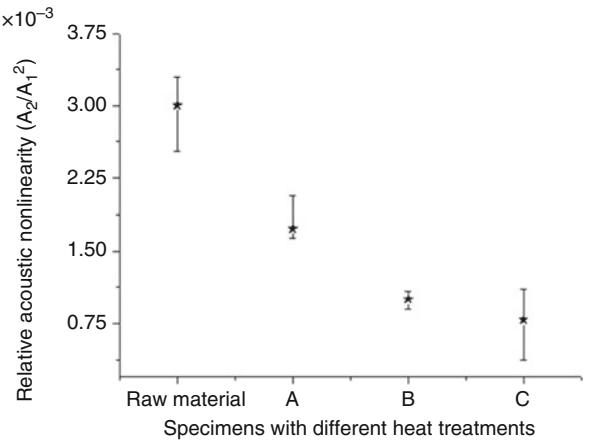

Fig. 1.5 Variation of relative acoustic nonlinearity in specimens after different heat treatments (from [10])

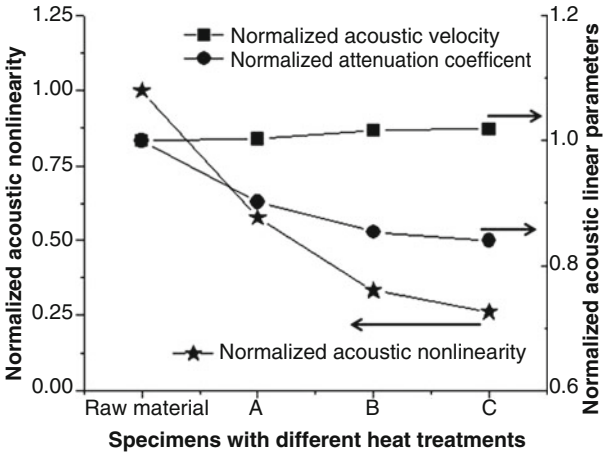

Fig. 1.6 Variations of linear and nonlinear acoustic parameters as the specimens underwent three different heat treatments—(**a**–**c**). All values were normalized with respect to their pristine values obtained before heat treatment $\overline{\beta}_{\text{Raw}} = 3 \times 10^{-3}$, $C_{\text{Raw}} = 5.92$ km/s and $\alpha_{\text{Raw}} = 0.246$ dB/mm (from [10])

Figure 1.6 shows the sensitivities of different linear and nonlinear acoustic parameters to heat treatment conditions. All acoustic parameters in the heat treated specimens have been normalized with respect to their initial values for the pristine material, to show the relative changes for each parameter. The experimental results show that the maximum change of wave velocity after heat treatment C is about 0.8% while the maximum change for the acoustic attenuation coefficient is 16%. However, the acoustic nonlinearity parameter shows most noticeable change with a variation of over 70% after heat treatment C. In Figs. 1.5 and 1.6 the nonlinear acoustic parameter value shows a 40% drop after heat treatment A and over 70% drop after heat treatment C [10].

Figure 1.6 clearly shows that compared to linear parameters nonlinear acoustic parameter is much more sensitive to the variations of the material properties caused by heat treatments. Thus variations of nonlinear parameters can be efficiently used for monitoring material degradation as well as enhancement.

1.3 Higher Harmonic Generation for Guided Waves

Ultrasonic guided waves such as Lamb waves can propagate over considerable distance exciting the entire thickness of the waveguide (such as plates and pipes). Therefore, guided waves can be used to find the surface defects as well as internal defects in plate, rod, and pipe-like structures. Low energy consumption and cost-effectiveness are two main advantages of guided wave-based damage detection techniques. Because of the high sensitivity of the nonlinear ultrasonic parameters to material damage and advantages of guided wave techniques for inspecting large structures, the nonlinear guided wave techniques have drawn considerable attention. Although guided wave nonlinearity is affected by the material nonlinearity the second harmonic generation is much more difficult for the guided wave due to its dispersive nature and multi-mode propagation characteristics. The multi-mode feature of guided waves makes it difficult to generate single pure mode experimentally. The investigation of second harmonic generation for guided waves in isotropic plate is presented in this section. To measure the nonlinear effect with sufficient signal-to-noise ratio one needs the second harmonic generation with cumulative effect. The key concept is to use those modes with a good "phase matching" so that significant energy transmission from the fundamental wave mode to the second harmonic mode occurs. The phase matching condition becomes important for the nonlinear guided wave NDE for having cumulative effect of the second harmonic while a nonlinear bulk wave technique does not require such precise frequency tuning. For this purpose, a new definition of guided wave nonlinear parameter is derived with some modifications of the conventional bulk wave nonlinearity. This section analyzes the second harmonic generation for guided waves in an isotropic plate. It discusses nonlinear features of both Rayleigh surface waves and Lamb waves.

1.3.1 Acoustic Nonlinear Parameter for Surface Wave Propagation

Particle displacements for surface waves, travelling along a free surface of an elastic half-space, decay exponentially with depth. Thus the energy of surface waves is concentrated near the surface. Surface waves can be efficiently used for the nondestructive evaluation of defects located on or near the surface. Advantages

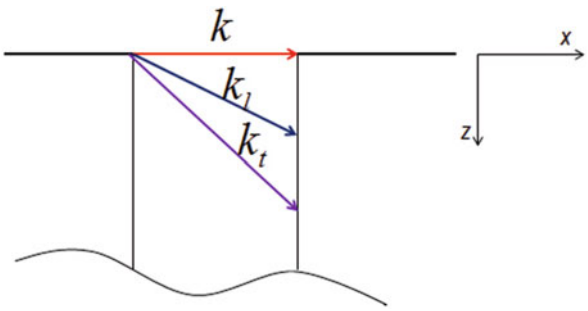

Fig. 1.7 Surface wave propagation in x direction

of surface wave-based NDE include longer propagation distance than conventional bulk waves to interrogate regions that are not suitable for visual inspection in large, complex structural components.

Let us consider a half-space with Rayleigh surface waves propagating in positive x direction, while z axis is pointing into the half-space as shown in Fig. 1.7. The displacement field associated with the Rayleigh surface wave propagating in an isotropic half-space with traction-free boundary conditions can be given as [1, 11].

$$u = \frac{\partial \phi}{\partial x} - \frac{\partial \psi}{\partial z} \tag{1.46}$$

$$w = \frac{\partial \phi}{\partial z} + \frac{\partial \psi}{\partial x}, \tag{1.47}$$

The longitudinal and shear wave potentials that describe Rayleigh wave propagation are,

$$\phi = \frac{A}{ik} e^{-pz} e^{i(kx-\omega t)}, \tag{1.48}$$

$$\psi = \frac{B}{ik} e^{-qz} e^{i(kx-\omega t)}, \tag{1.49}$$

where $p = \sqrt{k^2 - k_l^2}$ and $q = \sqrt{k^2 - k_t^2}$. Three wave numbers for the longitudinal wave, transverse wave, and surface wave in the material are k_l, k_t, and k, respectively. ω is the angular frequency. The boundary stresses σ_{zz} and σ_{xz} are zero on the surface ($z = 0$) because of the traction-free boundary conditions. Satisfying these boundary conditions the relationship between the constants A and B is obtained in the following form:

$$B = -iA \frac{2kp}{k^2 + q^2}. \tag{1.50}$$

Using partial wave technique, the surface wave can be decomposed into the cross-interaction and self-interaction of longitudinal and shear wave components on the surface. Thus, the partial displacement components of primary wave at the fundamental frequency and second harmonic waves at double frequency can be expressed as

$$u(f) = A\left(e^{-pz} - \frac{2pq}{k^2+q^2}e^{-qz}\right)e^{i(kx-\omega t)} \tag{1.51}$$

$$w(f) = iA\frac{p}{k}\left(e^{-pz} - \frac{2k^2}{k^2+q^2}e^{-qz}\right)e^{i(kx-\omega t)} \tag{1.52}$$

$$u(2f) = D\left(e^{-2pz} - \frac{2pq}{k^2+q^2}e^{-2qz}\right)e^{-i2\omega t} \tag{1.53}$$

$$w(2f) = iD\frac{p}{k}\left(e^{-2pz} - \frac{2k^2}{k^2+q^2}e^{-2qz}\right)e^{-i2\omega t} \tag{1.54}$$

Using normal modal expansion method, the relation between the amplitudes of fundamental wave and second harmonic wave generated displacements can be expressed as [12–14].

$$D = \sum_{n=1}^{3} C^{(n)} e^{ik^{(n)}x} \tag{1.55}$$

where

$$C^{(1)} = -\left(\frac{3\rho c_l^2 + C_{111}}{8\rho c_l^2}\right)k_l^2 A^2 x, \quad k^{(1)} = 2k_l, \tag{1.56}$$

$$C^{(2)} = -\left(\frac{\rho c_l^2 + C_{166}}{4\rho c_l^2}\right)\frac{k_t^3 A^2}{\left(k_t^2 - k_l^2\right)}\sin\left[\left(k_t - k_l\right)x\right], \quad k^{(2)} = k_l + k_t. \tag{1.57}$$

$$C^{(3)} = -\left(\frac{\rho c_l^2 + C_{166}}{\rho c_t^2}\right)\frac{\left(k_l k_t^2 + k_t k_l^2\right)A^2}{(k_l + k_t)^2 - 4k_t^2}\sin\left[\left(\frac{k_t - k_l}{2}\right)x\right], \quad k^{(3)} = \frac{3k_t + k_l}{2}. \tag{1.58}$$

It is found that $C^{(2)}$ and $C^{(3)}$ oscillate and vanish at certain propagation distances, which means these two components have no cumulative contributions to the second harmonic Rayleigh surface wave field. However, $C^{(1)}$ increases with propagation distance x. Therefore, when the wave propagation distance is sufficiently large, $C^{(1)}$

mostly contributes to the second harmonic field. From the above analysis, it is found that the relationship between D and A on the surface can be expressed as

$$D = \frac{\beta k_l^2 A^2 x}{8} e^{i2kx} \tag{1.59}$$

where $\beta = -\frac{3\rho c_l^2 + C_{111}}{\rho c_l^2}$ is the acoustic nonlinearity parameter for the surface wave; x is the wave propagation distance. Generally, the displacement component w is easier to detect experimentally, so in the following, w is used to calculate the nonlinear parameter of the surface wave. After substituting Eq. (1.59) into Eq. (1.54), the nonlinear parameter is expressed in terms of the vertical displacement amplitude w on the surface ($z = 0$) as

$$\beta = \frac{w(2f)}{w^2(f)} \frac{8i}{k_l^2 x} \frac{p}{k} \left(1 - \frac{2k^2}{k^2 + q^2}\right) \tag{1.60}$$

If attenuation is taken into consideration, then the acoustic nonlinear parameter is modified by the attenuation correlation factor as [12]

$$D_\alpha = \left(\frac{m}{1 - e^{-m}}\right), \quad m = (\alpha_2 - 2\alpha_1)\, x \tag{1.61}$$

where α_1 is the attenuation coefficient of the fundamental wave and α_2 is that for the second harmonic wave. Thus, the nonlinear parameter of the surface wave is modified as [12, 15]

$$\beta = \frac{A_2}{A_1^2} \frac{8i}{k_l^2 x} \frac{p}{k} \left(1 - \frac{2k^2}{k^2 + q^2}\right) D_\alpha \tag{1.62}$$

where A_1 and A_2 are the out-of-plane displacement amplitudes of the fundamental and the second harmonic wave, respectively, shown by the two peaks at 1 and 2 MHz frequencies in Fig. 1.8.

1.3.2 NDE Application Potential of Nonlinear Surface Waves

In this example, the frequency spectrum analysis to filter out undesirable frequency components is first conducted.

During nonlinear guided wave tests, nonlinear responses due to instruments, coupling media, and ambient noise are inevitable. However, amplitude of the higher harmonic induced by the material nonlinearity of the specimen is a function of the wave propagation distance as shown in Eq. (1.62), but the nonlinearity coming from the other sources listed above is independent of the wave path length.

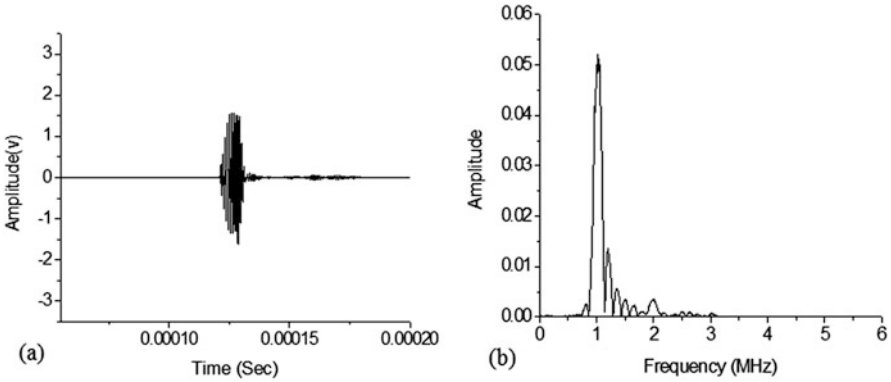

Fig. 1.8 Typical received signal: (**a**) time-domain signal, (**b**) frequency spectrum showing the strong fundamental frequency peak at 1 MHz and a relatively weak but noticeable second harmonic peak at 2 MHz (from [12])

Therefore, when the guided wave propagation distance increases, the amplitude of the second harmonic generated by the experimental setup or ambient noise remains same and only the second harmonic amplitude generated by the nonlinearity of the specimen increases. Thus the cumulative effect or the growth of the second harmonic amplitude with the propagation distance is very useful for distinguishing material nonlinearity from other sources of nonlinearity. To ensure that what is measured is due to the material nonlinearity induced by the micro-damages in the specimen and not arising from the measurement system one needs to demonstrate this cumulative effect.

To ensure that the experimental measurements of the nonlinear parameter are due to acoustic nonlinearity effect, the experiments were conducted for different propagation distances [12]. Wave propagation distance was varied from 50 to 250 mm with 25 mm interval. Note that the nonlinear parameter of Rayleigh surface waves is also a function of material properties and frequency. Since the same surface wave mode and frequency were chosen in this investigation to detect the acoustic nonlinearity in the specimens made of the same material, no correction for material or frequency variations was needed to study the nonlinear response. As shown in Fig. 1.9 it is found that the relative nonlinear parameter grows with the propagation distance because of the cumulative effect. The increase in the nonlinear parameter value is observed up to a certain distance (about 200 mm) after which it does not grow because then the material attenuation effect becomes more dominant.

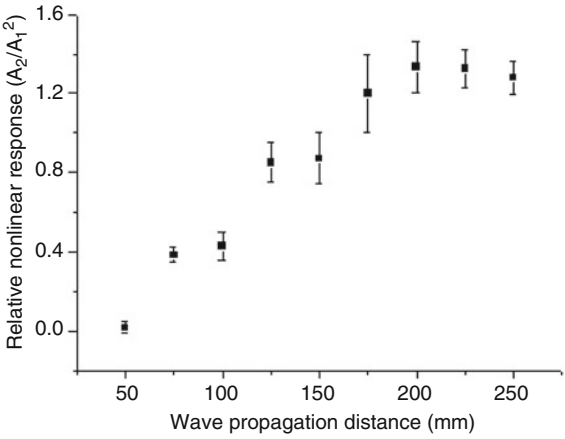

Fig. 1.9 Cumulative effect is responsible for the growth of the nonlinear parameter with propagation distance (from [12])

1.3.3 Nonlinear Lamb Waves

Compared to the Rayleigh surface waves, second harmonic generation for Lamb waves is much more difficult because of dispersion and multi-mode nature of Lamb waves. In general, the second harmonic wave amplitude is very small and can be easily overlooked due to the dispersive nature of Lamb waves. Consequently, proper mode tuning is absolutely necessary for nonlinear Lamb wave generation and reception. For this reason conducting nonlinear Lamb wave experiment can be quite challenging. Second harmonic generation of Lamb waves in an isotropic plate has been theoretically investigated using perturbation method and normal modal analysis technique. If the two conditions—phase matching and nonzero power transfer from the fundamental to the second harmonic mode—are satisfied, then the second harmonic mode shows a cumulative effect for nonlinear Lamb wave propagation. Group velocity of the primary wave mode and the higher harmonic wave mode should also be equal to achieve cumulative harmonic generation; however, this idea is still in dispute. For experimental investigation, it is necessary to have the second harmonic generation with cumulative effect to enable measurements of the nonlinear effects with sufficient signal-to-noise ratio.

We start with the nonlinear version of the Navier's equation for solving the Lamb wave propagation problem,

$$(\lambda + 2\mu)\,\nabla\,(\nabla \cdot \mathbf{u}) - \mu\nabla \times (\nabla \times \mathbf{u}) + \mathbf{f} = \rho_0 \frac{\partial^2 \mathbf{u}}{\partial t^2} \tag{1.63}$$

where, as before, $\mathbf{u}$ is the displacement, λ and μ are the elastic constants, ρ_0 is the material density, and $\mathbf{f}$ is the nonlinear term as defined in Landau and Lifshitz [2].

The body force is neglected in this wave equation. The nonlinear wave equation is solved by the perturbation method, by decomposing the total displacement field into two components—displacement component $\mathbf{u_1}$ from the primary wave and component $\mathbf{u_2}$ from the second harmonic:

$$\mathbf{u} = \mathbf{u_1} + \mathbf{u_2} \tag{1.64}$$

where $\mathbf{u_2}$ is assumed to be much smaller than $\mathbf{u_1}$, and the primary wave with frequency-wave number (ω, k) is written as follows:

$$\mathbf{u_1} = \mathbf{u}(z)e^{i(kx-\omega t)} \tag{1.65}$$

Constructing the second-order solution using modal expansion, the total second harmonic field can be written as [16–19].

$$\mathbf{u_2} = \frac{1}{2}\sum\nolimits_{m=1}^{\infty} A_m(x)\mathbf{u_2}(z)e^{-i2\omega t}, \tag{1.66}$$

where $\mathbf{u_2}$ is the displacement field. As shown in Fig. 1.10, x is the wave propagation direction. $A_m(x)$ is the expansion coefficient to be determined for the second-order modal amplitude and $2h$ is the thickness of the waveguide. The multiplier 1/2 in this equation is needed to have the final results in real quantities. The $A_m(x)$ is the solution of the following ordinary differential equation:

$$4p_{mn}\left(\frac{d}{dx} + ik_n^*\right)A_m(x) = \left(f_n^{\text{surf}} + f_n^{\text{vol}}\right)e^{i2kx}, \tag{1.67}$$

where

$$p_{mn} = -\frac{1}{4}\int_{\Omega}\left(\mathbf{v_n^*}\cdot\mathbf{s_m} + \mathbf{v_m}\cdot\mathbf{s_n^*}\right)\cdot\mathbf{n_x}d\Omega, \tag{1.68}$$

$$f_n^{\text{surf}}(x) = \int_{\Gamma}\mathbf{v_n^*}\cdot\mathbf{s^{2\omega}}\cdot\mathbf{n_x}d\Gamma, \tag{1.69}$$

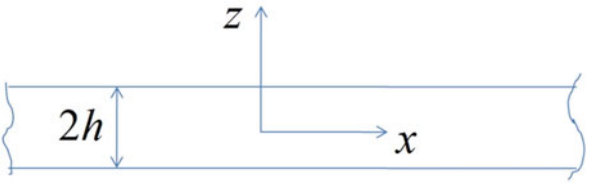

Fig. 1.10 Schematic of a plate with two traction-free boundary surfaces

$$f_n^{\text{vol}}(x) = \int_{\Omega} \mathbf{v_n^*} \cdot \mathbf{f^{2\omega}} d\Omega, \tag{1.70}$$

Ω is the waveguide's cross-sectional area and Γ is the curve enclosing Ω per unit length along the y axis. The terms f_n^{surf} and f_n^{vol} represent the complex external power related to the surface traction $\mathbf{s^{2\omega}}$ and body force $\mathbf{f^{2\omega}}$, respectively. The condition $u_2 = 0$ at $x = 0$ is satisfied when solving the equation to obtain $A_m(x)$:

$$A_m = \overline{A}_m(x) e^{i2kx} - \overline{A}_m(0) e^{-ik_n^* x}, \tag{1.71}$$

$$\overline{A}_m(x) = \frac{i\left(f_n^{\text{surf}} + f_n^{\text{vol}}\right)}{4p_{mn}\left(k_n^* - 2k\right)}, k_n^* \neq 2k, \tag{1.72}$$

$$\overline{A}_m(x) = \frac{\left(f_n^{\text{surf}} + f_n^{\text{vol}}\right)}{4p_{mn}} x, \quad k_n^* = 2k. \tag{1.73}$$

1.3.3.1 Phase Matched Lamb Wave Modes

Considering that single primary mode propagation in the waveguide generates multiple secondary modes, the second harmonic field of Lamb wave propagation could be assumed as superpositions of a series of double frequency Lamb wave components. However, only the component whose phase velocity is same as that of the fundamental wave mode is of our interest, because this mode having proper phase matching can get energy from the primary wave mode as it propagates with the primary mode. All other modes decay due to destructive interference with one another. For this reason, the cumulative effect of this double frequency component dominates the second harmonic field, up to a point, then it starts to decay due to the material attenuation. The contributions of other wave modes to the second harmonic field are negligible if they have different phase velocity than that of the fundamental mode. This is because they become out-of-phase with the fundamental mode after some propagation distance. Thus the energy transfer from the fundamental to an out-of-phase higher harmonic mode does not occur. For this reason the primary and the second harmonic Lamb wave modes whose phase and group velocities match are considered as the perfect mode pair. Some primary Lamb wave modes which satisfy the phase matching condition are shown in Fig. 1.11.

It has been shown in Eq. (1.73) that the amplitude of the higher harmonic wave grows with the propagation distance when the conditions of $k_n^* = 2k$ (synchronism) and $f_n^{\text{surf}} + f_n^{\text{vol}} \neq 0$ (nonzero power flux) are satisfied [17–19]. Thus, although several second harmonic Lamb wave modes at double frequency can be generated by the primary or fundamental Lamb wave mode in a nonlinear material, only the second harmonic component that has cumulative effect is of our interest. The second harmonic that has cumulative effect eventually dominates the generated group of

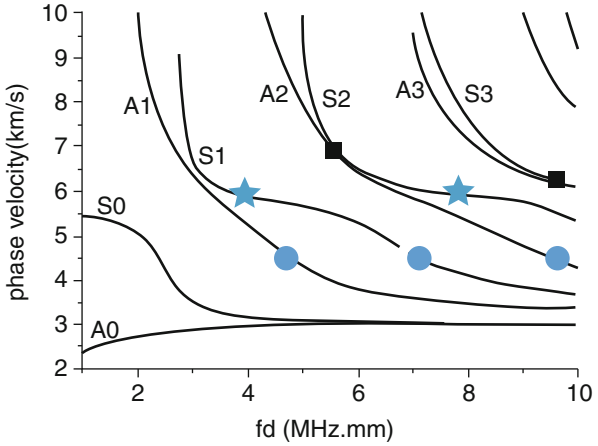

Fig. 1.11 Some phase matching guided wave modes that can serve as fundamental and higher harmonic modes in a plate are shown by different marker pairs on the dispersion curve plots

second harmonic waves after a certain propagation distance. From the dispersion curve plots, the phase matched guided wave modes can be found. The fundamental Lamb modes and double frequency second harmonic Lamb modes should have the same phase velocity for efficient generation of higher harmonic modes. All modes marked in Fig. 1.11 satisfy the phase matching conditions and have potential to generate cumulative second harmonic waves.

1.3.4 NDE Applications of Nonlinear Lamb Waves

1.3.4.1 Example 1: Detection of Thermal Fatigue in Composites by Second Harmonic Lamb Waves

All experiments were conducted on unidirectional carbon/epoxy composite laminates. The 400 × 400 mm square specimens with 1.0 mm thickness were made of 6 plies $[0]_6$ [8, 9]. All specimens had the same dimensions and provided by the same supplier. Material properties of the specimens are listed in Table 1.2. Thermal fatigue was imposed on the specimens to cause thermal degradation. The upper and lower limits of the temperature for the thermal fatigue cycle were 70 and −55 °C, respectively. Heating and cooling times of a thermal cycle were kept constant at 15 min, as shown in Fig. 1.12. The nonlinearity parameter in the specimens was measured before applying any thermal fatigue, and after applying 100, 200, and 1000 thermal fatigue cycles.

The S1 mode at frequency 2.25 MHz with phase velocity 9.6 km/s was chosen as the fundamental mode, because this mode satisfied the phase matching condition with S2 mode at 4.5 MHz (see Fig. 1.13). Under this condition, a double frequency

Table 1.2 Density and elastic stiffness coefficients of carbon/epoxy composites

ρ (kgm^{-3})	C_{11} (GPa)	C_{12} (GPa)	C_{13} (GPa)	C_{22} (GPa)	C_{23} (GPa)	C_{33} (GPa)	C_{44} (GPa)	C_{55} (GPa)	C_{66} (GPa)
1.5	146	5.81	5.81	11.07	6	11.07	2.55	3.82	4

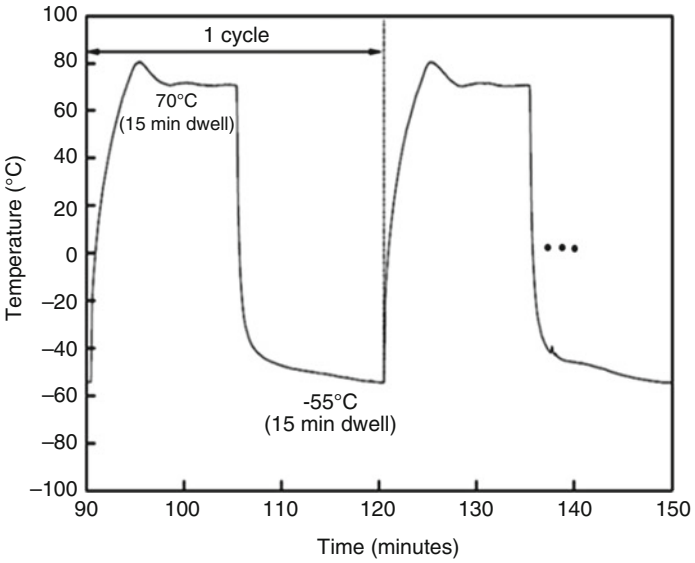

Fig. 1.12 Thermal fatigue cycle (from [8, 9])

Lamb mode (S2 mode) is likely to be generated due to the cumulative effect. Figure 1.13a, b shows that the "phase velocity matching" and "group velocity matching" conditions are satisfied between the fundamental S1 mode and double frequency second harmonic Lamb wave mode S2.

Experimentally, when the S1 mode is generated, it is inevitable that A1 mode is also generated since they are very close to each other in the phase velocity dispersion curve plot. Because of the difference in group velocities of S1 and A1 modes, wave-packets formed by S1 and A1 modes separate after a certain propagation distance. However, as shown in Fig. 1.13b, the group velocity of the S1 mode is different from that of the A1 mode, it is faster than A1 mode. Therefore, after the multi-mode signal propagates a certain distance, the wave-packages containing the S1 mode and A1 mode separate because of their different group velocities. Figure 1.14 shows how these two modes separate as the propagation distance increases. If the propagation distance is short, as shown in Fig. 1.14a, then multi-modes do not properly separate. As the propagation distance increases to 12 and 16 cm (see Fig. 1.14b, c), the mode separation becomes visible, since the gap in the time of flight due to the group velocity difference becomes noticeable. Since S2 mode has the same group velocity as the S1 mode the generated higher harmonic (S2) stay together with the fundamental mode (S1) but separate away from the A1 mode as

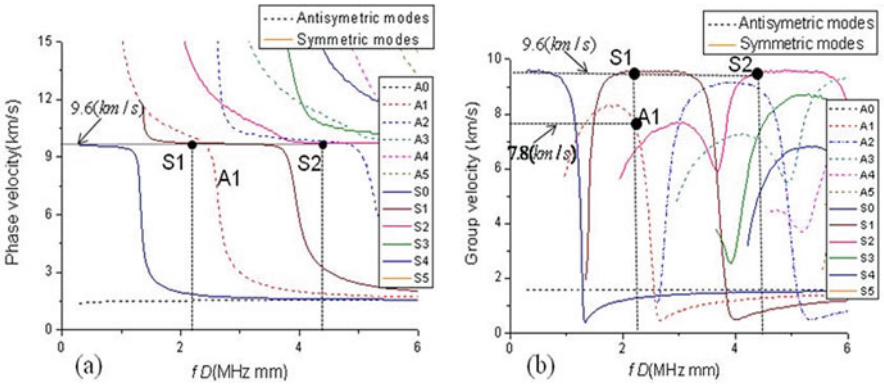

Fig. 1.13 Dispersion curves for Lamb wave propagation in the fiber direction of a composite plate specimen—(**a**) Phase velocity and (**b**) group velocity curves (from [8, 9])

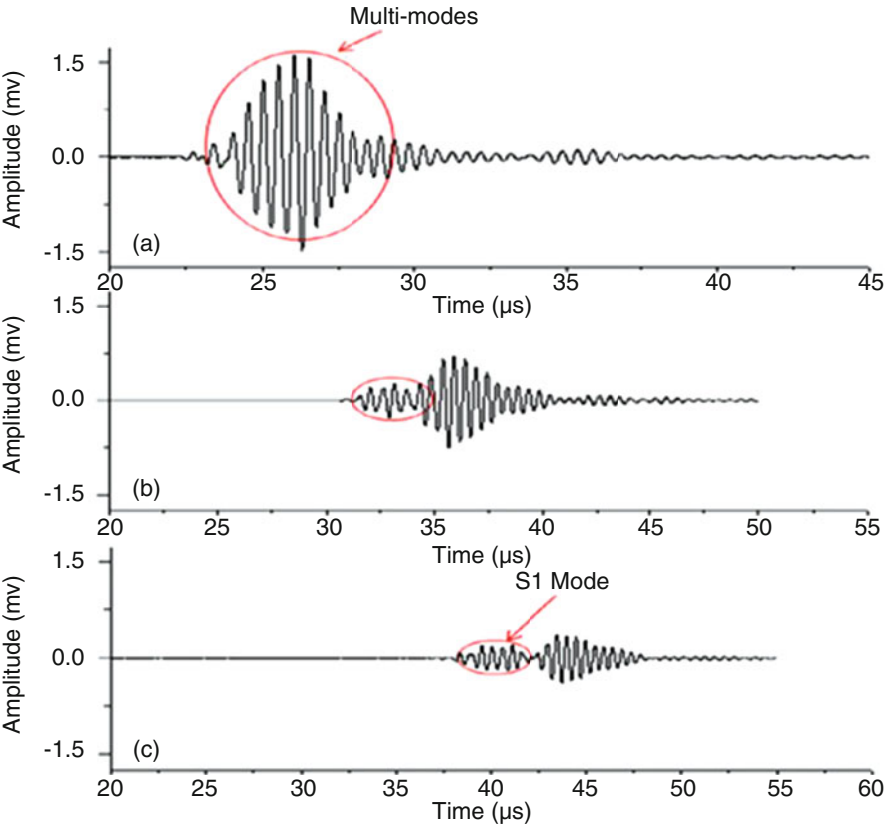

Fig. 1.14 The multi-mode separation process—time-domain signals at (**a**) 4 cm, (**b**) 12 cm, and (**c**) 16 cm propagation distances (from [8, 9])

shown in Fig. 1.14. Thus, it is possible to filter away A1 mode from S1 and S2 modes as shown in Fig. 1.14.

The S1–S2 mode pair was well separated from the A1 mode after 15 cm propagation distance. Then, a time gate was used to record only the S1 mode wave-packet avoiding A1 and other wave modes to accurately analyze the frequency spectrum of the second harmonic Lamb wave due to S1 mode only. Then, the frequency spectrum analysis to separate the second harmonic signal was conducted by placing the time gate over the S1–S2 wave-packet, at a propagation distance of 15 cm to avoid the influence of A1 and other modes. The measured time-domain signal was then processed by fast Fourier transform (FFT) to get the frequency spectrogram. From this spectral plot, the amplitude (A_1) of the fundamental S1 Lamb mode and the amplitude (A_2) of the double frequency second harmonic S2 mode were measured.

As shown in the above section, the acoustic nonlinear parameter β is a function of the ratio of the second harmonic amplitude and the square of the fundamental wave amplitude $\left(A_2/A_1^2\right)$, and the wave propagation distance x. For a given wave number k and nonlinearity feature function f, the normalized second harmonic amplitude can be expressed as:

$$\overline{\beta} = \frac{A_2}{A_1^2} \propto \beta x \tag{1.74}$$

As mentioned before, the normalized second harmonic amplitude grows with the propagation distance because of the cumulative effect up to certain distance, then it stops growing when the material attenuation becomes the dominating factor. To ensure that the measured nonlinearity is arising from the damages in specimens and not due to the measurement system's nonlinearity the demonstration of this cumulative effect is essential. The normalized second harmonic amplitudes $\left(A_2/A_1^2\right)$ have been measured at several distances as illustrated in Fig. 1.15.

The composite laminates are damaged due to the coefficient of thermal expansion (CTE) mismatch between the fibers and the matrix when the specimens are subjected to thermal fatigue. The appearance of transverse matrix micro-cracks and micro-debondings in composites are mainly caused by the thermal cycle induced thermal stresses. If the cyclic temperature variations occur in an oxidative environment, matrix oxidation appears in composites. It results in reduction in volume due to the resin induced shrinkage of the matrix relative to fibers. Scanning electron microscope (SEM) images of tested specimens shown in Fig. 1.16 confirms the existence of micro-damages in composites after thermal fatigue. The appearance of micro-damage, delamination, and fiber/matrix debonding caused by thermal fatigue can be seen in the right image of Fig. 1.16. These distributed micro-defects in composites are the main reason for the nonlinear behavior of the damaged composite laminates.

As shown in Eq. (1.74), the wave propagation distance affects the normalized second harmonic amplitude. It increases with the propagation distance. Therefore, at two different propagation distances, x_1 and x_2 two different values of the

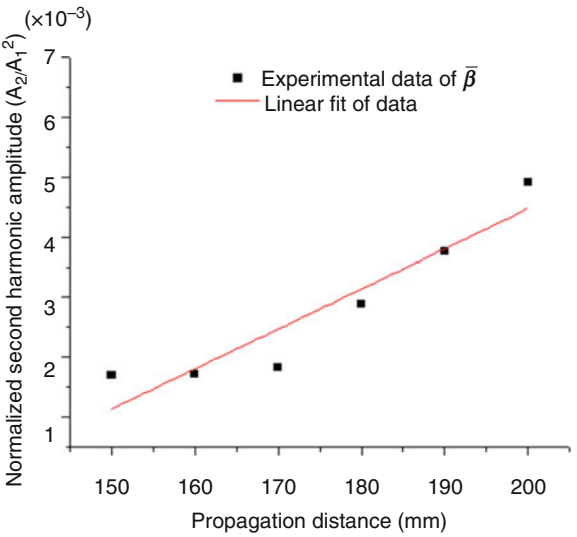

Fig. 1.15 Variation of the normalized second harmonic amplitude as a function of propagation distance of the Lamb wave (from [8, 9])

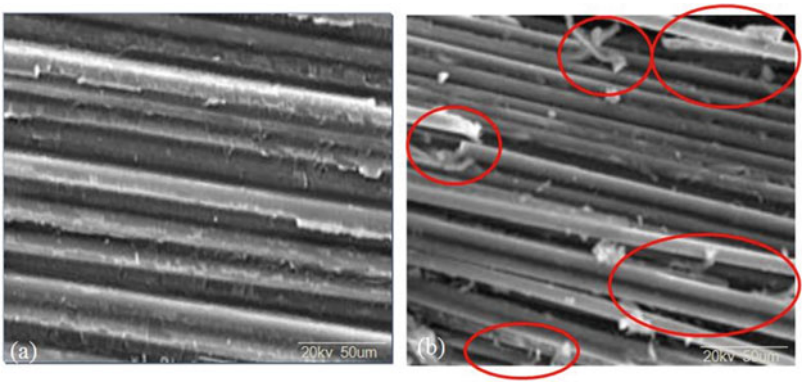

Fig. 1.16 SEM micrographs of specimens (**a**) without thermal loading, (**b**) after 1050 cycles of thermal fatigue loading (from [8, 9])

normalized second harmonic amplitude are obtained due to this cumulative effect—$\overline{\beta}_1 = \left(A_2/A_1^2\right)_1 \propto \beta x_1$ and $\overline{\beta}_2 = \left(A_2/A_1^2\right)_2 \propto \beta x_2$. Then, the relative acoustic nonlinearity is defined from the slope of the line obtained from the two points of data acquisition. It is defined in this manner to extract a term which is dependent only on the material damage and not on the propagation distance as shown in Eq. (1.75),

$$\tilde{\beta} = \frac{\left(\overline{\beta}_2 - \overline{\beta}_1\right)}{(x_2 - x_1)}, \tag{1.75}$$

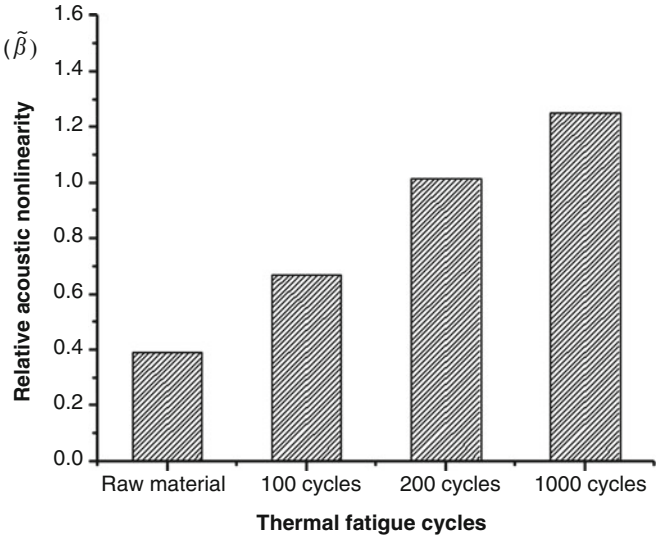

Fig. 1.17 Relative acoustic nonlinearity ($\tilde{\beta}$, see Eq. (1.75)) as a function of thermal cycles (from [8, 9])

The relative acoustic nonlinearity parameter defined in Eq. (1.75) should be nonzero only when the cumulative effect is present. In this way, the nonlinearity arising from other sources like couplant or instruments can be eliminated from the measurement since those nonlinearities do not have cumulative effect. The variation of relative acoustic nonlinearity in the specimens for different thermal fatigue cycles is shown in Fig. 1.17. One can see that the acoustic nonlinearity changes significantly as the number of thermal cycles increases.

The sensitivities of the linear acoustic parameters—the wave velocity and the attenuation coefficient—to the thermal cycles are also investigated for comparison. Figure 1.18 shows the variations of linear and nonlinear acoustic parameters in four specimens subjected to different levels of thermal cyclic loadings. One can see in this figure that there is a slight decrease of wave speed in the specimen with the increasing number of thermal cycles, while the attenuation coefficient and the nonlinearity parameter increase with thermal cycles. It clearly shows that the change of the linear parameters is not as noticeable as that for the nonlinear parameter. For example, after 100 cycles of thermal fatigue the micro-damage accumulated in the specimen almost does not change the linear parameters (velocity and attenuation) but shows a significant change in the nonlinear parameter (over 50%). To show only the relative changes of acoustic parameters in specimens with and without thermal loadings, all recorded values have been normalized with respect to the values of the undamaged pristine (or raw) specimen. This experimental investigation demonstrates that nonlinear Lamb waves can effectively detect micro-damages at their early stages.

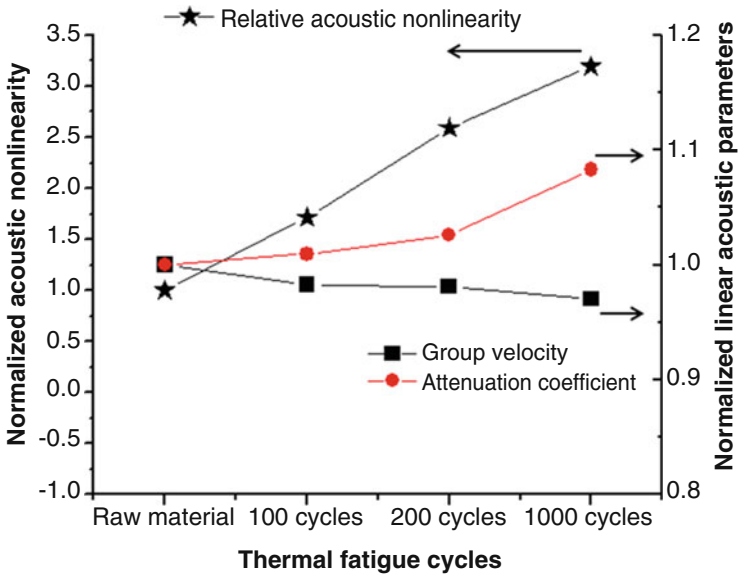

Fig. 1.18 Relative changes of linear parameters (group velocity and attenuation coefficient) and nonlinear acoustic parameters for a composite specimen subjected to different thermal fatigue loading cycles. All values are normalized with respect to the corresponding values of the undamaged specimen before it was subjected to the thermal fatigue loading. These values are ($C_{g.\,\mathrm{Raw}} = 9.36768$km/s), ($\alpha_{\mathrm{Raw}} = 0.079651 dB \cdot \mathrm{cm}^{-1}$), ($\beta_{\mathrm{Raw}} = 0.39157$) (from [8, 9])

1.3.4.2 Example 2: Assessment of Thermal Fatigue in Pipes by Nonlinear Guided Waves

To analyze nonlinear cylindrical guided wave propagation in a pipe having a constant cross-section, the total acoustic field can be decomposed into two parts, the primary waves (containing fundamental frequency components) and the second harmonic waves (containing double frequency components). Both waves satisfy the boundary conditions and the second harmonic waves show cumulative effect [20]. The nonlinear wave equation is solved by the perturbation method. The approximate solution of the wave equation can be expressed as the sum of the primary wave u_1 and its second harmonic u_2:

$$u = u_1 + u_2 \tag{1.76}$$

It is assumed that u_2 is much smaller than u_1, where the primary wave u_1 with frequency-wave number (ω, k) can be written as:

$$u_1 = u(r)e^{i(kz-\omega t)} \tag{1.77}$$

Constructing the second-order solution using modal expansion, the total second harmonic field can be written as

$$u_2 = \frac{1}{2}\sum_{m=1}^{\infty} A_m(z)u_{(2,m)}(r)e^{-i2\omega t} \tag{1.78}$$

$$v_2 = \frac{1}{2}\sum_{m=1}^{\infty} A_m(z)v_{(2,m)}(r)e^{-i2\omega t} \tag{1.79}$$

$$s_2 = \frac{1}{2}\sum_{m=1}^{\infty} A_m(z)s_{(2,m)}(r)e^{-i2\omega t} \tag{1.80}$$

where $u_{(2,m)}$ is the displacement field function for the mth double frequency component; the particle velocity ($v = \partial u/\partial t$) is denoted as $v_{(2,m)}$ and the stress tensor as $s_{(2,m)}$. The second-order modal amplitude $A_m(z)$ is the corresponding expansion coefficient and is to be determined, multiplier 1/2 is necessary to ensure real quantities. $A_m(z)$ is the solution of the following ordinary differential equation [17–19, 21, 22]:

$$4p_{mn}\left(\frac{d}{dz} - ik_n^*\right)A_m(z) = \left(f_n^{\text{surf}} + f_n^{\text{vol}}\right)e^{i2kz} \tag{1.81}$$

where

$$p_{mn} = -\frac{1}{4}\int_{\Omega}\left(v_n^* \cdot s_m + v_m \cdot s_n^*\right)\cdot n_z d\Omega \tag{1.82}$$

$$f_n^{\text{surf}}(z) = \int_{\Gamma} v_n^* \cdot s^{2\omega} \cdot n_z d\Gamma \tag{1.83}$$

$$f_n^{\text{vol}}(z) = \int_{\Omega} v_n^* \cdot f^{2\omega} d\Omega \tag{1.84}$$

where Ω denotes the waveguide's cross-sectional area and Γ is the curve that encloses Ω. Terms f_n^{surf} and f_n^{vol} define the complex external power corresponding to the surface traction $s^{2\omega}$ and the body force $f^{2\omega}$, respectively. Equation (1.81) is solved for the condition $u_2 = 0$ at $z = 0$ to obtain,

$$A_m = \overline{A}_m(z)e^{i2kz} - \overline{A}_m(0)e^{ik_n^* z} \tag{1.85}$$

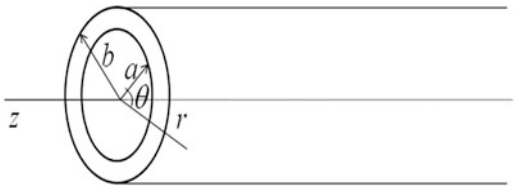

Fig. 1.19 Cylindrical shell

where

$$\overline{A}_m(z) = \frac{i\left(f_n^{\text{surf}} + f_n^{\text{vol}}\right)}{4p_{mn}\left(k_n^* - 2k\right)}, \quad k_n^* \neq 2k \tag{1.86}$$

$$\overline{A}_m(z) = \frac{\left(f_n^{\text{surf}} + f_n^{\text{vol}}\right)}{4p_{mn}} z, \quad k_n^* = 2k \tag{1.87}$$

It is found that the second harmonic amplitude is proportional to the propagation distance when $k_n^* = 2k$ (synchronism) and $f_n^{\text{surf}} + f_n^{\text{vol}} \neq 0$ (nonzero power flux). If the wave mode chosen satisfies these two conditions, then the generated second harmonic shows cumulative effect. As mentioned before the second harmonic generation with cumulative effect is essential for reliable experimental investigation.

Therefore, for a pipe with constant cross-sectional area as shown in Fig. 1.19, from the above analysis the expressions of p_{mn}, f_n^{surf}, and f_n^{vol} are given as,

$$p_{mn} = -\frac{1}{16}\int_0^{2\pi}\int_a^b \left[v_m^*(r,\theta)\cdot s_n(r,\theta) + v_n(r,\theta)\cdot s_m^*(r,\theta)\right]\cdot n_z r dr d\theta \tag{1.88}$$

$$f_n^{\text{surf}} = \frac{1}{2}b\int_0^{2\pi} v_n^*(b,\theta)\cdot s^{2\omega}(b,\theta)\cdot n_z d\theta - \frac{1}{2}a\int_0^{2\pi} v_n^*(a,\theta)\cdot s^{2\omega}(a,\theta)\cdot n_z d\theta \tag{1.89}$$

$$f_n^{\text{vol}} = \frac{1}{2}\int_a^b\int_0^{2\pi} v_n^*(r,\theta)\cdot f^{2\omega}(r,\theta)\cdot r dr d\theta \tag{1.90}$$

The assumed primary wave field of particle displacement components has the form:

$$u_1^r = u_r(r)\cos(n\theta)\, e^{i(kz-\omega t)} \tag{1.91}$$

$$u_1^\theta = u_\theta(r)\sin(n\theta)\, e^{i(kz-\omega t)} \tag{1.92}$$

$$u_1^z = u_z(r)\cos(n\theta)\, e^{i(kz-\omega t)} \tag{1.93}$$

where the circumferential order is $n = 0, 1, 2, \ldots\ldots$. For axi-symmetric modes $n = 0$. It is found that $f_n^{\text{surf}} + f_n^{\text{vol}} \neq 0$ (nonzero power flux) condition will always be satisfied if we substitute the axi-symmetric condition ($n = 0$) into the above equations.

As mentioned before, to generate cumulative second harmonic waves in a tube-like structure, certain conditions need to be satisfied: (1) nonzero power flux from the primary wave to the secondary wave field $\left(f_n^{\text{surf}} + f_n^{\text{vol}} \neq 0\right)$. The analysis has shown that all axi-symmetric modes, both longitudinal and torsional modes in pipes, satisfy this condition; (2) synchronism $\left(k_n^* = 2k\right)$ condition implies that the phase velocity of the secondary wave at double frequency is equal to that of the primary wave at fundamental frequency. This synchronism condition can physically explain the phenomenon that the second harmonic wave grows linearly with propagation distance because the energy is transferred continuously from the primary wave to the second harmonic wave as they propagate together satisfying the "phase matching" condition.

Acoustic field for the second harmonic guided wave propagation can be decomposed into several guided wave components at double frequency but having different phase velocities. However, the contribution of every double frequency guided wave component to the generated second harmonic field is not the same. Which component contributes how much depends on how close the phase and group velocities of the fundamental wave mode are with those of the double frequency wave modes. In this investigation, the second harmonic wave mode whose phase velocity is equal to that of the fundamental wave mode is of our interest, since only this mode satisfying the phase matching condition can grow with the propagation distance due to energy transfer from the fundamental mode while all other modes that do not satisfy phase matching condition decay due to material attenuation and destructive interference with other modes. The primary guided wave mode and phase matched secondary wave mode are a perfect mode pair for nonlinear guided wave-based inspection.

As shown in Fig. 1.20, $L(0, 6)$ and $L(0, 10)$ are a mode pair that satisfies phase matching condition since both phase velocity and group velocity of this mode pair are equal to each other. Therefore, for this mode pair the second harmonic waves at double frequency exhibit cumulative effect with the propagation distance for the longitudinal axi-symmetric mode $L(0, 6)$ at $fD = 5.05$ MHz-mm.

It is important to note that when one generates the $L(0, 6)$ mode at $fD = 5.05$ MHz-mm, it is inevitable to generate $L(0, 5)$ mode also, however, since the group velocities of these two modes are different they move away from each other after some propagation distance. The second harmonic guided wave mode $L(0, 10)$ generated by the fundamental mode $L(0, 6)$ has phase and group velocities same as those for the fundamental mode, so they can propagate together.

As mentioned before the measurement of the second harmonic amplitude is necessary for characterization of material nonlinearity. The nonlinear parameter is

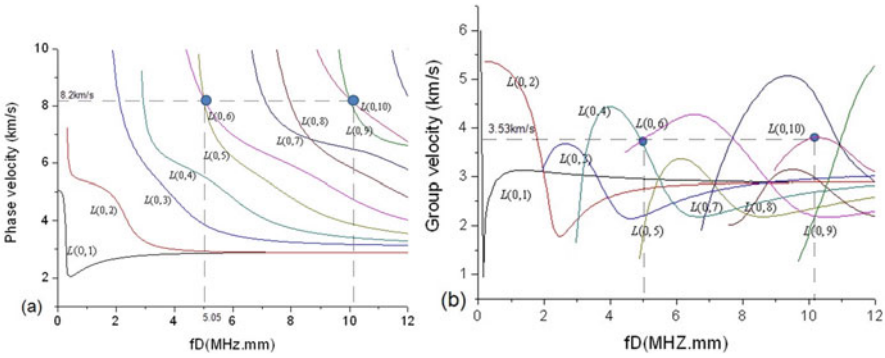

Fig. 1.20 Dispersion curves of an aluminum pipe: (**a**) phase velocity versus frequency; (**b**) group velocity versus frequency (from [8, 9])

related to the amplitudes of second harmonic and fundamental waves. The acoustic nonlinear parameter for the guided wave propagation is defined as,

$$\beta = \frac{8}{k^2 x} \frac{A_2}{A_1^2} F \tag{1.94}$$

where F is the feature function and x is the wave propagation distance. The nonlinear parameter of guided waves is a function of the frequency, mode type, material properties, and thickness of the waveguide. In this example, since the wave mode, frequency, and thickness of the waveguide do not change F is a constant. In the experimental investigation, the relative parameter $\overline{\beta}$ is used to represent the relative acoustic nonlinearity which is defined as $\overline{\beta} = A_2/A_1^2$, from Eq. (1.94),

$$\beta \propto \overline{\beta}/x \tag{1.95}$$

It is found that for the cylindrical guided wave also the ratio of the amplitude of the second harmonic and the fundamental wave grows with the propagation distance because of the cumulative effect. The amplitude grows up to a certain distance after which the material attenuation effect dominates and it starts to go down. Amplitudes of the higher harmonic waves induced by the material nonlinearity are functions of wave propagation distance as indicated in Eq. (1.95), but the harmonics induced by the instrumental nonlinearity are not. So, if we keep the experimental setup and conditions same, as the guided wave propagation distance increases, the strength of the second harmonic wave generated by the nonlinearity in the experimental setup or ambient noise will not change, but that generated by the nonlinearity of the specimen will increase due to the cumulative effect. To ensure that what is measured from the specimens are truly due to the damage induced nonlinearity rather than the nonlinearity in the measurement system, demonstration of this cumulative effect is necessary.

Aluminum pipes having outer diameter 20 mm, length 400 mm, and wall thickness 3 mm were inspected. In order to induce thermal fatigue in the specimen, the temperature and time of thermal fatigue were strictly controlled, especially in its early stage. The specimen was subjected to 5 and 10 cycles of thermal fatigue loading. In one thermal-loading cycle, the pipe specimen was heated at 204 °C for 30 min, and then for another 30 min it was kept at room temperature 20 °C.

In this study, the flexible PVDF sensor was used to generate and detect the guided wave modes in a pipe. The mode $L(0,6)$ at $fD = 5.05$ MHz-mm was excited by adjusting the wavelength of the flexible PVDF sensor generated wave. The wavelength of $L(0,6)$ mode is given by:

$$\lambda = \frac{c_{ph}}{f} \tag{1.96}$$

where λ is the wavelength; $c_{ph} = 8.2 km/s$ is the phase velocity shown in the dispersion curve plot (Fig. 1.20a); f is frequency.

Equation (1.96) can be also written as:

$$\frac{\lambda}{D} = \frac{c_{ph}}{fD} \tag{1.97}$$

where D is the wall thickness of the pipe. For a given pipe, a specific wave mode can be excited and detected by using a special transducer called comb transducer which is designed for a fixed wavelength controlled by the electrode finger spacing [23]. The spacing between successive fingers and the width of one finger determines the wavelength of the generated signal as shown in Fig. 1.21. In this study, the wavelength of $L(0,6)$ was about 5 mm for $fD = 5.05$ MHz-mm and phase velocity 8.2 km/s.

$$\lambda = \frac{c_{ph}}{f} = \frac{8.2}{1.68}\text{mm} \approx 5\text{mm} \tag{1.98}$$

Figure 1.21 shows the experimental setup and the comb transducer. A high voltage sinusoidal tone burst signal of 15 cycles at a frequency of 1.68 MHz was generated. An internal trigger generator, an internal waveform generator, and a high power gated RF amplifier were used to generate the signal. The attenuator and receiver unit were equipped with an amplifier connected to the transducers. Spacing of electrode fingers in flexible PVDF comb transducers controls the generated wave length. Axi-symmetric modes were generated in the pipe by wrapping the designed transducers around the pipe specimen. Specific holders were designed and placed on the transmitter and receiver to ensure uniform coupling condition. To increase the signal-to-noise ratio (SNR), time-domain signals were recorded and averaged 1000 times. On the steady state part of the signal a 256 point Hanning window was applied. To obtain the amplitudes A_1 of the fundamental wave and A_2 of the higher harmonic, the fast Fourier transform (FFT) of the measured time-domain signals

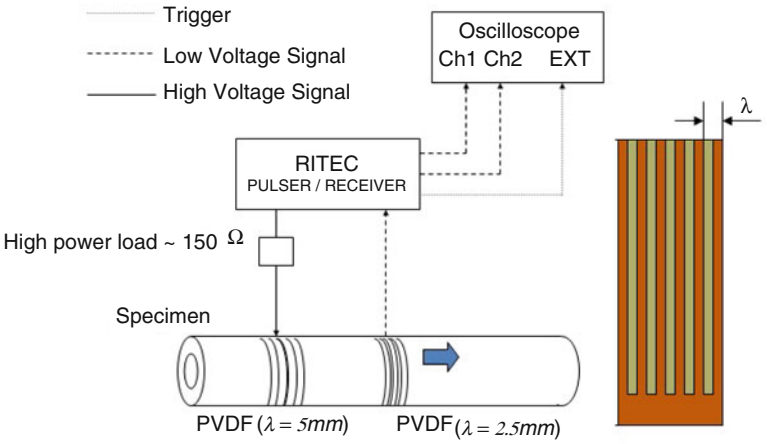

Fig. 1.21 Block diagram of nonlinear ultrasonic measurement system on the left and typical PVDF transducer for pipe inspection on the right (from [20])

was obtained. To detect the corresponding double frequency components, the width of the electrode fingers of the receiver (PVDF) was set equal to the half of that of the generator.

Generating the suitable wave mode is critical for finding the cumulative second harmonic wave. For guided wave test, one needs to verify that the mode chosen is indeed the mode generated experimentally. To this aim the group velocity of the generated wave mode and its frequency are measured and compared with the theoretical values shown in the dispersion curves. The group velocity can be calculated by measuring the time difference of wave signals propagating certain distance. As shown in Fig. 1.20, the group velocity of the propagating wave signal was 3.53 km/s, and the fundamental frequency was 1.68 MHz for waveguide thickness of 3 mm. By comparing this experimental signal with the theoretical value shown in Fig. 1.20b, it was concluded that this value was close to the theoretical value; therefore, the propagation signal was indeed the expected wave mode.

The $L(0,6)$ mode at $fD = 5.05$ MHz mm was selected as the primary mode. Experimentally, when the $L(0,6)$ mode was generated, $L(0,5)$ mode was also generated since they are very close in the phase velocity dispersion curve plot (Fig. 1.20a). However, as shown in Fig. 1.20b, the group velocities of $L(0,6)$ and $L(0,5)$ modes are different. However, $L(0,6)$ mode has the same group velocity as that of the double frequency $L(0,10)$ mode.

If the propagation distance is short, multiple modes having different group velocities do not separate properly. However, as the propagation distance increases, the modes with different group velocities separate more and become distinct. As a result, it is possible to selectively choose only the wave-packet of $L(0,6)$ and

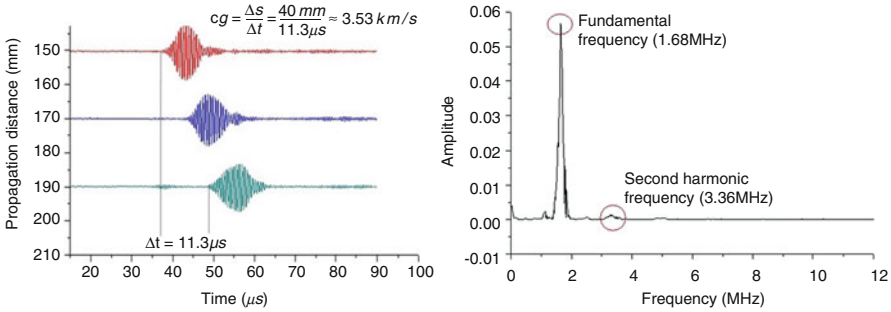

Fig. 1.22 Verification of $L(0,6)$ mode by (**a**) group velocity, (**b**) frequency [20]

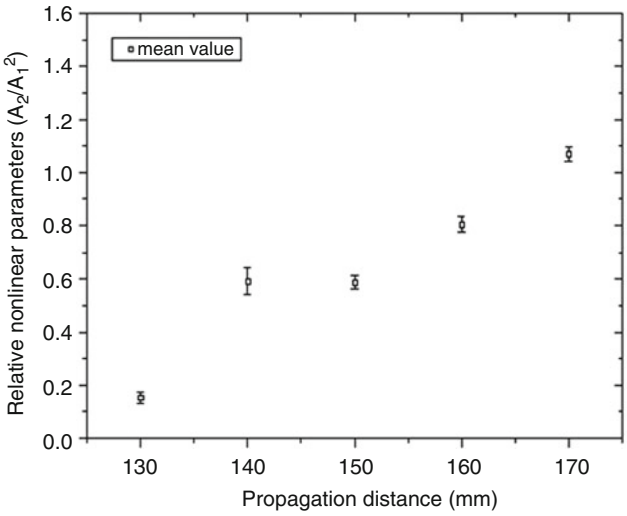

Fig. 1.23 Relative nonlinear parameter $\overline{\beta}$ versus propagation distance (from [20])

$L(0,10)$ after certain propagation distance. The $L(0,6) - L(0,10)$ wave-packet is well separated from the $L(0,5)$ mode after 130 mm propagation. The second harmonic mode was separated by applying FFT to the part of the signal within the time gate placed over the $L(0,6) - L(0,10)$ wave-packet, at a propagation distance of 150 mm to minimize the influence of $L(0,5)$ and other modes. Figure 1.22 shows a typical waveform of a received signal and its spectrum. In the spectral plot the fundamental wave amplitude A_1 and the higher harmonic mode amplitude A_2 were obtained at the fundamental frequency (1.68 MHz) and the second harmonic frequency (3.36 MHz), respectively.

The plot in Fig. 1.23 shows the average data with error bars from three measurements. The increase of the nonlinear parameter values with propagation distance confirms cumulative effect in the second harmonic generation.

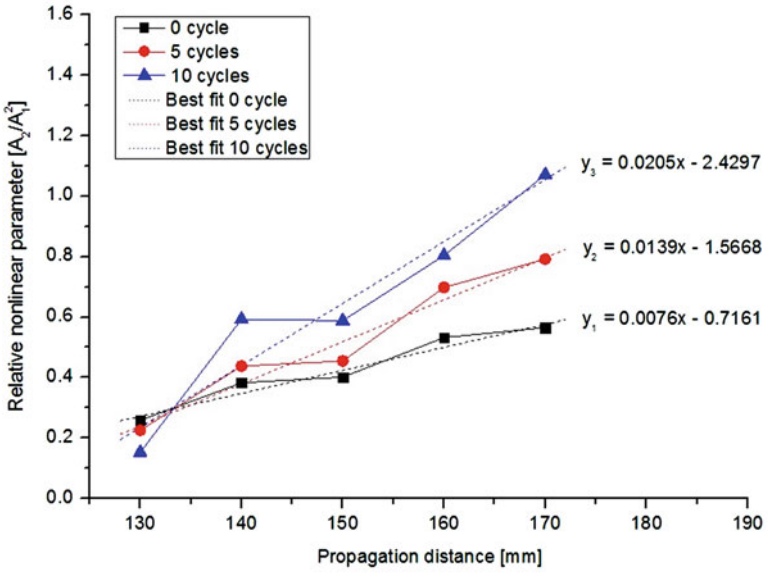

Fig. 1.24 Variations of relative nonlinear parameter with propagation distance for three specimens subjected to three different numbers of thermal fatigue cycles [20]

Second harmonic fields in a waveguide can be decomposed into a series of double frequency guided wave modes. However, during the above discussed experimental investigation, only a synchronous longitudinal mode pair was selected, whose wave velocities were the same. For this reason, the cumulative effect of this double frequency component dominated the second harmonic field, after the wave-packet propagated certain distance. The cumulative effect of the second harmonic amplitude helped to increase the signal-to-noise ratio, and it was concluded that under certain conditions, acoustic nonlinearity of the ultrasonic guided wave could be used for tracking micro-damages in pipe.

Figure 1.24 shows how the measured acoustic nonlinearity parameter of the specimen varies for different heat-loading cycles. The slope of the plotted curves increases with increasing number of heating–cooling cycles. These results demonstrated that nonlinear ultrasonic guided wave technique is a promising tool for detecting the thermal fatigue damage in their early stages in pipe and tube-like structures. Note that this technique of comparing slopes of the plotted curves can be used as a qualitative monitoring tool. In this investigation the correlation between the ultrasonic nonlinearity parameter and the damage level is made in a relative manner.

1.4 Higher Harmonic Generation by Different Types of Material Nonlinearity

Materials presented in Sects. 1.2 and 1.3 can be summarized in the following manner. Frequency (ω) of a propagating monochromatic acoustic wave remains unchanged during its propagation in a linear material. Its amplitude (A_1) can be reduced, owing to dissipation and diffraction in the linear material. However, in a nonlinear material the propagating wave is distorted resulting in higher harmonic generation. The amplitudes of generated higher harmonics give insight in the nonlinear mechanism. Figure 1.25 shows input and output waveforms for three representative cases: linear elastic, classical nonlinear elastic, and nonlinear hysteretic (non-classical) cases. The classical nonlinear elastic case for nonlinear quadratic stress–strain relation has been discussed in detail in Sects. 1.2 and 1.3. The process of higher harmonic generation for non-classical nonlinear response is more complex and is to be modeled by considering a nonlinear hysteretic stress–strain relationship in the wave equation. In this more general nonlinear model linear and classical nonlinear elastic cases can be considered as a special case [24]. The displacement amplitudes of the higher harmonics are directly related to the nonlinear mechanisms contributing to the wave distortion.

The nonlinear classical stress–strain relation can be expressed as a polynomial expansion of any order of our choice as [25],

$$\sigma = K_0 \cdot \left(\varepsilon + \beta\varepsilon^2 + \delta\varepsilon^3 + \ldots\right) \tag{1.99}$$

where K_0 is the linear elastic modulus, β and δ are higher-order elastic coefficients.

One-dimensional wave propagation along coordinate x ($\rho \cdot \partial^2 u/\partial t^2 = \partial\sigma/\partial x$, where ρ is the material density) through a rod whose stress–strain relationship obeys Eq. (1.99) leads to a nonlinear equation of motion. As mentioned before the solution of the displacement u is normally obtained through the perturbation theory, where the zero-order solution assumes a single frequency wave, $u_0 = A_1\cos(kx\text{-}\omega t)$. The first- and second-order perturbation solutions predict an increase of the spectral frequency content at twice (2ω) and thrice (3ω) the frequency of the initial

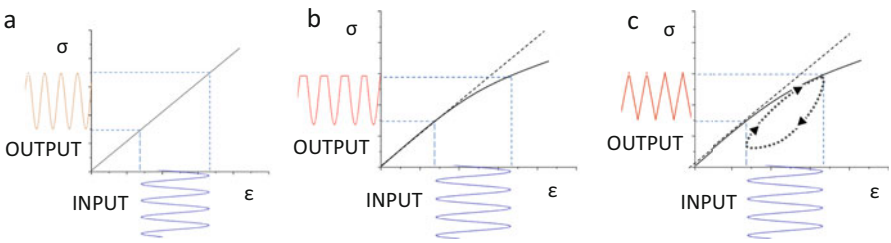

Fig. 1.25 Relationship between input and output signals for wave propagation through (**a**) a linear medium, (**b**) a nonlinear classical medium, and (**c**) a nonlinear hysteretic medium

monochromatic wave. The displacement amplitudes A_2 and A_3 corresponding to the second and third harmonics, respectively, are thus related to the higher-order parameters (β and δ). The higher-order elastic constants can be obtained as (see Eq. 1.28 for β),

$$\beta = -\frac{8 \cdot A_2 \cdot c_0^2}{A_1^2 \cdot \omega^2 \cdot x} \tag{1.100}$$

and

$$\delta = -\frac{48 \cdot A_3 \cdot c_0^3}{A_1^3 \cdot \omega^3 \cdot x} \tag{1.101}$$

where x is the propagation distance, and c_0 is the phase velocity. An example of attenuation corrections for second and third harmonics can be found in [26]. In any event, the second and third harmonic amplitudes are proportional to $A_1{}^2$ and $A_1{}^3$, respectively. The relation between third harmonic amplitude and β is approximately obtained as [27]

$$A_3 \approx \frac{\beta^2 \cdot A_1^3 \cdot \omega^4 \cdot x^2}{32 \cdot c_0^4}. \tag{1.102}$$

The deviation from such relation in the harmonic response of a material may indicate that higher-order elastic terms must be considered, or that hysteresis is contributing to the material nonlinearity [27]. A hysteretic equation of state can be considered as

$$\sigma = K_0 \cdot \varepsilon + U\,(\varepsilon, \dot{\varepsilon}) \tag{1.103}$$

where $U\,(\varepsilon, \dot{\varepsilon})$ is a function that adds a hysteretic departure from the linear behavior. The hysteretic behavior was considered to be elastic [28] and anelastic [24] in the wave equation. For both these cases, the second harmonic is not generated and A_3 is proportional to $A_1{}^3$. These conclusions also apply for higher harmonic generation in nonlinear acoustic resonance experiments—see Sect. 1.6 *Nonlinear resonance techniques*.

In other instances, the material nonlinearity stems from moving surfaces and interfaces within the material, such as a clapping crack being the most representative case. This is known as the contact acoustics nonlinearity (CAN). The generation of harmonics arises from the relative opening and closing of an interface (kissing bonds, delamination, cracks and/or crack tips, etc.). Even a perfect isotropic material can generate higher harmonics because of a structural inhomogeneity [29]. The material nonlinearity can be modeled from the nonlinear characteristics of the interface contact [30]. This is generally achieved considering a nonlinear spring model to describe the nonlinear stiffness of the contacting interface. Figure 1.26 illustrates

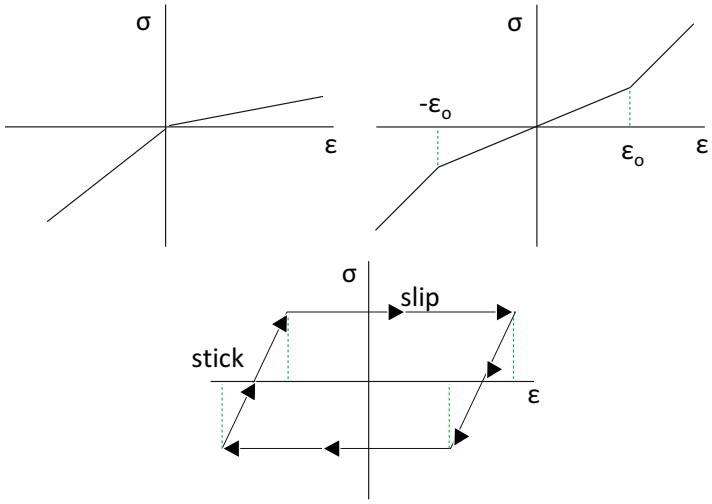

Fig. 1.26 Various nonlinear spring models

different nonlinear spring models used to describe the contact acoustic nonlinearity [31]. The propagation of a monochromatic wave through the contacting interface gives rise to considerable wave distortion which manifests as an enrichment of the frequency spectra with higher harmonics. These type of models have been applied and validated for specific cases involving contact acoustics nonlinearity in steel and polymeric materials [32–34].

In addition to the few examples discussed in Sects. 1.2 and 1.3 the higher harmonic methods have been used to characterize the material nonlinearity of various other metals [26, 35], rocks [36], and concrete [37, 38]. Second and third harmonics have been found to be sensitive to fatigue induced damage in different materials [5, 39–41]. Most common test configurations for higher harmonic detection use longitudinal waves in transmission mode; however, higher harmonics have been used in reflection mode as well [42]. As stated earlier besides bulk waves Rayleigh [13, 43] and Lamb waves [44] have also been used successfully for nonlinear ultrasonic NDE using higher harmonics. An extensive review of test configurations has been given by Zheng et al. [29]. Figure 1.27a illustrates the test configuration in transmission mode. It shows a single frequency burst with a preset number of cycles entering the nonlinear system. The distorted output signal contains the fundamental frequency and higher harmonics. Figure 1.27b shows typical transmitted and received signals. Spectral plots of the received signal shows peaks at the fundamental frequency and at double and triple frequencies.

The signal processing is normally conducted in the frequency domain through the fast Fourier transform, or bispectral analysis [7, 45]. These analyses allow a quantification of the amplitudes of the higher harmonics while other nonlinear mechanisms such as nonlinear attenuation or amplitude dependent effects are overlooked. In

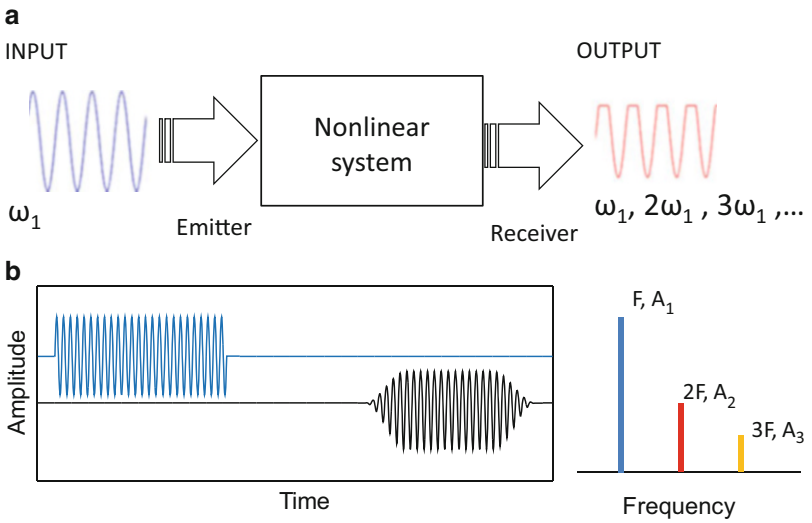

Fig. 1.27 (**a**) Schematic test configuration for higher harmonic generation—the transmission of a pure tone burst signal through a nonlinear system results in higher harmonic generation; (**b**) Representative transmitted and received signals and analysis of the received signal in frequency domain. Adapted from [7]

addition, the results may be affected by the signal processing parameters, such as windowing, zero-padding, and band-pass filtering. Bruno and coworkers [46] pointed out these disadvantages, and proposed a time-domain feature extraction method called scaling subtraction method (SSM). It requires subtracting a linear reference synthetic signal from the received signal. The resulted residuals contain the nonlinear contributions of the signal, which in turn can reveal the dominant mechanisms in the material nonlinearity—phase shift, nonlinear attenuation, and higher harmonic generation [46]. The SSM has been satisfactorily applied in the assessment of different damage mechanisms in concrete [47, 48], bricks [49], and steel [50].

1.5 Acoustoelastic Technique

The nonlinear mechanical behavior of materials has been traditionally tested by applying a stress or confining pressure onto the material under inspection and measuring changes in the wave speed due to applied stress [51]. This effect is known as acoustoelastic effect. The wave speed in a material stressed beyond the linear elastic regime can be expressed as a polynomial expansion of the applied strain—or alternately stress—as [52]

$$c(\varepsilon) = c_0 + c_1 \cdot \varepsilon + c_2 \cdot \varepsilon^2 + \ldots \tag{1.104}$$

where c_0 is the velocity in the unstressed material, and c_n is the n-th order acoustoelastic coefficient. The relative velocity variations may thus be related to either higher-order Murnaghan's [53] or Landau's [25] elastic coefficients. This method has been applied to characterize the nonlinear mechanical properties of steel [54], rock [55, 56], wood [57], and concrete [58]. The ultrasonic attenuation is also affected by the applied stress, as the crack type defects are closed and opened under compression and tension loadings, respectively [59]. Analogous to the strain dependent wave speed (Eq. 1.104), the acoustoelastic effect on the attenuation properties can be also expressed as [6]

$$\xi(\varepsilon) = \xi_0 + \xi_1 \cdot \varepsilon + \xi_2 \cdot \varepsilon^2 + \ldots \tag{1.105}$$

where ξ_0 is the attenuation in the unstressed material, and ξ_n is the nth order acoustoelastic attenuation coefficient. A modified version of the acoustoelastic technique investigates the acoustoelastic effects under low-cycle dynamic loading conditions—frequency up to 10 Hz, and strain amplitude 10^{-4} to 10^{-3} [6, 60]. The dynamic loading conditions allow reducing creep effects in the material, and improve the accuracy of the measured acoustoelastic coefficients when compared with static measurements [60]. Such a test configuration was used to assess the fatigue strength of polymeric materials and aluminum alloys [6]. The experimental results demonstrated that second-order acoustoelastic coefficients (c_2 and ξ_2) show enhanced sensitivity to fatigue damage when compared with the zero-order coefficients (c_0 and ξ_0)—those corresponding to the unstressed material.

Besides fatigue strength, and higher-order constant characterization, the acoustoelastic tests have been adapted to monitor damage and stress condition of infrastructure materials, using test configurations that allow one-sided measurements. This condition is sought by many researchers, since often the inspection of in-service structural components does not give access to two facing sides. Shokouhi et al. [61] used Rayleigh waves to monitor the stress-dependent velocity in concrete samples subjected to uniaxial compressive stress. Fröjd and Ulriksen [62] used a continuous sine wave excitation on the bottom side of a reinforced concrete slab subjected to static three-point bending loading condition. The variations in phase and amplitude of the received continuous wave signal exhibited similar variations as pulse transmission measurements subjected to increasing load. The authors pointed out that continuous wave excitation shows promise for structural health monitoring applications. This is because the continuous excitation can propagate with higher energy than ultrasonic pulses, and hence allowing inspection of large structures. The acoustoelastic experimental configurations are summarized in Fig. 1.28.

Testing the acoustoelastic effects in heterogeneous materials such as concrete is indeed more challenging because of scattering and dissipation [58]. Recently, different studies leveraged the enhanced sensitivity of multiple scattered waves in heterogeneous media to investigate the relative variations of wave velocity

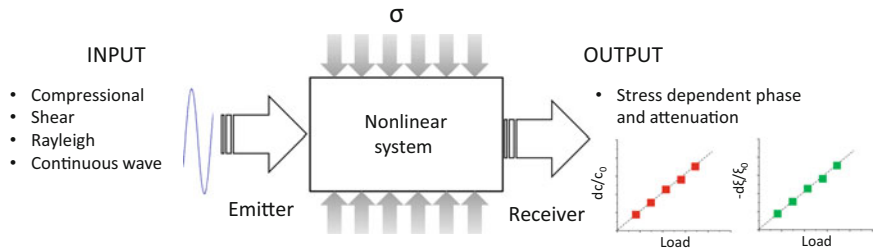

Fig. 1.28 Schematic representation of acoustoelastic tests. The ultrasonic pulses propagate through a material which is subjected to a static load

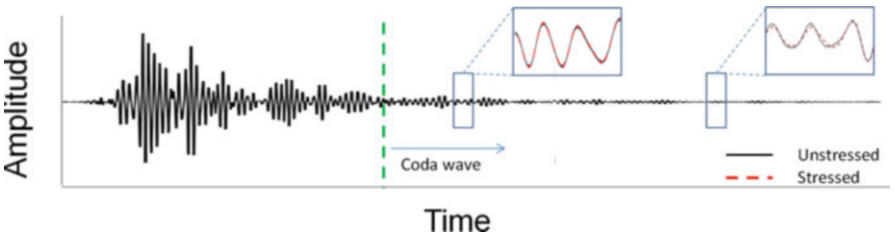

Fig. 1.29 Typical recorded signals in coda wave interferometry experiments. Insets show the time shift produced in the coda wave after loading the concrete samples

when subjected to compressive loading. This technique is referred as coda wave interferometry [63]. The test employs high-frequency ultrasonic pulses where multiple scattering effects are expected. At such frequencies, the received wave exhibits long-lasting waves (coda wave) that have been scattered multiple times by different heterogeneities within the material. Figure 1.29 shows a typical recorded signal. Different signals are recorded at different load steps. The variations of wave velocity are obtained by cross-correlating the coda wave in the received signal with the unstressed coda wave. Larose and Hall [64] used high-frequency ultrasonic pulses at 500 kHz in concrete, where multiple scattering effects are expected. The acoustoelastic effect was investigated under compressive load, from the time shift produced in the coda wave with respect to the reference signal. The authors argued that the test configuration might be used for in situ determination of the first-order acoustoelastic coefficient in concrete structures. Using similar experimental configuration and signal analysis, Payan et al. [58] derived the Murnaghan's constants in concrete. This procedure has also been used for assessing distributed anomalies, as produced by a thermal shock in concrete [65].

1.6 Nonlinear Resonance Techniques

Nonlinear resonance techniques monitor the resonance frequency shift and attenuation variations with increasing amplitude of excitation. For different excitation levels the resonance frequency and attenuation are determined. The material nonlinearity is manifested as a downward resonance peak shift, and decrease of quality factor (Q)—inverse of attenuation—with increasing excitation amplitude. Figure 1.30 shows the schematic diagram of a nonlinear resonance experiment. The test configuration consists of a sweeping frequency excitation over a range to match the resonance frequency of interest. Alternately, the resonance frequencies can be determined by hitting the specimen by an impactor. Multiple resonance spectra

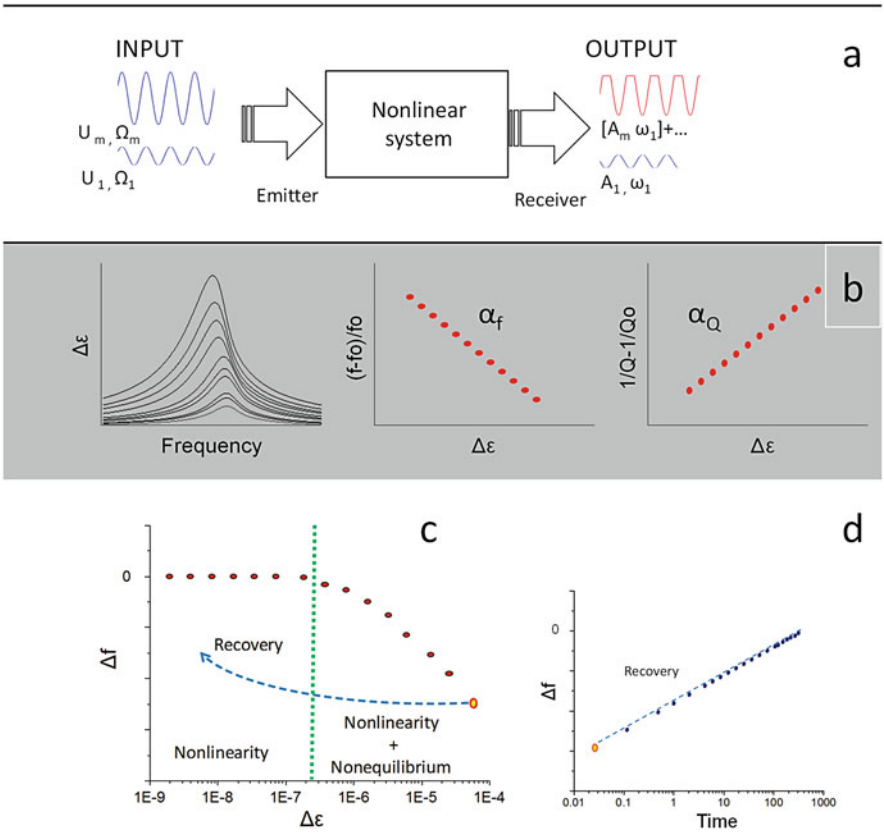

Fig. 1.30 (**a**) Schematic test configuration for nonlinear resonance acoustic spectroscopy, (**b**) typical resonance frequency shift observed in nonlinear resonance experiments, and evaluation of the hysteretic parameters—amplitude dependent resonance frequency and attenuation; (**c**) resonance frequency shift regimes (adapted from [84]), and (**d**) resonance frequency relaxation with time produced after an excitation in the non-equilibrium regime

are recorded by continuously increasing the excitation amplitude in consecutive experiments. This technique is referred as Nonlinear Impact Resonance Acoustic Spectroscopy or NIRAS [66, 67]. Figure 1.30b shows representative frequency spectra obtained in a nonlinear resonance experiment and the evaluation of the amplitude dependent frequency and quality factor (Q). The magnitudes of both shifts are related to the degree of damage.

The consideration of higher-order terms in the stress–strain relation leads to the generation of higher harmonics. From the acceleration amplitude corresponding to the fundamental resonance peak (A_1) and the higher harmonic amplitudes (A_2 and A_3) at twice and thrice the fundamental resonance frequency, the quadratic and cubic elastic constants can be obtained as [55, 56]

$$\beta = -\frac{A_2 \cdot \omega_0^2 \cdot L}{A_1^2}. \tag{1.106}$$

and

$$\delta = -\frac{A_3 \cdot \omega_0^4 \cdot L^2}{A_1^3} \tag{1.107}$$

where L and ω_0 are specimen dimension and fundamental frequency, respectively. Usually, the average strain over one strain cycle is zero; thus, the quadratic term β is eliminated [55, 56]. Therefore, from the downward resonance frequency shift, the third-order elastic nonlinear term can be obtained as

$$\frac{f - f_o}{f_o} \approx \frac{\delta}{2} \cdot \varepsilon^2 \tag{1.108}$$

where ε is strain, f_o is the resonance frequency in the linear strain range. In practice, f_o is the resonance frequency for the lowest excitation level. Determination of the third-order elastic nonlinearity has been the objective of many researchers, as it provides insight into the ultimate stress in brittle materials such as concrete, and the yield stress for ductile materials [68]. However, experimental evidences in polycrystalline solids and rocks revealed a linear dependence of the resonance frequency and attenuation shifts with strain amplitude, along with an unexpectedly high third harmonic amplitudes [55, 56, 69–71]. These observations do not comply with the classical nonlinear behavior, and were associated with hysteresis in the stress–strain relationship. Such behavior was found to be the characteristic of materials with defects at the mesoscale level: rocks, concrete, soil, cracked materials, etc., which are collectively termed nonlinear mesoscopic elastic materials, NMEM [69]. By including hysteresis in modeling resonance experiments [72–74], it was demonstrated that the resonance frequency shift is proportional to the strain amplitude ($\Delta\varepsilon$), so that

$$\frac{\Delta f}{f_o} = \alpha_f \cdot \Delta\varepsilon \tag{1.109}$$

along with a linear decrease of attenuation as

$$\frac{1}{Q} - \frac{1}{Q_o} = \alpha_Q \cdot \Delta\varepsilon \tag{1.110}$$

where Q is the quality factor (inverse of attenuation) and Q_o is the quality factor obtained in linear strain regime. These dependences (Eqs. 1.109 and 1.110) may be of higher order for different hysteretic stress-strain relations [75]. The parameters α_f and α_Q quantify the extent of hysteresis, and are presumed to have the same physical origins [76–78]. Such behavior was demonstrated to ensue from the bond and relative contact between grains [79]. These effects are regarded as fast dynamic effects [76] or amplitude dependent internal friction (ADIF) effects [80].

Along with hysteresis, NMEM exhibits a "creep-like" behavior upon dynamic excitation. It manifests in dynamic experiments as a progressive softening of the material towards a new equilibrium state while the material is under dynamic excitation (material conditioning). Once the excitation ceases, the material experiences a relaxation process whereby the material temporarily memorizes the attained strain amplitude, and progressively recovers the resonance frequency obtained at linear strain regime. Such a relaxation process may take hours and is referred as slow dynamics or SD [69].

SD based nondestructive testing monitors changes in the thermodynamic state of the material. This may be done, for example, by recording the change in the resonance frequency of the specimen for a specific resonance mode and change in its acoustic wave speed. The change in resonance frequency can be recorded by probing the specimen with a low amplitude acoustical wave before and after the disturbance.

A single frequency wave that monitors the frequency of a resonance mode can be used for SD experiment. Mechanical tapping or change in ambient temperature and pressure can disturb the thermodynamic equilibrium state. In the presence of damage the resonance frequency decreases. After several minutes or hours the resonance frequency returns to its equilibrium state. The return time depends on the type of material, severity of damage, and sensitivity of measurement. Since the return time is generally much longer than the time the specimen takes to stop its vibratory motion after the tapping it is known as the slow dynamics. SD can be used as a fast NDT technique. For example, the amplitude of a specific frequency (such as a resonance frequency) of the equilibrium state of the material is first measured and then after a disturbance like tapping it is again measured. A big change in that amplitude would indicate the presence of damage.

Slow dynamics is modeled in a phenomenological way by using rheological models [80–82]. However, although the nonlinear hysteresis and relaxation can be fairly well represented by rheological models, the underlying mechanisms may be

different in different materials [80]. Indeed, the physical origins of slow dynamics are still not very well understood [83].

On the other hand, there seems to exist a strain amplitude threshold, from which fast and slow dynamic effects are triggered [84]. Figure 1.30c illustrates the nonlinear regimes observed in resonance experiments on NMEM. At low strain amplitudes, say below 10^{-7}, the material exhibits nonlinear classical behavior. Beyond this threshold amplitude, hysteresis is activated which is accompanied by a slow dynamic recovery; that is non-equilibrium or non-classical regime. The recovery process is illustrated in Fig. 1.30d. After a resonance experiment driven at excitation amplitudes within the non-equilibrium regime, the recovery can be probed by monitoring the resonance frequency with time at low strain amplitude (linear regime). The strain threshold value is not a characteristic property of the material but it seems to depend on the stress rate [85]. Indeed, the size of the hysteresis loop depends on the strain rate excitation as revealed through dynamic acoustoelastic tests [86]. Therefore, the strain amplitude value from which hysteresis is activated depends on frequency.

Since the fast and slow dynamic effects appear to be related to the damage features such as micro-cracking, different resonance-based techniques have been developed to assess the mechanical integrity of various materials [77, 78]. The fast dynamic effect has been used to discern damage in polymer composites [77, 78], fatigued steel [72], and concrete [87]. The less sophisticated nonlinear resonance test using an impactor was used to qualitatively assess alkali–silica reaction [88], fire damage [89], and freezing–thawing damage [90, 91] in concrete-like materials. Fast and slow dynamic effects coexist during dynamic excitation [76], so that the measurement of the hysteretic parameters may be affected by slow dynamic effect. Such an effect can be minimized by increasing the time lapse between consecutive acquisitions.

Other resonance test configurations do not differ from the basic test configuration equipment, but they differ in the signal processing and testing protocols. Novak and colleagues [92] used a nonlinear convolution signal processing for identifying higher harmonics in damaged polymer composites. Interestingly, it was found that higher harmonics exhibit considerably larger shifts compared to the fundamental mode of vibration. These observations suggest a dispersive behavior of the nonlinear parameters as postulated by Gusev et al. [93]. On the other hand, Van Den Abeele et al. [94] used a pure tone burst excitation close to the resonance frequency of a plate-like sample. The resonance frequency tests were performed in a fully noncontact manner by using a loudspeaker as the emitter and a laser vibrometer as the sensor. The pure tone burst was generated at different amplitudes and the signal was analyzed during the ring down once the monochromatic excitation was switched off. The frequency and attenuation variations were observed during the ring down of the signal. It was found that both frequency shift and amplitude dependency investigated during the ring down differed from the observation of the amplitude dependent frequency and attenuation from consecutive experiments. Such a discrepancy is owed to the slow dynamic effect, which is present during the signal ring down.

Similar effects were observed by Eiras et al. [90, 91], Van Damme and Van Den Abeele [95], and Dahlen et al. [96].

1.7 Pump Wave and Probe Wave-Based Techniques

A number of nonlinear techniques require exciting the specimen simultaneously at two different frequencies—a pump frequency and a probe frequency. Different variations of these techniques are discussed in this section.

1.7.1 Nonlinear Wave Modulation Spectroscopy (NWMS)

Nonlinear wave modulation spectroscopy (NWMS) is a widely used technique and was conceptually introduced in the 1960s. The technique utilizes a continuous high-frequency probe wave (at frequency f_{probe}), and a low-frequency vibration or pump wave (at frequency f_{pump}). The pump wave is generally a given resonance mode of the tested sample. The pump vibration aims to induce stresses within the sample, while the probe wave senses the variation of modulus produced by the pump vibration. If the material under inspection behaves linearly, the frequency of the probe wave does not depend on the stresses induced by the pump wave excitation. However, in a nonlinear material the frequency of the probe wave is modulated by the pump wave excitation. The interaction of both waves—with frequencies f_{probe} and f_{pump}—manifests as sideband components in the frequency spectra of the received signal. This process is commonly illustrated through the nonlinear behavior ensued by the existence of a crack in a sample [97]; the probe wave propagates through the crack surfaces, while the pump vibration makes the contact area between the crack surfaces to increase in compression and decrease in tension. By this process, amplitude and phase of the received wave are modulated, according to the frequency of the pump vibration. The frequency domain plots of the received signal exhibit higher harmonics and modulated frequencies. This process is schematically shown in Fig. 1.31. Indeed, vibro-acoustic modulation techniques were formerly conceived to detect localized defects such as cracks in structural parts [98, 99].

As in nonlinear resonance and finite-amplitude techniques, the scaling relations between strain amplitude corresponding to every harmonic are affected by the type of nonlinearity: classical or non-classical hysteretic [66, 67]. In the case of quadratic nonlinearity, first-order sidebands $f_{\text{probe}} \pm f_{\text{pump}}$ are produced, with amplitude proportional to $\beta * A_{\text{pump}} * A_{\text{probe}}$. In the case of cubic nonlinearity, second-order sidebands $f_{\text{probe}} \pm 2 * f_{\text{pump}}$ are produced, with amplitude proportional to $C_{\beta\delta} * (A_{\text{probe}})^2$, where $C_{\beta\delta}$ is related to β and δ. In case of non-classical hysteretic behavior, second-order sidebands $f_{\text{probe}} \pm 2 * f_{\text{pump}}$ are proportional to $\alpha \cdot A_{\text{probe}} \cdot A_{\text{pump}}$ where α is the hysteretic parameter. In case of localized defects such as cracks, the modulation

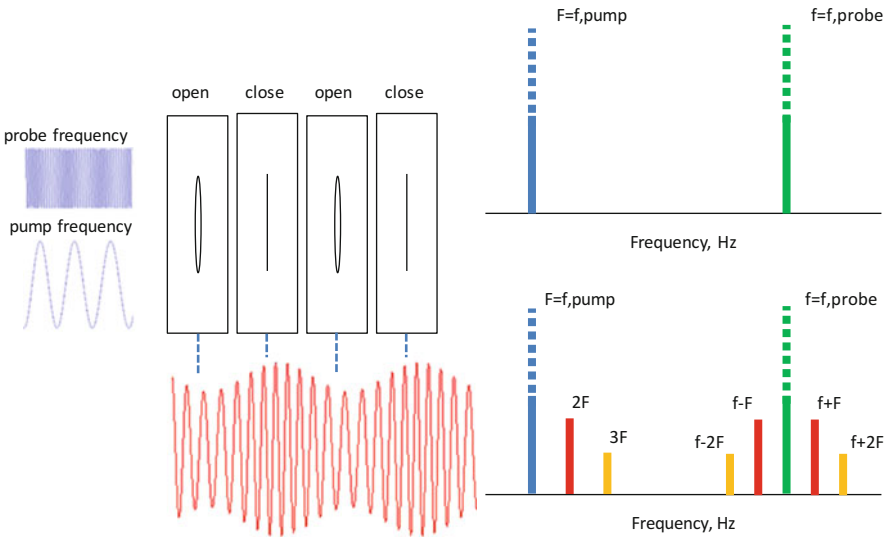

Fig. 1.31 Left figure: Schematic representation of the acoustic modulation process, Right figure: resulted spectra for an undamaged sample (top right) and for a cracked sample (bottom right). Adapted from [31]

arises from the nonlinear stiffness that ensues from the interfacial contact. In this case the behavior can be even chaotic [100].

Compared to the higher harmonic generation technique the modulation technique offers some advantages [101]. First, higher harmonic generation requires a homogeneous travelling path to take advantage of the cumulative effect; thus, this is difficult to fulfill in the presence of reflecting boundaries and other structural inhomogeneities. Second, high voltages are needed which frequently add some nonlinear background signal, which may affect the sensitivity of the technique.

1.7.1.1 Mathematical Proof of the Side Band Generation

How are these modulated frequencies and sidebands generated by the nonlinear material? This question can be answered from the following simple mathematical analysis.

The displacement field for a harmonic wave generated by the pumping frequency f_1 can be expressed as

$$u_1(\mathbf{x}, \mathrm{t}) = A_1(\mathbf{x}) \sin(\omega_1 t) + B_1(\mathbf{x}) \cos(\omega_1 t) \tag{1.111}$$

where $\omega_1 = 2\pi f_1$. Similarly, the displacement field in the material for the probing wave of frequency f_2 is given by

$$u_2(\mathbf{x}, t) = A_2(\mathbf{x}) \sin(\omega_2 t) + B_2(\mathbf{x}) \cos(\omega_2 t) \tag{1.112}$$

Therefore, the total displacement field is

$$\begin{aligned} u(\mathbf{x}, t) = & u_1(\mathbf{x}, t) + u_2(\mathbf{x}, t) = A_1(\mathbf{x}) \sin(\omega_1 t) + B_1(\mathbf{x}) \cos(\omega_1 t) \\ & + A_2(\mathbf{x}) \sin(\omega_2 t) + B_2(\mathbf{x}) \cos(\omega_2 t) \end{aligned} \tag{1.113}$$

The strain field for one-dimensional problem is given by,

$$\begin{aligned} \varepsilon(\mathbf{x}, t) = \frac{\partial u(\mathbf{x}, t)}{\partial x} = & A_1'(\mathbf{x}) \sin(\omega_1 t) + B_1'(\mathbf{x}) \cos(\omega_1 t) \\ & + A_2'(\mathbf{x}) \sin(\omega_2 t) + B_2'(\mathbf{x}) \cos(\omega_2 t) \end{aligned} \tag{1.114}$$

where $A_1'(\mathbf{x})$ denotes derivative of $A_1(\mathbf{x})$. For classical nonlinear quadratic stress – strain relation

$$\sigma(\mathbf{x}, t) = E\varepsilon(\mathbf{x}, t) = [E_0 + E_1(\varepsilon)]\varepsilon(\mathbf{x}, t) = E_0\varepsilon(\mathbf{x}, t) + E_1 \varepsilon^2(\mathbf{x}, t) \tag{1.115}$$

Then the total harmonic stress field can be expressed as,

$$\begin{aligned} \sigma(\mathbf{x}, t) &= E_0\varepsilon(\mathbf{x}, t) + E_1 \varepsilon^2(\mathbf{x}, t) \\ &= E_0 \left[A_1'(\mathbf{x}) \sin(\omega_1 t) + B_1'(\mathbf{x}) \cos(\omega_1 t) + A_2'(\mathbf{x}) \sin(\omega_2 t) \right. \\ &\quad \left. + B_2'(\mathbf{x}) \cos(\omega_2 t)\right] + E_1 \left[M_1 \sin^2(\omega_1 t) + M_2 \cos^2(\omega_1 t) + M_3 \sin^2(\omega_2 t) \right. \\ &\quad + M_4 \cos^2(\omega_2 t) + M_5 \sin(\omega_1 t) \cos(\omega_1 t) + M_6 \sin(\omega_1 t) \sin(\omega_2 t) \\ &\quad + M_7 \sin(\omega_1 t) \cos(\omega_2 t) + M_8 \sin(\omega_2 t) \cos(\omega_1 t) \\ &\quad \left. + M_9 \cos(\omega_1 t) \cos(\omega_2 t) + M_{10} \sin(\omega_2 t) \cos(\omega_2 t)\right] \end{aligned} \tag{1.116}$$

Or,

$$\begin{aligned} \sigma(\mathbf{x}, t) = & E_0 \left[A_1'(\mathbf{x}) \sin(\omega_1 t) + B_1'(\mathbf{x}) \cos(\omega_1 t) + A_2'(\mathbf{x}) \sin(\omega_2 t) \right. \\ & \left. + B_2'(\mathbf{x}) \cos(\omega_2 t)\right] + E_1 [N_1 \cos(2\omega_1 t) + N_2 \cos(2\omega_2 t)(\omega_1 t) \\ & + N_3 \cos(\omega_1 + \omega_2) t + N_4 \cos(\omega_1 - \omega_2) t + N_5 \sin(2\omega_1 t) \\ & + N_6 \sin(2\omega_2 t)(\omega_1 t) + N_7 \sin(\omega_1 + \omega_2) t + N_8 \sin(\omega_1 - \omega_2) t] \end{aligned} \tag{1.117}$$

In the above equations multiplying factors $M_1, M_2, M_3, \ldots N_1, N_2, N_3, \ldots$ for different trigonometric terms are functions of $A_1{}'(\mathbf{x})$, $B_1{}'(\mathbf{x})$, $A_2{}'(\mathbf{x})$, *and* $B_2{}'(\mathbf{x})$. For example,

$$M_1 = \left[A_1{}'(\mathbf{x})\right]^2 \tag{1.118}$$

$$M_2 = \left[B_1{}'(\mathbf{x})\right]^2 \tag{1.119}$$

$$M_5 = 2A_1{}'(\mathbf{x})\, B_1{}'(\mathbf{x}) \tag{1.120}$$

$$M_7 = 2A_1{}'(\mathbf{x})\, B_2{}'(\mathbf{x}) \tag{1.121}$$

In Eq. (1.117) one can clearly see that the linear term which is multiplied by E_0 only produces waves of angular frequency ω_1 and ω_2 while the nonlinear term generates waves with frequencies $2\omega_1$ and $2\omega_2$ (higher harmonic waves) as well as $\omega_1 \pm \omega_2$ (modulated waves). If cubic terms are also kept in the stress–strain relation, then one can show in the same manner that waves with frequencies $3\omega_1$, $3\omega_2$, $\omega_1 \pm 2\omega_2$, and $2\omega_1 \pm \omega_2$ are also generated, thus producing more higher harmonics and sidebands.

1.7.1.2 Experimental Configuration

Two most popular test configurations that are frequently discussed in the literature are shown in Fig. 1.32. These two testing techniques are referred as vibro-acoustic modulation and impact induced modulation techniques. The former consists of a continuous harmonic excitation with a weak probing frequency while the resonant vibration is produced by an electromagnetic shaker. The technique requires careful coupling between the shaker rig and the sample, otherwise additional contact nonlinearities may arise [102]. On the other hand, impact modulation techniques use a shock vibration to excite the resonance modes. One major advantage of the impact modulation technique is the absence of nonlinear contacts for the source of excitation. However, its drawback is that it is impossible to have the same impact force for all experiments [102, 103]. In general the impact induced modulation shows improved sensitivity compared to the vibro-acoustic modulation technique [104, 105].

The damage severity is generally evaluated through damage parameters that relate the intensity of the spectral sideband with respect to the amplitude of the probing wave. Donskoy et al. [106] proposed a modulation index (MI) as

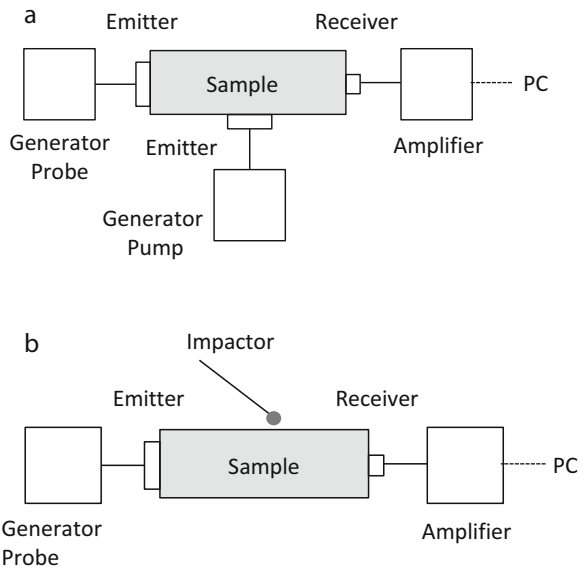

Fig. 1.32 Schematic of nonlinear wave modulation spectroscopy experiments—(**a**) vibro-acoustic modulation, (**b**) impact induced modulation

$$\mathrm{MI} = \sum_{m=1}^{M} \frac{A_{m\pm n}}{A_m \cdot A_n}, \tag{1.122}$$

where $A_{m\pm n}$ are the spectral magnitudes at the sideband frequencies $f_{m\pm n}$, A_m is the spectral magnitude at the probe frequency, and A_n is the spectral magnitude at the pump frequency. Distributed damages do not always produce clear sidebands to measure their amplitudes. An alternative modulation index from the energy of the sideband spectrum ($E_{m\pm n}$), pump signal (E_n), and probe signal (E_m) has also been defined for better accuracy [66, 67].

$$\mathrm{MI} = \frac{E_{m\pm n}}{E_m E_n} \tag{1.123}$$

1.7.2 Dynamic Acoustoelastic Test (DAET)

The dynamic acoustoelastic test (DAET) consists of monitoring the variations of modulus while the inspected sample is subjected to dynamic loading conditions. Nagy et al. [60] used DAET to evaluate the adhesive joints in composite materials under superimposed dynamic shear stress loading. The test configuration and signal analysis conducted therein allowed relating the average variations of wave velocity to the attained shear stress produced upon dynamic loading. Therefore, the analysis

was based on "classical" higher-order expansion of wave velocity as a function of stress (see Eq. 1.104).

Unlike the approach presented by Nagy et al. [60], Renaud et al. [107] presented a test configuration that allowed extracting the variations of modulus across different stress levels imparted during dynamic loading. In this case, the test allowed not only the description of higher-order terms, but also hysteresis and relaxation of elastic and attenuation properties [108]. Figure 1.33a shows a schematic representation of a basic DAET configuration. Normally, the test consists of a long low-frequency burst that matches a fundamental resonance mode (pump wave), while repeated ultrasonic pulses (probe wave) sense the variation of modulus across different strain values of the pump excitation. The received ultrasonic pulses are modulated in phase and amplitude, as in vibro-acoustic modulation discussed in the previous section. However, the analysis is focused on the instantaneous variations of modulus and attenuation properties, rather than on sideband spectral components, which may arise from the same physical effects. Figure 1.33b shows typical recorded signals in a DAET experiment.

Considering that the variations of the wave speed (Δc) with respect to the wave speed in the linear elastic range (c_0) are very small one can state that $c \approx c_0$—and hence, $c^2 - c_0^2 \approx 2c_0\,(c - c_0)$, the corresponding relative variations of time of flight ($\Delta t/t_o$) can be approximately related to the material nonlinearity as

$$\frac{\Delta M}{M_o} - 2 \cdot \frac{\Delta t}{t_o} \approx C_E\,(\Delta\varepsilon) + \beta\varepsilon + \delta\varepsilon^2 + \cdots + H_E\,(\varepsilon, \dot{\varepsilon}) \tag{1.124}$$

where, in addition to the quadratic and cubic nonlinear classical parameters (β and δ), the ad hoc function $C_E(\Delta\varepsilon)$ is introduced to describe the material conditioning effect: the offset between the relative variation of modulus and the strain. In addition, during low-frequency burst excitations the material attenuation variations can be obtained from the ultrasonic pulse amplitudes as

$$\Delta\xi \approx -\ln\left(1 + \frac{\Delta A}{A_o}\right) \Big/ d \approx C_D\,(\Delta\varepsilon) + \beta_D\varepsilon + \delta_D\varepsilon^2 + \cdots + H_D\,(\varepsilon, \dot{\varepsilon}) \tag{1.125}$$

Similarly, the same terms can be defined for the variation of the attenuation properties, which are denoted herein with subscript D. These tests allowed revealing also dispersive behavior of the nonlinear mechanisms.

Dynamic acoustoelastic experiments have been successfully used for the assessment of trabecular bone [107], rocks [109], and fatigued metallic samples [110], under controlled laboratory conditions. The test configurations for such studies are not very convenient for field applications. Yet some field application attempts have been made. Renaud et al. [111] performed in situ DAET to measure the elastic properties of soil. The tests were performed by using a thumper truck as pump wave source, and a buried system consisting of high-frequency generation and sensing. In other instances, the ultrasonic pulses were modulated by using a

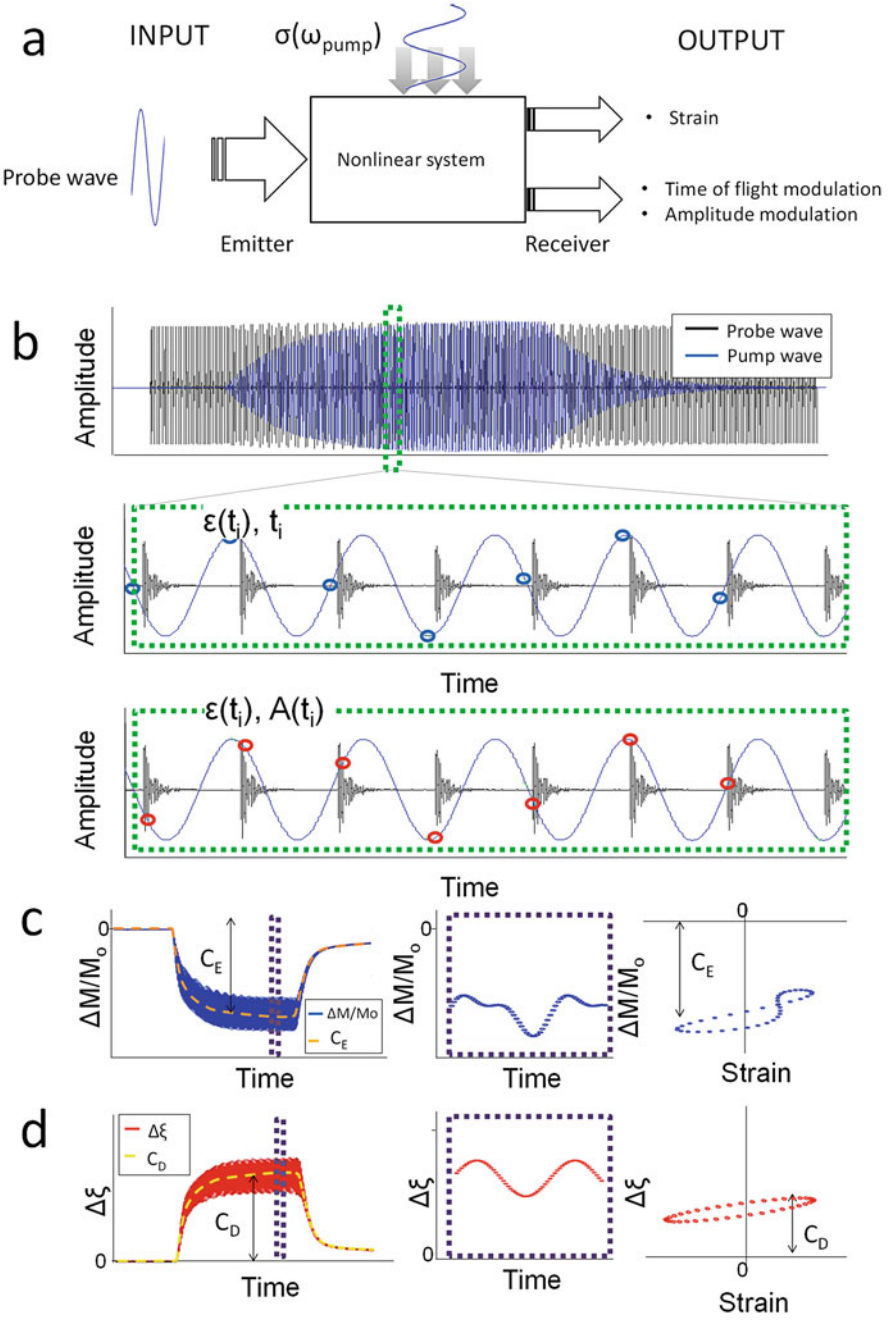

Fig. 1.33 (**a**) Schematic diagram representing a dynamic acoustoelastic test, (**b**) typical recorded signals in a DAET experiment, (**c**) resulted variation of modulus, and (**d**) attenuation properties, after processing the received signals

shock load. Such an approach aims on field monitoring of concrete structures by using a hammer blow [112], or passive structural health monitoring applications, for instance, by using traffic loads on bridges [113, 114]. The signal analysis conducted in such studies is based on the simultaneous comparison between a number of time segments of the received ultrasonic pulses, before and after shock wave perturbation, through the cross-correlation technique. The summation of the time shift obtained in every time segment is used as a quantification of the material nonlinearity. The approaches proposed in Bui et al. [112] and Moradi-Marani et al. [114] do not allow description of the strain dependent nonlinear elastic and dissipative characteristics, but a quantification of the material nonlinearity as a sole parameter. Moreover, such studies pointed out that the major contribution to the cumulative time shift primarily comes from the late coda wave segments [112, 114]. These results further confirm the sensitivity of the coda wave to detect induced subtle microstructural changes [63]. Indeed, the analyses of the coda wave have been leveraged to diagnose the material nonlinearity after a pump wave excitation. This approach is described in the following subsection on *Pump wave after-effect monitoring through coda wave interferometry*.

1.7.3 Pump Wave After-Effect Monitoring Through Coda Wave Interferometry

Coda wave refers to the tail of an ultrasonic signal that has gone through multiple scattering within the internal microstructure of the material. Therefore, the coda wave travels longer paths and is capable of detecting small changes in the microstructure. The analysis is normally performed through the cross-correlation function between a reference and a stressed waveform. From this analysis the relative variations of velocity produced in the heterogeneous material as a result of loading or temperature changes can be obtained. Coda wave interferometry technique has been used to monitor the variations of velocity produced after a pump excitation. Tremblay et al. [115] monitored the modulus recovery after an impact by analyzing consecutive ultrasonic pulses after dropping a ball in a concrete sample. Such a test configuration was used to assess mechanical and thermally damaged concrete [116]. Hilloulin et al. [117] used coda wave interferometry to discern the material nonlinearity as produced by a localized crack in concrete samples. In this case, the pump wave was provided by a short low-frequency sweep over a range of frequencies.

1.8 Subharmonic Phased Array for Crack Evaluation (SPACE)

To enhance the selectivity in nonlinear ultrasonic response induced by micro-cracks, recently, some researchers developed the nonlinear ultrasonic phased array technique. It combines the sensitivity of nonlinear ultrasonics and high power input of phased array technique. SPACE or the subharmonic phased array for crack evaluation was proposed by Ohara et al. [118] for closed-crack imaging. They used phased array subharmonic generation by short burst and frequency filtering.

Figure 1.34 shows a typical experimental setup for SPACE. An intense ultrasonic field was generated by a $LiNbO_3$ single-crystal transmitter with a wedge. The received signals were measured by a phased array sensor system, thus focusing on reception. As the high energy ultrasonic wave propagates through the specimen with defects, the interactions between ultrasonic waves and closed cracks cause clapping effect, thus the subharmonic waves are generated. The scattered waves were digitally filtered at fundamental and subharmonic frequencies, after those waves were received by the sensor array and converted to digital signals. The recorded signals were added after their phase shift following the delay law. The intensity at a focal point was obtained by calculating the root-mean-square value corresponding to that point. The image of a scan area was created by repeating the process described above over that area with incremental steps. The open and

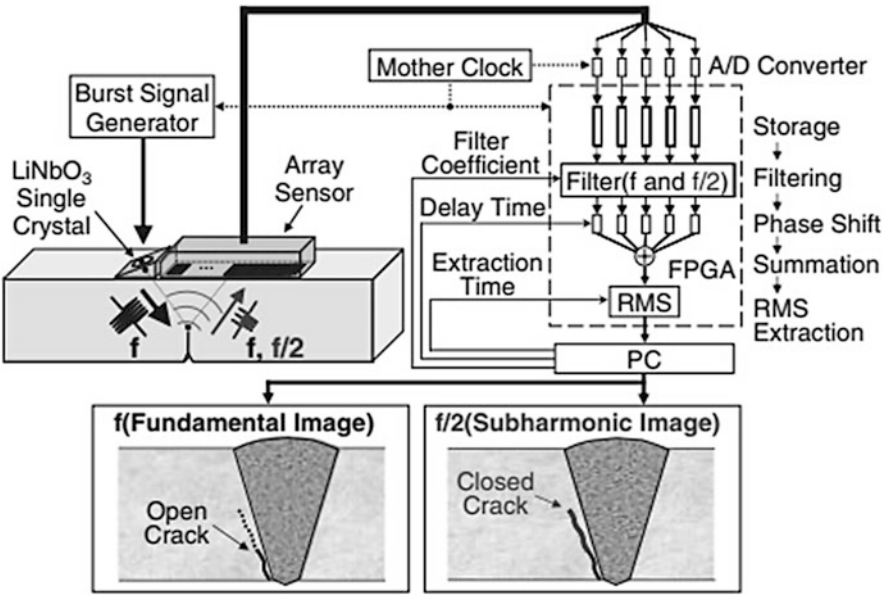

Fig. 1.34 Experimental configuration of SPACE (from [118])

closed parts of the cracks can be distinguished by comparing the fundamental and subharmonic wave generated images.

Researchers used the SPACE technique to evaluate the closed fatigue cracks and stress corrosion cracks. The measurement accuracy of SPACE for such micro-cracks is yet to be determined. It has been demonstrated that SPACE is very useful for correcting the underestimation of crack depths.

1.9 Collinear and Non–Collinear Wave Mixing Techniques

The major difficulty with the popular nonlinear NDT techniques based on higher harmonic generation lies in isolating the causes of nonlinearity. Specifically, amplifiers, transducers, and coupling mechanisms all can contribute to the generation of higher harmonic signals; their contributions can be even greater than that of the material nonlinearity. Determining whether the measured nonlinearity is caused by the instrument or the material is a difficult task. Wave mixing technique can overcome some of these difficulties as described below.

1.9.1 Collinear Wave Mixing Technique

Researchers used collinear wave mixing technique to evaluate the material nonlinearity in various solids. Two plane waves propagating collinearly in opposite directions in a nonlinear elastic medium generate a new wave. The resonance wave that is generated by mixing two bulk waves is studied and used to evaluate the material nonlinearity. The schematic of the nonlinear collinear beam-mixing measurement setup is shown in Fig. 1.35 [119].

Figure 1.35 shows two source waves propagating through the material to intersect and interact with each other in a comparatively large region or zone. The new shear wave generated from this interaction is received by the shear wave transducer and digitized. The digitized time-domain signal is then sent to the computer for post processing. In this experiment a broadband piezoelectric (PZT) shear wave transducer with a center frequency of 5 MHz was used as both transmitter and receiver. Another broadband PZT longitudinal transducer with a center frequency of 10 MHz was used to generate the longitudinal wave. Excitation signals for both input transducers were 30-cycles tone bursts at 500 Volts. Measurements were made at fixed shear wave frequency and variable longitudinal wave frequency to generate both resonance and non-resonance conditions, and to obtain the bandwidth of the generated resonance. To isolate the wave generated from the interaction of two primary incident waves, time-domain signals of the two primary waves generated separately were recorded and subtracted from the total signal. The total signal was recorded by the shear wave transducer when both transducers were exciting

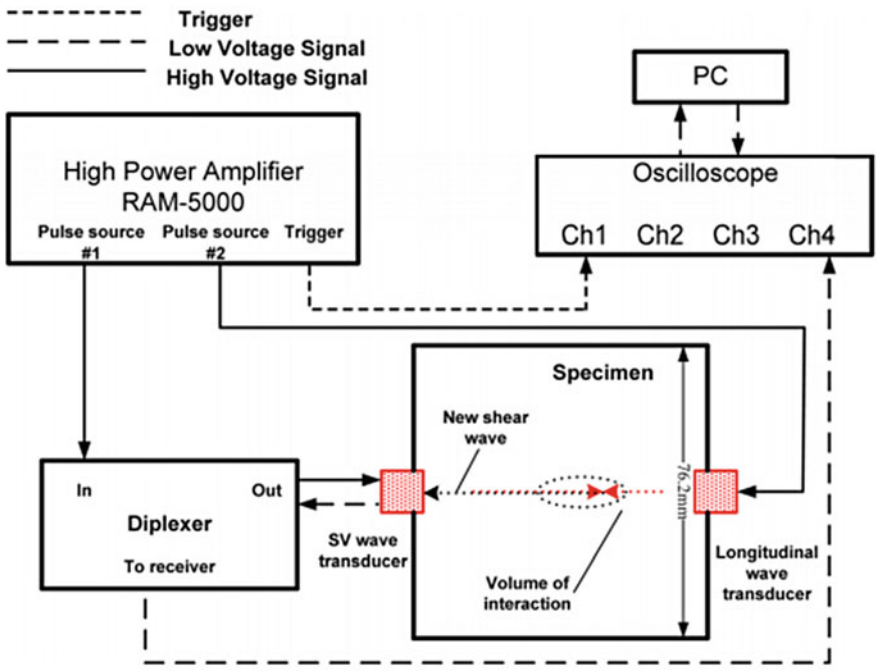

Fig. 1.35 Experimental setup for collinear wave mixing technique (from [119])

the specimen simultaneously. The resulting signal was then transformed into the frequency domain by the fast Fourier transform.

The collinear wave mixing method has the potential to measure the acoustic nonlinearity parameter without many of the experimental difficulties inherent in some of the existing second harmonic methods. Chief among them is the ability to select the resonance frequency that does not coincide with those associated with typical measurement systems. Thus, the collinear mixing technique shows higher sensitivity in measuring the acoustic nonlinearity parameter.

1.9.2 Non-Collinear Wave Mixing Technique

Non-collinear wave mixing technique has been used for the evaluation of plasticity, fatigue, and aging of PVC. Figure 1.36 shows an experimental arrangement for non-collinear wave mixing [120, 121]. Longitudinal wave transducers of frequency 5 MHz mounted on 60° Perspex wedges were used to generate two shear waves. These two intersecting shear waves generate a third longitudinal wave due to nonlinear interaction of the two waves. Once generated, this wave propagates through the material in a conventional manner and is detected by the receiver.

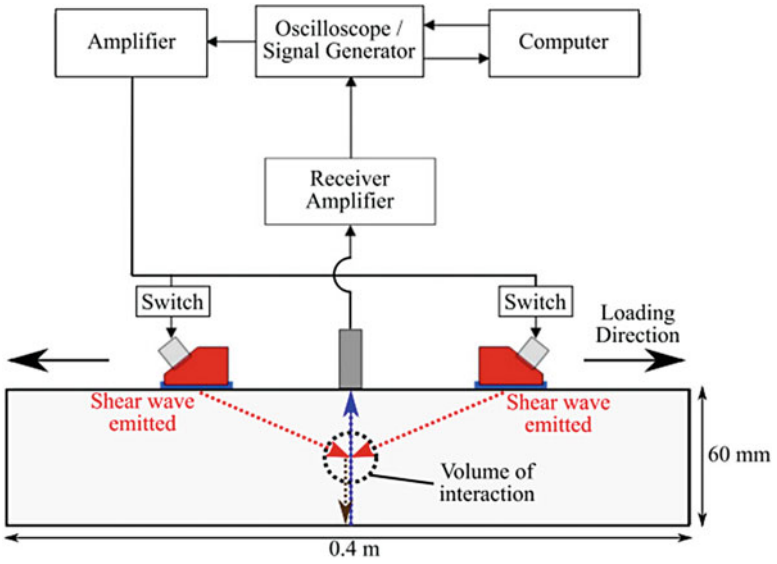

Fig. 1.36 Experimental setup for non-collinear wave mixing technique [120]

There are several advantages of the non-collinear wave mixing technique when compared with the conventional nonlinear ultrasonic harmonic generation technique. First, non-collinear wave mixing technique can limit the region where nonlinear interaction of the incident beams occurs. It is only the interaction region of the two beams. This capability of spatial selectivity makes this technique less sensitive to system nonlinearities. Another advantage of non-collinear wave mixing technique is modal selectivity which means the generated signal can be a different wave mode from the incident wave modes. The third advantage is the frequency selectivity, meaning frequency of the generated signal can be different from that of the incident ones or their higher harmonics when the frequencies of the two driving signals are not the same. The fourth advantage is the directional selectivity—meaning propagation direction of the generated signal can be different from the incident signals. The non-collinear wave mixing technique can isolate the nonlinear response of the material from the nonlinearities of the measuring instruments. Such separation is necessary for materials with weak nonlinearity.

1.10 Recent Advances of Wave Modulation Techniques

Higher harmonic generation and nonlinear wave modulation spectroscopy are probably two most popular nonlinear ultrasonic techniques. Section 9 discusses some of the limitations of the higher harmonic generation technique and how to overcome those limitations by collinear and non-collinear wave mixing techniques.

Wave modulation techniques are also difficult to use for monitoring plate type structures. This section discusses some new developments to overcome those limitations. Experimental evidence is provided to show the advantages of these new techniques.

1.10.1 Finding Optimal Combinations of Probing and Pumping Frequencies

Figure 1.13 shows phase velocity and group velocity dispersion curves for Lamb wave propagation in a plate. For generating sidebands and higher harmonics the frequency, phase velocity, and group velocity of the input waves should be such that there exist other wave modes of desired frequencies. Frequencies of these other modes should match with the expected sideband frequencies (for sideband generation) or that of the higher harmonic (for higher harmonic generation). The other wave preferably should have the same phase and group velocities as those of the input wave modes. Then without knowing the material properties of the plate how can one select the input excitations? Since all excitation frequencies cannot satisfy the conditions required for generating sidebands in a plate the question remains how to select the probing and pumping frequencies for NWMS experiments when the material properties of the plate are unknown. In other words, what combination of these two frequencies should be most sensitive to material nonlinearity?

Yoder and Adams [122] kept the pumping signal fixed and swept the probing signal to find the right combinations of these two signal frequencies to maximize the modulation level. Their results are shown in Fig. 1.37. Then Sohn et al. [123] created the sideband spectrogram by sweeping both pumping and probing signals over specified frequency ranges to study the effectiveness of pumping and probing waves in sensing material nonlinearity at different frequencies. Figure 1.38 shows their results.

Another shortcoming of NWMS for plate inspection is that for optimal generation of sidebands the pumping and probing frequencies need to be precisely controlled. Therefore, they must be generated by narrow band surface-mounted PZT ultrasonic transducers, accelerometers, piezoelectric stack actuators, or mechanical shakers in direct contact with the specimen, to excite the target structure and get the response (see Fig. 1.39) [123–126]. Noncontact excitation and detection arrangement as shown in Fig. 1.40 does not have restriction of requiring narrowband excitation. This figure shows laser beam induced acoustic excitation and detection of the propagating Lamb wave by a laser vibrometer. A new technique called sideband peak count (SPC) has been recently developed that does not require narrow band excitation and is ideal for noncontact monitoring of structures. This technique is described in the following section.

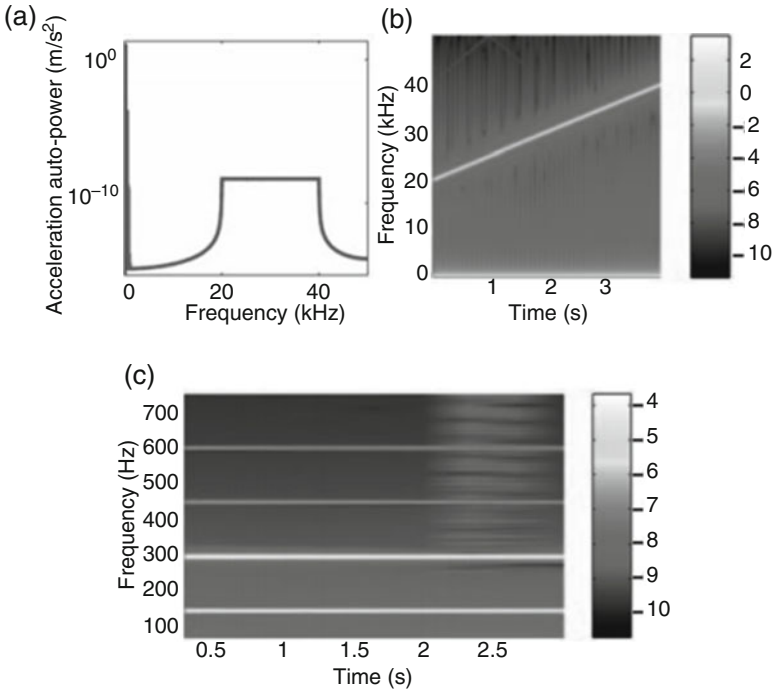

Fig. 1.37 The response of a nonlinear system for 150 Hz pumping signal and probing signal sweeping from 20 to 40 kHz, plotted in (**a**) frequency and (**b**) time–frequency domains. (**c**) The spectrogram obtained from the Hilbert envelope shows amplitude modulation [122]

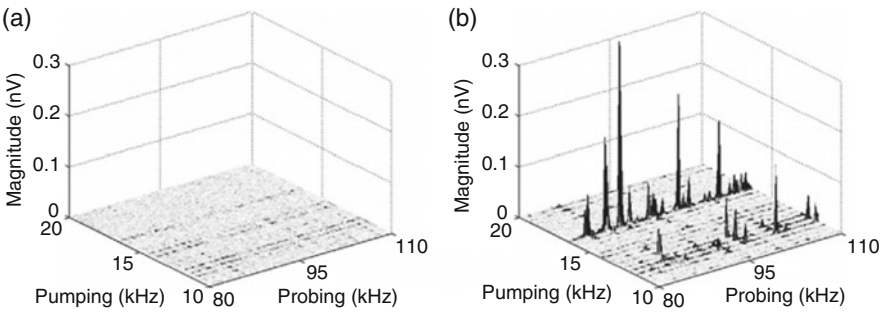

Fig. 1.38 The sideband spectrogram obtained by sweeping both the pumping frequency (from 10 to 20 kHz with a 500 Hz increment) and the probing frequency (from 80 to 110 kHz) for (**a**) intact and (**b**) damaged dog bone specimens (after [123])

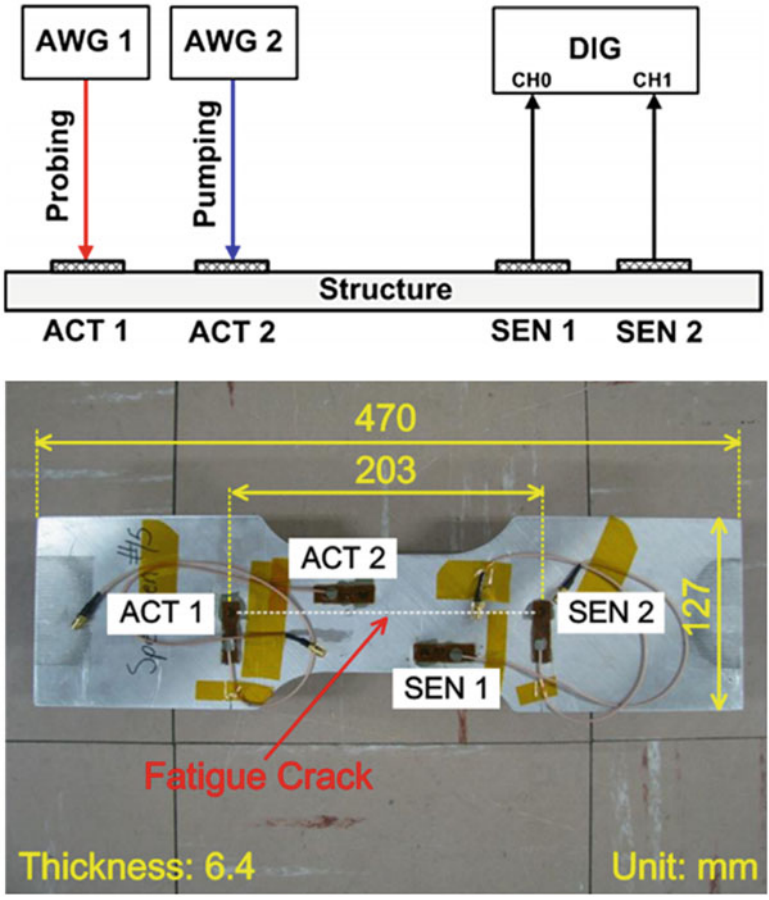

Fig. 1.39 Contact-type experimental setup using surface-mounted PZTs [123]

1.10.2 Sideband Peak Count (SPC) Technique

Instead of generating sidebands by nonlinear interaction between a pump wave and a probe wave, in SPC technique interaction between different Lamb wave modes is monitored. If the Lamb wave is generated by a broadband excitation (such as a laser beam striking a plate), then multiple Lamb modes are generated in the plate over a wide frequency range. If the plate material is nonlinear, then the interaction between these various Lamb modes can generate multiple sidebands. Instead of measuring the amplitudes of these sidebands, in SPC technique the number of peaks of the sidebands above a threshold value is counted. The SPC technique was first introduced in Eiras et al. [127]. In a plate with unknown material properties since it is not known a priori which Lamb mode peaks appear at what frequencies the only way to distinguish between sidebands and main Lamb modes is to examine their

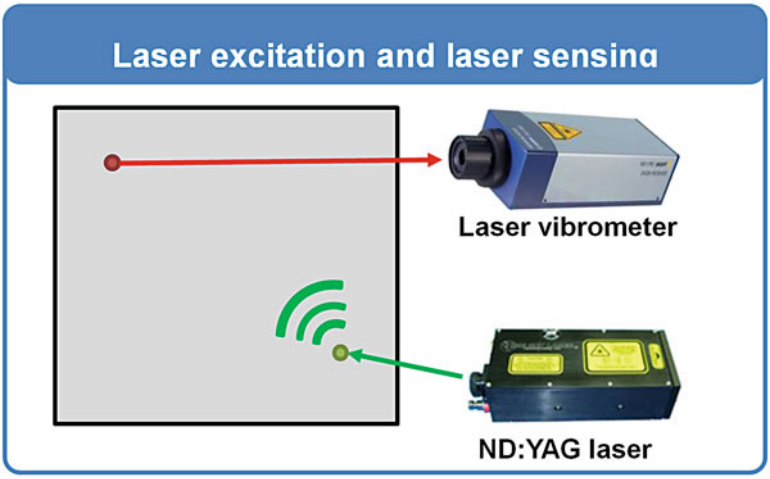

Fig. 1.40 Noncontact excitation and sensing arrangement for plate inspection

amplitudes. Generally sideband amplitudes are much smaller than the Lamb mode amplitudes.

The SPC technique is illustrated in Fig. 1.41. If waves of multiple frequency pass through a linear material, then their frequency values do not change. The top left spectral plot of Fig. 1.41 shows multiple peaks that can represent multiple Lamb modes propagating in a plate or multiple body waves of different frequency passing through a bulk material. On the receiving side for a linear material peaks appear at the same frequencies. However, peak amplitudes generally vary on the sending and receiving sides due to material attenuation and scattering. In a nonlinear material interactions between these waves of different frequency produce additional peaks due to frequency modulation effect as shown in the top-right spectral plot of Fig. 1.41. These minor peaks generated due to frequency modulation effect are generally much smaller than the highest peak value, typically less than 10%, and often even less than 1%. Therefore, all peaks in these spectral plots above the dotted line can be considered as main peaks and below this line are the modulated peaks or sideband peaks. If a threshold line is moved from 0 to 20% (or 10%) of the highest peak value and all peaks that are above this threshold line but below the 20% (or 10%) line are counted and plotted against the moving threshold value, then that graph is called SPC plot. The SPC plot is sensitive to the degree of material nonlinearity; higher value of SPC is obtained for a nonlinear material compared to a linear material. Hafezi et al. [128] have shown theoretically using peri-ultrasound modeling technique based on peridynamics principle that SPC plot for a structure containing a thin crack is much greater than that containing a thick crack or no crack when elastic waves propagate through the structure, as shown in the bottom plot of Fig. 1.41. This result is expected because thin crack surfaces come in contact more often causing nonlinearity in the material as the elastic wave passes through it. For

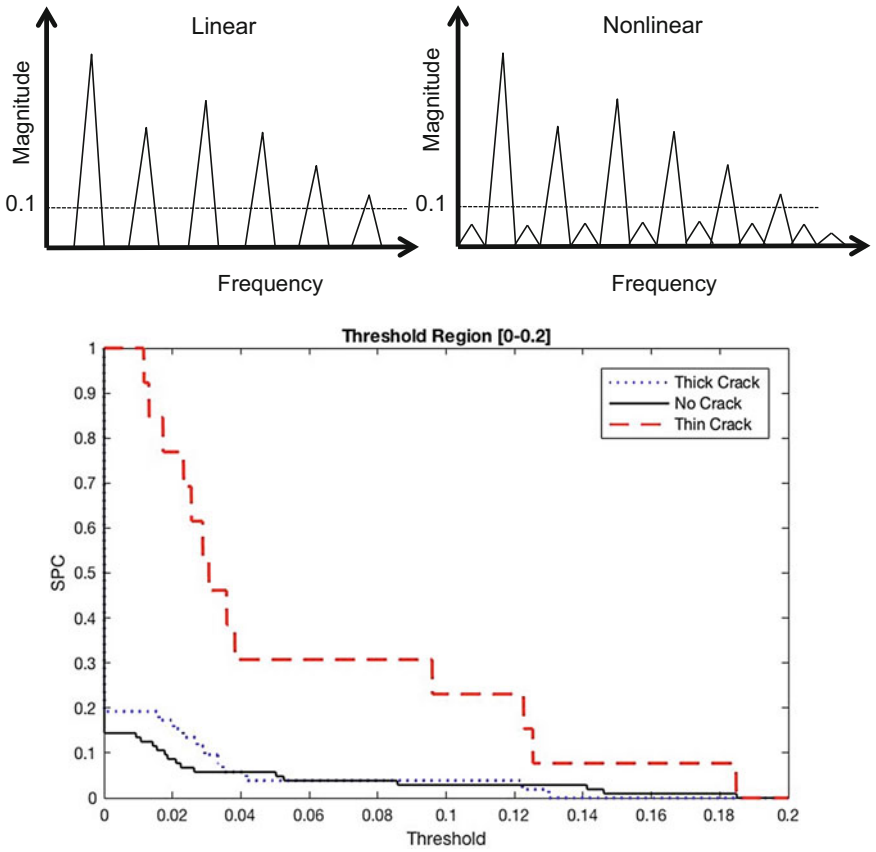

Fig. 1.41 Illustration of sideband peak count (SPC) technique (From [128])

a thick crack maybe only the region near the crack tip can come in contact and contribute to nonlinearity as the wave passes through and a linear elastic material having no crack shows no nonlinearity. Thus the correlation between the material nonlinearity and SPC has been demonstrated both theoretically by Hafezi et al. [128] and experimentally by Eiras et al. [127] and Liu et al. [129, 130].

The SPC technique has been successfully used to detect material nonlinearity variation in glass–fiber reinforced cement (GRC), cement composites subjected to accelerated aging process [127], and in aluminum plates and aircraft fitting-lugs with complex geometries containing fatigue cracks [129, 130].

For noncontact monitoring of the degree of nonlinearity in the plate material, ultrasonic waves were generated by shooting a pulse laser beam on the target surface, and a laser Doppler vibrometer (LDV) was used to measure the corresponding ultrasonic responses [129, 130]. This complete noncontact system setup allows this technique to scan a large inspection area with high spatial resolution.

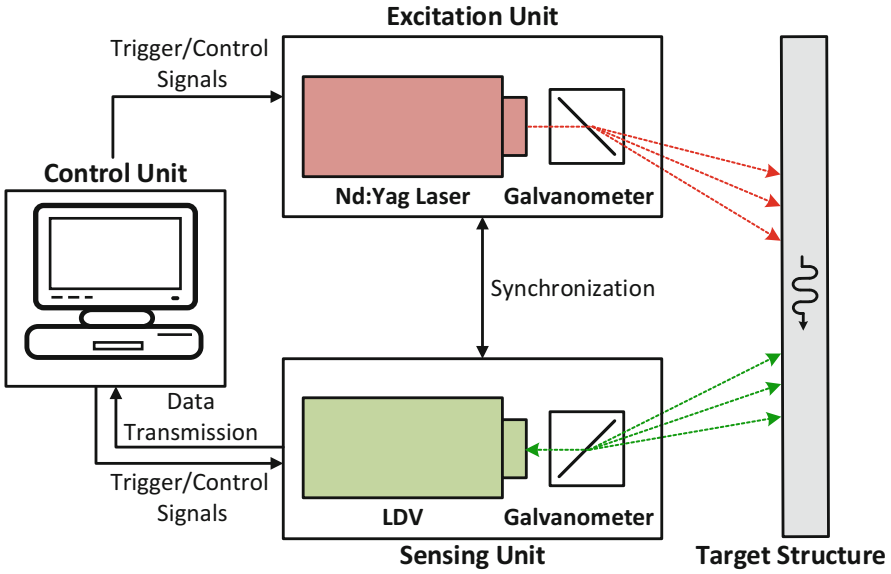

Fig. 1.42 Schematic diagram of the noncontact laser ultrasonic system

The use of contact transducers for structural monitoring has several shortcomings: (1) high spatial resolution is difficult to achieve for small incipient defect detection due to the installation issue of contact transducers, (2) imperfect contact interface between the transducers and the sample surface can introduce additional nonlinearity that can hide the material nonlinearity that we are interested in, (3) it is quite labor-intensive and expensive to install a large number of transducers, (4) transducers and cables are vulnerable to damage in harsh environments, potentially degrading the system reliability and increasing the maintenance cost, and (5) contact transducers attached on the target structure may alter its dynamic characteristics in certain situations [131].

To overcome these shortcomings, noncontact laser technique has been introduced as an alternative technique. Ultrasonic excitation has been successfully generated using noncontact pulse lasers [131, 132] and continuous lasers [133]. Ultrasonic sensing has been performed using laser interferometry [134]. The collected responses are processed to detect various types of defects in metal and composite structures [134, 135].

The noncontact system is composed of an excitation unit, a sensing unit, and a control unit, as shown in Fig. 1.42. When the material surface is illuminated by a pulse laser beam, a localized heating will cause thermal expansion and generate ultrasonic waves in the material [136]. To avoid laser caused surface damage (e.g., ablation), parameters for the pulse laser excitation should be carefully monitored for the laser peak power, pulse duration, and laser beam size.

It should be noted that the nonlinear ultrasonic modulation does not always occur even when the material shows some nonlinear behavior due to crack existing in the structure. It occurs only if several binding conditions are satisfied, which can be briefly summarized as [104, 122, 136]: (1) Crack perturbation condition: The strain (displacement) at the crack location should be oscillated by both of the two input excitations. In vibrations, this condition can be interpreted as nonlinear modulation components are not generated when the crack is located at the nodes of the vibration modes; (2) Mode matching condition: One of the inputs should be modulated at the crack location by the crack motion induced by the other input. Hence, the modulation generation significantly relies on the choice of two input frequencies and can be easily altered by crack configurations and even by environmental and operational conditions (e.g., temperature and loading) of the target structure.

It is difficult to find the optimal input frequencies satisfying all binding conditions. To tackle this issue in a robust manner Eiras et al. [127] proposed a broadband excitation of the plate specimen instead of frequency sweeping for probe and pump waves. Broadband excitation of the plate generates multiple Lamb modes and interaction between several of these modes can generate a number of sidebands in nonlinear materials. As the material nonlinearity increases the number of measurable sideband peaks above the threshold value increases. Thus from the sideband peak counts (SPCs) the degree of material nonlinearity can be estimated.

Figures 1.42, 1.43, 1.44, and 1.45 help the readers to understand how SPC technique should be used in laboratory and field environments. Figures 1.40 and 1.42 show a specimen is struck by a laser beam. Laser pulse excitation generates broad band Lamb wave in the plate. Generated Lamb wave propagates through the plate and is detected by a laser vibrometer in a noncontact manner. When the frequency spectrum is calculated from the recorded time history then the spectrum shows multiple peaks as shown in Fig. 1.43. These peaks correspond to different Lamb modes propagating through an intact plate. For a damaged plate due to the nonlinearity introduced in the plate by internal damages multiple sidebands are generated near the main peaks as shown in Fig. 1.43. If the number of peaks above a threshold value (see Fig. 1.44) is counted, then this number should be higher for a nonlinear material as long as the threshold value is small enough to count the sideband peaks. If the SPC values are plotted as a function of the threshold value, then they continuously decrease as shown in Fig. 1.44. This figure shows how the SPC decreases with the threshold value for three different plate specimens made of glass–fiber reinforced cement (GRC) composite before and after aging. These specimens were aged artificially by soaking them in hot water for several hours [127]. Note that in spite of experimental variations from specimen to specimen the SPC values clearly show a noticeable decrease as the specimens were aged. Mechanical destructive tests and NIRAS tests confirmed that with aging these samples became more brittle and weaker but their stress–strain behavior became more linear. Similarities between the experimental results of Fig. 1.44 and theoretical plots of Fig. 1.41 should be noted.

One question that needs to be answered is whether multiple sideband peaks observed in the nonlinear material are due to nonlinear wave modulation phe-

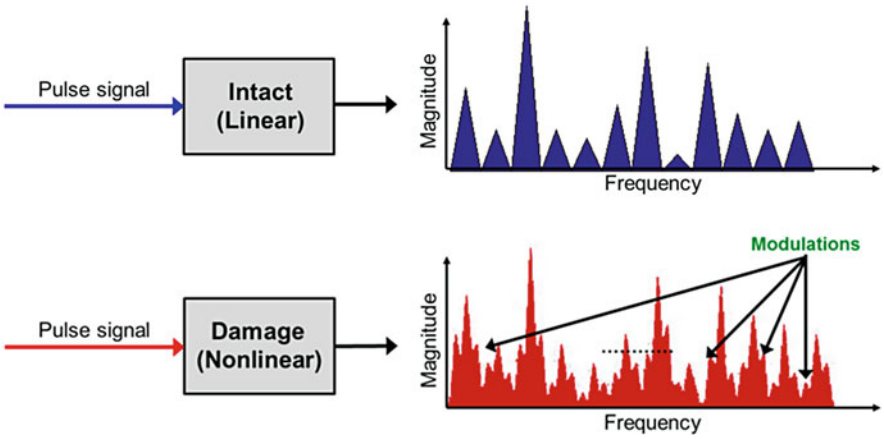

Fig. 1.43 Illustration of the SPC technique—spectral plots in the right column show more sideband peaks generated by the nonlinear material [129, 130]

nomenon between various Lamb modes or because of some other mechanisms. For classical NWMS high amplitude pump wave is needed to magnify the nonlinear effect. However, Van Den Abeele et al. [66, 67] investigated the effect of the strength of the pumping signal on the modulation energy, and showed that the nonlinear modulation in a structure with nonlinearity remains significant and measurable even when the strength of the pumping signal is almost zero. Sohn et al. [123] also succeeded in applying low strength input for both pumping and probing signals to detect the nonlinear modulation. Therefore, even when the energy level for each frequency component caused by a pulse laser excitation is relatively low, the nonlinear behavior of a damaged structure can still be detected using the pulse input.

The SPC technique proposed by Eiras et al. [127] kept track of the relatively weak spectral peaks, rather than the dominant peaks, generated due to material nonlinearity or the damage induced nonlinearity. Eiras et al. used two PZT transducers for excitation and sensing to monitor the aging process of GRC and investigated the variation of the sideband peak count results with the aging process. They observed that the number of minor peaks increased as the material nonlinearity increased.

Liu et al. [129, 130] redefined SPC as the ratio of the frequency peak number (N_p) above a moving threshold (T) to the total number of peaks (N_t) within a specified frequency range, as shown in Fig. 1.45a:

$$\mathrm{SPC}(T) = \frac{N_p(T)}{N_t} \tag{1.126}$$

Note that when the dominant peak number is much smaller than the number of weaker sideband peaks, then it is not necessary to separate the dominant peaks from the sideband peaks while counting the peaks. If the defect size is small enough to

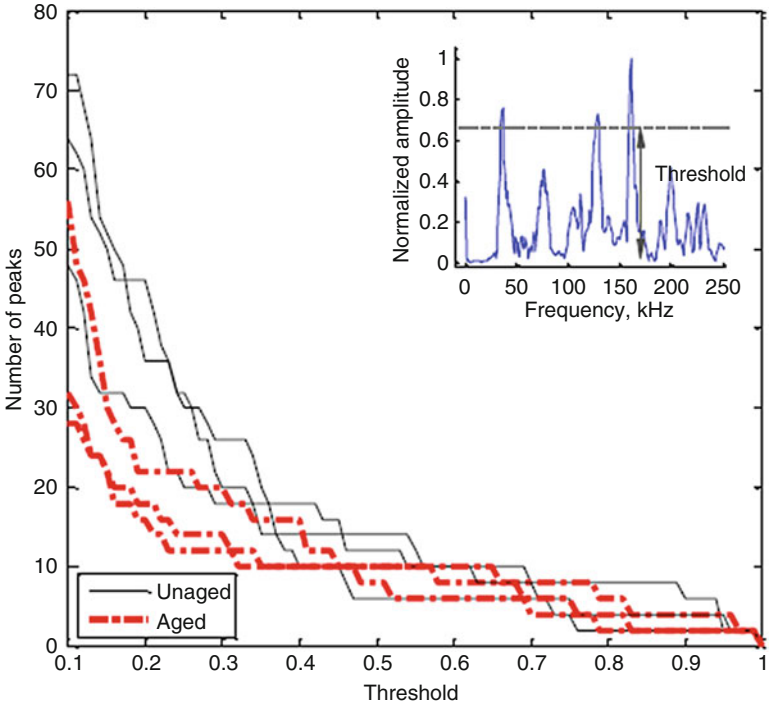

Fig. 1.44 SPC technique applied to glass–fiber reinforced cement (GRC) composite specimens—number of peaks above a preset normalized threshold value decreases as the normalized threshold value increases. For a specific value of the threshold the peak count is higher for the unaged material indicating the unaged material is more nonlinear than the aged material. Destructive test confirmed this observation. Three curves for aged and unaged samples were obtained from three different specimens [127]

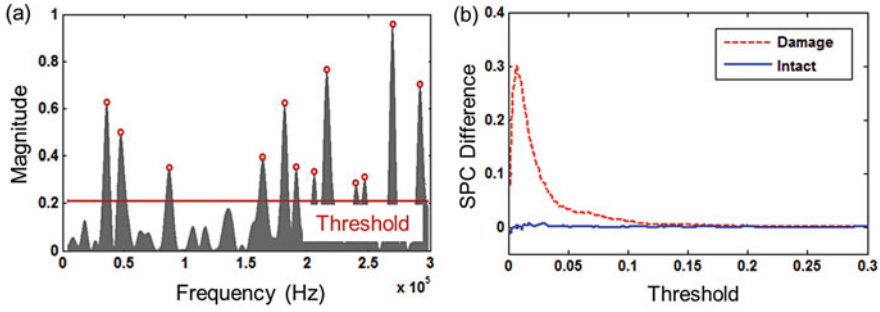

Fig. 1.45 Illustration of sideband peak count (SPC): (**a**) SPC here is counted as the ratio of the frequency peak number above a moving threshold to the total number of peaks within a specified frequency range; (**b**) Example of the SPC difference showing more peaks for the damaged case especially with a low threshold value [129, 130]

cause nonlinear effect (Fig. 1.41 shows how the defect size affects the degree of nonlinearity), then more sideband peaks appear in the spectrum and the amplitudes of the sideband peaks increase. Therefore, a damaged specimen should have larger SPC values than an intact specimen, especially for a low threshold value.

Figure 1.45b presents a typical test result of the SPC difference. The definition of the SPC difference is the difference of the SPC values between the current stage and an initial stage. In Fig. 1.45b, one can see that the SPC difference becomes positive for the damaged material, and for a low threshold value (around 1.5% of the largest spectral peak in Fig. 1.45b) the maximum SPC difference is observed. The maximum SPC difference is then defined as the damage index (DI) and used in the following experiments.

Though a pulse excitation can generate both symmetric and anti-symmetric wave modes in a plate-like structure, LDV mainly measures the anti-symmetric wave modes with predominant out-of-plane displacement. Therefore, the best condition for the phase and group velocities of the anti-symmetric wave modes for propagation is that they should be nondispersive in the selected optimal frequency band, as shown in Fig. 1.46a, b. It has also been reported that once the modulation frequencies coincide with the resonance frequencies of the target structure, the amplitude of the modulation components can be further amplified [122]. Furthermore, as

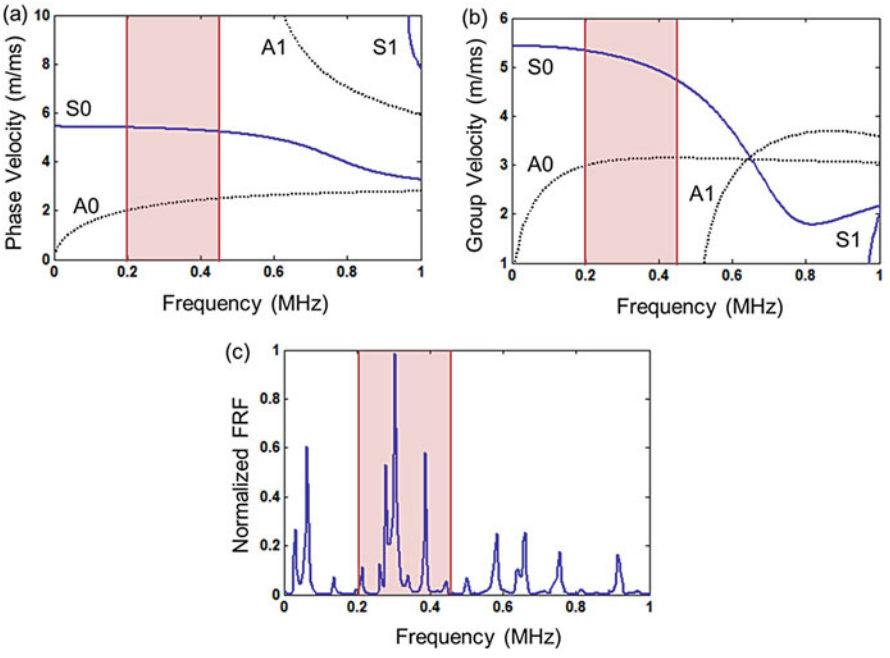

Fig. 1.46 Frequency band selection for SPC analysis: note that (**a**) phase and (**b**) group velocities of the anti-symmetric wave modes are almost nondispersive within the selected frequency band, (**c**) several strong resonance peaks should also be present in the selected frequency band [129, 130]

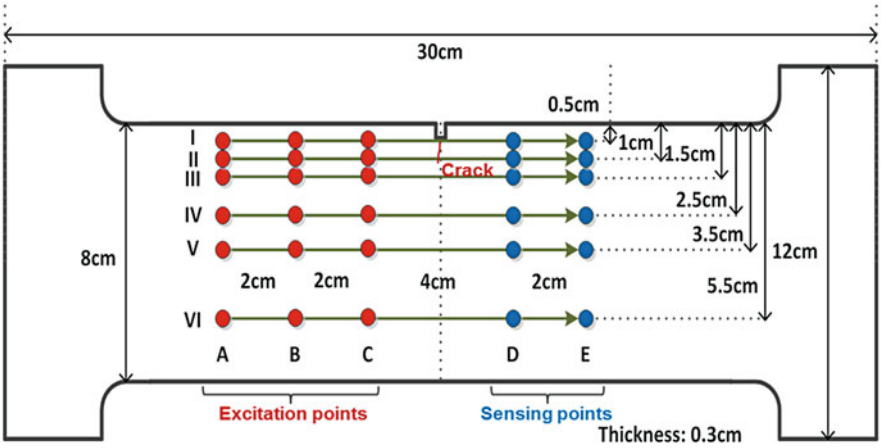

Fig. 1.47 Geometric dimensions of the specimen and its excitation and sensing points [129, 130]

shown in Fig. 1.46c, the selected frequency band should also include several strong resonance peaks. For some complex target structures, however, it is advised that the SPC analysis be conducted over the entire spectrum.

1.10.2.1 Crack Detection in Aluminum Plate Specimens

Experimental Setup

Three identical aluminum plate specimens with a notch on one side were fabricated using 6061-T6 aluminum alloy [129, 130]. The geometric dimensions of these plate specimens are shown in Fig. 1.47. Every specimen has a fatigue crack that was introduced by cyclic loading tests with a 10 Hz cyclic loading rate and a maximum load of 25 kN. As shown in Fig. 1.48, the introduced fatigue cracks have a length less than 6 mm and a width less than 10 μm. Traditional ultrasonic techniques based on linear analysis often miss these cracks.

Pairs of excitation and sensing laser beam locations are selected as shown in Fig. 1.47 to examine how the locations of the excitation/sensing pairs relative to the fatigue crack position affect the sensitivity of the proposed SPC technique. Excitation/sensing pair I A–D implies that along path I the excitation and sensing laser beams are aimed at points A and D, respectively. Other excitation/sensing pairs are defined in a similar manner. The previously described noncontact laser ultrasonic system was adopted in this experiment (see Fig. 1.49). The peak power of the Nd:YAG excitation laser was set at 0.4 MW, and the generated pulse laser was shot at the target points on the target surface using a galvanometer. A 12.8 ms ultrasonic response was measured by LDV from every target sensing point with a

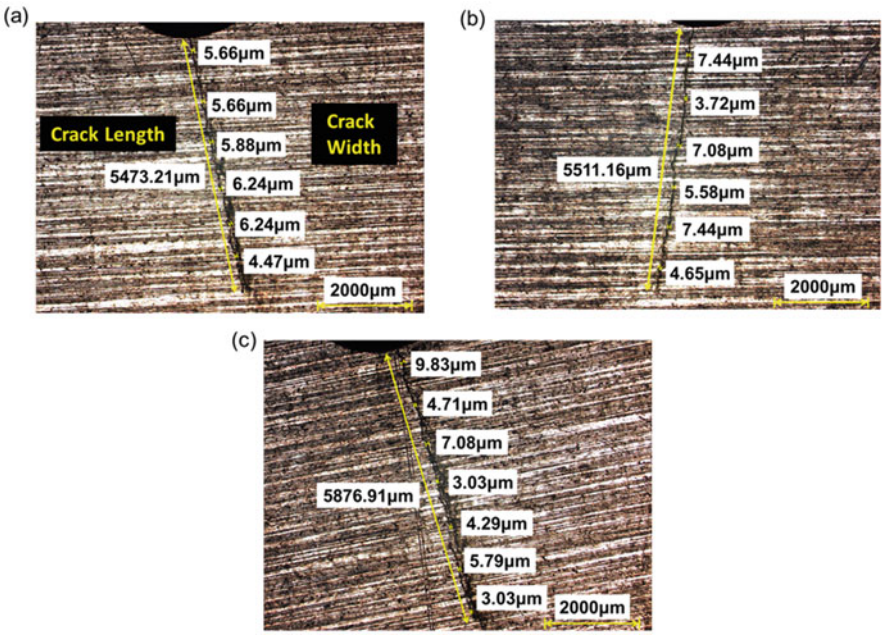

Fig. 1.48 Microscopic images of the fatigue cracks in three identical aluminum specimens: (**a**) specimen I, (**b**) specimen II, and (**c**) specimen III [129, 130]

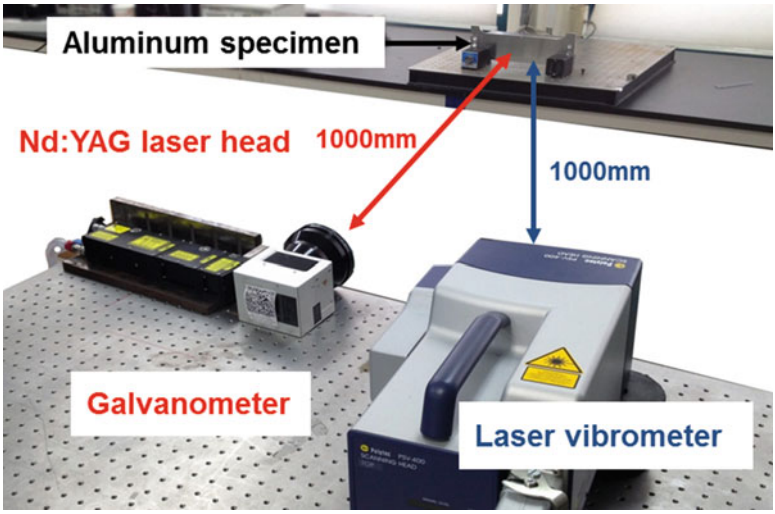

Fig. 1.49 Experimental setup for crack detection using noncontact laser ultrasonic system [129, 130]

sampling rate of 5.12 MHz. All responses were measured after averaging 100 time-domain signals to improve the signal-to-noise ratio.

For all excitation/sensing pair combinations in every specimen, the responses were measured two times before introducing any crack. The first measurement was used as the reference signal. After recording the reference signal the system was reset by removing the intact specimen from its holder, turning off the lasers and then putting the specimen back into the holder and turning on the lasers. The second measurement after resetting the intact specimen is denoted as the response signal for the intact case. After the fatigue loading had been applied to create the fatigue crack the responses were measured again for the damaged specimen.

Experimental Results

Figure 1.50 shows some representative responses and their frequency spectra collected from pair I A–D. Although the spectra in Fig. 1.50 are plotted in logarithmic scale, the SPC analysis is conducted in a linear scale. The entire response signal (12.8 ms) was used in the spectral analysis with a spectral resolution around 80 Hz. In Fig. 1.50, it is not easy to differentiate the signals or identify their distinctive features. Some variations were speculated to be caused by the system re-setup and the measurement noises. The root-mean-square-error (RMSE) of the damage and intact signals were calculated with respect to the reference signal in the frequency domain. The RMSE values from pair I A–D and pair IV A–D are summarized in Table 1.3. It clearly shows that the RMSE (a linear feature) cannot reliably detect the fatigue crack regardless of the location of the excitation/sensing pairs.

In this experiment, the SPC analysis was conducted within a frequency band 50–250 kHz. Figure 1.51a, b shows the SPC difference results obtained from pair I A–D and pair IV A–D, respectively. It was observed that the fatigue crack can be successfully detected using the SPC difference whose value was much larger for the damaged case in comparison to that in the intact case, especially for a relatively low threshold value (around 0.8% of the largest spectral peak value for pair I A–D and 1% for pair IV A–D). Figure 1.51 thus demonstrates that the existence of fatigue crack can be detected by the maximum SPC difference which can also be considered as a damage index or DI value. It does not matter whether the direct wave propagation path for the excitation/sensing pair goes through the crack or not, in both cases the DI value indicates the presence of a fatigue crack when there is one.

Then, DI values calculated from all excitation/sensing pairs were plotted in Fig. 1.52. For all three specimens, significantly larger DI values were obtained for the damaged case while for the intact case most DI values were below 5%. System re-setup and the measurement noises could be the main cause for obtaining nonzero DI values for the intact case. Note that some DI values obtained for a few damaged cases are not significantly higher than the intact cases. Since DI is not zero but a small value for the intact case and it is slightly or significantly greater

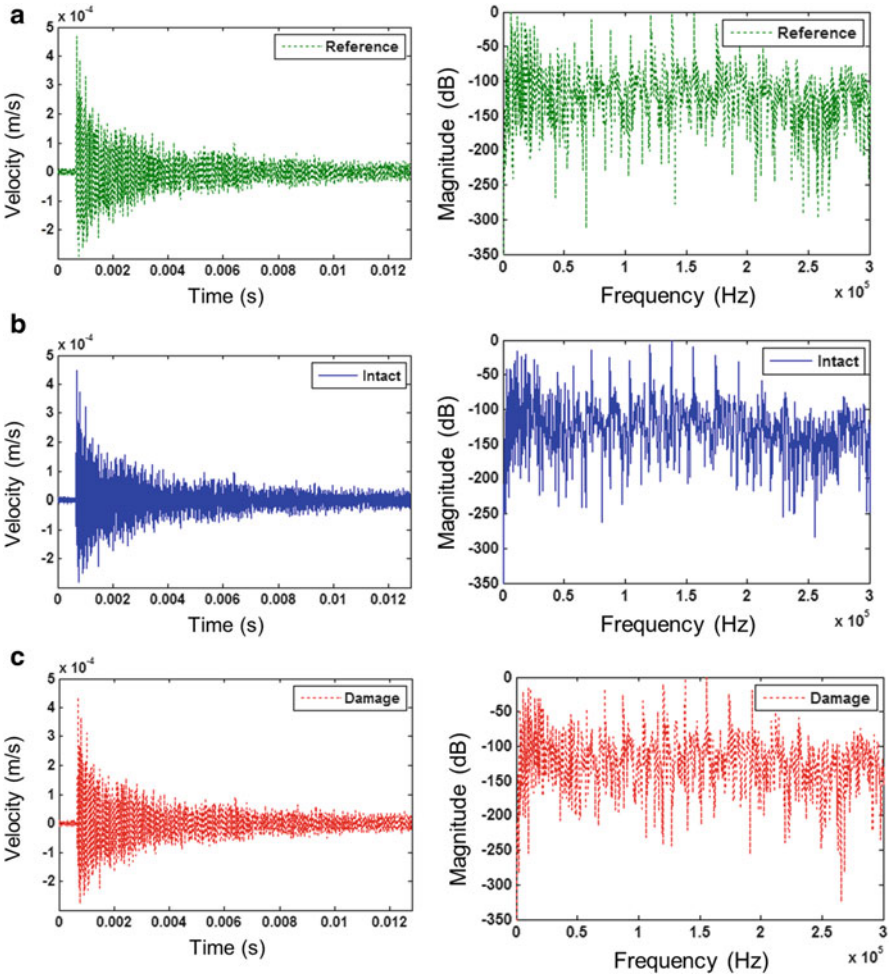

Fig. 1.50 Representative response signals (left column) and the corresponding normalized frequency spectra (right column) acquired from pair I A–D in specimen I: (**a**) reference, (**b**) intact and (**c**) damage signals [129, 130]

Table 1.3 Results of the root-mean-square-error (RMSE) [129, 130]

Excitation/sensing pair	Specimen I		Specimen II		Specimen III	
	Intact	Damage	Intact	Damage	Intact	Damage
I A–D	0.0058	0.0052	0.0061	0.0068	0.0042	0.0054
IV A–D	0.0069	0.0043	0.0054	0.0059	0.0051	0.0057

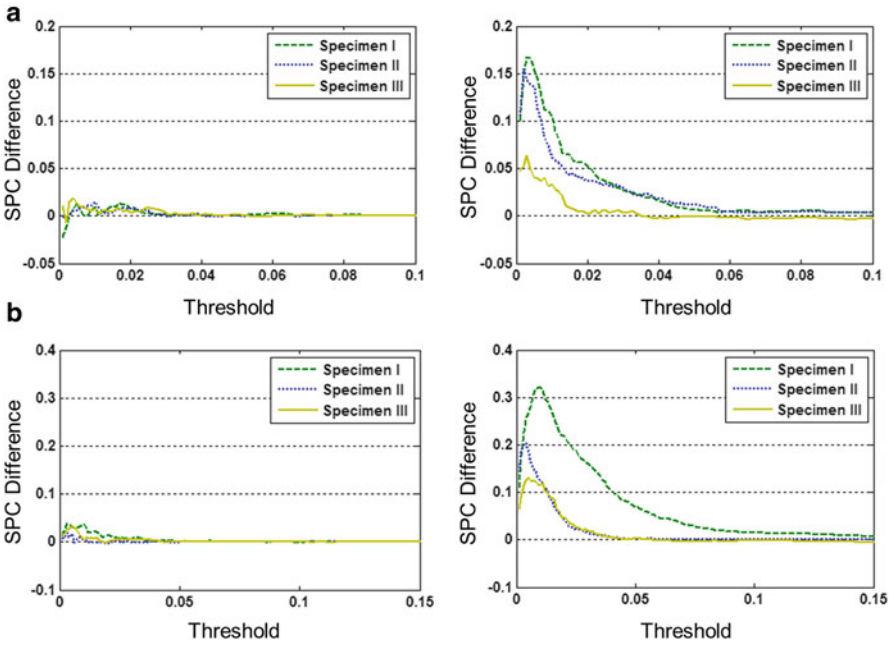

Fig. 1.51 SPC difference plots for intact case (left column) and damaged case (right column) in three specimens: (**a**) for sensor pair I A-D; (**b**) for sensor pair IV A–D [129, 130]

for the damaged case, some criteria need to be established to identify the damaged specimen as described below.

Let us assume that the specimen is damaged only when the DI value is twice or larger than that for the intact case. After all excitation/sensing pairs were considered for all specimens, the resulting diagnosis success rate was listed in Table 1.4. This table shows that the success rate of the SPC technique for micro-crack detection was very high. It should also be noted that for this experimental arrangement the DI value did not show any clear correlation with the location of the fatigue crack and the excitation/sensing pair.

1.10.2.2 Crack Detection in Aircraft Fitting-Lugs

Experimental Setup

As shown in Fig. 1.53, two mock-up 6061-T6 aluminum specimens were prepared. The specimens represent fitting-lugs used to connect an aircraft wing with the main fuselage frame [129, 130]. A fatigue crack was introduced to one specimen by cyclic loading test. This cyclic loading test is equivalent to a real operational loading over 1000 h of flight time. The detailed information can be found in [123]. For each

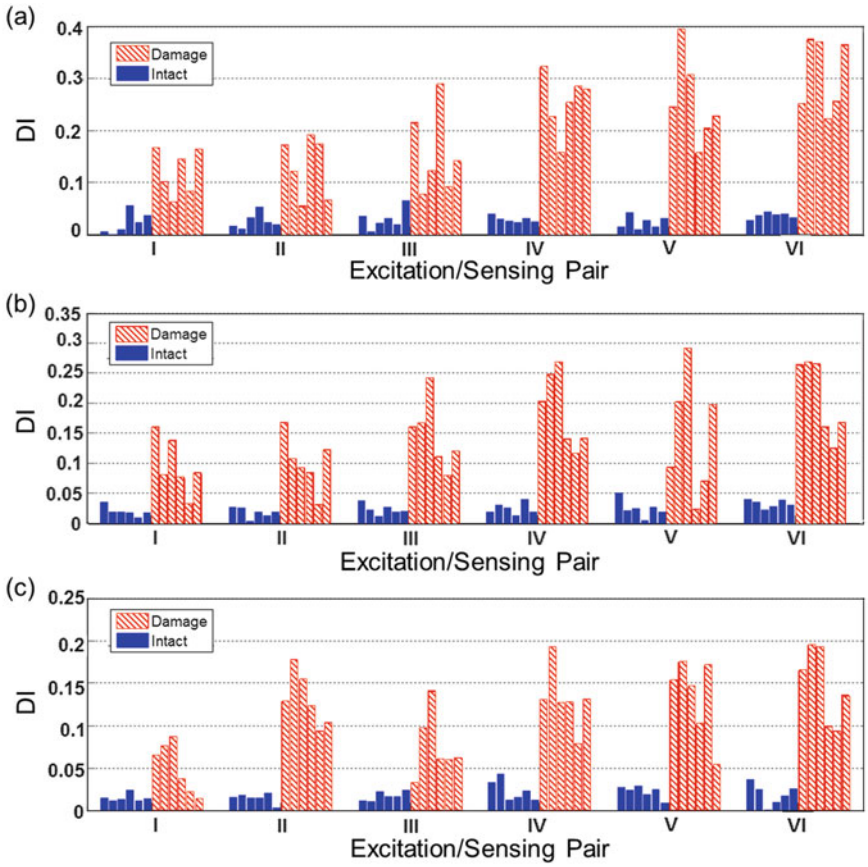

Fig. 1.52 DI values from all excitation/sensing pairs: (**a**) specimen I; (**b**) specimen II; and (**c**) specimen III (six bars from left to right in the bar diagrams represent sensor pairs A–D, B–D, C–D, A–E, B–E, and C–E)

Table 1.4 Diagnosis success rate for the three specimens considering multiple diagnosis excitation/sensing pairs [129, 130]

	Success rate (%)
Specimen I	100
Specimen II	100
Specimen III	94.4

specimen, one excitation point (Act) and one sensing point (Sen2) were located 40 mm away from each other on the same surface. A second sensing point (Sen1) was placed on another surface with a distance of approximately 40 mm from point Act. Here, only the excitation/sensing pair Act-Sen1 goes directly through the crack. The rest of the experimental setup is identical to that in the previous experiment.

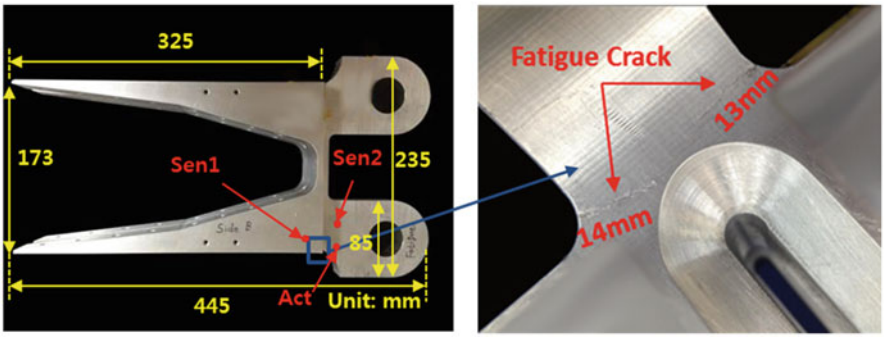

Fig. 1.53 A mock-up aluminum fitting-lug with fatigue crack, and the arrangement of the excitation (Act) and sensing points (Sen1 and Sen2) [129, 130]

Experimental Results

Figure 1.54a, b compares the intact and damaged frequency spectra obtained from sensor pairs Act-Sen1 and Act-Sen2, respectively. Here, the SPC analysis is conducted over the entire frequency band (0–600 kHz) since the waves propagating in such a specimen behave like nondispersive Rayleigh waves. Figure 1.54c plots the SPC difference results, by treating the response signals obtained from the intact specimen as the reference signal. It is observed that the SPC difference results from pairs Act-Sen1 and Act-Sen2 show the same trend as the previous experiment. The maximum SPC difference (DI) value is obtained for a relatively low threshold even for the pair Act-Sen2 for which the wave path does not directly pass through the fatigue crack.

1.10.2.3 Crack Localization in Aluminum Plate Specimens

Experimental Setup

Two identical 6061-T6 aluminum plate specimens were fabricated with a notch located in the middle of one side of the plate, as shown in Fig. 1.55 [10]. 15 mm long fatigue cracks were formed in each specimen by fatigue loadings. As shown in Fig. 1.56, the crack widths are generally less than 10 μm, and it is less than 5 μm near the crack tips. These cracks are difficult to detect using conventional linear ultrasonic techniques.

In this experiment, the same noncontact laser ultrasonic system described above was adopted but the power level was kept below 0.2 MW for generating the laser beam. Low power excitation was done to make sure that the crack opening and closing occur only when the laser beam generated ultrasonic wave passes through the crack but not when the path is bypassing the crack. A 12.8 ms ultrasonic response is measured by LDV from the desired sensing point with a sampling rate

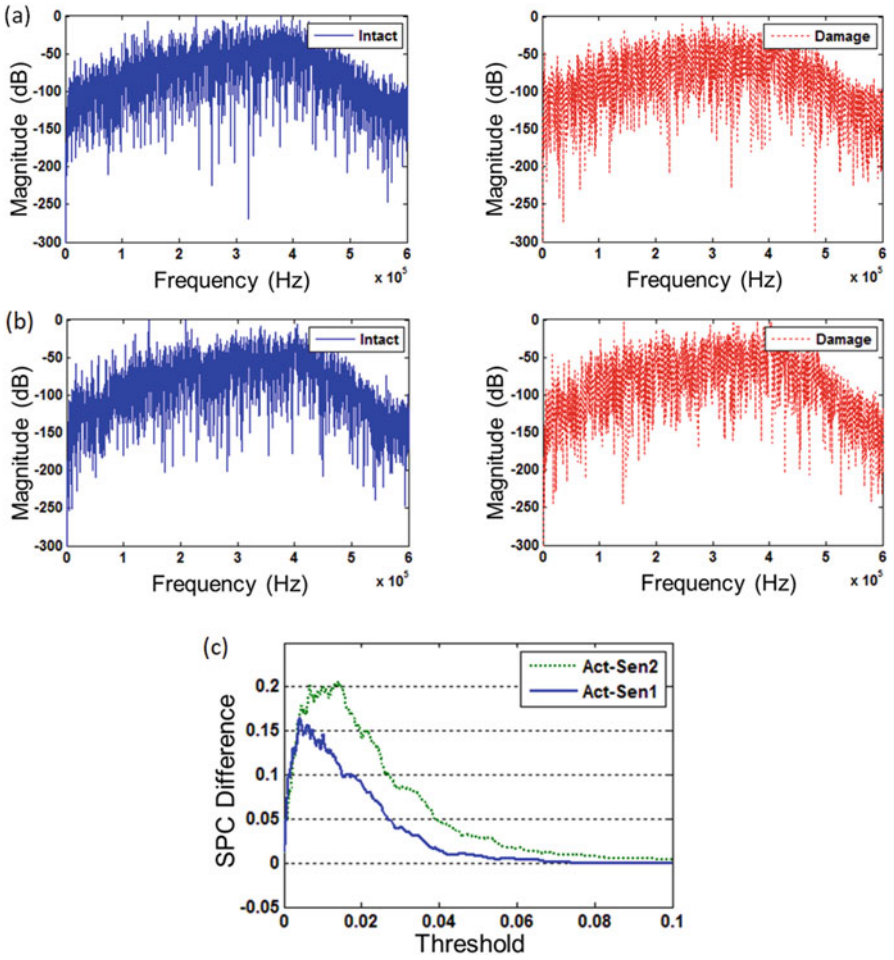

Fig. 1.54 Fatigue crack detection results from the mock-up aluminum fitting-lugs: normalized frequency spectra from (**a**) sensor pair Act-Sen1 and (**b**) sensor pair Act-Sen2; (**c**) SPC difference results for the two sensor pairs [129, 130].

of 5.12 MHz. All responses are recorded after averaging 100 time-domain signals to improve the signal-to-noise ratio.

Figure 1.55 shows six pairs of excitation and sensing points for the laser beam for examining the capability of SPC technique to localize damage. For each specimen, ultrasonic responses were measured three times for each path in the intact condition. Among the three measured responses, one was treated as the reference signal and the other two as the signals collected for the intact specimen. After the fatigue test, ultrasonic responses were recorded again for the damaged case. The system was also reset in between collecting various responses for the intact case to take into account

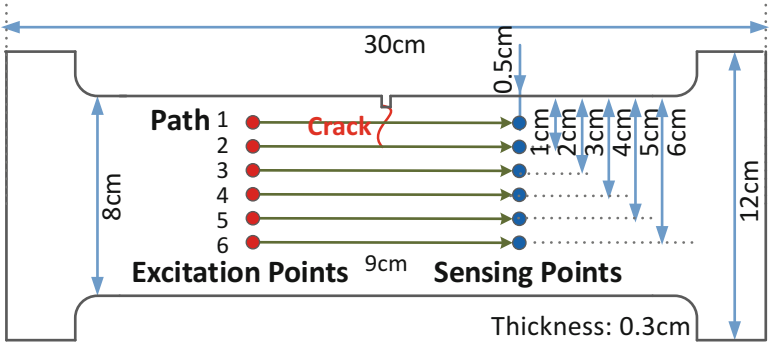

Fig. 1.55 Specimen dimensions, crack location, and excitation/sensing points [129, 130]

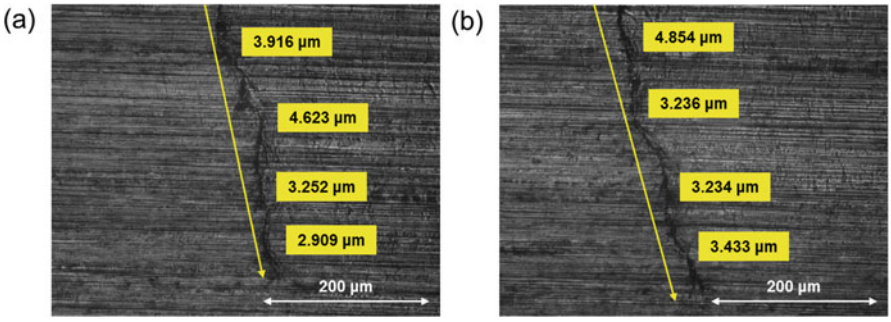

Fig. 1.56 Microscopic images of fatigue cracks in aluminum specimens: (**a**) specimen I, (**b**) specimen II [129, 130]

the potential variations in the ultrasonic responses for the damaged case caused by resetting of the measurement system and specimens.

Experimental Results

Figure 1.57 shows some representative SPC values and their differences obtained in the frequency range 20–400 kHz. As path 2 passes through the crack tip, SPC difference can be clearly observed between the intact and damaged cases for this path, as shown in Fig. 1.57a. When the threshold is relatively low, the maximum SPC difference (the DI) value becomes greater than 0.15 for the damaged case. For path 3 that does not go through the crack, the SPC values and their differences are plotted in Fig. 1.57b. Comparison of Fig. 1.57a, b shows that when the generated ultrasonic waves propagate directly through the crack tip, a higher SPC difference value is obtained for the damaged case than the intact case. Furthermore, the fatigue crack tip can be localized by comparing the SPC difference values along different paths.

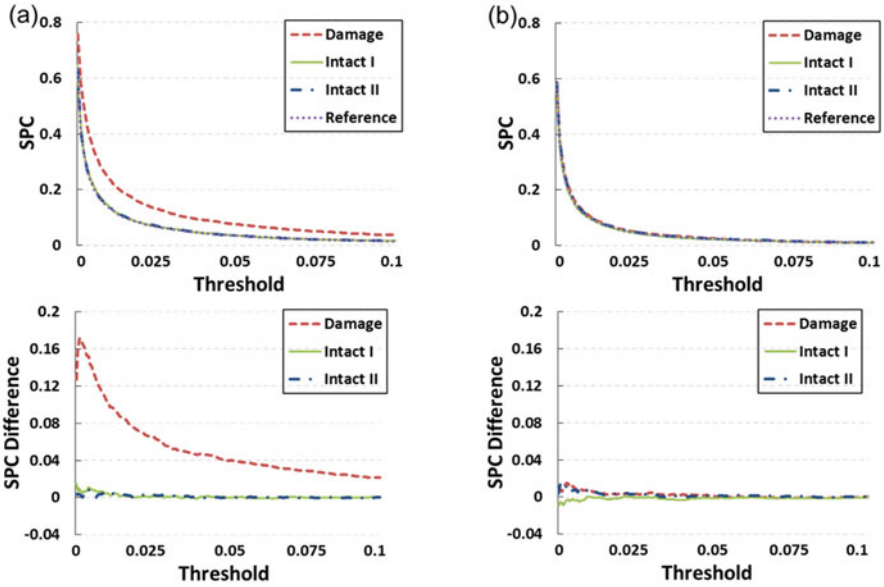

Fig. 1.57 Plots of SPC and SPC-difference variations with threshold value in specimen I along two different paths—(**a**) Path 2 and (**b**) Path 3 [129, 130]

The DI values for all six paths in the two specimens are calculated and plotted in Fig. 1.58. It shows that the DI value is much higher for the path passing through the crack, especially through the crack tip. DI values obtained for the paths that do not go through the cracks are probably caused by the measurement noises due to the measurement system reconfiguration after every fatigue test. Note that, in the previous experiments, the DI value was significantly high even when the path did not pass through the crack. This is because in those experiments the power level of the laser excitation was much higher (0.4 MW peak power) and all signals that were analyzed contained reflected and scattered signals from the plate boundaries, crack and the crack tip. The power level of the excitation laser beam for the crack localization experiment was kept below 0.2 MW so that it can cause crack opening and closing only when the generated ultrasonic waves pass directly through the crack. Figure 1.58 also shows that the crack tip region has the highest nonlinearity since the crack width there is minimum and the crack opening and closing is most prominent at the crack tip. These experimental results are in good agreement with the modeling results presented in Fig. 1.41 where it was shown that a thin crack produces higher nonlinearity than a thick crack.

In order to prove the cause of this difference, the same experiment was repeated with a higher power laser excitation (0.4 MW peak power, same as the earlier experiments) and the obtained results are shown in Fig. 1.59. In this figure the DI values for all six paths are much higher for the damaged case than the intact case. Clearly, the high power laser excitation fails to localize the fatigue crack

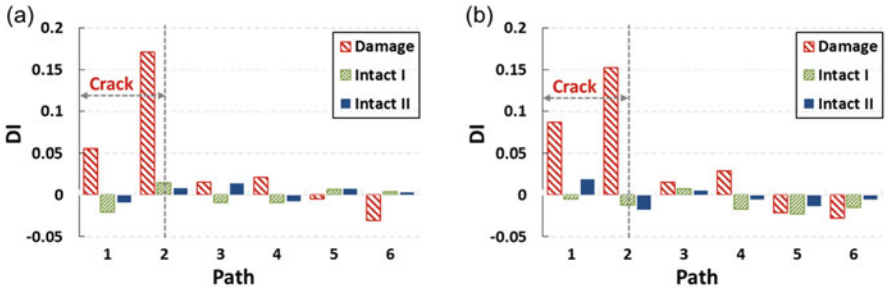

Fig. 1.58 DI values obtained using 0.2 MW peak power laser pulse excitation: (**a**) specimen I, (**b**) specimen II—only the two paths going through the crack indicate the presence of a crack in the damaged specimen in contrast to what is shown in Fig. 1.59 [129, 130]

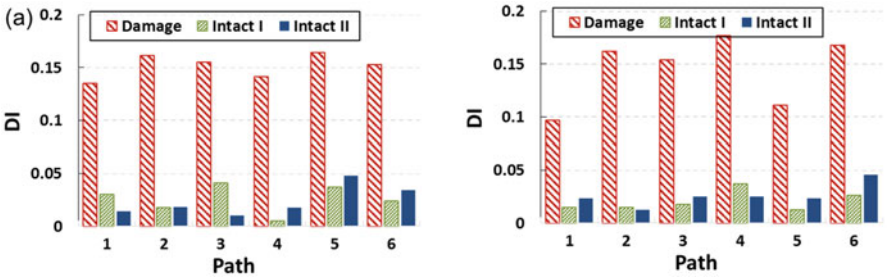

Fig. 1.59 DI values obtained using 0.4 MW peak power laser pulse excitation: (**a**) specimen I, (**b**) specimen II—all six paths indicate the presence of the fatigue crack in the damaged specimen—in contrast to what is shown in Fig. 1.58 [129, 130]

tip. Therefore, ideally, a high powered laser excitation can be initially used to identify the existence of damage, and then a lower power laser can be applied for the damage localization. Taking advantage of the laser scanning techniques, the proposed approach has the potential to be used as a noncontact technique for fatigue crack detection and localization.

1.11 Concluding Remarks

Nonlinear acoustical/ultrasonic technique for damage detection simply means sensing and recording the damage induced material nonlinearity by appropriate use of acoustic/ultrasonic waves. Ultrasonic waves generally produce very small stress in a material. Minute and almost negligible nonlinearity induced in the material by such small stress field is difficult to detect by traditional mechanics of materials approach. To investigate if a material is behaving linearly or nonlinearly in traditional mechanics of materials approach the material is loaded to check if the

stress–strain relation is linear or nonlinear. Many materials, such as metals, behave linearly at low stress levels but nonlinearly under high stress. Some people may argue that a metal when loaded by a low amplitude ultrasonic wave should exhibit linear response since the induced stress by low amplitude ultrasonic waves is very small. Therefore, one may think that there is no need to discuss nonlinear ultrasonic techniques for low amplitude ultrasonic waves.

However, it should be noted that a stress–strain curve that looks linear may not be linear. It may be a nonlinear curve that has a very large radius of curvature. Such nonlinearity cannot be detected from simple stress–strain plot since over a small segment it always looks like a straight line. In such a material even a small amplitude wave can cause very small nonlinear response of the material. This nonlinearity can be detected by appropriate techniques, such as higher harmonic, subharmonic, frequency modulation, sideband peak count, resonance acoustic spectroscopy, and various other techniques that are briefly discussed in this chapter. Detailed descriptions of these techniques are given in the following chapters by the experts on those techniques. One recently developed new technique discussed in this chapter is called sideband peak count or SPC technique. This new technique is described in detail in Sect. 1.10.2, in such a manner that it can be read and understood without reading the rest of the chapter.

References

1. T. Kundu, Chapter 1: Mechanics of elastic waves and ultrasonic NDE, in *Ultrasonic and electromagnetic NDE for structure and material characterization – engineering and biomedical applications*, ed. by T. Kundu, (CRC Press, Taylor and Francis, Boca Raton, 2012), pp. 1–108
2. L.D. Landau, E.M. Lifshitz, *Theory of elasticity* (Oxford University Press, Oxford, 1956)
3. Z.A. Goldberg, On the propagation of plane waves of finite amplitude. Sov. Phys. (Acoustics) **2**, 346–352 (1956)
4. A.N. Norris (1998), Finite-amplitude waves in solids, in Nonlinear acoustics. M. F. Hamilton and D T. Blackstocks, Academic press, New York, pp. 267-269
5. J.H. Cantrell, W.T. Yost, Nonlinear ultrasonic characterization of fatigue microstructures. Int. J. Fatigue **23**, S487–S490 (2001)
6. P.B. Nagy, Fatigue damage assesstment by nonlinear ultrasonic materials characterization. Ultrasonics **36**, 375–381 (1998)
7. K.Y. Jhang, Applications of nonlinear ultrasonics to the NDE of material degradation. IEEE Trans. Ultrason. Ferroelectr. Freq. Control **47**(3), 540–548 (2000)
8. W. Li, Y. Cho, J.D. Achenbach, Detection of thermal fatigue in composites by second harmonic Lamb waves. Smart Mater. Struct. **21**(8), 085019 (2012)
9. W. Li, Y. Cho, S. Hyun, Characteristics of ultrasonic nonlinearity by thermal fatigue. Int. J. Precis. Eng. Manuf. **13**(6), 935–940 (2012)
10. W. Li, Y. Cho, J.D. Achenbach, Assessment of heat treated Inconel X-750 alloy by nonlinear ultrasonics. Exp. Mech. **53**(5), 775–781 (2013)
11. J.D. Achenbach, *Wave Propagation in Elastic Solids* (North-Holland Preess, Amsterdam, 1973)
12. W. Li, Y. Cho, Combination of nonlinear ultrasonics and guided wave tomography for imaging the micro-defects. Ultrasonics **65**, 87–95 (2016)

13. G. Shui, J.–.Y. Kim, J. Qu, Y.S. Wang, L.J. Jacobs, A new technique for measuring the acoustic nonlinearity of materials using Rayleigh waves. NDT&E Int. **41**(5), 326–329 (2008)
14. Y. Shui, I.Y. Solodov, Nonlinear properties of Rayleigh and Stoneley waves in solids. J. Appl. Phys. **64**(11), 6155–6165 (1988)
15. J. Herrmannn, J. Kim, L.J. Jacobs, J. Qu, Assessment of material damage in a nickel-based superalloy using nonlinear Rayleigh surface waves. J. Appl. Phys. **99**, 124913 (2006)
16. B.A. Auld, *Acoustic fields and waves in solids, Vols. I and Vols. II* (Wiley, London, 1990)
17. W.J.N. de Lima, *Harmonic Generation in Isotropic Elastic Waveguides*., Ph.D. Dissertation (The University of Texas at Austin, Austin, 2000)
18. W.J.N. de Lima, M.F. Hamilton, Finite amplitude waves in isotropic elastic plates. J. Sound Vib. **265**(4), 819–839 (2003)
19. M. Deng, Analysis of second harmonic generation of Lamb modes using a modal analysis approach. J. Appl. Phys. **94**(6), 4152–4159 (2003)
20. W. Li, Y. Cho, Thermal fatigue damage assessment in an isotropic pipe using nonlinear ultrasonic guided waves. Exp. Mech. **54**(8), 1309–1318 (2014)
21. W.J.N. de Lima, M.F. Hamilton, Finite amplitude waves in isotropic elastic waveguides with arbitrary constant cross-sectional area. Wave Motion **41**(1), 1–11 (2005)
22. N. Matsuda, S. Biwa, Phase and group velocity matching for cumulative harmonic generation in Lamb waves. J. Appl. Phys. **109**(9), 094903 (2011)
23. T.R. Hay, J.L. Rose, Flexible PVDF comb transducers for excitation of axi-symmetric guided waves in pipe. Sens. Actuator A Phys. **100**, 18–23 (2002)
24. K.E.-A. Van Den Abeele, P.A. Johnson, R.A. Guyer, K.R. McCalld, On the quasi-analytic treatment of hysteretic nonlinear response in elastic wave propagation. J. Acoust. Soc. Am. **101**(4), 1885–1898 (1997)
25. L.D. Landau, E.M. Lifshitz, *Theory of elasticity* (Oxford University Press, Oxford, 1970)
26. A. Hikata, C. Elbaum, Generation of ultrasonic second and third harmonics due to dislocations. Phys. Rev. **144**(2), 469–477 (1966)
27. K.E.–.A. Van Den Abeele, Elastic pulsed wave propagation in media with second- or higher-order nonlinearity. Part I. Theoretical framework. J. Acoust. Soc. Am. **99**, 3334–3345 (1996)
28. V.E. Nazarov, L.A. Ostrovsky, A.M. Sutin, Nonlinear acoustics of micro-inhomogeneous media. Phys. Earth Planet. Inter. **50**(1), 65–73 (1988)
29. Y. Zheng, R.G. Maev, I.Y. Solodov, Nonlinear acoustic applications for material characterization: A review. Can. J. Phys. **77**, 927–967 (1999)
30. C. Pecorari, I. Solodov, Nonclassical nonlinear dynamics of solid surfaces in partial contact for NDE applications, in *Universality of nonclassical nonlinearity*. ed. by P. P. Delsanto, (Springer, Berlin, 2006), pp. 309–326
31. A. Klepka, Nonlinear acoustics. in *Advanced structural damage detection: from theory to engineering applications*. ed. by T. Stepinski, T. Uhl, W. Staszewski, (Wiley; Hoboken, 2013), pp. 73–107
32. S. Biwa, S. Nakajima, N. Ohno, On the acoustic nonlinearity of solid-solid contact with pressure-dependent Interface stiffness. J. Appl. Mech. **71**(4), 508–515 (2004)
33. J.-Y. Kim, A. Baltazar, J.W. Hu, S.I. Rokhlin, Hysteretic linear and nonlinear acoustic responses from pressed interfaces. Int. J. Solids Struct. **43**(21), 6436–6452 (2006)
34. D. Yan, B.W. Drinkwater, S. Neild, Measurement of the ultrasonic nonlinearity of kissing bonds in adhesive joints. NDT&E Int. **42**(5), 459–466 (2009)
35. K.H. Matlack, J.–.Y. Kim, L.J. Jacobs, J. Qu, Review of second harmonic generation measurement techniques for material state determination in metals. J. Nondestruct. Eval. **34**(1), 273 (2015)
36. G.D. Meegan, P.A. Johnson, R.A. Guyer, K.R. McCall, Observations of nonlinear elastic wave behavior in sandstone. J. Acoust. Soc. Am. **94**(6), 3387–3391 (1993)
37. A.A. Shah, Y. Ribakov, S. Hirose, Nondestructive evaluation of damaged concrete using nonlinear ultrasonics. Mater. Des. **30**(3), 775–782 (2009)
38. J.D. Stauffer, C.B. Woodward, K.R. White, Nonlinear ultrasonic testing with resonant and pulse velocity parameters for early damage in concrete. ACI Mater. J. **102**(2), 4–7 (2005)

39. M. Amura, M. Meo, F. Amerini, Baseline-free estimation of residual fatigue life using a third order acoustic nonlinear parameter. J. Acoust. Soc. Am. **130**(4), 1829–1837 (2011)
40. O. Buck, W.L. Morris, J.M. Richardson, Acoustic harmonic generation at unbonded interfaces and fatigue cracks. Appl. Phys. Lett. **33**(5), 371 (1978)
41. K.-Y. Jhang, K.–.C. Kim, Evaluation of material degradation using nonlinear acoustic effect. Ultrasonics **37**(1), 39–44 (1999)
42. A. Romer, J.–.Y. Kim, J. Qu, L.J. Jacobs, The second harmonic generation in reflection mode: An analytical, numerical and experimental study. J. Nondestruct. Eval. **35**(1), 6 (2016)
43. S. Thiele, J.–.Y. Kim, J. Qu, L.J. Jacobs, Air-coupled detection of nonlinear Rayleigh surface waves to assess material nonlinearity. Ultrasonics **54**, 1470–1475 (2014)
44. C. Bermes, J.–.Y. Kim, J. Qu, L.J. Jacobs, Experimental characterization of material nonlinearity using Lamb waves. Appl. Phys. Lett. **90**(2), 1–4 (2007)
45. A.J. Hillis, S.A. Neild, B.W. Drinkwater, P.D. Wilcox, Global crack detection using bispectral analysis. Proc. Royal Soc. A **462**, 1515–1530 (2006)
46. C.L.E. Bruno, A.S. Gliozzi, M. Scalerandi, P. Antonaci, Analysis of elastic nonlinearity using the scaling subtraction method. Phys. Rev. B **79**(6), 064108 (2009)
47. P. Antonaci, C.L.E. Bruno, A.S. Gliozzi, M. Scalerandi, Monitoring evolution of compressive damage in concrete with linear and nonlinear ultrasonic methods. Cem. Concr. Res. **40**(7), 1106–1113 (2010)
48. M. Scalerandi, M. Griffa, P. Antonaci, M. Wyrzykowski, P. Lura, Nonlinear elastic response of thermally damaged consolidated granular media. J. Appl. Phys. **113**(15), 154902 (2013)
49. P. Antonaci, A. Formia, A.S. Gliozzi, M. Scalerandi, J.M. Tulliani, Diagnostic application of nonlinear ultrasonics to characterize degradation by expansive salts in masonry systems. NDT&E Int. **55**, 57–63 (2013)
50. M. Scalerandi, A.S. Gliozzi, D. Olivero, Discrimination between cracks and recrystallization in steel using nonlinear techniques. J. Nondestruct. Eval. **33**(2), 269–278 (2014)
51. D.S. Hughes, J.L. Kelly, Second-order elastic deformation of solids. Phys. Rev. **92**(5), 1145–1149 (1953)
52. L. Adler, P.B. Nagy, Second order nonlinearities and their application in NDE. in *Review of progress in quantitative nondestructive evaluation*, ed. by D.O. Thompson, D.E. Chimenti, (Plenum Press, New York, 1991), Vol. **10B**, pp. 1813–1820
53. F.D. Murnaghan, *Finite deformation of an elastic solid* (Wiley, Hoboken, 1951)
54. R.H. Bergman, R.A. Shahbender, Effect of statically applied stresses on the velocity of propagation of ultrasonic waves. J. Appl. Phys. **29**(12), 1736–1738 (1958)
55. P.A. Johnson, P.N.J. Rasolofosaon, Nonlinear elasticity and stress-induced anisotropy in rock. J. Geophys. Res. **101**, 3113–3124 (1996)
56. P.A. Johnson, P.N.J. Rasolofosaon, Resonance and elastic nonlinear phenomena in rock. J. Geophys. Res. **101**(B5), 553–564 (1996)
57. V. Bucur, P.N.J. Rasolofosaon, Dynamic elastic anisotropy and nonlinearity in wood and rock. Ultrasonics **36**(7), 813–824 (1998)
58. C. Payan, V. Garnier, J. Moysan, P.A. Johnson, Determination of third order elastic constants in a complex solid applying coda wave interferometry. Appl. Phys. Lett. **94**(1), 011904 (2009)
59. W.L. Morris, O. Buck, R.V. Inman, Acoustic harmonic generation due to fatigue damage in high-strength aluminum. J. Appl. Phys. **50**(11), 6737–6741 (1979)
60. P.B. Nagy, P. McGowan, L. Adler, Acoustic nonlinearities in adhesive joints, in *Review of progress in quantitative nondestructive evaluation*, D.O. Thompson, D.E. Chimenti, (Plenum Press, New York, 1990), Vol. **9**, pp. 1685–1692
61. P. Shokouhi, A. Zoëga, H. Wiggenhauser, G. Fischer, Surface wave velocity-stress relationship in uniaxially loaded concrete. ACI Mater. J. **109**(2), 141–148 (2012)
62. P. Fröjd, P. Ulriksen, Amplitude and phase measurements of continuous diffuse fields for structural health monitoring of concrete structures. NDT&E Int. **77**, 35–41 (2016)
63. R. Snieder, A. Gret, H. Douma, J. Scales, Coda wave interferometry for estimating nonlinear behavior in seismic velocity. Science (New York, N.Y.) **295**(5563), 2253–2255 (2002)

64. E. Larose, S. Hall, Monitoring stress related velocity variation in concrete with a 2x10(−5) relative resolution using diffuse ultrasound. J. Acoust. Soc. Am. **125**(4), 2641 (2009)
65. D.P. Schurr, J.–.Y. Kim, K.G. Sabra, L.J. Jacobs, Damage detection in concrete using coda wave interferometry. NDT&E Int **44**(8), 728–735 (2011)
66. K.E.-A. Van Den Abeele, J. Carmeliet, J.A. Ten Cate, P.A. Johnson, Nonlinear Elastic Wave Spectroscopy (NEWS) techniques to discern material damage, part II: Single-mode nonlinear resonance acoustic spectroscopy. Res. Nondestruct. Eval. **12**(1), 31–42 (2000)
67. K.E.-A. Van Den Abeele, P.A. Johnson, A. Sutin, Nonlinear Elastic Wave Spectroscopy (NEWS) techniques to discern material damage, part I: Nonlinear Wave Modulation Spectroscopy (NWMS). Res. Nondestruct. Eval. **12**(1), 17–30 (2000)
68. L.K. Zarembo, V.A. Krasil'nikox, I.E. Shkol'nik, Nonlinear acoustics in a problem of diagnosing the strength of solids. Problemy Prochnosti **21**(11), 86–92 (1989)
69. R.A. Guyer, P.A. Johnson, Nonlinear mesoscopic elasticity: Evidence for a new class of materials. Phys. Today **52**(4), 30–36 (1999)
70. R.A. Guyer, K.R. McCall, G.N. Boitnott, Hysteresis, discrete memory, and nonlinear wave propagation in rock. Phys. Rev. Lett. **74**(17), 3491–3494 (1995)
71. T.A. Read, The internal friction of single metal crystals. Phys. Rev. **58**, 371–380 (1940)
72. C. Campos-Pozuelo, C. Vanhille, J.A. Gallego-Juárez, Comparative study of the nonlinear behavior of fatigued and intact samples of metallic alloys. IEEE Trans. Ultrason. Ferroelectr. Freq. Control **53**(1), 175–184 (2006)
73. R.A. Guyer, K.R. McCall, K. Van Den Abeele, Slow elastic dynamics in a resonant bar of rock. Geophys. Res. Lett. **25**(10), 1585–1588 (1998)
74. V.E. Nazarov, A.V. Radostin, L.A. Ostrovsky, I.A. Soustova, Wave processes in media with hysteretic nonlinearity: Part 2. Acoust. Phys. **49**(4), 444–448 (2003)
75. C. Pecorari, D.A. Mendelsohn, Forced nonlinear vibrations of a one-dimensional bar with arbitrary distributions of hysteretic damage. J. Nondestruct. Eval. **33**(2), 239–251 (2014)
76. P.A. Johnson, A. Sutin, Slow dynamics and anomalous nonlinear fast dynamics in diverse solids. J. Acoust. Soc. Am. **117**(1), 124–130 (2005)
77. K.E.–.A. Van Den Abeele, A. Sutin, J. Carmeliet, P.A. Johnson, Micro-damage diagnostics using nonlinear elastic wave spectroscopy (NEWS). NDT&E Int. **34**(4), 239–248 (2001)
78. K.E. Van Den Abeele, K. Van de Velde, J. Carmeliet, Inferring the degradation of pultruded composites from dynamic nonlinear resonance measurements. Polym. Compos. **22**(4), 555–567 (2001)
79. T.W. Darling, J.A. Ten Cate, D.W. Brown, B. Clausen, S.C. Vogel, Neutron diffraction study of the contribution of grain contacts to nonlinear stress-strain behavior. Geophys. Res. Lett. **31**(16), 31–34 (2004)
80. V.E. Nazarov, A.V. Radostin, *Nonlinear acoustic waves in micro-inhomogeneous solids* (Wiley, Hoboken, 2015)
81. M. Bentahar, H. El Agra, R. El Guerjouma, M. Griffa, M. Scalerandi, Hysteretic elasticity in damaged concrete: Quantitative analysis of slow and fast dynamics. Phys. Rev. B **73**(1), 014116 (2006)
82. N. Favrie, B. Lombard, C. Payan, Fast and slow dynamics in a nonlinear elastic bar excited by longitudinal vibrations. Wave Motion **56**, 221–238 (2015)
83. J.A. Ten Cate, Slow dynamics of earth materials: An experimental overview. Pure Appl. Geophys. **168**(12), 2211–2219 (2011)
84. D. Pasqualini, J.A. Ten Cate, S. Habib, D. Higdon, P.A. Johnson, Nonequilibrium and nonlinear dynamics in Berea and Fontainebleau sandstones: Low-strain regime. J. Geophys. Res. **112**(B1), B01204 (2007)
85. C. Pecorari, A constitutive relationship for mechanical hysteresis of sandstone materials. Proc. Royal Soc. London A Math. Phys. Eng. Sci. **471**(2184), 20150369 (2015)
86. J. Rivière, G. Renaud, R.A. Guyer, P.A. Johnson, Pump and probe waves in dynamic acousto-elasticity: Comprehensive description and comparison with nonlinear elastic theories. J. Appl. Phys. **114**(5), 054905 (2013)

87. C. Payan, V. Garnier, J. Moysan, P.A. Johnson, Applying nonlinear resonant ultrasound spectroscopy to improving thermal damage assessment in concrete. J. Acoust. Soc. Am. **121**(4), EL125–EL130 (2007)
88. J. Chen, J.-Y. Kim, K.E. Kurtis, L.J. Jacobs, Rapid evaluation of alkali-silica reactivity of aggregates using a nonlinear resonance spectroscopy technique. Cem. Concr. Res. **40**(6), 914–923 (2010)
89. S.-J. Park, G.-K. Park, H.J. Yim, H.-G. Kwak, Evaluation of residual tensile strength of fire-damaged concrete using a non-linear resonance vibration method. Mag. Concr. Res. **67**(5), 235–246 (2015)
90. J.N. Eiras, T. Kundu, J.S. Popovics, J. Monzó, L. Soriano, J. Payá, Evaluation of frost damage in cement-based materials by a nonlinear elastic wave technique, in *Health Monitoring of Structural and Biological Systems VII*, ed. by T. Kundu, *SPIE Proceedings Vol.* 9064, SPIE's 2014 Annual international symposium on smart structures and nondestructive evaluation, (San Diego, California, March 10–13, 2014)
91. J.N. Eiras, T. Kundu, J. Popovics, J. Monzo, J. Paya, Non-classical nonlinear feature extraction from standard resonance vibration data for damage detection. J. Acoust. Soc. Am. Exp. Lett. **135**(2), EL82–EL87 (2014)
92. A. Novak, M. Bentahar, V. Tournat, R. El Guerjouma, L. Simon, Nonlinear acoustic characterization of micro-damaged materials through higher harmonic resonance analysis. NDT&E Int. **45**(1), 1–8 (2012)
93. V.E. Gusev, W. Lauriks, J. Thoen, Dispersion of nonlinearity, nonlinear dispersion, and absorption of sound in micro-inhomogeneous materials. J. Acoust. Soc. Am. **103**(6), 3216–3226 (1998)
94. K.E.–.A. Van Den Abeele, P.Y. Le Bas, B. Van Damme, T. Katkowski, Quantification of material nonlinearity in relation to microdamage density using nonlinear reverberation spectroscopy: Experimental and theoretical study. J. Acoust. Soc. Am. **126**(3), 963–972 (2009)
95. B. Van Damme, K.E.–.A. Van Den Abeele, The application of nonlinear reverberation spectroscopy for the detection of localized fatigue damage. J. Nondestruct. Eval. **33**(2), 263–268 (2014)
96. U. Dahlén, N. Ryden, A. Jakobsson, Damage identification in concrete using impact non-linear reverberation spectroscopy. NDT&E Int. **75**, 15–25 (2015)
97. A.M. Sutin, V.E. Nazarov, Nonlinear acoustic methods of crack diagnostics. Radiophys. Quant. Electron. **38**(3), 109–120 (1995)
98. A.S. Korotkov, M.M. Slavinskii, A.M. Sutin, Variations of acoustic nonlinear parameters with the concentration of the defects in steel. Acoust. Phys. **40**(1), 71–74 (1994)
99. V.Y. Zaitsev, A.M. Sutin, I.Y. Belyaeva, V.E. Nazarov, Nonlinear interaction of acoustical waves due to cracks and its possible usage for cracks detection. J. Vib. Control. **1**(3), 335–344 (1995)
100. I.Y. Solodov, B.A. Korshak, Instability, chaos, and "memory" in acoustic-wave-crack interaction. Phys. Rev. Lett. **88**(1), 014303 (2002)
101. D.M. Donskoy, A.M. Sutin, Vibro-acoustic modulation nondestructive evaluation technique. J. Intell. Mater. Syst. Struct. **9**, 765–771 (1998)
102. P. Duffour, M. Morbidini, P. Cawley, A study of the vibro-acoustic modulation technique for the detection of cracks in metals. J. Acoust. Soc. Am. **119**(3), 1463 (2006)
103. A.E. Ekimov, I.N. Didenkulov, V.V. Kazakov, Modulation of torsional waves in a rod with a crack. J. Acoust. Soc. Am. **106**(3), 1289 (1999)
104. V.Y. Zaitsev, L.A. Matveev, A.L. Matveyev, On the ultimate sensitivity of nonlinear-modulation method of crack detection. NDT&E Int. **42**(7), 622–629 (2009)
105. V.Y. Zaitsev, L.A. Matveev, A.L. Matveyev, Elastic-wave modulation approach to crack detection: Comparison of conventional modulation and higher-order interactions. NDT&E Int. **44**(1), 21–31 (2011)
106. D. Donskoy, A. Sutin, A. Ekimov, Nonlinear acoustic interaction on contact interfaces and its use for nondestructive testing. NDT&E Int. **34**(4), 231–238 (2001)

107. G. Renaud, S. Callé, J.P. Remenieras, M. Defontaine, Exploration of trabecular bone nonlinear elasticity using time of flight modulation. IEEE Trans. Ultrason. Ferroelectr. Freq. Control **55**(7), 1497–1507 (2008)
108. G. Renaud, S. Callé, M. Defontaine, Remote dynamic acoustoelastic testing: Elastic and dissipative acoustic nonlinearities measured under hydrostatic tension and compression. Appl. Phys. Lett. **94**(011905), 1–4 (2009)
109. G. Renaud, M. Talmant, S. Callé, M. Defontaine, P. Laugier, Nonlinear elastodynamics in micro-inhomogeneous solids observed by head-wave based dynamic acoustoelastic testing. J. Acoust. Soc. Am. **130**(6), 3583 (2011)
110. S. Haupert, J. Rivière, B. Anderson, Y. Ohara, T.J. Ulrich, P. Johnson, Optimized dynamic acousto-elasticity applied to fatigue damage and stress corrosion cracking. J. Nondestruct. Eval. **33**(2), 226–238 (2014)
111. G. Renaud, J. Rivière, C. Larmat, J.T. Rutledge, R.C. Lee, R.A. Guyer, K. Stokoe, P.A. Johnson, In situ characterization of shallow elastic nonlinear parameters with dynamic acousto-elastic testing. J. Geophys. Res. Solid Earth **119**(9), 6907–6923 (2014)
112. D. Bui, S.A. Kodjo, P. Rivard, B. Fournier, Evaluation of concrete distributed cracks by ultrasonic travel time shift under an external mechanical perturbation: Study of indirect and semi-direct transmission configurations. J. Nondestruct. Eval. **32**(1), 25–36 (2013)
113. F. Moradi-Marani, S.A. Kodjo, P. Rivard, C.-P. Lamarche, Application of the mechanical perturbation produced by traffic as a new approach of nonlinear acoustic technique for detecting microcracks in the concrete: A laboratory simulation, in *AIP Conference proceedings*. 1430, (2012), pp. 1493–1499
114. F. Moradi-Marani, S.A. Kodjo, P. Rivard, C.-P. Lamarch, Nonlinear acoustic technique of time shift for evaluation of alkali-silica reaction damage in concrete structures. ACI Mater. J. **111**(5), 581–592 (2014)
115. N. Tremblay, E. Larose, V. Rossetto, Probing slow dynamics of consolidated granular multicomposite materials by diffuse acoustic wave spectroscopy. J. Acoust. Soc. Am. **127**(3), 1239–1243 (2010)
116. E. Larose, N. Tremblay, C. Payan, V. Garnier, V. Rossetto, Ultrasonic slow dynamics to probe concrete aging and damage, in *Review of progress in quantitative nondestructive evaluation*, 32, (American Institute of Physics Proceedings 1511, 2013), pp. 1317–1324
117. B. Hilloulin, O. Abraham, A. Loukili, O. Durand, V. Tournat, Small crack detection in cementitious materials using nonlinear coda wave modulation. NDT&E Int. **68**, 98–104 (2014)
118. Y. Ohara, H. Endo, T. Mihara, K. Yamanaka, Ultrasonic measurement of closed stress corrosion crack depth using subharmonic phased array. Jpn. J. Appl. Phys. **48**, 07GD01 (2009)
119. M. Liu, J. Kim, L.J. Jacobs, J. Qu, Experimental study of nonlinear Rayleigh wave propagation in shot-peened aluminium plates-feasibility of measuring residual stress. NDT&E Int. **44**(1), 67–74 (2011)
120. A.J. Croxford, P.D. Wilcox, B.W. Drinkwater, P.B. Nagy, The use of non-collinear mixing for nonlinear ultrasonic detection of plasticity and fatigue. J. Acoust. Soc. Am. **126**(5), 117–122 (2009)
121. A. Demčenko, R. Akkerman, P.B. Nagy, Non-collinear wave mixing for nonlinear ultrasonic detection of physical ageing in PVC. NDT&E Int. **49**(1), 34–39 (2012)
122. N.C. Yoder, D.E. Adams, Vibro-acoustic modulation using a swept probing signal for robust crack detection. Struct. Health Monit. **9**, 257–267 (2010)
123. H. Sohn, H.J. Lim, M.P. DeSimio, K. Brown, M. Derisso, Nonlinear ultrasonic wave modulation for fatigue crack detection. J. Sound Vib. **333**, 1473–1484 (2013)
124. X.J. Chen, J.–.Y. Kim, K.E. Kurtis, J. Qu, C.W. Shen, L.J. Jacobs, Characterization of progressive microcracking in Portland cement mortar using nonlinear ultrasonics. NDT&E Int. **41**, 112–118 (2008)

125. A. Klepka, W.J. Staszewski, R.B. Jenal, M. Szwedo, J. Iwaniec, Nonlinear acoustics for fatigue crack detection – Experimental investigations of vibro-acoustic wave modulations. Struct. Health Monit. **11**, 197–211 (2012)
126. C. Zhou, M. Hong, Z. Su, Q. Wang, L. Cheng, Evaluation of fatigue cracks using nonlinearities of acousto-ultrasonic waves acquired by an active sensor network. Smart Mater. Struct. **22**, 015018 (2013)
127. J.N. Eiras, T. Kundu, M. Bonilla, J. Payá, Nondestructive monitoring of ageing of alkali resistant glass fiber reinforced cement (GRC). J. Nondestruct. Eval. **32**(3), 300–314 (2013)
128. M.H. Hafezi, R. Alebrahim, T. Kundu, Peri-ultrasound for modeling linear and nonlinear ultrasonic response. Ultrasonics **80**, 47–57 (2017)
129. P. Liu, H. Sohn, T. Kundu, S. Yang, Noncontact detection of fatigue cracks by laser nonlinear wave modulation spectroscopy (LNWMS). NDT&E Int. **66**, 106–116 (2014)
130. P. Liu, H. Sohn, T. Kundu, Fatigue crack localization using laser nonlinear wave modulation spectroscopy (LNWMS). J. Korean Soc. Nondestruct. Test. **34**(6), 419–427 (2014)
131. Y.K. An, B. Park, H. Sohn, Complete noncontact laser ultrasonic imaging for automated crack visualization in a plate. Smart Mater. Struct. **22**, 025022 (2013)
132. S. Yashiro, J. Takatsubo, H. Miyauchi, N. Toyama, A novel technique for visualizing ultrasonic waves in general solid media by pulsed laser scan. NDT&E Int. **41**, 137–144 (2008)
133. J.N. Caron, G.P. DiComo, S. Nikitin, Generation of ultrasound in materials using continuous-wave lasers. Opt. Lett. **37**, 830–832 (2012)
134. H. Sohn, D. Dutta, J.Y. Yang, M.P. Desimo, S.E. Olson, E.D. Swenson, Automated detection of delamination and disbond from wavefield images obtained using a scanning laser vibrometer. Smart Mater. Struct. **20**, 045017 (2011)
135. T.E. Michaels, J.E. Michaels, M. Ruzzene, Frequency–wavenumber domain analysis of guided wavefields. Ultrasonics **51**, 452–466 (2011)
136. C.B. Scruby, L.E. Drain, *Laser ultrasonics: Techniques and Applications* (Taylor and Francis, London, 1990)

Chapter 2
Nonlinear Resonant Ultrasound Spectroscopy: Assessing Global Damage

James A. TenCate and Paul A. Johnson

2.1 Introduction and Motivation

This chapter begins with a broad question, why is (linear) acoustic resonance spectroscopy useful for damage detection? After all, standard acoustic techniques are quite good at locating flaws and damage; industrial ultrasonic imaging and inspection are well-established techniques for non-destructive evaluation (NDE). For example, full and complete robotic scans of critical large aerospace components are routinely done. What does a resonance technique offer for NDE? Perhaps the biggest advantages of resonance techniques are speed and the concomitant ability to quickly sort a large number of parts. In addition, it is an excellent way to detect differences in parts, e.g., [1]. For example, plinking a dozen coffee cups with a finger and listening to the sounds each make is a very easy way to find a damaged cup [2]. Standards for resonance inspection exist, e.g., ASTM E2001-8 "Standard Guide for Resonant Ultrasound for Defect Detection in Both Metallic and Non-Metallic Parts." In addition there are companies that will do this service as well, e.g., MTS Systems (http://www.modalshop.com/ndt.asp).

At Los Alamos National Laboratory, resonance techniques have been used for a wide variety of non-standard applications too. Some examples are to (1) quantify differences in aging plastic bonded explosives, (2) assess fatigue cracking in special parts, (3) track accumulating radiation damage to parts in inaccessible places, and (3) assess growing damage in waste-storage-vault concrete from repeated freeze/thaw cycles, etc. However, most of the research and development of resonance techniques has been on reservoir rocks, for oil and gas exploration, monitoring water resources, and predicting efficacy of carbon sequestration and storage.

J. A. TenCate (✉) · P. A. Johnson
Geophysics Group, Earth and Environmental Sciences, Los Alamos National Laboratory, Los Alamos, NM, USA
e-mail: tencate@lanl.gov; paj@lanl.gov

T. Kundu (ed.), *Nonlinear Ultrasonic and Vibro-Acoustical Techniques for Nondestructive Evaluation*, https://doi.org/10.1007/978-3-319-94476-0_2

Perhaps thinking of a rock as a damaged (inhomogeneous) material is unusual. Yet the "damage" (inhomogeneity) in a rock is its porosity and permeability—directly related to the frack structure at many scales—and it is global and extensive. Rocks, in fact, are a perfect "poster child" for the study of fatigued, cracked, and damaged engineered parts encountered in many NDE applications.

So why resonance *spectroscopy*? For standard resonance inspection techniques, an entire suite of resonance modes is used as a template for correlation or as a standard to compare against; hence measuring a wide spectrum of resonances is best. It is the differences between parts that matter in this case. However, it is often advantageous to focus on one or a small handful of modes instead of a complete set of spectral lines, concentrating on a few frequencies of particular interest. Often, for bulk characterization, just a single acoustic mode will best interrogate an item of interest. For determining global damage throughout a part, lower order (frequency) modes are best suited to quantify differences. However, for particular shapes (e.g., fatigue cracks at a bend in a tube), modes that "sample" a specific region might be better choices. For example, one of the lower frequency eigenmodes of a long thin core, the compressional (Young's) mode, works well for characterizing damage of a core sample taken from an oil and gas wellbore. Rocks are made up of cemented grains, and often poorly cemented, full of "cracks." So, our discussion will now focus on what we can learn from the "global" damage found in rocks knowing that much of what we describe also applies to general NDE, especially fatigue damage.

What modal frequencies are used? The answer, as you might guess, depends on feature size and the size of the part under examination. For example, in most oil and gas bearing sandstones the quartz grains are on the order of 100 microns, so frequencies and wavelengths are chosen where the details of the individual features don't matter and the overall *average* global behavior is sampled. For a standard sandstone rock core (2–3 cm diam and 20–30 cm long), resonance frequencies around a few kHz are often used. For detecting fatigue or stress-corrosion cracking on the radius of a pipe in a nuclear power plant on the other hand, the feature sizes are much smaller and higher frequencies are necessary.

2.2 Nonlinearity in General: Background

So why is *nonlinear* resonant ultrasound spectroscopy (NRUS) useful? Rocks and many other fatigued parts are nonlinear [3] and measuring nonlinearity as an additional variable adds an entirely new and valuable dimension to characterizing damage in a sample. For example, take a right circular cylinder sample of rock and put it in a load frame and make a quasi-static stress-strain curve on it—staying well below the region where any damage starts to occur. If the sample is linear, the stress-strain curve is a straight line—or very nearly so, sample dimensions do matter somewhat. However, the reality is that as the rock is compressed, cracks close up and the rock gets much stiffer; for a material like concrete shown here, the stress-strain curve is not a straight line (see Fig. 2.1). Reword the highlighted

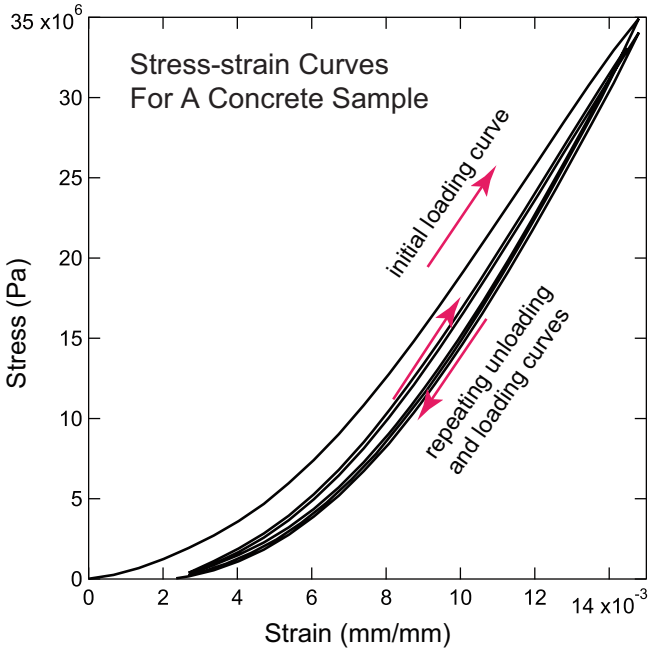

Fig. 2.1 Repeated loading and unloading stress-strain curves for a right circular cylinder of concrete. Note the banana-shape characteristic of hysteresis curves

sentence to read as follows: The amount of nonlinearity measured depends not only on the density of cracks but also some average details of how the cracks close up. The simplest way to model such a rock, for example, is with an ensemble of cracks with some distribution of sizes and spring constants; these cracks turn into very stiff springs when the cracks close [4]. But it's hard to tease out specific knowledge of the crack size distributions or the extent of the fracture networks or to even assess global damage from a simple stress-strain curve. In addition, obtaining or preparing a sample for a quasi-static stress-strain experiment is not always practical for NDE. Furthermore, most rocks like the concrete sample shown and some fatigued metals have some hysteresis as well, i.e., up and down curves are different, depending on the rate. The focus of this chapter is on how Resonant Ultrasound Spectroscopy (RUS) can be used to extract *nonlinearity*.

Large-amplitude waves interacting in various sorts of nonlinear media have been extensively studied. In most fluids a large (or finite) amplitude wave will form a shock (e.g., harmonic distortion and sonic booms). Two waves of different frequencies interacting in a nonlinear medium will produce nonlinear sum and difference frequency waves (e.g., intermodulation distortion, modulation of sound by sound [5]). The physics of nonlinearity and wave interactions in fluids has, in fact, been extensively studied starting back to the development of jet engines [6] to the present [7]. On the other hand, the physics of the nonlinearity and its effect

on wave propagation in (homogeneous and isotropic) solids is more complicated than in fluids but also well studied, an excellent summary can be found in [8]. The physics of nonlinearity in a material like a rock, however, is *not* well understood. A rock is a complicated, imperfect assemblage of various solids often filled with different fluids too; how to model a rock is the subject of a great deal of research even today. A particular experiment of relevance to the relevance of cracks in rocks illustrates this point well.

A square slab of sandstone filled with cracks oriented mostly in one direction was used in a nonlinear two-wave interaction experiment [9] similar to the modulation of sound by sound experiment mentioned above. A low-frequency large-amplitude shear (S) wave was launched *across* the sample at the same time a short small-amplitude compressional (P) wave was launched perpendicularly. The time of flight of the short P wave across the slab was very carefully measured as a function of different launch times. Depending on which part of the shear wave it encountered in its travels through the sample, the compressional wave sped up or slowed down, depending on when it was launched. Notably, this speeding up or slowing down not only depended on launch time but was also different depending on slab/crack orientation. Rotating the sample so the cracks were oriented vertically or horizontally gave different results (Fig. 2.2) shows the overall propagation time delay across the slab for the two different orientations described (as a function of

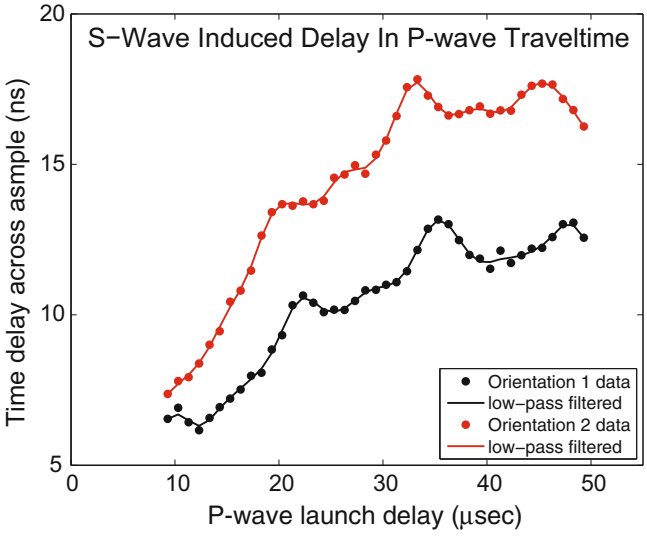

Fig. 2.2 Effects of crack orientation in a sample of Crab Orchard sandstone. A low frequency large amplitude shear wave affects the speed at which a short high frequency compressional wave travels across the sample. The propagation delay due to the shear wave differs depending on (1) which part of the shear wave the compressional wave travels through, (2) the overall softening provided by the shear wave's passage and (3) the sample orientation, parallel to the cracks or perpendicular to them (black and red data, respectively)

P wave launch time). For this experiment, cracks and their orientation matter! A theory of nonlinear wave interaction in a "simple" solid without cracks would have a very difficult time predicting these results, the cracks are an important part of the behavior of this rock.

In a bit of foreshadowing towards discussion further along in this chapter and elsewhere in this book, it's worth noting here that nonlinear measurements based on wave interactions within many solids are also rate dependent. Like the quasi-static stress-strain measurements already discussed, the loading stress-strain curve yields a different nonlinearity than the unloading curve. Even though the experiment is slow enough to be "quasi-static," the *rate* that data is taken matters. Indeed, [10] reports on results where nonlinearity obtained quasi-statically ("DC") yields different values than nonlinear wave (dynamic, "AC") interaction experiments. Similar conclusions are reported in [11], etc. and described in more detail in Chap. 13 of this book. Time dependent effects cannot be ignored in many cases; care is needed in making any nonlinear measurement, a point which will be expanded upon later in this chapter: a rock (or fatigued material for that matter) does not respond instantaneously to the insult of being measured.

2.3 Nonlinear Resonance Techniques: History

So, knowing the advantages and limitations of quasi-static and wave mixing measurements for determining nonlinearity, we now focus on a third, simpler measurement. In so doing, we explore some of the history of how the technique of nonlinear resonance ultrasound spectroscopy—the subject of this chapter—came about. As mentioned before, it has been found that measuring the resonance frequency curve of just one low frequency mode is a very good way to determine bulk nonlinearity and to infer the related bulk damage of a sample. These classic nonlinear spring-mass systems are often described by a Duffing equation [12] with a softening or hardening resonance peak shift with increase of driving amplitude. Sweeping through the lowest resonance frequency of a long thin rock core at successively increasing amplitudes leads to an intriguing result, the resonance frequency depends on driving amplitude and there is a noticeable *drop* in resonance frequency with increasing amplitude. Most rocks, concretes, even many fatigued parts all show this resonance frequency *decrease* with increasing drive amplitude, a *softening nonlinearity* in terms of the Duffing equation model [3]. The physics of the processes at work is likely different for different samples, many mechanisms have been proposed and perhaps more than one process is at play. For example, larger drive amplitudes may be "felt" by more of the rock's interior (e.g., more and more force chains come into play) or perhaps some grain-to-grain bond chemistry is activated by the driving excitation. Large amplitude sound in turn frees up cracks previously bound tightly together and results in a softer rock, at least until those bonds reform or heal. The exact physics of this softening and healing process is, in most cases, still a mystery.

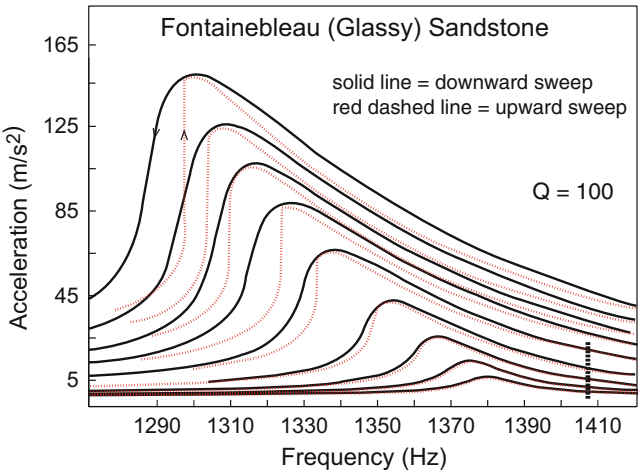

Fig. 2.3 A family of resonance curves for a long thin bar of Fontainebleau sandstone done at a series of increasing drive levels. Sweeps were done upward in frequency (red dashed lines) and then downward in frequency (black lines). The resonance frequency of the sample before these curves were made at around 1405 Hz was the initial resonance frequency of the sample. The downward shift is characteristic of most all rocks

Earlier work by Winkler [13] using single-mode resonance measurements was expanded in a collaborative effort between the Institut Français du Pétrole and Los Alamos National Laboratory and reported in [14]. The samples were all thin-rod geometries, long (>30 cm) and thin (25 mm diam) bars of a variety of rocks, all showed an easy-to-measure softening nonlinearity with increasing amplitude. As an example, an imperfectly-cemented Fontainebleau sandstone sample produced the very striking resonance curve family shown here, adapted from the curves shown in the paper (see Fig. 2.3). Initial attempts were made to quantify the frequency shift as a function of increasing amplitude for many different rock samples and then use that as a new-at-the-time way to characterize damage. Considerable work was done around that time, there was even a patent granted [15] with these ideas, namely to quantify nonlinearity with a resonant bar method. The chief advantage of the NRUS measurement was that it was repeatable, relatively insensitive to changes in room conditions, easy to perform, and it appeared to hold great promise for a wide variety of NDE applications.

2.3.1 Complication: Rate Dependence

All is not so easy however. In [14], after presenting families of nonlinear resonance curves for several different rocks, the *Discussion* section has a paragraph titled "Sweep Rate and Relaxation Effects" where the issue of measurement rate is mentioned. "We have noted that it make take tens of seconds or up to several minutes

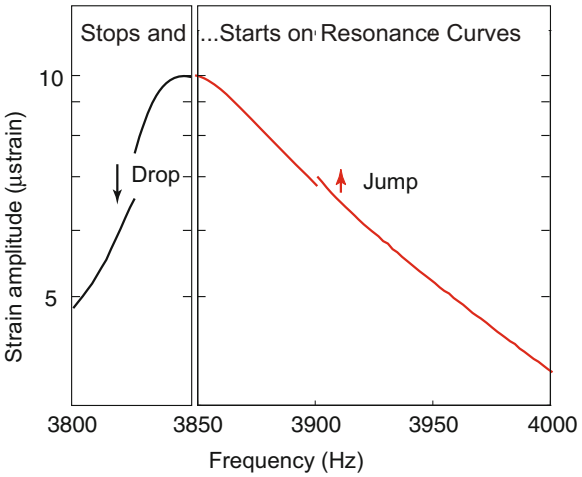

Fig. 2.4 Jumps and drops during 30 s interrupted sweeps for a resonance frequency measurement. Red curve was made sweeping up in frequency, past the peak at 3850 Hz and then stopping at 3900 Hz for 30 s and then continuing. Black curve was made sweeping down in frequency, past the peak and then stopping at 3825 for 30 s and then continuing. Noticeable jumps and drops are visible, demonstrating the resonance frequency of the rock moving around based on its acoustic excitation

for a rock to return to an original "linear" elastic state after a large-amplitude frequency sweep." That rate dependence was then studied extensively in [16]. They observed and reported on many different rate effects. Sweeping frequency upward in a resonance measurement yields a different curve than sweeping downward through the resonance frequency. Stopping partway during a resonance sweep and then continuing leads to a jump in the curve, and the initial resonance curve has a very different shape all following repeating curves (Fig. 2.4). Moreover, very-long-sweep resonance curves look very different than short duration sweeps. Many of these observations are reminiscent of pre-conditioning seen in standard stress-strain measurements and thus the terms *conditioning* and *recovery* of a rock were adopted to describe this rate behavior in rocks. All these rate effects together were dubbed *Slow Dynamics* and describe changes in the rock that take tens of minutes to sometimes hours to stabilize to a new "state" after a perturbation. Measuring slow dynamics has, in fact, been proposed as yet another useful nonlinear measurement in itself and will be discussed elsewhere in this book.

Both rate effects and nonlinearity are easily observed in resonance experiments and in fact, the rate effects are often more of a curse than anything. Can rate effects and nonlinearity be decoupled from one another? If not, using NRUS as a technique to quantify damaged materials is no longer the easy measurement once envisioned. To answer this question [17], made a series of careful resonance experiments at very low strains, trying to precisely see where rate effects start to play a significant role in resonance measurements. What they found (for representative cores of sandstone) is that below source strains of around 5×10^{-7} the samples could be very well described with a simple Duffing equation, i.e., a nonlinear spring and mass system.

Above that strain level rate effects started to become noticeable and really began to dominate at strains of around 10^{-6} for these samples. This result would come as no surprise to [13], where the authors looked at several resonant bars of various rock samples for changes of resonance Q (inverse attenuation) and velocity as a function of amplitude. They too chose 10^{-6} to be the strain where "nonlinearity" began to dominate in reservoir rocks. While the change in the apparent width of the resonance curve (Q) or attenuation at higher amplitudes is due to rate effects and the rate of the sweep measurement—Winkler et al. attributed these effects to Coulomb frictional heating—their results almost exactly match those of [18].

This is important and we summarize its relevance here. The amount of frequency shift as a function of amplitude depends on the rate at which the measurement is made. What this means is that an NRUS measurement is an excellent example of the *Observer Effect.* The very act of making a resonance measurement alters the state of the rock. As the rock approaches its resonance frequency, it experiences higher and higher strains which, in turn, successively softens the rock and drives the resonance frequency down more and more.

To demonstrate how important rate can be, two experiments were performed on the same long bar of sandstone. The first experiment was a sweep done in such a way as to minimally affect the sample; the sweep was done with very short excitation-ON steps with a long wait between steps to allow the sample to "recover" from the acoustic probing. The second experiment was done on the same sample except this time using a very long sweep rate, allowing the state of the sample to fully "equilibrate" (soften) at each new frequency step. The results are shown in Fig. 2.5; at this drive level, the resonance peak frequency varies by 10 Hz; the effects vary

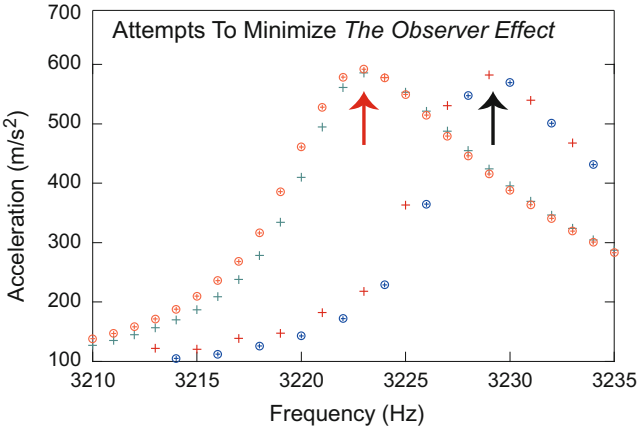

Fig. 2.5 Attempts to eliminate the Observer Effect by altering the way the resonance measurement is made. Leftmost resonance peak data were taken very slowly, dwelling at each datapoint for several hours to allow the rock to fully equilibrate before the next data point. Rightmost resonance peak data were taken quickly, the rock was "pinged" just long along to get a measurement and then allowed to rest for several hours before the next measurement. Upward and downward data (circles and pluses) in both cases are essentially identical given varying room environment conditions over the experiment

but are even more pronounced at higher strains and with different samples. NRUS measurements must therefore be made slowly and carefully to avoid the Observer Effect.

2.3.2 *Complication: Hysteresis*

There is another physics complication that can occur in an NRUS measurement. Quasi-static stress-strain curves for many materials with bulk damage exhibit hysteresis. As already noted, their stress-strain loops are also rate dependent—but the effect is less pronounced than in resonance measurements. Most stress-strain measurements show hysteresis "banana-shaped" curves and are generally repeatable for most practical time scales for most rocks. However, for very long, extended stress-strain measurements, the banana shape thins out and eventually the up and down curves merge and follow the same path [19]. The effect is called *elastic aftereffect* and was seen as early as 1900 by [20] and first discussed carefully in [21] and again by [22]. While hysteresis and elastic aftereffect manifest themselves at strains almost three orders of magnitude higher than an NRUS measurement, hysteresis can still be a concern.

For example, a significant measurement of hysteresis in rocks that is not often noted is reported in [23]. The authors saw evidence of hysteresis (cusping) at strains typical of NRUS measurements, even with a sinusoidal excitation. Cusping simply is not possible with standard models of attenuation/damping with sinusoidal driving, hysteresis must be present, even at the low strains used in their experiments and in a typical NRUS measurement. While the frequencies in their research were also very low, e.g., "seismic" frequencies (tenths of Hz), there has been evidence of cusping in [24] at higher frequencies (1000s of Hz) as well. Some DAE results also suggest cusping may be evident at the ends of the "butterfly" loops typical of those measurements [25]. The exact effect hysteresis has on a typical NRUS measurement is currently part of an ongoing discussion; the effect is mentioned and modeled in [26]. Exactly how hysteresis affects NRUS measurements remains an active area of research.

2.4 Demonstration: Nonlinearity Correlates with Damage

Now that the details—and the pitfalls—of NRUS measurements have been carefully laid out, a demonstration of the value of an NRUS style measurement is in order. Rocks can be thought of as highly globally damaged systems. Concrete too, as it cures and ages, also becomes globally damaged. However, modern NDE problems these days are more likely to encounter damage in, say, Carbon Fiber Reinforced Plastics (CFRP), which frequently delaminate with fatigue or heat cycling. To this end we conclude by reporting on an excellent study by [27] which measured

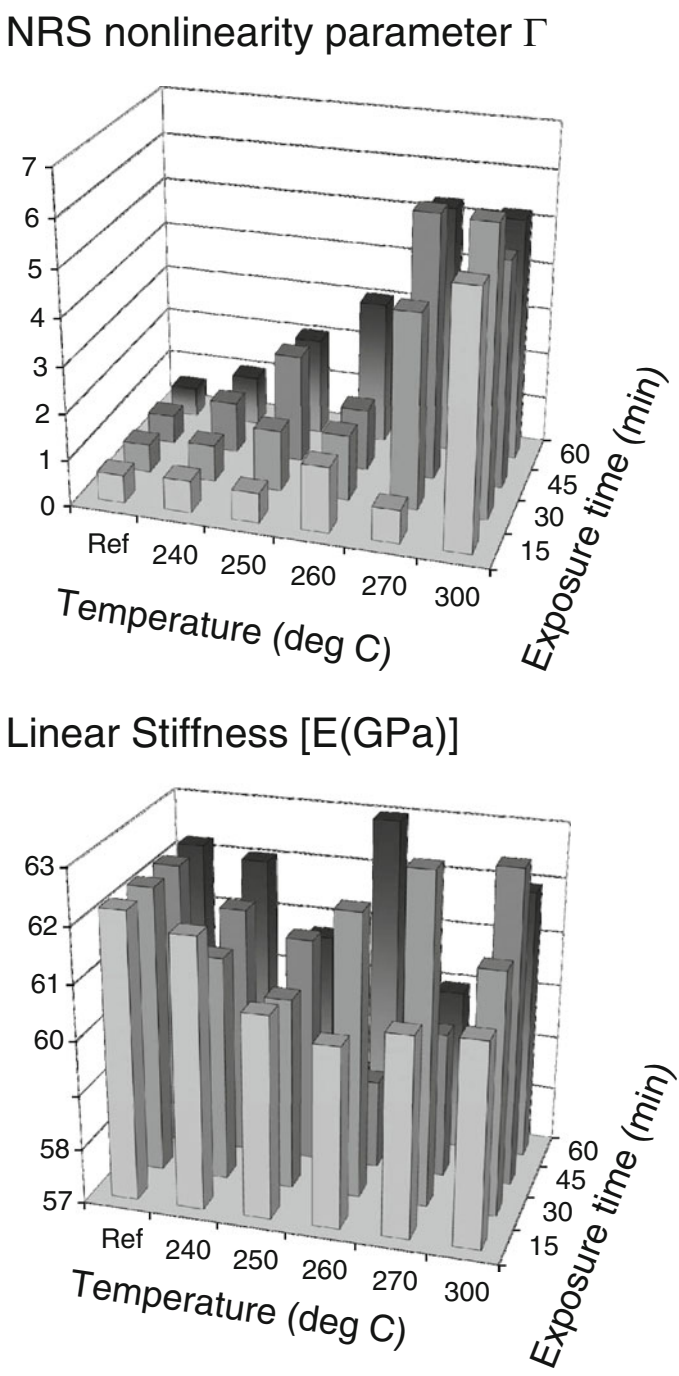

Fig. 2.6 A comparison of (Top) the nonlinear parameter Γ (related to peak shift) as a function of exposure time and temperature and (Bottom) changes of stiffness of the same set of heat damaged composites. As shown later in that paper, nonlinearity correlates well with the actual damage measured in these samples. Taken and adapted from [27]

the nonlinearity of several heat-damaged CFRP plates to see how the nonlinearity correlates with the actual amount of damage.

For this research, the authors used a variation of NRUS they dubbed nonlinear reverberation spectroscopy (NRS). The equivalence of an NRUS technique and NRS is demonstrated in the paper. Several (21) samples of CFRP underwent carefully controlled heat cycling protocols and then each was measured with linear methods (stiffness and quality factory) and compared with NRS. One such result (Fig. 2.6) demonstrates how much more sensitive the nonlinear parameters are than classic acoustic measures like stiffness or quality factor. The samples were then destructively cut apart and an optical imaging technique was used to count crack density. The nonlinear results were plotted as a function of exposure time and temperature and actual crack density. The correlation is excellent and shown in Fig. 8 of that paper. This result was one of the first conclusive results which shows how nonlinearity directly correlates with crack density.

2.5 Conclusions

NRUS is a promising technique for determining the nonlinearity of a sample and in some cases, a direct correlation between nonlinearity and a desired measurable (crack density) has been demonstrated. There seems to be recent renewed interest in NRUS. In [28] the authors seek to apply NRUS to materials where rate effects and hysteresis are negligible. In [26] the authors have modelled everything seen in an experiment, "classical" as well as "nonclassical" nonlinearities. In fact, the new and highly effective approach of dynamic acousto-elasticity [29] is an outgrowth of these resonance measurements (see Chap. 13). Rate effects were once a cause of great concern but there is now much better understanding of how they affect nonlinear measurements. Why has NRUS not been more widely adopted to date? We think that the early patent filed handcuffed a lot of development research at the time and in retrospect was probably a bad idea. In addition rate effects were poorly understood at the time. We feel that now is the time for a closer look at what can be learned from this technique.

Acknowledgements This work was funded by the DOE Office of Basic Energy Sciences and by DOE Fossil Energy. We thank Koen E. A. Van den Abeele and Pierre-Yves Le Bas for data use and discussions.

References

1. J. TenCate, M. Remillieux, J.D. Montalvo, C. Knapp, T.J. Ulrich, T. Saleh, B. Mitchell, *Acoustic Resonance Spectrum Analysis of Rings*, Los Alamos Report (available upon request), LA-UR-17-24940 (2017)

2. A. Migliori, T.W. Darling, Resonant ultrasound spectroscopy for materials studies and nondestructive testing. Ultrasonics **34**, 473–476 (1996)
3. R.A. Guyer, P.A. Johnson, Nonlinear mesoscopic elasticity: Evidence for a new class of materials. Phys. Today **52**(4), 30–36 (1999). https://doi.org/10.1063/1.882648
4. Y. Zheng, R. Gr Maev, I. Yu Solodov, Nonlinear acoustic applications for material characterization: A review. Can. J. Phys. **77**, 927–967 (1999)
5. V.A. Zverev, A.I. Kalachev, Modulation of sound by sound in the interaction of sound waves. Sov. Phys. Acoust. **16**, 204–208 (1970)
6. J. Lighthill, *Waves in Fluids* (Cambridge University Press, Cambridge, 1978)
7. M. F. Hamilton, D. T. Blackstock (eds.), *Nonlinear Acoustics* (Acoustical Society of America, San Diego, 2008)
8. A.N. Norris, in *Finite-Amplitude Waves in Solids in Nonlinear Acoustics*, ed. by M. F. Hamilton, D. T. Blackstock. (Acoustical Society of America, San Diego, 2008)
9. J.A. TenCate, A.E. Malcolm, X. Feng, M.C. Fehler, The effect of crack orientation on the nonlinear interaction of a P wave with an S wave. Geophys. Res. Lett. **43**, 6146–6152 (2016). https://doi.org/10.1002/2016GL069219
10. R.M. D'Angelo, K.W. Winkler, D.L. Johnson, Three wave mixing test of hyperelasticity in highly nonlinear solids: Sedimentary rocks. J. Acoust. Soc. Am. **123**, 622 (2008). https://doi.org/10.1121/1.2821968
11. J. Riviére, G. Renaud, R.A. Guyer, P.A. Johnson, Pump and probe waves in dynamic acousto-elasticity: Comprehensive description and comparison with nonlinear elastic theories. J. Appl. Phys. **114**, 054905 (2013). https://doi.org/10.1063/1.4816395
12. J.J. Stoker, in *Volume II of Pure and Applied Mathematics, a Series of Texts and Monographs*, ed. by H. Bohr, R. Courant, J. J. Stoker. Nonlinear vibrations in mechanical and electrical systems (Interscience, France, 1950)
13. K. Winkler, A. Nur, M. Gladwin, Friction and seismic attenation in rocks. Nature **277**, 528–531 (1979)
14. P.A. Johnson, B. Zinszner, P.N.J. Rasolofosaon, Resonance and elastic nonlinear phenomena in rock. J. Geophys. Res. **101**, 11553–11564 (1996)
15. P.A. Johnson, J.A. TenCate, R.A. Guyer, K.E.A. Van Den Abeele, *Resonant Nonlinear Ultrasound Spectroscopy*, US Patent 6330827, 18 2001
16. J.A. TenCate, T.J. Shankland, Slow dynamics in the nonlinear elastic response of Berea sandstone. Geophys. Res. Lett. **23**, 3019–3022 (1996)
17. D. Pasqualini, K. Heitmann, J.A. TenCate, S. Habib, D. Higdon, P.A. Johnson, Nonequilibrium and nonlinear dynamics in Berea and Fontainebleau sandstones: Low-strain regime. J. Geophys. Res. **112**, B01204 (2007). https://doi.org/10.1029/2006JB004264
18. J.A. TenCate, D. Pasqualini, S. Habib, K. Heitmann, D. Higdon, P.A. Johnson, Nonlinear and nonequilibrium dynamics in geomaterials. Phys. Rev. Lett. **93**, 065501 (2004). https://doi.org/10.1103/Phys Rev Lett.93.065501
19. K.E. Claytor, J.R. Koby, J.A. TenCate, Limitations of Preisach theory: Elastic aftereffect, congruence and end point memory. Geophys. Res. Lett. **36**, L06304 (2009). https://doi.org/10.1029/2008GL036978
20. H. Nagaoka, Elastic constants of rocks and the velocity of seismic waves. Publ. Earthquake Invest. Commit. Foreign Lang. **2**, 47–67 (1900)
21. C. Mack, Plastic flow, creep, and stress relaxation. J. Appl. Phys. **17**, 1101–1107 (1946)
22. D.J. Holcomb, Memory, relaxation, and microfracturing in dilatant rock. J. Geophys. Res. **86**, 6235–6248 (1981)
23. B. McKavanagh, F.D. Stacey, Mechanical hysteresis in rocks at low strain amplitudes and seismic frequencies. Phys. Earth Planet. Int. **8**, 246–250 (1974)
24. P.M. Roberts, *Conference Presentation, LAUR number (searching . . .)*, 2006
25. G. Renaud, J. Rivière, P.-Y. Le Bas, P.A. Johnson, Hysteretic nonlinear elasticity of Berea sandstone at low-vibrational strain revealed by dynamic acousto-elastic testing. Geophys. Res. Lett. **40**, 715–719 (2013). https://doi.org/10.1002/grl.50150

26. M.C. Remillieux, J.A. TenCate, T.J. Ulrich, H.E. Goodman, Propagation of a finite-amplitude elastic pulse in a bar of Berea sandstone: A detailed look at the mechanisms of classical nonlinearity, hysteresis, and nonequilibrium dynamics. J. Geophys. Res. Solid Earth **122**(11), 8892–8909 (2017)
27. K. Van den Abeele, P.Y. Le Bas, B. Van Damme, T. Katkowski, Quantification of material nonlinearity in relation to microdamage density using nonlinear reverberation spectroscopy: Experimental and theoretical study. J. Acoust. Soc. Am. **126**, 963–972 (2009). https://doi.org/10.1121/1.3184583
28. S.K. Chakrapani, D.J. Barnard, Determination of acoustic nonlinear parameter beta using nonlinear resonance ultrasound spectroscopy: Theory and experiment. J. Acoust. Soc. Am. **141**, 919 (2017). https://doi.org/10.1121/1.4976057
29. J. Riviére, P. Shokouhi, R.A. Guyer, P.A. Johnson, A set of measures for the systematic classification of the nonlinear elastic behavior of disparate rocks. J. Geophys. Res. Solid Earth **120**, 1587–1604 (2015). https://doi.org/10.1002/2014JB011718

Chapter 3
Modeling and Numerical Simulations in Nonlinear Acoustics Used for Damage Detection

Pawel Packo, Rafal Radecki, Michael J. Leamy, Tadeusz Uhl, and Wieslaw J. Staszewski

3.1 Introduction

Structural damage detection is frequently accomplished by interrogation with elastic waves [1, 2]. A wave is introduced to the structure by means of a bonded or contact-less source, e.g. a piezoelectric transducer, MEMS device, laser, air-coupled actuator, or other. Along the propagation path the wave interacts with the structure and its features, namely external boundaries, internal material interfaces, defects—e.g., voids, cracks, delaminations—and the medium itself. Consequently, the acquired response carries information on the propagation path that can potentially be extracted for damage detection and localization. As detection of a defect at its early stage is of primary interest, subtle waveform features are sought as damage indicators. This in turn requires high frequency waves and short wavelengths, as the resolution of a damage detection method relates to the ratio of the characteristic damage size to the wavelength. For widely employed wave propagation-based damage detection techniques linearity of the wavefield is assumed and wave–structure interaction phenomena, such as reflection, refraction, and diffraction, are studied to correlate specific signal features with possible defects. Recently, nonlinear properties of wavefields have been intensively studied for their potential use in NDT/SHM. Nonlinear systems break the superposition principle, thus result in more complex wave interaction phenomena. This includes wave–wave and wave–damage nonlinear interactions, internal resonances, generation of higher harmonics, and others [3–11]. Also, in nonlinear systems, it is known that spectral properties

P. Packo (✉) · R. Radecki · T. Uhl · W. J. Staszewski
Department of Robotics and Mechatronics, AGH University of Science and Technology, Kraków, Poland
e-mail: pawel.packo@agh.edu.pl; staszews@agh.edu.pl

M. J. Leamy
School of Mechanical Engineering, Georgia Institute of Technology, Atlanta, GA, USA

T. Kundu (ed.), *Nonlinear Ultrasonic and Vibro-Acoustical Techniques for Nondestructive Evaluation*, https://doi.org/10.1007/978-3-319-94476-0_3

depend on the propagating wave's amplitude, resulting in an even more complex picture of the wavefield. In nonlinear systems the energy is re-distributed in the frequency domain giving rise to additional waves, possibly at different frequencies and wavenumbers, propagating in the structure. Typically, these are shorter waves of higher frequencies that are appealing as a tool for structural health evaluation due to increased spatial resolution and sensitivity to damage.

Complex dynamic transient phenomena need to be investigated and thoroughly understood for their application in damage detection and structural state evaluation. Due to the nature of the nonlinear wavefields, it is impractical or impossible to analyze engineering problems through analytical studies. When complex geometries are considered, even linear elastic wave propagation cases cannot be solved or even described analytically. Experimental testing, on the other hand, is also difficult—without prior theoretical studies—since many other sources of nonlinearities can superimpose and contribute to the response. Hence, it is a common practice to employ numerical simulations for studying underlying wave interactions, perform parameter search, and to design and develop new inspection techniques [12, 13].

The spatial and temporal character of wave propagation, namely wave speeds and wavelengths, determine the spatio-temporal requirements for a numerical method. These two aspects for a modeling method translate into large model sizes and long analysis time that must be handled for effective and reliable simulations. Also, when dealing with wave propagation problems, one need to obviously consider time-dependent problems and numerical time integration methods, in addition to spatial discretization schemes.

Among all time integration schemes, namely implicit and explicit techniques, the latter has been widely adopted and employed for wave propagation problems. The solution procedure based on the explicit time integration requires operations on the mass matrix only. Further, if the mass lumping is employed—as it is frequently the case for wave propagation—the mass matrix inversion reduces to independent inversion operations on the elements of the diagonal, hence decoupling the solution from other DOFs at the same time step. Although not perfectly accurate and conditionally stable, the explicit time integration combined with the mass lumping procedure is widely used due to the following reasons. First, decoupling DOFs makes the operations independent when advancing the solution. As a consequence, extremely efficient massively parallel processing procedures can be adopted for simulations [14, 15]. Second, the solution procedure does not require actual matrix inversion (no stiffness matrix inversion) since the mass-related operations can be carried out element-wise. Next, high wave propagation speeds need dense time stepping, hence the time step limitation due to the stability condition is not a serious drawback. As wave propagation simulations involve a number of time steps, the efficiency becomes critical and the number of operations performed per time step should be limited and simplified. This becomes even more important for nonlinear problems where special procedures are required for implicit advancing in time, while the explicit approach retains certain degree of its original simplicity. Nevertheless, despite computational effort, the implicit time integration is occasionally considered for wave propagation as it possesses favorable numerical properties [16, 17].

There is a wide selection of numerical procedures that can be employed for space discretization in wave propagation problems. Historically first, and one of the most widely utilized, are methods based on finite differences (FD) [18]. In the FD approach the governing PDEs are transformed into a set of algebraic equations by approximating partial derivatives with the finite difference formulas. FDs are among the most effective and simple methods, however their solutions may suffer from energy conversation violation, difficulties in representing complex geometries through regular grid of points and other. An improvement over classical FDs was with the velocity–stress finite differences [19] where the staggered grid concept was combined with a mixed variable (stresses and velocities) approach. A similar concept of separation of variables has been employed in [20] where the elastodynamic finite integration technique (EFIT) was proposed. The EFIT belongs to the finite volume methods and improves over the standard FDs. Specifically, the integration over the control volume helps in the energy conservation of a scheme. As a drawback the fact that velocities and stresses are defined in different spatial locations, making the boundary conditions definition cumbersome, can be mentioned. Another spin–off of the finite difference approach was the local interaction simulation approach (LISA) [14, 21]. The LISA employs a special procedure for interface treatment through the stress continuity imposition, improving modeling of wave propagation and interaction with interfaces of two media with drastically different material properties. As LISA departs from the governing PDEs and introduces the discretization procedure to arrive at the iteration equations defining the local interactions, the method can be seen as a top-down methodology. An opposite approach, termed the bottom-up strategy, yields when local rules, applied to an elementary unit (point, element, cell etc.), build up and lead to the global structural response [22]. Such a method was employed in [23, 24] as the cellular automata for elastodynamics (CAFE) method. In CAFE, the wave propagation problem is seen from the cellular automaton perspective and the state transition rules are constructed through neighboring cells and fundamental principles of mechanics.

Most frequently, the above-outlined approaches for elastic waves propagation simulations involve only closest vicinity, i.e. nearest neighboring, of points or cells, to construct approximation. Hence, those can be seen as the local computational models [25]. Another important group of methods, that under certain conditions can be formulated as local ones, are finite element (FE) based approaches [26, 27]. Apart from the classical FE formulations for wave propagation, employing the explicit time integration procedure, a number of other concepts have been developed. Combining the FE spatial discretization and interpolation techniques with the fundamental solutions, boundary element method has been proposed [28]. Boundary elements reduce the problem dimensionality by one, hence are attractive for wave propagation simulation. However, when the volume to surface ratio becomes small and nonlinear problems are considered, the BEM performance drops significantly. Well suited for numerical studies of elastic waves propagation are spectral element methods. There are two substantially different approaches to the spectral formulation for FE as outlined in [29] and [30]. As the first method involves special derivation of shape functions and resembles the classical FE, it is frequently

termed a higher order FE technique. The latter [30] employs Fourier transform of a problem into the spectral domain and constructs dynamic shape functions dependent on wavenumbers. The spectral element method formulated in [30] has been shown effective for linear 1-D and 2-D systems. For complex domains and nonlinear problems spectral formulations applicability requires further developments [31].

Numerical models are discrete systems where one wants to obtain approximation to wave propagation in continuous media. Precisely, starting from a set of PDEs, subsequent transformations are applied in order to arrive at an algebraic formulation, convenient for computer implementation. This fundamental difference is reflected in model response in the form of spurious oscillations, wave velocity and wavelength errors, artificial modes, and other [18, 23, 32]. Those errors are further amplified when nonlinear systems are considered. Spectral properties of numerical models—dispersion and excitability properties—clearly differ from exact solutions [32, 33], hence detailed analysis of numerical spectral properties and their nonlinear influence on the results is of particular interest.

Besides the general numerical procedures adopted for continua, various techniques have been proposed for damage modeling. In general, the physical understanding of nonlinear mechanisms involved in classical and non-classical methods used for damage detection is very important to separate reliably damage-related nonlinearities from other nonlinear effects (e.g., material nonlinearity, measurement chain). Therefore modeling of damage is very important but not easy. The major difficulty relates to the facts that similar nonlinear effects exhibited by damage can be manifested by different physical mechanism and vice versa. For example, energy dissipation may result from frictional, hysteretic, or non-classical LG phenomena. Hysteresis in turn involves both elasticity and dissipation, and could be linear or nonlinear. In addition, various nonlinear effects can be observed experimentally when nonlinear ultrasonic/acoustic methods are used for damage detection, as illustrated in [10]. Physical mechanisms behind nonlinear ultrasonic/acoustic damage–wave interactions are scale-dependent, strain-dependent and involve different types of elastic and dissipative effects, as explained in [34]. Research studies of classical and non-classical phenomena in solids have a long history and involved various physical models of damage, as reviewed in [34]. Altogether, these models can be classified into five major groups: (1) classical nonlinear elasticity; (2) classical nonlinear crack and crack-wave models; (3) hysteretic models; (4) classical contact models; (5) non-classical dissipation. A summary of these models is given in Table 3.1.

As one can notice, there are a number of approaches to model analytically the damage behavior and its interaction with the propagating wave. Moreover, there exist methods predicting damage initiation and propagation in various materials [52], however their discussion is beyond the scope of this chapter. In the following, only numerical methods related to wave–damage interactions will be outlined. The main focus is directed to the damage models implemented in two major numerical frameworks—i.e., FE and FD. Such approaches are considered as, penalty method, stick-slip contact or element activation/deactivation in order to imitate the clapping or breathing behavior of the damage surfaces.

Table 3.1 Analytical approaches used for damage modeling [34]

Models	Model examples and remarks	Examples of references
Classical nonlinear elasticity	Higher-order elements in the Hooke's law (nonlinear stress–strain, quadratic and cubic stiffness nonlinearity; used to model material, nonlinearity; not applicable to nonlinear phenomena in rocks)	[35, 36]
Classical nonlinear crack and crack-wave interaction	Bi-linear stiffness	[37]
	Breathing crack	[38–40]
	"Mechanical diode"—acoustic waves rectification	[41]
	Clapping	[42, 43]
	Contact Acoustic Nonlinearity (CAN) (relates to stiffness asymmetry; simplified models from the physical point of view; can take a form of an oscillator or relaxator—different force to close and open cracks; can be used to model adhesive, bond defects)	[41]
Hysteretic models	Elastic and inelastic hysteretic nonlinearity	[44, 45]
	Quasi-static (frequency-independent) model—dependence of the modulus on the strain-rate sign	[36]
	Phenomenological models—e.g., the Preisach-Mayergoyz (PM) model (always associated with energy dissipation; generates odd harmonics; can explain amplitude-dependent frequency shift and modulations; used to model nonlinearities in rocks)	[46, 47]
Classical contact models	Hertzian contact	[48]
	Rough-surface contact (involves contact of crack faces; can be used to model partial contact; can involve adhesion forces)	[48, 49]
Non-classical dissipation	Solid containing high-compliant inclusions	[50]
	The Luxemburg-Gorki effect (observed mainly in mesoscopic materials; often an addition to the hysteretic nonlinearity)	[51]

From the numerical viewpoint the two distinct types of nonlinearities, namely distributed and localized, require different treatment. The distributed nonlinearities affect the governing PDEs, and consequently the iteration equations of a model, in the global sense. Localized nonlinear wave interactions, typically related to damage, are reflected through additional or modified equations in a predefined part of the model. These two approaches have direct consequences to the implementation strategy of a numerical scheme.

In this chapter the discussion of modeling and numerical simulations for nonlinear acoustics will be separated into two main parts. First, the general theory for waves in nonlinear media will be presented, followed by the discussion of widely used methods for wave propagation. Besides the finite element method, recalled for completeness, the local computational approach for constructing approximate solutions will be briefly discussed. This will contribute to the idea of distributed nonlinearities that are of interest in nonlinear wave propagation. Next, the localized sources of nonlinear effects will be addressed. These are typically related to defects that interact nonlinearly with the wavefield through contact and friction, such as kissing bonds and breathing cracks. Local sources of nonlinear interactions deform elastic waves signals differently than the distributed sources.

3.2 Nonlinear Elastic Wave Propagation Problem Formulation

This section outlines the fundamental equations relevant to the nonlinear elastic wave propagation problem in continuous media. The following equations set serves as a basis for subsequent discretization and leads to various numerical models. Extensive discussions and theoretical derivations for nonlinearly elastic dynamical problems can be found in literature, see, e.g., [3, 35, 53–55].

In the following, two fundamental descriptions of the problem will be introduced, namely seen from the Eulerian—where the equilibrium is most generally formulated—and Lagrangian—which is the most convenient for the numerical implementation. Hence, two coordinate frames are distinguished. The deformed material configuration is described by the current coordinates $\boldsymbol{x}$ while the original, undeformed state by $\boldsymbol{X}$. The deformation of a solid is therefore described by a displacement field $\boldsymbol{U}(\boldsymbol{X}, t)$ relating the undeformed material point $\boldsymbol{X}$ with its new, deformed state $\boldsymbol{x}$ through the relation $\boldsymbol{x} = \boldsymbol{X} + \boldsymbol{U}(\boldsymbol{X}, t)$. The two states, namely deformed and undeformed, are related through the deformation gradient tensor $\boldsymbol{F} = \frac{\partial \boldsymbol{x}}{\partial \boldsymbol{X}} = \boldsymbol{I} + \frac{\partial \boldsymbol{U}}{\partial \boldsymbol{X}}$.

For the most general description, the Cauchy stress tensor—denoted by $\boldsymbol{\sigma}$ and describing the force acting on unit area in the deformed configuration—will be employed. Please note that other stress measures, combining forces in the deformed configuration and the undeformed unit area (the first Piola-Kirchoff stress tensor, $\boldsymbol{P}$) and forces in the undeformed configuration acting on the undeformed unit area

(the second Piola-Kirchoff stress tensor, $\boldsymbol{\Sigma}$) can be employed in the description of the equilibrium of a solid. From Eulerian perspective, the elastodynamic equation of an infinitesimal volumetric element yields

$$\rho \frac{D\dot{\boldsymbol{x}}}{Dt} = \nabla \cdot \boldsymbol{\sigma} \tag{3.1}$$

where ρ is the density in the deformed configuration, $\dot{\boldsymbol{x}} = \dot{\boldsymbol{x}}(\boldsymbol{x}, t)$ denotes the particle velocity as a function of Eulerian coordinates and time, and ∇ introduces differentiation with respect to the deformed coordinates $\boldsymbol{x}$, i.e. $\nabla = \frac{\partial}{\partial \boldsymbol{x}}$. In Eq. (3.1), $\frac{D()}{Dt}$ is used for the material (substantial or convective) derivative.

In solid mechanics, however, the Lagrangian description—referring to fixed *material* rather than fixed *spatial* points—is preferred. In order to re-formulate Eq. (3.1) in the Lagrangian framework, the following observations are made. First, note that the velocity $\dot{\boldsymbol{x}} = \frac{\partial \boldsymbol{U}(\boldsymbol{X},t)}{\partial t}$, according to the specified form of the deformation. Next, the material derivative in Eq. (3.1) can be written as

$$\frac{D\dot{\boldsymbol{x}}(\boldsymbol{x}, t)}{Dt} = \frac{\partial^2 \boldsymbol{U}(\boldsymbol{X}, t)}{\partial t^2} \tag{3.2}$$

where the convective part of the material derivative is zero due to the assumed form of deformation that does not depend on the deformed coordinates $\boldsymbol{x}$.

The right-hand side of Eq. (3.1) can be expressed in terms of the undeformed configuration through either the first or second Piola–Kirchoff stress tensor, $\boldsymbol{P}$ or $\boldsymbol{\Sigma}$, respectively. Despite the first Piola–Kirchoff stress is employed [3, 56] more frequently, $\boldsymbol{P}$ is a non-symmetric tensor. Hence, for convenience of numerical implementation, the general formulation through the second Piola–Kirchoff stress, $\boldsymbol{\Sigma}$, will be given for completeness. The stress tensors $\boldsymbol{\sigma}$, $\boldsymbol{P}$, and $\boldsymbol{\Sigma}$ are related by

$$\boldsymbol{\sigma} = \frac{\rho}{\rho_X} \boldsymbol{P} \boldsymbol{F}^T = \frac{\rho}{\rho_X} \boldsymbol{F} \boldsymbol{\Sigma} \boldsymbol{F}^T \tag{3.3}$$

where ρ_X is the material density in the undeformed configuration. Using Eqs. (3.2) and (3.3) in Eq. (3.1) gives

$$\rho_X \frac{\partial^2 \boldsymbol{U}}{\partial t^2} = \nabla_X \cdot \boldsymbol{P} \tag{3.4}$$

or, equivalently

$$\rho_X \frac{\partial^2 \boldsymbol{U}}{\partial t^2} = \nabla_X \cdot \left(\boldsymbol{F} \cdot \boldsymbol{\Sigma} \right) \tag{3.5}$$

In Eqs. (3.4) and (3.5) spatial derivatives are taken with respect to the undeformed coordinates $\boldsymbol{X}$. Please note that the only difference between Eqs. (3.4) and (3.5) is in the stress definition. Both stress measures, $\boldsymbol{P}$ and $\boldsymbol{\Sigma}$, refer to the undeformed

configuration, however the former takes the force in the deformed state, while the latter in the undeformed configuration.

In addition to the elastodynamic equation, Eq. (3.4) or (3.5), the constitutive equation—relating stresses and strains, and the geometrical relation between strains and displacements are required for a complete wave propagation problem definition. When wave propagation in nonlinear media is considered, it is convenient to adopt the hyper-elastic framework—allowing for large strains and large displacements—and further introduce certain simplifications in order to develop efficient and reliable numerical models.

For a nonlinearly elastic problem, the strain is taken in the most general form of the Green–Lagrange tensor

$$\boldsymbol{E} = \frac{1}{2}\left(\boldsymbol{F}^{\boldsymbol{T}} \cdot \boldsymbol{F} - \boldsymbol{I}\right) \tag{3.6}$$

or, in the component form

$$E_{ij} = \frac{1}{2}\left(\frac{\partial U_i}{\partial X_j} + \frac{\partial U_j}{\partial X_i} + \frac{\partial U_k}{\partial X_i}\frac{\partial U_k}{\partial X_j}\right) \tag{3.7}$$

accounting for large displacements and rotations, and being suitable for nonlinear strain–stress relationships. More important, however, from the nonlinear wave propagation point of view—the quadratic terms in Eq. (3.6) need to be retained for consistency with the higher order terms in the constitutive equation.

The constitutive relationship—for path-independent deformations—is conveniently derived from the strain energy density function W written as a function of the Green–Lagrange strain tensor or the deformation gradient tensor components, $W = W(\boldsymbol{E})$ or $W = W(\boldsymbol{F})$, where the two forms are related by Eq. (3.6). The strain energy density is written up to the desired order of expansion in strains (or deformation gradient components) and—for the case of retaining elastic constants up to fourth order—is given by [7, 35]

$$W = \frac{\lambda}{2}I_1^2 + \mu I_2 + \frac{A}{3}I_3 + BI_1I_2 + \frac{C}{3}I_1^3 + EI_1I_3 + FI_1^2I_2 + GI_2^2 + HI_1^4 \tag{3.8}$$

where I_1, I_2, and I_3 denote the strain tensor invariants, λ and μ the Lamé constants, and $A - H$ denote higher order elastic constants. By substituting strain invariant expressions in Eq. (3.8), the strain energy density formula is given in terms of deformation gradient tensor components, $W = W(\boldsymbol{F})$.

Please note that the strain energy density given by Eq. (3.8) retains the fourth order terms in displacements (and higher). Hence, employing the general formula for the strain, Eq. (3.6), where quadratic terms are included, is necessary for consistency—despite small but finite strains and displacements analyzed in nonlinear wave propagation problems.

The constitutive relation for a general nonlinear material is then obtained by differentiating the strain energy density function with respect to the strain tensor components $\frac{\partial W(\boldsymbol{E})}{\partial \boldsymbol{E}}$ and for a 2-D space yields

$$\begin{aligned}\Sigma_{11} = {} & (\lambda + 2\mu)E_{11} + \lambda E_{22} \\ & + (A + 3B + C)E_{11}^2 + (B + C)E_{22}^2 + (A + 2B)E_{12}^2 + 2(B + C)E_{11}E_{22} \\ & + 4(E + F + G + H)E_{11}^3 + (E + 2F + 4H)\left(E_{22}^3 + 3E_{11}^2 E_{22}\right) \\ & + 4(F + G + 3H)E_{11}E_{22}^2 + \left[(6E + 4F + 8G)E_{11} + (4F + 6E)E_{22}\right]E_{12}^2\end{aligned} \tag{3.9}$$

$$\begin{aligned}\Sigma_{22} = {} & (\lambda + 2\mu)E_{22} + \lambda E_{11} \\ & + (A + 3B + C)E_{22}^2 + (B + C)E_{11}^2 + (A + 2B)E_{12}^2 + 2(B + C)E_{11}E_{22} \\ & + 4(E + F + G + H)E_{22}^3 + (E + 2F + 4H)\left(E_{11}^3 + 3E_{11}E_{22}^2\right) \\ & + 4(F + G + 3H)E_{11}^2 E_{22} + \left[(6E + 4F)E_{11} + (6E + 4F + 8G)E_{22}\right]E_{12}^2\end{aligned} \tag{3.10}$$

$$\begin{aligned}\Sigma_{12} = {} & 2\mu E_{12} + (A + 2B)(E_{11} + E_{22})E_{12} \\ & + (3E + 2F + 4G)\left(E_{11}^2 + E_{22}^2\right)E_{12} + (6E + 4F)E_{11}E_{22}E_{12} + 8GE_{12}^3\end{aligned} \tag{3.11}$$

and $\Sigma_{21} = \Sigma_{12}$ due to the symmetry of $\boldsymbol{\Sigma}$. Please note that Eqs. (3.9)–(3.11) give the second Piola–Kirchoff stress tensor components, since $\boldsymbol{\Sigma}$ and $\boldsymbol{E}$ are a work-conjugate pair. Analogously, for the first Piola-Kirchoff stress tensor and the deformation gradient tensor, $\boldsymbol{P}$ and $\boldsymbol{F}$, the stresses are calculated from $\frac{\partial W(\boldsymbol{F})}{\partial \boldsymbol{F}}$ and for a 2-D medium read

$$\begin{aligned}P_{11} = {} & (\lambda + 2\mu)\frac{\partial U_1}{\partial X_1} + \lambda\frac{\partial U_2}{\partial X_2} + \left(\frac{3}{2}\lambda + 3\mu + A + 3B + C\right)\left(\frac{\partial U_1}{\partial X_1}\right)^2 \\ & + \left(\frac{1}{2}\lambda + B + C\right)\left(\frac{\partial U_2}{\partial X_2}\right)^2 \\ & + \left(\frac{1}{2}\lambda + \mu + \frac{1}{4}A + \frac{1}{2}B\right)\left[\left(\frac{\partial U_2}{\partial X_1}\right)^2 + \left(\frac{\partial U_1}{\partial X_2}\right)^2\right] \\ & + \left(\mu + \frac{1}{2}A + B\right)\frac{\partial U_1}{\partial X_2}\frac{\partial U_2}{\partial X_1} + (\lambda + 2B + 2C)\frac{\partial U_1}{\partial X_1}\frac{\partial U_2}{\partial X_2}\end{aligned}$$

$$
\begin{aligned}
&+\left(\frac{1}{2}\lambda+\mu+2A+6B+2C+4E+4F+4G+4H\right)\left(\frac{\partial U_1}{\partial X_1}\right)^3\\
&+(B+C+E+2F+4H)\left(\frac{\partial U_2}{\partial X_2}\right)^3\\
&+\left(\frac{1}{2}\lambda+\mu+\frac{5}{4}A+\frac{7}{2}B+C+\frac{3}{2}E+F+2G\right)\\
&\times\frac{\partial U_1}{\partial X_1}\left[\left(\frac{\partial U_2}{\partial X_1}\right)^2+\left(\frac{\partial U_1}{\partial X_2}\right)^2\right]\\
&+\left(\frac{1}{2}A+2B+C+\frac{3}{2}E+F\right)\frac{\partial U_2}{\partial X_2}\left[\left(\frac{\partial U_2}{\partial X_1}\right)^2+\left(\frac{\partial U_1}{\partial X_2}\right)^2\right]\\
&+(\mu+A+2B+3E+2F)\frac{\partial U_1}{\partial X_2}\frac{\partial U_2}{\partial X_1}\frac{\partial U_2}{\partial X_2}\\
&+\left(\frac{3}{2}A+3B+3E+2F+4G\right)\frac{\partial U_1}{\partial X_1}\frac{\partial U_1}{\partial X_2}\frac{\partial U_2}{\partial X_1}\\
&+\left(\frac{1}{2}\lambda+2B+2C+4F+4G+12H\right)\frac{\partial U_1}{\partial X_1}\left(\frac{\partial U_2}{\partial X_2}\right)^2\\
&+(3B+3C+3E+6F+12H)\frac{\partial U_2}{\partial X_2}\left(\frac{\partial U_1}{\partial X_1}\right)^2
\end{aligned}
\tag{3.12}
$$

$$
\begin{aligned}
P_{22}=&(\lambda+2\mu)\frac{\partial U_2}{\partial X_2}+\lambda\frac{\partial U_1}{\partial X_1}+\left(\frac{1}{2}\lambda+B+C\right)\left(\frac{\partial U_1}{\partial X_1}\right)^2\\
&+\left(\frac{1}{2}\lambda+\mu+\frac{1}{4}A+\frac{1}{2}B\right)\left[\left(\frac{\partial U_1}{\partial X_2}\right)^2+\left(\frac{\partial U_2}{\partial X_1}\right)^2\right]\\
&+(\lambda+2B+2C)\frac{\partial U_1}{\partial X_1}\frac{\partial U_2}{\partial X_2}\\
&+\left(\frac{3}{2}\lambda+3\mu+A+3B+C\right)\left(\frac{\partial U_2}{\partial X_2}\right)^2+\left(\mu+\frac{1}{2}A+B\right)\frac{\partial U_1}{\partial X_2}\frac{\partial U_2}{\partial X_1}\\
&+\left(\frac{1}{2}\lambda+\mu+2A+6B+2C+4E+4F+4G+4H\right)\left(\frac{\partial U_2}{\partial X_2}\right)^3\\
&+(B+C+E+2F+4H)\left(\frac{\partial U_1}{\partial X_1}\right)^3\\
&+\left(\frac{1}{2}\lambda+2B+2C+4F+4G+12H\right)\left(\frac{\partial U_1}{\partial X_1}\right)^2\frac{\partial U_2}{\partial X_2}
\end{aligned}
$$

$$
\begin{aligned}
&+\left(\frac{1}{2}A+2B+C+\frac{3}{2}E+F\right)\frac{\partial U_1}{\partial X_1}\left[\left(\frac{\partial U_1}{\partial X_2}\right)^2+\left(\frac{\partial U_2}{\partial X_1}\right)^2\right]\\
&+(\mu+A+2B+3E+2F)\frac{\partial U_1}{\partial X_1}\frac{\partial U_1}{\partial X_2}\frac{\partial U_2}{\partial X_1}\\
&+\left(\frac{3}{2}A+3B+3E+2F+4G\right)\frac{\partial U_1}{\partial X_2}\frac{\partial U_2}{\partial X_1}\frac{\partial U_2}{\partial X_2}\\
&+(3B+3C+3E+6F+12H)\frac{\partial U_1}{\partial X_1}\left(\frac{\partial U_2}{\partial X_2}\right)^2+\left(\frac{1}{2}\lambda+\mu+\frac{5}{4}A\right.\\
&\left.+\frac{7}{2}B+C+\frac{3}{2}E+F+2G\right)\left[\left(\frac{\partial U_1}{\partial X_2}\right)^2+\left(\frac{\partial U_2}{\partial X_1}\right)^2\right]\frac{\partial U_2}{\partial X_2}
\end{aligned}
\tag{3.13}
$$

$$
\begin{aligned}
P_{12}=&\,\mu\left(\frac{\partial U_2}{\partial X_1}+\frac{\partial U_1}{\partial X_2}\right)+\left(\mu+\frac{1}{2}A+B\right)\left(\frac{\partial U_2}{\partial X_1}\frac{\partial U_2}{\partial X_2}+\frac{\partial U_1}{\partial X_1}\frac{\partial U_2}{\partial X_1}\right)\\
&+\left(\lambda+2\mu+\frac{1}{2}A+B\right)\left(\frac{\partial U_1}{\partial X_2}\frac{\partial U_2}{\partial X_2}+\frac{\partial U_1}{\partial X_1}\frac{\partial U_1}{\partial X_2}\right)\\
&+\left(\frac{1}{4}A+\frac{1}{2}B+G\right)\left(\frac{\partial U_2}{\partial X_1}\right)^3\\
&+\left(\frac{1}{2}\lambda+\mu+\frac{5}{4}A+\frac{7}{2}B+C+\frac{3}{2}E+F+2G\right)\\
&\times\frac{\partial U_1}{\partial X_2}\left[\left(\frac{\partial U_1}{\partial X_1}\right)^2+\left(\frac{\partial U_2}{\partial X_2}\right)^2\right]\\
&+\left(\frac{3}{4}A+\frac{3}{2}B+\frac{3}{2}E+F+2G\right)\frac{\partial U_2}{\partial X_1}\left[\left(\frac{\partial U_1}{\partial X_1}\right)^2+\left(\frac{\partial U_2}{\partial X_2}\right)^2\right]\\
&+\left(\frac{1}{2}\lambda+\frac{1}{2}A+B+3G\right)\frac{\partial U_1}{\partial X_2}\left(\frac{\partial U_2}{\partial X_1}\right)^2\\
&+\left(\frac{3}{4}A+\frac{3}{2}B+3G\right)\frac{\partial U_2}{\partial X_1}\left(\frac{\partial U_1}{\partial X_2}\right)^2\\
&+\left(\frac{1}{2}\lambda+\mu+\frac{1}{2}A+B+G\right)\left(\frac{\partial U_1}{\partial X_2}\right)^3\\
&+(\mu+A+2B+3E+2F)\frac{\partial U_1}{\partial X_1}\frac{\partial U_2}{\partial X_1}\frac{\partial U_2}{\partial X_2}\\
&+(A+4B+2C+3E+2F)\frac{\partial U_1}{\partial X_1}\frac{\partial U_1}{\partial X_2}\frac{\partial U_2}{\partial X_2}
\end{aligned}
\tag{3.14}
$$

$$
\begin{aligned}
P_{21} = {} & \mu\left(\frac{\partial U_2}{\partial X_1} + \frac{\partial U_1}{\partial X_2}\right) + \left(\mu + \frac{1}{2}A + B\right)\left(\frac{\partial U_1}{\partial X_1}\frac{\partial U_1}{\partial X_2} + \frac{\partial U_1}{\partial X_2}\frac{\partial U_2}{\partial X_2}\right) \\
& + \left(\lambda + 2\mu + \frac{1}{2}A + B\right)\left(\frac{\partial U_1}{\partial X_1}\frac{\partial U_2}{\partial X_1} + \frac{\partial U_2}{\partial X_1}\frac{\partial U_2}{\partial X_2}\right) \\
& + \left(\frac{1}{4}A + \frac{1}{2}B + G\right)\left(\frac{\partial U_1}{\partial X_2}\right)^3 \\
& + \left(\frac{1}{2}\lambda + \mu + \frac{5}{4}A + \frac{7}{2}B + C + \frac{3}{2}E + F + 2G\right) \\
& \times \frac{\partial U_2}{\partial X_1}\left[\left(\frac{\partial U_1}{\partial X_1}\right)^2 + \left(\frac{\partial U_2}{\partial X_2}\right)^2\right] \\
& + \left(\frac{3}{4}A + \frac{3}{2}B + \frac{3}{2}E + F + 2G\right)\frac{\partial U_1}{\partial X_2}\left[\left(\frac{\partial U_1}{\partial X_1}\right)^2 + \left(\frac{\partial U_2}{\partial X_2}\right)^2\right] \\
& + \left(\frac{1}{2}\lambda + \frac{1}{2}A + B + 3G\right)\frac{\partial U_2}{\partial X_1}\left(\frac{\partial U_1}{\partial X_2}\right)^2 \\
& + \left(\frac{3}{4}A + \frac{3}{2}B + 3G\right)\frac{\partial U_1}{\partial X_2}\left(\frac{\partial U_2}{\partial X_1}\right)^2 \\
& + \left(\frac{1}{2}\lambda + \mu + \frac{1}{2}A + B + G\right)\left(\frac{\partial U_2}{\partial X_1}\right)^3 \\
& + (\mu + A + 2B + 3E + 2F)\frac{\partial U_1}{\partial X_1}\frac{\partial U_1}{\partial X_2}\frac{\partial U_2}{\partial X_2} \\
& + (A + 4B + 2C + 3E + 2F)\frac{\partial U_1}{\partial X_1}\frac{\partial U_2}{\partial X_1}\frac{\partial U_2}{\partial X_2}
\end{aligned}
\tag{3.15}
$$

Substituting Eqs. (3.12)–(3.15) into Eq. (3.4) gives the elastodynamic equation for wave propagation in nonlinear, hyper-elastic media, in terms of displacements. Analogously, using Eq. (3.6) in Eqs. (3.9)–(3.11), and the results in Eq. (3.5), yields nonlinear wave propagation problem expressed in terms of the second Piola–Kirchoff stress.

For guided wave propagation in bounded media, the elastodynamic equation is supplemented by a set of boundary conditions. In general, two types of boundary conditions (and their combinations) are met, namely, natural and essential boundary conditions. For mechanical problems, these types of boundary conditions refer to prescribed tractions and prescribed displacements, i.e.

$$
\boldsymbol{\sigma} \cdot \boldsymbol{n} = \hat{\boldsymbol{t}}, \quad \text{on} \quad \Omega_t \quad \text{and} \quad \boldsymbol{x} = \hat{\boldsymbol{x}}, \quad \text{on} \quad \Omega_x \tag{3.16}
$$

For the particular case of Lamb waves—of wide practical importance—and 2-dimensional media, stress-free boundary conditions for two parallel surfaces are

considered such that

$$\sigma_{ij} n_j = 0, \quad \text{at} \quad y = \pm h, \quad i, j = 1, 2; \tag{3.17}$$

where $\boldsymbol{n} = [0, \ \pm 1]^T$ is the horizontal surface outward pointing normal and the layer enclosed by the two surfaces has thickness $2h$.

3.3 Numerical Models for Wave Propagation in Nonlinear Media

Numerical modeling of dynamic transient phenomena, such as wave propagation, is inherently related to time-dependency. The left-hand side of the elastodynamic equation, Eq. (3.4) or (3.5), contains the second derivative of particle displacements with respect to time and need to be resolved for advancing the solution in the time domain. For general time-dependent problems, two groups of solution methods exist, namely direct time integration and modal superposition [57]. In the first approach the solution is evaluated for discrete time steps, while in the second a transformation of governing equations of motion is performed, decomposing the system into a set of simple systems which are then integrated in time. The solution in the original domain is obtained by an inverse transform.

The direct time integration techniques group can be further subdivided into two categories: explicit and implicit time integration. Each time integration procedure is suitable for a particular class of problems and displays different properties in terms of mathematical formulation. As a consequence, time-domain solution methods are suitable for different classes of structural mechanics problems. For details, the reader should refer to [26, 57]. For wave propagation problems, the explicit time integration techniques are most frequently used, and therefore will be outlined in more detail.

Regardless—for the moment—of the space discretization, i.e. the discretized form of the right-hand side of Eq. (3.4) or (3.5), the time derivatives are substituted by formal expressions that approximate the time evolution of the system. The finite difference formulas are used for this purpose. Particular selection of FD formulas depends on many aspects and determines the efficiency and robustness of a solution technique. In the explicit time integration approach, the elastodynamic equation (Eq. (3.4) or (3.5)) is rewritten for the current time step t, while the solution is sought in the next time step $t + \Delta t$. Subsequently, the approximation for time derivatives is introduced. For wave propagation, an advantageous choice is the central difference method. Employing the central difference scheme for a grid point (or, equivalently, nodal point or cell) denoted by (i, j) for a 2-D domain, the LHS of Eq. (3.4) or (3.5) yields

$$\rho_X \frac{\partial^2 \boldsymbol{U}}{\partial t^2} \approx \rho_X \frac{U^{i,j,t+\Delta t} - 2U^{i,j,t} + U^{i,j,t-\Delta t}}{\Delta t^2} \tag{3.18}$$

where $U^{i,j,t}$ denotes a grid point (node or cell) (i, j) displacement at time instance t and Δt is the time step. Using Eq. (3.18) with the space-discretized version of Eq. (3.4) or (3.5) leads to the set of algebraic equations governing the numerical model response. The solution for $U^{i,j,t+\Delta t}$ requires only the inversion of the mass matrix (see ρ_X in Eq. (3.18)) with no operations on the stiffness components. The solution procedure is effective if the inversion can be achieved without significant computational burden. When the mass matrix is diagonal, the inversion reduces to the inversion of its diagonal elements, hence the common choice of local computational strategies and/or lumping procedure for the mass matrix in wave propagation simulations. The remaining part of the solution consists of operations on matrix components and may be processed relatively fast. Please also note that regardless of the form of the right-hand side of Eq. (3.4) or (3.5), the solution procedure does not change—also when the RHS contains nonlinear terms.

The main disadvantage of the explicit schemes is the conditional stability. Namely, time step need to be smaller than the critical time step, $\Delta t \leq \Delta t_{cr}$ in order to ensure stability. The critical time step can be calculated from the Courant–Friedrichs–Lewy condition [58] and combines space discretization parameters and numerical properties of the model. Practically, Δt_{cr} is related to the highest possible wave velocity expected in the model. Despite the conditional stability, explicit time integration is widely employed for wave propagation due to its computational efficiency. High temporal resolution of the model, i.e. short time steps, as required by the stability criterion, is favorable due to high frequencies and velocities of elastic waves than need to be captured in the numerical simulation.

Similarly to the distinction made in Sect. 3.1 numerical models for the two types of nonlinear response sources, namely distributed and localized, can be constructed. Continuum mechanics-based numerical schemes consider—by definition—a continuous piece of material. Consequently, no discontinuities in the field variables are allowed without special treatment. For wave propagation, elastodynamic equations (Eqs. (3.4) and (3.5))—governing particle motion in an unbounded, continuous space—are transformed into algebraic form by employing a specific numerical procedure (e.g., FE, FD, SE, FV, LISA, CAFE, etc.). Please note that only distributed-type nonlinearities, e.g. geometric, quadratic, cubic nonlinearity, or hysteresis, etc., may be accounted for in these equations. Discontinuities, typically related to localized damage, require special analytical and numerical treatment. Internal boundaries due to crack or delamination faces are frequently modeled as stress-free boundaries. From numerical perspective duplicated nodes of the FE mesh [59], specific FD equations for boundary nodes [11], free faces of cellular automata [25], or other mechanisms are frequently employed. If an interaction between the crack or delamination faces exists, nonlinearity in the wavefield is introduced. The interaction is typically due to mechanical contact phenomena and friction.

In the following sections, numerical modeling strategies for the two types of nonlinearities—relevant from wave propagation perspective—are addressed, namely distributed and localized nonlinearities.

3.3.1 Nonlinear Media Models

This section outlines numerical strategies for wave propagation in nonlinear media. Specifically, the case of distributed nonlinearities will be addressed, leaving damage models for the next section. Technically, the current section considers various approaches to the space discretization, i.e. converting the RHS of Eq. (3.4) or (3.5) into algebraic form. Numerical model assumptions and simplifications will be discussed first, before presenting the details of discretization procedures.

The wave propagation problem in nonlinear media is fully described by Eq. (3.4) or (3.5) (elastodynamic equations), Eq. (3.6) (the geometric relation) and Eqs. (3.9)–(3.11) or (3.12)–(3.15) (the constitutive relationship). Recalled equations involve a number of variables that need to be analyzed in detail, before formulating a numerical model. In the following several simplifications are made leading to an effective numerical modeling strategy for wave propagation. The major assumptions on physical quantities used in the model are as follows.

Deformations It should be realized that in wave propagation problems, typically encountered in mechanical engineering, small—but finite—amplitude waves (approximately $\sim 10^{-6}$ to $\sim 10^{-3}$ mm) are considered. As a result, small displacements conditions are assumed. Therefore, differences in orientations of line segments between the deformed and undeformed configurations can be neglected. Mathematically, this means $\boldsymbol{F} = \frac{\partial \boldsymbol{x}}{\partial \boldsymbol{X}} = \boldsymbol{I}$. Please note, however, that this assumption relates to this particular point in derivation of the numerical model and cannot be generalized to simplify other quantities. A significant practical consequence of not distinguishing between the original, $\boldsymbol{X}$, and current, $\boldsymbol{x}$, configurations is that the model geometry does not need to be updated. A direct impact on the solution efficiency can be observed, as for the FE method the assembly of the stiffness and mass matrices in each iteration are avoided. For local computational strategies, this assumption is critical as the finite difference formalisms can be evaluated in the standard way. Also, no iteration formulas updates are required during the solution process. Accuracy of this simplification can be verified by comparing differently formulated numerical models. Figure 3.1 shows frequency spectra of the responses from an FD-based nonlinear local interaction simulation and an FE model [11]. In both models, the same numerical parameters have been used, with the only difference in the model geometry update. It can be seen that the differences are negligible even for high frequencies.

Strains Despite the above and the assumption of small displacements, the nonlinear geometric relation in the form of the Green–Lagrange strain is invoked (Eq. (3.6)). The quadratic terms in the strain-displacement relation are required for consistency with the order of expansion of the strain energy density function (Eq. (3.8)).

Stresses The hyper-elastic stress formulas including higher order terms, according to Eqs. (3.9)–(3.11) or (3.12)–(3.15) are adopted. Please note that due to the assumption on deformations, all stress measures are equal.

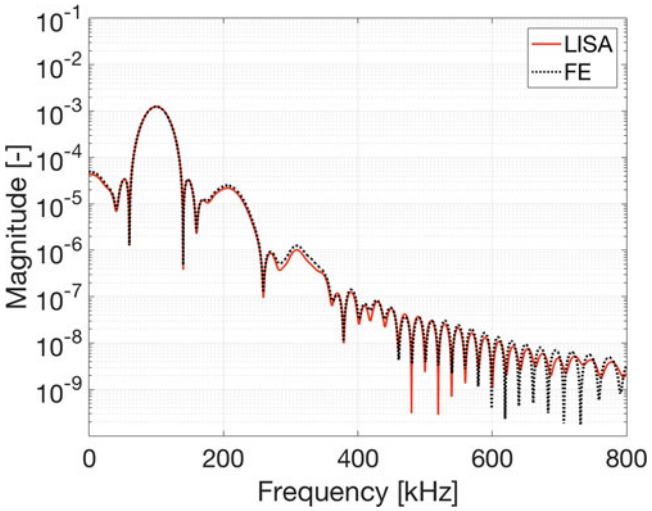

Fig. 3.1 Frequency spectra of time signals recorded from two numerical models of a plate: the LISA and FE models. For the FE model, in contrast to the LISA case, the geometry was updated every time step of the simulation [11]

Based on the above assumptions on deformations, strains and stresses, numerical models for wave propagation in nonlinear media are constructed. In the following three numerical techniques will be briefly outlined. First, the FE method will be shortly recalled. Next, the Local Interaction Simulation Approach (LISA) will be addressed.

3.3.1.1 The Finite Element Method for Wave Propagation in Nonlinear Media

The finite element method is probably the most widely used numerical procedure for solving mechanical engineering and other disciplines problems. It is therefore instructive to briefly address the wave propagation simulation in FE when nonlinear media are considered. The FE method departs from an alternative description of the equilibrium and boundary conditions from those described in Eqs. (3.1) and (3.16), namely the weak form.

The weak form can be obtained by multiplying the formulas in Eqs. (3.1) and (3.16) by an arbitrary continuous function of displacements $\delta \boldsymbol{U}$ (that is zero at and corresponding to the prescribed displacements). In the following it was assumed, however, that the natural boundary conditions are zero. The integration of the resulting formulas over the volume, for a selected time instant, and employing the divergence theorem, leads to

$$\int_{V^t} \boldsymbol{\sigma} \cdot \delta \boldsymbol{\epsilon} dV^t = \int_{V^t} \rho \ddot{\boldsymbol{U}} \delta \boldsymbol{U} dV^t \tag{3.19}$$

where $\boldsymbol{\epsilon}$ is the (virtual) strain tensor (corresponding to the virtual displacements; δ denotes the variation in strains due to the variation in displacements), $\boldsymbol{\sigma}$ is the Cauchy stress tensor, V is the volume and the right-hand side corresponds to the inertial contribution. Please note that other alternative descriptions yield the same description for mechanical systems [26, 27]. In Eq. (3.19) all quantities are taken at the same time instant t and calculated with respect to the current coordinate $\boldsymbol{x}$. In general it is difficult to work with Eq. (3.19) since the equilibrium is referenced with respect to the already deformed state (given by coordinates $\boldsymbol{x}$).

In order to transform Eq. (3.19) into a form suitable for the solution proper stress and strain measures need to be introduced. Instead of the Cauchy stress tensor $\boldsymbol{\sigma}$, the second Piola–Kirchoff stress tensor $\boldsymbol{\Sigma}$—relating the force and the area in the undeformed state—will be used. Similarly, instead of the strain given by $\boldsymbol{\epsilon}$, the Green–Lagrange strain $\boldsymbol{E}$ is employed. Both $\boldsymbol{\Sigma}$ and $\boldsymbol{E}$ are defined with respect to the undeformed coordinates $\boldsymbol{X}$. With these quantities, the left-hand side of Eq. (3.19) can be re-written as

$$\int_{V^t} \boldsymbol{\sigma} \cdot \delta\boldsymbol{\epsilon} dV^t = \int_{V^0} \boldsymbol{\Sigma} \cdot \delta\boldsymbol{E} dV^0 \tag{3.20}$$

and, analogously the inertial term reads

$$\int_{V^t} \rho\ddot{\boldsymbol{U}}\delta\boldsymbol{U} dV^t = \int_{V^0} \rho_X\ddot{\boldsymbol{U}}\delta\boldsymbol{U} dV^0 \tag{3.21}$$

where the mass conservation relation $\rho dV = \rho_X dV^0$ has been used. The superscript 0 refers to the initial, undeformed configuration. The equation of motion, Eq. (3.19) can be therefore re-written as

$$\int_{V^0} \boldsymbol{\Sigma} \cdot \delta\boldsymbol{E} dV^0 = \int_{V^0} \rho_X\ddot{\boldsymbol{U}}\delta\boldsymbol{U} dV^0 \tag{3.22}$$

Please note the quantities in Eq. (3.22) are taken at time instant t and with respect to the undeformed state. Equation (3.22) describes the elastodynamic problem with the reference to the known original (undeformed) configuration.

The solution of a nonlinearly elastic problem cannot be carried out in a single step, as it is the case for static linear elastic problem. There are many types of nonlinearities, hence there exist no general algorithms for solving a set of nonlinear equations. Therefore, in the FE formulation, approaches based on incremental solutions are frequently adopted. Two main solution strategies to nonlinear problems can be distinguished when considering the approximate solution with the finite element method, namely the total Lagrangian (TL) and updated Lagrangian (UL). When considering wave propagation (small deformations, small but finite strains and explicit time integration) the TL formulation is adopted. The solution for displacements is typically carried out incrementally by applying the decompositions for stresses, strains, and displacements. We note, however, that for wave propagation problems explicit time integration is employed, hence no equilibrium iterations are required.

After defining the integral form of the equilibrium, the finite element equations are derived as follows. First, interpolation scheme and functions (i.e., the type of an element) are assumed $\boldsymbol{U} = \boldsymbol{N}\bar{\boldsymbol{U}}$, where $\boldsymbol{N}$ is the shape functions matrix and $\bar{\boldsymbol{U}}$ stores nodal displacements. For wave propagation problems solved through the explicit time integration, the finite element interpolation formula is applied directly to Eq. (3.22). The following relations are used to convert Eq. (3.22) into the FE (matrix) equation of motion

$$\int_{V^0} \rho_X \ddot{\boldsymbol{U}} \delta \boldsymbol{U} dV^0 \approx \boldsymbol{M}\ddot{\bar{\boldsymbol{U}}} = \left(\int_{V^0} \rho_X \boldsymbol{N}^T \boldsymbol{N} dV^0 \right) \ddot{\bar{\boldsymbol{U}}} \tag{3.23}$$

$$\int_{V^0} \boldsymbol{\Sigma} \cdot \delta \boldsymbol{E} dV^0 \approx \boldsymbol{F}_{NL} = \int_{V^0} \boldsymbol{B}^T \hat{\boldsymbol{\Sigma}} dV^0 \tag{3.24}$$

where

- $\boldsymbol{M}$ is the mass matrix; frequently a mass lumping procedure is employed resulting in a diagonal matrix
- $\boldsymbol{N}$ is the matrix of shape functions
- $\boldsymbol{F}_{NL}$ is the general nonlinear loading vector depending on stresses and strains at time t; please note that $\boldsymbol{F}_{NL}$ depends on $\boldsymbol{\Sigma}$, $\boldsymbol{E}$ and, consequently, $\bar{\boldsymbol{U}}$, and involves the constitutive relationship
- $\boldsymbol{\Sigma}$ and $\boldsymbol{E}$ are the second Piola–Kirchoff and the Green–Lagrange strain, respectively
- $\hat{\boldsymbol{\Sigma}}$ is a vector collecting the second Piola–Kirchoff stress components
- $\boldsymbol{B}$ is the linear strain-displacement matrix

Finally, the finite element equation of motion, corresponding to Eq. (3.22), in the matrix form—in the absence of volumetric and surface loads—yields

$$\boldsymbol{F}_{NL} = \boldsymbol{M}\ddot{\bar{\boldsymbol{U}}} \tag{3.25}$$

where all quantities are taken at time t. If the explicit time integration scheme is employed, the acceleration vector $\ddot{\bar{\boldsymbol{U}}}$ in Eq. (3.25) is approximated by the second order central difference formula $\ddot{\bar{\boldsymbol{U}}} = \left(\bar{\boldsymbol{U}}^{t+1} - 2\bar{\boldsymbol{U}}^{t} + \bar{\boldsymbol{U}}^{t-1}\right)/\Delta t^2$. Subsequently, Eq. (3.25) can be solved for $\bar{\boldsymbol{U}}^{t+1}$ without additional iterations

$$\bar{\boldsymbol{U}}^{t+1} = \boldsymbol{M}^{-1}\Delta t^2 \boldsymbol{F}_{NL}\left(\bar{\boldsymbol{U}}^{t}\right) + 2\bar{\boldsymbol{U}}^{t} - \bar{\boldsymbol{U}}^{t-1} \tag{3.26}$$

where it can be seen that the solution requires calculation of internal stresses and the inversion of the mass matrix $\boldsymbol{M}$.

The nonlinear constitutive relation $\boldsymbol{\Sigma} = f(\boldsymbol{E})$, where f is a general nonlinear function of strains $\boldsymbol{E}$, is employed in the solution process during: (a) evaluation of stresses in $\boldsymbol{F}_{NL}$ and (b) evaluation of the tangent stiffness matrix (when

incremental solution process is adopted). Technically, the evaluation of the nonlinear stresses required in $\boldsymbol{F}_{NL}$ depends on the solution strategy (implicit or explicit) and specific software implementation. In general, most of the FE packages require an additional subroutine to be implemented, in order to simulate the wave propagation in nonlinear media.

3.3.1.2 The Local Interaction Simulation Approach for Wave Propagation in Nonlinear Media

The Local Interaction Simulation Approach is a well-established FD-based method for simulating wave propagation. The original method was proposed in [21, 60] and later developed in [61, 62] for wave propagation in complex heterogeneous media with sharp impedance changes. The LISA follows a particular application of finite difference (FD) formulas for space and explicit central difference approach for the time domain. It is therefore well suited for parallel processing. Derivation details are beyond the scope of this chapter and can be found in [21, 62]. In general, the LISA scheme can be employed various types of PDEs involving arbitrarily complex heterogeneous, anisotropic, and nonlinear materials. This section briefly outlines the LISA-based treatment of arbitrarily nonlinear media.

For a 2-D medium, the LISA discretizes the structure under investigation into a regular grid of rectangular cells. The material properties are assumed to be constant within each cell but may differ between cells. The LISA iteration equations are derived for a grid point—located at the intersection of four adjacent material cells as shown in Fig. 3.2a—from the elastodynamic wave equation, Eq. (3.4) or (3.5). Initially, each cell is treated as discontinuous and displacement and stress continuity conditions are applied to derive the LISA iteration equation. First, the elastodynamic equation is evaluated for each cell I–IV at points $P1$–$P4$ located close to point 0 based on the stress components distribution as shown in Fig. 3.2b. The four equations yield

$$\frac{2\Delta\Sigma_{11}^{(i)}}{\Delta x} + \frac{2\Delta\Sigma_{12}^{(i)}}{\Delta y} \approx \rho^{(i)}\ddot{u} \tag{3.27}$$

$$\frac{2\Delta\Sigma_{12}^{(i)}}{\Delta x} + \frac{2\Delta\Sigma_{22}^{(i)}}{\Delta y} \approx \rho^{(i)}\ddot{v} \tag{3.28}$$

where the superscripts (i) refer to the cell number, $i = \{I, II, III, IV\}$, and $\Delta\Sigma_{kl}^{(i)}$ defines a finite difference derivative of kl stress component in ith cell. The stress formulas, $\Delta\Sigma_{kl}^{(i)}$, are evaluated from displacement components in respective (i) cell nodes only, according to Eqs. (3.9)–(3.11).

Due to material properties discontinuity across the cells, some of the spatial derivatives appearing in the stress expressions cannot be evaluated and remain unknown. The set of equations needs therefore to be supplemented by enforcing

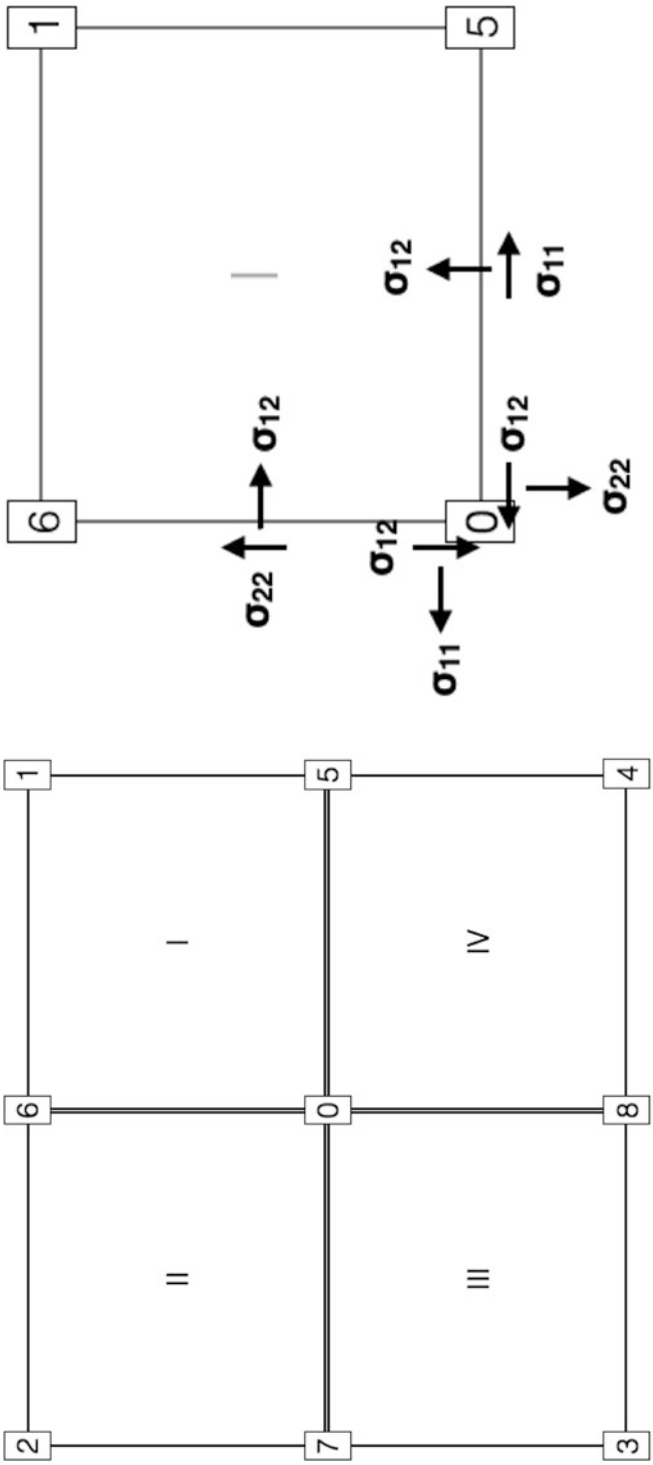

Fig. 3.2 Discretization scheme for the LISA approach (**a**). In (**b**) the stress tensor components used for iteration equations derivation are illustrated

stress continuity between the adjacent cells. Effectively, this procedure leads to the reduction of stress tensor components involved in the matching conditions between adjacent cells, collapsing to a unique stress tensor at the grid point of interest. Finally, the stress-based iteration equations can be written as

$$\frac{\Sigma_{11}^{(I)} - \Sigma_{11}^{(II)} - \Sigma_{11}^{(III)} + \Sigma_{11}^{(IV)}}{\frac{\Delta x}{2}} + \frac{\Sigma_{12}^{(I)} + \Sigma_{12}^{(II)} - \Sigma_{12}^{(III)} - \Sigma_{12}^{(IV)}}{\frac{\Delta y}{2}} = \sum_i \rho \ddot{u} \tag{3.29}$$

$$\frac{\Sigma_{12}^{(I)} - \Sigma_{12}^{(II)} - \Sigma_{12}^{(III)} + \Sigma_{12}^{(IV)}}{\frac{\Delta x}{2}} + \frac{\Sigma_{22}^{(I)} + \Sigma_{22}^{(II)} - \Sigma_{22}^{(III)} - \Sigma_{22}^{(IV)}}{\frac{\Delta y}{2}} = \sum_i \rho \ddot{v} \tag{3.30}$$

where the summation is carried over the four cells.

Please note that the LISA derivation procedure relies on evaluating the elastodynamic equation and imposing continuity of selected stress tensor components across the cell interfaces. As a consequence, the procedure can be carried out regardless of the form of the constitutive relation and the geometrical relation. Please also note that due to the explicit time integration procedure for advancing the solution in the time domain, the nonlinear contributions are accounted for through additional forcing terms in the iteration equation and no changes to the solution procedure are required. A similar procedure is invoked for the inertial part of Eq. (3.4) or (3.5). Namely, it is assumed that the second time derivatives across the four cells, at points $P1$–$P4$, converge towards a common value.

3.3.2 Nonlinear Damage Models

The approaches of modeling the local type of the structures' nonlinearity, namely the nonlinear crack induced through the fatigue of the monitored material, are of particular interest in the following section.

In general there are a number of techniques to exhibit the presence of the fatigue crack in the obtained ultrasonic respond. In particular, one can find it through such means as higher- [63–65] or sub- [66] harmonics generation, mixed frequency responses [67] (e.g., nonlinear wave modulation spectroscopy), shift of resonance frequency [8] (e.g., nonlinear resonant ultrasound spectroscopy), nonlinear surface waves [68, 69], or dual frequency mixing [70]. All the above-mentioned methods are surveyed comprehensively in [6]. However, among all the above-mentioned techniques the higher- and sub-harmonics generation are in the advantageous position, where the specific behavior of the crack interfaces upon the interaction with the propagating ultrasonic wave can be observed. Solodov et al. [42] presented an analytical description of the crack–wave interaction characteristics exhibited on the generated higher-order harmonics. Two types of the cracks movement, i.e. the breathing (clapping) of the crack interfaces and the shear transverse between

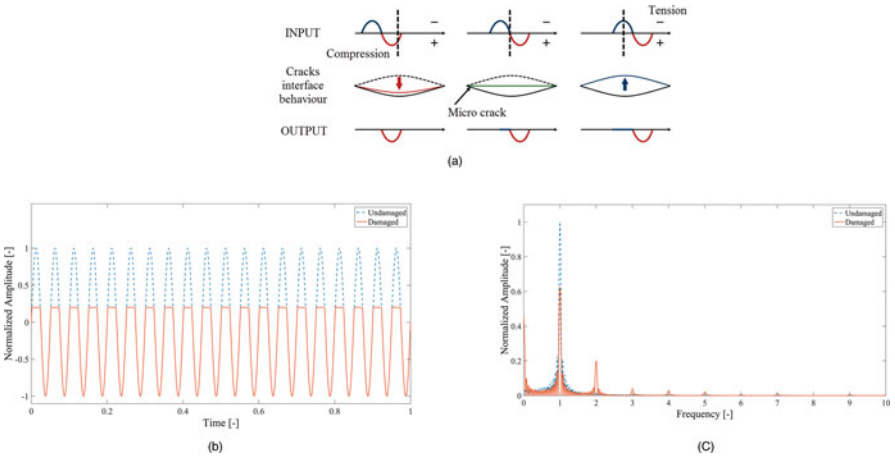

Fig. 3.3 Schematic of a breathing crack phenomenon (**a**) along with the displacement signal representations for ideal cases with and without the crack in the: (**b**) time domain; and (**c**) frequency domain (adopted from [11])

the interfaces with the exhibited friction were investigated. The concept of these phenomena is also presented in the following part of this section.

The breathing crack phenomenon described the movement of crack interfaces forced by a propagating ultrasonic wave with large enough amplitude. In the results a contact between the faces of the crack can be observed through the opening and closing of the gap. A graphical presentation of the breathing pattern of the fatigue crack is illustrated in Fig. 3.3a. The crack closes because of the compressional part of the propagating wave, which reaches its interface. While the crack is closed, the wave penetrates through it undisturbed and propagates further into the structure. The tensile part causes the crack to open, resulting in the partial wave reflection.

The result of this phenomenon can be observed in the deformation of the time signal and moreover, the generation of all higher-order harmonics in the frequency domain (time and frequency visualization are shown in Fig. 3.3b and c, respectively).

The second case of the crack faces movement is focused on the shear component forced by the propagating ultrasonic wave. Due to the shear drive of the propagating wave the faces of the crack are mechanically connected by the friction force resulting through the interaction between the asperities (see Fig. 3.4) [42]. However, if the amplitude of the shear component in the propagating wave is greater than the contact static friction, the transverse motion (sliding) between the crack interfaces with asperities is obtained.

In the result, the propagating shear wave is characterized by the cyclic transition between the static and kinematic friction (known as the stick-and-slip interface motion). Additionally, such a behavior leads the contact stress–strain relation to follow a hysteric loop. The contact tangential stiffness is independent of the

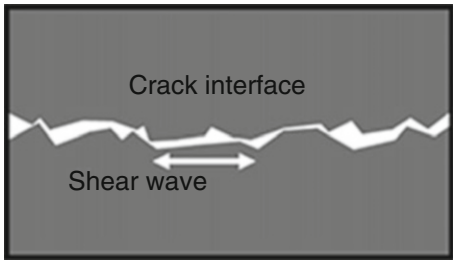

Fig. 3.4 Crack rough interface in shear traction (adopted from [42])

direction of the shear motion and causes stiffness variation twice for the input strain signal period. A symmetrical nonlinearity is introduce by such a restraint and only odd higher-order harmonics are to be expected in the structures respond.

3.3.3 Models Implemented Within the Finite Element Method Framework

In the most recent years there are two approaches with which the modeling of the crack-wave interaction is performed within the framework of the Finite Element Methods (FEM). Namely, (1) the activation/deactivation of the crack element and (2) the contact definition within the FEM solver based on the penalty method.

3.3.3.1 Activation/Deactivation Method

The former method is focused on activating or deactivating the chosen elements depending on the settled criteria. In order to deactivate the elements, their stiffness matrices are multiplied by the so-called reduction parameter, where the mass, damping, loads, and other such effects are set to zero. Therefore, as a result of the deactivation of the element the stiffness, mass matrices, and associated load will no longer contribute to the assembled global matrices. It should be emphasized that this approach does not remove the elements from the model, but keeps them instead in the position with greatly reduced properties. Furthermore, upon the reactivation of the elements, no new elements are added to the model, but instead the properties of the elements are resumed to the original values. The assembled original global equation will take the following form

$$\begin{pmatrix} M_{11} & \dots & 0 \\ \vdots & M^e & \vdots \\ 0 & \dots & M_{nn} \end{pmatrix} \begin{Bmatrix} \ddot{u}_{11} \\ \vdots \\ \ddot{u}_{nn} \end{Bmatrix} + \begin{pmatrix} C_{11} & \dots & 0 \\ \vdots & C^e & \vdots \\ 0 & \dots & C_{nn} \end{pmatrix} \begin{Bmatrix} \ddot{u}_{11} \\ \vdots \\ \ddot{u}_{nn} \end{Bmatrix} + \begin{pmatrix} K_{11} & \dots & 0 \\ \vdots & K^e & \vdots \\ 0 & \dots & K_{nn} \end{pmatrix} \begin{Bmatrix} \ddot{u}_{11} \\ \vdots \\ \ddot{u}_{nn} \end{Bmatrix} = \begin{Bmatrix} Q_1 \\ \vdots + Q^e \\ Q_n \end{Bmatrix} \tag{3.31}$$

where with the deactivated elements, the global equation takes form as

$$\begin{pmatrix} M_{11} & \dots & 0 \\ \vdots & +\Phi & \vdots \\ 0 & \dots & M_{nn} \end{pmatrix} \begin{Bmatrix} \ddot{u}_{11} \\ \vdots \\ \ddot{u}_{nn} \end{Bmatrix} + \begin{pmatrix} C_{11} & \dots & 0 \\ \vdots & +\Phi & \vdots \\ 0 & \dots & C_{nn} \end{pmatrix} \begin{Bmatrix} \ddot{u}_{11} \\ \vdots \\ \ddot{u}_{nn} \end{Bmatrix} + \begin{pmatrix} K_{11} & \dots & 0 \\ \vdots & \eta K^e & \vdots \\ 0 & \dots & K_{nn} \end{pmatrix} \begin{Bmatrix} \ddot{u}_{11} \\ \vdots \\ \ddot{u}_{nn} \end{Bmatrix} = \begin{Bmatrix} Q_1 \\ \vdots + \Phi \\ Q_n \end{Bmatrix} \tag{3.32}$$

The M^e, C^e, K^e, and Q^e are the mass, damping, stiffness matrices, and external load of the chosen elements, which undergoes the activation/deactivation process. The η symbol is the reduction parameter, which can be set to a very small value (usually $\eta < 1e^{-6}$ [71]). And finally, Φ is a zero matrix or vector. Through the analysis of Eqs. (3.31) and (3.32) it can be noticed, that the nonlinear effect is impose by the periodical change of matrices M, K and C.

The conditions for opening/closing the gap were presented by Shen in [71], where the status of the stress within the thin layer of elements simulating the crack (whether it is a compressional or tensional stress) is taken into account. Following the approach presented in the previous section, the tension imposed on the elements leads to the opening of the crack (deactivation of the elements), where the compression forces the crack to close (activation of the elements). Moreover, the condition to initiate such a behavior takes form as [71]

$$(U_2 - U_1 < 0) \cap \left(\overline{\varepsilon} = \frac{\sum_1^n \varepsilon_n}{n} < 0 \right) \tag{3.33}$$

where U_2 and U_1 are the nodes displacements in the direction of the cracks opening, located at the opposite edges of the chosen element. The $\overline{\varepsilon}$ is the average strain (also in the direction of the opening) of the elements within the thin layer of the crack. In Fig. 3.5 a depiction of the methods concept is presented. In Fig. 3.5a the closed state of the crack is shown, where the elements of the crack layer have the same material properties as the rest of the model, i.e. these elements are activated. In Fig. 3.5b the opened state of the crack is exhibited through the deactivated elements specified by

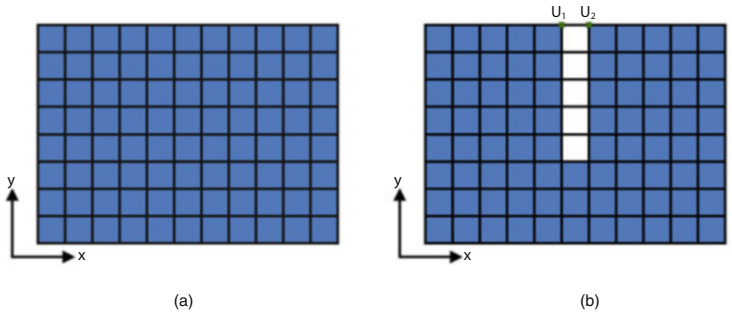

Fig. 3.5 Schematic of a breathing crack phenomenon using the deactivation/activation method: (**a**) crack closed (elements activated); (**b**) crack opened (elements deactivated)

the user, i.e. the stiffness of these elements is reduced by factor η and the remaining properties are set to zero.

3.3.3.2 Penalty Method

The next method which can be utilized to model the contact phenomenon within the FEM framework is the penalty method. In general, this was explored to find the solution to the constrained optimization problems and on the way of doing so, it was applied to simulate the contact problems within the FEM framework as one of the primary approaches.

In the physical world no penetration between the contact surfaces can be observed. However, in the case of the FEM, such an event can occur in order to ensure the equilibrium. Figure 3.6 illustrates the interaction between the two surfaces simulated with the penalty method. When the node from the slave surface penetrates the other fixed surface (i.e., master surface) during the ith step of the simulation, an interface spring is enforced during the $i+1$th step between the slave mode and the master surface to minimize the contact penetration.

Forces correlated to the interface spring is equal to the spring stiffness (k_{normal}, k_{slip}) multiplied by the distance of the penetration (Δ_N, Δ_T). The import part of the contact analysis is the choice of the stiffness parameter of the interface spring, due to the fact that it has a big influence on both accuracy and convergence of the solution. Through the analysis of the contact problem, it was shown in [71] that a small amount of penetration can lead to more accurate solution. Therefore, a large contact stiffness should be chosen. However, such a choice may lead to ill-conditioning of the global stiffness matrix resulting with convergence problems. Another choice may lead to decision of setting a lower stiffness value, which will lead to a certain amount of the penetration and/or slip. As a result, the solution is easier to converge, but also it will become less accurate. Thus, a compromise has to be found for the value of the stiffness parameter in order for the penetration and/or slip be to small enough giving accurate results and also for the solution to

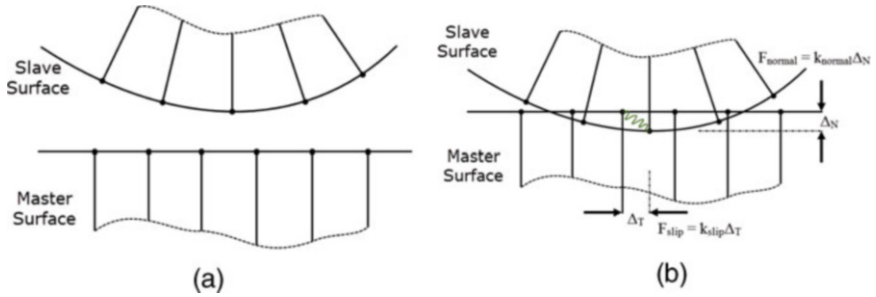

Fig. 3.6 Schematic of a penalty method: (**a**) before the penetration between contact surfaces; (**b**) during the penetration between contact surfaces exhibiting contact tractions (adopted from [72])

be convergent. A common approach is to first chose the lower value of the stiffness parameter which leads to a convergent solution and then examine if the penetration of the contact surfaces is acceptable. Then one can increase the stiffness value to the point where penetration distance is reasonable and the solutions between two respective penalty coefficients do not change.

3.3.4 Models Within the Local Interaction Simulation Approach Framework

As it was mentioned in the introduction of this chapter, the Local Interaction Simulation Approach (LISA) is receiving a burgeoning attention within the last decade due to its attractive computational cost-effectiveness [59, 61, 62, 73]. Moreover, in the most recent years LISA is also used to model the nonlinear behavior of the damage. Several approaches to model such phenomenon were used within LISA environment such as the activation/deactivation of elements [74] (whose working concept is similar to the one presented for the FEM), spring model [11, 75] or the penalty method [59]. Moreover, in [59] the Coulomb friction model between the crack interfaces was introduced.

In the following part of this section the spring model and the Coulomb friction model are reviewed.

3.3.4.1 Spring Model

The spring model was first introduced in [75] and as the name suggests, the propagation of the ultrasonic pulse or wave in the structure is substituted by the movement of the equivalent set of excited *tensorial* springs. The discretization scheme and material definition in SM follow those of LISA. The major difference between the two methods is found in the nodal displacement analysis. In a two-

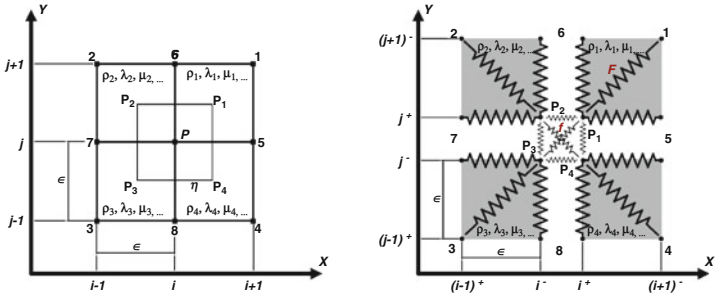

Fig. 3.7 Discretization of the model using: (**a**) LISA (adopted from [21]); and (**b**) SM (adopted from [75])

dimensional case in LISA, each nodal point belongs to four cells; while in SM, each nodal point is divided into four sub-nodal points, each of which belongs to a cell. Then, the relations between the sub-nodes are defined via *tensorial* springs and used for force representation. Forces between the sub-nodes within one cell are named external forces F and forces between the cells, introduced in order to keep the continuity of the structure, are named internal forces f. A graphical comparison of discretization between both methods is shown in Fig. 3.7.

Although the procedure of receiving the final iteration equations in the SM method differs from the one of the LISA method, the same result can be achieved for both methods, assuming that there is a perfect contact between the cells of the structure. It will have a form of

$$w_{t+1} = 2w - w_{t-1} + \frac{(\Delta t)^2}{\rho \epsilon^2} \sum_{k=1}^{4} \bar{F}^k, \tag{3.34}$$

where w_{t+1}, w, w_{t-1} are the respective iteratives of displacement in time, Δt is the time discretization step, ρ is the sum of the densities of the cells around the node for which the displacement values are calculated, ϵ is the size of the element, and $\sum_{k=1}^{4} \bar{F}^k$ is the sum of the resultant forces from the four cells (k is the cell number) surrounding the analyzed node. In that case, the structure taken into account is the one presented in Fig. 3.7a and the displacements are calculated for node $\boldsymbol{P}$ in each time step.

In order to introduce to the model an imperfect contact between the cells interfaces, node $\boldsymbol{P}$ from Fig. 3.7a needs to be divided in two-dimensional case into four sub-nodes $\boldsymbol{P}_{1-4}$ as it is shown in Fig. 3.7b. This approach redefines the final iteration equations into four independent ones, each for one sub-node in the form as follows:

$$w_{t+1}^{(k)} = 2w^{(k)} - w_{t-1}^{(k)} + \frac{(\Delta t)^2}{\rho \epsilon^2} \left(\bar{F}^k + \sum_{l \neq k} \bar{f}_{kl}^{(pc)} \right), \quad (k, l = 1, \ldots, 4), \tag{3.35}$$

where in order to maintain the continuity of the structure, the internal forces $\bar{f}_{kl}^{(pc)}$ for perfect contact are introduced in the form

$$\bar{f}_{kl}^{(pc)} = \frac{\rho_k \bar{F}_l - \rho_l \bar{F}_k}{\rho}, \tag{3.36}$$

where ρ_k and ρ_l are the densities of the cells between which the internal force is determined. $\bar{F}_k$ and $\bar{F}_l$ are the respective external forces of each cell. This component allows to extend the model to use the imperfect contact between the interfaces. It can be done by introducing a contact quality factor Q_{kl} for each sub-node through the relationship

$$\bar{f}_{kl} = Q_{kl} \bar{f}_{kl}^{(pc)}. \tag{3.37}$$

The Q_{kl} factor may vary between 0 and 1, which gives the possibility of modeling different types of imperfections in the structure. The contact quality factor may differ from one sub-node to the other and moreover, different values can be defined for the **x** and **y** components of the internal forces.

In the earlier works, in order to model the nonlinear contact between the crack interfaces, the changing state of the factor Q_{kl} was defined by monitoring the sub-nodes displacement in the horizontal direction (for the two-dimensional case)[75, 76]. The conditions are as follows:

$$\begin{aligned} u_i^+ - u_i^- &\leq 0 \qquad Q_{kl} = 1, \\ u_i^+ - u_i^- &> 0 \qquad Q_{kl} = 0. \end{aligned} \tag{3.38}$$

However, most recently a new way of defining the contact between the interfaces was stated [11], where the normal stress component in the direction of the wave propagation. Through such action the position of the sub-node in both direction (for two-dimensional case) is taken into consideration. The opening/closing condition takes form as

$$\begin{aligned} \sigma_{xx} &\leq 0 \qquad Q_{kl} = 1, \\ \sigma_{xx} &> 0 \qquad Q_{kl} = 0. \end{aligned} \tag{3.39}$$

Nonetheless, in both approaches the state of the Q_{kl} factor is calculated at every simulation time step. Furthermore, when the compressional part of the propagating stress wave reaches the crack surfaces, the perfect contact is imposed by setting Q_{kl} as 1 where for the tensile part of the wave it is set to 0. Thus, through such an action the nonlinearities are imposed into the propagating ultrasonic wave.

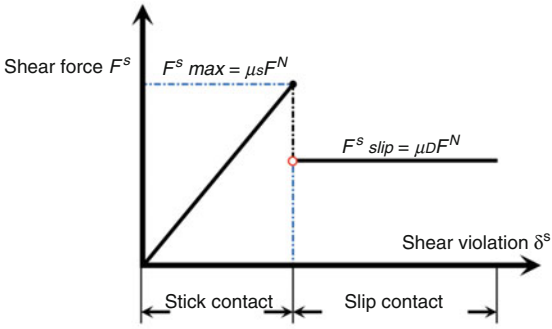

Fig. 3.8 Stick-slip contact condition based on the Coulomb friction model (adopted from [59])

Finally, the contact quality factor Q_{kl} may vary between the nodes, which means that the condition of opening and closing is considered separately and independently for each node. This gives a flexibility for the crack interfaces to adjust to more complex mode shapes of the propagating guided ultrasonic waves.

3.3.4.2 Coulomb Friction Model

The modeling approach allowing to imitate the slip motion between the crack interface is reviewed in this section. The Coulomb friction model is implemented in the framework of LISA, which was first done and presented in [59]. The condition of enabling the Coulomb friction is illustrated in Fig. 3.8.

When the tangential force at the interfaces is below the critical value F^S_{max}, the crack interfaces follow the breathing motion, which was described in the previous section. Moreover, through the process of varying contact, the tangential force will linearly increase with the tangential violation δ^2. In the result it will exceed the critical value and a relative slip motion will be imposed into the model.

In order to simulate the slip motion within the LISA framework, an additional term is added to the iterative Eq. (3.35) and the changed form is as follows:

$$w^{(k)}_{t+1} = 2w^{(k)} - w^{(k)}_{t-1} + \frac{(\Delta t)^2}{\rho\epsilon^2}\left(\bar{F}^k + \sum_{l\neq k}\bar{f}^{(pc)}_{kl} + F_{slip}\right), \qquad (k, l = 1, \ldots, 4), \tag{3.40}$$

where

$$F_{slip} = Q_{kl}\, Q_{slip}\, \bar{F}_{slip}. \tag{3.41}$$

In Eq. (3.41) the Q_{kl} is the contact quality factor introduced in the previous section. It varies between 0 and 1 using the conditions shown in Eqs. (3.38) or (3.39). Furthermore, the Q_{slip} is the friction quality factor which defines the presence of the

slip motion between the interfaces. As in the case of the contact quality factor, the friction quality factor also varies between 0 and 1. The condition to state its value for the two-dimensional case is as follows:

$$\begin{aligned} F^S &> \mu_S F^N \qquad Q_{slip} = 1, \\ F^S &\leq \mu_S F^N \qquad Q_{slip} = 0. \end{aligned} \tag{3.42}$$

The F^S and F^N are the tangential and normal forces at the crack interfaces, and the μ_S is the static friction coefficient of the material.

Finally, it should be emphasized that the material properties of the cells remain unchanged. Moreover, in the presented case the linear elastic relation is assumed and the breathing crack with the slip friction motion is the only source of nonlinearity imposed into the propagating ultrasonic wave. However, the nonlinear material definition was introduced in the LISA framework [11, 22, 77, 78] which leads to further investigation on the influence of the respective sources on the generated nonlinearity exposed in the structure response signal.

3.4 Discussion and Conclusions

In this chapter selected aspects of numerical modeling of wave propagation in nonlinear media have been outlined. The sources of nonlinearities were classified into two groups, namely distributed and localized ones. In the former, geometrical and material-related nonlinearities were considered, while in the latter damage-related localized nonlinear sources were addressed. Theoretical background and numerical modeling techniques have been summarized for the most frequently considered types of nonlinear wave interactions.

Numerical models for nonlinear acoustics, as those given in this chapter, serve as tools for predicting complex wavefields and studying wave propagation and interaction with defects in complex structural components. For completeness, however, guidelines for their application and parameters selection, allowing for accurate results, should be given.

The time step size selection is determined by the time integration procedure through the stability condition, as discussed in Sect. 3.3. The time step is therefore a parameter that depends on material properties of the medium and space discretization constants. For the latter, it is widely accepted that wavelength-based criteria are adopted for adjusting characteristic element sizes. For bulk wave propagation it is straightforward to determine the anticipated wavelengths at the fundamental, higher harmonics and potential modulated frequencies. In real practical problems, however, guided (opposed to bulk) wave propagation conditions prevail. For those complex wavefield patterns, spectral characteristics should be used to evaluate model accuracy.

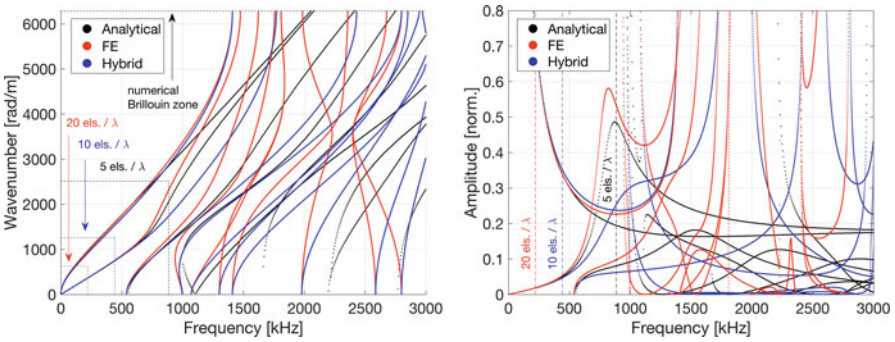

Fig. 3.9 Dispersion curves for a 2 mm copper plate for the hybrid and FE methods for $\Delta x = \Delta y = 0.5$ mm, superimposed with the exact solution [22, 33]

Figure 3.9 [22, 33] shows spectral characteristics, i.e. dispersion and excitability curves, for a 2 mm copper plate. In the plots the exact (analytical) solution is superimposed on the numerical spectral characteristics for a given discretization of the model. Several important factors should be addressed here in the context of nonlinear wave propagation. First, significant qualitative discrepancies can be seen. Numerical dispersion curves, Fig. 3.9a, display periodicity in the wavenumber domain. At the Nyquist wavenumber, the so-called Brillouin zone [33] exists, where all guided wave modes group velocity vanishes. At the same time, significantly increased amplitude response is observed in these frequency bands (Fig. 3.9b), resulting in potential artifacts in numerical model responses. Also, negative group velocities and other distortions can be observed. Subsequently, it can be noted that the wavelength-based (or, equivalently, wavenumber-based) criterion is difficult to use without a priori analyzing the dispersion curves. As the wavenumber-based accuracy condition limits the vertical axis only, it can be seen that higher order wave modes exist at high frequencies and propagate with significant errors. Specifically, for nonlinear wave propagation higher harmonic waves can be excited as those higher order modes. Dashed horizontal lines were plotted in Fig. 3.9a for the cases of 5, 10, and 20 elements per wavelength. Auxiliary conditions should be therefore employed to limit the effective frequency range for model application.

Waves propagating in nonlinear media give rise to the secondary wavefields (higher harmonics, modulations, etc.). From perturbation solutions for those problems [9, 78, 79] it can be seen that the higher order forcing terms strongly depend on wave amplitudes in the preceding orders of expansion. It is therefore critical to predict wave amplitudes precisely, not only wave speeds. Amplitude-frequency characteristics, known as excitability curves for the exact and numerical solutions are shown in Fig. 3.9b. Clearly, much higher discrepancies are observed in amplitudes than wavenumbers for the same excitation frequencies, suggesting that much finer discretizations are required for accuracy for nonlinear wave propagation numerical models.

References

1. T. Stepinski, T. Uhl, W.J. Staszewski, *Advanced Structural Damage Detection: From Theory to Engineering Applications*, 1st edn. (Wiley, Chichester, 2013)
2. C. Boller, F.-K. Chang, Y. Fujino, *Encyclopedia of Structural Health Monitoring* (Wiley, Chichester, 2009)
3. A.N. Norris, Finite-amplitude waves in solids, in *Nonlinear Acoustics*, ed. by M.F. Hamilton, D.T. Blackstock (Academic Press, San Diego, 1998), pp. 263–277
4. N. Rauter, R. Lammering, Numerical simulation of elastic wave propagation in isotropic media considering material and geometrical nonlinearities. Smart Mater. Struct. **24**(4), 045027 (2015)
5. V.K. Chillara, C.J. Lissenden, Review of nonlinear ultrasonic guided wave nondestructive evaluation: theory, numerics and experiments. Opt. Eng. **55**(1), 011002 (2015)
6. K.-Y. Jhang, Nonlinear ultrasonic techniques for nondestructive assessment of micro damage in material: a review. Int. J. Precis. Eng. Manuf. **10**(1), 123–135 (2009)
7. M. Destrade, R.W. Ogden, On the third- and fourth-order constants of incompressible isotropic elasticity. J. Acoust. Soc. Am. **128**, 3334–3343 (2010)
8. M. Muller, A. Sutin, R. Guyer, M. Talmant, P. Laugier, P.A. Johnson, Nonlinear resonant ultrasound spectroscopy (nrus) applied to damage assessment in bone. J. Acoust. Soc. Am. **118**(6), 3946–3952 (2005)
9. W.J.N. de Lima, M.F. Hamilton, Finite-amplitude waves in isotropic elastic plates. J. Sound Vib. **265**, 819–839 (2003)
10. A. Klepka, W.J. Staszewski, R.B. Jenal, M. Szwedo, J. Iwaniec, Nonlinear acoustics for fatigue crack detection - experimental investigations of vibroacoustic wave modulations. Struct. Health Monit. **11**, 197–211 (2012)
11. R. Radecki, Z. Su, L. Cheng, P. Packo, W.J. Staszewski, Modelling nonlinearity of guided ultrasonic waves in fatigued materials using a nonlinear local interaction simulation approach and a spring model. Ultrasonics. **84**, 272–289 (2008). https://doi.org/10.1016/j.ultras.2017.11.008
12. G.B. Santoni, L. Yu, B. Xu, V. Giurgiutiu, Lamb wave-mode tuning of piezoelectric wafer active sensors for structural health monitoring. J. Vib. Acoust. **129**(6), 752–762 (2007)
13. P.Y. Moghadam, N. Quaegebeur, P. Masson, Mode selective generation of guided waves by systematic optimization of the interfacial shear stress profile. Smart Mater. Struct. **24**(1), 015003 (2015)
14. P. Packo, T. Bielak, A.B. Spencer, W.J. Staszewski, T. Uhl, K. Worden, Lamb wave propagation modelling and simulation using parallel processing architecture and graphical cards. Smart Mater. Struct. **21**(7), 075001 (2012)
15. P. Packo, T. Bielak, A.B. Spencer, T. Uhl, W.J. Staszewski, K. Worden, T. Barszcz, P. Russek, K. Wiatr, Numerical simulations of elastic wave propagation using graphical processing units—comparative study of high-performance computing capabilities. Comput. Methods Appl. Mech. Eng. **290**, 98–126 (2015)
16. G. Noh, S. Ham, K.-J. Bathe, Performance of an implicit time integration scheme in the analysis of wave propagations. Comput. Struct. **123**, 93–105 (2013)
17. K.-T. Kim, K.-J. Bathe, Transient implicit wave propagation dynamics with the method of finite spheres. Comput. Struct. **173**, 50–60 (2016)
18. J.C. Strickwerda, *Finite Difference Schemes and Partial Differential Equations* (Wadsworth-Brooks, Belmont, 1989)
19. J. Virieux, P-sv wave propagation in heterogeneous media: velocity-stress finite difference method. Geophysics **51**, 889–901 (1986)
20. P. Fellinger, R. Marklein, K.J. Langenberg, S. Klaholz, Numerical modeling of elastic wave propagation and scattering with efit - elastodynamic finite integration technique. Wave Motion **21**(1), 47–66 (1995)
21. P.P. Delsanto, R.S. Schechter, H.H. Chaskelis, R.B. Mignogna, R. Kline, Connection machine simulation of ultrasonic wave propagation in materials. II: the two-dimensional case. Wave Motion **20**(4), 295–314 (1994)

22. P. Packo, R. Radecki, P. Kijanka, W.J. Staszewski, T. Uhl, M.J. Leamy, Local numerical modelling of ultrasonic guided waves in linear and nonlinear media, in *Proceedings of SPIE Health Monitoring of Structural and Biological Systems 2017*, vol. 10170 (2017), pp. 1017023–1017023-10
23. M.J. Leamy, Application of cellular automata modeling to seismic elastodynamics. Int. J. Solids Struct. **45**(17), 4835–4849 (2008)
24. R.K. Hopman, M.J. Leamy, Triangular cellular automata for computing two-dimensional elastodynamic response on arbitrary domains. J. Appl. Mech. **78**(2), 021020 (2011)
25. M.J. Leamy, T.B. Autrusson, W.J. Staszewski, T. Uhl, P. Packo, Local computational strategies for predicting wave propagation in nonlinear media, in *Proceedings of SPIE Health Monitoring of Structural and Biological Systems 2014*, vol. 9064 (2014), pp. 90641J–90641J-15
26. K.J. Bathe, *Finite Element Procedures in Engineering Analysis* (Prentice-Hall, Englewood Cliff, 1982)
27. O.C. Zienkiewicz, *The Finite Element Method* (McGraw-Hill, London, 1989)
28. A.A. Becker, *The Boundary Element Method in Engineering: A Complete Course* (McGraw-Hill, London, 1992)
29. A.T. Patera, A spectral element method for fluid dynamics: laminar flow in a channel expansion. J. Comput. Phys. **54**(3), 468–488 (1984)
30. S. Gopalakrishnan, A. Chakraborty, D.R. Mahapatra, *Spectral Finite Element Method* (Springer, Berlin, 2008)
31. S. Ham, K.J. Bathe, A finite element method enriched for wave propagation problems. Comput. Struct. **94–95**, 1–12 (2012)
32. P. Packo, T. Uhl, W.J. Staszewski, Generalized semi-analytical finite difference method for dispersion curves calculation and numerical dispersion analysis for Lamb waves. J. Acoust. Soc. Am. **136**(3), 993 (2014)
33. P. Kijanka, W.J. Staszewski, P. Packo, Simulation of guided wave propagation near numerical brillouin zones, in *Proceedings of SPIE Health Monitoring of Structural and Biological Systems 2016*, vol. 9805 (2016), pp. 98050Q–98050Q-6
34. D. Broda, W.J. Staszewski, A. Martowicz, T. Uhl, V.V. Silberschmidt, Modelling of nonlinear crack–wave interactions for damage detection based on ultrasound—a review. J. Sound Vib. **333**(4), 1097–1118 (2014)
35. L.D. Landau, E.M. Lifshitz, *Theory of Elasticity*, 2nd edn. (Pergamon Press, Oxford, 1970)
36. V. Gusev, V. Tournat, B. Castagnede, Nonlinear acoustic phenomena in micro-inhomogeneous media, in *Materials and Acoustic Handbook*, ed. by C. Potel, M. Bruneau (ISTE Ltd, London, 2009)
37. K. Worden, G.R. Tomlinson, *Nonlinearity in Structural Dynamics: Detection, Identification and Modelling* (IoP, Bristol, 2001)
38. R. Ruotolo, C. Surace, P. Crespo, D. Storer, Harmonic analysis of the vibrations of a cantilevered beam with a closing crack. Comput. Struct. **61**(6), 1057–1074 (1996)
39. T.G. Chondros, A.D. Dimarogonas, J. Yao, Vibrations of a beam with a breathing crack. J. Sound Vib. **239**(1), 57–67 (2001)
40. M.I. Friswell, J.E.T. Penny, Crack modeling for structural health monitoring. Struct. Health Monit. **1**(2), 139–148 (2002)
41. I.Y. Solodov, N. Krohn, G. Busse, CAN: an example of nonclassical acoustic nonlinearity in solids. Ultrasonics **40**(1–8), 621–625 (2002)
42. I.Y. Solodov, N. Krohn, G. Busse, Nonlinear ultrasonic NDT for early defect recognition and imaging, in *Proceedings of the 10th European Conference on Non-destructive Testing, Moscow* (2010)
43. F. Semperlotti, K.W. Wang, E.C. Smith, Localization of a breathing crack using super-harmonic signals due to system nonlinearity. AIAA J. **47**(9), 2076–2086 (2009)
44. V.E. Nazarov, L.A. Ostrovsky, I.A. Soustova, A.M. Sutin, Nonlinear acoustics of micro-inhomogeneous media. Phys. Earth Planet. Inter. **50**(1), 65–73 (1988)
45. V.E. Nazarov, A.V. Radostin, L.A. Ostrovsky, I.A. Soustova, Wave processes in media with hysteretic nonlinearity. Part I. Acoust. Phys. **49**(3), 344–355 (2003)

46. K.R. McCall, R.A. Guyer, Equation of state and wave propagation in hysteretic nonlinear elastic materials. J. Geophys. Res. Solid Earth **99**(B12), 23887–23897 (1994)
47. R.A. Guyer, K.R. McCall, G.N. Boitnott, Hysteresis, discrete memory, and nonlinear wave propagation in rock: a new paradigm. Phys. Rev. Lett. **74**, 3491–3494 (1995)
48. L.A. Ostrovsky, S.N. Gurbatov, J.N. Didenkulov, Nonlinear acoustics in nizhni novgorod (a review). Acoust. Phys. **51**(2), 114–127 (2005)
49. I.Y. Belyaeva, V.Y. Zaitsev, L.A. Ostrovsky, Nonlinear acousto-elastic properties of granular media. Acoust. Phys. **39**(1), 11–14 (1993)
50. V. Zaitsev, P. Sas, Dissipation in microinhomogeneous solids: inherent amplitude-dependent losses of a non-hysteretical and non-frictional type. Acta Acust. united Ac. **86**(3), 429–445 (2000)
51. V.Y. Zaitsev, V. Gusev, B. Castagnède, Observation of the "luxemburg–gorky effect" for elastic waves. Ultrasonics **40**(1), 627–631 (2002)
52. J. Lemaitre, R. Desmorat, *Engineering Damage Mechanics: Ductile, Creep, Fatigue and Brittle Failures* (Springer, Berlin, 2005)
53. J. Rushchitsky, *Nonlinear Elastic Waves in Materials* (Springer, Berlin, 2014)
54. A. Jeffrey, J. Engelbrecht, *Nonlinear Waves in Solids*. CISM Courses and Lectures (Springer, Berlin, 1994)
55. A.F. Bower, *Applied Mechanics of Solids* (CRC Press, Boca Raton, 2010)
56. M. Destrade, G. Saccomandi, M. Vianello, Proper formulation of viscous dissipation for nonlinear waves in solids. Acoust. Soc. Am. J. **133**, 1255 (2013)
57. P. Packo, Numerical simulation of elasticwave propagation, in *Advanced Structural Damage Detection: From Theory to Engineering Applications* (Wiley, Chichester, 2013)
58. R. Courant, K. Friedrichs, H. Lewy, Über die partiellen differenzengleichungen der mathematischen physik. Math. Ann. **100**(1), 32–74 (1928)
59. Y. Shen, C.E.S. Cesnik, Modeling of nonlinear interactions between guided waves and fatigue cracks using local interaction simulation approach. Ultrasonics **74**, 106–123 (2017)
60. P.P. Delsanto, T. Whitcombe, H.H. Chaskelis, R.B. Mignogna, Connection machine simulation of ultrasonic wave propagation in materials. I: the one-dimensional case. Wave Motion **16**(1), 65–80 (1992)
61. P. Packo, T. Bielak, A.B. Spencer, W.J. Staszewski, T. Uhl, K. Worden, Lamb wave propagation modelling and simulation using parallel processing architecture and graphical cards. Smart Mater. Struct. **21**(7), 075001 (2012)
62. P. Packo, T. Bielak, A.B. Spencer, T. Uhl, W.J. Staszewski, K. Worden, T. Barszcz, P. Russek, K. Wiatr, Numerical simulations of elastic wave propagation using graphical processing units—comparative study of high-performance computing capabilities. Comput. Methods Appl. Mech. Eng. **290**, 98–126 (2015)
63. D. Dutta, H. Sohn, K.A. Harries, P. Rizzo, A nonlinear acoustic technique for crack detection in metallic structures. Struct. Health Monit. **8**(3), 251–262 (2009)
64. M. Deng, Analysis of second-harmonic generation of lamb modes using a modal analysis approach. J. Appl. Phys. **94**(6), 4152–4159 (2003)
65. C. Zhou, M. Hong, Z. Su, Q. Wang, L. Cheng, Evaluation of fatigue cracks using nonlinearities of acousto-ultrasonic waves acquired by an active sensor network. Smart Mater. Struct. **22**(1), 015018 (2013)
66. I. Solodov, J. Wackerl, K. Pfleiderer, G. Busse, Nonlinear self-modulation and subharmonic acoustic spectroscopy for damage detection and location. Appl. Phys. Lett. **84**(26), 5386–5388 (2004)
67. F. Aymerich, W.J. Staszewski, Experimental study of impact-damage detection in composite laminates using a cross-modulation vibro-acoustic technique. Struct. Health Monit. **9**(6), 541–553 (2010)
68. D.T. Zeitvogel, K.H. Matlack, J.-Y. Kim, L.J. Jacobs, P.M. Singh, J. Qu, Characterization of stress corrosion cracking in carbon steel using nonlinear rayleigh surface waves. NDT & E Int. **62**, 144–152 (2014)

69. J.-Y. Kim, V.A. Yakovlev, S.I. Rokhlin, Parametric modulation mechanism of surface acoustic wave on a partially closed crack. Appl. Phys. Lett. **82**(19), 3203–3205 (2003)
70. T. Stratoudaki, R. Ellwood, S. Sharples, M. Clark, M.G. Somekh, I.J. Collison, Measurement of material nonlinearity using surface acoustic wave parametric interaction and laser ultrasonics. J. Acoust. Soc. Am. **129**(4), 1721–1728 (2011)
71. Y. Shen, V. Giurgiutiu, Predictive modeling of nonlinear wave propagation for structural health monitoring with piezoelectric wafer active sensors. J. Intell. Mater. Syst. Struct. **25**(4), 506–520 (2014)
72. T.J.R. Hughes, R.L. Taylor, J.L. Sackman, A. Curnier, W. Kanoknukulchai, A finite element method for a class of contact-impact problems. Comput. Methods Appl. Mech. Eng. **8**(3), 249–276 (1976)
73. M.B. Obenchain, K.S. Nadella, C.E.S. Cesnik, Hybrid global matrix/local interaction simulation approach for wave propagation in composites. AIAA J. **53**(2), 379–393 (2015)
74. A. Martowicz, P. Packo, W.J. Staszewski, T. Uhl, Modelling of nonlinear vibro–acoustic wave interaction in cracked aluminium plates using local interaction simulation approach, in *6th European Congress on Computational Methods in Applied Sciences and Engineering, Vienna, Austria* (2012)
75. P.P. Delsanto, M. Scalerandi, A spring model for the simulation of the propagation of ultrasonic pulses through imperfect contact interfaces. J. Acoust. Soc. Am. **104**(5), 2584–2591 (1998)
76. M. Scalerandi, V. Agostini, P.P. Delsanto, K. Van Den Abeele, P.A. Johnson, Local interaction simulation approach to modelling nonclassical, nonlinear elastic behavior in solids. J. Acoust. Soc. Am. **113**(6), 3049–3059 (2003)
77. P. Kijanka, R. Radecki, P. Packo, W.J. Staszewski, T. Uhl, M.J. Leamy, Nonlinear dispersion effects in elastic plates: numerical modelling and validation, in *Proceedings of SPIE Health Monitoring of Structural and Biological Systems 2017*, vol. 10170 (2017), pp. 101701U–101701U-8
78. P. Packo, T. Uhl, W.J. Staszewski, M.J. Leamy, Amplitude-dependent lamb wave dispersion in nonlinear plates. J. Acoust. Soc. Am. **140**(2), 1319–1331 (2016)
79. M.F. Müller, J.-Y. Kim, J. Qu, L.J. Jacobs, Characteristics of second harmonic generation of lamb waves in nonlinear elastic plates. J. Acoust. Soc. Am. **127**(4), 2141–2152 (2010)

Chapter 4
Structural Damage Detection Based on Nonlinear Acoustics: Application Examples

Andrzej Klepka, Lukasz Pieczonka, Kajetan Dziedziech, Wieslaw J. Staszewski, Francesco Aymerich, and Tadeusz Uhl

4.1 Introduction

Integrity of structural components is one of the most important problems in engineering applications. The delicate link between performance and safety—that cannot be compromised—is not easy to maintain in practice. This problem relates not only to existing but also to newly developed structures. Existing and ageing structures need to be maintained and inspected to guarantee safe operation. New structures are often designed to include monitoring systems that can do the same job. Whatever the scenario, maintenance has a major impact on safe operation of structures and structural components. Effective maintenance procedures often offer additional advantages, leading to minimized operational/repair costs.

There exist a number of different techniques that are being used for structural damage detection and material testing. Methods based on nonlinear vibration/acoustic phenomena are of special interest, gaining an increasing attention in the scientific and engineering communities. The reason for this is that nonlinear damage detection methods are usually more sensitive and are able to detect defects earlier than methods based on linear properties of structures. These methods can therefore complement the commonly used linear techniques.

Vibration, ultrasonic and acoustic nonlinear phenomena have been used for many years to detect material defects and structural damage. A fatigue crack that opens and closes under dynamic loading and alters natural frequencies is probably the

A. Klepka (✉) · L. Pieczonka · K. Dziedziech · W. J. Staszewski · T. Uhl
Department of Robotics and Mechatronics, AGH University of Science and Technology, Kraków, Poland
e-mail: klepka@agh.edu.pl

F. Aymerich
Department of Mechanical, Chemical and Materials Engineering, University of Cagliari, Cagliari, Italy

T. Kundu (ed.), *Nonlinear Ultrasonic and Vibro-Acoustical Techniques for Nondestructive Evaluation*, https://doi.org/10.1007/978-3-319-94476-0_4

best-known example of nonlinear vibration phenomenon. Vibration-based damage detection methods are relatively well understood, but used mainly for global detection of large damage severities. In contrast, physical understanding of many ultrasonic and acoustic nonlinear phenomena is still not clear but their application for local damage detection has been gaining a fast growing interest for the last two decades. This is mainly due to the fact that relatively small defects exhibit strong nonlinearities resulting from relatively small strain amplitudes in these applications.

The following sections discuss the theoretical background and more importantly practical aspects of the nonlinear acoustic techniques that can be used for damage detection in engineering materials. The major focus is on the nonlinear vibro-acoustic modulation (VAM) technique.

4.2 Theoretical Background

Nonlinear ultrasonic and acoustic phenomena involve various classical and non-classical effects. Classical nonlinear effects in ultrasonic wave propagation have been investigated for decades [1–3] and also explored for damage detection [4, 5]. Classical effects are related to various material imperfections (e.g. intrinsic nonlinearities due to anharmonicity or imperfections in atomic lattices) and contribute to accumulated distortion of propagating waves, leading to higher harmonic generation. This effect is enhanced when additional imperfections—such as localized fatigue cracks or distributed microcracks—are present in material. Research work in this area also involves higher harmonic generation of Lamb waves used for the detection of material nonlinearity [6] and damage [7]. Recent years have demonstrated a growing interest of theoretical and applied research related to various non-classical effects in ultrasonic wave propagation [8–20]. The non-classical nonlinearities can be manifested in different ways. The scientific literature reports many different effects such as: higher harmonics generation with amplitude decay different than classical case, *sinc* modulation of spectral harmonic amplitudes, frequency mixing, subharmonic generation or chaotic dynamics. These effects result from various physical mechanisms including: the stress–strain hysteresis, amplitude-dependent non-classical (i.e. non-frictional and non-hysteretic) dissipation, acoustic equivalent of the Luxemburg–Gorky (LG) effect, the contact acoustic nonlinearity (CAN) and other phenomena that are often not easy to investigate and explain [10, 13, 21–26]. All these nonlinear effects are remarkably enhanced in the presence of contact-type and small-severity defects in materials.

There are many possible experimental arrangements that can be used to analyse various non-classical nonlinearities. The majority of these arrangements are based on the so-called pump-probe techniques that have been successfully used in nonlinear acoustics [27–29]. The ‘pump-probe’ idea involves two simultaneously applied dynamic fields. The ‘pump’ wave generates an intensive, high-amplitude field in order to perturb material defects and the ‘probe’ wave is used monitor changes induced in local elasticity.

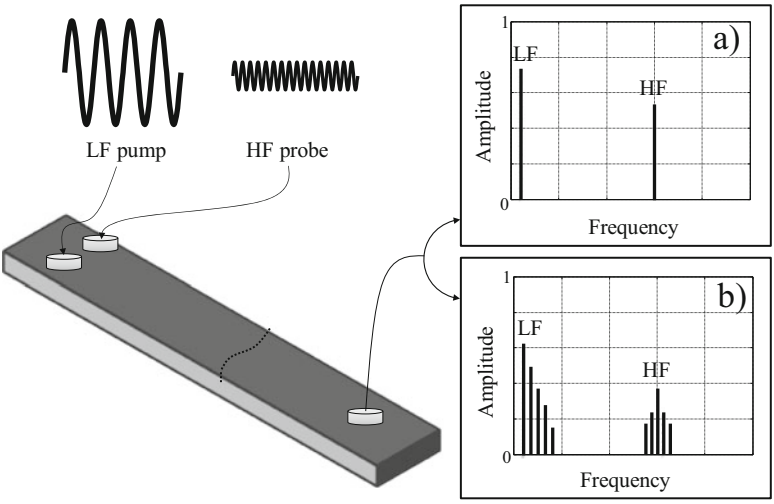

Fig. 4.1 Schematic presentation of the vibro-acoustic modulation (VAM) technique. Response spectrum of: (**a**) undamaged structure, and (**b**) damaged structure

The nonlinear Vibro-Acoustic wave Modulation technique (*VAM*) that is frequently used for damage detection belongs to this category. In most applications, the weak high-frequency (HF) ultrasonic wave is used as the 'probe' wave whereas the 'pump' wave involves the application of a strong, low-frequency (LF) excitation. The frequency of the LF wave usually corresponds to modal structural resonances. These two waves are simultaneously introduced to monitored structure, as illustrated in Fig. 4.1. For an ideal/linear (undamaged) structure, the spectrum of the response signal exhibits only two frequency components, i.e. frequencies of the LF pump and HF probe waves, as shown schematically in Fig. 4.1a. When structures are nonlinear (e.g. due to damage), the response spectrum reveals extra frequency components such as higher harmonics and modulation sidebands around the HF component (Fig. 4.1b).

The measure of nonlinearity of the monitored system—that can be attributed to the severity of damage—is often expressed in terms of modulation intensity. The intensity of modulation R can be calculated as the sum of theA^i_{LSB} and A^i_{RSB} amplitudes of the i-th pair of left (LSB) and right (RSB) sidebands over the high-frequency component amplitude A_{HF}:

$$R = \frac{\sum_{i=1}^{n} \left(A^i_{\mathrm{LSB}} + A^i_{\mathrm{RSB}}\right)}{A_{\mathrm{HF}}} \tag{4.1}$$

This parameter is often used to discern damaged and undamaged samples and to assess damage severity.

Other excitation scenarios in the VAM technique are also possible, including impulse excitation to provide a broadband LF pump, or frequency sweep signals instead of mono-harmonic signals for only the HF or both LF and HF signals [12, 30–33]. Structural response signals acquired during VAM experiments have to be processed to extract damage-related features. Various signal processing workflows and damage indicators have been used in practice and are reported in the literature. The vast majority of these approaches analyses response signals in the frequency domain, but some methods also focus on the instantaneous characteristics of the response. The latter involves the application of the Hilbert or Hilbert–Huang transforms [34]. The experimental examples described in the successive sections will discuss some of these different approaches.

Finally, it is important to note that in the scientific literature the vibro-acoustic wave modulation technique is also referred to as nonlinear wave modulation spectroscopy (NWMS) [10], the combination-frequency method or nonlinear acoustic modulation (NAM) method.

The cross-modulation damage detection technique is one of the non-classical, nonlinear acoustic methods. This technique is based on the acoustic equivalent of the Luxemburg–Gorky (L–G) effect [35]. The L–G effect was first observed in the early 1930s as an interaction between one radio station in Luxemburg and another Swiss radio station in Beromunster [36]. The observation was that the transmissions of the Swiss radio, received in Holland, appeared to be modulated in the ionosphere by the radiation from the powerful Luxemburg station. The same phenomenon was observed in the city of Gorky, where powerful Moscow stations could be heard during the reception of radio stations located to the west of Moscow. The phenomenon was related to radio waves propagation in upper layers of the atmosphere, leading to the modulation transfer between a strong amplitude-modulated wave and another weaker wave. It is assumed that the transfer of modulation was caused by variable absorption of the ionosphere inducted by the amplitude-modulated stronger wave [37, 38]. Later, very similar effects have been also observed in damaged solids and granular media [13, 39].

When the structure with damage is excited simultaneously by two waves—i.e. the 'pump' and 'probe' wave (Fig. 4.2)—at the response spectrum, the sidebands around the frequency related to the 'pump' wave can be observed in the response spectrum together with sidebands coming from the modulation transfer. For linear/intact structures, the component related to the 'pump' wave and the mono-harmonic wave can be observed.

The mechanisms of the modulation transfer in this case are different from the classical nonlinear effects and they are related to the inelastic part of the stress–strain characteristic. Some studies [13, 39, 40] show also that the L–G effect could be connected with the acoustic absorption due to thermo-elastic properties of a crack. The acoustic absorption model is based on contact phenomena produced by the pumping wave and properties of nonlinear medium. Strong interactions of the acoustic wave and the crack are generated in the stress field of the contact area. This results in thermal gradients. When the 'pump' wave ($\omega_1 \pm \omega_m$) is introduced, the area of contact interactions changes, leading to a change in the acoustic absorption.

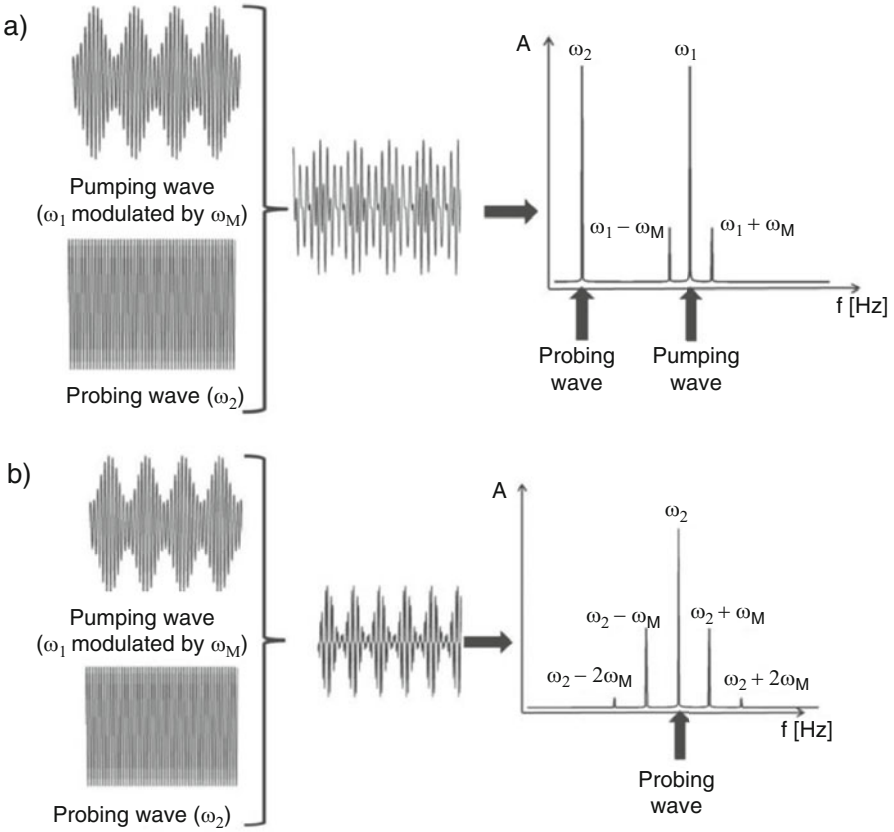

Fig. 4.2 The principle of Luxemburg–Gorky effect: (**a**) undamaged structure, and (**b**) damaged structure

During this action, the response of the structure is temporally averaged over the period of pumping wave carrier and causes the modulation processes. As a result, a new signal with the frequency corresponding to

$$(\omega_1 - (\omega_1 \pm \omega_m)) = \pm\omega_m \tag{4.2}$$

is generated and the 'probe' wave with the frequency ω_2 is modulated with the frequency ω_m, coming from changes in the absorption. The physics staying behind this modulation transfer has not been fully explained yet but there is some experimental evidence showing amplitude-dependent, non-hysteretic dissipation nonlinear mechanism related to the L–G effect [41, 42].

4.3 Experimental Examples

This chapter demonstrates selected application examples in which nonlinear acoustics was successfully used for damage detection. After a general overview of application areas and different experimental arrangements, case studies are described in more detail. The reported examples reflect mostly the experiences of the authors, gathered over many years of working with nonlinear acoustics, and by no means cover all possible applications in this multidisciplinary, exciting field of research. Wherever possible, the readers are directed to the relevant literature, where more information and other applications can be found.

4.3.1 Overview

A general scheme for the experimental arrangements used in VAM testing is shown in Fig. 4.3. The common components present in these experimental configurations include: Data Management System (typically a personal computer with appropriate software procedures to communicate with peripherals, orchestrate the measurement, acquire, store and process measurement data); Signal Generator and Signal Amplifier to drive the actuators. More differences can be found in the way the test sample is excited and vibration responses are acquired.

On the excitation side, there are several possibilities ranging from impulse excitation with an impact hammer through various contact transducers attached to the test samples (including piezoceramics and electrodynamic shakers), to non-contact excitation with lasers, speakers and air-coupled ultrasonic transducers.

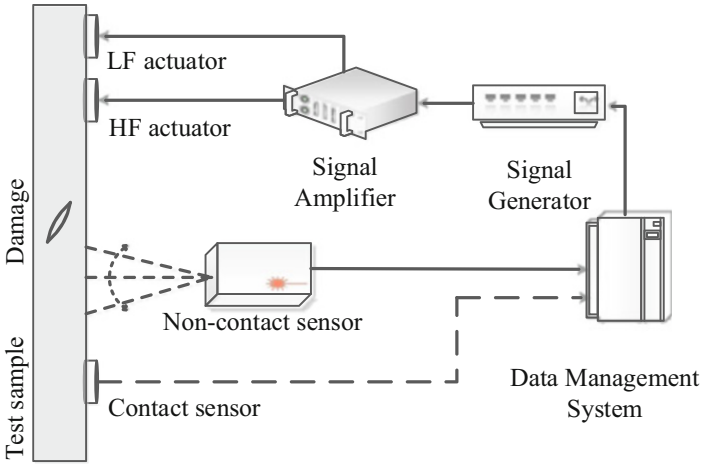

Fig. 4.3 General experimental set-up used for VAM testing

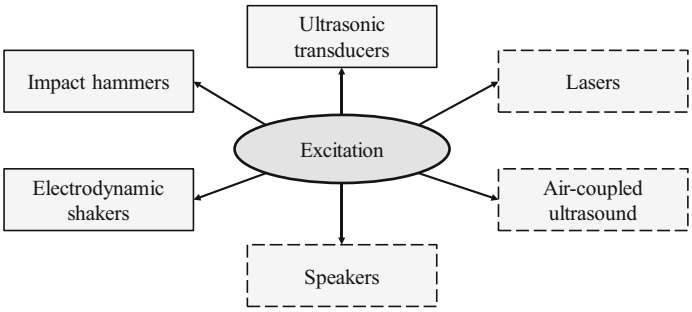

Fig. 4.4 Excitation methods used for damage detection based on non-classical nonlinear acoustics. The solid box frames indicate contact techniques while dashed box frames indicate non-contact techniques

Different possibilities are summarized in Fig. 4.4. Thus, the 'LF actuator' and 'HF actuator', in Fig. 4.3, correspond to different excitation sources reported in Fig. 4.4.

On the measurement side, the most frequently used solutions to acquire vibro-acoustic responses include: contact piezoceramic transducers and non-contact measurements with laser Doppler vibrometers (LDVs) or scanning laser Doppler vibrometers (SLDVs). These are included in the general scheme of the experimental set-up, shown in Fig. 4.3, as the 'Contact sensor' or the 'Non-contact sensor'. Laser vibrometers offer many advantages. These lasers are broadband and allow for flexible choice of measurement locations. This is very important when spatial mapping of signal modulations for damage localization is needed. LDVs and SLDVs are useful for laboratory experiments, where measurement capabilities and flexibility outweigh costs of the system, whereas contact transducers are more useful for field tests and real engineering applications, where less measurement flexibility is necessary and costs need to be optimized.

It appears that nonlinear acoustics has been applied to damage detection for many types of structures, materials and geometries. The scientific literature on this topic is very extensive. It is virtually impossible to provide a comprehensive overview of all these developments. Although the vast majority of applications, that can be found in the scientific literature, are related to crack detection in metallic structures, some attempts have been made to detect damage in other materials, e.g. composites, concrete and bones. It appears that damage detection applications are scattered and demonstrated by the Nondestructive Testing, Structural Health Monitoring, Geophysics and Applied Physics research communities. Very few publications discuss monitoring strategies with respect to excitation frequencies, sensor location and damage severities [43, 44]. Table 4.1 refers to example references in this field.

The following sections discuss in more detail selected application examples, in order to illustrate the experimental/modelling effort undertaken, signal processing used and more importantly to demonstrate the potential of the method for structural damage detection.

Table 4.1 Application examples of non-classical nonlinear ultrasonic/acoustic methods for structural damage detection

Type of damage	Examples of references
Cracks in steel	[35, 45]
Cracks in aluminium	[14, 19, 46]
Delamination in composites	[15, 17, 18, 20, 47, 48]
Debonding and kissing bonds	[49, 50]
Impact damage in sandwich structures	[15, 51, 52]
Cracks in glass	[53]
Cracks in concrete, ceramics	[11, 35]
Cracks in bones	[54, 55]

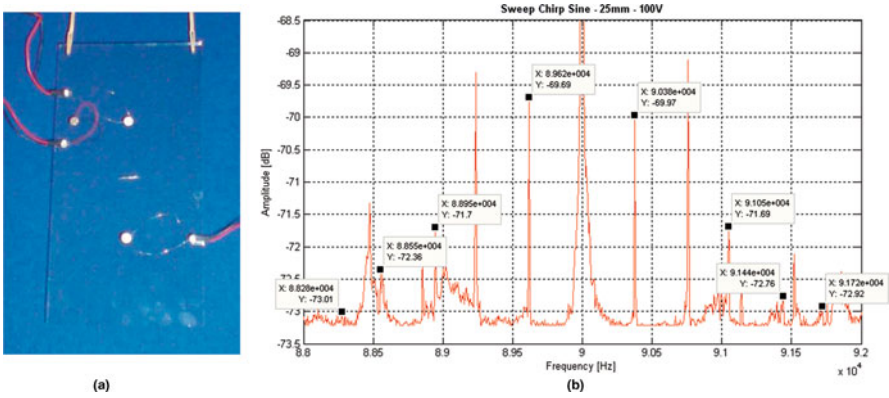

Fig. 4.5 Crack detection based on non-classical nonlinear acoustics in a glass plate: (**a**) glass plate instrumented with low-profile, surface-bonded piezoceramic transducers; and (**b**) power spectrum revealing nonlinear VAM sidebands [53]

4.3.2 Glass

Soda lime glass material is commonly used in many industrial applications (e.g. mirrors, optical windows or filters). Detection for manufacturing/operational crack defects in such applications is an important issue. This example involves the application of the VAM technique to a cracked glass plate.

The 150 × 375 × 6-mm glass plate was used in these investigations (Fig. 4.5a). The Vickers indenter was used to introduce a crack in the middle of the glass plate. Firstly, a 5-mm scratch line was made on the plate surface. Next, to prevent chipping a 3 × 5-mm rectangular steel plate was put between the glass plate and cone-shaped indenter tool. The sample was provided with surface-bonded piezoceramic transducers; one stack actuator *PI Ceramics PL-055.31* (5 × 5 × 2 mm) and two round *PI Ceramics PIC155* transducers (with diameter 10 mm and thickness 1 mm).

The glass sample was suspended to provide free–free boundary conditions. Next, the ultrasonic wave with frequency 90 kHz was introduced to the structure using

one of the *PI Ceramics* transducers. Simultaneously, the plate was excited using the stack actuator. The LF excitation frequency was set as 380 Hz. This value corresponds to one of the structural resonances. Signals used for excitation were generated by a two-channel *TTi-TGA 1242*, 40-MHz arbitrary waveform generator and next amplified by *PI E-505 LVPZT* piezo-amplifier. The amplitudes of low- and high-frequency excitations were equal to 100 and 10 V, respectively. The third piezoceramic transducer was used to measure vibro-acoustic responses of the structure. The responses were acquired with a four-channel *LeCroy Waverunner LT264*, 350 MHz, 1 GS/s digital oscilloscope.

Figure 4.5b shows a clear pattern of VAM sidebands produced by a nonlinear crack wave. The normalized amplitude of these sidebands can be used to estimate the modulation intensity and severity of damage investigated.

4.3.3 Aluminium

The following example involves the application of the VAM technique to a simple cracked plate. The plate was made of aluminium 2024, i.e. the aluminium alloy that includes copper as a primary alloying element. The most important mechanical properties of this material are as follows: Young's modulus—72400 MPa, Poisson ratio—0.33 and mass density—2780 kg/m^3. The 2024 aluminium is isotropic and homogeneous. The experiments were performed using a flat plate of the size equal to 150 × 400 × 2 mm. Firstly, the intact plate was investigated. Then, the fatigue crack was introduced to this plate. The final length of the crack reached 73 mm. The cracked specimen was freely suspended using elastic cords to avoid nonlinearities from boundary conditions. Modal testing together with the Crack Divergence Analysis was performed initially. The latter numerical modelling analysis is intended to identify three basic crack modes:

- Crack mode-I—crack surfaces move directly from each other (the so-called opening–closing mode);
- Crack mode-II—crack surfaces slide on each other; the direction of movement is perpendicular to the leading edge of the crack (the so-called sliding mode);
- Crack mode-III—crack surfaces move relative to each other; the direction of movement is parallel to the leading edge of the crack (the so-called tearing mode).

Following this analysis, the crack modes were correlated with the corresponding experimental mode shapes. Figure 4.6 illustrates three selected mode shapes that exhibit three different dominant crack modes. Natural frequencies corresponding to these mode shapes were selected as LF excitation frequencies.

When the VAM test was performed, the plate was excited at one of these identified resonant frequencies (LF excitation) using an electromagnetic shaker. Mono-harmonic excitation was used with the frequencies selected in the first step of analysis. Amplitude levels for the LF mono-harmonic excitation ranged from 0.25

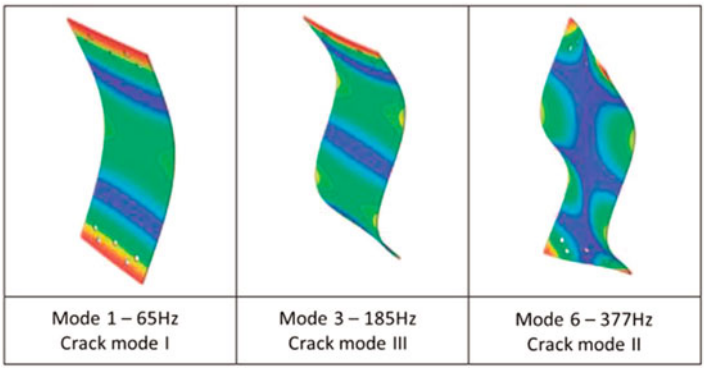

Fig. 4.6 Three vibration modes selected for experimental analysis of VAMs [19]

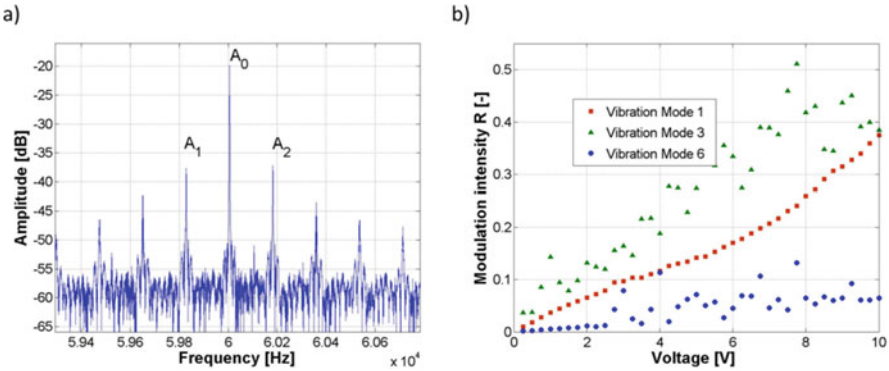

Fig. 4.7 Crack detection in an aluminium plate using the VAM technique: (**a**) example of power spectrum exhibiting nonlinear VAMs resulting from damage, and (**b**) modulation intensity for selected vibration modes and different levels of the LF excitation [19]

to 10 V. Simultaneously, a 60-kHz constant amplitude sine wave (HF excitation) was introduced to the plate using *PI Ceramics PIC155* transducers. Figure 4.7a presents an example of the response power spectrum. Figure 4.7b gives the modulation intensity parameter R—as defined by Eq. (4.1)—for three selected vibration modes.

The results in Fig. 4.7 show that nonlinear modulation sidebands—due to damage—can be observed in the response spectrum. However, different vibration (or crack) modes produce different modulation intensity. Additional tests and analyses were performed in order to explain possible physical mechanisms behind these results. The next test was performed to investigate the link between the closing–opening action of the crack and the modulation intensity. A *Leica MVD1024E-40-CL* camera was used in this test. The camera operating mode was set to a 'lock-in' option to observe the crack closing–opening action [19]. The study revealed that the crack started to open when the amplitude of excitation reached about 6 V. The maximum opening distance of the crack faces was equal to 5 μm.

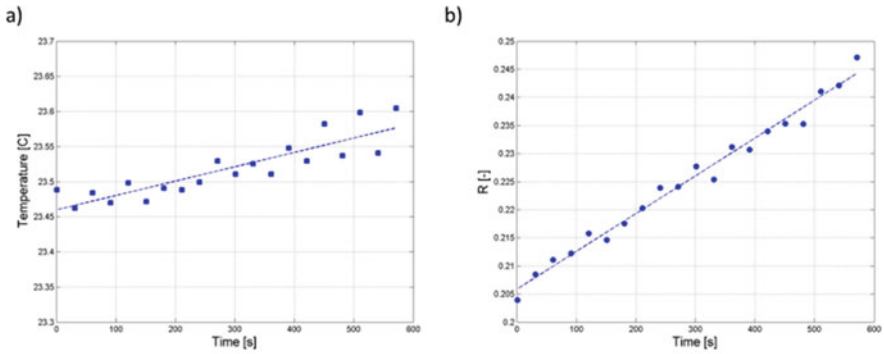

Fig. 4.8 The experimental evidence illustrating the coupling between the thermal and strain fields: (**a**) temperature vs. time, and (**b**) modulation intensity vs. time [19]

For the amplitudes lower than 6 V, the relative motion between crack edges was not observed. When these findings are confronted with Fig. 4.6b, one can see that the slope of the modulation intensity for the Mode I of the crack changes slightly in the excitation range between 6 and 7 V. This behaviour corresponds to the opening action of the crack. However, the modulation intensity R increases also for the lower amplitude levels of the LF excitation. In conclusion, the modulations are stronger when the closing–opening action takes place but the closing–opening action is clearly not required to generate VAMs. Further experimental tests were performed to analyse the temperature field in the vicinity of the crack when the VAM technique was used for damage detection. A photon detector thermographic camera *Cedip Silver 420M* was applied in this experiment. Constant amplitude mono-harmonic LF and HF excitations signals were introduced to the plate for a total duration of 600 s. Temperature changes around the crack area and modulation intensity R were monitored simultaneously in this test. The results are presented in Fig. 4.8.

The results illustrate that the modulation intensity increases when the temperature near the crack increases for one of the analysed vibration (or crack) modes that involves interaction between crack faces. The coupling between the strain (modulated) field and the thermal field is clear, indicating that a dissipative nonlinear mechanisms are important in the VAM technique to reveal damage. For more details, the readers are referred to [19].

The cross-modulation technique, based on the acoustic equivalent of the LG effect, has been applied on the same aluminium samples. In this case, two piezoceramic transducers were attached to excite the plate. An *Agilent DSO-X 3024a* oscilloscope was used as a pumping wave generator. The built-in *Polytec PSV-400* generator was used to generate the 'probe' wave. The excitation frequencies ω_1, ω_2 and the modulation frequency ω_n were selected following the initial experimental modal analysis test. The high-voltage *PAQ-G* amplifier was applied to amplify input signals. The *Polytec PSV-400* laser vibrometer was used to acquire the vibro-acoustic responses.

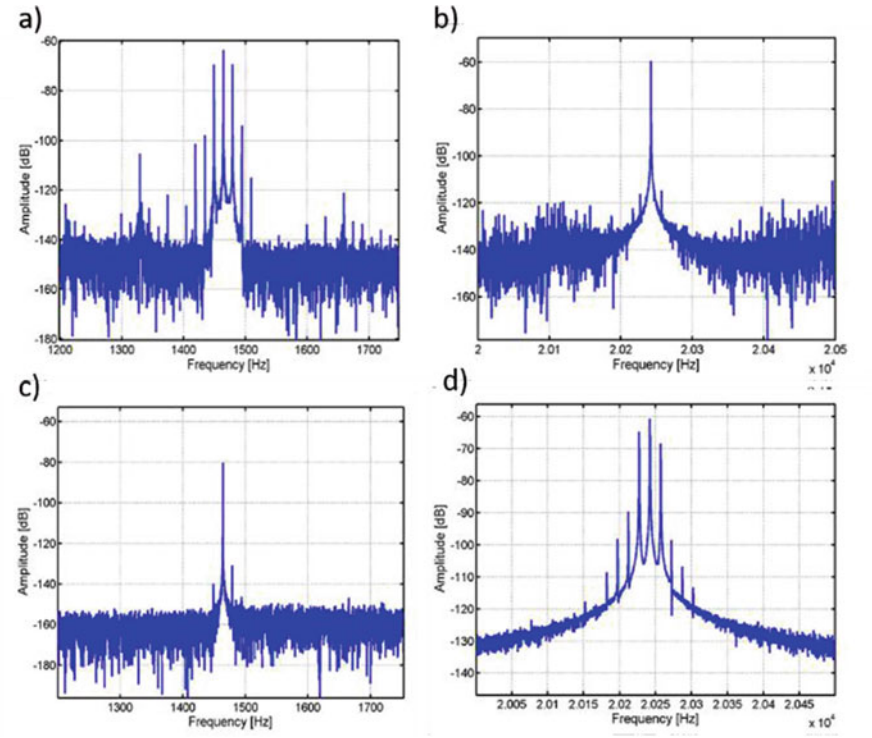

Fig. 4.9 Examples of ultrasonic response power spectra from the cross-modulation technique used for damage detection: (**a**) spectrum zoomed around the 'pump' wave for the undamaged plate, (**b**) spectrum zoomed around the 'probe' wave for the undamaged plate, (**c**) spectrum zoomed around the 'pump' wave for the damaged plate and (**d**) spectrum zoomed around the 'probe' wave for the damaged plate [56]

A series of tests were performed to detect fatigue damage. Both plates were simultaneously excited with the 'pump' and 'probe' waves. The modulation frequency of the 'pump' wave was chosen arbitrarily as $f_{\text{mod}} = 15$ Hz. The 'probe' wave amplitude was set up as constant and equal to 24 V. The 'probe' wave amplitude ranged from 5 to 50 V, with the step of 5 V applied.

Selected examples of the response spectra are presented in Fig. 4.9a, b for the undamaged plate and in Fig. 4.9c, d for damaged plate. The results clearly show that when the plate is undamaged the 'pump' wave exhibits modulation sidebands (Fig. 4.9a), as expected. However, there is no modulation transfer between the 'pump' and 'probe' waves. In contrast, when the damaged structure is investigated a set of modulation sidebands can be observed (Fig. 4.9d) around the main HF component of the 'probe' wave. In this case, the modulation transfer from the 'pump' to the 'probe' wave is clearly visible.

The modulation transfer mechanism for the damaged plate can be also confirmed when the modulation transfer index is investigated in Fig. 4.10. The results show

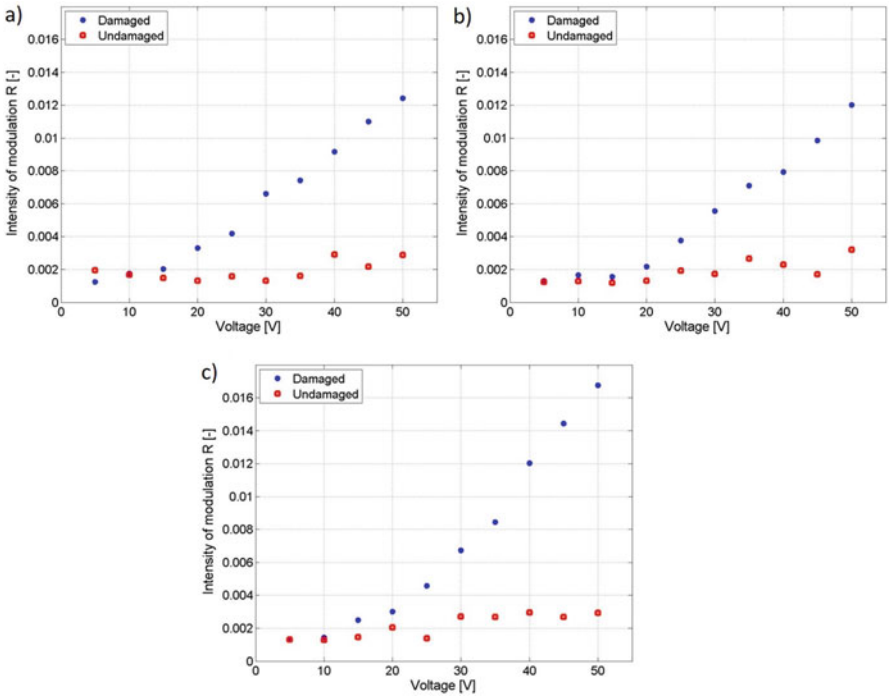

Fig. 4.10 Modulation intensity vs. excitation amplitude for the 'pump' wave resonance frequency equal to: (**a**) 1242 Hz, (**b**) 1464 Hz and (**c**) 3882 Hz

that the R parameter increases monotonically with the excitation amplitude for the damaged plate. In contrast, the relevant parameter remains relatively unchanged for the undamaged specimen when the excitation amplitude increases. When the highest excitation level is used, the modulation intensity is about five times larger for the damaged plate than for the undamaged plate. Similar qualitative and quantitative results can be obtained for other excitation/modulation frequencies used in this test (Fig. 4.10).

This study demonstrates that the modulation transfer, observed previously in cracked glass and granular materials, can be also found in cracked aluminium samples. The potential for structural damage detection applications is clear.

The VAM-based techniques are very efficient and can be used for different types of structures. However, two major observations can be made from all these investigations. Firstly, different vibration modes selected for the VAM test can potentially lead to different damage detection results with respect to damage sensitivity. The method works better for some values of the LF excitation frequency (or mode shapes) and does not work properly for other LF excitation frequencies (or mode shapes). Secondly, the proper frequency selection of the HF excitation is also important and can significantly enhance or amplify damage-related nonlinear

effects. The difficulties related with the selection of excitation frequencies in the nonlinear VAM technique can be overcome when broadband excitation is used simultaneously for the LF and HF excitation. It is well known that the chirp excitation frequency varies as a function of time. Thus, when chirp LF and HF excitations are used, time-varying vibro-acoustics responses are obtained. Then, the classical Fourier analysis cannot be used to extract modulation sidebands. The adaptive resampling procedure was proposed in [33] to transfer the vibro-acoustic response from the time domain to the angle domain. In this method, the signal is sampled with the angular sampling rate $F_s = \frac{1}{\Delta\theta}$, where $\Delta\theta$ is the angular spacing. When the signal with N samples is transformed, the order spacing is equal to

$$\Delta O = \frac{1}{N\Delta\theta}. \tag{4.3}$$

The adaptive resampling procedure guarantees that time-varying data are resampled uniformly following equal angle spacing rather than equal time spacing. Details of this procedure are explained in [33].

The proposed adaptive resampling procedure can be demonstrated using a simple experimental example. Two linear LF and HF chirp excitation signals were introduced to a cracked beam. The LF modulating wave was a linear chirp signal with the frequency content ranging from 500 to 2000 Hz. The HF modulated chirp was a linear chirp signal with frequencies changing from 60 to 240 kHz. The duration time t for both signals was equal to 10 s. The ratio between LF/HF = 1/120 was constant over the whole observation period. Figure 4.11 presents schematically the experimental set-up used for the crack detection experiment. Figure 4.12a shows the vibro-acoustic response of the structure in the time domain. This response was acquired with a LDV. The relevant amplitude spectrum—given in Fig. 4.12b—demonstrates that nonlinear modulation sidebands cannot be extracted reliably from this spectrum.

Therefore, the original response data was processed using the proposed adaptive resampling procedure. The resulting order spectrum—presented in Fig. 4.13—displays a clear pattern of sidebands around the carrier frequency component. After the adaptive resampling procedure, the LF and HF swept sine chirp excitation leads to the spectrum that clearly shows regular and strong modulation sidebands for the cracked specimen. The response resulting from the combined LF and HF swept sine chirp excitation can be directly transformed to the angle domain and then the Fourier order spectrum of this signal can be used to detect damage.

In order to demonstrate the potential of this technique for damage detection, the method was also applied to an intact (or undamaged) beam for comparison. The experiment was performed for different levels of LF excitation signals ranging from 0 to 0.7 V (the input voltage to the electrodynamic shaker driving the beam). Then, the Fourier order spectra were estimated for all signals. Finally, the modulation intensity R parameters were calculated. Figure 4.14 presents the modulation intensity parameter R calculated for the intact and cracked beams, for

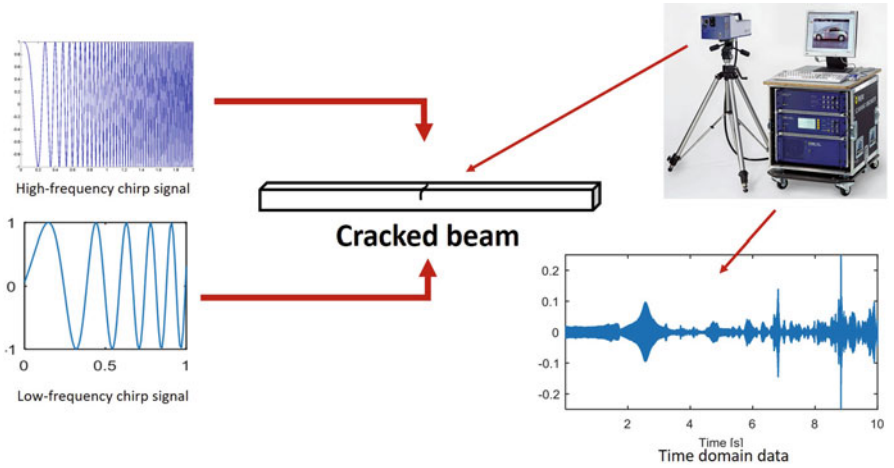

Fig. 4.11 Experimental set-up used for crack detection based on the combined broadband LF and HF excitation

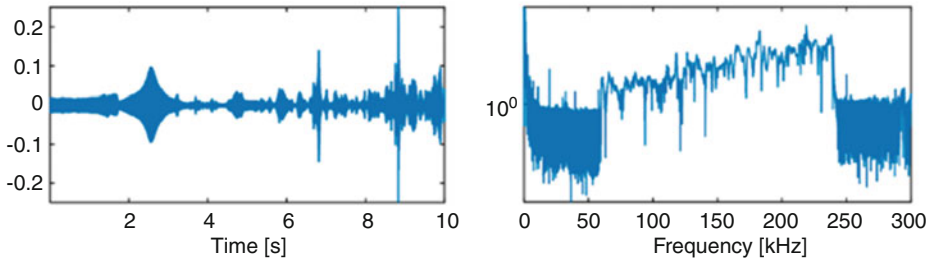

Fig. 4.12 Vibro-acoustic responses for the cracked beam: (**a**) time-domain data, and (**b**) amplitude spectrum

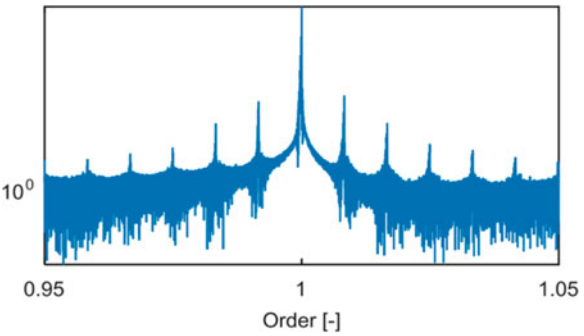

Fig. 4.13 Order domain amplitude spectrum for the vibro-acoustic response given in Fig. 4.12a, after the adaptive resampling procedure

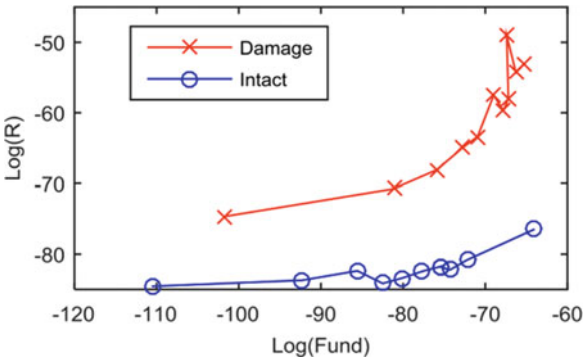

Fig. 4.14 Modulation indices for the intact and crack beams for various amplitude levels of swept sine chirp LF excitation

different driving amplitude levels. The results show that nonlinear modulations increase with the excitation level for both specimens. However, the values of R parameter are always significantly larger (about 10 dB for low-amplitude levels and about 25 dB for high-amplitude levels of excitation) for the cracked beam. The two plots are clearly separated and could be used for damage detection purposes.

In summary, the experimental approach, based on the proposed resampling procedure, removes all the hassles related with the selection of the excitation frequency and amplitude. No a priori knowledge on modal structural behaviour is needed. The procedure is simple, does not require any initial experimental modal testing and works relatively well for all amplitudes of excitation. A major step towards simplicity and robustness is the advantage of the proposed approach. This is exactly what would be needed when the method was used for damage detection in engineering applications.

4.3.4 Composite Laminates

Applications of the nonlinear VAM technique have been also demonstrated in materials with much more complex microstructure and mechanical properties. Composite laminates are an example of layered, anisotropic and inhomogeneous media that are not particularly easy to inspect for damage. The following paragraphs discuss selected application cases where the VAM technique was used to detect damage.

Firstly, a composite 420 × 120 × 2-mm plate, made of Seal Texipreg® HS160/REM carbon/epoxy prepreg layers and laminated with a $[0/\pm 45]_{2s}$ layup, was examined. The composite plate was monitored for damage of different severities, as introduced through low-velocity impacts with energies up to about 10 J. The resulting damage (Fig. 4.15) ranged from barely visible damage, introduced by an impact energy of 2.0 J (damage area = 104 mm^2; residual indentation depth = 0.08 mm), to near penetration, achieved by an impact energy of 10.1 J (damage area = 558 mm^2; residual indentation depth = 0.85 mm).

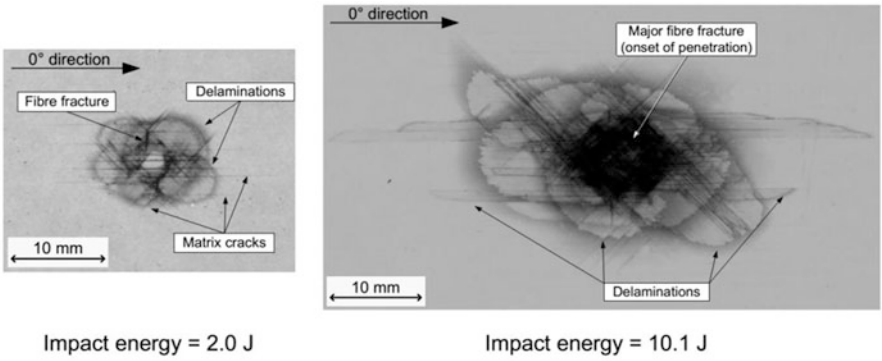

Fig. 4.15 X-radiographs of impact damage for 2.04 J and 10.1 J impacts

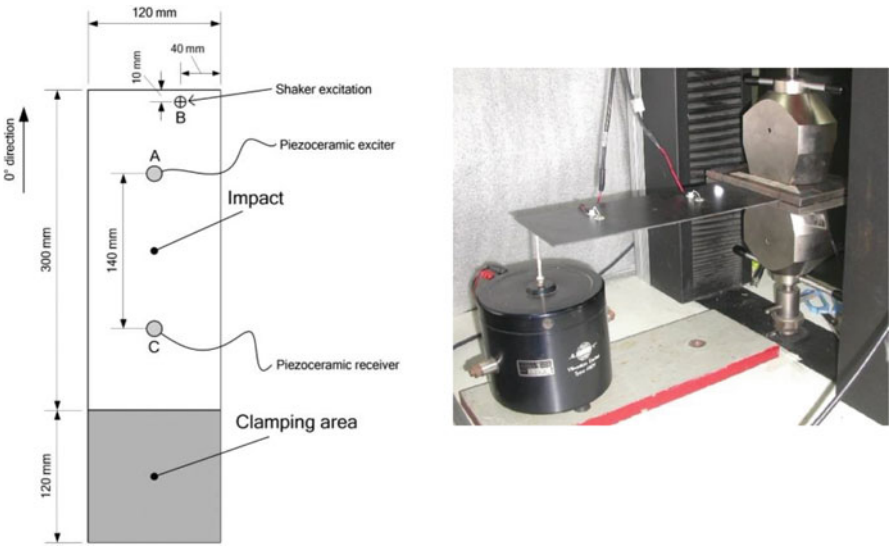

Fig. 4.16 Schematics of the composite sample (left) and experimental clamping arrangement (right)

The plate was instrumented with two *PI Ceramic PIC 151* low-profile piezoceramic transducers bonded at opposite sides of the damage area, as shown in Fig. 4.16. During the experiments, the composite plate was clamped at one end between two steel plates by a 5-kN servoelectric testing machine, which allowed to monitor and control the applied clamping force.

Preliminary tests were carried out on the intact plate to identify modal and ultrasonic structural resonance frequencies that exhibited sufficiently high signal-to-noise ratio responses for subsequent use in the VAM technique. Resonance modal frequencies (LF) of 77,262 and 2934 Hz and acoustic frequencies (HF) of 17.63 and 98.04 kHz were finally selected as pumping and probing frequencies for the damage detection tests.

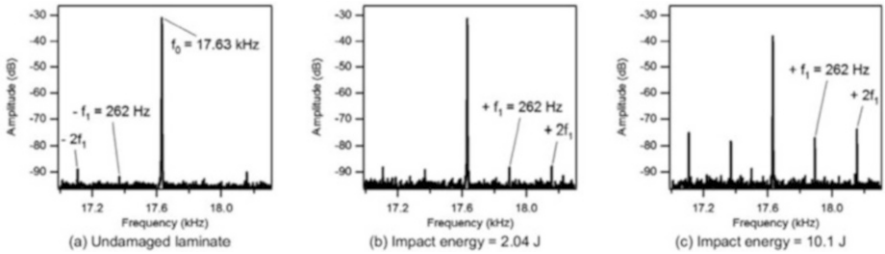

Fig. 4.17 Power spectra of signals acquired with 262 Hz pumping excitation and 17.63 kHz probing excitation: (**a**) undamaged laminate; (**b**) laminate damaged with 2.04 J impact energy; (**c**) laminate damaged with 10.12 J impact energy

Vibro-acoustic modulation tests were first carried out on the undamaged plate and then on the plates as damaged by impact at increasing energy levels. In all tests, the 'pump' wave was introduced to the plate at location B using an electromagnetic shaker, while the 'probe' wave was introduced to the piezo actuator at location A (Fig. 4.16). Sine waves were used for probing excitation, while either pure or amplitude-modulated sinusoidal signals were used as probing waves; the response signal was acquired from the piezoceramic transducer at position C.

Figure 4.17 gives examples of power spectra for a vibro-acoustic excitation characterized by 262 Hz pumping frequency and 17.63 kHz probing frequency. The graphs in Fig. 4.17 show that a pattern of sidebands appears around the probing excitation frequency and that the amplitude of sidebands increases with increasing damage severity. A significant drop in the amplitude of the acoustic excitation frequency is also observed for the plate damaged by the 10 J impact with respect to the intact plate. Similar trends were observed when exciting the plate with the other pumping and probing frequencies selected was the preliminary phase, as well as when an amplitude-modulated sinusoidal signal is used for pumping excitation. In all testing configurations, the experimental results show that nonlinear modulation effects are generated in the presence of damage and that the intensity of modulation generally increases with the extent of damage. As an example, the graph of Fig. 4.18 plots the damage index DI, as obtained through an amplitude-modulated pumping excitation, versus impact damage area; the DI is defined here as

$$DI\,(dB) = \left|A_{f_0} - A_{\mathrm{sb}}\right|_{\mathrm{undamaged}} - \left|A_{f_0} - A_{\mathrm{sb}}\right|_{\mathrm{damaged}} \tag{4.4}$$

where A_{f_0} is the amplitude (in dB) of the fundamental frequency of the probing wave and A_{sb} is the average amplitude (in dB) of the first pair of sidebands.

As visible in Fig. 4.17, sidebands around the probing frequency could be observed even in the response of the plate in the undamaged state. The presence of these sidebands may be related to intrinsic material nonlinearities or to contact type phenomena, such as those associated to the specific boundary or support conditions of the structure.

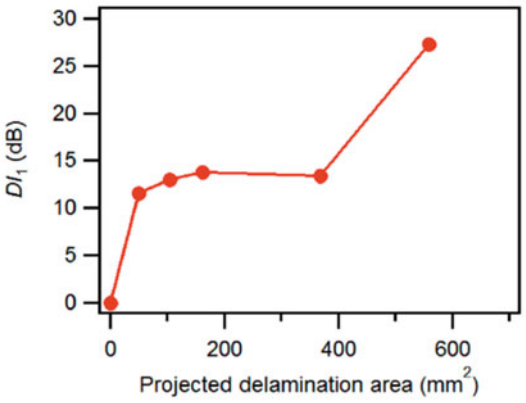

Fig. 4.18 Damage index DI vs projected delamination area. An amplitude-modulated sine wave was used for pumping excitation

The influence of the boundary conditions as a source of nonlinearity was investigated by analysing the results of vibro-acoustic experiments carried out on the composite plate when subjected to an increasing clamping force. The graphs of Fig. 4.19 show that the amplitude of the first sidebands decreases and the amplitude of the probing frequency increases with the clamping force for the undamaged plate. On the other hand, opposite trends were observed for the damaged plate thus suggesting possible differences in the nonlinear mechanisms activated by the boundary contact phenomena with respect to those induced by the waves-damage interaction.

4.3.4.1 Local Defect Resonance

The concept of the local defect resonance (LDR) is based on local stiffness loss due to damage and the fact that every localized damage in a material will have a resonant frequency that can be utilized for damage detection [57]. The problem of the LDR frequency in application to the VAM technique is presented in this subsection.

As an example, two composite plates manufactured from carbon/epoxy system (*Seal HS160/REM*) with dimension 150 × 300 × 2 mm were investigated. Firstly, the specimens were ultrasonically C-scanned to exclude any manufacturing defects. Next, a drop-weight testing machine was used to introduce impact damage. After impact, the structure was ultrasonically C-scanned once again to illustrate the severity of damage. The calculated hidden damage area was 326 mm^2; no visible evidence of damage was observed on plate's surfaces.

Simultaneously, the Finite Element (FE) model of the damaged plate was developed using the *MSC Patran* preprocessor in order to estimate modal properties of the plate and perform delamination divergence analysis [20], to find the possible scenarios of relative movement between delamination plies. In theory, two possible scenarios are assumed: (1) out-of-plane motion when two delaminated surfaces

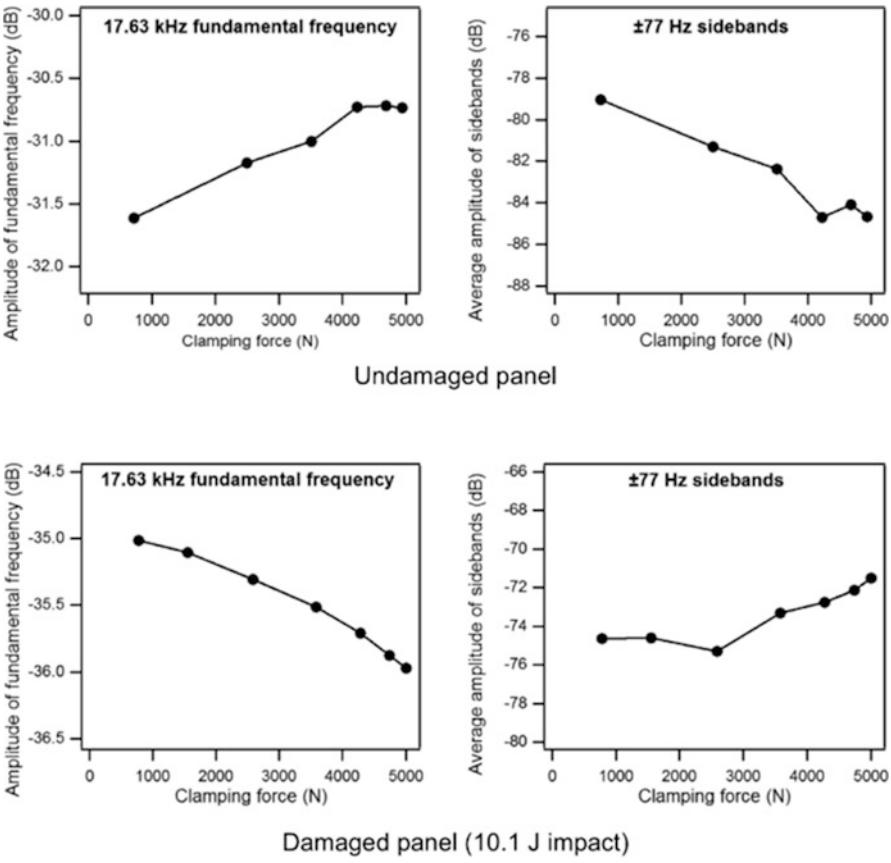

Fig. 4.19 Effect of clamping force on the amplitude of the fundamental frequency of the probing wave and of the first sidebands for the undamaged and damaged (10.1 J impact energy) plate. Pumping frequency = 77 Hz; probing frequency = 17.63 kHz

move creating the gap (Fig. 4.20a); (2) in-plane motion when delaminated surfaces are in contact and move relative to each other (Fig. 4.20b). In practice, both movements are mixed; however, in this case the dominant type of motion for a given mode shape was investigated.

The second task of numerical modelling was to find the frequency which corresponds to resonance of damage (LDR). For this reason, the frequency range of simulation was extended to 50 kHz, and geometry of the defect was introduced to the numerical model. The results of the analysis are presented in Fig. 4.21c.

Following these results, two mode shapes were selected for further analysis, i.e. the 5th vibration mode (325 Hz) displaying the dominant out-of-plane motion and 7th vibration mode (460) Hz displaying the dominant in-plane motion. The LDR frequency—estimated numerically as 29, 852 Hz—was selected as the HF

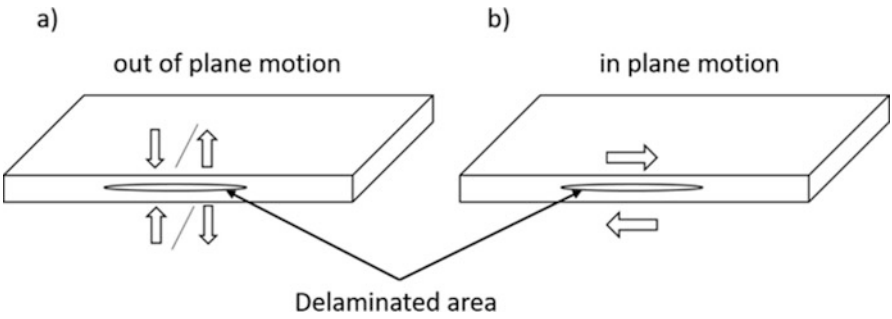

Fig. 4.20 Delamination motion scenarios: (**a**) out-of-plane motion, and (**b**) in-plane motion

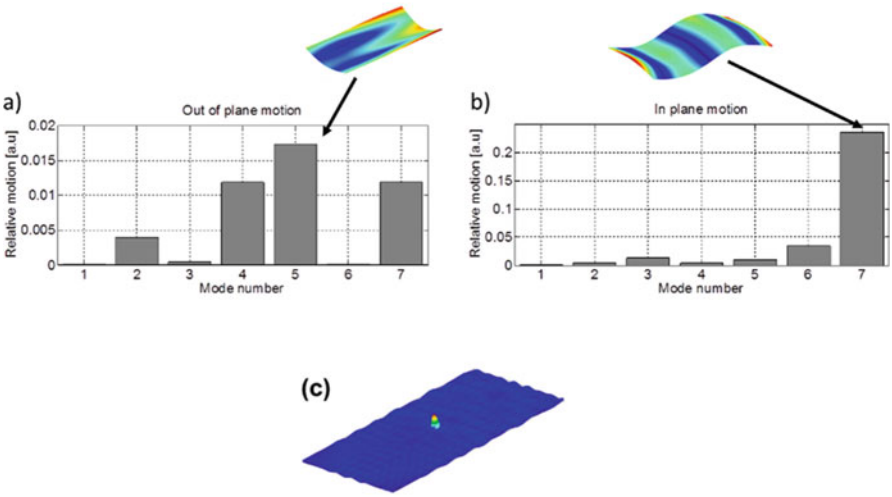

Fig. 4.21 Contribution of two distinct delamination behaviour scenarios for the first seven vibration mode shapes: (**a**) dominant opening and closing action ("breathing") for the 5th vibration (325 Hz), (**b**) dominant in-plane sliding action (frictional motion) for the 7th vibration mode (460 Hz) and (**c**) the 364th vibration mode (29,852 Hz) exhibiting the LDR behaviour

frequency. Next, the experimental validation was performed to verify the proposed model. Comparison of the numerical and experimental results is presented in Fig. 4.22.

The frequencies of the modes selected numerically and validated experimentally were chosen for further analysis. Once the VAM test was performed for the undamaged and damaged composite plate, power spectra were estimated for the vibro-acoustic acoustic response signals in order to reveal the possible modulation sidebands. Figure 4.23 presents examples of power spectra zoomed around the HF excitation frequency.

Finally, the R parameter representing the intensity of modulation was calculated for different levels of excitation amplitudes. The results are shown in Fig. 4.24.

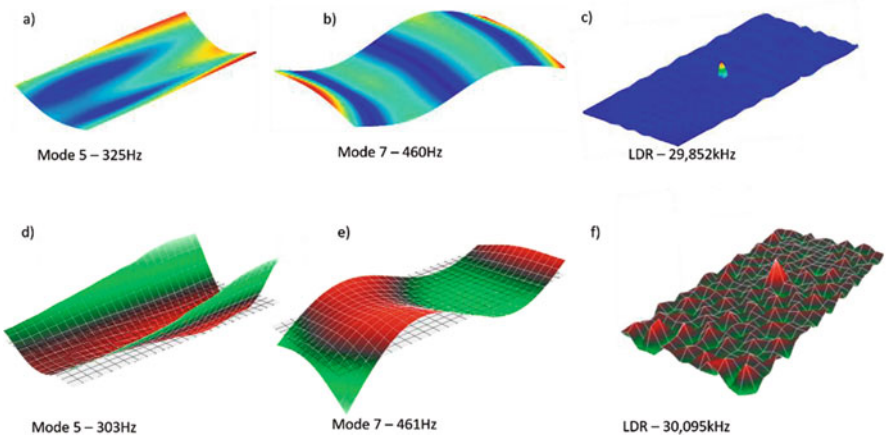

Fig. 4.22 Comparison of numerically predicted (**a**–**c**) and experimentally estimated (**d**–**f**) mode shapes of the investigated laminate damaged plate

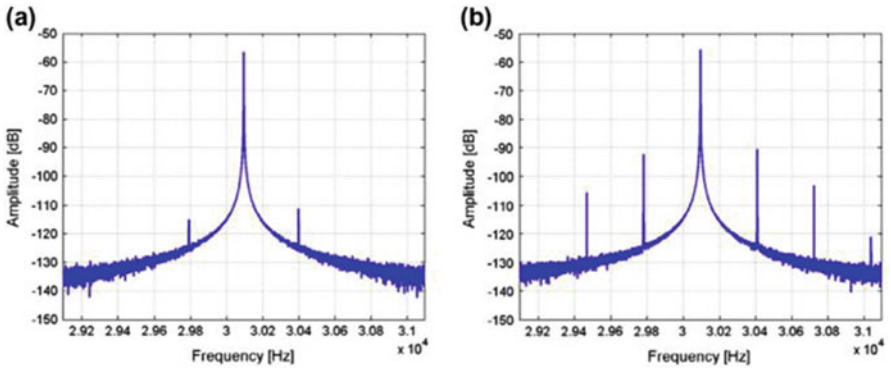

Fig. 4.23 Examples of zoomed vibro-acoustic response power spectra for: (**a**) undamaged plate, and (**b**) damaged plate

The presented results show that for the fifth vibration mode (Fig. 4.24a, c) the difference in intensity of modulation between undamaged and damaged sample is still significant for both HF excitation frequencies. However, for larger excitation amplitudes the R parameter starts increasing more sharply when the HF frequency does not correspond to the LDR (Fig. 4.23a). It is also clearly visible that for the HF = 30,095 Hz ultrasonic excitation—corresponding to the LDR—the modulation intensity parameter is about five times larger than when the 43 kHz HF excitation (selected a priori) is used. Two main conclusions can be made when the results are analysed. Firstly, the out-of-plane movement of delaminated area produces higher modulation than the in-plane movement in the case investigated. Secondly, the intensity of modulation is significantly amplified when the LDR frequency is applied for ultrasonic excitation.

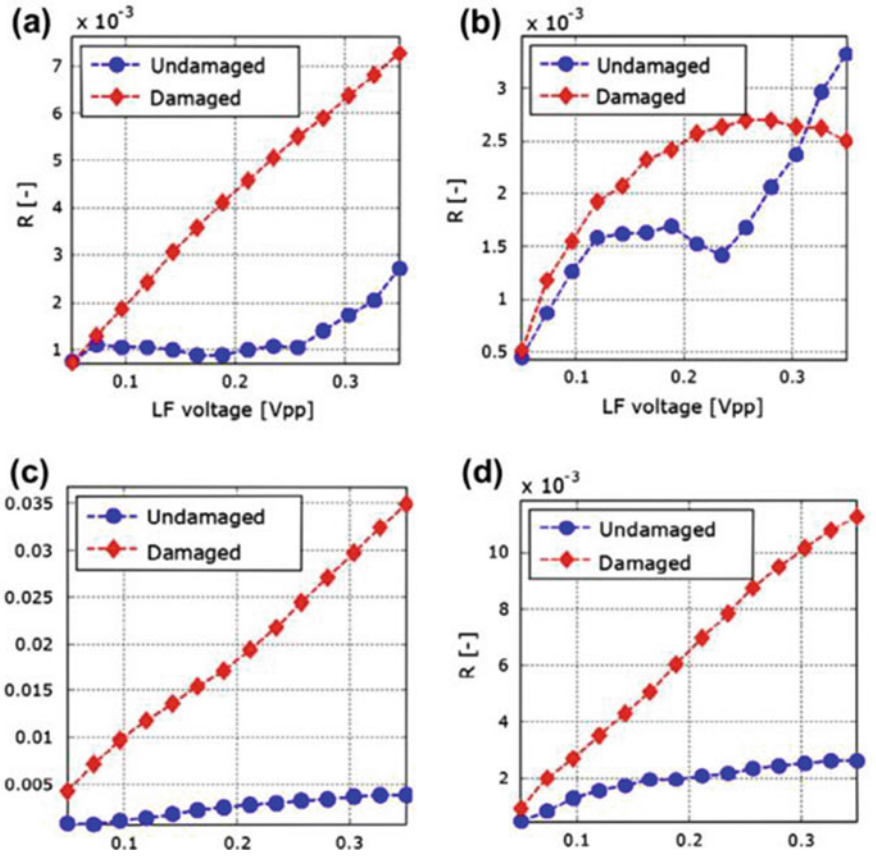

Fig. 4.24 Intensity of modulation vs. low-frequency excitation amplitude level: (**a**) 5th vibration mode used for the LF excitation and HF = 43 kHz, (**b**) 7th vibration mode used for the LF excitation and HF = 43 kHz, (**c**) 5th vibration mode used for the LF excitation and the LDR frequency used for the HF excitation and (**d**) 7th vibration mode used for the LF excitation and the LDR frequency used for the HF excitation

4.3.4.2 Vibro-Acoustic Modulation-Based Damage Imaging

The application examples presented in the previous sections demonstrated so far the presence of damage (damage detection). The following paragraphs present an approach that can be used to localize or "image" damage. The standard VAM technique is used in this approach. In principle, the proposed technique is similar to the previously used spatial mapping-based methods [58–60]. However, in contrast to higher harmonics and subharmonics analysis, the nonlinear modulation sidebands are used for damage localization.

It is well known that nonlinear higher harmonic generation is highly localized and particularly strong in the vicinity of damage, as has been documented in the

literature [58–61]. More recently, it has been also demonstrated that nonlinear modulation sidebands exhibit the same localization property. Therefore, sideband imaging—rather than higher harmonic imaging—can be used to localize damage without the need to increase the measurement bandwidth to the higher harmonics regime [62]. The procedure proposed for damage localization is similar to the procedures based on higher harmonics imaging known from the literature. That is, surface-bonded piezoceramic transducers are used for the LF and HF excitation and a laser vibrometer is used for response measurements. However, in contrast to the typical damage detection test, responses are acquired for locations at a predefined grid on the entire surface of monitored specimens using the scanning capability of laser vibrometer. Power spectra from measured responses are calculated to reveal modulation sidebands at frequencies equal to HF $\pm$ n·LF components, where n is a positive integer. The modulation intensity—based on the amplitude of sidebands—is then analysed for all scanned points to reveal areas of large modulation intensities due to structural damage. In the proposed case, the modulation intensity defined by the mean value of the first modulation sidebands amplitudes is mapped.

Experimental example presented in this chapter involved the same composite specimen as described in the preceding paragraphs. The frequency of the LF excitation was equal to 491 Hz and the frequency of the HF excitation was equal to 50 kHz. The results of the imaging procedure can be seen in Fig. 4.25.

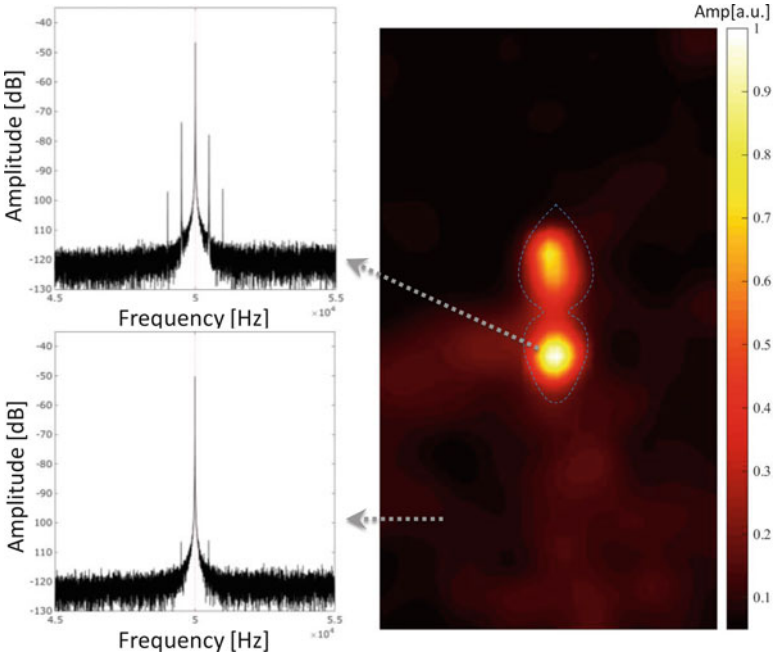

Fig. 4.25 Comparison of power spectra measured at two different and indicated locations on the plate for excitation frequencies equal to LF = 491 Hz and HF = 50 kHz [62]

Figure 4.25 shows the comparison of two power spectra measured at two different locations on the plate for excitation frequencies equal to LF = 491 Hz and HF = 50 kHz. The results show that the level of modulation sidebands is much higher around the damage location if compared with the healthy (undamaged) area of the plate. Firstly, the potential for damage imaging is evident from this example. Secondly, the results clearly indicate that a proper choice of the measurement point for the classical nonlinear VAM testing is very important. Although the modulation sidebands can be seen in all measurement points across the plate, the amplitude level of sideband components is significantly different depending on the location on the plate. As a consequence, an inappropriate choice of measurement location may lead to false-negative damage detection.

4.3.4.3 Triple Correlation for Damage Detection in Composite Structures

First investigations of the triple correlation (TC) were made in the early 1960s for examining non-Gaussian random processes. The main applications of the technique mainly concern statistical observation of ocean waves and laser spectroscopy. From mathematical point of view, the auto-triple correlation can be defined as [63]:

$$c(\tau_1, \tau_2) = \int x(t)x(t+\tau_1)\,x(t+\tau_2)\,dt \tag{4.5}$$

where $x(t)$ is time-domain signal and τ_1 and τ_2 are time delay intervals. When τ_1 and τ_2 are zeros, the triple correlation remains in proportion to the autocorrelation function. It means that information on amplitude and phase of the signal is still available. It is important that the time delay intervals τ_1 and τ_2 should correspond to frequency values in the spectral domain. Then, the Fourier transform of the auto-triple correlation becomes the bispectrum and can be written as

$$B(f_1 + f_2) = X^*(f_1 + f_2)\;X(f_1)\;X(f_2) \tag{4.6}$$

where $X(\bullet)$ means the Fourier transform of $x(\bullet)$ and symbol "*" indicates the complex conjugate value. This function is very often used to find nonlinear interactions in signals due to quadratic phase coupling.

This signal processing method was used to analyse response signals recorded during the VAM test. In this case, only harmonics of the low frequency were analysed. Firstly, the delamination divergence numerical test was performed to characterize relative motion of delaminated plies. Based on Finite Element (FE) model, the relative displacement in-plane and out-of-plane were investigated. Next, the experimental modal test was performed. For further testing, the mode shapes fulfilling the following condition were investigated:

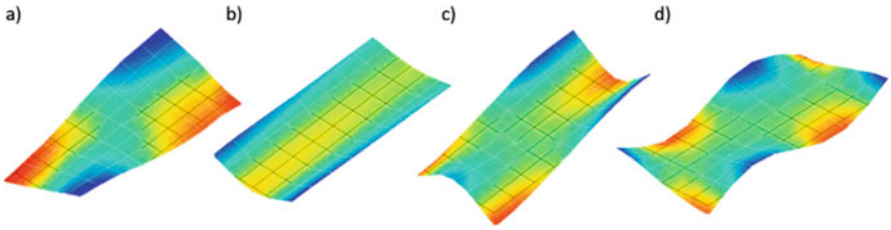

Fig. 4.26 Investigated mode shapes; (**a**) 1st—79 Hz, (**b**) 4th—334 Hz, (**c**) 5th—365 Hz and (**d**) 8th—736 Hz

- Should exhibit strong out-of-plane movement of delamination,
- Should exhibit strong in-plane movement of delamination,
- Should exhibit weak (i.e. very little movement) of delamination.

The modes 1st, 4th, 5th and 8th—presented in Fig. 4.26 were selected for VAM test.

In the last stage of testing, the triple correlation coefficients were calculated and the results are presented in Fig. 4.27.

For Mode 1 (Fig. 4.27a), where the relative movement between delamination interfaces is minimal, the TC coefficient has very low values and increases insignificantly with excitation amplitude. The small difference is observed after the excitation amplitude reaches 50 V. For Mode 4 (Fig. 4.27b), difference between damaged and undamaged plate in TC values is also small. In both above cases, the out-of-plane motion was dominant. The coefficients are almost constant for all excitation amplitude levels but generally for the damaged plate the TC values are larger. This indicates that weak nonlinearities in the analysed responses are rather not related to damage since the relevant nonlinear parameters do not increase significantly with excitation amplitude levels and a similar behaviour occurs for both, i.e. damaged and undamaged, plates. Here, material nonlinearities could be involved. The results for Mode 5 (Fig. 4.27c) show that the TC coefficient increases monotonically until the 50 V excitation amplitude level is reached in the case of damaged specimen. In contrast, the relevant parameter remains almost at the same level for the undamaged plate. The relevant characteristics for the undamaged and damaged specimens are also well separated. Large values of triple correlation coefficient indicate that there is a strong correlation between the fundamental frequency and its higher harmonics. Here, higher harmonics are clearly related to damage. When the plates are excited with the frequency of Mode 8 (Fig. 4.27d), the analysed characteristics for the undamaged and damaged plates are also well separated for all excitation amplitude levels. The above-presented results show that:

- The nonlinear effects are mainly related to delamination movements. This behaviour is particularly observed when weaker vibration modes (selected on the basis of delamination divergence analysis) and low-excitation level is used.

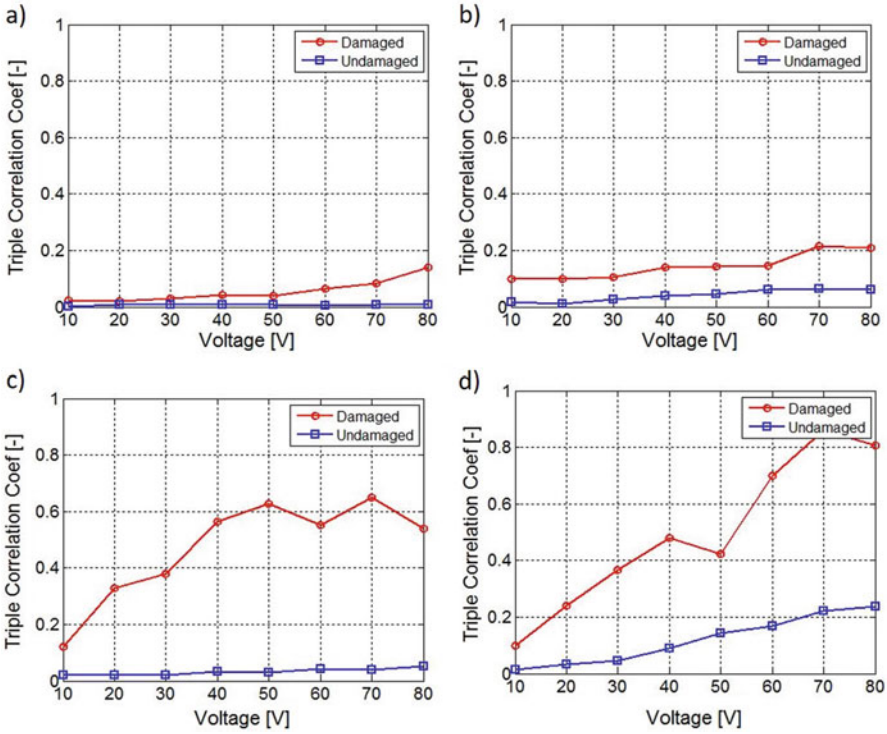

Fig. 4.27 Triple correlation coefficients for damaged and undamaged plates: (**a**) 1st vibration mode; (**b**) 4th vibration mode, (**c**) 5th vibration mode and (**d**) 8th vibration mode [63]

- The in-plane motion of the delaminated plies produces the most significant nonlinear effects. In the case of out-of-plane motion (or very low relative motion between delamination surfaces), nonlinear effects are much weaker. Thus, the mechanism of higher harmonics generation is related to dissipation (friction and/or hysteresis) rather than to elasticity.
- For higher amplitude levels of excitation, the stronger nonlinear effects are produced but unfortunately these excitation levels may also lead to intrinsic nonlinear effects that are not related to damage.

4.3.5 Composite Sandwich Panels

4.3.5.1 Chiral Core Sandwich Panel

The chiral composites are the new type of structures that could be used for many potential engineering applications. In these structures, the chirality is used to obtain auxetic cores with negative Poisson's ratio.

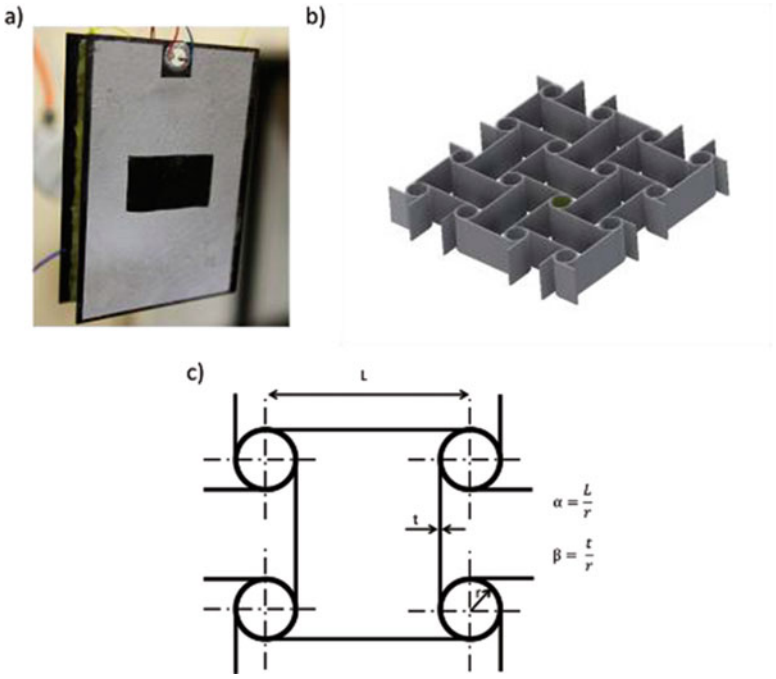

Fig. 4.28 Chiral sandwich composite panel: (**a**) general view with the location of piezoceramic transducer used for high-frequency ultrasonic excitation, (**b**) vires of anti-tetrachiral core joined to composite plates and (**c**) geometry of anti-tetrachiral topology [51]

The investigated chiral composite sandwich panel (Fig. 4.28) was manufactured using a truss-core with an anti-tetrachiral configuration (Fig. 4.28b). The skin was made with two quasi-isotropic composite plates. The aspect ratio α of the cells was 6 and relative thickness β is 0.4. The size of the unit cell L was 25.4 mm, with a gauge thickness of 25 mm. The parameters of the anti-tetrachiral topology are presented in Fig. 4.28c. The honeycomb panel was made of 5 × 3 unit cells. The *PI Ceramics PIC155* transducers were fixed to the skin of the structure, as shown in Fig. 4.28a.

The method based on nonlinear vibro-acoustic wave modulations is used in this case for damage detection. The low- and high-frequency excitations are introduced to the chiral structures simultaneously. Experimental modal testing was performed initially to obtain modal properties of the chiral panel and select values of LF excitation used in nonlinear acoustic tests [51]. The frequencies of three vibration modes (Fig. 4.29b), i.e. 1512 Hz, 2363 Hz and 3801 Hz, were selected for damage detection application in these tests. The first frequency was related to global torsion, the second frequency led to flexural deflection and the third frequency exhibited a combined torsional and flexural movement.

Drop-weight impact tests were carried out to introduce impact-type damage to the composite structure. Three impacts with energy 2, 9 and 30 J were performed to

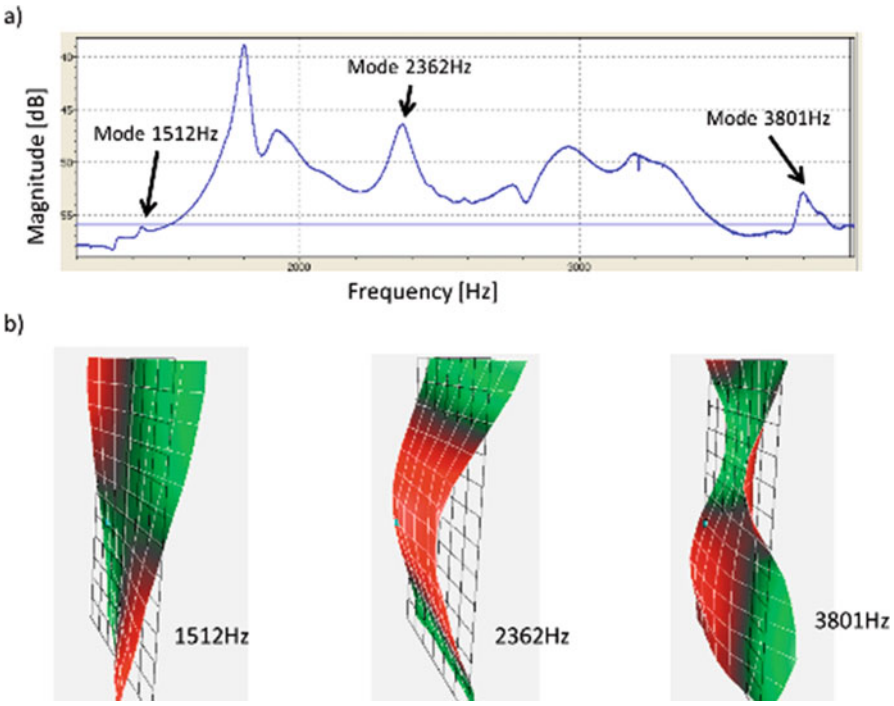

Fig. 4.29 Experimental modal analysis results for the composite chiral sandwich panel: (**a**) frequency response function magnitude, and (**b**) selected vibration modes

introduce damage in the middle of the top composite skin. After every impact, the modal analysis and the VAM technique were performed.

A series of VAM tests were carried out to analyse the intensity of modulation for various LF excitation amplitude levels. The HF excitation amplitude was kept constant during these tests. Finally, the modulation intensity was estimated using the *R* parameter, as defined by Eq. (4.1).

The results presented in Fig. 4.30 give the *R* parameter for three selected vibration modes. The results show that for the undamaged panel the intensity of modulation does not increase when the excitation amplitude increases. Similar behaviour can be observed for the third vibration mode and all impact energies investigated (Fig. 4.30c). For the first vibration mode, intensity of modulation increases significantly but only for the damaged chiral panel after the 30 J impact (Fig. 4.30a). When the second vibration mode is analysed, the modulation intensity increases with the excitation amplitude level for all impacts (damages) investigated. The weakest growth can be observed for the 2 J impact. For the 9 J impact, the *R* parameter increases significantly when excitation amplitude reaches 17 V. For the 30 J impact, the R parameter increases rapidly even for very low-excitation amplitude levels.

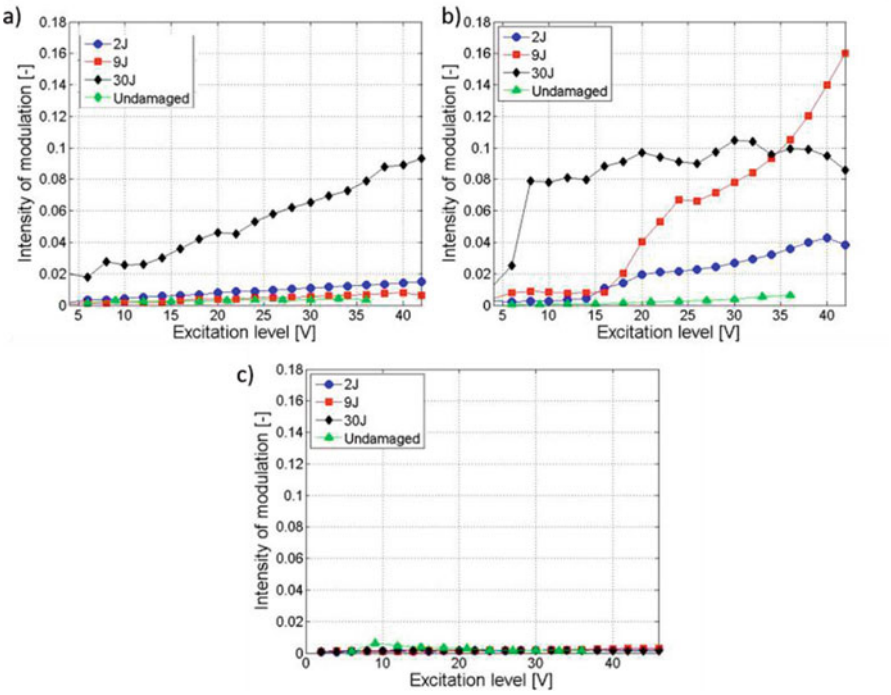

Fig. 4.30 Intensity of modulation vs. low-frequency excitation: (**a**) 1st vibration mode, (**b**) 2nd vibration mode and (**c**) 3rd vibration mode

In summary, the results show that it is possible to detect damage in complex chiral structures when the nonlinear VAM technique is used. However, the proper selection of excitation parameters is the key element in these investigations. The results are satisfactory only for the second vibration mode. For this mode, even after the relatively small 2 J impact the modulation intensity increases monotonically with the excitation amplitude level.

4.3.5.2 Foam Core Sandwich Panel

Another type of composite sandwich panels that were investigated with VAM contained a foam core. Closed-cell rigid foams allow to produce comparatively low-priced high-integral sandwich components having a complex geometry in terms of a curved and a variable lateral cut. The dimensions of the samples were 400 × 120 × 13.2 mm. The external panels were made of Seal Texipreg HS300/ET223 prepreg system. Ply stacking sequence was $[0/90_3/0]$. The thickness of the face laminate was 1.6 mm. The core of the panel was a closed-cell polyvinyl

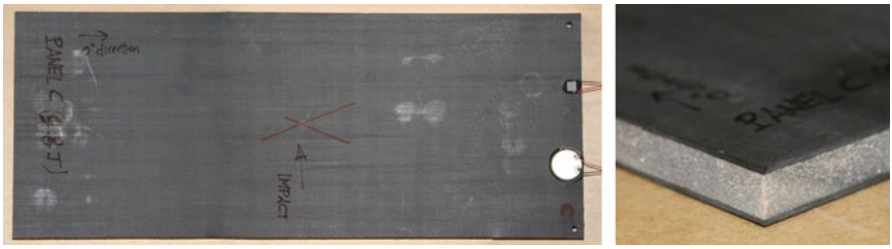

Fig. 4.31 Composite sandwich panel investigated with the VAM technique: (**a**) top view, and (**b**) details of the sandwich structure [52]

chloride (PVC) foam DIAB Divinycell HP60. The total thickness of the core was 10 mm. Figure 4.31 presents the panel.

For one of the panels, the impact test with the energy of 9.8 J was performed to produce a barely visible impact damage (BVID). The area of the damage was estimated as 640 mm^2. The VAM tests were performed on both, i.e. damaged and healthy/reference, panels using the same experimental set-up. The LF and HF excitations were introduced using the *PI Ceramic PL055.30* piezoelectric stack actuator and *PI Ceramic* 15 × 1-mm piezoelectric disc, respectively. The excitation signals were generated by an *Agilent 33522A* signal generator and amplified by an *EC Systems PAQG* amplifier. Structural responses were measured using a *Polytec PSV400* SLDV. The value of the selected LF excitation corresponded to the first bending mode of the sample (approximately 700 Hz). The HF excitation was arbitrarily selected as 40 kHz. The LF excitation amplitude was monotonically increased in the range from 10 to 70 Vp-p with step 10 Vp-p.

The results of the experimental works are presented in Fig. 4.32. The calculated response power spectrum for the undamaged sample (Fig. 4.32a) shows no modulation sidebands around the high-frequency component. In contrast, the spectrum in Fig. 4.32b—calculated for the damaged panel—exhibits modulation sidebands around the HF component. Figure 4.32c shows the intensity of modulation parameter R (calculated from Eq. (4.1)) for the undamaged and damaged panels and various LF excitation amplitudes. The results show that the damaged and undamaged conditions can be easy distinguished. The presented method has one more advantage, as already mentioned in the introduction to this chapter. For industrial applications, the experimental set-up can be easily simplified. The expensive SLDV can be replaced by a piezo-ceramic transducer, to obtain an effective health monitoring system. The presented example shows that the application of VAM technique is easy to use and does not need highly specialized equipment or/and signal processing techniques.

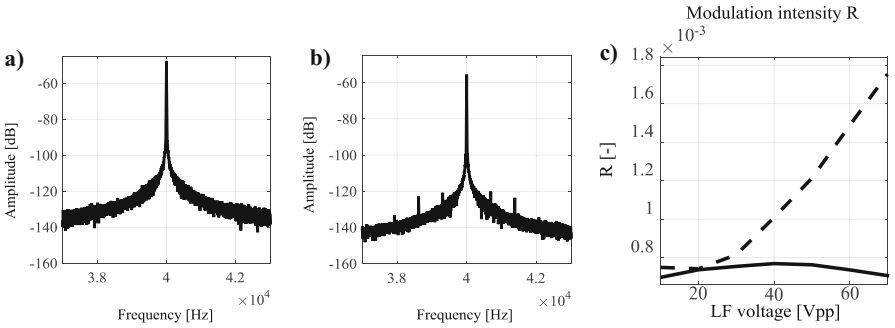

Fig. 4.32 Results of the VAM technique used for a composite sandwich panel: (**a**) response power spectrum for the undamaged panel, (**b**) response power spectrum for the damaged panel and (**c**) modulation intensity for different LF excitation amplitudes; the results are given for the undamaged (solid line) and damaged (dashed line) panels [52]

4.4 Final Remarks

Recent years have demonstrated the growing interest in the application of classical and non-classical nonlinear techniques for damage detection. The scientific literature related to this topic is voluminous. This chapter presented an overview of applications related to non-classical nonlinear acoustic phenomena used for damage detection and localization. The major focus was on the application of VAM. These applications were demonstrated for different materials, structural components and types of damage.

In particular, the VAM technique was discussed in detail. The technique provides the first level of SHM capability and allows obtaining global information about the presence of damage in the structure. Some of the VAM techniques also allow damage localization and estimation damage size. This means that the technique can detect damage in the structure and can be also used for continuous structural monitoring. Additionally, experimental set-up and hardware necessary to implement VAM techniques is fairly simple. It needs only three piezo-ceramic transducers: one for low-frequency excitation, one for high-frequency excitation and one for signal acquisition. These three transducers can be fixed to the structure or also integrated in a single VAM sensor. Over the last 20 years, a lot of progress has been done in the transducer development field, signal processing techniques and theory related to the VAM phenomena. We also demonstrated that the VAM technique can be extended to provide damage localization using sidebands imaging. Despite the advantages, the technique still faces challenges. One of the most important is to separate the intrinsic nonlinearities from that observed in nonlinear responses. These problems have been discussed many times in the literature but still a lot of research work is necessary to introduce VAM techniques to practical engineering applications.

The examples presented lead to the following conclusions:

- Damage detection methods based on nonlinear acoustics (ultrasonic wave propagation and wave interaction with damage) have been successfully used to reveal

different types of structural damage in different materials. However, the vast majority of these applications relates to laboratory demonstrations rather than to real field tests and engineering applications.

- The results presented illustrate that the proper selection of parameters in nonlinear acoustic tests is essential for reliable damage detection. Unfortunately, very little studies have been performed to establish reliable monitoring strategies with respect to excitation frequencies/amplitudes, sensor location, signal processing or uncertainty analysis. It is clear that major research effect is also required to distinguish between damage-related and non-damage-related (or intrinsic) nonlinear effects in order to avoid false-positive and false-negative damage detection.
- Non-contact excitation/measurement, damage visualization and hybrid approaches (i.e. approaches that combine different nonlinear techniques) are the major recent trends in structural damage detection applications based on nonlinear acoustics.
- The potential of nonlinear acoustics for nondestructive evaluation is very large. The presented examples together with provided references indicate that significant progress has been achieved so far in this field. This progress gives hope that the application of nonlinear acoustic methods for structural damage detection and nondestructive testing is closer than ever and will be possible in the near future.

Acknowledgments Andrzej Klepka and Lukasz Pieczonka would like to acknowledge the Polish National Science Centre for financial support (research project OPUS 9 2015/17/B/ST8/03399 and research project SONATA no. 2015/19/D/ST8/01905, respectively).

References

1. M.A. Breazeale, J. Ford, Ultrasonic studies of the nonlinear behavior of solids. J. Appl. Phys. **36**, 3486–3490 (1965)
2. W.B. Gauster, M.A. Breazeale, Ultrasonic measurement of the nonlinear parameters of copper single crystal. Phys. Rev. **168**(3), 655–661 (1968)
3. M.F. Hamilton, D.T. Blackstock, *Nonlinear Acoustics* (Acoustical Society of America, New York, 2008)
4. P.B. Nagy, Excess nonlinearity in material containing microcracks. Rev. Prog. QNDT **13**, 1987–1994 (1994)
5. P.B. Nagy, Fatigue damage assessment by nonlinear ultrasonic material characterization. Ultrasonics **36**, 375–381 (1998)
6. C. Bermes, J.-Y. Kim, J. Qu, L.J. Jacobs, Nonlinear lamb waves for the detection of material nonlinearity. Mech. Syst. Signal Process. **22**(3), 638–646 (2008)
7. C. Pruell, J. Kim, J. Qu, L.J. Jacobs, Experimental characterization of material nonlinearity using Lamb waves. Smart Mater. Struct. **18**, 035003 (2009)
8. V.Y. Zaitsev, A.M. Sutin, I.Y. Belyaeva, V.E. Nazarov, Nonlinear interaction of acoustical waves due to cracks and its possible usage for cracks detection. J. Vib. Control. **1**(3), 335–344 (1995)
9. P.A. Johnson, The new wave in acoustic testing. Mater. World **7**, 544–546 (1999)

10. K. Van Den Abeele, P. Johnson, A. Sutin, Nonlinear elastic wave spectroscopy (NEWS) techniques to discern material damage, part I: Nonlinear wave modulation spectroscopy (NWMS). Res. Nondestruct. Eval. **12**(1), 17–30 (2000)
11. K. Van Den Abeele, A. Sutin, J. Carmeliet, J.P. Johnson, Micro-damage diagnostics using nonlinear elastic wave spectroscopy (NEWS). NDT&E Int. **34**(4), 239–248 (2001)
12. D. Donskoy, A. Sutin, A. Ekimov, Nonlinear acoustic interaction on contact interfaces and its use for nondestructive testing. NDT&E Int. **34**(4), 231–238 (2001)
13. V.Y. Zaitsev, V. Gusev, B. Castagnede, Observation of the Luxemburg Gorki effect for elastic waves. Ultrasonics **40**(1–8), 627–631 (2002)
14. Z. Parsons, W.J. Staszewski, Nonlinear acoustics with low-profile piezoceramic excitation for crack detection in metallic structures. Smart Mater. Struct. **15**(4), 1110–1118 (2006)
15. M. Meo, G. Zumpano, Nonlinear elastic wave spectroscopy identification of impact damage on a sandwich plate. Compos. Struct. **71**(3), 469–474 (2005)
16. P. Duffour, M. Morbidini, P. Cawley, A study of the vibro-acoustic modulation technique for the detection of cracks in metals. J. Acoust. Soc. Am. **119**(3), 1463–1475 (2006)
17. F. Aymerich, W. Staszewski, Impact damage detection in composite laminates using nonlinear acoustics. Compos. Part A Appl. Sci. Manuf. **41**(9), 1084–1092 (2010)
18. F. Aymerich, W. Staszewski, Experimental study of impact damage detection in composite laminates using a cross-modulation vibro-acoustic technique. Struct. Health Monit. **9**(6), 541–553 (2010)
19. A. Klepka, W.J. Staszewski, R. Jenal, M. Szwedo, J. Iwaniec, T. Uhl, Nonlinear acoustics for fatigue crack detection–experimental investigations of vibro-acoustic wave modulations. Struct. Health Monit. **11**(2), 197–211 (2012)
20. A. Klepka, L. Pieczonka, W.J. Staszewski, F. Aymerich, Impact damage detection in laminated composites by non-linear vibro-acoustic wave modulations. Compos. Part B **65**, 99–108 (2014)
21. R.A. Guyer, P.A. Johnson, *Nonlinear Mesoscopic Elasticity: The Complex Behaviour of Rocks, Soil, Concrete*, 1st edn. (Wiley, Weinheim, 2009)
22. V.Y. Zaitsev, P. Sas, Nonlinear response of a weakly damaged metal sample: A dissipative modulation mechanism of Vibro-acoustic interaction. J. Vib. Control. **6**(6), 803–822 (2000)
23. V.Y. Zaitsev, V. Gusev, B. Castagnede, Thermoelastic mechanism for logarithmic slow dynamics and memory in elastic wave interactions with individual cracks. Phys. Rev. Lett. **90**(7), 075501 (2003)
24. A. Klepka et al., Nonlinear acoustics for fatigue crack detection – experimental investigations of vibro-acoustic wave modulations. Struct. Heal. Monit. **11**(2), 197–211 (2011)
25. I.Y. Solodov, B. Korshak, Instability, chaos, and 'memory' in acoustic-wave–crack interaction. Phys. Rev. Lett. **88**(1), 2001–2003 (2001)
26. I.Y. Solodov, N. Krohn, G. Busse, CAN: An example of nonclassical acoustic nonlinearity in solids. Ultrasonics **40**, 621–625 (2002)
27. K.U. Ingard, D.C. Pridmore-Brown, Scattering of sound by sound. J. Acoust. Soc. Am. **28**(3), 67–369 (1956)
28. P.J. Westervelt, Scattering of sound by sound. J. Acoust. Soc. Am. **29**(8), 934–935 (1957)
29. L.A. Ostrovsky, S.N. Gurbatov, A.N. Didenkulov, Nonlinear acoustics in Nizhni Novgorod (a review). Acoust. Phys. **51**(2), 114 (2005)
30. N.C. Yoder, D.E. Adams, Vibro-acoustic modulation utilizing a swept probing signal for robust crack detection. Struct. Heal. Monit. **9**(3), 257–267 (2010)
31. H. Sohn et al., Nonlinear ultrasonic wave modulation for online fatigue crack detection. J. Sound Vib. **333**, 1473–1484 (2013)
32. L. Pieczonka et al., *Optimal selection of parameters for impact damage detection in composites based on nonlinear Vibro- acoustics modulations* (ECCM16, Seville, 2014)
33. K. Dziedziech, L. Pieczonka, M. Adamczyk, A. Klepka, W.J. Staszewski, Efficient swept sine chirp excitation in the non-linear vibro-acoustic wave modulation technique used for damage detection. Struct. Heal. Monit. **17**, 147592171770463 (2017)

34. H.F. Hu, W.J. Staszewski, N.Q. Hu, R.B. Jenal, G.J. Qin, Crack detection using nonlinear acoustics and piezoceramic transducers—Instantaneous amplitude and frequency analysis. Smart Mater. Struct. **19**(6), 65017 (2010)
35. R.A. Guyer, P.A. Johnson, *Nonlinear Mesoscopic Elasticity* (Wile-VCH, Germany, 2009)
36. B.D.H. Tellegen, Interaction between radiowaves? Nature **131**, 840 (1933)
37. V.L. Ginzburg, To the theory of the Luxemburg–Gorky effect, Izvestia. Acad. Sci. USSR, Ser. Phys. **12**, 253 (1948). (in Russian)
38. V.A. Bailey, Some nonlinear phenomena in the ionosphere. Radio Sci. J. Res. NBS/USNC-URSI **69D**(1), 9–24 (1965)
39. V.Y. Zaitsev, V.E. Nazarov, V. Tournat, V.E. Gusev, B. Castagnède, Luxemburg-Gorky effect in a granular medium: Probing perturbations of the material state via cross-modulation of elastic waves. EPL (Europhys. Lett.) **70**(5), 607 (2005)
40. L. Fillinger, V.Y. Zaitsev, V.E. Gusev, B. Castagnede, Nonlinear relaxational absorption/transparency for acoustic waves due to thermoelastic effect. Acta acustica united with acustica **92**(1), 24–34 (2006)
41. A. Moussatov, B. Castagnede, *Ultrasonic Defectoscopy of Damaged Materials by Modulation Transfer Method: Nonlinear Pump-Probe Interaction* (WCU, Paris, 2003)
42. P. P. Delsanto (ed.), *Universality of Nonclassical Nonlinearity: Applications to Non-destructive Evaluations and Ultrasonics* (Springer, Berlin, 2006)
43. A. Klepka, W.J. Staszewski, K. Dziedziech, F. Aymerich, Non-linear vibro-acoustic wave modulations – analysis of different types of low-frequency excitation. Key Eng. Mater. **569–570**, 924–931 (2013)
44. L. Pieczonka, A. Klepka, A. Martowicz, W.J. Staszewski, Nonlinear vibroacoustic wave modulations for structural damage detection: An overview. Opt. Eng. **55**(1), 011005 (2016)
45. D. Dutta, H. Sohn, K.A. Harries, P. Rizzo, A nonlinear acoustic technique for crack detection in metallic structures. Struct. Health Monit. **8**(3), 251–262 (2009)
46. H.F. Hu, W.J. Staszewski, N.Q. Hu, R.B. Jenal, G.J. Qin, Crack detection using nonlinear acoustics and piezoceramic transducers – Instantaneous amplitude and frequency analysis. Smart Mater. Struct. **19**(6), 065017 (2010)
47. I. Solodov, N. Krohn, G. Busse, Nonlinear ultrasonic NDT for early defect recognition and imaging. in *Proceedings of 10th European Conference on Non-Destructive Testing, Moscow*, 2010
48. U. Polimeno, M. Meo, Detecting barely visible impact damage detection on aircraft composites structures. Compos. Struct. **91**(4), 398–402 (2009)
49. W.J. Staszewski, K. Swiercz, L. Pieczonka, D. Broda, A. Klepka, Kissing bonds monitoring using nonlinear vibro-acoustic wave modulations. in *Proceedings of the 7th ECCOMAS Thematic Conference on Smart Structures and Materials* (*SMART*), 2015
50. B.-Y. Chen, S.-K. Soh, H.-P. Lee, T.-E. Tay, V.B.C. Tan, A vibro-acoustic modulation method for the detection of delamination and kissing bond in composites. J. Compos. Mater.., Published online before print, 0021998315615652 **50**(22), 3089–3104 (2016)
51. A. Klepka, W.J. Staszewski, D. di Maio, F. Scarpa, Impact damage detection in composite chiral sandwich panels using nonlinear vibro-acoustic modulations. Smart Mater. Struct. **22**(8), 084011 (2013)
52. L. Pieczonka, P. Ukowski, A. Klepka, W.J. Staszewski, T. Uhl, F. Aymerich, Impact damage detection in light composite sandwich panels using piezo-based nonlinear vibro-acoustic modulations. Smart Mater. Struct. **23**, 105021 (2014)
53. R.B. Jenal, W.J. Staszewski. Crack detection in glass plates using nonlinear acoustics with low-profile piezoceramic transducers. in *Proceedings of SPIE, Health Monitoring of Structural and Biological Systems, 7650*, 2010
54. D.M. Donskoy, A. Sutin, Nonlinear acoustic parameter of trabecular bone. J. Acoust. Soc. Am. **102**, 3155 (1997)
55. G. Renaud, S. Callé, J.-P. Remenieras, M. Defontaine, Non-linear acoustic measurements to assess crack density in trabecular bone. Int. J. Nonlin. Mech. **43**(3), 194–200 (2008)

56. T. Trojniar, A. Klepka, L. Pieczonka, W.J. Staszewski, Fatigue crack detection using nonlinear vibro-acoustic cross-modulations based on the Luxemburg-Gorky effect, in *SPIE Smart Structures and Materials+ Nondestructive Evaluation and Health Monitoring, 90641F–90641F*, 2014
57. I. Solodov, J. Bai, S. Bekgulyan, G. Busse, A local defect resonance to enhance acoustic wave-defect interaction in ultrasonic nondestructive evaluation. Appl. Phys. Lett. **99**(21), 211911–211911–3 (2011)
58. W.S. Gan, *Acoustical Imaging: Techniques and Applications for Engineers* (Wiley, Chichester, 2012)
59. N. Krohn, R. Stoessel, G. Busse, Acoustic non-linearity for defect selective imaging. Ultrasonics **40**, 633–637 (2002)
60. U. Polimeno, M. Meo, D.P. Almond, S.L. Angioni, Detecting low velocity impact damage in composite plate using nonlinear acoustic/ultrasound methods. Appl. Comp. Mat. **17**(5), 481–488 (2010)
61. D. Broda, L. Pieczonka, V. Hiwarkar, W.J. Staszewski, V.V. Silberschmidt, Generation of higher harmonics in longitudinal vibration of beams with breathing cracks. J. Sound Vib. **381**, 206–219 (2016)
62. L. Pieczonka, L. Zietek, A. Klepka, W.J. Staszewski, F. Aymerich, T. Uhl, Damage imaging in composites using nonlinear vibro-acoustic wave modulations. Struct. Control Heal. Monit. **25**, e2063 (2017)
63. A. Klepka, M. Strączkiewicz, L. Pieczonka, W.J. Staszewski, L. Gelman, F. Aymerich, T. Uhl, Triple correlation for detection of damage-related nonlinearities in composite structures. Nonlin. Dyn. **81**(1–2), 453–468 (2015)

Chapter 5
Nonlinear and Hysteretic Constitutive Models for Wave Propagation in Solid Media with Cracks and Contacts

V. V. Aleshin, S. Delrue, O. Bou Matar, and K. Van Den Abeele

5.1 Introduction

Only a tiny part of the materials produced, treated, or used by mankind are free from any type of damage, defects, or internal structural features. Defects are often categorized into three types: 1D dislocations (e.g., irregularities, impurities, etc.), 2D internal contacts (e.g., cracks, delaminations, etc.), and 3D defects (e.g., pores, voids, etc.). All these defects particularly influence mechanical and physical properties of a material. However, internal contacts impact materials performance in the most crucial way. The reason lies in the inherent instability of the process of cracking which can be illustrated using the following considerations. Suppose that an elastic continuum contains a circular crack of zero thickness, and that a uniform tensile stress σ is applied to each face of the crack. Then the critical stress σ_0 at which the crack starts growing equals

$$\sigma_0^2 = \frac{\pi E G}{2R\left(1-\nu^2\right)}, \tag{5.1}$$

V. V. Aleshin (✉)
National Center for Scientific Research, Joint International Laboratory LICS-LEMAC, Institute of Electronics, Microelectronics and Nanotechnologies, Villeneuve d'Ascq, France
e-mail: vladislav.aleshin@iemn.univ-lille1.fr

S. Delrue · K. Van Den Abeele
Department of Physics, Wave Propagation and Signal Processing Research Group, KU Leuven Kulak, Kortrijk, Belgium
e-mail: steven.delrue@kuleuven.be; koen.vandenabeele@kuleuven.be

O. Bou Matar
Ecole Centrale de Lille, Joint International Laboratory LICS-LEMAC, Institute of Electronics, Microelectronics and Nanotechnologies, Villeneuve d'Ascq, France
e-mail: olivier.boumatar@iemn.univ-lille1.fr

T. Kundu (ed.), *Nonlinear Ultrasonic and Vibro-Acoustical Techniques for Nondestructive Evaluation*, https://doi.org/10.1007/978-3-319-94476-0_5

where G is the surface energy (i.e., the energy needed to form a unit area of free surface), and E andν are, respectively, Young's modulus and Poisson's ratio of the material [1]. The instability effect is explained by the inverse proportionality to the crack radius R. Indeed, if the applied stress reaches σ_0, the crack radius increases, and the new critical stress becomes even less than the applied one, so that the cracking process continues until the whole sample fails. For this reason, it is extremely important to develop realistic models that allow the mechanical behavior of solids with internal contacts to be accurately described.

The presence of internal contacts in a material is the reason for contact acoustic nonlinearity that appears at both normal and tangential (relative to the crack faces) loading of the crack. During normal straining the elastic reaction of an open and closed crack is different. The tangential loading engenders friction and associated hysteretic effects. In addition, friction described via the Coulomb friction law couples normal and tangential behavior. A successful theory for contact acoustic nonlinearity should appropriately deal with those issues.

Theoretical and numerical modeling approaches for elasticity in materials with internal contacts address at least two situations: distributed damage or localized damage. In the first case, the solid contains a large number of cracks whose exact positions are not known and not important. Typical examples of this class are geo-materials or construction materials consisting of consolidated grains with imperfect bounds between them, or fatigued metals. In this case, contact nonlinearity shows up as nonlinear or, frequently, hysteretic stress–strain relationships that results from a cumulative influence of the crack ensemble or crack network. Materials belonging to the second class contain only a few cracks whose positions are important. Since the internal contacts represent unique or rare "events" in the material, a statistical analysis is not suitable in that case. The response strongly depends on the geometry and locations of the cracks so that numerical models of finite element type (or similar based on a detailed meshing of the sample) are most appropriate. An internal contact constitutes an additional boundary at which proper boundary conditions should be defined. In a general case, these boundary conditions are neither of the first type (known displacement) nor of the second type (known stress, with a particular exception of open cracks when stress-free boundaries can be assumed), but of the third type, representing a link between contact displacements and stresses. Therefore, in this situation, contact acoustic nonlinearity originates from nonlinear load–displacement relationships at contact faces.

The modeling approach described in this chapter is related to the second class of materials (i.e., materials with internal contacts). To adequately reflect the physical nature of contact interactions, the model should take into account friction. Nowadays, there is a large and growing number of numerical contact mechanical models [2, 3] capable of solving frictional contact problems in a variety of situations, including shift, rolling, and torsion movement types. Usually they are applicable to general (non-plane) contact geometries and require detailed meshing of the contact zone. At the same time, the case of wave propagation in materials with localized damage-induced contacts has two essential features. Firstly, contact surfaces obtained by cracking are typically rough which means that the

microscopic details of the contact geometry are not known and are too complex to be fully represented. Secondly, common acoustical signals, such as sweeps and wave packages, can include high-frequency components and therefore require a huge number of time discretization points.

These arguments motivated the development of an alternative approach based on a multiscale consideration and semi-analytical contact mechanical solutions sketched in the next section.

5.2 Multiscale Approach and Three Contact Regimes

The numerical tool elaborated in this chapter consists of two parts: the contact model and the solid mechanics unit. The solid mechanics unit is created using available finite element software (COMSOL in our study). The contact model, which has to provide appropriate boundary conditions for the solid mechanics unit, is described in Sects. 5.4–5.7 of this chapter.

The account for interface roughness is essential for the proposed approach, as it leads to a different formulation of the problem when compared to the case of ideally flat crack surfaces that are subject to the Coulomb friction law. In the latter case, depending on the loading conditions, one of the three following cases can occur at each pair of close points located at opposite faces. First, if contact between the surfaces is lost, the local normal (σ) and tangential (τ) stresses both equal zero, while local normal and tangential displacements between this pair of points are defined by external conditions and not by the crack model itself. Second, in the case where $|\tau| < \mu\sigma$ (μ is the coefficient of friction), the normal displacement equals zero and the tangential one does not change, i.e., the stick event occurs. Finally, when $|\tau| = \mu\sigma$ the event of slip takes place. In that situation, some tangential displacement is developed which depends on external conditions, whereas the normal displacement still equals zero. It is important to note that the case $|\tau| > \mu\sigma$ is prohibited by the Coulomb friction law. In addition, the normal displacement can be negative (corresponding to a locally open interface) or equal zero (in the presence of contact), but is never positive since ideally flat surfaces do not have any asperities receding under load (here and in what follows we assume positive normal characteristics in compression). Thus, the Coulomb friction law for flat contact faces does not provide an explicit load–displacement relationship that could be used as the boundary condition by the solid mechanics part.

The fact that displacements cannot be calculated directly from loads in the framework of the traditional flat-surface approach suggests the idea of flipping the arguments and calculating loads for given displacements. As we will see, this is possible when the faces are not flat, but have some nontrivial surface relief. In this case a pair of close macroscopic points is replaced by a mesoscopic cell (see Fig. 5.1a, b) which should be, on the one hand, small enough to assume macroscopic elastic fields to be uniform within each cell and, on the other hand, sufficiently large to contain a lot of microscopic geometric features (asperities). In each mesoscopic

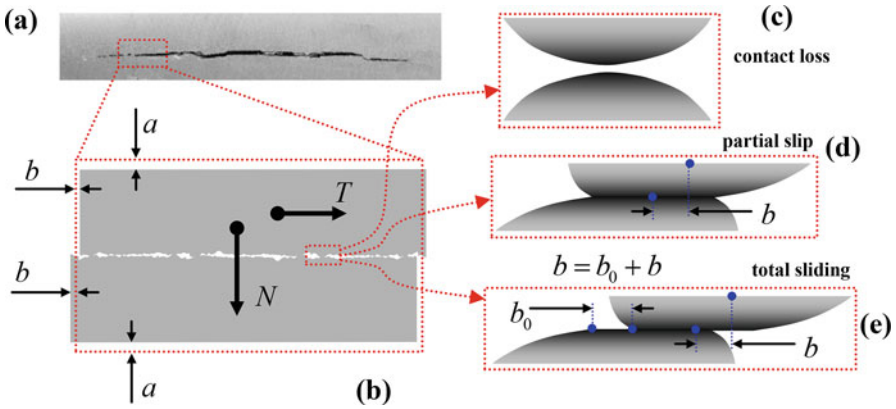

Fig. 5.1 Illustration of the proposed multiscale contact model. (**a**) Macro-level of the sample. (**b**) Mesoscopic cell in which contact forces and displacements are defined. (**c**–**e**) Contact regimes illustrated at the microscopic level (asperities): (**c**) contact loss, (**d**) partial slip, (**e**) total sliding

cell, a vector loading force and vector displacement is defined. The force has normal and tangential components, N and T in the considered 2D case, which correspond to macroscopic normal and shear stress, respectively. In the proposed model, the time-independent Coulomb friction law is postulated and the inertial reaction of asperities and surrounding material layers is neglected. In this quasi-static situation, the external force is equilibrated by the contact force, i.e., N and T also have the sense of the contact force components. The normal and tangential displacements (Fig. 5.1b) are denoted a and b, respectively, and are related to bulk parts of each body, so that the total displacements equal $2a$ and $2b$. In order to construct a valid contact model, the forces N and T have to be calculated for arbitrary displacements a and b. As friction produces memory effects, the forces will also depend on the history of the displacement components.

We assume that the normal components are linked by a biunique function $N = N(a)$ which, in particular, means that adhesion, plasticity as well as dissimilarity effects (when normal action alone produces slip) are neglected. Moreover, it is supposed that the function $N = N(a)$ does not depend on any tangential interactions, which is true when all normals to all microcontacts are aligned and stay aligned during loading. The link $N = N(a)$ is given by a normal loading model for nominally flat surfaces with roughness (Sect. 5.4).

The account for frictional tangential contact interaction is more complex. Besides the case of contact loss with $N = T = 0$ (Fig. 5.1c), two other regimes can be recognized: partial slip and total sliding (Fig. 5.1d, e). The regime of partial slip appears due to the presence of roughness, for ideally flat infinite surfaces it does not exist. The reason is that asperities recede not only under normal load but under tangential load as well. This process of local deformation of asperities and neighboring material layers (shown highly exaggerated in Fig. 5.1d) is accompanied by the development of slip that starts at the periphery of each microcontact and

propagates towards its center, defined as a local minimum of a random gap z between the profiles. The central zones, however, remain stuck. The corresponding tangential displacement of the bulk area is denoted here $\tilde{b}$. Then, if the tangential action exceeds the Coulomb threshold, the slip zone reaches the center of each microcontact. In this regime of total sliding (Fig. 5.1e), a new displacement component b_0 appears that corresponds to the mismatch between centers of contacting asperities (the same for all of them). The sum of both components equals the total displacement considered as a drive parameter of the contact model (see Sect. 5.7 for more details).

The solution in the total sliding regime is trivial: $N = N(a)$, $T = \pm \mu N$. The only remaining question is how to calculate the tangential force in the case of partial slip. Such solutions are known for many years for particular loading histories of two spheres (Hertz-Mindlin problem [4], also called Cattaneo-Mindlin problem [5]). This situation is addressed by the recent method of dimensionality reduction [6]. Here we propose to use a similar semi-analytical approach especially suitable for complex acoustical signal, including random ones.

The method is based on the recent theorem in contact mechanics that allows one to replace contact between rough surfaces by an equivalent axisymmetric contact geometry. The contact problem is then reduced to a sort of generalized Hertz-Mindlin problem for which the exact solutions for particular loading histories are known. Finally, for an arbitrarily complex excitation protocol, the full memory-dependent load–displacement relationship can be built up as a superposition of the particular solutions. The process of combining the particular solutions with appropriate parameters is automated with the help of the original method of memory diagrams (MMD, Sect. 5.6) that allows one to represent all memory information in the contact system as an internal functional dependency (memory diagram).

Finally, in Sect. 5.8 we integrate the developed contact model into the solid mechanics unit programmed in COMSOL. To illustrate the functionality of the created numerical toolbox we consider examples of wave propagation in a sample containing a frictional crack of a given configuration. It is shown in detail how the crack, excited by an elastic wave, generates nonlinear elastic field components radiated into the surrounding material.

5.3 Brief History of the Mechanical Contact Problem

The history of the contact problem started in 1880s when H. Hertz (see [7]) published the classical solution for two elastic spheres compressed by a normal force. In the absence of adhesion and plasticity, this solution is fully reversible. However, the addition of a tangential force and friction [4, 5] makes the problem hysteretic and memory-dependent. It was noted that even a small tangential force acting on two pre-compressed spheres results in appearance of a slip annulus at the periphery of the contact circle where the surfaces are compressed weakly. The coexistence of the stick (central) and slip (peripheral) zones actually means mixed-type

boundary conditions that correspond to zero local tangential displacement in the central region and, in the slip annulus, to the Coulomb friction law written for local tangential and normal stresses, $\tau = \mu\sigma$. The increase in the tangential force results in slip propagation towards the contact center. If, eventually, the tangential force starts decreasing, a new slip annulus develops at the contact periphery in which $\tau = -\mu\sigma$. Hence, the same values of the normal and tangential forces can correspond to different distributions of stresses and displacements in the contact zone. This fact explains a complex hysteretic character of the solution.

Allowing the normal force to evolve [4] adds a new complexity factor to the problem. The reason is that the slip zone always arises at the contact border where $\sigma = 0$ and propagates inward, but, if the normal force increases, the contact border itself propagates outward. The result depends on the value of the derivative dN/dT.

Finally, the introduction of a general contact geometry instead of spherical profiles introduces even more complexity in the description. Indeed, for two rough surfaces, the contact zone consists of a multitude of contact spots having random geometry. For changing normal force, those contact spots can merge or split. Further, each of them supports slip and stick zones, and traction distribution in the stick zones can contain residual stresses left from the previous moments of evolution. With continuously varying normal and tangential loading, this complicated picture continuously evolves.

The first step to solve the problem of contact between rough surfaces with friction would be to establish the load–displacement relationship in case of pure normal compression. The modeling of a force–displacement relationship corresponding to normal loading of contacts with rough surfaces is an extensive research topic since 1950–1970s. In particular, in the model proposed by Whitehouse and Archard [8], the concept of asperities is explicitly introduced and a distribution of asperities over heights and radii is deduced. The assumption that all asperities have equal radii but different heights produced the classical model by Greenwood and Williamson [9]. In our approach, we try to avoid using the concept of asperity and preserve the continuous character of roughness. The derivation of the model load–displacement relationship for normal compression is discussed in the next section.

5.4 Normal Load–Displacement Relationship for Contact Between Rough Surfaces

Contact of rough surfaces can be described using three different parameters related to the contact area: the nominal contact area A_n defined by replacing rough surfaces by ideally plane ones, the real (atomic) contact area A, and the geometric (truncated) contact area A_g obtained in a virtual situation when rough profiles can freely penetrate into each other or, equivalently, when all roughness elements of each surface located higher than a certain height are virtually cut off. Two of these contact

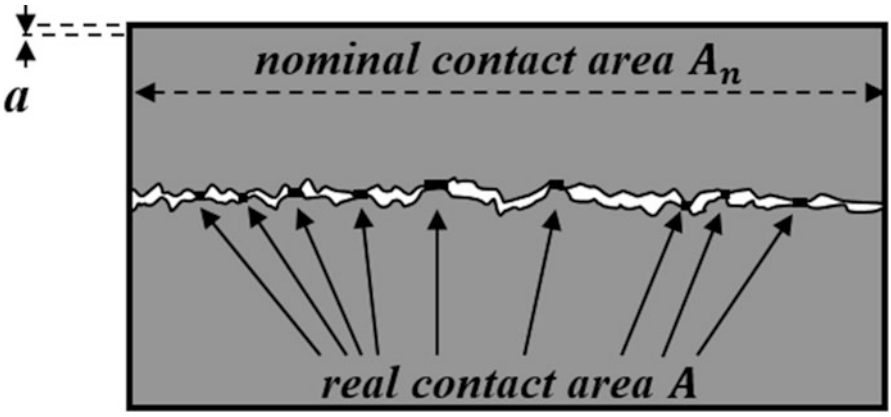

Fig. 5.2 Illustration of the nominal contact area A_n and the real contact area A

areas are also illustrated in Fig. 5.2. As can be observed, the real atomic contact area A between two bodies with rough surfaces is only a small part of the nominal area A_n.

The proportionality $A \sim N$ was proposed by Bowden and Tabor in 1939 [10]; a more recent discussion on the proportionality can be found in [11]. Both empirical and theoretical arguments suggest that

$$A = \frac{2\kappa\left(1-\nu^2\right)}{Eh'}N, \tag{5.2}$$

with h' equal to the root mean square of the random surface slope, and $\kappa \approx 2$ (see [12] and references therein for experiments, [13] for theory, [14] for the discussion on the coefficient κ, [15] for theoretical and numerical examples).

Further, we introduce the random gap ξ between the surfaces (2ξ is the full gap, ξ is related to one body) and denote $\varphi(z)$ as its distribution. Then it is easy to express the ratio A_g/A_n from purely geometric consideration as

$$\frac{A_g}{A_n} = \int_0^a \varphi(z)dz. \tag{5.3}$$

Finally, the real and geometric contact areas can be linked by a model relationship. In particular, if all microcontact spots are approximated by strained spheres, a simple relation

$$\frac{A}{A_g} = \upsilon = \frac{1}{2} \tag{5.4}$$

follows from the Hertz theory [7] (see also Eq. (5.14) below). For non-spherical shapes of asperities, the value of υ can deviate from 1/2. Combining Eqs. (5.2), (5.3), and (5.4) we obtain an analytical expression linking N and a,

$$N(a) = \frac{\upsilon h' E}{2\kappa\left(1-\nu^2\right)} \int_0^a \varphi(z) dz, \quad a \geq 0. \tag{5.5}$$

In case of negative normal displacement a, we set N equal to zero which actually corresponds to the absence of adhesion. Equation (5.5) means that the normal reaction of a crack section is determined by the gap (aperture) distribution which, in turn, depends on the nature of a crack. Since typical acoustical excitations can always be considered as small perturbations, the normal reaction in the acoustical strain range will mainly depend on the tangent to the curve $\varphi(z)$ at $z = 0$ (i.e., the first-order Taylor series approximation). As such, three cases can be distinguished: a vertical tangent, a horizontal one, or a tangent with inclination angle between 0 and $\pi/2$. A vertical tangent implies that even for a small compressive displacement a, a non-zero contact area will be immediately formed. In practice, this refers to highly conforming surfaces at the atomic level. Secondly, a horizontal tangent refers to an essentially open crack in which points in atomic contact practically do not appear. Finally, an intermediate tangent inclination coefficient k ($0 < k < \infty$) results in the approximation $\varphi(z) \approx kz$ which yields the following result:

$$N(a) = \frac{\upsilon h' E k}{4\kappa\left(1-\nu^2\right)} a^2, \quad a \geq 0 \tag{5.6}$$

The same second-order dependency ($N(a) \sim a^2$) has been introduced by Biwa et al. [16] based on existing experimental data for aluminum–aluminum contact and was already used by Yuan et al. [17] for modeling the nonlinear interaction of a compressive wave with a contact interface between two solid blocks of aluminum. This suggests that the quadratic dependency is a possible approximation for two globally plane surfaces with uncorrelated roughness brought into contact. As an extension we assume that Eq. (5.6) is also approximately valid for fatigue cracks since the internal stresses released during cracking and the associated microscopic displacements result in a similar loss of conformity at the atomic scale. Microscale composite roughness that mainly contributes to the acoustical response can thus be considered as uncorrelated.

The quadratic approximation is not the only possible form for modeling the normal load–displacement relationship. In [18, 19] it is shown that rough surfaces with various fractal dimensions correspond to different powers in approximation of the kind of Eq. (5.6). Nevertheless, based on experiments [16], we here accept Eq. (5.6) as a model equation for the normal reaction curve keeping in mind that, for the proposed theory, the specific form of $N(a)$ is not essential.

Certainly, a tangential excitation may considerably displace the contacting asperities in the lateral direction and therefore alter the normal reaction curve $N(a)$. However, this effect can be neglected if we assume that the random gap between the crack surfaces is a stationary process whose characteristics h' and $\varphi(z)$ do not depend on the tangential shift. Therefore, $N(a)$ is supposed to be a portrait of the system which is not affected by any other interactions, and incorporates all geometric information about the rough surfaces in contact.

Concluding this section it is appropriate to cite the existing solution for two equal axisymmetric bodies for comparison [20–22]:

$$N = \frac{2E}{1-\nu^2}\left(ca - \int_0^c \frac{\rho z\,(\rho)}{\sqrt{c^2-\rho^2}}d\rho\right), \tag{5.7}$$

$$a = \int_0^c \frac{cz'\,(\rho)}{\sqrt{c^2-\rho^2}}d\rho, \tag{5.8}$$

$$\sigma\,(\rho) = \frac{E}{\pi\left(1-\nu^2\right)}\int_\rho^c \left(\int_0^r \frac{z'(p)+pz''(p)}{\sqrt{r^2-p^2}}dp\right)\frac{dr}{\sqrt{r^2-\rho^2}}, \tag{5.9}$$

where ρ is the radial coordinate, c is the contact radius, $z(\rho)$ is a function describing the gap between the two bodies in the unstrained state (the total gap equals 2 $z(\rho)$), and $z'(\rho)$ and $z''(\rho)$ are its first and second derivatives, respectively. Equations (5.7) and (5.8) produce an implicit form of the normal force–displacement relationship $N = N(a)$.

It is straightforward to verify that Eqs. (5.7), (5.8), and (5.9) yield the classical Hertz solution [7] for two equal spheres when

$$z\,(\rho) = R - \sqrt{R^2-\rho^2} \tag{5.10}$$

is assumed, with R the radius of the spheres. In this derivation, only the lowest term in the expansion over the small parameter c/R is kept. In particular, the normal load for spheres

$$N(a) = \frac{4}{3}\frac{ER^{1/2}}{\left(1-\nu^2\right)}a^{3/2} \tag{5.11}$$

depends on a as $a^{3/2}$ and not a^2 as in the accepted model Eq. (5.6) for rough surfaces.

In a similar way, the normal stress distribution $\sigma_a(\rho)$ corresponding to normal displacement a is obtained from Eq. (5.9):

$$\sigma_a(\rho) = \begin{cases} \frac{2E}{\pi R(1-\nu^2)}\sqrt{c^2-\rho^2}, & \rho \le c \\ 0, & c < \rho \end{cases}. \tag{5.12}$$

The distribution of local normal displacement $u_a(\rho)$ is also known [6]:

$$u(\rho) = \begin{cases} \frac{2c^2-\rho^2}{2R}, & \rho \le c \\ \frac{1}{\pi R}\left(\arcsin\left(\frac{c}{\rho}\right)(2c^2-\rho^2) + c\sqrt{\rho^2-c^2}\right), & c < \rho \end{cases} \tag{5.13}$$

with

$$c^2 = Ra. \tag{5.14}$$

These solutions will be used below to illustrate contact between two spheres as a case where all analytical dependencies can be easily calculated.

5.5 Reduced Elastic Friction Principle

As it was mentioned, application of a tangential force or displacement makes the problem hysteretic; its solution becomes memory-dependent. Prior to automating the account for memory effects, it is necessary to formulate the solution for some basic loading protocols. The simplest of them is constant loading when application of a constant normal displacement a is followed by addition of a constant tangential displacement b.

A successful representation of the constant-loading situation is given using a modern theorem of contact mechanics called the Reduced Elastic Friction Principle (REFP, see [20, 23] or sometimes the Ciavarella-Jäger theorem [24, 25]). The theorem states that, for constant loading and for a wide range of contact geometries, the tangential force and displacement can be expressed through the normal force and displacement. This principle is illustrated in Fig. 5.3 for axisymmetric bodies (two upper sets). Consider two situations: the first one where the system is loaded only by normal displacement q (left upper set), and the second one where both displacement components, a and b, are applied ($a > q$). In the second case (right upper set), an annulus of slip surrounds the central stick zone. The normal displacement q is chosen in such a way that the stick zone in the second case coincides with the contact zone in the first case. Then the tangential force and displacement in the second situation are given by

$$\begin{cases} T = \mu\left(N(a) - N(a)|_{a=q}\right) \\ b = \theta\mu\,(a-q) \end{cases}, \tag{5.15}$$

where the dependency of the normal force on the normal displacement $N = N(a)$ is considered as known, and θ is a material constant that depends only on Poisson's ratio ν,

$$\theta = \frac{2-\nu}{2\,(1-\nu)}. \tag{5.16}$$

Equation (5.15) is written here for the displacement-driven system and can be easily reformulated in the case when the drive parameters are forces. Here and in Sect. 5.6 related to the partial slip regime description, for brevity we omit tilde in the notation $\tilde{b}$ introduced for the partial slip displacement. In other words, we consider the case when the Coulomb friction threshold is not achieved ($|T| < \mu N$), and therefore $\tilde{b} = b$.

Another, more detailed form of the REFP suitable for arbitrarily shaped plane contact with possible multiple contact spots is written for the shear stress distribution $\tau\left(\overrightarrow{r}\right)$ and local tangential displacement distribution $w\left(\overrightarrow{r}\right)$:

$$\tau\left(\overrightarrow{r}\right) = \tau_a^q\left(\overrightarrow{r}\right) \equiv \mu\left(\sigma_a\left(\overrightarrow{r}\right) - \sigma_q\left(\overrightarrow{r}\right)\right), \tag{5.17}$$

$$w\left(\overrightarrow{r}\right) = w_a^q\left(\overrightarrow{r}\right) \equiv \theta\mu\left(u_a\left(\overrightarrow{r}\right) - u_q\left(\overrightarrow{r}\right)\right), \tag{5.18}$$

where $\overrightarrow{r}$ is the coordinate in the global contact plane, $\sigma_a\left(\overrightarrow{r}\right)$ and $u_a\left(\overrightarrow{r}\right)$ are distributions of normal stress and of local normal displacement corresponding to the normal displacement a while in $\sigma_q\left(\overrightarrow{r}\right)$ and $u_q\left(\overrightarrow{r}\right)$ the normal displacement is substituted by parameter q.

In the purpose of creation of a contact model for an arbitrary contact geometry, it is appropriate to introduce the notation $\mathbb{C}_{a_2}^{a_1}$ for the contact area obtained under compression determined by displacement a_2 minus the contact area obtained under compression determined by displacement a_1 ($a_1 \le a_2$). Several examples of area configurations denoted by $\mathbb{C}_{\bullet}^{\bullet}$ with various subscripts and superscripts are illustrated in Fig. 5.3 (two lower sets). In particular, normal compression characterized by displacement a produces contact area $\mathbb{C}_a^0$, smaller displacement q creates contact configuration $\mathbb{C}_q^0$ which probably contains more contact spots since they can split when releasing compression. Similarly, $\mathbb{C}_a^q$ is the slip area produced by normal displacement a and tangential shift b. Further, the contact boundary is denoted $\mathbb{C}_a^a$, the boundary between stick and slip zones $\mathbb{C}_q^q$, etc.

Note that $\tau\left(\overrightarrow{r}\right)$ is affected by both distributions $\sigma_a\left(\overrightarrow{r}\right)$ and $\sigma_q\left(\overrightarrow{r}\right)$ in the stick zone $\mathbb{C}_q^0$, equals $\mu\sigma_a\left(\overrightarrow{r}\right)$ in the slip zone $\mathbb{C}_a^q$ as it is required by the Coulomb friction law, and is zero outside of the contact (in $\mathbb{C}_\infty^a$). The properties of the local tangential displacement $w\left(\overrightarrow{r}\right)$ are different. Since $u_a\left(\overrightarrow{r}\right) > 0$ everywherein $\mathbb{C}_\infty^0$

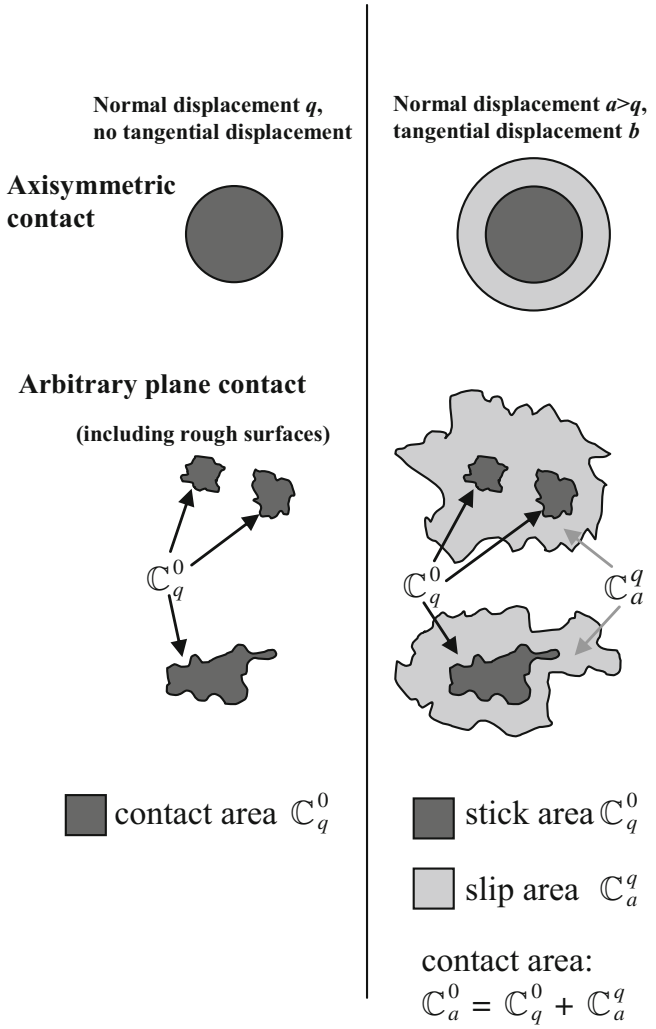

Fig. 5.3 Illustration of the reduced elastic friction principle. Left: contact created by normal displacement q; right: contact created by normal displacement $a > q$ and tangential displacement b. Two upper sets correspond to contact between axisymmetric bodies, two lower ones illustrate arbitrary plane contact including rough surfaces with multiple contact spots. Areas $\mathbb{C}_q^0$, $\mathbb{C}_a^q$, and $\mathbb{C}_a^0$ from Eqs. (5.17) and (5.18) are also shown. Note that areas $\mathbb{C}_q^0$ at the right and at the left coincide

in contrast to $\sigma_a\left(\overrightarrow{r}\right)$ which equals 0 outside of the contact, the distribution $w\left(\overrightarrow{r}\right)$ is everywhere affected by both $u_a\left(\overrightarrow{r}\right)$ and $u_q\left(\overrightarrow{r}\right)$. Moreover, inside the stick zone $\mathbb{C}_q^0$

$$w\left(\overrightarrow{r}\right)\big|_{\overrightarrow{r}\in\mathbb{C}_q^0} = \theta\mu\left[u_a\left(\overrightarrow{r}\right) - u_q\left(\overrightarrow{r}\right)\right]_{\overrightarrow{r}\in\mathbb{C}_q^0} = const\left(\overrightarrow{r}\right) \equiv b \tag{5.19}$$

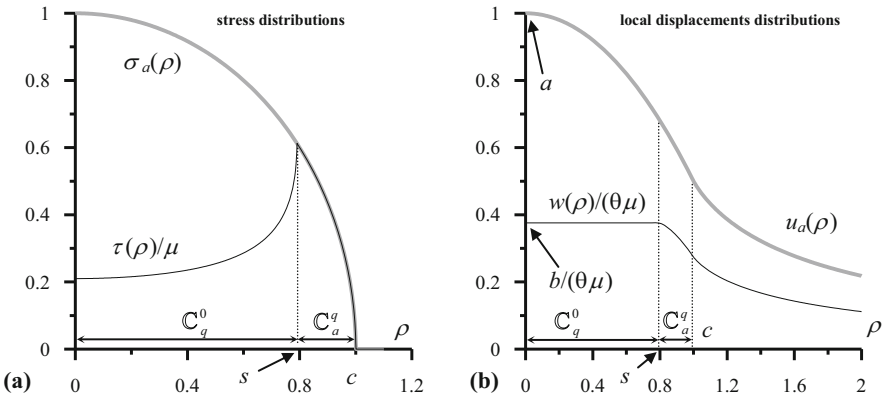

Fig. 5.4 The REFP solution for spheres satisfies the Coulomb friction law: (**a**) $\tau = \mu\sigma$ in the slip zone, (**b**) local tangential displacement $w(\rho) = b = \text{const}(\rho)$ in the stick zone

in accordance to the definition of stick. In other words, since in the zone $\mathbb{C}_q^0$ slip is absent, all points in that zone should displace equally, as a rigid body, i.e., independent of a current coordinate $\overrightarrow{r}$. This property guarantees the fulfillment of the Coulomb boundary condition in the stick zone.

The compliance with the Coulomb friction law is illustrated in Fig. 5.4 where normal and tangential stress and displacement distributions are calculated for spheres using the known Hertz solution [7] and Eqs. (5.17) and (5.18). In these figures, the radial coordinate ρ replaces $\overrightarrow{r}$, s is the radius of the boundary between the stick zone $\{0 < \rho < s\} = \mathbb{C}_q^0$ and the slip zone $\{s < \rho < c\} = \mathbb{C}_a^q$, c is the contact radius, with a simple link between parameters: $c^2 = Ra$, $s^2 = Rq$. The curves are obtained using Eqs. (5.12), (5.13), and (5.14).

The detailed REFP formulation in Eqs. (5.17) and (5.18) corresponds to the short form Eq. (5.15) for forces and displacements. Indeed, by setting $\overrightarrow{r} = 0$ in Eqs. (5.18) and (5.19) and noticing that $u_a(0) = a$ and $u_q(0) = q$ we retrieve the second Eq. (5.15). The first Eq. (5.15) is obtained by integration of Eq. (5.17) over the contact area $\mathbb{C}_a^0$.

The use of the REFP in the form of Eq. (5.15) as well as of Eqs. (5.17) and (5.18) requires some further explanation.

1. Contact theories of the considered kind use the following assumptions: All deformations are elastic, the normal vectors to all individual contacts are aligned and stay aligned during loading, the Coulomb's law is postulated at the level of local contact stresses, and torsion and rolling are absent.
2. The REFP is valid only for elastically similar materials with Dundur's constant

$$\beta = \frac{G_2(\kappa_1 - 1) - G_1(\kappa_2 - 1)}{G_2(\kappa_1 + 1) + G_1(\kappa_2 + 1)} \tag{5.20}$$

equal to 0. Here $G_{1,2}$ are shear moduli, $\kappa_{1,2} = 3 - 4\nu_{1,2}$, and $\nu_{1,2}$ are Poisson's ratios of the materials (see, for instance, [25]). In the latter paper, $\nu_{1,2} = 0$ is required in addition. The elastic similarity means that normal and tangential interactions are uncoupled in some sense. In contrast, for dissimilar bodies, normal loading alone generates partial slip since the bodies deform in the lateral direction differently. In many practical cases, even if the above conditions of elastic similarity are not exactly fulfilled, the dissimilarity effects are found to be small [20, 23, 26, 27].

3. Strictly speaking, the REFP with θ given by Eq. (5.16) is valid for axisymmetric profiles only (including surfaces with exactly axisymmetric asperities). For other contact shapes, the value of θ can slightly deviate from Eq. (5.16). It was numerically demonstrated [28] that the precision of the REFP becomes worse in the case of a very strong asymmetry in the contact shape, i.e., the situation where one dimension (say, x) considerably exceeds another one (y). For shifting along x the effective θ will deviate from the effective θ for movements along the y-axis. However, for surfaces with isotropic random roughness this effect does not appear.

An important feature of Eq. (5.15) is that it does not contain explicitly any geometry-related characteristics. All geometric information is contained in the dependency $N = N(a)$ linking the normal force with the normal displacement. Thus, a simple consequence of the REFP is a statement that, for two contact systems with the same normal response, the tangential responses are also identical. Consequently, a contact between isotropic rough surfaces can be replaced by an equivalent axisymmetric contact geometry. The related restrictions that limit the class of the considered contact types are discussed in [20, 23–25].

The REPF in the form of Eqs. (5.15), (5.17), and (5.18) is formulated for a contact system driven by displacements. The force-driven counterpart is described in a similar way:

$$\begin{cases} T = \mu\,(N - Q) \\ b = \theta\mu\left(a(N) - a(N)|_{N=Q}\right) \end{cases},$$

$$\tau\left(\overrightarrow{r}\right) = \tau_N^Q\left(\overrightarrow{r}\right) \equiv \mu\left(\sigma_N\left(\overrightarrow{r}\right) - \sigma_Q\left(\overrightarrow{r}\right)\right),$$

$$w\left(\overrightarrow{r}\right) = w_N^Q\left(\overrightarrow{r}\right) \equiv \theta\mu\left(u_N\left(\overrightarrow{r}\right) - u_Q\left(\overrightarrow{r}\right)\right).$$

5.6 Method of Memory Diagrams for Partial Slip

The REFP allows one to obtain the load–displacement relationship in the partial slip regime, for a particular case where the contact system is loaded in the normal direction and then a constant tangential load is added. For arbitrary loading histories,

the solution can be searched in the form of a superposition of constant-loading solutions with proper parameters. An automatic calculation of these parameters is arranged in the method of memory diagrams (MMD, see [29]) discussed in this section. The method is valid for arbitrary loading histories and provides, in 2D, a two-parametric output for a two-parametric input, i.e., $(a, b) \Rightarrow (N, T)$ for a displacement-driven and $(N, T) \Rightarrow (a, b)$ for a force-driven system. 3D extensions are also possible but are not discussed here. A memory diagram is an internal functional dependency that replaces complex distributions of shear stress and local tangential displacement but contains at the same time the equivalent amount of information.

5.6.1 Case of Constant Compression

A memory diagram (or memory function) $D(\alpha)$ for the constant-loading case can be formally introduced by rewriting Eq. (5.12) in the form:

$$\begin{cases} b/(\theta\mu) = \int\limits_0^a D(\alpha)\, d\alpha \\ T/\mu = \int\limits_0^a D(\alpha)\, \frac{dN}{da}\big|_{a=\alpha} d\alpha \end{cases}, \tag{5.21}$$

where $D(\alpha)$ is defined as

$$D(\alpha) = \begin{cases} 0,\ 0 \le \alpha < q \\ 1,\ q \le \alpha \le a \end{cases}. \tag{5.22}$$

The ends of the interval $q \le \alpha \le a$ on which the memory function equals 1 fully determine the solutions Eqs. (5.14) and (5.15) for distributions of stresses and local displacements. These distributions have the following property: in the slip zone $\mathbb{C}_a^q$ $\tau\left(\overrightarrow{r}\right) = \mu\sigma_a\left(\overrightarrow{r}\right)$, in the stick zone $\mathbb{C}_q^0$ $w\left(\overrightarrow{r}\right) = const$, and $\tau\left(\overrightarrow{r}\right)$ and $w\left(\overrightarrow{r}\right)$ are solutions to the equations of solid mechanics. Note that all results obtained so far are applicable for positive direction of slip, otherwise the minus sign should be added in the expressions for $T, b, \tau\left(\overrightarrow{r}\right)$, and $w\left(\overrightarrow{r}\right)$. An example of the shear stress distribution for two spheres and the corresponding memory diagram Eq. (5.22) are shown in Fig. 5.5a, b.

Suppose now that at some moment the drive parameter b starts decreasing. In this situation, we first assume that slip starts propagating anew from the contact boundary $\mathbb{C}_a^a$ with a different sign, and then we show that by a proper choice of parameters the conditions of the contact problem can be satisfied. To do that, we denote the new boundary between stick and slip zones $\mathbb{C}_{q'}^{q'}$ where q' is close to a. Then the new solution for stress and displacement distributions ($\tau'\left(\overrightarrow{r}\right)$ and $w'\left(\overrightarrow{r}\right)$, respectively) is obtained in the form

$$\tau'\left(\overrightarrow{r}\right) = \tau\left(\overrightarrow{r}\right) - \tau_a^{q'}\left(\overrightarrow{r}\right) - \tau_a^{q'}\left(\overrightarrow{r}\right),$$

$$w'\left(\overrightarrow{r}\right) = w\left(\overrightarrow{r}\right) - w_a^{q'}\left(\overrightarrow{r}\right) - w_a^{q'}\left(\overrightarrow{r}\right),$$

where $\tau\left(\overrightarrow{r}\right)$ and $w\left(\overrightarrow{r}\right)$ are given by Eqs. (5.14) and (5.15). Here subtraction $-\tau_a^{q'}\left(\overrightarrow{r}\right)$ removes any shear stress in the zone $\mathbb{C}_a^{q'}$ and the second subtraction $-\tau_a^{q'}\left(\overrightarrow{r}\right)$ sets the shear stress equal to $\tau\left(\overrightarrow{r}\right) = -\mu\sigma_a\left(\overrightarrow{r}\right)$, as it is easy to see from the definitions of notation $\tau_{\bullet}^{\bullet}\left(\overrightarrow{r}\right)$ given in Eq. (5.17). At the same time, adding $-2w_a^{q'}\left(\overrightarrow{r}\right)$ results in the creation of a constant additional displacement in the stick zone $\mathbb{C}_{q'}^0$, i.e., does not violate with the stick condition. For contact between two spheres, the shear stress distribution $\tau'\left(\overrightarrow{r}\right)$ is easy to calculate using Eq. (5.12) (see Fig. 5.5c). The two above equations produce expressions for the tangential displacement and force

$$b' = b - 2\theta\mu\left(a - q'\right)$$

$$T' = T - 2\mu\left(N(a) - N\left(a = q'\right)\right).$$

Taking into account Eq. (5.21), it is straightforward to check that these expressions correspond to the memory function $D(\alpha)$ shown in Fig. 5.5d. Again, calculating this solution we comply with the Coulomb friction conditions in the stick and slip zones and operate only with stresses and displacement satisfying the equations of solid mechanics.

5.6.2 *Case of Overloading*

The above example shows how the contact system evolves under fixed compression. Suppose now that the normal displacement a varies. Continuously changing inputs can be accounted for by considering infinitely small increments Δa and Δb as it was proposed for the first time in [4]. If Δa is positive, its application creates an additional contact zone $\mathbb{C}_{a+\Delta a}^a$ which can support additional shear stress necessary to satisfy the slip condition. If Δa is negative mechanical contact in the zone $\mathbb{C}_a^{a+\Delta a}$ disappears; therefore prior to application of Δa it is necessary to remove any pre-existing shear stress in that zone.

Increasing compression can produce a specific slip-free behavior referred to as "overloading" or "quick" enlargement of the contact zone in [30, 31], or "complete overlapping" by Jäger [23]. Assume a small increment Δa that creates an additional contact zone $\mathbb{C}_{a+\Delta a}^a$ and introduce a small increment Δb that produces

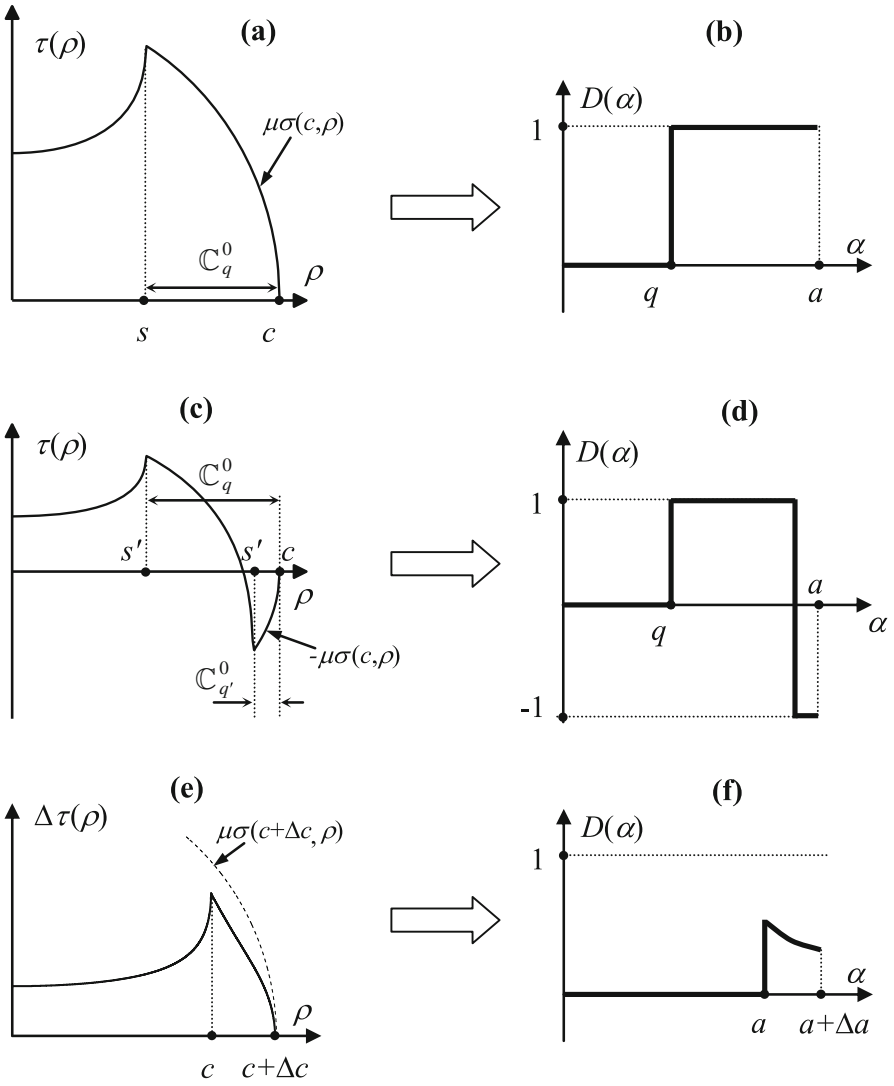

Fig. 5.5 Examples of the shear stress distributions (at the left) and corresponding memory diagrams (at the right) for the following situations. (**a**, **b**) Constant-loading case where application of positive a is followed by an application of positive b. (**c**, **d**) Same as (**a**, **b**) but followed by subsequent decreasing tangential displacement to a lower value. (**e**, **f**) Displacements a and b change simultaneously so that the condition Eq. (5.24) is satisfied (case of overloading)

slip characterized by the parameter q. Then if the slip zone $\mathbb{C}^q_{a+\Delta a}$ lies within $\mathbb{C}^a_{a+\Delta a}$, i.e., $a \le q \le a + \Delta a$ no slip actually occurs. Applying increments to Eq. (5.15) we obtain

$$\begin{cases} \Delta T/\mu = \frac{dN}{da}\Delta a - \frac{dN}{da}\big|_{a=q}\Delta q \approx \frac{dN}{da}\left(\Delta a - \Delta q\right) \\ \Delta b/\left(\theta\mu\right) = \Delta a - \Delta q \end{cases},$$

where the small increment of parameter q equals $\Delta q = q - a$. The above equations provide the tangential load–displacement relationship in the incremental form:

$$\frac{\Delta T}{\Delta b} = \frac{1}{\theta}\frac{dN}{da}. \tag{5.23}$$

Besides, the condition representing the absence of slip $a \le q \le a + \Delta a$ corresponds to the validity condition

$$\left|\Delta b/\Delta a\right|/\left(\theta\mu\right) < 1, \;\; \Delta a > 0 \tag{5.24}$$

for this solution.

It is also straightforward to get the following expressions for incremental shears stress and local tangential displacement:

$$\Delta\tau\left(\overrightarrow{r}\right) = \frac{1}{\theta}\frac{\partial\sigma_a\left(\overrightarrow{r}\right)}{\partial a}\Delta b,$$

$$\Delta w\left(\overrightarrow{r}\right) = \frac{\partial u_a\left(\overrightarrow{r}\right)}{\partial a}\Delta b.$$

Since we always operate with tangential solutions keeping identical local displacements for each point in the stick zone (see Eq. (5.19)), the latter equation actually means that

$$\Delta w\left(\overrightarrow{r}\right) = \frac{\partial u_a\left(\overrightarrow{r}\right)}{\partial a}\Delta b = \frac{\partial a}{\partial a}\Delta b = \Delta b = const\left(\overrightarrow{r}\right).$$

Finally, in the overloading regime, the incremental local fields are given by

$$\begin{cases} \Delta\tau\left(\overrightarrow{r}\right) = \frac{1}{\theta}\frac{\partial\sigma_a\left(\overrightarrow{r}\right)}{\partial a}\Delta b \\ \Delta w\left(\overrightarrow{r}\right) = \Delta b \end{cases} \tag{5.25}$$

everywhere in the contact zone $\mathbb{C}_a^0$. Slip in this regime is absent. An illustration for contact between two spheres is presented in Fig. 5.5e in which small increments are highly exaggerated.

In defining the related memory diagram, our intention is to keep the link Eq. (5.21) for any loading history. The result is shown in Fig. 5.5f where the curvilinear piece of the memory function is given by

$$D(\alpha) = \frac{1}{\theta\mu}\left.\frac{db}{da}\right|_{a=\alpha}. \tag{5.26}$$

The absolute value of the memory function on the new segment $a < \alpha < a + \Delta a$ is less than 1 which follows from Eq. (5.24) indicating the absence of slip in the considered case (see also Fig. 5.5e where the shear stress does not exceed the Coulomb threshold). The "overloading" solution holds also in the situation when before application of the increments the area $\mathbb{C}_a^0$ already supported some residual shear stress distribution. Indeed, the above derivations apply independently of the residual stress presence.

5.6.3 *Memory Diagrams for Arbitrary Loading Histories*

The two considered examples show how to extend our reasoning to arbitrary loading histories. First of all, we check whether the condition of overloading Eq. (5.24) is satisfied or not. If the solution is slip-free, i.e., is given by Eqs. (5.23) and (5.25), then the memory diagram should be updated according to Eq. (5.26) in a new contact zone $\mathbb{C}_{a+\Delta a}^a$. If it is not, a two-stage procedure involving slip should be applied. At the first stage, all residual shear stress in a guessed slip zone should be removed. Then the slip solution of the kind Eqs. (5.15), (5.17), and (5.18) should be added. In other words, the procedure consists in the proper selection of a superposition of known elementary solutions to the solid mechanics equations such that both stick (rigid-body displacement) and slip (tangential stress equals normal one times μ) conditions are satisfied. Each time when a shear stress component is added or subtracted, the corresponding amount of local tangential displacement should be added or subtracted. Note that the latter does not violate the stick condition since the corresponding tangential displacement fields are constant in the stick zone.

The usefulness of the memory diagram is related to the fact that "cleaning up" some part of the contact zone and the subsequent application of the slip solution consists in updating the memory diagram only in that zone. In contrast to memory diagrams, distributions of the shear stress and local tangential displacement do not have this property. Application of infinitely small displacement increments modifies $\tau\left(\overrightarrow{r}\right)$ and $w\left(\overrightarrow{r}\right)$ everywhere in the contact zone whereas the memory diagrams are updated only locally. In that sense, the memory diagram represents an economic and efficient way of storing memory information physically kept in the residual parts of distributions $\tau\left(\overrightarrow{r}\right)$ and $w\left(\overrightarrow{r}\right)$.

The parameter q of the slip zone (if slip takes place) is determined by the drive parameter b of the system. The corresponding output parameter T is calculated by the MMD algorithm illustrated in Figs. 5.6 and 5.7 and explained below in detail.

The MMD aims at calculating parameters at the next step (subscript "n") using parameters at the previous step (subscript "p"); the increments are denoted as Δ (e.g., $\Delta a = a_n - a_p$, $\Delta b = b_n - b_p$, etc.). Since the normal solution to the contact problem is known, the normal displacement increment

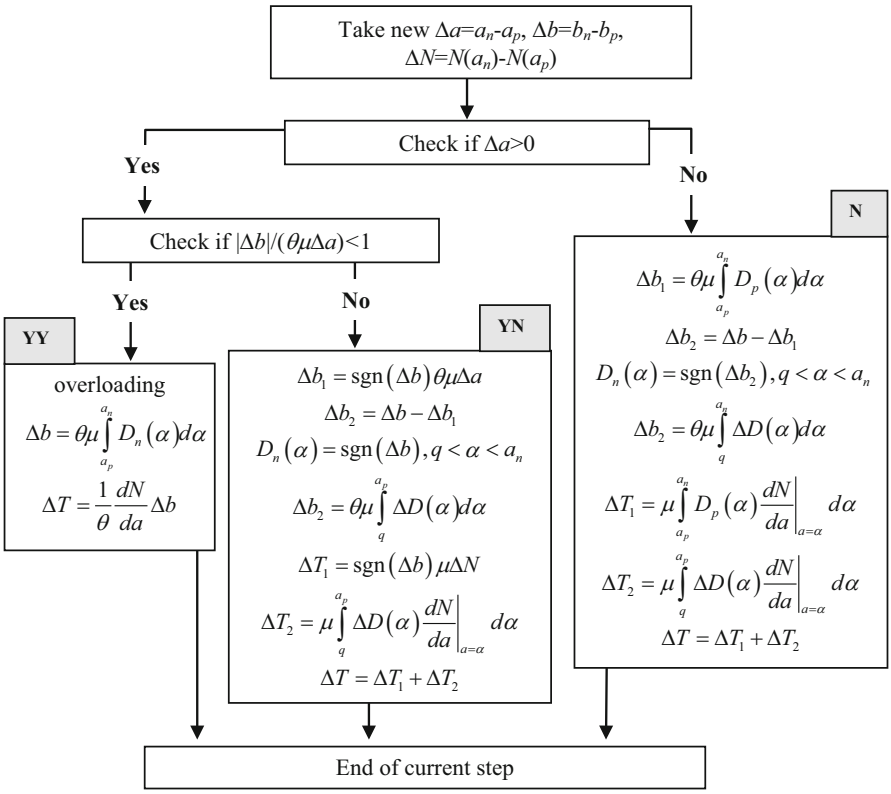

Fig. 5.6 Complete algorithm of the method of memory diagrams. The equations displayed in the boxes correspond to Eqs. (5.27), (5.28), (5.29), (5.30), (5.31), (5.32), (5.33), (5.34), (5.35), (5.36), (5.37), (5.38), (5.39), (5.40), (5.41), (5.42), and (5.43)

$$\Delta N = N\left(a_n\right) - N\left(a_p\right) \tag{5.27}$$

can be immediately calculated, while ΔT has to be determined as the result of the MMD procedure. The algorithm involves only two binary choices and thus consists of three cases in which the calculations differ. As illustrated in Fig. 5.6, we have called these cases YY, YN, and N. In all illustrations, the values of "small force increments" are exaggerated.

5.6.3.1 Case YY

As it was mentioned, the calculation is different for increasing and decreasing a. If a increases ($\Delta a > 0$, Fig. 5.7a–c), a new segment $a_p < \alpha < a_n = a_p + \Delta a$ should be added to the diagram as shown in Fig. 5.7a which means that an additional contact area $\mathbb{C}_{a_n}^{a_p}$ is created. Then the condition Eq. (5.24) of overloading should be checked.

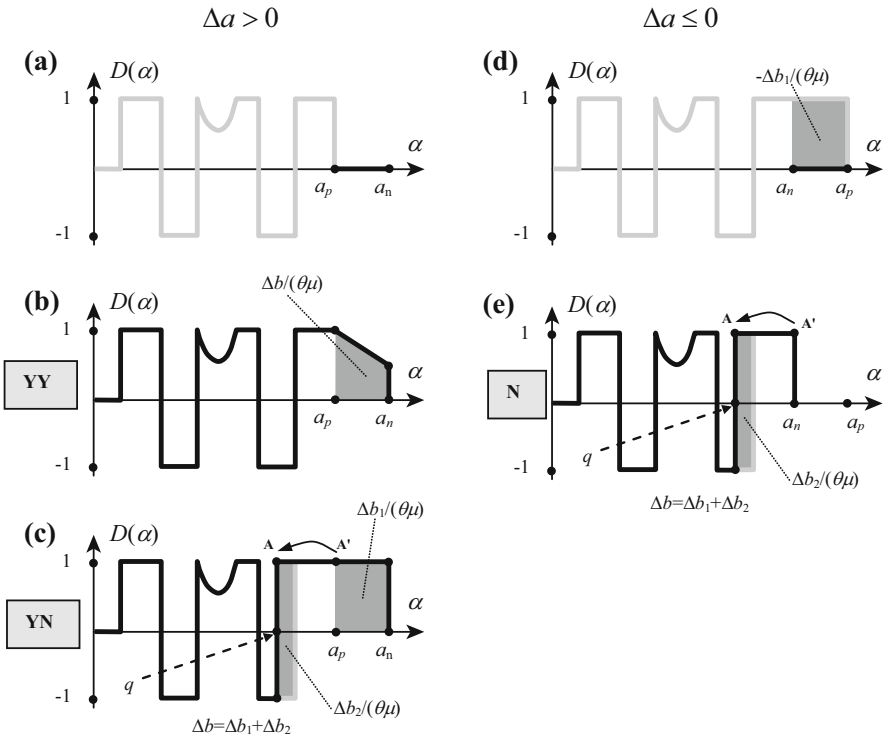

Fig. 5.7 Illustrations of the evolution algorithm. (**a**) Original memory diagram (gray), a increases from a_p to a_n. (**b**) Case YY, i.e., $|\Delta b/\Delta a|/(\theta\mu) < 1,\ \Delta a > 0$; the displacement increment Δb can be equilibrated by the proper choice of $D(\alpha)$ on the new interval $a_p < \alpha < a_n$. (**c**) Case YN, i.e., $|\Delta b/\Delta a|/(\theta\mu) \geq 1,\ \Delta a > 0$; the increment Δb is too large to be equilibrated by setting $D(\alpha) = 1$ only on the new interval $\alpha_p < \alpha < \alpha_n$, therefore the slip zone $\mathbb{C}^q_{a_n}$ with $D(\alpha) = 1$ penetrates closer to the contact center $\mathbb{C}^0_0$. (**d**) Original memory diagram (gray), a decreases from a_p to a_n releasing displacement Δb_1. (**e**) The remaining displacement increment $\Delta b_2 = \Delta b\text{-}\Delta b_1$ is equilibrated by slip propagation

Suppose it is verified (situation marked YY in Fig. 5.6). It is exactly the case where the slip-free solution Eqs. (5.23) and (5.25) is applicable. Thus on a new segment Eq. (5.26) should be required which means that

$$\int_{a_p}^{a_n} D_n(\alpha)\, d\alpha = \Delta b/(\theta\mu), \tag{5.28}$$

or, for small increments (see case YY in Figs. 5.6 and 5.7b),

$$\frac{D_n(a_p) + D_n(a_n)}{2}\Delta a = \Delta b/(\theta\mu). \tag{5.29}$$

Here $D_n(a_p) = D_p(a_p)$ since we modify the memory function only on the new interval, leaving it unchanged on the old one (compare thick gray line in Fig. 5.7a for the old diagram $D_p(\alpha)$ with the thick black line in Fig. 5.7b for the new one, $D_n(\alpha)$). Correspondingly, Eq. (5.29) determines the updated value $D_n(a_n)$.

It can be easily shown using the overloading condition Eq. (5.24) that if $|D_n(a_p)| \leq 1$ then $|D_n(a_n)| < 1$. Hence, it can be concluded that the slip-free regime corresponds to the memory diagram that ends with a value $D(a)$ such that $|D(a)| < 1$.

5.6.3.2 Case YN

Suppose now that the normal displacement increases, $\Delta a > 0$, but $|\Delta b/\Delta a|/(\theta\mu) \geq 1$. As in the previous case, an additional contact zone $\mathbb{C}_{a_n}^{a_p}$ is created. However, since the condition Eq. (5.24) of the slip-free solution is not fulfilled, slip develops starting from the contact border $\mathbb{C}_{a_n}^{a_n}$ and occupies some slip zone $\mathbb{C}_{a_n}^{q}$ with q a priori unknown. In order to fix q, we can gradually decrease it by infinitesimally small steps starting from a_n and apply the two-stage procedure that consists in (1) setting the memory diagram to 0 at each small interval $a_n - (i+1)\Delta a \leq \alpha \leq a_n - i\Delta a$ ($i = 0, 1, \ldots$, and Δa is small) and (2) applying the slip solution in the zones $\mathbb{C}_{a_n}^{a_n-(i+1)\Delta a}$ with the sign $\mathrm{sgn}(\Delta b)$ corresponding to the direction of slip. In other words, the new value of the memory function is

$$D_n(\alpha) = \mathrm{sgn}(\Delta b), \; q < \alpha < a_n. \tag{5.30}$$

For the newly created interval $a_p \leq \alpha \leq a_n$ on which $D(\alpha) \equiv 0$, the first stage of the procedure is not necessary. Setting new $D_n(\alpha)$ on that interval corresponds to the tangential displacement

$$\Delta b_1 = \mathrm{sgn}(\Delta b)\,\theta\mu\Delta a. \tag{5.31}$$

while the remaining part

$$\Delta b_2 = \Delta b - \Delta b_1. \tag{5.32}$$

This means that for compliance with the first MMD equation (Eq. 5.21),

$$b/(\theta\mu) = \int_0^a D(\alpha)\, d\alpha,$$

the following relationship should be required:

$$\int_q^{a_p} \Delta D d\alpha = \Delta b_2/(\theta\mu), \tag{5.33}$$

where $\Delta D(\alpha) = D_n(\alpha) - D_p(\alpha)$. Here we assume that at the previous moment of time the MMD equations (Eq. (5.21)) were fulfilled.

The situation is illustrated in Fig. 5.7c where the case of positive slip with $D = +1$ is shown for definiteness, while in a general case D should be set to $\mathrm{sgn}(\Delta b_2) = \mathrm{sgn}(\Delta b)$. Firstly, the memory function $D(\alpha)$ has been set to $\mathrm{sgn}(\Delta b)$ on the interval $a_p < \alpha < a_n$, thereby equilibrating the partial displacement increment $\Delta b_1 = \theta\mu\Delta a$. Subsequently, the remaining part $\Delta b_2 = \Delta b - \Delta b_1$ is compensated for by setting $D_n(\alpha) = 1$ in the contact zone adjacent to the new segment $a_p < \alpha < a_n$. In other words, we have to shift point A in Fig. 5.7c starting from position A' and setting the memory function to $\mathrm{sgn}(\Delta b)$ on the interval AA' until the desired value $\Delta b_2/(\theta\mu)$ is reached. Then the new parameter q of the slip zone $\mathbb{C}_{a_n}^{q}$ is determined via Eq. (5.33).

Once $\Delta b_{1,2}$ and q are determined, the solution for the force increment corresponding to Δb_1 easily follows from Eq. (5.31) and reads

$$\Delta T_1 = \mathrm{sgn}\,(\Delta b)\,\mu\Delta N, \tag{5.34}$$

while the remaining part ΔT_2 is given by

$$\Delta T_2 = \mu \int_{q}^{a_p} \Delta D\,(\alpha)\,\left.\frac{dN}{da}\right|_{a=\alpha} d\alpha \tag{5.35}$$

where q is known. Finally, it suffices to sum both contributions to obtain the total force increment:

$$\Delta T = \Delta T_1 + \Delta T_2. \tag{5.36}$$

These equations are reproduced in Fig. 5.6 (set "YN").

While shifting q towards $\alpha = 0$ some elements of the previously saved memory diagram can be erased. Point q can even attain $\alpha = 0$ reaching the threshold of the partial slip regime. Erasing previously saved structure elements correspond to subtraction of proper residual shear stress distributions; rectangular segments correspond to slip solution while curvilinear ones mark the overloading regime (see Fig. 5.7). The validity of the procedure is guaranteed by the fact that the final superposition of particular solutions satisfies both slip and stick Coulomb conditions.

5.6.3.3 Case N

We now consider the situation in which the normal displacement is constant or decreasing, $\Delta a \leq 0$. In this case, the memory diagram should shrink to the new size a_n, and therefore release some tangential displacement Δb_1, as shown in Fig. 5.7d:

$$\Delta b_1 = \theta\mu \int_{a_p}^{a_n} D_p(\alpha)\, d\alpha \tag{5.37}$$

($\Delta b_1 = 0$ in a particular case $\Delta a = 0$). In order to achieve the force equilibrium, i.e., satisfy the second Eq. (5.21), we have to account only for the partial displacement increment

$$\Delta b_2 = \Delta b - \Delta b_1. \tag{5.38}$$

As previously, there is no other option than to allow slip to penetrate closer to the contact center $\mathbb{C}_0^0$ (except in a particular case when Δb_2 coincidentally equals 0). This means that we have to shift point A, starting from position A' (Fig. 5.7e), while setting

$$D_n(\alpha) = \operatorname{sgn}(\Delta b_2) \tag{5.39}$$

on interval AA', until the condition

$$\Delta b_2 = \theta\mu \int_{q}^{a_n} \Delta D(\alpha)\, d\alpha \tag{5.40}$$

is satisfied. As previously mentioned, various slip scenarios are possible depending on the structure of the memory function on the segment $0 < \alpha < a_n$.

Once the values of Δb_1 and Δb_2 are determined for this case, the related T-increments then read

$$\Delta T_1 = \mu \int_{a_p}^{a_n} D_p(\alpha) \left.\frac{dN}{da}\right|_{a=\alpha} d\alpha, \tag{5.41}$$

$$\Delta T_2 = \mu \int_{q}^{a_p} \Delta D(\alpha) \left.\frac{dN}{da}\right|_{a=\alpha} d\alpha, \tag{5.42}$$

with the total

$$\Delta T = \Delta T_1 + \Delta T_2. \tag{5.43}$$

Equations (5.37), (5.38), (5.39), (5.40), (5.41), (5.42), and (5.43) then represent the full solution to the problem in case N; they are cited in the proper set in Fig. 5.6.

The solutions that correspond to slip (cases YN and N) have an interesting feature. In the case YN where the normal displacement increases, the maximal

setting $|D(\alpha)| = 1$ in the new segment is not enough for equilibrating the tangential force, so that we have to engage other segments. As Δb_1 and Δb_2 have the same sign (which also equals the sign of Δb), the direction of slip always coincides with the direction of the tangential displacement increment. However, in the case N, corresponding to normal unloading, this is not always true. Decreasing the normal displacement releases some amount Δb_1 whose value and sign are defined by the system's history and therefore are completely independent on the increment Δb. In the situation presented in Fig. 5.7e, the direction of slip is positive since $D_n(\alpha) = +1$ at the end of the new diagram, but the released area $\Delta b_1/(\theta\mu)$ is larger than the area $\Delta b_2/(\theta\mu)$ generated by slip. This implies that the sum $\Delta b = \Delta b_1 + \Delta b_2$ is negative, and the slip direction is opposite to the direction of the tangential displacement change.

The strength of the proposed approach lies in the fact that the memory effects are automatically accounted for. Indeed, the fulfillment of the principal MMD Eq. (5.21) by the application of the algorithm in Fig. 5.7 automatically complies with the force balance, without specifying or classifying all structural changes that can potentially occur to the memory diagram.

5.6.4 *Retrieving Physical Characteristics from Memory Diagram*

As it was mentioned, the memory diagram represents a compact way of storing information on physical quantities characterizing the current state of contact, such as tangential displacement b, tangential force T, and distributions of shear stress $\tau\left(\overrightarrow{r}\right)$ and of local tangential displacement $w\left(\overrightarrow{r}\right)$. As an example, we show how to retrieve these quantities from the memory diagram shown in Fig. 5.8a. For that, it is sufficient to specify one particular loading history that results in the given memory diagram. This loading history can be as follows:

1. Start with the contact zone $\mathbb{C}^0_{\alpha_3}$ and apply positive slip in the zone $\mathbb{C}^{\alpha_1}_{\alpha_3}$ keeping constant compression.
2. Apply negative slip in the zone $\mathbb{C}^{\alpha_2}_{\alpha_3}$ keeping the constant compression.
3. Increase contact zone to $\mathbb{C}^0_{\alpha_4}$ using the slip-free (overloading) regime.
4. Extend contact zone till $\mathbb{C}^0_{\alpha_5}$ simultaneously creating positive slip in $\mathbb{C}^{\alpha_4}_{\alpha_5}$.
5. Extend contact zone till $\mathbb{C}^0_{\alpha_6}$ simultaneously creating negative slip in $\mathbb{C}^{\alpha_5}_{\alpha_6}$.
6. Extend contact zone till $\mathbb{C}^0_a$ simultaneously creating positive slip in $\mathbb{C}^{\alpha_6}_a$.

Correspondingly, the final solutions read

$$b = \theta\mu\,(\alpha_3 - \alpha_1) - 2\theta\mu\,(\alpha_3 - \alpha_2) + \int_{\alpha_3}^{\alpha_4} \frac{db}{da}\,da$$
$$+ \theta\mu\,(\alpha_5 - \alpha_4) - \theta\mu\,(\alpha_6 - \alpha_5) + \theta\mu\,(a - \alpha_6)\,, \tag{5.44}$$

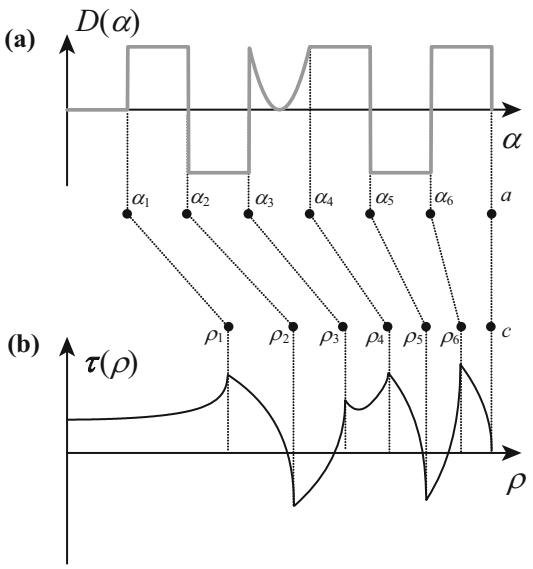

Fig. 5.8 Exemplar memory diagram (**a**) and corresponding traction distribution (**b**) for contact of two identical spheres. The scale transformation is given by $\rho = (R\alpha)^{1/2}$, equation immediately following from the Hertz theory

$$T = \mu\left(N\left(\alpha_3\right) - N\left(\alpha_1\right)\right) - 2\mu\left(N\left(\alpha_3\right) - N\left(\alpha_2\right)\right) + \frac{1}{\theta}\int_{\alpha_3}^{\alpha_4}\frac{dN}{da}\frac{db}{da}da$$

$$+\mu\left(N\left(\alpha_5\right) - N\left(\alpha_4\right)\right) - \mu\left(N\left(\alpha_6\right) - N\left(\alpha_5\right)\right) + \mu\left(N(a) - N\left(\alpha_6\right)\right), \quad (5.45)$$

$$w\left(\overrightarrow{r}\right) = w_{\alpha_3}^{\alpha_1}\left(\overrightarrow{r}\right) - 2w_{\alpha_3}^{\alpha_2}\left(\overrightarrow{r}\right) + \int_{\alpha_3}^{\alpha_4}\frac{db}{da}da + w_{\alpha_5}^{\alpha_4}\left(\overrightarrow{r}\right) - w_{\alpha_6}^{\alpha_5}\left(\overrightarrow{r}\right) + w_{a}^{\alpha_6}\left(\overrightarrow{r}\right), \quad (5.46)$$

$$\tau\left(\overrightarrow{r}\right) = \tau_{\alpha_3}^{\alpha_1}\left(\overrightarrow{r}\right) - 2\tau_{\alpha_3}^{\alpha_2}\left(\overrightarrow{r}\right) + \frac{1}{\theta}\int_{\alpha_3}^{\alpha_4}\frac{\partial\sigma_a\left(\overrightarrow{r}\right)}{\partial a}\frac{db}{da}da$$

$$+ \tau_{\alpha_5}^{\alpha_4}\left(\overrightarrow{r}\right) - \tau_{\alpha_6}^{\alpha_5}\left(\overrightarrow{r}\right) + \tau_{a}^{\alpha_6}\left(\overrightarrow{r}\right), \quad (5.47)$$

with notations $w_{\bullet}^{\bullet}\left(\overrightarrow{r}\right)$ and $\tau_{\bullet}^{\bullet}\left(\overrightarrow{r}\right)$ which have been introduced in Eqs. (5.17) and (5.18). Here the derivative *db*/*da* during the slip-free process is known. The radial shear stress distribution for contact of two spheres when all solutions are given analytically Eqs. (5.11), (5.12), (5.13), and (5.14) is presented in Fig. 5.8b. In this case, the link between radial coordinate ρ and the parameter α (argument of memory functions) is provided by the relationship $\rho = (R\alpha)^{1/2}$, equation corresponding to the Hertzian link $c = (Ra)^{1/2}$ between contact radius and normal displacement.

Whereas the physical solution corresponding to a given memory diagram is unique, the loading history that engenders the given memory diagram is not. For instance, points (1) and (2) in the above loading history could be replaced by the following ones:

(1′) Start with the contact zone $\mathbb{C}^0_{\alpha_2}$ and apply positive slip in the zone $\mathbb{C}^{\alpha_1}_{\alpha_2}$ keeping constant compression.

(2′) Extend contact zone till $\mathbb{C}^0_{\alpha_3}$ simultaneously creating negative slip in $\mathbb{C}^{\alpha_2}_{\alpha_3}$.

The first two terms in the new expression of b will produce the same result as previously in Eq. (5.44):

$$\theta\mu\,(\alpha_2-\alpha_1)-\theta\mu\,(\alpha_3-\alpha_2)\equiv\theta\mu\,(\alpha_3-\alpha_1)-2\theta\mu\,(\alpha_3-\alpha_2)\,,$$

as well as for other physical quantities in Eqs. (5.45), (5.46), and (5.47).

Another example is the simplest memory diagram (Eq. 5.22):

$$D\,(\alpha)=\begin{cases}0,\ 0\le\alpha<q\\ 1,\ q\le\alpha\le a\end{cases}.$$

It can be created by a process that consists of any arbitrary transformation in the zone $q<\alpha<a$, concluded by application of $b=\theta\mu(a-q)$ at constant normal displacement a. Slip created in the zone $\mathbb{C}^q_a$ will erase the entire previously saved structure in that zone.

5.6.5 *Numerical Implementation and Examples*

The MMD formulation discussed in the previous paragraphs does not impose any requirements with respect to the numerical implementation procedure; the only assumption used concerns the linear interpolation in Eq. (5.29). The simplest numerical implementation can consist of introducing a fixed-point grid α_j on the α-axis and in defining the corresponding function values $D(\alpha_j)$ on that grid. However, this method is time consuming, inaccurate, and generally not suitable for ultrasound excitations with millions of oscillations. The use of adaptive grids is more relevant in this case. One "adaptive" feature consists in setting grid points α_j at the points $a_i=a(t_i)$ of the loading history. More precisely, increasing compression results in adding new α-points coinciding with points $a_i=a(t_i)$, while decreasing compression down to some value a means deleting all α-points exceeding a and adding an additional α-point equal to a. Another opportunity of increasing the calculations performance is to use the fact that the memory function is constant on certain intervals and thus can be represented only by the pairs of the two boundary values of α defining the intervals. For curvilinear sections, not only the interval boundaries but all intermediate points $\alpha=a(t_i)$ are to be memorized. Thus, in general, function $D(\alpha)$ can be defined on a non-equidistant and adaptive grid. In those cases where the memory function has to be determined in between two points

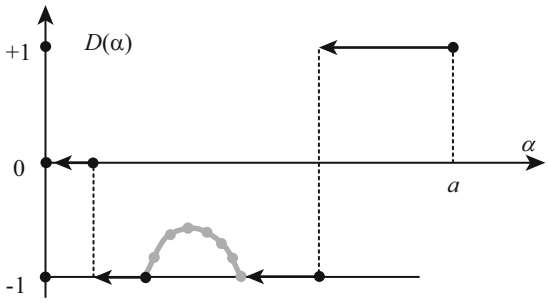

Fig. 5.9 Adaptive grid for representing a memory diagram. Black points mark ends of constant sections. Gray points are placed on curvilinear segments; the linear interpolation is used in between them

of a curvilinear section, we use linear interpolation (see Fig. 5.9). As a result, the complexity of this numerical code exceeds only slightly the complexity of the method itself (see Fig. 5.7).

A simple example illustrating all three cases (or regimes) YY, YN, and N is shown in Fig. 5.10 for a monotonous time dependence of the tangential displacement $b(t)$ (see the inset in Fig. 5.10a), the response $T(b)$ (main Fig. 5.10a) is monotonous as well. However, the normal displacement $a(t)$ in Fig. 5.10a is not monotonous which makes it possible to see various regimes in the corresponding memory diagrams (see Fig. 5.10b–e), corresponding to moments in time $t = 5000$, 8000, 9000, 19,000 in arbitrary units, marked by dotted lines in Fig. 5.10a. The curve $a(t)$ begins with an increasing segment on which the condition Eq. (5.27) is fulfilled (case YY, thick gray lines in Fig. 5.10a). According to the given explanation, a curvilinear segment appears in the memory diagram (Fig. 5.10b). Further, $a(t)$ still increases but the condition Eq. (5.27) is not satisfied anymore resulting in appearance of the regime YN (thick black line in Fig. 5.10a). A typical behavior is shown in Fig. 5.10c; a straight-line segment $q < \alpha < a$ on which $D(\alpha) = 1$ corresponds to slip. Slip propagates inward (i.e., to the left in the figures) erasing the previously saved curvilinear segment (Fig. 5.10d). At the moment $t = 10{,}000$ the normal force starts decreasing, therefore the total length of the memory diagram shrinks (future evolution of the memory diagrams is shown with arrows in all sets (b–e)), and the system runs in the regime N. Further, point q shifts closer to the left end of the memory diagram $\alpha = 0$ (Fig. 5.10e); at the moment $t = 20{,}000$ q reaches 0 which means that partial slip transforms into total sliding when $T = \mu N$ and $b = \theta \mu a$.

Fig. 5.10 (a, main figure) also illustrates the situation discussed in Sect. 5.6.3 (after Eq. (5.43)) where decreasing normal compression releases some preciously saved tangential stress in the vicinity of the contact boundary. In this case, the signs of increments Δb and ΔT can be different as it occurs at the concluding part of the curve $T(b)$.

Two more general cases of the MMD application are presented in Fig. 5.11. Set (a) illustrates the particular situation where the two displacement arguments, a and b, are linked by a functional relationship, $a = a(b)$, so that there actually is only one independent argument, but it evolves in a nontrivial manner. The resulting curve

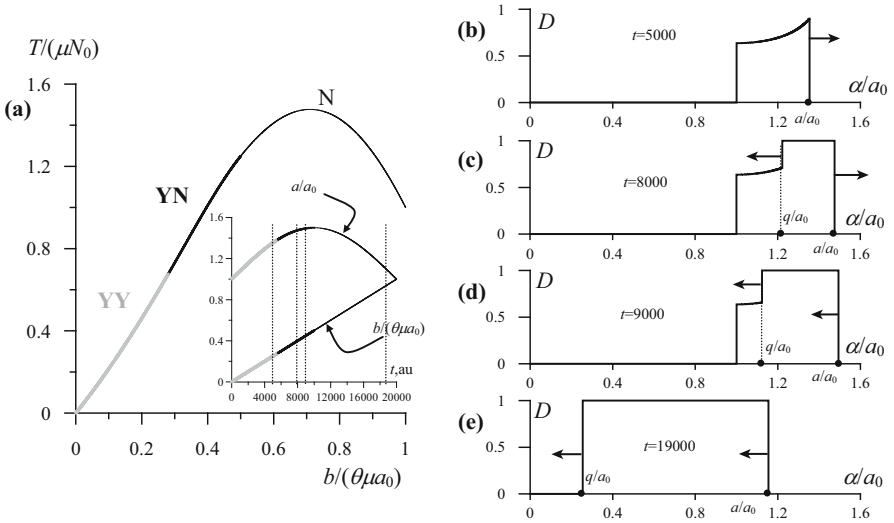

Fig. 5.10 Tangential force displacement relationship in which cases YY, YN, and N of the MMD algorithm (Figs. 5.6 and 5.7) are identified (gray, thick black, and thin black lines, respectively). In the inset: loading history, i.e., time dependencies of normal and tangential displacements; the regimes are marked as in the main figure. Four moments in time are selected; memory diagrams at these moments are shown in sets (**b–e**). In all plots, a_0 is a characteristic value of the normal displacement; $N_0 = N(a_0)$

$T(b)$ shown in Fig. 5.11a is typical for one-parametric hysteresis response; it exhibits closed loops for periodic $b(t)$, partial increase in the argument b on a globally decreasing branch results in the creation of an inner loop, and each completed inner loop has the property of end-point memory, where the curve exits the outer loop with the same tangent as just before entering it, etc.

In the more general case of two independent arguments, a and b without functional link, the hysteretic behavior differs considerably. Since variations in a are independent on the $b(t)$-protocol, it occurs that, even for a periodic $b(t)$ loading history, the "loops" are not closed. Indeed, as illustrated in Fig. 5.11b, the same $b(t)$-history as used in Fig. 5.11a produces a curve in which all monotonous parts are displaced, deformed, etc. It is important to emphasize that the generation of such curves via the direct analysis of the traction and without the use of an algorithm of the MMD type is an extremely cumbersome task. The formulation in terms of the MMD drastically reduces the complexity.

Finally, it can be analytically verified that all classical results, e.g., those discussed in [4] for spheres loaded by an oblique force, follow in a simple and straightforward manner from the MMD equations.

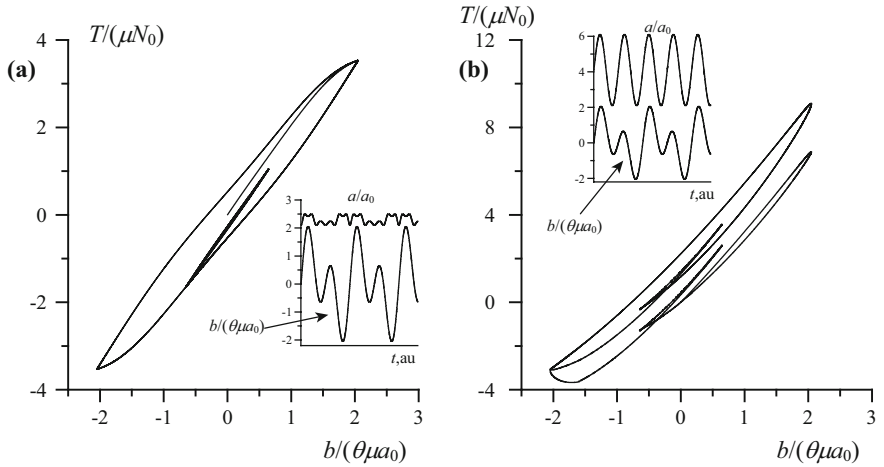

Fig. 5.11 Tangential force–displacement curves for some particular loading histories as shown in the insets. (**a**) One-parametric hysteresis, in which a and b are linked via a functional dependence. (**b**) Two-parametric hysteresis in which a and b are independent. In all plots, a_0 is a characteristic value of the normal displacement; $N_0 = N(a_0)$

5.6.6 Summary of the Method of Memory Diagrams

As it was mentioned in Sect. 5.2, in order to create a displacement-driven contact model providing an explicit relationship between contact displacements and forces, an algorithm for the description of hysteretic friction-induced behavior in the partial slip case is necessary. This algorithm is presented by the MMD that links forces and displacements via simple integral expressions (Eq. 5.21):

$$\begin{cases} b = \theta\mu \int\limits_0^a D(\alpha)\, d\alpha \\ T = \mu \int\limits_0^a D(\alpha)\, \frac{dN}{da}\big|_{a=\alpha} d\alpha \end{cases}$$

written for the displacement-driven system. Although it is not required in the framework of the general description, the partial slip theory can be developed in the case where the drive parameters are loads instead of displacements. The principal MMD equations for the load-driven system are:

$$\begin{cases} T = \mu \int\limits_0^N D(\eta)\, d\eta \\ b = \theta\mu \int\limits_0^N D(\eta)\, \frac{da}{dN}\big|_{N=\eta} d\eta \end{cases}, \tag{5.48}$$

where η is the argument of the memory function having the dimension of force. Finally, replacing contact of rough surfaces by an equivalent axisymmetric contact system (see Sect. 5.5) makes it possible to use the symmetric representation with radial coordinate ρ:

$$\begin{cases} T = \mu \int_0^c D(\rho) \left. \frac{dN}{dc} \right|_{c=\rho} d\rho \\ b = \theta \mu \int_0^c D(\rho) \left. \frac{da}{dc} \right|_{c=\rho} d\rho \end{cases}, \tag{5.49}$$

where $N(c)$ and $a(c)$ are the known solutions linking normal force and displacement with the contact radius c in the equivalent axisymmetric system. With Eqs. (5.48) and (5.49), the rest of the MMD equations have to be modified accordingly.

The MMD Eq. (5.21) is analytical, but in order to update the memory diagram $D(\alpha)$ following to the evolution of displacement b, an algorithm based on two binary choices (see cases YY, YN, and N above) and small increments is needed. Therefore the obtained solutions can be considered semi-analytical.

The MMD is not equivalent to a detailed numerical contact modeling (such as [2, 3]) and uses a number of assumptions:

1. Loading is in one plane only (i.e., in 2D); 3D extensions are discussed in [32].
2. Only shift is considered; torsion and rolling are ignored.
3. The Coulomb friction law with friction coefficient μ is postulated for contact stress fields.
4. The model is quasi-static: differences between static and dynamic friction are not considered, inertial behavior in the material in the vicinity of the contact zone is neglected.
5. Only partial slip is considered, i.e., the condition $|b| < \theta \mu a$ has to be fulfilled.
6. Plasticity and adhesion are ignored.
7. All individual contact spots are aligned (i.e., they have the same normal directions) and stay aligned during loading.
8. The normal solution is a known biunique function $N = N(a)$ independent of the tangential loading.
9. Dissimilarity effects are neglected.
10. The reduced elastic friction principle is valid for the considered geometry (it is a good approximation for isotropic rough surfaces).

The method is equivalent to another known semi-analytical solution known as the method of dimensionality reduction (MDR, [6]) which is also based on the axisymmetric solution Eqs. (5.7), (5.8), and (5.9). The MDR interprets an axisymmetric contact as the deformation of a half-space filled with infinitesimally spaced elastic springs against a rigid axisymmetric indentor. The only substantial difference is in the numerical implementation; in our case, we use adaptive grids which correspond to the MDR springs "moving" in accordance to the loading

history in the purpose of reducing their number. The adaptive-grid implementation is especially useful for acoustical and random signals.

It is important to mention that the MMD has no hidden parameters; the tangential load is calculated from the tangential displacement using the normal reaction curve $N(a)$ only. Therefore, it makes sense to denote the MMD result as

$$T = MMD(b), \tag{5.50}$$

having in mind that T can be calculated from b and its history, with any desired precision.

5.7 Complete Contact Model Accounting for Three Contact Regimes

As we have mentioned in Sect. 5.2, the Coulomb friction law for flat contact faces does not provide an explicit load–displacement relationship. We have avoided this difficulty by introducing crack face roughness and the corresponding partial slip regime addressed via the MMD. The next step is to complete the description and to show how to calculate the load–displacement response in all cases that can occur for arbitrary contact excitations.

5.7.1 Partial Slip and Total Sliding Displacement Components

In order to complete the description, we split the total tangential displacement into two parts: one part, b_0, corresponding to total sliding and the other one, $\tilde{b}$, to partial slip (Fig. 5.1d, e):

$$b = b_0 + \tilde{b}, \tag{5.51}$$

The idea [33] behind this separation can be illustrated as follows. Suppose the tangential loading increases under a fixed normal compression $N = N(a)$, corresponding to a certain normal displacement a. Asperities recede under load in both normal and tangential direction. In addition, the tangential receding $\tilde{b}$, in contrast to the normal one, a, is accompanied by partial slip. According to the MMD based on the Coulomb friction law, $\tilde{b}$ is not allowed to grow infinitely. Once the maximum value $\tilde{b}_{\max} = \theta\mu a$ is achieved, the asperities cannot deform anymore and a total sliding process develops when the very last stick point $\mathbb{C}_0^0$ belonging to one face separates from its neighbor at the opposite one. The tangential displacement between those points is denoted b_0 and corresponds to the contribution from total sliding. In other words, b_0 is a reference point mismatch, in some sense.

Contact state	If	Then	Memory diagram
(i) Contact loss	$a < 0$	$\tilde{b} := 0 \quad b_0 := b$ $T = N = 0$	
(ii) Total sliding	$a \geq 0$ $\lvert\tilde{b}\rvert \geq \theta\mu a$	$\tilde{b} := \pm\theta\mu a \quad b_0 := b - \tilde{b}$ $T = \pm\mu N$	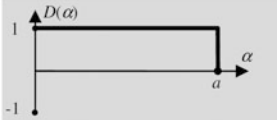
(iii) Partial slip	$a \geq 0$ $\lvert\tilde{b}\rvert < \theta\mu a$	$b_0 := b_0 \quad \tilde{b} := b - b_0$ $T = MMD(\tilde{b})$	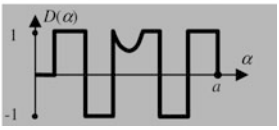

Fig. 5.12 Three possible contact states in the model of cracks with rough surfaces. For each case, the following information is supplied: conditions under which the case occurs, solutions for components b_0 and $\tilde{b}$, solutions for forces N and T, and memory diagrams

In case where the normal compression is also allowed to vary, the maximum value $\tilde{b}_{\max} = \theta\mu a$ changes too. In addition, the contact in a particular mesoscopic cell can be lost at some moment in time so that both stick and slip zones disappear. Figure 5.12 provides an overview of the full concept in case both normal and tangential displacements a and b evolve in an arbitrary manner. The scheme explains how to calculate the forces N and T for any given value of displacements a and b. In order to do so, the tangential displacement components b_0 and $\tilde{b}$ together with the corresponding memory diagram should be updated. The updating operation for the tangential displacement components is denoted using the assignment operator ":=", which means that values obtained at the previous time step are overwritten by new ones.

The full model [33] for cracks with rough faces assumes three possible contact states: contact loss when there is no contact between any two corresponding points from opposite crack faces, total sliding when slip occurs at each contact point and $|T| = \pm\mu N$ according to the Coulomb friction law, and partial slip when both stick and slip areas are present in the contact zone. Below we consider these three cases in more detail:

5.7.1.1 Contact Loss

If $a < 0$, the contact is lost which obviously means that $N = T = 0$. In this case, the repartition in Eq. (5.51), as well as the memory diagram, has no sense. However, it is useful to formally define these characteristics even in the absence of contact, having in mind that at the next time step contact can be reestablished. If so, the

process should start with a "virgin" memory diagram $D(\alpha) = 0$, since the contact zone contains no residual tangential stress. The asperities are not strained at this moment, meaning that $\tilde{b} := 0$, and hence $b_0 = b$. Accepting these modifications will guarantee the correct evolution representation once the crack faces will ever get in contact.

5.7.1.2 Total Sliding

Suppose now that $a \geq 0$ and that the old (i.e., obtained at the previous time step) value of $\tilde{b}$ is such that $\left|\tilde{b}\right| \geq \theta\mu a$, with a, the newly calculated normal displacement. In this case, the new value of $\tilde{b}$ should obviously be corrected, since the maximum tangential displacement corresponding to the elastic deformation of asperities can only be $\tilde{b}_{\max} = \theta\mu a$, and any attempt to further increase the tangential action will result in total sliding. We therefore have to set the new $\tilde{b} := \pm\theta\mu a$, with the sign corresponding to the direction of sliding. The remaining part of the tangential displacement corresponds to the total sliding contribution, $b_0 := b - \tilde{b}$. In other words, the reference point for measuring the tangential deformation of asperities is shifted. In accordance to the Coulomb friction law, $T = \pm \mu N$ and $D(\alpha) = \pm 1$, with the sign again corresponding to the sliding direction. The magnitude of the normal force $N = N(a)$ is calculated using the known normal reaction curve.

5.7.1.3 Partial Slip

Assume now that $a \geq 0$ and the old value of $\tilde{b}$ is such that $\left|\tilde{b}\right| < \theta\mu a$. In this situation, some points of the contact zone stick, and slip, if it occurs at all, can only be partial. The reference value b_0 corresponding to total sliding is therefore not affected, which is symbolically expressed by assigning $b_0 := b_0$. Obviously, the remaining part of the tangential displacement corresponds to the partial slip contribution, $\tilde{b} := b - b_0$. In this regime, the MMD algorithm should be executed using $\tilde{b}$ as an argument, i.e., $T = MMD\left(\tilde{b}\right)$. The magnitude of the normal force $N = N(a)$ is again calculated using the known normal reaction curve. Note that for this partial slip case, there is, however, the risk that the new $\left|\tilde{b}\right|$ will exceed $\theta\mu a$, even though the old $\left|\tilde{b}\right|$ does not. Such a situation should be additionally checked for, and if this happens, the appropriate solution should be taken as discussed in the total sliding regime.

The algorithm in Fig. 5.12 completes the description of the contact model. The result is the possibility to calculate contact forces per unit area, N and T, for any normal and tangential displacement, a and b, i.e.:

$$N = N(a), T = T(b, a). \tag{5.52}$$

This is the main difference of the proposed approach when compared to the simple flat crack model. The introduction of roughness on internal contacting surfaces and the account for partial slip allowed us to organize and perform calculations in an explicit manner. The advancement of this approach is related to the fact that accounting for roughness, or an equivalent axisymmetric contact shape, produces the Coulomb sliding condition for displacements, in the form $\left|\tilde{b}\right| = \theta\mu a$, instead of the traditional form $|T| = \mu N$, written for forces.

The notations N and T used in this chapter were introduced for contact forces. The reason is the consideration of contact between two axisymmetric bodies replacing the actual randomly rough surface topography. However, for mesoscopic cells containing the nominal area A_n of a crack, it is less convenient since the actual small value of A_n is not important. Therefore, in what follows, we normalize the forces on the nominal contact area,

$$N \to N/A_n, T \to T/A_n. \tag{5.53}$$

As a result, the new variables N and T have the sense of average stresses (remember that the normal stress is -N) applied at crack faces due to contact interactions, i.e., stresses defined at the level of the mesoscopic cell (Fig. 5.1b). They are not to be confused with microscopic stress fields $\sigma_a\left(\overrightarrow{r}\right)$ and $\tau\left(\overrightarrow{r}\right)$ which result from the presence of loaded asperities.

5.7.2 Numerical Example

In order to illustrate how the full crack model algorithm works, we study the following numerical example. Suppose a contact system is fed by time-dependent displacement protocols a and b, depicted in Fig. 5.13a. Both protocols consist of three sine waves with different frequencies and amplitudes. Each curve contains about ten local extrema, and therefore the contact system experiences a lot of "switching" events when either the normal or the tangential loading is reverted. In view of practical applications, one should think of the exemplary protocols as short fragments of a real ultrasonic signal coming from the direct propagation, possible reverberations, mode conversions, etc. Time in Fig. 5.13 is represented in time steps of the algorithm. The actual time interval corresponding to these steps is not essential since our contact model is quasi-static.

An intermediate result of the protocol execution is the repartitioning of the tangential displacement b in the components b_0 and $\tilde{b}$ related to respectively the total sliding shift and the partial slip accompanied by deformation of asperities relative to this shift. Both components are shown in Fig. 5.13b. The final outcome of the algorithm, i.e., the calculated normal and tangential forces as functions of time, is shown in Fig. 5.13c in which, for the tangential force, the absolute value is plotted. A closer look at Fig. 5.13 allows us to easily identify the three evolution

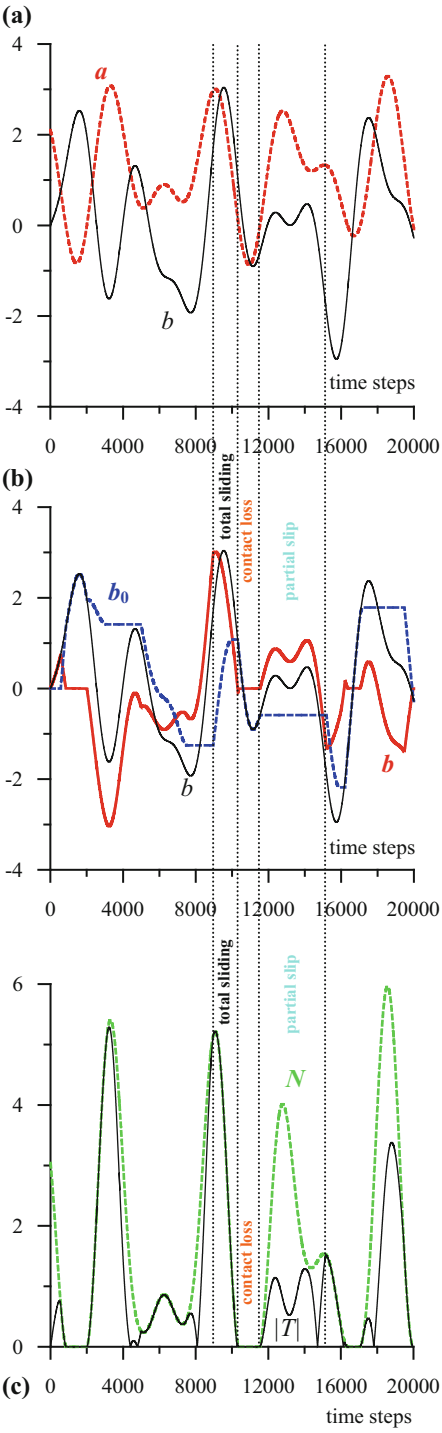

Fig. 5.13 (**a**) Excitation protocol in the considered example: normalized normal and tangential displacements, a and b, as a function of time. (**b**) Calculated components b_0 and $\tilde{b}$ in the considered numerical example. (**c**) The appropriate forces N and T calculated in our contact model

regimes. The total sliding regime occurs when $|T| = \mu N$ (Fig. 5.13c). In this case, the component b_0 evolves since the reference points at both faces shift (Fig. 5.13b). The other component $\tilde{b}$ changes as long as a is not constant, since the maximum tangential deformation of asperities depends on the normal compression. In the case marked as "total sliding" in Fig. 5.13, the normal displacement a decreases, and therefore $\tilde{b}$ diminishes as well. The regime of contact loss is also easy to identify. When a becomes negative (Fig. 5.13a), $\tilde{b}$ is set to zero since no asperity deformation is possible (Fig. 5.13b), and the normal force equals zero too (Fig. 5.13c). There are two different identification criteria for the partial slip regime: (1) b_0 does not change as the reference points do not shift, and (2) $|T|$ is less than μN. In Fig. 5.13, only one instance for each regime is shown, however, using the above criteria, it is possible to identify the regime at each time instance during the protocol.

The calculations have been performed assuming the normal contact reaction in the form

$$N(a) = C^2 a^2, \tag{5.54}$$

where $C = 6 \times 10^{10}$ Pa$^{1/2}$ m^{-1}, corresponding to the value obtained by matching the experimental relation between the contact pressure and the gap distance, as exemplified by Biwa et al. [16] and used in the numerical study of contact between two solid blocks of aluminum by Yuan et al. [17] (see discussion in Sect. 5.4).

Finally, using the parametric representations $b(t)$ and $T(t)$, the desired dependency of the tangential force T on the displacement b is plotted in Fig. 5.14. The code allows one to rapidly generate such responses for any excitation protocol. Clearly, this would be extremely difficult without an automated accounting of the memory-dependent processes.

Note that in Figs. 5.13 and 5.14, the forces and displacements are normalized on values N_0 and a_0, respectively. Here, N_0 is a typical stress magnitude of elastic

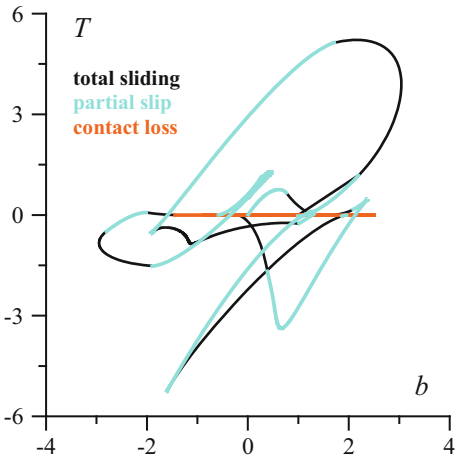

Fig. 5.14 The tangential load–displacement curve calculated for the displacement protocol from Fig. 5.13

waves propagating in the system (remember that in accordance to Eq. (5.53) N and T denote stresses now). The link between normalization constants N_0 and a_0 is given by the quadratic dependency $N_0 = C^2 a_0^2$ corresponding to Eq. (5.54).

In the next section, we present some numerical examples of wave propagation in a 2D aluminum bar containing a crack.

5.8 Finite Element Simulations Using the Developed Contact Model

5.8.1 General Remarks

Modeling of elastic wave propagation in cracked samples requires two different components, the first of which is needed to describe the microscopic normal and tangential behavior of the crack walls, whereas the second describes the wave propagation itself. In this study, the Structural Mechanics Module [34] of the finite element-based, software package COMSOL Multiphysics is used. On the one hand, this specific module has been particularly designed to solve elastic wave propagation problems, while, on the other hand, it contains sufficient tools to incorporate external user-supplied contact models. These contact models do not necessarily have to be implemented as closed form equations in the software itself, but can also be written as external functions in MATLAB which can be easily introduced in COMSOL using the LiveLink for MATLAB [35]. Using this approach, the more complex contact model described in Sects. 5.4–5.7 can be directly linked to COMSOL, and hence, allows the time-dependent interaction of an elastic wave with a frictional crack to be studied as follows [36, 37]:

(a) Calculation of displacements in Structural Mechanics Module of COMSOL.

At each particular time step of the procedure, relative normal and tangential displacements Δu_n and Δu_t are calculated at the discretization points on the crack interface and transferred to the displacement-driven crack model implemented in MATLAB.

(b) Calculation of contact stresses in MATLAB.

From the relative normal and tangential displacement values, the contact model in MATLAB allows to directly and explicitly calculate normal and tangential contact stresses (-N and T), which are then considered as an input in COMSOL to update the boundary conditions at the crack interface.

(c) Repeated calculations of displacements and contact stresses.

Steps (a) and (b) are repeated for the next time step, until the desired calculation time is reached.

The above-mentioned approach allows the problem of wave propagation in a sample containing a crack with rough surfaces to be numerically solved in a simple and straightforward way. Since roughness is only considered at the microscopic level, crack faces at the mesoscopic level can be modeled as flat in the Structural Mechanics Module of COMSOL.

5.8.2 *Numerical Implementation of the Constitutive Crack Model*

Cracks are introduced as internal boundaries using the "thin elastic layer" feature [34] that allows one to implement user-defined boundary conditions. These conditions are defined on discretization points located at the same positions but related to different sides of a crack. In other words, the actual number of nodes is doubled. Relative movement of both sides occurs due to the action of forces denoted by F_n for the normal component and F_t for the tangential component (here forces per unit area are meant). The relative normal and tangential displacements between the crack faces are here denoted by Δu_n and Δu_t, respectively. The appropriate choice of boundary conditions makes it possible to separately model various contact phenomena, e.g., to avoid crack faces to freely penetrate into each other or to use the normal reaction curve of the kind of Eqs. (5.6) or (5.54), to "switch" on and off friction, etc.

Technically, in theoretical contact mechanics and in the Structural Mechanics Module of COMSOL different notations are used. To help the reader identify the correct forces and displacements which are necessary to introduce into COMSOL, we provide here the explicit link:

$$\Delta u_n = -2a, \;\; \Delta u_t = 2b, \tag{5.55}$$

$$F_n = -N(a) + F_0, \;\; F_t = T\,(b, a)\,. \tag{5.56}$$

The terms $N(a) \equiv N$ and $T(b, a) \equiv T$ are solutions of Eq. (5.52) for the contact forces per unit area provided by the constitutive contact model. The mean normal and shear or tangential contact stresses at the mesoscopic level equal

$$-N = F_n - F_0, \;\; T = F_t$$

respectively. They are created by the contact interactions at the internal boundaries and can be calculated for any value of normal and tangential displacements Δu_n and Δu_t depending on the current contact state (contact loss, total sliding, or partial slip). The term F_0 ($F_0 \geq 0$) is introduced to account for a possible pre-stress created as a result of another physical process such as plasticity, fatigue, thermal changes,

and irregularities of molecular structure. When differing from zero, the pre-stress induces both positive a and $N(a)$ in a situation where any external excitation, such as an acoustical wave, is absent.

5.8.3 Test Sample Geometry and Physical Parameters

In order to illustrate the potential of the proposed model, two instructive examples of a shear wave propagating in a 2D rectangular aluminum sample of 50 mm width and 100 mm height containing a crack are studied. The aluminum sample has a density $\rho = 2700$ kg/m^3, Young's modulus $E = 70$ GPa, and Poisson's ratio $\nu = 0.33$. A crack with a length of 20 mm is positioned in the center of the sample. In the first example, the crack orientation is horizontal, whereas in the second example the crack is inclined at 20°, as illustrated in Fig. 5.15. In both examples, a continuous shear wave excitation with a frequency of 100 kHz and tangential displacement amplitude of 100 nm is defined on the top boundary of the sample. At the side and bottom boundaries of the sample, non-reflecting boundary conditions were applied in order not to mask the crack-wave interactions by parasite reflections. At the internal crack boundaries, a thin elastic layer boundary condition is specified as described in Sect. 5.8.2. The friction coefficient value $\mu = 1$ was used, which is close to known data for aluminum on aluminum [38].

As illustrated in Fig. 5.15, the full geometry is meshed using triangular elements with a maximum size of approximately 2.6 mm (i.e., 12 second-order mesh elements

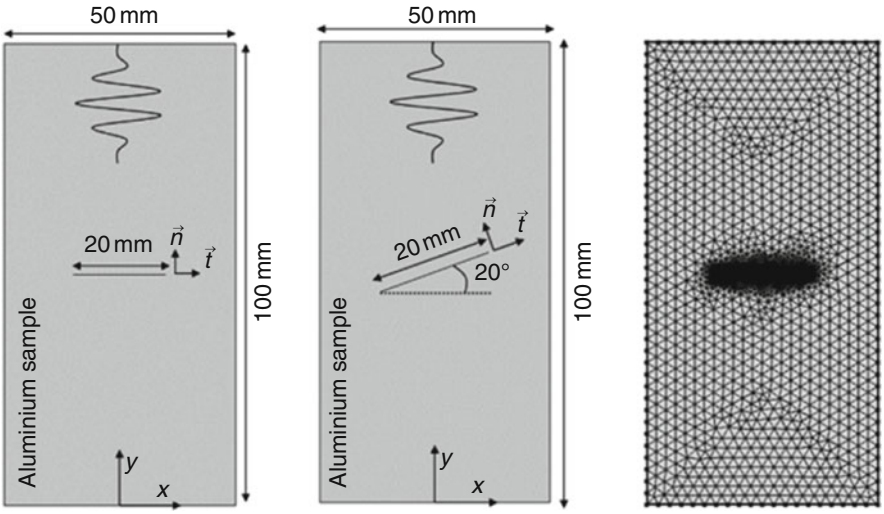

Fig. 5.15 Illustration of two geometries implemented in COMSOL, together with the mesh generated for one of the geometries. The samples represent 2D rectangles of aluminum with cracks (horizontal and inclined at 20°) of finite length positioned in the center domain. Both geometries are meshed with triangular mesh elements, with a higher mesh density in the region of the crack

per wavelength). At the internal crack boundary, however, a fixed number of 150 mesh elements (i.e., element size of approximately 0.13 mm) was used. By choosing such small elements, the macroscopic elastic fields used in the MMD algorithm can be considered uniform enough within each mesh cell. The solution to the problem is calculated using the implicit generalized alpha time-dependent solver typically used for structural mechanics problems in COMSOL. Accurate solutions are obtained using a time step $\Delta t = 25$ ns, corresponding to 400 time steps per wave cycle.

5.8.4 *Nonlinear Hysteretic Tangential Behavior of Horizontal Crack*

In the first example, the interaction of the excited shear wave, propagating in the vertical direction, with a horizontal crack is considered, with a particular focus on the influence of pre-stress on wave propagation. At weak pre-stress, a sufficiently high wave amplitude may engender total sliding, while strong compression can only induce partial slip. To avoid the influence of the clapping effect (repeated opening and closing of crack faces) and concentrate on tangential interactions only, the weak pre-stress should be still large enough to keep the crack faces always in contact.

In this study, we consider two pre-loading magnitudes, $F_0 = 0.36$ MPa and $F_0 = 0.09$ MPa, satisfying those criterion for the chosen shear wave excitation with tangential displacement amplitude of 100 nm. Figure 5.16 shows snapshots of the calculated total displacement in the cracked aluminum sample illustrating the interaction of the ultrasonic shear wave with the crack. In set (a), a snapshot at $t = 10$ μs is shown. In this case, the wave has not yet reached the crack. In figures (b) and (c), snapshot at $t = 18$ μs is presented for both pre-loading magnitudes. The

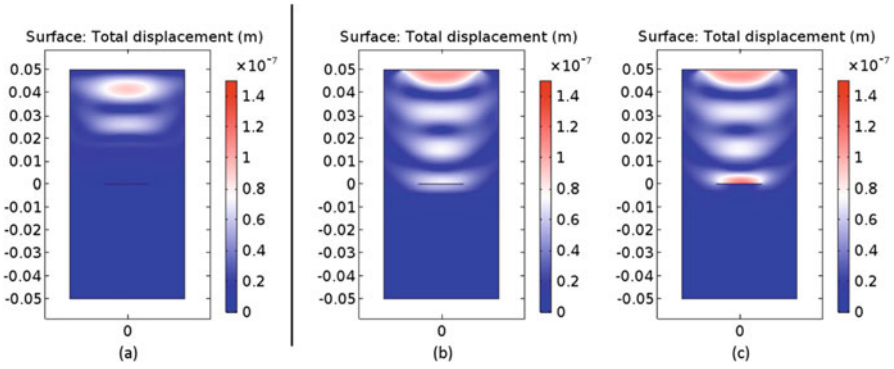

Fig. 5.16 Snapshots of the calculated total displacement in the cracked aluminum sample. (**a**) $t = 10$ μs: shear wave has not reached the crack yet. (**b**) $t = 18$ μs and $F_0 = 0.36$ MPa: shear wave propagation is practically not influenced by the crack. (**c**) $t = 18$ μs and $F_0 = 0.09$ MPa: shear wave propagation is highly influenced by the crack

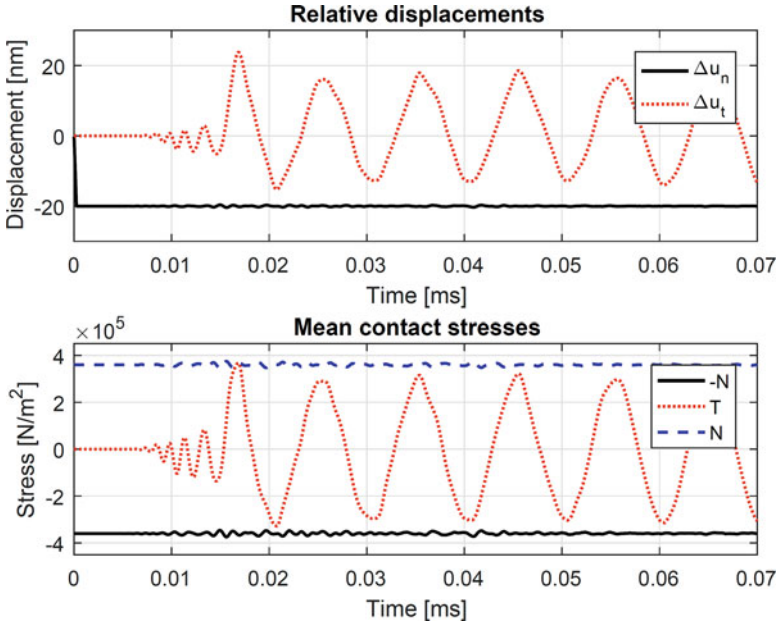

Fig. 5.17 Calculated normal and tangential relative displacements Δu_n and Δu_t (upper set), and mean contact stresses -N and T (lower set) at the central point on the crack interface in case of a shear wave excitation at 100 kHz with amplitude of A100 nm, and a pre-loading $F_0 = 0.36$ MPa. The curves for both -N and N are included to show that shear stress T always lies in between them ($\mu = 1$ in our examples)

2D color plots illustrate the situation in general; fine nonlinear effects are not visible in this representation. However, the difference between the two cases is clearly seen. Partial slip plastically does not modify the linear propagation (Fig. 5.16b), whereas total sliding domination results in strong refection (Fig. 5.16c).

Two other pictures, Figs. 5.17 and 5.18, justify our choice of the pre-stress magnitudes. The figures display contact displacements $\Delta u_n = -2a$ and $\Delta u_t = 2b$ as well as the mean contact stresses -N and T at the center of the crack, for $F_0 = 0.36$ MPa and $F_0 = 0.09$ MPa, respectively. In both situations, application of the normal pre-loading closes the crack, resulting in the appearance of a negative normal displacement Δu_n due to the fact that asperities in contact can recede under load. The normal displacement Δu_n increases with increasing pre-load F_0. Figure 5.17 illustrates the case with the largest pre-loading which forces the crack to stay in the state of partial slip. Indeed, the condition $|T| < \mu N$ is satisfied everywhere (except at one short instant in time). It can be verified (not shown here) that this will also be the case for other positions on the crack. In the case of weaker pre-loading (Fig. 5.18), $|T|$ often equals μN, i.e., the contact state frequently switches between partial slip and total sliding. In this case as well, it can be verified (not shown here) that at other positions on the crack the stresses behave in the same way.

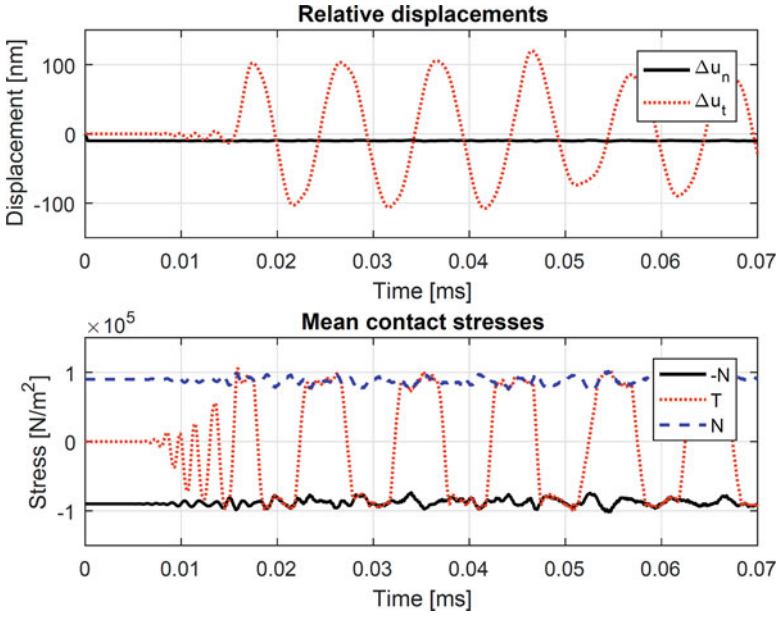

Fig. 5.18 Calculated normal and tangential relative displacements Δu_n and Δu_t (upper set), and mean contact stresses -N and T (lower set) at the central point on the crack interface in case of a shear wave excitation at 100 kHz with amplitude of A 100 nm, and a pre-loading $F_0 = 0.09$ MPa. The curves for both -N and N are included to show that shear stress T always lies in between them ($\mu = 1$ in our examples)

The hysteretic tangential load–displacement curves corresponding to the shear wave excitation are shown in Fig. 5.19 for both considered pre-stress values. The partial slip and total sliding regime are indicated with different colors. Again, the total sliding regime frequently appears for the weaker pre-stress (bottom figure) whereas stronger pre-compression (top figure) disables this regime. Correspondingly, contact acoustic nonlinearity is much stronger in the weak pre-compression case. However, it is clearly discernible for the higher pre-stress as well, as hysteresis in the upper set of Fig. 5.19 is still strongly pronounced. The same effect can be seen in Fig. 5.17, in which the shape of the stress and displacement signals are visibly different. This confirms the fact that contact acoustic nonlinearity remains relatively strong, even in situations of high pre-loading due to the partial slip effects and highly nonlinear normal reaction.

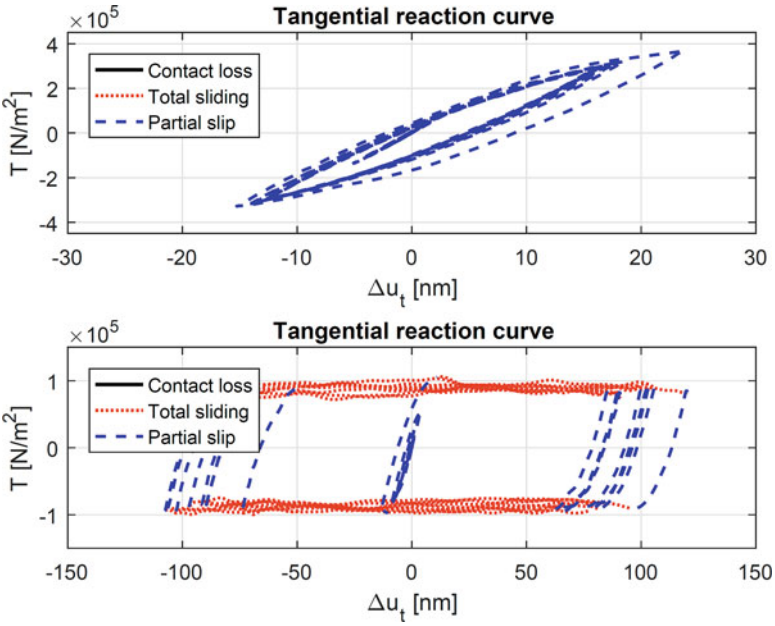

Fig. 5.19 Tangential reaction curves at the central point on the crack interface in case of a shear wave excitation at 100 kHz with a tangential displacement amplitude of 100 nm. (**a**) Hysteretic curve in case of partial slip (pre-load $F_0 = 0.36$ MPa), (**b**) Hysteretic curve in case of partial slip and total sliding (pre-load $F_0 = 0.09$ MPa)

5.8.5 Nonlinear Normal and Tangential Behavior of Inclined Crack

The second example illustrates the interaction of the excited shear wave with an inclined crack. No pre-loading has been introduced in this example. Due to crack's inclination, both clapping (i.e., opening and closing) and friction at the crack interface are efficiently excited.

In Fig. 5.20, relative normal and tangential displacements and mean contact stresses are plotted as functions of time. The normal displacement time curve is highly asymmetric as negative excursions of Δu_n meet much higher counter-action. Indeed, negative normal displacements engender both the straining of surrounding material layers and the resistance of the deformed asperities. In contrast, positive excursions (contact loss regime) only strain the surrounding material; the reaction of asperities is not activated. Moments of contact and contact loss in the upper figure can be identified in the contact stress curves at the bottom. When contact is lost both normal and tangential contact stresses equal zero. The absolute value of the negative (in compression) normal stress is plotted in order to show that the Coulomb friction law is fulfilled; the tangential stress can only reach the Coulomb threshold but never exceeds it.

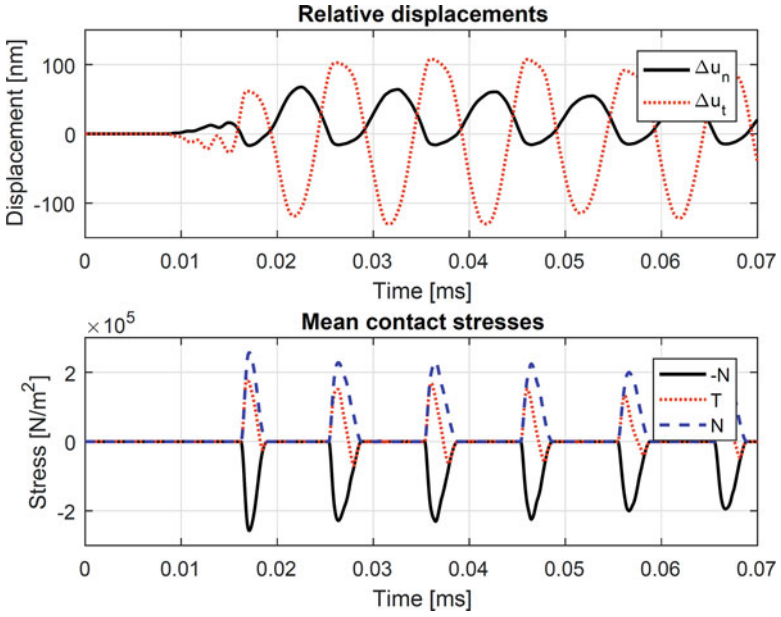

Fig. 5.20 Calculated relative displacements Δu_n and Δu_t (upper set) and mean contact stresses $-N$ and T (lower set) at the central point on the crack interface in case of a shear wave excitation at 100 kHz with amplitude of 100 nm, and no pre-loading. The curves for both $-N$ and N are included to show that shear stress T always lies in between them ($\mu = 1$ in our examples)

Figure 5.21 shows the normal and tangential reaction curves calculated at the central point on the inclined crack. According to Eqs. (5.52) and (5.54), the mean normal stress $-N$ differs from zero only in case of contact (i.e., $a > 0$ or $\Delta u_n < 0$). This can be observed in Fig. 5.21 (upper set). Moreover, in accordance to the accepted assumptions, the normal reaction curve is fully reversible. On the other hand, the tangential reaction curve (lower set) is hysteretic. Depending on loading conditions, all three contact regimes appear which is shown in the lower set with different colors.

Mechanical contact interactions are highly nonlinear due to the nonlinear normal reaction curve, as well as due to hysteretic friction effects. Therefore, the crack behaves as a source of secondary nonlinear waves. Figure 5.22 provides an overview of both linear and nonlinear wave dynamics. In particular, the top figures show the time evolution of the normal and shear contact stresses ($-N$ and T) at all positions along the crack interface in the sample excited by the shear wave at 100 kHz with an amplitude of 100 nm. The figures clearly demonstrate the dynamic switching that occurs between the non-contact ($N = T = 0$) and contact states ($N > 0$, $T \neq 0$), with different behavior for different positions on the crack. The set of figures in the second row shows snapshots of the displacement component u_x in the aluminum sample at four instances in time, thus illustrating the propagation of the incident wave. The considered time instances are also indicated by the vertical white lines in

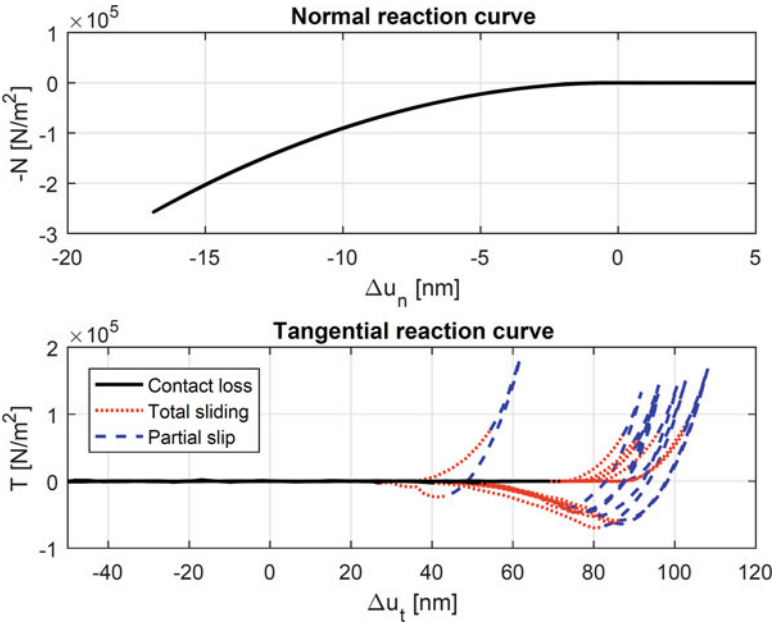

Fig. 5.21 Normal (upper set) and tangential (lower set) reaction curves at the central point on the crack interface in case of a shear wave excitation at 100 kHz with a tangential displacement amplitude of 100 nm

the top figures. The third row and bottom set of figures illustrate the nonlinear wave propagation. To evaluate the nonlinear wave components, the Scaling Subtraction Method (SSM) [39] has been used. This method exploits the distorted scaling of the received signals with increasing excitation amplitude due to nonlinearity. To use SSM, a sample has to be excited twice, once at a low excitation amplitude A_{low}, and once at a high excitation amplitude $A_{high} = n\, A_{low}$, where n denotes the scaling factor. By subtracting the properly scaled relative displacement signals obtained using the low excitation amplitude from the ones obtained using the high excitation amplitude, all linear contributions in the signals will be eliminated and the nonlinearities will be enhanced. Here, two simulations were performed, one at a low excitation amplitude $A_{low} = 10$ nm, and another one at a high excitation amplitude $A_{high} = 100$ nm. Hence, snapshots of respectively the scale subtracted normal and tangential displacement signals, u_n and u_t, at four instances in time (same as the ones used before) can be shown. The color scale in each set of snapshot figures runs from blue (most negative displacement value over time) over green (zero displacement) to yellow (most positive displacement value over time). At the first time instant ($t = 15$ μs), there is no sign of nonlinearities at all. This is due to the fact that it takes the excited shear wave approximately 16 μs to travel from the top boundary to the crack (shear wave velocity $v_S = 3122$ m/s). Once the first part of the shear wave has reached the crack, the dynamic wave-crack interaction

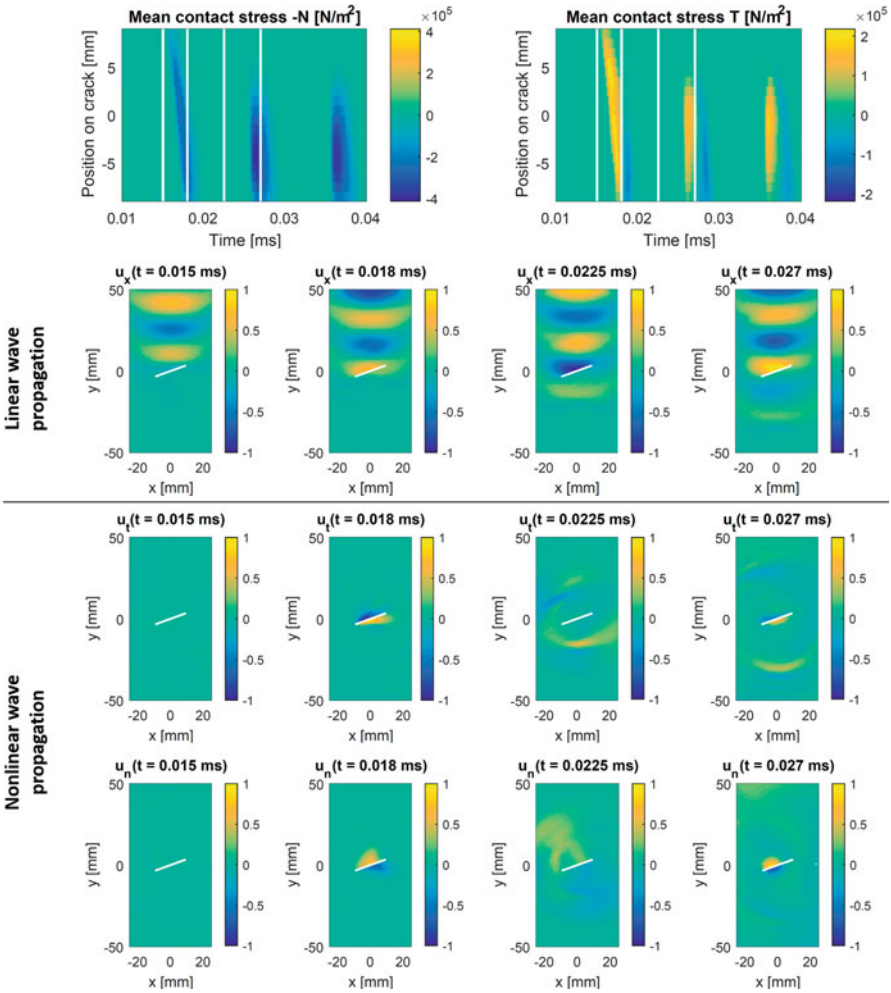

Fig. 5.22 First row: color coded plots illustrating the time evolution of the normal (-*N*) and shear (*T*) contact stresses at the crack interface in case of a shear wave excitation at 100 kHz with a tangential displacement amplitude of 100 nm; contact is lost when both contact stresses equal zero. Second row: snapshots of the displacement component u_x in the aluminum sample at four different moments in time. Third and fourth row: snapshots of respectively the scale subtracted normal and tangential displacements u_n and u_t at four different moments in time. The four time instances are marked by white vertical lines in the top figures

starts, resulting in the generation of both normal and tangential nonlinearities at the crack interface, as illustrated by the snapshots at $t = 18$ μs, for u_n and for u_t, respectively. The contact stress evolution (top figures) shows that around $t \approx 20$ μs the entire crack is again in an open state. In this case, the crack faces temporarily do not interact, and there will be no activation of contact nonlinearities, which can, for

instance, be seen in the snapshots at time $t = 22.5$ μs. Yet, at that particular time, the previously generated nonlinear wave components have propagated some distance in the sample, while generation of new nonlinear components is not detected. As the energy of a quasi-point source is redistributed circularly for 2D cases, the amplitude quickly diminishes. At $t \approx 25$ μs, the contact between crack faces is reestablished, inducing again the nonlinear ultrasound generation at the crack faces, clearly observed at the snapshot at time $t = 27$ μs. The performed time evolution study of the nonlinear content in the wave propagation confirms that a crack starts to behave as a nonlinear source when triggered by a wave-crack interaction. The signals excited by this nonlinear source and detected at the surface of the object can in turn be used for defect detection, localization, and/or characterization, provided the recorded amplitudes are measurable.

5.9 Conclusions

In this chapter, we developed a theoretical and numerical approach to model elastic wave propagation in solid structures containing cracks at known positions. The key component of the created numerical toolbox is a contact model accounting for friction and roughness of crack faces. The model allows to calculate the load–displacement relationships in three different contact states: contact loss, total sliding, and partial slip. The first one occurs when there is no contact between every two corresponding points from opposite crack faces. Total sliding occurs when both crack faces are sliding against each other. The last case corresponds to the situation when both stick and slip areas are present in the contact zone and appears due to surface roughness. The load–displacement relationship in the partial slip regime is obtained with the help of the method of memory diagrams that allows one to automate the account for friction-induced hysteresis by introducing an internal functional dependency responsible for all memory effects in the contact system.

The load–displacement relationship represents a boundary condition that has to be defined at internal boundaries, such as cracks. To do this, the constitutive model has been combined with an elastic wave propagation model of final element type. We have used the Structural Mechanics Module of the commercially available finite element-based software package COMSOL Multiphysics. Using the LiveLink for MATLAB feature, the crack model, implemented in MATLAB, was incorporated into COMSOL in a simple and straightforward way.

The working principle of the numerical toolbox is illustrated by means of two instructive examples of shear wave propagation in a 2D rectangular aluminum sample containing a crack with rough surfaces, oriented either horizontally or inclined at 20 degrees. Calculations of all elastic fields in the sample allow one to check the fulfillment of the postulated friction laws, to identify the three contact regimes, to separate the linear and nonlinear components of the waves, to detect several nonlinear signatures including those that can be experimentally measured, etc.

The created numerical toolbox drastically increases visibility of all wave or vibration processes used in experimental nondestructive testing methods for defect detection and imaging. One of its final objectives is to estimate physical and geometric parameters of defects which is only possible once a relevant nonlinear wave propagation model is implemented.

References

1. I. Sneddon, *Fourier series* (Routledge & Kegan, New York, 1951)
2. V.A. Yastrebov, *Numerical methods in contact mechanics* (Wiley-ISTE, Hoboken, 2013)
3. E.A.H. Vollebregt. User Guide for CONTACT, rolling and sliding contact with friction Technical report TR09-03, version 16.1, VORtech BV, Delft, 2016, www.kalkersoftware.org
4. R. Mindlin, H. Deresiewicz, Elastic spheres in contact under varying oblique forces. J. Appl. Mech. **20**, 327–344 (1953)
5. C. Cattaneo, Sul contatto di due corpi elastici: distribuzione locale degli sforzi. Accad. Lincei. Rend. **27**(6), 342–348 (1938)
6. V. Popov, M. Hess, *Method of dimensionality reduction in contact mechanics and friction* (Springer, New York, 2015)
7. L. Landau, E. Lifschitz, *Theory of elasticity* (Pergamon Press, Oxford, 1993)
8. D.J. Whitehouse, J.F. Archard, The properties of random surfaces of significance in their contact. Proc. Roy. Soc. Lond. A **316**(1524), 97–121 (1970)
9. J. Greenwood, J. Willianson, Contact of nominally flat surfaces. Proc R Soc Lond A **295**, 300–319 (1966)
10. F. Bowden, D. Tabor, The area of contact between stationary and between moving surfaces. Proc R Soc Lond A **169**, 391–413 (1939)
11. G. Carbone, F. Bottiglione, Asperity contact theories: Do they predict linearity between contact area and load? J. Mech. Phys. Solids **56**, 2555–2572 (2008)
12. S. Hyun, M. Robbins, Elastic contact between rough surfaces: Effect of roughness at large and small wavelengths. Tibol. Int. **40**, 1413–1422 (2007)
13. B. Persson, F. Bucher, B. Chiaia, Elastic contact between random rough surfaces: Comparison of theory with numerical results. Phys. Rev. B **65**(18), 184106 (2002)
14. M. Paggi, M. Ciavarella, The coefficient of proportionality between real contact area and load, with new asperity models. Wear **268**, 1020–1010 (2010)
15. M. Paggi, R. Pohrt, V. Popov, Partial-slip frictional response of rough surfaces. Sci. Rep. **4**, 5178 (2014)
16. S. Biwa, S. Nakajima, N. Ohno, On the acoustic nonlinearity of solid-solid contact with pressure-dependent interface stiffness. J. Appl. Mech. **71**(4), 508–515 (2004)
17. M. Yuan, J. Zhang, S. Song, H. Kim, Numerical simulation of Rayleigh wave interaction with surface closed cracks under external pressure. Wave Motion **57**, 143–153 (2015)
18. R. Pohrt, V. Popov, Normal contact stiffness of elastic solids with fractal rough surfaces. Phys. Rev. Lett. **108**, 104301 (2012)
19. R. Pohrt, V.L. Popov, Contact stiffness of randomly rough surfaces. Sci. Rep. **3**, 3293 (2013)
20. J. Jäger, Axisymmetric bodies of equal material in contact under torsion or shift. Arch. Appl. Mech. **65**, 478–487 (1995)
21. L.A. Galin, *Contact problems in the theory of elasticity* (North Carolina State College, Raleigh, 1961)
22. I.N. Sneddon, The relation between load and penetration in the axisymmetric Boussinesq problem for a punch of arbitrary profile. Int. J. Eng. Sci. **3**, 47–57 (1965)
23. J. Jäger, A new principle in contact mechanics. J. Tribol. **120**(4), 677–684 (1998)

24. M. Ciavarella, The generalized Cattaneo partial slip plane contact problem. I – theory, II - examples. Int. J. Solids Struct. **35**, 2349–2362 (1998)
25. M. Ciavarella, Tangential loading of general 3D contacts. ASME J. Appl. Mech. **65**, 998–1003 (1998)
26. R.L. Munisamy, D.A. Hills, D. Nowell, Contact of Similar and Dissimilar Elastic Spheres under Tangential Loading. *Contact Mechanics* (Presses polytechniques et universitaires romandes, Lausanne, 1992)
27. R.L. Munisamy, D.A. Hills, D. Nowell, Static axisymmetrical Hertzian contacts subject to shearing forces. ASME J. Appl. Mech. **61**, 278–283 (1994)
28. R. Pohrt, personal communication
29. V. Aleshin, O. Bou Matar, K. Van Den Abeele, Method of memory diagrams for mechanical frictional contacts subject to arbitrary 2D loading. Int. J. Solids Struct. **60–61**, 84–95 (2015)
30. V.V. Aleshin, K. Van Den Abeele, Hertz-Mindlin problem for arbitrary oblique 2D loading: General solution by memory diagrams. J. Mech. Phys. Solids **60**, 14–36 (2012)
31. V.V. Aleshin, K. Van Den Abeele, General solution to the Hertz-Mindlin problem via Preisach formalism. Int. J. Non Linear Mech. **49**, 15–30 (2013)
32. V.V. Aleshin, O. Bou Matar, Solution to the frictional contact problem via the method of memory diagrams for general 3D loading histories. Phys. Mesomech. **19**, 130–135 (2016)
33. V.V. Aleshin, S. Delrue, O. Bou Matar, K. Van Den Abeele, Two dimensional modeling of elastic wave propagation in solids containing cracks with rough surfaces and friction – Part I: Theoretical background. Ultrasonics **82**, 11–18 (2018)
34. COMSOL AB, *Structural mechanics module, user's guide* (COMSOL Multiphysics v. 5.2, Stockholm, 2015)
35. COMSOL AB, *LiveLink for MATLAB, user's guide* (COMSOL Multiphysics v. 5.2, Stockholm, 2015)
36. S. Delrue, V. Aleshin, M. Sorensen, L. De Lathauwer, Simulation study of the localization of a near-surface crack using an air-coupled ultrasonic sensor array. Sensors **17**(4), 930 (2017)
37. S. Delrue, V.V. Aleshin, K. Truyaert, O. Bou Matar, K. Van Den Abeele, Two dimensional modeling of elastic wave propagation in solids containing cracks with rough surfaces and friction – Part II: Numerical implementation. Ultrasonics **82**, 19–30 (2018)
38. http://www.engineershandbook.com/Tables/frictioncoefficients.htm, Accessed on 14 Sept 2017
39. M. Scalerandi, A. Gliozzi, C. Bruno, D. Masera, P. Bocca, A scaling method to enhance detection of a nonlinear elastic response. Appl. Phys. Lett. **92**, 101912 (2008)

Chapter 6
Nonlinear Ultrasonic Techniques for Material Characterization

J.-Y. Kim, L. Jacobs, and J. Qu

6.1 Time Harmonic Wave Motion in Elastic Solids with Quadratic Nonlinearity

6.1.1 Governing Equations

The three-dimensional equations of motion for waves propagating in an elastic medium with quadratic nonlinearity will be derived in this section. The derivation follows closely the approach used in [1].

First, to describe the wave motion, we affix a Cartesian coordinate x_i ($i = 1, 2, 3$) to the continuum elastic body of interest, where the coordinate x_i is also used to label the material particle that was located at x_i in the initial (undeformed) configuration. This way of describing the wave motion is called the Lagrangian description and x_i is called the Lagrangian coordinate. At any given time t, the displacement of the particle x_i from its initial location is denoted by $u_i = u_i(\mathbf{x}, t)$. The deformation of the continuum can then be described by the Lagrangian strain

$$\varepsilon_{ij} = \frac{1}{2}\left(u_{i,j} + u_{j,i} + u_{k,i}u_{k,j}\right), \tag{6.1}$$

where, and in the rest of this paper, the summation convention has been adopted.

Next, let the continuum medium be a hyperelastic body [2] with quadratic nonlinearity, i.e.,

J.-Y. Kim · L. Jacobs
Georgia Institute of Technology, Atlanta, GA, USA

J. Qu (✉)
Tufts University, Medford, MA, USA
e-mail: Jianmin.Qu@Tufts.edu

T. Kundu (ed.), *Nonlinear Ultrasonic and Vibro-Acoustical Techniques for Nondestructive Evaluation*, https://doi.org/10.1007/978-3-319-94476-0_6

$$\sigma_{ij} = C_{ijkl}u_{k,l} + \frac{1}{2}\left(D_{ijklmn} + C_{ijklmn}\right)u_{k,l}u_{m,n} + \cdots, \tag{6.2}$$

where σ_{ij} is the first Piola-Kirchhoff stress, C_{ijkl} and C_{ijklmn} are the second and third order elastic constants of the hyperelastic body, and

$$D_{ijklmn} = C_{ijln}\delta_{km} + C_{jlmn}\delta_{ik} + C_{jnkl}\delta_{im}, \tag{6.3}$$

with δ_{ij} being the Kronecker delta.

Finally, consider the equations of motion

$$\frac{\partial \sigma_{ij}}{\partial x_j} = \rho \frac{\partial^2 u_i}{\partial t^2}, \tag{6.4}$$

where ρ is the mass density of the undeformed body. Substituting (6.2) into (6.4) leads to the displacement of equation of motion

$$\rho \frac{\partial^2 u_i}{\partial t^2} - C_{ijkl}\frac{\partial^2 u_k}{\partial x_j \partial x_l} = \left(D_{ijklmn} + C_{ijklmn}\right)\frac{\partial u_m}{\partial x_n}\frac{\partial^2 u_k}{\partial x_j \partial x_l} + \frac{1}{2}\frac{\partial C_{ijklmn}}{\partial x_j}\frac{\partial u_k}{\partial x_l}\frac{\partial u_m}{\partial x_n}. \tag{6.5}$$

Furthermore, we will limit ourselves to isotropic materials only. Under these assumptions, the elastic constants can be simplified to [1],

$$C_{ijkl} = \lambda \delta_{ij}\delta_{kl} + 2\mu I_{ijkl}, \tag{6.6}$$

$$\begin{aligned} C_{ijklmn} = {} & (2l - 2m + n)\, I_{ijklmn} + (2m - n)\left(J_{ijklmn} + J_{klmnij} + J_{mnijkl}\right) \\ & + \frac{n}{2}\left(J_{ikjlmn} + J_{iljkmn} + J_{jkilmn} + J_{jlikmn}\right), \end{aligned} \tag{6.7}$$

$$D_{ijklmn} = \lambda\left(I_{ijlnkm} + I_{jlmnik} + I_{jnklim}\right) + 2\mu\left(J_{kmijln} + J_{ikjlmn} + J_{imjnkl}\right), \tag{6.8}$$

where λ and μ are the Lamé constants, and l, m, and n are the Murnaghan third order elastic constants [1], and

$$I_{ijklmn} = \delta_{ij}\delta_{kl}\delta_{mn},\ J_{ijklmn} = \frac{1}{2}\left(I_{ijkmln} + I_{ijknlm}\right) = \frac{1}{2}\left(\delta_{ij}\delta_{km}\delta_{ln} + \delta_{ij}\delta_{kn}\delta_{lm}\right). \tag{6.9}$$

Making use of (6.6) and (6.7) in (6.5) yields

$$\frac{1}{c_L^2}\frac{\partial^2 u_i}{\partial t^2} - \left(1 - \frac{1}{\kappa^2}\right)\frac{\partial^2 u_j}{\partial x_j \partial x_i} - \frac{1}{\kappa^2}\frac{\partial^2 u_i}{\partial x_j \partial x_j} = f_i + g_i, \tag{6.10}$$

where $\kappa = c_L/c_T$, and $c_L = \sqrt{(\lambda + 2\mu)/\rho}$ and $c_T = \sqrt{\mu/\rho}$ are the longitudinal and transverse phase velocities, respectively. The right-hand side of (6.10) is given by

$$f_i = \frac{C_{ijklmn}}{\lambda + 2\mu} \frac{\partial u_m}{\partial x_n} \frac{\partial^2 u_k}{\partial x_j \partial x_l} + \frac{1}{2} \frac{\partial C_{ijklmn}}{\partial x_j} \frac{\partial u_k}{\partial x_l} \frac{\partial u_m}{\partial x_n}, \; g_i = \frac{D_{ijklmn}}{\lambda + 2\mu} \frac{\partial u_m}{\partial x_n} \frac{\partial^2 u_k}{\partial x_j \partial x_l}, \tag{6.11}$$

Clearly, f_i arises from the material nonlinearity and g_i comes from the geometrical nonlinearity. It can be easily shown that g_i vanishes if small strain assumption, i.e.,

$$\varepsilon_{ij} = \frac{1}{2} \left(u_{i,j} + u_{j,i} \right) \tag{6.12}$$

is made.

In the foregoing derivations, we had implicitly assumed that C_{ijklmn} is spatially dependent so that $\partial C_{ijklmn}/\partial x_j \neq 0$. In the rest of this paper, we will assume that C_{ijklmn} is uniform throughout the body so that $\partial C_{ijklmn}/\partial x_j = 0$.

We now define boundary value problems for the wave propagation in a weakly nonlinear *bounded* elastic medium. In such a medium, the displacement field can be written as the sum of the primary field, $u_i^{(1)}$ and the secondary field, $u_i^{(2)}$ as the first correction term to the primary field:

$$u_i = u_i^{(1)} + u_i^{(2)}. \tag{6.13}$$

with

$$\left| u_i^{(2)} \right| << \left| u_i^{(1)} \right|. \tag{6.14}$$

Experimental results on numerous engineering materials including pure metals and metallic alloys show that the amplitude of the secondary wave displacement (the second harmonic) is typically 10^{-3} to 10^{-2} times smaller than the amplitude of the primary wave displacement (the first harmonic). Therefore, the perturbation condition, Eq. (6.14), is well supported by experimental results. By this condition, it follows

$$\left| u_i^{(2)} u_j^{(2)} \right| << \left| u_i^{(1)} u_j^{(2)} \right| << \left| u_i^{(1)} u_j^{(1)} \right|. \tag{6.15}$$

Substituting (6.13) into (6.5) and then applying (6.15), one obtains the equations of motion for the primary and secondary fields as follows:

$$\rho \frac{\partial^2 u_i^{(1)}}{\partial t^2} - C_{ijkl} \frac{\partial^2 u_k^{(1)}}{\partial x_j \partial x_l} = 0, \tag{6.16}$$

$$\rho \frac{\partial^2 u_i^{(2)}}{\partial t^2} - C_{ijkl} \frac{\partial^2 u_k^{(2)}}{\partial x_j \partial x_l} = \widehat{f_i}. \tag{6.17}$$

where

$$\widehat{f_i} = \left(D_{ijklmn} + C_{ijklmn}\right) \frac{\partial u_m^{(1)}}{\partial x_n} \frac{\partial^2 u_k^{(1)}}{\partial x_j \partial x_l}. \tag{6.18}$$

It is seen in (6.17) that the secondary field is excited by the interaction of the primary field and this excitation appears as the body force term $\left(\widehat{f_i}\right)$ in (6.17).

Now consider the boundary conditions. First, for the stress-free boundary, the condition for the primary and secondary fields is written

$$\sigma_{ij}^{(L)} \left(u_i^{(1)}\right) n_j = 0, \tag{6.19}$$

$$\sigma_{ij}^{(L)} \left(u_i^{(2)}\right) n_j = -\sigma_{ij}^{(NL)} \left(u_i^{(1)}\right) n_j, \tag{6.20}$$

where $\sigma_{ij}^{(L)}$ is the linear stress, the first term on the right-hand side of (6.2); $\sigma_{ij}^{(NL)}$ is the nonlinear portion of the first Piola-Kirchhoff stress, the second and third terms on the right-hand side of (6.2); n_j is the surface normal vector. The nonlinear stress in (6.20) is quadratic in the primary displacement and higher order terms are neglected. Eq. (6.20) states that the primary field also produces sources of the secondary field, the nonlinear tractions, on the boundary.

The conditions for a rigid (no displacement or velocity) boundary for the primary and secondary fields are

$$u_i^{(1)} = 0, \tag{6.21}$$

$$u_i^{(2)} = 0. \tag{6.22}$$

Unlike in the stress-free boundary, the condition for the secondary field at the rigid boundary is linear and no sources are generated by the action of the primary at the boundary. In summary, Eqs. (6.16), (6.17), (6.18), (6.19), and (6.20) define the nonlinear boundary value problems with the stress-free boundary condition, and Eqs. (6.16), (6.17), and (6.21) define those with the rigid boundary condition, both in the framework of the perturbation approach. Using the relationships in Eqs. (6.6), (6.7), and (6.8), the explicit expressions for $\widehat{f_i}$ and $\sigma_{ij}^{(NL)}$ for an isotropic solid are

$$\begin{aligned}\widehat{f_i} &= \left(\mu+\frac{n}{4}\right)\left(\frac{\partial^2 u_l^{(1)}}{\partial x_k^2}\frac{\partial u_l^{(1)}}{\partial x_i}+\frac{\partial^2 u_l^{(1)}}{\partial x_k^2}\frac{\partial u_i^{(1)}}{\partial x_l}+2\frac{\partial^2 u_i^{(1)}}{\partial x_l \partial x_k}\frac{\partial u_l^{(1)}}{\partial x_k}\right)\\ &+\left(\lambda+\mu+m-\frac{n}{4}\right)\left(\frac{\partial^2 u_i^{(1)}}{\partial x_l \partial x_k}\frac{\partial u_l^{(1)}}{\partial x_k}+\frac{\partial^2 u_k^{(1)}}{\partial x_l \partial x_k}\frac{\partial u_i^{(1)}}{\partial x_l}\right)\\ &+\left(\lambda+m-\frac{n}{2}\right)\frac{\partial^2 u_i^{(1)}}{\partial x_k^2}\frac{\partial u_l^{(1)}}{\partial x_l}+\left(2l-m+\frac{n}{2}\right)\frac{\partial^2 u_k^{(1)}}{\partial x_i \partial x_k}\frac{\partial u_l^{(1)}}{\partial x_l}\\ &+\left(m-\frac{n}{4}\right)\left(\frac{\partial^2 u_k^{(1)}}{\partial x_l \partial x_k}\frac{\partial u_l^{(1)}}{\partial x_i}+\frac{\partial^2 u_l^{(1)}}{\partial x_i \partial x_k}\frac{\partial u_k^{(1)}}{\partial x_l}\right),\end{aligned} \tag{6.23}$$

$$\begin{aligned}\sigma_{ij}^{(NL)} = &\left\{\left(\frac{\lambda}{2}+\frac{m}{2}-\frac{n}{4}\right)\frac{\partial u_k^{(1)}}{\partial x_l}\frac{\partial u_k^{(1)}}{\partial x_l}+\left(l-m+\frac{n}{2}\right)\frac{\partial u_k^{(1)}}{\partial x_k}\frac{\partial u_l^{(1)}}{\partial x_l}\right.\\ &\left.+\left(\frac{m}{2}-\frac{n}{4}\right)\frac{\partial u_k^{(1)}}{\partial x_l}\frac{\partial u_l^{(1)}}{\partial x_k}\right\}\delta_{ij}+\left(m-\frac{n}{2}\right)\frac{\partial u_k^{(1)}}{\partial x_k}\frac{\partial u_i^{(1)}}{\partial x_j}\\ &+\frac{n}{4}\frac{\partial u_i^{(1)}}{\partial x_k}\frac{\partial u_k^{(1)}}{\partial x_j}+\left(\lambda+m-\frac{n}{2}\right)\frac{\partial u_k^{(1)}}{\partial x_k}\frac{\partial u_j^{(1)}}{\partial x_i}\\ &+\left(\mu+\frac{n}{4}\right)\left(\frac{\partial u_i^{(1)}}{\partial x_k}\frac{\partial u_j^{(1)}}{\partial x_k}+\frac{\partial u_k^{(1)}}{\partial x_i}\frac{\partial u_k^{(1)}}{\partial x_j}+\frac{\partial u_j^{(1)}}{\partial x_k}\frac{\partial u_k^{(1)}}{\partial x_i}\right)\end{aligned} \tag{6.24}$$

If the domain is infinite, instead of these boundary conditions, the radiation condition should be used. The fact that the secondary waves are generated by the primary waves implies that there is a power flow from the primary to secondary waves. For the total energy in the domain to be conserved, the amplitude of the primary wave should decrease as the secondary wave is generated. However, this is not taken into account in this perturbation approach, but the relative error should be on the order of $\left|u_i^{(2)}\right| / \left|u_i^{(1)}\right|$, which we assumed to be much smaller than unity.

6.1.2 One-Dimensional Wave Propagation

To simplify the algebra, we consider the wave field in the form of

$$u_1 = u_1(x_1, t), u_2 = u_2(x_1, t), u_3 = 0, \tag{6.25}$$

In this case, only two of the equations of motion (6.10) are non-trivial. They are

$$L[u_1; c_L] \equiv \frac{\partial^2 u_1}{\partial t^2} - c_L^2 \frac{\partial^2 u_1}{\partial x_1^2} = \beta_L c_L^2 \frac{\partial u_1}{\partial x_1}\frac{\partial^2 u_1}{\partial x_1^2} + \beta_T c_T^2 \frac{\partial u_2}{\partial x_1}\frac{\partial^2 u_2}{\partial x_1^2}, \tag{6.26}$$

$$L\left[u_2; c_T\right] \equiv \frac{\partial^2 u_2}{\partial t^2} - c_T^2 \frac{\partial^2 u_2}{\partial x_1^2} = \beta_T c_T^2 \left(\frac{\partial^2 u_1}{\partial x_1^2} \frac{\partial u_2}{\partial x_1} + \frac{\partial u_1}{\partial x_1} \frac{\partial^2 u_2}{\partial x_1^2} \right), \tag{6.27}$$

where

$$\beta_L = 3 + \eta_L, \beta_T = \kappa^2 + \eta_T \tag{6.28}$$

are called, respectively, the longitudinal and transverse acoustic nonlinearity parameters. In the above, $\kappa = c_L/c_T$, and

$$\eta_L = \frac{2\left(l + 2m\right)}{\lambda + 2\mu}, \eta_T = \frac{m}{\mu} \tag{6.29}$$

represent the material nonlinearity. Clearly, the acoustic nonlinearity parameters account for both geometrical and material nonlinearities. Note that the β_L defined in (6.28) differs in sign from some of the acoustic nonlinearity parameter β used in some publications, i.e., $\beta_L = -\beta$.

The corresponding stresses follow from (6.2)

$$\sigma_{11} = \rho c_L^2 \left[\frac{\partial u_1}{\partial x_1} + \frac{\beta_L}{2} \left(\frac{\partial u_1}{\partial x_1} \right)^2 + \frac{\beta_T}{2\kappa^2} \left(\frac{\partial u_2}{\partial x_1} \right)^2 \right], \tag{6.30}$$

$$\sigma_{22} = \rho c_T^2 \left[\left(\kappa^2 - 2 \right) \frac{\partial u_1}{\partial x_1} + \left[\kappa^2 \left(1 + \frac{\beta_L}{2} \right) - 2\beta_T - 1 \right] \left(\frac{\partial u_1}{\partial x_1} \right)^2 + \frac{\beta_T}{2} \left(\frac{\partial u_2}{\partial x_1} \right)^2 \right], \tag{6.31}$$

$$\sigma_{12} = \rho c_T^2 \left[\frac{\partial u_2}{\partial x_1} + \left(1 - \kappa^2 + \beta_T \right) \frac{\partial u_1}{\partial x_1} \frac{\partial u_2}{\partial x_1} \right]. \tag{6.32}$$

Next, we consider a half-space defined by $x_1 \geq 0$. Let the boundary of the half-space be subjected to prescribed displacement condition

$$u_1\left(0, t\right) = U \sin\left(\omega t\right), u_2\left(0, t\right) = 0, \tag{6.33}$$

where $\omega = k_L c_L$ is the circular frequency and k_L is the wavenumber for the longitudinal propagating wave. It can be easily shown by a straightforward perturbation technique that, for $\left|\beta_L U k_L^2 x_1\right| \ll 1$, the solution to the boundary value problem defined by (6.26) and (6.33) can be written as [3],

$$\frac{u_1}{U} = \sin\left[\omega \left(t - \frac{x_1}{c_L} \right) \right] - \frac{\beta_L U k_L^2 x_1}{8} \left(A + \cos\left[2\omega \left(t - \frac{x_1}{c_L} \right) \right] \right), \tag{6.34}$$

$$\frac{\sigma_{11}}{\rho c_L^2} = -Uk_L \cos\left[\omega\left(t - \frac{x_1}{c_L}\right)\right] + \frac{\beta_L U^2 k_L^2}{8}\left[A + \cos\left[2\omega\left(t - \frac{x_1}{c_L}\right)\right] - 2kx_1 \sin\left[2\omega\left(t - \frac{x_1}{c_L}\right)\right]\right], \tag{6.35}$$

where A is an arbitrary constant. Note that, unlike the corresponding linear problem where A must be zero because the solution must be bounded as $x \to \infty$, the constant A in (6.34) does not have to be zero because (6.34) is valid only for finite x. To uniquely determine this constant, we use the following consistency condition

$$\frac{\partial u_1}{\partial t} = -\frac{2c_L}{3\beta_L}\left[\left(1 + \beta_L \frac{\partial u_1}{\partial x_1}\right)^{3/2} - 1\right]. \tag{6.36}$$

This is valid for any β_L and is independent of the boundary conditions. It can be easily shown that in the limit of $\beta_L \to 0$, the above reduces to the well-known Eq. (6.37),

$$\frac{\partial u_1}{\partial t} = -c_L \frac{\partial u_1}{\partial x_1}. \tag{6.37}$$

The consistency condition (6.36) provides an additional equation to uniquely determine the constant A. By substituting (6.34) into (6.36), we arrive at $A = 1$. Thus, the solution becomes

$$\frac{u_1}{U} = \sin\left[\omega\left(t - \frac{x_1}{c_L}\right)\right] - \frac{\beta_L U k_L^2 x_1}{8}\left(1 + \cos\left[2\omega\left(t - \frac{x_1}{c_L}\right)\right]\right), \tag{6.38}$$

$$\frac{\sigma_{11}}{\rho c_L^2} = -Uk_L \cos\left[\omega\left(t - \frac{x_1}{c_L}\right)\right] + \frac{\beta_L U^2 k_L^2}{8}\left[1 + \cos\left[2\omega\left(t - \frac{x_1}{c_L}\right)\right] - 2kx_1 \sin\left[2\omega\left(t - \frac{x_1}{c_L}\right)\right]\right]. \tag{6.39}$$

The above solutions satisfy (6.26) and (6.33) up to the order of $\beta_L U^2 k_L^2$.

Note that $A_1 = U$ represents the amplitude of the fundamental frequency, and $A_2 = -\beta_L A_1^2 k_L^2 x/8$ is the amplitude of the second harmonic. If the time-domain signal is recorded in an ultrasonic test, both A_1 and A_2 can be obtained by taking the Fourier transform of the time-domain signal. Once A_1 and A_2 are known, the acoustic nonlinearity parameter can be obtained as $\beta_L = -8A_2/\left(A_1^2 k_L^2 x_1\right)$. This is the fundamental principle used in many NLU methods to measure the acoustic nonlinearity parameter.

6.1.3 Nonlinear Wave Mixing

We consider the mixing of two primary plane waves in the x_1x_2-plane,

$$u_i^{(0)} = U_1 d_i^{(1)} \sin\left(\omega_1 t - k_1 p_j^{(1)} x_j\right) + U_2 d_i^{(2)} \sin\left(\omega_2 t - k_2 p_j^{(2)} x_j\right), u_3^{(0)} = 0 \tag{6.40}$$

where $d_i^{(m)}$ and $p_i^{(m)}$, $(m = 1, 2)$ are the displacement and propagation vectors, respectively, for the two primary waves.

If the medium is linear elastic, it is well known that the two primary waves would simply propagate on their own without interfering each other. However, in a nonlinear medium, not only each wave will generate its own higher harmonics as discussed in the previous section, the two waves would also interact and generate an additional wave field. In this section, we will focus on this additional wave field generated by the interactions between two primary plane waves.

Substituting (6.40) into the right-hand side of (6.10) for isotropic material with spatially uniform elastic constants and retaining only the cross terms between the two waves due to nonlinear interactions lead to

$$f_i + g_i = U_1 U_2 \left[b_i^+ \sin\left(\omega_+ t - k_j^+ x_j\right) + b_i^- \sin\left(\omega_- t - k_j^- x_j\right)\right] + U_1^2 A + U_2^2 B, \tag{6.41}$$

where

$$\omega_\pm = \omega_1 \pm \omega_2, k_j^\pm = k_1 p_j^{(1)} \pm k_2 p_j^{(2)} \tag{6.42}$$

and $\mathbf{b}^\pm = \left(b_1^\pm, b_2^\pm\right)^T$ are known functions of the materials and frequencies, which have been derived previously in [6]. The symbols A and B are used to indicate higher harmonics of ω_1 and ω_2, respectively. We note that (6.10) is a linear system of equations. Thus, its solution can be obtained by superimposing solutions corresponding to the different terms in (6.41). The solutions that correspond to U_1^2 and U_2^2 are given in the previous section. Here, our interest is the nonlinear interaction, so we will neglect terms associated with U_1^2 and U_2^2, i.e., we will consider only the solution to the following:

$$\begin{aligned} \frac{1}{c_L^2}\frac{\partial^2 u_i^{(1)}}{\partial t^2} &- \left(1 - \frac{1}{\kappa^2}\right)\frac{\partial^2 u_j^{(1)}}{\partial x_j \partial x_i} - \frac{1}{\kappa^2}\frac{\partial^2 u_i^{(1)}}{\partial x_j \partial x_j} \\ &= U_1 U_2 \left[b_i^+ \sin\left(\omega_+ t - k_j^+ x_j\right) + b_i^- \sin\left(\omega_- t - k_j^- x_j\right)\right]. \end{aligned} \tag{6.43}$$

It can be seen that a possible solution to (6.44) might be written as

$$u_i^{(1)} = a_i^+ \sin\left(\omega_+ t - k_j^+ x_j\right) + a_i^- \sin\left(\omega_- t - k_j^- x_j\right), \tag{6.44}$$

where $\mathbf{a}^{\pm} = \left(a_1^{\pm}, a_2^{\pm}\right)^T$ are constants to be determined. Substituting (6.44) into (6.43) yields a system of four algebraic equations for $\mathbf{a}^{\pm}$,

$$\mathbf{A}^{\pm}\mathbf{a}^{\pm} = U_1 U_2 \mathbf{b}^{\pm}, \tag{6.45}$$

where

$$\mathbf{A}^{\pm} = \begin{bmatrix} h_1^{\pm} & s^{\pm} \\ s^{\pm} & h_2^{\pm} \end{bmatrix} \tag{6.46}$$

and

$$\begin{aligned} h_1^{\pm} &= \frac{1}{\kappa^2 c_L^2}\left[c_L^2\left[\left(k_2^{\pm}\right)^2 + \kappa^2\left(k_1^{\pm}\right)^2\right] - \kappa^2\omega_{\pm}^2\right], \\ h_2^{\pm} &= \frac{1}{\kappa^2 c_L^2}\left[c_L^2\left[\left(k_1^{\pm}\right)^2 + \kappa^2\left(k_2^{\pm}\right)^2\right] - \kappa^2\omega_{\pm}^2\right], \end{aligned} \tag{6.47}$$

$$s^{\pm} = \frac{\kappa^2 - 1}{\kappa^2} k_1^{\pm} k_2^{\pm}. \tag{6.48}$$

The determinants of $\mathbf{A}^{\pm}$ are given by

$$D_{\pm} = \det\left(\mathbf{A}^{\pm}\right) = \frac{1}{\kappa^2}\left(k_j^{\pm}k_j^{\pm} - \frac{\omega_{\pm}^2}{c_L^2}\right)\left(k_j^{\pm}k_j^{\pm} - \frac{\omega_{\pm}^2}{c_T^2}\right). \tag{6.49}$$

If $D_+ D_- \neq 0$, Eq. (6.45) will have a unique solution given by

$$\mathbf{a}^{\pm} = U_1 U_2 \left(\mathbf{A}^{\pm}\right)^{-1} \mathbf{b}^{\pm}. \tag{6.50}$$

Substituting (6.49) into (6.44) yields the solution to the wave fields generated by the nonlinear interactions between the two primary waves. It is seen that such waves propagate with constant amplitude and frequencies that are the sum and difference of the frequencies of the two primary waves. In fact, even when $D_+ D_- = 0$, a unique solution to $\mathbf{a}^{\pm}$ may still exit if

$$\operatorname{rank}\left(\mathbf{A}^{\pm}|\mathbf{b}^{\pm}\right) = \operatorname{rank}\left(\mathbf{A}^{\pm}\right), \tag{6.51}$$

where $(\mathbf{A}^{\pm}|\,\mathbf{b}^{\pm})$ is to donate the augmented matrix, i.e., a matrix obtained by appending the columns of $\mathbf{b}^{\pm}$ to $\mathbf{A}^{\pm}$.

For convenience, we call (6.44) with $\mathbf{a}^{\pm}$ being given by (6.50) the mixing wave field induced by the nonlinear interactions between the two primary waves. It is seen that such mixing wave field generally consists of two propagating waves in the directions of $\mathbf{k}^{+}$ and $\mathbf{k}^{-}$, respectively.

A more interesting, and practically useful case is when $D_+D_- = 0$, i.e.,

$$\left(k_j^+k_j^+ - \frac{\omega_+^2}{c_L^2}\right)\left(k_j^+k_j^+ - \frac{\omega_+^2}{c_T^2}\right)\left(k_j^-k_j^- - \frac{\omega_-^2}{c_L^2}\right)\left(k_j^-k_j^- - \frac{\omega_-^2}{c_T^2}\right) = 0, \quad (6.52)$$

and either $\text{rank}(\mathbf{A}^+|\,\mathbf{b}^+) \neq \text{rank}(\mathbf{A}^+)$ or $\text{rank}(\mathbf{A}^-|\,\mathbf{b}^-) \neq \text{rank}(\mathbf{A}^-)$. In these cases, one or both of the sinusoidal functions in (6.44) become the eigenfunctions of the homogeneous equation of (6.43). Thus, the solution to (6.43) is no longer in the form of (6.44). In fact, the solution to (6.43) in these cases will grow linearly with the propagation distance. This phenomenon is called resonance. The waves generated by the nonlinear interaction under such resonant conditions will be called the resonant waves. In what follows, we will discuss several special cases.

6.1.3.1 Mixing of Two Collinear Longitudinal Plane Waves

Without loss of generality, we consider the mixing of the following two collinear longitudinal waves:

$$\mathbf{p}_1 = \mathbf{p}_2 = \mathbf{d}_1 = \mathbf{d}_2 = (1, 0)^T. \quad (6.53)$$

Clearly, use of (6.53) in (6.52) leads to $D_+D_- = 0$. Furthermore, one can show that

$$\mathbf{A}^\pm = \begin{bmatrix} 0 & 0 \\ 0 & -\frac{(c_L^2 - c_T^2)\omega_\pm^2}{c_L^4} \end{bmatrix}, \mathbf{b}^\pm = \frac{\beta_L}{2c_L}k_1k_2\begin{bmatrix} \omega_\pm \\ 0 \end{bmatrix}. \quad (6.54)$$

It is easy to see that $\text{rank}(\mathbf{A}^\pm|\,\mathbf{b}^\pm) \neq \text{rank}(\mathbf{A}^\pm)$, which means that (6.44) is no longer the solution to (6.43). In other words, the mixing of two collinear longitudinal waves will generate a resonant wave. One can show that this resonant wave is a longitudinal wave given by

$$u_1^s = \frac{-\beta_L}{4}k_1k_2U_1U_2x_1\left[\cos\left[\omega_+\left(t - \frac{x_1}{c_L}\right)\right] + \cos\left[\omega_-\left(t - \frac{x_1}{c_L}\right)\right]\right], u_2^s = 0. \quad (6.55)$$

We see that indeed the mixing wave grows with propagating distance x_1.

Interestingly, it can be shown that in the limit of $\omega_1 \to \omega_1 = \omega$ and $U_2 \to U_1 = U$, (6.55) reduces to

$$u_1^s = -\frac{\beta_L}{4}k_L^2U^2x_1\left[1 + \cos\left[2\omega\left(t - \frac{x_1}{c_L}\right)\right]\right]. \quad (6.56)$$

This is the same as to the generation of second harmonic given in (6.38). In fact, by including the terms generated by U_1^2 and U_2^2, the total solution now becomes

$$u_1 = 2U \sin\left[\omega\left(t - \frac{x_1}{c_L}\right)\right] - \frac{\beta_L U^2 k_L^2 x_1}{2}\left(1 + \cos\left[2\omega\left(t - \frac{x_1}{c_L}\right)\right]\right). \quad (6.57)$$

This is identical to (6.38) if the amplitude of the primary wave is 2 U in (6.38). In other words, the generation of second harmonic by a longitudinal wave is really the result of "self-mixing" of the longitudinal wave with itself.

6.1.3.2 Mixing of Two Collinear Transverse Plane Waves

Again, without loss of generality, we consider the mixing of the following two collinear transverse waves:

$$\mathbf{p}_1 = \mathbf{p}_2 = (1, 0)^T, \mathbf{d}_1 = \mathbf{d}_2 = (0, 1)^T. \quad (6.58)$$

Clearly, this also satisfies $D_+ D_- = 0$. However, we also have

$$\mathbf{A}^{\pm} = \begin{bmatrix} \frac{(\kappa^2-1)\omega_{\pm}^2}{c_L^2} & 0 \\ 0 & 0 \end{bmatrix}, \mathbf{b}^{\pm} = \frac{\beta_T}{2c_T} k_1 k_2 \begin{bmatrix} \omega_{\pm} \\ 0 \end{bmatrix}, \quad (6.59)$$

i.e., $\text{rank}(\mathbf{A}^{\pm} | \mathbf{b}^{\pm}) = \text{rank}(\mathbf{A}^{\pm}) = 1$. Thus, there is still a unique solution to (6.45), which is given by

$$u_1^s = \frac{\beta_T \kappa^2 \omega_1 \omega_2 U_1 U_2}{2c_T\left(\kappa^2 - 1\right)}\left[\frac{1}{\omega_-}\sin\left[\omega_-\left(t - \frac{x_1}{c_T}\right)\right] + \frac{1}{\omega_+}\sin\left[\omega_+\left(t - \frac{x_1}{c_T}\right)\right]\right], u_2^s = 0. \quad (6.60)$$

We see that the mixing wave field generated by two collinear transverse share waves consists of two longitudinal waves of constant amplitude with frequencies ω_- and ω_+, respectively. However, they are not resonant waves as they do not accumulate in amplitude with as they propagate through the mixing zone. Interestingly, the velocity of these longitudinal waves is c_T instead of c_L. This is possible only as mixing wave in the presence of the two primary shear waves. Such a mixing wave cannot propagate outside the mixing zone.

6.1.3.3 Mixing of Collinear Longitudinal and Transverse Plane Waves

Let us first consider the case when the two waves propagate in the same direction, i.e.,

$$\mathbf{p}_1 = \mathbf{p}_2 = (1, 0)^T, \mathbf{d}_1 = \mathbf{p}_1, \mathbf{d}_2 = (0, 1)^T. \quad (6.61)$$

It can be shown that $D_+D_- = 0$ when either $\omega_2/\omega_1 = (\kappa + 1)/(2\kappa)$, or $\omega_2/\omega_1 = 2/(\kappa + 1)$. However, only the former leads to $\text{rank}(\mathbf{A}^{\pm} | \mathbf{b}^{\pm}) \neq \text{rank}(\mathbf{A}^{\pm})$. That is, only when $\omega_2/\omega_1 = (\kappa + 1)/(2\kappa)$, a resonant wave occurs, which is given by

$$u_1^s = 0, u_2^s = \frac{\beta_T \omega_1^2 U_1 U_2}{2c_T^2 (\kappa + 1)} x_1 \cos\left(\omega_- \left(t + \frac{x_1}{c_T}\right)\right). \tag{6.62}$$

Clearly, this resonant wave is a pure shear wave propagating in the opposite direction as that of the two primary waves. Its phase velocity is the shear wave phase velocity, and its frequency is $\omega_- = \omega_1 - \omega_2$.

Next, consider the case when the two waves propagate in the opposite directions, i.e.,

$$\mathbf{p}_1 = -\mathbf{p}_2 = (-1, 0)^T, \mathbf{d}_1 = \mathbf{p}_1, \mathbf{d}_2 = (0, 1)^T. \tag{6.63}$$

This leads to

$$\mathbf{A}^{\pm} = -\frac{\kappa + 1}{c_T^2 \kappa^4} \begin{bmatrix} \kappa^2 \omega_1 (\omega_1 - \kappa\omega_1 \pm 2\omega_2) & 0 \\ 0 & \omega_2 (-\omega_2 + \kappa\omega_2 \pm 2\kappa\omega_1) \end{bmatrix}, \tag{6.64}$$

$$\mathbf{b}^{\pm} = \frac{\beta_T \omega_1 \omega_2}{2c_T^3 \kappa^4} \begin{bmatrix} 0 \\ \omega_2 \mp \kappa\omega_1 \end{bmatrix}. \tag{6.65}$$

It can be shown that $D_+D_- = 0$ has two physically meaningful roots, $\omega_2/\omega_1 = 2\kappa/(\kappa - 1)$ and $\omega_2/\omega_1 = (\kappa - 1)/2$. Only the former leads to $\text{rank}(\mathbf{A}^- | \mathbf{b}^-) \neq \text{rank}(\mathbf{A}^-)$. That is, only when $\omega_2/\omega_1 = 2\kappa/(\kappa - 1)$, does a resonant wave occurs, which is given by

$$u_1^s = 0, u_2^s = -\frac{\beta_T \omega_1^2 U_1 U_2}{2c_T^2 (\kappa - 1)} x_1 \cos\left[\omega_- \left(t + \frac{x_1}{c_T}\right)\right] \tag{6.66}$$

It is seen that the resonant wave is a shear wave of frequency $\omega_- = \omega_1 - \omega_2$ propagating in the direction opposite to that of the primary transverse wave.

6.1.4 Rayleigh Surface Waves

Consider a half-space defined by $x_2 \geq 0$. A Rayleigh wave propagating in the positive x_1-direction along the free surface $x_2 = 0$ can be described by a two-dimensional displacement field,

$$u_\alpha (x_1, x_2, t) = u_\alpha^{(1)} (x_1, x_2, t) + u_\alpha^{(2)} (x_1, x_2, t), \alpha = 1, 2. \tag{6.67}$$

where $\left|u_\alpha^{(1)}(x_1, x_2, t)\right| \gg \left|u_\alpha^{(2)}(x_1, x_2, t)\right|$. Making use of such displacements in (6.10) leads to

$$\frac{1}{c_L^2}\frac{\partial^2 u_\alpha^{(1)}}{\partial t^2} - \left(1 - \frac{1}{\kappa^2}\right)\frac{\partial^2 u_\beta^{(1)}}{\partial x_\beta \partial x_\alpha} - \frac{1}{\kappa^2}\frac{\partial^2 u_\alpha^{(1)}}{\partial x_\beta \partial x_\beta} = 0, \tag{6.68}$$

$$\frac{1}{c_L^2}\frac{\partial^2 u_\alpha^{(2)}}{\partial t^2} - \left(1 - \frac{1}{\kappa^2}\right)\frac{\partial^2 u_\beta^{(2)}}{\partial x_\beta \partial x_\alpha} - \frac{1}{\kappa^2}\frac{\partial^2 u_\alpha^{(2)}}{\partial x_\beta \partial x_\beta} = \frac{\partial H_{\alpha\beta}}{\partial x_\beta}, \tag{6.69}$$

where

$$\begin{aligned} H_{11} = {} & \frac{\beta_L}{2}\left(\frac{\partial u_1^{(1)}}{\partial x_1}\right)^2 + c_2\frac{\partial u_2^{(1)}}{\partial x_2}\left(2\frac{\partial u_1^{(1)}}{\partial x_1} + \frac{\partial u_2^{(1)}}{\partial x_2}\right) \\ & + c_3\frac{\partial u_1^{(1)}}{\partial x_2}\frac{\partial u_2^{(1)}}{\partial x_1} + \frac{\beta_T}{2}\left[\left(\frac{\partial u_1^{(1)}}{\partial x_2}\right)^2 + \left(\frac{\partial u_2^{(1)}}{\partial x_1}\right)^2\right], \end{aligned} \tag{6.70}$$

$$\begin{aligned} H_{22} = {} & \frac{\beta_L}{2}\left(\frac{\partial u_2^{(1)}}{\partial x_2}\right)^2 + c_2\frac{\partial u_1^{(1)}}{\partial x_1}\left(2\frac{\partial u_2^{(1)}}{\partial x_2} + \frac{\partial u_1^{(1)}}{\partial x_1}\right) \\ & + c_3\frac{\partial u_1^{(1)}}{\partial x_2}\frac{\partial u_2^{(1)}}{\partial x_1} + \frac{\beta_T}{2}\left[\left(\frac{\partial u_1^{(1)}}{\partial x_2}\right)^2 + \left(\frac{\partial u_2^{(1)}}{\partial x_1}\right)^2\right], \end{aligned} \tag{6.71}$$

$$\begin{aligned} H_{12} &= \left(c_3\frac{\partial u_2^{(1)}}{\partial x_1} + \beta_T\frac{\partial u_1^{(1)}}{\partial x_2}\right)\left(\frac{\partial u_1^{(1)}}{\partial x_1} + \frac{\partial u_2^{(1)}}{\partial x_2}\right), \\ H_{21} &= \left(c_3\frac{\partial u_1^{(1)}}{\partial x_2} + \beta_T\frac{\partial u_2^{(1)}}{\partial x_1}\right)\left(\frac{\partial u_1^{(1)}}{\partial x_1} + \frac{\partial u_2^{(1)}}{\partial x_2}\right), \end{aligned} \tag{6.72}$$

and

$$c_2 = 1 - \frac{1}{\kappa^2} + \frac{\beta_L}{2} - 2\beta_T, c_3 = -1 + \frac{1}{\kappa^2} + \beta_T$$

The corresponding stresses follow from (6.24)

$$\sigma_{12} = \rho c_T^2\left(\frac{\partial u_1}{\partial x_2} + \frac{\partial u_2}{\partial x_1} + \kappa^2 H_{12}\right), \sigma_{22} = \rho c_L^2\left(\frac{\partial u_2}{\partial x_2} + \left(1 - \frac{2}{\kappa^2}\right)\frac{\partial u_1}{\partial x_1} + H_{22}\right). \tag{6.73}$$

On the free surface ($x_2 = 0$), traction must vanish, i.e.,

$$\frac{\partial u_1^{(1)}}{\partial x_2} + \frac{\partial u_2^{(1)}}{\partial x_1} = 0,\ \frac{\partial u_2^{(1)}}{\partial x_2} + \left(1 - \frac{2}{\kappa^2}\right)\frac{\partial u_1^{(1)}}{\partial x_1} = 0 \text{ at } x_2 = 0. \tag{6.74}$$

$$\frac{\partial u_1^{(2)}}{\partial x_2} + \frac{\partial u_2^{(2)}}{\partial x_1} = -\kappa^2 H_{12},\ \frac{\partial u_2^{(2)}}{\partial x_2} + \left(1 - \frac{2}{\kappa^2}\right)\frac{\partial u_1^{(2)}}{\partial x_1} = -H_{22} \text{ at } x_2 = 0. \tag{6.75}$$

The first order solution can be obtained from standard textbooks, e.g., [5],

$$\begin{aligned} u_1^{(1)}(x_1, 0, t) &= U\sqrt{b_1 b_2}\exp\left(i\omega\left(t - \frac{x_1}{c_R}\right)\right), u_2^{(1)}(x_1, 0, t) \\ &= iUb_1\exp\left[i\omega\left(t - \frac{x_1}{c_R}\right)\right]. \end{aligned} \tag{6.76}$$

where c_R is the Rayleigh wave velocity that satisfies the Rayleigh equation

$$\left(2 - c_r^2\right)^2 - 4b_1 b_2 = 0, \tag{6.77}$$

and

$$b_1 = \sqrt{1 - \frac{c_r^2}{\kappa^2}},\ b_2 = \sqrt{1 - c_r^2},\ c_r = \frac{c_R}{c_T}. \tag{6.78}$$

Finding the second order solution is rather difficult and the solutions are fairly complex. Different authors have presented various types of solutions [7–21]. For many engineering applications, the quantity of most interest is the ratio of the second order and first order out-of-plane displacements on the surface, which was derived in [22],

$$\frac{u_2^{(2)}(x_1, 0, t)}{\left[u_2^{(1)}(x_1, 0, t)\right]^2} = \frac{\beta_L k_L^2 x_1}{8ib_1\left[1 - 2/\left(1 - b_2^2\right)\right]}. \tag{6.79}$$

Consequently,

$$\beta_L = \frac{8ib_1\left[1 - 2/\left(1 - b_2^2\right)\right]}{k_L^2 x_1}\frac{u_2^{(2)}(x_1, 0, t)}{\left[u_2^{(1)}(x_1, 0, t)\right]^2}. \tag{6.80}$$

Once $u_2^{(2)}(x_1, 0, t) / \left[u_2^{(1)}(x_1, 0, t)\right]^2$ is measured experimentally, the longitudinal acoustic nonlinearity parameter β_L can be obtained from the above. This is used later in Sect. 6.2.3 to characterize fatigue damage in metallic materials.

6.1.5 Lamb Waves

6.1.5.1 Solution for the Secondary Field

Consider a flat, stress-free, lossless, elastic plate with a thickness $2\,h$ as shown in Fig. 6.1. The z axis coincides with the direction of propagation while the y axis is normal to the thickness. Therefore, all wave motions occur in y-z plane, implying $u_x \equiv 0$ and $\partial F/\partial x \equiv 0$ for any field variable F. The boundary value problems relevant to the weakly nonlinear wave motion in this plate have been defined by (6.16), (6.17), (6.18), (6.19), and (6.20). The derivation of the primary field solution to (6.16) with the boundary condition (6.19), that is, the linear Lamb waves, can be found in many textbooks, e.g., [5], so it is not repeated here. The two essential steps in the analysis of the secondary field are, first to calculate the body force term $\widehat{f_i}$ (or $\widehat{\mathbf{f}}$) in (6.18) and the boundary traction term $\sigma_{ij}^{(NL)} n_j$ (or $\mathbf{n} \cdot \boldsymbol{\sigma}^{(NL)}$) in (6.20), both in a quadratic function of the known primary displacement field $u_i^{(1)}$ (or $\mathbf{u}^{(1)}$), and then to solve the resulting linear differential Eq. (6.17) with the body force term and the prescribed traction term at boundary. The vector (dyadic) notation will be used for brevity of expressions hereafter. Obtaining $\widehat{\mathbf{f}}$ and $\boldsymbol{\sigma}^{(NL)}$ in terms of $\mathbf{u}^{(1)}$ involves tedious manipulations of products of the trigonometric functions, and the expressions are quite lengthy and thus are omitted here. It is assumed that we have obtained $\widehat{\mathbf{f}}$ and $\boldsymbol{\sigma}^{(NL)}$, and have expressed them as follows:

$$\widehat{\mathbf{f}} = \tilde{\mathbf{f}}(y) e^{2i(\kappa z - \omega t)} + \text{const.} \tag{6.81}$$

$$\boldsymbol{\sigma}^{(NL)} = \tilde{\boldsymbol{\sigma}}^{(NL)}(y) e^{2i(\kappa z - \omega t)} + \text{const.} \tag{6.82}$$

where the "tilde" denotes the amplitude of the harmonic fields, the "*const.*" stands for a real constant representing a static (DC) deformation or stress in the plate. This is closely related to the interesting phenomenon of the radiation stress and strain [4, 23]. Our analysis focuses on the phenomenon of the second harmonic generation. Thus, these constants will be neglected.

An efficient way to solve the forced guided wave problem is the method based on the elastodynamic reciprocity principle [24]. The general framework presented below was originally developed by Auld [25] for a linear anisotropic piezoelectric waveguide problem, and then was extended by de Lima [26] to the nonlinear Lamb wave problem.

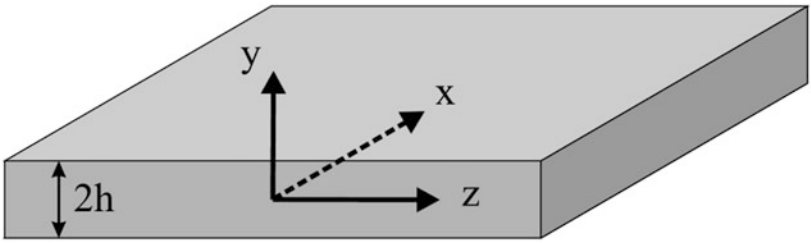

Fig. 6.1 Coordinate system of the infinite plate

Consider two situations in which body forces $\widehat{\mathbf{f}}_k$, $k = 1, 2$ produce wave fields $\{\mathbf{v}_k, \boldsymbol{\sigma}_k\}$, where $\mathbf{v}$ denotes the particle velocity, i.e., $\mathbf{v} = \dot{\mathbf{u}}$. The elastodynamic reciprocity principle stipulates that,

$$\nabla \cdot \left(\mathbf{v}_2^* \cdot \boldsymbol{\sigma}_1 + \mathbf{v}_1 \cdot \boldsymbol{\sigma}_2^*\right) = -\mathbf{v}_2^* \cdot \widehat{\mathbf{f}}_1 - \mathbf{v}_1 \cdot \widehat{\mathbf{f}}_2^*. \tag{6.83}$$

where "*" denotes the complex conjugate. If any two plate modes m and n with the same time dependence $e^{i\omega t}$ are taken as the two wave fields in (6.83), the traction-free boundary conditions on the plate surfaces mean $\widehat{\mathbf{f}}_1 = \widehat{\mathbf{f}}_2 = 0$. Thus, (6.83) leads to

$$P_{mn} = \begin{cases} -\frac{1}{2}\,\mathrm{Re}\int_{-h}^{h} \tilde{\mathbf{v}}_n^* \cdot \tilde{\boldsymbol{\sigma}}_n \cdot \mathbf{n}_z dy & \text{if} \quad n = m \\ 0 & \text{if} \quad n \neq m \end{cases} \tag{6.84}$$

Inspection of the integrand in (6.84) reveals that P_{mm} is the power flow density in the z direction carried by the mode m, and there is no power flow between two different modes because of their orthogonality.

Having introduced these concepts, we are ready to solve (6.17) with (6.20) for the secondary field $\{\mathbf{v}^{(2)}, \boldsymbol{\sigma}^{(2)}\}$ under the action of the body force $\widehat{\mathbf{f}}\left(\mathbf{u}^{(1)}\right)$ in the bulk and the traction $\boldsymbol{\sigma}^{(NL)}(\mathbf{u}^{(1)}) \cdot \mathbf{n}$ on the surfaces of the plate. Now consider an arbitrary known free mode $\{\mathbf{v}_n, \boldsymbol{\sigma}_n\}$ under zero body force ($\mathbf{b}_n = 0$) at the second harmonic frequency,

$$\mathbf{v}_n = \tilde{\mathbf{v}}_n(y) e^{i(\kappa_n z - 2\omega t)}, \; \boldsymbol{\sigma}_n = \tilde{\boldsymbol{\sigma}}_n(y) e^{i(\kappa_n z - 2\omega t)}. \tag{6.85}$$

where κ_n is the propagation constant of mode n. If this free mode and the unknown secondary solution are taken as the two wave fields in the reciprocity Eq. (6.83), one obtains

$$-\frac{\partial}{\partial z}\left\{\left(\tilde{\mathbf{v}}_n^* \cdot \boldsymbol{\sigma}^{(2)} + \mathbf{v}^{(2)} \cdot \tilde{\boldsymbol{\sigma}}_n^*\right) e^{-i\kappa_n^* z}\right\} \cdot \mathbf{n}_z \;\; -\frac{\partial}{\partial y}\left\{\left(\tilde{\mathbf{v}}_n^* \cdot \boldsymbol{\sigma}^{(2)} + \mathbf{v}^{(2)} \cdot \tilde{\boldsymbol{\sigma}}_n^*\right) e^{-i\kappa_n^* z}\right\} \cdot \mathbf{n}_y = \tilde{\mathbf{v}}_n^* \cdot \widehat{\mathbf{f}} e^{-i\kappa_n^* z}. \tag{6.86}$$

The secondary field is now expressed in a series expansion of the normal modes at the second harmonic frequency:

$$\mathbf{u}^{(2)} = \sum_{m=0}^{\infty} A_m(z)\tilde{\mathbf{u}}_m^{(2)}(y)e^{-2i\omega t} \tag{6.87}$$

$$\mathbf{v}^{(2)} = \sum_{m=0}^{\infty} A_m(z)\tilde{\mathbf{v}}_m^{(2)}(y)e^{-2i\omega t} \tag{6.88}$$

$$\boldsymbol{\sigma}^{(2)} = \sum_{m=0}^{\infty} A_m(z)\tilde{\boldsymbol{\sigma}}_m^{(2)}(y)e^{-2i\omega t} \tag{6.89}$$

Note that in (6.87), (6.88), and (6.89), $A_m(z)$ is introduced to reflect any variation of the secondary field amplitude in the z direction due to the nonlinearities. This is motivated by the linear increase of the secondary field in the one-dimensional longitudinal waves, see, Sect. 6.1.2. Substituting (6.88) and (6.89) into (6.86) and integrating the resulted equation over the thickness of the plate, one obtains

$$\begin{aligned} &-\frac{\partial}{\partial z}\int_{-h}^{h}\left\{\sum_{m=0}^{\infty} A_m(z)\left(\tilde{\mathbf{v}}_n^{*}\cdot\tilde{\boldsymbol{\sigma}}_m^{(2)}+\mathbf{v}_m^{(2)}\cdot\tilde{\boldsymbol{\sigma}}_n^{*}\right)e^{i(\omega t-\kappa_n^{*}z)}\right\}\cdot\mathbf{n}_z dy \\ &-\left(\tilde{\mathbf{v}}_n^{*}\cdot\boldsymbol{\sigma}^{(2)}+\mathbf{v}^{(2)}\cdot\tilde{\boldsymbol{\sigma}}_n^{*}\right)\cdot\mathbf{n}_y\Big|_{-h}^{h}e^{-i\kappa_n^{*}z}=\int_{-h}^{h}\tilde{\mathbf{v}}_n^{*}\cdot\widehat{\mathbf{f}}dy e^{-i\kappa_n^{*}z}. \end{aligned} \tag{6.90}$$

Because of the traction-free boundary condition on the plate surfaces, $\tilde{\boldsymbol{\sigma}}_n(\pm h)=0$, and the orthogonality in (6.84), Eq. (6.85) is written as

$$4P_{nn}\frac{d}{dz}\left\{A_n(z)e^{i(\omega t-\kappa_n^{*}z)}\right\}-\tilde{\mathbf{v}}_n^{*}\cdot\boldsymbol{\sigma}^{(2)}\cdot\mathbf{n}_y\Big|_{-h}^{h}e^{-i\kappa_n^{*}z}=\int_{-h}^{h}\tilde{\mathbf{v}}_n^{*}\cdot\widehat{\mathbf{f}}dy e^{-i\kappa_n^{*}z}. \tag{6.91}$$

Note that the partial differentiation in the first term on the left-hand side has changed to the ordinary differentiation since the y dependences were absorbed in P_{nn} upon integration. Finally, applying the boundary condition (6.20), $\boldsymbol{\sigma}^{(2)}=\boldsymbol{\sigma}^{(L)}(\mathbf{u}^{(2)})=-\boldsymbol{\sigma}^{(NL)}(\mathbf{u}^{(1)})$ and inserting (6.81) and (6.82) into (6.91), one arrives at an ordinary differential equation for the modal amplitude of the secondary field $A_n(z)$:

$$4P_{nn}\left(\frac{d}{dz}-i\kappa_n^{*}\right)A_n(z)=\left(f_n^{\mathrm{vol}}+f_n^{\mathrm{surf}}\right)e^{2i\kappa z}, \tag{6.92}$$

where the two modal driving forces are defined as

$$f_n^{\text{vol}} = \int_{-h}^{h} \tilde{\mathbf{v}}_n^* \cdot \widehat{\mathbf{f}} dy, \tag{6.93}$$

$$f_n^{\text{surf}} = -\tilde{\mathbf{v}}_n^* \cdot \tilde{\boldsymbol{\sigma}}^{(NL)} \cdot \mathbf{n}_y \Big|_{-h}^{h}, \tag{6.94}$$

Since the secondary field is produced by the primary field during propagation, the condition at $z = 0$ may be written as,

$$\mathbf{u}^{(2)} = \mathbf{v}^{(2)} = 0, \text{ at } z = 0. \tag{6.95}$$

Due to the orthogonality of normal modes, the modal amplitude should vanish independently, that is,

$$A_n(0) = 0, n = 0, 1, 2, \ldots, \tag{6.96}$$

Solving (6.92) with the initial condition (6.96), one obtains the modal amplitude of the secondary field

$$A_n(z) = \frac{f_n^{\text{vol}} + f_n^{\text{surf}}}{4P_{nn}} \begin{cases} \frac{i}{\kappa_n^* - 2\kappa} \left(e^{2i\kappa z} - e^{i\kappa_n^* z} \right) & \text{if} \quad \kappa_n^* \neq 2\kappa \\ z e^{2i\kappa z} & \text{if} \quad \kappa_n^* = 2\kappa \end{cases}. \tag{6.97}$$

Since the plate is assumed to be lossless, the propagation constants of the propagating modes are real and thus $\kappa_n^* = \kappa_n$.

6.1.5.2 Some Properties of the Secondary Lamb Wave Modes

1. Equation (6.97) shows that when the propagation constant of the secondary wave mode (κ_n) coincides with twice the propagation constant of the primary wave (2κ), the amplitude of mode n will increase linearly with the propagation distance. This is another case of the "internal resonance" of the self-interacted primary field. The condition $\kappa_n = 2\kappa$ is equivalent to $c_p(\omega) = c_p(2\omega)$, that is, the phase velocity matching. This is analogous to the resonance in the forced vibration of a simple oscillator: When the excitation (the primary wave) and the response (the secondary wave) have a certain phase relationship (the phase velocity matching), the resonance occurs (the amplitude grows linearly). When this condition is not met, the modal amplitude is spatially oscillatory as ($e^{2i\kappa z} - e^{i\kappa_n^* z}$) in (6.97) suggests. In the experiment, detection of the second harmonic

wave is very difficult for its small amplitude. Therefore, it is important to select a pair of modes (fundamental and second harmonic) that satisfy the phase velocity matching condition. The unbounded linear growth of the secondary field in (6.97) violates the perturbation condition in (6.14). When the secondary wave amplitude grows similar in magnitude to the primary wave amplitude, the waveform distorts significantly. The initially sinusoidal shape is changed to be more and more like a saw-tooth shape and finally discontinuity (the separation of continuum) occurs at the crest of the saw-tooth wave, forming a shock by which accumulated energy is discharged.

2. It is noticed that $f_n^{\text{vol}} + f_n^{\text{surf}}$ in (6.97) has the dimension of "power per unit distance." Physically, this is the amount of power leaks out of the primary to secondary field through the bulk and surfaces of the plate. Furthermore, these two terms should not vanish simultaneously for the second harmonic mode to be excited. It has been found that this power has the dependence on the kind of the mode of the primary field, [26–29]. Since f_n^{vol} and f_n^{surf} in (6.97) are the driving forces of the modal amplitude $A_n(z)$, it is worthwhile to examine the properties of these driving forces and their dependences on the primary mode. It can be shown that regardless of the symmetry of the primary wave mode the nonlinear body force and surface stress are in the following forms:

$$\tilde{\mathbf{f}} = \begin{pmatrix} A(y) \\ S(y) \end{pmatrix}, \tag{6.98}$$

$$\tilde{\boldsymbol{\sigma}}^{(NL)} = \begin{pmatrix} S(y) & A(y) \\ A(y) & S(y) \end{pmatrix}. \tag{6.99}$$

where $A(y)$ and $S(y)$ are generic functions which are antisymmetric and symmetric, respectively, with respect to the $y = 0$ axis. The proof of it is tedious but straightforward. For example, take the first term on the right-hand side in (6.24) and assume a primary symmetric mode, then we have

$$\begin{aligned} \frac{\partial u_k^{(1)}}{\partial x_l}\frac{\partial u_k^{(1)}}{\partial x_l} &= \frac{\partial u_y^{(1)}}{\partial y}\frac{\partial u_y^{(1)}}{\partial y} + \frac{\partial u_y^{(1)}}{\partial z}\frac{\partial u_y^{(1)}}{\partial z} + \frac{\partial u_z^{(1)}}{\partial y}\frac{\partial u_z^{(1)}}{\partial y} + \frac{\partial u_z^{(1)}}{\partial z}\frac{\partial u_z^{(1)}}{\partial z} \\ &= S^2(y) + A^2(y) + A^2(y) + S^2(y) = S(y) + S(y) + S(y) + S(y) \\ &= S(y) \end{aligned} \tag{6.100}$$

Performing the same algebra for all terms in (6.23) and (6.24), one arrives at the above conclusions, (6.98) and (6.99). Now, the velocity vector of a symmetric secondary mode can be written as

$$\tilde{\mathbf{v}}_{sym} = \begin{pmatrix} A(y) \\ S(y) \end{pmatrix}, \tag{6.101}$$

and $\mathbf{n}_y = (1, 0)$. Then, the modal driving forces in (6.93) and (6.94) become

$$f_n^{\text{vol}} = \int_{-h}^{h} \begin{pmatrix} A(y) \\ S(y) \end{pmatrix}^T \cdot \begin{pmatrix} A(y) \\ S(y) \end{pmatrix} dy = \int_{-h}^{h} S(y) dy \neq 0, \tag{6.102}$$

$$f_n^{\text{surf}} = -\begin{pmatrix} A(y) \\ S(y) \end{pmatrix}^T \cdot \begin{pmatrix} S(y) & A(y) \\ A(y) & S(y) \end{pmatrix} \cdot \begin{pmatrix} 1 \\ 0 \end{pmatrix} \Bigg|_{y=-h}^{y=h} = A(y)|_{y=-h}^{y=h} \neq 0. \tag{6.103}$$

In other words, the driving forces and thus the power flow from a symmetric or antisymmetric primary mode to a symmetric secondary mode is nonzero. Similar algebra for an antisymmetric secondary mode reveals that $f_n^{\text{vol}} = f_n^{\text{surf}} = 0$, i.e., an antisymmetric secondary mode cannot be excited since the driving forces cancel out by themselves.

3. One of the assumptions made in the aforementioned analysis is that the waves are time harmonic, i.e., waves are infinitely long in time and space, while in the real-world experiments, tone burst signals with a finite numbers cycles are used. In this case, one more condition in addition to the phase velocity matching is required for the cumulative growth of the secondary field, namely the group velocity of the secondary wave should match or at least be very close to that of the primary wave. The reason is quite obvious. As shown in the above, the primary field continuously gives its energy out to the secondary field. But this energy will be accumulated in the secondary wave only when the secondary wave travels at the same speed with the primary wave.
4. The analysis in [30] shows that certain types of Lamb modes satisfy the conditions for both excitability (nonzero power flow) and cumulative growth (phase and group velocity matching). Two different mode pairs have been successfully used in the experiments. First, the symmetric primary modes whose phase velocity coincides with the bulk longitudinal wave speed c_L. The lowest two pairs, (S1, S2) and (S2, S4) have been used in the experiments [31, 32]. Experimental aspects of using these mode pairs are discussed in the next section. In the regime $c_{ph} > c_L$, it is possible that the phase velocity dispersion curves of a symmetric mode and an antisymmetric mode have crossovers. Furthermore, it can be shown that this crossing occurs periodically as can be seen in the phase velocity dispersion curves. Pairs of a symmetric primary mode and the corresponding antisymmetric secondary mode along this line satisfy all necessary conditions for the excitability and cumulative growth. Deng et al. [33] have used some of these modes.

6.2 Measurement Techniques for Nonlinear Ultrasound and Their Applications

6.2.1 Through-Transmission of Bulk Waves

A number of investigators have applied nonlinear ultrasonic techniques to assess fatigue damage in different materials under a variety of laboratory conditions. Yost and Cantrell [34] and Cantrell and Yost [35] have conducted extensive experimental studies on different structural alloys to investigate the correlation between fatigue induced microstructural changes such as dislocation dipoles and slip bands and the acoustic nonlinearity parameter. Frouin et al. [36] performed in situ nonlinear ultrasonic measurements during fatigue test on Ti-6-4 alloy, and related the measured increase in the acoustic nonlinearity parameter—in the vicinity of the fracture surface—to an increase in the dislocation density. Among these studies, only Frouin et al. [36] reported using nonlinear ultrasonic results to track fatigue damage throughout the entire fatigue life of a specimen. Moreau [37] and Hurley and Fortunko [38] used a laser interferometer to measure the second order harmonic in through-transmitted longitudinal waves. Recently Kim et al. [39] developed a robust experimental procedure to track the evolution of fatigue damage in a nickel-base superalloy (IN 100) with the acoustic nonlinearity parameter, β, and demonstrate its effectiveness by making repeatable measurements of β in multiple specimens, subjected to both high- and low-cycle fatigue. The measurement procedure developed in this research is robust in that it is based on conventional piezoelectric contact transducers, which are readily available off the shelf, and it offers the potential for field applications. In addition, the measurement procedure enables the user to isolate sample nonlinearity from measurement system nonlinearity. The experimental results show that there is a significant increase in β which is linked to the high plasticity of low-cycle fatigue, and illustrate how these nonlinear ultrasonic measurements quantitatively characterize the damage state of a specimen in the early stages of fatigue. One application of these results is to serve as a master curve for life prediction based on nonlinear ultrasonic measurements.

The measurement of nonlinear longitudinal waves with contact piezoelectric transducers is fairly straightforward, and a typical schematic is shown in Fig. 6.2. A tone burst signal determined by the specimen thickness is generated by a function generator and is fed into a high-power gated amplifier to simulate a propagating wave in a single direction, the number of cycles of the tone burst is selected as the number of cycles that fits in twice the thickness of the specimen. Both the transmitter and receiver are commercial narrow-band PZT (Lead Zirconate Titanate) based transducers. Light lubrication oil is used to couple the transducers to the specimen. A special fixture is used to keep both the transmitting and receiving transducers aligned on the same centerline axis, and to also allow for the removal of either transducer (transmitter or receiver) without disturbing the coupling (and position) of the other; this capacity is critical for the calibration procedure described next. The receiver is terminated with a 50 Ω passive load to have the same terminal load

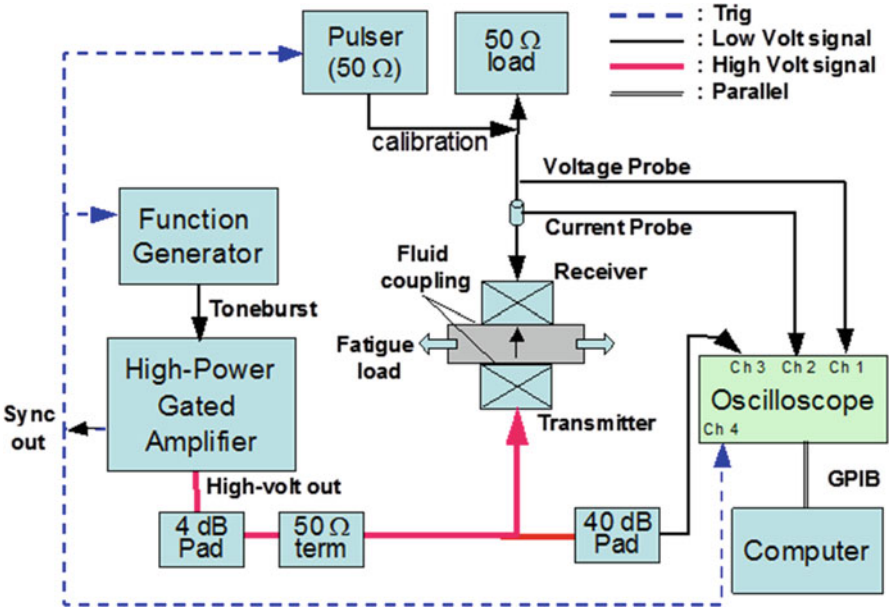

Fig. 6.2 Schematic of experimental setup for through transmission

in the calibration. Both voltage and current signals of the transmitted ultrasonic waves are recorded and time averaged with an oscilloscope, and then transferred to a computer for further signal processing. Then, diffraction corrections are made to the measured fundamental and the second-harmonic signal amplitudes. The calibration procedure for the piezoelectric receiving transducer is based on the principle of self-reciprocity [40] and is employed in order to obtain a conversion transfer function from the measured electrical signal to the absolute amplitude of the particle displacement, and to compensate for any small variations in the coupling of the receiving transducer. Note that this calibration is performed prior to every nonlinear measurement, with the transmitter transducer removed. The current and voltage signals of the incident and the reflected pulse from the bottom surface of the specimen that is kept stress-free (when the transmitter is removed) are measured and used to calculate a transfer function that converts the measured current signal to the particle displacement of the incident wave at the receiver.

One clever way to improve SNR is through the pulse-inversion technique to accentuate the contribution of the even, second harmonic signal, while reducing the dominance of the fundamental contribution. The pulse-inversion technique is employed to extract the second-harmonic amplitude by canceling out any odd harmonics; the even harmonic signal is extracted by adding two 180° out-of-phase input signals.

6.2.2 *Collinear Wave Mixing*

The method of second harmonic generation discussed in the previous section usually measures the average β in the volume of material between the transmitter and the receiver. It is thus difficult to measure the spatial distribution of β which is crucial in monitoring fatigue damage. Nonlinear wave mixing techniques [41–47] offer the advantage of finding localized damage in the material. These techniques are based on the mixing of two propagating waves. When the frequencies and polarization of these two propagating waves satisfy certain resonant or phase-matching conditions, a third propagating wave is generated at a frequency different from those of primary waves. This generated third propagating wave is called the resonant wave. Its amplitude is proportional to the size of the mixing zone and the acoustic nonlinearity parameter of the material in the mixing zone [6]. By measuring the amplitude of the resonant wave, the acoustic nonlinearity parameter of the material in the mixing zone can be obtained. Since the measured β is only associated with the acoustic nonlinearity within the mixing zone. This spatial selectivity provides a tool to obtain the spatial distribution of β.

As a feasibility study of the scanning capability of mixing waves, Tang, et al. [47] conducted experimental measurements on circular cross-section bars with localized plastic zone in known locations. Their experimental setup [46] is schematically shown in Fig. 6.3.

The test samples are circular cross-section bars with localized plastic zone [47]. On the left end of the bar, a shear wave transducer is attached that sends a 5-cycle

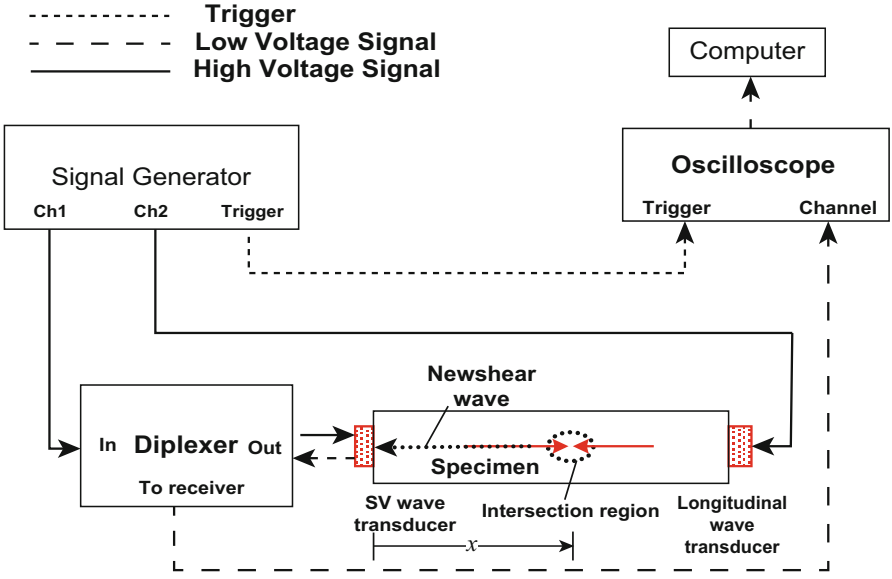

Fig. 6.3 Schematic of experimental setup for the collinear wave mixing method

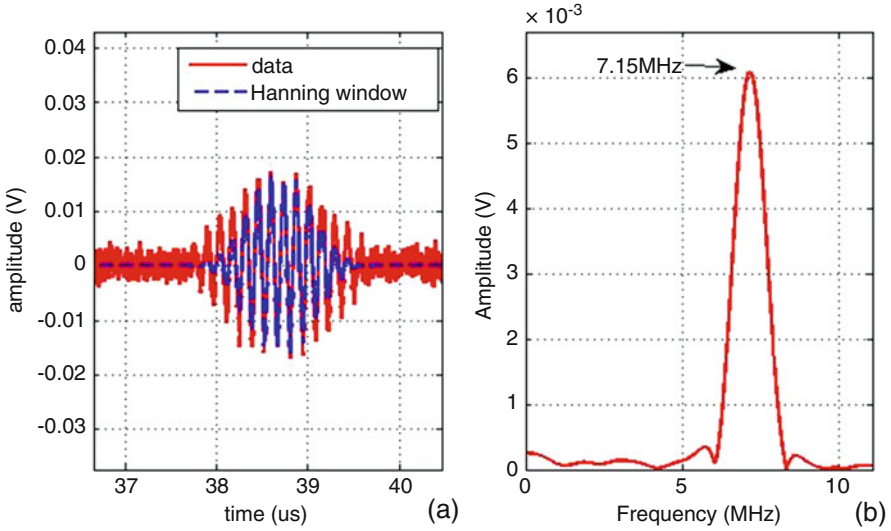

Fig. 6.4 (**a**) Resonant wave received by the shear wave transducer (red solid line) and the same signal after applying a Hann window (blue dashed line), (**b**) Frequency spectrum of the resonant wave after applying a Hann window

tone burst (6.3 mm spatially) with frequency $\omega_T = 2.5$ MHz. On the right end of the sample, a longitudinal wave transducer is attached that sends a nine-cycle tone burst (5.9 mm spatially) with frequency $\omega_L = 9.65$ MHz. These two frequencies satisfy the resonant condition given by (6.61) and (6.62). By adjusting the delay times of the two transducers, the two input wave-pulses can be mixed at any desired location along the bar. The resonant wave generated by such mixing is a shear wave that will propagate towards the left end of the bar. This resonant wave can be recorded by the shear wave transducer attached at the left end. Amplitude of this resonant shear wave is proportional to the acoustic nonlinearity parameter β_T at the location of mixing zone. By moving the mixing zone from the left to the right, one can then obtain the spatial distribution of β_T along the bar sample.

A typical time-domain resonant wave signal received by the shear wave transducer is shown in Fig. 6.4a and its frequency spectrum is shown in Fig. 6.4b. The solid red line in Fig. 6.4a shows the resonant wave received by the shear wave transducer, while the dashed blue line is the signal after applying a Hann window to the original time-domain signal to help smooth the frequency-domain signal shown in Fig. 6.4b. We will use $A(x)$ to donate the amplitude of the resonant shear wave when the center of the mixing zone is located at a distance x away from the left end of the bar. For Sample 0, which has no localized plastic zone, showing in Fig. 6.5 is the normalized amplitude $\overline{A}(x) = A(x)/A(x_0)$, where x_0 is the location of the first measurement point. In this case, $x_0 = 37.9$ mm.

According to the results derived in (6.66) for plane waves in a lossless medium, the amplitude $A(x)$ should be independent of the location of the mixing zone if the

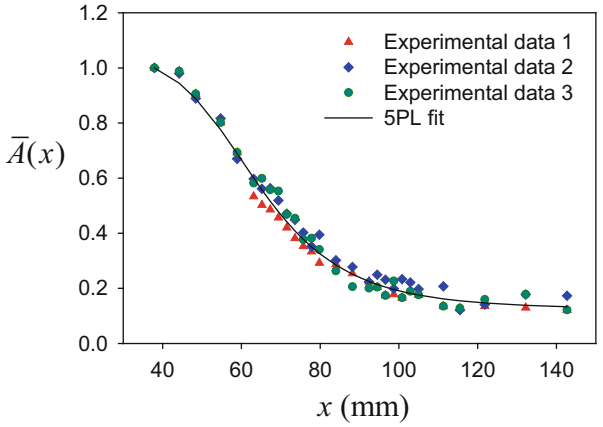

Fig. 6.5 Normalized amplitude of the resonant shear wave as a function of location x in a uniform bar sample

sample is uniform, i.e., the acoustic nonlinearity parameter is a constant throughout the sample. However, in the bar, the waves generated by the transducers are no longer plane waves. They are beams of finite diameter, and the material has loss. Thus, wave amplitude will decay due to beam divergence and material loss. In other words, the amplitudes of the incident waves, as well as the amplitude of the resonant waves, are all functions of locations, even though the acoustic nonlinearity parameter β_T is a constant throughout the sample.

Without carrying out detailed analysis of the effects of beam divergence and material loss, we opted for using a curve fitting technique to account for these effects. Based on the experimental data shown in Fig. 6.5, it seems that the five-parameter logistic (5PL) function [48] provides a good fit. Thus, the 5PL function is used as a baseline for $A(x)$. Any deviation of $A(x)$ from the 5PL function would indicate a non-uniform spatial distribution of β_T. Symbolically, one may re-write

$$A(x) = \beta_T(x) f(x), \tag{6.104}$$

where x indicates the location of mixing zone and $f(x)$ is a 5PL function as shown in Fig. 6.5. It then follows that the normalized acoustic nonlinearity parameter is given by

$$\overline{\beta}_T(x) = \frac{\beta_T(x)}{\beta_T(x_0)} = \frac{\overline{A}(x)}{\overline{f}(x)}, \tag{6.105}$$

where $\overline{A}(x) = A(x)/A(x_0)$ and $\overline{f}(x) = f(x)/f(x_0)$ with x_0 being the location of the first measurement point. It is now clear from (6.105) that if $\overline{A}(x) \propto \overline{f}(x)$, then β_T will be independent of x. Vice versa, if $\overline{A}(x)$ deviates from a 5PL function, $\overline{\beta}_T(x)$ will depend on x.

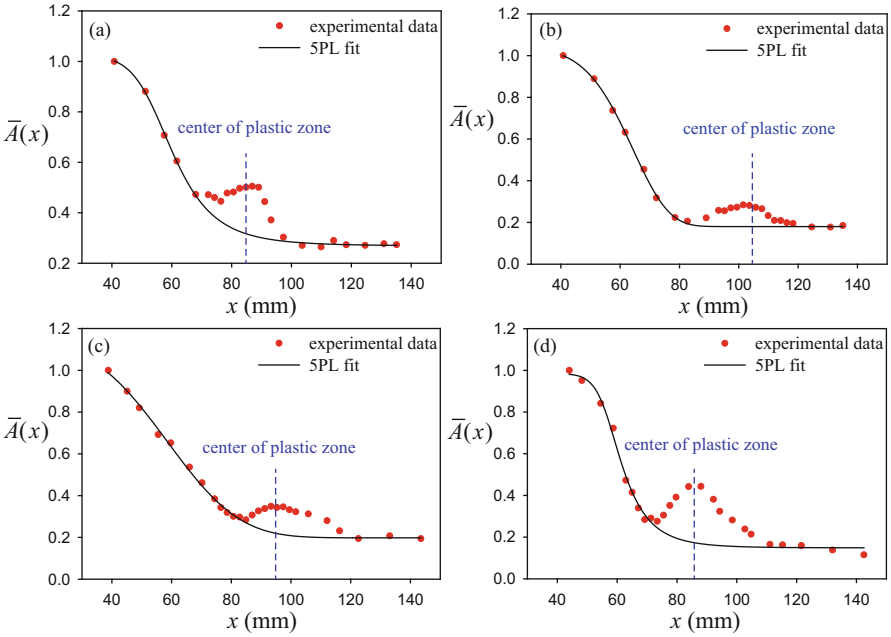

Fig. 6.6 Normalized amplitude of the resonant shear wave $\overline{A}(x)$. (**a**) from Sample 1 (center of plastic zone is at $x = 85$ mm), (**b**) from Sample 1 (center of plastic zone is at $x = 104$ mm), (**c**) from Sample 2 (center of plastic zone is at $x = 94$ mm), and (**d**) from Sample 3 (center of plastic zone is at $x = 86$ mm)

Similar tests were carried out on Samples 1, 2, and 3. Shown in Fig. 6.6 is the amplitude $A(x)$ from these samples plotted as a function of x. Figure 6.6a is from Sample 1. Figure 6.6b is also from Sample 1, but the positions of the shear wave and longitudinal wave transducers are switched such that the distance between the shear wave transducer (receiver) and the location of the plastic zone is different between Fig. 6.6a, b. In obtaining Fig. 6.6a, the center of the plastic zone is 85 mm from the shear wave transducer and 104 mm away from the longitudinal wave transducer. In obtaining Fig. 6.6b, the center of plastic zone is 104 mm from the shear wave transducer and 85 mm away from the longitudinal wave transducer. Figure 6.6c, d are from Samples 2 and 3, respectively.

In all these figures, the dots are experimental data points, and the solid lines are the 5PL function best-fitted to the experimental data outside the notched region. All experimental data are an average of three sets of tests. The location of the plastic zone center is indicated by the vertical dash-lines in these figures. Data from Fig. 6.6 shows that for the samples with a localized plastic zone, the amplitude of the resonant shear wave no longer follows a 5PL function of x. The region over which $\overline{A}(x)$ deviates from the 5PL function coincides exactly with the location of the plastic zone, indicating that the acoustic nonlinearity β_T in the plastic zone is higher its values than elsewhere in the sample.

These results demonstrated the feasibility of using co-linear wave mixing techniques to map spatial distribution of plastic strain along a slender bar. In other words, nonlinear wave mixing has the potential for imaging spatial distribution of damage in structural components.

6.2.3 Rayleigh Surface Waves

Rayleigh surface waves have also been used to characterize fatigue damage and material nonlinearity. Barnard et al. [49] and Blackshire et al. [50] used Rayleigh surface waves to evaluate the fatigue damage in high temperature alloys. Blackshire et al. [50] employed a scanning heterodyne interferometer for detecting the Rayleigh waves. Herrmann et al. [22] developed a technique to measure the second order harmonic amplitude of a Rayleigh surface wave propagating in metallic specimens, using a wedge transducer and a laser interferometer. This system is used to measure the fundamental and second harmonic components in Rayleigh surface waves, and these results are interpreted in terms of the nonlinearity parameter derived in terms of the measured out-of-plane displacement of the Rayleigh surface waves. The proposed measurement technique is used to assess damage in nickel-base high temperature alloy specimens where the evolution of material nonlinearity under various loading conditions is measured in terms of the increasing amplitude of the second order harmonic. These results show that there is a large increase in the acoustic nonlinearity parameter at monotonic tensile loads above the material's yield stress, and that during low-cycle fatigue tests, the increase in the second order harmonic amplitude is considerable. The results from this study show that accumulated plasticity plays the major role in the increase in material nonlinearity, and demonstrate the effectiveness of the proposed experimental procedure to track damage in high temperature alloys.

The experimental setup for the generation and detection of nonlinear Rayleigh waves is similar to the procedure described in 2.1 for bulk waves. The main difference is that a wedge is needed to generate and detect the Rayleigh waves. The wedge angle is selected so the projection of the longitudinal wave in the wedge matches the wavelength of the Rayleigh wave in the specimen.

One advantage of using Rayleigh waves in the generation of higher harmonics is that the value of the measured material nonlinearity should increase with increasing propagation distance. This is not the case for instrumentation nonlinearity, which should remain a constant as a function of increasing propagation distance. It is important to note that it is difficult, if not impossible, to increase the propagation distance of a longitudinal wave in a specimen since the specimen thickness is a fixed constant. Consider the results in Fig. 6.7, which show how the measured nonlinearity in an A-36 steel plate increases with increasing propagation distance. The two sets of data shown in this figure correspond to the nonlinearities measured with Rayleigh waves before fatigue and after 88 cycles. The maximum load level in the fatigue is 110% of the yield stress and R ratio is 0. This figure shows an increasing slope with the number fatigue cycles.

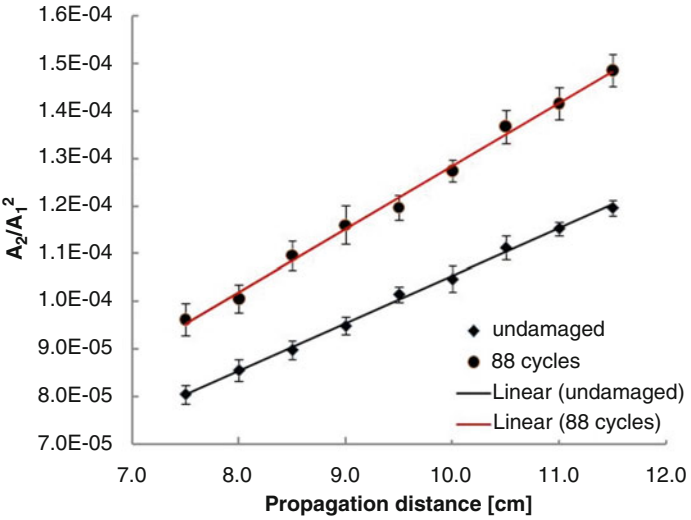

Fig. 6.7 Change in measured nonlinearity as a function of propagation distance

As an example, consider a set of both nonlinear longitudinal and Rayleigh wave measurements in low-cycle fatigue damaged IN100 specimens. Figure 6.8 shows a rapid increase in the measured material nonlinearity (up to 30%) during the first 40% of fatigue life. This behavior demonstrates that NLU can be used to quantitatively characterize the damage state in this material in the early stages of fatigue life. There is also excellent agreement in the material nonlinearity measured with either Rayleigh or longitudinal waves.

There are a few different ways to experimentally realize the nonlinear Rayleigh wave measurement. Techniques that adopt the pulsed laser, laser interferometer, electromagnetic acoustic transducer (EMAT), ultrasonic wedge transducer, and air-coupled ultrasonic transducer as excitation and detection methods have been proposed [22, 51–54]. A fully non-contact method would be most desirable but a critical issue in selecting a combination of excitation and detection methods is the capability of getting signals with sufficiently high signal-to-noise ratio (SNR). Thiele et al. [46] proposed recently a technique that uses an air-coupled transducer for detection and a wedge transducer for excitation. This technique has been successfully applied to the evaluation of microstructural damage in materials [55, 56]. Figure 6.9a shows the measurement setup. An air-coupled transducer, with its reception angle adjusted at the Rayleigh critical angle, detects the sound wave radiated from the propagating Rayleigh wave. It can be shown that the leaked sound wave preserves the information on harmonics contents that are carried by the Rayleigh wave propagating in the solid. This is because the impedance mismatch at the solid–air interface is so high that the amplitude of the leaked sound wave is reduced to be in the linear acoustics regime and thus the radiation from solid into air can be regarded as a linear process. In other words, the propagation through the

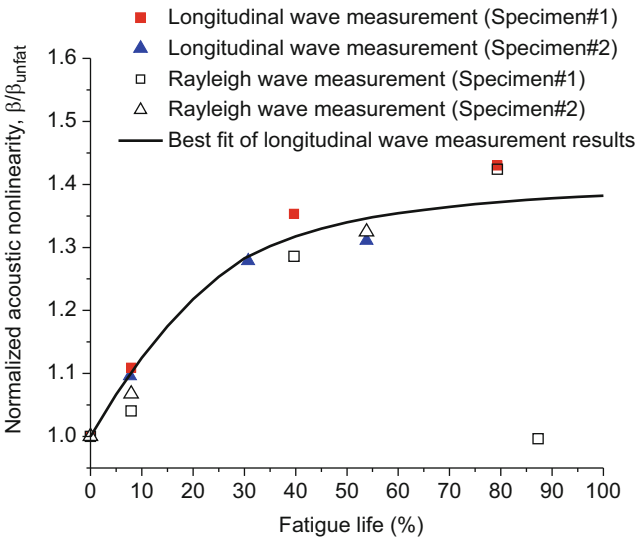

Fig. 6.8 Normalized acoustic nonlinearity as a function of fatigue life

air does not cause any additional nonlinearity. Since the leaked sound is due to the surface normal displacement, the air-coupled detection measures the nonlinearity of the surface normal displacement component of the Rayleigh wave. Compared to the detections based on the laser interferometry and EMAT, this method is much more sensitive and reliable. With the setup shown in Fig. 6.9a, it is possible to obtain excellent-shaped signals with amplitude 100 mV and SNR higher than 50 dB.

Among numerous applications of this technique, two interesting cases are discussed. In the first case [55], dislocations and precipitates evolve simultaneously during thermal aging such that a non-monotonic behavior is seen in the measured material nonlinearity. In the second case [56], a single mechanism of the grain boundary precipitation is dominant. Marino et al. [55] investigated thermal aging at 650 °C of modified 9%-Cr ferritic-martensitic steel, a high temperature material that is often used in thermal and nuclear power plants. This material experiences significant changes in its microstructure and deterioration in mechanical properties when aged at a temperature 600 °C and higher. Exposure to heat causes two microstructural changes to occur simultaneously: the formation of various kinds of precipitates and change in the dislocation density. These microstructural changes influence the long term thermo-mechanical properties of the material and also the measured nonlinearity parameter. Two different groups of precipitates evolve during tempering and post thermal aging in this material: First, $M_{23}C_6$, MX, and M_2X precipitates during tempering and the Laves phase and Z-phase during thermal aging. Previous investigations [55 and the references therein] report that: (1) the $M_{23}C_6$ and MX particles are relatively stable against coarsening and grow little at 650 °C; (2) Laves phase does not nucleate during tempering like the other

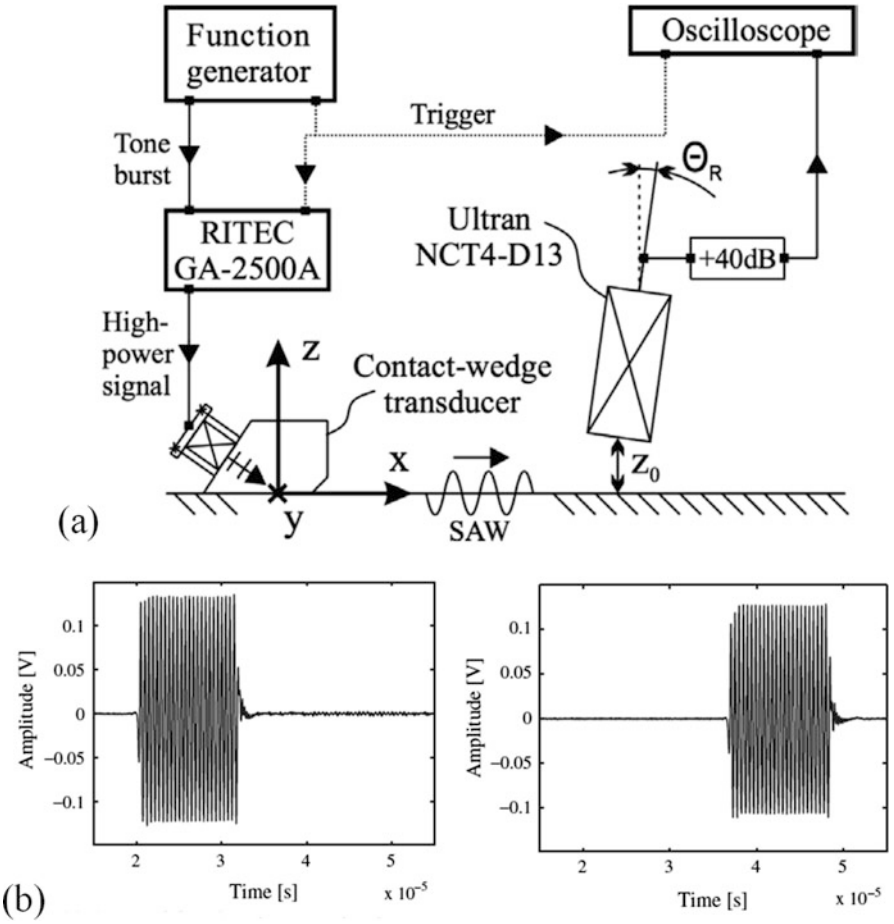

Fig. 6.9 (**a**) Experimental setup using non-contact air-coupled receiver; (**b**) Time-domain signals obtained at propagation distances, $x = 30$ mm and 78 mm from the source (Al 7075 specimen)

precipitates but starts to precipitate during thermal aging and rapidly grows up to a size of about 400 nm in the first 1000–10,000 h; (3) Z-phase precipitates during thermal aging only for longer holding times. Not only the precipitates but also the dislocations evolve during tempering and aging. The initial dislocation density after normalizing at 19×10^{14} m^2 steadily decreases to 6.1×10^{14} m^2 after tempering and 1.6×10^{14} m^2 immediately after aging [55].

Nonlinear ultrasonic measurements are performed using the setup shown in Fig. 6.9a intermittently during aging up to 3000 h. In addition, hardness, longitudinal wave speed, and attenuation are measured. Figure 6.10a shows the trend of material nonlinearity with aging time. Based on the above-mentioned microstructure changes during aging, the initial sharp drop is due to the decreased dislocation density for the

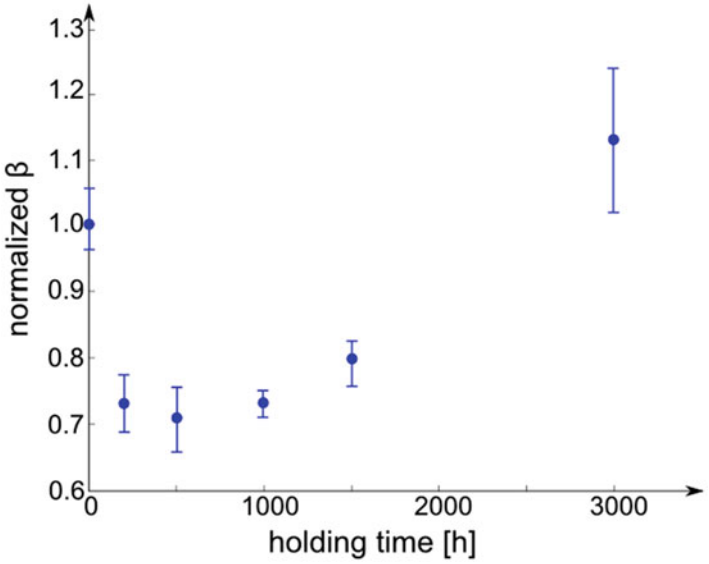

Fig. 6.10 Change of the material nonlinearity parameter in 9%Cr ferritic-martensitic steel aged at 650 °C

first 500 h and the following gradual rise is because of the increased number density and size of the Laves precipitates. The changes in the nonlinearity are significant as compared to the wave speed and attenuation which change less than a few percent. These results are confirmed with SEM microscopy and hardness results [55] and demonstrate that the measured material nonlinearity is well correlated with the microstructure evolution during the thermal again in this material.

Doerr et al. [56] investigated the sensitization phenomenon in austenite 304 and 304 L stainless steels using nonlinear Rayleigh waves. These austenite stainless steels contain about 18% of chromium and this chromium content (>12%) makes these stainless steels corrosion resistant. Sensitization is a result of the chromium carbide ($Cr_{23}C_6$) precipitation along the grain boundaries, causing the formation of a chromium depletion zone around the grain boundary which is susceptible to intergranular stress corrosion cracking (IGSCC). Note that IGSCC is the major corrosion problem, for example, in boiling water nuclear reactors. Sensitization occurs when a stainless steel is exposed to a certain range of high temperature, such as during welding. For this reason, the detection of sensitization as a precursor of IGSCC is of great importance to prevent failure of the components in 304 and 304 L stainless steels due to IGSCC. The annealed 304 and 304 L stainless steel samples are exposed at temperature 675 °C and nonlinear ultrasonic measurements are performed at different exposure times. The electrochemical potentiodynamic reactivation (EPR) test which is a direct laboratory measurement of degree of sensitization (DOS) and optical microscopy are used to monitor the progress of sensitization.

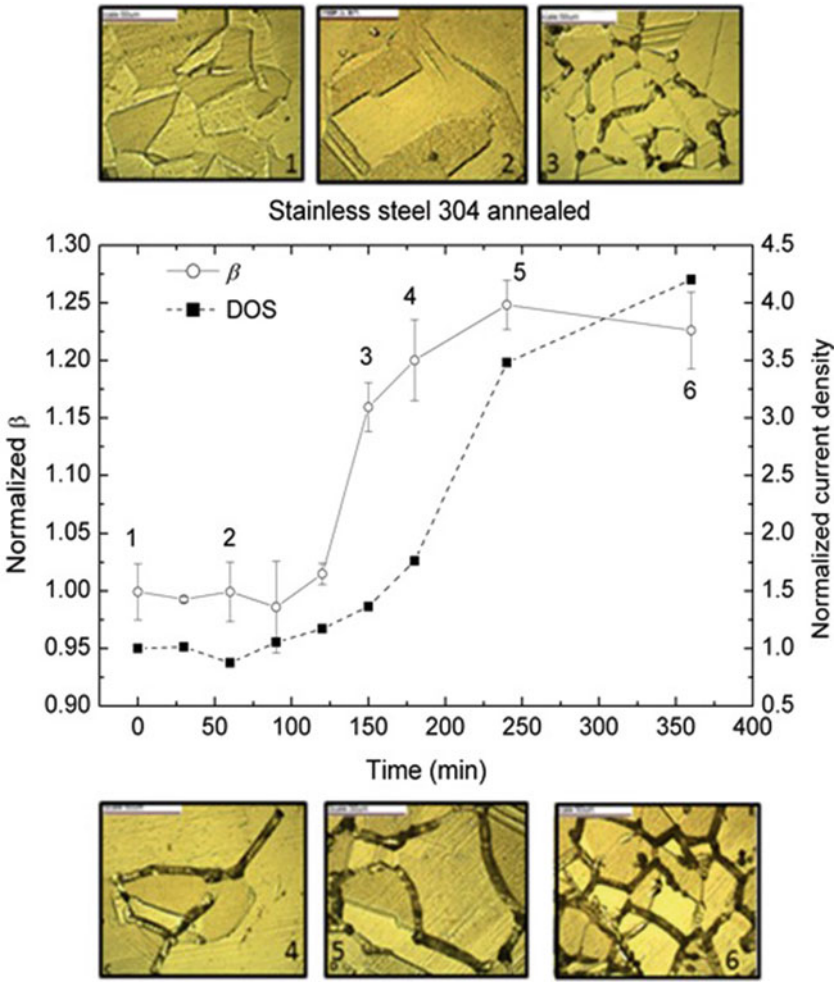

Fig. 6.11 Changes of the material nonlinearity parameter and DOS in annealed 304 stainless steel aged at 675 °C. The micrographs at different aging times are shown together

Figure 6.11 shows changes in the material nonlinearity parameter and DOS as a function of exposure time. Both parameters increase and then saturate and their trends are very well correlated. In other words, from the measured nonlinearity one can estimate how much sensitization has occurred in this material. The accompanied micrographs taken at different moments exhibit the progress of sensitization; the black lines indicate the chromium deplete zones. Saturation of DOS means all grain boundaries are sensitized. Figure 6.12 shows those results for 304 L material. Note that 304 L has reduced amount of carbon content (<0.02 wt.% versus 0.05 wt.% in 304) with intention to minimize the sensitization. The trends in 304 L are similar to those in 304 and the trends of the material nonlinearity parameter and DOS

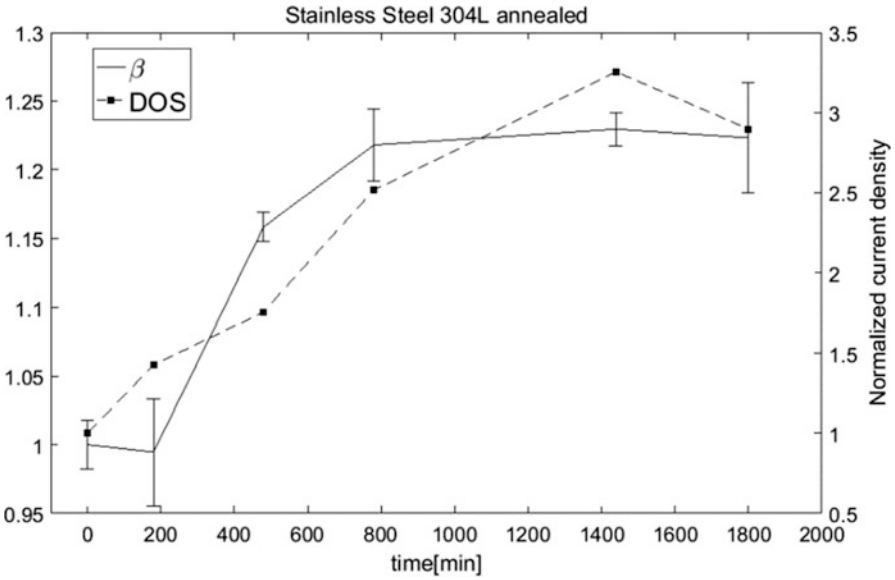

Fig. 6.12 Changes of the material nonlinearity parameter and DOS in annealed 304 stainless steel aged at 675 °C

in this material also are very close to each other. However, the whole process of sensitization is retarded, more than five times slower than in 304, possibly due to the lower carbon content. Note that the same saturation occurs in this material, meaning that the reduced carbon content is still more than enough to sensitize all grain boundaries in this material. The phenomenon of sensitization in 304 and 304 L stainless steels is investigated using nonlinear Rayleigh wave as a practical application of the developed measurement setup in Fig. 6.9. The good correlation between the measured material nonlinearity parameter and DOS suggests the feasibility of taking the nonlinear ultrasonic technique to field applications. Also interesting is that the grain boundary precipitation is a new mechanism of generating material nonlinearity that has not been observed in the literature so far. A theoretical description of the nonlinearity generation from grain boundary precipitates is the topic to be explored.

6.2.4 Lamb Waves

Techniques based on guided waves including Lamb waves have advantages over other NDE techniques based on bulk ultrasonic waves. These guided-wave-based techniques can interrogate large areas and inaccessible parts of a structure, and have been successful in evaluating discontinuity type defects such as cracks in

metallic plates and delamination/debonding in laminate composite materials. Most of the existing guided wave techniques are based on linear ultrasound. It is therefore desirable to combine the long-range coverage capability of guided waves with the higher sensitivity of nonlinear ultrasound to material damage. This combination may render a unique opportunity to develop an NDE technique which can inspect fast and quantitatively microstructural damage in plate-like structural components. Unfortunately an experimental realization of Lamb wave propagation in the nonlinear regime [26, 27, 57] is quite difficult because of the dispersive and multi-mode nature of these guided waves. Nonlinear Lamb wave measurements in aluminum specimens subjected to cyclic fatigue have been conducted by Deng and Pei [33]. They introduced a parameter called stress wave factor that is defined as the absolute magnitude of the second harmonic wave integrated over the excitation frequency range and is taken an acoustic nonlinearity parameter. An experimental procedure for characterizing fatigue damage in metallic plates using nonlinear Lamb waves has been developed by Pruell et al. [31] and Bermes et al. [58]. They first considered conditions for efficient second harmonic generation in propagating nonlinear Lamb waves, and then performed measurements for S1-S2 mode pair and showed the expected linear increase of the second-harmonic amplitude. It was concluded that not only the phase velocity matching but also the group velocity matching is essential for the practical generation of nonlinear guided elastic waves where tone burst input signals with limited number of cycles are used. The acoustic nonlinearity parameter of aluminum specimens under low-cycle fatigue measured with Lamb waves showed a direct correlation with fatigue damage which was represented by the cumulative plastic strain. A similar correlation of the acoustic nonlinearity to fatigue damage has been observed in nonlinear longitudinal and Rayleigh waves. This result demonstrates that Lamb waves can be used to quantitatively assess fatigue damage using established higher harmonic generation measurement concept.

6.3 Summary

This chapter summarizes the potential of using nonlinear ultrasonic techniques to characterize material state and to develop the framework for accurate life prediction of components under mechanical and thermo-mechanical loading. These nonlinear ultrasonic measurements are done at the material level, before macroscopic damage appears. Starting from mechanics fundamentals, we first developed the theoretical equations of wave motion in an elastic solid with quadratic nonlinearity, covering bulk, surface, and guided waves. The final section considers measurement techniques for nonlinear ultrasonic measurements, including examples of the assessment of fatigue and thermal damage in metals with nonlinear ultrasounds.

References

1. A. Norris, in *Finite Amplitude Waves in Solids*, ed. By M.F. Hamilton, D.T. Blackstock. Nonlinear Acoustics (Acoustical Society of America, New York, 2008)
2. L. Malvern, in *Introduction to the Mechanics of a Continuous Medium*. ed. By J.B. Reswick, W.M. Rohsenow. Prentice-Hall Series in Engineering of the Physical Sciences, (Prentice-Hall, Inc, Englewood, 1969)
3. D.O. Thompson, M.A. Breazeale, Ultrasonic waves of finite amplitude in solids. J. Acoust. Soc. Am. **35**(11), 1884 (1963)
4. J.H. Cantrell, Acoustic radiation stress in solids. IEEE Transac. Sonics Ultrason. **32**(1), 100–100 (1985)
5. J.D. Achenbach, *Wave Propagation in Elastic Solids* (North-Holland, Amsterdam, 1973)
6. G.L. Jones, D.R. Korbett, Interaction of elastic waves in an isotropic solid. J. Acoust. Soc. Am. **35**(1), 5 (1963)
7. N. Kalyanasundaram, Non-linear surface acoustic-waves on an isotropic solid. Int. J. Eng. Sci. **19**(2), 279–286 (1981)
8. N. Kalyanasundaram, Non-linear mixing of surface acoustic-waves propagating in opposite directions. J. Acoust. Soc. Am. **73**(6), 1956–1965 (1983)
9. N. Kalyanasundaram, G.V. Anand, Surface acoustic-waves of finite-amplitude excited by a monochromatic line source. J. Acoust. Soc. Am. **68**(2), 567–574 (1980)
10. N. Kalyanasundaram, G.V. Anand, Periodic rayleigh-waves of finite-amplitude on an isotropic solid. J. Acoust. Soc. Am. **72**(5), 1518–1523 (1982)
11. N. Kalyanasundaram, D.F. Parker, E.A. David, The spreading of nonlinear elastic surface-waves. J. Elast. **24**(1-3), 79–103 (1990)
12. N. Kalyanasundaram, R. Ravindran, P. Prasad, Coupled amplitude theory of non-linear surface acoustic-waves. J. Acoust. Soc. Am. **72**(2), 488–493 (1982)
13. R.W. Lardner, Non-linear surface-waves on an elastic solid. Int. J. Eng. Sci. **21**(11), 1331–1342 (1983)
14. A.P. Mayer, Nonlinear surface acoustic waves: Theory. Ultrasonics **48**(6-7), 478–481 (2008)
15. A.P. Mayer, Surface acoustic-waves in nonlinear elastic media. Phys. Rep. Rev. Sect. Phys. Lett. **256**(4-5), 237–366 (1995)
16. M.F. Hamilton, Y.A. Ilinskii, E.A. Zabolotskaya, in *Nonlinear Surface Wave Propagation in Crystals*, ed. By R.J. Wei. Nonlinear Acoustics in Perspective (Nanjing University Press, Nanjing, 1996), pp. 64–69
17. M.F. Hamilton, Y.A. Il'inskii, E.A. Zabolotskaya, *Nonlinear Surface Acoustic Waves*. ed. by W. Lauterborn, T. Kurz. Nonlinear Acoustics at the Turn of the Millennium (AIP, Melville, 2000), p. 55–64
18. M.F. Hamilton, Y.A. Il'inskii, E.A. Zabolotskaya, Nonlinear surface acoustic waves in crystals. J. Acoust. Soc. Am. **105**(2), 639–651 (1999)
19. M.F. Hamilton, Y.A. Ilinsky, E.A. Zabolotskaya, Local and nonlocal nonlinearity in rayleigh-waves. J. Acoust. Soc. Am. **97**(2), 882–890 (1995)
20. M.F. Hamilton, Y.A. Ilinsky, E.A. Zabolotskaya, Evolution-equations for nonlinear rayleigh-waves. J. Acoust. Soc. Am. **97**(2), 891–897 (1995)
21. M.F. Hamilton, Y.A. Ilinsky, E.A. Zabolotskaya, On the existence of stationary nonlinear rayleigh-waves. J. Acoust. Soc. Am. **93**(6), 3089–3095 (1993)
22. J. Herrmann, J.Y. Kim, L.J. Jacobs, J. Qu, J.W. Littles, M. Savage, Assessment of material damage in a Nickel-Base superalloy using nonlinear Rayleigh surface waves. J. Appl. Phys. **99**, 124913 (2006)
23. J.M. Qu, L.J. Jacobs, P.B. Nagy, On the acoustic-radiation-induced strain and stress in elastic solids with quadratic nonlinearity (L). J. Acoust. Soc. Am. **129**(6), 3449–3452 (2011)
24. J.D. Achenbach, *Reciprocity in Elastodynamics* (Cambridge University Press, London, 2004)
25. B.A. Auld, *Acoustic Fields and Waves in Solids*, vol 2 (Wiley, New York, 1973)

26. W.J.N. de Lima, M.F. Hamilton, Finite-amplitude waves in isotropic elastic plates. J. Sound Vib. **265**(4), 819–839 (2003)
27. M.X. Deng, Analysis of second-harmonic generation of Lamb modes using a modal analysis approach. J. Appl. Phys. **94**(6), 4152–4159 (2003)
28. T.O. Mueller, J.Y. Kim, J. Qu, L.J. Jacobs, Nonlinear acoustic measurements and Rayleigh waves. *32nd Annual Review of Process in Quantitative Nondestructive Evaluation* (American Institute of Physics, Brunswick, 2005)
29. A. Srivastava, F.L. di Scalea, On the existence of antisymmetric or symmetric Lamb waves at nonlinear higher harmonics. J. Sound Vib. **323**(3-5), 932–943 (2009)
30. M.F. Muller, J.Y. Kim, J.M. Qu, L.J. Jacobs, Characteristics of second harmonic generation of Lamb waves in nonlinear elastic plates. J. Acoust. Soc. Am. **127**(4), 2141–2152 (2010)
31. C. Pruell, J.Y. Kim, J. Qu, L.J. Jacobs, Evaluation of plasticity driven material damage using Lamb waves. Appl. Phys. Lett. **91**(23), 231911 (2007)
32. K.H. Matlack, J.Y. Kim, L.J. Jacobs, J.M. Qu, Experimental characterization of efficient second harmonic generation of Lamb wave modes in a nonlinear elastic isotropic plate. J. Appl. Phys. **109**(1), 014905 (2011)
33. M.X. Deng, P. Wang, X.F. Lv, Experimental observation of cumulative second-harmonic generation of Lamb-wave propagation in an elastic plate. J Phys. D Appl. Phys. **38**(2), 344–353 (2005)
34. W.T. Yost, J.H. Cantrell, *The Effects of Fatigue on Acoustic Nonlinearity in Aluminum Alloys* (IEEE, Tucson, 1992)
35. J.H. Cantrell, W.T. Yost, Nonlinear ultrasonic characterization of fatigue microstructures. Int. J. Fatigue **23**(SUPPL 1), 487–490 (2001)
36. J. Frouin, T.E. Matikas, J.K. Na, S. Sathish, In-situ monitoring of acoustic linear and nonlinear behavior of titanium alloys during cycling loading. in *Proceedings of SPIE – The International Society for Optical Engineering,* Vol. 3585, 1999, pp. 107–116
37. A. Moreau, Detection of acoustic 2nd-harmonics in solids using a heterodyne laser interferometer. J. Acoust. Soc. Am. **98**(5), 2745–2752 (1995)
38. D.C. Hurley, C.M. Fortunko, Determination of the nonlinear ultrasonic parameter beta using a Michelson interferometer. Meas. Sci. Technol. **8**(6), 634–642 (1997)
39. J.Y. Kim, L.J. Jacobs, J.M. Qu, J.W. Littles, Experimental characterization of fatigue damage in a nickel-base superalloy using nonlinear ultrasonic waves. J. Acoust. Soc. Am. **120**(3), 1266–1273 (2006)
40. G.E. Dace, R.B. Thompson, O. Buck, Measurement of the acoustic harmonic generation for materials characterization using contact transducers. Rev. Prog. Quant. Nondestr. Eval. **11**, 2069–2076 (1992)
41. F.R. Rollins, Interaction of ultrasonic waves in solid media. Appl. Phys. Lett. **2**(8), 147–148 (1963)
42. F.R. Rollins, P.H. Todd, L.H. Taylor, Ultrasonic study of 3-phonon interactions .2. Experimental results. Phys. Rev. **136**(3A), A597–A601 (1964)
43. L.H. Taylor, F.R. Rollins, Ultrasonic study of 3-phonon interactions .I. Theory. Phys. Rev. **136**(3A), A591–A596 (1964)
44. A.J. Croxford, P.D. Wilcox, B.W. Drinkwater, P.B. Nagy, The use of non-collinear mixing for nonlinear ultrasonic detection of plasticity and fatigue. J. Acoust. Soc. Am. **126**(5), El117–El122 (2009)
45. Z.M. Chen, G.X. Tang, Y.X. Zhao, L.J. Jacobs, J.M. Qu, Mixing of collinear plane wave pulses in elastic solids with quadratic nonlinearity. J. Acoust. Soc. Am. **136**(5), 2389–2404 (2014)
46. M.H. Liu, G.X. Tang, L.J. Jacobs, J.M. Qu, Measuring acoustic nonlinearity parameter using collinear wave mixing. J. Appl. Phys. **112**(2), 024908 (2012)
47. G.X. Tang, M.H. Liu, L.J. Jacobs, J.M. Qu, Detecting localized plastic strain by a scanning collinear wave mixing method. J. Nondestruct. Eval. **33**(2), 196–204 (2014)
48. R.A. Dudley, P. Edwards, R.P. Ekins, D.J. Finney, I.G.M. McKenzie, G.M. Raab, D. Rodbard, R.P.C. Rodgers, Guidelines for immunoassay data processing. Clin. Chem. **31**, 1264–1271 (1985)

49. D.J. Barnard, L.J.H. Brasche, D. Raulerson, A.D. Degtyar, *Monitoring Fatigue Damage Accumulation with Rayleigh Wave Harmonic Generation Measurements*. ed. By D.O. Thompson, D.E. Chimenti. Review of Progress in Quantitative Nondestructive Evaluation, Vols. 22a and 22b, Vol 20, (Springer, New York, 2003), pp. 1393–1400
50. J.L. Blackshire, S. Sathish, J. Na, J. Frouin, *Nonlinear Laser Ultrasonic Measurements of Localized Fatigue Damage*. ed. by D.O. Thompson, D.E. Chimenti. Review of Progress in Quantitative Nondestructive Evaluation, Vols 22a and 22b, Vol. 20 (American Institute of Physics, Melville, 2003), pp. 1479–1488
51. T. Stratoudaki et al., Measurement of material nonlinearity using surface acoustic wave parametric interaction and laser ultrasonics. J. Acoustic. Soc. Am. **129**(4), 1721–1728 (2011)
52. A. Cobb et al., Nonlinear ultrasonic measurments with EMATs for detecting pre-cracking fatigue damage. Review of progress in quantitative nondestructive evaluation. AIP Conf. Proc. **1430**, 299–306 (2012)
53. C.B. Swacek. et al., Opical excitation of narrowband Rayleigh surface waves for secod harmonic generation. in *Review of Progress in Quantitative Nondestructive Evaluation, AIP Conference Proceeding 1511* (2013), pp. 375–381
54. S. Thiele et al., Air-coupled detection of nonlinear Ryleigh surface waves to assess material nonlinearity. Ultrasonics **54**, 1470–1475 (2014)
55. D. Marino et al., Using nonlinear ultrasound to track microstructural changes due to thermal again in modifies 9% ferritic martenstic steel. NDT&E Int. **79**, 46–52 (2016)
56. C. Doerr et al., Evaluation of sensitization in stainless 304 and 304L using nonlinear Rayleigh waves. NDT&E Int. **88**, 17–23 (2017)
57. M.X. Deng, Cumulative second-harmonic generation of Lamb-mode propagation in a solid plate. J. Appl. Phys. **85**(6), 3051–3058 (1999)
58. C. Bermes, J.Y. Kim, J.M. Qu, L.J. Jacobs, Experimental characterization of material nonlinearity using Lamb waves. Appl. Phys. Lett. **90**(2), 021901 (2007)

Chapter 7
Second-Harmonic Generation at Contacting Interfaces

Shiro Biwa

7.1 Nonlinear Spring-Type Interface Model for Contacting Rough Surfaces

Real surfaces of solid bodies possess roughness to some extent. Therefore, when two solid bodies with nominally flat surfaces are in contact with each other under compressive loading, the load is supported by a distribution of asperities on the surfaces. When the load, or the nominal contact pressure, is increased, the supporting asperities undergo further flattening while other asperities newly come into contact. This leads to the increase of the true area of contact and the reduction of the gap distance between the surfaces (the distance between the nominal planes of average height of both surfaces). The resulting relation between the nominal contact pressure and the gap distance of contacting surfaces is schematically shown in Fig. 7.1.

The contact between rough surfaces has been extensively studied as it is related to some important physical characteristics of the interface such as friction, and thermal and electrical conductance [1, 2]. Elastic or ultrasonic waves have been utilized to characterize contacting interfaces between solid bodies for a long time, based on the linear wave characteristics such as the reflection/transmission [3–6] and the wave-guiding properties [7]. Recently, nonlinear ultrasonic responses of contacting interfaces have attracted much attention in the field of nondestructive evaluation as a sensitive measure of the presence of closed defects and weakly bonded interfaces [8–13]. Granular media and other micro-inhomogeneous materials also show highly nonlinear responses to acoustic waves due to weak contacts between

S. Biwa (✉)
Department of Aeronautics and Astronautics, Graduate School of Engineering, Kyoto University, Kyoto, Japan
e-mail: biwa@kuaero.kyoto-u.ac.jp

T. Kundu (ed.), *Nonlinear Ultrasonic and Vibro-Acoustical Techniques for Nondestructive Evaluation*, https://doi.org/10.1007/978-3-319-94476-0_7

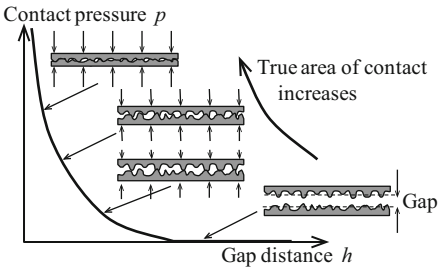

Fig. 7.1 Schematic of the pressure–gap distance relation of contacting surfaces

the grains or other micro-constituents [14]. In order to facilitate nonlinear ultrasonic characterization of materials and structural components, it is of fundamental interest to understand nonlinear responses of contacting interfaces to ultrasonic waves from a theoretical point of view.

As shown in Fig. 7.1, the nominal contact pressure p is a nonlinear function of the gap distance h. Many authors attempted to construct the pressure–gap relation of contacting rough surfaces based on micromechanical modeling of asperity deformation and statistical modeling of geometrical features of surfaces, e.g., Baltazar et al. [15]. From a macroscopic point of view, the mechanical response of contacting rough surfaces can be expressed as a relation between the surface traction and the relative displacement of the two surfaces, i.e., change of gap distance h in the normal direction and sliding displacement s in the tangential direction. When the roughness features are independent of the orientation in the plane of interface, the nominal shear stress is expected to be parallel with the sliding displacement. Then, the nominal normal stress $\sigma = -p$ and the nominal shear stress τ can be described as functions of h and s,

$$\sigma = \mathbf{n} \cdot \mathbf{T}\mathbf{n} = \sigma(h, s), \quad \tau = \mathbf{t} \cdot \mathbf{T}\mathbf{n} = \tau(h, s), \tag{7.1}$$

where $\mathbf{T}$ is the stress tensor, $\mathbf{n}$ is the outward unit normal to the surface, and $\mathbf{t}$ is the unit vector in the direction of shear stress. Furthermore, when the surface features are orientation-independent, it is natural to assume that σ is an even function of s, while τ is an odd function of s. Let the gap distance of the interface at equilibrium be denoted by h_0, and assume that the Taylor expansions of Eq. (7.1) exist at $h = h_0$ and $s = 0$. Then σ and τ can be approximated by

$$\sigma = -p_0 + K_{\mathrm{N}}(h - h_0) - K_{\mathrm{NN}}(h - h_0)^2 - K_{\mathrm{TT}}s^2, \tag{7.2a}$$

$$\tau = K_{\mathrm{T}}s - K_{\mathrm{NT}}(h - h_0)s, \tag{7.2b}$$

up to the second order in h and s, where $p_0 = -\sigma(h_0, 0)$ is the static pressure at equilibrium, and

$$K_{\mathrm{N}} = \frac{\partial \sigma}{\partial h}(h_0, 0)\,, \quad K_{\mathrm{NN}} = -\frac{1}{2}\frac{\partial^2 \sigma}{\partial h^2}(h_0, 0)\,,$$
$$K_{\mathrm{TT}} = -\frac{1}{2}\frac{\partial^2 \sigma}{\partial s^2}(h_0, 0)\,, \quad K_{\mathrm{T}} = \frac{\partial \tau}{\partial s}(h_0, 0)\,,$$
$$K_{\mathrm{NT}} = -\frac{\partial^2 \tau}{\partial h \partial s}(h_0, 0)\,. \tag{7.3}$$

Neglecting the second-order terms in the above expression gives the celebrated linear spring-type interface model;

$$\sigma = -p_0 + K_{\mathrm{N}}(h - h_0)\,, \quad \tau = K_{\mathrm{T}} s. \tag{7.4}$$

The parameters K_{N} and K_{T} are the interfacial normal and tangential stiffnesses, respectively. The other parameters in Eq. (7.3) characterize the quadratic nonlinear response of the contacting interface.

Nonlinear ultrasonic responses of contacting interfaces have been discussed in the literature using different models of the relation between the surface traction and the relative surface displacement. The simplest is the one used by Richardson [16] for the analysis of the longitudinal wave at normal incidence on the interface, which requires that either one of the following two sets of conditions is met, i.e.,

$$h > 0 \quad \text{and} \quad \sigma = 0 \quad (\text{perfect opening})\,, \tag{7.5a}$$

$$h = 0 \quad \text{and} \quad \sigma < 0 \quad (\text{perfect closure})\,. \tag{7.5b}$$

In this model the two surfaces are either traction-free (perfect opening) or moving without relative displacements (perfect closure). This model has been used in a number of subsequent investigations, e.g., Hirose and Achenbach [17]. A piecewise linear spring-type interface model with two constants K_{N}^{+} and K_{N}^{-},

$$\sigma = K_{\mathrm{N}}^{+}(h - h_0)\,, \quad \sigma \geq 0, \tag{7.6a}$$

$$\sigma = K_{\mathrm{N}}^{-}(h - h_0)\,, \quad \sigma < 0 \tag{7.6b}$$

was used by Shui et al. [18], which accompanies switching of the interfacial stiffness when the normal stress changes between tension and compression. Another piecewise linear spring-type interface model incorporating perfect closure and perfect opening was used by Wu [19].

With the above models, however, it is not possible to describe the pressure-dependent reflection/transmission characteristics of contacting interfaces commonly observed experimentally. Based on the Hertz contact of asperities with the statistical

distribution of the radius of curvature and height, Pecorari [20] proposed the following boundary conditions at a contacting interface:

$$p - p_0 = -K_{\mathrm{N}}\,(h - h_0) + K_{\mathrm{NN}}(h - h_0)^2, \tag{7.7a}$$

$$\tau = K_{\mathrm{T}} s - K_{\mathrm{NT}}\,(h - h_0)\,s - \frac{1}{2}K'_{\mathrm{T}}\left\{\left(s^2 - s_{\max}^2\right)\mathrm{sgn}\,(\partial s/\partial t) + s_{\max} s\right\}, \tag{7.7b}$$

where K'_{T} is a constant of the interface and $s_{\max}$ is the maximum positive sliding displacement during the loading cycle. The function $\mathrm{sgn}(\partial s/\partial t)$ is defined to be 1 (or -1) when $\partial s/\partial t$ is positive (or negative). Equation (7.7a) can be obtained from Eq. (7.2a) when the term with the constant K_{TT} is dropped. On the other hand, Eq. (7.7b) contains an additional term with the constant K'_{T}, which represents a hysteretic response of the interface for sliding displacements. As shown by Pecorari [20], this additional term affects the nonlinear ultrasonic response of the contacting interface by giving the generation of the third and higher odd-order harmonics. The relation given by Eq. (7.7a) has been used by several authors [21–24] to analyze the nonlinear response of a contacting interface subjected to normal incidence of longitudinal waves. Furthermore, the effect of adhesive force has been considered by Gusev et al. [25] and Gusev [26] using a bistable interface model, which leads to certain hysteretic responses to acoustic waves.

In this chapter, the interaction of ultrasonic waves with contacting interfaces modeled by Eqs. (7.2a) and (7.2b) is considered. To this purpose, it is assumed that Eqs. (7.2a) and (7.2b) hold not only in the case of static loading of contacting bodies but also in the case of dynamic loading by incident waves. Hysteresis and adhesion are thus not accounted for in the analysis. It is noted that in order to justify the use of the model without hysteresis, the supporting asperities should be already flattened in the previous loading history and show elastic responses with minimal elasto-plastic or frictional effects.

Suppose that two solid bodies in contact are in static equilibrium with the nominal contact pressure $p = -\sigma = p_0$ and the vanishing shear stress $\tau = 0$. At this equilibrium, the gap distance is h_0 and the relative sliding displacement is set as $s = 0$. An elastic wave impinging on the contacting interface brings about time-dependent change of the gap distance and sliding, i.e., $h(t)$ and $s(t)$, which are related to the normal stress $\sigma(t)$ and the shear stress $\tau(t)$ on the contacting surfaces given by Eqs. (7.2a) and (7.2b). In this chapter, the contacting bodies are assumed to be the same homogeneous, isotropic, and linear elastic half-spaces. Therefore, the motions in the contacting bodies are governed by linear elastodynamic field equations: the nonlinearity only lies in the boundary conditions at the interface, Eqs. (7.2a) and (7.2b). In the following sections, some representative cases of the interaction of elastic waves with the nonlinear spring-type interface are considered.

7.2 Second-Harmonic Generation by Plane Longitudinal Wave at Normal Incidence

7.2.1 Time-Domain Formulation

The one-dimensional problem of normal incidence of time-harmonic longitudinal wave on the nonlinear spring-type interface between two identical elastic bodies (density ρ and longitudinal wave speed c_L) is first considered. The following formulation basically follows the approach presented by Biwa et al. [21], but similar problems are also analyzed by, e.g., Pecorari [20], Gusev et al. [25], Kim and Lee [23]. As shown in Fig. 7.2, the x-axis is taken along the propagation direction and the interface is located at $x = 0$. The governing equation is given by the following uniaxial stress–strain relation and the equation of motion in the absence of body force,

$$\sigma = -p_0 + \rho {c_\mathrm{L}}^2 \frac{\partial u}{\partial x}, \quad \rho \frac{\partial^2 u}{\partial t^2} = \frac{\partial \sigma}{\partial x}, \tag{7.8}$$

where $u(x,t)$ is the longitudinal displacement of the wave and $\sigma(x,t)$ is the sum of the constant static pressure p_0 and the normal stress associated with the wave. Combining the two equations gives the linear wave equation,

$$\frac{\partial^2 u}{\partial t^2} = {c_\mathrm{L}}^2 \frac{\partial^2 u}{\partial x^2}. \tag{7.9}$$

The incident wave propagating in the positive direction of x-axis is a solution of the above equation and can be expressed as $u^{\mathrm{inc}}(x,t) = F(x - c_\mathrm{L}t)$ in d'Alembert's form. Its interaction with the interface gives rise to the reflected wave $u^{\mathrm{ref}}(x,t) = G(x + c_\mathrm{L}t)$ and the transmitted wave $u^{\mathrm{tra}}(x,t) = H(x - c_\mathrm{L}t)$, respectively. The displacement and stress fields are then given by

$$u\,(x,t) = \begin{cases} F\,(x - c_\mathrm{L}t) + G\,(x + c_\mathrm{L}t)\,, & x < 0, \\ H\,(x - c_\mathrm{L}t)\,, & x > 0, \end{cases} \tag{7.10}$$

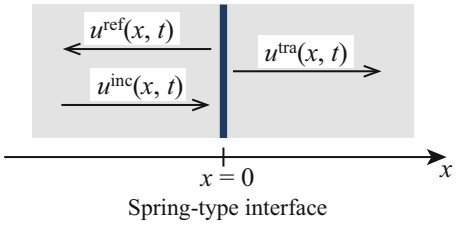

Fig. 7.2 Reflection and transmission of longitudinal wave at a spring-type interface

$$\sigma(x,t) = \begin{cases} -p_0 + \rho {c_\mathrm{L}}^2 \left\{ F'(x - c_\mathrm{L} t) + G'(x + c_\mathrm{L} t) \right\}, & x < 0, \\ -p_0 + \rho {c_\mathrm{L}}^2 H'(x - c_\mathrm{L} t), & x > 0, \end{cases} \tag{7.11}$$

where the superscript $(\quad)'$ denotes differentiation of a function with respect to its argument.

The wave motion causes dynamic variation of the gap distance $h(t)$ accompanied by the change in the normal stress, but no relative slip displacement, i.e., $s = 0$ and $\tau = 0$ in Eqs. (7.2a) and (7.2b). The boundary conditions at $x = 0$ are given by

$$\sigma\left(0^+, t\right) = \sigma\left(0^-, t\right) = -p_0 + K_\mathrm{N} \xi(t) - K_\mathrm{NN} \xi(t)^2, \tag{7.12}$$

from Eq. (7.8), where

$$\xi(t) = h(t) - h_0 = u\left(0^+, t\right) - u\left(0^-, t\right) \tag{7.13}$$

is the time-dependent change of gap distance. Combining Eq. (7.11) and $(7.12)_1$ gives

$$F'(-c_\mathrm{L} t) + G'(c_\mathrm{L} t) = H'(-c_\mathrm{L} t). \tag{7.14}$$

Substituting Eq. (7.10) in Eq. (7.13), differentiating with respect to t, and using Eq. (7.14) gives

$$\frac{\mathrm{d}\xi}{\mathrm{d}t} = 2 c_\mathrm{L} \left\{ F'(-c_\mathrm{L} t) - H'(-c_\mathrm{L} t) \right\}. \tag{7.15}$$

Substitution of the last expression in Eq. $(7.12)_2$ gives the following nonlinear first-order ordinary differential equation for $\xi(t)$,

$$\frac{\mathrm{d}\xi}{\mathrm{d}t} = 2 c_\mathrm{L} F'(-c_\mathrm{L} t) - \frac{2}{\rho c_\mathrm{L}} \left\{ K_\mathrm{N} \xi(t) - K_\mathrm{NN} \xi(t)^2 \right\}, \tag{7.16}$$

when the incident waveform is given explicitly. If once $\xi(t)$ is determined, the reflected and transmitted waves are given by

$$u^\mathrm{ref}(x,t) = G(x + c_\mathrm{L} t) = -\frac{1}{2} \xi\left(t + x/c_\mathrm{L}\right), \tag{7.17a}$$

$$u^\mathrm{tra}(x,t) = H(x - c_\mathrm{L} t) = F(x - c_\mathrm{L} t) + \frac{1}{2} \xi\left(t - x/c_\mathrm{L}\right), \tag{7.17b}$$

respectively, where the integration constants are arbitrarily set as zero.

In the following, the incident wave is assumed to be time-harmonic and characterized by the amplitude A_0 and the angular frequency ω_0,

$$u^{\text{inc}}(x,t) = A_0 \cos\left\{\omega_0 (x - c_{\text{L}} t)/c_{\text{L}}\right\}. \tag{7.18}$$

Then, Eq. (7.16) is reduced to

$$\frac{\mathrm{d}\xi}{\mathrm{d}t} = 2\omega_0 \left[A_0 \sin\omega_0 t - \kappa_{\text{N}} \left\{\xi(t) - \beta\xi(t)^2\right\}\right], \tag{7.19}$$

where the constants κ_{N} and β are defined by

$$\kappa_{\text{N}} = \frac{K_{\text{N}}}{\rho c_{\text{L}} \omega_0}, \quad \beta = \frac{K_{\text{NN}}}{K_{\text{N}}}. \tag{7.20}$$

7.2.2 *Perturbation Analysis*

In order to carry out a perturbation analysis of the nonlinear equation in Eq. (7.19), the following non-dimensional variables are introduced,

$$\tilde{\xi} = \frac{\xi}{A_0}, \quad \tilde{t} = \omega_0 t, \quad \varepsilon = A_0 \beta, \tag{7.21}$$

and the parameter ε is assumed to be a sufficiently small quantity. Using these non-dimensional variables, Eq. (7.19) is rewritten as

$$\frac{\mathrm{d}\tilde{\xi}}{\mathrm{d}\tilde{t}} = 2\sin\tilde{t} - 2\kappa_{\text{N}} \left\{1 - \varepsilon\, \tilde{\xi}\left(\tilde{t}\right)\right\} \tilde{\xi}\left(\tilde{t}\right). \tag{7.22}$$

Now the following power expansion is assumed for $\tilde{\xi}\left(\tilde{t}\right)$,

$$\tilde{\xi}\left(\tilde{t}\right) = \tilde{\xi}_1\left(\tilde{t}\right) + \varepsilon\, \tilde{\xi}_2\left(\tilde{t}\right) + \varepsilon^2\, \tilde{\xi}_3\left(\tilde{t}\right) + \cdots. \tag{7.23}$$

Equation (7.23) is substituted in Eq. (7.22) and the terms are arranged in the same order in ε to yield

$$\varepsilon^0; \quad \frac{\mathrm{d}\tilde{\xi}_1}{\mathrm{d}\tilde{t}} + 2\kappa_{\text{N}}\tilde{\xi}_1 = 2\sin\tilde{t}, \tag{7.24}$$

$$\varepsilon^1; \quad \frac{\mathrm{d}\tilde{\xi}_2}{\mathrm{d}\tilde{t}} + 2\kappa_{\text{N}}\tilde{\xi}_2 = 2\kappa_{\text{N}}\tilde{\xi}_1^2, \tag{7.25}$$

$$\varepsilon^2; \quad \frac{\mathrm{d}\tilde{\xi}_3}{\mathrm{d}\tilde{t}} + 2\kappa_{\text{N}}\tilde{\xi}_3 = 4\kappa_{\text{N}}\tilde{\xi}_1\tilde{\xi}_2, \tag{7.26}$$

and so on. Then, each function $\tilde{\xi}_m(t)$ in Eq. (7.23) can be obtained by solving Eqs. (7.24) and the others one by one from the lowest order in ε. In dimensional variables, Eq. (7.23) gives

$$\xi = A_0\tilde{\xi}_1 + \beta {A_0}^2\tilde{\xi}_2 + \beta^2 {A_0}^3\tilde{\xi}_3 + \cdots, \tag{7.27}$$

which indicates that $\xi_1(t) = A_0\tilde{\xi}_1(\omega_0 t)$ represents the linear response whose amplitude is proportional to the incident wave amplitude A_0, and $\xi_2(t) = \beta {A_0}^2\tilde{\xi}_2(\omega_0 t)$ represents the quadratic nonlinear response in proportion to ${A_0}^2$ which contains the effect of the contact nonlinearity.

The solution to Eq. (7.24) is given by

$$\begin{aligned} \tilde{\xi}_1 &= -\frac{2}{\sqrt{1+4{\kappa_\mathrm{N}}^2}}\cos\left(\tilde{t}+\alpha_1\right), \\ \cos\alpha_1 &= \frac{1}{\sqrt{1+4{\kappa_\mathrm{N}}^2}}, \quad \sin\alpha_1 = \frac{2\kappa_\mathrm{N}}{\sqrt{1+4{\kappa_\mathrm{N}}^2}}, \end{aligned} \tag{7.28}$$

or

$$\xi_1(t) = -\frac{2A_0}{\sqrt{1+4{\kappa_\mathrm{N}}^2}}\cos\left(\omega_0 t+\alpha_1\right) \tag{7.29}$$

in dimensional variables, which depends only on the linear property of the interface.

The quadratic nonlinear response is obtained from Eq. (7.25) which reduces to

$$\frac{\mathrm{d}\tilde{\xi}_2}{\mathrm{d}\tilde{t}} + 2\kappa_\mathrm{N}\tilde{\xi}_2 = \frac{8\kappa_\mathrm{N}}{1+4{\kappa_\mathrm{N}}^2}\cos^2\left(\tilde{t}+\alpha_1\right), \tag{7.30}$$

The solution is given by

$$\begin{aligned} \tilde{\xi}_2 &= \frac{2}{1+4{\kappa_\mathrm{N}}^2} + \frac{2\kappa_\mathrm{N}}{\left(1+4{\kappa_\mathrm{N}}^2\right)\sqrt{1+{\kappa_\mathrm{N}}^2}}\cos\left(2\tilde{t}+2\alpha_1-\alpha_2\right), \\ \cos\alpha_2 &= \frac{\kappa_\mathrm{N}}{\sqrt{1+{\kappa_\mathrm{N}}^2}}, \quad \sin\alpha_2 = \frac{1}{\sqrt{1+{\kappa_\mathrm{N}}^2}}, \end{aligned} \tag{7.31}$$

or, in dimensional variables,

$$\xi_2(t) = \frac{2\beta {A_0}^2}{1+4{\kappa_\mathrm{N}}^2} + \frac{2\beta\kappa_\mathrm{N}{A_0}^2}{\left(1+4{\kappa_\mathrm{N}}^2\right)\sqrt{1+{\kappa_\mathrm{N}}^2}}\cos\left(2\omega_0 t+2\alpha_1-\alpha_2\right). \tag{7.32}$$

This expression shows that the quadratic nonlinear response of the interface contains the stationary (DC) term ($\omega = 0$) and the second-harmonic ($\omega = 2\omega_0$) of the incident wave. As a result,

$$\xi(t) = \xi_1(t) + \xi_2(t) = A_0\tilde{\xi}_1(\omega_0 t) + \beta {A_0}^2 \tilde{\xi}_2(\omega_0 t) \tag{7.33}$$

gives the gap opening of the interface in the approximation up to the second order in the small parameter ε.

In dimensional variables, the reflected and transmitted waves are given by

$$u^{\mathrm{ref}}(x,t) = -\frac{\beta {A_0}^2}{1+4{\kappa_{\mathrm{N}}}^2} + \frac{A_0}{\sqrt{1+4{\kappa_{\mathrm{N}}}^2}}\cos(\omega_0 x/c_{\mathrm{L}} + \omega_0 t + \alpha_1) - \frac{\beta \kappa_{\mathrm{N}} {A_0}^2}{\left(1+4{\kappa_{\mathrm{N}}}^2\right)\sqrt{1+{\kappa_{\mathrm{N}}}^2}}\cos(2\omega_0 x/c_{\mathrm{L}} + 2\omega_0 t + 2\alpha_1 - \alpha_2) \tag{7.34a}$$

$$u^{\mathrm{tra}}(x,t) = \frac{\beta {A_0}^2}{1+4{\kappa_{\mathrm{N}}}^2} - \frac{2A_0\kappa_{\mathrm{N}}}{\sqrt{1+4{\kappa_{\mathrm{N}}}^2}}\sin(\omega_0 x/c_{\mathrm{L}} - \omega_0 t - \alpha_1) + \frac{\beta \kappa_{\mathrm{N}} {A_0}^2}{\left(1+4{\kappa_{\mathrm{N}}}^2\right)\sqrt{1+{\kappa_{\mathrm{N}}}^2}}\cos(2\omega_0 x/c_{\mathrm{L}} - 2\omega_0 t - 2\alpha_1 + \alpha_2) \tag{7.34b}$$

up to the second order in the parameter ε (these expressions are equivalent to Eqs. (7.17a) and (7.17b) of Biwa et al. [21] when $X_+ = X_- = 0$ therein). From these expressions, the fundamental amplitudes in the reflected and transmitted waves are given by

$$A_1^{\mathrm{ref}} = \frac{A_0}{\sqrt{1+4{\kappa_{\mathrm{N}}}^2}}, \quad A_1^{\mathrm{tra}} = \frac{2A_0\kappa_{\mathrm{N}}}{\sqrt{1+4{\kappa_{\mathrm{N}}}^2}}. \tag{7.35}$$

The second-harmonic components in the reflected and transmitted waves have the following amplitudes

$$A_2^{\mathrm{ref}} = A_2^{\mathrm{tra}} = \frac{\beta \kappa_{\mathrm{N}} {A_0}^2}{\left(1+4{\kappa_{\mathrm{N}}}^2\right)\sqrt{1+{\kappa_{\mathrm{N}}}^2}}, \tag{7.36}$$

For practical applications, the ratio of the second-harmonic amplitude to the square of the fundamental amplitude is often used as an effective measure of harmonic generation. For the reflected and transmitted waves, this ratio is given by

$$\frac{A_2^{\mathrm{ref}}}{\left(A_1^{\mathrm{ref}}\right)^2} = \frac{\beta\kappa_{\mathrm{N}}}{\sqrt{1+{\kappa_{\mathrm{N}}}^2}}, \quad \frac{A_2^{\mathrm{tra}}}{\left(A_1^{\mathrm{tra}}\right)^2} = \frac{\beta}{4\kappa_{\mathrm{N}}\sqrt{1+{\kappa_{\mathrm{N}}}^2}}, \tag{7.37}$$

whose right-hand sides are independent of the amplitude of the incident wave. In Sect. 7.5, the validity of the above expressions is examined from an experimental point of view.

7.2.3 Frequency-Domain Analysis

The results in the previous section for the incidence of time-harmonic waves can also be derived by formulating the problem in the frequency domain. This type of formulation can be more convenient for the problems of oblique incidence on the interface considered below, and multilayered structures with nonlinear spring-type interfaces [27].

The governing equations for the interaction of a normally incident longitudinal wave with a nonlinear spring-type interface between identical elastic media are summarized as

$$\frac{\partial^2 u}{\partial t^2} = {c_\mathrm{L}}^2 \frac{\partial^2 u}{\partial x^2}, \tag{7.38a}$$

$$\rho {c_\mathrm{L}}^2 \frac{\partial u}{\partial x}\left(0^+, t\right) = \rho {c_\mathrm{L}}^2 \frac{\partial u}{\partial x}\left(0^-, t\right) = K_\mathrm{N}\xi(t) - K_\mathrm{NN}\xi(t)^2, \tag{7.38b}$$

$$\xi(t) = u\left(0^+, t\right) - u\left(0^-, t\right). \tag{7.38c}$$

According to the perturbation analysis presented in the previous section, the displacement field can be decomposed as the sum of two solutions $u(x,t) = u_1(x,t) + u_2(x,t)$ up to the second order of small parameter ε. The linear response is characterized by $u_1(x,t)$, which is governed by

$$\frac{\partial^2 u_1}{\partial t^2} = {c_\mathrm{L}}^2 \frac{\partial^2 u_1}{\partial x^2}, \tag{7.39a}$$

$$\rho {c_\mathrm{L}}^2 \frac{\partial u_1}{\partial x}\left(0^+, t\right) = \rho {c_\mathrm{L}}^2 \frac{\partial u_1}{\partial x}\left(0^-, t\right) = K_\mathrm{N}\xi_1(t), \tag{7.39b}$$

$$\xi_1(t) = u_1\left(0^+, t\right) - u_1\left(0^-, t\right), \tag{7.39c}$$

and the incident wave of the form given by Eq. (7.18). The quadratic nonlinear response is given by $u_2(x,t)$, which is governed by

$$\frac{\partial^2 u_2}{\partial t^2} = {c_\mathrm{L}}^2 \frac{\partial^2 u_2}{\partial x^2}, \tag{7.40a}$$

$$\rho {c_{\mathrm{L}}}^2 \frac{\partial u_2}{\partial x}\left(0^+, t\right) = \rho {c_{\mathrm{L}}}^2 \frac{\partial u_2}{\partial x}\left(0^-, t\right) = K_{\mathrm{N}} \xi_2(t) - K_{\mathrm{NN}} \xi_1(t)^2, \tag{7.40b}$$

$$\xi_2(t) = u_2\left(0^+, t\right) - u_2\left(0^-, t\right). \tag{7.40c}$$

The first problem given by Eqs. (7.39a), (7.39b), and (7.39c) can be converted to the frequency domain by introducing the following complex-value representation

$$u_1(x, t) = \mathrm{Re}\left[U_1(x) \exp\left(-\mathrm{i}\omega_0 t\right)\right], \tag{7.41a}$$

$$\xi_1(t) = \mathrm{Re}\left[\Xi_1 \exp\left(-\mathrm{i}\omega_0 t\right)\right], \tag{7.41b}$$

where i denotes the imaginary unit. Then the frequency-domain displacement field $U_1(x)$ is governed by

$$\frac{\mathrm{d}^2 U_1}{\mathrm{d}x^2} + \frac{{\omega_0}^2}{{c_{\mathrm{L}}}^2} U_1 = 0, \tag{7.42a}$$

$$\rho {c_{\mathrm{L}}}^2 \frac{\mathrm{d}U_1}{\mathrm{d}x}\left(0^+\right) = \rho {c_{\mathrm{L}}}^2 \frac{\mathrm{d}U_1}{\mathrm{d}x}\left(0^-\right) = K_{\mathrm{N}} \Xi_1, \tag{7.42b}$$

$$\Xi_1 = U_1\left(0^+\right) - U_1\left(0^-\right), \tag{7.42c}$$

with the incident wave

$${U_1}^{\mathrm{inc}}(x) = A_0 \exp\left(\mathrm{i}\omega_0 x / c_{\mathrm{L}}\right). \tag{7.43}$$

The displacement field $U_1(x)$ is given by the sum of the forward-propagating wave $U_{1\mathrm{F}}(x) \propto \exp\left(\mathrm{i}\omega_0 x / c_{\mathrm{L}}\right)$ and the backward-propagating wave $U_{1\mathrm{B}}(x) \propto \exp\left(-\mathrm{i}\omega_0 x / c_{\mathrm{L}}\right)$, i.e.,

$$U_1(x) = U_{1\mathrm{F}}(x) + U_{1\mathrm{B}}(x). \tag{7.44}$$

The boundary condition of Eq. (7.42b) is rewritten as

$$\begin{aligned} &\mathrm{i}\left\{U_{1\mathrm{F}}\left(0^+\right) - U_{1\mathrm{B}}\left(0^+\right)\right\} = \mathrm{i}\left\{U_{1\mathrm{F}}\left(0^-\right) - U_{1\mathrm{B}}\left(0^-\right)\right\} \\ &= \kappa_{\mathrm{N}}\left\{U_{1\mathrm{F}}\left(0^+\right) + U_{1\mathrm{B}}\left(0^+\right) - U_{1\mathrm{F}}\left(0^-\right) - U_{1\mathrm{B}}\left(0^-\right)\right\}, \end{aligned} \tag{7.45}$$

where κ_{N} is defined in Eq. (7.20). The above two equations can be rearranged to yield

$$\begin{pmatrix} U_{1\mathrm{F}}(0^+) \\ U_{1\mathrm{B}}(0^+) \end{pmatrix} = \begin{bmatrix} 1+\frac{1}{2}\mathrm{i}/\kappa_{\mathrm{N}} & -\frac{1}{2}\mathrm{i}/\kappa_{\mathrm{N}} \\ \frac{1}{2}\mathrm{i}/\kappa_{\mathrm{N}} & 1-\frac{1}{2}\mathrm{i}/\kappa_{\mathrm{N}} \end{bmatrix} \begin{pmatrix} U_{1\mathrm{F}}(0^-) \\ U_{1\mathrm{B}}(0^-) \end{pmatrix}, \tag{7.46}$$

in a matrix form.

The forward and backward waves can be assumed to have the following forms (see Fig. 7.3a):

$$U_{1\mathrm{F}}(x) = \begin{cases} U_{1\mathrm{F}}^-(x) = A_0 \exp\left(\mathrm{i}\omega_0 x/c_{\mathrm{L}}\right), & x < 0 \\ U_{1\mathrm{F}}^+(x) = T_{\mathrm{L}} A_0 \exp\left(\mathrm{i}\omega_0 x/c_{\mathrm{L}}\right), & x > 0 \end{cases} \tag{7.47}$$

$$U_{1\mathrm{B}}(x) = \begin{cases} U_{1\mathrm{B}}^-(x) = R_{\mathrm{L}} A_0 \exp\left(-\mathrm{i}\omega_0 x/c_{\mathrm{L}}\right), & x < 0 \\ 0, & x > 0 \end{cases} \tag{7.48}$$

where R_{L} and T_{L} are the complex reflection and transmission coefficients, respectively. Then Eq. (7.46) reduces to

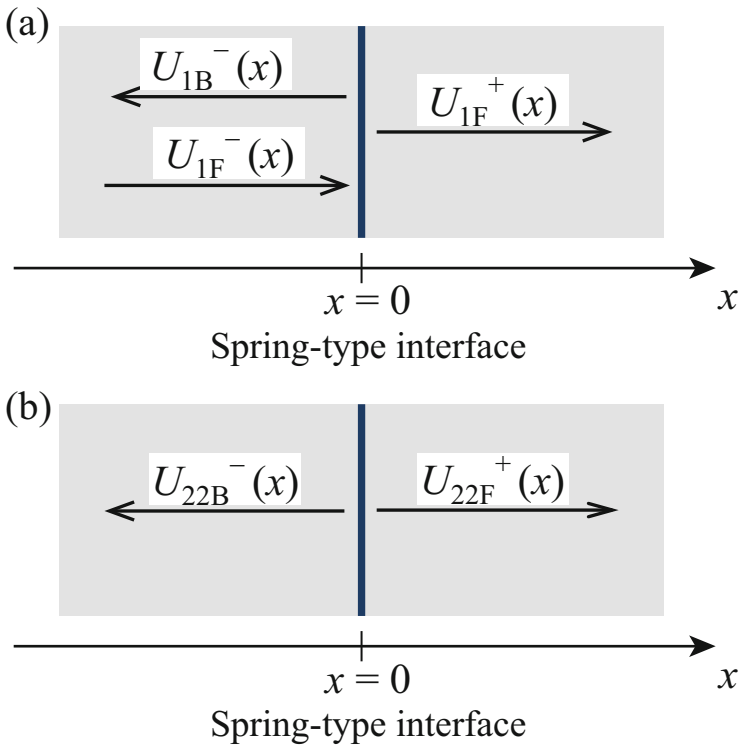

Fig. 7.3 (**a**) The fundamental and (**b**) the second-harmonic components associated with the interaction of normal-incidence longitudinal wave with the nonlinear spring-type interface

$$\begin{pmatrix} T_{\mathrm{L}}A_0 \\ 0 \end{pmatrix} = \begin{bmatrix} 1+\frac{1}{2}\mathrm{i}/\kappa_{\mathrm{N}} & -\frac{1}{2}\mathrm{i}/\kappa_{\mathrm{N}} \\ \frac{1}{2}\mathrm{i}/\kappa_{\mathrm{N}} & 1-\frac{1}{2}\mathrm{i}/\kappa_{\mathrm{N}} \end{bmatrix} \begin{pmatrix} A_0 \\ R_{\mathrm{L}}A_0 \end{pmatrix}, \tag{7.49}$$

which immediately yields

$$R_{\mathrm{L}} = \frac{1}{1+2\mathrm{i}\kappa_{\mathrm{N}}}, \quad T_{\mathrm{L}} = \frac{2\mathrm{i}\kappa_{\mathrm{N}}}{1+2\mathrm{i}\kappa_{\mathrm{N}}}. \tag{7.50}$$

These results are equivalent to Eq. (7.35).

From the above solution, the gap change is given by

$$\Xi_1 = \{T_{\mathrm{L}} - (1+R_{\mathrm{L}})\}\, A_0 = -\frac{2A_0}{1+2\mathrm{i}\kappa_{\mathrm{N}}} = -\frac{2A_0}{\sqrt{1+4{\kappa_{\mathrm{N}}}^2}} \exp\left(-\mathrm{i}\alpha_1\right), \tag{7.51}$$

in the frequency domain and by

$$\xi_1(t) = -\frac{2A_0}{\sqrt{1+4{\kappa_{\mathrm{N}}}^2}} \cos\left(\omega_0 t + \alpha_1\right), \tag{7.52}$$

in the time domain, where α_1 is defined by Eq. (7.28). Its square appearing in Eq. (7.40b) yields

$$\xi_1(t)^2 = \frac{4{A_0}^2}{1+4{\kappa_{\mathrm{N}}}^2}\cos^2\left(\omega_0 t + \alpha_1\right) = \frac{2{A_0}^2}{1+4{\kappa_{\mathrm{N}}}^2}\left\{1+\cos\left(2\omega_0 t + 2\alpha_1\right)\right\}. \tag{7.53}$$

Therefore, the driving force for the secondary wave contains the stationary term ($\omega = 0$) and the second-harmonic term ($\omega = 2\omega_0$). The problem of Eqs. (7.40a), (7.40b), and (7.40c) further reduces to the following two problems for $\omega = 0$ and $\omega = 2\omega_0$.

The stationary component $U_{21}(x)$ is governed by

$$\frac{\mathrm{d}^2 U_{21}}{\mathrm{d}x^2} = 0, \tag{7.54a}$$

$$\rho {c_{\mathrm{L}}}^2 \frac{\mathrm{d}U_{21}}{\mathrm{d}x}\left(0^+\right) = \rho {c_{\mathrm{L}}}^2 \frac{\mathrm{d}U_{21}}{\mathrm{d}x}\left(0^-\right) = K_{\mathrm{N}}\Xi_{21} - \frac{2K_{\mathrm{NN}}{A_0}^2}{1+4{\kappa_{\mathrm{N}}}^2}, \tag{7.54b}$$

$$\Xi_{21} = U_{21}\left(0^+\right) - U_{21}\left(0^-\right). \tag{7.54c}$$

From Eq. (7.54a) and for the boundedness of the solution, $U_{21}(x)$ is constant for each of $x < 0$ and $x > 0$. Then Eq. (7.54b) gives

$$\Xi_{21} = \frac{2\beta {A_0}^2}{1+4{\kappa_{\mathrm{N}}}^2}, \tag{7.55}$$

which corresponds to the stationary opening of the interface, in consistency with the first term on the right-hand side of Eq. (7.32).

The second-harmonic component $U_{22}(x)$ is governed by

$$\frac{\mathrm{d}^2 U_{22}}{\mathrm{d}x^2} + \frac{(2\omega_0)^2}{{c_\mathrm{L}}^2} U_{22} = 0, \tag{7.56a}$$

$$\rho {c_\mathrm{L}}^2 \frac{\mathrm{d}U_{22}}{\mathrm{d}x}\left(0^+\right) = \rho {c_\mathrm{L}}^2 \frac{\mathrm{d}U_{22}}{\mathrm{d}x}\left(0^-\right) = K_\mathrm{N} \Xi_{22} - \frac{2K_\mathrm{NN} {A_0}^2}{1+4{\kappa_\mathrm{N}}^2} \exp\left(-2\mathrm{i}\alpha_1\right), \tag{7.56b}$$

$$\Xi_{22} = U_{22}\left(0^+\right) - U_{22}\left(0^-\right). \tag{7.56c}$$

Again, the second-harmonic wave field $U_{22}(x)$ can be expressed as the sum of the forward and the backward waves, $U_{22}(x) = U_{22\mathrm{F}}(x) + U_{22\mathrm{B}}(x)$, and Eq. (7.56b) is rewritten as

$$\begin{aligned} &2\mathrm{i}\rho c_\mathrm{L}\omega_0 \left\{U_{22\mathrm{F}}\left(0^+\right) - U_{22\mathrm{B}}\left(0^+\right)\right\} = 2\mathrm{i}\rho c_\mathrm{L}\omega_0 \left\{U_{22\mathrm{F}}\left(0^-\right) - U_{22\mathrm{B}}\left(0^-\right)\right\} \\ &= K_\mathrm{N}\left\{U_{22\mathrm{F}}\left(0^+\right) + U_{22\mathrm{B}}\left(0^+\right) - U_{22\mathrm{F}}\left(0^-\right) - U_{22\mathrm{B}}\left(0^-\right)\right\} \\ &-\frac{2K_\mathrm{NN} {A_0}^2}{1+4{\kappa_\mathrm{N}}^2} \exp\left(-2\mathrm{i}\alpha_1\right). \end{aligned} \tag{7.57}$$

These equations can be cast in the following matrix form:

$$\begin{pmatrix} U_{22\mathrm{F}}\left(0^+\right) \\ U_{22\mathrm{B}}\left(0^+\right) \end{pmatrix} = \begin{bmatrix} 1+\mathrm{i}/\kappa_\mathrm{N} & -\mathrm{i}/\kappa_\mathrm{N} \\ \mathrm{i}/\kappa_\mathrm{N} & 1-\mathrm{i}/\kappa_\mathrm{N} \end{bmatrix} \begin{pmatrix} U_{22\mathrm{F}}\left(0^-\right) \\ U_{22\mathrm{B}}\left(0^-\right) \end{pmatrix} + \frac{\beta {A_0}^2}{1+4{\kappa_\mathrm{N}}^2} \exp\left(-2\mathrm{i}\alpha_1\right) \begin{pmatrix} 1 \\ 1 \end{pmatrix}, \tag{7.58}$$

The second-harmonic component is generated at the interface, and radiated into both directions (see Fig. 7.3b). The physically reasonable form for the second-harmonic field satisfies $U_{22\mathrm{F}}(0^-) = 0$ and $U_{22\mathrm{B}}(0^+) = 0$. Substituting these into Eq. (7.58) directly leads to

$$U_{22\mathrm{B}}\left(0^-\right) = -\frac{\beta\kappa_\mathrm{N} {A_0}^2}{\left(1+4{\kappa_\mathrm{N}}^2\right)\sqrt{1+{\kappa_\mathrm{N}}^2}} \exp\left\{-\mathrm{i}\left(2\alpha_1 - \alpha_2\right)\right\}, \tag{7.59a}$$

$$U_{22\mathrm{F}}\left(0^+\right) = \frac{\beta\kappa_\mathrm{N} {A_0}^2}{\left(1+4{\kappa_\mathrm{N}}^2\right)\sqrt{1+{\kappa_\mathrm{N}}^2}} \exp\left\{-\mathrm{i}\left(2\alpha_1 - \alpha_2\right)\right\}, \tag{7.59b}$$

where α_2 is defined in Eq. (7.31). The second-harmonic field is given by

$$U_{22\mathrm{F}}(x) = \begin{cases} 0, & x < 0 \\ U^{+}_{22\mathrm{F}}(x) = U_{22\mathrm{F}}\left(0^{+}\right) \exp\left(2\mathrm{i}\omega_0 x/c_{\mathrm{L}}\right), & x > 0 \end{cases}, \tag{7.60a}$$

$$U_{22\mathrm{B}}(x) = \begin{cases} U^{-}_{22\mathrm{B}}(x) = U_{22\mathrm{B}}\left(0^{-}\right) \exp\left(-2\mathrm{i}\omega_0 x/c_{\mathrm{L}}\right), & x < 0 \\ 0, & x > 0 \end{cases} \tag{7.60b}$$

As a consequence, the time-domain displacement field in this approximation is given by

$$u\,(x,t) = U_{21}(x) + \mathrm{Re}\left[U_1(x) \exp\left(-\mathrm{i}\omega_0 t\right) + U_{22}(x) \exp\left(-2\mathrm{i}\omega_0 t\right)\right], \tag{7.61}$$

which coincides with the results Eqs. (7.34a) and (7.34b) derived in the time-domain formulation.

7.2.4 Note on the Power-Law Stiffness–Pressure Relation

The interfacial stiffness K_{N} defined in Eq. (7.3) is a function of the interface gap h_0, or equivalently, a function of the applied pressure p_0. The contact-pressure dependence of the interfacial stiffness has been studied by many investigators [3, 5, 15, 22, 28–30]. The experimental data show that the interfacial normal stiffness is an increasing function of the applied pressure. As one of the simplest forms to meet this property, a power-law pressure dependence of the stiffness is tentatively considered here, i.e.,

$$K_{\mathrm{N}} = C{p_0}^m, \tag{7.62}$$

where C and m are constants characteristic of the interface. A functional form of $\sigma(h,s)$ which is compatible with Eq. (7.62) is given by

$$\sigma\,(h,s) = \begin{cases} -\left\{{p_0}^{1-m} - (1-m)\,C\,(h-h_0)\right\}^{1/(1-m)} + g(s), & m \neq 1, \\ -\,p_0 \exp\left\{-C\,(h-h_0)\right\} + g(s), & m = 1, \end{cases} \tag{7.63}$$

where $g(s)$ is an even function of s with the property $g(0) = g'(0) = 0$. It should be noted that this relation is valid for the following range of h:

$$h < h_0 + \frac{{p_0}^{1-m}}{(1-m)\,C}, \quad \text{if} \quad m < 1, \tag{7.64a}$$

$$h > h_0 - \frac{{p_0}^{1-m}}{(m-1)\,C}, \quad \text{if} \quad m > 1. \tag{7.64b}$$

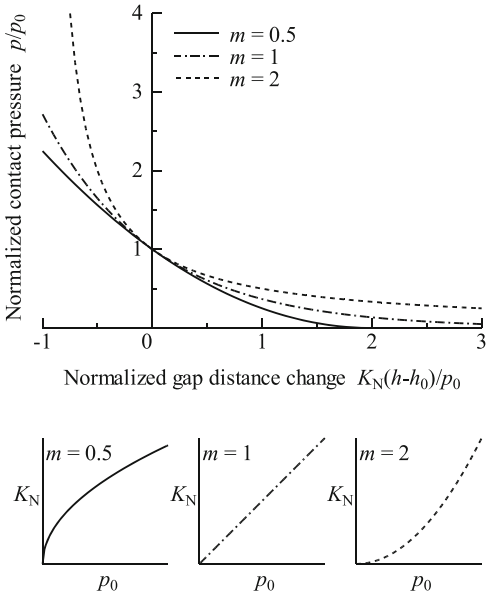

Fig. 7.4 Pressure–gap distance relation with power-law pressure-dependence of the interfacial stiffness

In Fig. 7.4, the relation of Eq. (7.63) when $s = 0$ is shown for different values of the parameter m.

The relation of Eq. (7.63) gives the nonlinear stiffness parameter K_{NN} as

$$K_{\mathrm{NN}} = \frac{1}{2} m C^2 {p_0}^{2m-1}. \tag{7.65}$$

Then, for relatively weak contact when $\kappa_{\mathrm{N}} \ll 1$, Eq. $(7.37)_2$ reduces to

$$\frac{A_2^{\mathrm{tra}}}{\left(A_1^{\mathrm{tra}}\right)^2} \approx \frac{m \rho c_{\mathrm{L}} \omega_0}{8 p_0}, \tag{7.66}$$

which predicts the inverse dependence on the applied static pressure, irrespective of the power-law exponent m. As shown in the analysis by Biwa et al. [21], the experimental data by Buck et al. [31] for contacting interfaces of aluminum blocks are in conformity with this inverse pressure dependence.

7.3 Second-Harmonic Generation by Plane Shear Wave at Normal Incidence

When a plane, time-harmonic transverse (shear) wave is incident on the interface in the normal direction, it gives rise to relative tangential motion $s(t)$. This motion

accompanies not only the shear stress but also the normal stress as implied by the boundary conditions in Eqs. (7.2a) and (7.2b), so the incident shear wave can couple with the longitudinal wave as an outcome of the nonlinear interaction. With the spirit of perturbation analysis similar to the previous section, the linear response is described by the following set of equations for the transverse displacement $v_1(x,t)$.

$$\frac{\partial^2 v_1}{\partial t^2} = {c_\mathrm{T}}^2 \frac{\partial^2 v_1}{\partial x^2}, \tag{7.67a}$$

$$\rho {c_\mathrm{T}}^2 \frac{\partial v_1}{\partial x}\left(0^+,t\right) = \rho {c_\mathrm{T}}^2 \frac{\partial v_1}{\partial x}\left(0^-,t\right) = K_\mathrm{T} s_1(t), \tag{7.67b}$$

$$s_1(t) = v_1\left(0^+,t\right) - v_1\left(0^-,t\right), \tag{7.67c}$$

where c_T is the shear wave speed. The time-harmonic incident wave is assumed to have the form

$$v^{\mathrm{inc}}(x,t) = B_0 \cos\left\{\omega_0 \left(x - c_\mathrm{T} t\right)/c_\mathrm{T}\right\}, \tag{7.68}$$

where B_0 is its amplitude. In the frequency domain, the solution is given as the sum of the forward and backward waves $V_1(x) = V_{1\mathrm{F}}(x) + V_{1\mathrm{B}}(x)$ with

$$V_{1\mathrm{F}}(x) = \begin{cases} V_{1\mathrm{F}}^-(x) = B_0 \exp\left(\mathrm{i}\omega_0 x/c_\mathrm{T}\right), & x < 0, \\ V_{1\mathrm{F}}^+(x) = T_\mathrm{T} B_0 \exp\left(\mathrm{i}\omega_0 x/c_\mathrm{T}\right), & x > 0, \end{cases} \tag{7.69a}$$

$$V_{1\mathrm{B}}(x) = \begin{cases} V_{1\mathrm{B}}^-(x) = R_\mathrm{T} B_0 \exp\left(-\mathrm{i}\omega_0 x/c_\mathrm{T}\right), & x < 0, \\ 0, & x > 0, \end{cases} \tag{7.69b}$$

in analogy with the analysis in Sect. 7.2.3, where R_T and T_T are the complex reflection and transmission coefficients of the shear wave, respectively (see Fig. 7.5a). With the boundary conditions in Eq. (7.67b), these coefficients are given by

$$R_\mathrm{T} = \frac{1}{1 + 2\mathrm{i}\kappa_\mathrm{T}}, \quad T_\mathrm{T} = \frac{2\mathrm{i}\kappa_\mathrm{T}}{1 + 2\mathrm{i}\kappa_\mathrm{T}}, \tag{7.70}$$

where

$$\kappa_\mathrm{T} = \frac{K_\mathrm{T}}{\rho c_\mathrm{T} \omega_0}. \tag{7.71}$$

The quadratic nonlinear response is given by the longitudinal displacement $u_2(x,t)$, which is governed by

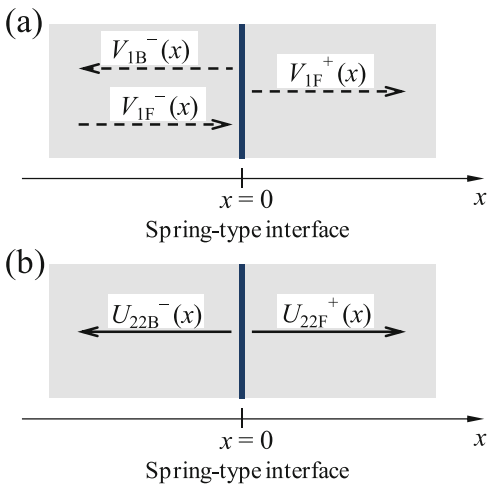

Fig. 7.5 (**a**) The fundamental and (**b**) the second-harmonic components associated with the interaction of normal-incidence shear wave with the nonlinear spring-type interface

$$\frac{\partial^2 u_2}{\partial t^2} = {c_\mathrm{L}}^2 \frac{\partial^2 u_2}{\partial x^2}, \tag{7.72a}$$

$$\rho {c_\mathrm{L}}^2 \frac{\partial u_2}{\partial x}\left(0^+, t\right) = \rho {c_\mathrm{L}}^2 \frac{\partial u_2}{\partial x}\left(0^-, t\right) = K_\mathrm{N}\xi_2(t) - K_\mathrm{TT} s_1(t)^2, \tag{7.72b}$$

$$\xi_2(t) = u_2\left(0^+, t\right) - u_2\left(0^-, t\right). \tag{7.72c}$$

Following the approach in Sect. 7.2.3, the frequency-domain solution for $u_2(x,t)$ is given by

$$U_2(x) = U_{21}(x) + U_{22}(x), \tag{7.73}$$

with the constant stationary displacement satisfying

$$U_{21}\left(0^+\right) - U_{21}\left(0^-\right) = \frac{2\gamma {B_0}^2}{1 + 4{\kappa_\mathrm{T}}^2}, \tag{7.74}$$

where

$$\gamma = \frac{K_\mathrm{TT}}{K_\mathrm{N}} \tag{7.75}$$

and the second-harmonic longitudinal displacement field

$$U_{22}(x) = \begin{cases} U_{22\mathrm{B}}^{-}(x) = -\frac{\gamma\kappa_{\mathrm{N}}{B_0}^2}{(1+4\kappa_{\mathrm{T}}{}^2)\sqrt{1+\kappa_{\mathrm{N}}{}^2}} \exp\{-\mathrm{i}\,(2\delta_1-\alpha_2)\} \exp\left(-2\mathrm{i}\omega_0 x/c_{\mathrm{L}}\right), & x<0, \\ U_{22\mathrm{F}}^{+}(x) = \frac{\gamma\kappa_{\mathrm{N}}{B_0}^2}{(1+4\kappa_{\mathrm{T}}{}^2)\sqrt{1+\kappa_{\mathrm{N}}{}^2}} \exp\{-\mathrm{i}\,(2\delta_1-\alpha_2)\} \exp\left(2\mathrm{i}\omega_0 x/c_{\mathrm{L}}\right), & x>0. \end{cases} \tag{7.76}$$

where

$$\cos\delta_1 = \frac{1}{\sqrt{1+4\kappa_{\mathrm{T}}{}^2}}, \quad \sin\delta_1 = \frac{2\kappa_{\mathrm{T}}}{\sqrt{1+4\kappa_{\mathrm{T}}{}^2}}. \tag{7.77}$$

The displacement fields are given by

$$v\,(x,t) = \mathrm{Re}\left[V_1(x)\exp\left(-\mathrm{i}\omega_0 t\right)\right], \tag{7.78a}$$

$$u\,(x,t) = U_{21}(x) + \mathrm{Re}\left[U_{22}(x)\exp\left(-2\mathrm{i}\omega_0 t\right)\right]. \tag{7.78b}$$

Namely, the interaction of a time-harmonic shear wave with the interface results in the fundamental reflected and transmitted shear waves, together with the stationary opening and the second-harmonic longitudinal waves radiated from the interface (see Fig. 7.5b).

The harmonic generation for the normal incidence of shear wave has been analyzed by Pecorari [20] using the model given by Eqs. (7.7a) and (7.7b). Due to the absence of the term with the coefficient K_{TT}, the model by Eqs. (7.7a) and (7.7b) does not predict the generation of the second-harmonic longitudinal waves. Instead, the hysteretic term in Eq. (7.7b) gives the occurrence of the odd-order harmonic shear waves.

7.4 Second-Harmonic Generation by Plane Longitudinal Wave at Oblique Incidence

7.4.1 Formulation

In this section, the interaction of plane time-harmonic elastic waves with the nonlinear spring-type interface is considered in the two-dimensional framework. Two identical semi-infinite isotropic, linear elastic solids are in contact at $x = 0$ as shown in Fig. 7.6. The governing equations are Navier's equations without body forces

$$\frac{\partial^2 u}{\partial t^2} = \left({c_{\mathrm{L}}}^2 - {c_{\mathrm{T}}}^2\right)\frac{\partial}{\partial x}\left(\frac{\partial u}{\partial x} + \frac{\partial v}{\partial y}\right) + {c_{\mathrm{T}}}^2\left(\frac{\partial^2}{\partial x^2} + \frac{\partial^2}{\partial y^2}\right)u, \tag{7.79a}$$

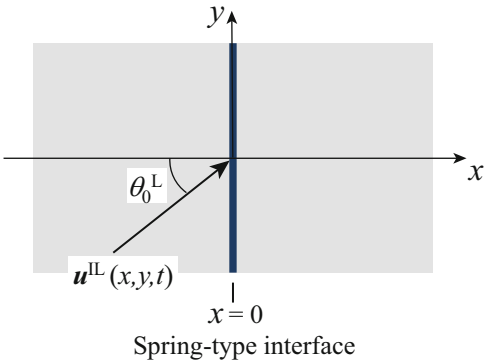

Fig. 7.6 Oblique incidence of plane longitudinal wave on a spring-type interface

$$\frac{\partial^2 v}{\partial t^2} = \left({c_{\mathrm{L}}}^2 - {c_{\mathrm{T}}}^2\right) \frac{\partial}{\partial y}\left(\frac{\partial u}{\partial x} + \frac{\partial v}{\partial y}\right) + {c_{\mathrm{T}}}^2 \left(\frac{\partial^2}{\partial x^2} + \frac{\partial^2}{\partial y^2}\right) v, \tag{7.79b}$$

for the displacement fields $u(x, y, t)$ and $v(x, y, t)$.

The incident wave is assumed to be a plane time-harmonic longitudinal wave of amplitude A_0 and angular frequency ω_0, whose displacement is written as

$$\mathbf{u}^{\mathrm{IL}}(x, y, t) = \begin{pmatrix} u^{\mathrm{IL}}(x, y, t) \\ v^{\mathrm{IL}}(x, y, t) \end{pmatrix} = A_0 \begin{pmatrix} n_x \\ n_y \end{pmatrix} \cos\left\{\omega_0 \left(n_x x + n_y y - c_{\mathrm{L}} t\right)/c_{\mathrm{L}}\right\}, \tag{7.80}$$

where $(n_x, n_y)^{\mathrm{T}}$ is a unit vector in the incident direction and related to the angle of incidence θ_0^{L} as

$$n_x = \cos\theta_0^{\mathrm{L}}, \quad n_y = \sin\theta_0^{\mathrm{L}}. \tag{7.81}$$

The case of the incidence of a plane shear wave can be considered likewise, except that it needs to be taken into account that the mode-converted longitudinal waves become evanescent for the shear wave with the incident angle greater than the critical one.

The boundary conditions at $x = 0$ are, from Eqs. (7.2a) and (7.2b),

$$\begin{aligned} &\rho {c_{\mathrm{L}}}^2 \frac{\partial u}{\partial x}\left(0^+, y, t\right) + \rho\left({c_{\mathrm{L}}}^2 - 2{c_{\mathrm{T}}}^2\right) \frac{\partial v}{\partial y}\left(0^+, y, t\right) \\ &= \rho {c_{\mathrm{L}}}^2 \frac{\partial u}{\partial x}\left(0^-, y, t\right) + \rho\left({c_{\mathrm{L}}}^2 - 2{c_{\mathrm{T}}}^2\right) \frac{\partial v}{\partial y}\left(0^-, y, t\right) \\ &= K_{\mathrm{N}}\, \xi(y, t) - K_{\mathrm{NN}}\, \xi(y, t)^2 - K_{\mathrm{TT}}\, s(y, t)^2, \end{aligned} \tag{7.82a}$$

$$\rho {c_{\mathrm{T}}}^2 \left\{ \frac{\partial u}{\partial y}\left(0^+, y, t\right) + \frac{\partial v}{\partial x}\left(0^+, y, t\right) \right\}$$
$$= \rho {c_{\mathrm{T}}}^2 \left\{ \frac{\partial u}{\partial y}\left(0^-, y, t\right) + \frac{\partial v}{\partial x}\left(0^-, y, t\right) \right\} = K_{\mathrm{T}}\ s\left(y, t\right) - K_{\mathrm{NT}}\, \xi\left(y, t\right)\ s\left(y, t\right), \tag{7.82b}$$

where

$$\xi\left(y, t\right) = u\left(0^+, y, t\right) - u\left(0^-, y, t\right), \quad s\left(y, t\right) = v\left(0^+, y, t\right) - v\left(0^-, y, t\right). \tag{7.83}$$

The perturbation approach presented in Sect. 7.2 is applied to decompose the displacement field $\mathbf{u}(x, y, t) = (u(x, y, t), v(x, y, t)))^{\mathrm{T}}$ into the linear part $\mathbf{u}_1(x, y, t) = (u_1(x, y, t), v_1(x, y, t)))^{\mathrm{T}}$ and the quadratic nonlinear part $\mathbf{u}_2(x, y, t) = (u_2(x, y, t), v_2(x, y, t)))^{\mathrm{T}}$, i.e.,

$$u\left(x, y, t\right) = u_1\left(x, y, t\right) + u_2\left(x, y, t\right), \quad v\left(x, y, t\right) = v_1\left(x, y, t\right) + v_2\left(x, y, t\right). \tag{7.84}$$

and likewise for the interfacial displacements,

$$\xi\left(y, t\right) = \xi_1\left(y, t\right) + \xi_2\left(y, t\right), \quad s\left(y, t\right) = s_1\left(y, t\right) + s_2\left(y, t\right). \tag{7.85}$$

7.4.2 Linear Response

The linear response $\mathbf{u}_1(x, y, t)$ is governed by the following equations:

$$\frac{\partial^2 u_1}{\partial t^2} = \left({c_{\mathrm{L}}}^2 - {c_{\mathrm{T}}}^2\right) \frac{\partial}{\partial x}\left(\frac{\partial u_1}{\partial x} + \frac{\partial v_1}{\partial y}\right) + {c_{\mathrm{T}}}^2 \left(\frac{\partial^2}{\partial x^2} + \frac{\partial^2}{\partial y^2}\right) u_1, \tag{7.86a}$$

$$\frac{\partial^2 v_1}{\partial t^2} = \left({c_{\mathrm{L}}}^2 - {c_{\mathrm{T}}}^2\right) \frac{\partial}{\partial y}\left(\frac{\partial u_1}{\partial x} + \frac{\partial v_1}{\partial y}\right) + {c_{\mathrm{T}}}^2 \left(\frac{\partial^2}{\partial x^2} + \frac{\partial^2}{\partial y^2}\right) v_1, \tag{7.86b}$$

$$\rho {c_{\mathrm{L}}}^2 \frac{\partial u_1}{\partial x}\left(0^+, y, t\right) + \rho\left({c_{\mathrm{L}}}^2 - 2{c_{\mathrm{T}}}^2\right) \frac{\partial v_1}{\partial y}\left(0^+, y, t\right)$$
$$= \rho {c_{\mathrm{L}}}^2 \frac{\partial u_1}{\partial x}\left(0^-, y, t\right) + \rho\left({c_{\mathrm{L}}}^2 - 2{c_{\mathrm{T}}}^2\right) \frac{\partial v_1}{\partial y}\left(0^-, y, t\right) = K_{\mathrm{N}}\, \xi_1\left(y, t\right), \tag{7.86c}$$

$$\rho {c_{\mathrm{T}}}^2 \left\{ \frac{\partial u_1}{\partial y}\left(0^+, y, t\right) + \frac{\partial v_1}{\partial x}\left(0^+, y, t\right) \right\}$$
$$= \rho {c_{\mathrm{T}}}^2 \left\{ \frac{\partial u_1}{\partial y}\left(0^-, y, t\right) + \frac{\partial v_1}{\partial x}\left(0^-, y, t\right) \right\} = K_{\mathrm{T}}\, s_1\left(y, t\right), \tag{7.86d}$$

$$\xi_1\left(y, t\right) = u_1\left(0^+, y, t\right) - u_1\left(0^-, y, t\right), \quad s_1\left(y, t\right) = v_1\left(0^+, y, t\right) - v_1\left(0^-, y, t\right), \tag{7.86e}$$

with the incident wave given by Eq. (7.80). In the frequency domain, the displacement $\mathbf{U}_1(x, y) = (U_1(x, y), V_1(x, y))^{\mathrm{T}}$ obeys

$$\left({c_{\mathrm{L}}}^2 - {c_{\mathrm{T}}}^2\right) \frac{\partial}{\partial x}\left(\frac{\partial U_1}{\partial x} + \frac{\partial V_1}{\partial y}\right) + {c_{\mathrm{T}}}^2 \left(\frac{\partial^2}{\partial x^2} + \frac{\partial^2}{\partial y^2}\right) U_1 + {\omega_0}^2 U_1 = 0, \tag{7.87a}$$

$$\left({c_{\mathrm{L}}}^2 - {c_{\mathrm{T}}}^2\right) \frac{\partial}{\partial y}\left(\frac{\partial U_1}{\partial x} + \frac{\partial V_1}{\partial y}\right) + {c_{\mathrm{T}}}^2 \left(\frac{\partial^2}{\partial x^2} + \frac{\partial^2}{\partial y^2}\right) V_1 + {\omega_0}^2 V_1 = 0, \tag{7.87b}$$

$$\rho {c_{\mathrm{L}}}^2 \frac{\partial U_1}{\partial x}\left(0^+, y\right) + \rho \left({c_{\mathrm{L}}}^2 - 2{c_{\mathrm{T}}}^2\right) \frac{\partial V_1}{\partial y}\left(0^+, y\right)$$
$$= \rho {c_{\mathrm{L}}}^2 \frac{\partial U_1}{\partial x}\left(0^-, y\right) + \rho \left({c_{\mathrm{L}}}^2 - 2{c_{\mathrm{T}}}^2\right) \frac{\partial V_1}{\partial y}\left(0^-, y\right) = K_{\mathrm{N}}\, \Xi_1(y), \tag{7.87c}$$

$$\rho {c_{\mathrm{T}}}^2 \left\{ \frac{\partial U_1}{\partial y}\left(0^+, y\right) + \frac{\partial V_1}{\partial x}\left(0^+, y\right) \right\} = \rho {c_{\mathrm{T}}}^2 \left\{ \frac{\partial U_1}{\partial y}\left(0^-, y\right) + \frac{\partial V_1}{\partial x}\left(0^-, y\right) \right\}$$
$$= K_{\mathrm{T}}\, S_1(y), \tag{7.87d}$$

$$\Xi_1(y) = U_1\left(0^+, y\right) - U_1\left(0^-, y\right), \quad S_1(y) = V_1\left(0^+, y\right) - V_1\left(0^-, y\right), \tag{7.87e}$$

with the incident wave

$$\mathbf{U}_1^{\mathrm{IL}}\left(x, y\right) = \begin{pmatrix} U_1^{\mathrm{IL}}\left(x, y\right) \\ V_1^{\mathrm{IL}}\left(x, y\right) \end{pmatrix} = A_0 \begin{pmatrix} n_x \\ n_y \end{pmatrix} \exp\left\{ \mathrm{i}\omega_0 \left(n_x x + n_y y\right) / c_{\mathrm{L}} \right\}. \tag{7.88}$$

Since two semi-infinite media are the same isotropic elastic solid, the propagation angles of the reflected longitudinal (RL), reflected transverse (RT), transmitted longitudinal (TL), and transmitted transverse (TT) waves are given by

$$\theta^{\mathrm{RL}} = \theta^{\mathrm{TL}} = \theta_0^{\mathrm{L}}, \quad \theta^{\mathrm{RT}} = \theta^{\mathrm{TT}} = \theta_0^{\mathrm{T}}, \quad \frac{\sin\theta_0^{\mathrm{T}}}{c_{\mathrm{T}}} = \frac{\sin\theta_0^{\mathrm{L}}}{c_{\mathrm{L}}}, \tag{7.89}$$

according to Snell's law. The reflected and transmitted wave fields can be assumed to have the following forms:

$$\mathbf{U}_1^{\mathrm{RL}}(x,y) = \begin{pmatrix} U_1^{\mathrm{RL}}(x,y) \\ V_1^{\mathrm{RL}}(x,y) \end{pmatrix} = R_{\mathrm{L}} A_0 \begin{pmatrix} -n_x \\ n_y \end{pmatrix} \exp\left\{\mathrm{i}\omega_0 \left(-n_x x + n_y y\right)/c_{\mathrm{L}}\right\}, \tag{7.90a}$$

$$\mathbf{U}_1^{\mathrm{RT}}(x,y) = \begin{pmatrix} U_1^{\mathrm{RT}}(x,y) \\ V_1^{\mathrm{RT}}(x,y) \end{pmatrix} = R_{\mathrm{T}} A_0 \begin{pmatrix} l_y \\ l_x \end{pmatrix} \exp\left\{\mathrm{i}\omega_0 \left(-l_x x + l_y y\right)/c_{\mathrm{T}}\right\}, \tag{7.90b}$$

$$\mathbf{U}_1^{\mathrm{TL}}(x,y) = \begin{pmatrix} U_1^{\mathrm{TL}}(x,y) \\ V_1^{\mathrm{TL}}(x,y) \end{pmatrix} = T_{\mathrm{L}} A_0 \begin{pmatrix} n_x \\ n_y \end{pmatrix} \exp\left\{\mathrm{i}\omega_0 \left(n_x x + n_y y\right)/c_{\mathrm{L}}\right\}, \tag{7.90c}$$

$$\mathbf{U}_1^{\mathrm{TT}}(x,y) = \begin{pmatrix} U_1^{\mathrm{TT}}(x,y) \\ V_1^{\mathrm{TT}}(x,y) \end{pmatrix} = T_{\mathrm{T}} A_0 \begin{pmatrix} -l_y \\ l_x \end{pmatrix} \exp\left\{\mathrm{i}\omega_0 \left(l_x x + l_y y\right)/c_{\mathrm{T}}\right\}, \tag{7.90d}$$

where

$$l_x = \cos\theta_0^{\mathrm{T}}, \quad l_y = \sin\theta_0^{\mathrm{T}}, \tag{7.91}$$

and R_{L}, R_{T}, T_{L}, and T_{T} are the complex reflection and transmission coefficients of longitudinal and transverse waves, respectively (see Fig. 7.7a). By applying the boundary conditions in Eqs. (7.87c) and (7.87d), these coefficients are determined by the following set of equations:

$$\begin{bmatrix} n_x & -l_y & n_x - \mathrm{i}\left(1 - 2\eta^2 {n_y}^2\right)/\kappa_{\mathrm{N}} & -l_y + 2\mathrm{i}\eta l_x l_y/\kappa_{\mathrm{N}} \\ -n_y & -l_x & n_y - 2\mathrm{i}\eta n_x n_y/\kappa_{\mathrm{T}} & l_x + \mathrm{i}\left({l_y}^2 - {l_x}^2\right)/\kappa_{\mathrm{T}} \\ 1 - 2\eta^2 {n_y}^2 & -2\eta l_x l_y & -1 + 2\eta^2 {n_y}^2 & 2\eta l_x l_y \\ 2\eta n_x n_y & {l_x}^2 - {l_y}^2 & 2\eta n_x n_y & {l_x}^2 - {l_y}^2 \end{bmatrix}$$

$$\begin{pmatrix} R_{\mathrm{L}} \\ R_{\mathrm{T}} \\ T_{\mathrm{L}} \\ T_{\mathrm{T}} \end{pmatrix} = \begin{pmatrix} n_x \\ n_y \\ -1 + 2\eta^2 {n_y}^2 \\ 2\eta n_x n_y \end{pmatrix}, \tag{7.92}$$

where

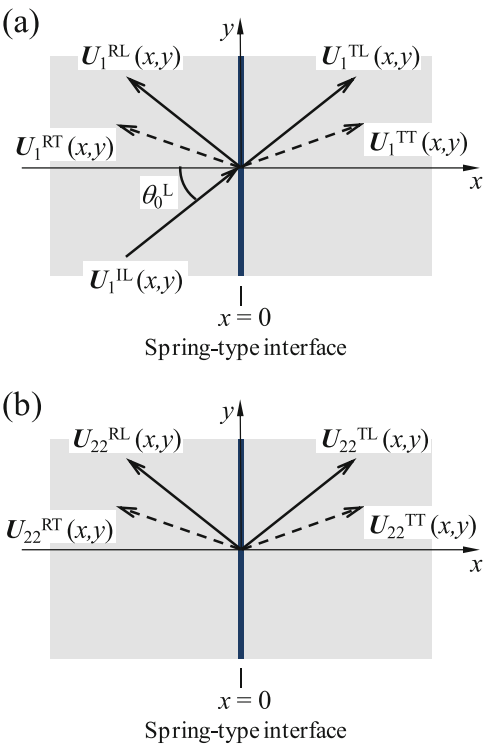

Fig. 7.7 (**a**) The fundamental and (**b**) the second-harmonic components associated with the interaction of oblique-incidence longitudinal wave with the nonlinear spring-type interface

$$\eta = \frac{c_T}{c_L} \tag{7.93}$$

is the ratio of wave speeds and κ_N and κ_T are the normalized interfacial stiffnesses defined in Eqs. (7.20) and (7.71). Once these coefficients are obtained, the interfacial displacements are given by

$$\Xi_1(y) = A_0 M_1 \exp\left(i\omega_0 n_y y/c_L\right), \tag{7.94a}$$

$$S_1(y) = A_0 N_1 \exp\left(i\omega_0 n_y y/c_L\right), \tag{7.94b}$$

where the complex constants M_1 and N_1 are defined by

$$M_1 = \mid M_1 \mid \exp(i\varphi_1) = -n_x + n_x R_L - l_y R_T + n_x T_L - l_y T_T, \tag{7.95a}$$

$$N_1 = \mid N_1 \mid \exp(i\psi_1) = -n_y - n_y R_L - l_x R_T + n_y T_L + l_x T_T, \tag{7.95b}$$

where φ_1 and ψ_1 are the phases of M_1 and N_1, respectively.

7.4.3 Quadratic Nonlinear Response

The quadratic nonlinear response $\mathbf{u}_2(x, y, t)$ is governed by

$$\frac{\partial^2 u_2}{\partial t^2} = \left({c_\mathrm{L}}^2 - {c_\mathrm{T}}^2\right) \frac{\partial}{\partial x}\left(\frac{\partial u_2}{\partial x} + \frac{\partial v_2}{\partial y}\right) + {c_\mathrm{T}}^2 \left(\frac{\partial^2}{\partial x^2} + \frac{\partial^2}{\partial y^2}\right) u_2, \tag{7.96a}$$

$$\frac{\partial^2 v_2}{\partial t^2} = \left({c_\mathrm{L}}^2 - {c_\mathrm{T}}^2\right) \frac{\partial}{\partial y}\left(\frac{\partial u_2}{\partial x} + \frac{\partial v_2}{\partial y}\right) + {c_\mathrm{T}}^2 \left(\frac{\partial^2}{\partial x^2} + \frac{\partial^2}{\partial y^2}\right) v_2, \tag{7.96b}$$

$$\begin{aligned}
&\rho {c_\mathrm{L}}^2 \frac{\partial u_2}{\partial x}\left(0^+, y, t\right) + \rho\left({c_\mathrm{L}}^2 - 2{c_\mathrm{T}}^2\right) \frac{\partial v_2}{\partial y}\left(0^+, y, t\right) \\
&= \rho {c_\mathrm{L}}^2 \frac{\partial u_2}{\partial x}\left(0^-, y, t\right) + \rho\left({c_\mathrm{L}}^2 - 2{c_\mathrm{T}}^2\right) \frac{\partial v_2}{\partial y}\left(0^-, y, t\right) \\
&= K_\mathrm{N}\, \xi_2\left(y, t\right) - K_\mathrm{NN}\, \xi_1(y, t)^2 - K_\mathrm{TT}\, s_1(y, t)^2,
\end{aligned} \tag{7.96c}$$

$$\begin{aligned}
&\rho {c_\mathrm{T}}^2 \left\{\tfrac{\partial u_2}{\partial y}\left(0^+, y, t\right) + \tfrac{\partial v_2}{\partial x}\left(0^+, y, t\right)\right\} = \rho {c_\mathrm{T}}^2 \left\{\tfrac{\partial u_2}{\partial y}\left(0^-, y, t\right) + \tfrac{\partial v_2}{\partial x}\left(0^-, y, t\right)\right\} \\
&= K_\mathrm{T}\, s_2\left(y, t\right) - K_\mathrm{NT}\, \xi_1\left(y, t\right)\, s_1\left(y, t\right),
\end{aligned} \tag{7.96d}$$

$$\xi_2\left(y, t\right) = u_2\left(0^+, y, t\right) - u_2\left(0^-, y, t\right), \quad s_2\left(y, t\right) = v_2\left(0^+, y, t\right) - v_2\left(0^-, y, t\right). \tag{7.96e}$$

The driving force terms in Eqs. (7.96c) and (7.96d) can be evaluated from Eqs. (7.94a) and (7.94b) and using the following relations:

$$\begin{aligned}
\xi_1(y, t)^2 &= \left\{\mathrm{Re}\left[\Xi_1(y) \exp\left(-\mathrm{i}\omega_0 t\right)\right]\right\}^2 \\
&= \frac{1}{2} {A_0}^2 |M_1|^2 \left[1 + \cos\left\{2\omega_0\left(t - n_y y / c_\mathrm{L}\right) - 2\varphi_1\right\}\right],
\end{aligned} \tag{7.97a}$$

$$\begin{aligned}
s_1(y, t)^2 &= \left\{\mathrm{Re}\left[S_1(y) \exp\left(-\mathrm{i}\omega_0 t\right)\right]\right\}^2 \\
&= \frac{1}{2} {A_0}^2 |N_1|^2 \left[1 + \cos\left\{2\omega_0\left(t - n_y y / c_\mathrm{L}\right) - 2\psi_1\right\}\right],
\end{aligned} \tag{7.97b}$$

$$\xi_1\left(y, t\right) s_1\left(y, t\right) = \mathrm{Re}\left[\Xi_1(y) \exp\left(-\mathrm{i}\omega_0 t\right)\right] \mathrm{Re}\left[S_1(y) \exp\left(-\mathrm{i}\omega_0 t\right)\right]$$

$$= \frac{1}{2} {A_0}^2 \, |M_1| \, |N_1| \left[\cos\left(\varphi_1 - \psi_1\right) + \cos\left\{ 2\omega_0 \left(t - n_y y / c_\mathrm{L} \right) - \varphi_1 - \psi_1 \right\} \right], \tag{7.97c}$$

which consist of the stationary ($\omega = 0$) and the second-harmonic ($\omega = 2\omega_0$) components. As a consequence, the quadratic nonlinear response $\mathbf{U}_2(x, y) = (U_2(x, y), V_2(x, y))^\mathrm{T}$ can then be decomposed into the stationary part $\mathbf{U}_{21}(x, y) = (U_{21}(x, y), V_{21}(x, y))^\mathrm{T}$ and the second-harmonic part $\mathbf{U}_{22}(x, y) = (U_{22}(x, y), V_{22}(x, y))^\mathrm{T}$.

The stationary field $\mathbf{U}_{21}(x, y)$ is governed by

$$\left({c_\mathrm{L}}^2 - {c_\mathrm{T}}^2 \right) \frac{\partial}{\partial x} \left(\frac{\partial U_{21}}{\partial x} + \frac{\partial V_{21}}{\partial y} \right) + {c_\mathrm{T}}^2 \left(\frac{\partial^2}{\partial x^2} + \frac{\partial^2}{\partial y^2} \right) U_{21} = 0, \tag{7.98a}$$

$$\left({c_\mathrm{L}}^2 - {c_\mathrm{T}}^2 \right) \frac{\partial}{\partial y} \left(\frac{\partial U_{21}}{\partial x} + \frac{\partial V_{21}}{\partial y} \right) + {c_\mathrm{T}}^2 \left(\frac{\partial^2}{\partial x^2} + \frac{\partial^2}{\partial y^2} \right) V_{21} = 0, \tag{7.98b}$$

$$\begin{aligned} &\rho {c_\mathrm{L}}^2 \frac{\partial U_{21}}{\partial x} \left(0^+, y\right) + \rho \left({c_\mathrm{L}}^2 - 2{c_\mathrm{T}}^2 \right) \frac{\partial V_{21}}{\partial y} \left(0^+, y\right) \\ &= \rho {c_\mathrm{L}}^2 \frac{\partial U_{21}}{\partial x} \left(0^-, y\right) + \rho \left({c_\mathrm{L}}^2 - 2{c_\mathrm{T}}^2 \right) \frac{\partial V_{21}}{\partial y} \left(0^-, y\right) \\ &= K_\mathrm{N} \, \Xi_{21}(y) - \frac{1}{2} {A_0}^2 K_\mathrm{NN} |M_1|^2 - \frac{1}{2} {A_0}^2 K_\mathrm{TT} |N_1|^2, \end{aligned} \tag{7.98c}$$

$$\begin{aligned} &\rho {c_\mathrm{T}}^2 \left\{ \frac{\partial U_{21}}{\partial y} \left(0^+, y\right) + \frac{\partial V_{21}}{\partial x} \left(0^+, y\right) \right\} \\ &= \rho {c_\mathrm{T}}^2 \left\{ \frac{\partial U_{21}}{\partial y} \left(0^-, y\right) + \frac{\partial V_{21}}{\partial x} \left(0^-, y\right) \right\} \\ &= K_\mathrm{T} \, S_{21}(y) - \frac{1}{2} {A_0}^2 K_\mathrm{NT} \, |M_1| \, |N_1| \cos\left(\varphi_1 - \psi_1\right), \end{aligned} \tag{7.98d}$$

$$\Xi_{21}(y) = U_{21}\left(0^+, y\right) - U_{21}\left(0^-, y\right), \quad S_{21}(y) = V_{21}\left(0^+, y\right) - V_{21}\left(0^-, y\right). \tag{7.98e}$$

The solution to the above set of equations is given by the strain-free field with the constant interfacial displacements

$$\begin{aligned} \Xi_{21}(y) &= \frac{1}{2} {A_0}^2 \beta |M_1|^2 + \frac{1}{2} {A_0}^2 \gamma |N_1|^2, \\ S_{21}(y) &= \frac{1}{2} {A_0}^2 \chi \, |M_1| \, |N_1| \cos\left(\varphi_1 - \psi_1\right), \end{aligned} \tag{7.99}$$

where

$$\chi = \frac{K_{\mathrm{NT}}}{K_{\mathrm{T}}}. \tag{7.100}$$

The second-harmonic field $\mathbf{U}_{22}(x, y)$ is governed by

$$\left({c_{\mathrm{L}}}^2 - {c_{\mathrm{T}}}^2\right) \frac{\partial}{\partial x} \left(\frac{\partial U_{22}}{\partial x} + \frac{\partial V_{22}}{\partial y} \right) + {c_{\mathrm{T}}}^2 \left(\frac{\partial^2}{\partial x^2} + \frac{\partial^2}{\partial y^2} \right) U_{22} + (2\omega_0)^2 U_{22} = 0, \tag{7.101a}$$

$$\left({c_{\mathrm{L}}}^2 - {c_{\mathrm{T}}}^2\right) \frac{\partial}{\partial y} \left(\frac{\partial U_{22}}{\partial x} + \frac{\partial V_{22}}{\partial y} \right) + {c_{\mathrm{T}}}^2 \left(\frac{\partial^2}{\partial x^2} + \frac{\partial^2}{\partial y^2} \right) V_{22} + (2\omega_0)^2 V_{22} = 0, \tag{7.101b}$$

$$\begin{aligned} &\rho {c_{\mathrm{L}}}^2 \frac{\partial U_{22}}{\partial x} \left(0^+, y\right) + \rho \left({c_{\mathrm{L}}}^2 - 2{c_{\mathrm{T}}}^2\right) \frac{\partial V_{22}}{\partial y} \left(0^+, y\right) \\ &= \rho {c_{\mathrm{L}}}^2 \frac{\partial U_{22}}{\partial x} \left(0^-, y\right) + \rho \left({c_{\mathrm{L}}}^2 - 2{c_{\mathrm{T}}}^2\right) \frac{\partial V_{22}}{\partial y} \left(0^-, y\right) \\ &= K_{\mathrm{N}} \left[\Xi_{22}(y) - \beta {A_0}^2 W_{\mathrm{N}} \exp\left(2\mathrm{i}\omega_0 n_y y / c_{\mathrm{L}}\right) \right], \end{aligned} \tag{7.101c}$$

$$\begin{aligned} &\rho {c_{\mathrm{T}}}^2 \left\{ \frac{\partial U_{22}}{\partial y} \left(0^+, y\right) + \frac{\partial V_{22}}{\partial x} \left(0^+, y\right) \right\} \\ &= \rho {c_{\mathrm{T}}}^2 \left\{ \frac{\partial U_{22}}{\partial y} \left(0^-, y\right) + \frac{\partial V_{22}}{\partial x} \left(0^-, y\right) \right\} \\ &= K_{\mathrm{T}} \left[S_{22}(y) - \beta {A_0}^2 W_{\mathrm{T}} \exp\left(2\mathrm{i}\omega_0 n_y y / c_{\mathrm{L}}\right) \right], \end{aligned} \tag{7.101d}$$

$$\Xi_{22}(y) = U_{22}\left(0^+, y\right) - U_{22}\left(0^-, y\right), \quad S_{22}(y) = V_{22}\left(0^+, y\right) - V_{22}\left(0^-, y\right), \tag{7.101e}$$

where the complex constants W_{N} and W_{T} are given by

$$W_{\mathrm{N}} = \frac{1}{2} {M_1}^2 + \frac{\gamma}{2\beta} {N_1}^2, \tag{7.102a}$$

$$W_{\mathrm{T}} = \frac{\chi}{2\beta} M_1 N_1. \tag{7.102b}$$

The solution to the above problem is assumed to have the following forms:

$$\mathbf{U}_{22}^{\mathrm{RL}}(x,y)=\begin{pmatrix}U_{22}^{\mathrm{RL}}(x,y)\\ V_{22}^{\mathrm{RL}}(x,y)\end{pmatrix}=\beta {A_0}^2 w^{\mathrm{RL}}\begin{pmatrix}-n_x\\ n_y\end{pmatrix}\exp\left\{2\mathrm{i}\omega_0\left(-n_x x+n_y y\right)/c_{\mathrm{L}}\right\}, \tag{7.103a}$$

$$\mathbf{U}_{22}^{\mathrm{RT}}(x,y)=\begin{pmatrix}U_{22}^{\mathrm{RT}}(x,y)\\ V_{22}^{\mathrm{RT}}(x,y)\end{pmatrix}=\beta {A_0}^2 w^{\mathrm{RT}}\begin{pmatrix}l_y\\ l_x\end{pmatrix}\exp\left\{2\mathrm{i}\omega_0\left(-l_x x+l_y y\right)/c_{\mathrm{T}}\right\}, \tag{7.103b}$$

$$\mathbf{U}_{22}^{\mathrm{TL}}(x,y)=\begin{pmatrix}U_{22}^{\mathrm{TL}}(x,y)\\ V_{22}^{\mathrm{TL}}(x,y)\end{pmatrix}=\beta {A_0}^2 w^{\mathrm{TL}}\begin{pmatrix}n_x\\ n_y\end{pmatrix}\exp\left\{2\mathrm{i}\omega_0\left(n_x x+n_y y\right)/c_{\mathrm{L}}\right\}, \tag{7.103c}$$

$$\mathbf{U}_{22}^{\mathrm{TT}}(x,y)=\begin{pmatrix}U_{22}^{\mathrm{TT}}(x,y)\\ V_{22}^{\mathrm{TT}}(x,y)\end{pmatrix}=\beta {A_0}^2 w^{\mathrm{TT}}\begin{pmatrix}-l_y\\ l_x\end{pmatrix}\exp\left\{2\mathrm{i}\omega_0\left(l_x x+l_y y\right)/c_{\mathrm{T}}\right\}, \tag{7.103d}$$

where w^{RL}, w^{RT}, w^{TL}, and w^{TT} are complex coefficients related to the amplitude of the second harmonics. These forms represent the second-harmonic fields of longitudinal and transverse waves radiating into the negative and positive directions (Fig. 7.7b). They satisfy Eqs. (7.101a), (7.101b), (7.101c), (7.101d), and (7.101e) when these coefficients are determined from

$$\begin{bmatrix} n_x & -l_y & n_x-2\mathrm{i}\left(1-2\eta^2{n_y}^2\right)/\kappa_{\mathrm{N}} & -l_y+4\mathrm{i}\eta l_x l_y/\kappa_{\mathrm{N}}\\ -n_y & -l_x & n_y-4\mathrm{i}\eta n_x n_y/\kappa_{\mathrm{T}} & l_x+2\mathrm{i}\left({l_y}^2-{l_x}^2\right)/\kappa_{\mathrm{T}}\\ 1-2\eta^2{n_y}^2 & -2\eta l_x l_y & -1+2\eta^2{n_y}^2 & 2\eta l_x l_y\\ 2\eta n_x n_y & {l_x}^2-{l_y}^2 & 2\eta n_x n_y & {l_x}^2-{l_y}^2 \end{bmatrix}$$

$$\begin{pmatrix}w^{\mathrm{RL}}\\ w^{\mathrm{RT}}\\ w^{\mathrm{TL}}\\ w^{\mathrm{TT}}\end{pmatrix}=\begin{pmatrix}W_{\mathrm{N}}\\ W_{\mathrm{T}}\\ 0\\ 0\end{pmatrix}. \tag{7.104}$$

From the above solution, it is seen that the second-harmonic component propagates in the same directions with the reflected longitudinal, reflected transverse, transmitted longitudinal, and transmitted transverse components of the fundamental wave.

It is noted that the three parameters describing the interfacial nonlinearity, K_{NN}, K_{TT}, and K_{NT}, need to be specified in order to obtain the second-harmonic amplitudes based on the above theory. Establishing an effective method to quantify these parameters for actual contacting interfaces requires further investigations. Some numerical results of the nonlinear interaction of obliquely incident plane waves with a contacting interface are presented by Pecorari [20] for the model

given by Eqs. (7.7a) and (7.7b). Nam et al. [32] show experimental data for the harmonic generation at a contacting interface at oblique incidence of longitudinal wave, together with some theoretical results to interpret the experimental results.

7.5 Experimental Aspects

7.5.1 Quantitative Evaluation of the Second-Harmonic Amplitude

In this section, the second-harmonic generation at a contacting interface is examined from an experimental point of view based on the work by Biwa et al. [33]. As shown in Fig. 7.8, two cubic aluminum alloy blocks with side length 30 mm were mated together under compressive loading of different levels. The measured load was divided by the nominal area of contact (30 × 30 mm) to give the nominal contact pressure. A ten-cycle longitudinal tone-burst wave of the center frequency 1 MHz was emitted from the end of one block by aid of a piezoelectric transducer (nominal center frequency 1 MHz). The transmitted wave was detected at the other end by another piezoelectric transducer (nominal center frequency 2.25 MHz) and recorded in a personal computer. The recorded transmission waveforms were analyzed in the frequency domain by the fast Fourier transform (FFT) technique to obtain the amplitudes of the fundamental (1 MHz) and the second-harmonic (2 MHz) components. At each contact pressure, the emitting transducer was also excited by a spike pulse to send an ultrasonic wave pulse to the contacting interface, and the reflection waveform was measured by the same transducer. This measurement enabled the identification of the amplitude reflection coefficient and the interfacial normal stiffness K_N of the contacting interface as a function of the applied pressure.

The measured transmission waveforms are shown in Fig. 7.9 at different contact pressures in a loading/unloading cycle. It can be observed that the waveforms at relatively low contact pressures are distorted significantly from the original sinusoidal shape. On the other hand, the waveforms at higher pressures retain the sinusoidal shape of the emitted wave signal. These transmission waveforms were analyzed by the FFT to obtain the amplitudes of the fundamental (1 MHz) and the second-harmonic (2 MHz) components. These amplitudes, obtained from the voltage signal detected by the receiving piezoelectric transducer, are denoted by A_{1V} and A_{2V}, respectively. It should be noted that the relative magnitudes of these amplitudes are affected by the frequency characteristics of the receiving transducer, which makes direct comparison of these amplitudes or their ratio with the theoretical prediction, Eqs. (7.35), (7.36), and (7.37), less meaningful. Therefore, in order to evaluate the fundamental and the second-harmonic amplitudes in a quantitative manner, the frequency characteristics of the receiving transducer was compensated in the following manner.

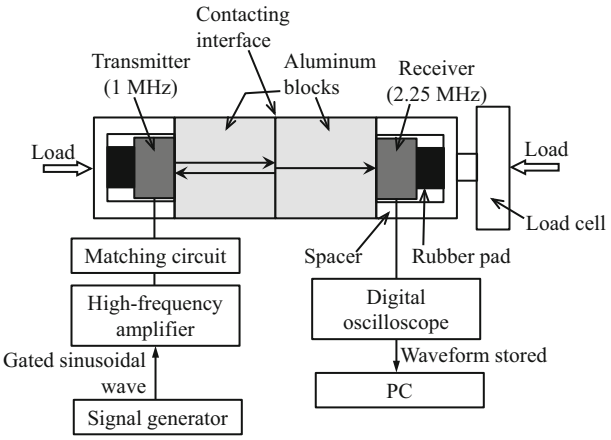

Fig. 7.8 Schematic of the experimental setup for the transmission of longitudinal tone-burst wave through a contacting interface

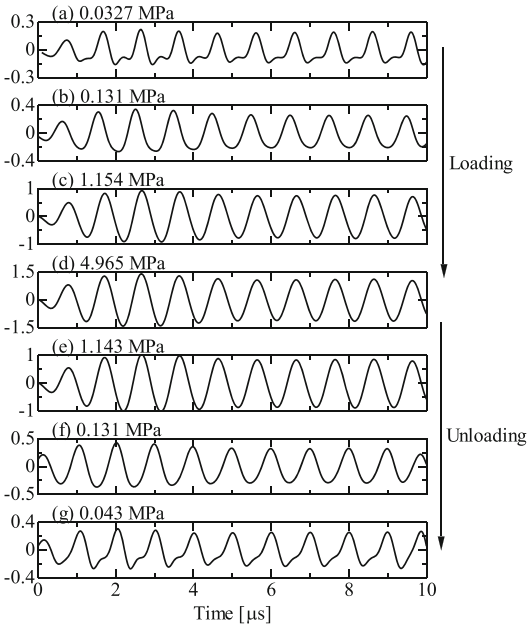

Fig. 7.9 Transmission waveforms through the contacting interface at different contact pressures

As shown in Fig. 7.10a, the longitudinal tone-burst waves with center frequencies 1 MHz, 2 MHz, and 3 MHz were emitted to the aluminum alloy block (the same block as used in the above measurements) from the bottom surface. The transmitted waveforms on the upper surface were measured by using the same receiving transducer (nominal center frequency 2.25 MHz). The FFT of the sinusoidal part of each transmission waveform was calculated, and the inverse FFT of its value at

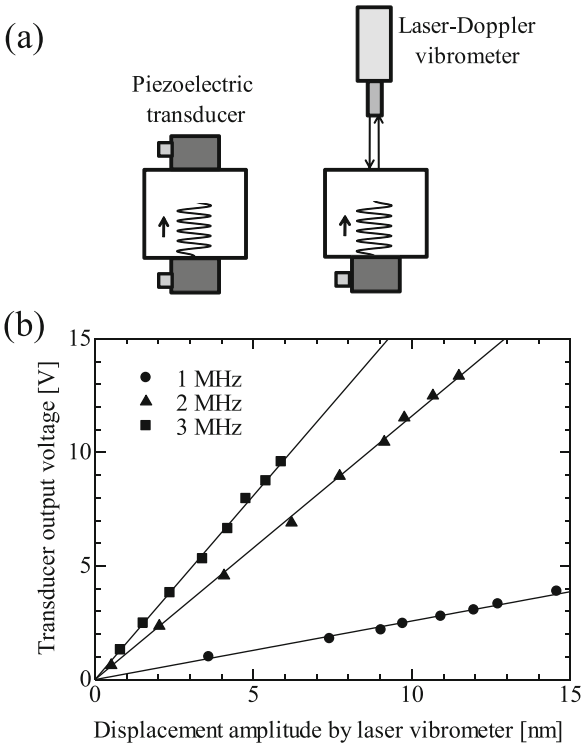

Fig. 7.10 (**a**) Schematic of the calibration of the frequency characteristics of the receiving transducer by a laser Doppler vibrometer, (**b**) the relation between the output of the receiving transducer and the displacement amplitude obtained by the laser Doppler vibrometer for different frequencies (reproduced from Biwa et al. [33] with the permission of AIP Publishing)

the center frequency was regarded as the voltage output at this frequency. Next, instead of the piezoelectric transducer, a laser Doppler vibrometer was used to measure the particle velocity of the upper surface accompanying the arrival of the ultrasonic wave. This enabled the determination of the velocity amplitude of the sinusoidal tone burst, which can then be converted to its displacement amplitude by dividing it by the angular frequency. Since the laser vibrometry was applied to the free surface of the block, the displacement amplitude of the tone-burst wave propagating in the block is the half of the so-determined displacement amplitude. The relations between the displacement amplitudes obtained by the laser Doppler vibrometer and the output voltage amplitudes obtained by the receiving transducer are shown in Fig. 7.10b for the frequencies 1, 2, and 3 MHz. The results show that there is good linearity between them. The least-square fits (shown in Fig. 7.10b) to the experimental results can be used to convert the output voltage amplitude of the receiving transducer to the displacement amplitude, provided that the same specimen and the transducer are used.

Using the above calibration method, the fundamental as well as the second-harmonic displacement amplitudes, denoted by A_1 and A_2, were obtained. The ratio A_2/A_1 is plotted in Fig. 7.11 together with A_{2V}/A_{1V}. It is found that the calibrated

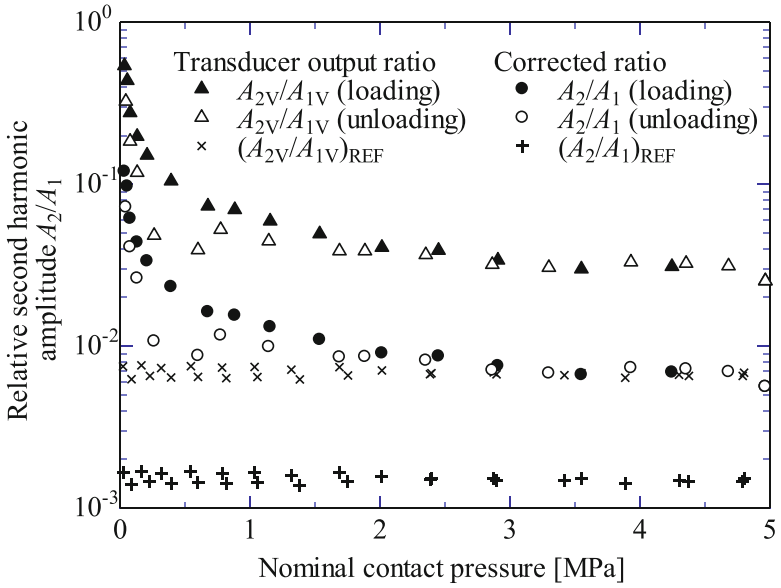

Fig. 7.11 Contact-pressure dependence of the relative second-harmonic amplitude (reproduced from Biwa et al. [33] with the permission of AIP Publishing, with additional data)

ratios are smaller than the corresponding raw data given by the transducer voltage. This can be understood naturally since the receiving transducer had the nominal frequency of 2.25 MHz and should detect the second-harmonic component (2 MHz) with greater sensitivity than the fundamental component (1 MHz).

When evaluating the second-harmonic generation at contacting interfaces, attention should be paid to the fact that the contact nonlinearity is not the only source of the second-harmonic component. Other sources include the transient excitation signal to the transducer which involves high-frequency components, nonlinearity of the equipment hardware, material nonlinearity of the specimen, and so on. To estimate their overall effect, an aluminum block of the length 60 mm (but with the same lateral dimensions as the contacting blocks used in the measurement) was used to perform the same tone-burst transmission measurement under compressive loading as described above. For this reference block, the relative second-harmonic amplitudes in the transmission waveform are denoted by $(A_{2V}/A_{1V})_{REF}$ and $(A_2/A_1)_{REF}$ before and after the calibration for the frequency characteristics of the receiving transducer, respectively. In Fig. 7.11, these relative second-harmonic amplitudes keep constant levels irrespective of the contact pressure, and are shown to be an order of magnitude smaller than those measured for the contacting blocks.

7.5.2 Comparison with the Prediction Based on the Nonlinear Spring-Type Interface Model

In the above measurement, the pulse reflection waveform from the contacting interface was also measured at each contact pressure. From the FFT of the reflection waveform, the amplitude reflection coefficient was obtained as a function of the applied pressure. Based on Eqs. (7.35) or (7.50), the interfacial normal stiffness was determined by

$$K_{\mathrm{N}} = \frac{\rho c_{\mathrm{L}} \omega_0 \sqrt{1 - |R_{\mathrm{L}}|^2}}{2 \mid R_{\mathrm{L}} \mid}. \tag{7.105}$$

The results are shown in Fig. 7.12, where the interfacial stiffness increases monotonically with the contact pressure during the loading, and decreases with slight hysteresis at the unloading. Instead of the power-law form discussed in Sect. 7.2.4, the following simple logarithmic form was found to fit the measurements reasonably well:

$$K_{\mathrm{N}}(p_0) = a \ln p_0 + b, \tag{7.106}$$

with $a = 2.40 \times 10^{-2}$ (MPa/nm), $b = 7.16 \times 10^{-2}$ (MPa/nm) for the loading, and $a = 1.88 \times 10^{-2}$ (MPa/nm), $b = 7.94 \times 10^{-2}$ (MPa/nm) for the unloading.

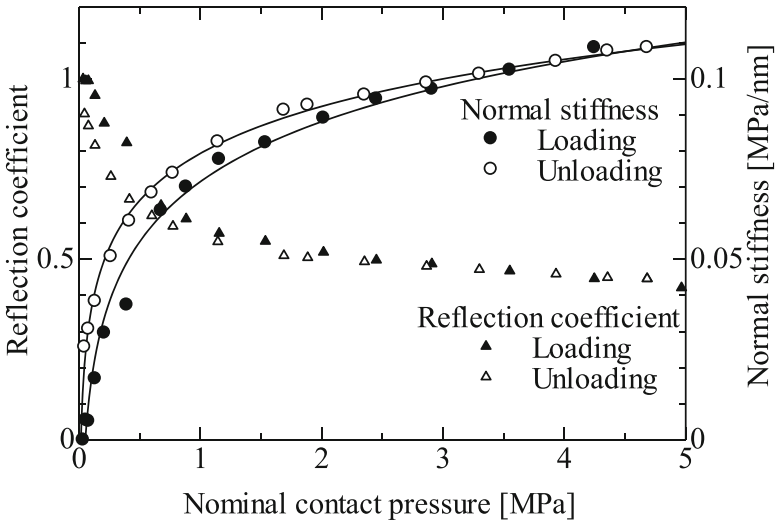

Fig. 7.12 Contact-pressure dependence of the reflection coefficient and the interfacial normal stiffness

From the above results, the nonlinear interfacial parameter K_{NN} was estimated in the following way. The relation in Eq. $(7.1)_1$ was restricted to the pressure-gap distance relation

$$p = p(h), \tag{7.107}$$

by neglecting the effect of the tangential sliding s. The derivative $\mathrm{d}p/\mathrm{d}h$ is a function of the gap distance h or a function of the pressure p through the inverse relation of Eq. (7.107). Now the functional form of $\mathrm{d}p/\mathrm{d}h$ as a function of p is identified with $-K_{\mathrm{N}}(p_0)$ in Eq. (7.106), i.e.,

$$\frac{\mathrm{d}p}{\mathrm{d}h} = -\tilde{K}(p), \quad \tilde{K}(p) \equiv a \ln p + b. \tag{7.108}$$

This identification amounts to assuming that the variation of the interfacial normal stiffness for dynamic pressure variation is identical with the variation for static change of pressure. Based on this assumption, the second-order derivative of $p(h)$ is given by

$$\frac{\mathrm{d}^2 p}{\mathrm{d}h^2} = -\frac{\mathrm{d}}{\mathrm{d}h}\tilde{K}(p) = -\frac{\mathrm{d}p}{\mathrm{d}h}\frac{\mathrm{d}\tilde{K}(p)}{\mathrm{d}p} = \tilde{K}(p)\frac{\mathrm{d}\tilde{K}(p)}{\mathrm{d}p}. \tag{7.109}$$

Therefore, the nonlinear interfacial parameter K_{NN} at the contact pressure p_0 is given by, from Eq. (7.3),

$$K_{\mathrm{NN}} = \frac{1}{2}\frac{\mathrm{d}^2 p}{\mathrm{d}h^2}\bigg|_{p=p_0} = \frac{a\ K_{\mathrm{N}}(p_0)}{2p_0} \tag{7.110}$$

and the parameter β is given by

$$\beta = \frac{K_{\mathrm{NN}}}{K_{\mathrm{N}}} = \frac{a}{2p_0}. \tag{7.111}$$

Based on the above estimation of K_{NN} and β for each of the loading and the unloading results, the ratio of the second-harmonic amplitude to the square of the fundamental amplitude in the transmitted wave was estimated by Eq. (7.37). With the parameters for aluminum alloy ($\rho = 2700$ kg/m^3, $c_{\mathrm{L}} = 6400$ m/s) and $\omega_0 = 2\pi$ (MHz), the results are shown in Fig. 7.13 together with the experimental data, where $A_2^{\mathrm{tra}}/\left(A_1^{\mathrm{tra}}\right)^2$ is simply denoted by $A_2/{A_1}^2$. It is noted that the calibration of the receiver frequency characteristics has enabled direct and quantitative comparison between the theory and the experimental data. In Fig. 7.13, the results based on the nonlinear spring-type interface model are in reasonable agreement with the experimental data as far as the order of magnitude is concerned. The discrepancy

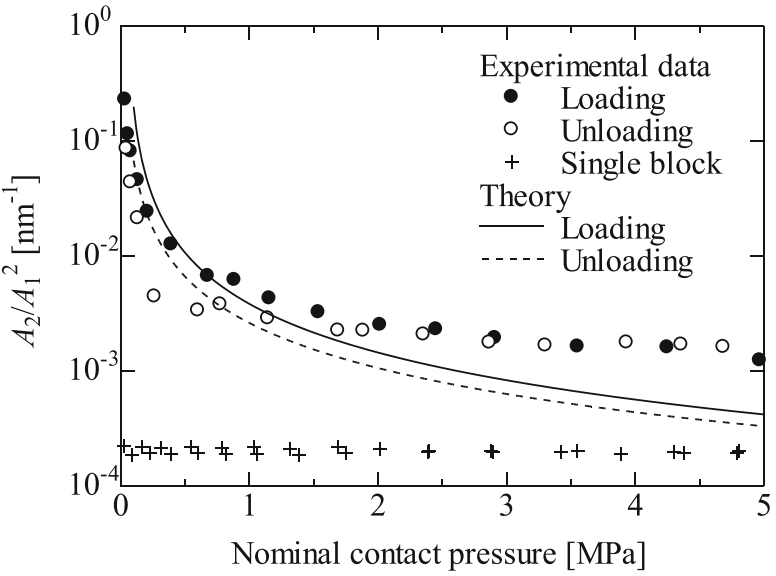

Fig. 7.13 Comparison between theory and experiment for the ratio of the second-harmonic amplitude to the square of the fundamental amplitude

between the theory and the experiment at relatively high pressures is likely due mainly to the effect of other sources of second-harmonics than the contacting interface, as it is of comparable magnitude to the results for the single reference block.

7.5.3 Other Experimental Investigations

Since the pioneering experiments by Buck et al. [31] on a contacting interface and a fatigue crack, many investigators have studied the harmonic generation at contacting interfaces from the viewpoints of fundamental experimental study as well as application to nondestructive evaluation. Theoretical discussions of the experimental results, including those based on the nonlinear spring-type interface model described here, can also be found in the works by, e.g., Barnard et al. [8], Wu [19], Kim et al. [22], Chen et al. [34], Biwa et al. [29, 35], Kim and Lee [23], Guo et al. [36], and Nam et al. [32]. The harmonic generation at a kissing bond at an adhesive interface has been studied by Yan et al. [13, 37] from a theoretical point of view based on a nonlinear spring-type interface model.

Acknowledgments The experimental results presented in Sect. 7.5 were obtained during 2006–2008 in collaboration with Mr. Shigeru Yamaji, a graduate student of Kyoto University, and Prof. Eiji Matsumoto. The writing of this chapter has been conducted partly for the basis of the author's current research project sponsored by the JSPS KAKENHI Grant Number JP16H04235.

References

1. G.W. Stachowiak, A.W. Batchelor, *Engineering Tribology* (Elsevier, Amsterdam, 1993)
2. T. R. Thomas (ed.), *Rough Surfaces* (Longman, London, 1982)
3. B.W. Drinkwater, R.S. Dwyer-Joyce, P. Cawley, A study of the interaction between ultrasound and a partially contacting solid-solid interface. Proc. R. Soc. Lond. A **452**, 2613–2628 (1996)
4. R.S. Dwyer-Joyce, The application of ultrasonic NDT techniques in tribology. Proc. IMechE J. J. Eng. Trib. **219**, 347–366 (2005)
5. K. Kendall, D. Tabor, An ultrasonic study of the area of contact between stationary and sliding surfaces. Proc. R. Soc. Lond. A **323**, 321–340 (1971)
6. P.B. Nagy, Ultrasonic classification of imperfect interfaces. J. Nondestruct. Eval. **11**, 127–139 (1992)
7. B. Gu, K.T. Nihei, L.R. Myer, L.J. Pyrak-Nolte, Fracture interface waves. J. Geophys. Res. **101**, 827–835 (1996)
8. D.J. Barnard, G.E. Dace, D.K. Rehbein, O. Buck, Acoustic harmonic generation at diffusion bonds. J. Nondestruct. Eval. **16**, 77–89 (1997)
9. I.Y. Solodov, Ultrasonics of non-linear contacts: Propagation, reflection and NDE-applications. Ultrasonics **36**, 383–390 (1998)
10. A.M. Sutin, V.E. Nazarov, Nonlinear acoustic methods of crack diagnosis. Radiophys. Quant. El. **38**, 109–120 (1995)
11. I.Y. Solodov, CAN: An example of nonclassical acoustic nonlinearity in solids. Ultrasonics **40**, 621–625 (2002)
12. R. Yamada, K. Kawashima, M. Murase, Application of nonlinear ultrasonic measurement for quality assurance of diffusion bonds of gamma titanium aluminum alloy and steel. Res. Nondestruct. Eval. **17**, 223–239 (2006)
13. D. Yan, B.W. Drinkwater, S.A. Neild, Measurement of the ultrasonic nonlinearity of kissing bonds in adhesive joints. NDT&E Int. **42**, 459–466 (2009)
14. O.V. Rudenko, Giant nonlinearities in structurally inhomogeneous media and the fundamentals of nonlinear acoustic diagnostic techniques. Phys. Usp. **49**, 69–87 (2006)
15. A. Baltazar, S.I. Rokhlin, C. Pecorari, On the relationship between ultrasonic and micromechanical properties of contacting rough surfaces. J. Mech. Phys. Solids **50**, 1397–1416 (2002)
16. J.M. Richardson, Harmonic generation at an unbonded interface-I. Planar interface between semi-infinite elastic media. Int. J. Eng. Sci. **17**, 73–85 (1979)
17. S. Hirose, J.D. Achenbach, Higher harmonics in the far field due to dynamic crack-free contacting. J. Acoust. Soc. Am. **93**, 142–147 (1993)
18. G. Shui, Y. Wang, J. Qu, A theoretical model for nondestructive evaluation of damage of adhesive joints. Key Eng. Mater. **324–325**, 339–342 (2006)
19. P. Wu, Nonlinear interaction of ultrasound with an unbounded rough interface. in: *2005 IEEE Ultrasonics Symposium*, 2005, pp. 289–292
20. C. Pecorari, Nonlinear interaction of plane ultrasonic waves with an interface between rough surfaces in contact. J. Acoust. Soc. Am. **113**, 3065–3072 (2003)
21. S. Biwa, S. Nakajima, N. Ohno, On the acoustic nonlinearity of solid-solid contact with pressure-dependent interface stiffness. ASME J. Appl. Mech. **71**, 508–515 (2004)
22. J.Y. Kim, A. Baltazar, J.W. Hu, S.I. Rokhlin, Hysteretic linear and nonlinear acoustic responses from pressed interfaces. Int. J. Solids Struct. **43**, 6436–6452 (2006)

23. J.Y. Kim, J.S. Lee, A micromechanical model for nonlinear acoustic properties of interfaces between solids. J. Appl. Phys. **101**, 043501 (2007)
24. O.V. Rudenko, C.A. Vu, Nonlinear acoustic properties of a rough surface contact and acoustodiagnostics of a roughness height distribution. Acoust. Phys. **40**, 593–596 (1994)
25. V. Gusev, B. Castagnède, A. Moussatov, Hysteresis in response of nonlinear bistable interface to continuously varying acoustic loading. Ultrasonics **41**, 643–654 (2003)
26. V. Gusev, Frequency dependence of dynamic hysteresis in the interaction of acoustic wave with interface. J. Acoust. Soc. Am. **115**, 1044–1048 (2004)
27. S. Biwa, Y. Ishii, Second-harmonic generation in an infinite layered structure with nonlinear spring-type interfaces. Wave Motion **63**, 55–67 (2016)
28. S. Biwa, S. Hiraiwa, E. Matsumoto, Stiffness evaluation of contacting surfaces by bulk and interface waves. Ultrasonics **47**, 123–129 (2007)
29. S. Biwa, S. Hiraiwa, E. Matsumoto, Pressure-dependent stiffnesses and nonlinear ultrasonic response of contacting surfaces. J. Solid Mech. Mater. Eng. **3**, 10–21 (2009)
30. S. Biwa, A. Suzuki, N. Ohno, Evaluation of interface wave velocity, reflection coefficients and interfacial stiffnesses of contacting surfaces. Ultrasonics **43**, 495–502 (2005)
31. O. Buck, W.L. Morris, J.M. Richardson, Acoustic harmonic generation at unbonded interfaces and fatigue cracks. Appl. Phys. Lett. **33**, 371–373 (1978)
32. T. Nam, T. Lee, C. Kim, K.Y. Jhang, N. Kim, Harmonic generation of an obliquely incident ultrasonic wave in solid-solid contact interfaces. Ultrasonics **52**, 778–783 (2012)
33. S. Biwa, S. Yamaji, E. Matsumoto, in *Nonlinear Acoustics – Fundamentals and Applications, CP 1022*, ed. by B. O. Enflo, C. M. Hedberg, L. Kari. Quantitative Evaluation of Harmonic Generation at Contacting Interface (AIP, New York, 2008), pp. 505–508
34. J. Chen, D. Zhang, Y. Mao, J. Cheng, Contact acoustic nonlinearity in a bonded solid-solid interface. Ultrasonics **44**, e1355–e1358 (2006)
35. S. Biwa, S. Hiraiwa, E. Matsumoto, Experimental and theoretical study of harmonic generation at contacting interface. Ultrasonics **44**, e1319–e1322 (2006)
36. X. Guo, D. Zhang, J. Wu, Quantitative evaluation of contact stiffness between pressed solid surfaces using dual-frequency ultrasound. J. Appl. Phys. **108**, 034902 (2010)
37. D. Yan, S.A. Neild, B.W. Drinkwater, Modelling and measurement of the nonlinear behaviour of kissing bonds in adhesive joints. NDT&E Int. **47**, 18–25 (2012)

Chapter 8
Nonlinear Acoustic Response of Damage Applied for Diagnostic Imaging

Igor Solodov

8.1 Introduction

The concept of using acoustic nonlinear response for material characterization stems from the first experimental observations of the second harmonic generation in solids in the early 1960s by Vladimir Krasilnikov in Russia and Mack Breazeale in the USA [1, 2]. The second (and the higher harmonic (HH)) generation implies that the stiffness of a nonlinear material is a function of strain that results in a local variation of acoustic wave velocity and the waveform distortion. In crystalline (flawless) materials, acoustic nonlinearity reveals a weak nonlinear behavior of inter-atomic forces so that even at high ultrasonic strains $\approx 10^{-4}$ in homogeneous and free from defects materials, the amplitude-dependent stiffness variation is usually below 10^{-3}. As a result, noticeable nonlinear effects are measured due to the HH accumulation along the propagation distance, and reasonable generation efficiency is observed only for the second harmonic signal.

Further experiments revealed a substantial increase of nonlinearity in materials with localized imperfections: a dramatic enhancement of the second harmonic signal was measured in a high-purity aluminum single crystal with dislocations induced by mechanical stress [3]. An important role of internal boundaries in acoustic nonlinearity of imperfect materials was then experimentally confirmed for dislocations in fatigued materials [4] and matrix–precipitate interfaces in alloys [5].

A further enhancement of nonlinear response was traced for the defects with a higher severity: anomalously efficient HH generation was measured for weakly bonded contacts of cracked defects (cracks, delaminations, impacts, etc.) due to specific Contact Acoustic Nonlinearity (CAN) [6]. Besides the much higher efficiency

I. Solodov (✉)
IKT, University of Stuttgart, Stuttgart, Germany
e-mail: igor.solodov@ikt.uni-stuttgart.de

T. Kundu (ed.), *Nonlinear Ultrasonic and Vibro-Acoustical Techniques for Nondestructive Evaluation*, https://doi.org/10.1007/978-3-319-94476-0_8

of the higher-order harmonic generation, the CAN-based nonlinear effects included qualitatively different "non-classical" acoustical phenomena, like frequency down conversion (subharmonics), hysteresis, instabilities, chaotic dynamics, etc. [7, 8] that are well known in other branches of nonlinear physics. These localized effects can be identified as nonlinear "tags" of the damage and applied to its recognition and imaging [9].

Unlike conventional (linear) nondestructive evaluation (NDE), which uses the amplitude and phase variation (primary effects) induced in the probing wave reflection/transmission/scattering by the defect, the nonlinear approach is based on the frequency variation as a result of the wave-defect interaction. In this regard, the nonlinear defect response can be referred as a derivative effect in the wave-defect interaction produced due to activating derivative material properties by an acoustic wave (nonlinear, thermal, acousto-optic responses, etc.). These secondary effects are generally the higher-order nonlinear functions of the acoustic wave amplitude and therefore relatively inefficient so that corresponding NDE and defect imaging techniques require an elevated acoustic power and specific instrumentation particularly adapted to high-power ultrasonics.

Another way to increase the vibration amplitude is to excite the specimen at one of its natural frequencies. This approach widely used in ultrasonic NDE has an obvious drawback of "missing" the defect due to the presence of nodal lines in a standing wave pattern [10, 11]. A more rational way to activate a defect has been found in driving the specimen at a natural frequency of the damaged area to result in the so-called Local Defect Resonance (LDR) [12]. Unlike the resonance vibration of the whole specimen, the LDR addresses the impact of the defect severity to its own resonance response, which is far stronger and is closely confined in the damaged area. It identifies the damage by its resonant response clearly distinguished and independent of the rest (intact) part of the specimen. The increase in local vibration of the damage results in enhanced efficiency and sensitivity of the derivative effects in acoustic wave-defect encounter. They include LDR activated nonlinear, thermosonic, and shearosonic responses demonstrated to be beneficial for NDE and imaging of damage [13].

This chapter starts with a brief summary of basic mechanisms of CAN and phenomenology of local frequency conversion scenarios under assumption of the damaged area to combine both resonance and nonlinear properties (Sect. 8.1). In Sect. 8.2, the methodologies of scanning laser vibrometry and Nonlinear Air-Coupled Emission (NACE) will be applied to nonlinear defect-selective imaging at different spectral components of local nonlinear spectra for various defects. The concept of LDR will be presented in Sect. 8.3 along with experimental evidence and characteristics of the damage mechanical resonance. A combined effect of LDR-CAN and new "nonclassical" features characteristic of nonlinear and parametric resonances are considered in Sect. 8.4, followed by the case studies of highly efficient and sensitive resonant nonlinear acoustic imaging and NDE of damage in composite materials and components (Sect. 8.5).

8.2 CAN Mechanisms and Nonlinear Vibration Spectra of Fractured Defects

According to the Introduction, the strength of contact bonding is a crucial factor for the build-up of nonlinearity in damaged areas. A weakly bonded interface of a cracked defect driven by intense in-plane or out-of-plane tractions exhibits nonlinear dynamics of an intermittent contact associated with either symmetrical or asymmetrical stiffness variation.

The asymmetrical modulation of the local stiffness (C_0) is, apparently, characteristic of the compression-tension contact vibration of the defect elements: it is higher for compression ($+\Delta C$) and lower ($-\Delta C$) for the contact tension. Such "bi-modular" behavior (clapping) of a pre-stressed contact interface can be approximated as a piece-wise stress (σ)–strain (ε) relation by using the Heaviside function $H(\varepsilon)$ [14]:

$$\sigma = C_0 \left[1 - H\left(\varepsilon - \varepsilon^0\right) \Delta C / C_0\right] \varepsilon, \tag{8.1}$$

where $\Delta C/C_0$ is the modulation depth of the compressed (ε^0 is the pre-strain) contact stiffness that, generally, can be as high as $\sim$1, i.e., about three orders of magnitude higher than that in the classical (flawless) case. The clapping contact, therefore, acts as a mechanical diode (Fig. 8.1) and results in an unusual rectified nonlinear waveform distortion. As soon as $\varepsilon > \varepsilon^0$, the Fourier series expansion of the nonlinear term in (8.1) indicates the generation of multiple both odd and even HH produced locally in the defect area. The clapping model entails a pulse-type stiffness variation so that the envelope of the HH amplitudes features the modulation by *sinc* function (Fig. 8.2).

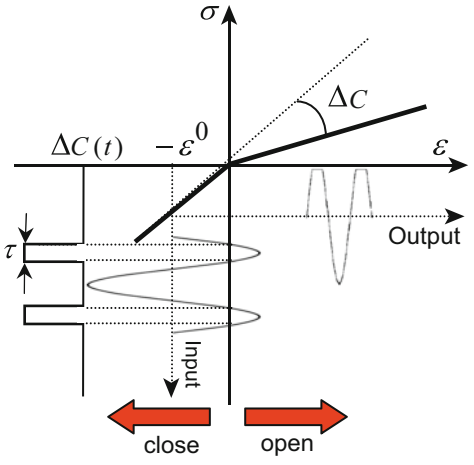

Fig. 8.1 Mechanical diode model of clapping CAN

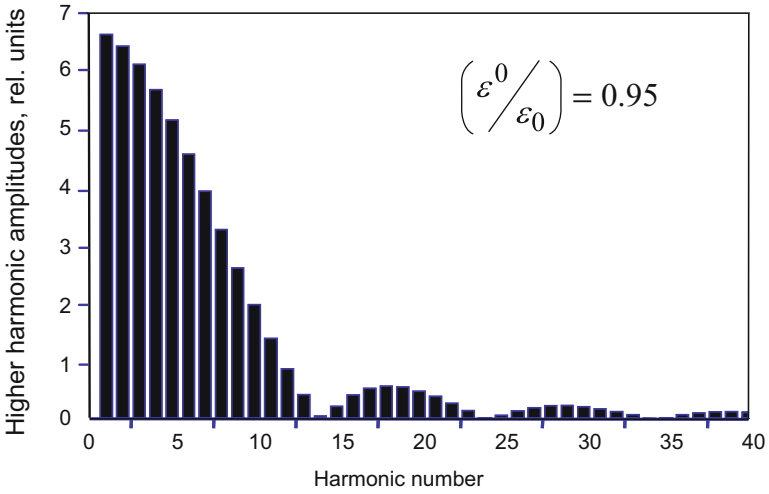

Fig. 8.2 HH spectrum modulation for clapping CAN

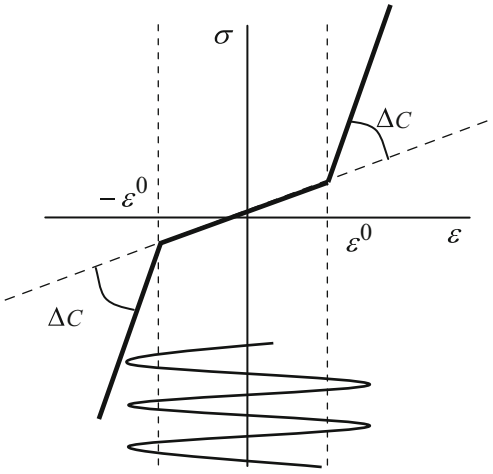

Fig. 8.3 Mechanical diode mode for micro-slip mechanism of CAN

For an in-plane drive (shear wave excitation), mechanical coupling of the contact interface is provided by the friction force caused by the interaction between asperities (micro-slip). This interaction constrains the in-plane vibration of the contact (in-plane clapping) and leads to a step-wise variation in tangential contact stiffness (Fig. 8.3):

$$\sigma = \left\{ C_0 - \left[H\left(\varepsilon + \varepsilon^0\right) - H\left(\varepsilon - \varepsilon^0\right) \right] \Delta C \right\} \varepsilon \tag{8.2}$$

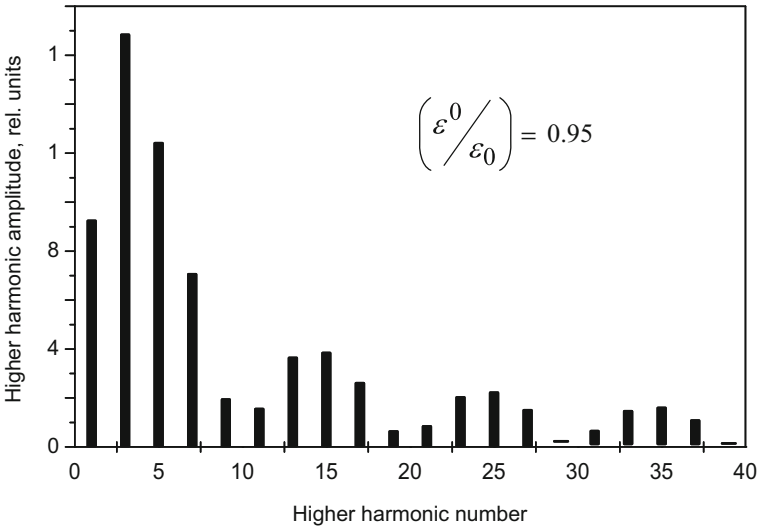

Fig. 8.4 Odd HH spectrum for micro-slip mechanism of CAN

For a harmonic excitation, the stiffness modulation is independent of the direction of in-plane motion (symmetrical nonlinearity) and provides only odd higher harmonic generation. Similar to the above, the step-wise stiffness variation manifests itself in *sinc*-modulation of the higher harmonic amplitudes (Fig. 8.4).

In realistic fractured damage, both CAN mechanisms are activated and result in an efficient generation of the nonlinear spectra that contain dozens of the higher-order HH. Provided the damage vibrates at local resonance (will be discussed in detail below) the HH is being confined inside the defect area that sets up the background for defect-selective nonlinear imaging of fractured flaws. Fortunately, this group of flaws includes the most typical defects in composite materials: micro- and macro-cracks, delaminations, disbonds, impact damages, etc., which will be discussed within the scope of this chapter.

The HH spectra analyzed above is not the only possible scenario of nonlinear defect vibrations. Inclusion of a cracked defect leads to a local decrease in stiffness of a certain mass of the damaged material, which should manifest in a particular characteristic frequency (ω_0) and therefore identified as a nonlinear oscillator (see Sect. 8.3). The contact nonlinearity can be introduced in the equation of forced vibrations of the oscillator as displacement (X) dependent nonlinear force $F^{NL}(X)$. For a harmonic driving force$f(t) = F_0 \cos \nu t$, the driven vibrations of the nonlinear oscillator are found as a solution to the nonlinear equation:

$$\ddot{X} + \omega_0^2 X = f(t) + F^{NL}(X). \tag{8.3}$$

In the second order of the perturbation approach, the nonlinear force in (8.3) accounts for the interaction between driving and natural frequency vibrations, so that $F^{NL} \sim \cos(\nu - \omega_0)t$.

Therefore, if the driving frequency is chosen as $\nu - \omega_0 \approx \omega_0$, the nonlinearity leads to a resonance increase in the output at $\omega_0 \approx \nu/2$ (subharmonic (SB) resonance). Taking into account the higher-order nonlinearity one obtains $F^{NL}(X) \sim m\nu - n\omega_0$ and the frequency matching relation $m\nu - n\omega_0 \approx \omega_0$ provides resonance output at $\omega_0 \approx m\nu/(n+1)$. For $n = 1$, the nonlinear spectrum acquires ultra-subharmonics (USB) of the second order $m\nu/2$, while the higher values of n bring about the USB of the higher orders.

In reality, a damaged area has a complicated mechanical structure that can be conceived as a set of coupled nonlinear oscillators with different natural frequencies [8]. If the defect is introduced as a pair of oscillators with normal frequencies $\omega_\alpha, \omega_\beta$ and the driving frequency is chosen as: $\nu \approx \omega_\alpha + \omega_\beta$, the second-order nonlinearity generates the difference frequency components $\nu - \omega_\alpha \approx \omega_\beta$ and $\nu - \omega_\beta \approx \omega_\alpha$, which provide simultaneous excitation of the both coupled oscillators. The two resonant spectral lines ω_α, ω_β in the nonlinear vibration spectrum are centered around the subharmonic position $\omega_\alpha \approx \nu/2 + \delta, \omega_\beta \approx \nu/2 - \delta$ and called a frequency pair (FP).

After taking into account the Nth-order nonlinear terms in the driving force, the spectrum acquires the following frequency components:

$$F^{NL}(\omega) \sim \sum\nolimits_{m,n,p} F_{mnp}\left(n\nu + m\omega_\alpha + p\omega_\beta\right). \tag{8.4}$$

Besides the higher harmonics $n\nu$, nonlinear spectrum (8.4) comprises the ultra-frequency pairs (UFP) $(n\nu + m\omega_\alpha + p\omega_\beta)$ and $(n\nu + p\omega_\alpha + m\omega_\beta)$. They are separated by $|m - p|\Delta$ $(\Delta = \omega_\beta - \omega_\alpha)$, centered around $[n\nu + (m + p)\nu/2]$ frequencies and structured into two sets around higher harmonics ($(m + p)$ even) and USB ($(m + p)$ odd). These features are illustrated in Fig. 8.5, where the results of calculations based on (8.4) are shown for the normalized amplitudes $F_{mnp} = 1$ and $N = 8$. The experimental results on the nonlinear spectra of local vibrations of damage and their applications for defect-selective imaging will be given in the next section.

8.3 Nonlinear Spectra of Damage and Defect–Selective Imaging

To observe the vibration spectra of damage the laser scanning vibrometry was adapted for nonlinear measurements (nonlinear scanning laser vibrometry (NSLV)). A continuous wave high-power Branson PG generator was used for excitation of flexural ultrasonic waves (frequencies 20, 40 kHz, strain amplitudes up to $\sim 10^{-3}$) by means of the piezo-stack transducers attached to plate-like composite specimens.

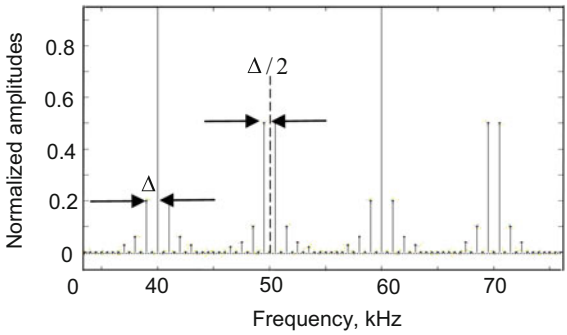

Fig. 8.5 Section of calculated UFP spectrum: $\nu = 20$ kHz; $\omega_\alpha = 9$ kHz; $\omega_\beta = 11$ kHz; $N = 8$

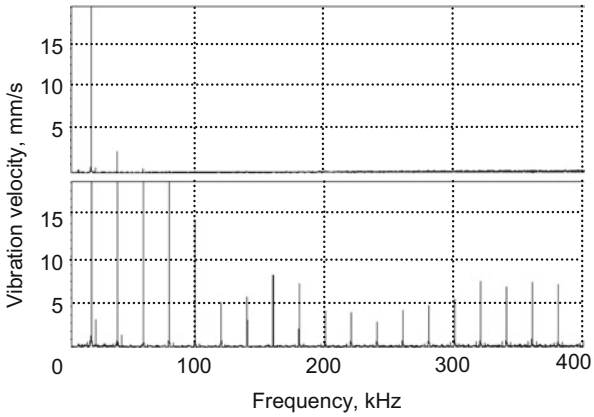

Fig. 8.6 Vibration spectra measured outside (top) and inside (bottom) damaged area in CFRP specimen. Excitation frequency is 20 kHz

The out-of-plane particle vibration velocity induces a frequency modulation of the laser light reflected from the surface of the specimen. After demodulation in the controller OFV 3001S of Polytec scanning vibrometer PSV 300 and A/D conversion, the spectrum of the vibrations is obtained at any point of the specimen surface over 1 MHz bandwidth by Digital Fourier Transform (DFT) in the PC-unit.

Figure 8.6 shows typical vibration spectra measured in a cracked carbon fiber-reinforced plastic (CFRP) specimen. In the intact region, the driving frequency (20 kHz) dominates in the vibration spectrum while the second harmonic content amounts to a few percent with a minor indication of the higher-order harmonics (Fig. 8.6, top). In the damaged area (Fig. 8.6, bottom), the spectrum reveals extremely efficient generation of multiple HH: their amplitudes are comparable to that of the driving frequency with evident indication of the *sinc*-modulation envisaged in Sect. 8.1.

The micro-slip mechanism of CAN, which according to Sect. 8.1 provides only odd higher harmonics, was found to prevail in wood, which is a natural fiber-reinforced composite. In an intact specimen, the HH spectrum shows an evident odd harmonic domination (Fig. 8.7). Then the specimen was damaged and the spectrum measured in the crack area acquired even-order higher harmonics generated due to contact clapping in the crack.

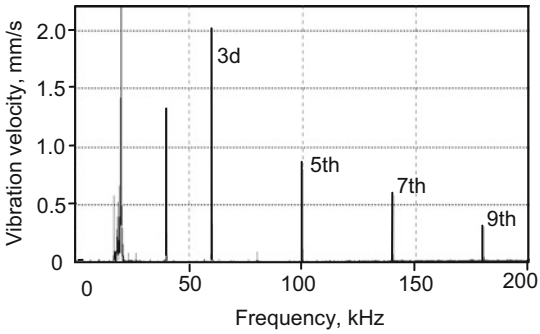

Fig. 8.7 Odd harmonic generation in intact wood; specimen driven at 20 kHz

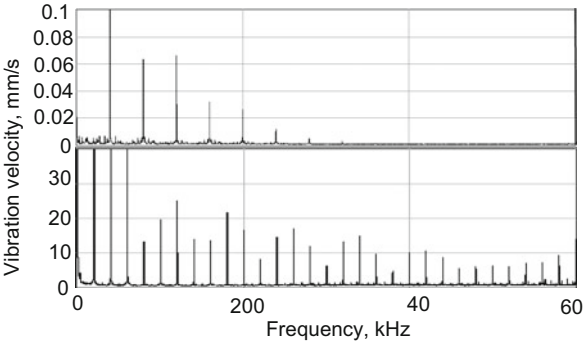

Fig. 8.8 Bifurcation of the higher harmonic spectrum (top) into USB (bottom) in damaged CFRP specimen

Figure 8.8 shows the USB-spectra measured in a cracked area of a CFRP rod ($8 \times 25 \times 350$ mm^3) driven by 40 kHz excitation. For a low-amplitude drive, the nonlinear spectrum consists of only HH of the driving frequency (top). As the driving amplitude grows beyond a certain threshold value, the HH pattern changes abruptly for the USB spectrum (period doubling bifurcation). The resonance enhancement of the USB components by orders of magnitude (compare the scales in Fig. 8.8) demonstrates the nonlinear instability, which switches the HH spectrum to multiple USB instantly (bottom)). The "wavy" amplitude modulation of the USB spectral components indicates involvement of the CAN clapping mechanisms in the USB generation.

As it was mentioned in Sect. 8.1, a realistic damage has a complicated mechanical structure and might display multi-frequency nonlinear resonances leading to the UFP generation. Such behavior is experimentally illustrated in Fig. 8.9, which shows a part of the UFP spectrum measured in the impact damage area of a glass fiber-reinforced composite (GFRP) for a 20-kHz excitation. The higher frequency section of the spectrum in the figure includes the second (40 kHz) and third (60 kHz) HH as well as ultra-subharmonics (50 and 70 kHz). The UFP lines are centered around the USB positions and distanced from them by $\Delta/2 \cong 0.6$ kHz. As expected, the UFP around higher harmonics reveal twice larger shift $\Delta \approx 1.2$ kHz. Overall agreement between the theory and the experiment becomes evident by comparing Figs. 8.9 and 8.5.

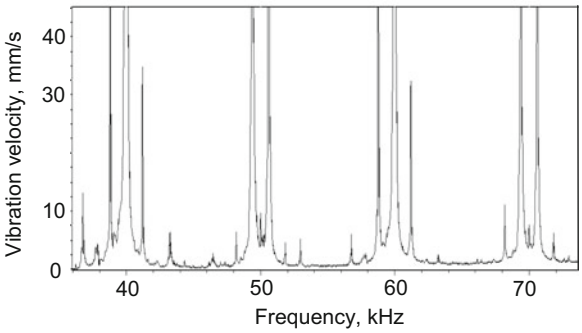

Fig. 8.9 Section of UFP spectrum in impact damage area of GFRP specimen; excitation frequency is 20 kHz. See Fig. 8.5 for comparison with theoretical results

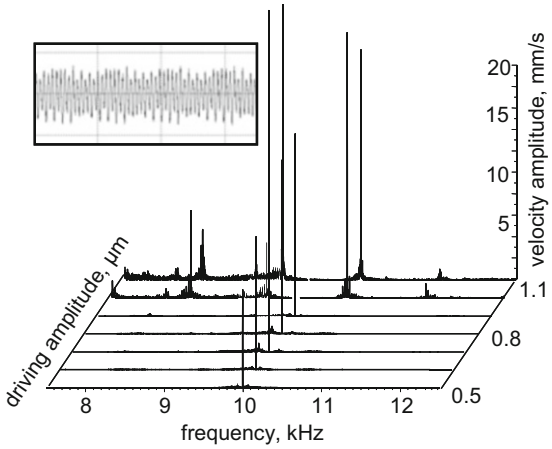

Fig. 8.10 USB-UFP bifurcation in delamination area of C/C-SiC-composite

Similar to the USB dynamics, the avalanche-like growth of the UFP components is observed when the input excitation exceeds a certain threshold level and is caused by the amplitude instability. The instable behavior of the UFP is demonstrated in Fig. 8.10 by spectral conversion beyond the subharmonic threshold. As the amplitude of the driving 20-kHz vibration is above the subharmonic threshold ($\approx$0.5 μm in Fig. 8.10), another instability threshold gives rise to a bifurcation into the UFP spectrum (at $\approx$1 μm-drive). The oscilloscope inset in Fig. 8.10 also shows the amplitude modulation (self-modulation) of the output signal in the USB-UFP transition due to emerging low-frequency side-lobes. A further growth of the driving amplitude results in broadening of the UFP lines into noise-like quasi-continuous frequency bands, which are the forerunners of the transition to chaos (Fig. 8.11).

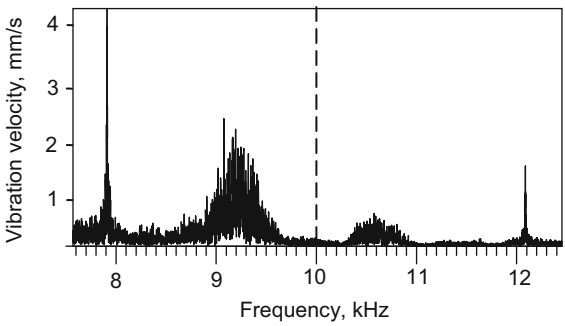

Fig. 8.11 Transition of UFP to noise-like spectrum in C/C SiC damaged composite. Driving frequency is 20 kHz

8.3.1 Nonlinear Imaging Via Laser Scanning Vibrometry

The nonlinear spectral components shown above are generated locally in the damaged area, while an intact part of material vibrates linearly, i.e., without frequency variation in the vibration spectrum. The emergence of the nonlinear spectral components is, therefore, a defect-selective indicator of damage presence and development. The localization of the nonlinear vibrations around the origin (in the damaged area) is a basis for nonlinear imaging of damage. To this end in the NSLV methodology, after a C-scan of the specimen surface any nonlinear spectral line is selected from the total spectrum detected by the laser vibrometer, and the distribution of this component over the specimen surface is presented as a color-coded image. Since normally (see the experimental data above) the total spectrum contains multiple nonlinear spectral components for a fixed input frequency, a single C-scan yields a number of images of the defect corresponding to various nonlinearly generated frequencies. Usually these nonlinear images are similar but not identical because the optimal conditions for generation of different nonlinear components depend on the input amplitude and also vary over the damaged area. In the images below, the selection of particular frequencies for nonlinear imaging is based on the best signal-to-noise ratio (SNR) to provide at least (10–20) dB difference between the nonlinear response of the damage and the outside (intact) background.

The defect-selective character of the nonlinear imaging is demonstrated by the example shown in Fig. 8.12. A linear (fundamental frequency 20 kHz) image of the damaged fabric carbon-kevlar fiber-reinforced composite (left) reveals a pronounced standing wave pattern in the specimen without any indication of damage. The HH images (Fig. 8.12, center and right) selectively indicate the point impact damages. The SNR (against background standing wave) of the 3d harmonic nonlinear image is about 20 dB in Fig. 8.12. The measured SNR usually increases for the higher-order HH since their level is lower in the excitation signal.

The two examples in Figs. 8.13 and 8.14 demonstrate the capability of the higher-order USB imaging. The image of a crack in polymethyl methacrylate (PMMA) specimen excited at 1.75 kHz (Fig. 8.13) is obtained at as high as the 33d USB of the excitation frequency (28.9 kHz). The maxima in the USB amplitude indicate

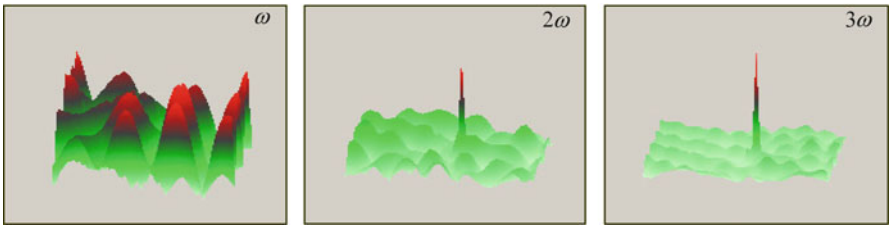

Fig. 8.12 Linear (left), second (center), and third harmonic (right) NSLV-images of a point impact damage in carbon-kevlar composite

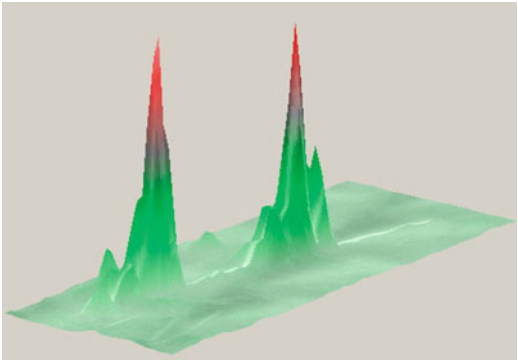

Fig. 8.13 33d USB image of a crack in Perspex specimen

particularly close contact areas between the crack faces. The photo in Fig. 8.14 (top) shows a hairline fatigue crack produced by cyclic loading in Ni-base super-alloy. The crack of less than 2 mm length, with average distance between the edges of only ≈5μm, is clearly detected in the 70 kHz USB ($7\nu/2$) image (Fig. 8.14, bottom), whereas traditional linear NDE by using slanted ultrasonic reflection failed to work with such tiny cracks.

The benefit of the UFP-imaging is demonstrated in Figs. 8.15 for the 14-ply epoxy-based GFRP specimen with a 9.5 J-impact damage (a). The linear image taken at the driving frequency of 20 kHz reveals only a well-developed standing wave pattern over the whole sample (b), whereas the image at the first UFP-side-lobe of the 10th HH of the driving frequency (198.8 kHz) reveals a very clear indication of the damage in the central area (c).

The example of the UFP nonlinear imaging of extended damaged areas in constructional materials is shown in Fig. 8.16 for a slab of GFR-concrete ($15 \times 30 \times 1.5$ cm^3) (a). For intense 20 kHz excitation, the image at 30.5 kHz UFP around the third USB clearly indicates the large delamination areas (b, dark color).

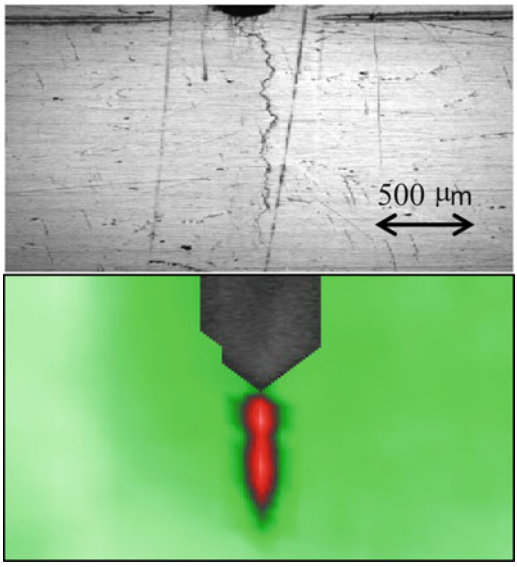

Fig. 8.14 Ultra-subharmonic (70 kHz) image (bottom) of a fatigue crack Ni-base super-alloy (top) driven by 20 kHz input

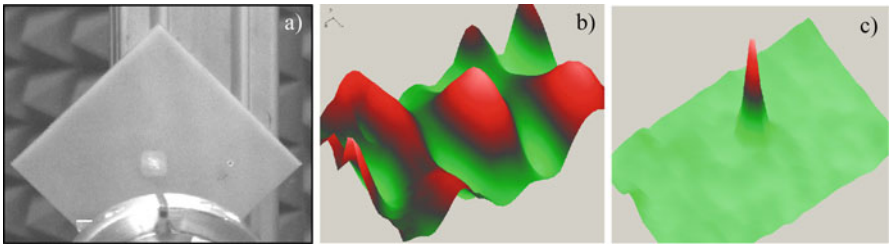

Fig. 8.15 Nonlinear imaging of an impact damaged area in the GFR-composite plate. (**a**, **b**) Linear image (20 kHz); (**c**) UFP-side-lobe image around 10th HH (198.8 kHz)

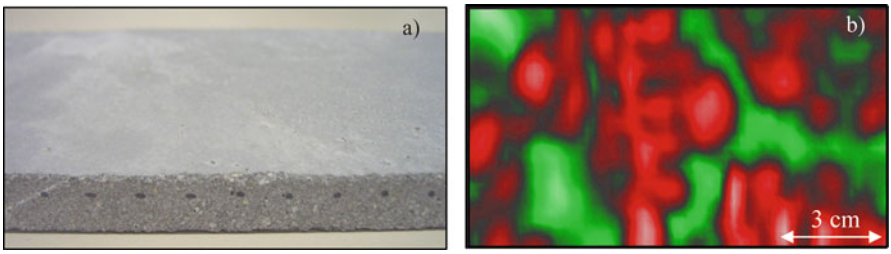

Fig. 8.16 UFP imaging of delamination areas (**b**) in GFR-concrete plate (**a**)

8.3.2 Nonlinear Air-Coupled Emission (NACE)

Our experiments [15] also showed that fractured defects as localized sources of nonlinear vibrations efficiently radiate nonlinear airborne ultrasound. Such Nonlinear Air-Coupled Emission (NACE) was proposed as an alternative methodology

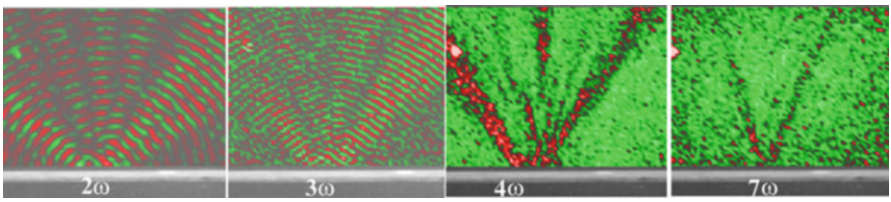

Fig. 8.17 NACE radiation patterns for various higher harmonics from a delamination in GFRP specimen driven by 50 kHz excitation

to NSLV to locate and visualize the defects. To experimentally evidence this effect, the air-coupled laser vibrometry was used [16] to visualize and quantify the airborne radiation of defects. Figure 8.17 shows a few HH NACE patterns for a delamination in GFRP specimen that reveals two main symmetrical side-lobes with frequency dependent radiation angles.

The directivity of airborne radiation assessed by calculation of a spatial Fourier transform of the vibration velocity distribution in the source area. If a defect (delamination) provides a homogeneous distribution of nonlinear (n-th order harmonic) velocity over length D along the x-axis, then the envelope of the nonlinear radiation source is:

$$w_n = w_0 \Pi\,(x/D) \exp\,(jn\omega t)\,, \tag{8.5}$$

where the rectangle function $\Pi(x/D) = 1$ for $|x| < D/2$ and zero otherwise.

The HH vibrations are activated by the standing wave pattern (i.e., by the oppositely propagating waves in the specimen (velocity c)) which introduce progressive time delay $\pm x/c$ in subsequent excitation of the HH sources so that $t \to t \pm x/c$ in (8.5). After this change, the Fourier transform of (8.5) is found as follows:

$$W_n\,(\theta) = w_0 D\,\mathrm{sinc}\,\left[(nKD/2)\right)(\sin\theta \pm \sin\theta_0)\Big]\,, \tag{8.6}$$

where $K = \omega/c$, $\sin\theta_0 = c_{air}/c/$.

The first conclusion inferred from this equation is that the radiation pattern (8.6) includes two main side-lobes steered symmetrically to $\pm\theta_0$ determined by the well-known Cherenkov's radiation condition. Secondly, the angular width of the side-lobes (determined by nKD factor) reduces for the higher-order harmonic NACE. Both conclusions are traced in the images shown in Fig. 8.17. The two symmetrical main side-lobes are clearly observed for all higher harmonics while the second harmonic NACE field exhibits maximum angular width of the side-lobes. The images in Fig. 8.17 also demonstrate that the radiation angle θ_0 reduces as the harmonic number increases, which is attributed to frequency dependent increase in flexural wave velocity (c) at HH frequencies.

An experimental setup of the NACE imaging system includes a high-frequency focused air-coupled (ACU) transducer as a scanning receiver of the nonlinear

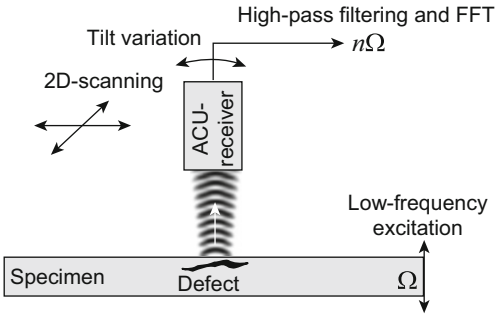

Fig. 8.18 Experimental setup for imaging of defects via NACE

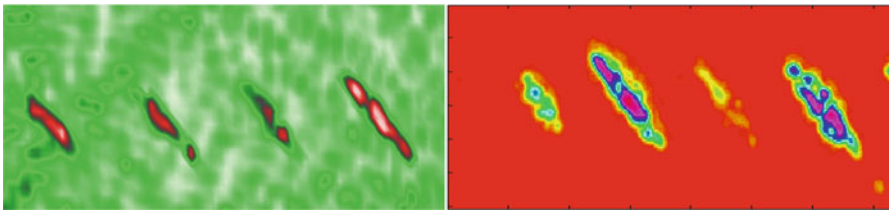

Fig. 8.19 Nonlinear imaging of multiple impact-induced damage in multi-ply $(+45^0; -45^0)$ CFRP-plate: laser vibrometry (second harmonic image, left); NACE (9–11th) higher harmonic image (right)

airborne ultrasound activated by a low-frequency excitation of the specimen. Similar to the NSLV, after a C-scan the output signal of the receiver is Fast Fourier Transformed (FFT) and a color-coded image of the amplitude distribution of any nonlinear frequency component over the specimen surface is obtained (Fig. 8.18).

In the experiments, a piezo-stack transducer and high-power supply (Branson Ultrasonics) were applied for low-frequency (around 20 and 40 kHz) excitation with $\geq 10^{-6}$ strain amplitude in the source. A focused (focus spot ~2–3 mm, focus distance 40 mm) ACU-transducer with frequency responses centered at ~450 kHz was used as a receiver in the C-scan mode. By changing the angle of inclination of the receiver one of the side-lobes of the NACE radiation pattern was selected. The transducer high frequency band-pass response (3 dB-bandwidth of the receiver ~20 kHz) combined with a high-pass filtering circuit provided a complete rejection of the low-frequency excitation signal. The nonlinear frequency components received (higher-order harmonics of the low-frequency vibration) are used as an input to acquisition unit of commercial air-coupled scanning system for computer imaging of NACE amplitude distribution over a specimen surface.

In Fig. 8.19, the NACE C-scan imaging results are compared with NSLV for multiple impact damage on a reverse side of a multi-ply $(+45^0; -45^0)$ CFRP composite plate ($175 \times 100 \times 1$ mm^3). Both techniques reliably visualize the defects with similar sensitivity.

A high NACE sensitivity to surface fractured defects is illustrated in Fig. 8.20 for μm-wide inter-ply delamination in a massive C/C/SiC-ceramic specimen (left). The NACE image (right) reproduces a discrete structure of cracking and demonstrates a good (mm-scale) lateral resolution along the crack.

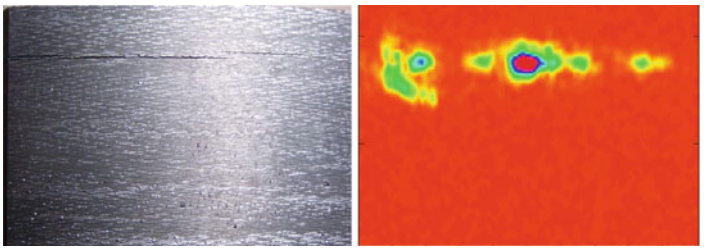

Fig. 8.20 NACE HH imaging (right) of inter-ply cracking (left) in a C/C/Si composite

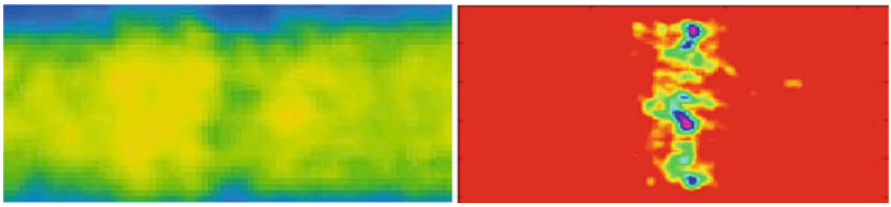

Fig. 8.21 A linear ACU-transmission (left) and NACE (right) images of a cold work strip (70×30 mm^2) in a steel plate

For weakly focused ACU-transducers with cm-range focus depth, the NACE was found to be insensitive to medium scale variations of the surface profile. Our experiments showed that the NACE operates well in various constructional materials (wood, concrete, and metals) with raw surfaces and rugged defects in components.

A very high sensitivity of NACE to micro-damage induced by plastic deformation was observed in metals. Figure 8.21 compares the linear ACU transmission (top) and the NACE (bottom) images of a cold work area in steel plate produced by hammer peening. An evident advantage in contrast to the NACE imaging over its linear counterpart is clearly seen.

The analysis of NACE angular patterns presented above is 2D, i.e., it describes the radiated field in the plane (xz) normal to the specimen surface. The defect is assumed to be infinite along the surface direction (y) normal to the wave propagation and the wave pattern is independent of y. In this case, for small D, $nKD << 1$ in (8.6), and the in-plane radiation is omni-directional, so that for the defect extended along the y-direction NACE produces a 2D-cylindrical wave in the xz-plane without radiation along the$y$-axis. Therefore, to detect such a cylindrical wave produced by the folded structure of the laser weld line in Fig. 8.22 (left), the ACU-transducer (tuned at 11th higher harmonic of the driving frequency 40 kHz) was aligned at an inclination angle in the xz-plane to result in the image of the line shown in Fig. 8.22 (center).

For a point-like nonlinear flaw in the center of the laser weld line (Fig. 8.22, center), the radiation pattern will apparently change for a 3D-spherical wave with NACE in both x- and y-directions. The defect size-dependent difference in the NACE radiation patterns enables to extract particular features in the images of

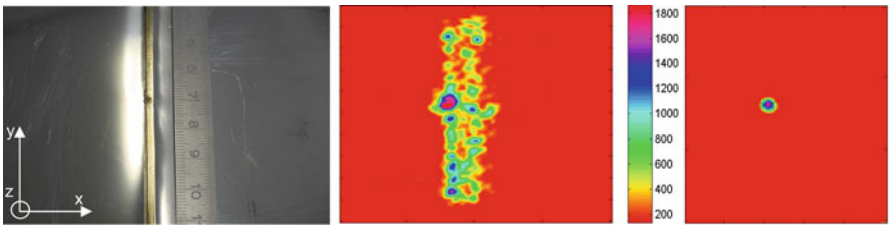

Fig. 8.22 3D-NACE imaging of the welding line with a point-like defect (left): NACE image for transducer orientation in the xz-plane (center) and in the yz-plane (right)

complex defects, as illustrated in Fig. 8.22 for a point-like extra-defect in the center part of the weld line. To visualize this point-like feature of the weld line image (Fig. 8.22, right), the orientation of the scanning ACU-receiver had to be changed for the *yz*-plane.

8.4 Local Defect Resonance: Concept, Simulations, and Experimental Evidence

The scenarios of local frequency conversion by nonlinear defects considered in the previous sections were based on the phenomenology of a resonant nonlinear defect (nonlinear oscillator) which was introduced in order to explain the manifestations of "nonclassical" nonlinear features and vibration spectra of damage (thresholds, instability, subharmonics, frequency pairs, etc.) observed in our early experiments [7–9]. A realistic concept and experimental evidence for the resonance in the damage vibrations were shaped up later and worked out in a series of our recent papers [12, 13, 17].

The resonance approach to "amplify" acoustical contribution of small inclusions has been introduced in ultrasonics of bubble liquids where a natural frequency of a bubble is used as a factor to increase an ultrasonic response of insonified μm-size spheres [18]. Further evidence of a strong enhancement of nonlinear acoustic response of the contrast agents due to resonance vibrations of incorporated gel bubbles made a breakthrough in ultrasonic medical diagnostics [19]. In solids, an opportunity of a resonance interaction of ultrasound with delaminations in composites was theoretically analyzed in [20] for plate waves. The nonlinear seismo-acoustic land mine detection methodology developed in [21] was also based on the model of a resonance inclusion in soil. Numerical simulations and shearographic imaging demonstrated a modal structure of resonant vibrations for delaminations [22] and flat-bottom holes [23] in composites.

8.4.1 LDR Concept and FEM Simulation

The concept of Local Defect Resonance (LDR) is based on the fact that inclusion of a defect leads to a local decrease in stiffness for a certain mass of the material around, which should manifest in a particular characteristic frequency (f_0) of the defect vibrations. The reduction in local stiffness is clearly seen for deformation of the defect modeled as a spherical cavity. A local stiffness (E_L) of such a defect for a stress normal to the cavity surface is given by [24]:

$$E_L = \frac{2\,(1-2\sigma)}{3\,(1-\sigma)} E_I \approx 0.3 E_I. \tag{8.7}$$

From (8.7), the stiffness of the intact material (E_I) reduces about three times for materials with Poisson's ratio $\sigma \approx 0.3$. For a disk-like crack of elliptical cross-section with semi-axes R (radius of the disk) and d (half of maximal opening), a local Young's modulus is [24]: $E_L \approx (d/R)E_I$. Provided that for realistic cracks $R \sim (10^{-3} - 10^{-2})$m and $d \sim 10^{-6}$m, a drop in local stiffness is very substantial: $E_L/E_I \sim (10^{-3} - 10^{-4})$.

We proceed with interpretation of the LDR concept for the defects presented as flat-bottomed holes (FBH), which simulate closely vibrations of such typical defects in composite plates as delaminations. The LDR frequency can be introduced as a natural frequency of the defect with an effective rigidity K_{eff} and mass M_{eff}: $f_0 = \frac{1}{2\pi}\sqrt{K_{\text{eff}}/M_{\text{eff}}}$. To derive the expressions for K_{eff} and M_{eff} we use the equations of the potential and kinetic vibration energy of the defect [25]. The parameters obtained for a circular FBH (radius R, thickness of residual material h) are:

$$K_{\text{eff}} = 192\pi D/R^2;\ M_{\text{eff}} = 1.8m, \tag{8.8}$$

while for a square FBH with side a and thickness h:

$$K_{\text{eff}} = 32\pi^4 D/a^2;\quad M_{\text{eff}} = 2.25m, \tag{8.9}$$

where $D = Eh^3/12(1-\nu^2)$ is the bending stiffness, E is Young's modulus, ν is Poisson's ratio, and m is the masses of the rest of plate with density ρ below the defect.

Equations (8.8) and (8.9) are then combined to yield the LDR frequencies for the defects in question:

$$f_0 = \frac{10h}{3\pi R^2}\sqrt{\frac{E}{5\rho\left(1-\nu^2\right)}}. \tag{8.10}$$

$$f_0 = \frac{4\pi h}{3a^2}\sqrt{\frac{E}{6\rho\left(1-\nu^2\right)}}. \tag{8.11}$$

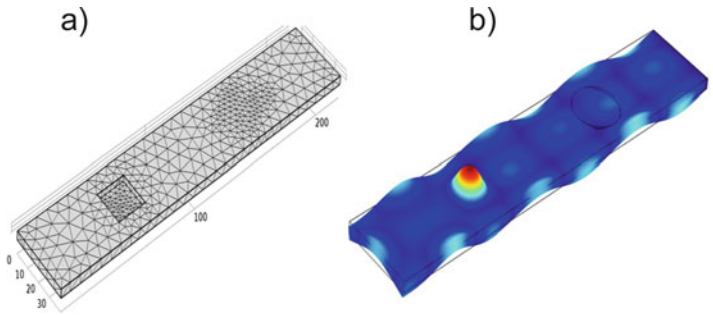

Fig. 8.23 FEM mesh (**a**) and fundamental LDR vibration pattern at $f_0 = 8255$ Hz (**b**) for 2×2 cm^2 square FBH in a PMMA plate

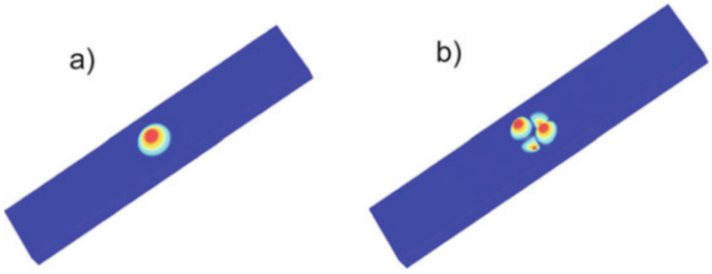

Fig. 8.24 A fundamental LDR (10.4 kHz) (**a**) and higher-order LDR (23.25 kHz) (**b**) for a FBH (radius 1 cm, depth 2 mm) in a PMMA plate (thickness 3 mm)

Equations (8.10) and (8.11) are also applicable to evaluation of the fundamental resonance frequencies of the defects, like laminar defects in rolled sheet metals and delaminations in composites. By using (8.11) for a square FBH in PMMA ($h = 1.2$ mm; $a = 2$ cm) we obtain: $f_0 = (7.2/9.4)$ kHz for Young's modulus values in the range (1.8/3.1) GPa given in the literature.

The problem of practical application of the analytical approach developed above is concerned with uncertainty in the boundary conditions for FBH of various geometries. Instead, the software COMSOL MULTIPHYSICS was used for analyzing the vibration characteristics of plates with FBH defects and estimating their LDR frequencies. By using eigen-frequency analysis package all possible resonances in the plate can be found and the vibration patterns plotted. Figure 8.23 shows a vibration pattern of a square FBH ($h = 1.2$ mm; $a = 2$ cm) in a PMMA plate at frequency 8255 Hz, which is readily identified as a fundamental LDR. A similar "bell-like" vibration pattern reveals a fundamental LDR in a circular FBH at 10.4 kHz (Fig. 8.24a), followed by the higher-order LDR at the higher driving frequency of 23.25 kHz (Fig. 8.24b). It is worth noting that the values of f_0 obtained are well within the frequency range covered by Eqs. (8.10) and (8.11).

8.4.2 LDR Experimental Evidence and Study

A direct way to experimentally reveal a Local Defect Resonance is to measure an individual contribution of each point of the specimen in its overall vibration frequency response in a wide frequency range. In the experiment, the specimen vibrations were activated with a wideband (400 Hz–100 kHz) piezoelectric transducer while a scanning laser vibrometer (Polytec 300) was used for interrogation of the specimen frequency response. The scanning mode enables to probe and indicate all possible resonances in the vibration spectrum for every point of the specimen. The spectrum obtained includes the resonance peaks corresponding to the natural frequencies of the specimen as well the LDR spectral lines. The task becomes simpler if a location of the defect is known: in this case the laser beam probing the defect area delivers the vibration spectrum dominated by the resonance peaks at a fundamental and the higher-order LDR frequencies.

An example of application of such an approach is shown in Fig. 8.25 for the circular FBH in PMMA plate used for FEM simulation in the preceding section. The origin of each maximum in Fig. 8.25 was verified by imaging the vibration pattern in the specimen at the corresponding frequency. The insets in Fig. 8.25 illustrate that the low-frequency resonant peak at about 8 kHz corresponds to one of the natural frequencies of the whole specimen. The main peak at $\approx$11 kHz is apparently a fundamental LDR (compare with simulation in Fig. 8.24a) followed by multiple higher-order LDR at higher frequencies. As it is seen from Fig. 8.25, both the fundamental and the higher-order LDR are caused by mechanical resonances (standing waves) within an area of reduced stiffness (a circular plate of residual material for a circular FBH defect). It is instructive noting that the LDR vibration patterns are similar to transverse modes of a cylindrical laser resonator (TEM_{nm} modes) [26] that points out the generality of resonant phenomena for different types of waves. The same notations are therefore also applied to the LDR vibration modes: n is the number of nodal rings and m denotes the number of nodal diameters in the images. The LDR vibration modes measured with laser vibrometry correspond to the extremes of out-of-plane vibration velocity (or displacement) whereas the patterns of nodal lines are identical to historical Chladni sand figures for a circular drum (Fig. 8.26).

As seen from Figs. 8.25 and 8.26, LDR is a clear "tag" of the defect location and a simple means for imaging of damage. The role of the high-order LDR is illustrated in Fig. 8.27 for imaging of a square insert (2.5×2.5 cm^2) in a ($300 \times 300 \times 5$ mm^3) CFRP specimen: Unlike vibration pattern of the fundamental LDR, which visualizes mainly the central part of the defect, the higher-order resonances also support vibrations at the periphery of the defect and thus contribute to imaging of its actual shape. Provided the frequencies of the higher-order resonances are within the wideband driving acoustic spectrum these resonances are excited along with the fundamental LDR and result in full scale imaging both shape and size of the defect (Fig. 8.27d).

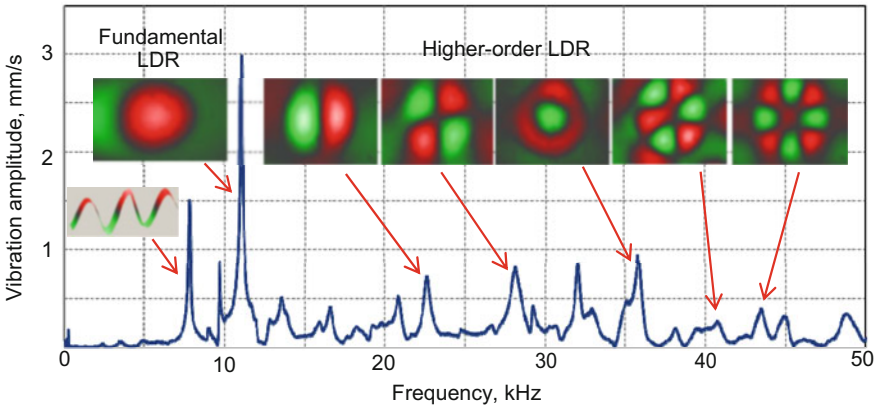

Fig. 8.25 Amplitude spectrum and vibration patterns at resonance peaks for the circular FBH in PMMA plate shown in Fig. 8.24

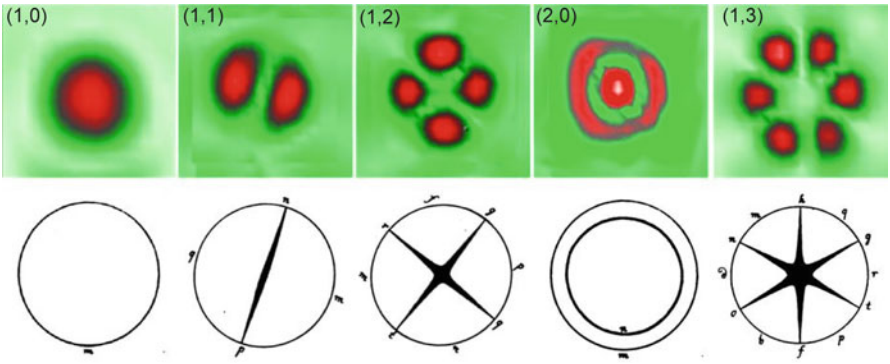

Fig. 8.26 Vibration patterns for various order LDR (*n*, *m*) in a circular FBH (top) and corresponding historical pictures of Chladni sand figures (from E.F.F. Chladni, *Entdeckungen über die Theorie des Klanges*, Beichmanns & Reich, 1787) (bottom)

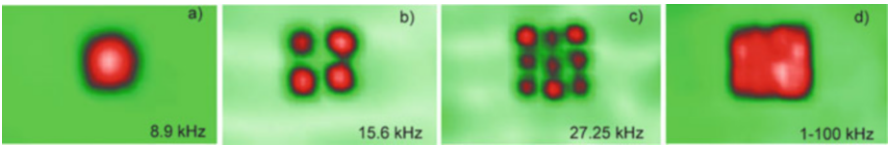

Fig. 8.27 Effect of the higher-order LDR: image of a square insert in CFRP plate at fundamental LDR (8980 Hz) (**a**), higher-order LDR (15600 Hz (**b**)), (27250 Hz (**c**)), and in a wideband (1–100 kHz) excitation mode (**d**)

Figure 8.28 demonstrates LDR frequency responses and the vibration patterns measured for a simulated (circular FBH in PMMA plate) and a realistic defect (impact damage in CFRP). Both LDR feature a classical resonance behavior and

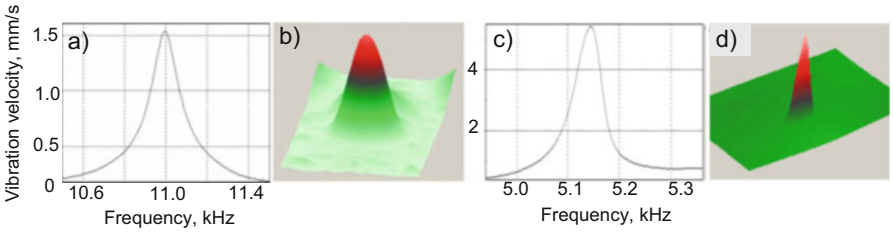

Fig. 8.28 LDR frequency responses and vibration patterns for a circular flat-bottomed hole (radius $a = 1$ cm; $h = 0.8$ mm) in PMMA plate ($200 \times 30 \times 3$ mm^3) (**a**, **b**) and impact damage in CFRP plate (**c**, **d**)

show a strong rise of the vibration amplitude confined strictly inside the defect areas with high-Q factors (Q ≈ 75 for FBH and Q ≈ 85 for the impact damage).

Similar to a conventional resonance, the value of Q factor determines the "amplification" of local vibrations due to LDR and is an important parameter in temporal development of the defect resonance. To illustrate this fact, the solution to the equation of forced defect vibrations in the presence of damping:

$$\ddot{x} + 2\lambda\dot{x} + \omega_0^2 x = F_0 \cos \nu t \tag{8.12}$$

is sought as a sum of the free and forced terms which for zero initial conditions and for takes the form of the transient vibration:

$$x = x_0 \left(1 - \exp\left(-\lambda t\right)\right) \cos \nu t \tag{8.13}$$

with the steady-state amplitude $x_0 \approx F_0/2\lambda\omega_0 = \left(F_0/\omega_0^2\right) Q$. This amplitude is $Q = \omega_0/2\lambda$ times higher than the vibration amplitude outside the resonance. By introducing Q value in (8.13) the exponential term takes the form $\exp(-(\pi/QT))$ so that Q periods of the driving signal $T$are required to reach the steady-state "amplification" of vibrations.

To verify the LDR "amplification" process, the CFRP impact damaged specimen (LDR frequency response shown in Fig. 8.28c) was excited with an ultrasonic burst while the transient development of vibration was monitored with the laser vibrometer. The results in Fig. 8.29 illustrate a good agreement between the experiment and the calculations based on the above relations. The values of Q factors measured for damage in various materials ranged from ~ 10 to 100 and provided LDR induced amplification of local vibrations as high as ~20 to 40 dB.

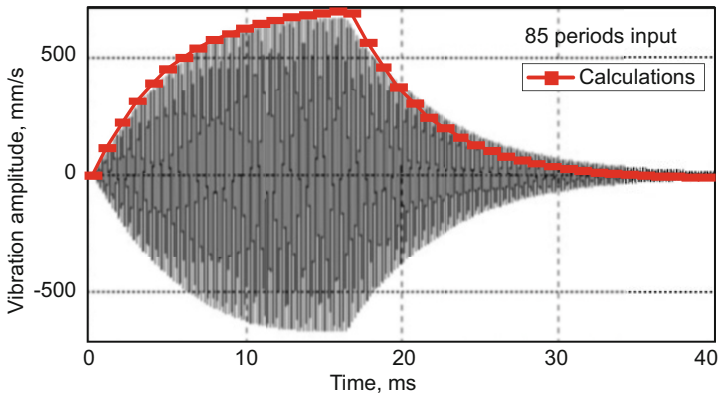

Fig. 8.29 LDR time response of an impact damage in CFRP to an 85 period burst signal at LDR frequency 5180 Hz

8.5 Resonant Nonlinearity of Defects

8.5.1 LDR: Enhanced "Classical" Nonlinear Effects

The high amplification of local damage vibration via LDR would contribute appreciably to defect nonlinearity. Due to LDR-induced enhancement of vibration amplitude by orders of magnitude, an efficient nonlinear frequency conversion is expected to develop at much lower acoustic inputs. In all the experiments below, acoustic powers for defect activation were in the mW range; with 20–30 dB transducer insertion losses it requires electrical inputs in the range of W, i.e., orders of magnitude lower that in the case of "classical" nonlinear acoustical NDE.

An extremely high resonant nonlinearity of a delamination in GFRP plate is seen in Fig. 8.30: the vibration spectrum of the damage acquires multiple HH even at a moderate input voltage of a few volts. A crucial contribution of LDR to the damage nonlinearity is illustrated in Fig. 8.31 for a crack in a unidirectional (UD-) CFRP rod. A strong enhancement of the HH amplitudes generated locally in the defect area is observed only as the driving frequency matches the LDR frequency (19.5 kHz).

The LDR-induced increase in nonlinearity can also be applied for efficiency enhancement of another "classical" nonlinear effect of frequency mixing. The method is based on the nonlinear interaction of ultrasonic waves of different frequencies (f_1,f_2) that results in a mixed frequency output: $f_{\pm} = f_1 \pm f_2$. For nonlinear experiments in "classical" materials, the efficiency of the interaction is highly critical to the geometry of the wave propagation and is generally rather low: the amplitude ratio $U_{\pm}/U_{1,2}$ is normally below $10^{-3} - 10^{-2}$. A high-Q LDR can enhance the output signal by matching either a combination frequency or the frequencies of the interacting waves to the LDR frequency response.

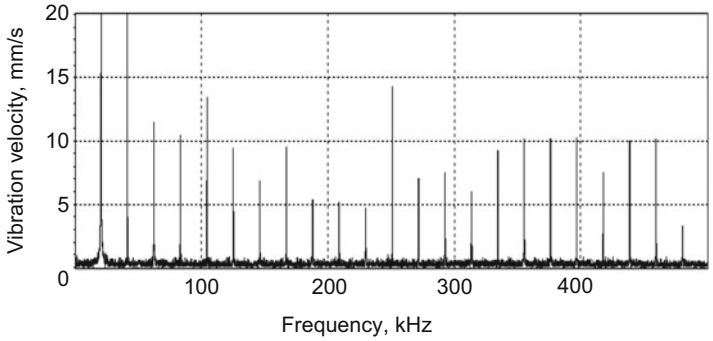

Fig. 8.30 HH spectrum for delamination in GFRP specimen driven at LDR frequency 20900 Hz. Input voltage is 7 V

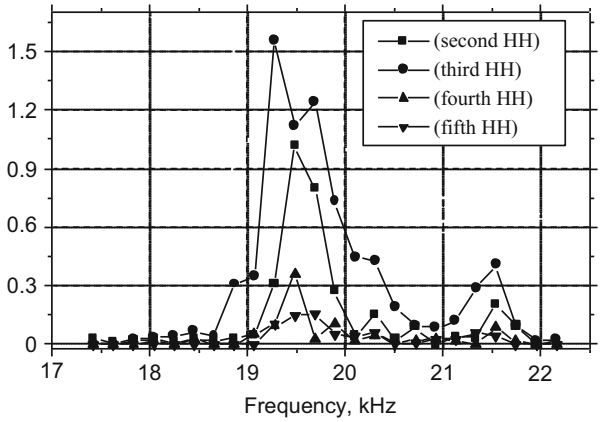

Fig. 8.31 HH LDR frequency response of a crack in CFRP rod (LDR frequency 19.5 kHz)

The "interacting wave amplifier" mode is demonstrated in Figs. 8.33 and 8.34 for a CFRP plate ($280 \times 40 \times 1$ mm^3) with an impact-induced damage area ($\sim 5 \times 5$ mm^2). A linear LDR frequency response of the defect manifests a well-defined double-maxima peak in (100–115) kHz frequency band with a high $Q \approx 100$ (Fig. 8.32).

In the experiment, the frequency of one of the waves (f_1=111500 kHz) is fixed to be matched to the LDR band while the frequency of the second wave (f_2) is swept within 80–130 kHz bandwidth. The nonlinear spectrum measured with laser vibrometer (Fig. 8.33) appears to be highly sensitive to the frequency match between f_2 and LDR: Only as soon as both frequencies are inside the damage resonance band and activate LDR, the interacting waves interact efficiently and combination frequency vibrations are generated in the damaged area (Fig. 8.34). Unlike the classical case, the nonlinear spectrum contains far greater number

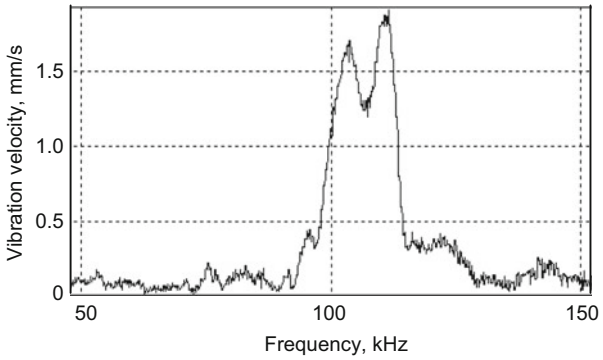

Fig. 8.32 LDR frequency response for an impact-induced damage in a CFRP plate

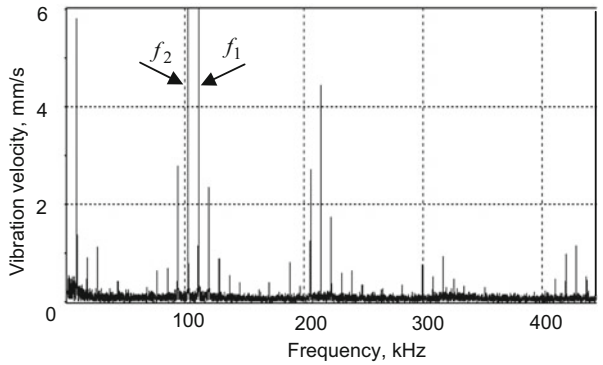

Fig. 8.33 Mixing frequency spectrum in an impact damage in a CFRP plate: f_1=111500 Hz; f_2=102800 Hz

Fig. 8.34 Variation of mixed frequency amplitudes as functions of f_2 frequency swept around LDR

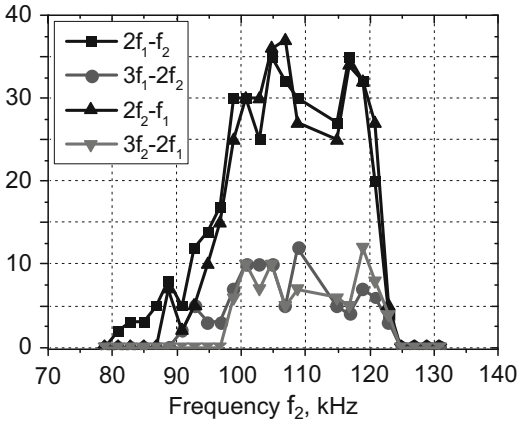

of mixed frequency components well described by $mf_1 \pm nf_2$ combination that indicates manifestation of the high order $((m + n)-)$ nonlinearity typical for CAN. The multiple side-lobe pattern in Fig. 8.33 reveals that the nonlinear interactions up to the 10th-order are developed by combining CAN and LDR.

The results in Figs. 8.30, 8.31, 8.32, 8.33, and 8.34 confirm that the activation of LDR enhances appreciably the nonlinearity of defects via local "amplification" of vibrations even at moderate input signals. It raises dramatically the efficiency of "conventional" nonlinear effects, like HH generation and frequency mixing. However, the classical nonlinear effects is not the only dynamic scenario of nonlinearity development and manifestation in resonant defects. At higher vibration level, a combined effect of resonance and nonlinearity results in qualitatively new "non-classical" acoustical phenomena characteristic of nonlinear and parametric resonances.

8.5.2 Superharmonic Resonances

To clarify the effect of nonlinearity on resonant higher level vibrations the higher order (second and third-) nonlinear terms are to be taken into account in the equation of forced vibrations of an oscillator with natural frequency ω_0 [27]:

$$\ddot{x} + 2\lambda\dot{x} + \omega_0^2 x + \alpha x^2 + \beta x^3 = F_0 \cos \nu t, \tag{8.14}$$

where λ is the dissipation factor, $\alpha$and β are the second and the third-order parameters of nonlinearity.

The superharmonic resonance is activated at integer multiples of the driving frequency so that if the input frequency is taken as $\approx\omega_0/n$ it is converted into ω_0 via the nth-order nonlinearity of the oscillator. The example analyzed below corresponds to $n = 2$ and uses the perturbation approach for obtaining solutions to Eq. (8.14).

The solution of the first approximation for the driving frequency $\nu = (\omega_0/2) + \varepsilon$ and small λ is a non-resonant linear driven vibration:

$$x_1 = \frac{4F_0}{3\omega_0^2} \cos\left[(\omega_0/2) + \varepsilon\right) t] \tag{8.15}$$

The resonance driving force is developed by means of the second-order nonlinearity, so that by inserting (8.15) in (8.14) and keeping only resonant terms in the right-hand side, one obtains in the second approximation:

$$\ddot{x}_2 + 2\lambda\dot{x}_2 + \omega_0^2 x_2 + \alpha x_2^2 + \beta x_2^3 = -\alpha x_1^2 \cos\left(\omega_0 + 2\varepsilon\right) \tag{8.16}$$

A solution to (8.16) could be readily found if one neglects the nonlinear terms in the left-hand side:

$$x_2^{2\omega} = \frac{4\alpha F_0^2}{9\omega_0^5\sqrt{4\varepsilon^2+\lambda^2}}\cos\left[(\omega_0+2\varepsilon)\,t\right] \tag{8.17}$$

A similar procedure for the input $\nu = (\omega_0/3) + \varepsilon$ leads to the solution for the resonant third HH vibration:

$$x_2^{3\omega} = \frac{\beta\left(x_1^0\right)^3}{8\omega_0\sqrt{9\varepsilon^2+\lambda^2}}\cos\left[(\omega_0+3\varepsilon)\,t\right], \tag{8.18}$$

where $x_1^0 = 9F_0/8\omega_0^2$.

Equations (8.17) and (8.18) demonstrate the resonant generation of the second and third HH vibrations for a fundamental frequency input (superharmonic resonances). The maximum amplitudes of the superharmonic resonant vibrations depend on the values of the high-order nonlinearity parameters resonances and the nonlinear driving force $\left(\sim F_0^n\right)$, which usually reduces strongly with increase of n. However, in the case of CAN a step-wise stiffness modulation triggers its higher-order nonlinearity, which does not necessarily decrease with n monotonically (see Sect. 8.1), so that one can expect a strong development of the superharmonic vibrations due to damage resonance.

In Figs. 8.35 and 8.36, the experimental evidence for superharmonic resonances in fractured defects is demonstrated for the third-order resonance in impact damaged CFRP specimen with LDR around 5140 Hz.

One-third of the LDR frequency (1714 Hz) was therefore selected for the excitation while the input voltage was increased up to 80 V. The temporal pattern of the vibrations in the damage area, however, indicates an exclusive presence of a "clean" third harmonic vibration (period ~0.19 ms in Fig. 8.36). The damage vibration spectrum (Fig. 8.35) confirms the domination of the third harmonic

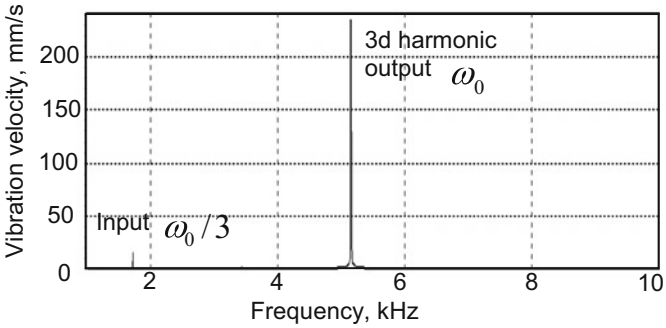

Fig. 8.35 Spectrum of the third-order superharmonic LDR in impact damaged CFRP plate

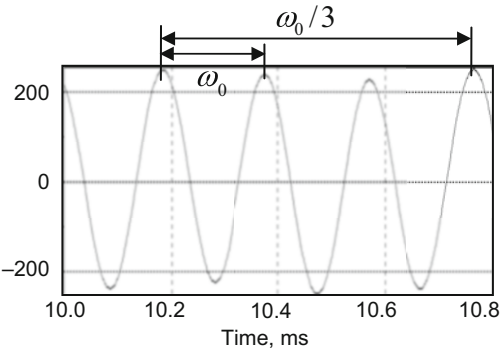

Fig. 8.36 Vibration pattern of the third-order superharmonic LDR in impact damaged CFRP plate

vibration: It is 25 dB higher than the fundamental in Fig. 8.35. Due to a high-Q of the fundamental LDR (Q ≈ 85, Fig. 8.28c), the superharmonic resonance required quite precise placing of the input (within 100 Hz) as one-third of the LDR frequency.

8.5.3 Combination Frequency Resonance

A high-Q LDR also modifies strongly the mixed frequency mode of nonlinear NDE. For a bi-frequency (ν_1, ν_2) excitation of a nonlinear defect, the equation of motion is:

$$\ddot{x} + 2\lambda\dot{x} + \omega_0^2 x + \alpha x^2 + \beta x^3 = F_1 \cos \nu_1 t + F_2 \cos \nu_2 t, \tag{8.19}$$

with the first-order (linear) solution:

$$x_1 = x_1^{\nu_1} \cos \nu_1 t + x_1^{\nu_2} \cos \nu_2 t \tag{8.20}$$

where $x_{1,2}^{\nu_{1,2}} = \frac{F_{1,2}}{\nu_{1,2}^2\left[\left(\omega_0^2/\nu_{1,2}^2\right)-1\right)}$.

The second-order term in (8.19) yields the driving force:

$$-\alpha x_1^2 = -\alpha x_1^{\nu_1} x_2^{\nu_2} \left[\cos\left(\nu_1 + \nu_2\right) + \cos\left(\nu_1 - \nu_2\right)\right], \tag{8.21}$$

which under the frequency match condition $\nu_1 \pm \nu_2 = \omega_0 + \varepsilon$ results in the resonant solution at the combination frequency:

$$x_2^{\pm} = -\frac{\alpha x_1^{\nu_1} x_1^{\nu_2}}{2\omega_0\sqrt{\varepsilon^2 + \lambda^2}} \cos\left[\left(\omega_0 + \varepsilon\right) t\right]. \tag{8.22}$$

An application of LDR as a "combination frequency resonator" was tested for an impact-induced circular damage in a CFRP plate with LDR frequency response

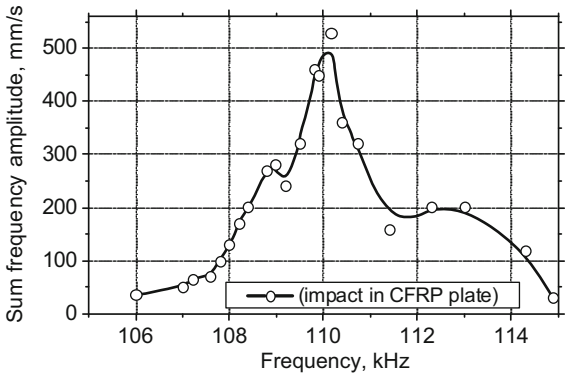

Fig. 8.37 LDR induced amplification at the sum frequency vibration for impact damage in CFRP plate

around 110 kHz shown in Fig. 8.32. The frequency of one of the interacting flexural waves was f_1=77.5 kHz while the other was swept from f_2=28.5 to 37.5 kHz to provide the sum frequency variation in the LDR bandwidth of the defect.

A laser scanning vibrometer in the vibration velocity mode was used for measurements of the vibration velocity amplitudes at f_1, f_2, and f_+ in the defect area. Figure 8.37 shows how the normalized velocity amplitude at sum frequency f_+ varied as the frequency f_2 changed over the sweeping range indicated above. Comparison of the results in this figure with the frequency response in Fig. 8.32 clearly indicates more than 20 dB increase in the output due to the combination frequency resonance activated when the combination frequency matches the frequency of LDR.

8.5.4 Parametric and Subharmonic Resonances

Resonant vibrations in a parametric system are triggered by varying a certain parameter at a frequency different from the natural frequency of the system. The parametric resonance of a mechanical system is different from conventional resonance because it exhibits the phenomenon of amplitude instability accompanied by an avalanche-like growth of the nonlinear vibration amplitude. This feature is obviously beneficial for boosting the nonlinear output in engineering applications. In resonant nonlinear defects, the activation of parametric effects is assumed to be due to the amplitude-dependent shift (modulation) of LDR frequency induced by the driving signal. The evidence for parametric resonance in realistic damage suggests a new extremely efficient and sensitive mode of nonlinear NDE and imaging of defects.

To analyze the opportunity of parametric resonance effects we apply again the perturbation method to Eq. (8.14). In the first approximation, for the driving frequency close to the resonance $\nu = \omega_0 + \varepsilon$, one obtains conventional linear vibration:

$$x_1 = \frac{F_0}{2\omega_0\sqrt{\varepsilon^2 + \lambda^2}} \cos \nu t. \tag{8.23}$$

In the next approximation, the quadratic nonlinearity in (8.14) produces the third-order interaction term in the form $\sim 2\alpha x_1 x_2$. By using (8.23) and taking into account this term only, one obtains:

$$\ddot{x}_2 + 2\lambda\dot{x}_2 + \omega_0^2\left[1 + \frac{\alpha F_0}{\omega_0^3\sqrt{\varepsilon^2+\lambda^2}}\cos\nu t\right]x_2 = 0. \tag{8.24}$$

Equation (8.24) is a Mathieu's-type equation of a general form:

$$\ddot{x} + \omega_0^2\left(1 + h\cos\gamma t\right)x = 0 \tag{8.25}$$

that reveals parametric resonance and instability phenomena [28, 29].

Equation (8.24) is obtained for $\nu \approx \omega_0$ and corresponds to the second-order parametric resonance. The solutions of this equation include unstable HH of the input signal: $\omega = n\nu$ $(n = 1, 2, 3, \ldots)$ [29], whose amplitudes grow in time exponentially above the input threshold (instability).

For $\nu \approx 2\omega_0$ input, the second approximation in (8.14) yields [27]:

$$\ddot{x}_2 + 2\lambda\dot{x}_2 + \omega_0^2\left[1 - \frac{2\alpha F_0}{3\omega_0^4}\cos\left(2\omega_0 + \varepsilon\right)t\right]x_2 = 0, \tag{8.26}$$

the equation for a fundamental parametric (subharmonic) resonance. In this case, the solutions to (8.26) yield unstable USB-vibrations: $\omega = m\nu/2 (m = 1, 2, 3, \ldots)$ [29].

Unlike conventional (linear) resonance, in a certain range of detuning ε the parametric resonances provide an exponential growth of the vibration in time even in the presence of damping. The instability develops in a step-wise manner is above as soon as the frequency modulation index I (input energy) is above a threshold level determined by the energy dissipated in the system. The critical values of I are the functions of ε (and vice versa): the higher modulation is generally required for larger frequency mismatch thus producing divergent boundaries of the V-shaped $I(\varepsilon)$curves for parametric resonances (Fig. 8.38) [30]. Thus, for the high excitation levels, the parametric resonances can be developed for driving frequencies outside the defect resonance. This explains that the parametric phenomena (thresholds, subharmonics, frequency pairs, etc.) were observed in Sect. 8.2 for the high input strain amplitudes (up to $\sim 10^{-3}$) even without precise frequency matching for the input frequencies 20 and 40 kHz. However, a "clever" frequency selection with an account of LDR enables to activate the resonance nonlinearity for 1–2 orders of magnitude lower inputs, i.e., to increase dramatically the efficiency of nonlinear NDE and defect imaging.

The experimental evidence for unstable parametric dynamics of the HH generation at the second-order parametric resonance is given in Fig. 8.39 for the impact damage (LDR at 5140 Hz, Fig. 8.28c) in CFRP sample. The parametric regime of the HH instability is activated beyond the threshold at ~30 V for the input at the

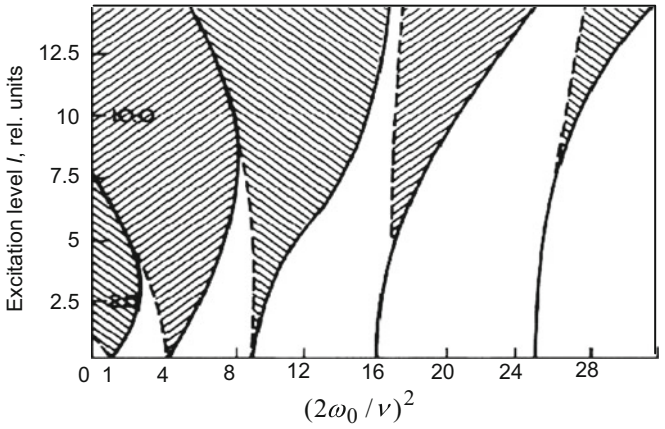

Fig. 8.38 Dynamics of parametric resonances of various orders (from A. Nafeh and D. Mook, Nonlinear oscillations, Wiley-Interscience 1979)

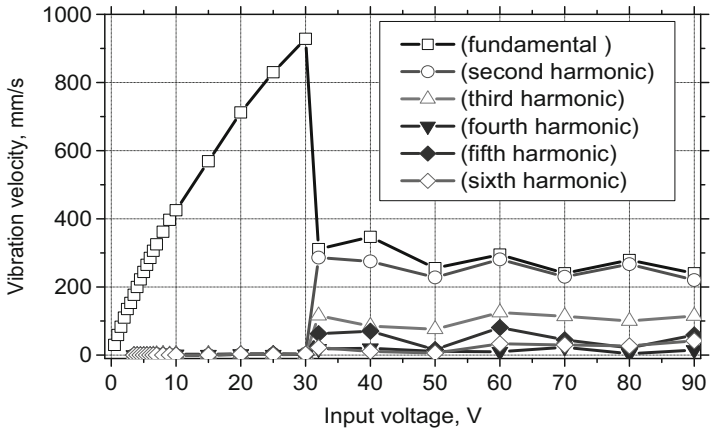

Fig. 8.39 Bifurcation nonlinear dynamics of resonant HH generation for an impact damage in a CFRP plate

LDR frequency (Fig. 8.39). It results in a strong nonlinear distortion of vibrations in the damage area with highly nonlinear spectrum of HH (Fig. 8.40). The fundamental vibration is depleted due to the energy outflow and heavily distorted (Fig. 8.40a) via frequency conversion to HH, whose amplitudes are comparable to the fundamental frequency vibration (Fig. 8.40b). The generation of the unstable HH vibrations is an expected result of the second-order parametric resonance that is activated for the input frequency equal to the LDR frequency of damage ($\nu \approx \omega_0$ in (8.24).

According to (8.26), the fundamental parametric (subharmonic) resonance requires the input at the second harmonic frequency. In the experiment, the excitation frequency was then changed to the second harmonic of the fundamental

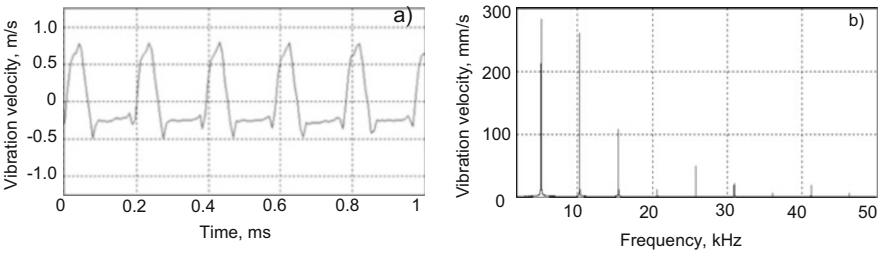

Fig. 8.40 Vibration pattern (**a**) and HH spectrum (**b**) beyond threshold for an impact damage in CFRP plate

LDR (10280 Hz) and the input voltage at the piezo-actuator increased further. The threshold for the instability was found to be ≈50 V (Fig. 8.41a); below the threshold (input 45 V) the vibration pattern of the damage follows closely the driving frequency 10280 Hz (Fig. 8.42, top). As the input passes the threshold, the subharmonic bifurcation develops: the vibration frequency turns into subharmonic (Fig. 8.42, (bottom), 55 V input), its amplitude bursts (compare the scales in Fig. 8.42a, b) due to parametric instability. According to Fig. 8.41b, the subharmonic component dominates in the damage vibration (velocity) spectrum beyond the threshold: $V_{\omega/2}/V_{\omega} \approx 30$ dB. At 10280 Hz input beyond the threshold, the temporal vibration pattern in the impact area is a pure sinusoidal subharmonic vibration of 5140 Hz (Fig. 8.42, bottom). Similar to the superharmonic case, the input frequency range for matching to the subharmonic resonance was measured to be within ∼100–200 Hz that corresponds to a high-Q factor of the LDR for this defect.

8.6 Resonant Nonlinear Defect-Selective Imaging

8.6.1 Contact Activation of Damage

In Sect. 8.4, diverse resonant nonlinear modes of defects vibrations have been shown to exist in various types of damage in composite materials. These resonant modes provide new options in developing nonlinear NDE and defect imaging applications based on either frequency selective nonlinear resonances (sub- and superharmonic resonance, combination frequency resonance) or simultaneous generation of multiple nonlinear frequencies (higher harmonics, various order combination frequencies). Due to the resonance, all these nonlinear frequency components are generated highly efficiently so that the input power can be reduced substantially. Therefore, the concept of LDR suggests a solution (applicable to NDE of localized damage) to a long-term bottleneck problem of a low efficiency of conversion from fundamental frequency to nonlinear frequency components in nonlinear ultrasonic applications in NDE&T.

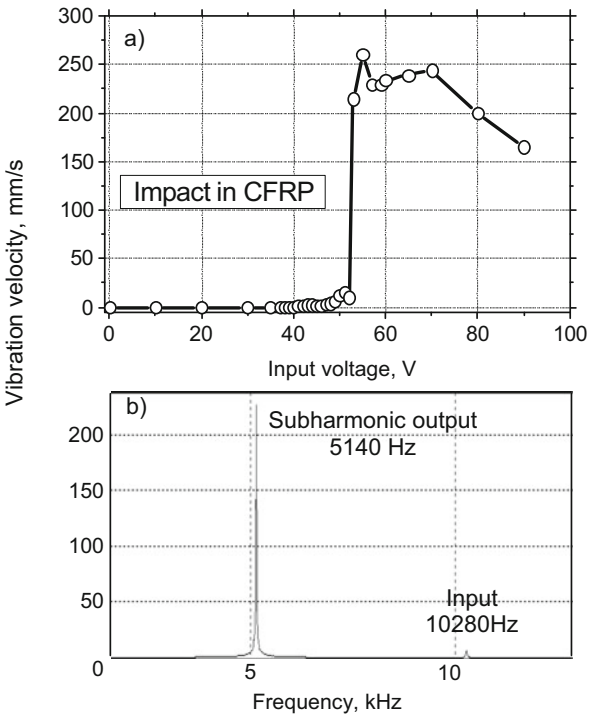

Fig. 8.41 Threshold dynamics (**a**) and vibration spectrum beyond the threshold (**b**) for fundamental parametric resonance in impact damage in CFRP

This modifies and simplifies considerably the experimental methodologies for laboratory investigations and NDE applications of the resonant nonlinear modes. Unlike specific equipment used in classical nonlinear studies, the LDR-based techniques admit using general purpose ultrasonic transducers, moderate-power and klirr-factor generators, avoid signal filtering, etc. In the experiments and applications below, the input electric power is usually well below 1 W; commercial off-the-shelf (*Conrad Elektronik GmbH*) piezo-ceramic transducers are used for ultrasonic excitation without any particular filtering of the input signals. Besides, due to LDR the nonlinear vibrations are being strictly confined inside the defect area. This makes LDR nonlinearity inherently defect-selective and provides the background for sensitive defect-selective nonlinear imaging of fractured flaws.

As it was shown in Sect. 8.3, a linear LDR also provides high-quality imaging of defects so that the benefits of nonlinear imaging have to be proved by comparison with its linear "competitor." An example of such a comparison is illustrated in Fig. 8.43 for the HH LDR imaging of a 10×20 mm^2 delamination with fundamental LDR frequency 36.77 kHz in 1 mm GFRP plate. The second harmonic LDR image (at 73.53 kHz) demonstrates a substantial improvement of the image quality: the signal-to-noise ratio (SNR) of the nonlinear image in Fig. 8.43b is ~24 dB, while ~12 dB was measured for the fundamental frequency LDR (a). A similar improvement in nonlinear image quality of ~20 mm long impact-induced fiber loss

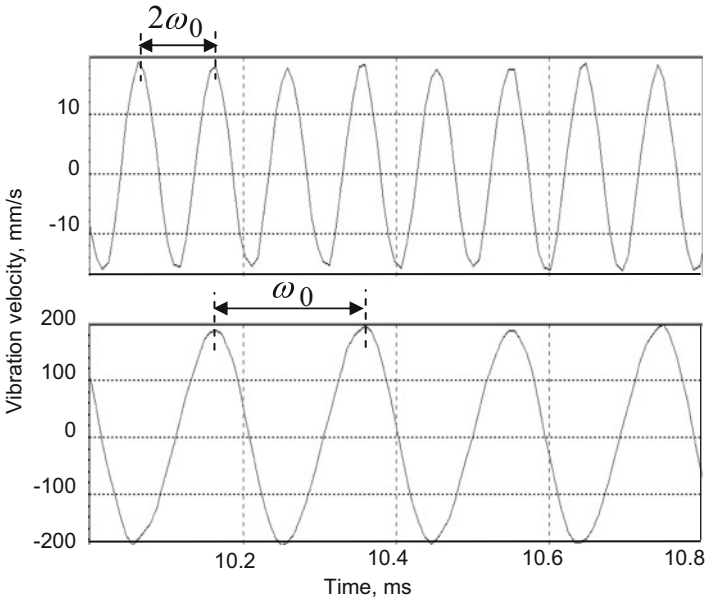

Fig. 8.42 Dynamic subharmonic bifurcation in impact damage in CFRP: Vibration pattern at driving frequency (input voltage 45 V, top); Bifurcation to subharmonic frequency at input voltage 55 V (bottom)

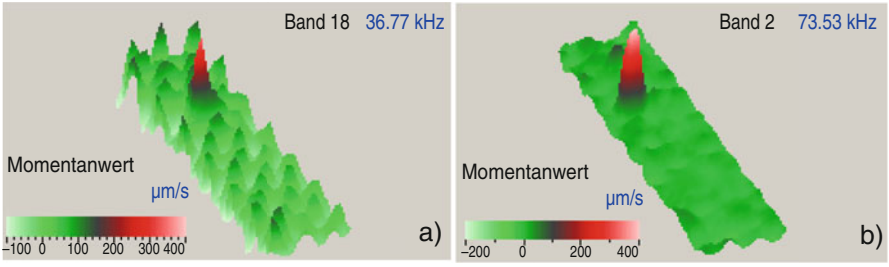

Fig. 8.43 LDR nonlinear imaging of defects: fundamental frequency (**a**) and the second harmonic LDR (**b**) images of $\sim 10 \times 20$ mm^2 delamination in GFRP plate

damage in CFRP plate is readily seen in Fig. 8.44 by comparing the linear LDR (3.66 kHz) (Fig. 8.44) and the second harmonic images (Fig. 8.44).

A substantial enhancement in SNR is also seen in Fig. 8.45 for the second harmonic of a high-velocity point impact in 5 mm thick CFRP window cut-out of a commercial airplane.

As shown in Sect. 8.4, the efficient mixing frequency mode is observed when both frequencies of the probing waves are within the range of the damage LDR frequency response. The test in Fig. 8.46 is concerned with a crack in a CFRP plate (top), whose LDR frequency is in the range of 37.5 ± 2.5 kHz. The defect

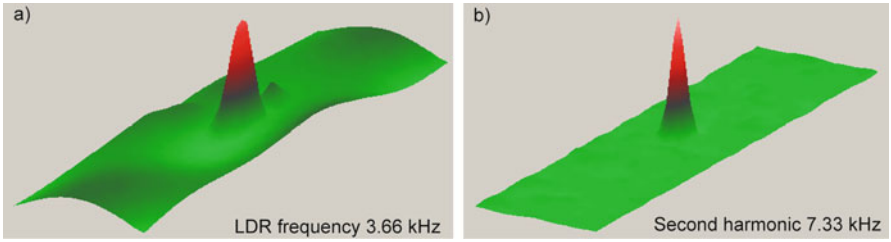

Fig. 8.44 Fundamental frequency (**a**) and the second harmonic (**b**) LDR images of impact-induced fiber loss in CFRP plate

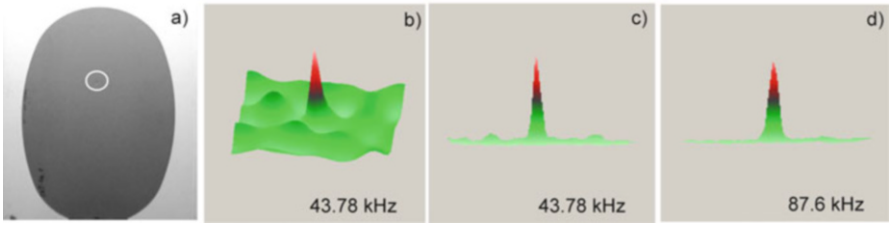

Fig. 8.45 A point impact damage in CFRP cut-out of aircraft window (in a white circle (**a**), LDR frequency 43.78 kHz), its fundamental LDR images (**b**, **c**) and the second harmonic (87.6 kHz) image (**d**)

is insonified with two oppositely propagating guided waves of the frequencies f_1=36 kHz and f_2=38 kHz. LDR amplified nonlinear interaction results in efficient generation of combination frequencies $mf_1 \pm nf_2$ in the defect area (Fig. 8.46, center) which produce multiple images of the defect (bottom). The SNR of the images is found to depend on the order of interactions (m, n) with maximum values ≈25 dB.

As it was suggested in Sect. 8.4, another opportunity of the frequency mixing is concerned with a combination frequency resonance, which amplifies selectively a single combination frequency component at LDR frequency. Such an image of the impact in a CFRP plate obtained via the combination frequency resonance (LDR frequency of the defect ∼107 kHz, see Fig. 8.32) by mixing two flexural waves of frequencies 77 and 30 kHz is shown in Fig. 8.47 and demonstrates a reasonable SNR (∼15 dB).

Other examples of the nonlinear and parametric resonance imaging are given in Figs. 8.48 and 8.49. Figure 8.48 illustrates a drastic increase of the SNR for the third-order superharmonic resonance in a CFRP specimen with an impact damage (fundamental LDR frequency 5145 Hz): the excitation frequency at 1715 Hz (one-third of the LDR frequency) obviously does not match the resonance conditions so that no image of damage is observed at this frequency (a), while the third HH output does and leads to ∼17 dB SNR in the superharmonic resonance image (b).

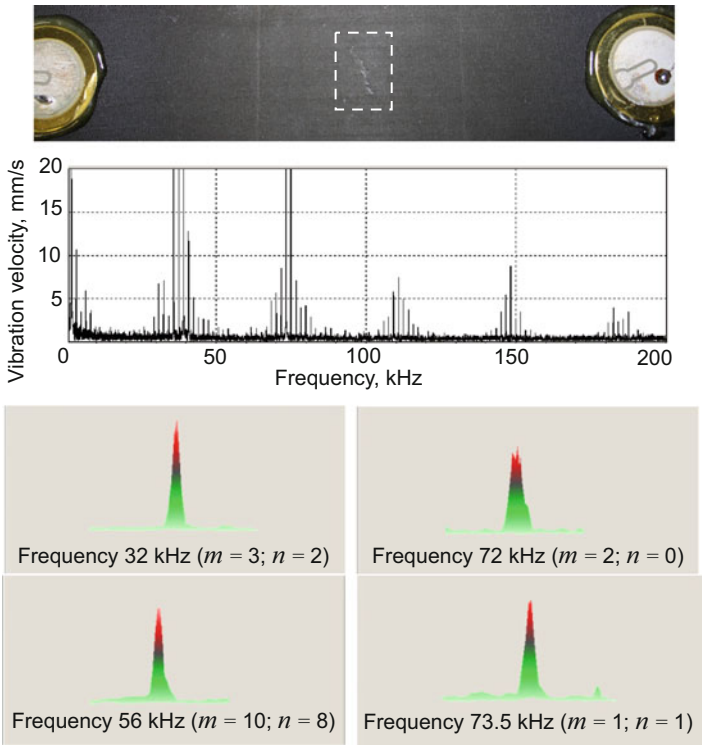

Fig. 8.46 Frequency mixing imaging of a crack in CFRP plate (top): Multiple frequency nonlinear spectrum (center) and a few combination frequency images (bottom)

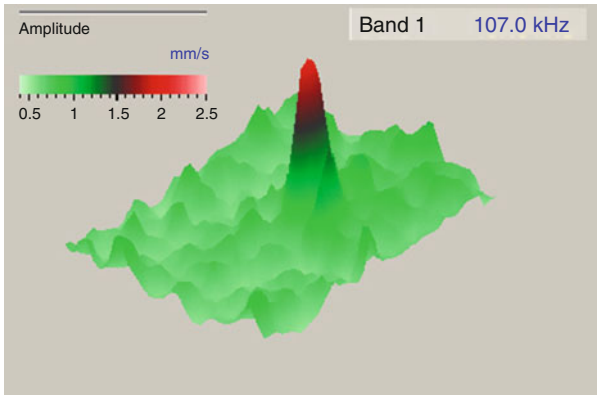

Fig. 8.47 Combination frequency resonance imaging: Sum-frequency image of the impact-induced damage ($\sim 5 \times 5$ mm^2) in a CFRP plate

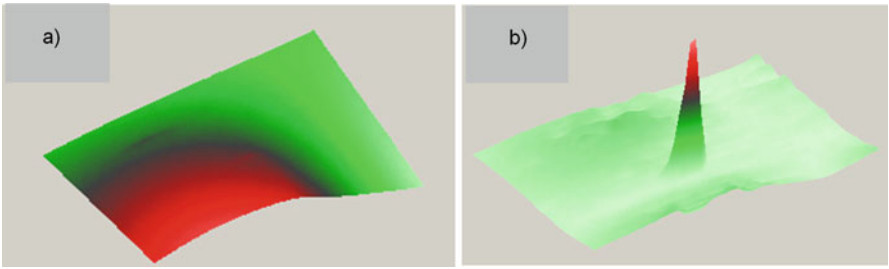

Fig. 8.48 Third-order superharmonic imaging of impact damage in CFRP: fundamental frequency (1715 Hz) image (**a**), the third HH (5145 Hz) image (**b**)

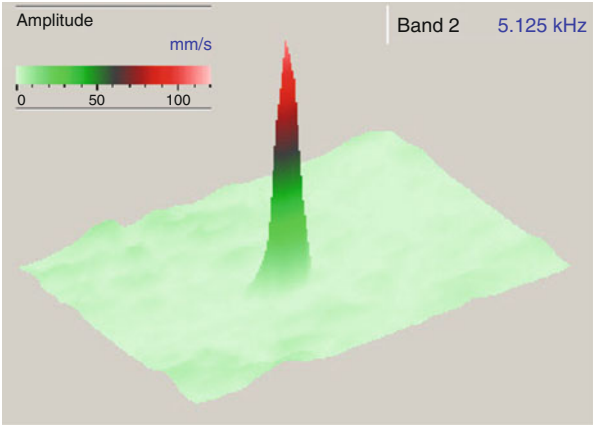

Fig. 8.49 Subharmonic LDR imaging of impact damage in a CFRP plate: Input 10250 Hz; output 5125 Hz

Figure 8.49 illustrates an application of a subharmonic resonance for imaging of the impact damage in the same CFRP specimen. In this case, the excitation frequency 10250 Hz is twice as the LDR fundamental frequency and the subharmonic image is visualized at LDR frequency 5125 Hz with an excellent SNR $\geq$35 dB.

8.6.2 Noncontact Nonlinear Imaging of Damage

To efficiently transmit the probing ultrasonic wave in conventional NDE methods, the ultrasonic transducer must usually be attached to the testing material via either solid ("permanent" bonding) or liquid (gel, water) couplants. In many cases, however, the contact to the component is not desirable (material deterioration) or possible (non-planar surface) and permitted (testing in production).

Development of remote techniques for elastic wave generation/detection enables to remove these limitations and to provide a great deal of flexibility in various NDT applications. The electromagnetic acoustic transducer (EMAT) is a well-known technology to be applied in ultrasonic frequency range (up to a few MHz) to conductive/ferromagnetic materials [31]. In laser ultrasonic testing [32], usually high-frequency (up to GHz range) ultrasonic pulses are generated remotely due to material thermal expansion/ablation caused by short laser pulses. The widely used air-coupled ultrasonics employs specially designed piezo-transducers to efficiently generate and transmit ultrasonic energy in air to be applied for noncontact testing in the frequency range about 50 kHz^{-1} MHz [33].

However, in the fiber-reinforced composite materials the high frequency ultrasound (MHz range) is not always applicable due to substantial damping. The low-frequency ultrasonic sensors (kHz range) are more adapted to inspection of large components in industrial environment, however, suffer from low scattering (and hence sensitivity) even for cm-size defects. For such defects (impacts, disbonds, and delaminations) in polymer composite materials, the LDR frequencies are in a low-kHz range that implies an opportunity of sonic NDE. Since the LDR vibrations are constrained exclusively in the defect area, the resonant techniques are not affected by diffraction, so that the lateral resolution of the resonant sonic imaging must be high despite the lower frequencies used.

Besides, the resonant response of the defect also entails a strong enhancement in sensitivity: the acoustic power required to activate the defects scales down to mW–μW range [34] and opens up an opportunity for remote airborne sonic testing. For this purpose, there exists a multitude of a high-quality commercial equipment (dynamic, piezoelectric, plasma-arc-, parametric speakers) to provide airborne sound intensities as high as 1 W/m^2 (120 dB) in m-distance ranges. The airborne sound sources can simultaneously insonify large areas and be applied for remote sonic testing of different materials and various scale components.

In the experiments below, two types of loudspeakers were applied for sonic activation of defects:

1. Commercial dynamic loudspeakers JBL Control One with RMS power of 150 W provided airborne excitation in the frequency range 2–19 kHz with sound intensity 85–100 dB.
2. Piezoelectric loudspeakers CTS 232 with maximal frequency response between 3 and 20 kHz and maximum sound intensity within 100–120 dB range.

To probe and quantify the radiated sound field, the air-coupled vibrometry technique [16] was used, which relates the laser vibrometer readings of "virtual" Doppler velocity V with the amplitude of vibration velocity $\Delta V_{\sim}$ in the sound field:

$$\Delta V_{\sim} \approx 3.5 \cdot 10^3 (KL)^{-1} V, \tag{8.27}$$

where K is the sound wave number and L is the sound field aperture.

Equation (8.27) was used to evaluate the vibration velocity $\Delta V_{\sim}$ at the "output" (at 1–2 cm distance) from the sound source where the beam diffraction is not

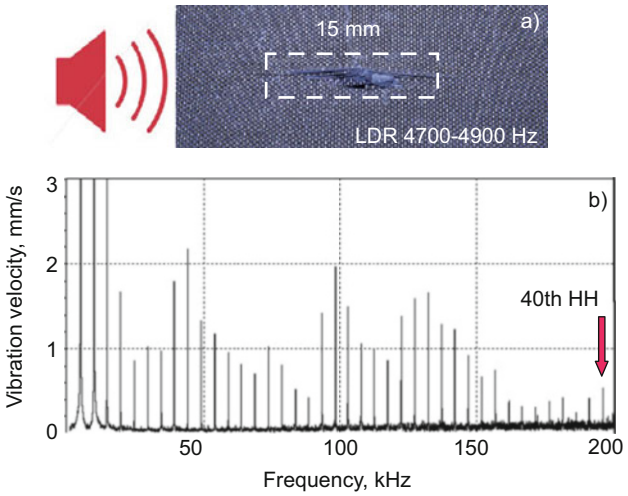

Fig. 8.50 Impact-induced damage in CFRP specimen used for noncontact nonlinear laser vibrometry (**a**); HH spectrum in the defect area (**b**)

developed and $L \approx$ diameter of the loudspeaker. In the case studies given below, the sound intensities used for noncontact nonlinear imaging were in the range of 100–110 dB derived from $\Delta V_{\sim}$ values at this measurement position. The speakers were positioned at a distance of 30–150 cm from either the front or reverse surface of the specimens. Both normal and slanted incidence setups were tested; in the latter case, the angle of sound incidence on the specimen surface was in the range of 30–45°.

In Fig. 8.50, the slanted setup is applied for a noncontact sonic activation of an impact damage with LDR frequency response within the range of 4700–4900 Hz in CFRP plate ($270 \times 40 \times 1$ mm^3, a). The dynamic speaker was positioned at a distance of 20–30 cm from the specimen surface. For the radiated sound intensities 85–100 dB, the amplitude of the plate wave generated in the CFRP plate measured with a laser vibrometer ranged from 10^{-9} to 5×10^{-8} m. Due to LDR "amplification" of 25 dB a local vibration amplitude in the damage area increased strongly (from 5×10^{-8} m to 0.85 μm) that was sufficient for triggering defect nonlinearity.

As a result, the nonlinear vibration spectrum recorded in the defect area (Fig. 8.50b) demonstrates a strong nonlinearity: more than 40 HH is generated in the noncontact nonlinear mode. A single C-scan of the specimen surface is then applied for mapping the distribution of HH amplitudes and delivers a number of HH defect images (Fig. 8.51). The multitude of the nonlinear images for a single measurement enables to select the images with the highest SNR. Figure 8.51 confirms a good repeatability of the image position for different HH; this feature of the nonlinear imaging increases the probability of defect detection.

The frequency mixing mode is considered as one of the most prospective for NDE applications due to the minimum number of spurious signals. According

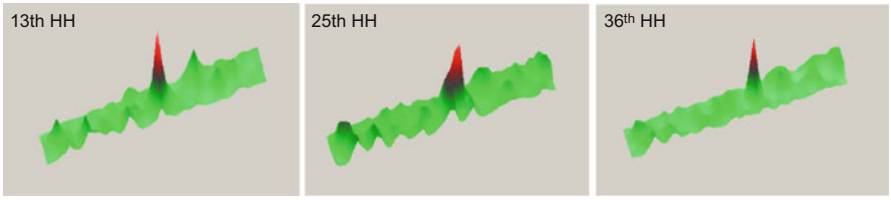

Fig. 8.51 Noncontact resonant imaging of the defect in Fig. 8.50 (**a**) at various higher harmonics

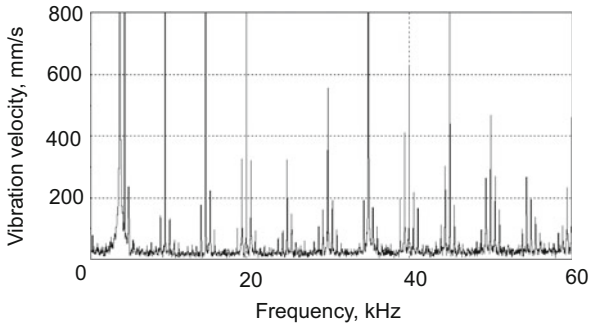

Fig. 8.52 Noncontact frequency mixing spectrum in impact damage area for input frequencies $f_1 = 4450$ Hz and $f_2 = 5000$ Hz

to Sect. 8.4, one of the highly efficient LDR versions of this mode requires the excitation frequencies to be positioned around the LDR bandwidth to make use of resonant amplification of interacting waves. A noncontact version of this mode was tested in the experiment for impact damage (LDR frequency around 5 kHz) in a CFRP plate. The specimen was insonified with sound waves radiated by two loudspeakers at frequencies $f_1 = 4450$ Hz and $f_2 = 5000$ Hz in the LDR bandwidth. The spectrum of damage vibrations (Fig. 8.52) demonstrates that similar to the contact excitation case (Fig. 8.30) the higher-order nonlinearity can be activated in a noncontact mode. Multiple mixed frequency components generated are also well described by $mf_1 \pm nf_2$ combination produced by the higher $(m + n)$-order of nonlinear interaction. Each of the nonlinear frequency components in Fig. 8.52 indicates the damage presence and its position as seen from Fig. 8.53 where a few examples of the noncontact higher-order mixing frequency images are given.

The opportunities for a noncontact excitation of the parametric resonances in the defect vibrations are illustrated in Fig. 8.54a, b for the impact damaged CFRP discussed above. To overcome the parametric threshold, the piezoelectric loudspeakers were used to provide the higher sound intensity ~110 dB. To detect a subharmonic resonance the driving frequency is chosen as a fraction of the damage resonance frequency while the defect responds at its LDR frequency. The spectrum in Fig. 8.54a is measured for the damage activation at the input frequency of $f_0 = 1600$ Hz (one-third of the fundamental LDR), however, the defect nonlinear

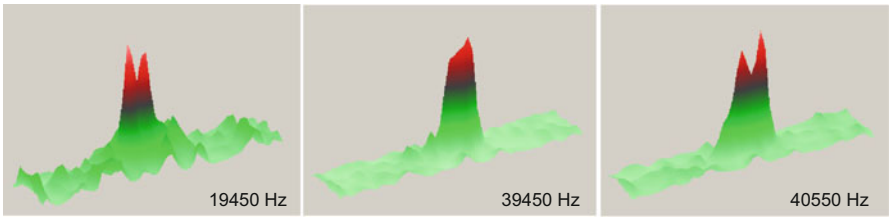

Fig. 8.53 Remote frequency mixing imaging of the impact damage for the input frequencies 4450 and 5000 Hz. The output frequencies are indicated on the images

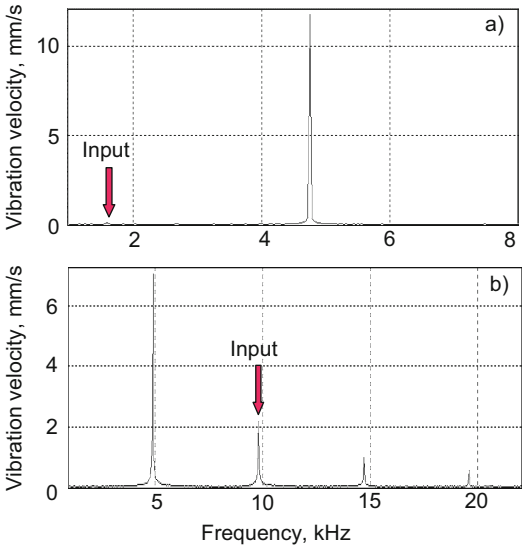

Fig. 8.54 Noncontact excitation of the third superharmonic (**a**) and subharmonic (**b**) resonances for the impact damage defect in CFRP

response peaks overwhelmingly at $f_0 = 4800$ Hz that indicates an extremely efficient development of the third-order superharmonic resonance in the defect area (similar to the contact excitation case). If, on the contrary, the excitation is switched to the double LDR frequency ($f \approx 2f_0 = 9800$ Hz) an efficient (and unstable) subharmonic output at $f_0 = f/2 = 4900$ Hz and the integer multiples of the LDR frequency (Fig. 8.54b) validate the feasibility of the noncontact mode of subharmonic (ultra-subharmonic) resonance.

Similar to all nonlinear vibration modes, the parametric resonance frequency components are also generated locally within the damage area and, therefore, are readily applied for noncontact nonlinear imaging of defects. This opportunity is demonstrated in Fig. 8.55a, b for input frequency $f = 9800$ Hz in the impact damaged CFRP discussed above. Both the third subharmonic (at $3f/2 = 14700$ Hz (a)) and the second harmonic resonance images ($2f = 19600$ Hz (b)) demonstrate a good reproducibility in visualizing the damage.

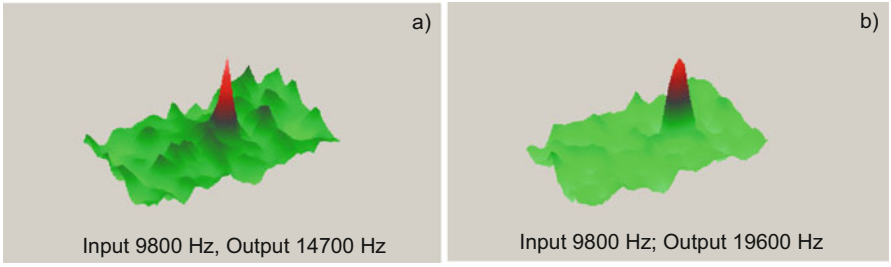

Fig. 8.55 Noncontact resonant imaging of the impact damage at the third subharmonic (**a**) and the second harmonic/fourth subharmonic (**b**) frequencies. The scanning area is 45×30 mm^2

8.7 Conclusions

A long-term bottleneck problem of nonlinear acoustical applications in NDE is concerned with a low efficiency of conversion from fundamental frequency to nonlinear components. The results presented in this chapter show that the nonlinear efficiency enhances dramatically in the localized damaged areas due to a combination of contact nonlinearity and mechanical resonance. A frequency match between the driving acoustic wave and the characteristic frequency of the damage activates its local resonance and provides an efficient energy transfer from the wave directly to the defect. Even at a moderate excitation level, the resonance "amplification" of damage vibrations results in a strong nonlinear response with efficient generation of the higher harmonics and combination frequency components. For the higher input, the damage nonlinear vibration dynamics acquires qualitatively new features characteristic of nonlinear and parametric resonances. The resonance-induced nonlinear dynamics should be seen not as exceptional or anomalous but rather conventional and peculiar to majority of fractured defects.

The experiments confirm unconventional nonlinear dynamics of realistic defects subject to resonant instability and highly efficient nonlinear frequency conversion. The nonlinear components like higher harmonics, mixed frequencies, and subharmonics may dominate in the vibration spectrum of resonant damage. This proposes nonlinear resonant modes as an extremely efficient approach for nonlinear NDE and diagnostic imaging. The nonlinear vibrations of all resonant modes are strongly confined in the defect area that brings about an opportunity for highly sensitive defect-selective imaging. Since the resonant vibrations are trapped in the damage area, the resonant techniques are not affected by diffraction so that the lateral resolution of the resonant acoustic imaging is high despite the lower (sonic) frequencies used. The resonant nonlinear modes require substantially lower acoustic power to energize the defects which modifies and simplifies the experimental methodologies for NDE applications and enables to realize for the first time noncontact nonlinear imaging via airborne sonic activation.

References

1. A.A. Gedroits, V.A. Krasilnikov, L.K. Zarembo, Elastic waves of finite amplitude in solids and anharmonicity of the lattice. Acust. **3**(2), 108 (1963)
2. M.A. Breazeale, D.O. Thompson, Finite amplitude ultrasonic waves in aluminum. Appl. Phys. Lett. **3**(5), 77–78 (1963)
3. A.A. Gedroitz, V.A. Krasilnikov, Elastic waves of finite amplitude and deviations from Hook's law. Sov. Phys. JETP **16**, 1122–1131 (1963)
4. W.T. Yost, J.H. Cantrell, Material characterization using acoustic nonlinearity parameters and harmonic generation: engineering materials. Rev. Prog. QNDE **9**, 1669–1676 (1990)
5. J. Cantrell, W. Yost, Effect of precipitate coherency strain on acoustic harmonic generation. J. Appl. Phys. **81**, 2957–2962 (1997)
6. I.Y. Solodov, Ultrasonics of nonlinear contacts: propagation, reflection and NDE applications. Ultrasonics **36**, 383–390 (1998)
7. I. Solodov, B. Korshak, Instability, chaos, and "memory" in acoustic wave-crack interaction. Phys. Rev. Lett. **88**, 014303 (2002)
8. I. Solodov, J. Wackerl, K. Pfleiderer, G. Busse, Nonlinear self-modulation and subharmonic acoustic spectroscopy for damage detection and location. Appl. Phys. Lett. **84**, 5386–5388 (2004)
9. I. Solodov, K. Pfleiderer, G. Busse, *Nonlinear Acoustic NDE: Inherent Potential of Complete Nonclassical Spectra*, ed. By P. Delsanto. Universality of Nonclassical Nonlinearity with Application to NDE and Ultrasonics (Springer, New York, 2006), pp. 465–484
10. R. Guyer, P. Johnson, Nonlinear Mesoscopic elasticity: Evidence for a new class of materials. Phys. Today **52**, 30–36 (1999)
11. K.V.D. Abeele, Multi-mode nonlinear resonance ultrasound spectroscopy for defect imaging: An analytical approach for the one-dimensional case. J. Acoust. Soc. Am. **122**, 73–90 (2007)
12. I. Solodov, J. Bai, S. Bekgulyan, G. Busse, A local defect resonance to enhance acoustic wave-defect interaction in ultrasonic nondestructive evaluation. Appl. Phys. Lett. **99**, 211911 (2011)
13. I. Solodov, Resonant ultrasonic imaging of defects for advanced nonlinear and thermosonic applications. Int. J. Microstruct. Mater. Prop. **9**(3/4/5), 261–273 (2004)
14. I. Solodov, N. Krohn, G. Busse, CAN: An example of nonclassical nonlinearity in solids. Ultrasonics **40**, 621–625 (2002)
15. I. Solodov, G. Busse, Nonlinear air-coupled emission: A signature to reveal and image micro-damage in solid materials. Appl. Phys. Lett. **91**(25), 251910 (2007)
16. I. Solodov, D. Döring, G. Busse, Air-coupled laser vibrometry: Analysis and applications. Appl. Opt. **48**(7), C33–C37 (2009)
17. I. Solodov, J. Bai, G. Busse, Resonant ultrasonic spectroscopy of defects: Case study of flat-bottomed holes. J. Appl. Phys. **113**, 223512 (2013)
18. N. De Jong, L. Hoff, Ultrasound scattering properties of albunex microspheres. Ultrasonics **31**, 175–181 (1993)
19. F. Tranquart, N. Grenier, V. Eder, L. Pourcelot, Clinical use of ultrasound tissue harmonic imaging. Ultrasound Med. Biol. **25**(6), 889–894 (1999)
20. S.I. Rokhlin, Resonance phenomena of lamb waves scattering by a finite crack in a solid layer. J. Acoust. Soc. Am. **69**, 922–928 (1981)
21. A. Zagrai, D. Donskoy, A. Ekimov, Structural vibrations of buried landmines. J. Acoust. Soc. Am. **118**, 3619–3628 (2005)
22. B. Sarens, B. Verstraeten, C. Glorieux, G. Kalogiannakis, D. Van Hemelrijck, Investigation of contact acoustic nonlinearity in delamination by shearographic imaging. IEEE Trans. Ultrason. Ferroel. Freq. Control. **57**, 1383–1395 (2010)
23. G. De Angelis, M. Meo, D.P. Almond, S.G. Pickering, S.L. Angioni, A new technique to detect defect size and depth in composite structures using digital shearography and unconstrained optimization. NDT&E Int. **45**, 91–96 (2012)

24. G. Mavko, T. Mukerji, J. Dvorkin, *The Rock Physics Handbook* (Cambridge University Press, Cambridge, 2003)
25. S.P. Timoshenko, *Vibration Problems in Engineering*, 4th edn. (D. Van Nostrand Company, New York, 1956)
26. A.E. Siegman, *Lasers* (University Science Books, Mill Valley, 1986)
27. L.D. Landau, E.M. Lifshitz, *Mechanics* (Pergamon Press, Oxford, 1960)
28. N.W. McLachlan, *Theory and Applications of Mathieu Functions* (University Press, Oxford, 1951)
29. E.K. Kneubuehl, *Oscillations and Waves* (Springer, Berlin, 1997)
30. A. Nafeh, D. Mook, *Nonlinear Oscillations* (Wiley, Hoboken, 1979)
31. R.B. Thompson, Physical principles of measurements with EMAT transducers, ed. by R.N. Thurston, A.D. Pierce, *in Ultrasonic Measurement Methods, Physical Acoustics,***XIX**, (Academic Press, Cambridge, 1990)
32. V.E. Gusev, A.A. Karabutov, *Laser Optoacoustics* (AIP, New York, 1993)
33. W. Hillger, R. Meiler, R. Heinrich, Inspection of CFRP components by ultrasonic imaging with air-coupled ultrasound. Insight **46**, 47–50 (2004)
34. I. Solodov, M. Rahammer, D. Derusova, G. Busse, Highly-efficient and noncontact vibrothermography via local defect resonance. QIRT J. **12**(1), 98–111 (2015)

Chapter 9
Nonlinear Guided Waves and Thermal Stresses

Francesco Lanza di Scalea, Ankit Srivastava, and Claudio Nucera

9.1 Nonlinear Guided Waves in Isotropic Plates and Rods (Analytical Method)

9.1.1 Introduction

The study of nonlinear elastic wave propagation has been of considerable interest for the last four decades primarily due to the higher sensitivity of nonlinear parameters to structural defects. Therefore, the application of guided waves to nondestructive evaluation and structural health monitoring has also drawn considerable research interest given that guided waves combine the nonlinear parametric sensitivities with large inspection ranges.

Problems of nonlinear acoustics have been studied since the eighteenth century [1] but few studies existed of guided nonlinear elastic waves. The mathematical complexity results from the fact that Navier equations themselves become nonlinear and is further complicated by the geometrical constraints essential to the generation and sustenance of guided waves. Thin nonlinear waveguides, under long wavelength assumption, have been studied using approximate 1-D theories [2–4] and the system is shown to accept solitary wave solutions.

F. Lanza di Scalea (✉)
Department of Structural Engineering, University of California San Diego, La Jolla, CA, USA
e-mail: flanza@ucsd.edu

A. Srivastava
Illinois Institute of Technology, Chicago, IL, USA
e-mail: asriva13@iit.edu

C. Nucera
Barclays Investment Bank, London, UK

T. Kundu (ed.), *Nonlinear Ultrasonic and Vibro-Acoustical Techniques for Nondestructive Evaluation*, https://doi.org/10.1007/978-3-319-94476-0_9

The first steps in regard to treating nonlinear Lamb waves (up to the second harmonic) were taken by Deng [5–7], who represented the primary and secondary fields by pairs of plane waves and stress-free boundary conditions on the surfaces. One of the main conclusions of the papers was that antisymmetric Lamb waves are not possible at the double harmonic. The problem was subsequently analyzed by de Lima and Hamilton [8] and Deng [9]. These authors built on Auld [10] in techniques of normal mode decomposition combined with forced response. They explained the generation of the double-harmonic guided mode and the cumulative growth of a synchronous higher harmonic. The study was further extended to include nonlinear guided waves in waveguides of arbitrary cross-section by De Lima and Hamilton [11] with specific application to the problem of double-harmonic generation in rods and shells. Deng [12] applied these findings for nonlinear ultrasonic experimental tests to detect fatigue damage in plates. Subsequently, researchers at UC San Diego [13–15] extended these ideas to explain certain additional aspects of nonlinear guided wave propagation in plates, rods, and waveguides of arbitrary cross-sections. For Lamb waves, they established the existence conditions on higher-harmonic antisymmetric and symmetric modes based upon their modeshape symmetries. Similarly, they established existence conditions for rod waves which were based on power flux considerations.

Authors at Georgia Tech also conducted parallel studies on nonlinear Lamb waves, from both a theoretical viewpoint [16] and an experimental viewpoint for both detection of fatigue damage and verification of theoretical nonlinear resonance conditions in plates [17–19].

Other work in theoretical methods to predict favorable nonlinear higher-harmonic generation conditions in Lamb waves was performed by a research group at Penn State University [19–21]. This work was also extended to guided waves in rods [22] and pipes [23]. Researchers in Japan have also conducted extensive studies of nonlinear Lamb waves [18, 24]. Researchers from Poland have also conducted theoretical studies [25] and experimental studies [26] on nonlinear Lamb waves. An excellent recent review of nonlinear guided waves was provided by Chillara and Lissenden [27].

Most authors agree that the existence and nonexistence conditions for higher-harmonic guided wave modes are based upon the following three conditions: (a) phase velocity matching between the primary mode and the higher-harmonic mode; (b) group velocity matching, although Deng et al. [28] showed that group velocity matching can be relaxed in the practical case of toneburst excitations of finite duration, and (c) nonzero power flow through the surface and through the volume from the primary mode to the higher-harmonic mode.

In this section, we present the essential founding ideas which have contributed to a significant portion of these developments. We note that the results presented here pertaining to nonlinear antisymmetric Lamb modes and first-order flexural rod modes are analogous to classical results by Goldberg [29] on transverse plane waves in unconstrained isotropic media.

9.1.2 Nonlinear Strain Energy Expression

Well-established models of nonlinear elasticity exist in classical references [30–32]. Some fundamental viewpoints of these references will be repeated here as the basis of the general nonlinear guided wave problem.

Among the possible sources of nonlinearity, the so-called *geometrical* and *physical* sources are considered. Geometrical nonlinearity is described by the following exact expression of the strain tensor [33]:

$$\boldsymbol{\epsilon} = \frac{1}{2}\left\{\nabla \mathbf{u} + (\nabla \mathbf{u})^T + \nabla \mathbf{u} \cdot (\nabla \mathbf{u})^T\right\} \tag{9.1}$$

which reduces to the linear strain expression when small deformations are considered. The finite deformation tensor is written in terms of the vector gradient $\nabla \mathbf{u}$ and its transpose $(\nabla \mathbf{u})^T$ of the displacement vector $\mathbf{u} = \{u_i\}$. The above definition includes considerations for possibly large geometrical variations of the initial configuration of an elastic solid. This constitutes a possible source of nonlinearity as it emerges from non-infinitesimal deformations.

Another possible source of nonlinearity is through the material constitutive relations. Murnaghan [34] proposed strain energy as a power series in the three invariants of the strain tensor:

$$\Pi = \frac{\lambda + 2\mu}{2} I_1^2 - 2\mu I_2 + \frac{l + 2m}{3} I_1^3 - 2m I_1 I_2 + n I_3 \tag{9.2}$$

where I_k, $k = 1, 2, 3$, are the invariants of the strain tensor:

$$I_1(\boldsymbol{\epsilon}) = tr\boldsymbol{\epsilon}, \quad I_2(\boldsymbol{\epsilon}) = \left[(tr\boldsymbol{\epsilon})^2 - tr\boldsymbol{\epsilon}^2\right]/2, \quad I_3(\boldsymbol{\epsilon}) = \det \epsilon \tag{9.3}$$

The first two terms in Eq. (9.2) account for linear elasticity in the case of small deformations. Other terms account for material nonlinearity of the first order by using the third-order elastic constants (*l, m, n*). *Geometrical nonlinearity* arises from terms in $\boldsymbol{\epsilon}$ proportional to $\nabla \mathbf{u} \cdot (\nabla \mathbf{u})^T$, whereas *physical nonlinearity* is caused by all terms in Π except the first two. It must be noted that both physical and geometrical nonlinearities are to be taken into consideration simultaneously, i.e., square and higher-order terms with respect to $\nabla \mathbf{u}$ in $\boldsymbol{\epsilon}$. Murnaghan further suggested that in order to account for still higher orders of nonlinearity, a more general energy expression may be used:

$$\Pi = \phi_2 + \phi_3 + \phi_4 \ldots \tag{9.4}$$

where ϕ_3 corresponds to the linear regime and consists of terms I_1^2, I_2, ϕ_3 that correspond to the first-order nonlinearity and consists of terms I_1^3, I_1, I_2, I_3. Similarly, ϕ_4 consists of all terms that can be formed from the different combinations of the three invariants such that the order of strain in each of them is 4. This can be extended to

further orders of nonlinearity. Another commonly used power series expansion of energy for Cartesian geometry was proposed by Landau and Lifshitz [35]. In terms of the strain components ε_{ij}, it is written as:

$$\Pi = \mu\varepsilon_{ik}^2 + \left(\frac{1}{2}K - \frac{1}{3}\mu\right)\varepsilon_{ll}^2 + \frac{1}{3}A\varepsilon_{ik}\varepsilon_{il}\varepsilon_{lk} + B\varepsilon_{ik}^2\varepsilon_{ll} + \frac{1}{3}C\varepsilon_{ll}^3 \tag{9.5}$$

where the bulk modulus K and the higher-order moduli (A, B, C) were introduced. Equation (9.5) can be expressed in terms of displacement differentials. Substituting Eq. (9.1) in Eq. (9.5) and neglecting terms of order higher than 3, we get the commonly used energy expression in Cartesian geometry:

$$\begin{aligned}\Pi = \ & \frac{1}{4}\mu\left(u_{i,k} + u_{k,i}\right)^2 + \left(\frac{1}{2}K - \frac{1}{3}\mu\right)\left(u_{l,l}\right)^2 + \left(\mu + \frac{1}{4}A\right)\left(u_{i,k}u_{l,i}u_{l,k}\right) \\ & + \left(\frac{1}{2}K - \frac{1}{3}\mu + \frac{1}{2}B\right)\left[u_{l,l}\left(u_{i,k}\right)^2\right] + \frac{1}{12}A\left(u_{i,k}u_{k,l}u_{l,i}\right) \\ & + \frac{1}{2}B\left(u_{i,k}u_{k,i}u_{l,l}\right) + \frac{1}{3}C\left(u_{l,l}^3\right) + \ldots\end{aligned} \tag{9.6}$$

All coefficients of one form can be transformed into those of another one and vice versa. Therefore, it can be shown that the higher-order moduli of Landau and Lifshitz in Eq. (9.5) can be expressed in terms of the higher-order moduli of Murnaghan in Eq. (9.2).

9.1.3 Nonlinear Equation of Motion for a Waveguide

The nonlinear equation of motion is given by:

$$\nabla \cdot \mathbf{P} = \rho_0 \frac{\partial^2 \mathbf{u}}{\partial t^2} \tag{9.7}$$

where the displacement vector is constrained to be in the region occupied by the waveguide, $\mathbf{P}$ is the Piola–Kirchhoff tensor, and ρ_0 is the initial density. The second Piola–Kirchhoff tensor is defined as:

$$\mathbf{P} = \mathbf{S} + \mathbf{S}\nabla\mathbf{u} \tag{9.8}$$

Now, consider a weakly nonlinear elastic medium for the waveguide for which the constitutive relation is given by Landau and Lifshitz [35]:

$$\mathbf{S} = \lambda\left(tr\boldsymbol{\epsilon}\right)\mathbf{I} + 2\mu\boldsymbol{\epsilon} + \mathbf{I}\left[\boldsymbol{\epsilon}(tr\left(\boldsymbol{\epsilon}\right))^2 + B\left(\boldsymbol{\epsilon} : \boldsymbol{\epsilon}^{\mathrm{T}}\right)\right] + 2B\left(tr\boldsymbol{\epsilon}\right)\boldsymbol{\epsilon} + A\boldsymbol{\epsilon}\boldsymbol{\epsilon}\right) \tag{9.9}$$

In the above, the second Piola–Kirchhoff tensor is calculated from the tensorial form of Eq. (9.5) and $\mathbf{I}$ is the identity matrix.

Substituting Eq. (9.1) into Eq. (9.9), we have:

$$\mathbf{S}(\mathbf{u}) = \mathbf{S}^{\mathbf{L}}(\mathbf{u}) + \mathbf{S}^{\mathbf{NL}}(\mathbf{u}) \tag{9.10}$$

where $\mathbf{S}^{\mathbf{L}}(\mathbf{u})$ and $\mathbf{S}^{\mathbf{NL}}(\mathbf{u})$ are the linear and nonlinear parts of the stress tensor, respectively. The linear part, $\mathbf{S}^{\mathbf{L}}(\mathbf{u})$, is given by the usual isotropic constitutive relation:

$$\mathbf{S}^{\mathbf{L}}(\mathbf{u}) = \frac{1}{2}\lambda tr\left[\nabla\mathbf{u} + (\nabla\mathbf{u})^{\mathrm{T}}\right]\mathbf{I} + \mu\left(\nabla\mathbf{u} + (\nabla\mathbf{u})^{\mathrm{T}}\right) \tag{9.11}$$

Substituting Eqs. (9.8), (9.10), and (9.11) into Eq. (9.7) gives us the nonlinear Navier equation of motion which governs elastodynamics in the current problem:

$$(\lambda + 2\mu)\nabla(\nabla\mathbf{u}) - \mu\nabla\times(\nabla\times\mathbf{u}) + \mathbf{f} = \rho_0\frac{\partial^2\mathbf{u}}{\partial t^2} \tag{9.12}$$

In the above, $\mathbf{f}$ is a body force which emerges from including all the nonlinear terms in the equation. Stress-free boundary conditions are assumed on the surface of the waveguide:

$$\left[\mathbf{S}^{\mathbf{L}}(\mathbf{u}) - \overline{\mathbf{S}}(\mathbf{u})\right]\cdot\mathbf{n} = 0 \quad \text{on} \quad \mathcal{S} \tag{9.13}$$

The expressions for $\mathbf{f}$ and $\overline{\mathbf{S}}(\mathbf{u})$ are given by [8]:

$$\mathbf{f} = \nabla\cdot\left(\mathbf{S}^{\mathbf{NL}} + \mathbf{S}^{\mathbf{L}}\nabla\mathbf{u} + \mathbf{S}^{\mathbf{NL}}\nabla\mathbf{u}\right) \tag{9.14}$$

$$\overline{\mathbf{S}}(\mathbf{u}) = \mathbf{S}^{\mathbf{NL}} + \mathbf{S}^{\mathbf{L}}\nabla\mathbf{u} + \mathbf{S}^{\mathbf{NL}}\nabla\mathbf{u} \tag{9.15}$$

We present the solution of the nonlinear boundary value problem through the method of perturbation. Here, $\mathbf{u}$ is written as the sum of a primary and a secondary solution:

$$\mathbf{u} = \mathbf{u^1} + \mathbf{u^2} \tag{9.16}$$

where $|\mathbf{u}^1| \ll |\mathbf{u}^2|$ is assumed. In the first approximation, we have:

$$(\lambda + 2\mu)\nabla\left(\nabla\mathbf{u^1}\right) - \mu\nabla\times\left(\nabla\times\mathbf{u^1}\right) = \rho_0\frac{\partial^2\mathbf{u^1}}{\partial t^2} \tag{9.17}$$

with boundary condition:

$$\mathbf{S^1} \cdot \mathbf{n} = 0 \quad \text{on} \quad \mathcal{S} \tag{9.18}$$

where $\mathbf{S^1} = \mathbf{S^L}(\mathbf{u^1})$ is the first-order approximation of the second Piola–Kirchhoff tensor. Equations (9.17) and (9.18) constitute a system of unforced linear Navier equations for a waveguide. Their solutions are the usual eigenvalues and mode shapes of the waveguide. For the second-order approximation, we have the following forced linear partial differential equation system:

$$(\lambda + 2\mu)\,\nabla\left(\nabla \mathbf{u^2}\right) - \mu \nabla \times \left(\nabla \times \mathbf{u^2}\right) + \mathbf{f^1} = \rho_0 \frac{\partial^2 \mathbf{u^2}}{\partial t^2} \tag{9.19}$$

with boundary condition,

$$\mathbf{S^2} \cdot \mathbf{n} = -\overline{\mathbf{S}}^{\mathbf{1}} \cdot \mathbf{n} \quad \text{on} \quad \mathcal{S} \tag{9.20}$$

where $\mathbf{u^2}$ is the secondary solution and $\mathbf{S^2} = \mathbf{S^L}(\mathbf{u^2})$ is the second-order approximation of the second Piola–Kirchhoff tensor. $\mathbf{f^1}$ and $\overline{\mathbf{S}}^{\mathbf{1}}$ are obtained by replacing $\mathbf{u}$ by $\mathbf{u^1}$ in the expressions for $\mathbf{f}$ and $\overline{\mathbf{S}}$, respectively and constitute the effect of nonlinearity.

It should be noted here that an unforced nonlinear partial differential equation has been reduced to two sets of equations through the use of perturbation. The first set of linear partial differential equations leads to the dispersion solutions of the waveguide (the primary solution). The second is a system of forced linear partial differential equation where the forcing terms emanate from the primary solution. Another observation about the solution is that since both $\mathbf{f}$ and $\overline{\mathbf{S}}$ have terms which are multiples of displacement $\mathbf{u^1}$, a primary solution at a frequency ω results in stress and body forces at frequency 2ω. This, in turn, gives rise to a part of the solution at the double harmonic. The effect is general in that a summed frequency and a subtracted frequency result from the perturbative process. This is seen if one considers:

$$\mathbf{u^1} = \frac{1}{2}\left[\mathbf{u}^a\,(\mathbf{r})\,e^{i(\kappa_a z - \omega_a t)} + \mathbf{u}^b\,(\mathbf{r})\,e^{i(\kappa_b z - \omega_b t)}\right] + c.c. \tag{9.21}$$

Then,

$$\mathbf{f^1} = \mathbf{f}^{\pm}\,(\mathbf{r}, z)\,e^{i\left[(\kappa_a \pm \kappa_b) z - \omega_{\pm} t\right]} + c.c. \tag{9.22}$$

and

$$\overline{\mathbf{S}}^{\mathbf{1}} = \overline{\mathbf{S}}^{\pm}\,(\mathbf{r}, z)\,e^{i\left[(\kappa_a \pm \kappa_b) z - \omega_{\pm} t\right]} + c.c. \tag{9.23}$$

In the above and in the following sections, z is the wave propagation direction, y is the thickness direction, and *c.c.* stands for complex conjugate. Normal mode expansion in terms of the primary solution is used at the double harmonic to represent the secondary solution. The amplitudes of the constituting modes are determined by enforcing the stress and body forces. This requires orthogonality relationships for the modes of the primary solution. The required orthogonality condition was derived by Auld [10] and is briefly reproduced below for the sake of completeness.

9.1.4 Waveguide Mode Orthogonality

The complex reciprocity relation between two elastodynamic states ($\mathbf{v}_1$,$\mathbf{T}_1$,$\mathbf{F}_1$) and ($\mathbf{v}_2$,$\mathbf{T}_2$,$\mathbf{F}_2$) where $\mathbf{v}$ is the velocity vector, $\mathbf{T}$ is surface traction, and $\mathbf{F}$ is the body force is given by [10]:

$$\nabla \cdot \left[-\mathbf{v}_2^* \cdot \mathbf{T}_1 - \mathbf{v}_1 \cdot \mathbf{T}_2^*\right] = \left[\mathbf{v}_2^* \cdot \mathbf{F}_1 - \mathbf{v}_1 \cdot \mathbf{F}_2^*\right] \tag{9.24}$$

Wavemode orthogonality is reproduced here for Lamb modes but the essential form of the final solution holds for arbitrary waveguides. First, body forces ($\mathbf{F_1}$, $\mathbf{F_2}$) are neglected since orthogonality is required for free modes. States 1 and 2, in the reciprocity relation, are now taken to be free modes with propagation factors, κ_m and κ_n, respectively. For the 2-dimensional problem under consideration, we have:

$$\begin{aligned} \mathbf{v_1} &= e^{i\kappa_m z} v_m(y) \\ \mathbf{v_2} &= e^{i\kappa_n z} v_n(y) \end{aligned} \tag{9.25}$$

Under these conditions, the complex reciprocity relation reduces to:

$$\nabla \cdot \{\} = \frac{\partial}{\partial z}\{\} \cdot \widehat{z} + \frac{\partial}{\partial y}\{\} \cdot \widehat{y} \tag{9.26}$$

where

$$\{\} = -\mathbf{v_2^*} \cdot \mathbf{T_1} - \mathbf{v_1} \cdot \mathbf{T_2^*} \tag{9.27}$$

After substitution, this becomes:

$$\begin{aligned} i\left(\kappa_m - \kappa_n^*\right)\left\{-\mathbf{v_n^*} \cdot \mathbf{T_m} - \mathbf{v_m} \cdot \mathbf{T_n^*}\right\} \cdot \widehat{z} e^{-i\left(\kappa_m - \kappa_n^*\right)z} \\ = \frac{\partial}{\partial y}\left\{-\mathbf{v_n^*} \cdot \mathbf{T_m} - \mathbf{v_m} \cdot \mathbf{T_n^*}\right\} \cdot \widehat{y} e^{-i\left(\kappa_m - \kappa_n^*\right)z} \end{aligned} \tag{9.28}$$

The above equation is integrated with respect to y across the waveguide to give the global reciprocity relationship. Upon doing so, the right-hand side of the above equation reduces to the value of {} at the plate edges from Gauss theorem. If there is either a stress-free or rigid boundary condition at the plate edges, that is:

$$\mathbf{T} \cdot \widehat{y} = 0 \quad \text{or} \quad \mathbf{v} = 0 \quad \text{at} \quad y = 0, b \tag{9.29}$$

then the right-hand side of Eq. (9.28) is zero. Consequently,

$$i\left(\kappa_m - \kappa_n^*\right) P_{mn} = 0 \tag{9.30}$$

Hence, the orthogonality relation for the waveguide modes is:

$$P_{mn} = 0 \quad \text{if} \quad \kappa_m \neq \kappa_n^* \tag{9.31}$$

where

$$P_{mm} = \Re\mathfrak{e}\frac{1}{2}\int \left\{-\mathbf{v_m^*} \cdot \mathbf{T_m}\right\} \cdot \widehat{z} dy \tag{9.32}$$

is also the average power flow in the z direction (z component of the *Poynting Vector*).

9.1.5 Complex Reciprocity Relation

The required complex reciprocity relation for the second-order problem is [10, 11]:

$$-\frac{\partial}{\partial z}\left[\left(\mathbf{v}_n^* \cdot \mathbf{S^2} + \mathbf{v^2} \cdot \sigma_n^*\right) \cdot \mathbf{n}_z e^{i\kappa_n^* z}\right] - \nabla_\perp \cdot \left(\mathbf{v}_n^* \cdot \mathbf{S^2} + \mathbf{v} \cdot \sigma_n^*\right) e^{i\kappa_n^* z} = \mathbf{v}_n^* \cdot \mathbf{f^1} e^{i\kappa_n^* z} \tag{9.33}$$

where $\mathbf{v}_n(\mathbf{r})$ is the velocity of the nth mode for a stress-free waveguide, $\sigma_n(\mathbf{r})$ the stress for the mode calculated from $\mathbf{v}_n(\mathbf{r})$, κ_n is the mode's wavenumber, $\mathbf{v^2} = \partial \mathbf{u^2}/\partial t$ is the particle velocity derived from taking the time derivative of the secondary solution, $\mathbf{S^2}(\mathbf{r})$ is the stress calculated from $\mathbf{u^2}(\mathbf{r})$, $\mathbf{n}_z$ the unit vector in the direction of propagation, and

$$\nabla_\perp = \mathbf{n}_x \frac{\partial}{\partial x} + \mathbf{n}_y \frac{\partial}{\partial y} \tag{9.34}$$

Expanding $\mathbf{v^2}$ and $\mathbf{S^2} \cdot \mathbf{n}_z$ in terms of waveguide modes

$$\mathbf{v^2}(\mathbf{r}, z, t) = \frac{1}{2}\sum\nolimits_{m=1}^{\infty} A_m(z)\mathbf{v}_m(\mathbf{r})\, e^{-i\omega_{\pm} t} + c.c. \tag{9.35}$$

$$\mathbf{S^2}\left(\mathbf{r},z,t\right).\mathbf{n}_z=\frac{1}{2}\sum\nolimits_{m=1}^{\infty}A_m(z)\sigma_m\left(\mathbf{r}\right)\cdot\mathbf{n}_z e^{-i\omega_{\pm}t}+c.c. \tag{9.36}$$

where $A_m(z)$ is modal amplitude. Substituting Eqs. (9.35) and (9.36) in Eq. (9.33), integrating the result over the cross-section of the waveguide, and from the divergence theorem applied to the left-hand side, we have:

$$-P_{mn}\frac{\partial}{\partial z}\left[e^{i\kappa_n^* z}\sum\nolimits_m 4A_m(z)\right]\ -e^{i\kappa_n^* z}\left[\int_{\Gamma}\left(\mathbf{v^2}\cdot\sigma_n^*+\mathbf{v}_n^*\cdot\mathbf{S}^2\right)\cdot\mathbf{n}d\Gamma\right]$$
$$=e^{i\kappa_n^* z}\int_{\Omega}\mathbf{f^1}\cdot\mathbf{v}_n^* d\Omega \tag{9.37}$$

where Γ is the surface of Ω, $\mathbf{n}$ is the unit vector normal to Γ, and

$$P_{mn}=-\frac{1}{4}\int_{\Omega}\left(\mathbf{v}_n^*\cdot\sigma_m+\mathbf{v}_m\cdot\sigma_n^*\right)\cdot\mathbf{n}_z d\Omega \tag{9.38}$$

In the secondary problem, only traction is prescribed and the modes correspond to a stress-free waveguide ($\sigma_n\,\mathbf{n}=0$). Therefore, (9.37) can be written as:

$$-P_{mn}\frac{\partial}{\partial z}\left[e^{i\kappa_n^* z}\sum\nolimits_m 4A_m(z)\right]-e^{i\kappa_n^* z}\left[\int_{\Gamma}\mathbf{v}_n^*\cdot\overline{\mathbf{S}}^{\mathbf{1}}\cdot\mathbf{n}d\Gamma\right]=e^{i\kappa_n^* z}\int_{\Omega}\mathbf{f^1}\cdot\mathbf{v}_n^* d\Omega \tag{9.39}$$

Now, the orthogonality relation of modes is:

$$P_{mn}=0\quad\text{if}\quad\kappa_m\neq\kappa_n^* \tag{9.40}$$

Therefore, we have:

$$4P_{mn}\left(\frac{d}{dz}+i\kappa_n^*\right)A_m(z)=\left[f_n^{surf}(z)+f_n^{vol}(z)\right]e^{i(\kappa_a\pm\kappa_b)z} \tag{9.41}$$

where the nth mode is orthogonal to the mth mode, and

$$f_n^{surf}(z)=\int_{\Gamma}\mathbf{v}_n^*\cdot\overline{\mathbf{S}}^{\pm}\cdot\mathbf{n}d\Gamma \tag{9.42}$$

$$f_n^{vol}(z)=\int_{\Omega}\mathbf{f}^{\pm}\cdot\mathbf{v}_n^* d\Omega \tag{9.43}$$

The terms ${f_n}^{surf}(z)$ and ${f_n}^{vol}(z)$ are the complex external modal power due to the surface stress $\overline{\mathbf{S}}^{\mathbf{1}}\cdot\mathbf{n}$ and volume force $\mathbf{f^1}$. If the source condition is assumed to be

$$\mathbf{u^2} = 0 \quad at \quad z = 0 \tag{9.44}$$

The solution to Eq. (9.41) is:

$$A_m(z) = \overline{A}_m(z)e^{i[(\kappa_a \pm \kappa_b)z]} - \overline{A}_m(0)e^{-i\kappa_n^* z} \tag{9.45}$$

where

$$\overline{A}_m(z) = \frac{i\left(f_n^{surf} + f_n^{vol}\right)}{4P_{mn}\left[\kappa_n^* - (\kappa_a \pm \kappa_b)\right]} \quad \kappa_n^* \neq (\kappa_a \pm \kappa_b) \tag{9.46}$$

and

$$\overline{A}_m(z) = \frac{\left(f_n^{surf} + f_n^{vol}\right)}{4P_{mn}} z \quad \kappa_n^* = (\kappa_a \pm \kappa_b) \tag{9.47}$$

9.1.6 Nonlinear Lamb Waves

The general solution process given above is now applied to the case of Lamb waves in plates.

9.1.6.1 Statement of the Problem

Nonlinear elasticity in a stress-free plate (Fig. 9.1) is governed by the following equation of motion:

$$(\lambda + 2\mu)\nabla(\nabla \cdot \mathbf{u}) - \mu\nabla \times (\nabla \times \mathbf{u}) + \mathbf{f} = \rho_0 \frac{\partial^2 \mathbf{u}}{\partial t^2} \tag{9.48}$$

with the condition (stress-free boundary):

$$\left(\mathbf{S^L} - \overline{\mathbf{S}}\right) \cdot \mathbf{n_y} = \mathbf{0} \quad \text{on} \quad \mathcal{L} \tag{9.49}$$

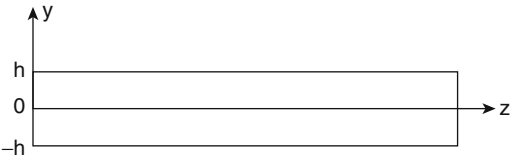

Fig. 9.1 Schematic of a stress-free plate

where $\mathbf{n_y}$ is a unit normal vector to the surface L, $\mathbf{S_L}$ is the linear part of the Piola–Kirchhoff stress tensor, and $\overline{\mathbf{S}}$ and $\mathbf{f}$ include all nonlinear terms. For Rayleigh–Lamb modes, $u_x = 0$ and $u_y, u_z \neq 0$.

Equation (9.7) is used for the energy expression. The nonlinear stress and volume forces in Eqs. (9.48) and (9.49) can be obtained from the nonlinear energy expression as [36]:

$$S_{ij} = \frac{\partial \Pi}{\partial \left(u_{i,j}\right)} \quad ; \quad f_i = S_{ij,j} \tag{9.50}$$

9.1.7 Solution to Nonlinear Problem

9.1.7.1 Forced Solution to Guided Waves

Following normal mode expansion from Auld [10], waves in a plate under arbitrary excitation can be written as:

$$\mathbf{v}\left(y, z, t\right) = \frac{1}{2}\sum\nolimits_{m=1}^{\infty} A_m(z)\mathbf{v}_m(y)e^{-i\omega t} \tag{9.51}$$

$$\mathbf{S}\left(y, z, t\right) \cdot \mathbf{n}_z = \frac{1}{2}\sum\nolimits_{m=1}^{\infty} A_m(z)\mathbf{S}_m(y) \cdot \mathbf{n_z}e^{-i\omega t} \tag{9.52}$$

where $\mathbf{v} = \partial \mathbf{u}/\partial t$, $\mathbf{S}_m$ is the stress tensor for the mth mode, $\mathbf{v}_m$ is the particle velocity of the mth mode, and A_m is the second-order modal amplitude to be determined. Auld shows how A_m can be found from the following differential equation:

$$4P_{mn}\left(\frac{d}{dz} - i\kappa_n^*\right)A_m(z) = \left(f_n^{\text{surf}} + f_n^{\text{vol}}\right)e^{i\kappa z} \quad ; \quad m = 1, 2, \ldots \tag{9.53}$$

where

$$P_{mn} = -\frac{1}{8}\int_{-h}^{h}\left(\mathbf{v_n^*} \cdot \mathbf{S_m} + \mathbf{v_m} \cdot \mathbf{S_n^*}\right) \cdot \mathbf{n}_z d\Omega, \tag{9.54}$$

$$f_n^{\text{surf}} = -\frac{1}{2}\mathbf{v_n^*}\mathbf{S} \cdot \mathbf{n}_y\Big|_{y=-h}^{y=h}, \tag{9.55}$$

$$f_n^{\text{vol}} = \frac{1}{2}\int_{-h}^{h}\mathbf{f} \cdot \mathbf{v_n^*}dy \tag{9.56}$$

and κ_n is the wavenumber of the mode which is not orthogonal to the mode with wavenumber κ_m. $\mathbf{f}$ and $\mathbf{S}$ are the body force and surface traction, respectively, from the primary wave.

9.1.7.2 Perturbation

De Lima and Hamilton [8] used perturbation, to derive the solution to Eqs. (9.48) and (9.49) as the sum of following two components:

$$\mathbf{u} = \mathbf{u^1} + \mathbf{u^2} \tag{9.57}$$

where $\mathbf{u^2}$ is the perturbation due to nonlinearity and is assumed to be small in comparison to $\mathbf{u^1}$. $\mathbf{u^1}$ is the solution to the following linear problem:

$$(\lambda + 2\mu)\,\nabla\left(\nabla \cdot \mathbf{u^1}\right) - \mu\nabla \times \left(\nabla \times \mathbf{u^1}\right) - \rho_0 \frac{\partial^2 \mathbf{u^1}}{\partial t^2} = 0, \tag{9.58}$$

$$\mathbf{S^L}\left(\mathbf{u^1}\right) \cdot \mathbf{n_y} = \mathbf{0} \quad \text{on} \quad \mathcal{L} \tag{9.59}$$

This represents the solution to the classical stress-free boundary plate. $\mathbf{u^2}$ can be found by solving the following forced problem:

$$(\lambda + 2\mu)\,\nabla\left(\nabla \cdot \mathbf{u^2}\right) - \mu\nabla \times \left(\nabla \times \mathbf{u^2}\right) - \rho_0 \frac{\partial^2 \mathbf{u^2}}{\partial t^2} = -\mathbf{f^1}, \tag{9.60}$$

$$\mathbf{S^L}\left(\mathbf{u^2}\right) \cdot \mathbf{n_y} = -\mathbf{S^1} \cdot \mathbf{n_y} \quad \text{on} \quad \mathcal{L} \tag{9.61}$$

where $\mathbf{S^1}$ and $\mathbf{f^1}$ are surface traction and body force as calculated from the primary solution $\mathbf{u^1}$.

9.1.7.3 Solution

Assuming that primary excitation is at ω, energy equation has first-order nonlinearity, and $\mathbf{S^1}$ and $\mathbf{f^1}$ would be harmonic at 2ω. If the energy equation contains higher nonlinearities, $\mathbf{S^1}$ and $\mathbf{f^1}$ would contain appropriate higher-harmonic terms as well. The solution to the current problem when only the double harmonic is considered is:

$$A_m(z) = \overline{A}_m(z)e^{i(2\kappa z)} - \overline{A}_m(0)e^{i\kappa_n^* z}, \tag{9.62}$$

where

$$\overline{A}_m(z) = i\frac{\left(f_n^{\text{vol}} + f_n^{\text{surf}}\right)}{4P_{mn}\left[\kappa_n^* - 2\kappa\right]} \;\; ; \;\; \kappa_n^* \neq 2\kappa \tag{9.63}$$

$$\overline{A}_m(z) = \frac{\left(f_n^{\text{vol}} + f_n^{\text{surf}}\right)}{4P_{mn}} z \;\; ; \;\; \kappa_n^* = 2\kappa \tag{9.64}$$

A_m are the κ -2ω amplitudes.

9.1.8 Condition for the Absence of Antisymmetric Modes

If appropriate **S** and **f** in Eqs. (9.55) and (9.56) are used in combination with normal mode expansion, the first-order nonlinear solution in Eq. (9.62) can be extended to higher orders. This allows us to consider different orders of nonlinearities separate from each other. Assuming that Eq. (9.5) consists of a single order of nonlinearity, **S** and **f** are due to that particular order of nonlinearity. Going forward, we will have Q^{Ay} (Q^{Sy}) represent that a quantity, Q, is antisymmetric (symmetric) with respect to the thickness direction (y direction).

Equations (9.63) and (9.64) indicate that a certain higher-harmonic mode will not be excited if both ${f_n}^{\text{surf}}$ and ${f_n}^{\text{vol}}$ are zero. We have the following in our notation:

$$\mathbf{v}_{ny} = v_y^{Sy} \quad ; \quad \mathbf{v}_{nz} = v_z^{Ay} \tag{9.65}$$

From Eq. (9.55), it can be seen that ${f_n}^{\text{surf}}$ would be zero if the quantity, **v**, is symmetric with respect to y. In this case, we find from Eq. (9.65) that **S** should be of the following form:

$$\mathbf{S} = \begin{bmatrix} S_{yy}^{Sy} & S_{yz}^{Ay} \\ S_{zy}^{Ay} & S_{zz}^{Sy} \end{bmatrix} \tag{9.66}$$

The above follows by considering the symmetry behavior of appropriate spatial derivatives. It is worth noting that a y-derivative turns a symmetric function into an antisymmetric one and vice versa. A z-derivative does not change the symmetry of the function (i.e., if Q^{Ay}, then ${Q^{Sy}}_{,y}$, etc.). Equation (9.56) also shows that f_n^{vol} is zero if the quantity, $\mathbf{f}\mathbf{v}_{\mathbf{n}}{}^*$, is antisymmetric with respect to y (due to integration over the y variable). For it to be true, we find that **f** should be of the following form:

$$\mathbf{f} = \begin{bmatrix} f_y^{Ay} & f_z^{Sy} \end{bmatrix} \tag{9.67}$$

It follows from $f_i = S_{ij,j}$ that if **S** follows Eq. (9.66), then **f** would follow Eq. (9.67). The reverse is also true and since one implies the other, it is important to satisfy only one of the two. From Eq. (9.50), we have the following for a plain strain, Rayleigh–Lamb mode:

$$\begin{aligned} f_i &= \left[\frac{\partial E}{\partial u_{i,j}}\right]_{,j} = \left[\frac{\partial}{\partial x_l}\frac{\partial x_l}{\partial u_{i,j}}(E)\right]_{,j} = \left[E_{,l}\frac{1}{u_{i,jl}}\right]_{,j} \\ &= \left[E_{,y}\frac{1}{u_{i,yy}} + E_{,z}\frac{1}{u_{i,yz}}\right]_{,y} + \left[E_{,y}\frac{1}{u_{i,zy}} + E_{,z}\frac{1}{u_{i,zz}}\right]_{,z} \end{aligned} \tag{9.68}$$

From Eq. (9.68), it can be verified that Eqs. (9.66) and (9.67) hold if the following conditions are satisfied (absence of antisymmetric harmonics):

$$\begin{aligned} &E^{Sy} \text{ when } u_y^{Ay} \text{ and } u_z^{Sy} \quad \text{(Symmetric Driving Mode)} \\ &E^{Ay} \text{ when } u_y^{Sy} \text{ and } u_z^{Ay} \quad \text{(Antisymmetric Driving Mode)} \end{aligned} \tag{9.69}$$

This implies that the symmetry of Π follows that of $u_{l,l}$ (whether an antisymmetric or a symmetric mode is the primary). A set of conditions necessary and sufficient for the absence of symmetric motion ($v_{ny} = v_y{}^{Ay}$, $v_{nz} = v_z{}^{Sy}$) can be similarly found:

$$\begin{aligned} &E^{Ay} \text{ when } u_y^{Ay} \text{ and } u_z^{Sy} \quad \text{(Symmetric Driving Mode)} \\ &E^{Sy} \text{ when } u_y^{Sy} \text{ and } u_z^{Ay} \quad \text{(Antisymmetric Driving Mode)} \end{aligned} \tag{9.70}$$

Conditions (9.69) and (9.70) imply that a given harmonic can allow both symmetric and antisymmetric motions when the following cases are true:

$$\begin{aligned} &E^{Sy} \text{ when } u_y^{Ay} \text{ and } u_z^{Sy} \quad \text{(Symmetric Driving Mode)} \\ &E^{Sy} \text{ when } u_y^{Sy} \text{ and } u_z^{Ay} \quad \text{(Antisymmetric Driving Mode)} \end{aligned} \tag{9.71}$$

or when Π is always symmetric.

9.1.9 Application to First-Order Nonlinearity

It can be seed that the energy relation for first-order nonlinearity from Eq. (9.5), also considering Eq. (9.1), contains cubic terms. The relation, after some albegra, is reproduced here for the sake of clarity:

$$\begin{aligned} E =& E_1\left(u_{i,j}u_{j,k}u_{k,i}\right) + E_2\left(u_{i,j}u_{k,i}u_{k,j}\right) + E_3\left(u_{i,i}u_{j,k}u_{k,j}\right) \\ &+ E_4\left[u_{i,i}\left(u_{j,k}\right)^2\right] + E_5\left(u_{i,i}^3\right) \end{aligned} \tag{9.72}$$

where E_1, E_2, E_3, E_4, and E_5 are constants. From Eq. (9.69), it is enough to show that first-order nonlinearity would not support any antisymmetric higher-order modes if each of the five terms in the above equation follows the symmetry of $u_{l,l}$. In other words, if each term in Eq. (9.72) can be written as $u_{l,l} \times Q^{Sy}$, where Q^{Sy} is a symmetric function, then antisymmetric modes will be absent. We first note:

$$u_{i,j}u_{j,i} = u_{y,y}u_{y,y} + u_{y,z}u_{z,y} + u_{z,y}u_{y,z} + u_{z,z}u_{z,z} \tag{9.73}$$

The terms in the expansion are all symmetric. Therefore:

Lemma 9.1 *All the terms in the expansion of $u_{i,j}\ u_{j,i}$ are symmetric, hence [ui,juj,i]Sy.*

We also have:

$$u_{i,i}u_{j,j} = \left(u_{y,y} + u_{z,z}\right)^2 \tag{9.74}$$

Hence.

Lemma 9.2 [*ui,iuj,j*]*Sy.*

Further,

$$u_{i,j}u_{i,j} = \left(u_{i,j}\right)^2 \tag{9.75}$$

Hence,

Lemma 9.3 [*ui,jui,j*]*Sy.*

Energy for first-order nonlinearity contains terms of displacement derivatives that are cubic. Expressing first term in Eq. (9.72) as $T = u_{i,j}u_{j,k}u_{k,i}$, the following cases can be identified

- $i = j = p$; $T = u_{\overline{p},\overline{p}}u_{\overline{p},k}u_{k,\overline{p}}$, where overbar indicates that the corresponding index does not follow Einstein convention. From Lemma (9.1), $u_{\overline{p},k}u_{k,\overline{p}} = Q^{Sy}$. Hence, $T = u_{\overline{p},\overline{p}}Q^{Sy}$.
- $i \neq j$; since i, j, and k can assume only y and z, and since $i \neq j$, the third index, k, must be equal to either i or j. When $k = i = p$, $T = u_{\overline{p},j}u_{j,\overline{p}}u_{\overline{p},\overline{p}}$. Conversely, when $k = j = p$, $T = u_{i,p^-}u_{p,^-p^-}u_{p,i^-}$. In either case, from Lemma (9.1), it follows that $T = u_{i,\overline{p}}u_{\overline{p},\overline{p}}u_{\overline{p},i}$.

For the second term in Eq. (9.72), $T = u_{i,j}u_{k,i}u_{k,j}$, the following two cases arise:

- $i = j = p$; $T = u_{\overline{p},\overline{p}}u_{k,\overline{p}}u_{k,\overline{p}}$. From Lemma (9.2), $T = u_{\overline{p},\overline{p}}Q^{Sy}$.
- $i \neq j$. Since i, j, and k can assume only y and z, and since $i \neq j$, the third index, k, must be equal to either i or j. When $k = i = p$, $T = u_{\overline{p},j}u_{\overline{p},\overline{p}}u_{\overline{p},j}$. Conversely, when $k = j = p$, $T = u_{i,\overline{p}}u_{\overline{p},i}u_{\overline{p},\overline{p}}$. In either case, from Lemmas (9.1, 9.3), it follows that $T = u_{\overline{p},\overline{p}}Q^{Sy}$.

It can be seen that the other terms in Eq. (9.72) ($u_{i,k}u_{k,i}u_{l,l}$, $u_{l,l}\left(u_{i,k}\right)^2$, $u_{l,l}^3$) trivially reduce to $T = u_{i,\ i}Q^{Sy}$ from Lemmas (9.1–9.3). Hence, from conditions (9.69), first-order nonlinearity under hyper-elasticity model cannot support antisymmetric Rayleigh–Lamb waves.

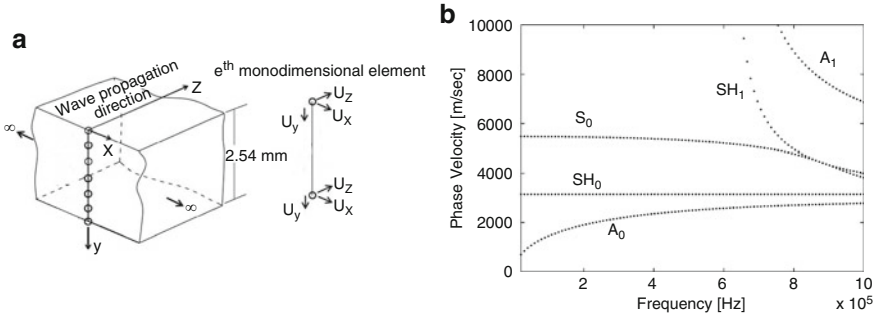

Fig. 9.2 SAFE discretization of a plate (reproduced from: Srivastava A, Bartoli I, Salamone S, and Lanza di Scalea F, Higher harmonic generation in nonlinear waveguides of arbitrary cross-section. J Acoust Soc Am 127:2790–2796, 2010, with the permission of the Acoustical Society of America)

Table 9.1 Material properties for the plate

$\rho 0$ (kg/m^3)	c_l (m/s)	c_t (m/s)	λ^b	μ^b	$A^{a,b}$	$B^{a,b}$	$C^{a,b}$
2727	6381	3150	57	27	−320	−200	−190

9.1.10 A Representative Simulation Confirmation: Nonlinear SAFE Analysis in Plates

Nonlinear Semi-Analytical Finite Element (SAFE) simulation was done to study the behavior of the nonlinear power flow at the double harmonic in plates [15]. The geometry of a plate is shown in Fig. 9.2. Since the waveguide is infinitely extended in the x direction, derivatives with respect to x vanish and the problem reduces to plain strain. Finite element discretization of the cross-section can be simply accomplished by a one-dimensional thickness discretization. Fourty, 2-node linear elements were used. Material properties are given in Table 9.1. Figure 9.2 shows the SAFE results for phase velocity dispersion curve for the Aluminum plate between 20 kHz and 1 MHz.

Figure 9.3 presents the results from SAFE as phase velocity dispersion curve for the Aluminum plate (20 kHz^{-1} MHz). It was discussed that, independently of the nature of the primary mode, double-harmonic antisymmetric Lamb modes will not be produced. This is due to the vanishing power transfer from the primary to the secondary mode $\left(f_n^{surf} + f_n^{vol}\right)$. This, in turn, follows from the specific cross-sectional profile of the integrands in Eqs. (9.55) and (9.56).

Figure 9.4 shows SAFE results for the thickness profiles of terms $v_n^* \cdot \overline{S} \cdot n_y$ and $v_n^* \cdot \overline{f}$ for modes A_0 and A_1 when the primary generating mode is S_0 and A_0, respectively. Irrespective of the primary mode, $v_n^* \cdot \overline{S} \cdot n_y$ is symmetric and $v_n^* \cdot \overline{f}$ is antisymmetric for a possible double-harmonic antisymmetric mode generation. A contour integral of $v_n^* \cdot \overline{S} \cdot n_y$ and a thickness integral of $v_n^* \cdot \overline{f}$ become zero. Consequently, no power

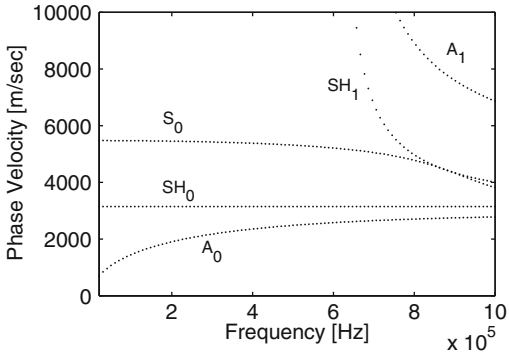

Fig. 9.3 Phase velocity dispersion curve for an Aluminum plate 2.54 mm thick

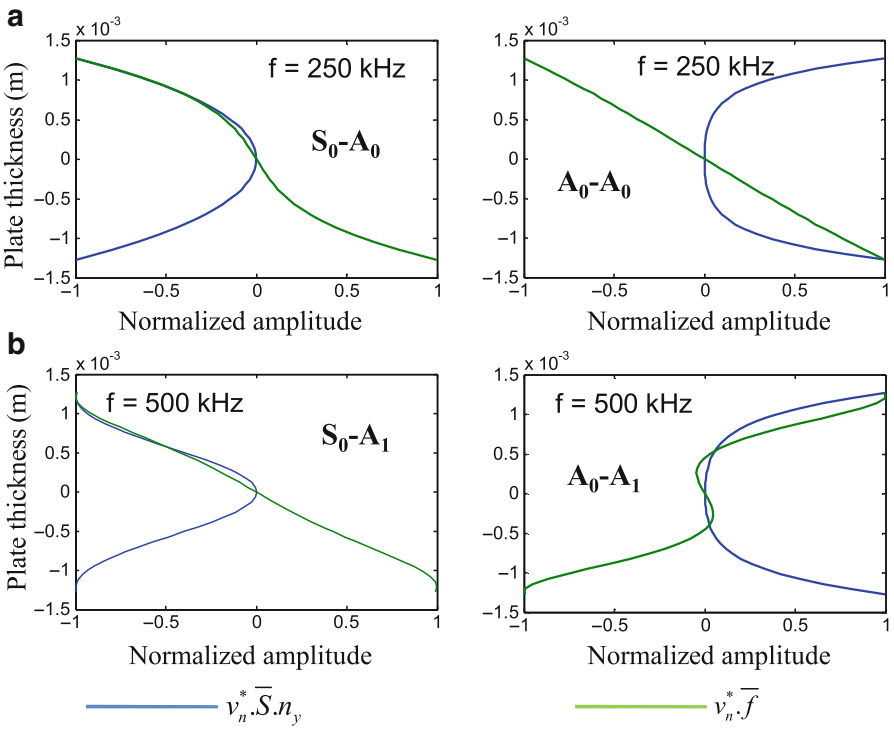

Fig. 9.4 Thickness profile of power flow. (**a**) S0 to A0 and A0 to A0 conversion. (**b**) S0 to A1 and A0 to A1 conversion (reproduced from: Srivastava A, Bartoli I, Salamone S, and Lanza di Scalea F, Higher harmonic generation in nonlinear waveguides of arbitrary cross-section. J Acoust Soc Am 127:2790–2796, 2010, with the permission of the Acoustical Society of America)

transfer occurs between any primary mode and an antisymmetric double-harmonic mode. The frequencies for the primary excitation were randomly chosen, since the symmetry attributes of these terms are not expected to change with frequency.

9.1.11 Application to Higher-Order Harmonics

Subsequent proofs to harmonics of order higher than two will be presented through mathematical induction.

Theorem 9.4 *If $E^n = u_{l,l}Q^{Sy}$, n is even and $E^{n+1} = P^{Sy}$ where P and Q are symmetric functions.* For an *n*th-order harmonic, all the terms in the energy expression contain $n + 1$ powers of strains. $E^n = u_{l,l}Q^{Sy}$ implies that any term in the expansion of E^n (denoted by T^n) behaves like $u_{l,l}Q^{Sy}$. By "any arbitrary term," we mean all $T^n = F^{n+1}(i_1,i_2,...i_{n+1})$ where $F^{n+1}(i_1,i_2,...i_{n+1})$ represents a function having $n + 1$ multiples of strains which depend upon $n + 1$ indices (i_1 to i_{n+1}) and where every index occurs exactly twice so that Einstein summation convention applies to all the indices.

Since $T^n = u_{l,l}Q^{Sy}$, n is even because if n was odd, at least one term in the expansion of E would equal $(u_{l,l})^{n+1}$ which is always symmetric. Hence, the assumption that all $T^n = u_{l,l}Q^{Sy}$ would become false.

The following two scenarios arise:

Lemma 9.5 *If T^{n+1} contains at least one strain term with repeated index, ui_m,i_m:*

$$\begin{aligned} T^{n+1} &= u_{i_m,i_m}F^{n+1}(i_1, i_2, \ldots i_{m-1}, i_{m+1}, \ldots i_{n+2}) \\ &= u_{i_m,i_m}F^{n+1}\left(i'_1, i'_2, \ldots i'_{n+1}\right) \\ &= u_{i_m,i_m}T^n = u_{i_m,i_m}u_{l,l}Q^{Sy} = P^{Sy} \end{aligned}$$

Lemma 9.6 *If T^{n+1} contains at least one strain term where the two indices assume equal values, or $i_j = i_k = p(p = y \text{ or } z)$:*

$$\begin{aligned} T^{n+1} &= u_{\overline{p},\overline{p}}F^{n+1}\left(i_1, i_2, \ldots \left(i_j = \overline{p}\right), \ldots (i_k = \overline{p}), \ldots i_{n+2}\right) \\ &= u_{\overline{p},\overline{p}}F^{n+1}\left(i'_1, i'_2, \ldots i'_{n+1}\right)\left(i_j, i_k = i'_n = \overline{p}\right) \\ &= u_{\overline{p},\overline{p}}T^n = u_{\overline{p},\overline{p}}u_{l,l}Q^{Sy} = P^{Sy} \end{aligned}$$

The most generic energy term for $(n + 1)$th-order harmonic is:

$$T^{n+1} = u_{i_1,i_2}F^{n+1}(i_1, i_2, \ldots i_{n+2})$$

The following two cases can be identified:

- $i_1 = i_2 = p$: In this case, $T^{n+1} = P^{Sy}$ from Lemma (9.6).
- $i_1 \neq i_2$; since each index from i_1 to i_{n+2} equals either y or z and since $i_1 \neq i_2$, each of i_3 to i_{n+2} equals either i_1 or i_2. Keeping in mind Lemmas (9.5, 9.6), we are only interested in the nontrivial case where all the terms T^{n+1} have indices with different value (i.e., every term in T^{n+1} is either $u_{i1,i2}$, or $u_{i2,i1}$). Since $(n + 2)$ is even, we can divide T^{n+1} into $(n + 2)/2$ multiplied sets of multiples of two terms each. Each such set is either $u_{i_1,i_2}u_{i_2,i_1}$ or $(u_{i_1,i_2})^2$ or $(u_{i_2,i_1})^2$. All of these (from Lemmas 9.1–9.3) are symmetric, hence their product is also symmetric, hence $T^{n+1} = P^{Sy}$.

This completes the proof.

Theorem 9.7 *If the energy relation for an nth-order harmonic, $E^n = Q^{Sy}$, n is odd and for the next higher order, $E^{n+1} = u_{l,l}\, P^{Sy}$ where P and Q are symmetric functions*. The fact that all $T^n = Q^{Sy}$ implies that n is odd since if n was an even number, at least one term in the expansion of Π would equal $(u_{l,l})^{n+1}$, becoming $u_{l,l}Q^{Sy}$. Hence, our initial assumption that all $T^n = Q^{Sy}$ would become false.

Following two scenarios arise:

Lemma 9.8 *If T^{n+1} contains at least one strain term with repeated index, ui_m,i_m*:

$$\begin{aligned} T^{n+1} &= u_{i_m,i_m} F^{n+1}\left(i_1, i_2, \ldots i_{m-1}, i_{m+1}, \ldots i_{n+2}\right) \\ &= u_{i_m,i_m} F^{n+1}\left(i'_1, i'_2, \ldots i'_{n+1}\right) \\ &= u_{i_m,i_m} T^n = u_{i_m,i_m} P^{Sy} \end{aligned}$$

Lemma 9.9 *If T^{n+1} contains at least one strain term where the two indices assume equal values, or $i_j = \mathrm{i_k} = \mathrm{p(p = y\ or\ z)}$*:

$$\begin{aligned} T^{n+1} &= u_{\overline{p},\overline{p}} F^{n+1}\left(i_1, i_2, \ldots \left(i_j = \overline{p}\right), \ldots \left(i_k = \overline{p}\right), \ldots i_{n+2}\right) \\ &= u_{\overline{p},\overline{p}} F^{n+2}\left(i'_1, i'_2, \ldots i'_{n+1}\right)\left(i_j, i_k = i'_n = \overline{p}\right) \\ &= u_{\overline{p},\overline{p}} T^n = u_{\overline{p},\overline{p}} P^{Sy} \end{aligned}$$

Moving forward, the most generic energy term for $(n + 1)$th-order harmonic can be expressed as:

$$T^{n+1} = u_{i_1,i_2} F^{n+1}\left(i_1, i_2, \ldots i_{n+2}\right)$$

The following two cases arise:

- $i_1 = i_2 = p$: In this case, $T^{n+1} = u_{\overline{p},\overline{p}} P^{Sy}$ from Lemma (9.9).
- $i_1 \neq i_2$; since each index from i_1 to i_{n+2} equals either y or z and since $i_1 \neq i_2$, each of i_3 to i_{n+2} equals either i_1 or i_2. Keeping in mind Lemmas (9.8, 9.9), the interest is to see if it is possible to have T^{n+1} with all the terms having indices with different values. Since n is odd, the total number of indices $n + 2$ is also odd. For a case of no index repetition and where every multiple in T^{n+1} is $u_{i1,i2}$ or $u_{i2,i1}$, the number of indices assuming value i_1 should be equal to the number of indices with value i_2. Since the total number of indices is odd, the following sets of indices can exist:
  - $i'_1, i'_2, \ldots i'_{(n+1)/2}$ where each is equal to i_1.
  - $i''_1, i''_2, \ldots i''_{(n+1)/2}$ where each is equal to i_2.
  - i_m equal to either i_1 or i_2.

It should be seen that the total number of indices in the above expressions is equal to $n + 2$. From the first two expressions, $n + 1$ displacement derivatives producing

a term in nth-order harmonic $F^{n+1}\left(i'_1, \ldots i'_{(n+1)/2}, i''_1, \ldots i''_{(n+1)/2}\right)$ is obtained by using each index exactly twice. The last $(n+2)$th term is thus left with one index since all the other indices have been used twice. Hence, that last term has a form $u_{im,im}$. Hence,

$$\begin{aligned} T^{n+1} &= u_{i_m,i_m} F^{n+1}\left(i'''_1, i'''_2, \ldots i'''_{n+2}\right) \\ &= u_{i_m,i_m} T^n = u_{i_m,i_m} P^{Sy} = u_{l,l} P^{Sy} \end{aligned}$$

This completes the proof. From Theorems (9.4 and 9.7) and conditions (9.69) and (9.71), all even harmonics (2ω, 4ω, 6ω, etc.) support only symmetric Lamb waves. Alternatively, all odd harmonics (3ω, 5ω, 7ω, etc.) support either symmetric or antisymmetric waves.

9.1.12 Experimental Confirmation

In order to test the theoretical predictions, two nonlinear ultrasonic experiments were carried out on an Aluminum plate. The plate had a thickness of 2.54 mm and a Physical Acoustics Corporation Pico transducer with 0.1–1 MHz band and central frequency 0.543 MHz was used to generate Lamb waves in it. A Pinducer sensor (Valpey Fisher VP-1093) was used to measure the response of the plate at a distance of 25 mm from the source. Both the Pico and the Pinducer excite and sense out of plane displacements; hence, they predominantly generate and receive antisymmetric motion—Fig. 9.5a. To induce high deformation nonlinearity, we loaded the plate quasi-statically to a level large enough to induce measurable nonlinearity-driven higher harmonics of the primary Rayleigh–Lamb mode. The excitation was driven at a monochromatic frequency of 320 kHz. The frequency content of the measurement is shown in Fig. 9.5b. As expected, only the odd harmonics are distinguishable in the figure because the motion is predominantly antisymmetric.

As a further confirmation, we performed joint time–frequency analysis (wavelet analysis) of the received signal using complex Morlet wavelet having a bandwidth parameter = 2 and applied a central frequency parameter = 2.5. Figure 9.6b shows the wavelet scalogram applied to signal shown in Fig. 9.6a and Fig. 9.6c shows a zoomed view in the range 0.5–1 MHz. The white lines are the expected arrival times of the relevant modes from Rayleigh–Lamb theory. As shown, strong antisymmetric mode exists at 320 kHz, and no antisymmetric mode exists at 640 kHz. Alternatively, the antisymmetric mode is present at the triple harmonic (960 kHz), as predicted by the theory and confirmed in the spectrum of Fig. 9.5.

In the second experiment, excitation and detection were accomplished by utilizing two Macro-Fiber Composite—MFC transducers (Smart Materials Corporation, M2814P1). MFCs work by generating and detecting in-plane strains, hence they are preferentially sensitive to symmetric waves—Fig. 9.7a. Figure 9.7b shows the frequency content of the received signal.

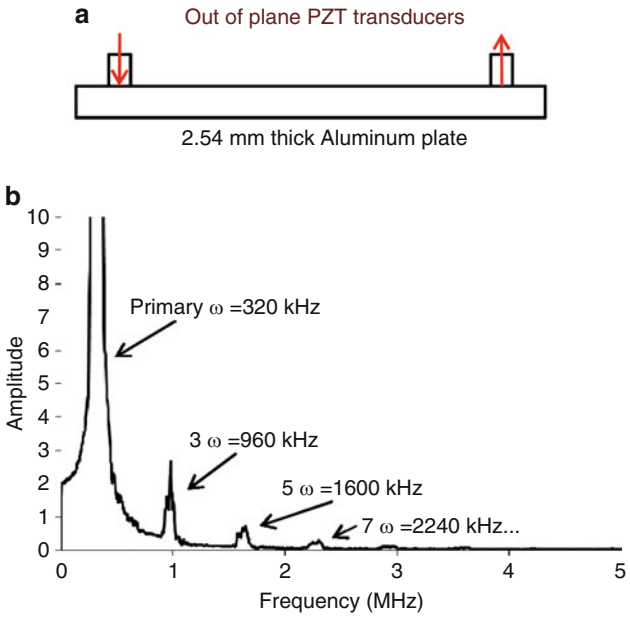

Fig. 9.5 (**a**) Schematic of the experiment for the measurement of nonlinear higher harmonics, and (**b**) response spectrum of the signal measured by the Pinducer (Reprinted from Srivastava A and Lanza di Scalea F, On the existence of antisymmetric or symmetric Lamb waves at nonlinear higher harmonics. J Sound Vibr 323:932–943, 2009)

The primary generation frequency was, again, 320 kHz. In this experiment, we expect a substantial sensitivity to symmetric waves and hence the presence of even harmonics. Figure 9.7b confirms the emergence of the double harmonic (640 kHz). The large odd harmonic at 960 kHz may be attributed to either (a) both symmetric and antisymmetric motion (MFC patches are not "pure mode" transducers), or (b) residual contributions from the undeformed plate. Figure 9.8 compares the frequency content of signals between unloaded plate and loaded plate. The harmonics present in the unloaded plate are much less significant than those present in the loaded plate. This confirms that the measured higher harmonics are in large part due to nonlinear elastic effects.

Figure 9.9 presents the wavelet scalogram of the measurement in the anti-symmetric experiment, with the theoretical Rayleigh–Lamb curves. Figure 9.9b shows that under both symmetric and antisymmetric primary excitation (320 KHz), the energy at the double harmonic (640 KHz) contains only the fundamental symmetric mode—Fig. 9.9c. The energy at the triple harmonic (960 kHz) consists of the fundamental antisymmetric, the fundamental symmetric, and the first-order antisymmetric modes. This is in accordance with the theoretical predictions that antisymmetric modes are only allowed at odd harmonics, whereas symmetric modes are allowed at both odd and even harmonics.

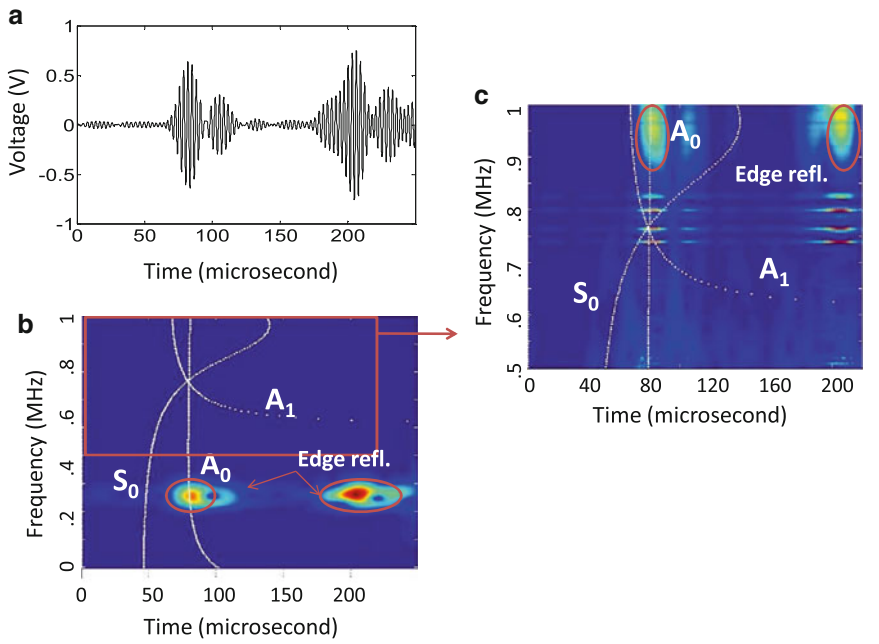

Fig. 9.6 Wavelet analysis of the antisymmetric excitation/detection in the plate: (**a**) time history, (**b**) wavelet scalogram of the measurement in the DC-1 MHz range, and (**c**) zoomed view of the wavelet scalogram. The theoretical arrival times from the Rayleigh–Lamb theory are shown as white lines (reprinted from Srivastava A and Lanza di Scalea F, On the existence of antisymmetric or symmetric Lamb waves at nonlinear higher harmonics. J Sound Vibr 323:932–943, 2009)

9.1.13 Conclusions

The inability of an even Lamb wave harmonic to support antisymmetric motion results from symmetry considerations in the corresponding energy equation. These predict that the double harmonic does not allow antisymmetric Rayleigh–Lamb waves. Mathematical induction was used to generalize to higher order of harmonics. The general conclusion is that antisymmetric Rayleigh–Lamb waves exist at odd harmonics; alternatively symmetric waves exist at either odd or even harmonics.

9.1.14 Nonlinearity in Rods

Consider now the case of nonlinear guided waves in rods. The equation of motion for nonlinear elasticity in a stress-free rod is given by (Fig. 9.10):

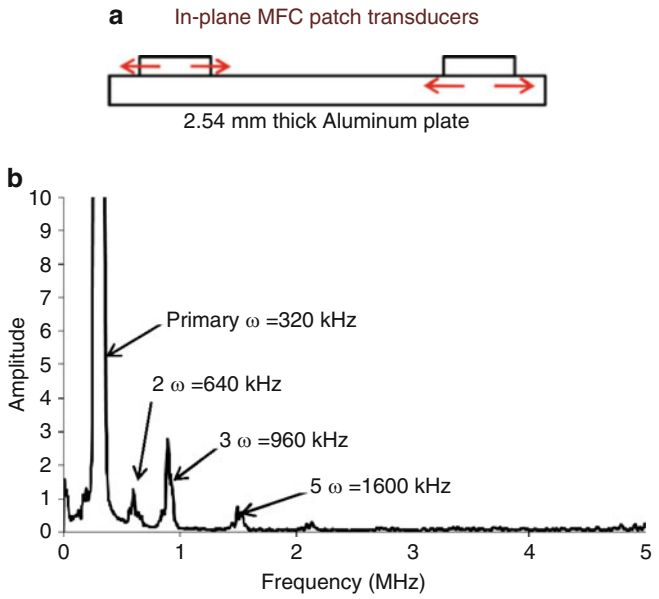

Fig. 9.7 Measurement of nonlinear higher harmonics: (**a**) scheme of the experiment, (**b**) frequency spetrum of the signal received by the MFC (reprinted from Srivastava A and Lanza di Scalea F, On the existence of antisymmetric or symmetric Lamb waves at nonlinear higher harmonics. J Sound Vibr 323:932–943, 2009)

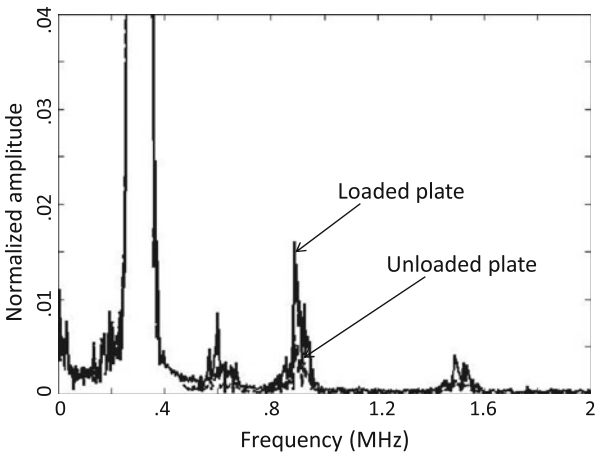

Fig. 9.8 Frequency content comparison of signals in unloaded and loaded cases (reprinted from Srivastava A and Lanza di Scalea F, On the existence of antisymmetric or symmetric Lamb waves at nonlinear higher harmonics. J Sound Vibr 323:932–943, 2009)

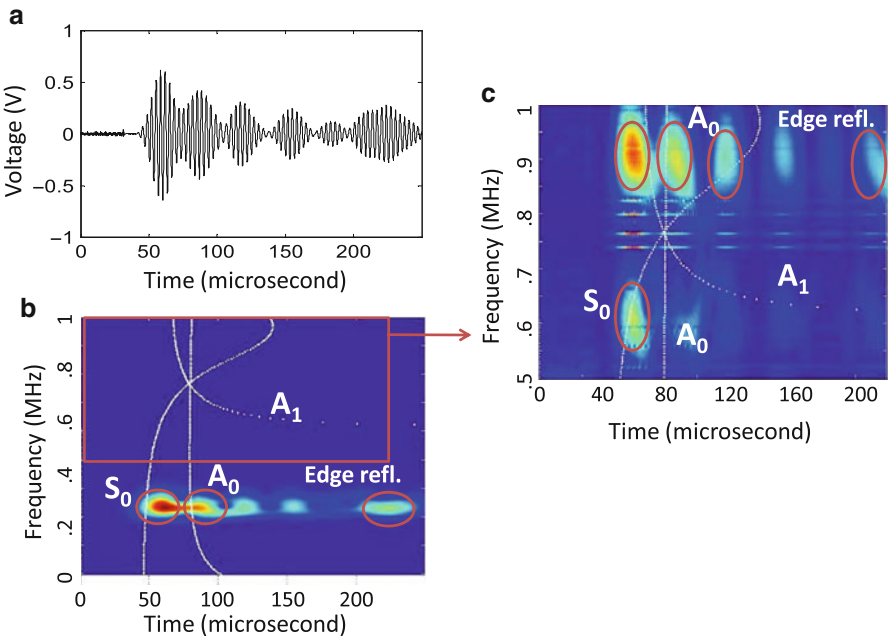

Fig. 9.9 Wavelet analysis of the symmetric excitation and detection in the plate: (**a**) time history, (**b**) wavelet scalogram, and (**c**) zoomed view of the wavelet scalogram. The theoretical arrival times from Rayleigh–Lamb theory are shown with white lines (reprinted from Srivastava A and Lanza di Scalea F, On the existence of antisymmetric or symmetric Lamb waves at nonlinear higher harmonics. J Sound Vibr 323:932–943, 2009)

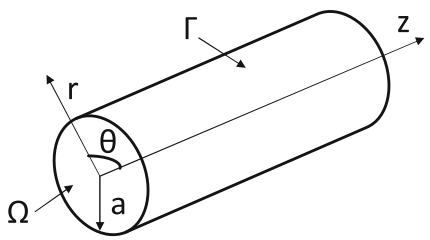

Fig. 9.10 Schematic of a stress-free rod

$$(\lambda + 2\mu)\,\nabla\,(\nabla \cdot \mathbf{u}) - \mu \nabla \times (\nabla \times \mathbf{u}) + \mathbf{f} = \rho_0 \frac{\partial^2 \mathbf{u}}{\partial t^2} \tag{9.76}$$

with stress-free boundary conditions on the free surface:

$$\left[\mathbf{S}^{\mathbf{L}}(\mathbf{u}) - \overline{\mathbf{S}}(\mathbf{u})\right] \cdot \mathbf{n_r} = \mathbf{0} \quad \text{on} \quad \Gamma \tag{9.77}$$

Murnaghan's approximation is again used for the energy expression, Eq. (9.4). To consider non-Cartesian geometry, strains are expressed by covariant differentials:

$$\varepsilon_{ij} = \frac{1}{2}\left(u_{i;j} + u_{j;i} + u_{k;i}u^{k}_{;j}\right) \tag{9.78}$$

where:

$$u_{i;j} = u_{i,j} - u_k \Gamma^{k}_{ij} \tag{9.79}$$

and

$$u^{i}_{;j} = u^{i}_{,j} + u^{k}\Gamma^{i}_{kj} \tag{9.80}$$

$\Gamma^{i}{}_{jk}$ are the Christoffel symbols. Stress is expressed by:

$$\sigma^{ij} = \frac{\partial E}{\partial \varepsilon_{ij}} \tag{9.81}$$

and the body force vector is:

$$f^{i} = \sigma^{ij}_{;j} \tag{9.82}$$

9.1.15 Solution to the Nonlinear Problem

Following normal mode expansion and perturbation from Auld [10] and de Lima and Hamilton [11], the first-order nonlinear solution becomes:

$$\mathbf{v}(\mathbf{r}, z, t) = \frac{1}{2}\sum\nolimits_{m=1}^{\infty} A_m(z)\mathbf{v}_m(\mathbf{r})\, e^{-i2\omega t} \quad + \quad c.c. \tag{9.83}$$

We have the solution:

$$A_m(z) = \overline{A}_m(z)e^{i(2\kappa z)} - \overline{A}_m(0)e^{i\kappa^{*}_{n} z}, \tag{9.84}$$

where

$$\overline{A}_m(z) = i\frac{\left(f^{\text{vol}}_n + f^{\text{surf}}_n\right)}{4P_{mn}\left[\kappa^{*}_{n} - 2\kappa\right]} \;\; ; \;\; \kappa^{*}_{n} \neq 2\kappa \quad \text{(asynchronous solution)} \tag{9.85}$$

$$\overline{A}_m(z) = \frac{\left(f^{\text{vol}}_n + f^{\text{surf}}_n\right)}{4P_{mn}} z \;\; ; \;\; \kappa^{*}_{n} = 2\kappa \quad \text{(synchronous solution)} \tag{9.86}$$

$$P_{mn} = -\frac{1}{4}\int_{\Omega}\left(\mathbf{v}^{*}_{\mathbf{n}} \cdot \mathbf{S}_{\mathbf{m}} + \mathbf{v}_{\mathbf{m}} \cdot \mathbf{S}^{*}_{\mathbf{n}}\right) \cdot \mathbf{n}_z d\Omega, \tag{9.87}$$

$$f_n^{\text{surf}}(z) = \int_{\Gamma} \mathbf{v}_{\mathbf{n}}^* \cdot \overline{\mathbf{S}} \cdot \mathbf{n}_{\mathbf{r}} \, d\Gamma \tag{9.88}$$

$$f_n^{\text{vol}}(z) = \int_{\Omega} \mathbf{v}_{\mathbf{n}}^* \cdot \bar{\mathbf{f}} \, d\Omega \tag{9.89}$$

κ is the mode wavenumber, κ_n is the wavenumber of the non-orthogonal mode to the mth mode at the higher harmonic and κ_n^* is the complex conjugate. $\mathbf{S}_m$ is the stress tensor of the mth mode, and $\mathbf{n}_z$ is the unit vector in direction z. Ω, Γ are the rod cross-sectional area and the rod surface, respectively (Fig. 9.10).

9.1.16 Analysis of Solution

If appropriate $\overline{\mathbf{S}}$ and $\bar{\mathbf{f}}$ are used in Eqs. (9.88) and (9.89), similarly to Lamb waves, the first-order nonlinear solution of Eq. (9.84) can be extended to higher orders. For an $(n-1)$th-order nonlinearity, surface stresses and body forces are $\overline{\mathbf{S}}^{\mathbf{n}}$ and $\bar{\mathbf{f}}^{\mathbf{n}}$, respectively. The subscripts for f^{surf} and f^{vol} are changed to "l."

For a cylindrical rod with radius a, flux integrals become:

$$f_l^{\text{surf}} = -\frac{a}{2} \int_0^{2\pi} \mathbf{v}_l^*(a,\theta) \cdot \overline{\mathbf{S}}^{\mathbf{n}}(a,\theta) \cdot \mathbf{n}_{\mathbf{r}} \, d\theta \tag{9.90}$$

$$f_l^{\text{vol}} = \frac{1}{2} \int_0^a \int_0^{2\pi} \mathbf{v}_l^*(r,\theta) \cdot \bar{\mathbf{f}}^{\mathbf{n}}(r,\theta) \, r \, d\theta \, dr \tag{9.91}$$

where the superscript n refers to the nonlinear effect of the primary excitation (at frequency $n\omega$) and the subscript l is referred to potential higher harmonic. Particle velocity for the lth Pochhammer Chree wave in rods at frequency $n\omega$ is [37]:

$$v_r = V_r(r) \cos(q\theta) \, e^{i(\kappa_l z - n\omega t)} \tag{9.92}$$

$$v_\theta = V_\theta(r) \sin(q\theta) \, e^{i(\kappa_l z - n\omega t)} \tag{9.93}$$

$$v_z = V_z(r) \cos(q\theta) \, e^{i(\kappa_l z - n\omega t)} \tag{9.94}$$

where $q = 0$ for longitudinal modes, and $q \geq 1$ for flexural modes. Substituting the expressions for f_l^{surf} and f_l^{vol} and ignoring the exponential harmonic term yields:

$$f_l^{\text{surf}} = -\frac{a}{2} \int_0^{2\pi} \left[V_r \overline{S}_{rr}^n \cos(q\theta) + V_\theta \overline{S}_{\theta r}^n \sin(q\theta) + V_z \overline{S}_{zr}^n \cos(q\theta) \right] d\theta \tag{9.95}$$

$$f_l^{vol} = \frac{1}{2}\int_0^a \int_0^{2\pi} \left[V_r \overline{f}_r^n \cos(q\theta) + V_\theta \overline{f}_\theta^n \sin(q\theta) + V_z \overline{f}_z^n \cos(q\theta) \right] r d\theta \, dr \tag{9.96}$$

The following identities must be noted for all integers $n \neq 0$:

$$\int_0^{2\pi} \sin(n\theta) \quad d\theta = 0 \tag{9.97}$$

$$\int_0^{2\pi} \cos(n\theta) \quad d\theta = 0 \tag{9.98}$$

From Eqs. (9.85) and (9.86), the lth mode would not be excited if both $f_l^{\text{surf}}, f_l^{\text{vol}} = 0$. This occurs if all terms in Eqs. (9.95) and (9.96) are zero. Hence, if all the terms in (9.95) and (9.96) can be expressed as one of the two integrals in (9.97) and (9.98) for an lth mode, that particular higher-harmonic mode will not be excited.

From De Moivre's formula, Euler's formula, and binomial expansion, the following expansions can be written:

If n is odd:

$$\cos^n(\theta) = \sum_{k=0}^{\frac{n-1}{2}} A_k \cos(n-2k)\theta \tag{9.99}$$

$$\sin^n(\theta) = \sum_{k=0}^{\frac{n-1}{2}} B_k \sin(n-2k)\theta \tag{9.100}$$

where A_k and B_k are only functions of n.

If n is even:

$$\cos^n(\theta) = X + \sum_{k=0}^{\frac{n}{2}-1} C_k \cos(n-2k)\theta \tag{9.101}$$

$$\sin^n(\theta) = X + \sum_{k=0}^{\frac{n}{2}-1} D_k \cos(n-2k)\theta \tag{9.102}$$

where X, C_k, and D_k are only functions of n.

For an $(n-1)$th-order nonlinearity, Eq. (9.4) will contain terms with $(n+1)$ multiples of strains. Therefore, from the velocities in Eqs. (9.92), (9.93), and (9.94), $\overline{\mathbf{S}}^{\mathbf{n}}$ and $\overline{\mathbf{f}}^{\mathbf{n}}$ contain n-strains (Eq. 9.81). Hence, for a $(n-1)$th-order nonlinearity, any term $\left(\overline{\mathbf{S}}^{\mathbf{n}}\right)$ and $\left(\overline{\mathbf{f}}^{\mathbf{n}}\right)$ can be expressed as:

$$T^n = f(r)\sin^t(p\theta)\cos^s(p\theta) \qquad t+s=n \tag{9.103}$$

where p identifies the type of primary excitation mode, $f(r)$ is an arbitrary function of the radius r, and either t or s can be equal to 0.

Equations (9.95) and (9.96) show that each term in the expressions for f_l^{surf} and f_l^{vol} involves an integral of the type:

$$I^n = \int_0^{2\pi} F(r)\sin^t(p\theta)\cos^s(p\theta)\sin(l\theta)\; d\theta \tag{9.104}$$

or

$$I^n = \int_0^{2\pi} F(r)\sin^t(p\theta)\cos^s(p\theta)\cos(l\theta)\; d\theta \tag{9.105}$$

For the ease of analysis, we denote $\sin^t(p\theta)\cos^s(p\theta) = E^n$.

Case 1: *n* Is Odd (Odd Harmonics)
Since n is odd and $t+s=n$, either t is odd or s is odd. If t is odd:

$$\begin{aligned} E^n &= \left(\sum\nolimits_{k_1=0}^{\frac{t-1}{2}} B_{k_1}\sin\{(t-2k_1)\,p\theta\}\right)\left(X+\sum\nolimits_{k_2=0}^{\frac{s}{2}-1} C_{k_2}\cos\{(s-2k_2)\,p\theta\}\right) \\ &= X\sum\nolimits_{k_1=0}^{\frac{t-1}{2}} B_{k_1}\sin\{(t-2k_1)\,p\theta\} \\ &\quad +\sum\nolimits_{k_1=0}^{\frac{t-1}{2}}\sum\nolimits_{k_2=0}^{\frac{s}{2}-1}\left(B_{k_1}\sin\{(t-2k_1)\,p\theta\}\;\; C_{k_2}\cos\{(s-2k_2)\,p\theta\}\right) \end{aligned} \tag{9.106}$$

where X, B_{k1}, and C_{k2} are independent of θ. Further,

$$\begin{aligned} S &= \sum\nolimits_{k_1=0}^{\frac{t-1}{2}}\sum\nolimits_{k_2=0}^{\frac{s}{2}-1} B_{k_1}\sin\{(t-2k_1)\,p\theta\}\;\; C_{k_2}\cos\{(s-2k_2)\,p\theta\} \\ &= \sum\nolimits_{k_1=0}^{\frac{t-1}{2}}\sum\nolimits_{k_2=0}^{\frac{s}{2}-1}\frac{1}{2}B_{k_1}C_{k_2}\left(\sin\{(t+s-2k_1-2k_2)\,p\theta\}\right. \\ &\quad \left.+\sin\{(t-2k_1-s+2k_2)\,p\theta\}\right) \end{aligned} \tag{9.107}$$

$(t+s-2k_1-2k_2)$ assumes all odd values between 3 $\left(k_1=\frac{t-1}{2}, k_2=\frac{s}{2}-1\right)$ and $t+s$ ($k_1=k_2=0$). Similarly, $(t-2k_1-s+2k_2)$ takes only odd values. It takes a value of -1 $\left(k_1=\frac{t-1}{2}, k_2=\frac{s}{2}-1\right)$ which is equivalent to 1. S can be expressed as:

$$S = \sum\nolimits_{k=1,3\ldots}^{t+s} B_k\sin(kp\theta) \tag{9.108}$$

where B_k are constants. Substituting this in Eq. (9.106), after some algebraic manipulations:

$$\begin{aligned} E^n &= \sum\nolimits_{k_1=1,3,\ldots}^{t} B_{k_1} \sin(k_1 p\theta) + \sum\nolimits_{k_2=1,3\ldots}^{t+s} B_{k_2} \sin(k_2 p\theta) \\ &= \sum\nolimits_{k=1,3,\ldots}^{t+s} E_k \sin(kp\theta) \end{aligned} \tag{9.109}$$

where E_k depend only on k. Similarly, it can be shown that if t is even, we have the following:

$$E^n = \sum\nolimits_{k=1,3\ldots}^{t+s} E_k \cos(kp\theta) \tag{9.110}$$

If Eq. (9.69) holds, we have:

$$I^n = \int_0^{2\pi} F(r) \left(\sum\nolimits_{k=1,3\ldots}^{t+s} E_k \sin(kp\theta) \right) \sin(l\theta)\ d\theta \quad ; \quad t \text{ odd} \tag{9.111}$$

or

$$I^n = \int_0^{2\pi} F(r) \left(\sum\nolimits_{k=1,3\ldots}^{t+s} E_k \cos(kp\theta) \right) \sin(l\theta)\ d\theta \quad ; \quad t \text{ even} \tag{9.112}$$

Trigonometric integration is such that the integral in Eq. (9.112) is always 0 whereas the integral in Eq. (9.111) is nonzero iff $l = kp$ for some value of k. Similarly, it can be shown that even if Eq. (9.105) holds, I^n is nonzero if $l = kp$ for some $k = 1, 3...n$.

Therefore, the families of higher-order modes that can be produced at odd harmonics are restricted by the specific primary mode. In fact, a primary flexural mode will not generate a longitudinal mode at an odd higher harmonic. Vice versa, a primary longitudinal mode cannot generate a flexural mode at an odd higher harmonic (n odd). In addition, a primary flexural mode will only generate at the nth harmonic those modes where $l = kp$ where $k = 1, 3...n$.

Case 2: n Is Even (Even Harmonics)
Since n is even and $t + s = n$, either both t and s are odd or both are even.

In the case that both t and s are odd, the following expansion holds:

$$\begin{aligned} E^n &= \left(\sum\nolimits_{k_1=0}^{\frac{t-1}{2}} B_{k_1} \sin\{(t-2k_1)\, p\theta\} \right) \left(\sum\nolimits_{k_2=0}^{\frac{s-1}{2}} A_{k_2} \cos\{(s-2k_2)\, p\theta\} \right) \\ &= \sum\nolimits_{k_1=0}^{\frac{t-1}{2}} \sum\nolimits_{k_2=0}^{\frac{s-1}{2}} B_{k_1} \sin\{(t-2k_1)\, p\theta\}\ A_{k_2} \cos\{(s-2k_2)\, p\theta\} \end{aligned} \tag{9.113}$$

It can be shown that the above expression reduces to:

$$E^n = \sum_{k=2,4,\ldots}^{t+s} E_k \sin(kp\theta) = \sum_{k=0,2,\ldots}^{t+s} E_k \sin(kp\theta) \tag{9.114}$$

Similarly, when t and s are even, we have:

$$\begin{aligned} E^n &= \left(X + \sum_{k_1=0}^{\frac{t}{2}-1} D_{k_1} \cos\{(t-2k_1)\, p\theta\} \right) \left(X + \sum_{k_2=0}^{\frac{s}{2}-1} C_{k_2} \cos\{(s-2k_2)\, p\theta\} \right) \\ &= Y + \sum_{k=2,4,\ldots}^{t+s} E_k \cos(kp\theta) = \sum_{k=0,2,\ldots}^{t+s} E_k \cos(kp\theta) \end{aligned} \tag{9.115}$$

where Y contains all terms independent of θ. If Eq. (9.104) holds, we have:

$$I^n = \int_0^{2\pi} F(r) \left(\sum_{k=0,2\ldots}^{t+s} E_k \sin(kp\theta) \right) \sin(l\theta)\ d\theta \quad ; \quad t, s \ \text{odd} \tag{9.116}$$

or

$$I^n = \int_0^{2\pi} F(r) \left(\sum_{k=0,2\ldots}^{t+s} E_k \cos(kp\theta) \right) \sin(l\theta)\ d\theta \quad ; \quad t, s \ \text{even} \tag{9.117}$$

The integral in Eq. (9.117) is always 0, whereas the integral in Eq. (9.116) is nonzero iff $l = kp$ for some value of $k \neq 0$. On the other hand, if Eq. (9.105) holds, we have:

$$I^n = \int_0^{2\pi} F(r) \left(\sum_{k=0,2\ldots}^{t+s} E_k \sin(kp\theta) \right) \cos(l\theta)\ d\theta \quad ; \quad t, s \ \textit{odd} \tag{9.118}$$

$$I^n = \int_0^{2\pi} F(r) \left(\sum_{k=0,2\ldots}^{t+s} E_k \cos(kp\theta) \right) \cos(l\theta)\ d\theta \quad ; \quad t, s \ \text{even} \tag{9.119}$$

The integral in Eq. (9.118) is 0. The integral in (9.119) is nonzero if and only if $l = kp$ for some value of k. Since f^{surf} and f^{vol} are a combination of the above terms, it can be said that a primary mode of order p can generate a higher-order mode with an angular order l if $l = kp$ for some value of $k = 0, 2 \ldots n$. Even a primary flexural mode can generate a longitudinal mode at an even higher harmonic. At the same time, a primary longitudinal mode ($p = 0$) still cannot produce a flexural mode ($l \neq 0$) at an even higher harmonic (n even).

9.1.17 Conclusions

In comparison with results from the Lamb wave case earlier, it can be seen that the flexure modes of angular order 1 in rods behave similarly to antisymmetric Lamb

modes and longitudinal rod modes behave similarly to symmetric Lamb modes. The set of first-order flexure modes and the set of antisymmetric Lamb modes are both absent at even harmonics. They are instead present, along with longitudinal and symmetric modes, at odd harmonics in rods and plates, respectively. These conclusions are not surprising, since first-order flexure and longitudinal mode symmetries in rods are analogous to those of antisymmetric and symmetric Lamb modes.

9.2 Nonlinear Waves in Waveguides of Arbitrary Cross-Sections (Semi-Analytical Computational Method)

9.2.1 Introduction

Despite several theoretical investigations pertaining to nonlinear effect in solids and second-harmonic generation were reported in the past, most studies focus on simple geometries (plates, rods, and shells) with well-known analytical solutions for the primary wave field. Nonlinear propagation in homogenous and isotropic waveguides of arbitrary cross-sections of the type of cylindrical rods and shells can be analyzed theoretically if the geometry is easily represented analytically [11]. Numerical approaches are needed for more general geometries, anisotropic elastic properties, or inhomogenous materials (or a combination of these characteristics). This section summarizes recent work in the numerical modeling of nonlinear wave in waveguides of arbitrary cross-section and material composition from Nucera and Lanza di Scalea [38–40] and Srivastava et al. [15]. Some other work in this area has been performed by Apetre et al. [41] and Radecki et al. [25]. For the solution of the nonlinear boundary value problem, perturbation theory and modal expansion from de Lima and Hamilton [8] are used in this section. A semi-analytical algorithm is presented to study the waveguides of different complexity. Four case studies are presented, namely a railroad track, a viscoelastic plate, a composite quasi-isotropic laminate, and a reinforced concrete slab. In each of these complex waveguides, favorable combinations of primary and resonant secondary modes (nonlinear resonance conditions) were successfully identified. These predictions can help designing experimental systems aimed at utilizing nonlinear waves for structural diagnostics or other purposes.

9.2.2 Waves in Nonlinear Elastic Regime: Internal Resonance

For finite deformations and/or large amplitude waves, nonlinear elasticity constitutive relations must be applied. For a homogeneous, isotropic,and hyperelastic body,

the second Piola–Kirchhoff stress tensor $\boldsymbol{S}$ can be expressed as a function of strain energy density ε and the Green–Lagrange strain tensor $\boldsymbol{E}$:

$$S_{ij} = \rho_0 \frac{\partial \varepsilon}{\partial E_{ij}} \tag{9.120}$$

where $\boldsymbol{\rho_0}$ is the initial density.

We are assuming finite strain theory:

$$E_{ij} = \frac{1}{2}\left(u_{i,j} + u_{j,i} + u_{k,i}u_{k,j}\right), u_{i,j} = \frac{\partial u_i}{\partial x_j} \tag{9.121}$$

The strain energy can be expressed as:

$$\varepsilon = \frac{1}{2}\lambda {I_1}^2 + \mu I_2 + \frac{1}{3}C {I_1}^3 + B I_1 I_2 + \frac{1}{3}A I_3 + O\left({E_{ij}}^4\right) \tag{9.122}$$

where $I_1 = E_{ii}$, $I_2 = E_{ij}E_{ji}$, $I_3 = E_{ij}E_{jk}E_{ki}$, λ and μ are the Lamé elastic constants, and A, B, and C are the Landau–Lifshitz third-order elastic constants [35] assuming first-order nonlinearity. From these relations and retaining the second-order terms, the nonlinear constitutive relation is:

$$S_{ij} = \lambda E_{kk}\delta_{ij} + 2\mu E_{ij} + \delta_{ij}\left(C E_{kk}E_{ll} + B E_{kl}E_{lk}\right) + 2B E_{kk}E_{ij} + A E_{jk}E_{ki} \tag{9.123}$$

where δ_{ij} is the Kronecker delta. If Eq. (9.123) is used in the momentum equation, the nonlinear wave equation in isotropic homogenous waveguides can be written as [29]:

$$\begin{aligned}
&\rho_0 \ddot{u}_i - \mu u_{i,kk} - (\lambda + \mu) u_{l,li} = \left(\mu + \frac{A}{4}\right)\left(u_{l,kk}u_{l,i} + u_{l,kk}u_{i,l} + 2u_{i,lk}u_{l,k}\right) \\
&++ \left(\lambda + \mu + \frac{A}{4} + B\right)\left(u_{l,ik}u_{l,k} + u_{k,lk}u_{i,l}\right) + (\lambda + B)\, u_{i,kk}u_{l,l} \\
&++ \left(\frac{A}{4} + B\right)\left(u_{k,lk}u_{l,i} + u_{l,ik}u_{k,l}\right) + (B + 2C)\, u_{k,ik}u_{l,l}
\end{aligned} \tag{9.124}$$

where $u_i(x_k,t)$ is the displacement vector in the Lagrange variables and $u_{i,j} = \partial u_i/\partial x_j$). By using vector notation, the governing equation of the guided waves becomes:

$$(\lambda + 2\mu)\nabla(\nabla \cdot \boldsymbol{u}) - \mu \nabla \times (\nabla \times \boldsymbol{u}) + \overline{\boldsymbol{f}} = \rho_0 \frac{\partial^2 u}{\partial t^2} \tag{9.125}$$

$$\mathbf{S_L}(\boldsymbol{u}) \cdot \boldsymbol{n}_r = -\overline{\boldsymbol{S}}(\boldsymbol{u}) \cdot \boldsymbol{n_r} \quad \text{on} \quad \Gamma \tag{9.126}$$

where $\boldsymbol{u}$ is the vector of particle displacements, $\boldsymbol{\rho_0}$, $\boldsymbol{\lambda}$, and $\boldsymbol{\mu}$ were as defined earlier, $\overline{\boldsymbol{f}}$ is the body force containing nonlinear terms, $\boldsymbol{n_r}$ is the unit vector perpendicular to the waveguide's surface Γ, and $\boldsymbol{S_L}$ and $\overline{\boldsymbol{S}}$ are the linear and nonlinear parts of the second Piola–Kirchhoff stress tensor. The nonlinear terms are given by:

$$\begin{aligned}\overline{f}_i = &\left(\mu + \frac{A}{4}\right)\left(u_{l,kk}u_{l,i} + u_{l,kk}u_{i,l} + 2u_{i,lk}u_{l,k}\right) + \left(\lambda + \mu + \frac{A}{4} + B\right)\\ &\times\left(u_{l,ik}u_{l,k} + u_{k,lk}u_{i,l}\right) + (\lambda+B)\left(u_{i,kk}u_{l,l}\right) + \left(\frac{A}{4}+B\right)\left(u_{k,lk}u_{l,i}+u_{k,ik}u_{k,l}\right)\\ &+ (B + 2C)\left(u_{k,ik}u_{l,l}\right) + O\left(E_{ij}\right)^3 \end{aligned} \tag{9.127}$$

$$\begin{aligned}\overline{S}_{ij} = &\left(\frac{\lambda}{2}u_{k,l}u_{k,l} + Cu_{k,k}u_{l,l}\right)\delta_{ij} + Bu_{k,k}u_{j,i} + \frac{A}{4}u_{j,k}u_{k,i}\\ &+\frac{B}{2}\left(u_{k,l}u_{k,l} + u_{k,l}u_{l,k}\right)\delta_{ij} + (\lambda + B)\,u_{k,k}u_{i,j}\\ &+\left(\mu + \frac{A}{4}\right)\left(u_{i,k}u_{j,k} + u_{k,i}u_{k,j} + u_{i,k}u_{k,j}\right) + O\left(E_{ij}\right)^3 \end{aligned} \tag{9.128}$$

The terms in Eqs. (9.127) and (9.128) highlight the presence of third-order displacement gradients. They act as forcing functions of the linearized boundary value problem, as better described below.

For second-order nonlinearity (Fig. 9.11), the boundary value problem in Eqs. (9.125) and (9.126) is solved using perturbation theory [8, 10]. Accordingly, the solution is a combination of two terms, namely $\boldsymbol{u} = \boldsymbol{u^{(1)}} + \boldsymbol{u^{(2)}}$, where $\boldsymbol{u^{(1)}}$ is the primary solution and $\boldsymbol{u^{(2)}}$ is the secondary solution due to nonlinearity (assumed small compared to $\boldsymbol{u^{(1)}}$—*perturbation condition*). So, two linear boundary value problems are derived, namely the first-order and second-order approximations. If $\boldsymbol{\omega}$ is the primary frequency, the first-order nonlinear solution at $2\boldsymbol{\omega}$ is calculated through modal expansion:

$$v\,(x,\,y,\,z,\,t) = \frac{1}{2}\sum\nolimits_{m=1}^{\infty} A_m(z)v_m\,(x,\,y)\,e^{-i2\omega t} + c.c. \tag{9.129}$$

where ***c.c.*** indicates complex conjugates, $\boldsymbol{v_m}$ is the vector of particle velocities for the mth mode at $2\boldsymbol{\omega}$, z is the direction of wave propagation and $\boldsymbol{A_m}$ is the modal amplitude of the higher-order mode given by:

$$A_m(z) = \overline{A}_m(z)e^{i\,(2kz)} - \overline{A}_m(0)e^{ik_n{}^*z} \tag{9.130}$$

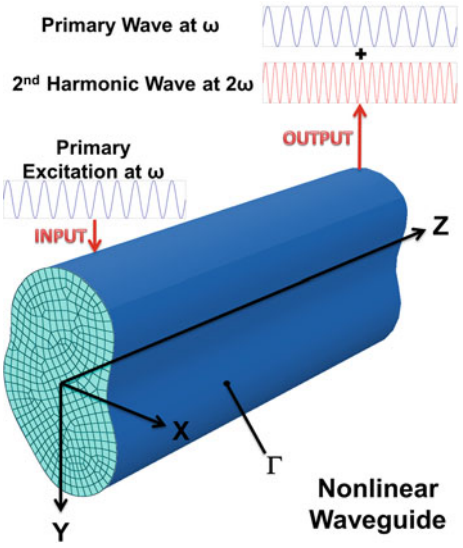

Fig. 9.11 Nonlinear waveguide (finite element mesh just on the cross-section) with second-harmonic generation mechanism highlighted (reprinted from Nucera C and Lanza di Scalea F, Modeling of nonlinear guided waves and applications to structural health monitoring. ASCE J Comput Civ Eng 29:B40140011–B401400115, 2015, with permission from ASCE)

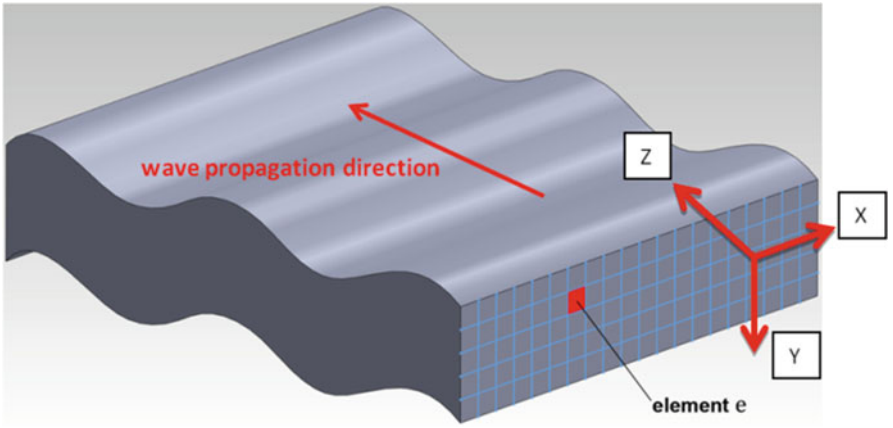

Fig. 9.12 Generic *eth* finite element on the waveguide cross-section for the SAFE modeling of ultrasonic guided waves (reprinted from Nucera C and Lanza di Scalea F, Modeling of nonlinear guided waves and applications to structural health monitoring. ASCE J Comput Civ Eng 29:B40140011–B401400115, 2015, with permission from ASCE)

Two conditions exists, namely an asynchronous (difference of phase velocity) and a synchronous (equality of phase velocity) condition:

$$\overline{A}_m(z) = i\frac{\left(f_n{}^{vol} + f_n{}^{surf}\right)}{4P_{mn}\left(k_n{}^* - 2k\right)} \quad \text{if} \quad k_n{}^* \neq 2k \quad \text{ASYNCHRONISM} \qquad (9.131)$$

$$\overline{A}_m(z) = \frac{\left(f_n{}^{vol} + f_n{}^{surf}\right)}{4P_{mn}} z \quad \text{if} \quad k_n{}^* = 2k \quad \text{SYNCHRONISM} \tag{9.132}$$

where P_{mn} is the complex power flow along the direction of wave propagation and $f_n{}^{vol}$ and $f_n{}^{surf}$ are the power from surface and volume forces, respectively.

As observed by de Lima and Hamilton [8], in the asynchronous case the modal amplitude of the generic mth secondary mode oscillates. Alternatively, in the synchronous case, the nonlinear amplitude increases linearly with propagation distance z (cumulative behavior). The internal resonance mechanism requires the simultaneous occurrence of two conditions, namely:

1. Phase matching: $k_n{}^* = 2\,k$.
2. Nonzero power transfer from primary to secondary wave field: $f_n{}^{surf} + f_n{}^{vol} \neq 0$.

Recent investigations performed by Deng et al. [28] have also considered the condition of group velocity matching. The authors conclude that the group velocity matching is not a necessary condition for cumulative higher-harmonic generation due to the finite time duration of practical wave tonebursts.

In light of these considerations, it is important to develop ways to identify "favorable" conditions of cumulative higher-harmonic generation in waveguides, and specifically for waveguides that are complex in terms of either their geometries or their constituent materials.

9.2.3 Nonlinear Semi-Analytical Algorithm

The Semi-Analytical Finite Element formulation (*S.A.F.E.*) in its linear fashion was proposed for the first time four decades ago [42, 43] and has been researched ever since [44–53]. The S.A.F.E. method has been traditionally limited to the linear elastic regime. The extension to the nonlinear case is not trivial. The authors of this chapter have utilized the COMSOL finite element code in conjunction with an S.A.F.E. analysis (CO.NO.SAFE—**CO**MSOL **No**nlinear **S**emi-**A**nalytical **F**inite **E**lement) for the identification of resonant and cumulative high-harmonic generation in complex waveguides.

The development of the proposed numerical algorithm started from the classical 3D elasticity field equations. Early nonlinear applications of S.A.F.E. were proposed by Bartoli et al. [51]. Accordingly, the displacement for the generic eth element of the cross-sectional discretization is:

$$u^e(x, y, z, t) = N^e(x, y)\, q^e e^{i(kz - \omega t)} \tag{9.133}$$

where k is the wavenumber, u^e is the displacement for the eth element, ω is frequency, q^e is the nodal displacement vector for the eth element, $N^e(x, y)$ is the shape functions matrix of order $(3\ x\ 3n)$, and n is the number of nodes per element.

Considering stress-free conditions at the waveguide's surface, the following twin-parameter eigenproblem can be formulated:

$$C_{ijkl}N_{j,kl} + i\left(C_{i3jk} + C_{ikj3}\right)\left(kN_j\right)_{,k} - kC_{i3j3}\left(kN_j\right) + \rho\omega^2\delta_{ij}N_j = 0 \quad \text{in} \quad \Omega \tag{9.134}$$

$$C_{ikjl}N_{j,l}n_k + iC_{ikj3}\left(kN_j\right)n_k = \widehat{t_i} \quad \text{on} \quad \Gamma_\sigma \tag{9.135}$$

where C_{ijkl} is the elasticity tensor, Ω is the waveguide's volume, Γ_σ is the part of the exterior surface Γ where surface tractions are present, $i = 1, 2, 3$, and summation is meant over the indices j, k, and l. The eigensolutions are pairs of k and ω (dispersion solutions). At each frequency ω, wavenumbers and mode shapes of propagative (real wavenumber) and non-propagative (complex wavenumber) modes are generated. However, a relatively complex second-order polynomial eigenvalue problem would have to be solved at each frequency ω. The second-order eigenproblem is reduced to a first-order eigensystem by introducing the vector variable $\boldsymbol{v}$:

$$\boldsymbol{M} \cdot \boldsymbol{v} = k\boldsymbol{M} \cdot \boldsymbol{u} \tag{9.136}$$

where $\boldsymbol{M}$ is a diagonal matrix that is arbitrary.

The following set of variables is introduced:

$$\overline{\boldsymbol{u}} = [u_1 \;\; u_2 \;\; u_3 \;\; v_1 \;\; v_2 \;\; v_3]^T \tag{9.137}$$

The SAFE coefficients become:

$$d_a = \begin{bmatrix} 0 & D \\ M & 0 \end{bmatrix}; \quad \alpha = \begin{bmatrix} 0 & iA \\ 0 & 0 \end{bmatrix}; \quad \beta = \begin{bmatrix} 0 & -iB \\ 0 & 0 \end{bmatrix}; c = \begin{bmatrix} C & 0 \\ 0 & 0 \end{bmatrix}; \quad a = \begin{bmatrix} M & 0 \\ 0 & M \end{bmatrix}; \tag{9.138}$$

where:

$$M = \begin{bmatrix} -\rho\omega^2 & 0 & 0 \\ 0 & -\rho\omega^2 & 0 \\ 0 & 0 & -\rho\omega^2 \end{bmatrix}; \quad D = \begin{bmatrix} -C_{55} & -C_{54} & -C_{53} \\ -C_{45} & -C_{44} & -C_{43} \\ -C_{35} & -C_{34} & -C_{33} \end{bmatrix};$$

$$A = \begin{bmatrix} \begin{bmatrix} C_{15} \\ C_{65} \end{bmatrix} & \begin{bmatrix} C_{14} \\ C_{64} \end{bmatrix} & \begin{bmatrix} C_{13} \\ C_{63} \end{bmatrix} \\ \begin{bmatrix} C_{65} \\ C_{25} \end{bmatrix} & \begin{bmatrix} C_{64} \\ C_{24} \end{bmatrix} & \begin{bmatrix} C_{63} \\ C_{23} \end{bmatrix} \\ \begin{bmatrix} C_{55} \\ C_{45} \end{bmatrix} & \begin{bmatrix} C_{54} \\ C_{44} \end{bmatrix} & \begin{bmatrix} C_{53} \\ C_{43} \end{bmatrix} \end{bmatrix}; \quad B = \begin{bmatrix} \begin{bmatrix} C_{51} \\ C_{56} \end{bmatrix} & \begin{bmatrix} C_{56} \\ C_{52} \end{bmatrix} & \begin{bmatrix} C_{55} \\ C_{54} \end{bmatrix} \\ \begin{bmatrix} C_{41} \\ C_{46} \end{bmatrix} & \begin{bmatrix} C_{46} \\ C_{42} \end{bmatrix} & \begin{bmatrix} C_{45} \\ C_{44} \end{bmatrix} \\ \begin{bmatrix} C_{31} \\ C_{36} \end{bmatrix} & \begin{bmatrix} C_{36} \\ C_{32} \end{bmatrix} & \begin{bmatrix} C_{35} \\ C_{34} \end{bmatrix} \end{bmatrix};$$

$$C = \begin{bmatrix} \begin{bmatrix} C_{11} & C_{16} \\ C_{61} & C_{66} \end{bmatrix} & \begin{bmatrix} C_{16} & C_{12} \\ C_{66} & C_{62} \end{bmatrix} & \begin{bmatrix} C_{15} & C_{14} \\ C_{65} & C_{64} \end{bmatrix} \\ \begin{bmatrix} C_{61} & C_{66} \\ C_{21} & C_{26} \end{bmatrix} & \begin{bmatrix} C_{66} & C_{62} \\ C_{26} & C_{22} \end{bmatrix} & \begin{bmatrix} C_{65} & C_{64} \\ C_{25} & C_{24} \end{bmatrix} \\ \begin{bmatrix} C_{51} & C_{56} \\ C_{41} & C_{46} \end{bmatrix} & \begin{bmatrix} C_{56} & C_{52} \\ C_{46} & C_{42} \end{bmatrix} & \begin{bmatrix} C_{55} & C_{54} \\ C_{45} & C_{44} \end{bmatrix} \end{bmatrix}; \tag{9.139}$$

and ρ is the density, ω is the frequency, and C_{ij} $(i,j = 1,...,6)$ are the stiffness coefficients (generally complex) expressed in Voigt notation.

$2\ M$ is the size of the linearized eigensystem. The $2\ M$ eigenvectors at each frequency ω are the M forward-propagating and the M backward-propagating modes.

The flowchart depicted in Fig. 9.13 presents the steps used by the proposed algorithm for internal resonance analysis of complex nonlinear waveguides. The first step is to calculate the dispersion solutions in the linear regime. In the second step, the nonlinear solutions are calculated by mode expansion and perturbation theory. Finally, the nonlinear generation condition for the various second-harmonic modes under a given primary excitation is checked for resonance (phase matching) and cumulative behavior (nonzero power transfer).

9.2.4 Application: Railroad Track

The first case study involves a waveguide with a complex cross-section, namely a 136-lb RE rail. Two cases of higher-harmonic generation are considered, one of synchronicity but no power transfer with oscillating second-harmonic amplitude (Eq. (9.131)), and the other one of synchronicity and nonzero power transfer leading to cumulative generation (Eq. (9.132)).

The material properties considered are given in Table 9.2, where the Landau–Lifshitz third-order constants from Sekoyan and Eremeev [54] were used.

Figure 9.14a depicts geometry and FE mesh used. The discretization employed 618 cubic Lagrangian triangular isoparametric finite elements [55]. The phase velocity dispersion curves are presented in Fig. 9.14b in the 0–200-kHz frequency range. The two selected combinations of primary and secondary modes as representative cases are shown in this figure.

The results show the multitude of modes that can be propagated in a rail. The complexities increase with increasing frequency. For a primary excitation frequency at 80 kHz, 500 propagative modes (real eigenvalues) were extracted at ω (80 kHz)

Table 9.2 Material properties assumed for the railroad track analysis

ρ (kg/m^3)	λ (GPa)	μ (GPa)	A (GPa)	B (GPa)	C (GPa)
7932	116.25	82.754	−760	−250	−90

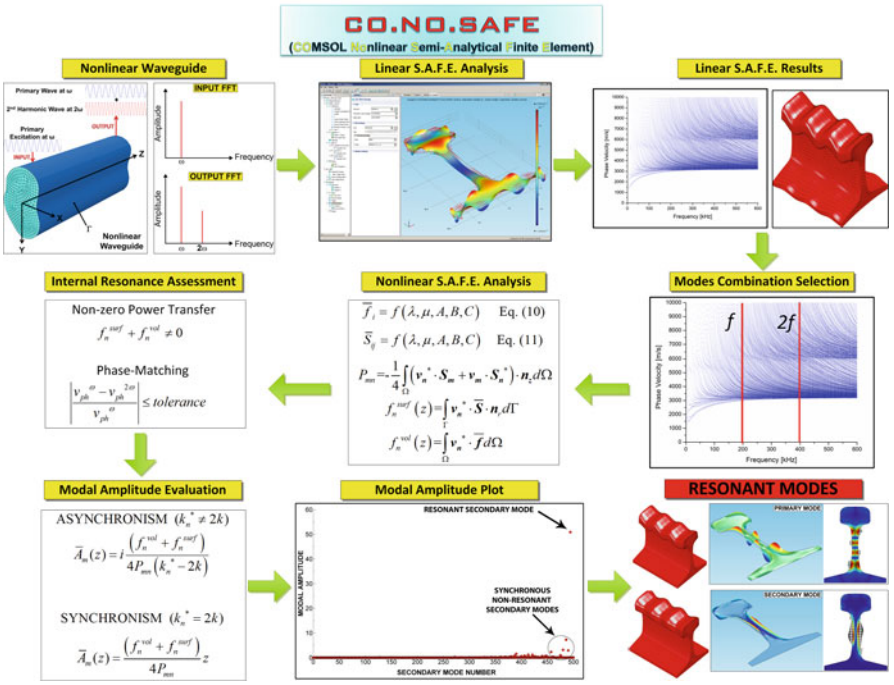

Fig. 9.13 CO.NO.SAFE algorithm flowchart (reprinted from Nucera C and Lanza di Scalea F, Modeling of nonlinear guided waves and applications to structural health monitoring. ASCE J Comput Civ Eng 29:B40140011–B401400115, 2015, with permission from ASCE)

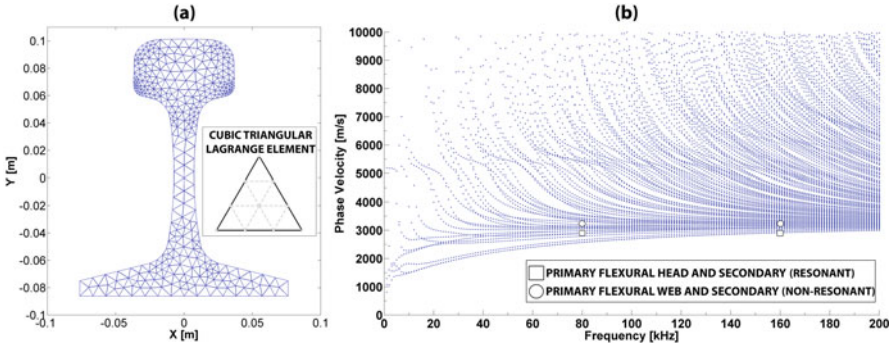

Fig. 9.14 (**a**) Geometry and mesh adopted of the railroad track, and (**b**) dispersion curve of phase velocity with selected combinations of primary and secondary modes (reprinted from Nucera C and Lanza di Scalea F, Modeling of nonlinear guided waves and applications to structural health monitoring. ASCE J Comput Civ Eng 29:B40140011–B401400115, 2015, with permission from ASCE)

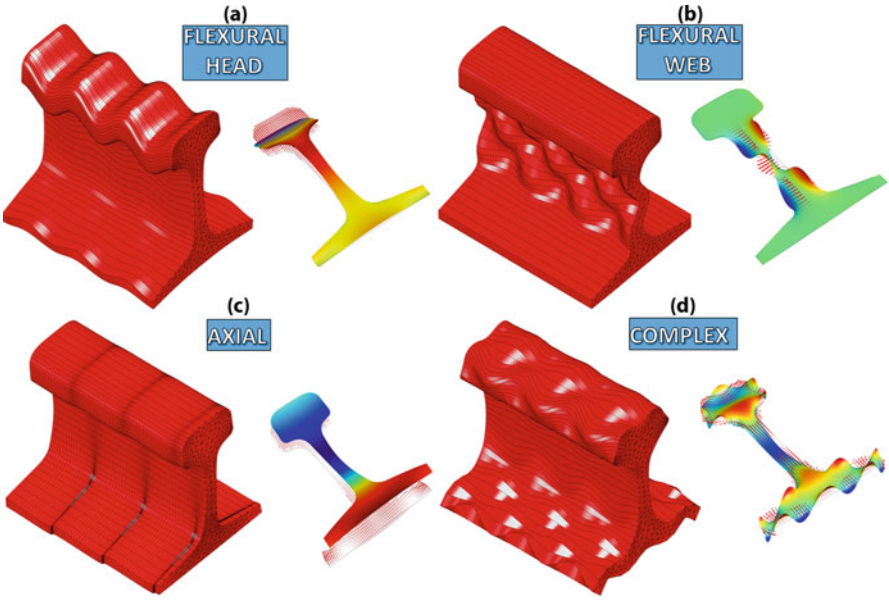

Fig. 9.15 Propagative modes in the 80–160-kHz range. (**a**) Flexural vertical mode (head mode), (**b**) flexural horizontal mode (web mode), (**c**) axial mode, and (**d**) complex mode (reprinted from Nucera C and Lanza di Scalea F, Modeling of nonlinear guided waves and applications to structural health monitoring. ASCE J Comput Civ Eng 29:B40140011–B401400115, 2015, with permission from ASCE)

and at 2ω (160 kHz). Figure 9.15 shows some propagative modes identified in this frequency range. These mode shapes indicate how the wave energy is distributed across the waveguides. This information is extremely useful to design appropriate wave transduction means for excitation and detection of these modes, and/or to focus a guided wave inspection to selected regions of the cross-section, whether the rail head, the rail web, or the rail base.

9.2.4.1 Nonresonant Combination

A flexural horizontal primary mode was selected as primary input for the CO.NO.SAFE analysis. The nonlinear analysis identified the presence of a synchronous secondary mode at 2ω. This mode is of a flexural horizontal type based on the cross-sectional displacement distribution. However, this mode has a zero power transfer from the primary mode resulting in a noncumulative behavior with amplitude oscillating along the propagation direction. At the same time, a significant power transfer is present between the selected primary mode and some asynchronous secondary modes; however, these modes are not synchronous with the primary mode and hence no cumulative behavior occurs.

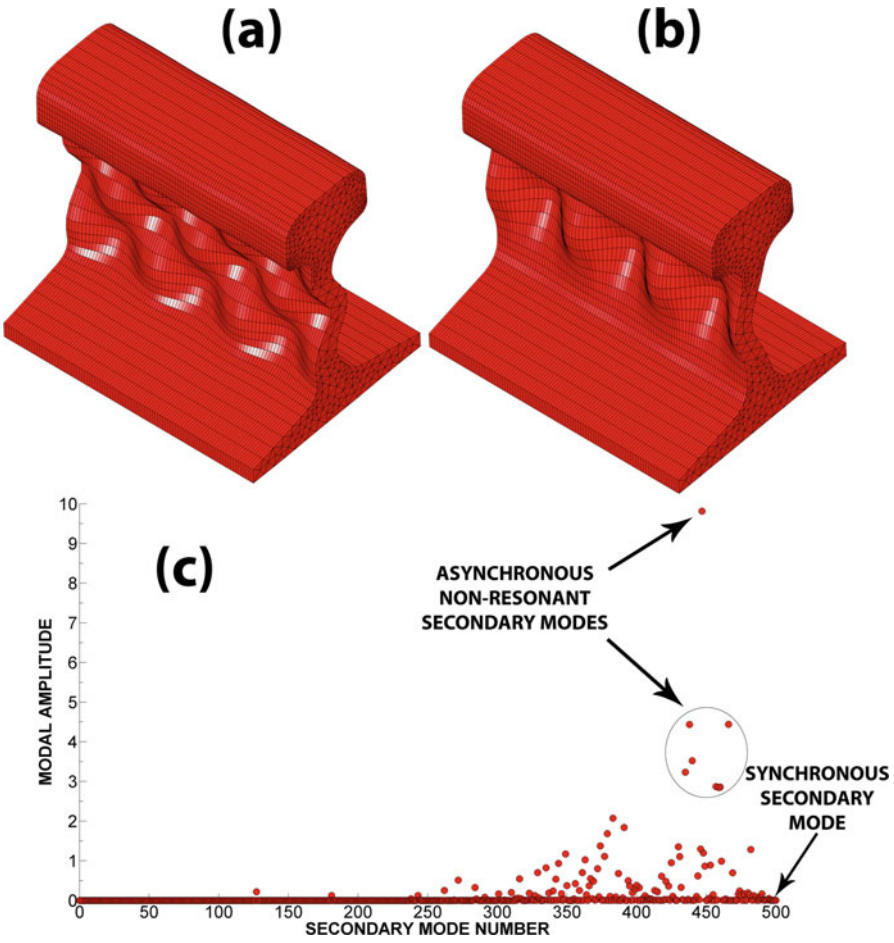

Fig. 9.16 (**a**) Primary mode at 80 kHz, (**b**) phase-matched (synchronous) but nonresonant secondary mode at 160 kHz, and (**c**) modal amplitudes for propagative secondary modes (reprinted from Nucera C and Lanza di Scalea F, Modeling of nonlinear guided waves and applications to structural health monitoring. ASCE J Comput Civ Eng 29:B40140011–B401400115, 2015, with permission from ASCE)

Figure 9.16a, b illustrates the selected primary and secondary modes, respectively. Figure 9.16c plots the modal amplitude results as calculated from Eqs. (9.131) and (9.132) for the propagative secondary modes present at 160 kHz.

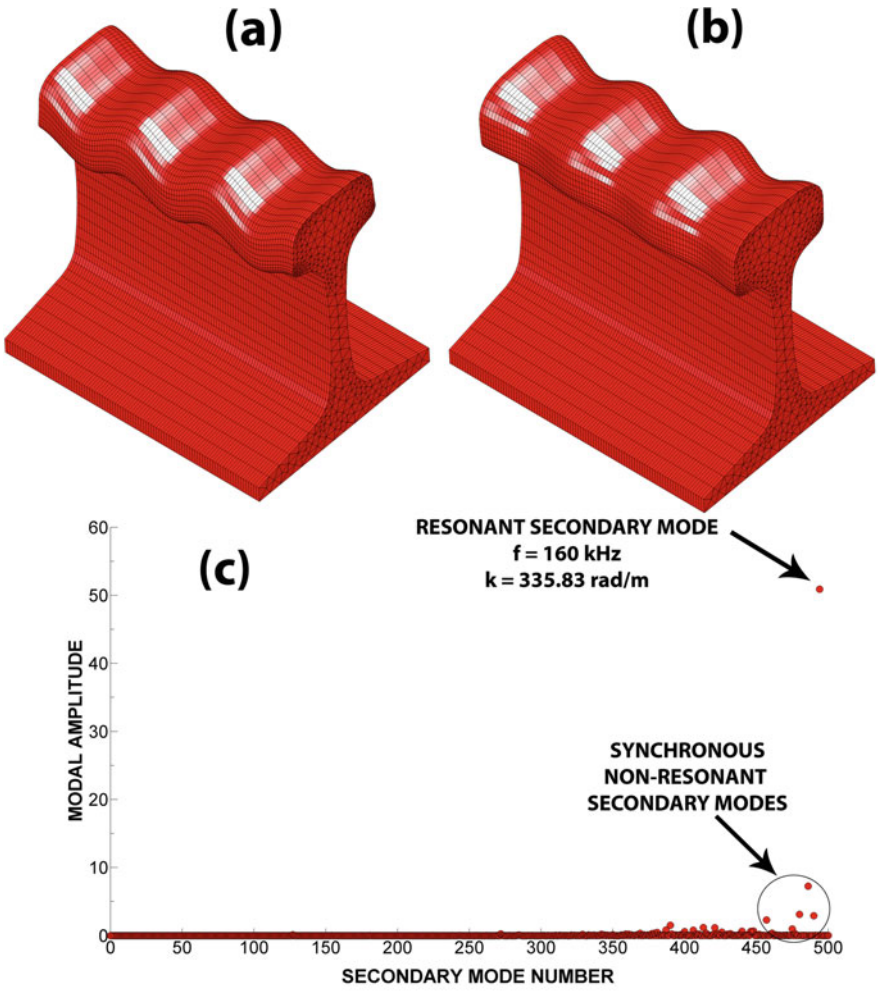

Fig. 9.17 (**a**) Primary mode at 80 kHz, (**b**) resonant secondary mode, and (**c**) modal amplitudes for secondary propagative modes (reprinted from Nucera C and Lanza di Scalea F, Modeling of nonlinear guided waves and applications to structural health monitoring. ASCE J Comput Civ Eng 29:B40140011–B401400115, 2015, with permission from ASCE)

9.2.4.2 Resonant Combination

In this case, a flexural vertical mode was selected as primary excitation. The nonlinear SAFE analysis revealed another flexural vertical mode that satisfies both synchronicity and power transfer requirements. This secondary mode can then propagate in a resonant cumulative fashion. Figures 9.16b and 9.17a display the selected modes, while Fig. 9.17c shows the very high value of modal amplitude

related to the secondary resonant mode; small amplitude values associated to the other synchronous modes, for which power transfer is absent, are also shown in the amplitude plot.

This analysis shows that it is indeed possible to find a combination of primary and secondary modes that is favorable to the practical utilization of nonlinear wave propagation for a rail waveguide. Interestingly, the primary mode considered here could also be easily generated by a piezoelectric transducer.

9.2.5 *Application: Viscoelastic Isotropic Plate*

The next study considered a viscoelastic isotropic polyethylene (HPPE) plate. Past investigations of this waveguide were conducted in the linear regime to identify dispersion curves and mode shapes [51, 56, 57]. This case is now extended to the nonlinear regime for the identification of favorable combinations of primary and secondary modes.

Material and geometrical properties for the plate are illustrated in Table 9.3 [56, 57], where ρ is the density, h is the thickness of the plate, c_L is the longitudinal bulk wave velocity, c_T is the shear bulk wave velocity, k_L is the longitudinal bulk wave attenuation, and k_T is the shear bulk wave attenuation.

A frequency-independent stiffness matrix was considered to account for the dissipative behavior of the plate via a hysteretic formulation [51]. The resulting complex Lame' constants are:

$$\tilde{\lambda} = \frac{\rho\tilde{c}_T^2\left(3\tilde{c}_L^2 - 4\tilde{c}_T^2\right)\left(\tilde{c}_L^2 - 2\tilde{c}_T^2\right)}{2\left(\tilde{c}_L^2 - \tilde{c}_T^2\right)^2\left(1 - \frac{\tilde{c}_L^2 - 2\tilde{c}_T^2}{\tilde{c}_L^2 - \tilde{c}_T^2}\right)\left(1 + \frac{\tilde{c}_L^2 - 2\tilde{c}_T^2}{2(\tilde{c}_L^2 - \tilde{c}_T^2)}\right)} = 3.51 + 0.06i\ GPa \quad (9.140)$$

$$\tilde{\mu} = \frac{\rho\tilde{c}_T^2\left(3\tilde{c}_L^2 - 4\tilde{c}_T^2\right)}{2\left(\tilde{c}_L^2 - \tilde{c}_T^2\right)\left(1 + \frac{\tilde{c}_L^2 - 2\tilde{c}_T^2}{2(\tilde{c}_L^2 - \tilde{c}_T^2)}\right)} = 0.86 - 0.08i\ GPa \quad (9.141)$$

In Eqs. (9.140) and (9.141), the complex bulk wave velocities (longitudinal and transverse) are calculated as:

$$\tilde{c}_{L,T} = c_{L,T}\left(1 + i\frac{k_{L,T}}{2\pi}\right)^{-1} \quad (9.142)$$

Table 9.3 HPPE plate material properties

ρ (kg/m^3)	h (mm)	c_L (m/s)	c_T (m/s)	k_L (Np/wavelength)	k_T (Np/wavelength)
953	12.7	2344	953	0.055	0.286

The resultant viscoelastic stiffness matrix, with terms expressed in GPa, is given by:

$$\tilde{C}=\begin{bmatrix} \tilde{\lambda}+2\tilde{\mu} & \tilde{\lambda} & \tilde{\lambda} & 0 & 0 & 0 \\ \tilde{\lambda} & \tilde{\lambda}+2\tilde{\mu} & \tilde{\lambda} & 0 & 0 & 0 \\ \tilde{\lambda} & \tilde{\lambda} & \tilde{\lambda}+2\tilde{\mu} & 0 & 0 & 0 \\ 0 & 0 & 0 & \tilde{\mu} & 0 & 0 \\ 0 & 0 & 0 & 0 & \tilde{\mu} & 0 \\ 0 & 0 & 0 & 0 & 0 & \tilde{\mu} \end{bmatrix}$$

$$=\begin{bmatrix} 5.23-0.09i & 3.51+0.06i & 3.51+0.06i & 0 & 0 & 0 \\ 3.51+0.06i & 5.23-0.09i & 3.51+0.06i & 0 & 0 & 0 \\ 3.51+0.06i & 3.51+0.06i & 5.23-0.09i & 0 & 0 & 0 \\ 0 & 0 & 0 & 0.86-0.08i & 0 & 0 \\ 0 & 0 & 0 & 0 & 0.86-0.08i & 0 \\ 0 & 0 & 0 & 0 & 0 & 0.86-0.08i \end{bmatrix} \tag{9.143}$$

The complex part of the third-order constants, not available in the literature, was neglected in the numerical results. This is a reasonable simplification, since the existence or the absence of resonant conditions primarily depends on general cross-sectional symmetries of the modes that are not affected in any substantial way by the material's third-order constants.

Dispersion curves were obtained adapting the linear SAFE algorithm to implement periodic boundary conditions (PBC) [58]. According to this approach, the present plate system was modeled using a mesh of just 60 quadrilateral cubic Lagrangian elements mapped and deployed in a 3.17 × 12.7-mm periodic cell, Fig. 9.18a. The dispersion solutions are shown in Fig. 9.18b, c in the 0–500-kHz frequency range, and show very good agreement with the previous results [59]. White circles are used to indicate the primary and secondary modes considered in the nonlinear analysis.

Since no reference value was available for the third-order Landau–Lifshitz elastic constants of the specific HPPE material, these properties were taken from a very similar plastic polymer (Polystyrene) [60] as $A = -10.8$, $B = -7.85$, and $C = -9.81$ GPa.

The nonlinear analysis was conducted between 250 kHz (primary mode) and 500 kHz (secondary mode), and by using a 10% threshold between real and imaginary wavenumber components to separate propagative modes from evanescent modes. One particular mode ($k = 669.62 + 87.56$i, $c_{ph} = 2345.80$ m/s at 250 kHz) was selected as input (primary mode). In Fig. 9.19, most of the double-harmonic modes have oscillatory amplitude, with one standing out with large amplitude suggesting cumulative behavior. Figure 9.19 also shows that the selected primary mode is a complex axial symmetric mode. The mode shape at the double harmonic is also typical of axial vibrations. The fact that the cross-sectional energy is confined

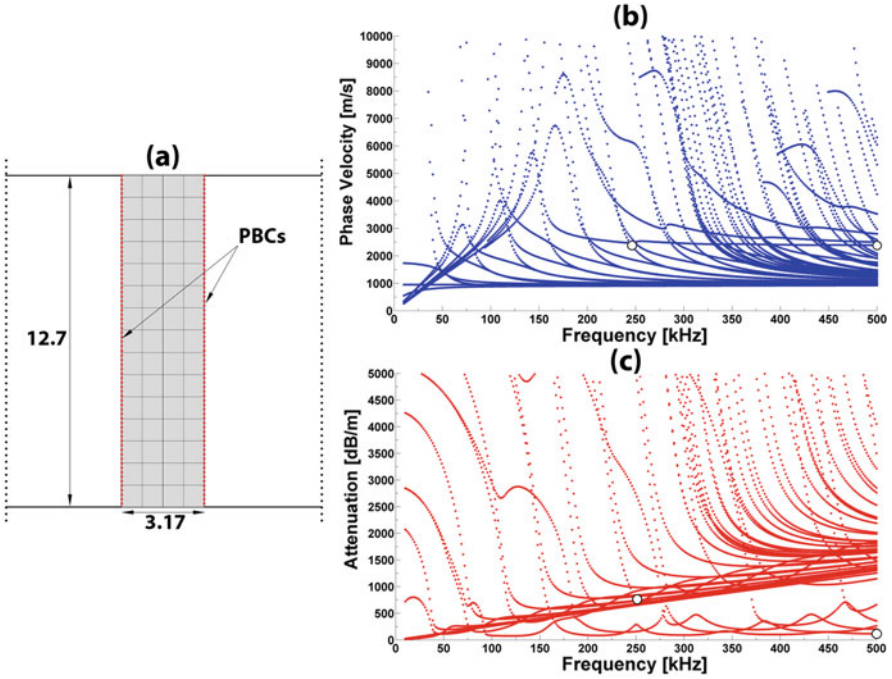

Fig. 9.18 (**a**) Geometry and mesh for the 2D periodic cell of the HPPE plate (dimensions in mm), (**b**) dispersion curves of phase velocity in the 0–500-kHz range with primary and secondary modes for nonlinear analysis indicated (circles), and (**c**) attenuation curve (dB/m) in the 0–500-kHz range with primary and secondary modes indicated (circles) (reprinted from Nucera C and Lanza di Scalea F, Modeling of nonlinear guided waves and applications to structural health monitoring. ASCE J Comput Civ Eng 29:B40140011–B401400115, 2015, with permission from ASCE)

to the central area of the waveguide's cross-section makes this secondary mode at 500 kHz quite suitable for practical structural diagnostics because of the reduced leakage into the surrounding medium. Furthermore, Fig. 9.18c shows that both primary and secondary modes have very small attenuation values (especially the secondary mode at 500 kHz), and hence large inspection ranges could be obtained by this combination.

9.2.6 Application: Anisotropic Elastic Composite Laminate

The following case study is that of a composite laminate made of T800/924 graphite epoxy with lay-up of $[\pm 45/0/90]_S$ (quasi-isotropic). The same components were investigated using the software DISPERSE in the linear regime [59]. Each lamina has a thickness of 0.125 mm for a laminate thickness of 1 mm. The properties for each single lamina are: $\rho = 1500$ kg/m^3, $E_{11} = 161$ GPa, $E_{22} = 9.25$ GPa,

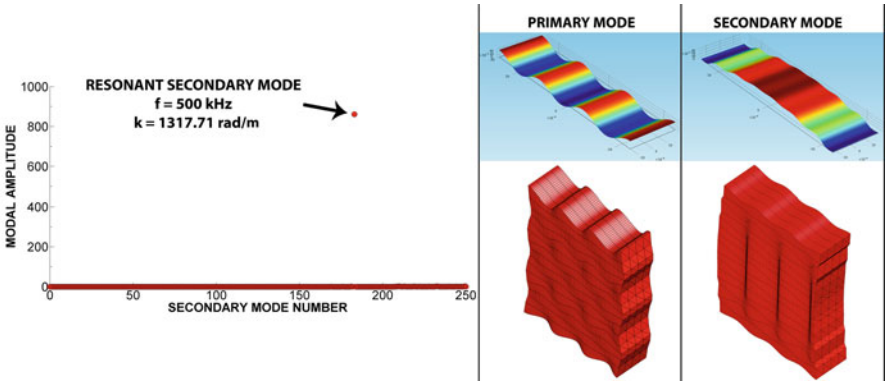

Fig. 9.19 Modal amplitudes for secondary modes with contour plots and 3D views of the selected primary and secondary modes for the viscoelastic HPPE plate (reprinted from Nucera C and Lanza di Scalea F, Modeling of nonlinear guided waves and applications to structural health monitoring. ASCE J Comput Civ Eng 29:B40140011–B401400115, 2015, with permission from ASCE)

$G_{12} = 6.0$ GPa, $\nu_{12} = 0.34$, and $\nu_{23} = 0.41$. The stiffness matrix is given by, in GPa:

$$C = \begin{bmatrix} C_{11} & C_{12} & C_{13} & 0 & 0 & 0 \\ C_{12} & C_{22} & C_{23} & 0 & 0 & 0 \\ C_{13} & C_{23} & C_{33} & 0 & 0 & 0 \\ 0 & 0 & 0 & C_{44} & 0 & 0 \\ 0 & 0 & 0 & 0 & C_{55} & 0 \\ 0 & 0 & 0 & 0 & 0 & C_{66} \end{bmatrix} = \begin{bmatrix} 168.4 & 5.45 & 5.45 & 0 & 0 & 0 \\ 5.45 & 11.3 & 4.74 & 0 & 0 & 0 \\ 5.45 & 4.74 & 11.3 & 0 & 0 & 0 \\ 0 & 0 & 0 & 3.28 & 0 & 0 \\ 0 & 0 & 0 & 0 & 6.0 & 0 \\ 0 & 0 & 0 & 0 & 0 & 6.0 \end{bmatrix} \quad (9.144)$$

The stiffness matrix of each of the transversely isotropic laminae was rotated opportunely according to the laminate's lay-up. The nonlinear part of the stiffness matrix (third-order elastic constants) has been approximated by an isotropic nonlinear matrix, because third-order constants are not available for this material in the literature. As discussed for the viscoelastic isotropic plate, this approximation is reasonable because the cross-sectional symmetry of the modes, and hence the existence or absence of resonant conditions, is not affected by the particular value of the third-order constants.

The results of this section were obtained for propagation along the fiber direction 1 of the 0° ply. A mesh of 48 quadrilateral cubic Lagrangian elements was applied to a 0.3 × 1-mm rectangular cell with PBC on both sides. Figure 9.20 shows the geometry of the laminate periodic cell, the finite element mesh, and the resultant Lamb wave solutions between 50 kHz and 5 MHz. The dispersion results agree extremely well with the previously published results [51, 59]. The primary and secondary modes considered for the nonlinear analysis, along with two particular propagative modes at 3 MHz (labeled as Mode M1 and Mode M2), are highlighted

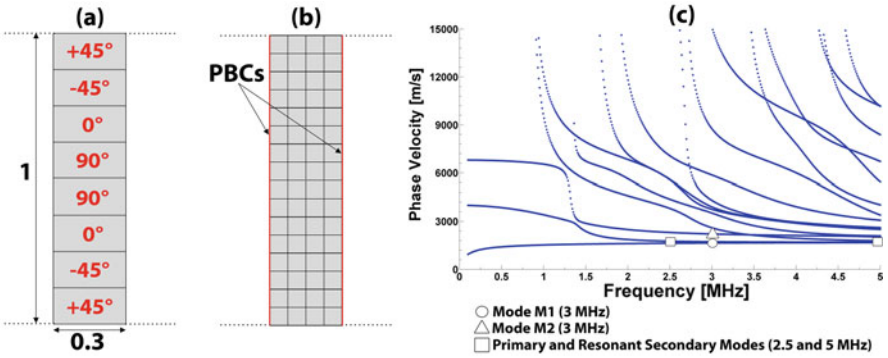

Fig. 9.20 (**a**) Geometry of the 2D periodic cell for the eight-layer quasi-isotropic laminate (dimensions in mm), (**b**) finite element mesh with periodic boundary conditions, and (**c**) dispersion curves of phase velocity between 50 kHz and 5 MHz with specific modes at 3 MHz, and with selected primary–secondary nonlinear mode combination (reprinted from Nucera C and Lanza di Scalea F, Modeling of nonlinear guided waves and applications to structural health monitoring. ASCE J Comput Civ Eng 29:B40140011–B401400115, 2015, with permission from ASCE)

in Fig. 9.20c using different symbols. Modes M1 and M2 have complex mode shapes due to the multilayered assembly, where abrupt changes in properties exist at the boundaries between two layers.

Correspondingly, sharp changes in slope in the displacement fields can be observed at the interfaces between adjacent layers, as depicted in Fig. 9.21. Figure 9.21a, c depicts the out-of-plane displacement field (along the direction of propagation) as a 3D contour plot for the M1 and M2 modes. Figure 9.21b, d shows the in-plane displacement field (in the cross-sectional plane) as a vector plot. The third-order elastic constants assumed for each lamina are: $A = 15$, $B = -33$, and $C = -14$ GPa [61]. The nonlinear post-processing was carried out between 2.5 MHz and 5.0 MHz. A complex primary mode that is a combination of axial and flexural horizontal modes was selected as the input. One of the propagative modes at the double harmonic (5 MHz) was found in internal resonance.

The modal amplitude plots are shown in Fig. 9.22 together with the mode shapes of the primary and the secondary modes. This figure shows one predominant resonant mode at 5 MHz with amplitude much larger than all others. Both primary and secondary modes concentrate the wave energy in the center of the waveguide. As remarked for a previous case study considered, this fact makes these modes attractive in a practical test because of the reduced leakage into the surrounding media that may be present (e.g., water, paint, ice, etc.).

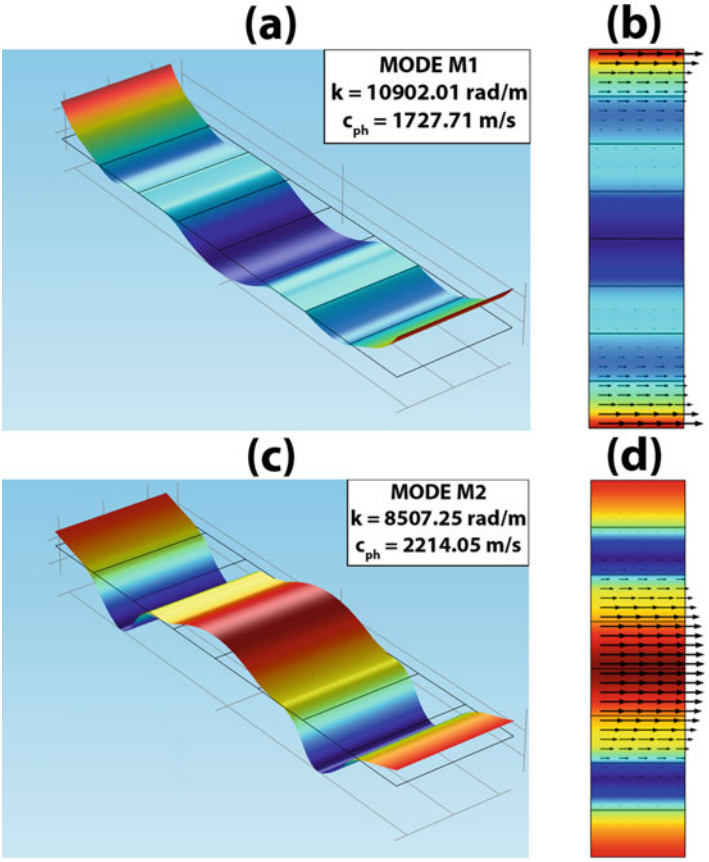

Fig. 9.21 Selected modes at 3 MHz for the composite laminate. (**a**) Contour plot of out-of-plane displacement field for mode M1, (**b**) vector plot of in-plane displacement field for mode M1, (**c**) contour plot of out-of-plane displacement field for Mode M2, and (**d**) vector plot of in-plane displacement field for Mode M2 (reprinted from Nucera C and Lanza di Scalea F, Modeling of nonlinear guided waves and applications to structural health monitoring. ASCE J Comput Civ Eng 29:B40140011–B401400115, 2015, with permission from ASCE)

9.2.7 Application: Reinforced Concrete Slab

The last case considered is that of a reinforced concrete slab. This is a case of a heterogeneous structure, made of two very different materials. Predoi et al. [57] have previously discussed how the reinforcement influences the guided waves dispersion in the slab. This chapter presents results pertaining to the nonlinear behavior of this propagation.

A 2D periodic cell (6 cm in width and 8 cm in height) with PBC was modeled. The steel bars are assumed to be 1.6 cm in diameter. The FE mesh consisted of 528 triangular cubic Lagrangian elements assembled using Delaunay's algorithm [61].

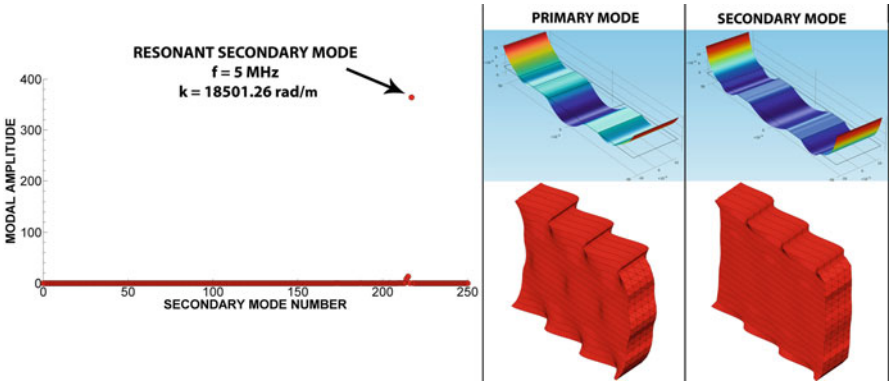

Fig. 9.22 Modal amplitude plot for secondary modes with contour plots and 3D views of the selected primary and secondary modes for the elastic composite laminate (reprinted from Nucera C and Lanza di Scalea F, Modeling of nonlinear guided waves and applications to structural health monitoring. ASCE J Comput Civ Eng 29:B40140011–B401400115, 2015, with permission from ASCE)

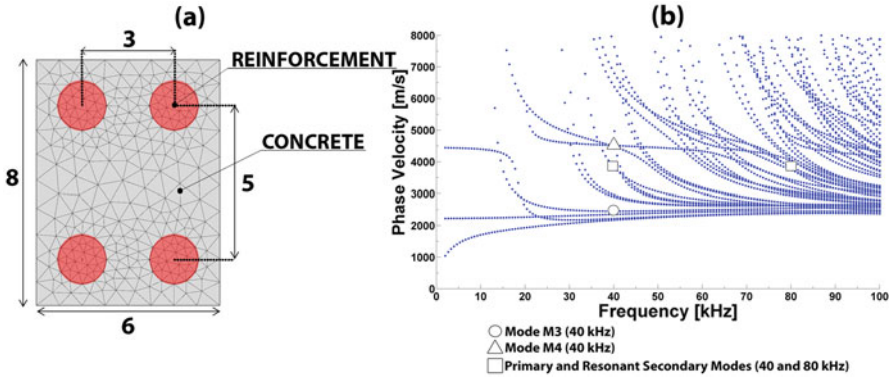

Fig. 9.23 (**a**) Geometry and finite element mesh for the periodic cell of a reinforced concrete slab (dimensions in cm), and (**b**) dispersion curves of phase velocity in the 0–100-kHz range with relevant modes at 40 kHz, along with primary and secondary modes for nonlinear analysis (reprinted from Nucera C and Lanza di Scalea F, Modeling of nonlinear guided waves and applications to structural health monitoring. ASCE J Comput Civ Eng 29:B40140011–B401400115, 2015, with permission from ASCE)

Material properties for the concrete domain were assumed as: $\rho = 2133$ kg/m^3, $C_{11} = 33.2$ GPa, $C_{66} = 11.8$ GPa [63], $A = -1813$ GPa, $B = -1376.5$ GPa, and $C = -1630.5$ GPa [64]. For the steel bars, values used were: $\rho = 7900$ kg/m^3, $C_{11} = 280$ GPa, $C_{66} = 80$ GPa [57], $A = -760$ GPa, $B = -250$ GPa, and $C = -90$ GPa [54]. Geometry and other details of the FE model are presented in Fig. 9.23a.

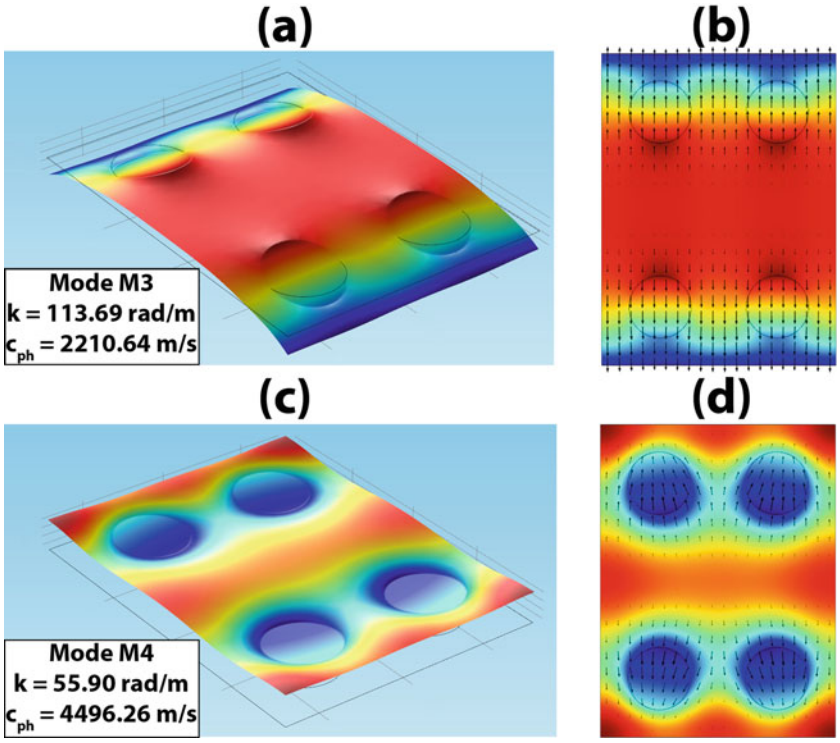

Fig. 9.24 Representative modes at 40 kHz for the reinforced concrete slab cell. (**a**) Contour plot of out-of-plane displacement field for Mode M3, (**b**) vector plot of in-plane displacement field for Mode M3, (**c**) contour plot of out-of-plane displacement field for Mode M4, and (**d**) vector plot of in-plane displacement field for Mode M4 (reprinted from Nucera C and Lanza di Scalea F, Modeling of nonlinear guided waves and applications to structural health monitoring. ASCE J Comput Civ Eng 29:B40140011–B401400115, 2015, with permission from ASCE)

Since specific material properties were considered separately for the steel FE domain and the concrete FE domain, the model properly represented the heterogeneity of the structure. The analysis carried out for the RC slab fully accounted for the material inhomogeneity because the model assumes also full bond (continuity) between rebars and surrounding steel. Since the emphasis of this study is the identification of nonlinear resonant conditions, neglecting rebar-concrete disbonds is a reasonable simplification.

Wave dispersion solutions for the reinforced concrete slab were obtained in the 0–100-kHz frequency range and are shown in Fig. 9.23b. Complex mode shapes are found, as a result of the substantial difference in properties between steel and concrete, with abrupt variations at the interfaces. Two of the propagative modes at 40 kHz (both highlighted in Fig. 9.23b and labeled as Mode M3 and Mode M4) are represented in detail in the following Fig. 9.24.

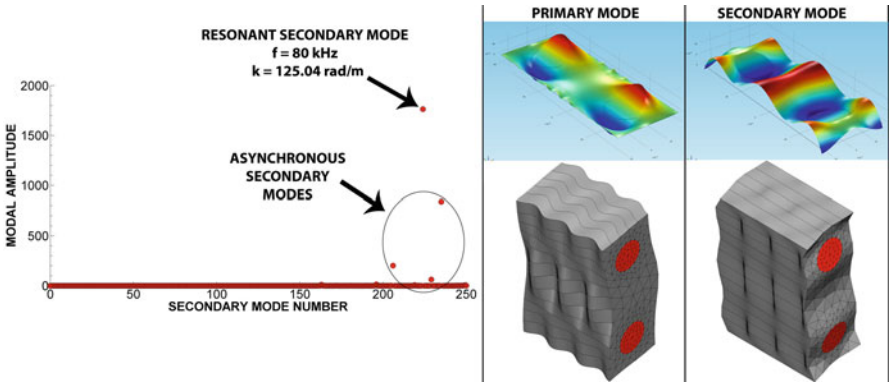

Fig. 9.25 Modal amplitudes of secondary modes of the reinforced concrete slab with contours and 3D views of the selected primary and secondary modes (reprinted from Nucera C and Lanza di Scalea F, Modeling of nonlinear guided waves and applications to structural health monitoring. ASCE J Comput Civ Eng 29:B40140011–B401400115, 2015, with permission from ASCE)

A flexural horizontal mode at 40 kHz was considered as the primary mode by the CO.NO.SAFE algorithm. A cell half in width was utilized to speed up the analysis. The smaller cell was defined by appropriately placing PBCs. The nonlinear results are shown in Fig. 9.25. This figure shows the presence of few asynchronous modes with relatively large power transfer (modal amplitude values inside the circle) and only a single resonant secondary mode that is also synchronous (phase-matching). The figure also shows the displacement distribution of this favorable primary–secondary mode combination.

9.2.8 Conclusions

This chapter examined the identification of suitable combinations of primary and second-harmonic mode that satisfy the resonance and cumulative propagation conditions in waveguides that are complex in either their geometry or their constituent materials. To model nonlinear propagation in such complex waveguides, the S.A.F.E. algorithm has been extended to the nonlinear regime and implemented in the COMSOL multipurpose commercial FEM code. This CO.NO.SAFE framework is able to first extract the full dispersion solutions for the waveguide and then identify cumulative resonant secondary modes for a given primary mode. Demonstrations of this algorithm were given for the following case studies: a railroad track, a viscoelastic isotropic plate, an anisotropic multilayered composite laminate, and a heterogeneous reinforced concrete slab. In all these cases, the proposed algorithm successfully identified appropriate combinations of resonant primary and secondary waveguide modes that exhibit the desired conditions of synchronicity and large cross-energy transfer. These combinations should be considered by any practical

system that aims at utilizing nonlinear wave propagation for structural diagnostics or other purposes (detect defects, measure quasi-static loads or instability conditions, and so on).

9.3 Nonlinear Waves in Constrained Solids Under Temperature Fluctuations (Thermal Stress Case)

9.3.1 Introduction

Much work exists in the literature on the theory of nonlinear thermoelasticy. For example, the work by Biot [65] considers geometrical nonlinearities, including isothermal and adiabatic buckling and the related thermoelastic creep buckling, using variational principles. The work by Dillon [66] identifies higher-order elastic constants for the case of material nonlinearity. It derives the constitutive equations to reflect nonlinear thermoelasticity of a solid and examines, in particular, torsional oscillations in a solid bar subjected to temperature variation. Slemrod [67] studied the existence of smooth solutions for a nonlinear elastic bar where heat conduction is a dissipative mechanism. This work also derives nonlinear thermoelasticity solutions applied to longitudinal motion.

Much less investigated is the case of nonlinearity-driven higher-harmonic wave generation for the measurement of quasi-static stresses/loads in structures. One specific application in this area is the measurement of thermal stresses arising from constrained thermal expansions of solids. A typical application of this problem is the management of the thermal load in Continuous-Welded Rail (CWR) during temperature excursion [68–70]. If left unchecked, this issue can lead to thermal buckling of the rail in hot weather. This section summarizes the work by Nucera and Lanza di Scalea [39] and Nucera et al. [70] in this area.

9.3.2 Model

The thermal expansion of solids, and the related elastic constants, is a topic that has been studied extensively in the previous literature. The work by Ledbetter [71] develops a model to link volumetric thermal expansion to elastic constants and atomic volume. This reference studies the case of free thermal expansion. The case at hand in this paper, however, regards the constrained thermal expansion case that requires a different approach to link wave nonlinearities to thermal stresses, as explained below.

Nonlinear phenomena arising in wave propagation have been classically treated using acoustoelasticity [72] or Finite-Amplitude Wave theory (Cantrell [73–75]). These studies rely on the application of finite strains (or, similarly, finite-amplitude

waves) as a requirement for the existence of nonlinearity. However, the generation of nonlinear effects (higher harmonics in particular) in solids that are constrained and subjected to thermal excursions requires a different theoretical perspective. In fact, in this case the solid cannot globally deform because of the boundaries. At the same time, the lattice particles acquire an increased energy of vibration (proportional to temperature) in agreement with classical material science theories [76]. Since quasi-static strains in constrained cases can be theoretically zero (fully constrained case), any nonlinear wave propagation must be explained with causes that are different from classical sources of nonlinearities.

9.3.2.1 Interatomic Potential

The interatomic potential defines the relationship between elastic potential energy and deformations at the atomistic level. The general Mie potential, that is commonly used for solids, can be written as [77]:

$$V_{MIE}(r) = \left(\frac{n}{n-m}\right)\left(\frac{n}{m}\right)^{\frac{m}{n-m}} w\left[\left(\frac{q}{r}\right)^{n} - \left(\frac{q}{r}\right)^{m}\right] \tag{9.145}$$

where r is the interatomic distance, w is the potential well depth, q is the Van der Waals radius, and n and m are material coefficient parameters. The Van der Waals radius represents the interatomic distance at which the interatomic potential is null, while the potential well depth quantifies the strength of the interaction between the two atoms. A schematic of this relationship is shown in Fig. 9.26a.

The interatomic force (Fig. 9.27b) is given by the first derivative of the potential, therefore:

$$F_{MIE}(r) = -\frac{dV_{MIE}}{dr} = -\frac{n\left(\frac{n}{m}\right)^{\frac{m}{n-m}} w\left[m\left(\frac{q}{r}\right)^{m} - n\left(\frac{q}{r}\right)^{n}\right]}{r\,(n-m)} \tag{9.146}$$

Equation (9.145) contains a "repulsive" part that is quite steep (first term in the square brackets), and an "attractive" part that is much smoother (second term in the square brackets). The minimum of the potential curve is the equilibrium position of the atoms, r_0, where the repulsive force is equal to the attractive force and the net force is zero (Fig. 9.26).

Most commonly, the coefficients n and m are taken such that $n = 2\,m$. A specific form of the interatomic potential most often used for its computational efficiency was proposed by Lennard-Jones [79–81], where $n = 12$ and $m = 6$. From Eq. (9.145), the Lennard-Jones potential is therefore:

$$V_{LJ} = 4w\left[\left(\frac{q}{r}\right)^{12} - \left(\frac{q}{r}\right)^{6}\right] \tag{9.147}$$

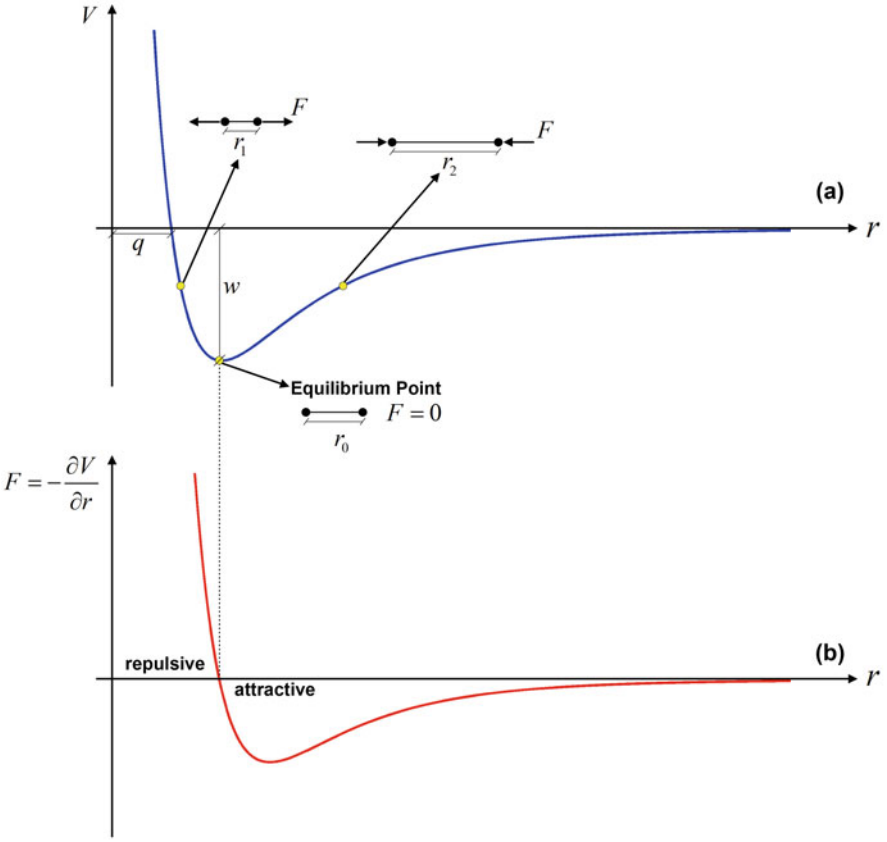

Fig. 9.26 General form of (**a**) interatomic potential and (**b**) interatomic force, as a function of interatomic distance (reprinted from [78])

9.3.2.2 Potential Energy for Constrained Thermal Expansion

When the temperature increases and the solid is free to expand, the atoms' equilibrium distance r_0 increases, according to the dashed curve in Fig. 9.27, also known as the Average Bonding Distance (ABD), or the points of equal distance with the repulsive and attractive branches of the potential. The ABD curve represents the well-known thermal expansion of the material, which directly results from the "anharmonicity," or asymmetry, of the interatomic potential curve. If, in fact, the potential curve were symmetric around the minimum point at $r = r_0$, the midpoint distance (ABD curve) would become a vertical straight line and no thermal expansion of the material would occur.

The ABD curve, $r_{\mathrm{ABD}}(V)$, can be easily calculated from the Mie potential with $n = 2\,m$ by equating the repulsive force to the attractive force:

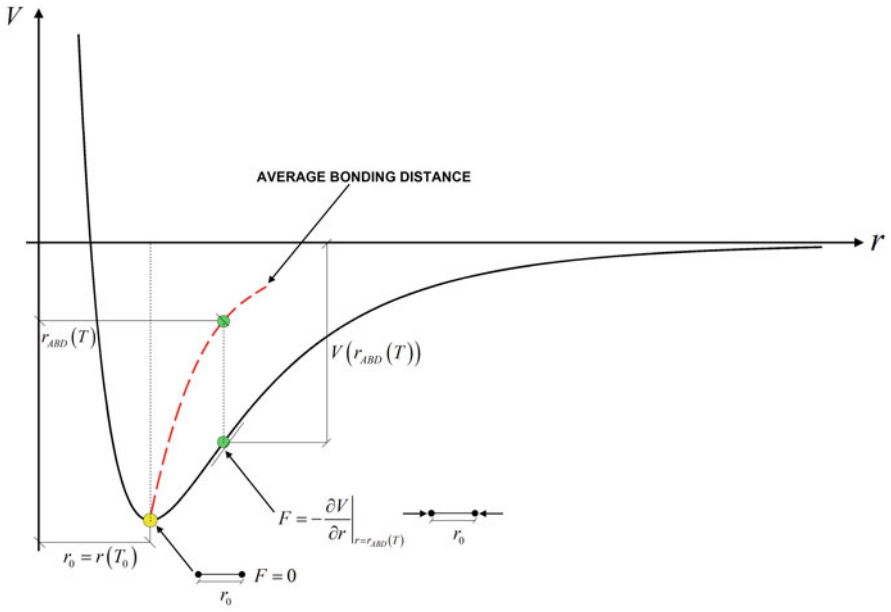

Fig. 9.27 Average Bonding Distance for free expansion and residual potential for perfectly constrained thermal expansion (boundaries with infinite stiffness) (reprinted from [78])

$$r_{ABD} = 2^{\left(\frac{1}{m}-1\right)} q \left[\left(1 - \sqrt{1 + \frac{V}{w}}\right)^{-\frac{1}{m}} + \left(1 + \sqrt{1 + \frac{V}{w}}\right)^{-\frac{1}{m}} \right] \tag{9.148}$$

Recalling conventional linear thermal expansion theory, the r_{ABD} curve can be also expressed as a function of temperature as:

$$r_{ABD}(T) = r_0 \left[1 + \alpha \left(T - T_0\right)\right] \tag{9.149}$$

where α is the thermal expansion coefficient of the material, and $\Delta T = T\text{-}T_0$ is the temperature excursion from the initial interatomic distance r_0.

If the solid is free to expand (free thermal expansion), the minima of the potential at the various temperatures lie on the r_{ABD} curve, and the potential well depth rises to reflect the additional kinetic energy imparted by the temperature increase. In this case, the new positions of the atoms at all temperatures are still at zero net force (strain without stress).

If, instead, the solid is prevented from expanding due to external constrains, it is known that it develops thermal stresses. Therefore, the interatomic potential at T does not have a minimum point (zero force). Rather, it takes a value that corresponds to the $V(r)$ curve for the original T_0 temperature, calculated at the current "free expansion" position $r_{\mathrm{ABD}}(T)$ (see Fig. 9.27). For this case of constrained thermal

expansion, the general form of the current interatomic potential at T can be found by expanding Eq. (9.145) around the $r_{\mathrm{ABD}}(T)$ value. Therefore:

$$V(r,T) = V(r_{ABD}(T)) + \left.\frac{\partial V}{\partial r}\right|_{r=r_{ABD}(T)} \cdot (r - r_{ABD}(T)) + \frac{1}{2}\left.\frac{\partial^2 V}{\partial r^2}\right|_{r=r_{ABD}(T)}$$
$$\times (r - r_{ABD}(T))^2 + \frac{1}{6}\left.\frac{\partial^3 V}{\partial r^3}\right|_{r=r_{ABD}(T)} \cdot (r - r_{ABD}(T))^3 + \ldots = A(T) + B(T) \quad (9.150)$$
$$(r - r_{ABD}(T)) + \frac{1}{2}C(T) \cdot (r - r_{ABD}(T))^2 + \frac{1}{6}D(T) \cdot (r - r_{ABD}(T))^3 + \ldots$$

where $A(T)$ is an initial energy, $B(T) = \partial V/\partial r$, $C(T) = \partial^2 V/\partial r^2$, and $D(T) = \partial^3 V/\partial r^3$, with the derivatives calculated at $r = r_{\mathrm{ABD}}(T)$.

The expansion above is only carried out to the cubic order $O(r^3)$ to account for second-harmonic wave generation. If higher harmonics are of interest, the expansion should be carried out further. The terms $C(T)$ and $D(T)$ are similar to the elastic constants of classical nonlinear elasticity caused by finite quasi-static deformations or finite-amplitude waves [73]. For example, the term C is analogous to the second-order elastic stiffness, and the term D is analogous to the third-order elastic stiffness. The difference with classical nonlinear elasticity, however, is that the nonlinearity (arising from the $O(r^3)$ term in the potential, or the term D) does not arise from finite deformations (these are ideally zero for perfectly constrained thermal expansion), but rather from the "residual" strain energy stored as internal forces.

Equation (9.150) strictly applies to the case of fully constrained solids (infinitely stiff boundaries), where the entirety of the free thermal expansion is prevented (zero deformations or strains), and therefore the full "residual" potential $V(r,T)$ is absorbed in the form of internal thermal forces (or stresses).

For partially constrained solids (boundaries with finite stiffness), the solid will *partially* expand under ΔT, and only the difference between the "free" thermal expansion and the "actual" thermal expansion will develop internal thermal forces. As shown in Fig. 9.28, in the partially constrained case, the solid will expand to a reduced distance, r_{PC}. For symmetric boundaries with spring stiffness k_{b} (Fig. 9.28), simple equilibrium indicates that the new interatomic distances $r_{\mathrm{PC}}(T)$ will be a function of the "free" expansion distance $r_{\mathrm{ABD}}(T)$ and the material linear stiffness S, in the following manner:

$$r_{PC}(T) = \frac{S \cdot r_{ABD}(T) - k_b \cdot r_0}{S - k_b} \quad (9.151)$$

For the simple case of a continuum rod of length L and cross-sectional area A, for example, the term S is the longitudinal rod stiffness EA/L, where E is the Young's modulus. For $k_{\mathrm{b}} \to \infty$ (infinitely stiff boundaries), Eq. (9.151) retrieves the fully constrained case, yielding $\lim_{k_b \to \infty} r_{PC}(T) = r_0$, therefore zero deformation.

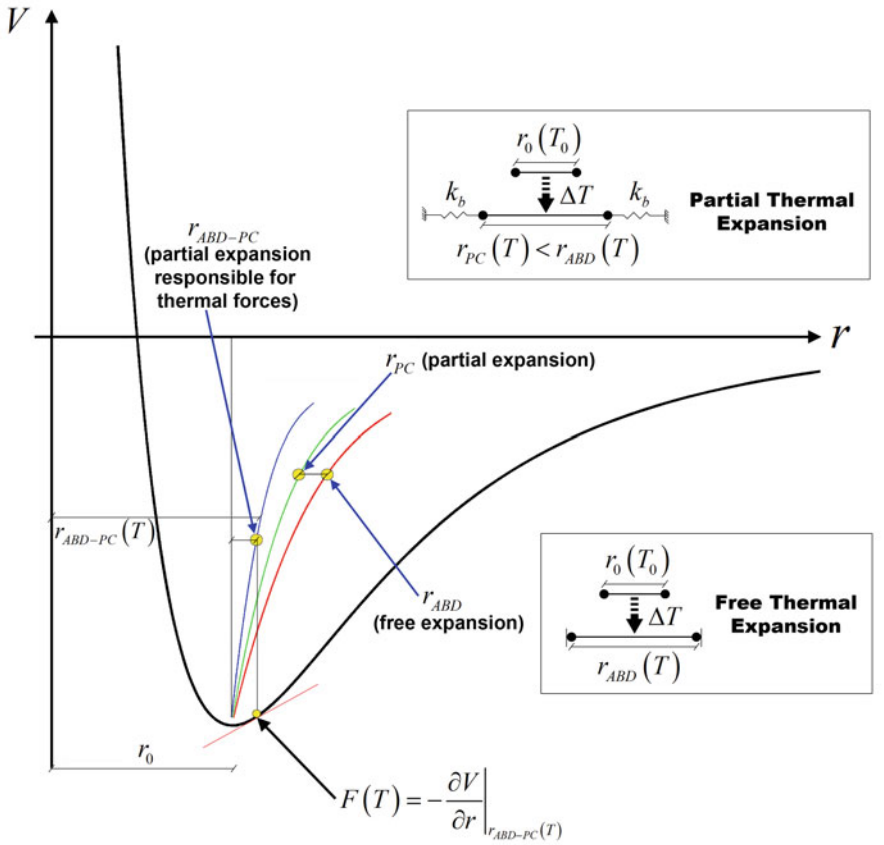

Fig. 9.28 Partially constrained thermal expansion (boundaries with finite stiffness) (reprinted from [78])

At the other limit, for $k_b \to 0$, Eq. (9.151) retrieves the free expansion case, yielding $\lim_{k_b \to 0} r_{PC}(T) = r_{ABD}(T)$.

Equation (9.150) can therefore be simply generalized to the partially constrained case by expanding $V(r)$ around the points $r_{\text{ABD-PC}}(T) = r_0 + (r_{\text{ABD}}(T) — r_{\text{PC}}(T))$ shown in Fig. 9.28, which is the portion of the free thermal expansion that is prevented by the supports:

$$V(r,T) = V(r_{ABD-PC}(T)) + \left.\frac{\partial V}{\partial r}\right|_{r=r_{ABD-PC}(T)} \cdot (r - r_{ABD-PC}(T)) + \frac{1}{2}\left.\frac{\partial^2 V}{\partial r^2}\right|_{r=r_{ABD-PC}(T)} \cdot (r - r_{ABD-PC}(T))^2 + \frac{1}{6}\left.\frac{\partial^3 V}{\partial r^3}\right|_{r=r_{ABD-PC}(T)} \cdot \times (r - r_{ABD-PC}(T))^3 + \ldots \quad (9.152)$$

This equation can also be expressed in terms of $A(T)$, $B(T)$, $C(T)$, and $D(T)$, where now the derivatives $\partial^n V/\partial r^n$ for the partial expansion case are calculated at $r = r_{\text{ABD-PC}}(T)$ instead of at $r = r_{\text{ABD}}(T)$ as for the free expansion case. The $r_{\text{ABD-PC}}(T)$ positions are easily calculated from Eq. (9.151) based on the stiffness of the partial constraints and that of the structure at hand. Therefore, for the purposes of this paper, the only relevant difference between the fully constrained case and the partially constrained case is a scaling down of the nonlinearity term $D(T)$ to reflect the reduced thermal forces caused by the partial expansion.

9.3.2.3 Nonlinear Wave Equation for Constrained Thermal Expansion

Once the expression of the elastic potential between two atoms up to cubic order $O(r^3)$ is obtained, the derivation of the nonlinear wave equation can follow classical equilibrium considerations.

Equation (9.150) can be extended to a 1-D lattice comprising p particles as shown in Fig. 9.29. Considering an infinitesimal deformation Δu from initial equilibrium, the elastic potential of the p particles can be written as:

$$V = A(T) + \sum\nolimits_p B(T) \cdot \Delta u + \frac{1}{2}\sum\nolimits_p C(T) \cdot \Delta u^2 + \frac{1}{6}\sum_p D(T) \cdot \Delta u^3 + \ldots \tag{9.153}$$

Applying Newton's second law to the nth particle, the differential equation governing its motion reads:

$$\begin{aligned} m\frac{d^2u_n}{dt^2} = F_n = -\frac{dV}{du_n} = -B(T) \cdot \textstyle\sum_p \frac{d}{du_n}\left(u_{p+1} - u_p\right) + \\ - \frac{1}{2}C(T) \cdot \textstyle\sum_p \frac{d}{du_n}\left(u_{p+1} - u_p\right)^2 - \frac{1}{6}D(T) \cdot \textstyle\sum_p \frac{d}{du_n}\left(u_{p+1} - u_p\right)^3 + \ldots \end{aligned} \tag{9.154}$$

Equation (9.154) can be simplified by making use of the Dirac delta function, namely:

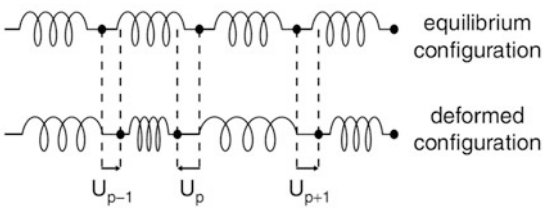

Fig. 9.29 1D Lattice of atoms connected by nonlinear springs before and after an infinitesimal deformation is imposed to the system [73]

$$\sum_p \left(\frac{du_{p+1}}{du_n} - \frac{du_p}{du_n} \right) = \delta_{p+1,n} - \delta_{p,n} = 0 \tag{9.155}$$

Substituting Eq. (9.155) into Eq. (9.154) brings to:

$$\begin{aligned} m\frac{d^2u_n}{dt^2} &= C(T) \cdot [(u_{n+1} - u_n) - (u_n - u_{n-1})] \\ &+ \frac{1}{2} D(T) \cdot \left[(u_{n+1} - u_n)^2 - (u_n - u_{n-1})^2 \right] + \ldots \end{aligned} \tag{9.156}$$

By reformulating Eq. (9.156), one can express the force exerted on the generic *n*th particle by adjacent particles *n + 1* and *n-1:*

$$\begin{aligned} m\frac{d^2u_n}{dt^2} &= F_{n,n+1} - F_{n,n-1} \\ &= \left[B(T) + C(T) \cdot \left(\frac{u_{n+1} - u_n}{h} \right) h + \frac{1}{2} D(T) \cdot \left(\frac{u_{n+1} - u_n}{h} \right)^2 h^2 \right] \\ &- \left[B(T) + C(T) \cdot \left(\frac{u_n - u_{n-1}}{h} \right) h + \frac{1}{2} D(T) \cdot \left(\frac{u_n - u_{n-1}}{h} \right)^2 h^2 \right] + \ldots \end{aligned} \tag{9.157}$$

where the term h indicates the original undeformed distance between adjacent particles.

All the concepts discussed for the 1D lattice of atoms can be easily extended to the 3D case (Fig. 9.30). In this scenario, everything that was applicable for the *n*th particle can be used now for the *n*th plane. The equation of motion will be derived for the case of 1D longitudinal bulk waves traveling along direction x_1. Introducing the unit surface S_1, perpendicular to axis x_1, the equation of motion for the *n*th plane is:

$$\begin{aligned} \frac{m}{S_1}\frac{d^2u_{1,n}}{dt^2} &= \frac{F_{n,n+1}}{S_1} - \frac{F_{n,n-1}}{S_1} \\ &= \frac{C(T)h_1}{S_1} \left[\left(\frac{u_{1,n+1} - u_{1,n}}{h_1} \right) - \left(\frac{u_{1,n} - u_{1,n-1}}{h_1} \right) \right] \\ &+ \frac{1}{2} \frac{D(T)\, {h_1}^2}{S_1} \left[\left(\frac{u_{1,n+1} - u_{1,n}}{h_1} \right)^2 - \left(\frac{u_{1,n} - u_{1,n-1}}{h_1} \right)^2 \right] + \cdots \end{aligned} \tag{9.158}$$

where the term h_1 is the original undeformed distance along direction x_1 between adjacent particles. If the term h_1 tends to zero in Eq. (9.158), one passes from the discrete system to the continuum system. From the definition of derivative, in the continuum limit Eq. (9.158) can be rewritten as:

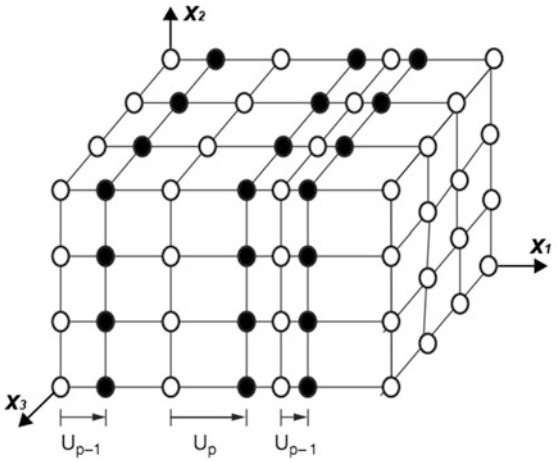

Fig. 9.30 3D Lattice of atoms connected by nonlinear springs before and after an infinitesimal deformation is imposed to the system [73]

$$\frac{m}{S_1}\frac{d^2u_{1,n}}{dt^2} = \frac{F_1(x_1)}{S_1} - \frac{F_1(x_1-h_1)}{S_1} = \sigma_{11}(x_1) - \sigma_{11}(x_1-h_1)$$
$$= \frac{C(T)\,h_1}{S_1}\left[\left(\frac{\partial u_1}{\partial x_1}\right)_{x_1} - \left(\frac{\partial u_1}{\partial x_1}\right)_{x_1-h_1}\right]$$
$$+\frac{1}{2}\frac{D(T)\,{h_1}^2}{S_1}\left[\left(\frac{\partial u_1}{\partial x_1}\right)^2_{x_1} - \left(\frac{\partial u_1}{\partial x_1}\right)^2_{x_1-h_1}\right] + \ldots \quad (9.159)$$

By dividing Eq. (9.159) by h_1, letting h_1 tend to zero for the continuum limit, and letting $m/(S_1h_1) = \rho$ (the mass density of the material in the initial configuration), one can derive:

$$\rho\frac{\partial^2 u_1}{\partial t^2} = \frac{\partial \sigma_{11}}{\partial x_1} = \overline{C_2}\frac{\partial^2 u_1}{\partial {x_1}^2} + \overline{C_3}\left(\frac{\partial u_1}{\partial x_1}\right)\frac{\partial^2 u_1}{\partial {x_1}^2} + \ldots$$

OR

$$\frac{\partial^2 u_1}{\partial t^2} = \overline{V_1}^2\left[1 - \overline{\gamma_1}\left(\frac{\partial u_1}{\partial x_1}\right)\right]\frac{\partial^2 u_1}{\partial {x_1}^2} \quad (9.160)$$

where $\overline{C_2} = C(T)\,h_1/S_1$ and $\overline{C_3} = D(T)\,h_1^2/S_1$ are new temperature-dependent elastic coefficients of second-order and third-order, respectively; the terms $\overline{C_2}$ and $\overline{C_3}$ combine the influence of the classical elastic potential with the new nonlinear effects caused by the prevented thermal expansion.

The closed-form expressions of the terms *C(T)* and *D(T)* can be simply obtained by differentiating the potential, and are given in Eqs. (9.A1), (9.A2), (9.A3), and (9.A4) of the Appendix.

Equation (9.160) represents the nonlinear partial differential equation for the propagation of longitudinal bulk waves in solids subjected to constrained thermal expansion.

In light of the above result, the two new definitions for longitudinal bulk wave velocity and nonlinear parameter are:

$$\overline{V_1} = \sqrt{\frac{\overline{C_2}}{\rho}} = \sqrt{\frac{C(T)\, h_1}{\rho S_1}} \quad \text{LONGITUDINAL WAVE SPEED} \tag{9.161}$$

$$\overline{\gamma_1} = -\frac{\overline{C_3}}{\overline{C_2}} = -\frac{D(T)\, h_1}{C(T)} \quad \text{NONLINEAR PARAMETER} \tag{9.162}$$

A dimensional analysis confirms the nature of these parameters. Since, from Eq. (9.153), $C(T)$ has units of *Joule/m*^{2}, and $D(T)$ has units of *Joule/m*^{3}, Eqs. (9.161) and (9.162) indicate that $\overline{V_1}$ has units of velocity (*m/sec*), and $\overline{\gamma_1}$ is dimensionless.

Equation (9.161) shows that the wave speed depends on the quadratic term $O(r^2)$ of the interatomic potential, $C(T)$. This term is associated with the curvature of the potential that is changing with interatomic distance. According to classical linear Hooke's theory, this curvature (hence material stiffness) is approximated constant through the deformation range, resulting in a constant wave velocity. By considering the full asymmetric potential as a function of the prevented thermal expansion, the wave velocity is found to change with thermal stresses. Trends of $\overline{V_1}$ from Eq. (9.161) are plotted in Fig. 9.31 assuming a Lennard-Jones interatomic potential ($n = 12$, $n = 6$) and sample values of Van der Waals radius $q = 4$ Angstroms, and potential well depth $w = 40$ kJ/mol. The material density is assumed that of steel, $\rho = 7800$ kg/m^3. The expression for $C(T)$ given in Eq. (9.A3) of the Appendix was used.

Specifically, Fig. 9.31a plots the relative change in wave speed $\left[\overline{V_1}(T) - \overline{V_1}(T_0)\right] / \overline{V_1}(T_0)$, as a function of interatomic distance r^*. The temperature T_0 is the stress-free value (corresponding to equilibrium distance $r_0^* = 4.489$ Angstroms—minimum of the assumed Lennard-Jones potential). The independent variable r^* represents the (prevented) thermal expansion $r_{\text{ABD}}(T)$ for the fully constrained case, or the (partially prevented) thermal expansion $r_{\text{ABD-PC}}(T)$ for the partially constrained case. The trend in Fig. 9.31a clearly indicates that the wave speed decreases with increasing (prevented) thermal expansion. This indicates a "softening" effect, consistently with the decrease in curvature of the interatomic potential, $C(T)$, when moving slightly to the right of the equilibrium position r_0^* (see, for example, Fig. 9.27).

Figure 9.31b plots the same velocity change $\left[\overline{V_1}(T) - \overline{V_1}(T_0)\right] / \overline{V_1}(T_0)$ as a direct function of the temperature change, $\Delta T = T - T_0$. This plot was obtained from the previous values in Fig. 9.31a by simply using the linear thermal expansion relation in Eq. (9.149), and assuming a thermal expansion coefficient for steel of $\alpha = 11 \times 10^{-6}$/°C and a fully constrained case. The range of temperature excursion considered in Fig. 9.31b was arbitrarily chosen as 100 °C. For the case considered,

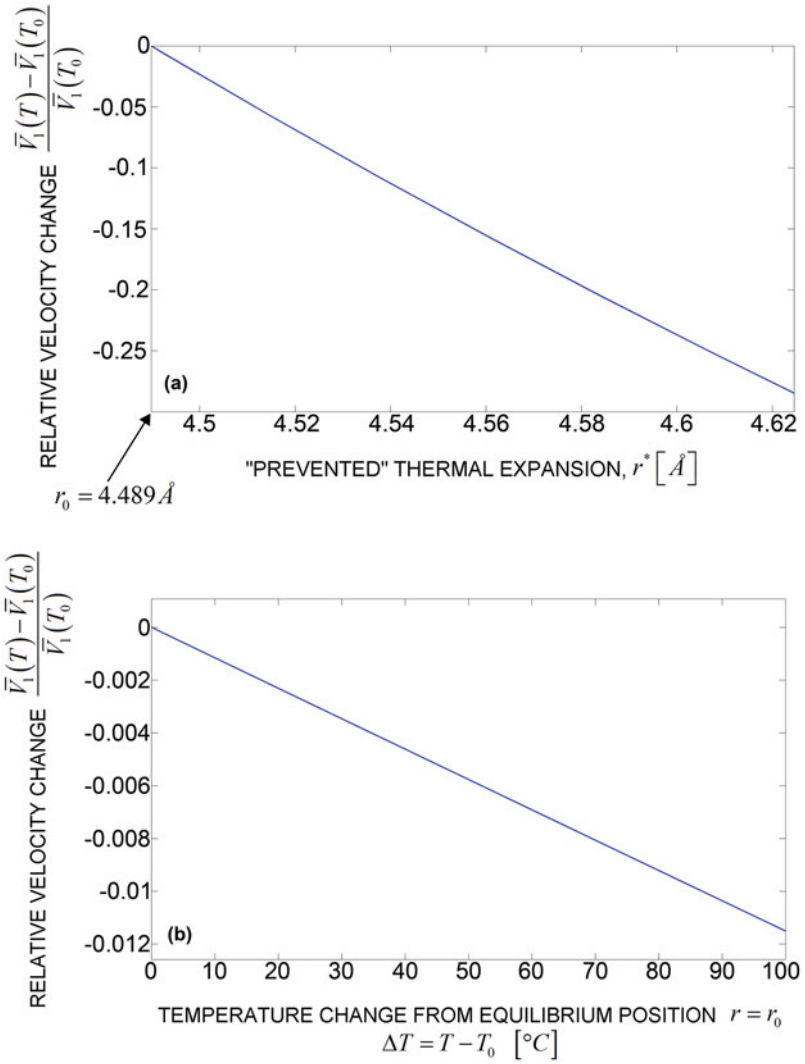

Fig. 9.31 Relative change in longitudinal wave velocity $\left[\overline{V}_1(T) - \overline{V}_1(T_0)\right]/\overline{V}_1(T_0)$ (**a**) as a function of "prevented" thermal expansion of interatomic distance, and (**b**) as a function of temperature change from equilibrium (Lennard-Jones potential, $n = 12$, $n = 6$, $q = 4$ Angstroms, $w = 40$ kJ/mol, $\alpha = 11 \times 10^{-6}$/°C, and $\rho = 7800$ kg/m^3) (reprinted from [78])

for example, the longitudinal wave velocity is expected to decrease by about 1% for a temperature increase of 100 °C in the fully constrained solid.

The parameter $\overline{\gamma_1}$ of Eq. (9.162) contains the nonlinear portion of the potential through the cubic term $O(r^3)$, $D(T)$. As mentioned above, the difference from classical nonlinear wave theory is that the cubic $O(r^3)$ energy term arises from

the prevented thermal expansion due to the asymmetry of the interatomic potential, rather than from applied finite deformations. The nonlinear parameter is discussed more in depth in the next section.

9.3.2.4 Solution of the Nonlinear Wave Equation: Second-Harmonic Wave Generation for Constrained Thermal Expansion

Equation (9.160) can be solved by using perturbation analysis [8], thereby decomposing the displacement field into the linear portion, ${u_1}^{(1)}$, and the nonlinear portion, ${u_1}^{(2)}$, with ${u_1}^{(1)} << {u_1}^{(2)}$.

The final solution to the nonlinear wave equation can be written in the classical form as:

$$u_1 = {u_1}^{(1)} + {u_1}^{(2)} = A_1 \cos(kx_1 - \omega t) - \frac{1}{8}\overline{\gamma_1} k^2 {A_1}^2 x_1 \sin 2(kx_1 - \omega t) \quad (9.163)$$

where x_1 is the wave propagation distance, and k is the wavenumber $k = \omega/\overline{V_1}$.

The nonlinearity thus generates a second-harmonic contribution at 2ω under a fundamental excitation at ω. The magnitude of the second-harmonic is proportional to the nonlinear parameter, $\overline{\gamma_1}$ (given in Eq. (9.162)), as well as to the wave propagation distance, x_1 ("cumulative" behavior). As in classical nonlinear wave theory, Eq. (9.163) only holds for a limited propagation distance that satisfies the perturbation condition ${u_1}^{(1)} << {u_1}^{(2)}$.

Experimentally, it is customary to directly measure the amplitudes of the second harmonic, A_2, and that of the fundamental frequency, A_1. Therefore, an "experimental" nonlinear parameter can be defined from the "theoretical" nonlinear parameter in Eq. (9.162) as:

$$\beta = \frac{|A_2|}{{A_1}^2} = \frac{1}{8}\overline{\gamma_1}\, k^2 x_1 = \frac{\pi^2}{2}\overline{\gamma_1}\frac{f^2}{{\overline{V_1}}^2} x_1 \quad \text{EXPER. NONLINEAR PARAMETER} \quad (9.164)$$

where f is the excitation wave frequency (fundamental), $\overline{V_1}$ is the longitudinal bulk wave speed, and x_1 is the wave propagation distance. Substituting Eqs. (9.161) and (9.162) into Eq. (9.164), the experimental nonlinear parameter can be also written in terms of the second-order and third-order energy terms, $C(T)$ and $D(T)$, as:

$$\beta(T) = \frac{|A_2|}{{A_1}^2} = -\frac{D(T)}{C^2(T)} \quad \frac{\pi^2 \rho\, S_1\, x_1\, f^2}{2} \quad \text{EXPER. NONLINEAR PARAMETER} \quad (9.165)$$

where $C(T) = \partial^2 V/\partial r^2$, $D(T) = \partial^3 V/\partial r^3$, and the derivatives are calculated at $r = r_{\text{ABD}}(T)$ for the fully constrained case, and at $r = r_{\text{ABD-PC}}(T)$ for the partially constrained case.

Plots of the nonlinear parameter β from Eq. (9.165) are given in Fig. 9.32 for a Lennard-Jones interatomic potential ($n = 12$, $n = 6$) and values of $q = 4$ Angstroms, and $w = 40$ kJ/mol, without loss of generality for the nonlinear trends. The β values in this figure have been normalized to all terms independent of temperature, to isolate clearly the temperature-dependent terms $C(T)$ and $D(T)$. Figure 9.32a plots β as a function of interatomic distance r^*, where the independent variable r^* represents the (prevented) thermal expansion $r_{\text{ABD}}(T)$ for the fully constrained case, or the (partially prevented) thermal expansion $r_{\text{ABD-PC}}(T)$ for the partially constrained case. The nonlinear parameter increases with increasing "prevented" thermal expansion, i.e., increasing thermal stress absorbed by the constrained solid. This trend is the combined effect of a decreasing curvature of the interatomic potential, $C(T)$ (that is also responsible for the wave velocity decrease discussed in the previous section), and an increasing cubic term $D(T)$. Figure 9.32b plots the same nonlinear parameter β as a direct function of the temperature change, $\Delta T = T - T_0$, from the initial, stress-free temperature T_0 (corresponding to equilibrium distance r_0). This plot was obtained directly from the previous values in Fig. 9.32a by simply using the linear thermal expansion relation in Eq. (9.149) and assuming, again, $\alpha = 11 \bullet 10^{-6}/°\text{C}$ (steel) and a fully constrained case. The range of temperature excursion considered in Fig. 9.32b was arbitrarily chosen as 100 °C. It is clear that the nonlinear parameter monotonically increases with increasing temperature, as the constrained thermal expansion builds nonlinear effects through thermal stresses. The slope of the $<\beta$ vs. $T>$ curve will, of course, depend on the coefficient of thermal expansion of the material, with larger slopes expected for larger α's. This slope will also decrease moving from a fully constrained case to a partially constrained case, according to Eq. (9.151).

The next section presents an experimental validation on a steel block subjected to constrained thermal expansion.

9.3.3 *Experimental Validation: Nonlinear Waves in a Steel Block under Constrained Thermal Expansion*

A series of experimental tests were performed on a steel block in order to confirm the existence of nonlinearity-driven higher harmonics in longitudinal bulk waves in solids where free thermal expansion is prevented. The block (Fig. 9.33) was wrapped with a high-temperature heating tape (electrical heating) to progressively increase its temperature from 30 to 80 °C. Temperature was measured by a thermocouple.

As shown in Fig. 9.33, a 2.25-MHz piezoelectric longitudinal transducer was installed on one side of the block. The wave was detected on the opposite side by a second piezoelectric transducer centered at 5.00 MHz (for second-harmonic measurement). High-temperature delay lines were placed between the transducers

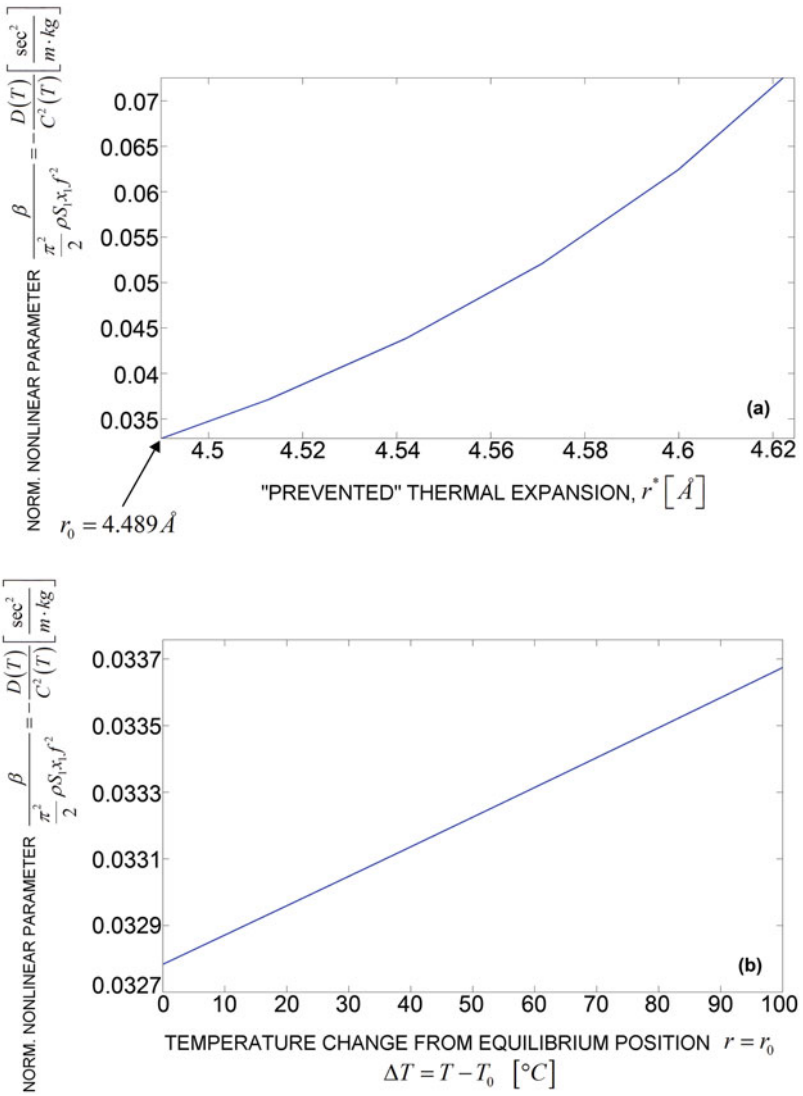

Fig. 9.32 Normalized nonlinear parameter β (**a**) as a function of "prevented" thermal expansion of interatomic distance, and (**b**) as a function of temperature change from stress-free position (Lennard-Jones potential, $n = 12$, $n = 6$, $q = 4$ Angstroms, $w = 40$ kJ/mol, and $\alpha = 11 \times 10^{-6}/°C$) (reprinted from [78])

and the block to account for the high temperatures. A National Instruments PXI DAQ unit generated the excitation and received the detection. A frequency sweep in the 1.5–2.5-MHz range was utilized with a step of 250 kHz. At each temperature level, the first arrival in the received signals at each frequency was analyzed by a fast

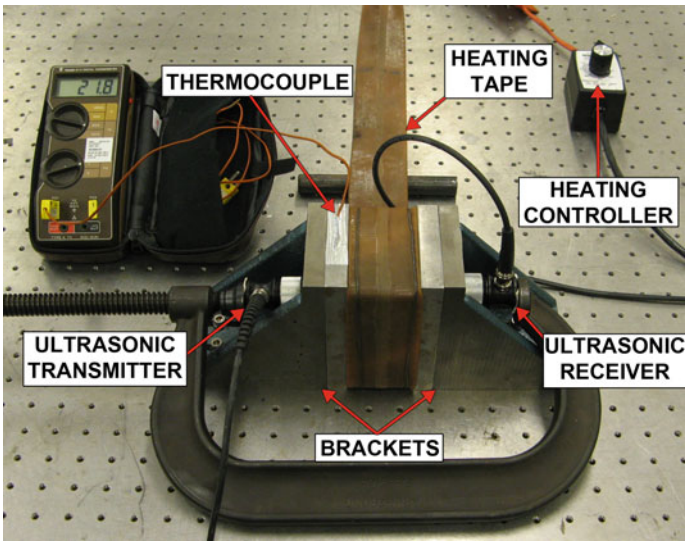

Fig. 9.33 Experimental setup used for the constrained steel block condition (reprinted from [78])

Fourier transform (FFT) and an experimental nonlinear parameter, β, was evaluated from the FFT spectra as the ratio between the amplitude of the second harmonic and the squared amplitude of the fundamental excitation frequency, i.e., $A_2/{A_1}^2$.The nonlinear parameter was plotted against temperature.

The measurements were performed under two test conditions. In one condition, the steel block was placed on two rollers and left unconstrained so that it could freely expand under the temperature increase. In the other condition (Fig. 9.33), the block was axially constrained using two stiff L-brackets specially designed to prevent the deformations due to the temperature increase. The two brackets were bolted on the test table.

A screenshot from an IR camera used to monitor the uniformity of the temperature distribution when heating is shown in Fig. 9.34.

A typical waveform measured at a 1.75-MHz excitation frequency is shown in Fig. 9.35, where the first arrival has been highlighted.

The results for both constrained and unconstrained cases are compared in Fig. 9.36 for two representative excitation frequencies, 1.75 MHz (Fig. 9.36a) and 2 MHz (Fig. 9.36b). The absolute values of β are not directly comparable between the unconstrained and constrained cases since the transducers were repositioned after the installation of the brackets, resulting in a change in transducer/part coupling. The trends of $<\beta$ vs. temperature > are, instead, comparable. The results show that when the block is free to expand, no clear trend is observed for the $<\beta$ vs. temperature> curve. However, in the constrained case, the nonlinear parameter increases monotonically with temperature (except for the very high temperatures) as a result of the prevented thermal expansion and the resulting thermal stresses.

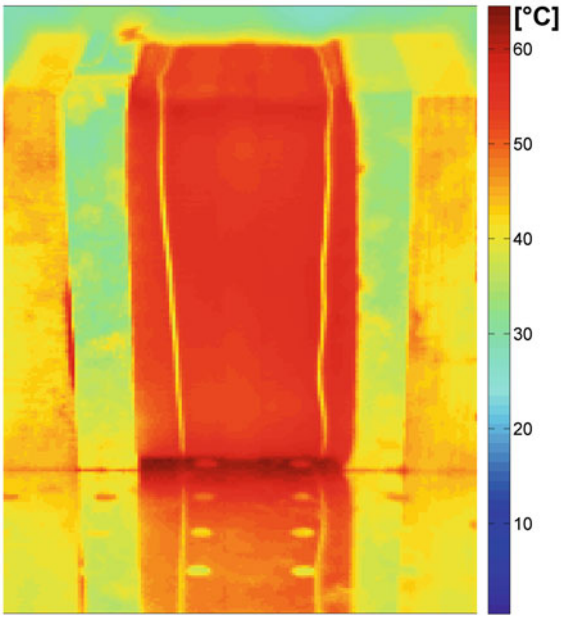

Fig. 9.34 Temperature distribution in the specimen assembly from infrared camera (reprinted from [78])

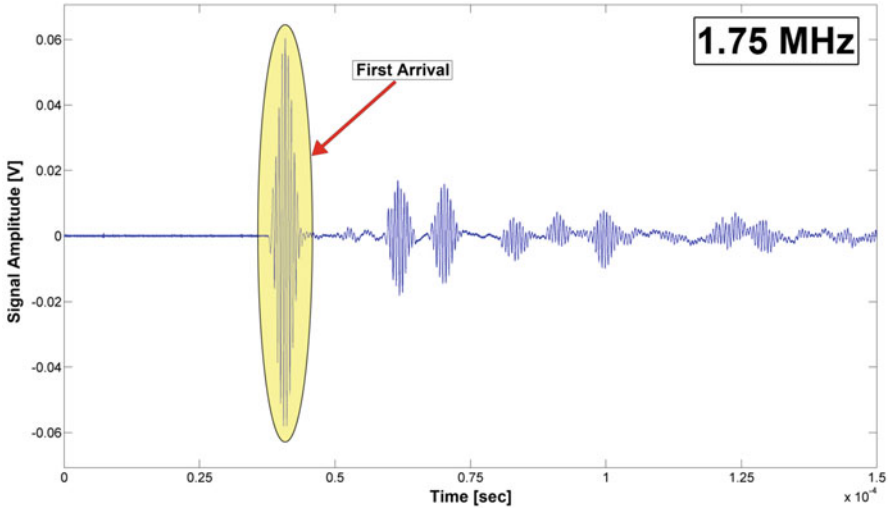

Fig. 9.35 Time history of received signal with 1.75 MHz as excitation frequency (first arrival is highlighted) (reprinted from [78])

The same trend is seen for both excitation frequencies of 1.75 and 2 MHz, and it is consistent with the theoretical predictions presented in the previous section (see Fig. 9.32).

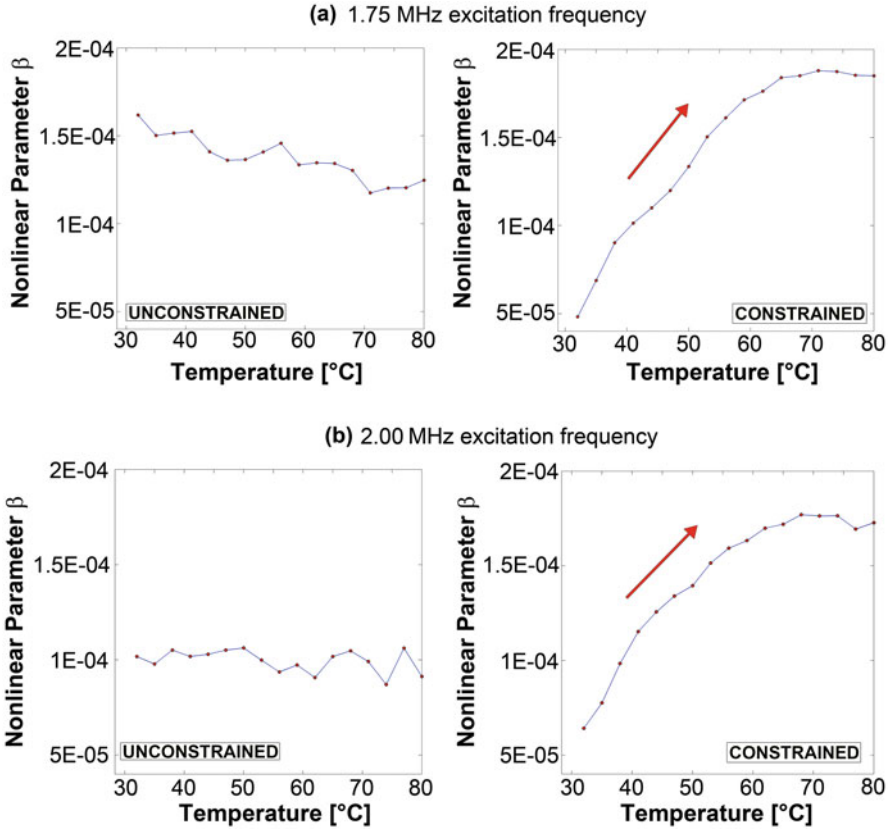

Fig. 9.36 Nonlinear parameter β vs. temperature measured for unconstrained and constrained steel block at two excitation frequencies: 1.75 MHz (**a**), and 2 MHz (**b**) (reprinted from [78])

In the constrained case, the slight drop in β at the very high temperatures could be due to either temperature-dependent wave attenuation effects (not considered in the theoretical model) or degradation of the transducer/couplant response at the high temperatures (the delay lines have a finite, although small, thermal conductivity).

The changes in β values between the two excitation frequencies for the constrained case can be compared since the transducers were not moved between the two excitations. It can be seen that, at ambient temperature ($T \approx 30$ °C), the β value measured for the 1.75-MHz case is somewhat smaller than the value measured for the 2-MHz case as expected from the frequency dependence expressed in Eqs. (9.164) and (9.165). With increasing temperature, the rate of increase of β is very comparable between the two frequencies. The slight increase in rate of β (T) curve of the 1.75-MHz excitation frequency versus the 2-MHz frequency could be due to temperature-dependent and frequency-dependent attenuation effects, again, not considered in the model.

9.3.4 Conclusions

This chapter has studied the generation of wave nonlinearities in solids that are constrained and subjected to temperature excursions, and are therefore subject to thermal stresses. Among the applications of this study is the monitoring of structures prone to thermal buckling, such as the continuous-welded rail. In the problem at hand, the classical assumption of applied finite strain or finite-amplitude wave used to model wave nonlinearity (e.g., acoustoelasticity) does not hold. Instead, the source of the nonlinearity is attributed to the anharmonicity of the interatomic potential and the "residual" energy that is stored in the solid when it is prevented from expanding. This residual energy corresponds to the full interatomic potential of the free thermal expansion for a fully constrained solid, and to a smaller potential for a partially constrained solid (depending on the stiffness of the solid and that of the boundaries). These considerations result in an interatomic potential expression that is at least cubic, $O(r^3)$, as a function of interatomic distance. This leads to a nonlinear wave equation that can be readily solved using perturbation techniques.

The model leads to closed-form solutions for the longitudinal wave velocity and second-harmonic nonlinear parameter that are explicitly dependent on the interatomic potential parameters and on temperature. The theoretical results indicate that the longitudinal wave speed decreases with increasing temperature for a constrained solid, as a result of the resulting thermal stresses. This sort of "softening" effect is attributed to the decrease in curvature of the interatomic potential vs. distance curve (quadratic term $O(r^2)$) near the equilibrium position. In addition, the theory concludes that the second-harmonic nonlinear parameter increases with increasing temperature for the constrained solid. This is, again, the result of the shape of the interatomic potential (quadratic and cubic terms $O(r^2)$ and $O(r^3)$) that is stored in the material as "residual" energy from the prevented thermal expansion.

The chapter presented experimental testing on a steel block with and without thermal stresses. The experiments confirmed that bulk wave nonlinearities are directly related to the thermal stresses and not to the free thermal expansion.

One possibility that arises from this study is the characterization of absolute values of thermal stresses from measurements of the nonlinear parameter. However, careful calibration of all material properties involved in Eq. (9.165) would be required for absolute measurements. This calibration is not an easy task, since the interatomic potential curve should be known to, at least, a cubic accuracy of $O(r^3)$, for the given test material. In addition, as in any nonlinear ultrasonic test, the nonlinearity of the instrumentation and that of the transducer/structure coupling will affect the absolute measurements. Because of these reasons and others, a direct comparison of the theoretical results with the experimental results on the steel block shown in this section is not feasible. However, it would be quite possible to determine the point of *zero thermal stress* of a solid under a temperature fluctuation, that corresponds to a minimum of the nonlinear parameter. For example, the zero thermal stress point is a key factor in the maintenance of continuous-welded rail tracks (the well-known "neutral temperature" point of rails).

The proposed model does not include changes of the first-order elastic properties with temperature (although that could be easily included). The model is also limited to longitudinal bulk waves and does not include wave attenuation/damping effects.

A.1 Appendix

The second-order and third-order coefficients of the interatomic potential for constrained thermal expansion, for the general case of the Mie potential, are given by the following expressions. These expressions are simply obtained by differentiating the potential V_{MIE} in Eq. (9.145), and calculating the derivatives at the temperature-dependent interatomic position r^*, where $r^* = r_{\mathrm{ABD}}(T)$ for the fully constrained case, and $r^* = r_{\mathrm{ABD\text{-}PC}}(T)$ for the partially constrained case.

$$C(T)=\left.\frac{\partial^2 V_{MIE}}{\partial r^2}\right|_{r=r\cdot(T)}=\frac{n\left(\frac{n}{m}\right)^{\frac{n}{n-m}}\left[n\,(1+n)\left(\frac{q}{r\cdot(T)}\right)^{n}-m\,(1+m)\left(\frac{q}{r\cdot(T)}\right)^{m}\right]w}{(n-m)\,(r\cdot(T))^2} \tag{9.A1}$$

and

$$D(T)=\left.\frac{\partial^3 V_{MIE}}{\partial r^3}\right|_{r=r\cdot(T)} \tag{A.2}$$

$$=\frac{n\left(\frac{n}{m}\right)^{\frac{n}{n-m}}\left[m\,(1{+}m)\,(2{+}m)\left(\frac{q}{r\cdot(T)}\right)^{m}-n\,(1{+}n)\,(2{+}n)\left(\frac{q}{r\cdot(T)}\right)^{n}\right]w}{(n{-}m)\,(r\cdot(T))^3}$$

For the specific case of the Lennard-Jones potential ($n = 12$, $m = 6$), these expressions simplify to:

$$C_{Lennard-Jones}(T)=\frac{24wq^6\left[26q^6-7(r\cdot(T))^6\right]}{(r\cdot(T))^{14}} \tag{9.A3}$$

and

$$D_{Lennard-Jones}(T)=\frac{672wq^6\left[-13q^6+2(r\cdot(T))^6\right]}{(r\cdot(T))^{15}} \tag{9.A4}$$

References

1. M.F. Hamilton, D.T. Blackstock, *Nonlinear Acoustics* (Acoustical Society of America, New York, 2008)
2. A. Jeffrey, J. Engelbrecht, *Nonlinear Waves in Solids* (Springer, Berlin-New York, 1994)
3. A.V. Porubov, *Amplification of Nonlinear Strain Waves in Solids* (World Scientific Pub Co, Singapore, 2003)
4. A.M. Samsonov, *Strain Solitons in Solids and how to Construct them* (CRC Press, Boca Raton, 2001)
5. M. Deng, Second-harmonic properties of horizontally polarized shear modes in an isotropic plate. Jap. J. Appl. Phys. **35**, 4004–4010 (1996)
6. M. Deng, Cumulative second-harmonic generation accompanying nonlinear shear horizontal mode propagation in a solid plate. J. Appl. Phys. **84**, 3500 (1998)
7. M. Deng, Cumulative second-harmonic generation of Lamb-mode propagation in a solid plate. J. Appl. Phys. **85**, 3051 (1999)
8. W.J.N. De Lima, M.F. Hamilton, Finite-amplitude waves in isotropic elastic plates. J. Sound Vibr. **265**, 819–839 (2003)
9. M. Deng, Analysis of second-harmonic generation of Lamb modes using a modal analysis approach. J. Appl. Phys. **94**, 4152 (2003)
10. B.A. Auld, *Acoustic Fields and Waves in Solids* (R.E. Krieger, Malabar, 1990)
11. W.J.N. De Lima, M.F. Hamilton, Finite amplitude waves in isotropic elastic waveguides with arbitrary constant cross-sectional area. Wave Motion **41**, 1–11 (2005)
12. M. Deng, Assessment of accumulated fatigue damage in solid plates using nonlinear Lamb wave approach. Appl. Phys. Lett. **90**, 121902 (2007)
13. A. Srivastava, F. Lanza di Scalea, On the existence of antisymmetric or symmetric Lamb waves at nonlinear higher harmonics. J. Sound Vibr. **323**, 932–943 (2009)
14. A. Srivastava, F. Lanza di Scalea, On the existence of longitudinal or flexural waves in rods at nonlinear higher harmonics. J. Sound Vibr. **329**, 1499–1506 (2010)
15. A. Srivastava, I. Bartoli, S. Salamone, F. Lanza di Scalea, Higher harmonic generation in nonlinear waveguides of arbitrary cross-section. J. Acoust. Soc. Am. **127**, 2790–2796 (2010)
16. M.F. Muller, J.K. Kim, J. Qu, L.J. Jacobs, Characteristics of second harmonic generation of lamb waves in nonlinear elastic plates. J. Acoust. Soc. Am. **127**, 2141–2152 (2010)
17. C. Bermes, J.Y. Kim, J.M. Qu, L.J. Jacobs, Experimental characterization of material nonlinearity using Lamb waves. Appl. Phys. Lett. **90**, 021901 (2007)
18. N. Matsuda, S. Biwa, Phase and group velocity matching for cumulative harmonic generation in lamb waves. J. Appl. Phys. **109**, 094903 (2011)
19. K.H. Matlack, J.J. Wall, J.Y. Kim, J. Qu, L.J. Jacobs, H.W. Viehrig, Evaluation of radiation damage using nonlinear ultrasound. J. Appl. Phys. **111**, 1–3 (2012)
20. V.K. Chillara, C.J. Lissenden, Interaction of guided wave modes in isotropic weakly nonlinear elastic plates: higher harmonic generation. J. Appl. Phys. **111**, 124909 (2012)
21. V.K. Chillara, C.J. Lissenden, D.O. Thompson, D.E. Chimenti, Higher harmonic guided waves in isotropic weakly nonlinear elastic plates. AIP Conf. Proc. **1511**, 145–150 (2013)
22. Y. Liu, V.K. Chillara, C.J. Lissenden, On selection of primary modes for generation of strong internally resonant second harmonics in plate. J. Sound Vibr. **332**, 4517–4528 (2013)
23. V.K. Chillara, C.J. Lissenden, Analysis of second harmonic guided waves in pipes using a large-radius asymptotic approximation for axis-symmetric longitudinal modes. Ultrasonics **53**, 862–869 (2013)
24. N. Matsuda, S. Biwa, Frequency dependence of second-harmonic generation in Lamb waves. J. Nondestruct. Eval. **33**, 169–177 (2014)
25. R. Radecki, M.J. Lemay, T. Uhl, W.J. Staszewski, Z. Su, L. Cheng, P. Packo, Investigation on high–order harmonic generation of guided waves using local computation approaches: theory and comparison with analytical modelling. in *7th European Workshop on Structural Health Monitoring, 8–11 July* (Nantes, France, 2014)

26. M. Ryles, F.H. Ngau, I. McDonald, W.J. Staszewski, Comparative study of nonlinear acoustic and Lamb wave techniques for fatigue crack detection in metallic structures. Fatigue Fract. Eng. Mech. **31**, 674–683 (2008)
27. V.K. Chillara, C.J. Lissenden, Review of nonlinear ultra sonic guided wave nondestructive evaluation: theory, numerics, and experiments. Opt. Eng. **55**, 011002–011002 (2016)
28. M. Deng, Y.X. Xiang, L.B. Liu, Time-domain analysis and experimental examination of cumulative second-harmonic generation by primary Lamb wave propagation. J. Appl. Phys. **109**, 113525 (2011)
29. Z.A. Goldberg, Interaction of plane longitudinal and transverse elastic waves. Sov. Phys. Acoust. **6**, 306–310 (1961)
30. A.C. Eringen, E.S. Suhubi, *Elastodynamics* (Academic Press, New York, 1975)
31. A.I. Lurie, *Nonlinear Elasticity* (Nauka Publishers, Moscow, 1980)
32. J. Engelbrecht, *Nonlinear Wave Processes of Deformation in Solids* (Pitman Advanced Pub. Program, Boston, 1983)
33. K.A. Lurie, *Nonlinear Theory of Elasticity* (North-Holland, Amsterdam, 1990)
34. F.D. Murnaghan, *Finite Deformations* (Wiley, New York, 1951)
35. L.D. Landau, E.M. Lifshitz, *Theory of Elasticity* (Addison-Wesley Pub. Co, London, 1959)
36. R. Truell, C. Elbaum, B. Chick, *Ultrasonic Methods in Solid State Physics* (Academic Press, New York, 1969)
37. A.H. Meitzler, Mode coupling occurring in the propagation of elastic pulses in wires. J. Acoust. Soc. Am. **33**, 435 (1961)
38. C. Nucera, F. Lanza di Scalea, Nonlinear semi-analytical finite element algorithm for the analysis of internal resonance conditions in complex waveguides. ASCE J Eng Mech **140**, 502–522 (2014)
39. C. Nucera, F. Lanza di Scalea, Nondestructive measurement of neutral temperature in continuous welded rails by nonlinear ultrasonic guided waves. J. Acoust. Soc. Am. **136**, 2561–2574 (2014)
40. C. Nucera, F. Lanza di Scalea, Modeling of nonlinear guided waves and applications to structural health monitoring. ASCE J Comput Civ Eng **29**, B40140011–B401400115 (2015)
41. N. Apetre, M. Ruzzene, S. Hanagud, S Gopalakrishnan, Nonlinear spectral methods for the analysis of wave propagation. in *49th AIAA/ASME/ASCE/AHS/ASC Structures, Structural Dynamics and Materials Conference* (Schaumburg, IL, 7–10 April, 2008)
42. B. Aalami, Waves in prismatic guides of arbitrary cross-section. J Appl Mech-T ASME **40**, 1067–1077 (1973)
43. P.E. Lagasse, Higher-order finite-element analysis of topographic guides supporting elastic surface-waves. J. Acoust. Soc. Am. **53**, 1116–1122 (1973)
44. L. Gavrić, Finite-element computation of dispersion properties of thin-walled waveguides. J. Sound Vib. **173**, 113–124 (1994)
45. L. Gavrić, Computation of propagative waves in free rail using a finite element technique. J. Sound Vib. **185**, 531–543 (1995)
46. K.H. Huang, S.B. Dong, Propagating waves and edge vibrations in anisotropic composite cylinders. J. Sound Vib. **96**, 363–379 (1984)
47. S. Finnveden, Spectral finite element analysis of the vibration of straight fluid-filled pipes with flanges. J. Sound Vib. **199**, 125–154 (1997)
48. A.C. Hladky Hennion, Finite element analysis of the propagation of acoustic waves in waveguides. J. Sound Vib. **194**, 119–136 (1996)
49. T. Mazuch, Wave dispersion modelling in anisotropic shells and rods by the finite element method. J. Sound Vib. **198**, 429–438 (1996)
50. U. Orrenius, S. Finnveden, Calculation of wave propagation in rib-stiffened plate structures. J. Sound Vib. **198**, 203–224 (1996)
51. I. Bartoli, A. Marzani, F. Lanza di Scalea, E. Viola, Modeling wave propagation in damped waveguides of arbitrary cross-section. J. Sound Vib. **295**, 685–707 (2006)
52. T. Hayashi, W.J. Song, J.L. Rose, Guided wave dispersion curves for a bar with an arbitrary cross-section, a rod and rail example. Ultrasonics **41**, 175–183 (2003)

53. P.W. Loveday, Semi-analytical finite element analysis of elastic waveguides subjected to axial loads. Ultrasonics **49**, 298–300 (2009)
54. S.S. Sekoyan, A.E. Eremeev, Measurement of the third-order elasticity constants for steel by the ultrasonic method. Meas. Tech. **0543–1972**, 888–893 (1966)
55. E. Onate, *Structural Analysis with the Finite Element Method. Linear Statics – Volume I* (Springer, Dordrecht, 2009)
56. A. Bernard, M. Deschamps, M.J.S. Lowe, Energy velocity and group velocity for guided waves propagating within an absorbing or non-absorbing plate in vacuum. Rev Progr Quant NDE **18**, 183–190 (1999)
57. A. Bernard, M.J.S. Lowe, M. Deschamps, Guided waves energy velocity in absorbing and non-absorbing plates. J. Acoust. Soc. Am. **110**, 186–196 (2001)
58. M.V. Predoi, M. Castaings, B. Hosten, C. Bacon, Wave propagation along transversely periodic structures. J. Acoust. Soc. Am. **121**, 1935–1944 (2007)
59. B. Pavlakovic, M.J.S. Lowe, *Disperse User Manual* (Imperial College, London, 2003)
60. C. Cattani, Y.Y. Rushchitskii, *Wavelet and Wave Analysis as Applied to Materials with Micro or Nanostructure* (World Scientific Pub. Co., Hackensack, 2007)
61. W.H. Prosser, Ultrasonic characterization of the nonlinear elastic properties of unidirectional graphite/epoxy composites. NASA Contr. Rep. **4100**, 75–120 (1987)
62. D.E. Knuth, *Axioms and Hulls* (Springer, Berlin-New York, 1992)
63. A. Bouhadjera, Simulation of in-situ concrete conditions using a novel ultrasonic technique. in *Proceedings of 16th World Conf Non-Destructive Testing* (2004)
64. C. Payan, V. Garnier, J. Moysan, Potential of nonlinear ultrasonic indicators for nondestructive testing of concrete. Adv. Civ. Eng. **2010**, 1–8 (2009)
65. M.A. Biot, Nonlinear thermoelasticity, irreversible thermodynamics and elastic instability. Indiana U. Math. J. **23**, 309–335 (1973)
66. O.W. Dillon, A nonlinear thermoelasticity theory. J. Mech. Phys. Solids **10**, 123–131 (1962)
67. M. Slemrod, Global existence, uniqueness, and asymptotic stability of classical smooth solutions in one-dimensional non-linear thermoelasticity. Arch. Ration. Mech. Ann. **76**, 97–133 (1981)
68. A.D. Kerr, Thermal buckling of straight tracks: fundamentals, analyses and preventive measures. Tech Rep FRA/ORD-78-49 (1978)
69. A. Kish, Fundamentals of CWR rail stress management. in *TRB 90th Annual Meeting* (Washington, DC, 2011)
70. C. Nucera, R. Phillips, F. Lanza di Scalea, M. Fateh, G. Carr, RAIL-NT system for the in-situ measurement of neutral temperature in CWR: Results from laboratory and field test. J. Transp. Res. Board **2374**, 154–161 (2013)
71. H. Ledbetter, Thermal-expansion and elastic-constants. Int. J. Thermophys. **12**, 637–642 (1991)
72. D.M. Egle, D.E. Bray, Measurement of acoustoelastic and 3rd-order elastic-constants for rail steel. J. Acoust. Soc. Am. **60**, 741–744 (1976)
73. J.H. Cantrell, in *Fundamentals and Applications of Nonlinear Ultrasonic Nondestructive Evaluation*, ed. By T. Kundu. Ultrasonic Nondestructive Evaluation: Engineering and Biological Material Characterization (CRC Press, Boca Raton, 2004), pp. 363–433
74. J.H. Cantrell, Quantitative assessment of fatigue damage accumulation in wavy slip metals from acoustic harmonic generation. Philos. Mag. **86**, 1539–1554 (2006)
75. J.H. Cantrell, W.T. Yost, Nonlinear ultrasonic characterization of fatigue microstructures. Int. J. Fatigue **23**, S487–S490 (2001)
76. R.J.D. Tilley, *Understanding Solids: The Science of Materials* (Wiley, Chichester, West Sussex, England and Hoboken, 2004)
77. G. Mie, Zur kinetischen theorie der einatomigen körper. Ann. Phys. **316**, 657–697 (1903)
78. C. Nucera, F. Lanza di Scalea, Nonlinear wave propagation in constrained solids subjected to thermal loads. J. Sound Vibr. **333**, 541–554 (2014)
79. J. Lennard-Jones, On the determination of molecular fields I – from the variation of the viscosity of a gas with temperature. Proc. R. Soc. Lond. **106**, 441–462 (1924)

80. J.E. Lennard-Jones, On the determination of molecular fields II – from the equation of state of a gas. Proc. R. Soc. Lond. **106**, 463–477 (1924)
81. J.E. Lennard-Jones, On the determination of molecular fields III – from crystal measurements and kinetic theory data. Proc. R. Soc. Lond. **106**, 709–718 (1924)

Chapter 10
Subharmonic Phased Array for Crack Evaluation (SPACE)

Yoshikazu Ohara, Tsuyoshi Mihara, and Kazushi Yamanaka

10.1 Introduction

Crack depth is one of the important factors determining material strength. Hence, the accurate measurement of crack depth is essential to ensure the reliability of aged structures and manufactured products. If cracks are open, crack depth can be measured by ultrasonics because ultrasound is strongly scattered by the crack tip (Fig. 10.1a) [1]. However, if cracks are closed because of compression residual stress [2, 3] and/or oxide debris generated between the crack faces [4], ultrasonic testing can result in the underestimation (Fig. 10.1b) or nondetection (Fig. 10.1c) of cracks since ultrasound penetrates through closed cracks. Subharmonic phased array for crack evaluation (SPACE) is a novel imaging method for measuring closed-crack depths [5, 6]. SPACE uses the subharmonics generated by short-burst waves and a phased array algorithm with frequency filtering. It enables the precise measurement of closed-crack depths. This chapter starts from fundamental aspects of subharmonic generation at closed cracks. It then describes the principle of SPACE and its application to several types of closed crack.

Y. Ohara (✉) · T. Mihara · K. Yamanaka
Tohoku University, Sendai, Japan
e-mail: ohara@material.tohoku.ac.jp

T. Kundu (ed.), *Nonlinear Ultrasonic and Vibro-Acoustical Techniques for Nondestructive Evaluation*, https://doi.org/10.1007/978-3-319-94476-0_10

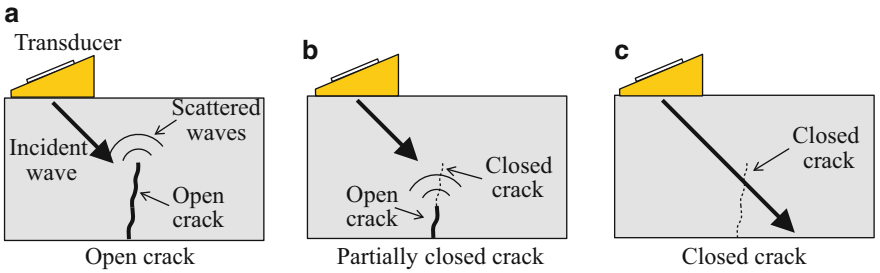

Fig. 10.1 Interaction of ultrasound with different types of crack. (**a**) Open crack, (**b**) partially closed crack, and (**c**) closed crack

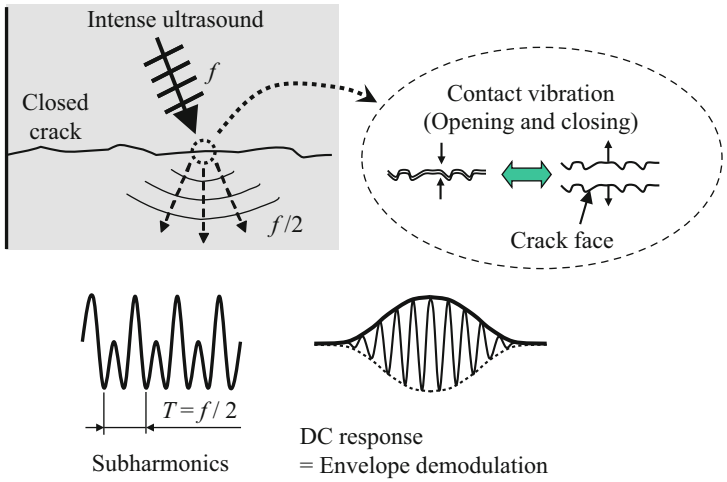

Fig. 10.2 Nonlinear interaction of intense ultrasound with a closed crack

10.2 Theory of Subharmonic Generation at Closed Cracks

10.2.1 Historical Context

In nonlinear acoustic techniques for detecting and measuring closed cracks, several types of nonlinear component, such as superharmonics, subharmonics, and sidebands, generated by the nonlinear interaction between cracks and intense ultrasound have been extensively studied [7, 8]. Among them, subharmonics has a few unique characteristics as described later. Subharmonics is a kind of nonlinear waveform distortion where the amplitudes of adjacent carrier waves become different. This results in the doubling of the period, which corresponds to the generation of a frequency of $f/2$ (Fig. 10.2), where the fundamental frequency is f. Subharmonic generation at closed cracks has been experimentally observed in many types of material such as metals [9–16], composites [17], glass [18], and ice [19]. The

most important advantage of subharmonics for nondestructive evaluation is that it is generated by closed cracks, although it is well known that superharmonics is generated not only at closed cracks but also at transducers, liquid couplants, and electrical circuits [20]. Subharmonic generation has mostly been observed by using long-burst waves including continuous waves to obtain a high-frequency resolution, whereas it has been found that subharmonics has a high temporal resolution [14, 15]. These advantages make subharmonics useful for closed-crack imaging with high selectivity and a high spatial resolution. On the other hand, the mechanism of subharmonic generation is different from that of superharmonic generation [21, 22]. To explain the mechanism of subharmonic generation, analytical and numerical theories have been studied, as described in Sects. 10.2.2 and 10.2.3, respectively. On the basis of fundamental studies, a closed-crack imaging method, SPACE, has been developed to measure the closed-crack depth, whose principle and applications are described in Sects. 10.3 and 10.4, respectively.

10.2.2 Analytical Theory [14, 15, 20]

In this section we describe the analytical theory of subharmonic generation using a simplified model [14, 15]. Superharmonic generation at closed cracks can be explained by the nonlinearity due to the contact vibration of crack faces [21, 22]. On the other hand, subharmonic generation at closed cracks is related to both the nonlinearity due to the contact vibration of crack faces and the resonance phenomenon, which was also confirmed in microbubbles in medical ultrasonics [23, 24]. As a phenomenon related to subharmonics, a DC response has been studied [12]. The DC response is a nonlinear rectifying effect resulting in amplitude demodulation (Fig. 10.2) [25], which was also discovered in the cantilever of an atomic force microscope [26, 27]. It is also referred to as the mechanical diode effect [28]. DC and subharmonic responses are common in terms of having a frequency range lower than that of the incident wave. Hence, these responses can be analyzed using a unified model. Actually, it was reported that DC and subharmonic responses are mutually connected by a quantitative relationship in some cases [29]; the subharmonic amplitude is proportional to the square root of the amplitude of the DC response.

For the analysis of the above effects, the asymmetric stiffness for a given tension and compression of a closed crack is insufficient; however, an effective mass is introduced to express inertial effects. Here the output side crack face (crack face B) cannot follow the vibration of the input side crack face (crack face A). For a high-frequency limit, the average force per cycle applied to crack face B by crack face A is balanced by the restoring force of the spring that supports crack face B. This theory successfully explained the DC effect observed in the interaction between a tip and a sample in ultrasonic force microscopy (UFM) [26], which is well known as a useful tool for the nanoscale imaging of subsurface defects.

Subharmonics generated in closed cracks exhibits the threshold behavior; the amplitude of subharmonics drastically increases above a certain amplitude of incident wave. The effect of the adhesion force on the threshold behavior has yet to be examined, although the analysis of hysteresis involving the threshold behavior has been reported [30]. However, the threshold behavior observed in UFM was successfully explained by introducing the adhesion force between the tip and the sample [31]. Although the analysis of introducing an adhesion force with hysteresis has been studied [32, 33], the threshold behavior can be explained by a model without hysteresis [31]. Thus, in a slightly different manner from that in UFM [31], the adhesion force is introduced in the reported model [14].

Figure 10.3 is a model of a partially closed crack in an elastic medium. Crack face A is assumed to be vibrated by incident wave. Crack face B has an effective mass of m that is supported by a spring with a stiffness of k. The parameter $x_s(t)$ denotes the initial displacement of crack face A because of crack closure stress. Crack face B is displaced by x_c from its free position because of a static repulsive force from crack face A. By solving $f(x_s - x_c) = kx_c$, the displacement x_c is determined. When crack face A is vibrated following an incident wave (amplitude a, angular frequency ω), the displacement x of crack face B satisfies

$$m\ddot{x} + \gamma\dot{x} + kx = f\left(x_s + a\sin\omega t - x\right), \tag{10.1}$$

where γ is the damping of crack face B and t is time. γ can be estimated in principle from the width of the resonance. $f(\Delta x)$ is the interaction force, which is a function of the compression of the crack faces Δx.

When ω is even higher than the resonance frequency $\omega_0 = \sqrt{k/m}$ of crack face B, crack face B cannot follow the vibration because of its inertia and the additional repulsive force is induced by the intermittent contact with crack face A. The time-averaged displacement of crack face B is changed from x_c to x_0. At the high-frequency limit, the vibration of crack face B is completely suppressed and thereby x_0 becomes constant. This phenomenon is essentially the same as the nonlinear rectifying effect in amplitude demodulation [25], which was also discovered in the field of atomic force microscopy [26, 27], or the mechanical diode effect [28]. Following the same analysis in that in [26, 27], we can derive x_0 by solving the integral equation

$$kx_0 = \frac{1}{f}\int_0^T f\left(x_s + a\sin\omega t - x_0\right)dt, \tag{10.2}$$

where $T = 2\pi/\omega$ is the period of the incident wave. The assumptions to obtain an analytical solution for the evaluation of the threshold behavior are as follows:

1. The vibration of crack face A corresponding to an incident wave is a triangular wave instead of a sinusoidal wave [14, 18, 26, 30].
2. During contact, crack faces are fixed by the adhesion force f_d as a short-range force. As shown in Fig. 10.4, the interaction force is expressed as

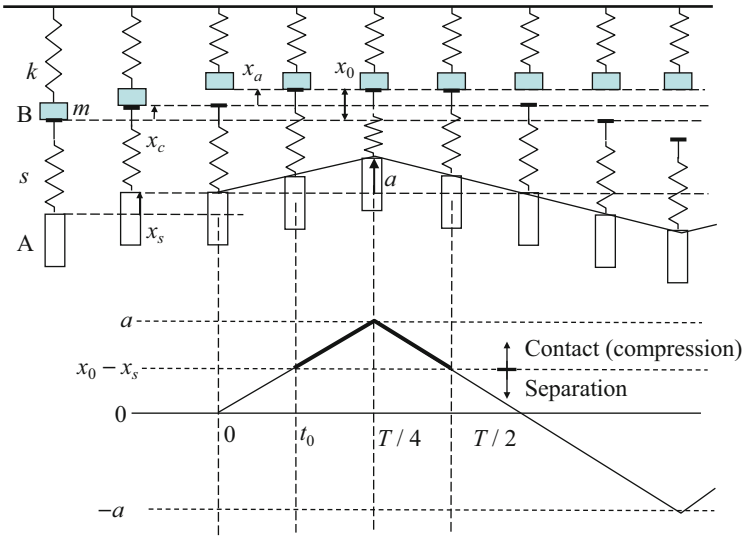

Fig. 10.3 Model of nonlinear interaction between crack faces when the frequency of the incident wave is much higher than the effective resonance frequency of the output crack face. Modified from [14] (Copyright (2004) The Japan Society of Applied Physics)

Fig. 10.4 Interaction force between crack faces

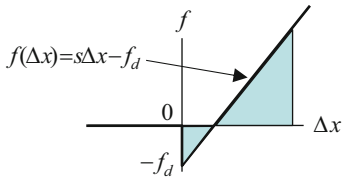

$f(\Delta x) = s\Delta x - f_d$ during contact, where s is the contact stiffness of the crack, while it is 0 during separation.

Under the above assumptions, as shown by the shaded area in Fig. 10.4, the integral with respect to t in Eq. (10.2) is replaced by an integral with respect to x; therefore,

$$kx_0 = \frac{1}{2a}\left[\frac{s}{2}(x_S - x_0 + a)^2 - f_d\,(x_s - x_0 + a)\right]. \tag{10.3}$$

Since $s(x_S - x_c) = kx_c$, the time-averaged displacement variation x_a is obtained from Eq. (10.3) as

$$x_a = \frac{k}{s}x_c + a\left(1 + 2\frac{k}{s}\right) - 2\sqrt{\frac{k}{s}a\left(\frac{k}{s} + 1\right)(a + x_c) + \frac{f_d^2}{4ks}}. \tag{10.4}$$

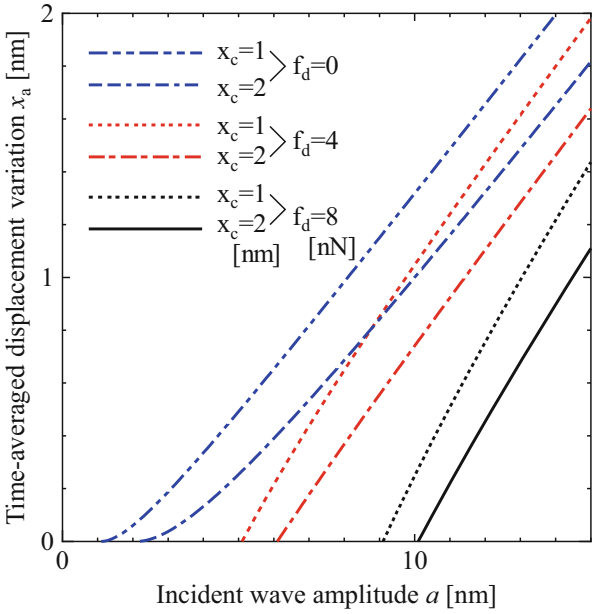

Fig. 10.5 Dependence of time-averaged displacement variation x_a on initial crack closure displacement x_c and adhesion force f_d. Taken from [15], with permission from Elsevier

The threshold a_{th} of the incident wave amplitude is derived at $x_a = 0$ in Eq. (10.4) as

$$a_{th} = \frac{k}{s} x_c + \frac{f_d}{\sqrt{ks}} \tag{10.5}$$

It should be noted that this analytical solution is a simple but powerful expression that clearly shows the effects of both the adhesion force and crack closure stress on subharmonics generated in closed cracks.

Subsequently, the effect of parameters on the analytical solution was examined. Figure 10.5 shows the analytical solution of Eq. (10.4) with different f_d and x_c plotted against the incident wave amplitude a. As x_c increases, x_a decreases at each f_d. This is because the preliminary crack closure displacement suppresses the effective force acting on crack face B from crack face A. As f_d increases, the threshold increases. It should be noted that depending on the presence or absence of an adhesion force, the shape of the threshold behavior significantly differs. The relation between x_a and a is upward concave for the absence of an adhesion force, but upward convex for the presence of f_d. Also, as f_d increases, the slope of x_a against a slightly increases steep.

To verify the aforementioned analytical theories, we carried out an experiment in a through-transmission configuration on a fatigue crack in an aluminum alloy (A7075) [15, 20]. The fatigue crack was extended from a starting notch by a three-

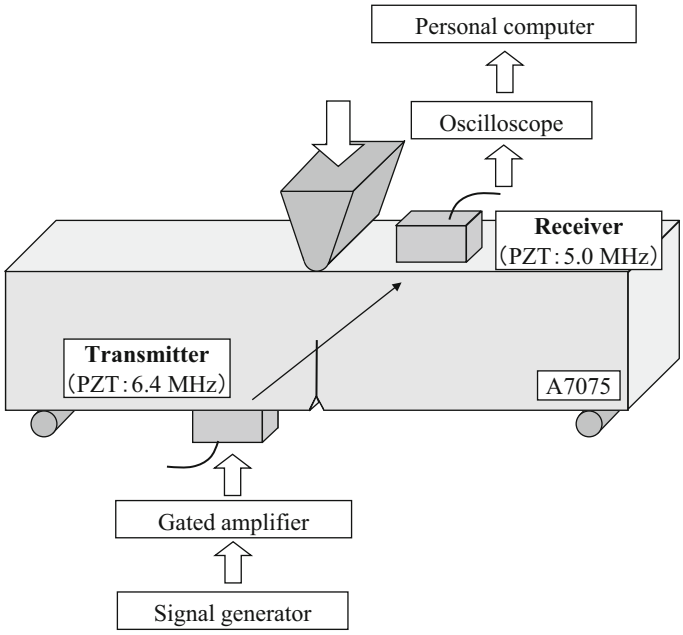

Fig. 10.6 Experimental configuration for through-transmission measurement in a fatigue crack specimen

point bending fatigue test, where the fatigue conditions were a maximum stress intensity factor K_{max} of 4.3 MPa $m^{1/2}$ and a minimum stress intensity factor K_{min} of 0.6 MPa $m^{1/2}$. As shown in Fig. 10.6, we performed the nonlinear ultrasonic measurement using an oblique-incidence longitudinal wave with a wedge made of polystyrene. A continuous sine wave with a center frequency of 6.4 MHz was produced by a signal generator. Subsequently, a gated amplifier was used to amplify this wave of 20 cycles up to a voltage of 1.2 kV peak to peak (p–p). To confirm that the incident wave is suited for the nonlinear ultrasonic measurement, we measured the displacement amplitude of a longitudinal wave at the crack position in a crack-free sample using a laser vibrometer, as shown in Fig. 10.7a. As a result, it was larger than 20 nm p–p (Fig. 10.7b). It is clear in Fig. 10.7c that the received waveform does not include subharmonics around 3.2 MHz, although it includes some superharmonics around 12.8 MHz generated at the liquid couplant and the piezoelectric transducer. For detection in the following experiments, however, we used a broadband piezoelectric transducer with a center frequency of 5 MHz because of its higher sensitivity and easy handling.

Figure 10.8a shows the transmitted waveforms at an incident wave amplitude of 10.7 nm for different loads, where the static bending load was applied to open the closed crack and has been converted to the stress intensity factor K. By applying a bending load of up to $K = 3.6$ MPa $m^{1/2}$, the amplitude of the transmitted waves decreased. This is because the partially closed crack was opened.

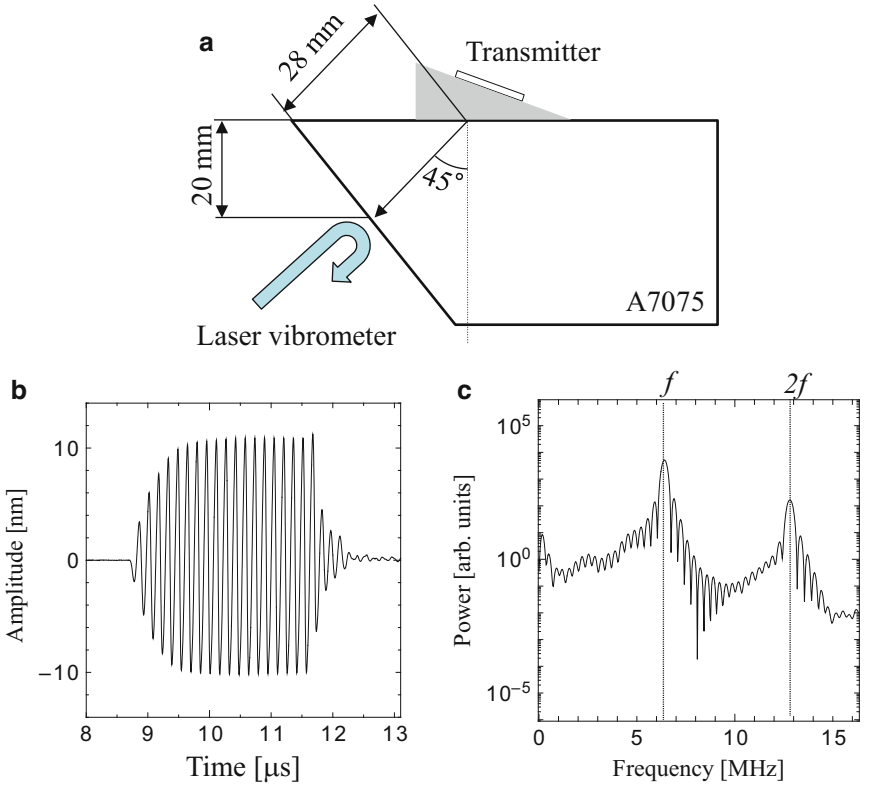

Fig. 10.7 Incident wave measured at an excitation voltage of 1.2 kVp-p in a crack-free sample using a laser vibrometer. (**a**) Experimental configuration, (**b**) received waveform, and (**c**) power spectrum corresponding to (**b**)

It is noteworthy that the amplitudes of adjacent carriers became clearly different. This results in subharmonic generation. In the corresponding power spectra in Fig. 10.8b, the subharmonic intensity is comparable to the fundamental intensity at $K = 3.6$ MPa $m^{1/2}$.

At a bending load of 0.6 kN, corresponding to $K = 3.6$ MPa $m^{1/2}$, the transmitted waveforms for different incident wave amplitudes are plotted in Fig. 10.9a. As the incident wave amplitude increased, the amplitudes of adjacent carriers became clearly different, resulting in the generation of subharmonics. In the corresponding power spectra in Fig. 10.9b, the subharmonic intensity was comparable to the fundamental intensity at an incident wave amplitude of 10.8 nm.

It is noteworthy that the subharmonics was evident even within the first two carriers in Figs. 10.8a and 10.9a. Although the twenty-cycle burst wave was employed to obtain a high signal-to-noise ratio (SNR) in spectrum analysis, it is easy to identify the waveform distortion even in an initial few cycles. This suggests that temporal resolution can be increased by extracting a clear variation of waveforms.

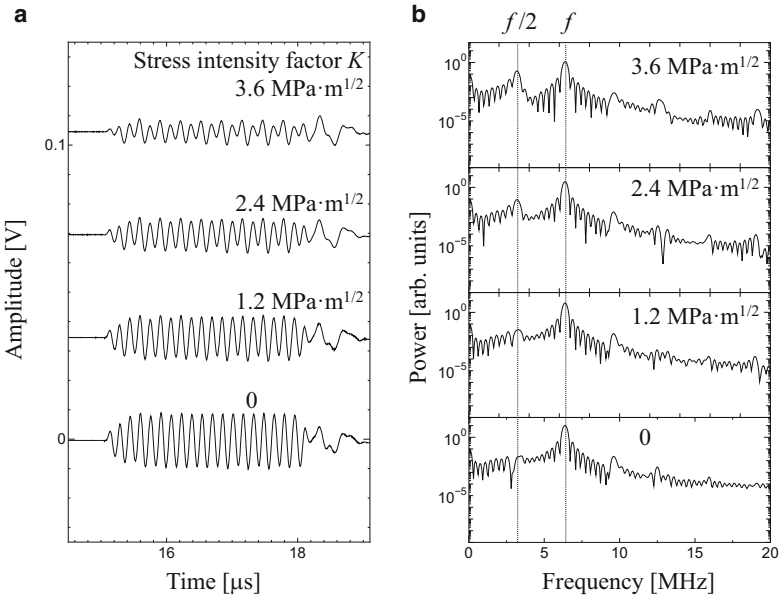

Fig. 10.8 Dependence of transmitted waveforms and their spectra on the stress intensity factor K at an incident wave amplitude of 10.7 nm. (**a**) Transmitted waveforms, (**b**) power spectra corresponding to (**a**)

Next, we compared the analytical solution with experimental results. Figure 10.10 (vertical axis on left side) shows the subharmonic amplitude $A_{3.2\,\mathrm{MHz}}$ of the transmitted waves as a function of the incident wave amplitude a at each K, where $a = 2.75$, 4.7, 6.8, and 10.7 nm and the increase in K in the experiment corresponds to a decrease in the initial crack closure displacement x_c in the analysis. To reproduce the experimental results using the analytical solution, the time-averaged displacement variation x_a calculated based on Eq. (10.4) was drawn as solid lines in Fig. 10.10, where $f_d = 3$ nN, x_c=0.4–2.8 nm, $s = k = 1$ N/m, and the vertical scale on the right side was adjusted to fit the experimental results.

At $K = 0$, the slope of $A_{3.2\mathrm{MHz}}$ against a was small below $a = 7$ nm. Above $a = 7$ nm, it markedly increased. Therefore, we evaluated the threshold was about 7 nm. This is in agreement with the analytical solution at x_c=2.8 nm. At $K = 1.2$ MPa m$^{1/2}$, $A_{3.2\,\mathrm{MHz}}$ was almost zero up to $a = 2.7$ nm and rapidly increased at $a = 4.7$ nm, showing that the threshold existed between $a = 2.7$ and 4.7 nm. This is consistent with the analytical solution at x_c=0.4 nm. Thus, the experimentally observed threshold with upward convex curves was reproduced using an analytical solution. Also, the clear threshold behavior that was reported in some experimental works [10–12] was reproduced well by the analytical solution. These results support the validity and usefulness of the proposed model.

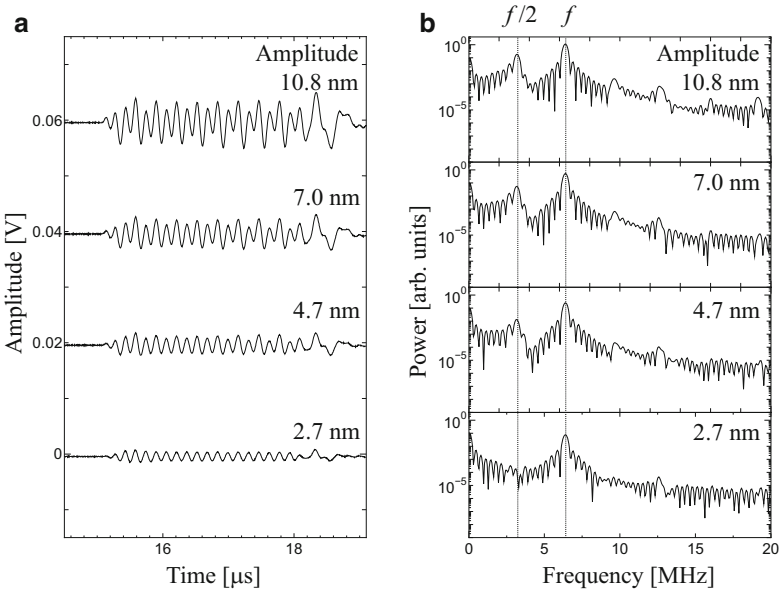

Fig. 10.9 Dependence of transmitted waveforms and their spectra on incident wave amplitude at a bending load of 0.6 kN, corresponding to $K = 3.6$ MPa $m^{1/2}$. (**a**) Transmitted waveforms, (**b**) power spectra corresponding to (**a**)

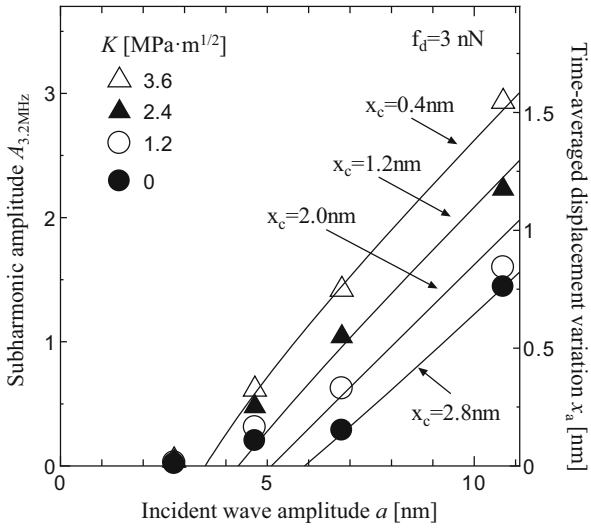

Fig. 10.10 Comparison of analytical solution with experimental results. Modified from [15], with permission from Elsevier

10.2.3 Numerical Theory [14, 34, 35]

In the previous section, we described an analytical solution that is valid for the DC effect and approximately explains the subharmonics. However, not only the intensity but also subharmonic waveforms should be calculated to obtain a precise understanding of the dynamic behavior of partially closed cracks and the interaction between crack faces.

To calculate subharmonic waveforms, we directly solve the equations governing the motion of crack faces. In the literature, a simple case of impact collision has been studied by performing such calculations [36, 37]. Here we extend Eq. (10.1) to an elastic-body-oscillator model [34, 35]. The input side is an elastic body where an incident wave and the reflected wave propagate, and the output side crack face is still an oscillator to express the resonance phenomenon, which is strongly related to subharmonic generation. The introduction of an elastic body into the model [14] follows Richardson's model [21]. Figure 10.11 shows the model used for the numerical simulation. Assuming that X_- is the position of crack face A and X_+ is the position of crack face B, which corresponds to the mass of the oscillator, the boundary condition at crack face A and the motion equation of crack face B are, respectively, given by

$$-x_p(t) + \rho c \dot{X}_-(t) - \sigma_C = -f\left(X_+ - X_-\right), \tag{10.6}$$

$$m\ddot{X}_+(t) + \gamma \dot{X}_+(t) + kX_+(t) = f\left(X_+ - X_-\right) - \sigma_C, \tag{10.7}$$

where σ_C is the crack closure stress, x_p is the position of crack face A perturbed by the incident wave, and $X_+ - X_-$ is a crack opening displacement. We directly solve Eqs. (10.6) and (10.7) simultaneously. We also deal with the more realistic force function of the van der Waals interatomic force, including an extension to the interaction between larger objects [38],

$$f\left(X_+ - X_-\right) = -f_0\left[\kappa\left(\frac{\sigma}{X_+ - X_-}\right)^M - \left(\frac{\sigma}{X_+ - X_-}\right)^N\right], \tag{10.8}$$

where f_0 is the magnitude of the force, κ is the ratio of the attractive to repulsive force, M is the repulsive force index, N is the attractive force index, and σ is a characteristic length for crack faces (e.g., interatomic distance, asperity height, or grain size), which was originally an interatomic distance in the Lennard–Jones-type atomic force. The parameters M, N, and κ characterize the force function and depend on the shape of the crack face, as listed in Table 10.1. Here we assume that the crack faces are a plane and a half space, and thus case (3) in Table 10.1 is employed. x_p essentially follows the motion of the incident wave. To reproduce the experimental results, an incident waveform with 20 cycles of carriers satisfying the following equations was used in a calculation:

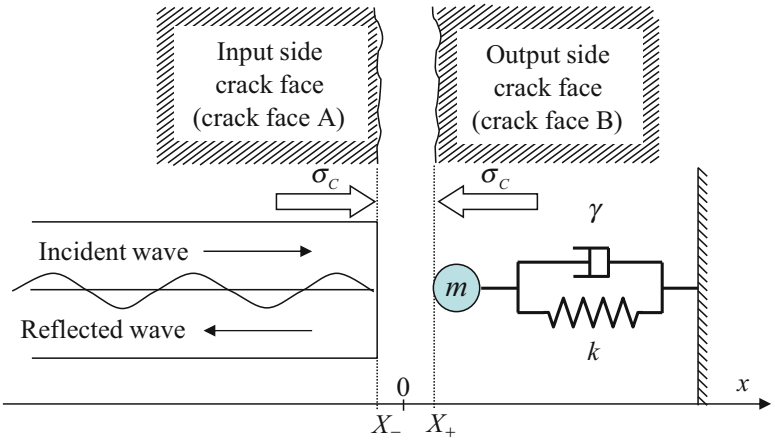

Fig. 10.11 Elastic-body-oscillator model used for numerical simulation

Table 10.1 Repulsive and attractive force indices and ratio of repulsive to attractive force

	M	N	κ
(1) Lennard–Jones atomic potential	13	7	2
(2) Sphere–half-space interaction	8	2	1/30
(3) Plane–half-space interaction	9	3	1

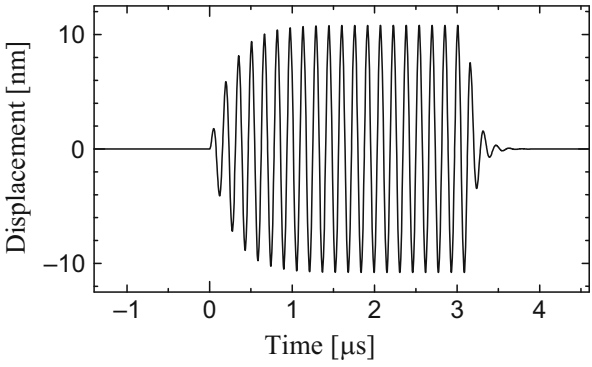

Fig. 10.12 Incident waveform used in the numerical simulation

$$x_p(t) = \begin{cases} a\left(1 - e^{-\frac{t}{\tau_R}}\right) \sin \omega t & 0 \le t < 20T \\ ae^{-\frac{t - 20T}{\tau_D}} \sin \omega t & 20T \le t, \end{cases} \tag{10.9}$$

where τ_R is the rising time constant and τ_D is the decaying time constant. τ_R and τ_D were, respectively, specified as 1.60 T and 0.64 T to obtain the best agreement with the measured waveforms (Fig. 10.7b). The incident waveform used in the numerical simulations is shown in Fig. 10.12.

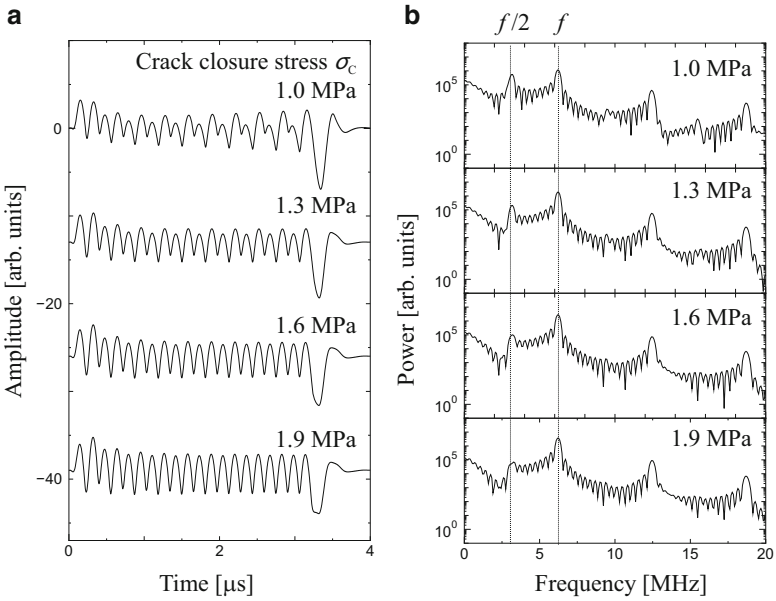

Fig. 10.13 Dependence of calculated waveforms and their spectra on crack closure stress σ_C at an incident wave amplitude of 10.7 nm. (**a**) Calculated waveforms, (**b**) the spectra corresponding to (**a**)

The transient solutions of X_+ and X_- were calculated by solving Eqs. (10.6) and (10.7) simultaneously with the incident wave of Fig. 10.12, where the other parameters were selected as follows to simulate the experimental conditions: density $\rho = 2790$ kg/m^3, elastic modulus $\lambda = 73.83$ GPa, $f = 6.4$ MHz, $a = 2.7$–10.8 nm, $\sigma_C = 1.0$–1.9 MPa, $m = 1.27$ kg/m^2, $\gamma = 2.5 \times 10^6$ kg/s/m^2, $k = 3.4 \times 10^{14}$ N/m/m^2, $f_0 = 1$ kPa, $\sigma = 5$ nm. Figures 10.13a and 10.14a show the waveforms X_+ calculated to investigate the σ_C and a dependences of subharmonic generation, respectively. When a increased or σ_C decreased, the waveform distortion became clear: the amplitudes of adjacent carriers became clearly different. Note that the waveforms (Figs. 10.13a and 10.14a) calculated by the numerical simulation are very similar to the experimentally observed ones (Figs. 10.8a and 10.9a). In the power spectra (Figs. 10.13b and 10.14b), the peaks at the subharmonic frequency and the threshold behavior were successfully reproduced. Figures 10.13b and 10.14b also show that second and third harmonics were generated, irrespective of the value of a or σ_C. This suggests that the threshold of superharmonics is lower than that of subharmonics and that subharmonics is more sensitive to closed cracks than superharmonics. Thus, the numerical model is useful for reproducing the waveforms of subharmonics and analyzing the behaviors of subharmonic generation.

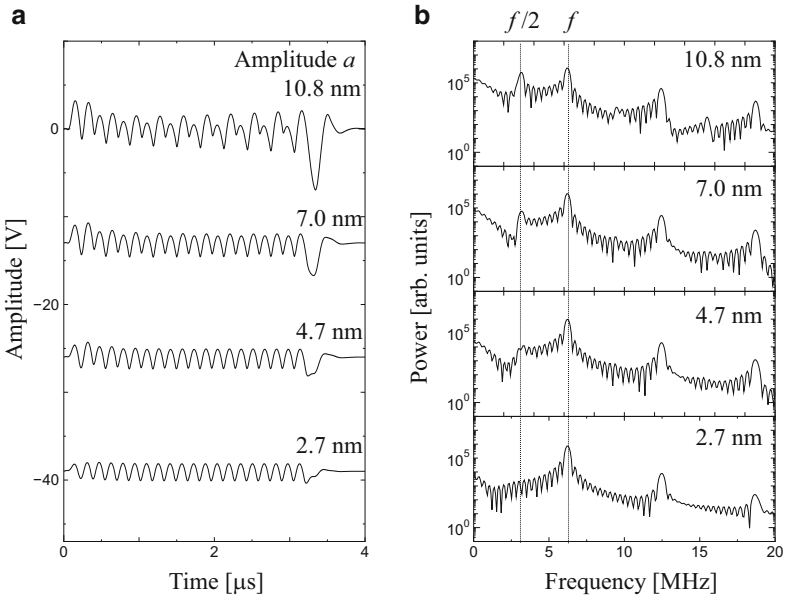

Fig. 10.14 Dependence of calculated waveforms and their spectra on incident wave amplitude a at σ_C=1.0 MPa. (**a**) Calculated waveforms, (**b**) the spectra corresponding to (**a**)

10.3 Principle of SPACE

On the basis of the findings that subharmonics has high selectivity for closed cracks and a high temporal resolution, a closed-crack imaging method, subharmonic phased array for crack evaluation (SPACE), was proposed. The first implementation of SPACE with a transmitter and an array transducer is shown in Fig. 10.15 [5, 6]. A $LiNbO_3$ (LN) single-crystal transmitter with a wedge made of polyimide is employed to realize large-amplitude incidence required for subharmonic generation. An array transducer is employed as a receiver to focus on receptions. Note that the LN transmitter of SPACE can be replaced with a different piezoelectric material and/or a different structure to generate more intense ultrasound. By inputting intense ultrasound, the fundamental and subharmonic scatterings take place at the open and closed parts of cracks, respectively. After the reception of the scattered waves by the array transducer, the fundamental and subharmonic components are extracted from the received waves by band-pass filters for fundamental and subharmonic frequencies, respectively. Subsequently, by focusing on reception in accordance with the delay law, which is described later, fundamental array (FA) and subharmonic array (SA) images are created. Note that the schematic configuration in Fig. 10.15 is similar to that used in the time-of-flight diffraction (TOFD) method [1], which uses forward-scattering waves, whereas a configuration that uses backward-scattering waves or both forward- and backward-scattering waves can also be used in SPACE.

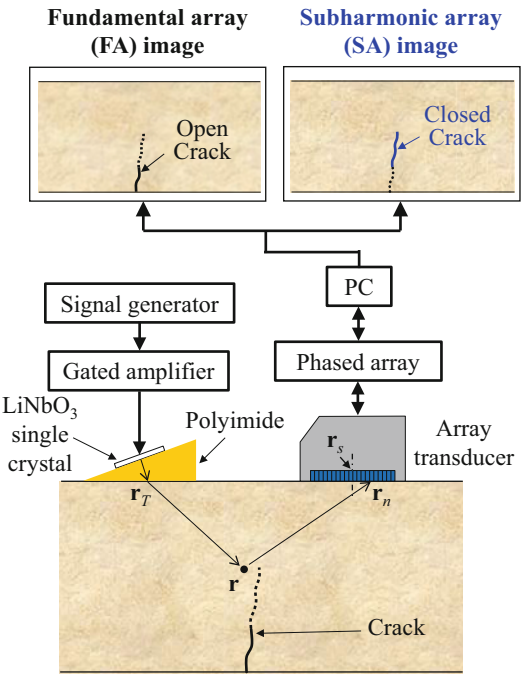

Fig. 10.15 Schematic of SPACE with a transmitter and an array transducer

Another implementation of SPACE that uses a single array transducer has also been proposed [4, 39, 40], of which a schematic is illustrated in Fig. 10.16. An array transducer is employed for both transmission and reception, and this implementation can thus be applied to a small testing area. The effect of focusing on the transmission is employed to increase the incident wave amplitude around a focal point. Here we define the focal point as a transmission focal point (TFP) at angle θ and distance r. To focus incident waves emitted from the elements of the array transducer on the TFP, each element is excited in accordance with a delay law, which is described later. The fundamental and subharmonic scatterings take place at the open and closed parts of cracks, respectively. After the reception of the scattered waves by the array transducer, the fundamental and subharmonic components are extracted from the received waves by band-pass filters for fundamental and subharmonic frequencies, respectively. Subsequently, by focusing on reception in accordance with the delay law, FA and SA images are created for the TFP, referred to as single-focus FA and single-focus SA images, respectively. The effective imaging area is limited to the region around the TFP because the transmission energy is low in the region away from the TFP, although a high imaging speed can be achieved.

To create an effective image over a wide area, multiple TFPs can also be set. By repeating the same imaging process for each TFP and thereafter merging single-focus FA and single-focus SA images, merged FA and merged SA images are created. This provides open and closed crack images over a wide area. This implementation of SPACE is called confocal SPACE [40] because both focusing on transmission and reception is used.

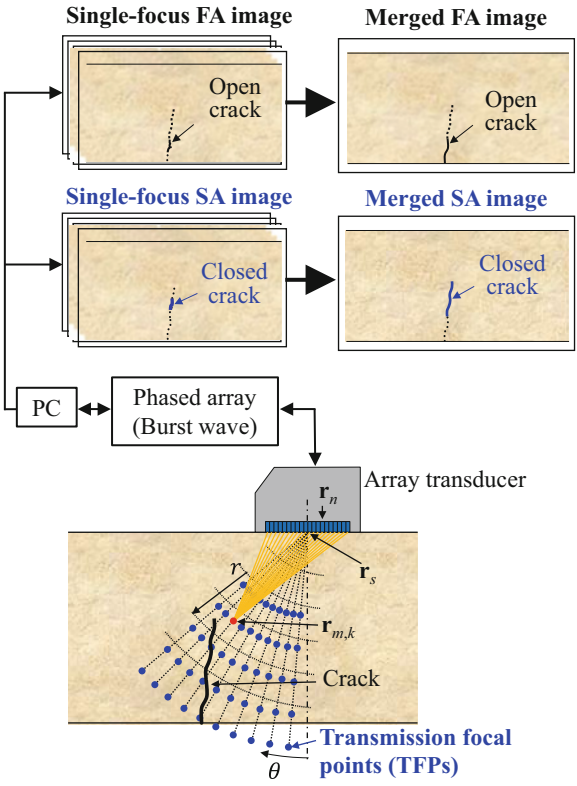

Fig. 10.16 Schematic of confocal SPACE with a single array transducer

As an option of confocal SPACE, a radarlike display was proposed to precisely observe linear and nonlinear scattering behaviors [40]. This is a display method that shows FA and SA images for TFPs with different incident angles, where a line indicating the incident direction is superimposed on the images. Hence, the linear and nonlinear scattering behaviors can be precisely observed by arranging some still images or displaying these images successively as a movie-like radar.

The imaging algorithm of SPACE with a transmitter and an array transducer is formulated as follows. Assuming that $u_{F,n}$ and $u_{S,n}$ are the waves received by the nth element of the array transducer filtered around the fundamental and subharmonic components by band-pass filters, respectively, the shift-summation waveforms at a point $\mathbf{r}$ in Fig. 10.15 are expressed as

$$U_F(\mathbf{r}, t) = \frac{1}{N}\sum_{n=1}^{N} u_{F,n}(t - t_n(\mathbf{r})), \tag{10.10}$$

$$U_S(\mathbf{r}, t) = \frac{1}{N}\sum_{n=1}^{N} u_{S,n}(t - t_n(\mathbf{r})), \tag{10.11}$$

where N is the total number of elements of the array transducer and $t_n(\mathbf{r})$ is the propagation time from the transmitter through $\mathbf{r}$ to the nth element of the array transducer and given by

$$t_n(\mathbf{r}) = \frac{|\mathbf{r} - \mathbf{r}_T| + |\mathbf{r}_n - \mathbf{r}|}{c_p} + t_W. \tag{10.12}$$

Here $\mathbf{r}_T$ is the position vector of the incidence point at the interface between the wedge and the specimen, $\mathbf{r}_n$ is the position vector of the nth element of the array transducer, c_p is the longitudinal wave speed in the specimen, and t_W is the propagation time in the wedge. Therefore, the intensities at $\mathbf{r}$ in the FA and SA images are, respectively, expressed as

$$I_F(\mathbf{r}) = \sqrt{\frac{1}{\tau}\int_{t_C}^{t_C+\tau} [U_F(\mathbf{r}, t)]^2 dt}, \tag{10.13}$$

$$I_S(\mathbf{r}) = \sqrt{\frac{1}{\tau}\int_{t_C}^{t_C+\tau} [U_S(\mathbf{r}, t)]^2 dt}, \tag{10.14}$$

where t_C is the correction term, such as the delay due to the trigger, and τ is the time window for the calculation of root-mean-square (RMS). τ is determined as the product of the time period of incident wave and the number of cycles, and is hereinafter referred to as the RMS period.

Likewise, the imaging algorithm of SPACE with a single array transducer is formulated as follows. The delay time for focusing on transmission is given by

$$t_{T,n}\left(\mathbf{r}_{m,k}\right) = \frac{\left|\mathbf{r}_n - \mathbf{r}_{m,k}\right|}{c_p}, \tag{10.15}$$

where $\mathbf{r}_{m,k}$ is the position vector of the TFP with the mth θ and the kth r. Assuming that $u_{F,n}^{m,k}$ and $u_{S,n}^{m,k}$ are the received waveforms of the nth element filtered around the f and $f/2$ components by band-pass filters, respectively, the shift-summation waveforms at $\mathbf{r}$ are expressed as

$$U_F^{m,k}(\mathbf{r}, t) = \frac{1}{N}\sum_{n=1}^{N} u_{F,n}^{m,k}(t - t_n(\mathbf{r})), \tag{10.16}$$

$$U_S^{m,k}(\mathbf{r}, t) = \frac{1}{N}\sum_{n=1}^{N} u_{S,n}^{m,k}(t - t_n(\mathbf{r})), \tag{10.17}$$

where in this case, $t_n(\mathbf{r})$ is the propagation time from the position vector of the array center $\mathbf{r}_s$ through $\mathbf{r}$ to $\mathbf{r}_n$ and given by

$$t_n(\mathbf{r}) = \frac{|\mathbf{r}_s - \mathbf{r}| + |\mathbf{r} - \mathbf{r}_n|}{c_p}. \tag{10.18}$$

Therefore, the intensities at $\mathbf{r}$ in the single-focus FA and single-focus SA images for the TFP are, respectively, expressed as

$$I_F^{m,k}(\mathbf{r}) = \sqrt{\frac{1}{\tau}\int_{t_C}^{t_C+\tau}\left[U_F^{m,k}(\mathbf{r},\ t)\right]^2 dt}, \tag{10.19}$$

$$I_S^{m,k}(\mathbf{r}) = \sqrt{\frac{1}{\tau}\int_{t_C}^{t_C+\tau}\left[U_S^{m,k}(\mathbf{r},\ t)\right]^2 dt}. \tag{10.20}$$

Merged FA and merged SA images are created on the basis of single-focus FA and single-focus SA images for each TFP, respectively. Here the following equations were used to select the areas of single-focus FA and single-focus SA images in the vicinity of the TFP for the merged images.

θ direction:

$$\frac{\arg\left(\mathbf{r}_{m,k}\right) + \arg\left(\mathbf{r}_{m-1,k}\right)}{2} \le \arg(\mathbf{r}) < \frac{\arg\left(\mathbf{r}_{m+1,k}\right) + \arg\left(\mathbf{r}_{m,k}\right)}{2}, \tag{10.21}$$

r direction:

$$\left|\frac{\mathbf{r}_{m,k} \pm \mathbf{r}_{m,k-1}}{2}\right| \le |\mathbf{r}| < \left|\frac{\mathbf{r}_{m,k+1} \pm \mathbf{r}_{m,k}}{2}\right|. \tag{10.22}$$

10.4 Experiments

10.4.1 Open and Closed Fatigue Cracks [5, 6]

To demonstrate the fundamental performance of SPACE, well-defined closed cracks were introduced in specimens made of aluminum alloy A7075 by performing a three-point bending fatigue test [14, 20]. To control the closure stress, the fatigue conditions were set to $K_{\max} = 5.3$ and $K_{\min} = 0.6$ MPa·m$^{1/2}$ for a high-stress-intensity specimen and $K_{\max} = 4.3$ and $K_{\min} = 0.6$ MPa m$^{1/2}$ for a low-stress-intensity specimen. For the imaging by SPACE, the selection of an appropriate incident frequency is important to optimize the tradeoff between the increase in spatial resolution and the decrease in SNR due to attenuation. In addition to this tradeoff, to generate the large-amplitude short-burst wave required for subharmonic generation, an input frequency of 7 MHz was selected as appropriate for the LN transmitter. The input signals were a three-cycle burst with 17 nm p-p, which was measured by a laser vibrometer in the configuration shown in Fig. 10.7. The experimental configuration is shown in Fig. 10.17. A forward-scattering configuration with a 32-element PZT array transducer having an element pitch of 0.5 mm and a center frequency of 5 MHz was selected for the measurement. The distance between the transmitter and the center of the array transducer was 52.5 mm.

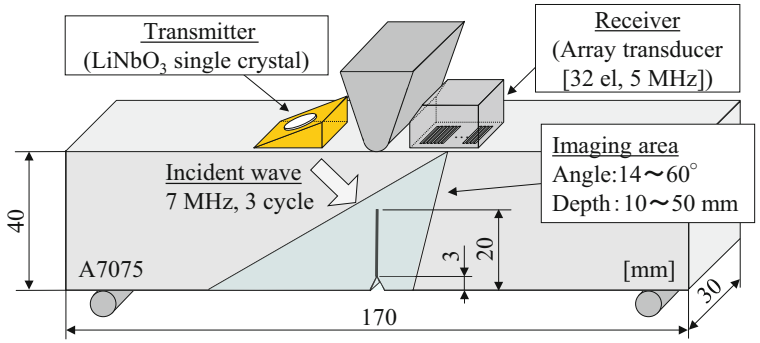

Fig. 10.17 Experimental configuration of SPACE for imaging a closed fatigue crack made of aluminum alloy A7075

The FA and SA images of fatigue cracks in the aluminum alloy specimens are shown in Fig. 10.18. In the high-stress-intensity specimen, the crack tip clearly appeared in the FA image (Fig. 10.18a), whereas it was absent in the SA image (Fig. 10.18b). This result suggests that the crack tip was dominantly open. It was also confirmed that the crack depth measured in Fig. 10.18a was in good agreement with the actual one confirmed on the side surface shown in the photograph (Fig. 10.18c). In contrast, in the low-stress-intensity specimen, the crack tip was not observed in the FA image (Fig. 10.18d), whereas it clearly appeared in the SA image (Fig. 10.18e). This result suggests that the crack tip was dominantly closed. It was also confirmed that the crack depth measured in Fig. 10.18e was in good agreement with the actual one confirmed on the side surface shown in the photograph (Fig. 10.18f). Thus, it was demonstrated that SA images accurately indicate the depth of closed cracks.

10.4.2 Dependence of a Fatigue Crack on Crack Closure Stress [5, 6]

To examine the dependence of SPACE images on crack closure, we formed a closed fatigue crack in a stainless-steel (SUS316L) specimen with thickness 40 mm, which is employed for the recirculation pipes of nuclear power plants, so as to simulate practical field testing. The fatigue conditions were set to $K_{\max} = 18.6$ and $K_{\min} = 0.6$ MPa $\mathrm{m}^{1/2}$. The crack depth on the side surface was optically observed to be approximately 8 mm.

We investigated the change in the FA and SA images while increasing the nominal bending stress induced by a static load to relieve the crack closure stress. The experimental configuration is shown in Fig. 10.19 and is similar to that of the experiment described in Sect. 10.4.1. Here, we used the nominal bending stress as

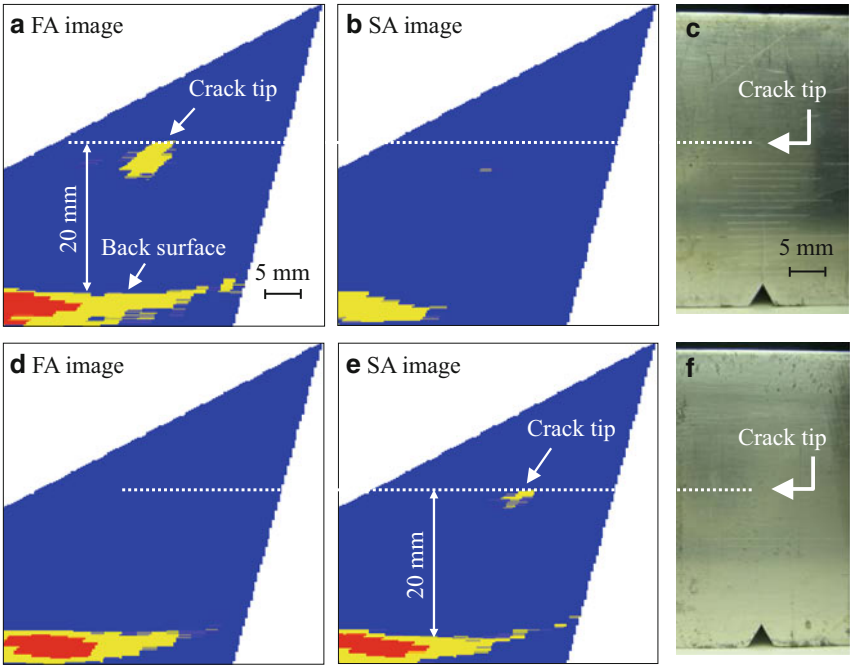

Fig. 10.18 Comparison of crack tip images obtained by SPACE for high- and low-stress-intensity A7075 specimens. (**a**) FA image, (**b**) SA image, and (**c**) photograph of high-stress-intensity specimen. (**d**) FA image, (**e**) SA image, and (**f**) photograph of low-stress-intensity specimen. Modified from [5] (Copyright © 2007 American Institute of Physics)

a measure of the stress relieved from the closure stress, although it is difficult to carry out the rigorous calculation of the closure stress owing to the complicated stress field around the crack. The nominal bending stress was calculated under the condition of a crack-free beam based on the applied static load, elastic properties, geometry, and density. Figure 10.20 shows the FA and SA images obtained at nominal bending stresses of 19, 84, and 112 MPa and schematic illustrations used for their interpretation.

At the bending stress of 19 MPa, only the notch part C appeared in the FA image (Fig. 10.20a). This suggests that C became a distinct linear scattering source at the boundary between the closed crack and the notch. On the other hand, not only C but also the crack tip A and the middle part B appeared in the SA image (Fig. 10.20b). This suggests that A and B were closed. This also shows that the present SPACE is able to visualize various parts of the crack, including the tip.

At the bending stress of 84 MPa, only the middle part B appeared in the FA image (Fig. 10.20d). This suggests that B became a distinct linear scattering source between the open and closed regions. Both A and B appeared in the SA image (Fig. 10.20e), although the intensity at B was less than that in Fig. 10.20b. This shows that the present SPACE is able to visualize the crack tip, regardless of the crack closure stress.

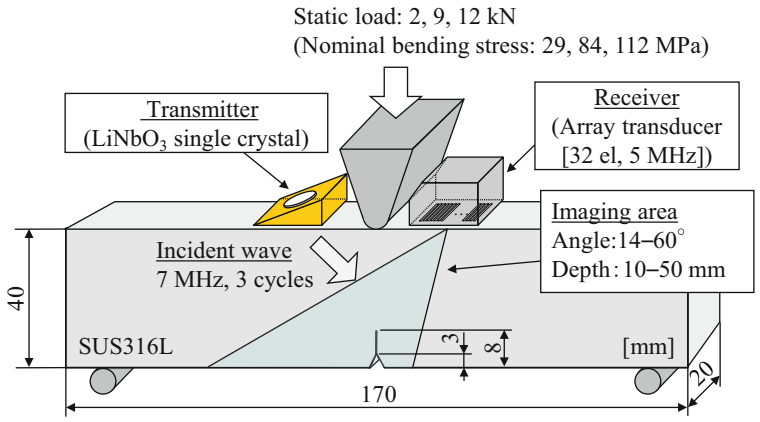

Fig. 10.19 Experimental configuration of SPACE for imaging a closed fatigue crack made of stainless steel SUS316L while varying the crack closure stress

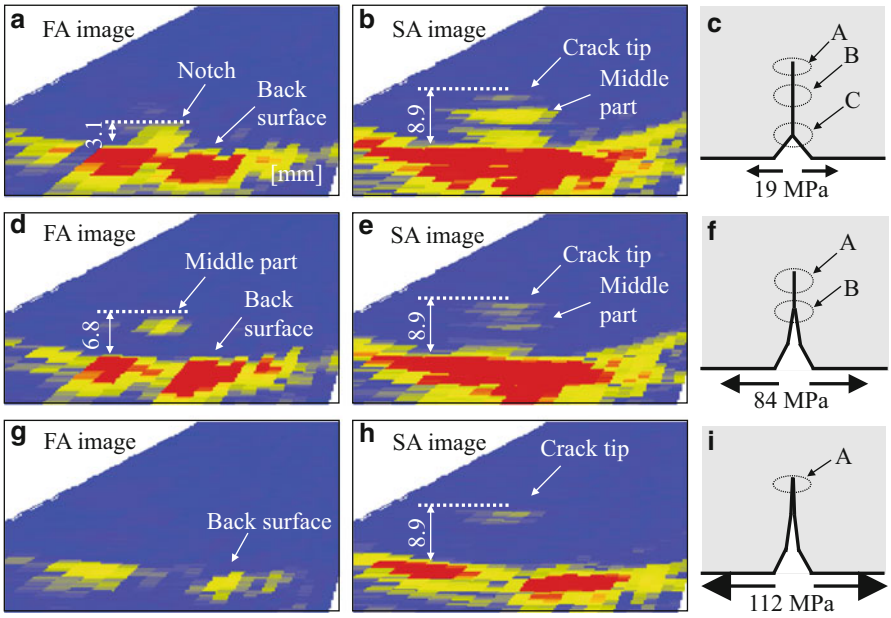

Fig. 10.20 Imaging results of fatigue crack with varying static bending stress. (**a**) FA and (**b**) SA images and (**c**) schematic illustration at the nominal bending stress of 19 MPa. (**d**) FA and (**e**) SA images and (**f**) schematic illustration at the nominal bending stress of 84 MPa. (**g**) FA and (**h**) SA images and (**i**) schematic illustration at the nominal bending stress of 112 MPa. A–C denote the crack tip, middle part, and notch, respectively, in (**c**, **f**, **i**). Modified from [6] (Copyright (2008) The Japan Society of Applied Physics)

At the bending stress of 112 MPa, no part of the crack appeared in the FA image (Fig. 10.20g), although a part of the back surface diminished due to the shade effect of the crack. It is surprising that the response of B observed in Fig. 10.20d disappeared, although the crack was more open. This can be interpreted by assuming that B became the ambiguous boundary between the open and closed regions with the increase in the nominal bending stress. In contrast, A was clearly observed in the SA image (Fig. 10.20h). This suggests that A was still closed.

Surprisingly, the aforementioned results clarified that the crack was tightly closed by a markedly high compression residual stress that was partly relieved by applying the nominal maximum bending stress of more than 100 MPa. Nevertheless, the change in the crack state was successfully imaged while varying the crack closure stress. In addition, the SA images always gave an accurate crack depth, although the FA image caused the underestimation of the crack depth or misdetection. Thus, the developed SPACE is expected to improve nondestructive inspection techniques.

10.4.3 Fatigue Crack Growth Monitoring [41, 42]

To monitor crack growth by SPACE, a compact tension (CT) specimen of which the shape was based on ASTM-E399 was selected (Fig. 10.21a). For the use in ultrasonic testing, the distance between the notch and top surface was 40 mm. The CT specimen was made of aluminum alloy A7075. The fatigue conditions were set to $K_{max} = 9.0$ and $K_{min} = 0.6$ MPa $m^{1/2}$ to form closed cracks. After 48,000 fatigue cycles, the crack had extended to a depth of approximately 5 mm, which was optically observed. Then the first measurement was carried out using SPACE. Subsequently, the fatigue test was continued to 87,000 cycles, after which the crack had extended to depths of 9.6 and 11 mm on the side surfaces, as can be seen in Fig. 10.21b, c. Then, a second measurement was carried out using SPACE, where the experimental configuration is shown in Fig. 10.21a. To monitor the distribution of the crack depths and closure behavior in the length direction, the measurement was carried out at five positions (a, b, c, d, and e) at 48,000 and 87,000 fatigue cycles. The incident wave was three-cycle burst with a center frequency of 7 MHz. Its displacement was measured to be 50 nm with a laser vibrometer. As a receiver, we employed a PZT 31-element array transducer with an element pitch of 0.5 mm and a center frequency of 5 MHz to receive both fundamental and subharmonic components simultaneously. The FA and SA images at 48,000 and 87,000 fatigue cycles and schematic illustrations used for their interpretation are shown in Figs. 10.22 and 10.23, respectively.

After 48,000 fatigue cycles, the middle part B was observed in the FA images (Fig. 10.22d, g, j). This suggests that B became a linear scattering source at a boundary between the open and closed regions. At the measurement positions “a” and “e,” only the notch part C was observed in the FA images (Fig. 10.22a). This suggests that C became a linear scattering source at a distinct boundary between the notch and the closed crack. On the other hand, at all measurement positions,

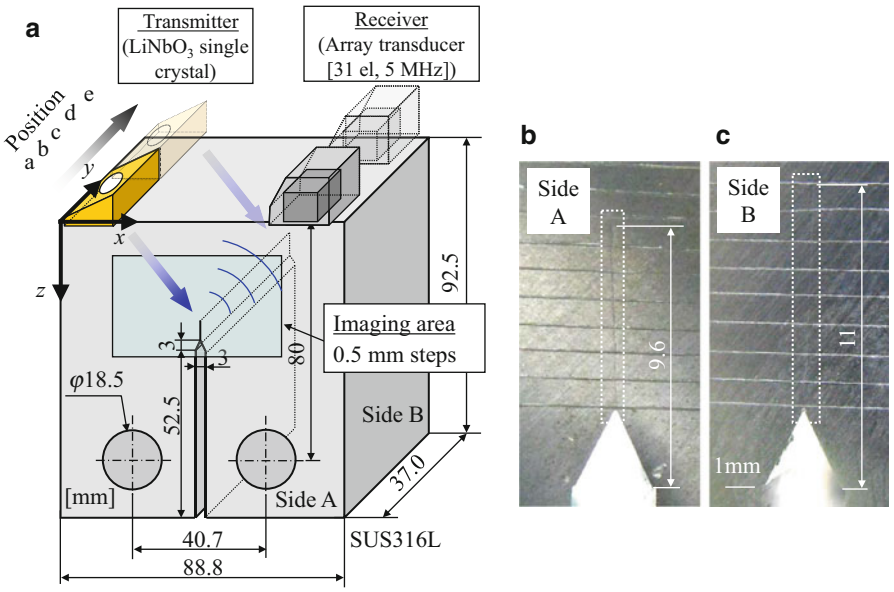

Fig. 10.21 Experimental configuration of SPACE for crack growth monitoring and photographs of side surfaces of specimen. (**a**) Experimental configuration. (**b**) and (**c**) Photographs of crack on the sides A and B, respectively. Modified from [42] (Copyright (2011) IEICE, 17RA0029)

the crack tip A was observed in the SA images (Fig. 10.22b, e, h, k, j). The depths measured in the SA images were larger than those measured in the FA images. These results show that the SA images gave an accurate crack depth irrespective of the measurement position. Also note that the region with a difference in crack depths between the FA and SA images indicated the closed region of the crack.

After 87,000 fatigue cycles, the middle part B was observed in the FA images (Fig. 10.23a, d, g, j). The depth and intensity were greater than those in Fig. 10.22. This suggests that B became a linear scattering source at a distinct boundary between the open and closed regions. At the measurement position "e," the FA image (Fig. 10.23m) gave no indication of any part of the crack. This result can be understood by assuming that the boundary between the open and closed regions became ambiguous, and thus the linear scattering source diminished. In contrast, at all measurement positions, the crack tip A was observed in the SA images (Fig. 10.23b, e, h, k, j). This shows that the crack tip A was still closed, which is favorable for subharmonic generation. Importantly, the SA images always gave an accurate crack depth, irrespective of the number of fatigue cycles and the measurement position, in contrast to the FA images, from which the crack depth was underestimated or the crack was overlooked.

To precisely examine the first and second measurement results, the distribution of crack depths and the closure behavior in the length direction are, respectively, shown in Figs. 10.24 and 10.25. The cracks at the center were deeper than those at

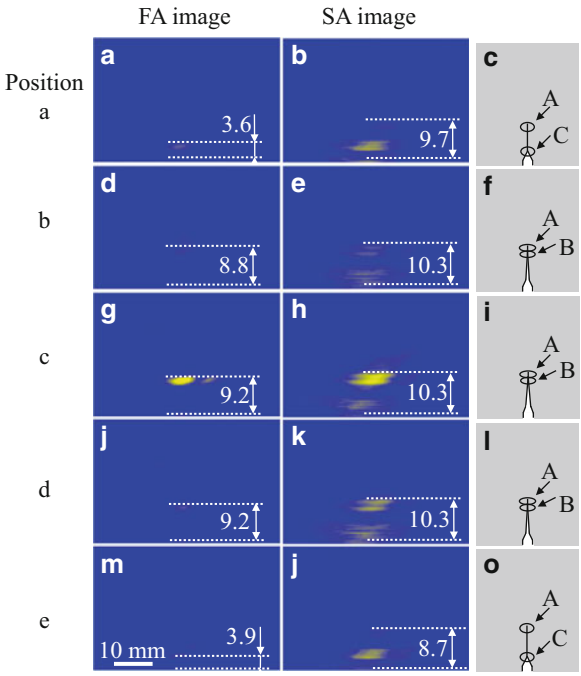

Fig. 10.22 Crack images in the length direction obtained by SPACE at 48,000 fatigue cycles. (**a**) FA and (**b**) SA images and (**c**) schematic illustration at measurement position "a". (**d**) FA and (**e**) SA images and (**f**) schematic illustration at measurement position "b". (**g**) FA and (**h**) SA images and (**i**) schematic illustration at measurement position "c". (**j**) FA and (**k**) SA images and (**l**) schematic illustration at measurement position "d". (**m**) FA and (**n**) SA images and (**o**) schematic illustration at measurement position "e". A–C denote the crack tip, middle part, and notch part, respectively, in (**c**, **f**, **i**, **l**, **o**). Modified from [42] (Copyright(2011) IEICE, 17RA0029)

the edge after each number of fatigue cycles. This is because the tensile stress at the center is larger than that in the vicinity of the edge since the former and the latter are subjected to the conditions of plane strain and plane stress, respectively [43]. This also clearly shows that the crack depths measured in the SA images were greater than those measured in the FA images at each position. Note that the difference was larger in the vicinity of the side surface than at the center, suggesting that the closed region was larger in the vicinity of the side surface than at the center. This can be qualitatively interpreted by the plasticity-induced crack closure proposed by Elber [2] and its extension [44]. A plastically transformed area is formed at the crack tip owing to the stress concentration around the crack tip, which leaves a wake of plastically deformed areas. This causes crack closure, and thus the crack closure depends on the plastic area formed around the crack tip. This fundamental theory can explain the reason why the closed region is larger in the vicinity of the edge than at the center, i.e., the plane stress at the center creates a larger plastic area than the plane strain in the vicinity of the edge [43]. The most striking finding is

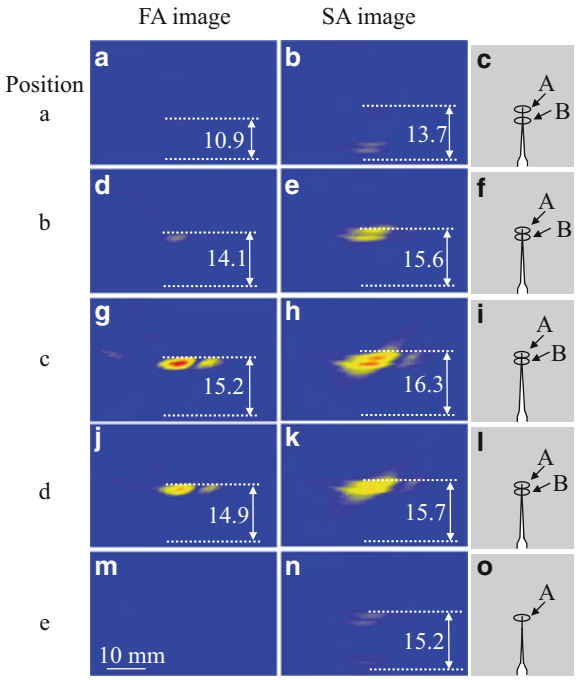

Fig. 10.23 Crack images in the length direction obtained by SPACE at 87,000 fatigue cycles. (**a**) FA and (**b**) SA images and (**c**) schematic illustration at measurement position "a". (**d**) FA and (**e**) SA images and (**f**) schematic illustration at measurement position "b". (**g**) FA and (**h**) SA images and (**i**) schematic illustration at measurement position "c". (**j**) FA and (**k**) SA images and (**l**) schematic illustration at measurement position "d". (**m**) FA and (**n**) SA images and (**o**) schematic illustration at measurement position "e". A–C denote the crack tip, middle part, and notch part, respectively, in (**c**, **f**, **i**, **l**, **o**). Modified from [42] (Copyright(2011) IEICE, 17RA0029)

that in spite of the same fatigue conditions, the percentage of the closed region was 63% in the vicinity of the side surface at 48,000 fatigue cycles, whereas was only 20% at 87,000 cycles. Thus, it was demonstrated that SPACE is useful for not only monitoring crack growth but also measuring the three-dimensional distribution of open and closed parts of cracks.

10.4.4 Closed Cracks Generated in Manufacturing Process [45]

Closed cracks are also a problem in the field of manufacturing. In this section we describe the measurement of cracks generated during the manufacturing of round-bar Ni-Cr-Mo steel. Ni-Cr-Mo steels are widely employed in bearings, shafts, and gears, which are used under harsh conditions. During the manufacturing process, nondestructive methods, such as ultrasonic testing and magnetic flux leakage testing, are generally applied. Nevertheless, some cracks are still difficult to inspect, probably due to crack closure. Cracks are initiated at the outer surface and then propagate inside in an oblique direction. This indicates that cracks initiated during casting or the initial stage of the rolling process are tilted by the rolling process. This also means that cracks are subjected to compression stress by the rolling process. This can result in crack closure.

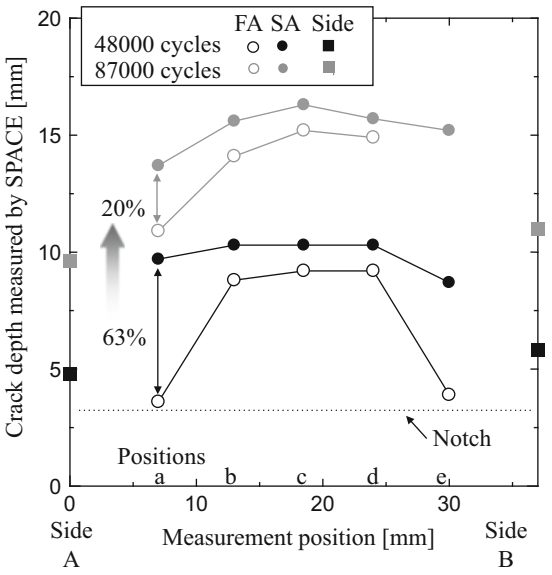

Fig. 10.24 Distribution of crack depths measured by SPACE in the length direction. Modified from [42] (Copyright(2011) IEICE, 17RA0029)

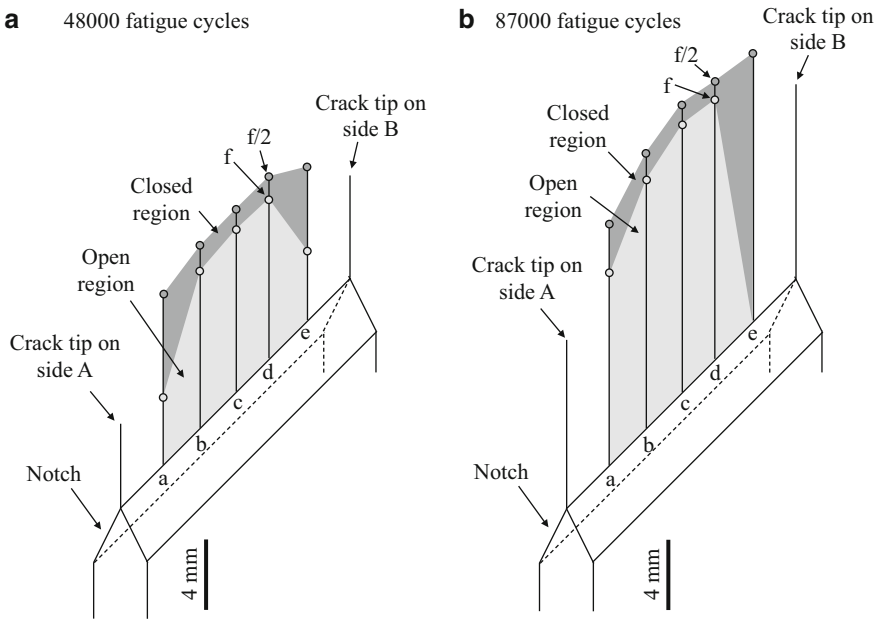

Fig. 10.25 Three-dimensional changes in open and closed regions of a fatigue crack with crack extension. (**a**) 48,000 fatigue cycles, (**b**) 87,000 fatigue cycles [42]. (Copyright(2011) IEICE, 17RA0029)

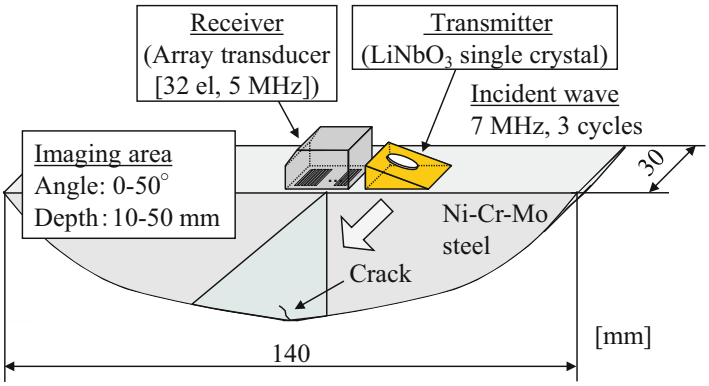

Fig. 10.26 Experimental configuration of SPACE with backscattering configuration for imaging tilted cracks in a round bar made of Ni-Cr-Mo steel

As a fundamental experiment, round-bar Ni-Cr-Mo steel was machined so that the cracks were positioned at the bottom (Fig. 10.26). Three specimens, C1, C2, and C3, were prepared. The experimental configuration is shown in Fig. 10.26, where the backscattering configuration was employed to achieve high sensitivity to such tilted cracks. An LN transmitter was excited by a three-cycle burst wave with a center frequency of 7 MHz. A 32-element PZT array transducer with a center frequency of 5 MHz was employed as a receiver. The distance between the transmitter and the center of the array transducer was 30 mm to receive the backscattering waves.

Figure 10.27 shows the FA and SA images obtained from the C1 specimen. Two tilted cracks, A and B, were observed in both images. For crack A, only the root part was observed in the FA image (Fig. 10.27a), whereas part of the crack tip was observed in the SA image (Fig. 10.27b). This shows that the crack tip was closed, which is favorable for subharmonic generation. On the other hand, for crack B, the crack tip was only imaged in the FA image. This shows that crack B was open. The crack depth was in agreement with an optical observation (Fig. 10.27c). On the other hand, only a single crack was observed in the photograph, although the imaging results show two cracks. This can be understood by assuming that the crack branched inside the specimen.

Figure 10.28 shows the FA and SA images obtained from the C2 specimen. A tilted crack appeared in both images. The response of the crack in the SA image (Fig. 10.28b) was greater than that in the FA image (Fig. 10.28a). This shows that the crack was mainly closed. The crack depth and shape were in agreement with an optical observation (Fig. 10.28c).

Figure 10.29 shows the FA and SA images obtained from C3 specimen. In the FA image (Fig. 10.29a), a tilted crack C was observed. On the other hand, in the SA image (Fig. 10.29b), two tilted cracks, C and D, were observed in parallel. This suggests that crack C had open and closed parts because it was observed in both images. It also suggests that crack D was mainly closed because crack D was only

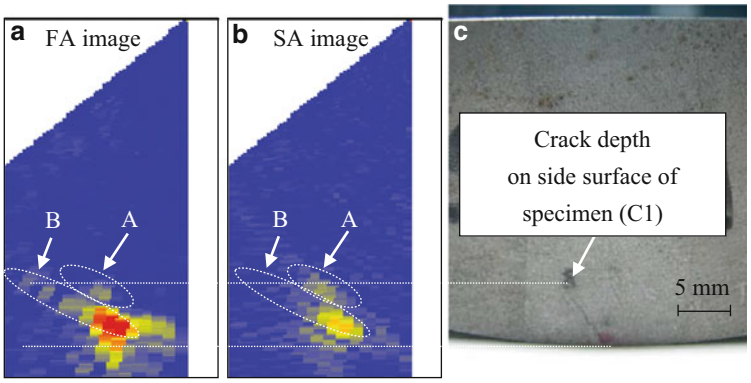

Fig. 10.27 Imaging results obtained from specimen C1 by SPACE with backscattering configuration. (**a**) FA and (**b**) SA images, and (**c**) photograph of the side surface

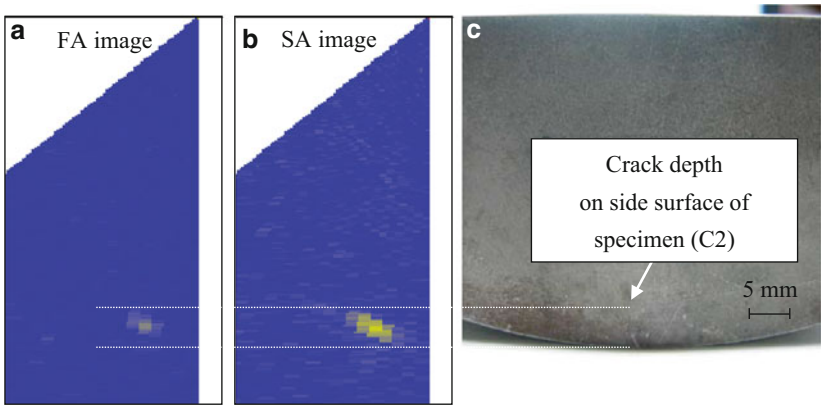

Fig. 10.28 Imaging results obtained from specimen C2 by SPACE with backscattering configuration. (**a**) FA and (**b**) SA images, and (**c**) photograph of the side surface

observed in the SA image. It was confirmed that the crack depth and shape including the branching were similar to those observed in the photographs of the side surface (Fig. 10.29c).

The imaging results and optical observation (Figs. 10.27, 10.28, and 10.29) clearly show that the cracks in specimens C1, C2, and C3 are more complicated than the fatigue cracks described in Sects. 10.4.1, 10.4.2, and 10.4.3. To precisely image complicated cracks, the spatial resolution of images should be increased. The lateral resolution Δr of images satisfies

$$\Delta r = \lambda \frac{z_d}{w_a}, \tag{10.23}$$

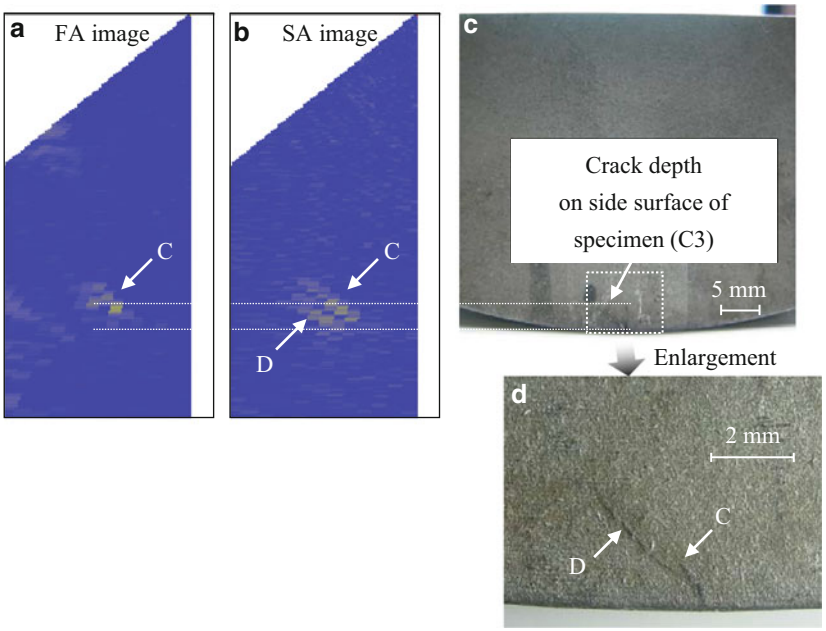

Fig. 10.29 Imaging results obtained from specimen C3 by SPACE with backscattering configuration. (**a**) FA and (**b**) SA images, (**c**) photograph of the side surface, and (**d**) enlarged photograph of rectangle surrounded by dotted line in (**c**)

where λ is the wavelength, z_d is the depth, and w_a is the width of the aperture [46]. From Eq. (10.23), Δr is enhanced as w_a increases.

To examine the dependence of crack images on the aperture of the array transducer in SPACE imaging, specimen C2 was imaged using array transducers with 32 elements and 96 elements. Here the element pitch was fixed to 0.5 mm, and thus the aperture of 96 elements was three times larger than that of 32 elements. To focus on reception, a step of 0.1 mm was employed to precisely examine the effect of the aperture. The imaging results are shown in Fig. 10.30. The crack was observed at the same position in both images. By increasing the aperture from 32 to 96 elements, the crack was extended to the left and right (Fig. 10.30b). This result suggests that the spatial resolution was enhanced and that the 96-element array transducer could receive scattered waves that were not received by the 32-element array transducer. Thus, an array transducer with a large aperture is useful in SPACE imaging. On the other hand, the cost of the array transducer and phased array hardware will increase with the number of elements. Therefore, appropriate imaging conditions should be selected depending on the situation.

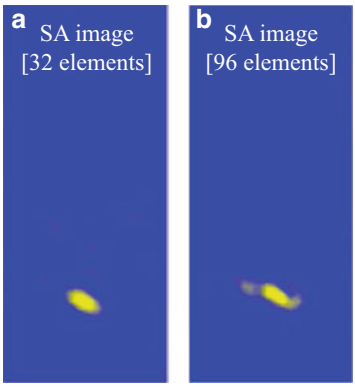

Fig. 10.30 Dependence of crack image (specimen C2) on the aperture of the array transducer. (**a**, **b**) SA images obtained with 32-element and 96-element array transducers, respectively

10.4.5 Stress Corrosion Crack (SCC) Extending from a Deep Fatigue Precrack [47]

The generation of SCCs in nuclear power, thermal power, and chemical plants has been frequently reported. The accurate measurement of SCCs is a key to ensuring the safety and reliability of such plants. The generation of SCCs involves a combination of three factors: the material, the tensile stress, and the corrosivity of the environment. Deep SCCs with depth exceeding 10 mm can endanger the safety of plants. It is, however, difficult to form deep SCCs in the laboratory owing to their low growth rate. Hence, the following method was used to form a deep SCC. The specimen was made of a sensitized austenitic stainless steel (SUS304 sensitized at 600 °C for 4 h). First, a fatigue precrack with approximately 10 mm deep was introduced by carrying out a three-point bending fatigue test. The fatigue conditions were set to $K_{max} = 28$ and $K_{min} = 0.6$ MPa $m^{1/2}$. Subsequently, using SCC apparatus (Fig. 10.31), the SCC was extended from the tip of the fatigue precrack. This apparatus has a cell with a corrosive environment. The entire specimen with a fatigue precrack was immersed under a static bending load of up to 100 kN, which is controlled with a hydraulic pump. The temperature of the corrosive environment is controlled with a thermostat. The growth of the SCC on the side surface of the specimen can be optically monitored in situ through a window in the cell. Here a solution of 30 wt.% $MgCl_2$ at 90 °C was used as the corrosive environment, and a nominal bending stress of 124 MPa was applied for 650 h.

Figure 10.32 shows the experimental configuration. To examine the SCC in the length direction, three positions A, B, and C were selected. An LN transmitter was excited by a three-cycle burst of a 7 MHz sinusoidal wave. The displacement amplitude was measured by a laser vibrometer to be 10.3 nm p-p at crack positions in another specimen cut from the same material. A 64-element PZT array transducer with a center frequency of 5 MHz was employed as a receiver. To focus on reception, images were created at 0.1 mm steps. To receive both forward- and backscattered waves from cracks, the distance between the transmitter and the center of the array transducer was set to 44.5 mm.

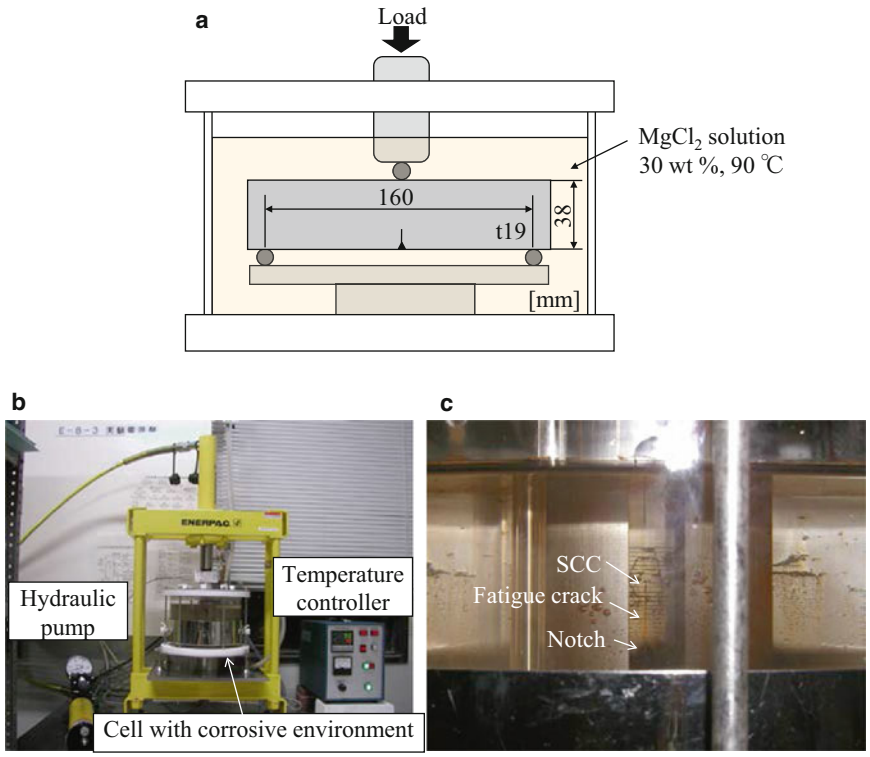

Fig. 10.31 Apparatus used to form deep SCCs. (**a**) Schematic illustration of the cell with a specimen and a corrosive environment. Modified from [47] (Copyright (2009) The Japan Society of Applied Physics). (**b**) Photograph of the entire apparatus. A static load is applied to the specimen in the cell by a hydraulic pump. The temperature of the corrosive environment in the cell is controlled by a temperature controller. (**c**) Enlarged photograph of the crack in the cell

The FA and SA images obtained at measurement positions A, B, and C are shown in Fig. 10.33. At each position, various cracks were successfully imaged. The crack responses in the images appeared not only in the vertical direction but also in the horizontal direction. This result suggests that the SCC did not linearly extend but complexly branched and had open and closed parts. We measured the crack depths from the FA and SA images. It turned out that the crack depths were greater in the SA images than in the FA images at all positions. This shows that the SCC tips were closed. By comparing the results of precise optical observation of cross sections with the imaging results, high measurement accuracy was also confirmed [47].

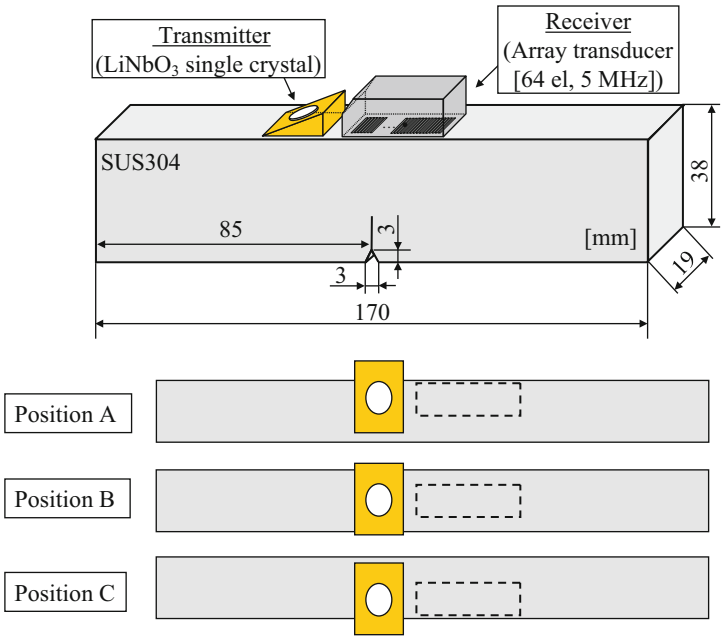

Fig. 10.32 Experimental configuration for imaging SCC in specimen made of stainless steel (SUS304). Modified from [47] (Copyright (2009). The Japan Society of Applied Physics)

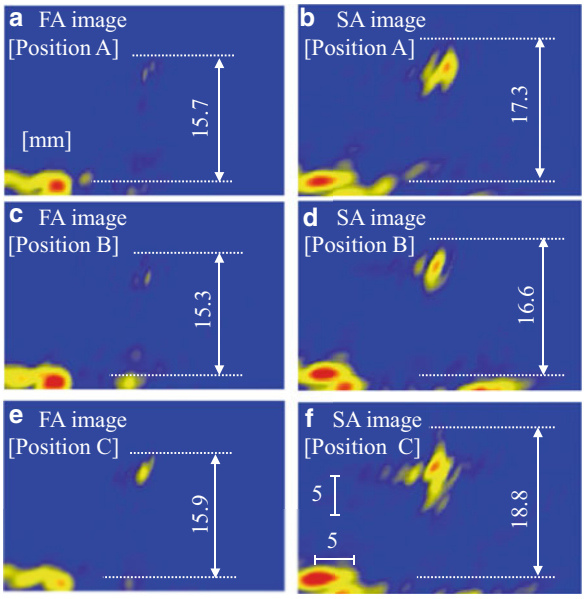

Fig. 10.33 Comparison of the FA and SA images of the SCC specimen. (**a**) FA and (**b**) SA images at measurement position A. (**c**) FA and (**d**) SA images at measurement position B. (**e**) FA and (**f**) SA images at measurement position C. Modified from [47] (Copyright (2009). The Japan Society of Applied Physics)

10.4.6 SCC Formed in a Weld Under Realistic Conditions [40]

In this section we describe the measurement of a realistic SCC specimen formed in an environment very similar to that of actual nuclear power plants. In nuclear power plants, the high-temperature pressurized water (HTPW) at a temperature of around 300 °C in pipelines produces an active corrosive environment. As a result, SCCs are generated even in stainless steels. To simulate an SCC generated in actual nuclear reactors, similar conditions such as the specimen material, stress, and environment should be selected. A sensitized stainless steel (SUS304) was used as the material of the specimen used here. The SCC was introduced in a heat-affected zone (HAZ) of a welded pipe by a tensile residual stress, where the corrosive environment was HTPW at 288 °C in an autoclave. The pipe specimen was machined to a bar shape for ultrasonic testing. Note that the specimen had coarse grains, which are linear scattering sources. The maximum grain size was approximately 200 μm, which is similar to that for materials used in actual nuclear power plants.

Figure 10.34 shows the experimental configuration. A 32-element PZT array transducer with a center frequency of 5 MHz was excited by a three-cycle burst with 7 MHz frequency and a voltage of 150 Vp-p. The position of the transducer was set to avoid the weld metal with strong anisotropy and high attenuation. Three hundred TFPs with $\theta = 12$–$71°$ (1° steps) and $r = 12$–42 mm (7.5 mm steps) were employed to image over a wide area.

Radarlike displays of FA and SA images for $\theta = 36$–$42°$ are shown in Fig. 10.35, where the white lines represent incident directions. In the single-focus FA image for $\theta = 36°$, many bright points were imaged over a wide area in the single-focus FA image (Fig. 10.35a), whereas point A was only imaged in the vicinity of the incident direction in the single-focus SA image (Fig. 10.35d).

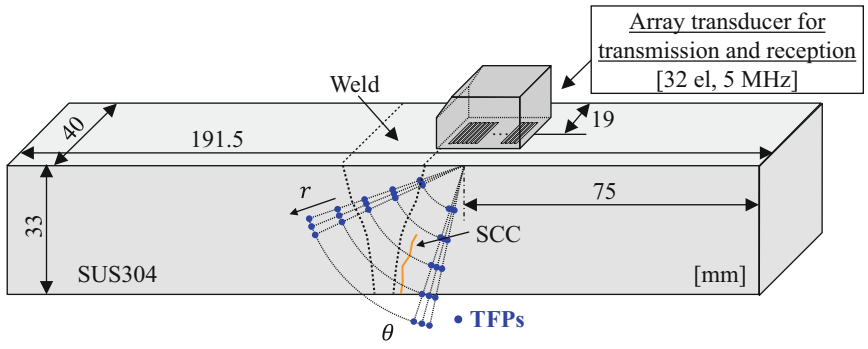

Fig. 10.34 Experimental configuration for imaging SCC formed in SUS304 in a heat-affected zone (HAZ) in high-temperature pressurized water (HTPW). Modified from [40] (Copyright (2015) The Japan Society of Applied Physics)

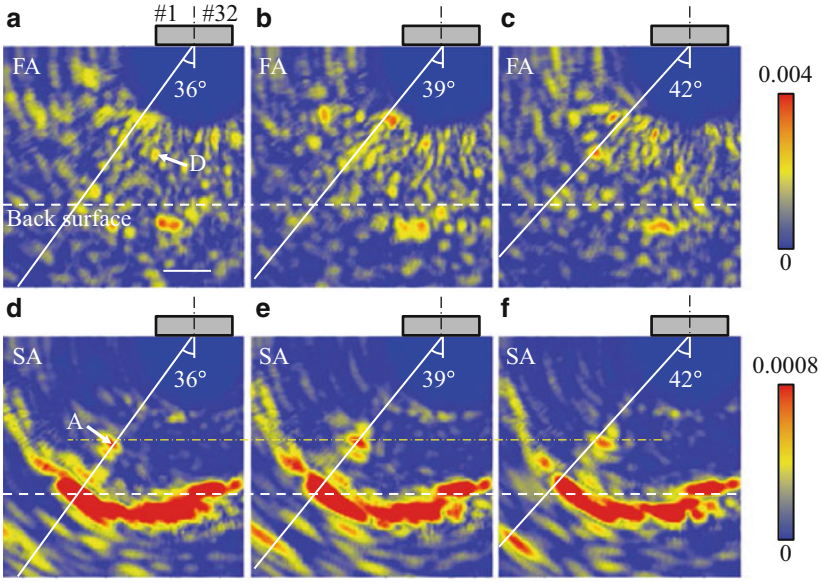

Fig. 10.35 Radarlike displays of unmoving crack response. (**a**–**c**) Single-focus FA images and (**d**–**f**) single-focus SA images for $\theta = 36, 39, 42°$, respectively [40]. (Copyright (2015) The Japan Society of Applied Physics)

To discuss the above results, we analyzed an incident sound field using the finite-difference time-domain (FDTD) method [48]. Here, we define the stress ratio as

$$\beta\,(\mathbf{r},\ \ t) = \frac{T_c\,(\mathbf{r},\ \ t)}{\sigma_C}, \tag{10.24}$$

where $\mathbf{r}$ is the position vector, $T_c(\mathbf{r},\ \ t)$ is the tensile stress of an incident wave at a crack, and σ_c is the crack closure stress. The maximum of $\beta(\mathbf{r},\ \ t)$ is defined as the maximum stress ratio, $\beta_{\max}(\mathbf{r})$.

A snapshot of the tensile stress in the x direction at $t = 5.85$ μs is shown in Fig. 10.36a. The maximum stress ratio $\beta_{\max}$ along the line OR in Fig. 10.36a was plotted against the angle ϕ formed by the z-axis and the line OR in Fig. 10.36b. It was confirmed that an incident wave had a large amplitude in the vicinity of $\phi = 36°$, which was due to the effect of beam focusing. In contrast, over a wide area including the area away from the incident direction, a small-amplitude wave appeared. These simulation results show that the linear scattering at coarse grains appeared as the bright points in the FA image. In contrast to the FA image, point A was only imaged in the vicinity of the incident direction of the large-amplitude wave in the SA image. This shows that point A was an SCC.

In addition, we analyzed the responses at points D and A in Fig. 10.35. Figure 10.37 shows the shift-summation waveforms for points D and A and the results of

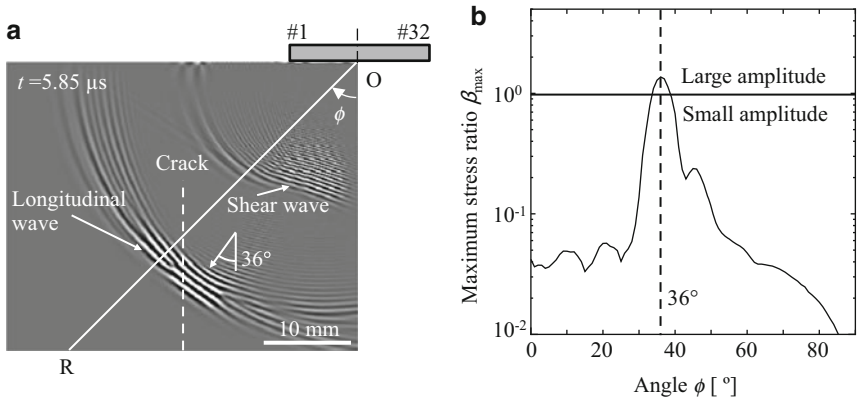

Fig. 10.36 Sound fields for $\theta = 36°$ calculated in simulation. (**a**) Snapshot at $t = 5.85$ μs that only shows the tensile stress in the x direction of the incident wave and (**b**) dependence of the maximum stress ratio β_{max} on angle ϕ [40]. (Copyright (2015) The Japan Society of Applied Physics)

their frequency analysis. The fundamental component for point D was dominant, as shown in Fig. 10.37c, showing that linear scattering at coarse grains appeared at point D. In contrast, the generation of subharmonic waves was clearly observed for point A, as shown in Fig. 10.37d, suggesting that the closed part of the SCC appeared at point A. Furthermore, point A did not move upon varying θ from 36 to 42°, as shown in Fig. 10.35d–f. This behavior can be understood by assuming that point A was the branched crack tip or a winding point on the crack.

Figure 10.38 shows radarlike display of single-focus FA and SA images for $\theta = 50$–56°. For $\theta = 50°$, point B was imaged in the single-focus SA image (Fig. 10.38d). Figure 10.39a, c shows shift-summation waveform for point B and the results of the frequency analysis. The generation of subharmonic waves was clearly observed. This suggests that point B was closed part of the SCC. Moreover, we found that the depth of point B increased to point C upon varying θ from 50 to 56° (Fig. 10.38e, f). For point C, the subharmonic generation was confirmed, as shown in Fig. 10.39b, d. We call this behavior a moving crack response (MCR). Although unmoving responses upon varying θ, as shown by point A, have previously been observed, this MCR upon varying θ, as shown by point B, was observed for the first time. It is assumed that the MCR is attributed to the change in the crack opening point (COP), where the tensile stress of an incident wave is equal to the tensile stress of an incident wave.

To image the closed SCC over a wide area, merged FA and SA images were created by merging single-focus FA and SA images for multiple TFPs, as shown in Fig. 10.40a, b, respectively. The merged FA image indicated the linear scattering at coarse grains over a wide area, similarly to the single-focus FA images. In contrast, the merged SA image indicated points A, B, and C. This is because large-amplitude incident waves covered the entire region of interest, as shown in Fig. 10.40c. In the merged SA image, the crack depth was 19.5 mm. This is comparable to the optically

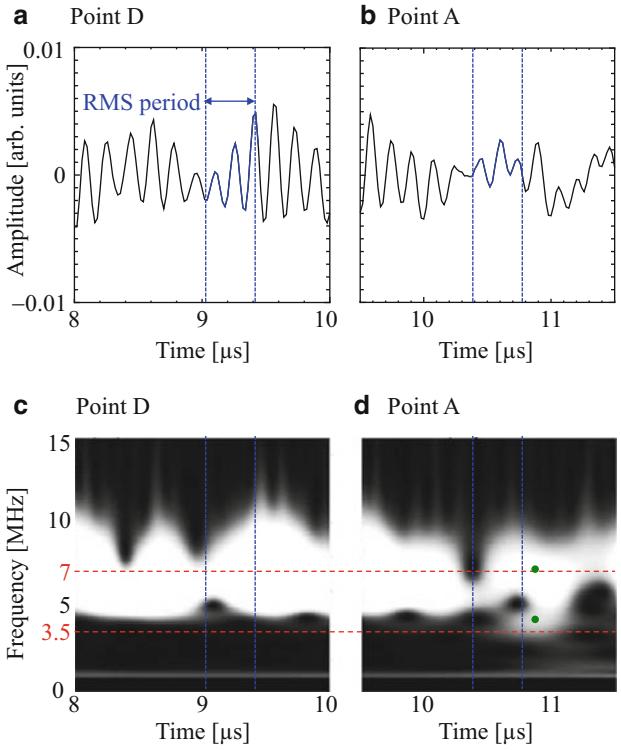

Fig. 10.37 Shift-summation waveforms for points D and A in Fig. 10.35 and their frequency analysis. (**a**) Shift-summation waveform for point D and (**b**) shift-summation waveform for point A. (**c**) Result of wavelet analysis for point D and (**d**) result of wavelet analysis for point A [40]. (Copyright (2015) The Japan Society of Applied Physics)

measured crack depth of 14.5 mm. Thus, it was demonstrated that confocal SPACE is useful for measuring closed-crack depths even in coarse-grained stainless steels.

To interpret the observed phenomena and extract useful information from them, the dependence of the scattering behavior on the incident angle was analyzed by the FDTD method using a damped double node (DDN) model [49, 50].

The DDN model in the FDTD method was proposed for the two-dimensional (2D) analysis of subharmonic generation at closed cracks. For the calculation of particle velocities and stresses by the FDTD method, staggered grids (Fig. 10.41) are used, as shown in Fig. 10.41, where $T_1 = \sigma_{xx}$ and $T_3 = \sigma_{zz}$ are the tensile stresses, $T_5 = \sigma_{xz}$ is the shear stress, $\dot{u}$ and $\dot{w}$ are the particle velocities in the x- and z-directions, respectively. Figure 10.41a shows the closed state, where crack faces are represented by normal nodes. Figure 10.41b shows the open state, where normal nodes are split into double nodes consisting of the particle velocity $\dot{u}^-$ of the incidence-side crack face and the particle velocity $\dot{u}^+$ of the transmission-side crack face. As shown by the gray circle in Fig. 10.41b, crack faces with compression

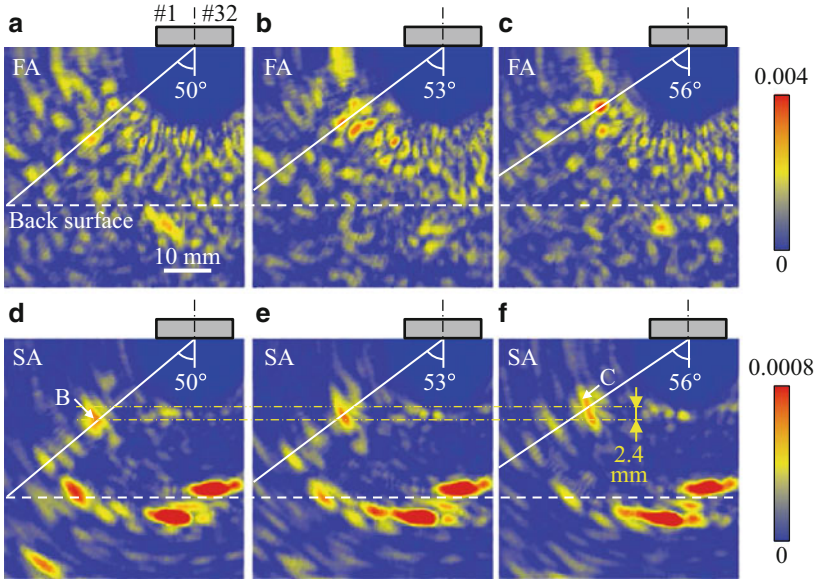

Fig. 10.38 Radarlike displays of moving crack response (MCR). (**a**–**c**) Single-focus FA images and (**d**–**f**) single-focus SA images for $\theta = 50, 53, 56°$, respectively [40]. (Copyright (2015) The Japan Society of Applied Physics)

residual stress were simulated by introducing viscous damping into the double nodes, which can also suppress the noise. The following criteria define the transition between the closed and open states.

1. In the closed state, the average tensile stress T_{1M} at the crack is used for the judgment of criteria. As shown in the following equation, T_{1M} is calculated as the average of the stresses of the left and right nodes of $i-1$ and i.

$$T_{1M} = \frac{1}{2}\left[T_1^n\,(i,\ \ j) + T_1^n\,(i-1,\ \ j)\right], \tag{10.25}$$

where n is the time step. If $T_{1M} \le \sigma_C$, the nodes remain closed, and if $T_{1M} > \sigma_C$, the nodes are open, where the threshold for the transition is σ_C.

2. In the open state, it is assumed that the particle velocity nodes $\dot{u}^+$ and $\dot{u}^-$ at the crack are subject to viscous damping proportional to the difference between the particle velocities $\dot{u}^+$ and $\dot{u}$, and thus

$$\dot{u}^{+^{n+1}}\,(i,\ \ j) = \dot{u}^{+^n}\,(i,\ \ j) + 2V_{PL}T_1^n\,(i,\ \ j) - \gamma\left[\dot{u}^{+^n}\,(i,\ \ j) - \dot{u}^n\,(i+1,\ \ j)\right], \tag{10.26}$$

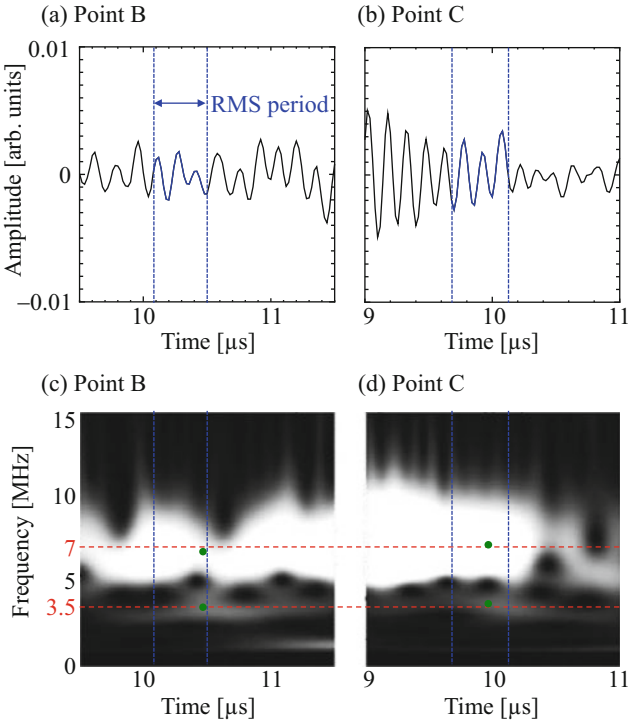

Fig. 10.39 Shift-summation waveforms for points B and C in Fig. 10.38 and their frequency analysis. (**a**) Shift-summation waveform for point B and (**b**) shift-summation waveform for point C. (**c**) Results of wavelet analysis for point B and (**d**) result of wavelet analysis for point C. The positions shown by green dots indicate locations where the subharmonic ratio was measured [40]. (Copyright (2015) The Japan Society of Applied Physics)

where γ is the damping coefficient and V_{PL} is the Courant factor. Likewise,

$$\dot{u}^{-n+1}(i,\ j) = \dot{u}^{-n}(i,\ j) + 2V_{PL}T_1^n(i-1,\ j) - \gamma\left[\dot{u}^{-n}(i,\ j) - \dot{u}^{n}(i-1,\ j)\right]. \tag{10.27}$$

The crack opening displacement is given by

$$\Delta u^n = u^{+n} - u^{-n}, \tag{10.28}$$

where u^+ and u^- are the particle displacements on the transmission-side and incidence-side crack faces, which are calculated by integrating $\dot{u}^+$ and $\dot{u}^-$, respectively. If $\Delta u > 0$, the crack remains the open state, and if $\Delta u \leq 0$, the crack is transited to the closed state.

A simulation model with a vertical closed crack based on the DDN model is shown in Fig. 10.42. To simulate the specimen in the experiment, the parameters

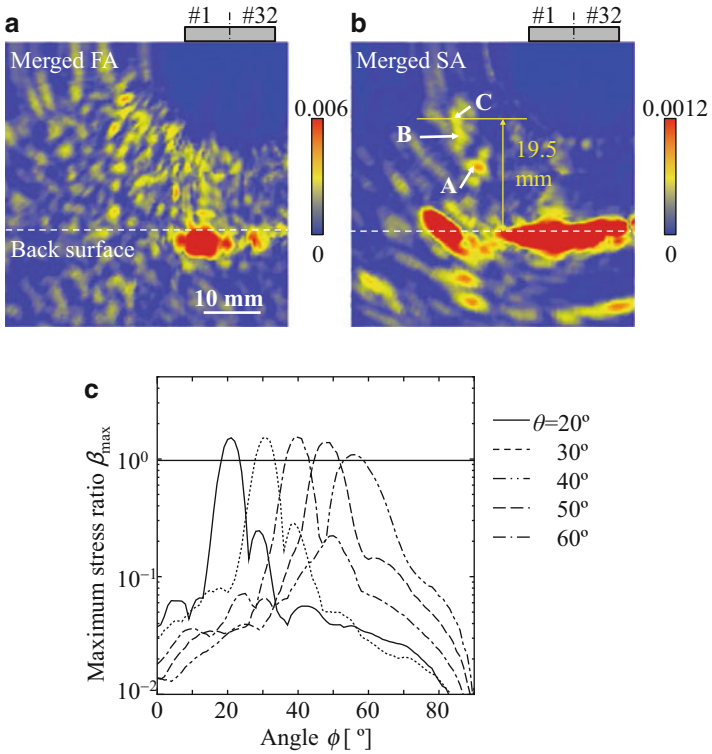

Fig. 10.40 Merged images. (**a**) Merged FA image, (**b**) merged SA image, and (**c**) angle ϕ dependence of the maximum stress ratio β_{max} for different incident angles θ [40]. (Copyright (2015) The Japan Society of Applied Physics)

Table 10.2 Parameters used for 2D simulation with DDN model

Discretization	Node interval (μm)	Time interval (ns)	Damping coefficient γ	Density ρ (kg/m^3)	Elastic constant ratio C_{44}/C_{11}
5000 × 1650	13	1.727	0.3	8000	0.296

listed in Table 10.2 were used. Gaussian windowed five-cycle burst waves with a frequency of 7 MHz were focused at $\theta = 50$ and 56° ($r = 27$ mm) to reproduce the scattering behavior observed in the experiment. For $\theta = 50^\circ$, we set $\beta_{max} = 1.13$ at $z = 17.3$ mm, where $\beta_{max}(\mathbf{r})$ was the maximum at the crack.

Figure 10.43 shows snapshots of the displacement in the x direction for $\theta = 50^\circ$. The crack was opened at the COP by the incident wave, as shown in Fig. 10.43b. Subsequently, the incident wave opened the lower part continuously along the crack face. This behavior continued to the crack closure point (CCP), where the tensile stress became less than σ_c (Fig. 10.43c).

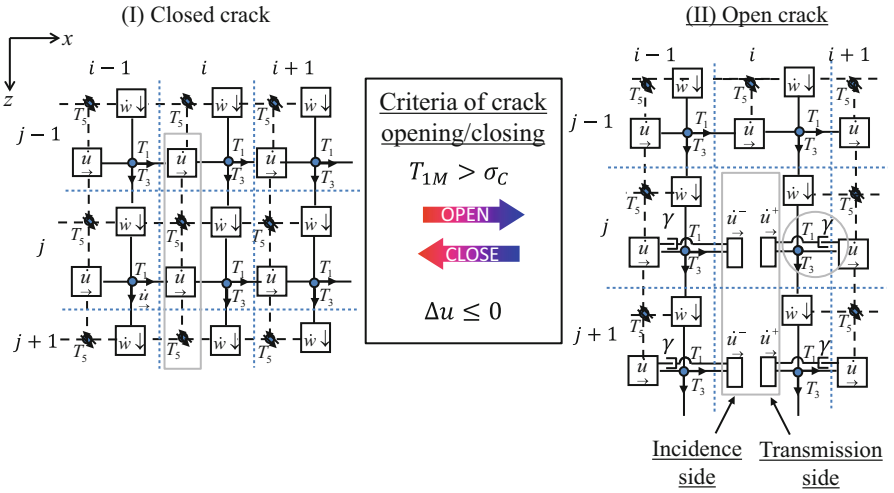

Fig. 10.41 FDTD model of closed crack with DDN. The gray rectangle represents the double nodes and the gray circle indicates the damper

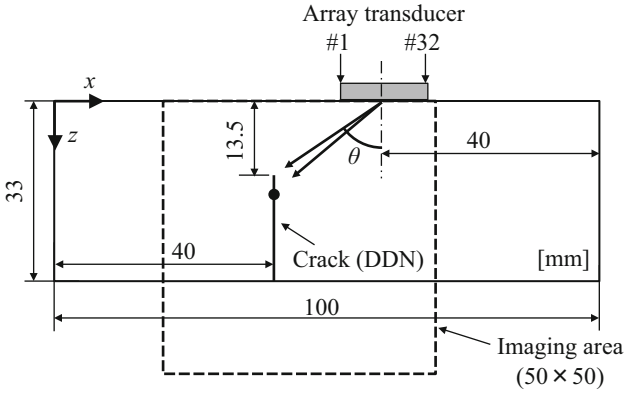

Fig. 10.42 Simulation model to reproduce the experiment. A closed crack was modeled based on the DDN model [40]. (Copyright (2015) The Japan Society of Applied Physics)

SA images created on the basis of the received waves in the simulation are shown in Fig. 10.44a, b. The COP and CCP were clearly observed. It should be noted that the center of the COP moved from the dashed-dotted line ($\theta = 50^\circ$) to the dashed-two-dotted line ($\theta = 56^\circ$). Thus, the MCR was successfully reproduced in the simulation. In snapshots of the displacement in the x direction, the COP and CCP moved upward from $\theta = 50^\circ$ (Fig. 10.44c) to $\theta = 56^\circ$ (Fig. 10.44d). This may be caused by the change in the tensile stress distribution of the incident wave in the crack with the increase in θ. This shows that the MCR is attributed to the changes in the COP and CCP.

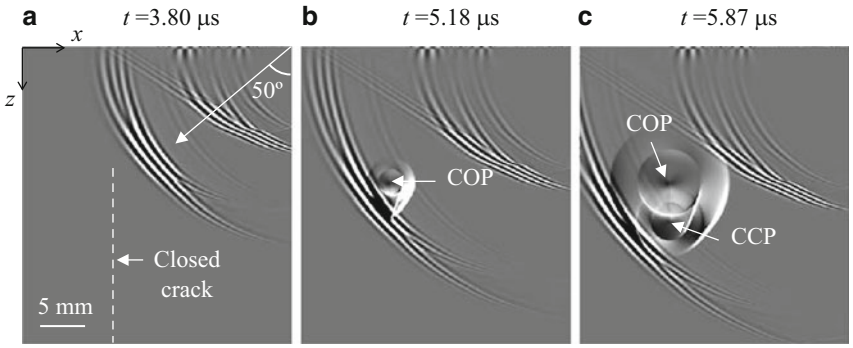

Fig. 10.43 Snapshots of the particle displacement in the x direction for $\theta = 50^{\circ}$. (**a**) $t = 3.80$ μs, (**b**) $t = 5.18$ μs, and (**c**) $t = 5.87$ μs. Taken from [40] (Copyright (2015) The Japan Society of Applied Physics)

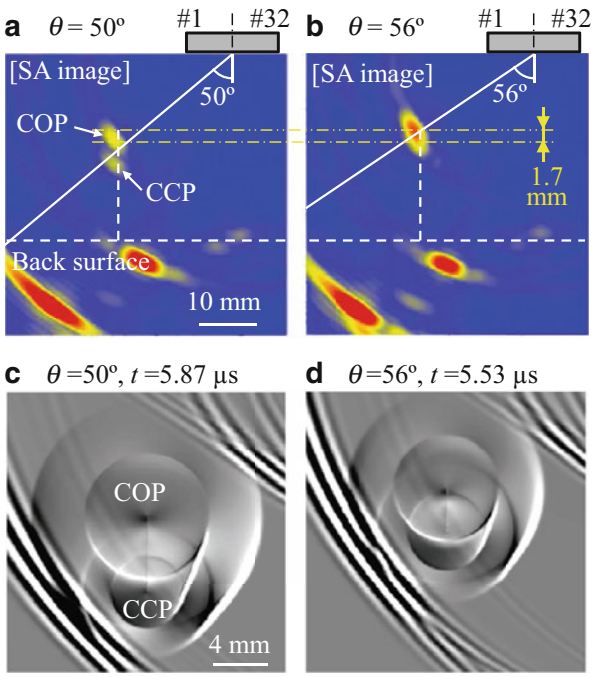

Fig. 10.44 Simulation results for different θ. Single-focus SA image (**a**) for $\theta = 50^{\circ}$ and (**b**) for $\theta = 56^{\circ}$, respectively. (**c**) Snapshots of the particle displacement in the x direction (**c**) for $\theta = 50^{\circ}$, $t = 5.87$ μs and (**d**) for $\theta = 56^{\circ}$, $t = 5.53$ μs, respectively [40]. (Copyright (2015) The Japan Society of Applied Physics)

10.4.7 SPACE Using Surface Acoustic Wave (SAW) [51, 52]

In this section we describe another type of SPACE that uses a SAW to measure the crack length. The crack length, which represents the size of a crack in the direction perpendicular to the crack depth, is also one of the important factors determining the material strength of structures. For the measurement of crack

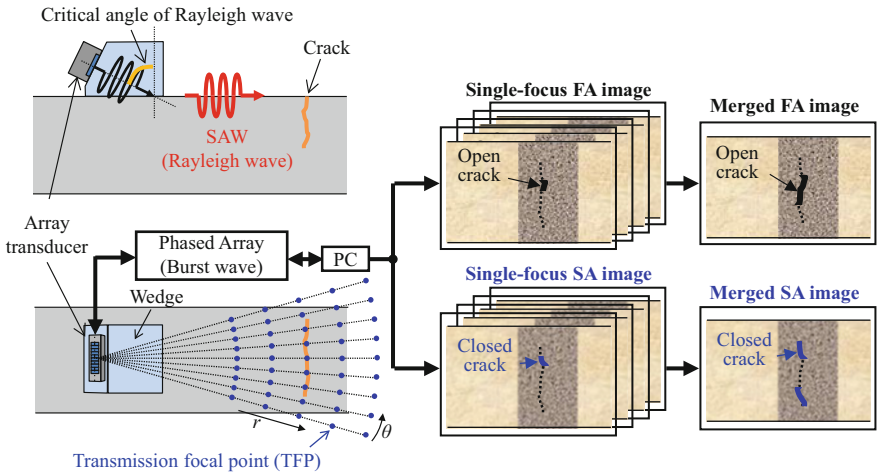

Fig. 10.45 Schematic of SAW SPACE with a wedge and surface acoustic wave (SAW)

length, the measurement from the side opposite to the crack opening is insufficient in terms of sensitivity because the depth in the edge of a crack in the length direction is generally small. To overcome this issue, we have developed SPACE with a SAW that is a Rayleigh wave.

Figure 10.45 shows the first implementation of SAW SPACE used for contact testing with a wedge that has a critical angle of the Rayleigh wave. An array transducer is employed for transmission and reception. Here the array transducer is placed on the wedge. The array transducer is positioned on the crack opening side, which is the opposite side to that for SPACE using bulk waves. The Rayleigh wave is focused at the TFP from the array transducer through a wedge in accordance with the delay law [52], which is formulated on the basis of Fermat's principle. By transmitting a Rayleigh wave to cracks, linear and nonlinear scattering takes place at the open and closed cracks, respectively. After the scattered waves are received by the array transducer, they are filtered around fundamental and subharmonic frequencies. Subsequently, they are delay-and-summed to create single-focus FA and single-focus SA images. For multiple TFPs, this process is repeated; thereafter, the images in the vicinity of the TFPs are merged to create an image of the cracks over the entire region of interest.

In our experiment, a fatigue crack was formed in a specimen made of an aluminum alloy (A7075) by carrying out a three-point bending fatigue test [5]. The fatigue conditions were set to $K_{\max} = 5.3$ and $K_{\min} = 0.6$ MPa $m^{1/2}$. The experimental configuration is shown in Fig. 10.46. A 32-element PZT array transducer with a center frequency of 5 MHz and an element pitch of 0.5 mm was employed. The input signals were a three-cycle burst with a frequency of 2 MHz, where the frequency was selected with consideration of the attenuation of the longitudinal wave in the acrylic resin wedge, the leaky loss of the Rayleigh wave,

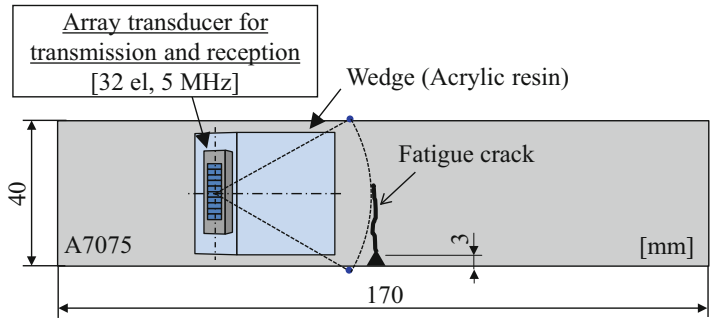

Fig. 10.46 Experimental configuration of SPACE with SAW for imaging a fatigue crack in an aluminum alloy (A7075)

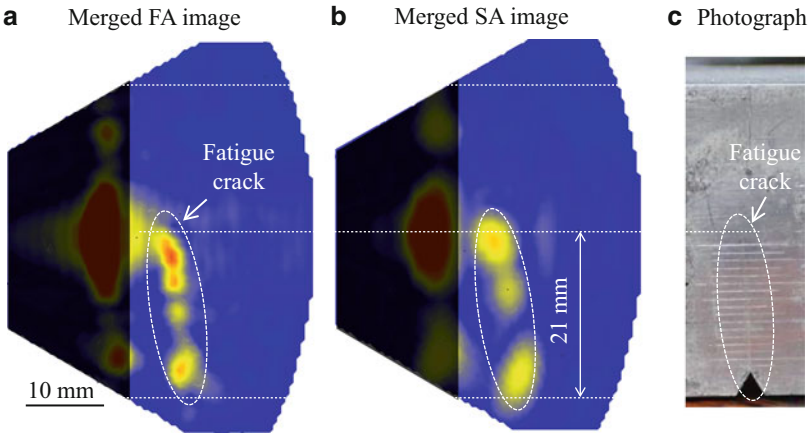

Fig. 10.47 Results of imaging a fatigue crack by SPACE with a SAW. (**a**) FA and (**b**) SA images, (**c**) photograph of side surface around the crack

and the transmission loss of the Rayleigh wave at the edge of the wedge. The wedge was made of acrylic resin because of its low cost and high workability. The wedge angle was 64°, which was the critical angle of the Rayleigh wave. Sixty TFPs with $\theta = -29$ to 30° (1° steps) and $r = 39.5$ mm were selected.

The results of imaging the fatigue crack are shown in Fig. 10.47. The fatigue crack was clearly observed in both the FA and SA images (Fig. 10.47a, b). The distributions of the crack responses were similar in both images, whereas the intensities differed. The crack lengths measured from the FA and SA images were almost the same as that measured by optical observation (Fig. 10.47c).

Furthermore, the interaction between the SAW and the cracks was directly observed by measuring the waveforms propagating on the top surface of the specimen by mechanically scanning a laser vibrometer (Fig. 10.48). The measurement area was 10 mm by 10 mm around the fatigue crack tip. Figure 10.49 shows

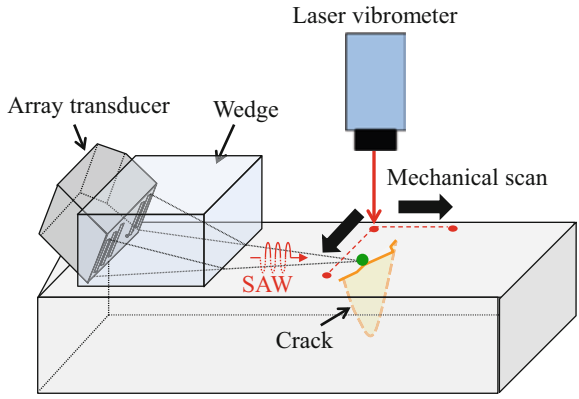

Fig. 10.48 Experimental configuration of direct observation of SAW propagating through the fatigue crack by scanning the laser vibrometer

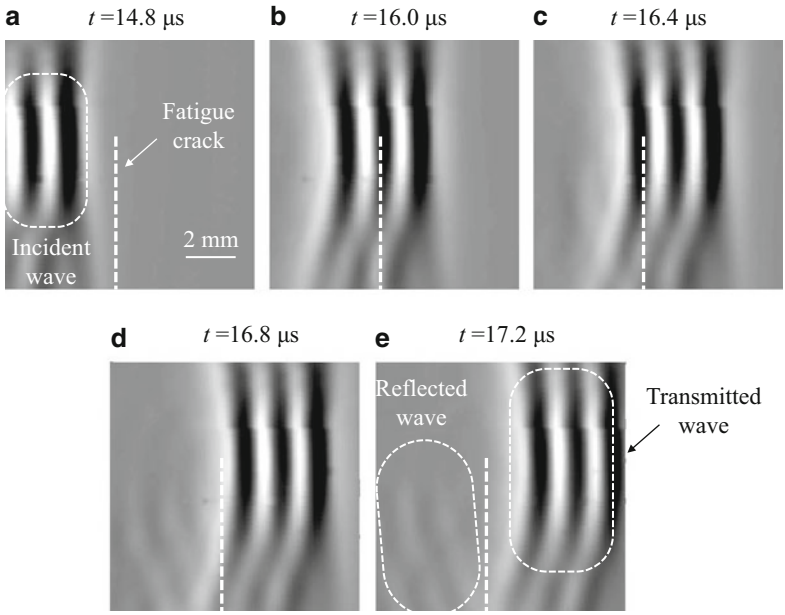

Fig. 10.49 Direct observation of SAW propagating through the fatigue crack by scanning a laser vibrometer. The white dashed line denotes the position of the fatigue crack

snapshots that show the behaviors of Rayleigh wave propagating through the fatigue crack. At $t = 14.8$ μs, the Rayleigh wave propagated to the fatigue crack from the left (Fig. 10.49a). At $t = 16.0$–16.4 μs, most of the Rayleigh wave was transmitted through the fatigue crack (Fig. 10.49b, c). At $t = 16.8$–17.2 μs, a small reflected wave was observed. This is direct evidence of the closure of the fatigue crack. Thus, it was demonstrated that the direct observation of a SAW by scanning a laser vibrometer is a powerful tool for clarifying the nonlinear interaction between a SAW and cracks and linear/nonlinear scattering behaviors.

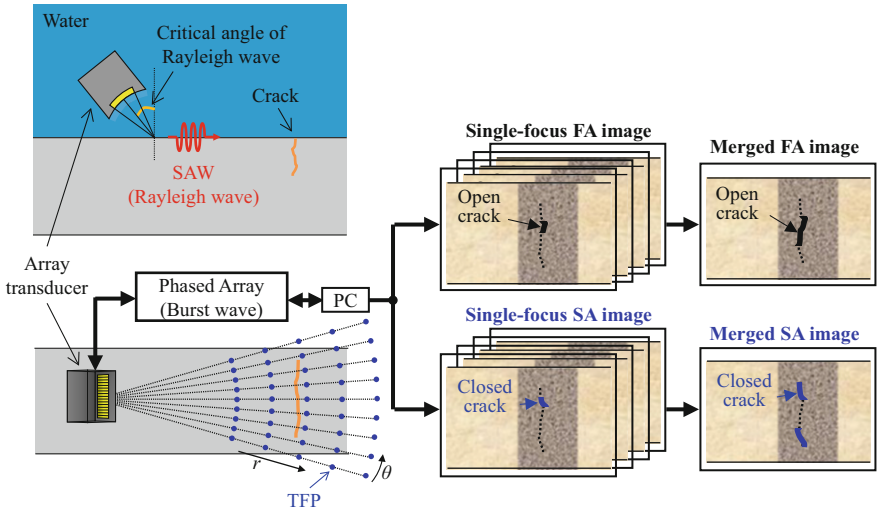

Fig. 10.50 Schematic of SAW SPACE used for water immersion testing. Modified from [52] (Copyright (2015) The Japan Society of Applied Physics)

As described above, the fatigue crack was imaged at the correct position by SAW SPACE with the wedge made of acrylic resin (Fig. 10.47). However, the spatial resolution was low because of the use of a low frequency (2 MHz). To achieve a higher resolution, SAW SPACE in water was proposed as shown in Fig. 10.50. For transmission and reception, a concave array transducer is employed. The array transducer was set so that the incident angle equals to a critical angle of a Rayleigh wave. By exciting each element in accordance with the delay law, [52] a SAW is focused at a TFP on the top surface of specimens. The imaging algorithm is the same as that for SAW SPACE with the wedge.

In an experiment, the same fatigue crack specimen (A7075) as that of Fig. 10.47 was used. The experimental configuration is shown in Fig. 10.51. A 32-element PZT array transducer with a center frequency of 15 MHz and an element pitch of 0.5 mm was selected. Each element of the array transducer was excited by a three-cycle burst of frequency 10 MHz with a voltage of 150 V. Two hundred and forty TFPs with $\theta = -39$ to 40° (1° steps) and $r = 33.4$–37.4 mm (2 mm steps) were set. To obtain high-resolution images over a large area, we performed five measurements at 8 mm intervals in the length direction.

The results of imaging the fatigue crack are shown in Fig. 10.52. The fatigue crack appeared in both FA and SA images (Fig. 10.52a, b). Note that the spatial resolution in Fig. 10.52 was even higher than that in Fig. 10.47. The distributions of the crack responses were similar in both images, whereas the intensities differed. The crack lengths measured from the FA and SA images were almost the same as that measured by optical observation (Fig. 10.52c).

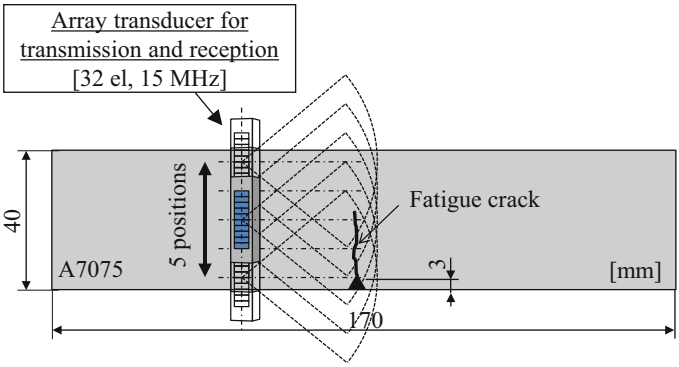

Fig. 10.51 Experimental configuration of SAW SPACE in water for imaging a fatigue crack in aluminum alloy A7075

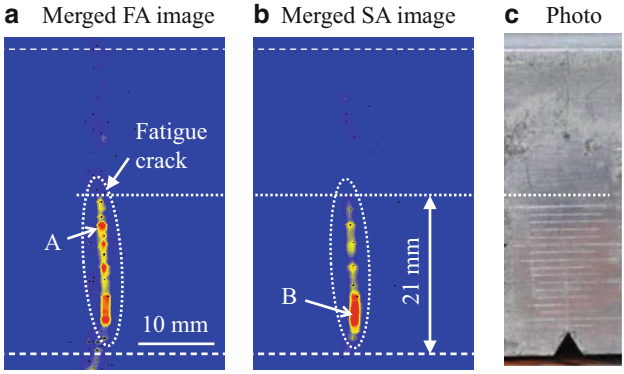

Fig. 10.52 Results of imaging a fatigue crack by SAW SPACE in water. (**a**) FA image, (**b**) SA image, (**c**) photograph of side surface of the specimen. Modified from [52] (Copyright (2015) The Japan Society of Applied Physics)

In addition, we analyzed the responses with high intensities, which are points A and B in the FA and SA images (Figs. 10.52a, b), respectively. Figure 10.53 shows the shift-summation waveforms for points A and B and their wavelet analysis. For point A (Fig. 10.53c), the fundamental component was dominant, suggesting that point A in the crack was open. In contrast, for point B (Fig. 10.53d), the generation of subharmonic waves was observed, suggesting that point B in the crack was closed.

Thus, it was demonstrated that SAW SPACE is useful in measuring crack lengths. SAW SPACE with a wedge can be readily applied to structures, whereas SAW SPACE in water can achieve a high resolution. An appropriate method should be selected depending on the situation.

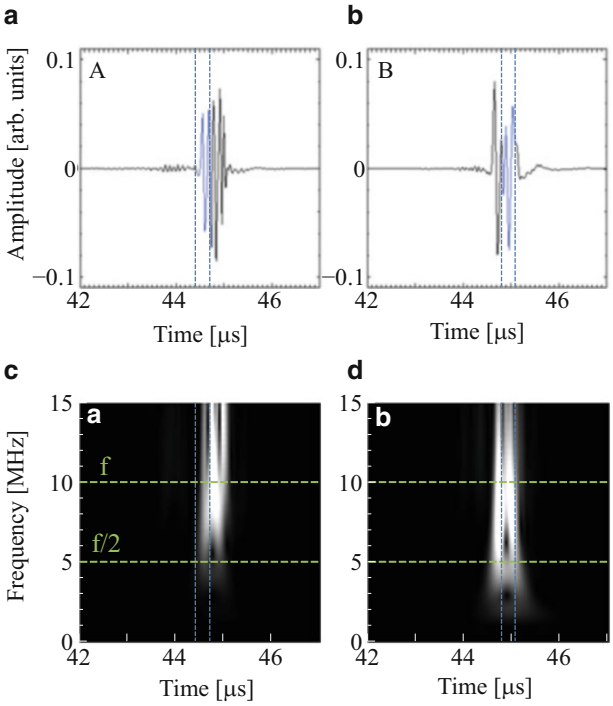

Fig. 10.53 Shift-summation waveforms for points A and B in Fig. 10.52 and their wavelet analysis. (**a**) Shift-summation waveform for point A and (**b**) shift-summation waveform for points B. (**c**) Result of wavelet analysis for point A and (**d**) result of wavelet analysis for point B [52]. (Copyright (2015) The Japan Society of Applied Physics)

10.5 Conclusions

This chapter has presented an overview of the development of an imaging method for closed cracks, subharmonic phased array for crack evaluation (SPACE), to accurately measure closed-crack depths. It is known that the mechanism of subharmonic generation is different from that of other nonlinear components. To explain the mechanism, analytical and numerical solutions for subharmonic generation were derived. In the analytical theory, a simplified model based on a model developed in the field of atomic force microscopy (AFM) was introduced. By introducing an adhesion force into a model comprising an oscillator with a damper, the threshold behavior of subharmonic generation was reproduced well. The validity of the simplified model was confirmed by comparison with experimentally observed subharmonics. In the numerical simulation, an elastic-body-oscillator model was directly solved to reproduce the subharmonic generation including the waveforms. The experimentally observed subharmonic waveforms were found to be reproduced well by the numerical simulation. The dependence of subharmonic generation on

the crack closure stress and incident wave amplitude was in good agreement with experimental results. In the theoretical and experimental studies, we found that subharmonics has high selectivity for closed cracks and a high temporal resolution, which are useful in increasing the spatial resolution and the selectivity for closed cracks in ultrasonic imaging.

On the basis of these significant findings, we have developed SPACE, which uses the subharmonics generated by short-burst waves and a phased array algorithm with frequency filtering. SPACE provides fundamental array (FA) and subharmonic array (SA) images that show open and closed cracks, respectively. The principle and imaging algorithm of SPACE were described. Then we introduced several examples of its application such as the identification of open and closed cracks, crack-closure-stress dependence, closed-crack growth monitoring, and the measurement of the depths of cracks generated in steel manufacturing process and stress corrosion cracks (SCCs). Thus, the usefulness of SPACE was demonstrated in terms of its high measurement accuracy of crack depth and high selectivity for closed cracks. Also the behavior of experimentally observed nonlinear scattering was analyzed by two-dimensional (2D) simulation using the finite-difference time-domain (FDTD) method with a damped double node (DDN) model. Furthermore, SPACE with a surface acoustic wave (SAW) was also described as a means of measuring crack lengths. The use of both SPACE with bulk waves and SAW can provide the accurate 2D crack shape, which enables the material strength of structures to be estimated more precisely.

In this chapter we described the fundamental applications of SPACE. On the other hand, SPACE-related studies have been widely carried out. In the examples introduced, an array transducer with a piezoelectric material was employed in SPACE, whereas the scanning of a laser vibrometer can be replaced into a receiver because it enables a flexible element pitch, a flexible number of elements, and a flat broadband receiving characteristics [53, 54]. To achieve higher selectivity for closed cracks, amplitude-difference and load-difference methods can be used [39, 55–57]. SPACE uses subharmonics with lower frequency than the fundamental frequency, and thus the spatial resolution for subharmonics is lower than that for fundamentals and superharmonic frequencies. To achieve a higher resolution in SA images, a combination of SPACE with a signal processing algorithm, such as multiple signal classification (MUSIC), will be useful [54].

Finally we describe the possible expansion of the range of SPACE applications. In actual industrial applications such as power plants, most of the cracks have been accurately measured by conventional ultrasonic methods, meaning that most of them may be open. However, it is difficult to measure the crack depth even for open cracks when the scattering noise due to the weld microstructures is greater than the crack tip echo. In this case, it is impossible to separate the crack tip echo from the scattering noise by frequency filtering since the scattering noise and the crack tip echo have the same frequency as the incident wave. For this problem, an even larger incidence in SPACE may be a solution. In SPACE, an incident amplitude on the order of tens of nm has been used to image closed cracks. If the amplitude of incident wave increases to the order of the crack opening displacement (COD) or the

distance between the asperities on the crack faces, subharmonics can be generated even at open cracks by the contact vibration of the crack faces. In this case, a crack tip echo with subharmonic frequency can be separated from the scattering noise by frequency filtering. In addition, subharmonics is less attenuative than fundamentals because the subharmonic frequency is half of the fundamental frequency. This concept can be applied to the inspection of highly attenuative materials such as concrete structures. The development of a high-output transmitter for SPACE will be an important research topic in nondestructive evaluation [58].

Acknowledgements It is our great pleasure to thank all those who have collaborated with us in the development of SPACE. Financial support by Japan Society for the Promotion of Science (JSPS) KAKENHI (Grants-in-Aid for Scientific Research) and other various projects for part of the work described in this chapter is gratefully acknowledged.

References

1. J. Blitz, G. Simpson, *Ultrasonic Methods of Non-Destructive Testing* (Chapman & Hall, London, 1996)
2. W. Elber, Fatigue crack closure under cyclic tension. Eng. Fract. Mech. **2**, 37–45 (1970)
3. J.D. Frandsen, R.V. Inman, O. Buck, A comparison of acoustic and strain gauge techniques for crack closure. Int. J. Fract. **11**, 345–348 (1975)
4. S. Horinouchi, M. Ikeuchi, Y. Shintaku, Y. Ohara, K. Yamanaka, Evaluation of closed stress corrosion cracks in Ni-based alloy weld metal using subharmonic phased array. Jpn. J. Appl. Phys. **51**, 07GB15-1–07GB15-5 (2012)
5. Y. Ohara, T. Mihara, R. Sasaki, T. Ogata, S. Yamamoto, Y. Kisihimoto, K. Yamanaka, Imaging of closed cracks using nonlinear response of elastic waves at subharmonic frequency. Appl. Phys. Lett. **90**, 011902-1–011902-3 (2007)
6. Y. Ohara, S. Yamamoto, T. Mihara, K. Yamanaka, Ultrasonic evaluation of closed cracks using subharmonic phased array. Jpn. J. Appl. Phys. **47**, 3908–3915 (2008)
7. Y. Zheng, R.G. Maev, I.Y. Solodov, Nonlinear acoustic applications for material characterization: A review. Can. J. Phys. **77**, 927–967 (1999)
8. K.-Y. Jhang, Nonlinear ultrasonic techniques for nondestructive assessment of micro damage in material: a review. Int. J. Precis. Eng. Manuf. **10**(1), 123–135 (2009)
9. I.Y. Solodov, C.A. Vu, Popping nonlinearity and chaos in vibrations of a contact interface between solids. Acoust. Phys. **39**, 476–479 (1993)
10. I.Y. Solodov, Ultrasonics of non-linear contacts: propagation, reflection and NDE-applications. Ultrasonics **36**, 383–390 (1998)
11. I.Y. Solodov, N. Krohn, G. Busse, CAN: an example of nonclassical acoustic nonlinearity in solids. Ultrasonics **40**, 621–625 (2002)
12. B.A. Korshak, I.Y. Solodov, E.M. Ballad, DC effects, sub-harmonics, stochasticity and "memory" for contact acoustic non-linearity. Ultrasonics **40**, 707–713 (2002)
13. I. Solodov, J. Wackerl, K. Pfleiderer, G. Busse, Nonlinear self-modulation and subharmonic acoustic spectroscopy for damage detection and location. Appl. Phys. Lett. **84**, 5386–5388 (2004)
14. K. Yamanaka, T. Mihara, T. Tsuji, Evaluation of closed cracks by model analysis of subharmonic ultrasound. Jpn. J. Appl. Phys. **43**, 3082–3087 (2004)
15. Y. Ohara, T. Mihara, K. Yamanaka, Effect of adhesion force between crack planes on subharmonic and DC responses in nonlinear ultrasound. Ultrasonics **44**, 194–199 (2006)

16. T. Hayashi, S. Biwa, Subharmonic wave generation at interfaces of a thin layer between metal blocks. Jpn. J. Appl. Phys. **52**, 07HC02-1–07HC02-6 (2013)
17. I. Solodov, G. Busse, Nonlinear air-coupled emission: the signature to reveal and image microdamage in solid materials. Appl. Phys. Lett. **91**, 251910-1–251910-3 (2007)
18. A. Moussatov, V. Gusev, B. Castagnede, Self-induced hysteresis for nonlinear acoustic waves in cracked material. Phys. Rev. Lett. **90**(2), 124301-1–124301-4 (2003)
19. A.E. Ekimov, A.V. Lebedev, L.A. Ostrovskii, A.M. Sutin, Nonlinear acoustic effects due to cracks in ice cover. Acoust. Phys. **42**(1), 51–54 (1996)
20. M. Akino, T. Mihara, K. Yamanaka, Fatigue crack closure analysis using nonlinear ultrasound. AIP Conf. Proc. **700**, 1256–1263 (2004)
21. J.M. Richardson, Harmonic generation at an unbonded interface – I. Planar Interface between semi-infinite elastic media. Int. J. Eng. Sci. **17**, 73–85 (1979)
22. B. O'Neill, R.G. Maev, F. Severin, Distortion of shear waves passing through a friction coupled interface. AIP Conf. Proc. **557**, 1261–1267 (2001)
23. P.M. Shankar, P.D. Krishna, V.L. Newhouse, Subharmonic backscattering from ultrasound contrast agents. J. Acoust. Soc. Am. **106**(4), 2104–2110 (1999)
24. P. Palanchon, A. Bouakaz, J. Klein, N.D. Jong, Subharmonic and ultraharmonic emissions for emboli detection and characterization. Ultrasound Med. Biol. **29**(3), 417–425 (2003)
25. F.M. Severin, I.Y. Solodov, Experimental observation of acoustic demodulation in reflection from a solid-solid interface. Sov. Phys. Acoust. **35**(4), 447–448 (1989)
26. K. Yamanaka, H. Ogiso, O. Kolosov, Ultrasonic force microscopy for nanometer resolution subsurface imaging. Appl. Phys. Lett. **84**(2), 178–180 (1994)
27. O. Kolosov, K. Yamanaka, Nonlinear detection of ultrasonic vibrations in an atomic force microscope. Jpn. J. Appl. Phys. **32**, L1095–L1098 (1993)
28. N.A. Burnham, A.J. Kulik, G. Gremaud, P.-J. Gallo, F. Oulevey, Scanning local-acceleration microscopy. J. Vac. Sci. Technol. B **14**(2), 794–799 (1996)
29. E.M. Abdel-Rahman, A.H. Nayfeh, Contact force identification using the subharmonic resonance of a contact-mode atomic force microscopy. Nanotechnology **16**, 199–207 (2005)
30. V. Gusev, B. Castagnede, A. Moussatov, Hysteresis in response of nonlinear bistable interface to continuously varying acoustic loading. Ultrasonics **41**, 643–654 (2003)
31. K. Yamanaka, H. Ogiso, O. Kolosov, Analysis of subsurface imaging and effect of contact elasticity in the ultrasonic force microscope. Jpn. J. Appl. Phys. **33**, 3197–3203 (1994)
32. K. Inagaki, O. Matsuda, O.B. Wright, Hysteresis of the cantilever shift in ultrasonic force microscopy. Appl. Phys. Lett. **80**(13), 2386–2388 (2003)
33. C. Pecorari, Adhesion and nonlinear scattering by rough surfaces in contact: beyond the phenomenology of the Presisach-Mayergoyz framework. J. Acoust. Soc. Am. **116**(4), 1938–1947 (2004)
34. K. Yamanaka, Y. Ohara, S. Yamamoto, H. Endo, Analysis of subharmonic phased Array for crack evaluation (SPACE) using elastic-body-oscillator model. AIP Conf. Proc. **1022**(577), 577–580 (2008)
35. Y. Ohara, Nondestructive evaluation of closed cracks by nonlinear ultrasound, PhD Thesis, Tohoku University, Sendai, 2007
36. S.R. Bishop, M.G. Thompson, S. Foale, Prediction of period-1 impacts in a driven beam. Proc. R. Soc. London Sec. A **452**, 2579–2592 (1996)
37. A.B. Pippard, *The Physics of Vibrations I* (Cambridge University Press, Cambridge, 1978)
38. D. Maugis, *Contact, Adhesion and Rupture of Elastic Solid* (Springer, Berlin, 1999)
39. Y. Ohara, Y. Shintaku, S. Horinouchi, M. Ikeuchi, K. Yamanaka, Enhancement of selectivity in nonlinear ultrasonic imaging of closed cracks using amplitude difference phased array. Jpn. J. Appl. Phys. **51**, 07GB18-1–07GB18-6 (2012)
40. A. Sugawara, K. Jinno, Y. Ohara, K. Yamanaka, Closed-crack imaging and scattering behavior analysis using confocal subharmonic phased array. Jpn. J. Appl. Phys. **54**, 07HC08-1–07HC08-8 (2015)
41. Y. Ohara, H. Endo, M. Hashimoto, Y. Shintaku, K. Yamanaka, Monitoring growth of closed fatigue crack using subharmonic phased array. AIP Conf. Proc. **1211**, 903–909 (2010)

42. H. Ohara, M. Hashimoto, M. Horinouchi, Y. Shintaku, K. Yamanaka, Closed crack growth monitoring using nonlinear ultrasonic imaging method. IEICE Trans. Fundam. Electron. Commun. Comput. Sci. **J94-A**(11), 800–808 (2011)
43. S.P. Timoshenko, J.N. Goodier, *Theory of Elasticity* (McGraw-Hill, New York, 1970)
44. A. Steuwer, M. Rahman, A. Shterenlikht, M.E. Fitzpatrick, L. Edwards, P.J. Withers, The evolution of crack-tip stresses during a fatigue overload event. Acta Mater. **58**, 4039–4052 (2010)
45. Y. Ohara, K. Yamanaka, Measurement of invisible cracks by ultrasonics: development of subharmonic phased array for crack evaluation (SPACE). Inspect. Eng. **13**(5), 8–14 (2008)
46. J.W. Goodman, *Introduction to Fourier Optics* (Roberts & Co, Englewood, 2004)
47. Y. Ohara, H. Endo, T. Mihara, K. Yamanaka, Ultrasonic measurement of closed stress corrosion crack depth using subharmonic phased array. Jpn. J. Appl. Phys. **48**, 07GD01-1–07GD01-6 (2009)
48. M. Sato, Comparing three methods of free boundary implementation for analyzing elastodynamics using the finite-difference time-domain formulation. Acoust. Sci. Tech. **28**(1), 49–52 (2007)
49. K. Yamanaka, Y. Ohara, M. Oguma, Y. Shintaku, Two-dimensional analyses of subharmonic generation at closed cracks in nonlinear ultrasonics. Appl. Phys. Express **4**, 076601-1–076601-3 (2011)
50. K. Jinno, A. Sugawara, Y. Ohara, K. Yamanaka, Analysis on nonlinear ultrasonic images of vertical closed cracks by damped double node model. Mater. Trans. **55**(7), 1017–1023 (2014)
51. A. Ouchi, A. Sugawara, Y. Ohara, K. Yamanaka, Subharmonic phased array for crack evaluation using refraction and/or mode conversion at an interface. Proc. Symp. Ultrason. Electron. **35**, 259–260 (2014)
52. A. Ouchi, A. Sugawara, Y. Ohara, K. Yamanaka, Subharmonic phased Array for crack evaluation using surface acoustic wave. Jpn. J. Appl. Phys. **54**, 07HC05-1–07HC05-6 (2015)
53. S. Yamamoto, Y. Ohara, T. Mihara, K. Yamanaka, Application of laser interferometer to subharmonic phased array for crack evaluation (SPACE). J. Jpn. Soc. Nondestr. Insp. **57**(4), 198–203 (2008)
54. C.-S. Park, J.-W. Kim, S. Cho, D.-C. Seo, A high resolution approach for nonlinear subharmonic imaging. NDT&E Int. **79**, 114–122 (2016)
55. M. Ikeuchi, K. Jinno, Y. Ohara, K. Yamanaka, Improvement of closed crack selectivity in nonlinear ultrasonic imaging using fundamental wave amplitude difference. Jpn. J. Appl. Phys. **52**, 07HC08-1–07HC08-6 (2013)
56. Y. Ohara, S. Horinouchi, M. Hashimoto, Y. Shintaku, K. Yamanaka, Nonlinear ultrasonic imaging method for closed cracks using subtraction of responses at different external loads. Ultrasonics **51**, 661–666 (2011)
57. Y. Ohara, K. Takahashi, S. Murai, K. Yamanaka, High-selectivity imaging of closed cracks using elastic waves with thermal stress induced by global preheating and local cooling. Appl. Phys. Lett. **103**, 031917-1–031917-5 (2013)
58. T. Mihara, G. Konishi, Y. Miura, H. Ishida, Accurate sizing of closed crack using nonlinear ultrasound of SPACE with high voltage transformer pulser technique. AIP Conf. Proc. **1581**, 727–732 (2014)

Chapter 11
A Unified Treatment of Nonlinear Viscoelasticity and Non-equilibrium Dynamics

H. Berjamin, G. Chiavassa, N. Favrie, B. Lombard, and C. Payan

11.1 Introduction

Understanding and modeling the complex coupling between nonlinear elasticity, non-equilibrium phenomena, and nonlinear attenuation during dynamic solicitation in geomaterials and consolidated granular media is of great interest in earth science and civil engineering. These so-called "nonclassical" [1] or "mesocopic" [2] class of materials exhibit two different, time-dependent, nonlinear mechanisms. The first is called fast dynamics. It relates the classical Landau and Lifshitz [3] nonlinear behavior by introducing higher order elastic constants. The latter is called slow dynamics, it relates the decrease of the elastic properties when subjected to high amplitude strain vibration (order 10^{-6}) as well as the slow, logarithmic in time, recovery (order 10^3 s) of initial properties. In rocks, experimental evidence of such a class of materials has been reported from decades [4–6]. It has been shown that all of these mechanisms play a role in understanding earthquake triggering [7–9], soils characterization [10, 11], and the dynamic response of buildings during ground motion [12]. The high sensitivity to microstructural changes of the nonlinear behavior in cement based materials is also of interest for nuclear energy within the actual context of license renewal [13, 14]. The physical origin of the nonlinear behavior of such solids is not fully understood yet. Although it has been established that contacts and soft boundaries between grains at the microstructural

H. Berjamin · B. Lombard · C. Payan (✉)
Aix Marseille Univ, CNRS, Centrale Marseille, LMA, Marseille, France
e-mail: cedric.payan@univ-amu.fr

N. Favrie
Aix Marseille Univ, CNRS, IUSTI, Marseille, France

G. Chiavassa
Aix Marseille Univ, CNRS, Centrale Marseille, M2P2, Marseille, France

T. Kundu (ed.), *Nonlinear Ultrasonic and Vibro-Acoustical Techniques for Nondestructive Evaluation*, https://doi.org/10.1007/978-3-319-94476-0_11

scale [1] contribute to the overall behavior. At this scale, authors state the role of thermal mechanisms [15, 16] as well as adhesion forces [16, 17]. Up to date, to model this complex nonlinear behavior, the literature mainly makes use of the Preisach–Mayergoyz model issued from electromagnetism [18, 19]. However, even if this phenomenological description successfully reproduces some experimental observations, it lacks in providing physical data related to the material. More physical approaches have been explored to describe slow dynamics [5, 16, 20] or hysteresis [17, 21] but none of them are able to describe the mutual interaction between fast and slow dynamics during dynamical loading. An original approach describing the entire coupling was proposed by Vakhnenko et al. [22, 23] but due to analytical derivation considerations, the mutual coupling was broken. Moreover, the attenuation was supposedly linear which is known to be also nonlinear [4]. Recent studies proposed in the literature [24] come back to this model including nonlinear viscoelasticity, and show its ability to reproduce every nonlinear signature (harmonic generation, softening, recovery, hysteresis). However, one can show [25] that several drawbacks such as violation of the second principle of thermodynamics or difficulty to extend this model to higher dimensions deters its use for practical applications with low predictive abilities.

Starting from the basic principles of continuum mechanics and thermodynamics, we present here a generalized model, including nonlinear viscoelasticity as well as a robust way to solve the entire problem. This model is a general framework allowing to describe the full nonlinear and non-equilibrium mechanisms as well as their mutual interactions occurring during dynamic solicitation using a limited number of physical parameters. It aims to relate the key nonlinear features reported in recent experimental data recently published in the literature using Dynamic Acousto Elasticity (DAE) [26, 27] or Nonlinear Resonance Ultrasound Spectroscopy (NRUS) [13, 28].

The chapter is organized as follows. In the first section, the governing equations are presented. The second section presents a numerical implementation based on finite-volume methods. In the third section, the numerical method is used to reproduce DAE and NRUS experiments.

11.2 Physical Modeling

A Cartesian coordinate system $(x_1 x_2 x_3)$ is used. We consider a continuum in the Lagrangian representation of motion, whose length L along the x_1-axis is very large compared to its other dimensions. Only longitudinal vibrations are considered. Thus, we make the approximation of a planar displacement field $\mathbf{u}$, which is described by its component $u_1(x_1, t)$ along the x_1-axis, oriented by the unit-vector $\mathbf{e}_1$. In the first subsection, 1D nonlinear elastodynamics is presented. Then, internal-variable modeling of the slow dynamics is achieved in agreement with the 3D model from [25]. Lastly, viscoelasticity is incorporated in a similar fashion to [24].

11.2.1 Nonlinear Elastodynamics

If no body force is applied to the material, the equation of motion reduces to $\varrho \ddot{u}_1 = \sigma_{11,1}$, where self-gravitation and heat transfer are neglected. This rewrites as a differential system of the form

$$\begin{cases} \dot{\varepsilon}_{11} = v_{1,1} \,, \\ \varrho \dot{v}_1 = \sigma_{11,1} \,, \end{cases} \tag{11.1}$$

where σ_{11} is the stress, $\varepsilon_{11} = u_{1,1} > -1$ is the strain, and $v_1 = \dot{u}_1$ is the particle velocity. The mass density in the reference (undeformed) configuration is denoted by ϱ. The system (11.1) is a system of conservation laws. For details about this kind of partial differential system, interested readers are referred to [29–31].

An expression of the stress σ_{11} is required. In the case of hyperelastic materials, the only variable of state is the (possibly large) strain ε_{11}. Therefore, the internal energy per unit volume reads $U = U_0(\varepsilon_{11})$, where U_0 is the strain energy density function in J/m^3. The stress is a function of the strain, expressed by

$$\sigma_{11} = \frac{\partial U}{\partial \varepsilon_{11}} = U_0'(\varepsilon_{11}) \,. \tag{11.2}$$

The speed of sound c_P deduced from (11.1) satisfies

$$\varrho {c_P}^2 = \frac{\partial \sigma_{11}}{\partial \varepsilon_{11}} = U_0''(\varepsilon_{11}) \,. \tag{11.3}$$

Therefore, the speed of sound is a function of the strain. Hyperelastic materials are elastic, which means that no dissipation occurs for all state and all evolution.

In the case of Landau's law, the strain energy density function reads

$$U_0 = \left(\frac{1}{2} - \frac{\beta}{3} \varepsilon_{11} - \frac{\delta}{4} {\varepsilon_{11}}^2 \right) E \, {\varepsilon_{11}}^2, \tag{11.4}$$

where $E > 0$ is Young's modulus. Hence, the stress is a cubic function of the strain, and $\varrho {c_P}^2$ is a quadratic function of the strain. The parameters β and δ in Landau's law are third-order elastic (TOE) constants, which are related to the Murnaghan parameters [25, 32]. The classical case of linear elasticity corresponds to $\beta = 0$ and $\delta = 0$. As expected, the sound speed in (11.3) then becomes $c_P = \sqrt{E/\varrho}$.

Possible strain limits are derived from the hyperbolicity condition, i.e. the fact that the sound speed c_P in (11.3) is real, or in other words, the fact that $\varrho {c_P}^2 > 0$. In the linear case $\beta = \delta = 0$, no strain limit is obtained, since $\sqrt{E/\varrho}$ is always real. This differs from the nonlinear case where $\delta > 0$. Indeed, both lower bound and upper bound for the strain ε_{11} are obtained:

$$\frac{1}{\beta - \sqrt{\beta^2 + 3\delta}} < \varepsilon_{11} < \frac{1}{\beta + \sqrt{\beta^2 + 3\delta}} \,. \tag{11.5}$$

Table 11.1 Physical parameters

ϱ (kg/m^3)	E (GPa)	β	δ	Q	γ (J/m^3)	τ_g (J/m^3 s)
2.6×10^3	10	100	10^7	20	1.0	0.01

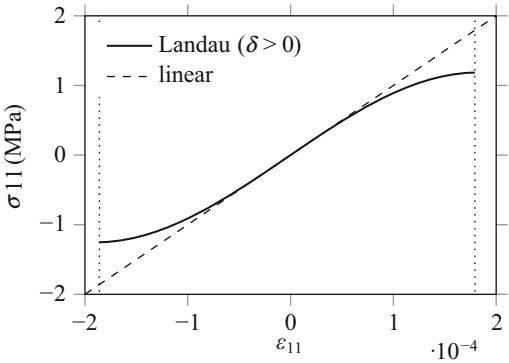

Fig. 11.1 Nonlinear stress–strain relationship deduced from Landau's law (11.4) with the parameters from Table 11.1. The vertical dotted lines denote the strain limits (11.5)

For nonlinear elasticity in rocks, typical values of β and δ are given in Table 11.1. Thus, the hyperbolicity condition (11.5) imposes $|\varepsilon_{11}| < 1.8 \times 10^{-4}$. The stress-strain relationship (11.2) deduced from Landau's law (11.4) is displayed in Fig. 11.1, where the parameters are taken from Table 11.1. The hyperbolicity limits (11.5) correspond to the strains where the slope of the curve equals zero.

11.2.2 Internal-Variable Model of Slow Dynamics

Several models of slow dynamics can be found in the literature. The soft-ratchet model of Vakhnenko et al. introduces a variable g which modifies the elastic modulus in time when the stress varies [22–24]. This idea has been reconsidered in the framework of continuum thermodynamics with internal variables [33, 34], resulting in a new model [25]. The internal-variable g modifies the stress according to

$$\sigma_{11} = \frac{\partial U}{\partial \varepsilon_{11}} = (1 - g)\, U_0'(\varepsilon_{11})\,. \tag{11.6}$$

If $g = 0$, the expression of the hyperelastic stress (11.2) is recovered. If $g = 1$, the stress does not depend on the strain anymore. Therefore, the value $g = 1$ destroys the material.

Integrating the constitutive law (11.6) with respect to the strain, the expression of the internal energy per unit volume $U = (1 - g)\, U_0(\varepsilon_{11}) + U_1(g)$ is obtained. The integration constant $U_1(g)$ is called storage energy hereinafter. In [25], an evolution equation for the internal variable of the form

$$\dot{g} = -\frac{1}{\tau_g}\frac{\partial U}{\partial g} = \frac{1}{\tau_g}\left(U_0(\varepsilon_{11}) - U_1'(g)\right) \tag{11.7}$$

is proposed, where $\tau_g > 0$ is proportional to a relaxation time. This evolution equation is thermodynamically admissible, i.e. the Clausius-Duhem inequality is satisfied for all state and all evolution. This type of material with internal variable dissipates energy.

The speed of sound c_P deduced from (11.1)–(11.7) satisfies $\varrho {c_P}^2 = (1-g)\,U_0''(\varepsilon_{11})$. If g is bounded by 1 and the hyperbolicity condition (11.5) is satisfied, then the speed of sound is real. Moreover, if the storage energy satisfies $U_1'(0) = 0$, then the evolution equation guarantees that g is positive. This condition points to the experimental fact that the sound speed decreases with respect to its value at equilibrium (softening of the material), when a dynamic loading is applied. The storage energy

$$U_1(g) = -\frac{1}{2}\gamma\,\ln(1-g^2)\,, \tag{11.8}$$

where $\gamma > 0$ is an energy per unit volume, is designed to ensure that the equilibrium point $\dot{g} = 0$ is unique, $g = 0$ is an equilibrium point, and g is bounded by 1 [25]. Given the expressions of the strain energy density (11.4) and the storage energy (11.8), the internal energy U is a surface in ε_{11}-g coordinates. This surface is represented in Fig. 11.2, where the parameters are issued from Table 11.1. One can notice the presence of an energy barrier (vertical asymptote) at $g = 1$.

11.2.3 Viscoelasticity

Nonlinear elastodynamics without attenuation poorly represents real media. In the framework of linear elasticity, many rheological models based on a frequency-dependent complex wave number can be found in the literature. Among them, the standard linear solid model, also known as generalized Zener or Maxwell body, is

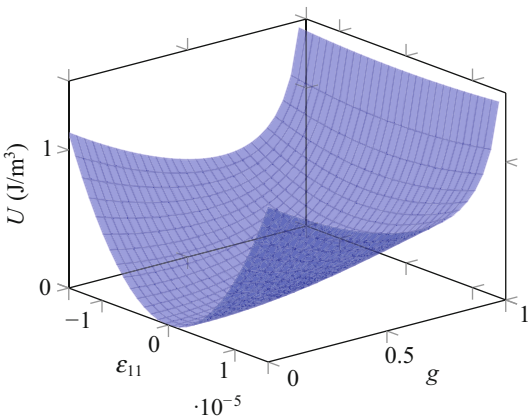

Fig. 11.2 Sketch of the internal energy $U = (1-g)\,U_0(\varepsilon_{11}) + U_1(g)$ of the slow dynamics model in ε_{11}-g coordinates

commonly used for the description of seismic wave propagation. It can be shown that this model adds a set of memory variables—or anelastic functions—to the variables of elastodynamics, and a set of equations satisfied by these new variables [35–37].

The generalized Zener body can be extended to hyperelasticity, as described in [24]. A set of N anelastic functions ξ_ℓ is introduced, which modify the equations of nonlinear elastodynamics (11.1) as follows. The anelastic functions ξ_ℓ satisfy

$$\dot{\xi}_\ell = v_{1,1} + \frac{\varepsilon_{11} - \xi_\ell}{\tau_{\varepsilon\ell}} - \frac{\tau_{\varepsilon\ell} - \tau_{\sigma\ell}}{\tau_{\varepsilon\ell}\tau_{\sigma\ell}} \frac{U_0'(\xi_\ell)}{E}\,, \tag{11.9}$$

where the parameters $\tau_{\varepsilon\ell}$ and $\tau_{\sigma\ell}$ are the relaxation times involved in the ℓth Zener mechanism. The stress is given by the weighted sum

$$\sigma_{11} = \mathrm{Re}(\mathscr{F})^2 \sum_{\ell=1}^{N} \frac{\tau_{\varepsilon\ell}}{\tau_{\sigma\ell}} U_0'(\xi_\ell)\,, \tag{11.10}$$

where

$$\mathscr{F} = \left(N + \sum_{\ell=1}^{N} \frac{\mathrm{i}\omega_{ref}(\tau_{\varepsilon\ell} - \tau_{\sigma\ell})}{1 + \mathrm{i}\omega_{ref}\tau_{\sigma\ell}} \right)^{-1/2} \tag{11.11}$$

and i denotes the imaginary unit. In the linear case, the normalizing factor $\mathrm{Re}(\mathscr{F})^2$ guarantees that the frequency-dependent phase velocity is equal to $\sqrt{E/\varrho}$ at the angular frequency ω_{ref} [37]. Finally, the stress (11.10) is not explicitly expressed in terms of the strain ε_{11} anymore, but in terms of the anelastic functions ξ_ℓ, whose evolution equations (11.9) involve the strain.

In practice, the value of the relaxation times $\tau_{\varepsilon\ell}$ and $\tau_{\sigma\ell}$ can be obtained by using a nonlinear optimization technique [37]. The procedure consists in minimizing the error between an objective quality factor and the quality factor of the linear Zener model. A typical value of the objective Q factor is given in Table 11.1. Now, the choice of the number of relaxation mechanisms N results from a compromise. In fact, the quality of the optimization increases with N, as well as the computational costs. Here, $N = 5$ Zener mechanisms are used. Nonlinear optimization of the relaxation times $\tau_{\varepsilon\ell}$ and $\tau_{\sigma\ell}$ is performed over the angular frequency range $\left[0.1\,\omega_{ref}, 10\,\omega_{ref}\right]$, where $\omega_{ref} = 2\pi \times 10^4$ rad/s.

Now, we describe how accounting for the slow dynamics modifies the previous rheological model. The coupling of the internal-variable model and the generalized Zener model gives the following set of equations:

$$\begin{cases} \dot{\varepsilon}_{11} = v_{1,1}\,, \\ \varrho \dot{v}_1 = \sigma_{11,1}\,, \\ \dot{\xi}_\ell = v_{1,1} + \dfrac{\varepsilon_{11} - \xi_\ell}{\tau_{\varepsilon\ell}} - \dfrac{\tau_{\varepsilon\ell} - \tau_{\sigma\ell}}{\tau_{\varepsilon\ell}\tau_{\sigma\ell}} \dfrac{U_0'(\xi_\ell)}{E}\,, \quad 1 \le \ell \le n\,, \\ \dot{g} = \dfrac{1}{\tau_g} \left(\mathrm{Re}(\mathscr{F})^2 \left[\displaystyle\sum_{\ell=1}^{N} \frac{\tau_{\varepsilon\ell}}{\tau_{\sigma\ell}} U_0(\xi_\ell) + \frac{E}{2} \frac{\tau_{\varepsilon\ell}\,(\varepsilon_{11} - \xi_\ell)^2}{\tau_{\varepsilon\ell} - \tau_{\sigma\ell}} \right] - U_1'(g) \right), \end{cases} \tag{11.12}$$

where the stress is

$$\sigma_{11} = (1-g)\,\mathrm{Re}(\mathscr{F})^2 \sum_{\ell=1}^{N} \frac{\tau_{\varepsilon\ell}}{\tau_{\sigma\ell}} U_0'(\xi_\ell)\,. \tag{11.13}$$

The speed of sound c_P deduced from this system satisfies

$$\varrho {c_P}^2 = \sum_{\ell=1}^{N} \frac{\partial \sigma_{11}}{\partial \xi_\ell} = (1-g)\,\mathrm{Re}(\mathscr{F})^2 \sum_{\ell=1}^{N} \frac{\tau_{\varepsilon\ell}}{\tau_{\sigma\ell}} U_0''(\xi_\ell)\,. \tag{11.14}$$

A sufficient condition for the sound speed to be real is that g is bounded by 1, and each relaxation function ξ_ℓ satisfies the inequality (11.5) instead of ε_{11}.

In order to close the system, we specify the boundary conditions and initial conditions. We consider a bounded physical domain of length L, such that $0 < x_1 < L$. The setup of DAE and NRUS experiments suggests to impose a time-dependent displacement $u_d(t)$ at the abscissa $x_1 = 0$. At the abscissa $x_1 = L$, a free edge condition is imposed, which results in zero stress. With the present set of variables, one has therefore $v_1 = \dot{u}_d$ at $x_1 = 0$, and $\varepsilon_{11} = 0$ at $x_1 = L$. By construction of the rheological model, the same conditions apply to the anelastic functions ξ_ℓ as to the strain ε_{11}. Therefore, one has $\xi_\ell = 0$ for all ℓ at the abscissa $x_1 = L$. None of these boundary condition involves g, as if the physical domain was unbounded for g. Lastly, all the unknowns are initialized to zero over the physical domain at the time $t = 0$.

11.3 Numerical Modeling

The system of partial differential equations in space and time (11.12) is a nonlinear hyperbolic system with relaxation. It rewrites as

$$\dot{\mathbf{U}} + \frac{\partial}{\partial x_1} \mathbf{F}(\mathbf{U}) = \mathbf{R}(\mathbf{U})\,, \tag{11.15}$$

where the unknowns $\mathbf{U} = (\varepsilon_{11}, v_1, \xi_1 \dots \xi_N, g)$ depend on space and time. The flux function $\mathbf{F}$ and the relaxation function $\mathbf{R}$ deduced from (11.12) are both nonlinear with respect to $\mathbf{U}$. Nevertheless, such a differential system can be solved efficiently by finite-volume methods [30, 31]. The procedure is described in the next subsections.

11.3.1 Numerical Strategy

The physical domain is discretized using a regular grid in space with step $\Delta x_1 = L/N_x$. Also, a variable time step $\Delta t = t_{n+1} - t_n$ is introduced. Therefore, $\mathbf{U}(i\,\Delta x_1, t_n)$ denotes the solution to (11.15) at the ith grid node, $0 \leq i \leq N_x$, and the time t_n. A straightforward strategy consists in discretizing explicitly the non-homogeneous system (11.15):

$$\tilde{\mathbf{U}}_i^{n+1} = \tilde{\mathbf{U}}_i^n - \frac{\Delta t}{\Delta x_1}\left(\tilde{\mathbf{F}}_{i+1/2} - \tilde{\mathbf{F}}_{i-1/2}\right) + \Delta t\, \mathbf{R}(\tilde{\mathbf{U}}_i^n)\,, \tag{11.16}$$

where $\tilde{\mathbf{U}}_i^n \simeq \mathbf{U}(i\,\Delta x_1, t_n)$ approximates the solution at the grid nodes, and $\tilde{\mathbf{F}}_{i+1/2}$ is the numerical flux of a finite-volume method. According to the time-marching formula (11.16), a forward Euler method may be used for the relaxation term.

The stability of the numerical method (11.16) is constrained by two upper bounds on the time step Δt. The first one is the Courant-Friedrichs-Lewy (CFL) condition, which is imposed by the physical sound speed c_P. It states that the Courant number $\kappa = \tilde{c}_P\,\Delta t/\Delta x_1$ must be smaller than 1, where $\tilde{c}_P$ denotes the maximum sound speed over the boxes with corners $\tilde{\mathbf{U}}_i^n$ and $\tilde{\mathbf{U}}_{i+1}^n$. The second one relates to the stiffness of the relaxation term, and states that the time step Δt cannot be arbitrarily larger than the inverse of the spectral radius of the Jacobian matrix $\partial\mathbf{R}/\partial\mathbf{U}$. If the material is viscoelastic, then the Jacobian of $\mathbf{R}$ can have a very large spectral radius, which imposes to choose a small time-step Δt. In this case, time-marching of (11.16) is very slow, and the straightforward numerical discretization is inefficient.

A more flexible and efficient numerical strategy results from splitting. This approach consists in splitting the system (11.15) in a propagative part

$$\dot{\mathbf{U}} + \frac{\partial}{\partial x_1}\mathbf{F}(\mathbf{U}) = \mathbf{0}\,, \tag{11.17}$$

and a relaxation part

$$\dot{\mathbf{U}} = \mathbf{R}(\mathbf{U})\,. \tag{11.18}$$

Numerically, both parts are solved successively at each time step, with a dedicated numerical method for each part. Here, a second-order accurate Strang splitting scheme is used [24]. It consists in solving the diffusive part (11.18) over half a time step, then the propagative part (11.17) over one time step, and again the diffusive part over half a time step.

Now, it remains to specify the dedicated methods for the numerical resolution of each part. In the relaxation part, the evolution equations (11.9) for ξ_ℓ are linearized with respect to ξ_ℓ, by using the approximation $U_0'(\xi_\ell)/E \simeq \xi_\ell$. Then, time-marching of the anelastic functions ξ_ℓ is performed by using matrix exponentials [24]. Time-marching of the evolution equation for g is carried out by using an explicit Euler method. The propagative part (11.17) is solved using a well-suited finite-volume method, which is described in the next subsection. The resulting numerical method is stable under the CFL condition, as long as the sound speed c_P in (11.14) is real for the numerical data $\tilde{\mathbf{U}}_i^n$.

11.3.2 Finite-Volume Method

Since the flux function $\mathbf{F}$ is nonlinear with respect to $\mathbf{U}$, an initial-value problem defined by the data $\mathbf{U}(x_1, t = 0)$ can have several solutions. It is not straightforward for a numerical method to converge towards the correct solution. In particular, the numerical fluxes $\tilde{\mathbf{F}}_{i+1/2}$ of the finite-volume method must be computed carefully. In the present case, Roe linearization can be used to construct a finite-volume scheme of any order of convergence [31, 38].

Based on Roe linearization, we implement the *flux-limiter method*, as described in [31, 39]. This method is a bit less than second-order accurate, but is well-suited to nonlinear flux functions. The numerical flux $\tilde{\mathbf{F}}_{i+1/2}$ is computed from a first-order accurate finite-volume method (Roe's approximate Riemann solver). Then, a second-order correction deduced from the Lax-Wendroff method is added. This correction is penalized by a limiter function, which avoids spurious oscillations to arise in the numerical solution. Here, the minmod flux limiter is used, which has shown to be very robust during validation steps, even in the case of nonconvex flux functions [40, 41].

By construction, the resulting numerical scheme has a five-point stencil. It means that the five numerical values of $\mathbf{U}$ at the grid nodes $i-2 \ldots i+2$ are required to carry out one iteration in time at the ith grid node. Therefore, two "ghost cells" are added on the left side and on the right side of the numerical domain. Setting the values of the unknowns $\mathbf{U}$ in the ghost cells makes it possible to account for various boundary conditions. At each time step, the imposed displacement at the abscissa $x_1 = 0$ is represented by setting the data $\mathbf{U}_{-2}^n$ and $\mathbf{U}_{-1}^n$ in a similar way to the "oscillating wall" in [31]. The free edge at the abscissa $x_1 = L$ is represented by setting the data $\mathbf{U}_{N_x+1}^n$ and $\mathbf{U}_{N_x+2}^n$ in a similar way to the "solid wall" in [31].

11.4 Numerical Experiments

In this section, two experiments are carried out with the numerical model described in the previous section. The first experiment reproduces DAE, and the second experiment reproduces NRUS. In both cases, a sample of length $L = 30\,\text{cm}$ is used.

If not specified, the material parameters are issued from Table 11.1. The physical domain is discretized using $N_x = 100$ points. To avoid instability, the Courant number is set to $\kappa = 0.95$.

11.4.1 Dynamic Acoustoelasticity

A sinusoidal particle velocity $\dot{u}_d(t)$ with amplitude V_0 and frequency 1585 Hz is imposed at the abscissa $x_1 = 0$. This source is turned on from $t = 0$ to $t \approx 50.4$ ms, which corresponds to a total duration of 80 periods of signal. A receiver records the numerical solution at the abscissa $x_1 = 0.1$ m, up to $t = 80$ ms.

Figure 11.3a displays the elastic modulus $\varrho {c_P}^2$ in (11.14), which is recorded at the position of the receiver. A slow decrease of the elastic modulus combined with fast oscillations is observed. The frequency of the fast oscillations is the frequency of the source signal. When the source is stopped, the amplitude of the fast oscillations diminishes, and the elastic modulus recovers slowly its initial value. The duration of the softening is related to the characteristic time $\tau_g/\gamma \approx 10$ ms of slow dynamics. As observed experimentally, the softening phenomenon is accentuated when the amplitude of forcing V_0 is increased.

Figure 11.3b focuses on the steady-state solution. Here, the last period of signal before $t = 50$ ms is used. When the elastic modulus (11.14) is represented with respect to the strain at the position of the receiver, a hysteresis curve is obtained. The shape of the hysteresis curve is related to the parameters β and δ of Landau's law (11.4), and to the dissipation in the material [25].

11.4.2 Resonance Curves

The imposed velocity $\dot{u}_d(t)$ is sinusoidal with amplitude V_0. The exciting frequency is increased every 200 ms, which is long enough to consider that the solution has reached the steady state. Here, twenty equally spaced frequencies between 1400 and 1700 Hz are chosen. A receiver records the numerical solution at the abscissa $x_1 = L$.

For linear viscoelastic solids, the frequency response function $FRF(\omega)$ of a sample which vibrates longitudinally at the angular frequency $\omega = 2\pi f$ can be computed analytically. In the case of a vibrating wall at the abscissa $x_1 = 0$ (input) and a free edge at the abscissa $x_1 = L$ (output), a plane-wave decomposition of the solution yields

$$FRF(\omega) = \frac{2}{\exp(\mathrm{i}\, k_P(\omega)\, L) + \exp(-\mathrm{i}\, k_P(\omega)\, L)}, \tag{11.19}$$

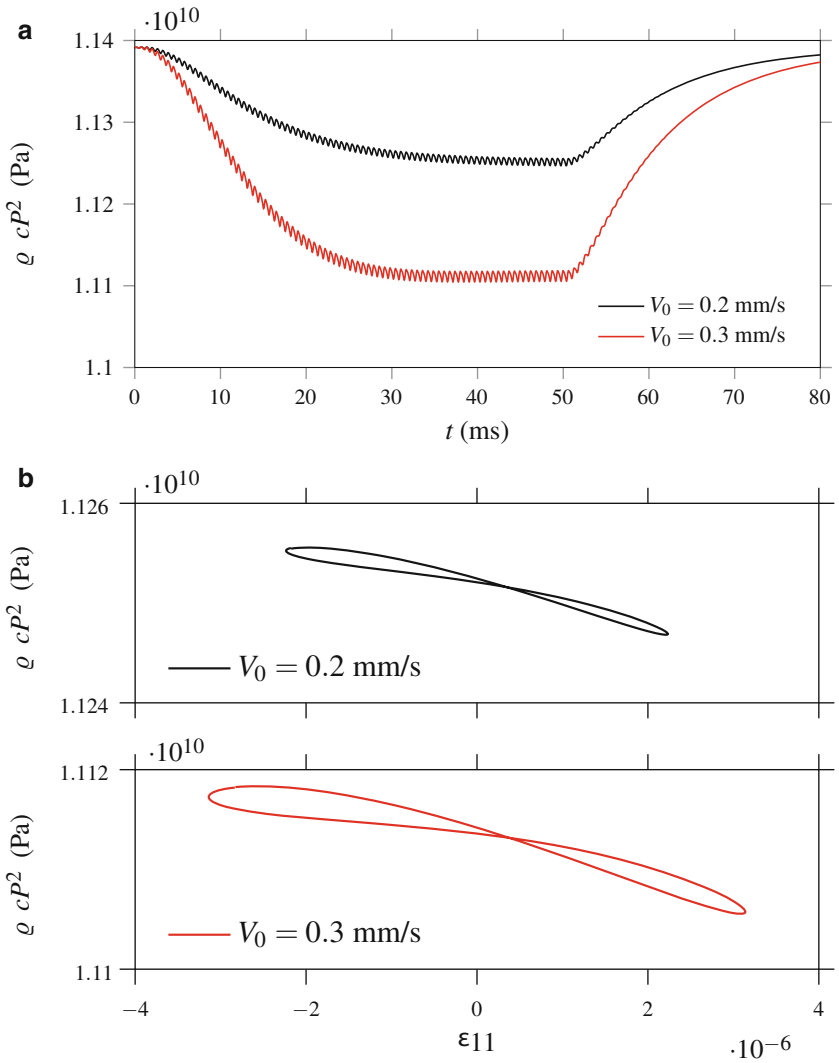

Fig. 11.3 Dynamic acoustoelasticity. (**a**) Softening of the material, as recorded by the receiver at the abscissa $x_1 = 0.1$ m. (**b**) Hysteresis curves in steady-state ($t \approx 50$ ms)

where $k_P(\omega)$ denotes the complex wave number

$$k_P(\omega) = \frac{\omega\sqrt{\varrho/E}}{\mathrm{Re}(\mathscr{F})}\left(N + \sum_{\ell=1}^{N} \frac{\mathrm{i}\omega(\tau_{\varepsilon\ell} - \tau_{\sigma\ell})}{1 + \mathrm{i}\omega\tau_{\sigma\ell}}\right)^{-1/2} \tag{11.20}$$

of the Zener model (11.9)–(11.11).

Numerically, the value of $FRF(\omega)$ is given by the ratio of two coefficients: the first Fourier coefficients of the output and input velocity signals. In practice, these coefficients are computed by numerical integration over one period of signal. Since a sufficiently long time must have elapsed, this computation is performed over the last period of signal before a higher exciting frequency is used. In Fig. 11.4a, the modulus of the analytical frequency response (11.19)–(11.20) is compared with the numerical estimation. The forcing amplitude is $V_0 = 1.0\,\text{mm/s}$, and the material parameters satisfy $\beta = 0$, $\delta = 0$, and $\tau_g \to \infty$. In the vicinity of the resonance, the frequency response is slightly underestimated by the numerical method, which can be resolved by increasing the number of points N_x of the spatial discretization.

In the case of nonlinear constitutive laws, no analytical expression of the frequency response is known. However, one can still compute numerically the Fourier coefficients of long-time numerical solutions. Figure 11.4b displays the results of the previous setup, which has been applied to a nonlinear viscoelastic solid with slow dynamics. In this figure, the output velocity amplitude is represented with respect to the frequency, for different forcing amplitudes V_0. The velocity amplitude is defined as twice the modulus of the first Fourier coefficient of the velocity signal. In the linear viscoelastic case from Fig. 11.4a, the output velocity amplitude was equal to the input velocity amplitude V_0 multiplied by the modulus of the frequency-response. Here, a frequency shift of the resonance peak is observed with increasing forcing amplitudes (Fig. 11.4b). The shape of the resonance curves relates the typical behavior of rocks [6, 28]. It includes stiffening of the curve with increasing frequency and amplitude. It is worth noticing that present simulations are carried out increasing the frequency of the exciting signal. Figure 11.5 presents the relative frequency shift as a function of the strain amplitude. Again, the shape of the curve is qualitatively comparable to the one reported in rocks [6, 28]. Also, at low forcing amplitudes, one recognizes the shape of the frequency response from Fig. 11.4a.

11.5 Conclusion

In this chapter, the main ingredients of a one-dimensional model of continuum which includes nonlinear elasticity, viscoelastic attenuation, and slow dynamics are exposed. A well-suited numerical method based on finite volumes is introduced, so as to solve the equations of motion efficiently. With a particular choice of parameters, DAE and NRUS experiments are reproduced, and qualitative agreement is obtained in both cases.

We mention here a few improvements to be introduced. Firstly, a quantitative experimental validation needs to be carried out, so as to estimate the value of the parameters for different materials. Secondly, higher-order methods can improve the accuracy of the computations (see, e.g., [38]), which has been carried out in recent works [42]. Lastly, frequency-domain approaches would be a more efficient tool rather than time-domain methods to deduce the resonance curves from long-time

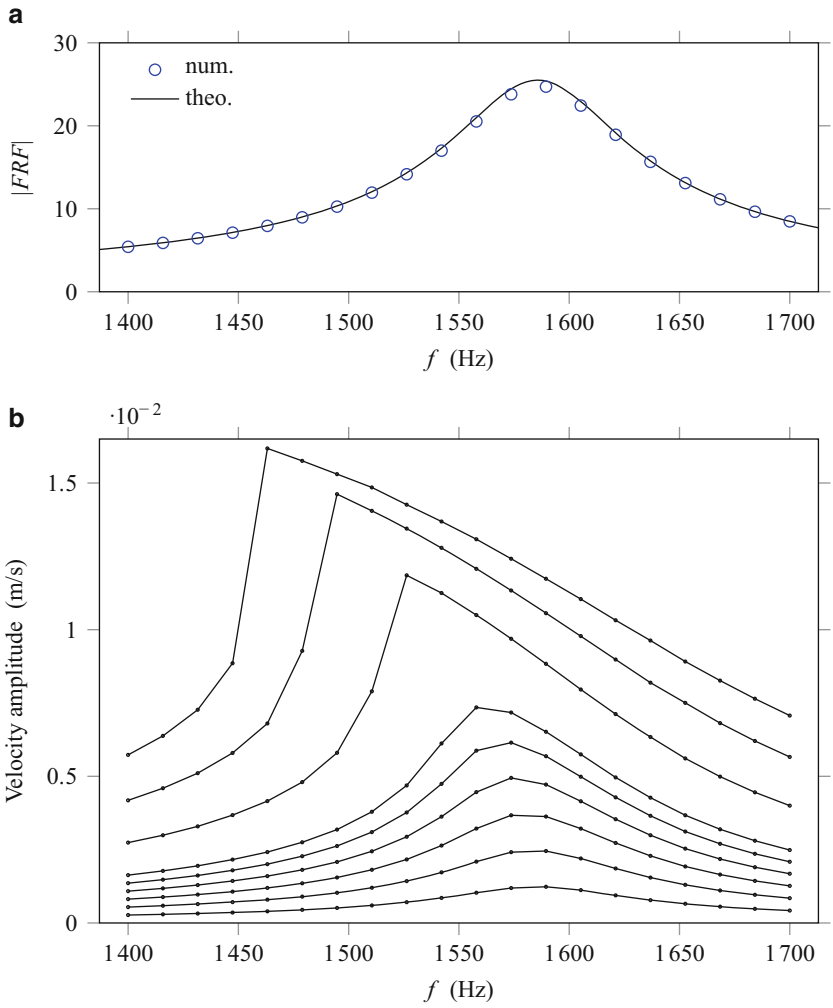

Fig. 11.4 Resonance curves. (**a**) Numerical and analytical frequency response of a linear viscoelastic solid. (**b**) Output velocity amplitude of a nonlinear viscoelastic solid with slow dynamics, at input velocity amplitudes increasing linearly from $V_0 = 0.05$ mm/s (bottom) to $V_0 = 0.3$ mm/s by steps of 0.05 mm/s, and from $V_0 = 0.25$ mm/s to $V_0 = 1$ mm/s (top) by steps of 0.25 mm/s

periodic solutions. Future work will be devoted to 2D and 3D numerical modeling. In particular, such tools can be used to implement imaging techniques.

Acknowledgements This work was supported by the interdisciplinary mission of CNRS (INFINITI). The project leading to this publication has received funding from Excellence Initiative of Aix-Marseille University—A*MIDEX, a French "Investissements d'Avenir" programme. It has been carried out in the framework of the Labex MEC.

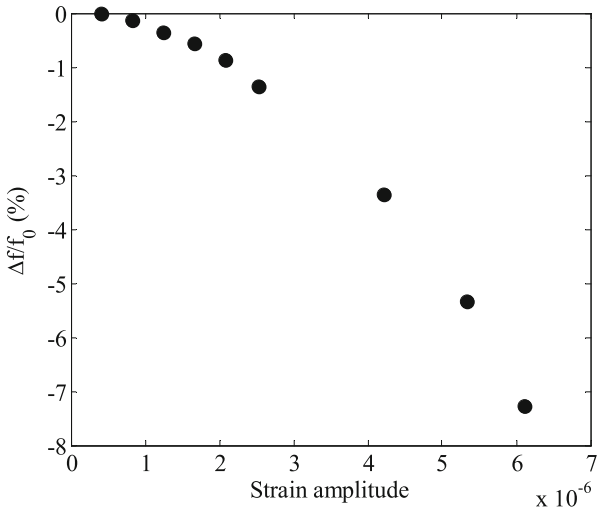

Fig. 11.5 Relative resonant frequency shift as a function of strain amplitude

References

1. R.A. Guyer, P.A. Johnson, Nonlinear mesoscopic elasticity: evidence for a new class of materials. Phys. Today **52**(4), 30–36 (1999)
2. R.A. Guyer, P.A. Johnson, *Nonlinear Mescopic Elasticity: The Complex Behaviour of Rocks, Soil, Concrete* (Wiley-VCH, Weinheim, 2009)
3. L.D. Landau, E.M. Lifshitz, *Course of Theoretical Physics Vol. 7: Theory of Elasticity* (Pergamon Press, London, 1959)
4. K. Winkler, N. Amos, M. Gladwin, Friction and seismic attenuation in rocks. Nature **277**, 528–531 (1979)
5. J.A. TenCate, E. Smith, R.A. Guyer, Universal slow dynamics in granular solids. Phys. Rev. Lett. **85**(5), 1020 (2000)
6. J.A. TenCate, D. Pasqualini, H. Salman, K. Heitmann, D. Higdon, P.A. Johnson, Nonlinear and nonequilibrium dynamics in geomaterials. Phys. Rev. Lett. **93**(6), 065501 (2004)
7. J. Gomberg, P.A. Johnson, Seismology: dynamic triggering of earthquakes. Nature **437**, 830 (2005)
8. P.A. Johnson, X. Jia, Nonlinear dynamics, granular media and dynamic earthquake triggering. Nature **437**, 871–874 (2005)
9. P.A. Johnson, H. Savage, M. Knuth, J. Gomberg, C. Marone, Effect of acoustic waves on stick–slip in granular media and implications for earthquakes. Nature **451**, 57–60 (2008)
10. P.A. Johnson, P. Bodin, J. Gomberg, F. Pearce, Z. Lawrence, F.-Y. Menq, Inducing in situ, nonlinear soil response applying an active source. J. Geophys. Res. Solid Earth **114**(B5), B05304 (2009)
11. G. Renaud, J. Rivière, C. Larmat, J.T. Rutledge, R.C. Lee, R.A. Guyer, K. Stokoe, P.A. Johnson, In situ characterization of shallow elastic nonlinear parameters with dynamic acoustoelastic testing. J. Geophys. Res. Solid Earth **119**(9), 6907–6923 (2014)
12. P. Guéguen, P. Johnson, P. Roux, Nonlinear dynamics induced in a structure by seismic and environmental loading. J. Acoust. Soc. Am. **140**(1), 582–590 (2016)
13. C. Payan, T.J. Ulrich, P.Y. Le Bas, T. Saleh, M. Guimaraes, Quantitative linear and nonlinear resonance inspection techniques and analysis for material characterization: application to concrete thermal damage. J. Acoust. Soc. Am. **136**(2), 537–546 (2014)

14. C. Payan, T.J. Ulrich, P.Y. Le Bas, M. Griffa, P. Schuetz, M.C. Remillieux, T.A. Saleh, Probing material nonlinearity at various depths by time reversal mirrors. Appl. Phys. Lett. **104**(14), 144102 (2014)
15. V. Zaitsev, V. Gusev, B. Castagnede, Thermoelastic mechanism for logarithmic slow dynamics and memory in elastic wave interactions with individual cracks. Phys. Rev. Lett. **90**(7), 075501 (2003)
16. V.Y. Zaitsev, V.E. Gusev, V. Tournat, P. Richard, Slow relaxation and aging phenomena at the nanoscale in granular materials. Phys. Rev. Lett. **112**(10), 108302 (2014)
17. V. Aleshin, K. Van Den Abeele, Friction in unconforming grain contacts as a mechanism for tensorial stress–strain hysteresis. J. Mech. Phys. Solids **55**(4), 765–787 (2007)
18. P. Antonaci, C.L.E. Bruno, A.S. Gliozzi, M. Scalerandi, Evolution of damage-induced nonlinearity in proximity of discontinuities in concrete. Int. J. Solids Struct. **47**(11–12), 1603–1610 (2010)
19. R.A. Guyer, K.R. McCall, G.N. Boitnott, Hysteresis, discrete memory, and nonlinear wave propagation in rock: a new paradigm. Phys. Rev. Lett. **74**(17), 3491–3494 (1995)
20. A.V. Lebedev, L.A. Ostrovsky, A unified model of hysteresis and long-time relaxation in heterogeneous materials. Acoust. Phys. **60**(5), 555–561 (2014)
21. C. Pecorari, A constitutive relationship for mechanical hysteresis of sandstone materials. Proc. R. Soc. A **471**(2184), 20150369 (2015)
22. O.O. Vakhnenko, V.O. Vakhnenko, T.J. Shankland, J.A. Ten Cate, Strain-induced kinetics of intergrain defects as the mechanism of slow dynamics in the nonlinear resonant response of humid sandstone bars. Phys. Rev. E **70**(1), 015602 (2004)
23. V.O. Vakhnenko, O.O. Vakhnenko, J.A. TenCate, T.J. Shankland, Modeling of stress-strain dependences for Berea sandstone under quasistatic loading. Phys. Rev. B **76**(18), 184108 (2007)
24. N. Favrie, B. Lombard, C. Payan, Fast and slow dynamics in a nonlinear elastic bar excited by longitudinal vibrations. Wave Motion **56**, 221–238 (2015)
25. H. Berjamin, N. Favrie, B. Lombard, G. Chiavassa, Nonlinear waves in solids with slow dynamics: an internal-variable model. Proc. R. Soc. A **473**(2201), 20170024 (2017)
26. G. Renaud, J. Rivière, P.Y. Le Bas, P.A. Johnson, Hysteretic nonlinear elasticity of Berea sandstone at low-vibrational strain revealed by dynamic acousto-elastic testing. Geophys. Res. Lett. **40**(4), 715–719 (2013)
27. M. Lott, C. Payan, V. Garnier, Q.A. Vu, J. Eiras, M.C. Remillieux, P.Y. Le Bas, T.J. Ulrich, Three-dimensional treatment of nonequilibrium dynamics and higher order elasticity. Appl. Phys. Lett. **108**(14), 141907 (2016)
28. M.C. Remillieux, R.A. Guyer, C. Payan, T.J. Ulrich, Decoupling nonclassical nonlinear behavior of elastic wave types. Phys. Rev. Lett. **116**(11), 115501 (2016)
29. J. Smoller, *Shock Waves and Reaction–Diffusion Equations*, 2nd edn. (Springer, New York, 1994)
30. E. Godlewski, P.-A. Raviart, *Numerical Approximation of Hyperbolic Systems of Conservation Laws* (Springer, New York, 1996)
31. R.J. LeVeque, *Finite-Volume Methods for Hyperbolic Problems* (Cambridge University Press, Cambridge, 2002)
32. A.N. Norris, Finite-amplitude waves in solids, in *Nonlinear Acoustics*, ed. by M.F. Hamilton, D.T. Blackstock (Academic Press, San Diego, 1998), pp. 263–277
33. G.A. Maugin, W. Muschik, Thermodynamics with internal variables. Part I. General concepts. J. Non-Equilib. Thermodyn. **19**(3), 217–249 (1994)
34. G.A. Maugin, The saga of internal variables of state in continuum thermo-mechanics (1893–2013). Mech. Res. Commun. **69**, 79–86 (2015)
35. J.M. Carcione, *Wave Fields in Real Media: Wave Propagation in Anisotropic, Anelastic, Porous and Porous Media* (Elsevier, Oxford, 2001)
36. P. Moczo, J. Kristek, On the rheological models used for time-domain methods of seismic wave propagation. Geophys. Res. Lett. **32**(1), L01306 (2005)

37. E. Blanc, D. Komatitsch, E. Chaljub, B. Lombard, Z. Xie, Highly accurate stability-preserving optimization of the Zener viscoelastic model, with application to wave propagation in the presence of strong attenuation. Geophys. J. Int. **205**(1), 427–439 (2016)
38. C.-W. Shu, High order weighted essentially nonoscillatory schemes for convection dominated problems. SIAM Rev. **51**(1), 82–126 (2009)
39. R. Velasco-Segura, P.L. Rendón, A finite volume approach for the simulation of nonlinear dissipative acoustic wave propagation. Wave Motion **58**, 180–195 (2015)
40. A. Voss, Exact Riemann solution for the Euler equations with nonconvex and nonsmooth equation of state, Ph.D. thesis, RWTH Aachen, 2005
41. A. Kurganov, G. Petrova, B. Popov, Adaptive semidiscrete central-upwind schemes for nonconvex hyperbolic conservation laws. SIAM J. Sci. Comput. **29**(6), 2381–2401 (2007)
42. H. Berjamin, B. Lombard, C. Chiavassa, N. Favrie, Modeling longitudinal wave propagation in nonlinear viscoelastic solids with softening. Int. J. Solids Struct. **141–142**, 35–44 (2018)

Chapter 12
Cement-Based Material Characterization Using Nonlinear Single-Impact Resonant Acoustic Spectroscopy (NSIRAS)

J. N. Eiras, T. Kundu, J. S. Popovics, and J. Payá

12.1 Introduction

The durability of infrastructure materials, such as concrete, has direct impact on society because the productivity of many industries and safety of human beings depend on infrastructure condition, and further because maintenance of the infrastructure can represent a significant portion of a government's budget. Thus the enhancement of concrete durability and improvement of infrastructure condition monitoring are significant concerns to the scientific community. The resonant frequency method has been traditionally used to assess the mechanical condition of concrete. Resonance frequencies of a solid body depend on test sample mass and dimensions, elastic properties, and boundary conditions. Resonance frequencies have been used to determine engineering properties such as the elastic moduli and material damping. The method is useful to assess the performance of materials within accelerated degradation durability test procedures, and to inspect quality of the products during manufacturing processes (pass/fail tests). Different testing standards and recommendations prescribe test configurations, and specific tests are recommended for different materials. A basic resonant frequency test requires

J. N. Eiras (✉)
Aix Marseille Univ, CNRS, Centrale Marseille, LMA, Marseille, France

T. Kundu
Department of Civil Engineering and Engineering Mechanics, Aerospace and Mechanical Engineering, University of Arizona, Tucson, AZ, USA

J. S. Popovics
Department of Civil and Environmental Engineering, University of Illinois at Urbana-Champaign, Urbana, IL, USA

J. Payá
Instituto de Ciencia y Tecnología del Hormigón (ICITECH), Universitat Politècnica de València, Valencia, Spain

T. Kundu (ed.), *Nonlinear Ultrasonic and Vibro-Acoustical Techniques for Nondestructive Evaluation*, https://doi.org/10.1007/978-3-319-94476-0_12

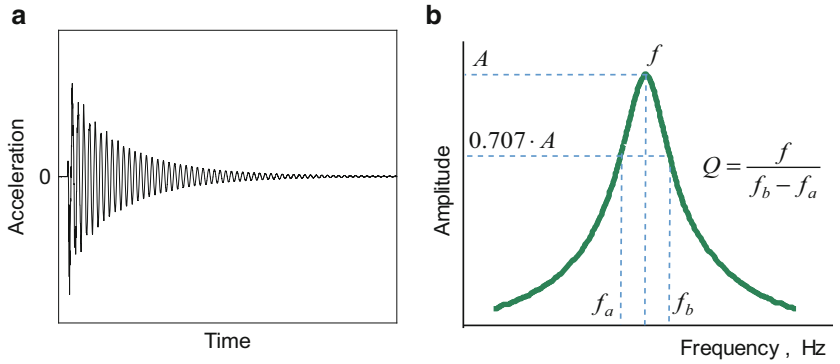

Fig. 12.1 (**a**) Typical time domain acceleration signal obtained in impact vibration resonant tests, and (**b**) typical resonant spectrum, from which resonant frequency and quality factor can be evaluated

a forced vibration system to set up mechanical resonances, and some system to sense the frequency content from the resonant vibration signals. For concrete-like materials, these specifications are given by ASTM C215 [1], wherein an impulsive impact event is applied to the test sample to excite the resonant frequencies and a small sensor is mounted on the surface of the test sample. From the impulsive impact vibration signals thus obtained, two standard parameters are usually derived: (1) the dynamic modulus, which depends on sample dimensions, mass, and the resonant frequency peak (f), and (2) the attenuation or damping capacity of the material. Figure 12.1a, b illustrates typical signals obtained from a single-impact vibration test, where the spectral (frequency domain) signal is computed from the time signal using a Fourier transform algorithm. The continuous reduction of the vibration signal amplitude with time during the signal "ring-down" is seen in the time domain signal. The resonant frequency and damping characteristics are extracted from the spectral signal in the region around the resonant frequency peak. The damping capacity of the material is determined from the quality factor (Q) (or inverse attenuation), which is defined as the ratio between the resonant frequency peak (f) and the bandwidth frequencies corresponding to a 50% reduction of vibration energy in the power frequency spectrum for a given vibration mode [2]. Meaningful application of the ASTM C215 test is found within other standard durability test methods [3, 4].

It is important to note that standardized wave propagation and vibration test methods, such as ASTM C215, assume that the test material behaves in a linear elastic fashion, even after the material accumulates damage, and as such these methods are identified as "linear" test methods. The assumption of linearity implies, among other things, that the test results are independent of the mechanical energy level (e.g., maximum strain amplitude of the vibration motion) used in

the measurement. However, infrastructure materials such as concrete are known to behave in a nonlinear and hysteretic fashion, especially at higher mechanical energy levels. It has been shown by many investigators that the *nonlinear* characteristics of the vibration signatures are very sensitive to the presence of damage and other microstructural characteristics within materials [5–8]. Because the nonlinear behavior is expected to be enhanced by increasing damage, considerable effort has been dedicated to develop nonlinear vibration techniques for improved damage content measurement. These nonlinear methods provide linear and nonlinear material characterization parameters. Different measurement modalities can be used to extract the nonlinear character, such as finite-amplitude and nonlinear wave mixing techniques [8–10]; some of these techniques are described elsewhere in this book. In nonlinear resonant frequency tests, the nonlinear and hysteretic behavior of concrete is exhibited by nonlinear harmonic mode generation and an apparent softening of the material with increasing vibration strain energy; as a result of the latter characteristic, the resonant frequency shifts downward and the attenuation shifts upward with increasing excitation amplitude [11, 12]. The nonlinear nature of the vibration response can be elicited by repeating the standard resonant frequency test configuration, but at varying vibration excitation amplitude through multiple acquisitions. The excitation amplitude can be changed by either changing the energy of the impulsive impact event or the driving voltage of an ultrasonic transmitter. Figure 12.2 illustrates the expected evolution of the amplitude dependent vibration resonant frequency (f) and attenuation (ξ) expressed with respect to those values at very low strain energy (linear) condition: f_o and ξ_o.

These phenomena have been leveraged by several researchers to measure nonlinear frequency and attenuation variation in a more simple and convenient manner by making use of the ring-down of a single forced vibration test. These types of approaches monitor instantaneous phase and attenuation information of the vibration as the amplitude of the signal naturally decreases during ring-down, and are referred as ring-down spectroscopies. The test configurations consist of either a burst excitation, wherein the signal is analyzed after switching off a monochromatic frequency burst [13], or a more straight-forward option that utilizes a single controlled impact event applied to the sample [14–16]. The latter approach enables implementation of standard test configurations and thus is less cumbersome when compared to other nonlinear measurement techniques, yet provides additional nonlinear material measurement characterization parameters.

In this chapter, different signal processing techniques that can be applied to investigate material nonlinearity derived from a single standard impact resonant frequency test are discussed. In addition, nonlinear multiple- and single-impact test approaches are compared, and the advantages and disadvantages of these techniques are discussed. Finally, some of the concerns related to impact resonant frequency tests, particularly those related to the investigation of the damage in cement-based materials, are addressed.

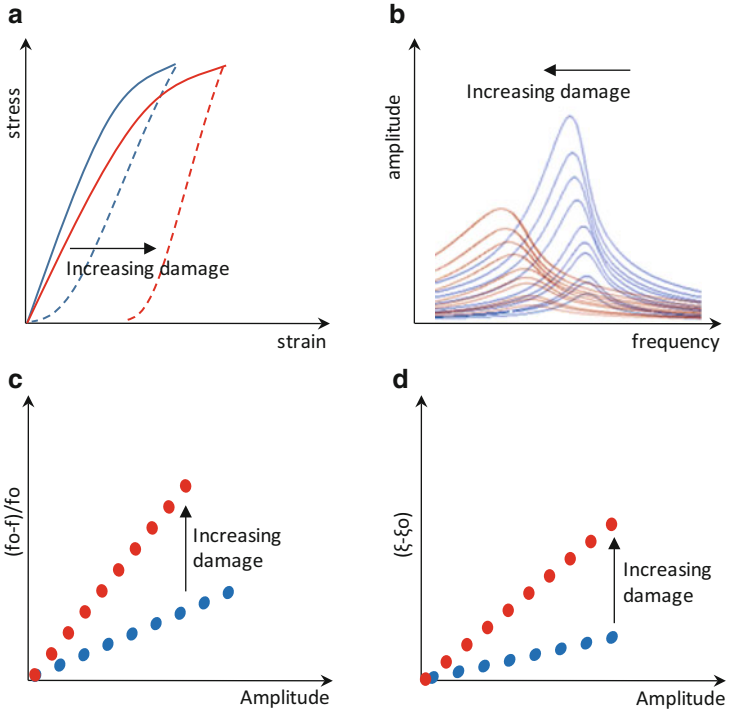

Fig. 12.2 (**a**) Expected behavior of the stress–strain behavior with increasing damage, (**b**) expected evolution of the resonant spectra with increasing damage, and amplitude dependence of the (**c**) resonant frequency, and (**d**) attenuation

12.2 Background

Material degradation (D) is often defined using the dynamic modulus as

$$D = 1 - \frac{E_{o,i}}{E_{o,p}} \tag{12.1}$$

where $E_{o,p}$ is the modulus of elasticity in the pristine state and $E_{o,i}$ is the modulus after an accelerated material degradation treatment. The subscript i may stand for a value indicating the number of cycles that imparted damage, the time of exposure in an aggressive environment, or another parameter characterizing the harshness of the treatment (e.g., the temperature, the concentration of a chemical solution, etc.). Usually, standard reference durability methods assume that the stress–strain relationship remains linear upon increasing damage, and hence the evaluation of damage depends on the variations of the linear resonant frequency. However, deviation from this assumption increases as the material damage level increases, and the material then behaves according to a nonlinear and hysteretic stress–strain

relationship. The resulting nonlinear modulus (E) can be described as

$$E = E_o + H\left(\varepsilon, \dot{\varepsilon}, \Delta\varepsilon\right), \tag{12.2}$$

where the function $H(\varepsilon, \dot{\varepsilon}, \Delta\varepsilon)$ describes a nonlinear and hysteretic departure from the linear elastic behavior, which in general depends on the strain (ε), the strain rate ($\dot{\varepsilon}$), and the dynamic strain amplitude ($\Delta\varepsilon$). In resonant frequency experiments, this nonlinear and hysteretic behavior results in harmonic mode generation, increasing attenuation, and an apparent softening of the material manifested by changing resonant frequency and attenuation with increasing strain amplitude [17, 18]. The latter effects have been referred as the amplitude dependent internal friction [19], or the fast dynamic effect [20]. The relationship between frequency and attenuation shifts with the strain amplitude depends on the type of mechanical hysteresis involved [18, 21]. However, for most materials the resonant frequency was found to vary inversely and proportionately to the strain amplitude ($\Delta\varepsilon$), within a certain level of strain amplitudes $\{\Delta\varepsilon_{\text{th}}, \Delta\varepsilon_{\text{upper}}\}$ [22, 23] usually above 10^{-7} [24]. Therefore, the downward frequency shift experienced with respect to the linear elastic frequency value (f_o) is expressed as

$$\frac{\Delta f}{f_o} = \alpha_f \cdot \Delta\varepsilon, \quad \text{and } \Delta\varepsilon \in \left\{\Delta\varepsilon_{th}, \Delta\varepsilon_{\text{upper}}\right\}. \tag{12.3}$$

The linear elastic frequency value (f_o) is obtained for strain amplitude at and below the threshold value of the strain amplitude ($\Delta\varepsilon_{\text{th}}$). The proportionality constant α_f is a measure of the hysteretic behavior. Analogously, the attenuation properties also become amplitude dependent, so the attenuation shifts from the attenuation in the linear strain regime (ξ_o) as

$$\xi\left(\Delta\varepsilon\right) - \xi_0 = \alpha_\xi \cdot \Delta\varepsilon, \quad \text{and } \Delta\varepsilon \in \left\{\Delta\varepsilon_{\text{th}}, \Delta\varepsilon_{\text{upper}}\right\}, \tag{12.4}$$

where α_ξ is the nonlinear attenuation parameter. Whenever a downward frequency shift is obtained, the attenuation properties are also shifted upward proportionately [25]. Thus, α_f and α_ξ are proportional, which may indicate that both effects arise from the same physical mechanisms [8]: internal friction and rough contacts between unbounded interfaces. Furthermore, materials that exhibit amplitude dependent internal friction effects also reveal a time-dependent creep-like behavior which is referred as the slow dynamics effect [26]. Upon dynamic excitation, slow dynamics manifests in the material response as a progressive softening of the elastic modulus towards a new equilibrium state. Once the dynamic excitation ceases the material experiences a relaxation process whereby the modulus gradually restores to its initial value [26]. The two mechanisms (fast and slow dynamics) are thought to coexist during dynamic excitation, so the material is said to experience material conditioning [23].

The incorporation of a nonlinear hysteretic modulus into Eq. (12.1)—hence $D(\Delta\varepsilon) = 1 - E_i(\Delta\varepsilon)/E_p(\Delta\varepsilon)$—reveals a damage parameter that depends on the

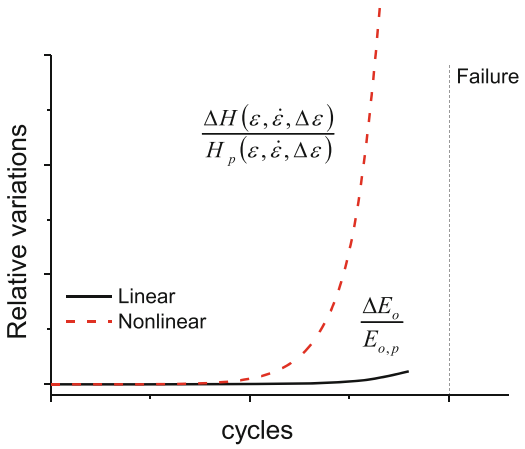

Fig. 12.3 Conceptual illustration of the evolution of linear and nonlinear parameters with increasing damage, expressed in progressive cycles of damage, in durability tests

strain amplitude. Alternately, the evolution of the nonlinear modulus upon material changes (i.e., degradation) can be described by including perturbation terms which reflect the variation of the linear and nonlinear elastic properties from those obtained in the pristine state (subscript p) as

$$E_i\,(\varepsilon,\dot{\varepsilon},\Delta\varepsilon) = \left(E_{o,p} + \Delta E_o\right) + \left(H_p\,(\varepsilon,\dot{\varepsilon},\Delta\varepsilon) + \Delta H\,(\varepsilon,\dot{\varepsilon},\Delta\varepsilon)\right). \qquad (12.5)$$

Every perturbation term can be used in a relative basis for quantifying the evolution of nonlinear and linear parameters with increasing damage content. This idea is illustrated in Fig. 12.3, which shows expected evolution of the linear and nonlinear parameters with increasing damage in durability tests, say with increasing number of fatigue cycles or cycles of exposure in an aggressive medium. In most cases, the relative variations of the linear and nonlinear parameters exhibit a power-law behavior with increasing damage. The nonlinear parameters are able to detect the damage progression at early states, and vary with greater extent with increasing damage as compared with linear measurement parameters [6]. But at the same time, nonlinear parameters also exhibit significantly greater variability, which is not illustrated in Fig. 12.3. In some cases, the rise of material nonlinearity with damage can also reverse itself, which may correspond to crossovers between dominating mechanisms of energy dissipation, for example, viscous vs. dry friction attenuation. This effect can be especially observed in cases where the mechanism of degradation involves chemical reactions, for instance, the alkali-silica reaction in concrete [27]. This effect can also be observed during increase of moisture uptake during durability tests, see also Sect. 12.5.4. In other instances, a particular material degradation mechanism may lead to an apparent healing of the material, whereby the material nonlinearity decreases during accelerated durability tests. These cases include carbonation [28–30] and the degradation of particular fiber types in fiber reinforced concrete [31].

12.3 Signal Processing for Single-Impact Vibration

Signal analysis techniques are used to investigate nonlinear behavior from single-impact vibration signals by extracting the instantaneous frequency and attenuation during the signal ring-down period. To achieve this, different time–frequency signal analysis techniques can be applied. Instead of providing an exhaustive review of time–frequency representations that are available, here we restrict our discussion to the Short-Time Fourier Transform, or "sliding window," method and the time domain fitting method.

12.3.1 Sliding Window

The Fourier transform of a complete time signal provides a composite (average) response over the entire duration of the signal and thus does not permit time–frequency localization for certain time periods within the signal. However, the Short-Time Fourier Transform (STFT) allows for tracking the instantaneous frequency and amplitude variations during the signal ring-down using a sliding widow approach. For a given vibration time signal, the discrete Fourier transform is performed at overlapped time segments of the signal, which are weighted by a window function. Figure 12.4 schematically describes the signal processing technique. In Fig. 12.4b the spectral maxima for each windowed signal illustrates nonlinear softening (frequency reduction) with increasing vibration amplitude. The analysis can be stopped when the spectral amplitude at a given window position reaches a preset low threshold amplitude or a preset number of windows.

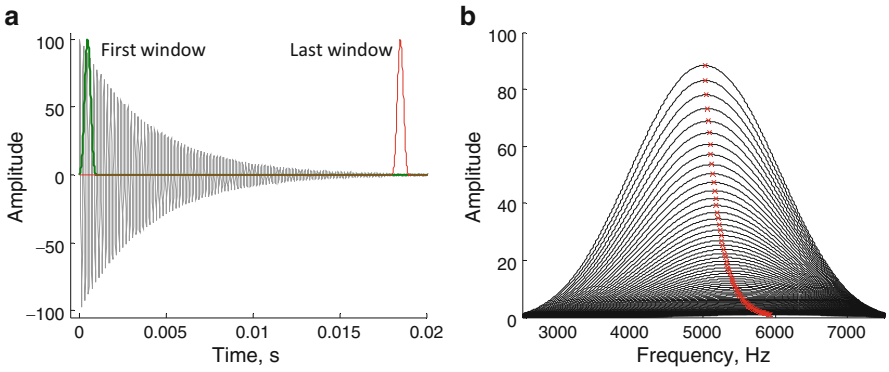

Fig. 12.4 (**a**) Simulated vibration time signal. First and last positions of the sliding window are shown, (**b**) stacked spectra from each window wherein the red points show the maximum amplitude values

The results depend on the signal analysis parameters, such as window length and window function type. Since the frequency resolution of the discrete Fourier transform depends on the signal length, there is a direct trade-off between time and frequency resolutions. Thus, shorter windows provide better time resolution but at the cost of poor frequency resolution. To improve frequency resolution, each signal for a given window position can be zero-padded to artificially increase the frequency step resolution [15]. However, when several modes are present in the signal, the frequency resolution decreases for higher frequency modes because the window length is kept constant. This does not pose a problem in standard test configurations (e.g., ASTM C215) because the test and the analysis of the resonant frequency are focused on only one resonant frequency mode. However, if the analysis of several modes is of interest, the resolution issue can be circumvented, for instance, through a wavelet analysis [32] or an adaptive window length approach [33], so that the frequency resolution can be kept constant along the time–frequency representation.

12.3.2 Time Domain Fitting

The analysis of single-impact vibration signals can be also conducted in the time domain. The time domain fitting method was first proposed by Van Den Abeele and De Visscher [13]. The method consists of fitting an exponentially decaying sine function

$$y(t)|_{\tau} = A_{\tau} \cdot \exp\left(-q_{\tau} \cdot t\right) \cdot \sin\left(2\pi \cdot f_{\tau} \cdot t + \varphi_{\tau}\right), \tag{12.6}$$

to the entire signal using τ overlapped time segments of equal duration; in Eq. (12.6), A_{τ} is the signal amplitude, q_{τ} is the decay parameter, f_{τ} is the frequency, and φ_{τ} is the phase for each of the τ segments. The analysis then retrieves the values of A, f, q, and φ for each time segment τ, allowing investigation of the amplitude dependent internal friction effects. The experimental configuration proposed by Abeele and De Visscher used a loudspeaker to emit a low frequency long sinusoidal burst that matches the resonant frequency of the sample under investigation. The analysis of the signal was then performed during the ring-down of the reverberation signal after the burst excitation had been switched off. Such an experimental configuration and signal analysis was applied to analyze the material nonlinearity of concrete [13], titanium alloys [34], and carbon fiber reinforced polymer samples [35, 36].

In case of a single-impact excitation, it is expected that several vibration modes of the sample will be excited simultaneously. Hence, the model can be adapted by considering the superposition of M vibration modes as

$$y(t)|_{\tau} = \sum_{m=1}^{M} A_{m,\tau} \cdot \exp\left(-q_{m,\tau} \cdot t\right) \cdot \sin\left(2\pi \cdot f_{m,\tau} \cdot t + \varphi_{m,\tau}\right) \tag{12.7}$$

where the subscript m stands for different vibration modes. One of the pitfalls of this technique is that the amplitude value corresponds to the maximum amplitude value within the measured time segment, while the frequency and decay parameter values are averaged (in the sense of least-squares) over the time segment. Also, the results depend on parameters such as the selected time segment length. Dahlén et al. [14] pointed out these concerns and proposed to fit the entire vibration signal to the model,

$$y(t) = \sum_{m=1}^{m=M} A_m \cdot \exp\left(\theta_m(t)\right) \cdot \sin\left(\varphi_m(t)\right), \tag{12.8}$$

where the functions $\theta_m(t)$ and $\phi_m(t)$ are time-dependent polynomial descriptions of the phase and attenuation of order N_m, and K_m

$$\varphi_m(t) = \sum_{n=0}^{n=N_m} p_{n,m} \cdot t^n, \quad \text{and} \tag{12.9}$$

$$\theta_m(t) = \sum_{k=1}^{k=K_m} q_{k,m} \cdot \ t^k, \tag{12.10}$$

where $p_{n,m}$ and $q_{k,m}$ are the coefficients of the polynomials corresponding to the vibration mode m. By fitting the entire signal, the instantaneous variations of signal amplitude can be precisely related to the instantaneous variations of frequency and attenuation; this approach is also called the global fitting method. It follows that the amplitude values are independent of the signal processing parameters (window length, window type, etc.), in contrast to the Fourier-based analysis or windowed fitting methods. The polynomial orders (N_m and K_m) should be selected by finding an appropriate compromise between the residuals of the fit and the number of parameters included in the model. This is normally achieved through either the Akaike's or the Bayesian Information Criteria. The latter favors the selection of parsimonious models, hence having lower polynomial orders. Two different algorithms to find the least-squares solution and polynomial order selection can be found in [14] and in [37].

The global fitting method becomes especially cumbersome when an increasing number of vibration modes coexist in the signal. Under certain circumstances, when the time-varying phase and attenuation exhibit non-monotonic variations with time, then higher order polynomials for the $\theta_m(t)$ and $\phi_m(t)$ functions are required. For instance, consider the case when the instantaneous frequency and attenuation appear to vary periodically. In this case, when the entire vibration signal is analyzed through a Fourier transform, the main resonant frequency peak may show a double hump or splitting of the resonant peak; this is further discussed in Sect. 12.5.3. In these cases, alternate functions $\theta_m(t)$ and $\phi_m(t)$ that are not polynomial in form can be

considered in order to better describe the nonlinear behavior. Otherwise, a model-free method is preferred, such as the sliding window analysis described in Sect. 12.3.1.

12.4 Damage Quantification from a Single-Impact Response

Regardless of the feature extraction technique used to investigate the instantaneous characteristics of a single-impact vibration signal, the material nonlinearity can be detected by observing relationships between the signal amplitude and instantaneous frequency or attenuation. Unlike the nonlinear techniques that investigate the amplitude dependent internal friction by varying the excitation amplitude in consecutive runs, ring-down spectroscopies allow investigation of the material nonlinearity in a single run. Yet, experimental observations in damaged materials [35, 37] have revealed that the nonlinear behaviors extracted from single- and multiple-runs are substantially different, especially with increasing amount of damage within the sample. Figure 12.5a, b compares nonlinear multiple- and single-impact resonance results obtained from the same damaged concrete sample. Differences in frequency–amplitude dependence obtained from the two approaches are apparent by comparing the solid and dashed lines in Fig. 12.5b. The multiple-impact approach (Fig. 12.5a) analyzes the downward shift of the resonant frequency with successively increasing impact force for each event. In this case, the frequency decreases linearly with increasing spectral amplitude (see inset plot in Fig. 12.5a). The spectral amplitude is proportional to strain amplitude, but precise quantification of the hysteretic behavior through the slope of the frequency–amplitude relationship is limited by the arbitrary units of the spectral amplitude; recall that the Fourier spectral amplitude and frequency values are averaged over the duration of the ring-down signal. This is the main downside of the multiple-impact approach: it does not permit physical quantification, but rather a qualitative comparison between different damage states.

Considering now the single-impact approach, every impact vibration response from that same data set is analyzed individually, following the global time domain fitting method—see Sect. 12.3.2 for more detail. In contrast to the multiple-impact approach, analysis of ring-down of the single-impact signal enables the frequency shift to be related to signal amplitude using the physical units with which the signal was measured, thus enabling quantitative evaluation of the nonlinear behavior. The signal amplitude can then be translated to strain using analytical [38] or numerical approaches [39]. Moreover, the results shown in Fig. 12.5b demonstrate that the instantaneous frequency–amplitude dependences for every individual single-impact vibration signal are nonlinear, and that the response form depends on the impact force. Yet the frequency obtained at the maximum amplitude of every impact, indicated by circle symbols, reveals a linear relationship as ascertained from the Fourier transform of every impact signal (inset in Fig. 12.5a). These results illustrate the point that the frequency–amplitude dependences from both approaches differ substantially.

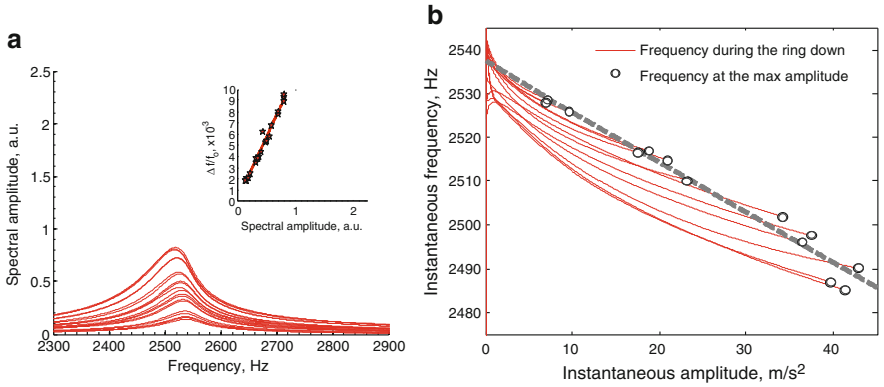

Fig. 12.5 Investigation of the material nonlinearity of a concrete sample: (**a**) resonant spectra corresponding to multiple-impact events each with varying amplitude, where the inset figure shows the relationship between the relative frequency shift and the spectral amplitude; (**b**) instantaneous frequency–amplitude variation obtained during the ring-down of every single-impact event using the global time domain fitting method (continuous lines) where circle symbols represent the frequency values corresponding to the maximum amplitude for each individual impact and the dashed line fit to the maximum amplitude results match the linear trend found in (**a**)

The dissimilarity between single- and multiple-impact method results can be attributed principally to the slow dynamics effect. In the multiple-impact method the slow dynamic effect is less significant assuming that the material is able to recover the resonant frequency to a reasonable amount between consecutive impacts. If sufficient recovery between impacts is achieved, then the variability of impact force on the resonant frequency is well represented by the strain amplitude and does not depend on the time lapse between consecutive impacts. In contrast, in the single-impact method, the frequency recovery during the ring-down signal depends not only on the strain amplitude, but also on the previous history of the dynamic load; the latter is represented in general form using the subscript "*t-1*," to recognize that frequency shift resulting from the slow dynamics contribution lags with respect to the instantaneous strain amplitude. Then, the total (measured) frequency shift experienced during a ring-down signal ($f_o - f(\Delta\varepsilon,\Delta\varepsilon_{t\text{-}1})$) can be considered as the superposition of two elastic subsystems: (1) one that depends on the instantaneous strain amplitude—or fast dynamics ($f_o - f(\Delta\varepsilon)$)—having no memory of the load history, and (2) another that depends on the load history—or slow dynamics ($f_o - f(\Delta\varepsilon_{\max},\Delta\varepsilon_{t\text{-}1})$). When expressed as a simple linear combination of effects, the expression for total frequency shift becomes

$$\frac{f_0 - f\,(\Delta\varepsilon,\,\Delta\varepsilon_{t-1})}{f_0} = \left\langle \frac{f_0 - f\,(\Delta\varepsilon)}{f_0} \right\rangle_{\text{fast}} + \left\langle \frac{f_0 - f\,(\Delta\varepsilon_{t-1},\,\Delta\varepsilon_{\max})}{f_0} \right\rangle_{\text{slow}}. \tag{12.11}$$

Experimental observations in concrete suggest that fast and slow dynamics are coupled during dynamic excitation, as indicated by Eq. (12.11). This coupled effect has been referred as material conditioning [23, 40]. It follows that in order to decompose fast and slow dynamic contributions from the total, a priori knowledge is required about (1) the frequency–amplitude dependence set up by the fast dynamic behavior, and (2) the linear resonant frequency value f_o. Thus, in the case of a linear relationship between frequency and strain amplitude (e.g., as shown in Fig. 12.5a for the case of spectral amplitude, which is proportional to the strain amplitude), the nonlinear hysteretic parameter can be extracted from the maximum value obtained from a single-impact response as

$$\alpha_f = \frac{\left(\frac{f_0 - f_{\Delta\varepsilon\,\max}}{f_0}\right)}{\Delta\varepsilon_{\max}}. \tag{12.12}$$

where $f_{\Delta\varepsilon\max}$ is the frequency value obtained at the maximum strain amplitude ($\Delta\varepsilon_{\max}$). In this way, the frequency shift corresponding to the fast dynamic effect is proportional to the amplitude variation over the signal ring-down, and the slow dynamics contribution deviates away the proportional frequency shift behavior. Figure 12.6a, b illustrates conceptually the fast and slow dynamic contributions as a function of time and as a function of the strain amplitude for a general case where the frequency–amplitude dependence corresponding to the fast dynamic effect is assumed to be linear; note, however, that other nonlinear relationships can be also considered for the fast dynamics effect as the frequency–amplitude relationship depends on the type of mechanical hysteresis [21]. The linear combination of fast and slow dynamics expressed in Eq. (12.11) is illustrated in Fig. 12.6b, illustrating the relationship between frequency and amplitude obtained for both single- and multiple-runs. Note also that a similar decomposition can be derived for the amplitude dependent attenuation. The investigation of the nonlinear behavior through a single-impact approach contains the slow dynamic response (dotted lines in Fig. 12.6a, b), which in a multiple-impact approach may be avoided with sufficient material recovery time between impact events. The latter can be achieved by controlling the time lapse between impacts and by verifying that the resonant frequency has been restored to the value obtained in the linear strain regime (f_o) between consecutive acquisitions.

12.5 Sources of Variability and Systematic Errors

The measurement of linear and nonlinear elastic properties from resonant frequency tests is affected by different sources of variability. These sources of measurement variability are inherent to the specific feature extraction technique employed, to the particular test configuration employed, or to the ambient environmental conditions. Some of these effects are disregarded, or only vaguely addressed, in

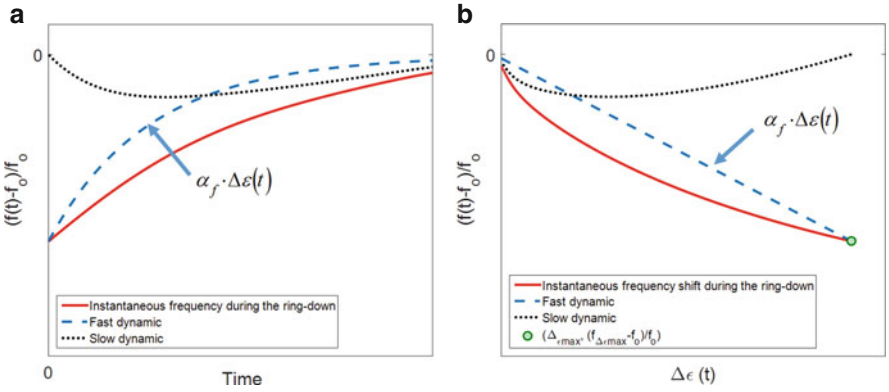

Fig. 12.6 Conceptual illustration of the resonant frequency shift during the signal ring-down and decomposed fast and slow dynamic contributions as a function of (**a**) time and (**b**) strain amplitude. The circular point indicates the maximum strain amplitude

the test standards even though they may significantly affect the results or lead to misinterpretation of data. A good understanding of the following sources of variability would further enhance the robustness of linear and nonlinear resonance frequency evaluation for material characterization.

12.5.1 Errors in Nonlinear Parameter Estimation

The signal processing used to extract and quantify nonlinear behavior from the raw signal data affects the obtained parameter values and variability. In general, the signal processing must provide enough frequency resolution to reveal the small frequency variations that occur with changing excitation amplitude. Therefore, the smallest hysteretic parameter value that can be ascertained will depend on the frequency and amplitude resolutions of the signals. However, the accuracy of the hysteretic parameter depends on the precision with which the defined frequency in the linear strain regime, f_o, is determined. The effects of incorrect selection of f_o on the hysteretic parameter were previously discussed by Johnson et al. [41]. They identified the likely causes leading to incorrect estimation of f_o are: (1) high material attenuation that can hinder the identification of f_o, (2) insufficient frequency step resolution used in the signal analysis, and (3) the effect of material conditioning, meaning the f_o value was not measured in the equilibrium state. Often, f_o and ξ_o values are assumed to be the value obtained from the lowest excitation amplitude event, which depends on the sensitivity of the measurement excitation and sensing systems, rather than being ascertained at the true linear strain regime. Consideration of a pair $\Delta\varepsilon_{th}, f_o$ values that are above the true linear strain regime leads to an overestimation of the hysteretic parameter. Figure 12.7a shows

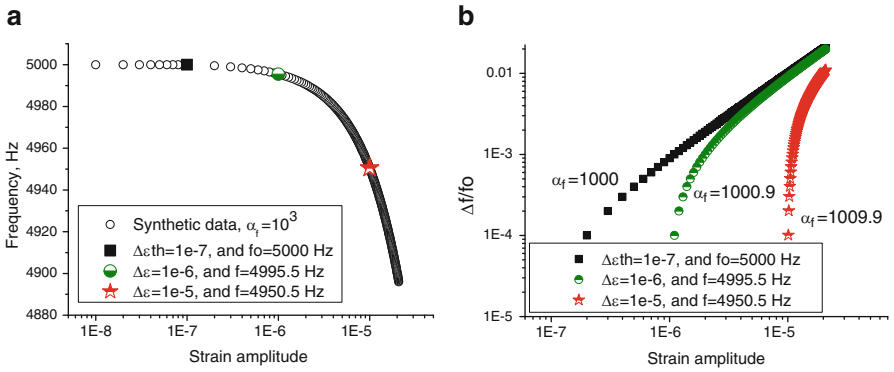

Fig. 12.7 (**a**) Synthetic data representing the frequency variation of the resonant frequency as a function of the strain amplitude with a value $\alpha_f = 1000$, and whose true linear frequency f_o is equal to 5000 Hz, and the true threshold strain amplitude $\Delta\varepsilon_{th}$ equals 10^{-7}, and (**b**) normalized frequency shift as a function of the strain amplitude, where the different curves represent normalized frequency shift obtained when the linear frequency is considered to be at higher values of strain amplitude than the true $\Delta\varepsilon_{th}$ values

synthetic data relating strain amplitude and frequency for $\alpha_f = 10^3$, $\Delta\varepsilon_{th} = 10^{-7}$, and $f_o = 5000$ Hz. Figure 12.7b shows the effects on the computation of the hysteretic parameter α_f when slightly high values of $\Delta\varepsilon_{th}$ and f_o are assigned. Also, separate discussion is needed to consider the transformation from the dynamic response of the sample (acceleration, velocity, or displacement) to its internal dynamic strain amplitude. Although these conversions are appealing because the nonlinear behavior is defined by strain response (see Eq. (12.2)), the relations to conduct such a transformation presume linear elastic behavior [38]. With increasing material damage, these conversions will deviate from the linear elastic assumption; a comprehensive study addressing this issue is needed.

12.5.2 Effect of Test Configuration

The test configuration that is employed may affect the obtained dynamic response results because of imperfect sample boundary conditions, varying mode excitation, or varying dynamic strain rate used in the dynamic excitation. Standard resonant frequency tests are normally performed on a sample assuming free boundary conditions. As such, samples are either supported on a foam mat, hung by elastic wires, supported on rods, or otherwise held at nodal positions. Some studies also have employed a cantilever configuration, however, non-ideal clamping conditions at the sample end may obscure the measurement of the material nonlinearity. For example, new sources of nonlinearity can be introduced to the overall system because of a loose clamp, while excessive torque on the clamped end can constrain

the sample, leading to a mitigation of the nonlinear behavior [42]. Also, additional care must be taken with coupling transducers and excitation sources to the test sample to avoid nonlinear effects and spurious frequencies that are not inherent to the mechanical behavior of the material under inspection, but are associated with the test configuration itself. For example, rattling between transducers, rigs, etc. and the sample under inspection can lead to such spurious nonlinear system behaviors [43]. These spurious effects can be avoided, where possible, by the selection of test configurations that let the sample freely vibrate as much as possible.

Experimental observations have also revealed that different modes of vibration can exhibit distinct hysteretic behavior [39, 44], and so each may evolve in different ways with increasing damage. Therefore, a complete characterization of the nonlinear behavior should consider different vibration mode families (e.g., compressional, flexural, and torsional). Also, the effects of varying test strain rate may be significant, considering that strain rate does affect the nonlinear and hysteretic behavior as described in Eq. (12.2). In general, nonlinear and hysteretic behavior is enhanced with increasing dynamic strain rate [45, 46]. These observations suggest that shorter samples may enhance the nonlinear effects when compared to longer ones, as the same vibration mode will subject the shorter sample to a higher strain rate dynamic loading (higher frequency). To the authors' knowledge, these issues have not yet been clearly addressed.

12.5.3 Double-Hump Effect

The resonant spectra of a standard flexural vibration test configuration may display closely spaced resonant frequencies mostly depending on the sample geometry, which are normally either prisms or cylinders. For samples that exhibit cross-sectional geometric symmetry, flexural modes in orthogonal directions appear at the same frequency value, and are said to be degenerate modes. If this symmetry is somehow disrupted, for example, because of imperfect geometry or the presence of an internal localized defect or density variation across the sample, the frequency of the degenerate modes separates. This effect has been dubbed as signal beating [47], double-hump effect [48], or splitting of degeneracies [49]. For concrete samples, in particular for imperfect cross-sectional geometry of the sample, the presence of a localized crack or honeycomb or chip within the material, non-uniform moisture distribution, or a density variation across the sample—for instance, because of bleeding of the concrete batch—may cause peak splitting. Also, in concrete durability tests, peak splitting effect may be enhanced as damage progresses in asymmetric fashion. Thus the double-hump effect can be observed upon increasing degradation, for example, with external chemical attack wherein the inward diffusion of aggressive chemical species can lead to a density variation across the sample, or in durability tests that subject the samples to thermal shocks or freezing-thawing cycles. In other cases, the peak splitting can be interpreted as a periodic variation of sample stiffness during opening and closing of an internal defect (e.g., a surface-breaking crack)

upon dynamic motion [50, 51]. In other instances, a double-hump effect can be also caused by poorly attached sensors on the sample [27].

Figure 12.8a, b shows the vibration response in time and frequency domains corresponding to the flexural mode of a concrete sample containing a vertical surface-breaking crack at the mid-span. The presence of the crack disrupts the continuous amplitude ring-down of the signal (Fig. 12.8a). When the whole vibration signal is interpreted in the frequency domain, the resonant peak appears to split (Fig. 12.8b). When the instantaneous frequency is investigated (Fig. 12.8c), the resonant frequency appears to vary periodically, giving the appearance that the stiffness of the sample varies with dynamic excitation. Thus peak splitting may be leveraged to identify defective samples and detect damage where the span of the frequency split correlates with the size of the defect [49, 52, 53]. However, within the context of material characterization, where the goal of the resonant frequency test is to obtain engineering properties (elastic moduli, damping, or the hysteretic parameter), peak splitting may disrupt the analysis. In this case non-degenerate

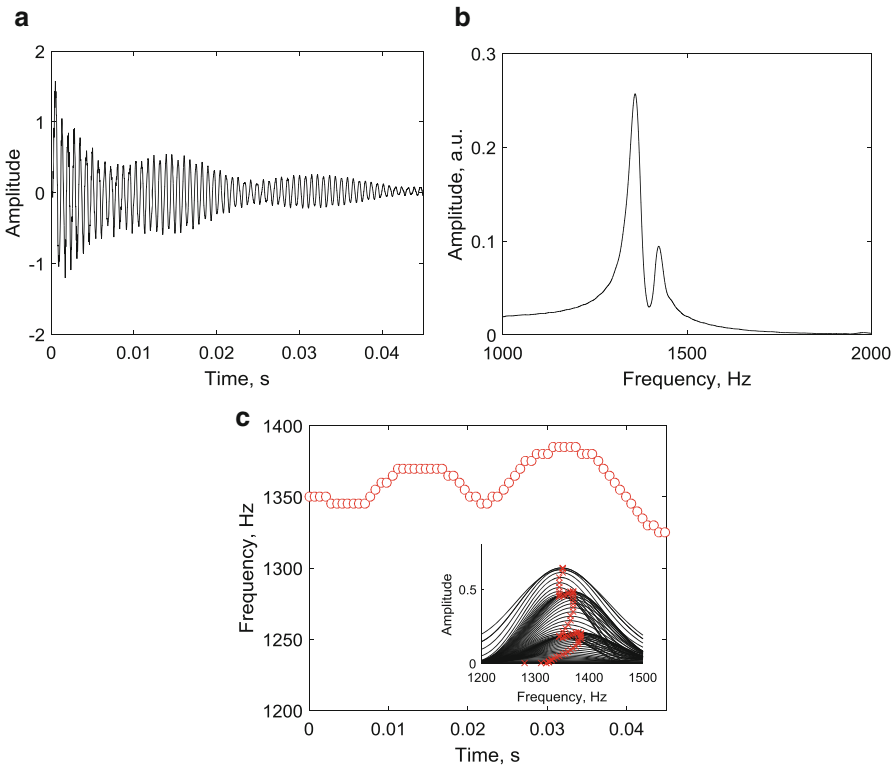

Fig. 12.8 (**a**) Vibration signal corresponding to the flexural mode of a concrete sample containing a surface breathing crack, (**b**) resulting spectra showing splitting of the resonant peak, and (**c**) time–frequency representation; the inset plot shows the stacked spectra obtained through the sliding window method

modes (e.g., from the longitudinal and torsional families of modes) should be selected to characterize the samples.

12.5.4 Environmental Factors: Internal Moisture and Temperature

The constitutive properties of porous materials such as concrete are affected by the internal moisture contained within the pore structure. In general, moisture in the internal pore structure exerts a buildup of internal (hydraulic) pressure, which results in an alteration of the apparent elastic properties. The way which moisture affects the linear and nonlinear elastic properties depends on the characteristics of the pore network [54]. For concrete-like materials, it has been shown that an increase of the apparent modulus and an increase of the apparent attenuation occur with increasing moisture content. The extent of variation of the dynamic properties with internal moisture variations depends, however, on the concrete properties and composition [55]. The increase of modulus with increasing moisture content appears to be controlled by capillary-sized porosity, which is usually in the pore size range of 10–0.01 μm [55, 56]. Loss of internal moisture can also produce tensile stresses leading to microcracking of brittle porous materials [57]. Hence, the hysteretic behavior of concrete can be enhanced after drying treatment because it can lead to shrinkage, cracking, and other microstructural modifications [56]. However, subsequent moisture uptake by the material can alleviate the mechanisms that give rise to the nonlinear behavior [37, 58]. These observations illustrate the important effect of moisture because it can obscure the presence of damage sensed by nonlinear parameters and lead to misinterpretations in durability tests. The elastic properties of materials depend also on the sample temperature [59]. The elastic modulus of different rock types exhibits hysteretic behavior during warming and cooling cycles [60]. These results may be also relevant for concrete-like materials. Environmental conditions (i.e., moisture and temperature) must be carefully maintained during durability test to avoid such misinterpretations.

12.5.5 Material Conditioning

Because of nonlinear hysteretic behavior exhibited by concrete, a memory effect may persist whereby the material temporarily "remembers" the previous load history [61]. As a consequence of this slow dynamics effect, the measured frequency and attenuation behavior may change if the standard resonant frequency test in concrete samples is repeated with short periods of rest in between [37, 62]. In other words, the resonant frequency and attenuation of a test may be affected by the previous impact test. Figure 12.9a shows the resonant frequency of concrete

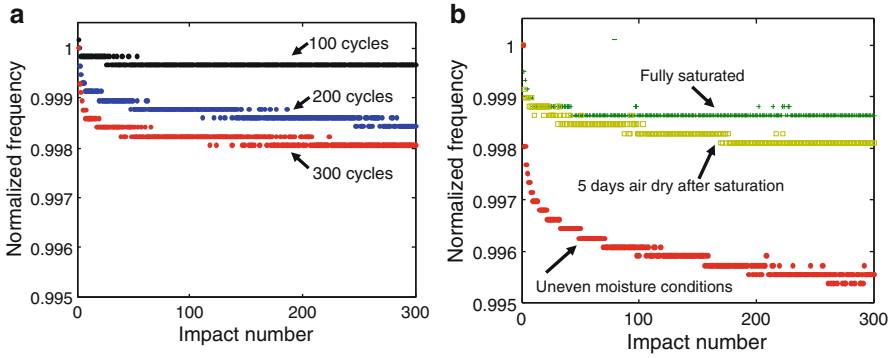

Fig. 12.9 (**a**) Repeated resonant frequency measurements in concrete samples that underwent 100, 200, and 300 freezing-thawing cycles, and (**b**) repeated resonant frequency measurements for varying moisture content in the concrete sample that underwent 300 cycles

samples that underwent 100, 200, and 300 standard freezing-thawing cycles [3] and thus are expected to exhibit increasing amounts of distributed cracking damage. The resonant frequency test was repeated at a constant impact rate (1 Hz) and with a constant impact energy by using an automated impactor device. The results demonstrate that the resonant frequency decreases with accrued number of impacts for these types of tests, and that the amount of this change depends on the extent of internal damage. Yet, the initial resonant frequency can be eventually restored if enough rest time between subsequent tests is provided for the sample to recover the initial properties through the slow dynamics process (not shown in these data). Furthermore, the influence of the slow dynamic effect can be affected by the internal moisture content of the material. Figure 12.9b shows that the slow dynamic effect is modified by changing internal moisture content. Thus slow dynamic behavior arises from significant and separate contributions from internal moisture and internal damage levels, which can lead to misinterpretation of the obtained results if sufficient care is not taken. The influence of the slow dynamic effect on the measurement of the hysteretic parameters can be minimized by increasing the time lapse between consecutive acquisitions, that is by providing sufficient "rest" time between measurements by verifying that the elastic modulus has been restored to that obtained at linear strain amplitude excitation; however, "sufficient" rest time can require up to ten to thousands of seconds between consecutive acquisitions, depending on the material and ambient conditions [40].

12.6 Concluding Remarks

This chapter describes the use of nonlinear single-impact resonant acoustic spectroscopy (NSIRAS) to quantify nonlinear material behavior of concrete, such as

amplitude dependent internal friction effects. NSIRAS is a ring-down spectroscopic method where the data are collected using the standard impact resonant frequency test configuration (e.g., ASTM C 215). The NSIRAS approach offers a balance of sensitivity to material damage, when compared with linear vibration methods, and test simplicity in comparison to other nonlinear test methods such as nonlinear elastic wave spectroscopy or the dynamic acousto-elasticity test. Several different signal processing alternatives that extract nonlinear features, which arise from the nonlinear and hysteretic behavior of concrete, from the measurement signal were described. Multiple- and single-impact (ring-down spectroscopy) methods were compared. The single-impact method offers advantages in comparison to multiple-impact methods. For example, material nonlinearity can be investigated using the physical units of the signal amplitude, rather than the arbitrary units of spectral amplitude. Also, the single-impact method reduces the operating time and the number of impacts needed to carry out the test; multiple repeated impacts could lead to local damage in concrete samples, especially in durability tests as the distress progresses in the material. Some of the concerns and limitations related to impact resonant frequency tests are finally presented, particularly those related to the investigation of the durability of cement-based materials.

Acknowledgements This work has been supported by the Spanish Administration (MINECO: BIA 2010-19933 and BIA2014-55311-C2-1-P, projects) and FEDER funds. Jesús N. Eiras wants to acknowledge the financial support provided by the Ministerio de Economía y Competitividad (MINECO Spain, grant BES-2011-044624).

References

1. ASTM C215-14, Standard Test Method for Fundamental Transverse, Longitudinal, and Torsional Resonant Frequencies of Concrete. West Conshohocken, PA, 2014
2. V.M. Malhotra, V. Sivasundaram, in Resonant Frequency Methods. *Handbook on Nondestructive Testing of Concrete* (CRC Press, Boca Raton, 2004). pp. 167–188
3. ASTM-C666/C666M-15, Standard Test Method for Resistance of Concrete to Rapid Freezing and Thawing. West Conshohocken, PA, 2015
4. ASTM C1012/C1012M-15, Standard Test Method for Length Change of Hydraulic-Cement Mortars Exposed to a Sulfate Solution. West Conshohocken, PA, 2015
5. J. Chen, A.R. Jayapalan, J. Kim, K.E. Kurtis, L.J. Jacobs, Rapid evaluation of alkali–silica reactivity of aggregates using a nonlinear resonance spectroscopy technique. Cem. Concr. Res. **40**(6), 914–923 (2010)
6. P.B. Nagy, Fatigue damage assesstment by nonlinear ultrasonic materials characterization. Ultrasonics **36**, 375–381 (1998)
7. C. Payan, V. Garnier, J. Moysan, P.A. Johnson, Applying nonlinear resonant ultrasound spectroscopy to improving thermal damage assessment in concrete. J. Acoust. Soc. Am. **121**(4), EL125–EL130 (2007)
8. K. Van Den Abeele, A. Sutin, J. Carmeliet, P.a. Johnson, Micro-damage diagnostics using nonlinear elastic wave spectroscopy (NEWS). NDT E Int. **34**(4), 239–248 (2001)
9. V. Gusev, V. Tournat, B. Castagnède, in Non-Destructive Evaluation of Micro-Inhomogenous Solids by Nonlinear Acoustic Methods. *Materials and Acoustics Handbook* (Wiley, Hoboken, 2010), pp. 473–503

10. Y. Zheng, R.G. Maev, I.Y. Solodov, Nonlinear acoustic applications for material characterization: a review. Can. J. Phys. **77**, 927–967 (1999)
11. V.E. Nazarov, L.A. Ostrovsky, I.A. Soustova, A.M. Sutin, Nonlinear acoustics of micro-inhomogeneous media. Phys. Earth Planet. Inter. **50**(1), 65–73 (1988)
12. L.A. Ostrovsky, P.A. Johnson, Dynamic nonlinear elasticity in geomaterials. Riv. Nuovo Cimento **24**(7), 1–46 (2001)
13. K. Van Den Abeele, J. De Visscher, Damage assessment in reinforced concrete using spectral and temporal nonlinear vibration techniques. Cem. Concr. Res. **30**(9), 1453–1464 (2000)
14. U. Dahlén, N. Ryden, A. Jakobsson, U. Dahlen, N. Ryden, A. Jakobsson, Damage identification in concrete using impact non-linear reverberation spectroscopy. NDT E Int. **75**(1), 15–25 (2015)
15. J.N. Eiras, J. Monzó, J. Payá, T. Kundu, J.S. Popovics, Non-classical nonlinear feature extraction from standard resonance vibration data for damage detection. J. Acoust. Soc. Am. **135**(2), EL82–EL87 (2014)
16. S.A. Neild, M.S. Williams, P.D. McFadden, Nonlinear vibration characteristics of damaged concrete beams. J. Struct. Eng. **129**(2), 260–268 (2003)
17. R.A. Guyer, K.R. McCall, K. Van Den Abeele, Slow elastic dynamics in a resonant bar of rock. Geophys. Res. Lett. **25**(10), 1585–1588 (1998)
18. V.E. Nazarov, A.V. Radostin, L.A. Ostrovsky, I.A. Soustova, Wave processes in media with hysteretic nonlinearity: part 2. Acoust. Phys. **49**(4), 444–448 (2003)
19. V.E. Nazarov, A.V. Radostin, *Nonlinear Acoustic Waves in Micro-Inhomogeneous Solids* (Wiley, Hoboken, 2015)
20. R.A. Guyer, P.A. Johnson, *Nonlinear Mesoscopic Elasticity* (Wiley, Wienhiem, 2009)
21. C. Pecorari, D.A. Mendelsohn, Forced nonlinear vibrations of a one-dimensional bar with arbitrary distributions of hysteretic damage. J. Nondestruct. Eval. **33**(2), 239–251 (2014)
22. R.A. Guyer, P.A. Johnson, Nonlinear mesoscopic elasticity: evidence for a new class of materials. Phys. Today **52**(4), 30–36 (1999)
23. P.A. Johnson, A. Sutin, Slow dynamics and anomalous nonlinear fast dynamics in diverse solids. J. Acoust. Soc. Am. **117**(1), 124–130 (2005)
24. D. Pasqualini, K. Heitmann, J.A. TenCate, S. Habib, D. Higdon, P.A. Johnson, Nonequilibrium and nonlinear dynamics in Berea and Fontainebleau sandstones: low-strain regime. J. Geophys. Res. **112**(B1), B01204 (2007)
25. T.A. Read, The internal friction of single metal crystals. Phys. Rev. **58**, 371–380 (1940)
26. J.A. TenCate, E. Smith, R.A. Guyer, Universal slow dynamics in granular solids. Phys. Rev. Lett. **85**(5), 1020–1023 (2000)
27. K.J. Leśnicki, J.-Y. Kim, K.E. Kurtis, L.J. Jacobs, Assessment of alkali–silica reaction damage through quantification of concrete nonlinearity. Mater. Struct. **46**(3), 497–509 (2013)
28. F. Bouchaala, C. Payan, V. Garnier, J.P.P. Balayssac, Carbonation assessment in concrete by nonlinear ultrasound. Cem. Concr. Res. **41**(5), 557–559 (2011)
29. J.N. Eiras, T. Kundu, J.S. Popovics, J. Monzó, M.V. Borrachero, J. Payá, Effect of carbonation on the linear and nonlinear dynamic properties of cement-based materials. Opt. Eng. **55**(1), 11004 (2015)
30. Q.A. Vu, V. Garnier, J.F. Chaix, C. Payan, M. Lott, J.N. Eiras, Concrete cover characterisation using dynamic acousto-elastic testing and rayleigh waves. Constr. Build. Mater. **114**, 87–97 (2016)
31. J.N. Eiras, T. Kundu, M. Bonilla, J. Payá, Nondestructive monitoring of ageing of alkali resistant glass fiber reinforced cement (GRC). J. Nondestruct. Eval. **32**(3), 300–314 (2013)
32. J.S. Walker, *A Primer on Wavelets and Their Scientific Applications* (Chapman & Hall/CRC, London, 1999)
33. S. Nisar, O.U. Khan, M. Tariq, An efficient adaptive window size selection method for improving spectrogram visualization. Comput. Intell. Neurosci. **2016**, 1–13 (2016)
34. K. Van Den Abeele, C. Campos-Pozuelo, J. Gallego-Juarez, F. Windels, B. Bollen, Analysis of the Nonlinear Reverberation of Titanium Alloys Fatigued at High Amplitude Ultrasonic Vibration. Proceedings Forum Acustica Sevilla, 2002

35. B. Van Damme, K. Van Den Abeele, The application of nonlinear reverberation spectroscopy for the detection of localized fatigue damage. J. Nondestruct. Eval. **33**(2), 263–268 (2014)
36. K. Van Den Abeele, P.-Y. Le Bas, B. Van Damme, T. Katkowski, Quantification of material nonlinearity in relation to microdamage density using nonlinear reverberation spectroscopy: experimental and theoretical study. J. Acoust. Soc. Am. **126**(3), 963–972 (2009)
37. J.N. Eiras, Studies on nonlinear mechanical wave behavior to characterize cement based materials and its durability, Dissertation, Universitat Politècnica de València, 2016
38. F.V. Hunt, Stress and strain limits on the attainable velocity in mechanical vibration. J. Acoust. Soc. Am. **32**(7), 1123–1128 (1960)
39. C. Payan, T.J. Ulrich, P.Y. Le Bas, T. Saleh, M. Guimaraes, Quantitative linear and nonlinear resonance inspection techniques and analysis for material characterization: application to concrete thermal damage. J. Acoust. Soc. Am. **136**(2), 537 (2014)
40. P.A. Johnson, in Nonequilibrium Nonlinear-Dynamics in Solids: State of the Art State of the Art in Nonequilibrium Dynamics. ed. By P.P. Delsanto. *Universality of Nonclassical Nonlinearity* (Springer, New York, 2006), pp. 49–69
41. P.A. Johnson, B. Zinszner, P.N.J. Rasolofosaon, F. Cohen-Tenoudji, K. Van Den Abeele, Dynamic measurements of the nonlinear elastic parameter α in rock under varying conditions. J. Geophys. Res. **109**(B2), B02202 (2004)
42. U. Polimeno, M. Meo, Understanding the effect of boundary conditions on damage identification process when using non-linear elastic wave spectroscopy methods. Int. J. Non-Linear Mech. **43**(3), 187–193 (2008)
43. P. Duffour, M. Morbidini, P. Cawley, Comparison between a type of vibro-acoustic modulation and damping measurement as NDT techniques. NDT E Int. **39**(2), 123–131 (2006)
44. M.C. Remillieux, R.A. Guyer, C. Payan, T.J. Ulrich, Decoupling nonclassical nonlinear behavior of elastic wave types. Phys. Rev. Lett. **116**(11), 115501 (2016)
45. K.E. Claytor, J.R. Koby, J.A. TenCate, Limitations of Preisach theory: elastic aftereffect, congruence, and end point memory. Geophys. Res. Lett. **36**(6), L06304 (2009)
46. V. Gusev, V. Tournat, in Thermally Induced Rate-Dependence of Hysteresis in Nonclassical Nonlinear Acoustics. *Universality of Nonclassical Nonlinearity* (Springer, New York, 2006), pp. 337–348
47. L. Meirovitch, *Fundamentals of Vibrations* (McGraw Hill, New York, 2001)
48. R. Jones, *Non Destructive Testing of Concrete* (Cambridge University Press, London, 1962)
49. A. Migliori, J.L. Sarrao, *Resonant Ultrasound Spectroscopy: Applications to Physics, Materials Measurements, and Nondestructive Evaluation* (Wiley, New York, 1997)
50. T.G. Chondros, A.D. Dimarogonas, J. Yao, Vibration of a beam with breathing crack. J. Sound Vib. **239**(1), 57–67 (2001)
51. E. Douka, L.J. Hadjileontiadis, Time–frequency analysis of the free vibration response of a beam with a breathing crack. NDT E Int. **38**(1), 3–10 (2005)
52. ASTM E2001-13, Standard Guide for Resonant Ultrasound Spectroscopy for Defect Detection in Both Metallic and Non-Metallic. West Conshohocken, PA, 2013.
53. K. Flynn, M. Radovic, Evaluation of defects in materials using resonant ultrasound spectroscopy. J. Mater. Sci. **46**(8), 2548–2556 (2011)
54. K. Van Den Abeele, J. Carmeliet, P.A. Johnson, B. Zinszner, Influence of water saturation on the nonlinear elastic mesoscopic response in earth materials and the implications to the mechanism of nonlinearity. J. Geophys. Res. **107**, 1–11 (2002)
55. L.O. Yaman, N. Hearn, H.M.I. Aktan, I.O. Yaman, Active and non-active porosity in concrete part I: experimental evidence. Mater. Struct. **35**(2), 102–109 (2002)
56. J.N. Eiras, J.S. Popovics, M.V. Borrachero, J. Monzó, J. Payá, The effects of moisture and micro-structural modifications in drying mortars on vibration-based NDT methods. Constr. Build. Mater. **94**, 565–571 (2015)
57. G.W. Scherer, Theory of drying. J. Am. Ceram. Soc. **14**(1), 3–14 (1990)
58. C. Payan, V. Garnier, J. Moysan, Effect of water saturation and porosity on the nonlinear elastic response of concrete. Cem. Concr. Res. **40**(3), 473–476 (2010)

59. J.B. Watchman, W.E. Tefet, D.G. Lam, C.S. Apstein, Exponential temperature dependence of young's modulus for several oxides. Phys. Rev. **122**(6), 1754 (1961)
60. T.J. Ulrich, T.W. Darling, Observation of Anomalous elastic behavior in rock at low temperatures. Geophys. Res. Lett. **28**(11), 2293–2296 (2001)
61. J.A. TenCate, T.J. Shankland, Slow dynamics in the nonlinear elastic response of Berea sandstone. Geophys. Res. Lett. **23**(21), 3019–3022 (1996)
62. J. Somaratna, Evaluation of Linear and Nonlinear Vibration Methods to Characterize Induced Microstructural Damage in Portland Cement-Based Materials, Dissertation, University of Illinois at Urbana-Champaign, 2014

Chapter 13
Dynamic Acousto-Elastic Testing

Sylvain Haupert, Guillaume Renaud, Jacques Rivière, and Parisa Shokouhi

13.1 Introduction

13.1.1 Inspirations and Principles of Dynamic Acousto-Elastic Testing

Pioneering measurements of elastic nonlinearity were static methods leading to the thermodynamic diagram that shows the relations between pressure, volume, and temperature (p-v-T diagram) [1]. The dependence of the bulk elastic modulus on the pressure, i.e., a measure of nonlinear elasticity, was deduced from this diagram. In the beginning of the twentieth century, resonance spectroscopy [2, 3] or methods based on interferometry [4] were proposed to measure the elastic moduli as functions of temperature and hydrostatic pressure. Finally, with the possibility of generating an ultrasonic short pulse [5, 6], acousto-elastic testing became an alternative way to assess elastic nonlinearity. Acousto-elastic testing consists in measuring changes of the speed of sound (by the determination of the travel time of an ultrasonic short pulse) induced by a hydrostatic or uniaxial stress (or strain). For metals and polymers, the relative variation in ultrasound wave-speed is found

S. Haupert · G. Renaud (✉)
Laboratoire d'Imagerie Biomédicale – INSERM – CNRS – Sorbonne Université, Paris, France
e-mail: guillaume.renaud@upmc.fr

J. Rivière · P. Shokouhi
Department of Engineering Science and Mechanics, Pennsylvania State University, University Park, PA USA

T. Kundu (ed.), *Nonlinear Ultrasonic and Vibro-Acoustical Techniques for Nondestructive Evaluation*, https://doi.org/10.1007/978-3-319-94476-0_13

between 10^{-5} and 10^{-4} per MPa of the applied stress. In cracked or granular media, contacts between the two lips of cracks or contacts between grains can greatly increase the variation in ultrasound wave-speed up to about 10^{-2} per MPa of applied stress, i.e., orders of magnitude larger than in metals and polymers [7].

A conventional acousto-elastic experiment is quasi-static; the applied stress is varied in discrete steps and the ultrasonic wave-speed is measured for each level of the applied stress [8–10]. While early conventional experiments applied a static stress up to 1 GPa [6, 11], recent studies have applied less than 10 MPa [12]. There exist several ways to monitor the change of wave-speed induced by the quasi-static loading. It can rely on an elastic wave (propagating short ultrasonic burst or resonance technique) or on a hybrid optical and ultrasonic approach using diffraction of light by standing elastic wave [13] or Brillouin spectroscopy [14].

In the past three decades, alternative ways to measure the acousto-elastic effect were proposed. A slowly varying sinusoidal loading was proposed instead of a quasi-static stress that is varied in discrete steps [15]. Methods based on the interaction of two bulk elastic waves [16] or surface waves [17, 18] were introduced, including a technique termed Dynamic Acousto-Elastic Testing (DAET) [19, 20]. DAET is the dynamic analog of a conventional experiment of acousto-elasticity, though with significant differences. Firstly, the applied stress is not produced by a universal testing machine in discrete steps but induced by an elastic wave. The elastic wave has typically a frequency of a few kHz in a lab experiment. Consequently the elastic constants at stake are all adiabatic elastic constants. On the contrary both adiabatic and isothermal elastic constants are involved in a quasi-static conventional acousto-elastic experiment (since a quasi-static deformation is considered to be an isothermal process). Secondly, a low vibrational strain is applied, typically 10^{-6}, while conventional quasi-static experiments operate with an applied strain exceeding 10^{-4}. Finally DAET explores the dynamic elastic behavior of a material about its equilibrium state. Unlike conventional quasi-static experiments where a compressive stress only (or tensile stress only) is applied, both tensile and compressive behaviors are investigated in DAET.

In a typical DAET lab experiment, the sample is dynamically excited by an acoustic/elastic wave whose wavelength is larger than the size of the sample (frequency is typically a few kHz if the sample size is several centimeters). This wave is called the “pump” wave. A sequence of identical ultrasonic short bursts (with a typical center frequency of 1 MHz) is simultaneously applied to measure the dynamic change of elasticity induced by this pump wave. The ultrasonic short bursts are called the “probe” wave, since they are broadcasted to capture the dynamic variation in material elasticity induced by the pump wave (see Fig. 13.1). The repetition rate of these ultrasonic short bursts is chosen to adequately sample the changes of elasticity produced at a rate imposed by the temporal frequency of the pump wave. Typically the pump wave produces a dynamic acoustic displacement of the order of 1 micrometer while the ultrasonic probe induces a dynamic acoustic displacement of the order of 1 nm. Therefore, the theory of acousto-elasticity as described in [7] can be applied to DAET.

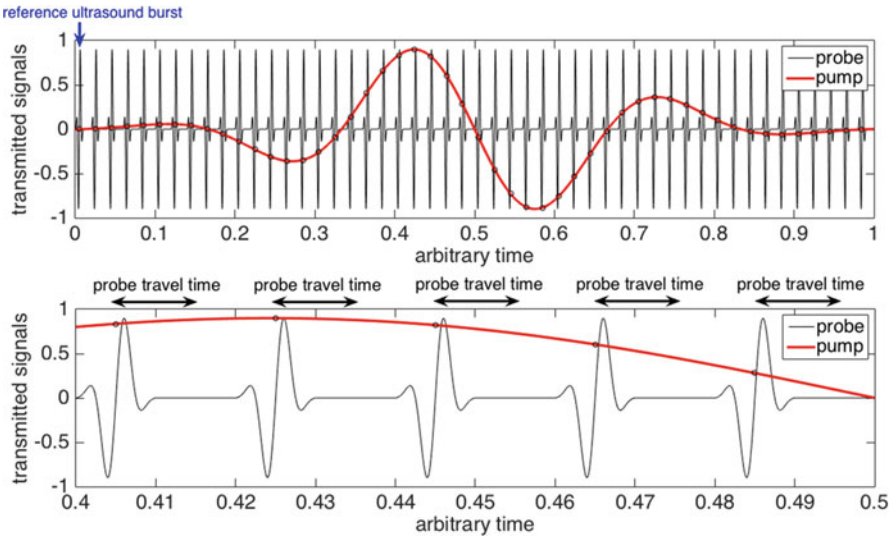

Fig. 13.1 Principles of DAET. Top: schematic representation of the pump wave and the probe wave. The very first ultrasonic pulse is used as a reference. Bottom: enlargement showing that the travel time of an ultrasonic pulse is much smaller than the temporal period of the pump wave

In order to apply the theory of acousto-elasticity [7], the strain field (produced by the pump wave) traversed by the ultrasonic pulses must be quasi-homogeneous and quasi-static with respect to the ultrasonic travel time in the sample. The geometry of the sample and/or the position of the ultrasound transducers that transmit and receive the ultrasonic pulses are then selected so that the travel time of the probe wave (ultrasonic pulses) is much smaller than the temporal period of the pump wave. Each ultrasonic pulse traverses the material as it experiences a different strain level and the large number of ultrasonic pulses in the sequence (typically 1000–10,000). This provides a dense sampling of the relation between the ultrasonic wave-speed measured by the probe wave and the applied strain (produced by the pump wave). The change of ultrasonic wave-speed is calculated from the change of travel time of the probe wave, since the length of the propagation path is known. The change of travel time can be precisely determined from a comparison of a given ultrasonic pulse in the sequence with the very first ultrasonic pulse that serves as a reference (see Fig. 13.1). Techniques to achieve this will be detailed later in this chapter. For each ultrasonic pulse, the strain level is taken as the spatial and temporal average of the strain experienced by the ultrasonic pulse during its propagation through the sample. Techniques to calculate the strain value associated with each ultrasonic pulse will also be explained later in this chapter.

13.1.2 Comparison with Other Methods

DAET belongs to the family of "pump-probe" methods that have existed in nonlinear acoustics from the 1950s [21, 22]. It involves two dynamic fields: one perturbs the material elasticity (the pump) and one measures the induced elastic changes (the probe). Experiments of this type are also termed nonlinear wave mixing. In such measurements, one is interested in the resulting effects of the nonlinear interaction after a propagation distance (i.e., length of interaction) that is much larger than both the pump wavelength and the probe wavelength (see Chaps. 1 and 6 in this book). In contrast, in DAET, we are interested in the nonlinear interaction between the pump wave and the probe wave over a distance that is much smaller than the pump wavelength. This situation is therefore more similar to a conventional quasi-static acousto-elastic experiment than an experiment of nonlinear wave mixing.

Nonlinear resonance ultrasound spectroscopy (NRUS, see Chaps. 2 and 12 in this book) measures a variation in the material elasticity (as the driving amplitude is increased) that is time-averaged over an acoustic period. In contrast DAET allows one to "read" the instantaneous variations in the elastic modulus during an entire acoustic cycle of the pump wave. In this respect, DAET provides more detailed insight into the dynamic elastic nonlinearity of a material than NRUS. Moreover nonlinear resonance ultrasound spectroscopy measures the global elastic nonlinearity of the entire sample. In contrast DAET provides a local measurement of elastic nonlinearity. The investigated region of the sample is the volume of the sample that is traversed by the ultrasonic short bursts (probe wave).

13.2 Experimental Setups

Dynamic acousto-elastic testing (DAET) was originally developed to evaluate microdamage in trabecular (spongious) bone [19, 23]. In this first configuration, the bone sample was immersed in a water tank. It was later shown that small modifications of this experimental setup allow one to investigate any material immersed in a coupling fluid, such as a plain block of a given solid material, water-saturated glass beads [24], gels or creams [25], or a suspension of particles [25, 26]. Meanwhile, DAET method was also extended to experimentations in contact (without the need of immersing the sample in a water tank) to study materials such as rocks [27, 28], concrete [29, 30], or metals with cracks [31, 32] under room-dry conditions.

13.2.1 Low-Frequency Pump Wave: Quasi-Homogeneous and Quasi-Static Requirements

Whether DAET is done in immersion or in contact, both setups are similar and consist in broadcasting a low-frequency (LF) pump wave and measuring changes of wave-speed experienced by an ultrasonic (US) probe wave that traverses the LF pressure/strain field generated in the probed volume. The analysis of the measurements is straightforward if two requirements are respected: the LF pressure field must be (1) quasi-homogeneous in the volume probed by the US probe wave and (2) quasi-static with regard to the travel time of the US probe wave. In these conditions, it is analogous to conventional quasi-static acousto-elastic testing.

It has been shown experimentally and validated by simulation [33] that the pressure/strain field seen by the US probe is quasi-homogeneous when the distance d_{probe} traveled by the US probe is at least 10 times smaller than the LF pump wavelength λ_{pump}, while the quasi-static requirement is reached when the US time of flight (TOF) propagation is at least 10 times smaller than the LF pump period T_{pump}. The two requirements are related via the wave-speed c since $d_{probe} = c^*TOF$ and $\lambda_{pump} = c^*T_{pump}$. In practice, the LF pump wave is either a standing wave (e.g., first compressional mode of a bar) [27, 34] or a propagative wave [20, 26, 35] (Fig. 13.2). Both configurations will be explained in detail in Sects. 13.2.4 and 13.2.5.

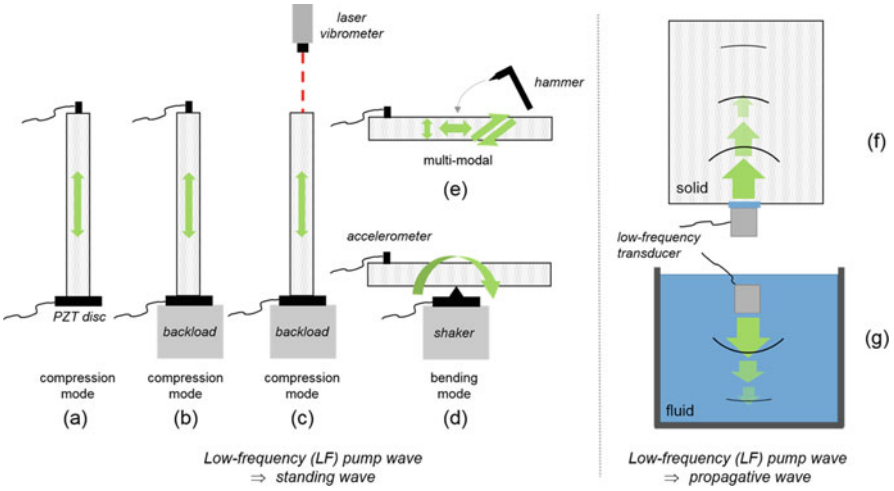

Fig. 13.2 Examples of different low-frequency (LF) pump wave configurations. For bars or cylinders, the LF pump wave can be a standing wave matching either the 1st compressional mode (**a**–**c**) or the 1st bending mode (**d**). The LF pump can also be multi-modal when using a hammer as exciter (**e**). Various boundary conditions and emitter/receiver types can be used depending on the application. For a (semi-)infinite solid (**f**) or fluid (**g**) sample, the pump can be a propagative wave induced by a LF transducer

13.2.2 Ultrasonic Probe Wave: Type, Amplitude, Position, and Orientation

A US probe wave is required to read the instantaneous change of phase velocity at different strain levels. While it is possible to use any kind of ultrasonic waves, bulk compressional wave is involved in most of the studies, while bulk shear wave [29, 36], or surface wave such as direct or head wave [27, 37], or Raleigh wave [29, 30] remain anecdotic. The only requirement is to be able to measure the TOF of the probe wave and its variation (induced by the pump wave, see Sect. 13.3) along a known propagation path for different strain levels. The propagation path of the probe wave is also needed to evaluate the pump strain experienced by the probe wave.

In practice, this can be done with two US transducers in direct or indirect transmission configuration or with one transducer in pulse-echo configuration (Fig. 13.3). The choice of configuration depends on the experimental conditions such as the workable surface of the sample, the material access, the attenuation in the material, or the orientation between the US probe beam and the LF pump wave (e.g., collinear, orthogonal, or with an arbitrary angle). It also depends on how large the TOF variation is along the propagation distance in the medium. If the one way direct transmission path is not enough to accumulate sufficient change in TOF (i.e., larger than the phase noise level), the use of multiple reflections (within the sample) along the same direct transmission path represents a good alternative [32].

In order to determine the propagation path of the US probe wave, a short US pulse is generally preferred as it is relatively easy to guess the propagation knowing the nature of the wave (e.g., compression or shear bulk wave, Rayleigh wave or Lamb

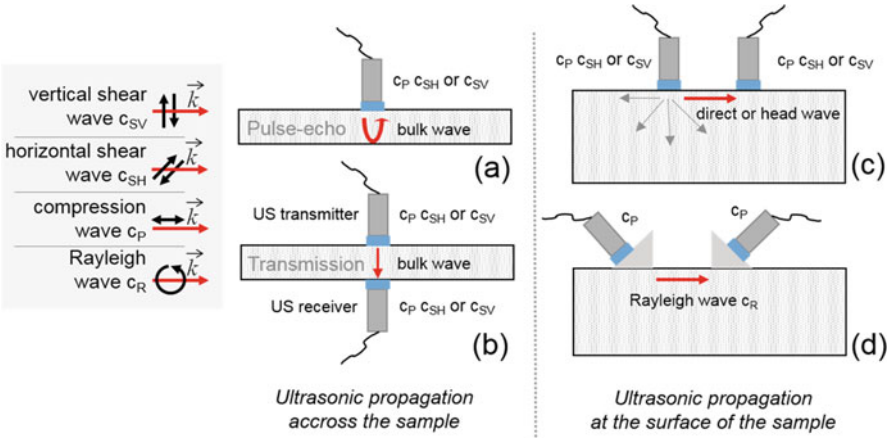

Fig. 13.3 Examples of different high-frequency (HF) probe wave configurations: bulk compression wave or bulk shear wave propagating across the sample in pulse-echo (**a**) or transmission (**b**); direct wave (**c**) or surface wave (**d**) propagating at the surface of the sample

wave). The use of a continuous monochromatic US wave may be used cautiously as waves may travel in the whole material, with possible multiple reflections and modes conversion. The probe signal recorded at the receiver contains the direct propagation signal superimposed with signals produced by reflections and mode conversion within the sample, which makes the analysis difficult. It is preferable to use a continuous probe in case of strong attenuation (e.g., due to multiple scattering and/or absorption) that reduces the amplitude of waves reflected at the sample boundaries [38].

For very heterogeneous media such as rocks or concrete, the direct or ballistic US wave is sometimes difficult to disentangle from the later arriving waves, the so-called coda. The coda is the result of multiple scattering that occurs when the US wavelength is close to the size of the scatterers and/or when the scattering efficiency is high (large contrast of mass density and/or compressibility). A coda-based technique called Coda Wave Interferometry (CWI) can be used to calculate small variations in wave-speed with a greater accuracy than ballistic wave arrival times, making it an interesting tool for measuring acousto-elastic effects [39, 40]. The main drawbacks of using coda wave instead of direct wave are (1) the LF strain field seen by the coda wave is no more quasi-homogeneous nor quasi-static and (2) the coda wave is a superposition of multiple shear and bulk waves having different speed of sound and polarization.

In the case of a porous medium like rocks, it is important to add treatment on the surface of the sample (e.g., polished nail or tape) to prevent coupling ultrasound gel from penetrating the material.

When a short US pulse is used, the pulse repetition frequency (PRF) is conditioned by the distance between the US emitter and receiver and by ultrasound attenuation. Indeed, for proper analysis, two successive US signals (including direct propagation, (multiple) reflections, guided propagation, and (multiple) scattering) must not overlap in the time domain. The ratio between the PRF and the frequency of the LF pump wave must not equal a rational number in order to create a stroboscopic effect, so that US pulses probe different LF strains during each LF cycle. In this manner, US pulses are able to probe discrete values well distributed over the entire LF strain excursion, both in tension and in compression, after several LF periods (e.g., generally between few tens to few hundreds).

13.2.3 Clock Synchronization and Phase Noise

The DAET measurement protocol involves three distinct phases (Figs. 13.1 and 13.14):

- *Pre-pump reference phase*—The US probe is turned on, and stays on until the end of the DAET measurement. During this phase, the reference TOF is measured while the noise floor (e.g., phase noise) is evaluated by computing the phase-shift between US signals (i.e., US pulses or US monochromatic continuous wave).

- *Pump phase*—The LF pump wave is then turned on. It can be an impact or continuous monochromatic wave, which lasts as long as it is needed for the US signal to probe the entire LF strain excursion. In case of standing wave, it is important to wait for the steady state. The TOF variation is evaluated by assessing the phase-shift between the instantaneous US signal and the reference US signal (see Sect. 13.3)
- *Post-pump reference phase or recovery phase*—The LF pump wave is finally turned off. In some cases, the phase velocity of the material does not return back instantaneously to its initial value, leading to a relaxation period, due to the so-called conditioning (see Sect. 13.4.2.3) that is tracked by the US probe.

The key for effective DAET measurements is to achieve high sensitivity to small TOF variations. For weakly nonlinear elastic materials, such as PMMA or duralumin, the maximum TOF variation is close to one nanosecond for a US wave traveling through a few centimeters if the maximum LF strain level is in the order of 10^{-5} [27, 41]. Although not straightforward, it is possible to achieve phase noise as low as 0.1 ns with conventional electronic devices (e.g., function generator, digitizer) if some essential rules are respected.

The most important rule is to maximize the signal-to-noise ratio of the recorded probe signal. Another important aspect is synchronization. All the electronic devices involved in the experimental setup must be synchronized by choosing a single master clock across all devices. This is generally done by connecting the 10 MHz reference clock from one of the devices (e.g., a function generator) to other electronic devices (e.g., the other function generators and digitizers). A good synchronization reduces drastically the electronic time deviation or phase-shift, also called jitter, which is one of the major sources of phase noise.

Phase noise can also be caused by relative movements of both US transducers due to low vibrations coming from the environment (e.g., vibration from the building). The use of the same holder for both US transducers overcomes this problem by suppressing the relative movements.

A good configuration for the digitizer (i.e., sampling frequency and quantization bits) is also required to achieve high sensitivity to small TOF variation. High sampling frequency is a necessity, but it does not determine directly the TOF resolution. Indeed, TOF resolution depends on the sampling frequency (i.e., sampling period) as well as the numerical tool used to compute the phase-shift between two probe signals (see Sect. 13.3).

The quantization bits (i.e., the number of vertical bits used for analog-to-digital conversion) are generally forgotten but this factor is as important as the sampling frequency. Indeed, the higher the number of quantization bits, the better will be the TOF resolution. The vertical range (i.e., in voltage) of the digitizer must also be adapted to the voltage of the US transmitted signal in order to reach at least 80% of the full range.

In practice, for short US pulses centered at around 2 MHz, a sampling frequency above 50 MHz (i.e., a sampling period of 20 ns) with a quantization above 14 bits reduces the phase noise below 0.1 ns.

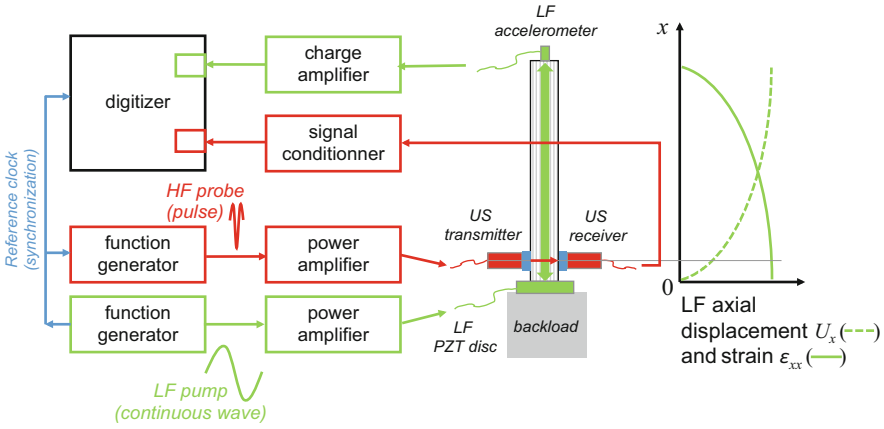

Fig. 13.4 Example of a DAET experimental setup with stationary wave (1st compression mode) as pump wave. The shape of the sample is either a bar or a cylinder

13.2.4 DAET with Stationary Pump Wave

DAET with stationary pump wave is recommended for laboratory measurements on calibrated samples such as bars, cylinders, or plates because it is possible:

(1) To achieve high strain level, up to 10^{-4}.
(2) To estimate the strain level along the US probe path as the strain distribution is known for a simple modal shape.

In practice, the first compressional [27] or flexural [30] mode is preferentially excited with a continuous monochromatic source tuned to match the frequency of the desired mode. The LF pump wave is broadcasted directly in the sample by means of a piezoelectric disk glued on the sample [27] or a shaker attached to the sample [30]. The frequency of the pump wave is chosen to match the fixed-free [27] or the free-free [42] boundary conditions (Fig. 13.2).

When using the first compressional mode with fixed-free boundary conditions, the most common configuration for the probe consists of two US transducers in through-transmission configuration, with a direction of propagation either normal to the pump stress direction (Fig. 13.4) [43], collinear to the pump stress direction [27], or at an angle [41]. The pair of US transducers is generally placed where the LF strain amplitude is the largest, i.e., close to the piezoelectric disk (Fig. 13.4).

Use of the first bending mode is more restrictive because the strain field across the sample is not uniformed. Nonetheless, along a short portion of the sample, the strain field can be considered quasi-uniform when the penetration depth (i.e., one wavelength) of the US beam is smaller than one tenth of the sample thickness. For this reason, only HF surface waves such as Rayleigh wave [30] or head wave may be used. In this configuration, the US probe is primarily sensitive to the strain component parallel to the US wave propagation direction.

For in situ measurements, when it is not possible/practical to glue or attach a LF source on the structure, a solution is the use of impact source, such as hammer (Fig. 13.2e). Indeed, impacting briefly the surface of the structure may select the resonant modes with the most excitability. The quick change of elasticity following the impact is either probed with short US bursts [29] or a continuous monochromatic US wave [38]. The main drawback is the difficulty to characterize the strain field seen by the US probe as multiple resonance modes are simultaneously excited.

Finally, the measurement of the in-plane or out-of-plane vibration of the sample is performed by either an accelerometer [27] or a laser vibrometer [34] (Fig. 13.2a–d). The strain is then derived directly from the particle's displacement/velocity/acceleration by analytical derivation [27]. Sometimes, when the boundary conditions are more complex, a numerical simulation is performed to compute the strain based on the experimentally measured out-of-plane or in-plane particle's displacement/velocity/acceleration [44].

13.2.5 DAET with Propagative Pump Wave

In case of in situ measurements (e.g., in soil, large concrete structures or water tank), propagating pump wave is generally the only option as no standing wave is feasible. DAET with propagative pump wave consists of a LF pressure wave that is broadcasted in an infinite medium, i.e., reflections at the boundaries of the medium are negligible (Fig. 13.5). DAET investigates the volume corresponding to the volume of interaction of the two acoustic beams (the probe beam and the pump beam).

When the infinite medium is a fluid, e.g., water, the LF pump wave can be generated by a circular piston attached to a shaker [19] or by a LF immersion transducer [26]. The LF hydrostatic pressure is measured with a hydrophone placed close to the probed volume, in order to evaluate the local pressure. Very different materials could be positioned at the volume of interaction, including solids (e.g., trabecular bone, beads), another fluid (e.g., gel or cream), or micro-particles (e.g., ultrasonic contrast agent).

When the infinite medium is a solid, e.g., soil, rock, or large concrete structure, the LF pump wave is generated at the accessible surface of the structure. In case of measurements in soil, the LF source can be the common LF source for underground prospection, such as a mobile hydraulic shaker [45]. The LF strain is deduced from two accelerometers buried in the soil at different depths [45]. These accelerometers are also used to measure the probe wave.

If one wants to reproduce propagation of seismic waves in the laboratory, a LF shear or compressional wave can be propagated in a rock [35, 46] while the LF velocity is measured by a laser vibrometer at the surface of the volume of interaction.

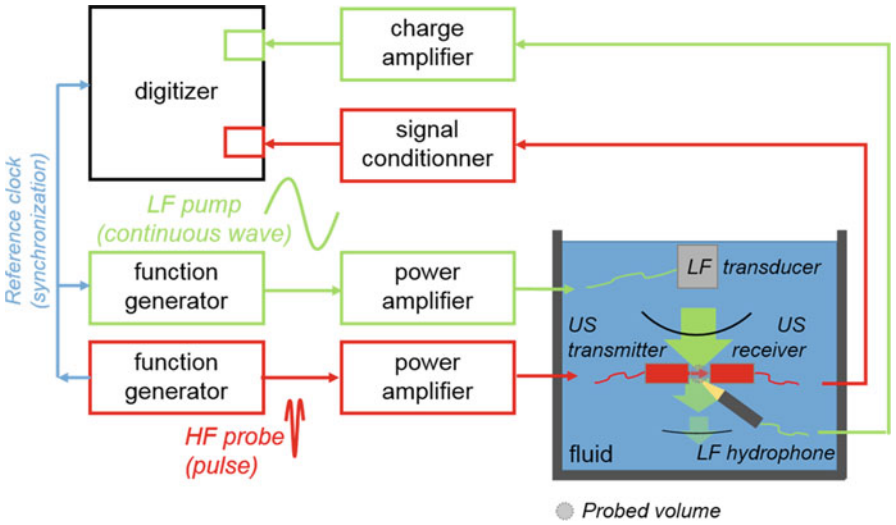

Fig. 13.5 Example of a DAET experimental setup with propagative wave as pump wave. The probed volume corresponds to the volume of interaction of the US beam and the LF beam. The medium is either a fluid or a solid

13.3 Signal Analysis

13.3.1 Analysis of the Pump: Calculation of Strain/Stress Produced by the Pump Wave That is Experienced by the Probe Wave

Most often, it is desired to know the absolute amplitude of the stress or strain generated by the pump wave. If known, it is possible to compare the elastic nonlinearity of different materials or to measure the third-order elastic constants of a material. Nonetheless, if the objective is to monitor relative changes in elastic nonlinearity of a sample over time (for instance, as a consequence of mechanical or thermal fatigue), the absolute amplitude of the pump wave is not required. In this case a non-calibrated transducer can be used to record the pump wave.

In general it is best to record the pump wave as close as possible to the path of the probe wave in the sample. In a water-borne DAET experiment, the pump wave is measured with a hydrophone, next to the sample immersed in a water tank (Fig. 13.5). In a dry DAET experiment, the pump wave is measured either with an accelerometer or with a laser interferometer or laser Doppler vibrometer (Fig. 13.2). However, the recording of the pump wave is often conducted at a position next to the path followed by the probe wave. If the absolute amplitude of the stress or strain generated by the pump wave is required, we need to determine the absolute amplitude of the pump wave experienced by the probe wave along its

path in the sample. Consequently it is necessary to take into account the differences of amplitude and phase between the recording position of the pump wave and the region traversed by the probe wave. To correct these discrepancies, it is usually necessary to measure or calculate the strain/stress field produced by the pump wave.

Moreover, the strain field produced by the pump wave is not perfectly uniform. Therefore, the strain/stress level experienced by the probe wave is taken to be the spatial average of the actual strain/stress field produced by the pump wave. Finally, even if the travel time of the probe wave is much smaller than the temporal period of the pump wave, there exists a slight temporal change of the pump amplitude during the travel time of the probe wave. Thus, for an accurate determination of the absolute amplitude of the pump wave, the strain/stress level experienced by the probe wave is taken to be the spatial and temporal average of the pump wave over the region traversed by the probe and during its travel time, respectively.

13.3.2 Analysis of the Probe: Determination of the Change of Travel Time of the Probe Wave

The objective of an experiment of acousto-elasticity is to measure the stress-dependence of the speed of sound. Since the distance of the propagation of the probe wave in the sample is known, one must determine the change of travel time of the probe wave induced by the pump wave. There are two ways to determine the change of travel time:

1. The cross-correlation method
2. The phase analysis in the frequency domain

The cross-correlation method consists in computing the cross-correlation function between a reference probe signal (the very first ultrasonic pulse of the sequence) and a second signal that is assumed to be the same waveform as the reference signal with a certain time lag. The time lag, i.e., the change of travel time, is determined by searching the time position of the maximum of the cross-correlation function (Fig. 13.6). It can be positive or negative. Any difference in the waveform that is not a simple difference of amplitude may cause a bias in the determination of the change of travel time. Furthermore a parabolic interpolation around the maximum of the cross-correlation function provides sub-sample estimation of the time delay (i.e., the change of travel time). This technique is widely used in medical ultrasound and is known to be very robust against noise [47]. With an excellent signal-to-noise ratio and an ultrasound frequency of 1 MHz, this technique is able to determine a time delay smaller than 0.1 ns.

Another way to determine a change of travel time is the phase analysis in the Fourier domain. At a given frequency f (within the frequency bandwidth of the probe wave), a phase lag $\Delta\varphi$ is simply related to a time lag Δt by $\Delta\varphi = 2\pi f \Delta t$. After computing the Fourier transform of the reference probe signal (the very first

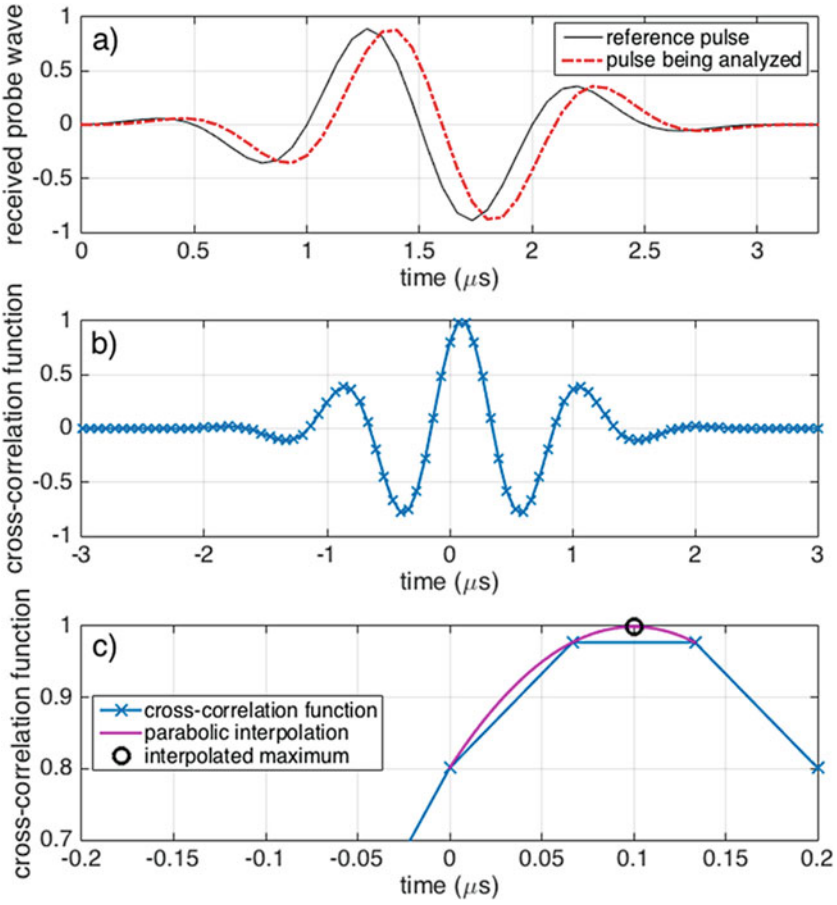

Fig. 13.6 Illustration of the cross-correlation method with synthetic signals. The ultrasonic pulse (probe wave) has a center frequency of 1 MHz and the sampling frequency is 25 MHz. (**a**) Recorded reference signal and signal to be analyzed, a time lag of 0.1 μs was introduced. (**b**) Cross-correlation function. (**c**) Enlargement of panel (**b**) showing the sub-sample determination of the time lag using a parabolic interpolation of the maximum of the cross-correlation function

ultrasonic pulse of the sequence) and the Fourier transform of one of the following ultrasonic pulses, the phase of the ratio of the two Fourier transforms gives the phase lag (Fig. 13.7). The time lag is then readily deduced. This method is less robust against noise than the cross-correlation technique, but it does not require that the two signals are identical in shape. Besides the phase method is sometimes necessary in a material where ultrasonic attenuation is significantly modified by the pump wave (see later in this chapter).

Once the change of travel time of the probe (dt) is accurately determined, the change of wave-speed of the probe (dc) can be calculated after evaluating the change in propagation distance of the probe (dL) induced by the pump strain:

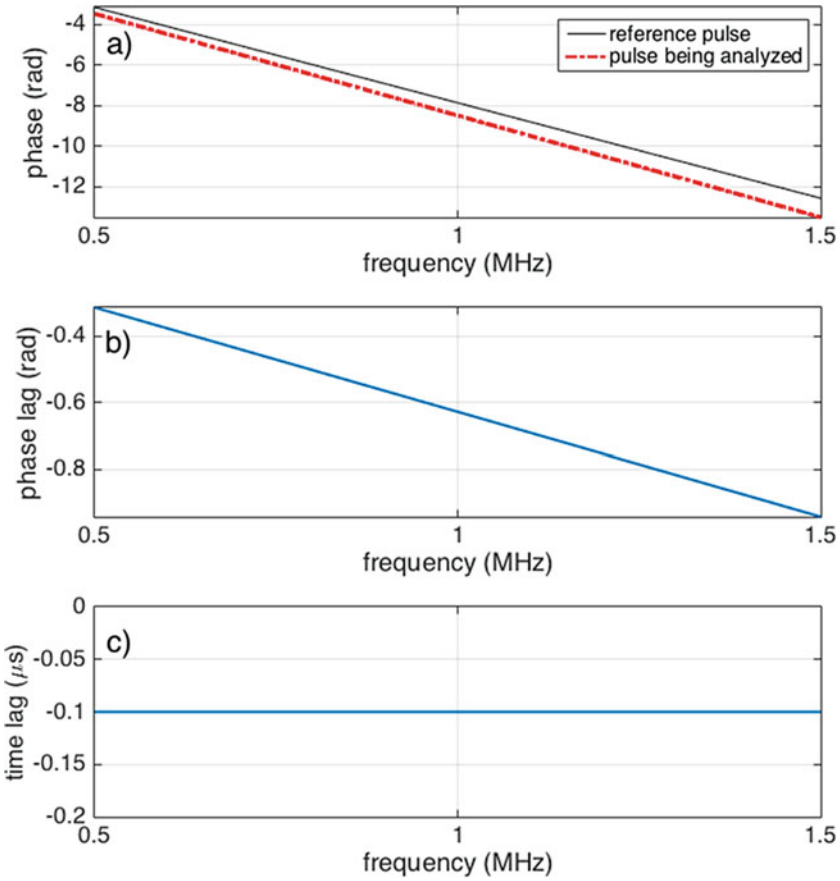

Fig. 13.7 Illustration of the phase method with the same synthetic signals as in Fig. 13.6. (**a**) Unwrapped phase of the two ultrasonic pulses. (**b**) Phase lag between the two signals. (**c**) Calculated time lag

$$\frac{dc}{c_0} = \frac{dL}{L_0} - \frac{dt}{t_0}$$

The subscript 0 refers to the value at zero pump strain (at equilibrium, in the absence of pump wave).

If the ultrasonic transducers employed to broadcast the probe and record it are attached to the sample, then dL is readily estimated knowing L_0 and the strain field produced by the pump wave.

If the ultrasonic transducers are coupled to the sample with water or gel, then the distance between the two transducers is fixed (not affected by the pump). And the formula above must be refined to take into account the variation in travel time in the coupling layer since the thickness of this coupling layer is dynamically modulated by the pump wave.

Note also that in materials with high elastic nonlinearity like granular media (rocks, concrete) the correction of the change of distance of propagation of the probe may be neglected since $\left|\frac{dt}{t_0}\right| \gg \left|\frac{dL}{L_0}\right|$. Nonetheless, in materials with small elastic nonlinearity like polymers, metals, or non-bubbly fluids, this correction must be considered since $\left|\frac{dt}{t_0}\right|$ and $\left|\frac{dL}{L_0}\right|$ have the same order of magnitude.

13.3.3 Investigating the Relation Between the Change of Wave-Speed of the Probe and the Magnitude of the Pump Stress/Strain

We have explained how to obtain two time signals:

1. The change of travel time of the probe as a function of time (i.e., for each ultrasonic pulse of the sequence)
2. The pump strain experienced by the probe as a function of time (i.e., for each ultrasonic pulse of the sequence)

The magnitude of the change of travel time of the probe generally increases as the magnitude of the pump stress/strain is increased. Therefore, a typical experimental protocol includes repeating the measurement while varying the amplitude of the pump wave. Thus we generally have in hand a set of measurements performed with different pump amplitudes. At this point, one has two options to study the relation between the change of wave-speed of the probe and the magnitude of the pump stress/strain:

1. Plot the peak amplitude of the change of travel time of the probe as a function of the peak amplitude of the pump strain/stress
2. Plot the instantaneous change of travel time of the probe as a function of the instantaneous pump strain/stress.

For the first approach, the peak amplitude of the change of travel time of the probe can be estimated directly in the time domain or in the Fourier domain. If the repetition rate of the probe is more than twice larger than the frequency of the pump wave, then a fast Fourier transform can be computed and the amplitude of the variation evaluated. If the repetition rate of the probe is not sufficient to compute a fast Fourier transform (Nyquist criterion is not respected), then a Gram–Schmidt process can be used to decompose the signal, knowing the frequency of the pump wave [34]. Such an analysis is shown in Figs. 13.16, 13.17, and 13.18.

The second option is only possible if the recordings of the pump and the probe signals are properly synchronized. This is the method of choice if one is interested in details of the relation between the change of wave-speed of the probe and the magnitude of the pump stress/strain. Such an analysis is shown in Figs. 13.8, 13.9, 13.10, 13.11, 13.12, and 13.13 as well as Fig. 13.15.

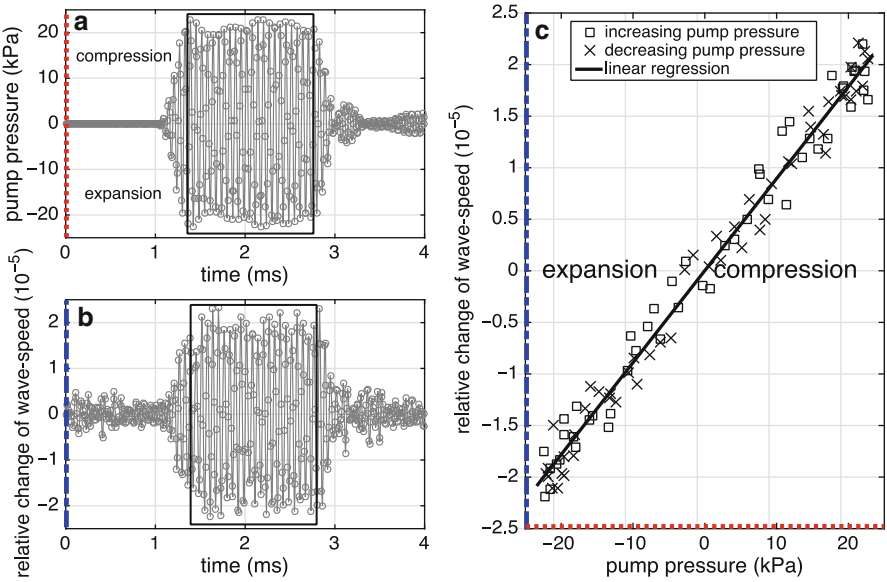

Fig. 13.8 Dynamic acousto-elastic response of water at 20 °C. The experimental setup shown in Fig. 13.5 was used. (**a**) Pump pressure as a function of time. (**b**) Relative change of speed of sound as a function of time obtained with the cross-correlation method. (**c**) Relative change of speed of sound as a function of the pump pressure. The two boxes in panels (**a**) and (**b**) show the data points that were selected to plot panel (**c**)

13.3.4 Alternative Measures of Acoustic Nonlinearity

Acoustic nonlinearity includes both elastic nonlinearity and dissipative nonlinearity. In our specific experimental situation, one investigates the effect of a "large-amplitude" pump wave on the propagation of a "small-amplitude" probe wave. The elastic nonlinearity of the material causes the acousto-elastic effect. In addition, in granular media or damaged/cracked media, the pump wave can also induce a variation in the attenuation experienced by the probe wave (dissipative nonlinearity).

The objective of a DAET measurement may be very practical, for instance, detecting and monitoring changes in a material like the accumulation of damage. In this case, the investigation of the change of wave-speed of the probe may not be the most sensitive parameter. The change of ultrasonic attenuation may be chosen as an alternative indicator of the level of damage [20, 37]. Such a change of ultrasonic attenuation can be simply implemented by tracking a change of the amplitude of the probe signal. Alternatively the cross-correlation method introduced earlier to estimate a change of travel time of the probe can be further exploited by tracking a change of the amplitude of the normalized cross-correlation function. If its amplitude equals 1 it means that the two input signals are identical waveforms (there may exist a time lag though). If the amplitude of the normalized cross-correlation function is less than 1, it means that the shape of the probe waveform has been modified, likely by a change of ultrasonic attenuation.

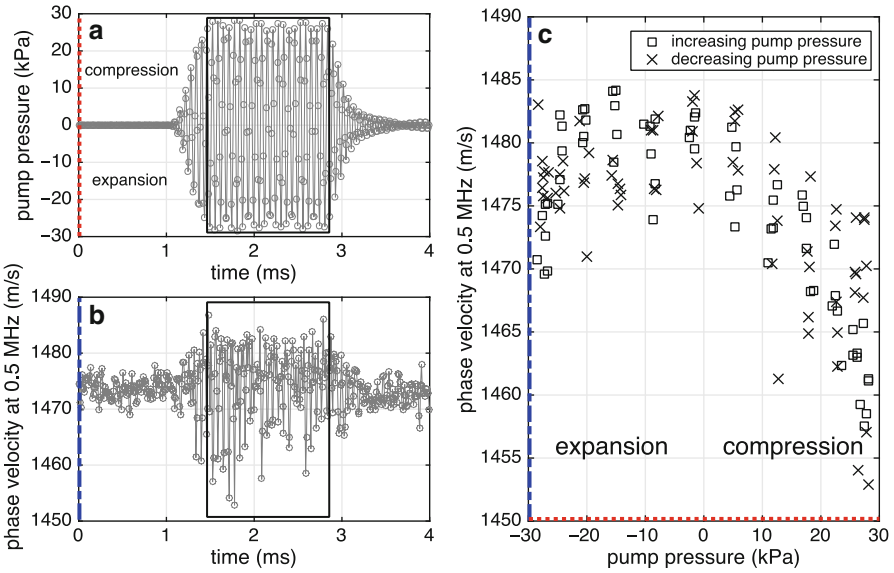

Fig. 13.9 Dynamic acousto-elastic response of a suspension of lipid-coated gas microbubbles in water at 0.5 MHz, i.e., at a frequency well below the resonance frequency of the microbubbles. The relative volume fraction occupied by microbubbles is 10^{-6}. The experimental setup shown in Fig. 13.5 was used. (**a**) Pump pressure as a function of time. (**b**) Phase velocity at 0.5 MHz as a function of time obtained with the frequency domain method. (**c**) Phase velocity at 0.5 MHz as a function of the pump pressure. The two boxes in panels (**a**) and (**b**) show the data points that were selected to plot panel (**c**)

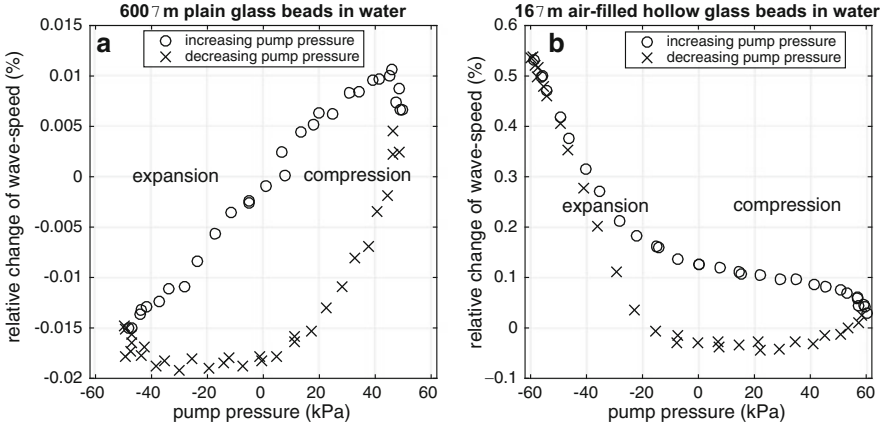

Fig. 13.10 Dynamic acousto-elastic response of (**a**) water-saturated plain glass beads with a diameter of 600 μm and (**b**) water-saturated air-filled hollow glass beads with a diameter of 16 μm. These measurements were performed with the system developed by RheaWave [25] which uses the experimental configuration described in Fig. 13.5

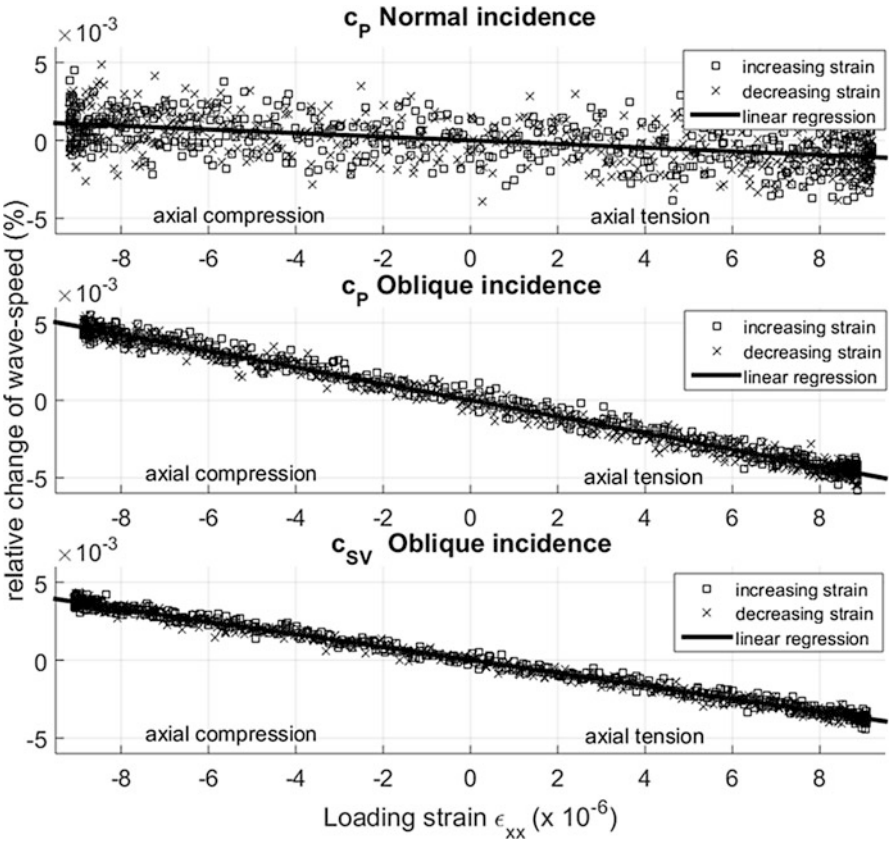

Fig. 13.11 Dynamic acousto-elastic response of PMMA with different orientations and types of US probe waves [41]. The orientations of the ultrasound transducers are chosen to probe the effect of a uniaxial strain (or stress) on the propagation velocity of compression bulk waves (c_P) with normal and oblique incidence and vertically polarized shear bulk waves (c_{SV}) with oblique incidence. The maximum axial strain is 9×10^{-6} while the relative change of wave-speeds varies between 0.001 and 0.005%

13.4 Observations in Different Materials

In this section, we present applications of dynamic acousto-elastic testing to different types of materials. This includes results in liquids and solids. We show how the addition of soft inclusions in a material, namely gas bubbles in a liquid or cracks in a solid, can dramatically change the dynamic acousto-elastic response of the material. More specifically, the reader shall appreciate that the addition of soft inclusions modifies the acousto-elastic effect quantitatively (soft inclusions enhance the elastic nonlinearity of the material) and qualitatively (hysteresis and DC component can appear).

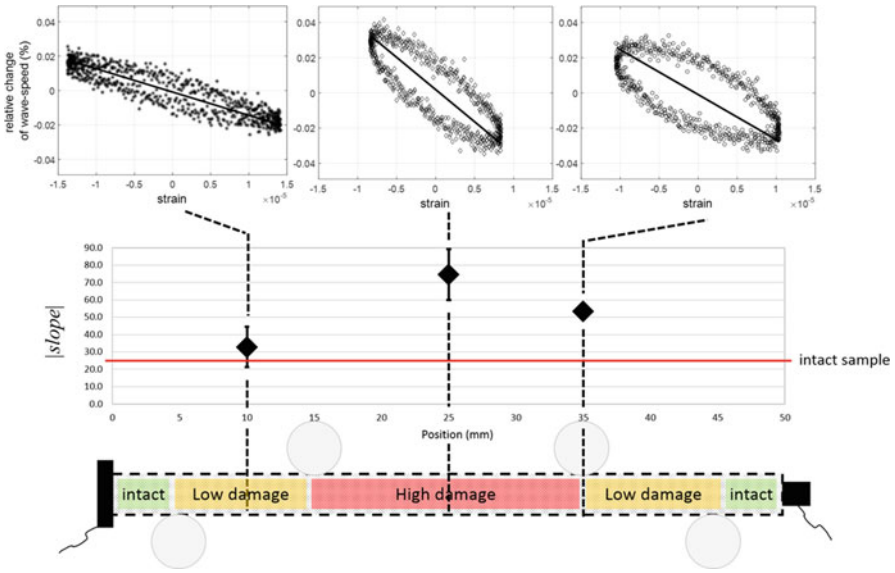

Fig. 13.12 Dynamic acousto-elastic responses measured at different positions along the fatigued bar of aluminum (i.e., 10, 25, and 35 mm). The slope and the hysteresis of the nonlinear signature are higher where the level of distributed fatigue damage is expected to be higher. Positive (negative) strain corresponds to tension (compression) phase of the sample

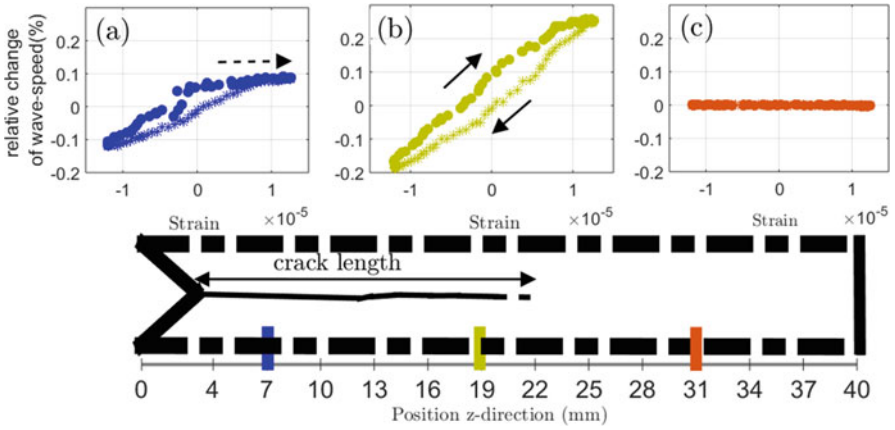

Fig. 13.13 Dynamic acousto-elastic responses for three characteristics positions along the sample width: (**a**) near the notch (**b**) at the crack tip (**c**) outside the cracked zone. Positive (negative) strain corresponds to tension (compression) phase of the sample

13.4.1 Liquids

13.4.1.1 Non-Bubbly Liquid

A typical experimental setup to apply dynamic acousto-elastic testing in a fluid is depicted in Fig. 13.5. The pump wave is a 16 kHz pressure wave generated by an underwater acoustic projector. The probe wave is a short ultrasound burst with a center frequency of 4 MHz that is generated by an immersion broadband ultrasound transducer. The ultrasound transducer broadcasts a sequence of short ultrasonic pulses with a repetition rate of 100 kHz. A plastic block is used as a reflector placed in front of the ultrasound transducer so that the ultrasound transducer can be operated in pulse-echo mode to transmit and receive the probe wave. The amplitude of the pump wave is first measured by a hydrophone that is inserted between the ultrasound transducer and the reflector, i.e., on the path of the ultrasound pulse (while the probe is turned off). Then the actual experiment of dynamic acousto-elasticity is conducted by turning on both the probe wave and the pump wave. The broadcasting of the pump wave is delayed by 1 ms. This delay is useful to appreciate the level of noise in the measurement of the change of travel time of the probe wave. The state-of-the-art equipment typically provides a noise level of 0.1 nanosecond or less for the measurement of travel time changes of the probe wave (dt).

The change of travel time of the probe wave is calculated using the cross-correlation method. Figure 13.8a shows the pump pressure experienced by each probe pulse as a function of time and the panel b depicts the relative change of speed of sound in water $(c - c_0)/c_0$ as a function of time. Finally a plot of the relative change of speed of sound as a function of the pump pressure is shown in panel c. There are several points to highlight when analyzing panel c. Firstly the magnitude of the relative change of wave-speed is small; the change of travel time of the probe wave is close to 0.1 ns while the total travel time of the probe wave is 5.8 μs. Secondly panel c shows that the relation between the relative change of wave-speed and the pump pressure is linear, with no DC offset (the change of wave-speed is null at zero pump pressure) and no hysteresis. When the pump pressure is positive (medium compression) the wave-speed increases. Conversely, when the pump pressure is negative (medium expansion) the wave-speed decreases.

Finally it was shown that DAET allows one to estimate the parameter of nonlinearity B/A in fluids [19, 25]. The parameter of nonlinearity B/A is proportional to the slope coefficient of the linear relation observed in panel c of Fig. 13.8.

13.4.1.2 Liquid with Suspension of Gas MicroBubbles

The experimental setup depicted in Fig. 13.5 can be used to investigate the influence of the addition of micrometric particles in a fluid. Figure 13.9 shows the acousto-elastic response of a suspension of lipid-coated gas microbubbles in water. Those lipid-coated gas microbubbles are used as an ultrasound contrast agent for medical

ultrasonography. Even if the microbubbles occupy a relative volume fraction of only 10^{-6}, the acousto-elastic response of the suspension is dramatically changed compared to that of water only (Fig. 13.8). First the variation in wave-speed is two orders of magnitude larger. Secondly the compression of the medium imposed by the pump wave reduces the wave-speed, while an increase is observed in water only (Fig. 13.8). The suspension of microbubbles has a resonance frequency close to 2 MHz. For a frequency well below this resonance frequency, attenuation is very small and the wave-speed is determined by the compressibility of the mixture. Figure 13.9 shows the acousto-elastic response of the suspension at 0.5 MHz, it was obtained by applying a frequency domain analysis (see Sect. 13.3 of this chapter). At this frequency, the wave-speed is determined by the compressibility of the medium. The decrease of wave-speed during medium compression is likely caused by the reversible buckling of the lipid shell of the microbubbles [26]. When shell buckling occurs, the stiffness of medium suddenly collapses and the wave-speed decreases.

13.4.1.3 Water-Saturated Glass Beads

The acousto-elastic response of water-saturated plain glass beads was investigated [24, 25]. Figure 13.10 shows the results in water-saturated plain glass beads with a diameter of 600 μm and water-saturated air-filled hollow glass beads with a diameter of 16 μm. The probe signal was a short ultrasound burst with a center frequency of 0.6 MHz. The frequency of the pump wave was 3.7 kHz. The pump wave is expected to modulate the contacts between the glass beads. As a result complicated dynamic changes of the ultrasonic wave-speed are observed, including expansion-compression asymmetry, hysteresis, and DC offset.

13.4.2 Solids

13.4.2.1 Undamaged Homogeneous Solids

Dynamic acousto-elastic testing has been successfully applied to study the classical nonlinear elasticity of two isotropic materials—a polymer, the polymethyl methacrylate (PMMA) and an aluminum alloy [27, 41, 43]. In these studies, both PMMA and aluminum samples have a cylindrical shape; therefore, the LF pump wave is tuned to match the frequency (i.e., few kHz) of the first compressional mode (or first Pochhammer-Chree mode) as explained in Sect. 13.2.4. The LF pump wave is broadcasted directly in the sample by means of a piezoelectric disk glued on the sample. The vibration is measured by an accelerometer glued at the top of the sample. The experimental setup of the LF pump corresponds to the configuration shown in Figs. 13.2b and 13.4.

A sequence of ultrasonic short bursts (with a typical center frequency of 1 or 2 MHz) is simultaneously applied to measure the dynamic change of elasticity

induced by the pump wave. The experimental setup corresponds to the typical configuration shown in Fig. 13.3b but with different angles for the ultrasound transducers that transmit and receive the probe wave. The orientations of the ultrasound transducers are chosen to probe the effect of a uniaxial strain (or stress) on the propagation velocity of compressional bulk waves (c_P) with normal and oblique incidence and with vertically polarized shear bulk waves (c_{SV}) with oblique incidence. The maximal pump strain experienced by the US probe is close to 10^{-5}.

The changes in travel time of the probe wave (dt) for different strain levels are calculated using the cross-correlation method. Then, the TOF variation due to the Poisson effect is subtracted from the total TOF variation in order to retrieve the TOF variation solely due to the variation in wave-speed (Sect. 13.3).

The results are shown in Fig. 13.11. For undamaged homogeneous solids such as PMMA and aluminum, the relative variation of wave-speed is very weak (between 0.001 and 0.005%) and exhibits a linear relation with the pump strain. When the pump strain is negative (axial compression), the wave-speed increases. Conversely, when the pump strain is positive (axial tension), the wave-speed decreases. Neither a DC offset nor hysteresis is observed: the change of wave-speed is null when the pump strain is zero.

In particular, a larger variation of compression bulk wave-speed (c_P) is observed when the direction of propagation has an oblique incidence compared with normal incidence. Indeed, it is well established that, even though a homogeneous solid sample exhibits isotropic elastic properties, the effect of a uniaxial strain (or stress) induces wave-speed anisotropy [7]. The propagation velocity of an elastic wave depends on the angle between the propagation direction and the axis of the applied loading [8]. Therefore, the acousto-elastic effect is stronger when the propagation direction of the probe wave is parallel to the direction of the uniaxial loading (produced by the pump wave).

Finally, it has been shown that it is possible to estimate the three independent third-order elastic constants (TOEC) for isotropic materials with DAET, by combining three different carefully chosen configurations for the US probe [41].

13.4.2.2 Damaged Homogeneous Solids

In the past decades, several nonlinear acoustical techniques were proposed for in situ nondestructive testing (NDT), such as wave frequency mixing or resonance measurements. Among them, DAET provides a unique way to observe nonlinear elastic features over an entire dynamic stress cycle while other techniques measure average bulk variations of modulus versus strain level. DAET also provides a local measurement of the nonlinear elasticity, which is particularly convenient to localize and characterize microdamage within a whole solid.

It has been demonstrated that DAET applied to steel and aluminum samples is sensitive to

1. Distributed fatigue damage [32] and
2. A localized single micro-crack [31, 32].

The experimental setup involves a stationary pump wave and two compressional bulk wave transducers in transmission configuration as described in Fig. 13.4.

In case of the fatigue damage protocol [32], two aluminum bars ($50 \times 4 \times 2$ mm) are machined from the same 2 mm thick aluminum plate. The first aluminum specimen is fatigued while the second one is kept intact and serves as control. Fatigue damage is induced by cycling 10,000 times within the elastic regime using a four-point bending configuration. Dislocation density and/or fatigue cracking on the external surface is suspected to be larger in the center of the bar where the stress concentration is the maximum, while both ends of the bar remain intact. DAET measurements have been performed on both aluminum samples (i.e., intact and damaged) at different positions along the bar (i.e., 10, 25, and 35 mm). For each position, the relative change of wave-speed is plotted against strain level in Fig. 13.12. Then, the slope is extracted from each acousto-elastic response. Negative slopes are observed, as expected for most metals, with the highest value obtained in the center of the specimen, where fatigue damage is expected to be the most severe. Moreover, a hysteresis is present in the nonlinear signature. For the intact sample, no hysteresis is observable and the slopes (horizontal red line in Fig. 13.12) remain constant along the sample with an average value smaller than the slopes measured in the damage sample.

In case of the localized single micro-crack protocol [31], a closed fatigue crack has been formed in an aluminum alloy bar ($170 \times 30 \times 40$ mm) by a three-point bending fatigue test. The fatigue crack is extended from a notch placed at mid-length. The notch is approximately 3 mm deep and the fatigue crack is 17 mm long. The fatigue crack is invisible to the eye. Twelve DAET measurements have been performed along the crack (i.e., in the z-direction). Three typical acousto-elastic responses are shown in Fig. 13.13. No change in wave-speed is observed outside of the crack (Fig. 13.13c) whereas large changes are observed along the crack (Fig. 13.13a, b). The largest slope and hysteresis are observed close to the crack tip (Fig. 13.13b). At the notch, the crack is expected to be more open than at any other location. A bi-state behavior is clearly observed near the notch (Fig. 13.13a), with the presence of a plateau, i.e., no change in velocity during the tension phase when the crack is opened. Therefore, near the notch, the crack induces elastic nonlinearly essentially during the compression phase while elasticity is virtually unchanged in the tension phase. This agrees with a simple model of Contact Acoustic Nonlinearity [48, 49] that describes asymmetry between compression and tension phases. On the other hand, at the crack tip, the change of wave-speed is more symmetric and a high elastic nonlinearity (large slopes in Fig. 13.13b) is observed. Finally the positive sign of the slope is somewhat surprising as it means that the velocity decreases during the compression phase, which would imply that asperities at the interface slow down the direct wave. Further investigation will be needed to understand such behavior.

13.4.2.3 Rocks, Cementitious, and Granular Materials

Unlike undamaged or single-cracked materials, poorly consolidated media such as rocks and concrete exhibit very large nonlinear behaviors [50]. Perhaps the most striking feature is the appearance of a transient elastic softening, as soon as the medium is subjected to dynamic strains as low as 10^{-7} [27, 37]. It is then followed by a $\log(t)$ relaxation back to the original elastic modulus as soon as the dynamic loading is turned off [51]. This elastic softening is also often referred to as "conditioning," or "dynamically induced conditioning" or "DC offset." In some poorly consolidated media, the elastic modulus can therefore be transiently reduced by several percent, depending on the loading amplitude and frequency. Understanding such behavior is critical to better estimate seismic hazard, for instance, for civil structures and buildings. One key step towards the development of robust diagnostic tools is therefore to relate these complex nonlinear responses to physical, quantitative microstructural features.

Beyond nondestructive evaluation and civil engineering applications, there is growing evidence that such nonlinear effects are key mechanisms for the understanding of earthquake triggering, when a large seismic wave transiently softens the Earth's crust and triggers a second earthquake [52]. Current research also focuses on the link between elastic softening [53] and transient increases in permeability observed following earthquakes [54]. Such relation with fluid processes is of particular significance for the understanding of induced seismicity in oil/gas and geothermal applications.

As shown in Fig. 13.14, the sound speed evolution in highly nonlinear media such as rock, concrete, and granular media can be decomposed in six consecutive phases.

The initial phase (Phase I) refers to the beginning of the experiment when the pump is "off." In this phase, the unperturbed local wave-speed of the specimen is registered. Upon turning "on" the pump, the pump strain first rings up towards the steady state (Phase II). In Phase III, the pump strain has reached a steady state, but the sound speed continues to drop. Phase IV is the time domain where the medium is in a non-equilibrium steady state. By analyzing the strain-dependency of sound speed in this phase, the different nonlinear material properties can be evaluated, as discussed in the next section (Phase IV: During the Dynamic Loading). In Phase V, the pump strain rings down towards zero. Finally in Phase VI, the pump strain is zero, but the sound speed is still recovering. The slow recovery of sound speed towards the speed of sound at the initial unperturbed state is referred to as "slow dynamics" and will be further detailed in section "After the Dynamic Loading: Slow Dynamics (Phase VI)".

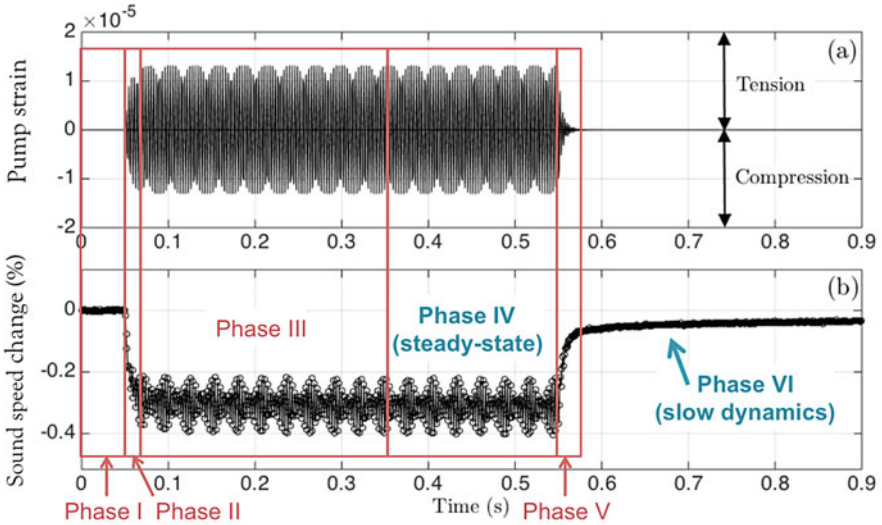

Fig. 13.14 Typical DAET results in a sample of Berea sandstone [28] using the experimental setup described in Fig. 13.4. (**a**) Pump strain as a function of time. (**b**) Sound speed change as a function of time. The sound speed changes in response to the pump strain. The evolution of sound speed can be studied in six time domains (Phases I–VI). Details on the fast (Phase IV) and slow (Phase VI) dynamics responses are presented in sections "Phase IV: During the Dynamic Loading" and "After the Dynamic Loading: Slow Dynamics (Phase VI)," respectively

Phase IV: During the Dynamic Loading

Instantaneous Velocity Changes

DAET is often performed at a single large strain amplitude, either to evaluate the third-order elastic constants in weakly nonlinear elastic materials (Fig. 13.11), to compare the nonlinear responses at different locations (Figs. 13.12 and 13.13), or to monitor a sample over time as it undergoes progressive damage. On the other hand, to further improve the theoretical description of nonlinear elasticity in complex (either damaged or granular-like) materials, one may want to perform DAET at multiple peak strain amplitudes, from a weakly nonlinear regime at low strain ($\sim 10^{-7}$) to a highly nonlinear regime at larger strain ($\sim 10^{-5}$).

Figure 13.15 shows some typical DAET results in two samples of Berea sandstone and Berkeley blue granite at room-dry conditions and multiple strain amplitudes ranging from 10^{-7} to 10^{-5}, using the experimental setup described in Fig. 13.4. Both samples exhibit a transient elastic softening that increases with the pump amplitude, reaching about $\sim 0.5\%$ at strain $\varepsilon_m = 8 \times 10^{-6}$. Further observations can be made depending on the strain range. At large strains ($\sim 10^{-5}$), complex loops are observed, with larger (lower) velocity during the compression (tension) phase, suggesting opening/closing of micro-cracks or grain contacts. This effect seems particularly strong for the granite sample (Fig. 13.15b). The acousto-

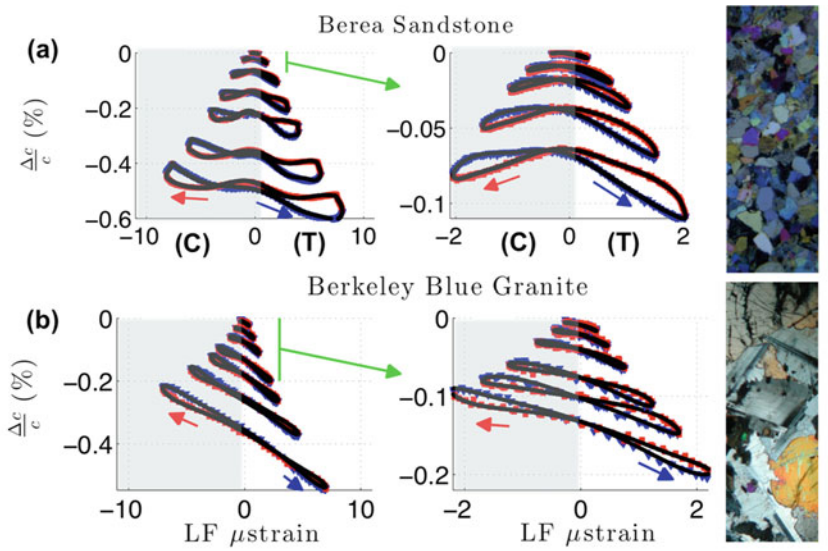

Fig. 13.15 Relative velocity change $\Delta c/c$ as a function of low-frequency pump strain ε for 10 increasing strain excitations ranging from 10^{-7} to 10^{-5}. (**a**) Berea sandstone. (**b**) Berkeley blue granite. Plots on the right side provide details on the nonlinear responses for strain amplitudes lower than 2×10^{-6}. Blue triangles (red squares) correspond to increasing (decreasing) strains. Negative strains correspond to the compression phase (C) whereas positive strains correspond to the tension phase (T). The black line shows the result of the Fourier analysis (cf. [28] for further details). On the right side, photomicrographs under plane polarized light. Height of the photo is 2.35 mm for Berea sandstone, 3.85 mm for Berkeley blue granite (Modified from [28])

elastic responses for the two samples differ at intermediate strains ($\sim 10^{-6}$); while the granite sample exhibits a larger velocity at negative pump strain (than at zero pump strain) and a smaller velocity at positive pump strain, the velocity in Berea sandstone at negative and positive pump strain maxima is found lower than at zero pump strain (right plots in Fig. 13.15). No certain evidence exists on a particular mechanism for such observation. However, the fact that it is observed for all tested sandstones [28, 43] suggests that it could arise from shearing processes at the grain boundaries, leading to a lower elastic modulus during maximum tension and compression, and larger moduli when strain passes through zero. Finally, the large slope for granite at intermediate and large strains suggests that the opening/closing mechanism dominates over shearing processes [43].

Amplitude Dependence

The dynamic acousto-elastic response of rocks is far more complicated than that of homogeneous undamaged solids (like PMMA, Fig. 13.11). While the velocity in homogeneous undamaged solids is modulated only at the frequency of the pump, the dynamic change of velocity in rocks exhibits a component at the frequency of

the pump, at its higher harmonics as well as at zero frequency. To further investigate the nonlinear elastic responses in rocks, the time series $\Delta c/c(t)$ can be decomposed using a Fourier analysis in combination with a Gram–Schmidt procedure [34]. The latter is needed to ensure orthogonality of the sine and cosine functions. From this analysis we find the amount of $\Delta c/c(t)$ oscillating at the pump frequency $\Delta c/c|_{\mathbf{1\omega}}$, twice the pump frequency $\Delta c/c|_{\mathbf{2\omega}}$, as well as the DC offset $\Delta c/c|_{\mathbf{0\omega}}$ (zero frequency component). When hysteretic effects are relatively small, as in Fig. 13.15, these quantities correspond approximately to the slope of the signature, the curvature, and the DC offset, respectively.

The $\Delta c/c|_{\mathbf{0\omega}}$—component is represented in Fig. 13.16 as a function of pump strain amplitude for both samples. This offset observed with DAET is equivalent to the frequency shift observed with NRUS (see Chap. 2 in this book) [28]. A progressive transition from quadratic dependence at low strain ($\sim 10^{-7}$) to linear at large strain ($\sim 10^{-5}$) is observed. This result, observed with both DAET [28, 34, 37] and NRUS [55], is typical of poorly cemented rocks. While no current theoretical model is able to fully capture the complex nonlinear response of rocks, cementitious, or granular-like materials, it is worth comparing these observations to some existing theories. One practical approach is to use the following 1D-equation (assuming material elastic nonlinearity is large and therefore neglecting changes in mass density):

$$\frac{\Delta M}{M} = 2\frac{\Delta c}{c} = \beta\varepsilon + \delta\varepsilon^2 + \alpha\left(\varepsilon_m + \text{sign}\left(\dot{\varepsilon}\right)\varepsilon\right),$$

where $\frac{\Delta M}{M}$, $\frac{\Delta c}{c}$, ε, $\dot{\varepsilon}$, and ε_m are, respectively, the relative change in modulus, the relative change in wave-speed, the pump strain, the strain rate, and the maximum strain excursion experienced by the material. The maximum strain excursion ε_m in our case is the amplitude of the pump strain, assuming $\varepsilon = \varepsilon_m \sin \omega t$. The terms β and δ represent the nonlinear quadratic and cubic coefficients, respectively, and arise from the classical nonlinear theory [7]. In particular, the term β is related to the third-order elastic coefficients (TOEC) [7]. The last term on the right-hand side results from the quadratic hysteretic nonlinear theory [50, 56–58]. Following such description, the quadratic dependence observed at low strain in Fig. 13.16 can be fitted with the cubic nonlinear parameter δ using $\left.\frac{\mathbf{\Delta M}}{M}\right|_{0\omega} = 2\left.\frac{\mathbf{\Delta c}}{c}\right|_{0\omega} = \frac{\delta\varepsilon_m^2}{2}$, whereas the linear dependence observed at large strain can be better fitted with the hysteretic parameter α using $\left.\frac{\mathbf{\Delta M}}{M}\right|_{0\omega} = 2\left.\frac{\mathbf{\Delta c}}{c}\right|_{0\omega} = \alpha\varepsilon_m$. However, it is important to note that such hysteretic model inherently couples hysteresis with softening which leads to an overestimation of hysteretic effects [34]. It also does not include the rate/frequency/relaxation effects that are described later.

Figure 13.17 shows the $\Delta c/c|_{\mathbf{1\omega}}$—component as a function of pump strain amplitude. The linear dependence over the whole strain range can be fitted with the classical quadratic nonlinear parameter β using $\left.\frac{\mathbf{\Delta M}}{M}\right|_{1\omega} = 2\left.\frac{\mathbf{\Delta c}}{c}\right|_{1\omega} = \beta\varepsilon_m$. The

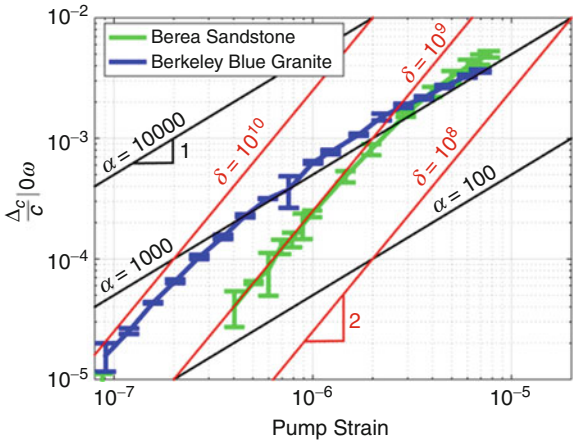

Fig. 13.16 Strain dependence for the offset component $\Delta c/c|_{0\omega}$ extracted from the Fourier analysis (black curves in Fig. 13.14) for two rock samples of Berea sandstone and Berkeley blue granite. This offset component corresponds to transient elastic softening that reaches about 0.5% at the maximum strain amplitude. Note the overall transition from quadratic to linear dependence as strain increases from 10^{-7} to 10^{-5}

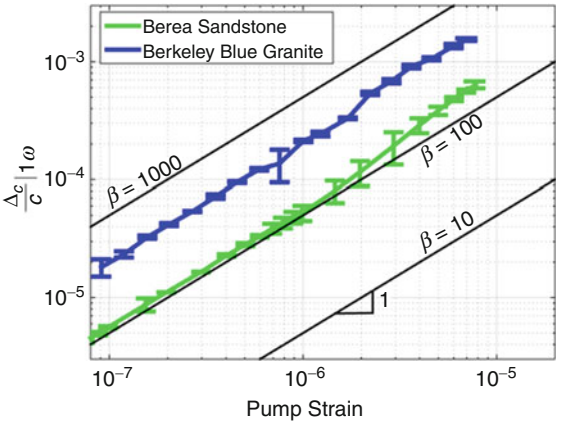

Fig. 13.17 Strain dependence for the slope component $\Delta c/c|_{1\omega}$ of Berea sandstone and Berkeley blue granite. Note the larger β value for the granite sample, as indicated by the larger slopes in Fig. 13.14

parameter β is found much larger in the granite sample than in the sandstone, as indicated by the larger slope observed for granite in Fig. 13.15.

Figure 13.18 shows the $\Delta c/c|_{2\omega}$—component as a function of pump strain amplitude, related to the curvature shape in Fig. 13.15. As for the offset component, we observe a scaling change over the strain range considered [45]. It transitions from quadratic to roughly linear for the Berea sandstone, while the Berkeley blue granite is roughly linear at low strain and lower than 1 at large strain. The quadratic dependence at low strain for Berea can be fitted with δ using $\frac{\Delta M}{M}\Big|_{2\omega} = 2\,\frac{\Delta c}{c}\Big|_{2\omega} = \frac{\delta\varepsilon_m^2}{2}$. The parameter δ estimated from either the offset in Fig. 13.16 or the curvature in Fig. 13.18 leads to a value comprised between 10^8 and 10^9 for Berea sandstone (a larger value is found from the offset estimation).

The scaling changes observed for $\Delta c/c|_{0\omega}$ and $\Delta c/c|_{2\omega}$ occur at strains where higher order harmonics (in particular, $\Delta c/c|_{4\omega}$ and $\Delta c/c|_{6\omega}$) emerge from noise [28, 34]. Rather than using two models corresponding to two different strain

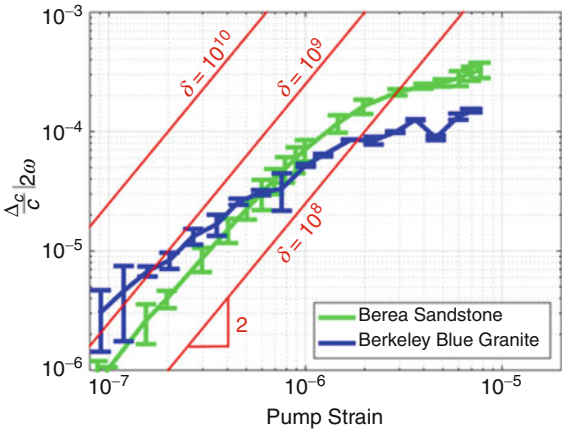

Fig. 13.18 Strain dependence for the curvature component $\boldsymbol{\Delta c/c|_{2\omega}}$ of Berea sandstone and Berkeley blue granite. As in Fig. 13.15 for the offset component, a progressive change in amplitude dependence is observed as strain increases from 10^{-7} to 10^{-5}

ranges, an alternative approach consists in introducing a critical strain level ε_c at which the sample transitions from a quadratic to a linear dependence, using $\frac{\boldsymbol{\Delta M}}{M}\Big|_{0\omega/2\omega} = 2\,\frac{\boldsymbol{\Delta c}}{c}\Big|_{0\omega/2\omega} = \Gamma\varepsilon_c \tanh\frac{\varepsilon_m}{\varepsilon_c}\varepsilon_m$ (Guyer, personal note). This critical strain, a characteristic of the material, could then also be used to describe the emergence of higher order harmonics.

Finally, a third—more systematic—approach is used in [28] to compare the responses from 6 different rock samples. Ignoring the changes in scaling, each curve in Figs. 13.16, 13.17, and 13.18 is fitted over the whole strain range with $\frac{\Delta c}{c}\big|_{n\omega} = a\varepsilon_m^{\nu}$. The power-law parameter ν is compared for all nonlinear components across samples. A correlation is found between the offset power-law $\nu_{0\omega}$, the curvature $\nu_{2\omega}$, and the hysteresis area of the loops ν_H, whereas the slope component $\nu_{1\omega}$ is found independent. This suggests that nonlinearity arises from two main mechanisms. The first one associated with the slope component $\Delta c/c|_{\boldsymbol{1\omega}}$ can be referred to as the classical nonlinearity, and as suggested above, is possibly related to opening/closing of cracks and grain contacts. The second one associated with all other components can be referred to as non-classical nonlinearity and is possibly related to shearing mechanisms of grain contacts.

Frequency Dependence: Transition from Static to Dynamic Acousto-Elasticity

One can ask whether the complex nonlinear effects measured at a few kilohertz still exist at much lower frequency. For instance, do these effects happen when a building vibrates at a few hertz due to the passage of seismic waves?

Both quasi-static tests and resonance-type experiments (see Chap. 2 in this book as well as [51, 59, 60]) have shown that rate effects are inherent to the nonlinear response of poorly cemented materials. For instance, when performing compressional tests on rocks, the hysteresis observed at typical experimental rate (∼several minutes to an hour) can completely disappear if one performs the same test at a much lower rate (∼several hours to a few days) [59]. This observation

suggests that the system has enough time to recover from each incremental stress step when cycled slowly: it remains in its original state and is not brought to a metastable state. On the other hand at larger rates, the initial increase in stress brings the sample to a new state and the subsequent decrease in stress does not follow the same path, leading to hysteresis. Resonance-type tests show similar behaviors when frequency is incrementally increased and decreased around the resonance frequency. The two upward and downward curves do not overlap when the test is performed quite fast, whereas they do overlap when the sweeps are conducted slowly [51]. To investigate such phenomena with DAET and provide further insights on the physical mechanisms at play, acousto-elastic measurements are performed at multiple loading frequencies ranging from quasi-static (~0.1 Hz) to dynamic (~10^3) regimes [61]. A rod-shaped sample of room-dry Berea sandstone is jacketed and placed upright in a pressure vessel. A large piezoelectric stack is forcing the sample to oscillate uniaxially. A small static overburden stress (0.5 MPa) is previously applied to maintain contact at all phases of the oscillation between the stack and the sample. Two longitudinal transducers operating at 500 kHz are glued on the sides of the sample to monitor the ultrasonic velocity before and during the steady-state oscillations. As for the standard DAET setup described in Fig. 13.4, the probing direction is normal to the loading direction. The Fourier analysis is performed on the nonlinear signatures and amplitudes $\Delta c/c|_{n\omega}$ are reported in Fig. 13.19 for frequencies spanning three orders of magnitude, constant strain amplitude ($\varepsilon = 1.4 \times 10^{-5}$), and constant confining pressure (1 MPa). Interestingly, the clustering found when studying multiple rocks at various strain amplitudes applies here too. Indeed, all nonlinear components but the slope ($\Delta c/c|_{1\omega}$) increase with frequency, suggesting that the mechanism related to $\Delta c/c|_{1\omega}$ is rather frequency independent (for instance, opening/closing of cracks). On the other hand, the frequency dependence observed for other components reinforces the assumption of friction/adhesion processes at crack interfaces and/or grain boundaries [62, 63].

The increase in nonlinearity with frequency corroborates former studies based on quasi-static and resonance tests [51, 59], that is, when dynamic tests are performed slowly enough, the specimen can continuously recover from the changes in loading conditions. Interestingly, the nonlinear components shown in Fig. 13.19 increase only by a factor 2 or 3 over 3 orders of magnitude in frequency, indicating that observations made at the laboratory scale in the kilohertz range are relevant to interpret larger scale observations (civil structures, geotechnical engineering, and seismology).

After the Dynamic Loading: Slow Dynamics (Phase VI)

The term “slow dynamics” was first used by [64] to describe the progressive recovery of the resonance frequency of rocks subsequent to acoustic straining or thermal shocking. Dynamic perturbations of sufficiently high amplitude (strain >10^{-6}) bring mesoscopic nonlinear materials such as rocks and cementitious materials [50] to a temporary metastable state that manifests itself by a sudden elastic softening (Phase II in Fig. 13.14). Once the perturbation is terminated,

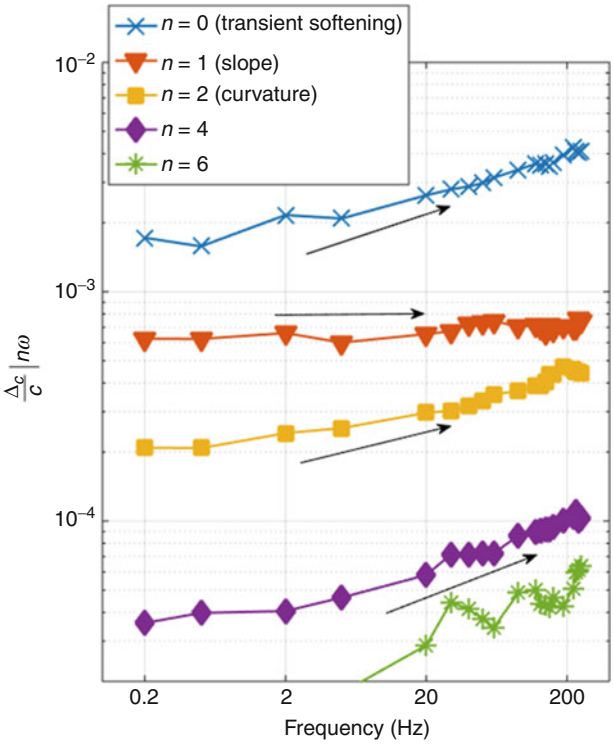

Fig. 13.19 Frequency dependence of the nonlinear components for a sample of Berea sandstone. All nonlinear components increase by a factor 2 or 3 over 3 orders of magnitude increase in frequency, except $\mathbf{\Delta c/c|_{1\omega}}$ (slope component) which is frequency independent. Note that these curves are obtained for a constant dynamic strain amplitude ($\varepsilon_m = 1.4 \times 10^{-5}$) and constant confining pressure (1 MPa). Similar observations are made at other confining pressures and oscillation amplitudes [61]

the elastic modulus slowly relaxes back towards its unperturbed equilibrium state (Phase VI in Fig. 13.14). This gradual transition of state is termed slow dynamics.

Early Time Vs. Late-Time Recovery

Earlier empirical observations have unanimously reported a time-logarithmic recovery at times t > 10 s after terminating the high-amplitude perturbation. The observed behavior appears to be independent of the test material or method used: resonance frequency in disparate rocks and concrete [64], Larsen frequency in cement paste and sandstone [65], and change of velocity in concrete [66]. Consequently, the handful of phenomenological models that have been developed to describe the post-perturbation recovery predict a log(t) behavior [67]. Despite the universal consensus about the time-logarithmic behavior, there is an experimental evidence for non-logarithmic recovery at earlier times, i.e., $t < 10$ s. For example, [65] have

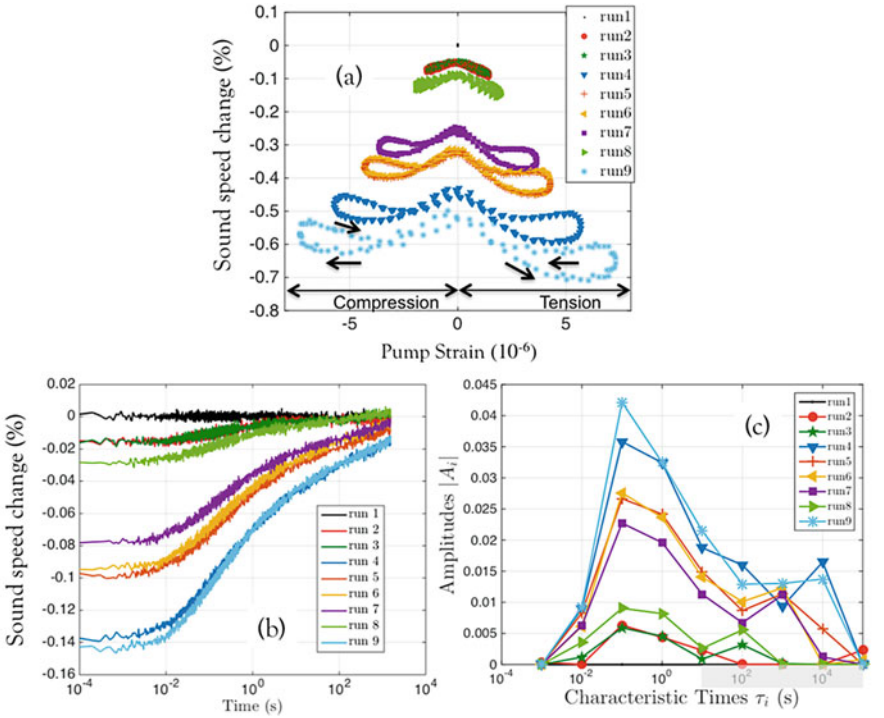

Fig. 13.20 DAET results on a sample of Berea sandstone. Runs 1–9 correspond to different pump strains: (**a**) Relative change in sound speed vs. pump strain during the non-equilibrium steady-state phase (Phase IV); (**b**) Progressive recovery of sound speed in Phase VI; (**c**) The corresponding relaxation spectra show a non-logarithmic recovery behavior at early times ($t < 10$ s). At later times, the spectrum is rather flat; the recovery is time-logarithmic, as found in previous studies [64]

measured faster than $\log(t)$ relaxation in cement paste and sandstone at $t \sim 10^{-3}$. The recent model proposed by Snieder et al. [68] describes a multi-scale relaxation phenomenon that takes place on different temporal and spatial scales.

DAET provides an unprecedented opportunity to investigate the recovery of mesoscopic nonlinear materials at times as early as $t \sim 10^{-4}$ s. Here, we present the results from a series of DAET experiments on a sample of Berea sandstone (Shokouhi et al. in preparation, to appear in 2017). The test apparatus, configuration, and parameters are very similar to those presented in [28] except that the sound speed is probed for a much longer time (about 30 min) after stopping the pump. Further, the test is conducted under controlled temperature $T(^{\circ}\mathrm{C}) = 23.0 \pm 0.2$ and relative humidity $\mathrm{RH}(\%) = 50.0 \pm 0.2$ conditions. Figure 13.20 presents the obtained results; the sound speed variations with pump strain at steady state (Fig. 13.20a) and the corresponding recoveries (Fig. 13.20b).

An examination of the recovery behavior suggests that the material recovers faster at $t > 10^{-2}$ s than at later times $t > 10$ s, after which the recovery appears to progress time-logarithmically. For a more quantitative representation, the observed recoveries are described in the form of an exponential series $\sum_{i=1}^{9} A_i e^{-t/\tau_i}$, where relaxation times τ_i are equally distributed (in a logarithmic way) over the entire time range. We find that a summation of nine exponentials is sufficient to fit the data without over fitting. The contribution of each exponential term to the recovery (A_i) or the "recovery spectrum" is shown in Fig. 13.20c. The recovery spectrum is a plot of exponential amplitudes A_i vs. the corresponding relaxation times τ_i.If wave-speeds were recovering time-logarithmically (i.e., linearly with $\log_{10}(t)$), the spectrum would be flat as was previously observed with resonance-based studies [64]. Unlike these studies, where later time recoveries were probed ($\tau \geq 10$ s), the early time recovery ($\tau < 10$ s) demonstrates preferential recovery time characteristics; the dominant recovery time for the sample is in the order of 10^{-1} s. Interestingly, the relaxation spectra for ($\tau \geq 10$ s) are almost flat, in close agreement with the earlier observations. Finally, the level of pump strain does not seem to alter the overall shape of the relaxation spectra; they all show a dominant recovery time at about 10^{-1} s. This latter observation suggests a link between the preferential recovery time and the rock microstructure. In fact, our recent observations indicate that the shape of the recovery spectrum is invariant to the changes in relative humidity of the test medium. While increasing the relative humidity increases the nonlinearity, it does not affect the multi-scale recovery rates. This latter observation provides additional evidence for the association of the recovery and microstructure. Furthermore, damage-induced microstructural changes have shown to alter the materials slow dynamics behavior. Earlier studies have shown that damage slows down the late-time recovery of cementitious materials. For example, TenCate et al. [64] show that damaged concrete recovers much slower than intact concrete. Tremblay et al. [66] made similar observations when comparing the late-time recoveries of an intact vs. a stress-damaged concrete sample. The study by Kodjo et al. [69] suggests that the rate of recovery may be used to differentiate two damage processes in concrete.

We use DAET to investigate the influence of damage on early and late-time recoveries [70]. Figure 13.21 compares the recoveries for two concrete samples: one intact and the other one damaged. Damage is induced by compressing one specimen to about 70% of its strength. The two specimens are from the same concrete mixture and visually indistinguishable (no visible surface cracking). Ultrasonic wave velocities measured (using compressional wave transducers of center frequency of 150 kHz) at two different locations across the samples are very similar. The damaged specimen has even a slightly higher linear dynamic modulus than the intact one: $E_{\text{intact}} = 33.1$ GPa and $E_{\text{damaged}} = 33.3$ GPa. Those moduli are measured by resonance ultrasonic spectroscopy (RUS) testing in the kHz range [71]. Despite their similar linear acoustic properties, the two samples differ significantly in terms of nonlinear signatures (Fig. 13.21a). The relaxation spectra in Fig. 13.21c show that the substantial recovery of the intact sample takes place for $t < 1$ s, whereas the damaged sample is still recovering even after 1 s. This

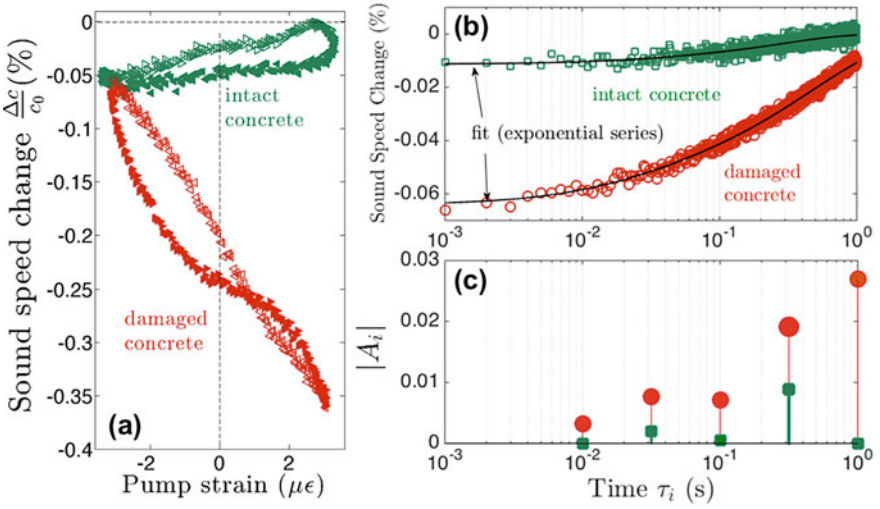

Fig. 13.21 Influence of damage on the DAET response of two concrete samples. (**a**) Fast dynamics response of intact and damaged concrete samples (phase IV). (**b**) Slow dynamics response (phase VI). (**c**) Corresponding relaxation spectra. Less than a second is needed for the intact sample to recover, whereas the damaged sample continues to recover after 1 s

observation suggests that damage-induced microstructural changes alter both fast and slow dynamics behaviors and that both signatures can be used to infer the state of damage in materials.

13.5 Conclusions

The objective of Dynamic Acousto-Elastic Testing (DAET) is the measurement of the dynamic stress (or strain) dependence of the elasticity of a material at the micro-strain level. In a typical DAET experiment, two elastic waves are simultaneously generated in a material, a low-frequency pump wave and a sequence of identical high-frequency probe waves. The sequence of probe waves determines the local changes of wave-speed induced by the pump wave. These changes can be related to local changes of elasticity of the material. Unlike methods like nonlinear resonant ultrasound spectroscopy and nonlinear wave mixing, DAET reveals the details of the nonlinear elastic behavior over a single wave cycle, including hysteresis and expansion-compression asymmetry. While non-bubbly fluids or homogeneous undamaged solids exhibit a weak and simple dynamic acousto-elastic response, bubbly liquids and damaged or granular solids show large and complicated dynamic acousto-elastic responses. Thus DAET can be a useful technique for nondestructive evaluation of materials.

References

1. P.W. Bridgman, Water, in the liquid and five solid forms, under pressure. Proc. Am. Acad. Arts Sci. **47**, 441–558 (1912)
2. F. Birch, The effect of pressure on the modulus of rigidity of several metals and glasses. J. Appl. Phys. **8**, 129–133 (1937)
3. P. Van't Klooster, N.J. Trappeniers, S.N. Biswas, Effect of pressure on the elastic constants of noble metals from -196 to $+25^{\circ}$C and up to 2500 bar. Physica B **97**(1), 65–75 (1979)
4. J.C. Swanson, Pressure coefficients of acoustic velocity for nine organic liquids. J. Chem. Phys. **2**, 689–693 (1934)
5. J.R. Pellam, J.K. Galt, Ultrasonic propagation in liquids: I. Application of pulse technique to velocity and absorption measurements at 15 Megacycles. J. Chem. Phys. **14**(10), 608–614 (1946)
6. D. Lazarus, The variation of the adiabatic elastic constants of KCl, NaCl, CuZn, Cu, and Al with pressure to 10,000 Bars. Phys. Rev. **76**(4), 545–553 (1949)
7. A.N. Norris, *Nonlinear Acoustics* (Academic, New York, 1998), pp. 263–277
8. D.S. Hughes, J.L. Kelly, Second-order elastic deformation of solids. Phys. Rev. **92**(5), 1145–1149 (1953)
9. T. Bateman, W.P. Mason, H.J. McSkimin, Third-order elastic moduli of germanium. J. Appl. Phys. **32**(5), 928–936 (1961)
10. P.B. Nagy, Fatigue damage assessment by nonlinear materials characterization. Ultrasonics **36**, 375–381 (1998)
11. J.R. Asay, D.L. Lamberson, A.H. Guenther, Pressure and temperature dependence of the acoustic velocities in polymethylmethacrylate. J. Appl. Phys. **40**(4), 1768–1783 (1969)
12. K.W. Winkler, L. McGowan, Nonlinear acoustoelastic constants of dry and saturated rocks. J. Geophys. Res. **109**, B10204 (2004)
13. S. Haussühl, W. Chmielewski, Third-order elastic constants of orthorhombic calcium formate. Acta Crystallogr. Sect. A **37**(3), 361–364 (1981)
14. J.K. Krüger, C. Grammes, K. Stockem, R. Zietz, M. Dettenmaier, Nonlinear elastic properties of solid polymers as revealed by Brillouin spectroscopy. Colloid Polym. Sci. **269**(8), 764–771 (1991)
15. G. Gremaud, M. Bujard, W. Benoit, The coupling technique: a two-wave acoustic method for the study of dislocation dynamics. J. Appl. Phys. **61**(5), 1795–1805 (1987)
16. X. Jacob, C. Christophe Barriere, D. Royer, Acoustic nonlinearity parameter measurements in solids using the collinear mixing of elastic waves. Appl. Phys. Lett. **82**(6), 886–888 (2003)
17. A. Zeiger, K. Jassby, Measurement of acoustoelastic coefficients of Rayleigh waves in steel alloys. J. Nondestruct. Eval. **3**(2), 115–124 (1982)
18. R. Ellwood, T. Stratoudaki, S.D. Sharples, M. Clark, M.G. Somekh, Determination of the acoustoelastic coefficient for surface acoustic waves using dynamic acoustoelastography: an alternative to static strain. J. Acoust. Soc. Am. **135**(3), 1064–1070 (2014)
19. G. Renaud, S. Callé, J.-P. Remenieras, M. Defontaine, Exploration of trabecular bone nonlinear elasticity using time-of-flight modulation. IEEE Trans. UFFC **55**(7), 1497–1507 (2008)
20. G. Renaud, S. Callé, M. Defontaine, Remote dynamic acoustoelastic testing: elastic and dissipative acoustic nonlinearities measured under hydrostatic tension and compression. Appl. Phys. Lett. **94**, 11905 (2009)
21. P.J. Westervelt, Scattering of sound by sound. J. Acoust. Soc. Am. **29**(2), 199–203 (1957)
22. L.H. Taylor, F.R.J. Rollins, Ultrasonic study of three-phonon interactions. I. Theory. Phys. Rev. **136**(3A), A59–A596 (1964)
23. H. Moreschi, S. Callé, S. Guerard, D. Mitton, G. Renaud, M. Defontaine, Monitoring trabecular bone microdamage using a dynamic acousto-elastic testing method. Proc. Inst. Mech. Eng. **225**(3), 282–295 (2010)
24. G. Renaud, M. Defontaine, S. Callé, Dynamic acoustoelastic testing of weakly pre-loaded unconsolidated water-saturated glass beads. J. Acoust. Soc. Am. **128**(6), 1–11 (2010)

25. C. Trarieux, S. Callé, H. Moreschi, G. Renaud, M. Defontaine, Modeling nonlinear viscoelasticity in dynamic acoustoelasticity. Appl. Phys. Lett. **105**(26), 264103 (2014)
26. G. Renaud, J.G. Bosch, A.F. van der Steen, N. de Jong, Dynamic acousto-elastic testing applied to a highly dispersive medium and evidence of shell buckling of lipid-coated gas microbubbles. J. Acoust. Soc. Am. **138**(5), 2668–2677 (2015)
27. G. Renaud, M. Talmant, S. Callé, M. Defontaine, P. Laugier, Nonlinear elastodynamics in micro-inhomogeneous solids observed by head-wave based dynamic acoustoelastic testing. J. Acoust. Soc. Am. **130**(6), 3583–3589 (2011)
28. J. Rivière, P. Shokouhi, R.A. Guyer, P.A. Johnson, A set of measures for the systematic classification of the nonlinear elastic behavior of disparate rocks. J. Geophys. Res. Solid Earth **120**(3), 1587–1604 (2015)
29. D. Bui, S.A. Kodjo, P. Rivard, B. Fournier, Evaluation of concrete distributed cracks by ultrasonic travel time shift under an external mechanical perturbation: study of indirect and semi-direct transmission configurations. J. Nondestruct. Eval. **32**(1), 25–36 (2013)
30. Q.A. Vu, V. Garnier, J.F. Chaix, C. Payan, M. Lott, J.N. Eiras, Concrete cover characterisation using dynamic acousto-elastic testing and Rayleigh waves. Constr. Build. Mater. **114**, 87–97 (2016)
31. J. Rivière et al., Dynamic acousto-elasticity in a fatigue-cracked sample. J. Nondestruct. Eval. **33**(2), 216–225 (2014)
32. S. Haupert, J. Rivière, B. Anderson, Y. Ohara, T.J. Ulrich, P. Johnson, Optimized dynamic acousto-elasticity applied to fatigue damage and stress corrosion cracking. J. Nondestruct. Eval. **33**(2), 226–238 (2014)
33. M. Scalerandi, A.S. Gliozzi, S. Haupert, G. Renaud, M. Ait Ouarabi, F. Boubenider, Investigation of the validity of dynamic acoustoelastic testing for measuring nonlinear elasticity. J. Appl. Phys. **118**(12), 124905 (2015)
34. J. Rivière, G. Renaud, R.A. Guyer, P.A. Johnson, Pump and probe waves in dynamic acousto-elasticity: comprehensive description and comparison with nonlinear elastic theories. J. Appl. Phys. **114**(5), 54905 (2013)
35. T. Gallot, A. Malcolm, T.L. Szabo, S. Brown, D. Burns, M. Fehler, Characterizing the nonlinear interaction of S- and P-waves in a rock sample. J. Appl. Phys. **117**(3), 34902 (2015)
36. M. Lott et al., Three-dimensional treatment of nonequilibrium dynamics and higher order elasticity. Appl. Phys. Lett. **108**(14), 141907 (2016)
37. G. Renaud, J. Rivière, S. Haupert, P. Laugier, Anisotropy of dynamic acoustoelasticity in limestone, influence of conditioning, and comparison with nonlinear resonance spectroscopy. J. Acoust. Soc. Am. **133**(6), 3706–3718 (2013)
38. J.N. Eiras, Q.A. Vu, M. Lott, J. Payá, V. Garnier, C. Payan, Dynamic acousto-elastic test using continuous probe wave and transient vibration to investigate material nonlinearity. Ultrasonics **69**, 29–37 (2016)
39. B. Hilloulin et al., Monitoring of autogenous crack healing in cementitious materials by the nonlinear modulation of ultrasonic coda waves, 3D microscopy and X-ray microtomography. Constr. Build. Mater. **123**, 143–152 (2016)
40. M.A. Ouarabi, F. Boubenider, A.S. Gliozzi, M. Scalerandi, Nonlinear coda wave analysis of hysteretic elastic behavior in strongly scattering media. Phys. Rev. B **94**(13), 134103 (2016)
41. G. Renaud, M. Talmant, G. Marrelec, Microstrain-level measurement of third-order elastic constants applying dynamic acousto-elastic testing. J. Appl. Phys. **120**(13), 135102 (2016)
42. M. Lott, M.C. Remillieux, P.-Y. Le Bas, T.J. Ulrich, V. Garnier, C. Payan, From local to global measurements of nonclassical nonlinear elastic effects in geomaterials. J. Acoust. Soc. Am. **140**(3), EL231–EL235 (2016)
43. G. Renaud, P.-Y. Le Bas, P.A. Johnson, Revealing highly complex elastic nonlinear (anelastic) behavior of Earth materials applying a new probe: dynamic acoustoelastic testing. J. Geophys. Res. **117**(B6), B06202 (2012)
44. C. Payan, T.J. Ulrich, P.-Y. Le Bas, T. Saleh, M. Guimaraes, Quantitative linear and nonlinear resonance inspection techniques and analysis for material characterization: Application to concrete thermal damage. J. Acoust. Soc. Am. **136**(2), 537–546 (2014)

45. G. Renaud et al., In situ characterization of shallow elastic nonlinear parameters with dynamic acoustoelastic testing. J. Geophys. Res. Solid Earth **119**(9), 6907–6923 (2014)
46. J.A. TenCate, A.E. Malcolm, X. Feng, M.C. Fehler, The effect of crack orientation on the nonlinear interaction of a P wave with an S wave. Geophys. Res. Lett. **43**(12), 6146–6152 (2016)
47. I. Céspedes, Y. Huang, J. Ophir, S. Spratt, Methods for estimation of subsample time delays of digitized echo signals. Ultrason. Imaging **17**, 142–171 (1995)
48. I.Y. Solodov, N. Krohn, G. Busse, CAN: an example of nonclassical acoustic nonlinearity in solids. Ultrasonics **40**(1–8), 621–625 (2002)
49. S. Delrue, K. Van Den Abeele, Three-dimensional finite element simulation of closed delaminations in composite materials. Ultrasonics **52**(2), 315–324 (2012)
50. R.A. Guyer, P.A. Johnson, *Nonlinear Mesoscopic Elasticity* (Wiley, New York, 2009)
51. J.A. TenCate, Slow dynamics of earth materials: an experimental overview. Pure Appl. Geophys. **168**(12), 2211–2219 (2011)
52. P.A. Johnson, X. Jia, Nonlinear dynamics, granular media and dynamic earthquake triggering. Nat. Lett. **437**(6), 871–874 (2005)
53. F. Brenguier, M. Campillo, C. Hadziioannou, N.M. Shapiro, R.M. Nadeau, E. Larose, Postseismic relaxation along the san andreas fault at parkfield from continuous seismological observations. Science **321**(5895), 1478–1481 (2008)
54. J.E. Elkhoury, E.E. Brodsky, D.C. Agnew, Seismic waves increase permeability. Nature **441**(7097), 1135–1138 (2006)
55. D. Pasqualini, K. Heitmann, J.A. TenCate, S. Habib, D. Higdon, P.A. Johnson, Nonequilibrium and nonlinear dynamics in Berea and Fontainebleau sandstones: low-strain regime. J. Geophys. Res. **112**, B01204 (2007)
56. K.R. McCall, Theoretical study of nonlinear elastic wave propagation. J. Geophys. Res. Solid Earth **99**(B2), 2591–2600 (1994)
57. K.E.-A. Van Den Abeele, P.A. Johnson, A. Sutin, Nonlinear elastic wave spectroscopy (NEWS) techniques to discern material damage, part I: nonlinear wave modulation spectroscopy (NWMS). Res. Nondestruct. Eval. **12**, 17–30 (2000)
58. K.R. McCall, R.A. Guyer, Equation of state and wave propagation in hysteretic nonlinear elastic materials. J. Geophys. Res. **99**(12), 23,887–23,897 (1994)
59. K.E. Claytor, J.R. Koby, J.A. TenCate, Limitations of Preisach theory: elastic aftereffect, congruence, and end point memory. Geophys. Res. Lett. **36**(6), L06304 (2009)
60. J.A. TenCate, T.J. Shankland, Slow dynamics in the nonlinear elastic response of Berea sandstone. Geophys. Res. Lett. **23**(21), 3019–3022 (1996)
61. J. Rivière et al., Frequency, pressure, and strain dependence of nonlinear elasticity in Berea sandstone. Geophys. Res. Lett. **43**, 2016GL068061 (2016)
62. V. Gusev, V. Tournat, Amplitude- and frequency-dependent nonlinearities in the presence of thermally-induced transitions in the Preisach model of acoustic hysteresis. Phys. Rev. B **72**, 054104 (2005)
63. C. Pecorari, A constitutive relationship for mechanical hysteresis of sandstone materials. Proc. R. Soc. Lond. Math. Phys. Eng. Sci. **471**(2184), 20150369 (2015)
64. J.A. TenCate, E. Smith, R.A. Guyer, Universal slow dynamics in granular solids. Phys. Rev. Lett. **85**(5), 1020–1023 (2000)
65. O.I. Lobkis, R.L. Weaver, On the Larsen effect to monitor small fast changes in materials. J. Acoust. Soc. Am. **125**(4), 1894–1905 (2009)
66. N. Tremblay, E. Larose, V. Rossetto, Probing slow dynamics of consolidated granular multicomposite materials by diffuse acoustic wave spectroscopy. J. Acoust. Soc. Am. **127**(3), 1239–1243 (2010)
67. O.O. Vakhnenko, V.O. Vakhnenko, T.J. Shankland, J.A. Ten Cate, Strain-induced kinetics of intergrain defects as the mechanism of slow dynamics in the nonlinear resonant response of humid sandstone bars. Phys. Rev. E **70**(1), 015602 (2004)
68. R. Snieder, C. Sens-Schönfelder, R. Wu, The time dependence of rock healing as a universal relaxation process, a tutorial. Geophys. J. Int. **208**(1), 1–9 (2017)

69. A.S. Kodjo, P. Rivard, F. Cohen-Tenoudji, J.-L. Gallias, Impact of the alkali–silica reaction products on slow dynamics behavior of concrete. Cem. Concr. Res. **41**(4), 422–428 (2011)
70. P. Shokouhi, J. Rivière, R.A. Guyer, P.A. Johnson, Slow dynamics of consolidated granular systems: multi-scale relaxation. Appl. Phys. Lett. **111**(25), 251604 (2017)
71. T.J. Ulrich, K.R. McCall, R.A. Guyer, Determination of elastic moduli of rock samples using resonant ultrasound spectroscopy. J. Acoust. Soc. Am. **111**(4), 1667–1674 (2002)

Chapter 14
Time Reversal Techniques

Brian E. Anderson, Marcel C. Remillieux, Pierre-Yves Le Bas, and T. J. Ulrich

Time reversal is a technique to focus wave energy to a selected point in space and time, localize and characterize a source of wave propagation, and/or communicate information between two points. This chapter will introduce the reader to the concept of time reversal and different implementations of this concept. The focus will then be directed to non-destructive evaluation applications using nonlinear elasto-dynamics together with time reversal.

14.1 What Is Time Reversal?

14.1.1 Pebble on a Pond

Imagine a pebble being dropped into a pond (see Fig. 14.1) [1]. Ripples will spread out circularly from the location at which the pebble enters the water. If we had recorded video of the dropped pebble and the corresponding ripples, we could play it backwards and watch the process in reverse. The ripples would collapse at the location where the pebble broke the surface of the pond.

B. E. Anderson (✉)
Department of Physics and Astronomy, Brigham Young University, Provo, UT, USA
e-mail: bea@byu.edu

M. C. Remillieux
Geophysics Group (EES-17), Los Alamos National Laboratory, Los Alamos, NM, USA
e-mail: mcr1@lanl.gov

P.-Y. LeBas · T. J. Ulrich
Detonation Science and Technology Group (Q-6), Los Alamos National Laboratory, Los Alamos, NM, USA
e-mail: pylb@lanl.gov; tju@lanl.gov

T. Kundu (ed.), *Nonlinear Ultrasonic and Vibro-Acoustical Techniques for Nondestructive Evaluation*, https://doi.org/10.1007/978-3-319-94476-0_14

Fig. 14.1 Photograph of the ripples spreading outward from the location where a pebble was cast into a pond

One practical realization of the above experiment could involve transducers placed on the surface of the pond. These transducers can detect the motion of the ripples. If the recordings from each of the transducers are all time-aligned, we can then reverse the recorded wave motions and use the transducers as sources that broadcast the reversed wave motion that they each originally sensed. These broadcasts create circular wave fronts emanating from each of the transducers. If the density of the transducers is sufficient, then an inward traveling circular wave front would be created (i.e., Huygens' principle) that would propagate inward to the drop location and would result in maximal constructive interference at this location compared to any other location on the pond. In this simple experiment, time reversal (TR) is akin to a triangulation method in which the propagation delays are recorded by the transducers. There is no need to determine the optimal propagation delays that result in maximal constructive interference since the appropriate time delays are encoded in the original signals recorded by the transducers. The array of transducers used in this fashion are often referred to as the time reversal mirror (TRM), and the individual transducers as TRM elements.

14.1.2 Time Reversal in a Bounded Medium

What happens to the procedure outlined in the previous section if there are boundaries reflecting the ripples? Imagine a bounded solid plate, such as the one illustrated in Fig. 14.2. Suppose two transducers (A and B) are placed on the boundaries of this plate. If an impulsive source signal excites transducer A into motion, a pulse will spread outward in the plate. There will be a direct propagation of this pulse energy to transducer B, which will be followed by reflected energy from the walls, as shown in the figure, finally arriving at B. In fact, there are numerous paths that the pulse energy can travel between A and B. The recording at B is, by

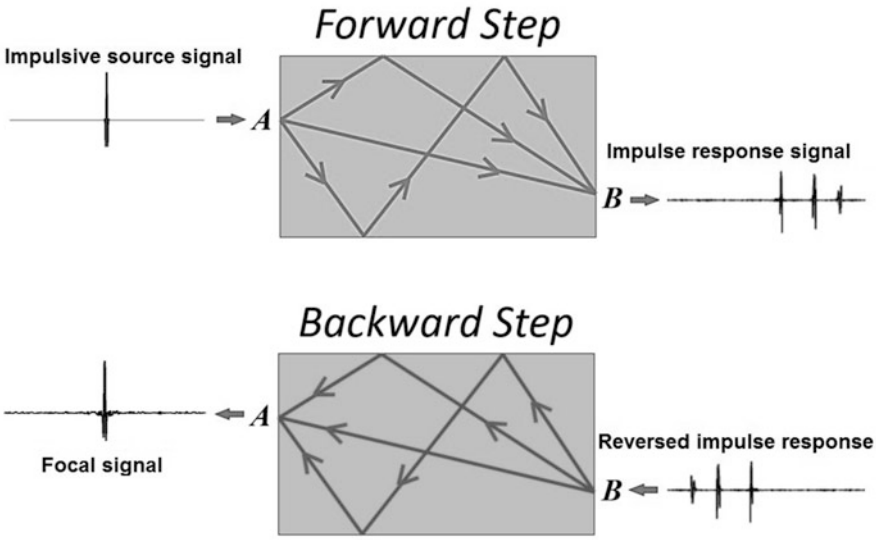

Fig. 14.2 Illustration of the forward and backward steps of the basic time reversal process

definition, the impulse response signal, often referred to as the transfer function or Green function. This signal contains the timing of the direct sound and all of the recorded reflections, within the time window of the recording, of this pulse energy. This recording of the impulse response is referred to as the forward step.

The impulse response may be reversed in time and used as an input signal to transducer B, which is now acting as a source rather than as a receiver. The energy that arrived last in the forward step is now broadcast first and the energy that arrived first in the forward step is now broadcast last. The energy emitted from B will travel along the same paths traversed during the forward step. Because the timing of the direct sound and the reflections is encoded in the impulse response, when it is played backwards the reflections and the direct sound will all arrive simultaneously at A to provide a constructive interference at that location. This is typically called the backward step, retro-focusing, or simply focusing. The focal signal recorded by A contains an impulse that is a recreation of the reverse of the impulse in the original source signal. The quality of the recreation depends upon many factors. Some of these factors were described by Anderson et al. [1]

Assuming that the transducers do not affect the signal for the generation and emission steps, the recorded signal at B, $r(t)$ (where t is time), in the forward step is mathematically represented by a convolution of the source signal,$s(t)$, with the impulse responses of the medium, $h(t)$,

$$r(t) = \int_{-\infty}^{\infty} h(\tau)\, s(t-\tau)\, d\tau. \tag{14.1}$$

In the frequency domain, this is the multiplication of the spectrum of the source signal,

$$S(f) = \int_{-\infty}^{\infty} s(t) e^{-i2\pi f t} dt, \tag{14.2}$$

where $i = \sqrt{-1}$ and f is the frequency in Hz, with the transfer functions of the medium,

$$H(f) = \int_{-\infty}^{\infty} h(t) e^{-i2\pi f t} dt, \tag{14.3}$$

$$R(f) = H(f) \cdot S(f), \tag{14.4}$$

where $R(f)$ is the spectrum of the received signal $r(t)$. A TR operation is represented by $g(t) \rightarrow g(-t)$ or a complex conjugate in the frequency domain $G(f) \rightarrow G^*(f)$. The focal signal, $y(t)$, in the backward step is then the convolution of $r(-t)$ with $h(t)$ (note that the medium's response from location A to location B is the same as the medium's response from location B to location A according to reciprocity),

$$y(t) = \int_{-\infty}^{\infty} h(\tau)\, r(-t - \tau)\, d\tau. \tag{14.5}$$

The spectrum of the focus signal, $Y(f)$, is the multiplication of $R^*(f)$ with $H(f)$,

$$Y(f) = H(f) \cdot R^*(f) = |H(f)|^2 S^*(f). \tag{14.6}$$

Since the TR process results in a magnitude-squared expression for the medium's transfer function, the TR process was originally called matched signal processing [2–5].

Another way to look at the backward step is to imagine removing the room boundaries and placing additional sources, termed image sources, at locations vertically above and below transducer B such that the distance between each image source and transducer A is the same as the distance traveled along a given reflected path that was traveled in the forward step. All these sources then emit the same source signal in the reversed order for the respective times in which they were received. The emissions from these image sources would arrive simultaneously at the original source position and constructively interfere at that location. This idea is conveyed in Fig. 14.3. Note that, in solid media, when a wave encounters a boundary the wave may partially convert into other types of motion, i.e., a longitudinal wave may reflect partly as a longitudinal wave and also partly as a shear wave. This effect is called mode conversion and requires the use of more than one image source to represent reflections of waves at boundaries.

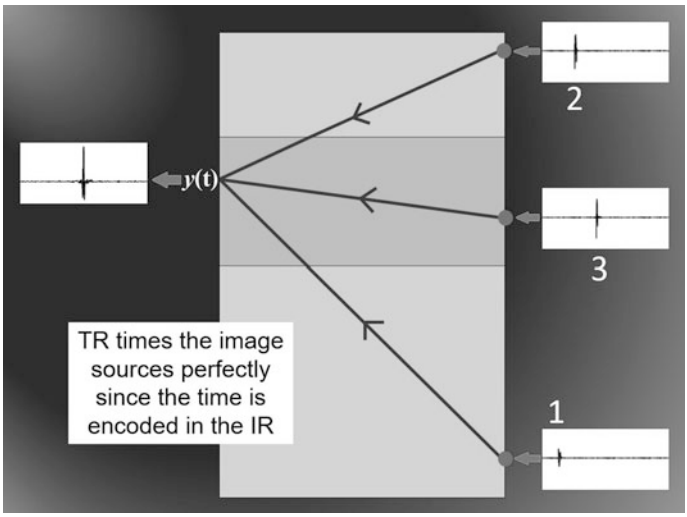

Fig. 14.3 Illustration of image sources, one above and one below transducer *B*, representing the reflections illustrated in Fig. 14.2

14.1.3 Characteristics of Time Reversal

Along with temporal reconstruction, TR provides a spatial focusing of energy. As the reversed waves reach the focal position, they interfere in space. If there are enough of these reversed waves coalescing at the focal position, a spherically converging wave is created that collapses at the focal position and then diverges out spherically. Spatial focusing is a linear superposition of these reversed waves, and thus, the TR process is diffraction limited, meaning that the size of the focusing cannot be smaller than half of a wavelength. A review of research aimed at beating the diffraction limit, often referred to as super-resolution, with time reversal techniques is beyond the scope of this chapter. Anderson et al. provided visual depictions which demonstrated the connection between temporal reconstruction and spatial focusing in the TR process [6]. Figure 14.4 provides an illustration of TR focusing before, during, and after focusing, from an experiment conducted with ultrasonic waves on the surface of a solid sample, as measured by a scanning laser Doppler vibrometer (SLDV).

TR is typically used to create impulsive focusing, however, the focusing properties at different bandwidths have been explored in room acoustics [7] and TR focusing has been demonstrated in solid media with individual sine waves when a sufficient number of TRM elements are used [8]. In general, as the bandwidth of the impulse response becomes narrower, the quality of the TR focusing deteriorates; the smaller the bandwidth of the impulse response, the weaker the TR focusing.

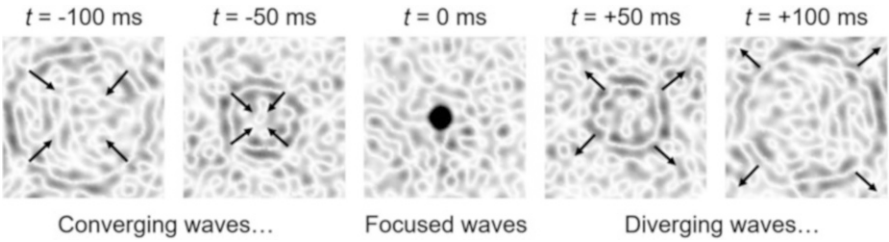

Fig. 14.4 Experimental data illustrating the convergence of waves before time reversal focusing, the coherent, constructive interference at the time of maximal focusing, and the divergence of waves after time reversal focusing

14.1.4 Methods of Time Reversal

The TR process of sending waves from *A* to *B* in the forward step and then sending waves from *B* to *A* in the backward step, as described previously, is referred to as standard TR [1]. Standard TR does not require any knowledge about the original source, be it location, temporal structure, radiation pattern, etc.; rather, it only requires the ability to measure a synchronized response across all elements of the TRM. As such, it has been used extensively in solid media for source localization and/or characterization applications, including locating, imaging, and characterizing large-scale disturbances in the earth as well as small-scale experiments involving crack motion, the latter having a direct application to non-destructive evaluation (NDE).

Due to the principle of reciprocity, a signal sent from *A* to *B* produces the same response at *B* that would be measured at A if the signal was sent from *B* to *A*, as long as the medium is identical between both operations. Thus, rather than using the standard TR process, one can instead take the signal recorded at *B* during the forward step, reverse it, and then broadcast the reversed signal from *A*. Due to reciprocity the TR focusing will now occur at *B*. This TR procedure is referred to as reciprocal TR [1]. Reciprocal TR is useful to remotely focus high-amplitude energy to any location *B* where an impulse response can be measured, or otherwise extracted, while the source transducer remains at the same location *A*. In order to focus energy at various locations of interest, the reciprocal TR process must be repeated in its entirety; i.e., the forward and backward steps must both be performed for each desired focal location. Reciprocal TR is the process typically used for NDE applications as it allows for high-amplitude targeted inspection and easy scanning of parts without having to move the source—only the receiver has to be moved to inspect another location.

Both standard and reciprocal TR require that a transfer function be obtained between the point(s) of the TRM element(s) and the focal location(s). In the above descriptions of the TR process the most basic response to an impulsive source was used. As the true impulse response, this is a simple method to obtain a suitable transfer function, and is thus sometimes referred to as the classic TR method. Due to

signal-to-noise issues, this classic process may not always be applicable. To obtain suitable transfer functions two other methods are primarily used: (1) a computed impulse response method and (2) a deconvolution method.

To conduct the computed impulse response method, a known source signal having a long duration (e.g., a chirp) is used to excite the system at location A. The response at location B is recorded, also for a long duration. This chirp response, $r(t)$, may be used, along with the source chirp signal, $s(t)$, to obtain a band-limited impulse response, $ir(t)$, through a cross-correlation operation,

$$ir(t) = \int_T s^*(\tau)\, r(t+\tau)\, d\tau, \tag{14.7}$$

where the symbol * denotes a complex conjugate (not needed for real signals) and T is the length of the signals. This cross-correlation operation is a cleaner method for obtaining an impulse response than the response from broadcasting an impulsive signal because of the higher signal-to-noise ratio afforded by the chirp signal. Example signals for $s(t)$, $r(t)$, and $ir(t)$ are displayed in Fig. 14.5.

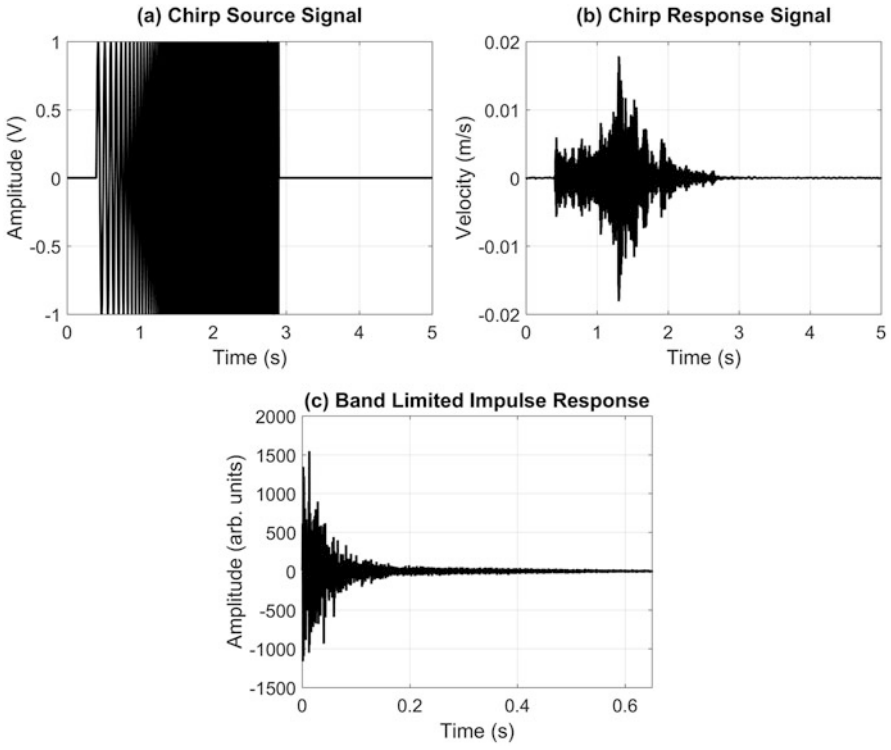

Fig. 14.5 Example signals illustrating the use of a (**a**) chirp signal and the corresponding (**b**) chirp response to obtain an (**c**) impulse response through the correlation of a known source

Alternatively, the deconvolution method can be used to obtain a suitable transfer function for TR focusing. This process, also known as inverse filtering, begins in the same manner as the computed impulse response method, i.e., with the broadcast of a long duration source signal such as a chirp. The measured response to this chirp source is then deconvolved from the source function. In the frequency domain, this is simply a division operation, as opposed to the multiplication operation that is a correlation, and is the origin of the term inverse filter. The explicit details of the process can be found in Refs. [9–13].

To compare the computed impulse response and deconvolution TR focusing methods, we refer to Figs. 14.6 and 14.7. The computed impulse response may simply be reversed and broadcast to produce a TR focus of energy. See Fig. 14.6a, b for examples of a reversed impulse response and a focal signal. The matched signal nature of the TR process, as shown by the magnitude squaring of the medium's impulse response in Eq. (14.6), results in the resonances of the system (transducers resonances and/or medium resonances) potentially distorting the temporal reconstruction provided by the TR process. Fortunately, Tanter and others have shown that the use of inverse filtering, or deconvolution, in conjunction

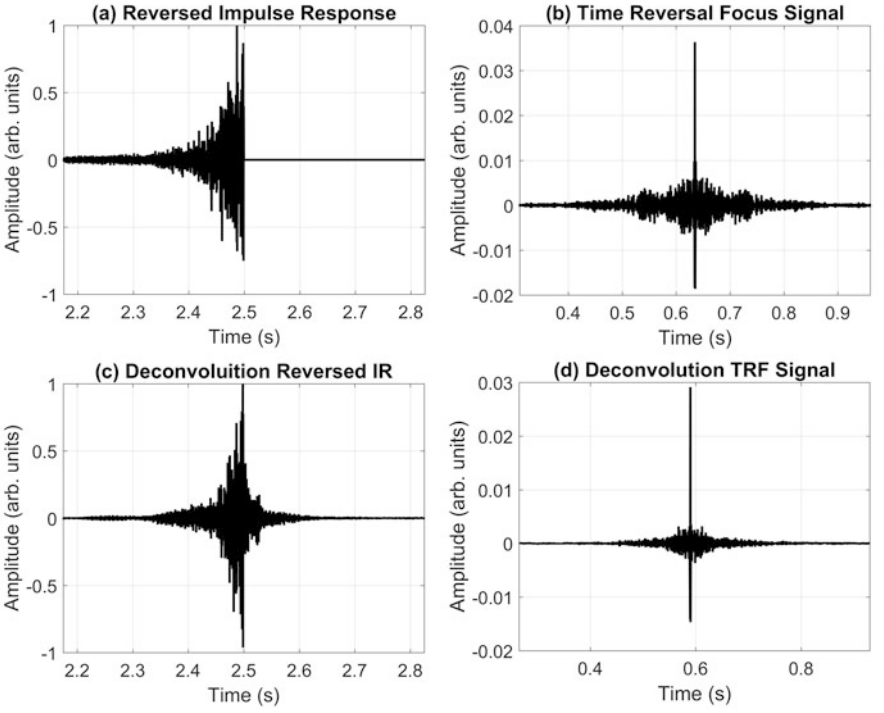

Fig. 14.6 Example signals illustrating the time reversal process during the backward step in which (**a**) a reversed impulse response (IR) is broadcast to create (**b**) a time reversal focus (TRF); (**c**) a reversed, deconvolution (or inverse filter) IR is broadcast to create (**d**) a corresponding TRF

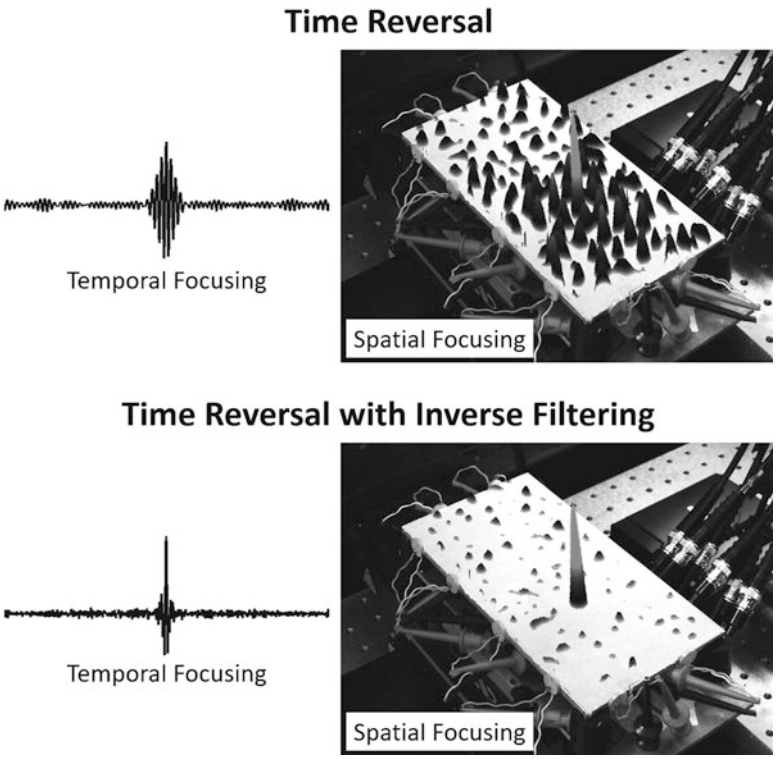

Fig. 14.7 Experimental data showing the spatial extent of time reversal focusing with (bottom) and without (top) the use of inverse filtering. On the left are images representing the temporal focal signal. On the right are the corresponding images representing the spatial extent of the focusing

with TR removes the effects of the system resonances to provide better temporal reconstruction and better spatial focusing [9, 11–13]. Inverse filtering attempts to adjust the amplitudes of the frequency content of the impulse response by reducing the amplitude at system resonance frequencies and boosting amplitude at non-resonance frequencies, while avoiding the amplification of noise.

Figure 14.6c, d displays example signals for the inverse-filter process. Figure 14.7 shows a comparison of the spatial mapping of TR focusing on a small (15.6 cm × 9.4 cm × 0.23 cm) aluminum plate. One can clearly note the improvement in the spatial focusing and the more impulsive nature of the temporal focusing. It should also be noted that this improvement in focusing quality is often obtained at the expense of a reduction in the peak amplitude of the focusing when using inverse filtering. Here, the reduction in amplitude seen between Fig. 14.6b, d is only 20% but similar experiments have reported a factor of 3 or more. Ultimately, the amplitude differences between the two methods are entirely system dependent and are not well understood.

The transfer functions obtained in both the computed impulse response and deconvolution methods are commonly referred to as being band-limited. This refers to the fact that the only information available in the signals comes from the bandwidth defined by the original chirp or other source. True impulse responses, also known as Green functions, have infinite bandwidth, a fact that cannot be realized experimentally.

A demonstration of the robust ability of TR to focus energy is provided in an example of reciprocal TR focusing, using the deconvolution method, in an aluminum plate. The localized high-amplitude focusing provided by TR can be demonstrated by placing Lego™ minifigures at various locations on the plate. A laser Doppler vibrometer (LDV) is aimed at the feet of one of the minifigures to sense the response to the chirp emanating from the single source transducer throughout the forward step. During the backward step, the vibrations in the plate are maximal at the location of this minifigure and only at this location. The vibration amplitude is such that the minifigure is launched into the air, while the other minifigures on the plate remain undisturbed. Refer to Fig. 14.8 for snapshots of

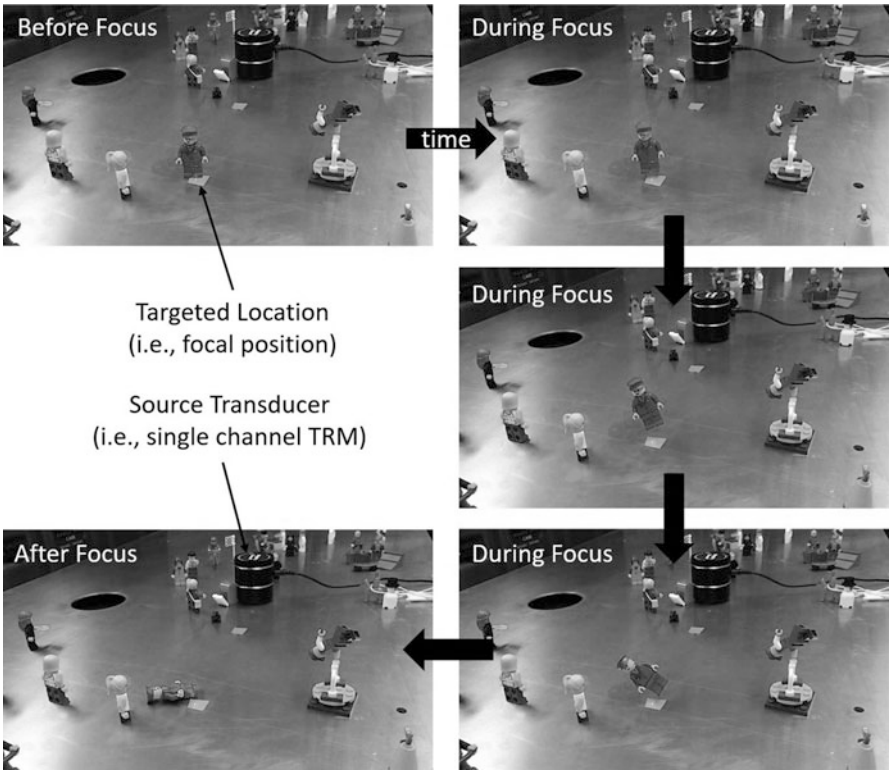

Fig. 14.8 Successive photographs of a time reversal demonstration in which a Lego™ minifigure, set up at the focal location, is being launched by the localized high-amplitude vibrations in the plate while other Lego™ minifigures, placed away from the focal location, remain relatively undisturbed throughout the process

the process. Anderson et al. calculated the peak accelerations at the focal location in a similar experiment to be approximately 250 times that of the acceleration due to gravity [14]. The ability to create such a high-amplitude localized focus of wave energy is useful for NDE where the TR focus can be used to interrogate mechanical properties of a material, in particular the nonlinear elastic parameters, as will be expounded upon later in Sect. 14.2.

The above example utilized only a single element TRM. Its success in focusing relied on the large amount of scattering that could be measured due to the multiple reflections and relatively low attenuation, which may not always be the case. In general the amplitude and quality of TR focusing requires some combination of many sources and a lot of reverberation (many reflections) in the impulse response. In media with high damping, the impulse response does not contain sufficient reverberation to compensate for the use of few sources. Similarly if a sample is small there is limited area for sources, such as piezoelectric transducers, to be bonded onto the sample's surface, and thus, the reverberation in the sample must be relied on. One method to overcome these limitations the use of a chaotic cavity (CC), in conjunction with the sample, has been introduced [15] and applied to NDE applications [16–18]. Transducers are bonded onto a CC that has low damping, such as a metallic material, and that may have a chaotic shape. This CC is then attached (i.e., bonded) onto the sample under test. During the forward propagation waves travel chaotically inside the CC and much of this energy is broadcast into the sample under test over time, providing the reverberation needed to improve the TR focusing. This idea has been termed a kaleidoscope smart transducer or a CC transducer (though this transducer may incorporate several physical transducers). The CC transducer thus provides extra reverberation to enhance TR focusing, with the caveat that this focusing principally comes from the direction of the CC transducer into the sample under test, meaning that the TR focal amplitude can be increased but the spatial extent of the focusing may or may not be confined to a diffraction limited spot.

Applying concepts similar to the idea of the CC transducer led to the development of a noncontact source that utilizes TR. Time Reversal Acoustic Non-Contact Excitation (TRANCE) exploits the reverberation of ultrasonic sound waves in an air-filled CC to create a TR focus of airborne acoustic waves onto the surface of a carbon fiber plate sample [19–23]. TRANCE was optimized through the bonding of piezoelectric transducers onto power-law profile wedges to increase the radiation of the energy from the piezoelectric transducer into the air-filled CC [24–26]. TRANCE has been shown to be able to image cracking that is perpendicular to the sample surface and a delamination that is parallel to the sample surface [27]. Imaging of these defects with TRANCE was accomplished by focusing wave motion in the plate both in the out-of-plane direction and in the in-plane directions.

In addition to the methods of direct focusing, i.e., focusing to a source/receiver as described above, several other TR-based methods have been developed to locate strong scatterers and/or weak sources/foci that may be masked due to the presence of stronger more dominant sources. These methods are more pertinent to standard TR.

The first uses of TR for NDE were aimed at the localization of linear scatterers (e.g., holes) in a sample. An array of transducers was used with each element

actively broadcasting in turn, one at a time, while the other array elements act as sensors. Once these sets of signals have been detected from each array element broadcast, a two-dimensional matrix of signals is constructed. A singular value decomposition procedure is then carried out in which the eigenvalues correspond to the signals that lead to TR focusing on the strongest scatterers in the medium (the number of scatterers that may be detected must be equal to or less than the number of array elements). This procedure is known as the Decomposition of the Time Reversal Operator (the French spelling leads to the acronym DORT) [28]. DORT was originally developed for underwater acoustics and later applied to NDE in solid media [29–31].

Depending on the application of TR, sometimes the focusing of waves to one location can be of sufficient amplitude to mask the presence of smaller amplitude TR focusing to a different location. Selective Source Reduction (SSR) was developed to progressively remove large amplitude foci and uncover smaller amplitude foci [32–34]. If nonlinear frequency content is being focused to locate a crack, a technique described in more detail in Sect. 14.2, the SSR technique may provide the means of discovering smaller nonlinear features that are masked by the TR focusing onto the largest nonlinear feature in a sample.

Time reversal is related to, though distinctly different, other methods, some of which are relevant to NDE applications. In free space, i.e., a non-scattering, environment, TR is equivalent to beamforming techniques [35, 36], an example of which is a phased array. To perform beamforming several transducers are utilized, each broadcasting/receiving the same signal but each transducer may have unique initial phases [37]. This allows a beam to be projected (i.e., steered) into a particular direction from an array of sources, or to determine the angle of incidence of an incident wave using the phase delays that produce maximal constructive interference when an array of receiver signals is summed. TR provides the delays for each transducer by obtaining the impulse responses and reversing them. Beamforming only attempts to utilize the direct signal and therefore struggles in a bounded medium with multiple reflections and/or inhomogeneity in the wave speed. On the contrary, TR utilizes the multiple reflections in a bounded medium to its advantage as will be discussed later. TR also automatically accounts for any spatial variation in the wave speed because this information is encoded in the impulse response during the forward step.

Matched field processing is another technique that is quite similar to TR used to locate sources [38–41]. In matched field processing, the backward step is done with a numerical model of the medium. Impulse responses are calculated between an array of receiving transducers and each suspected source location. When a source is detected and recorded by the receiver array, matched field processing is the process of determining which set of calculated impulse responses best matches the detected source to determine the location of the source. Matched field processing can be used to locate acoustic emissions in NDE [42], but it would not be useful to actively interrogate a sample with suspected damage since the backward step is not done experimentally, whereas TR provides the ability to do the backward step experimentally.

Finally, Reverse Time Migration (RTM) has been applied to image linear scatterers based on a technique that has been around for decades in seismic imaging applications [43, 44]. RTM involves a forward and a backward step just as in the TR process but instead of using this procedure for the purpose of creating TR focusing, RTM involves a comparison of time histories recorded during the forward and backward steps at several points of interest in which the forward and backward wave propagation occur. RTM was applied to the imaging of a partially delaminated object that was bonded onto a plate [45].

14.1.5 Benefits and Limitations of Time Reversal

As mentioned above, TR utilizes multiple reflections to its advantage where classic beamforming techniques typically struggle. One demonstration of how TR benefits from multiple reflections (reverberation) was described by Fink [46]. The experiment utilized standard TR in a water tank with a single transducer at A and an array of transducers at B. The experiment was initially conducted by transmitting from the single transducer, detecting with the array, reversing the array signals, broadcasting the reversed signals from the array, and using the single transducer to scan the spatial extent of the focusing. Next, a forest of rods was placed between A and B and the experiment was repeated. The resulting spatial extent of the focusing was 6 times narrower than for the case without the forest. This result not only demonstrated the ability of TR to perform robustly in complex media, but it also showed that multiple scattering improves the spatial focusing of TR.

Multiple transducers in a TRM may be used to record the wave propagation in the forward step. Each of these impulse responses may be reversed and subsequently broadcast simultaneously from the respective TRM transducers. The focusing generated by each transducer adds constructively to increase the focal amplitude. Thus, the TR focal amplitude may be increased through the use of more image sources (recording a longer impulse response) and/or more real sources (i.e., the multiple transducers referred to earlier in this paragraph). The energy that arrives at the focal location before or after the main coherent focus of energy, called side lobes, increases with more image sources and/or more real sources. Fortunately, the focal amplitude increases linearly with the number of TRM elements (N), while the incoherent side lobes increase in amplitude proportional to $\sqrt{N}$. Ultimately, this increase in amplitude will be used in Sect. 14.2 to achieve localized excitation with amplitudes and signal-to-noise sufficiently large for nonlinear elastic-wave measurements.

For standard TR, it is easy to see how spatial reciprocity, i.e., reciprocity along all paths between the TRM and the focal location, is involved since the paths traversed during the forward step are also traversed during the backward step. For simplicity, nothing should change between the forward and backward steps in order for TR to provide focusing. Thus, TR is limited in systems or media where mechanical properties are time dependent (such as a change in wave speed due to a global

change in temperature). Spatial reciprocity is not broken in systems with dispersion of velocity, mode conversion (waves changing form at boundaries) [47], multiple scattering as discussed previously, anisotropy, or refraction. A flowing medium can be statistically reciprocal as long as the flow does not change the velocity profile, for example. Propagation attenuation does not break spatial reciprocity unless the attenuation is a function of amplitude. Nonlinear wave steepening does not affect the TR process significantly unless a shock wave has been formed [48–50].

It has been recently shown that transducers that are directional in nature should be aimed away from the target focal location in a reverberant environment [51]. When a directional transducer is aimed at the focal location then the direct sound arrival tends to dominate the impulse response relative to the reflected (reverberant) sound in the impulse response. Prior to the broadcast of a reversed impulse response, this signal is normalized to take full advantage of the available amplification. Aiming the directional transducer away from the focal location reduces the direct sound arrival relative to the numerous reverberant sound arrivals, and thus, the normalization process essentially amplifies the many reflected arrivals for the TR broadcast. The result is a large focal amplitude. In a solid media sample, aiming the transducer directly away from the focal location may not be possible since the transducers are placed on the boundaries of the sample. Thus it may be best to aim the transducers away from the focal location(s) as much as possible, such as towards a different surface than the surface under evaluation.

It is worth mentioning that recordings made by a TRM should be simultaneous to ensure the proper timing for optimal constructive interference when conducting the backward propagation step. Additionally, for NDE applications, it is common to use multiple-channel generation systems to activate the nonlinear response of defects (typically activated at strain amplitudes ranging from 10^{-7} to 10^{-5}). As will be discussed in Sect. 14.2.3, the main advantage of using multiple-channel systems comes from the ability to generate a low-amplitude wave from each channel that will eventually coalesce into a high-amplitude wave at the focal point, thus avoiding the activation of inherent, background nonlinearity of the sample through the wave propagation from the elements of the TRM to the focal point. Further, when constructing a numerical model for either the forward or backward propagation steps, the models must be fairly accurate, though some errors may be tolerated [52, 53].

14.1.6 Applications of Time Reversal

TR has been developed for many applications in acoustics (including elastic waves in solid media) and also with electromagnetic waves [54, 55]. Within acoustics applications there are three main purposes for the use of TR focusing: to communicate information from one location to another, to locate and characterize a source of energy or a scatterer of energy, or to create a localized high-amplitude focus of energy.

The first application of TR was for underwater acoustic communication between ships [2–5]. In that early work, TR was referred to as matched signal processing since the focusing of a time reversed impulse response is equivalent to the autocorrelation of the impulse response. Later, researchers in underwater acoustics referred to the technique as phase conjugation (a phase conjugation of a complex spectrum in the frequency domain is equivalent to a TR operation on the corresponding temporal signal in the time domain), deriving the name from optical research on phase conjugate mirrors [56–58]. The reversed impulse response used in TR can be used as the carrier signal to deliver spatially focused communications. TR is especially useful in complex (multi-layered ocean), reverberant media [59]. There have been a significant number of published papers on the subject of underwater acoustic communications using TR. Recently TR was used to demonstrate acoustic communications through an elastic medium [60].

TR can be used to focus wave energy back to an unknown source location in order to localize it and the properties of the focused energy may be used to characterize the source. Tectonic plate earthquakes [61], glacial earthquakes [62], and geophysical tremor [63] have each been located and characterized with TR [64]. In addition to locating these seismic events, the TR focusing also enabled some understanding of the rupture process which may allow characterization of different types of seismic events. TR has been used in touchpad technology to locate finger taps [65, 66]. Various sources of sounds have been located in fluid media, including aeroacoustic sources [67–69], gun shots [70, 71], and gas leaks [72]. TR has been shown to accurately image the spatial extent of sources that are a half wavelength in size or less [73].

High-amplitude focusing has been used in the biomedical field of acoustics [74], room acoustics applications [75], and NDE of damage in solid media [76]. High amplitudes are useful in biomedical applications to destroy tissue without invasive surgery. Biomedical applications have included the acoustic lithotripsy of kidney stones [77] and brain tumors [78, 79], the development of a shock wave generator [80], and imaging of defects in human teeth [81]. Focusing high-amplitude sound has recently been shown in a reverberation chamber to study nonlinearities in loud, impulsive sounds, and to possibly simulate the sound of explosives [75]. For NDE applications in solid media, TR was first used to detect linear scatterer defects (i.e., holes) by coupling acoustic energy from an array of transducers into the sample through water or through the use of a plexiglass wedge [29–31, 82–85]. Later, high-amplitude TR was applied to find localized nonlinearities that are indicative of defects, cracks, and/or delaminations. The higher the amplitude, the more sensitive the TR techniques are to detecting nonlinearities. TR has been used to detect nonlinearities experimentally, to locate surficial cracks from impact damage [27, 86], surficial cracks from stress fatigue [87], surficial cracks from stress corrosion cracking [88, 89], near-surficial cracks and delaminations [45, 90], and internal delaminations [91].

The first experimental demonstrations of TR in solid media to locate linear scatterers and demonstrate TR focusing in solid media were conducted in the 1990s [29, 82–85, 92, 93]. In 2001, Guyer [94] proposed the idea of locating a crack

in solid media with TR and nonlinear techniques. Delsanto et al. then developed numerical simulations of TR in elastic media [95]. Experimental studies exploring the use of TR to detect nonlinearities and use TR techniques in granular media were then conducted by Sutin et al. at Los Alamos National Laboratory using transducers bonded onto the sample instead of submerging the samples [96, 97]. The first proof of concept of locating a nonlinear crack was demonstrated by Bou Matar et al. in 2005 using numerical analysis [98]. This was followed by the first experimental validation of using TR to locate a surficial crack in a solid sample in 2006 by Ulrich et al. [86]. Some key experiments demonstrating the use of TR for NDE of cracks, defects, and delaminations have been reviewed in Ref. [76].

14.2 Time Reversal for Locating Damage

14.2.1 Nonlinear Signatures of Defects

Damaged materials have in common the presence of internal defects, of various sizes and types. These defects include dislocations, micro-cracks, relatively large cracks, and delaminations, depending not only on the material but also on the process leading to damage (e.g., impact, exposure to harsh chemical environment, fatigue, non-optimal settings in the manufacturing process). As an elastic wave propagates in a solid, it interacts with its constituents, including its defects. It is not surprising then that elastic waves have been used for decades to characterize materials and evaluate structural integrity in various fields. Many material defects lead to nonlinear effects during the propagation of finite-amplitude elastic waves, manifested as wave distortions in the time domain or generation of harmonics in the frequency domain [99–101]. Unlike techniques relying on the linear scattering of an elastic wave by a defect, these effects may be observed even when the wavelength is much larger (by orders of magnitude) than the defects. This fact is of practical importance for NDE applications since it may be and has been used for the early detection of defects in materials. In fact, it has been demonstrated that nonlinear signatures are far more sensitive to the presence of microscopic-sized defects, which are precursors to larger defects and eventually system failure, than linear signatures, including linear scattering, changes in the propagation speed of the elastic waves, and linear attenuation [100, 101].

The interaction between an elastic wave with sufficiently large amplitude and a contact interface (e.g., crack, delamination, imperfect bonding) has been studied and described in depth by Solodov and his collaborators [102–104]. In brief, the nonlinear dynamic response of the interface may be described by a distributed nonlinear spring connecting two faces set in motion by an incident elastic wave. This spring stiffness depends on the stress conditions at the interface, thus leading to a complex spatio-temporal response. At relatively low amplitudes, this spring has a constant stiffness and behaves linearly. At larger amplitudes (with a threshold

determined by the size of the interface, material, roughness, etc.), the spring stiffness decreases with possibly a complex dependence on stress. Eventually, at much larger amplitudes, the spring "breaks" with its stiffness going to 0, thus allowing the two faces of the defect to vibrate independently from one another. When the amplitude of the incident elastic wave returns to a relatively small value, the spring regains its original linear stiffness properties and the dynamics of the faces are once again coupled. Similar approaches have been used in recent attempts to model the dynamics of cracks and their interactions with elastic waves [105–108].

Practically, an incident elastic wave will be distorted by an imperfect contact within an interface. For example, an incident monochromatic wave may be clipped at its peaks due to collisions between the two faces of the defect. The clipped waveform has the majority of its energy at the fundamental frequency of the incident wave but it also has a finite amount of energy at odd harmonic multiples of the fundamental frequency. Collisions that occur at any other time during the cycle of the fundamental frequency, or occur for anti-symmetric portions of the cycle, will result in finite amounts of energy at the even harmonic multiples of the fundamental frequency in addition to the odd harmonics. These effects of nonlinearity on waveforms and corresponding spectra are shown in Fig. 14.9. Two crack faces that are in constant contact, e.g., a closed crack, will rub against one another with a frictional interaction that may distort the incident wave throughout the cycle of the fundamental frequency [106]. If the interface is driven at two frequencies, f_1 and f_2, then the nonlinearly generated frequency content will consist of summation and difference frequency combinations of the two frequencies, $nf_1 \pm mf_2$ (where n and m may be any integer values). An experimental example of sum and difference frequencies will be given in Sect. 14.2.2. In some cases, where there is not enough energy for one side of a crack to vibrate far enough to contact the other side of the crack for more than a period of the wave (i.e., trampoline effect), there is a potential for the creation of sub-harmonics $f_1/2$, $f_2/2$, and linear combinations thereof.

14.2.2 Time Reversal of Nonlinear Features Detected Remotely (Standard Time Reversal)

As described in the previous section, in an otherwise linear medium, a crack (or more generally an imperfect interface) may be described as a localized nonlinear scatterer that distorts an incident elastic wave and generates additional harmonic content in the frequency domain. If the nonlinear features contained in the signal that are emitted by the scatterer can propagate away from the scatterer, be detected by remote sensors (e.g., piezoelectric transducers), isolated, time reversed, and broadcast into the same medium, then these features should coalesce to the source region and imaging is possible.

The feasibility of this idea was first demonstrated in a numerical study by Bou Matar et al. [98]. The first experimental realization of this idea can be found in

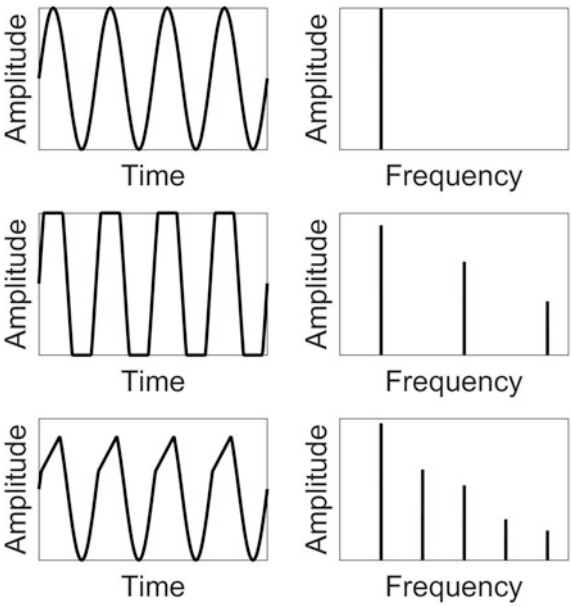

Fig. 14.9 Time waveforms and corresponding frequency spectra of three sample signals: a sine wave, a clipped sine wave, and a distorted peak sine wave

the work of Ulrich et al. [87] where a crack was imaged in a bearing cap. In this experiment, the modal response of a sample was excited (typically low frequency resonances are excited) with an impulsive excitation in conjunction with excitation of the sample with a narrowband high frequency tone burst from a transducer. The response was recorded by a piezoelectric transducer on the sample and analyzed to detect the presence of sum and difference frequencies on either side of the high frequency tone, as shown in Fig. 14.10. The recorded waveform was band-pass filtered to extract its nonlinear content that was presumably generated by a crack in the sample. The filtered waveform was then time reversed and broadcast by the piezoelectric transducer. Finally, a SLDV was used to measure the elastic response on the surface of the sample and locate positions where the TR focusing produced the highest amplitudes. Images of the crack detected in this experiment are shown in Fig. 14.11. Elastic wave energy refocuses at different parts of the crack at different times because of the complex space-time dependence of the crack dynamics discussed in the previous section. The time reversal process is able to capture such dynamics.

Another experimental realization of this concept was reported by Le Bas et al. to image nonlinearity at the interface between two solids: a glass block and an aluminum block [91]. A representation of their experimental setup is shown in Fig. 14.12. The optical properties of the two solids (i.e., transparent and opaque) allowed them to shine the beam of a LDV at the interface of the two solids and monitor its dynamic response. The rest of the setup consists of piezoelectric transducers to detect and emit elastic waves. This experiment is more complex than the one described previously because TR was used twice, for two distinct purposes. TR was

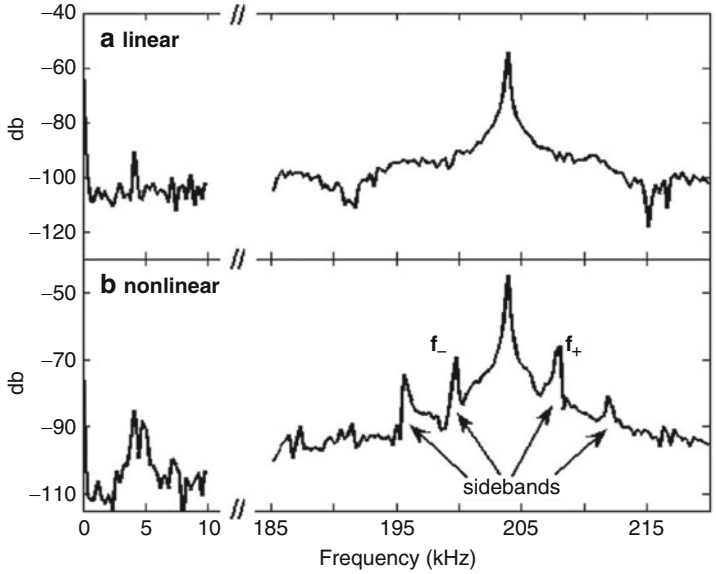

Fig. 14.10 (**a**) An example of a power spectrum for an elastically linear (undamaged) sample. Note in particular the lack of sidebands in the high frequency portion of the spectrum. (**b**) An example of a power spectrum for an elastically nonlinear (mechanically damaged) sample. Note the sidebands at multiples of ±4 kHz on either side of the 204 kHz pure tone. This spectrum demonstrates the nonlinear mixing of a normal mode with a pure tone. These identical samples only differ in that the damaged sample has a 1 cm crack

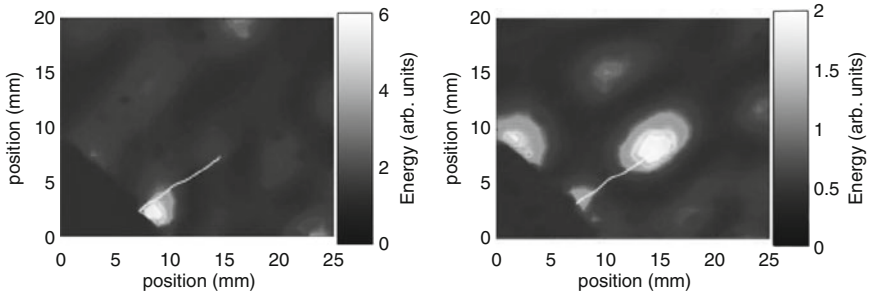

Fig. 14.11 Spatial maps of the time reversal focusing of energy on the damaged sample at two different time intervals. The true location of the crack is identified in white to illustrate how the focusing progresses from the mouth of the crack to the crack tip

used a first time through the time reversal mirror TRM1 (see Fig. 14.12) to stimulate a number of localized regions over the interface with high-amplitude elastic waves. More details about the application of this concept for NDE and imaging are given in the next section (Sect. 14.2.3). When a nonlinear scatterer was present within the focal region, it responded nonlinearly. The nonlinear features generated by the scatterer could be detected by the elements of a second time reversal mirror, TRM2.

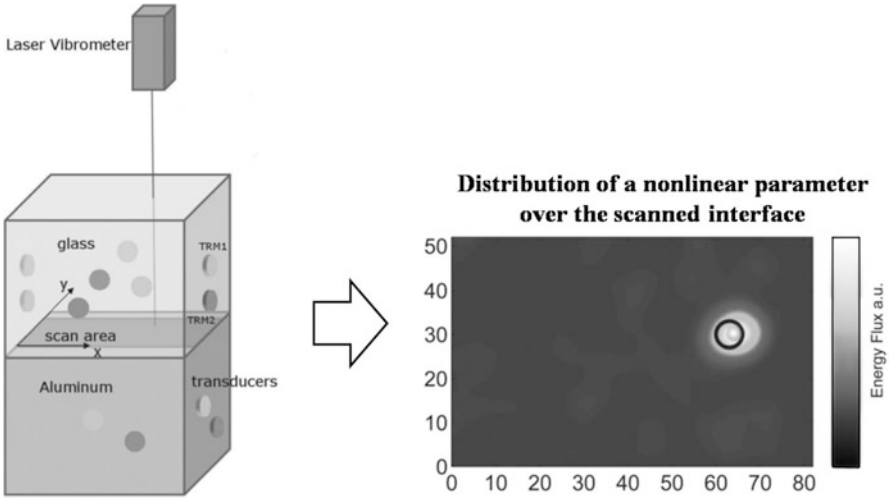

Fig. 14.12 Using time reversal to image nonlinearity at the interface between a glass block and an aluminum block

Once processed with time reversal and reemitted into the sample, these nonlinear features would coalesce where imperfections were intentionally introduced when creating the interface between the blocks, as shown in Fig. 14.12.

These two experiments have been complemented by numerous numerical studies where ways to optimize this technique were proposed [88, 109, 110]. However, widespread adoption of this technique by the NDE community may be a challenge because experimental implementation is not trivial. In addition, there is a caveat to be aware of. The nonlinear scatterer to be imaged is localized but the material may have some finite amount of inherent nonlinearity (e.g., micro-cracking from the damage process) in which case the elastic waves will propagate through this medium and experience additional distortions. If the nonlinear response emitted by the localized scatterer is much stronger than the background nonlinearity (i.e., that due to the distributed micro-defects in the material) and this background nonlinearity is quasi-uniform, then imaging of the defect is possible. If not, the techniques described in the next section can be a powerful alternative.

14.2.3 Focusing Elastic Wave Energy for Localized Nonlinear Inspection (Reciprocal Time Reversal)

As hinted in the previous section, TR can also be used to focus linear elastic waves to a region of interest by using the principle of reciprocity and thus be the basis of localized inspection techniques. The dynamic response within the focal region can be subsequently used for further processing and analysis, in particular to detect the

presence of nonlinear features. Relying on the fact that the dynamic response of a nonlinear scatterer does not scale with amplitude nor phase, the focal signal(s) can be exploited in multiple ways for imaging, each leading to a new NDE technique. These techniques are all based on reciprocal TR. While successful experiments have been conducted with as few as one transducer, using multiple transducers can be helpful to mitigate the issue of background nonlinearity caused by distributed micro-defects in the material. Using the principle of reciprocal TR, each transducer can be used independently to focus wave energy at a desired location. This fact allows for the use of multiple low-amplitude channels to produce a focused high-amplitude response at any point in the solid. In the following, some of the key experiments and signal processing techniques will be presented.

In 2003, Sutin et al. conducted a TR experiment in a cracked block using a single pair of source-receiver to focus elastic waves on and away from a crack [96]. They repeated the experiment at multiple amplitudes, tracked the harmonic content of the signals focused on the crack, and noticed that it scaled with amplitude as it should for a crack in a solid. Following this experiment, Ulrich et al. repeated the TR process, analyzed the focal signals for a grid of scan points around the nonlinear scatterers, and created images of these scatterers [86]. In this experiment, multiple transducers were used for wave focusing and nonlinearity was extracted via intermodulation distortion. In brief, reciprocal TR was conducted simultaneously at two different frequencies while the nonlinear scatterers generated difference and sum frequencies. The frequency components in the focal signals at each focal position on this experiment are shown in Fig. 14.13. The extent of the nonlinear features (difference and sum frequencies) is in excellent agreement with the extent of the actual damaged region bounded by dashed lines in the figure.

Phase inversion or pulse inversion (PI) is another technique used to extract the nonlinear features of a focal signal in a TR experiment. This technique was originally developed for medical imaging applications [111] and later applied to the detection of landmines [112]. In the PI technique the backward step is carried out twice, once with the reversed impulse response and then a second time with the reversed impulse response multiplied by -1 (i.e., phase inversion). The two focal signals, one with a positive phase focusing (0°) and the other with a negative phase focusing (180°), can then be added to one another. If the focusing is purely a linear process, then the addition of these signals should only consist of any background noise in both signals. The growth of even and odd harmonics is such that if the focusing generates any nonlinearities then the addition of the two focal signals will result in the elimination of all odd harmonics, including the fundamental frequency, leaving any even harmonics that were generated through nonlinear processes. For many types of nonlinear processes of interest, the amplitude of the second harmonic grows as the square of the amplitude of the fundamental frequency. The residual signal may then be characterized in any number of ways. Some example metrics that may be used to quantify the nonlinearities in the residue signal include the peak of the residue signal, the amplitude of the second harmonic extracted from the spectrum of the residue signal, or a summation of the squared residue signal (sometimes only centered on the time of peak focusing).

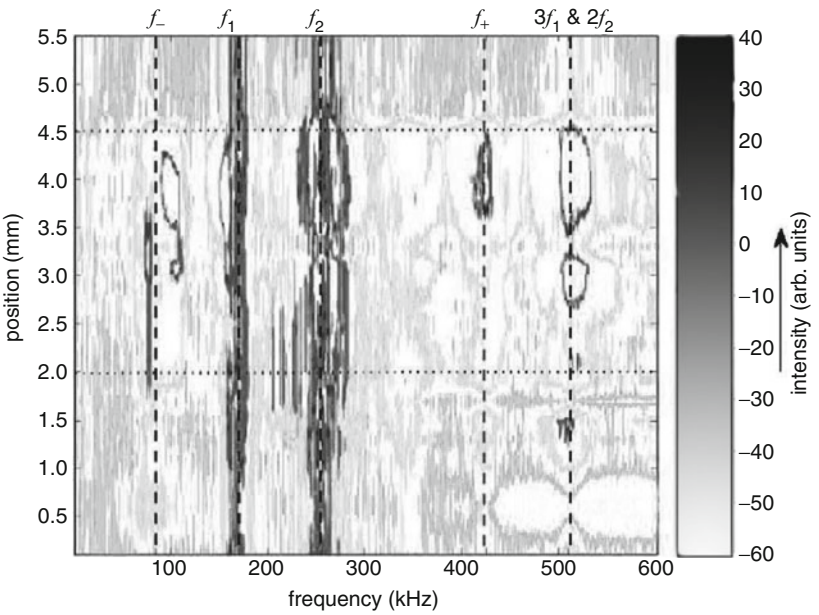

Fig. 14.13 Spatial dependence of the frequency content of focused energy. Note the presence of sum ($f_+ = f_1 + f_2 = 425$ kHz) and difference ($f_- = f_2 - f_1 = 85$ kHz) frequencies and harmonics of the two primary frequencies (e.g., 510 kHz) in the damaged region (identified by the dotted horizontal lines). Vertical lines denoted frequencies of interest

The PI technique was first combined to TR in experiments by Ulrich et al. [90] to image nonlinearity over the interface of two metallic disks that are diffusion bonded to one another. The types of defects found at the interface consist of holes and disbonded regions (i.e., cracks). The interface was imaged with linear C-scan at 15 MHz and with TR combined with PI at 200 kHz. The linear (C-scan) and nonlinear (TR scan) images of the interface are shown in Fig. 14.14. There are obvious differences between the two images. Each method is able to image different types of features. The linear C-scan is sensitive to large impedance contrasts, such as where a void is present or a free surface. The ability of the TR scan to detect nonlinear frequency content allows it to image defects where two surfaces are in contact with one another but no adhesion exists between the surfaces, such as with closed cracks and the edges of delaminations. Thus the methods are complimentary since the linear method (C-scan) cannot detect the cracks and delaminations whereas the nonlinear method (TR scan) cannot detect the large voids and free surfaces. The bonded disks were cut normally to the interface and imaged with a scanning electron microscope to verify that the C-scan correctly imaged voids in the diffusion bond, whereas the TR scan correctly imaged disbonding between the metals.

The loss of the odd harmonic energy, at the 3rd and 5th harmonic frequencies, for example, is one of the drawbacks to the PI technique. To address this issue, Ciampa and Meo proposed a variation on the PI technique that they termed third-

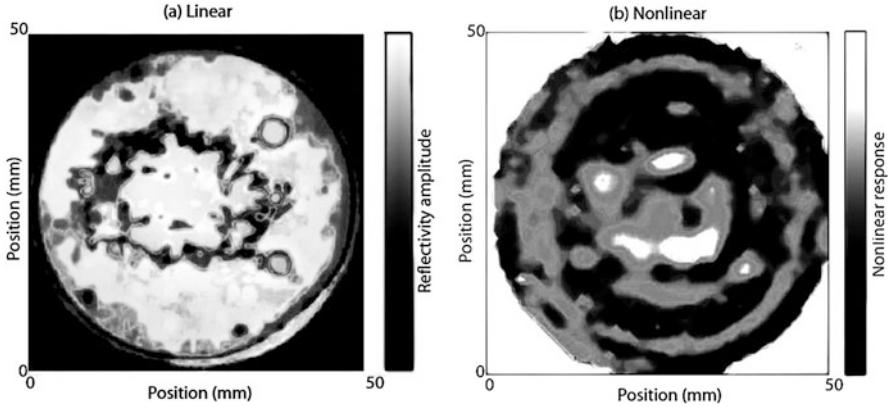

Fig. 14.14 Spatial maps imaging defects in the bonded sample. (**a**) The linear C-scan image on the left utilized a 15 MHz primary frequency whereas (**b**) the nonlinear TR scan image on the right utilized a 200 kHz primary frequency. The brightest white areas in the linear image near the center of the sample indicate voids. The white areas in the nonlinear image indicate disbonding or cracks

order phase symmetry analysis [113]. With third-order phase symmetry analysis, three time reversed impulse responses are used to create three different focal signals. Prior to the broadcast in the backward step, the first reversed impulse response signal is unchanged, the second reversed impulse response is shifted by 120°, and the third reversed impulse response is shifted by 240°. Ciampa and Meo showed that these three focal signals could be used to independently extract either the fundamental frequency content, the second-harmonic frequency content, or the third-order frequency content. They demonstrated that some systems generate more third harmonic content than second-harmonic content, and thus, the phase symmetry analysis they proposed is an improvement upon standard PI techniques, though it requires three focusing steps rather than just two.

The last technique discussed in this section to extract the nonlinear features of a signal in the context of TR experiment is the scaling subtraction method (SSM) [114, 115]. Since, by definition, nonlinear processes are amplitude dependent, if the focal signal is generated by broadcasting the same impulse response at two different amplitudes, then any differences in those two signals, when scaled appropriately, is due to nonlinear effects. For example, one reversed impulse response may be broadcast with an amplitude A_1. The same reversed impulse response may be broadcast with a larger amplitude of A_2. If the TR focusing is a linear process, then one can multiply the low-amplitude signal by A_2/A_1 and the two focal signals should be identical. The SSM specifies that the low-amplitude signal should be scaled up to match the large amplitude signal (according to the scaling factor used prior to broadcasting the signals) and then the scaled low-amplitude signal is subtracted from the large amplitude signal. SSM preserves the even- and odd-harmonic frequency content. Similar to the phase inversion technique, one is left with a residue signal. Scalerandi et al. proposed that one could sum the squared

residual signal (similar to an energy quantity depending on what type of signal is detected, i.e., squared particle velocity would be proportional to kinetic energy). Another type of processing of the residual signal involves the subtraction of the scaled low-amplitude spectrum from the large amplitude spectrum (where the spectra are the Fourier transforms of the focal signals) [89].

14.2.4 Surficial and Depth Imaging with Time Reversal

When elastic waves are focused via the TR process in a solid sample, one can easily image the surficial motion of the sample with a laser vibrometer. However, if the sample has an appreciable thickness, then one would expect that the converging waves do not solely travel on the surface of the sample but also through its bulk. Thus, one would expect that surficial TR focusing has a depth dependence to it besides the surficial spatial extent. Payan et al. probed the depth of bulk nonlinearity in concrete using this principle [116]. Remillieux et al. used a numerical model of the TR process to quantify the spatial profile and the depth profile of the TR focusing in a homogeneous elastic sample by simulating typical NDE sample sizes, transducers, and frequencies [117]. They found that the surficial extent of the focusing was half of a Rayleigh wavelength, whereas the depth penetration was one-third of a shear wavelength (both quantities defined in terms of the full width at half maximum of the focal amplitude). Recently TR was used to extract some information about the depth profile of a stress corrosion crack in a thick plate of stainless steel based on surficial measurements at different frequencies [89]. The sample is shown in Fig. 14.15. From visual inspection, the crack runs along the upper edge of the weld. It penetrates into the sample initially downward and then it curves under the weld such that the crack tip is approximately at a distance of 10 mm from the surface of the sample (see the image on the left in Fig. 14.15). Experiments were conducted with TR signals centered at 100 and 200 kHz. In these experiments, the nonlinear signature was extracted by a technique similar to the scaling subtraction method. Signals were scaled by the excitation amplitudes but processed in the frequency domain, in a relatively narrow frequency band centered around the second harmonic. An example of waveforms and corresponding amplitude spectra acquired at two amplitudes on the crack is shown in Fig. 14.16. Comparison of the amplitude spectra scaled with respect to the source amplitude shows a significant increase in second-harmonic amplitude for the high-source level (i.e., 3 V). Results from the scans are displayed in Fig. 14.17. At 200 kHz, the theoretical penetration depth is 5 mm, which only probes the portion of the crack that is perpendicular to the surface of the sample. As a result, the map of nonlinearity exhibits a strong but narrow contrast zone following the crack line on the surface. As the center frequency of the TR signal is decreased to 100 kHz, the theoretical penetration depth is 10 mm. The map of nonlinearity is discontinuous along the crack line, exhibiting larger contrast zones that appear only below the crack line, which coincides with the shape and depth of penetration of the crack into the sample.

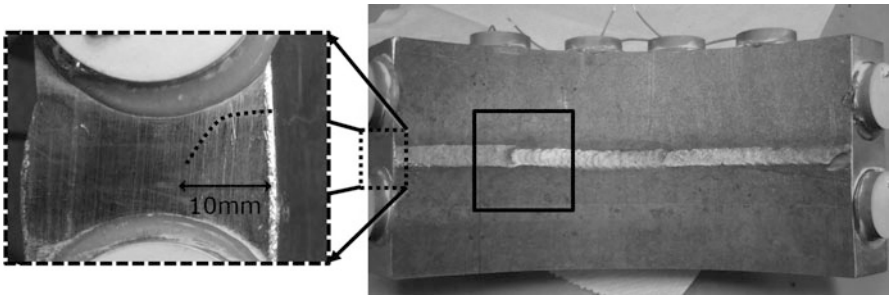

Fig. 14.15 Photographs of the sample used in the experiments conducted by Anderson et al. [89] The solid line box indicates the approximate scan area. The dashed line box (left) shows an edge view photograph of the side of the sample with a dotted line indicating the extent of a barely visible crack

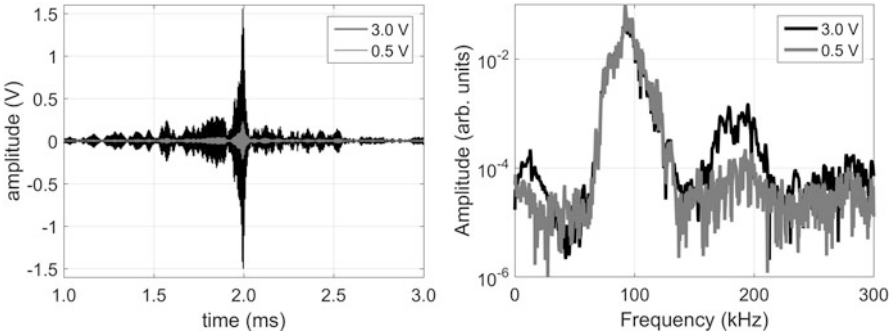

Fig. 14.16 Focal signals and corresponding scaled spectra measured on the crack for two difference source amplitudes, based on a TR signal centered at 100 kHz. In the frequency domain, the nonlinear response of the crack is well evidenced by the second-harmonic generation as the source amplitude is increased

14.2.5 Three-Dimensional Time Reversal Focusing

A development of particular interest for NDE is the ability to focus energy in different Cartesian directions (e.g., x, y, z, or linear combinations of these) using a scalar source [118, 119]. This property can be used for imaging the orientation of a crack [120] based on the simple fact that, dynamically, it is easier to activate the clapping than the friction mechanism at an interface. 3D focusing can be achieved with any receiver capable of sensing in multiple directions, which is the case of a 3D SLDV (e.g., 1 out-of-plane component +2 in-plane components). Focusing in a specific direction is again achieved with reciprocal time reversal where the direction of sensing will dictate the direction of focusing, regardless of the source characteristics. Focal signals and wave fields at the focal times for different focusing directions are shown in Figs. 14.18 and 14.19, respectively (only one in-plane direction is shown). If the signal recorded by an out-of-plane laser vibrometer

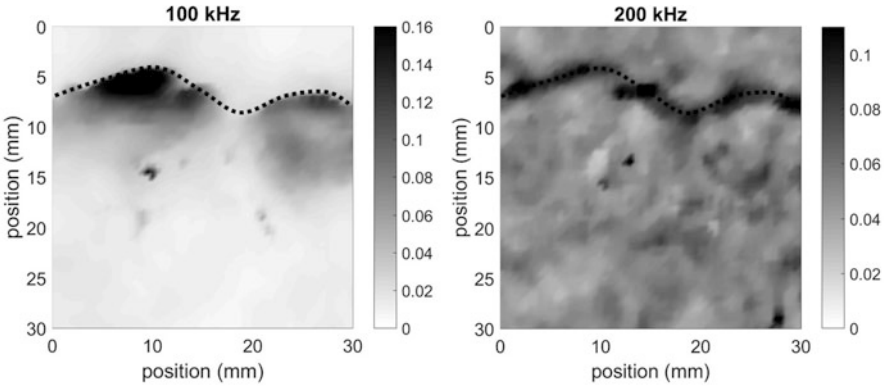

Fig. 14.17 Maps of nonlinearity produced with TR pulses centered at 100 and 200 kHz. The dotted line indicates the visible, surficial expression of the crack

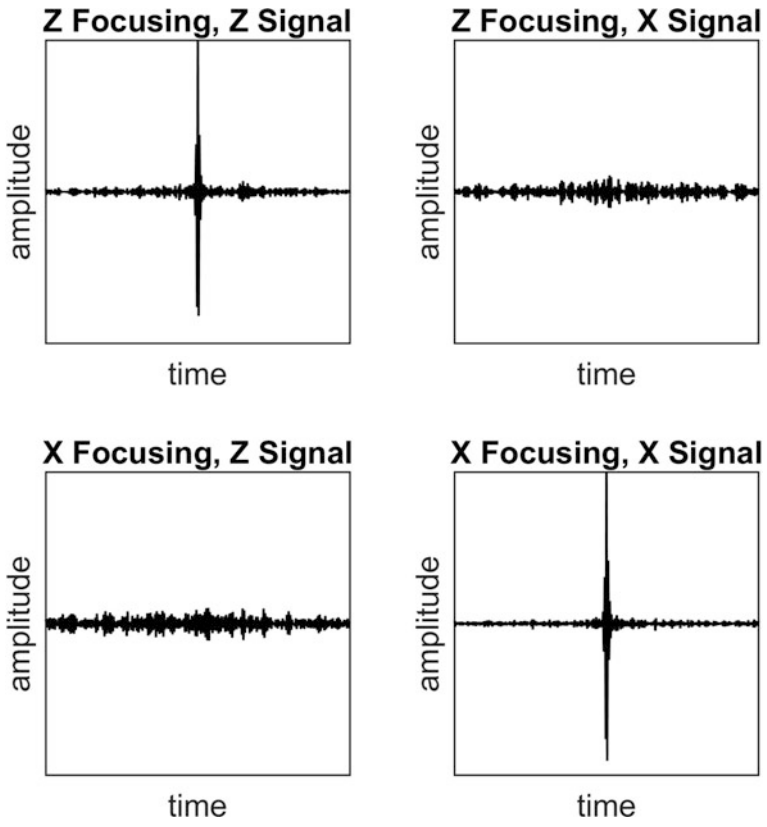

Fig. 14.18 Example temporal signals illustrating the time reversal focusing only in the direction in which the impulse response signal is detected during the forward step. These velocity signals were measured at the same locations. The first row displays the motion in the two directions for out-of-plane focusing while the second row displays the motion in the two directions for in-plane focusing

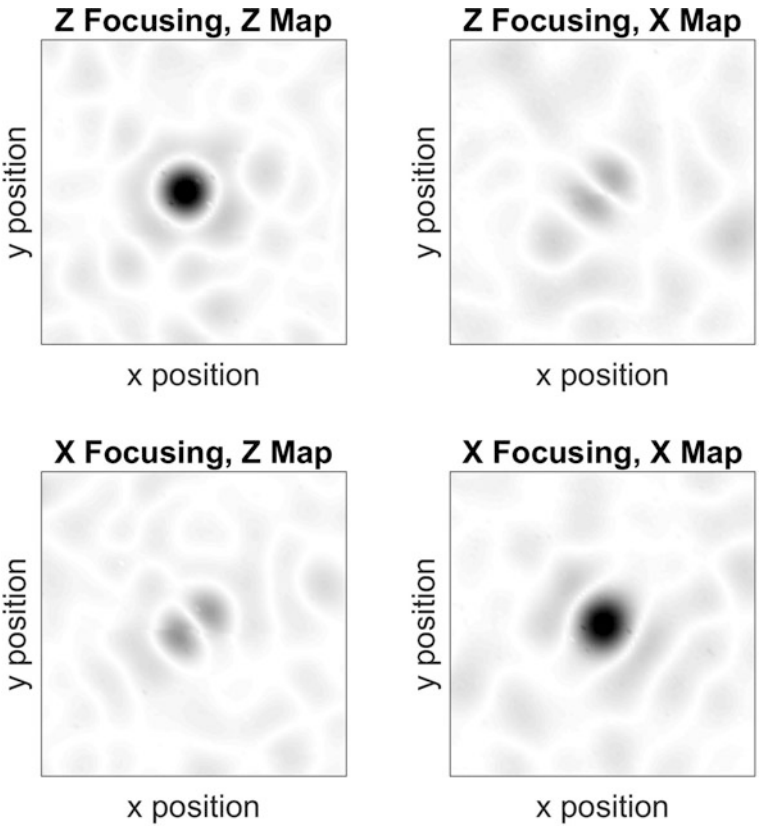

Fig. 14.19 Example spatial maps illustrating the time reversal focusing only in the direction in which the impulse response signal is detected during the forward step. These velocity amplitude maps were measured at the time of peak focusing. The first row displays the map of instantaneous motion in the two directions for out-of-plane focusing while the second row displays the map of instantaneous motion in the two directions for in-plane focusing. All color scales are equals on all images, with darker shades indicating higher amplitude

is used in the TR process, elastic waves will be mostly focused along the out-of-plane direction. Note that a fraction of the energy will also be visible in the in-plane directions due to the tensorial nature of elasticity (e.g., Poisson effect in an isotropic solid). However, the signals in the non-focused directions have such a small amplitude that they are not expected to interact significantly with the defect.

The ability of TR to image defect orientation was first tested in a sample of stainless steel with stress corrosion cracks [120, 121]. The sample and chosen system of coordinates for the analysis are shown in Fig. 14.20. A region was selected for the scan with TR being conducted at three orientations, x: in-plane normal to the crack line; y: in-plane in the direction of the crack line; and z: out-of-plane. TR was conducted successively in the x, y, and z directions. Results from these scans are

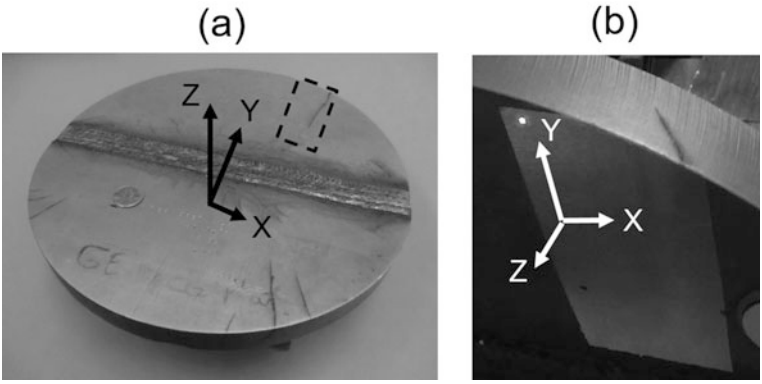

Fig. 14.20 Photographs of the sample used in the experiments to demonstrate the ability of TR to image defect orientation: (**a**) top view showing the presence of stress corrosion cracking near the weld area and outer boundaries, with the scan area displayed by a dashed line box, (**b**) side view showing an orientation of the crack of nearly 45° into the thickness of the sample

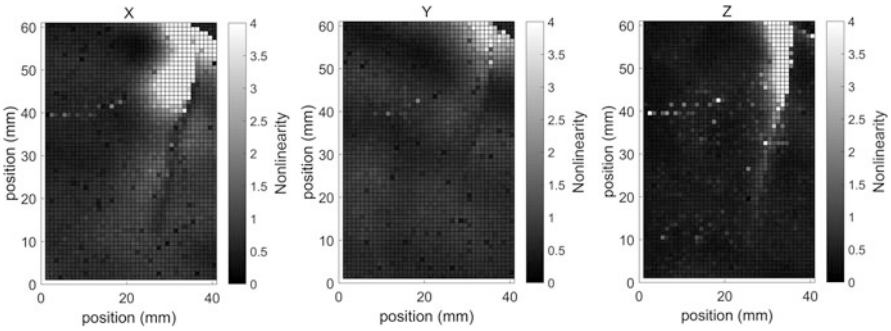

Fig. 14.21 Maps of nonlinearity obtained with TR in three orthogonal directions in the vicinity of the stress corrosion crack

displayed in Fig. 14.21. A strong nonlinear response (white contrast) is observed near the crack line in the *x*- and *z*-directions only. Since the normal to the crack surface is in the *x*–*z* plane, TR in these directions can induce a clapping mechanism. On the other hand, in the *y*-direction (along the crack line), TR tends to induce a friction mechanism, for which the nonlinear acoustic response is much weaker. For the same reason, if the crack was running perpendicular to the surface of the sample into the depth, we would observe little to no contrast by applying TR in the *z*-direction.

Another experiment conducted on a composite plate was reported recently by Le Bas et al. [27]. As a result of impact damage, the plate had two defects: a crack and a delamination. The two defects were located in the same region but had different orientations. The principle of time reversal could be used to image these two defects independently, as shown in Fig. 14.22. Other imaging techniques (e.g., X-ray, vibrothermography) show a similar extent of the defects but do not provide information about the orientation. The images shown in Fig. 14.22 were

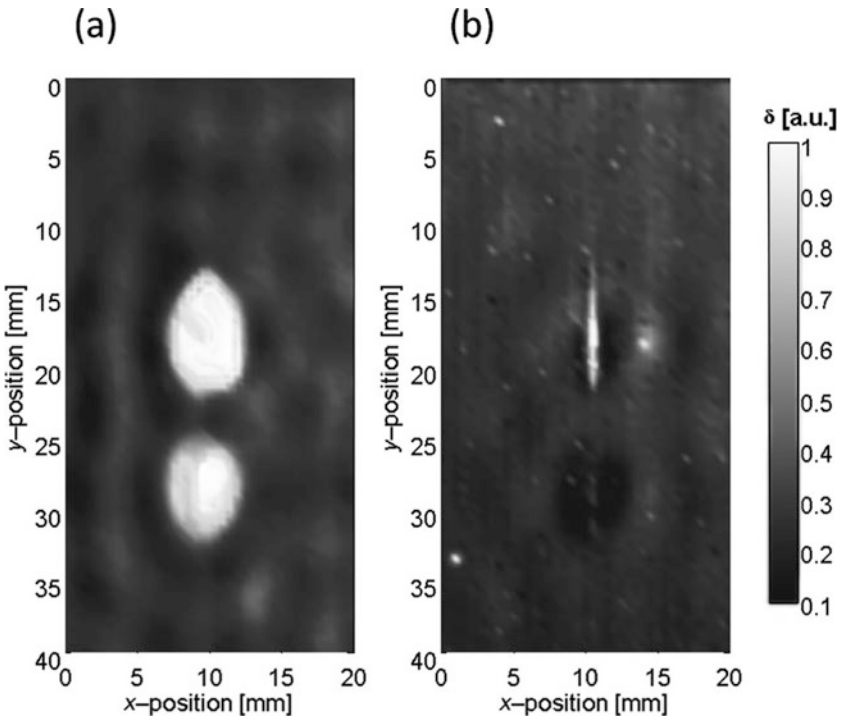

Fig. 14.22 Imaging of an impact damage in the composite plate with time reversal and linear post-processing. Images were obtained by focusing the (**a**) out-of-plane and (**b**) in-plane (along the x-direction) components of the particle velocity at each point of a scanning grid on the surface of the composite plate. The delamination (or crack) can be imaged when the out-of-plane (or in-plane) component of the velocity is used in the TR process

obtained using linear processing. Additional complementary images (not shown here) were also obtained using nonlinear processing. The nonlinear processing tends to illuminate the boundaries of the delaminations where a "sticky" contact exists whereas the center of the delamination generates a much smaller nonlinear response, possibly because the faces of the delamination are not in contact or very weakly so.

14.3 Conclusion

Time reversal may be used to focus energy remotely from a set of sources to any location on a sample where a receiver may be placed. This allows the surface of a sample to be interrogated with any number of sources at fixed positions and a mobile receiver, such as a laser vibrometer may be used to speed up the interrogation of a sample. The focused energy is large enough in amplitude and spatially confined such that localized regions of nonlinear elastic response may be excited and imaged. The

nonlinear signatures are indicative of various types of mechanical damage. Recent advances include the development of subsurface imaging of defects, 3D TR imaging in order to image the orientation of defects, and the development of a noncontact excitation source that can also be used to image defect orientation. The use of TR for NDE to image nonlinear defects may not be as rapid of a scanning process as traditional linear NDE techniques but it is far more sensitive to micro-cracking and allows imaging of the full extent of a crack and the crack's orientation.

Acknowledgements The authors wish to thank their various sources of funding over the years through the US Department of Energy. They also wish to thank Marci Harwood for helpful editing of the figures.

References

1. B.E. Anderson, M. Griffa, C. Larmat, T.J. Ulrich, P.A. Johnson, Time reversal. Acoust. Today **4**(1), 5–16 (2008)
2. A. Parvulescu, Signal detection in a multipath medium by M.E.S.S. processing. J. Acoust. Soc. Am. **33**(11), 1674 (1961)
3. A. Parvulescu, C.S. Clay, Reproducibility of signal transmission in the ocean. Radio Elec. Eng. **29**, 223–228 (1965)
4. I. Tolstoy, C.S. Clay, *Ocean Acoustics: Theory and Experiment in Underwater Sound* (Hudson Laboratories, Columbia Univerfsity, 1966, and reprinted by the Acoustical Society of America, 1987), pp. 241–266
5. C.S. Clay, B.E. Anderson, Matched signals: the beginnings of time reversal. Proc. Meet. Acoust. **12**, 055001 (2011)
6. B.E. Anderson, T.J. Ulrich, P.-Y. Le Bas, Comparison and visualization of the focusing wave fields of various time reversal techniques in elastic media. J. Acoust. Soc. Am. **134**(6), EL527–EL533 (2013)
7. S. Yon, M. Tanter, M. Fink, Sound focusing in rooms: the time-reversal approach. J. Acoust. Soc. Am. **113**(3), 1533–1543 (2003)
8. B.E. Anderson, R.A. Guyer, T.J. Ulrich, P.A. Johnson, Time reversal of continuous-wave, steady-state signals in elastic media. Appl. Phys. Lett. **94**(11), 111908 (2009)
9. M. Tanter, J.-L. Thomas, M. Fink, Time reversal and the inverse filter. J. Acoust. Soc. Am. **108**(1), 223–234 (2000)
10. M. Tanter, J.-F. Aubry, J. Gerber, J.-L. Thomas, M. Fink, Optimal focusing by spatio-temporal filter. I. Basic principles. J. Acoust. Soc. Am. **110**, 37–47 (2001)
11. T. Gallot, S. Catheline, P. Roux, M. Campillo, A passive inverse filter for Green's function retrieval. J. Acoust. Soc. Am. **131**(1), EL21–EL27 (2011)
12. T.J. Ulrich, B. Anderson, P.-Y. Le Bas, C. Payan, J. Douma, R. Snieder, Improving time reversal focusing through deconvolution: 20 questions. Proc. Meet. Acoust. XVII-ICNEM **16**, 045015 (2012)
13. B.E. Anderson, J. Douma, T.J. Ulrich, R. Snieder, Improving spatio-temporal focusing and source reconstruction through deconvolution. Wave Motion **52**(9), 151–159 (2015)
14. C. Heaton, B.E. Anderson, S.M. Young, Time reversal focusing of elastic waves in plates for educational demonstration purposes. J. Acoust. Soc. Am. **141**(2), 1084–1092 (2017)
15. G. Montaldo, D. Palacio, M. Tanter, M. Fink, Time reversal kaleidoscope: a smart transducer for three-dimensional ultrasonic imaging. Appl. Phys. Lett. **84**(19), 3879–3881 (2004)
16. O. Bou Matar, Y.F. Li, K. Van Den Abeele, On the use of a chaotic cavity transducer in nonlinear elastic imaging. Appl. Phys. Lett. **95**, 141913 (2009)

17. O. Bou Matar, Y. Li, S. Delrue, K. Van Den Abeele, Optimization of chaotic cavity transducers to nonlinear elastic imaging, in *Proceedings of the 10th French congress on acoustics*, Lyon (2010)
18. S. Delrue, K. Van Den Abeele, O. Bou Matar, Simulation study of a chaotic cavity transducer based virtual phased array used for focusing in the bulk of a solid material. Ultrasonics **67**, 151–159 (2016)
19. P.-Y. Le Bas, T.J. Ulrich, B.E. Anderson, J.J. Esplin, Toward a high power non-contact acoustic source using time reversal. Acoust. Soc. Am. ECHOES Newslett. **22**(3), 7–8 (2012)
20. S. Delrue, P.-Y. Le Bas, T.J. Ulrich, B.E. Anderson, K. Van Den Abeele, First simulations of the candy can concept for high amplitude non-contact excitation. Proc. Meet. Acoust. **16**, 045019 (2012)
21. B.E. Anderson, T.J. Ulrich, P.-Y. Le Bas, Improving the focal quality of the time reversal acoustic noncontact source using a deconvolution operation. Proc. Meet. Acoust. **19**, 065069 (2013)
22. P.-Y. Le Bas, T.J. Ulrich, B.E. Anderson, J.J. Esplin, A high amplitude, time reversal acoustic non-contact excitation (TRANCE). J. Acoust. Soc. Am. **134**(1), EL52–EL56 (2013)
23. S. Delrue, K. Van Den Abeele, P.-Y. Le Bas, T.J. Ulrich, B.E. Anderson, Simulations of a high amplitude air coupled source based on time reversal, in *Proceedings of the International Congress on Ultrasonics*, May 2–5 (2013), pp 591–596
24. M.C. Remillieux, B.E. Anderson, P.-Y. Le Bas, T.J. Ulrich, Improving the air coupling of bulk piezoelectric transducers with wedges of power-law profiles: a numerical study. Ultrasonics **54**(5), 1409–1416 (2014)
25. M.C. Remillieux, B.E. Anderson, T.J. Ulrich, P.-Y. Le Bas, M.R. Haberman, J. Zhu, Review of air-coupled transduction for nondestructive testing and evaluation. Acoust. Today **10**(3), 36–45 (2014)
26. B.E. Anderson, M.C. Remillieux, P.-Y. Le Bas, T.J. Ulrich, L. Pieczonka, Ultrasonic radiation from cubic-profile wedges: experimental results. Ultrasonics **63**, 141–146 (2015)
27. P.-Y. Le Bas, M.C. Remillieux, L. Pieczonka, J.A. Ten Cate, B.E. Anderson, T.J. Ulrich, Damage imaging in a laminated composite plate using an air-coupled time reversal mirror. Appl. Phys. Lett. **107**, 184102 (2015)
28. C. Prada, E. Kerbrat, D. Cassereau, M. Fink, Time reversal techniques in ultrasonic nondestructive testing of scattering media. Inv. Prob. **18**, 1761–1773 (2002)
29. C. Prada, M. Fink, Separation of interfering acoustic scattered signals using the invariant of the time-reversal operator. Application to Lamb waves characterization. J. Acoust. Soc. Am. **104**, 801–807 (1998)
30. E. Kerbrat, R.K. Ing, C. Prada, D. Cassereau, M. Fink, The DORT method applied to detection and imaging in plates using lamb waves, in *Review of Progress in Quantitative Nondestructive Evaluation, AIP Conference Proceedings*, pp 934–940 (2000)
31. E. Kerbrat, C. Prada, D. Cassereau, M. Fink, Ultrasonic nondestructive testing of scattering media using the decomposition of the time reversal operator. IEEE Trans. Ultrason. Ferroelectr. Freq. Control **49**, 1103–1113 (2002)
32. B.E. Anderson, M. Scalerandi, A.S. Gliozzi, M. Griffa, T.J. Ulrich, P.A. Johnson, Selective source reduction to identify masked smaller sources using time reversed acoustics (TRA), in *Review of Progress in Quantitative Nondestructive Evaluation, 27B, AIP Conference Proceedings,* pp 1520–1527 (2008)
33. M. Scalerandi, A.S. Gliozzi, B.E. Anderson, M. Griffa, P.A. Johnson, T.J. Ulrich, Selective source reduction to identify masked sources using time reversal acoustics. J. Phys. D. Appl. Phys. **41**, 155504 (2008)
34. B.E. Anderson, T.J. Ulrich, M. Griffa, P.-Y. Le Bas, M. Scalerandi, A.S. Gliozzi, P.A. Johnson, Experimentally identifying masked sources applying time reversal with the selective source reduction method. J. Appl. Phys. **105**(8), 083506 (2009)
35. C. Dorme, M. Fink, Focusing in transmit-receive mode through inhomogeneous media: the time reversal matched filter approach. J. Acoust. Soc. Am. **98**(2), 1155–1162 (1995)
36. M. Fink, Time-reversal acoustics. J. Phys. Conf. Ser. **118**(1), 012001–0120029 (2008)

37. B.E. Anderson, B. Moser, K.L. Gee, Loudspeaker line array educational demonstration. J. Acoust. Soc. Am. **131**(3), 2394–2400 (2012)
38. R.P. Porter, in *Generalized holography as a framework for solving inverse scattering and inverse source problems*, ed. by E. Wolf. Progress in Optics XXVII (Elsevier, New York, 1989)
39. H.P. Bucker, Use of calculated sound fields and matched-field detection to locate sound sources in shallow water. J. Acoust. Soc. Am. **59**(2), 368–373 (1976)
40. A.B. Baggeroer, W.A. Kuperman, H. Schmidt, Matched-field processing: source localization in correlated noise as an optimum parameter estimation problem. J. Acoust. Soc. Am. **83**(2), 571–587 (1988)
41. D.H. Chambers, J.V. Candy, S.K. Lehman, J.S. Kallman, A.J. Poggio, A.W. Meyer, Time reversal and the spatio-temporal matched filter (L). J. Acoust. Soc. Am. **116**(3), 1348–1350 (2004)
42. G. Turek, W.A. Kuperman, Applications of matched-field processing to structural vibration problems. J. Acoust. Soc. Am. **101**(3), 1430–1440 (1997)
43. E. Baysal, D. Kosloff, J.W.C. Sherwood, Reverse time migration. Geophysics **48**(11), 1514–1524 (1983)
44. W.-F. Chang, G.A. McMechan, Elastic reverse-time migration. Geophysics **52**(10), 1365–1375 (1987)
45. B.E. Anderson, M. Griffa, P.-Y. Le Bas, T.J. Ulrich, P.A. Johnson, Experimental implementation of reverse time migration for nondestructive evaluation applications. J. Acoust. Soc. Am. **129**(1), EL8–EL14 (2011)
46. M. Fink, Time reversed acoustics. Phys. Today **50**, 34–40 (1997)
47. I. Nunez, C. Negreira, Efficiency parameters in time reversal acoustics: applications to dispersive media and multimode wave propagation. J. Acoust. Soc. Am. **117**(3), 1202–1209 (2004)
48. K.B. Cunningham, M.F. Hamilton, A.P. Brysev, L.M. Krutyansky, Time-reversed sound beams of finite amplitude. J. Acoust. Soc. Am. **109**(6), 2668–2674 (2001)
49. M. Tanter, J.-L. Thomas, F. Coulouvrat, M. Fink, Breaking of time reversal invariance in nonlinear acoustics. Phys. Rev. E **64**, 016602 (2001)
50. C. Hedberg, Basics of nonlinear time reversal acoustics. AIP Conf Proc **1106**, 164–172 (2009)
51. B.E. Anderson, M. Clemens, M.L. Willardson, The effect of transducer directionality on time reversal focusing. J. Acoust. Soc. Am. **142**(1), EL95–El101 (2017)
52. M. Griffa, B.E. Anderson, R.A. Guyer, T.J. Ulrich, P.A. Johnson, Investigation of the robustness of Time Reversal Acoustics in solid media through the reconstruction of temporally symmetric sources. J. Phys. D. Appl. Phys. **41**(8), 085415 (2008)
53. M. Scalerandi, M. Griffa, P.A. Johnson, Robustness of computational time reversal imaging in media with elastic constant uncertainties. J. Appl. Phys. **106**(11), 114911 (2009)
54. J. de Rosny, G. Lerosey, A. Tourin, M. Fink, in *Time Reversal of Electromagnetic Waves*, ed. by H. Ammari. Modeling and Computations in Electromagnetics. Lecture Notes in Computational Science and Engineering, vol. 59 (Springer, Berlin, Heidelberg, 2008), pp. 187–202
55. B. Wu, W. Cai, M. Alrubaiee, M. Xu, S.K. Gayen, Time reversal optical tomography: locating targets in a highly scattering turbid medium. Optics Exp. **19**(22), 21956–21976 (2011)
56. O.S. Burdo, M.M. Dargeiko, Wave-field control in an acoustically inhomogeneous medium. Cybernet. Compu. Technol. **1**, 171–176 (1984)
57. O. Ikeda, An image reconstruction algorithm using phase conjugation for diffraction-limited imaging in an inhomogeneous medium. J. Acoust. Soc. Am. **85**(4), 1602–1606 (1989)
58. D.R. Jackson, D.R. Dowling, Phase conjugation in underwater acoustics. J. Acoust. Soc. Am. **89**(1), 171–181 (1991)
59. T. Shimura, Y. Watanabe, H. Ochi, H.C. Song, Long-range time reversal communication in deep water: experimental results. J. Acoust. Soc. Am. **132**(1), EL49–EL53 (2012)

60. B.E. Anderson, T.J. Ulrich, P.-Y. Le Bas, J.A. Ten Cate, Three-dimensional time reversal communications in elastic media. J. Acoust. Soc. Am. **139**(2), EL25–EL30 (2016)
61. C. Larmat, J.-P. Montagner, M. Fink, Y. Capdeville, A. Tourin, E. Clevede, Time-reversal imaging of seismic sources and applications to the great Sumatra earthquake. Geophys. Res. Lett. **33**(19), L19312 (2006)
62. C. Larmat, J. Tromp, Q. Liu, J.-P. Montagner, Time-reversal location of glacial earthquakes. J. Geophys. Res. **113**(B9), B09314 (2008)
63. C. Larmat, R.A. Guyer, P.A. Johnson, Tremor source location using time-reversal: selecting the appropriate imaging field. Geophys. Res. Lett. **36**(22), L22304 (2009)
64. C.S. Larmat, R.A. Guyer, P.A. Johnson, Time-reversal methods in geophysics. Phys. Today **63**(8), 31–35 (2010)
65. R.K. Ing, N. Quieffin, In solid localization of finger impacts using acoustic time-reversal process. Appl. Phys. Lett. **87**(20), 204104 (2005)
66. D. Vigoureux, J.-L. Guyader, A simplified time reversal method used to localize vibrations sources in a complex structure. Appl. Acoust. **73**(5), 491–496 (2012)
67. I. Rakotoarisoa, J. Fischer, V. Valeau, D. Marx, C. Prax, L.-E. Brizzi, Time-domain delay-and-sum beamforming for time-reversal detection of intermittent acoustic sources in flows. J. Acoust. Soc. Am. **136**(5), 2675–2686 (2014)
68. A. Mimani, Z. Prime, C.J. Doolan, P.R. Medwell, A sponge-layer damping technique for aeroacoustic time-reversal. J. Sound Vib. **342**, 124–151 (2015)
69. A. Mimani, Z. Prime, D.J. Moreau, C.J. Doolan, An experimental application of aeroacoustic time-reversal to the Aeolian tone. J. Acoust. Soc. Am. **139**(2), 740–763 (2016)
70. D.G. Albert, L. Liu, M.L. Moran, Time reversal processing for source location in an urban environment (L). J. Acoust. Soc. Am. **118**(2), 616–619 (2005)
71. S. Cheinet, L. Ehrhardt, T. Broglin, Impulse source localization in an urban environment: time reversal versus time matching. J. Acoust. Soc. Am. **139**(1), 128–140 (2016)
72. A.O. Maksimov, Y.A. Polovinka, Time reversal technique for gas leakage detection. J. Acoust. Soc. Am. **137**(4), 2168–2179 (2015)
73. B.E. Anderson, M. Griffa, T.J. Ulrich, P.A. Johnson, Time reversal reconstruction of finite sized sources in elastic media. J. Acoust. Soc. Am. **130**(4), EL219–EL225 (2011)
74. M. Fink, G. Montaldo, M. Tanter, Time-reversal acoustics in biomedical engineering. Annu. Rev. Biomed. Eng. **5**, 465–497 (2003)
75. M.L. Willardson, B.E. Anderson, S.M. Young, M.H. Denison, P.D. Patchett, Time reversal focusing of high amplitude sound in a reverberation chamber. J. Acoust. Soc. Am. **143**(2), 696–705 (2018)
76. B.E. Anderson, M. Griffa, T.J. Ulrich, P.-Y. Le Bas, R.A. Guyer, P.A. Johnson, *Crack localization and Characterization in Solid Media Using Time Reversal Techniques* (American Rock Mechanics Association, 2010), pp. 10–154
77. J.-L. Thomas, F. Wu, M.M. Fink, Time reversal mirror applied to litotripsy. Ultrason. Imaging **18**, 106–121 (1996)
78. J.-L. Thomas, M. Fink, Ultrasonic beam focusing through tissue inhomogeneities with a time reversal mirror: application to transskull therapy. IEEE Trans. Ultrason. Ferroelect. Freq. Contr. **43**(6), 1122–1129 (1996)
79. M. Tanter, J.-L. Thomas, M. Fink, Focusing and steering through absorbing and aberating layers: application to ultrasonic propagation through the skull. J. Acoust. Soc. Am. **103**(5), 2403–2410 (1998)
80. G. Montaldo, P. Roux, A. Derode, C. Negreira, M. Fink, Ultrasound shock wave generator with one-bit time reversal in a dispersive medium, application to lithotripsy. Appl. Phys. Lett. **80**(5), 87–89 (2002)
81. S. Dos Santos, Z. Prevorovsky, Imaging of human tooth using ultrasound based chirp-coded nonlinear time reversal acoustics. Ultrasonics **51**(6), 667–674 (2011)
82. N. Chakroun, M. Fink, F. Wu, Ultrasonic non destructive testing with time reversal mirrors, in *Proceedings IEEE Ultrasonics Symposium*, Tucson, vol. 2 (1992), pp. 809–814

83. N. Chakroun, M. Fink, F. Wu, Time reversal processing in ultrasonic nondestructive testing. IEEE Trans. Ultrason. Ferroelectr. Freq. Control **42**, 1087–1098 (1995)
84. V. Miette, L. Sandrin, F. Wu, M. Fink, Optimisation of Time Reversal Processing in Titanium Inspections, in *IEEE Ultrasonics Symposium Proceedings* (1996) pp. 643–647
85. R.K. Ing, M. Fink, Time Recompression of Dispersive Lamb Wave Using A Time Reversal Mirror. Applications to Flaw Detection in Thin Plates, in *IEEE Ultrasonics Symposium Proceedings*, San Antonio, USA, Nov. 1996, pp 659–664 (1996)
86. T.J. Ulrich, P.A. Johnson, A. Sutin, Imaging nonlinear scatterers applying the time reversal mirror. J. Acoust. Soc. Am. **119**(3), 1514–1518 (2006)
87. T.J. Ulrich, P.A. Johnson, R.A. Guyer, Interaction dynamics of elastic waves with a complex nonlinear scatterer through the use of a time reversal mirror. Phys. Rev. Lett. **98**, 104301 (2007)
88. G. Zumpano, M. Meo, A new nonlinear elastic time reversal acoustic method for the identification and localisation of stress corrosion cracking in welded plate-like structures–a simulation study. Int. J. Solids Struct. **44**(11), 3666–3684 (2007)
89. B.E. Anderson, L. Pieczonka, M.C. Remillieux, T.J. Ulrich, P.-Y. Le Bas, Stress corrosion crack depth investigation using the time reversed elastic nonlinearity diagnostic. J. Acoust. Soc. Am. **141**(1), EL76–EL81 (2017)
90. T.J. Ulrich, A.M. Sutin, T. Claytor, P. Papin, P.-Y. Le Bas, J.A. TenCate, The time reversed elastic nonlinearity diagnostic applied to evaluation of diffusion bonds. Appl. Phys. Lett. **93**(15), 151914 (2008)
91. P.-Y. Le Bas, T.J. Ulrich, B.E. Anderson, R.A. Guyer, P.A. Johnson, Probing the interior of a solid volume with time reversal and nonlinear elastic wave spectroscopy. J. Acoust. Soc. Am. **130**(4), EL258–EL263 (2011)
92. C. Draeger, D. Cassereau, M. Fink, Theory of the time-reversal process in solids. J. Acoust. Soc. Amer. **102**(3), 1289–1295 (1998)
93. C. Draeger, J.-C. Aime, M. Fink, One-channel time-reversal in chaotic cavities: experimental results. J. Acoust. Soc. Am. **105**(2), 618–625 (1999)
94. R. Guyer, Nonlinear Tomography and Time Reversed Acoustics, in *Presented at the 6th International Workshop on Nonlinear Elasticity in Materials*, Leuven, Belgium, 2001
95. P.P. Delsanto, P.A. Johnson, M. Scalerandi, J.A. TenCate, LISA simulations of time-reversed acoustic and elastic wave experiments. J. Phys. D. Appl. Phys. **35**(23), 3145–3152 (2002)
96. A. Sutin, P. Johnson, J. TenCate, Development of nonlinear time reverse acoustics (NLTRA) for application to crack detection in solids, in *Proceedings of the 5th World Congress on Ultrasonics*, Paris, France, pp. 121–124 (2003)
97. A.M. Sutin, J.A. TenCate, P.A. Johnson, Single-channel time reversal in elastic solids. J. Acoust. Soc. Am. **116**(5), 2779–2784 (2004)
98. O. Bou Matar, S. Dos Santos, J. Fortineau, T. Goursolle, L. Haumesser, F. Vander Meulen, Pseudo Spectral Simulations of Elastic Waves Propagation in Heterogeneous Nonlinear Hysteretic Medium, in *Proceedings of the 17th International Symposium on Nonlinear Acoustics*, State College, PA, pp. 95–98 (2005)
99. Y. Zheng, R.G. Maev, I.Y. Solodov, Nonlinear acoustic applications for material characterization: a review. Can. J. Phys. **77**(12), 927–967 (2000)
100. P. Nagy, Fatigue damage assessment by nonlinear ultrasonic materials characterization. Ultrasonics **36**(1–5), 375–381 (1998)
101. P.A. Johnson, The new wave in acoustic testing. Mat. World **7**, 544–546 (1999)
102. I.Y. Solodov, B.A. Korshak, Instability, chaos, and "memory" in acoustic-wave-crack interaction. Phys. Rev. Lett. **81**(1), 014303 (2001)
103. I.Y. Solodov, N. Krohn, G. Busse, CAN: an example of nonclassical acoustic nonlinearity in solids. Ultrasonics **40**(1), 621–625 (2002)
104. I. Solodov, J. Wackerl, K. Pfleiderer, G. Busse, Nonlinear self-modulation and subharmonic acoustic spectroscopy for damage detection and location. Appl. Phys. Lett. **84**(26), 5386–5388 (2004)

105. S. Delrue, K. Van Den Abeele, Three-dimensional finite element simulation of closed delaminations in composite materials. Ultrasonics **52**(2), 315–324 (2012)
106. P. Blanloeuil, A. Meziane, C. Bacon, Numerical study of nonlinear interaction between a crack and elastic waves under an oblique incidence. Wave Motion **51**(3), 425–437 (2014)
107. T.J. Ulrich, B.E. Anderson, M.C. Remillieux, P.Y. Le Bas, L. Pieczonka, in *Application of Nonlinear Ultrasonics to Inspection of Stainless Steel for Dry Storage*. Tech. rep. LA-UR-15-27382, Los Alamos National Laboratory (LANL), 2015
108. K. Kimoto, Y. Ichikawa, A finite difference method for elastic wave scattering by a planar crack with contacting faces. Wave Motion **52**, 120–137 (2015)
109. T. Goursolle, S. Dos Santos, O. Bou Matar, S. Calle, Non-linear based time reversal acoustic applied to crack detection: simulations and experiments. Int. J. of Nonlinear Mech. **43**(3), 170–177 (2008)
110. P. Blanloeuil, L.R.F. Rose, J.A. Guinto, M. Veidt, C.H. Wang, Closed crack imaging using time reversal method based on fundamental and second harmonic scattering. Wave Motion **66**, 156–176 (2016)
111. S. Krishnan, M. O'Donnell, Transmit aperture processing for nonlinear contrast agent imaging. Ultrason. Imaging **18**(2), 77–105 (1996)
112. A. Sutin, B. Libbey, V. Kurtenoks, D. Fenneman, A. Sarvazyan, Nonlinear detection of land mines using wide bandwidth time-reversal techniques. Proc. SPIE **6217**, 398–409 (2006)
113. F. Ciampa, M. Meo, Nonlinear elastic imaging using reciprocal time reversal and third order symmetry analysis. J. Acoust. Soc. Am. **131**(6), 4316–4323 (2012)
114. M. Scalerandi, A.S. Gliozzi, C.L.E. Bruno, D. Masera, P. Bocca, A scaling method to enhance detection of a nonlinear elastic response. Appl. Phys. Lett. **92**(10), 101912 (2008)
115. M. Scalerandi, A.S. Gliozzi, C.L.E. Bruno, K. Van Den Abeele, Nonlinear acoustic time reversal imaging using the scaling subtraction method. J. Physics D: Appl. Phys. **41**(21), 215404 (2008)
116. C. Payan, T.J. Ulrich, P.Y. Le Bas, M. Griffa, P. Schuetz, M.C. Remillieux, T.A. Saleh, Probing material nonlinearity at various depths by time reversal mirrors. Appl. Phys. Lett. **104**(14), 144102 (2014)
117. M.C. Remillieux, B.E. Anderson, T.J. Ulrich, P.-Y. Le Bas, C. Payan, Depth profile of a time-reversal focus in an elastic solid. Ultrasonics **58**, 60–66 (2015)
118. T.J. Ulrich, K. Van Den Abeele, P.-Y. Le Bas, M. Griffa, B.E. Anderson, R.A. Guyer, Three component time reversal: focusing vector components using a scalar source. J. Appl. Phys. **106**(11), 113504 (2009)
119. K. Van Den Abeele, T.J. Ulrich, P.-Y. Le Bas, M. Griffa, B.E. Anderson, R.A. Guyer, Vector component focusing in elastic solids using a scalar source in three component time reversal. Phys. Procedia **3**(1), 685–689 (2010)
120. B.E. Anderson, T.J. Ulrich, P.-Y. Le Bas, Imaging crack orientation using the time reversed elastic nonlinearity diagnostic with three component time reversal. J. Acoust. Soc. Am. **133**(5), 3562 (2013)
121. M.C. Remillieux, P.-Y. Le Bas, L. Pieczonka, B.E. Anderson, T.J. Ulrich, Estimating the penetration depth and orientation of stress corrosion cracks using time-reversal acoustics. Trans. Am. Nuclear Soc. **115**, 217–220 (2016)

Chapter 15
Nonlocal and Coda Wave Quantification of Damage Precursors in Composite from Nonlinear Ultrasonic Response

Sourav Banerjee and Subir Patra

Materials state awareness using conventional nondestructive evaluation (NDE) at the early stage of service life is extremely challenging because of the inherent material nonlinearity that initiates at the lower scales. Conventional NDE methods are limited by reporting location, size, and shape of the material discontinuities, e.g., cracks, voids, delamination, etc. In the past, several nonlinear ultrasonic methods are developed to detect the small discrete damages, whereas quantification of degraded material properties and detection of embryonic precursor damage in materials is currently challenging. Understanding the early stage of precursor damages using ultrasonic method inherently is to understand the material nonlinearity that arise from the bottom-up scales, which further requires to evaluate the ultrasonic signals with subtle nonlinearity in an innovative way that are essentially ignored in conventional ultrasonic NDE methods. Hence, in this chapter, it is hypothesized that such nonlinear effects at the early stage of damage at the lower scale are actually sensed by the ultrasonic NDE probes/sensors and hidden in the ultrasonic signals. Such hidden features are required to be extracted from the signals using innovative signal analysis method integrated with the microcontinuum physics. In this chapter defying the conventional nonlinear ultrasonic techniques, a newly formulated nonlocal approach is presented to quantify the damage precursor in materials at its early stage of the service life. Nonlocal parameter that carries information from the lower scale has a nonlinear dependency on the ultrasonic wave velocity at any particular frequency, which is assumed to be a constant in linear ultrasonics and no information could be extracted. Here, it should be noted that the nonlinear function of nonlocal parameter from a material that can be extracted from the material degradation state is not necessarily associated with the

S. Banerjee (✉) · S. Patra
Integrated Material Assessment and Predictive Simulation Laboratory (i-MAPS), Department of Mechanical Engineering, University of South Carolina, Columbia, SC, USA
e-mail: banerjes@cec.sc.edu

T. Kundu (ed.), *Nonlinear Ultrasonic and Vibro-Acoustical Techniques for Nondestructive Evaluation*, https://doi.org/10.1007/978-3-319-94476-0_15

material discontinuities like cracks or delamination at the macroscale but due to distributed nonlocal effect of lower scale defects and damages. Thus, a new term called nonlocal damage entropy (NLDE) was coined by the authors in their recent publications to quantify the multiscale damage state in materials while exploiting the high-frequency ultrasonic ($\geq$10 MHz) with microcontinuum field theory. In this chapter, first, a review of different "bottom-up" multiscale modeling approaches is discussed followed by the need of a "top-down" precursor quantification method is justified. Further, a review of the existing methods for quantifying damage precursor is presented followed by a mathematical and experimental derivation of NLDE is presented. To justify the findings with additional information from different scales, low-frequency ($\leq$500 kHz) Guided wave ultrasonic NDE was performed. It is further hypothesized that the lower frequency ultrasonic guided wave signal that carries the nonlinear effect from the lower scale is essentially manifested but can only be extracted from the coda part of the signals and thus in this chapter the coda part of the signals were analyzed. Frequency transformation of the signals could result very low and almost undetectable higher harmonics due to the very early stage of damage and may not be useful for precursor quantification. Hence, a time domain analysis is required to find this information on the nonlinearity that could be manifested but are buried deep inside the signal. Thus, Guided coda wave interferometry (CWI) for composite is formulated for the first time using high-speed Taylor series expansion method. Precursor damage index is then formulated to quantify the damage state. Precursor damage index from Guided CWI and high-frequency NLDE are then correlated to evaluate the equivalency of information. To prove the positive indication of precursor damage from the newly coined NLDE, a set of benchmark studied are presented using optical microscopy and scanning electron microscopy (SEM). As metallic structures are well studied by many researchers, in this chapter the example study of precursor damage is restricted to the composite specimens under fatigue.

15.1 Introduction

Structure-specific diagnostic and prognostic has become extremely important due to noticeable variances in real-life performance of the materials. Different batch of materials, batch of manufacturing, assembly, flight history, operational conditions, structures operating at various regimes, maintenance portfolios, etc. cause the variances in materials performance. Thus, structures, structural components, engine components, and power components will need individual attention in the near future. Parallel database must be maintained for each component containing the detailed fleet record, maintenance records, nondestructive test results, real-time sensory data, etc. for online digital certification. Digital certification has become an important and necessary step for composite materials.

Carbon fiber composites are widely used as structural material for aerospace and other mechanical, biomedical applications due to their superior properties over metals, like higher specific strength, higher specific modulus, etc. [1]. These superior material properties are engineered by design based on respective structural

requirements. In composites, after an initial reduction, the global stiffness of the material remains the same for major fraction of its lifespan, while damage incubates in a distributed fashion. We call it embryonic precursor damage state of composite which goes unnoticed, but gradually grows, only to compromise the remaining strength of the composite near the end of its life span. Therefore, with increasing demand [2, 3], routine maintenance of these composite parts received greater attention in the past two decades. The cost of maintenance [4] was proposed to be minimized by incorporating efficient condition-based maintenance(CBM^+) system which further required implementation of advanced structural health monitoring (SHM) and/or online NDE [4, 5] of composites.

Unfortunately, early detection and quantification of embryonic precursor damage is currently challenging due to lack of feasible reliable methods. Typical precursor damage in the composite develops in the form of matrix cracking, microcracks, voids, micro-buckling, local fiber breakage, local fiber-matrix deboning, etc. It is realized that the conventional ultrasonic Guided wave-based SHM (~100 KHz to ~500 KHz) is not sensitive to these precursor damages, often demands sophisticated off-line characterization employing advanced statistical signal processing, which further results in heavy computational burden. Guided wave signals carrying fundamental Guided wave modes, for example, symmetric S_0, and, antisymmetric A_0 Lamb wave modes that are predominantly analyzed for damage detection, are not sensitive enough [8, 9] to find the onset of embryonic damage in the materials. Structure made of composites are designed to experience extreme environments during its operation, therefore material state awareness for the structure is extremely important to improve the life management plan. Damage precursor in composites, like micro-cracks, fiber breakages, and crazing, starts to occur during the first 30% of the life span of the structure as shown in Fig. 15.1a. Current SHM and online NDE systems can only detect damages when 80–90% of the composite life is

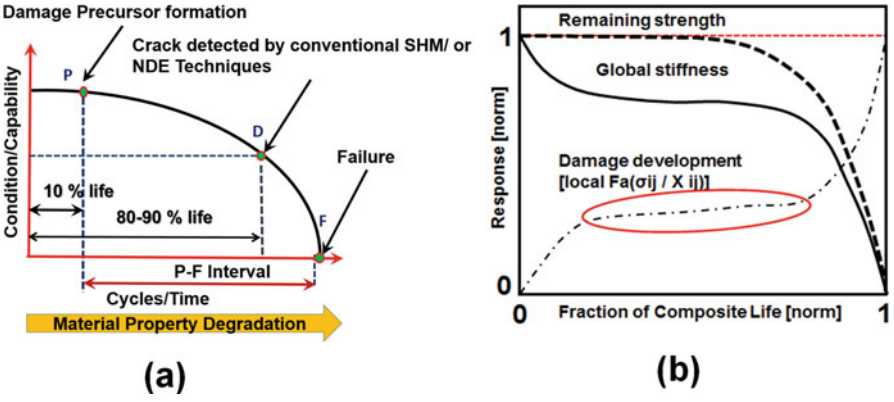

Fig. 15.1 (**a**) Condition monitoring of composite structure [4, 6] shows the P point when the early detection should be started, and (**b**) fatigue damage evolution in composite material [7] shows no change in global stiffness for a prolonged period of time when the incubation of embryonic damage precursor is underway

over. During the evolution of the fatigue damages, the interaction between the local damages in the materials and the global damage in the structure (during the 80–90% of the life span) is very rapid (Fig. 15.1b), and leads to catastrophic failure. So, it is argued that to avoid impeding failure of the structure, it is important to detect material damages as early as possible (∼during the first 30% of the life span of composites). Maintenance cost could be decreased significantly by avoiding unnecessary maintenance need. Thus, over the last few decades, many researchers attempted to address this problem with similar philosophy stated above. To secure the future of composites in structural applications, a reliable digital certification process for composites is a key step and is appropriately identified by the DoD and NASA [10, 11]. It is expected that the predictive failure models would be integrated with the "digital-twin" [10] software (identical twin of a real structure operates, virtually) where nondestructive evaluation (NDE) data will be integrated with predictive models as a feedback loop. It is conceptualized that the composites will be certified using digital failure prediction models based on its operational state.

15.1.1 Bottom-Up Multiscale Predictive Failure Models

Historically, the obvious route to understand the material behavior and unlock the secret of precursor damage is the "bottom-up" modeling approach. In this category, the damage modeling in composites can be broadly divided into four approaches:

- Failure criteria approach [12–27],
- Fracture mechanics approach [28–35],
- Plasticity approach [36–38],
- Damage mechanics approach [39–52].

The precursor damage is progressive in nature and thus, the damage mechanics approach is more suitable over the other approaches [53] in progressive failure models. Distributed damage may range from accumulated plastic strain, localization of voids, matrix cracking, fiber-matrix debonding, shearing to local fiber breakage, and interlaminar shear, etc. In the damage mechanics-based approach, damage variables are used to degrade material properties [40, 54]. Failure mechanisms are introduced by relating the damage variable to the strain energy release rate. Damage development and plasticity development laws depend on a few criteria and the parameters depend on material characteristics which are heuristically measured from specimen load test or are assumed. In spite of having significant advancements in the past decade [39–52], this current approach predicts uncertain behavior [53, 55], means that it reveals only a part of the story, thus, the criteria are still incomplete. As described to this date, the precursor to damage state evaluation in composites predominantly relies (theoretically) on "bottom-up" multiscale material models [56–65] utilizing multiple failure criteria. On the other side, ultrasonic sensing (NDE) methods [66–75] and/or digital image correlation (DIC) [76–78] methods are used to understand the material state, experimentally. Many multiscale

FEM and mesh less methods [79–81] are proposed with various modifications [82] but still the prediction remains uncertain. However, the possibility of having new multiscale observables in a "top-down" sense was not explored which could have reduced the uncertainty in the prediction. There has been a persistent disconnect between the sensing and modeling efforts.

Currently, it is required to design the composite structures with no growth criterion for explicit damage morphologies. And, that has become the shortcoming in the composite damage progression model because the existing NDE methods are not well equipped to provide certain parameter of interest, for example, degraded anisotropic material properties of damage variables. Although we have long way to go, it is identified that a significant opportunity exists to introduce a new multiscale process for precursor to damage quantification using a new method as presented in this chapter.

15.1.2 Unifying Bottom-Up and Top-Down Approaches

In material diagnostics, the "bottom-up" approach results in increasing uncertainty at the larger length and time scales as shown in Fig. 15.2. Diameter of the funnels at different scales is representative of the quantity of information that can be

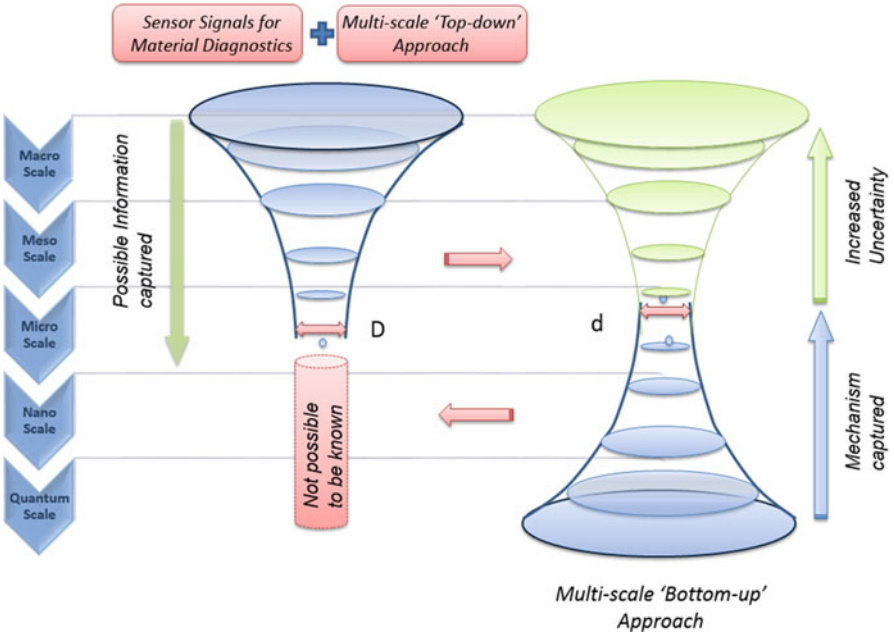

Fig. 15.2 A conceptual view of "bottom-up" and "top-down" approach

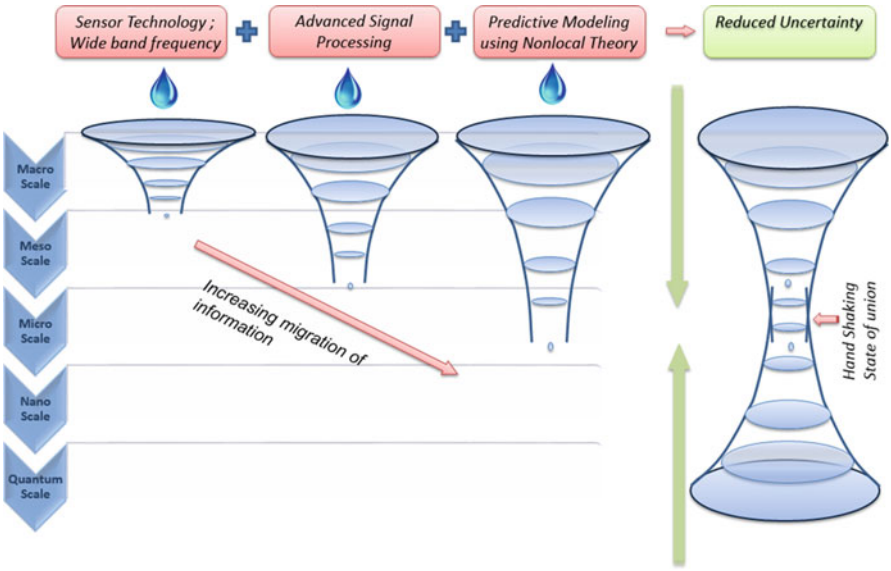

Fig. 15.3 Combining high-frequency ultrasonic, advanced signal and image processing, predictive modeling results state of union, reduced uncertainty

propagated to the subsequent length and time scales. It can be seen that using the "bottom-up" approach, most of the information can be lost through homogenization and could increase the uncertainties in the macroscale NDE sensor signals when simulated. On the other hand, it is possible to obtain information at multiple length scales by carefully selecting high-frequency ultrasonic methods, advanced signal processing methods, and unique predictive physics, which essentially conform a "top-down" approach. As shown in Figs. 15.2 and 15.3, it is not possible to extract information beyond certain length scales using any "top-down" approach. But, one could formulate a hybrid technique by fusing the "bottom-up" and "top-down" approaches by judicially selecting their respective advantages.

It is proposed to bring the modeling and ultrasonic sensing efforts under one unified umbrella. The most popular, "top-down" approaches in the multiscale mechanics that utilize the nonlocal behavior are peridynamic theory [83], and micromorphic theory [84–89]. They are actually the byproduct of many microcontinuum theories such as the microstructure theory [90], micropolar theory [85], coupled stress theory [91], Cosserat theory [92], etc. It has been found [93] that the newly devised quantitative ultrasonic image correlation (QUIC) is best compatible with the microcontinuum "top-down" approaches.

In QUIC, it is proposed to use high-frequency ($\geq$10 MHz) ultrasonic NDE method for this union. To quantify damages in a structure, conventionally, the signal decay, signal delay, amplitude changes, phase shifts, etc. are the predominant features that are extracted from the signals from low-frequency ($\leq$5 MHz) ultrasonic

NDE methods. However, contribution of the precursor damages to these features might be insignificant or undetectable, whereas these features from high-frequency ($\geq$25 MHz) ultrasonic NDE could be resonated if judicially transformed into new features that are entangled with microcontinuum mechanics. Nonlocal mechanics [89] have been greatly studied for material analysis, but as mentioned before there has been a persistent disconnect between the sensing and modeling efforts. To devise QUIC, high-frequency acoustic microscopy [94], which was previously used for quantifying residual stress [95] and determining the local mechanical properties [96–98] is used. Wave signals are analyzed in the context of nonlocal mechanics. QUIC utilizes the ultrasonic data from a bulk experiment in the top-down sense, and thus reduces the uncertainty in the prediction, unlike top-down models.

15.2 Theoretical Development for Quantitative Ultrasonic Image Correlation: High-Frequency Method

Quantifying the embryonic precursor damages in composite, by employing nonlocal continuum approach, was earlier proposed by Banerjee et al. [99]. In precursor damage state of materials, it is assumed that there exists a unique state where long-range forces influence the high-frequency wave propagation. At that state, the standard constitutive laws break down and the nonlocal process takes over. A suitable kernel function can be used to modify the constitutive law. Christofell's equation is then modified using the nonlocal constitutive law and the Eigenvalue problem is solved to obtain the dispersion curves for different wave modes (quasi-longitudinal, quasi-shear) and nonlocal parameters. Nonlocal parameters are calculated to quantify the microscale damaged from the macroscale signals. Experimentally measured wave velocity can be used to calculate the nonlocal parameters from the dispersion curves. Parametric variation of the nonlocal parameters can be used for damage quantification process. A detail discussion on this technique for damage state quantification can be found in the references [100–102]. In the following sections, the fundamental equations required for the QUIC method are discussed in detail.

15.2.1 Nonlocal Approach and Micromorphic Kernel Function

According to continuum mechanic, the fundamental balance laws are valid at a discrete point in the body, independently, without considering the influence of neighboring points. However, in micromorphic theory [84–89], this concept is argued, and says that the balance laws will be applicable for the entire body but locally invalid. This is expected if the long-range forces are effective. This means that a material point in a body is affected by the neighboring points mutually. These effects can be restricted within a certain zone around the material point or

can be spanned over the entire body. Diameters of such influence zone around a particle are conceptually similar to the concept of "horizon" in peridynamic theory [103–107]. This particular assumption is the basis for multiscale precursor damage quantification process using high-frequency ultrasonic. In case of high-frequency wave propagation, it is assumed that the deformable material particles cannot respond independently, but have to respond as a union. The response of a material point under external loading is a function of mutual interactions between neighboring material points with decaying effect at larger distance.

Experimental characterization of materials helped understanding the material responses obtained at variable length scales. Such responses could provide guidelines for the assumption of suitable material-dependent micromorphic (nonlocal) kernel function. Like the influence zone around a material particle, the material particle must have an influence function centered at that material point. Besides material characterization processes, ab initio dynamics studies [57] could also computationally calculate such influence functions or the kernel functions. After finding an influence function, a mathematical expression for that function can be devised and a unique operator can be found for the nonlocal kernel function. The kernel functions can be assumed as a Green's function in L^2 space [108]. Micromorphic approach includes the effect of long-range interatomic forces and can be used as a continuum model of the atomic lattice dynamics. Lattices are the periodic structure. Periodicity exists both in direct lattice and reciprocal lattice systems. In composites, we consider that at least the periodicity exists at the fiber dimension and periodicity exists between the layers. Thus, high-frequency ultrasonic waves are affected by the periodicity. Wave vectors in reciprocal lattice are the wave propagation vectors in direct lattice of the fiber dimension. Therefore, the wave frequency is a periodic function of the wave vectors in reciprocal lattice of wave number. According to the micromorphic description of material, materials are a cluster of deformable particles [6]. Here, it is assumed that a layer of composite is cluster of fibers in one direction. The deformable fibers have 9 degrees of freedom. Their external motion can create acoustic phonons but the internal deformation creates the optical phonons. With QUIC or any other ultrasonic method, it is not possible to gauge the optical phonons and hence, ultrasonic method is restricted to first acoustic branch. So, within the first Brillouin zone [109], our interest is restricted to the acoustic branch of the dispersion curves in the periodic material that consists of fibers, locally. Let us assume a position vector of a point in the fiber lattice $\overline{R} = a_1\widehat{e}_1 + a_2\widehat{e}_2 + a_3\widehat{e}_3$ where, $\widehat{e}_1, \widehat{e}_2$, and $\widehat{e}_3$ are the basis vectors for the lattice. The wave potential can be written as $\phi = A \exp\{i(\mathbf{k}.\ \mathbf{a} - \omega t)\}$. The function ϕ is periodic in $\overrightarrow{k} = k_1\widehat{b}_1 + k_2\widehat{b}_2 + k_3\widehat{b}_3$, where $\overrightarrow{k}$ is the wave vector. $\overrightarrow{k}$ wave vector is the reciprocal lattice of the special lattice. $\widehat{b}_1, \widehat{b}_2, \widehat{b}_3$ are the eigenvectors of the reciprocal system. There is an explicit relation between lattice vectors in reciprocal and direct lattices $\left(\widehat{e}_i \cdot \widehat{b}_k\right) = \delta_{ik}$, the Kronecker δ. Similar potential can be written for a wave vector $\overrightarrow{k}' = \overrightarrow{k} + \overrightarrow{g}$, where $\overrightarrow{g}$ is the translation vector $\left(\overrightarrow{g} = \xi_1\widehat{b}_1 + \xi_2\widehat{b}_2 + \xi_3\widehat{b}_3\right)$. The frequency ($\omega$) and wave vector $\mathbf{k}$ follow a periodic lattice scale relationship [109]. At the boundaries of the Brillouin zones

and specifically at the boundaries of the first Brillouin zone, the relation between the frequency (ω) and wave vector $\mathbf{k}$ must be satisfied. A functional relationship [108, 110, 111] presented by Born–Von Kármán is approximated at fiber scale and can be viz.

$$\frac{\omega_i(\mathbf{k})}{c_i|\mathbf{k}|} = \frac{1}{\left\{1+\varepsilon^2|\mathbf{k}|+\lambda^4|\mathbf{k}|^2\right\}} \tag{15.1}$$

where the problem of satisfying the boundary conditions at the Brillouin zones is avoided. Let $\varepsilon = \tau_0\ell$ and $\lambda = \nu_0\ell$ be the intrinsic length scale factors, and ℓ be the length scale, e.g., lattice dimension, the periodicity of fibers in composite. τ_0 and ν_0 are nonlocal parameters assumed to take values between 0 and 1. Lazar et al. [108], proposed a bi-Helmholtz-type operator L and can be viz.

$$L = \left(1+\tau_0{}^2\ell^2\nabla^2+\nu_0{}^4\ell^4\nabla^4\right) \tag{15.2}$$

where ∇^2 is a Laplace operator. Using the above operator, the suitable kernel function κ (which is a Green's function) can be written as

$$L\kappa = \delta(\mathbf{x}) \tag{15.3}$$

A specific length scale that is most influential was not identified. It has been foreseen that the governing length scale parameter is problem dependent. In this chapter, the influential length scale is identified for composite as fiber periodicity. The similar process can be used for identifying the governing intrinsic length scale for other similar problems.

15.2.2 Fundamental Equation of Motion with Nonlocal Parameters

As discussed in Chap. 1, let us consider a body Ω in a three-dimensional Cartesian coordinate system with boundary Γ. At any point $\mathbf{p}(x_1, x_2, x_3) \equiv \mathbf{p}(x_n)$ in Ω, where $n = 1, 2, 3$, the stress–strain relation can be written as

$$\sigma_{ij}(\mathbf{p}(x_n)) = C_{ijkl}(\mathbf{p}(x_n))\,\varepsilon_{kl}(\mathbf{p}(x_n)) \tag{15.4}$$

where $C_{ijkl}(\mathbf{p}(x_n))$ is the constitutive matrix that consists of material properties at the material point $\mathbf{p}(x_n)$. According to the nonlocal elasticity, the stress at another point $\mathbf{q}(x_n)$ of interest can be written as

$$t_{ij}(\mathbf{q}(x_n)) = \int_{\Omega} C_{ijkl}(\mathbf{p}(x_n))\,\kappa(|\mathbf{q}-\mathbf{p}|)\,\varepsilon_{kl}(\mathbf{p}(x_n))\,d\Omega(\mathbf{x}) \tag{15.5}$$

Further, the integrodifferential equation of motion at the material point $\mathbf{q}(x_n)$ can be written as

$$\int_{\Omega} \frac{\partial}{\partial x_j} \left(C_{ijkl}\left(\mathbf{p}\left(x_n\right)\right) \kappa\left(|\mathbf{q}-\mathbf{p}|\right) \varepsilon_{kl}\left(\mathbf{p}\left(x_n\right)\right)\right) d\Omega\left(\mathbf{x}\right) + F_i\left(\mathbf{q}\left(x_n\right)\right)$$

$$= \delta_{ik} \rho\left(\mathbf{q}\left(x_n\right)\right) \frac{\partial^2}{\partial t^2} u_k \tag{15.6}$$

where $\kappa(|\mathbf{q}-\mathbf{p}|)$ is an influence function or a micromorphic kernel function. A functional form of the kernel was developed from a molecular dynamic study and was presented by Picu [111]. As appropriate, it is also conceptualized that the kernel function can be considered as a probability density function in a stochastic media with random material properties if the kernels satisfy few specific properties [88, 89]. A suitable Gaussian kernel function can be viz. [108]

$$\kappa\left(|\mathbf{q}-\mathbf{p}|\right) = \frac{1}{4\pi} \frac{1}{c_p^2 - c_s^2} \frac{1}{|(\mathbf{q}-\mathbf{p})|} \left\{ \exp\left(-|(\mathbf{q}-\mathbf{p})|/c_p\right) - \exp\left(-|(\mathbf{q}-\mathbf{p})|/c_s\right) \right\} \tag{15.7}$$

where $c_{p,s}^2 = \frac{(\tau_0 \ell)^2}{2} \left(1 \pm \sqrt{1 - 4\frac{(v_0 \ell)^4}{(\tau_0 \ell)^4}}\right)$.

Eq. (15.6) can be further modified using the operator L written in Eq. (15.2) and the identity in Eq. (15.3)

$$C_{ijkl}\left(\mathbf{p}\left(x_n\right)\right) \varepsilon_{kl}\left(\mathbf{p}\left(x_n\right)\right) - L\left(\rho\left(\mathbf{p}\left(x_n\right) \frac{\partial^2}{\partial t^2} u_k\right) \delta_{ik}\right) = -L F_i\left(\mathbf{p}\left(x_n\right)\right) \tag{15.8}$$

where the material points $\mathbf{p}$ and $\mathbf{q}$ are reciprocal or synonymous in the above equations.

Homogeneous solution of Eq. (15.8) can be viz.

$$\left[C_{ijkl}\left(\mathbf{p}\left(x_n\right)\right) \frac{\partial^2 u_k\left(\mathbf{p}, t\right)}{\partial \mathrm{x}_j \partial \mathrm{x}_l} - \rho\left(\mathbf{p}\left(x_n\right) L\left(\frac{\partial^2}{\partial t^2} u_k\right) \delta_{ik}\right] = 0 \tag{15.9}$$

15.2.3 The Eigenvalue Problem

Assuming monochromatic harmonic wave potential for outgoing wave, the displacement potential can be written as $u_k = A_k \exp\left(i\mathbf{k}.\,\mathbf{x} - i\omega t\right)$. Hence, after substituting this expression in Eq. (15.9), we get

$$\left[\left[C_{ijkl} k_j k_l A_k e^{(i\mathbf{k}.\mathbf{x} - i\omega t)} - \rho\left(\mathbf{p}\right) \left(1 + \varepsilon^2 \nabla^2 \left(A_k e^{(i\mathbf{k}.\mathbf{x} - i\omega t)}\right) + \lambda^4 \nabla^4 \left(A_k e^{(i\mathbf{k}.\mathbf{x} - i\omega t)}\right)\right) \left(-\omega^2\right) \delta_{ik} \right]\right] = 0 \tag{15.10}$$

Simplifying the above equation, we can write

$$\left[\left[C_{ijkl}k_jk_l + \rho\,(\mathbf{p})\,\omega^2\left(1-\varepsilon^2|\mathbf{k}|^2+\lambda^4|\mathbf{k}|^4\right)\delta_{ik}\right]\right]\left(A_k e^{(i\mathbf{k}.\mathbf{x}-i\omega t)}\right)=0 \quad (15.11)$$

Nontrivial solution of Eq. (15.11) must satisfy

$$\left[\left[|\mathbf{k}|^2\frac{K_{ik}}{\rho\,(\mathbf{x})\,\omega^2}+\left(1-\varepsilon^2|\mathbf{k}|^2+\lambda^4|\mathbf{k}|^4\right)\delta_{ik}\right]\right]=0 \quad (15.12)$$

where $K_{ik}=C_{ijkl}n_jn_l$; defining $\frac{K_{ik}}{\rho\omega^2}=\Omega_{ik}$ and $|\mathbf{k}|^2=\left(k_1^2+k_2^2+k_3^2\right)$, Eq. (15.12) can be written in the matrix form:

$$\begin{bmatrix} \Omega_{11}-\varepsilon^2-\left(\lambda^4|\mathbf{k}|^2-\frac{1}{|\mathbf{k}|^2}\right) & \Omega_{12} & \Omega_{13} \\ \Omega_{21} & \Omega_{22}-\varepsilon^2-\left(\lambda^4|\mathbf{k}|^2-\frac{1}{|\mathbf{k}|^2}\right) & \Omega_{23} \\ \Omega_{31} & \Omega_{32} & \Omega_{33}-\varepsilon^2-\left(\lambda^4|\mathbf{k}|^2-\frac{1}{|\mathbf{k}|^2}\right) \end{bmatrix} = 0 \quad (15.13)$$

Therefore, the eigenvalue analysis is performed on the following nonlocal bi-Helmholtz-type Christoffel equation:

$$\left[\left(\Omega_{ij}-\varepsilon^2\delta_{ij}\right)-\left(\lambda^4|\mathbf{k}|^2-\frac{1}{|\mathbf{k}|^2}\right)\delta_{ij}\right]=0 \quad (15.14)$$

To solve for the eigenvalues, the first part of Eq. (15.14) was solved, where no fourth-order nonlocal parameter is coupled.

$$\left[\left(\Omega_{ij}-\left(\varepsilon^2+|\mathbf{k}|^2\right)\delta_{ij}\right)-\left(\left(\lambda^4-1\right)|\mathbf{k}|^2-\frac{1}{|\mathbf{k}|^2}\right)\delta_{ij}\right]=0 \quad (15.15)$$

After few steps of mathematical simplifications, Eq. (15.15) is obtained from Eq. (15.13). After the eigenvalues are obtained from $(\Omega_{ij}-(\varepsilon^2+|\mathbf{k}|^2)\delta_{ij})=0$, it is obvious that the homogeneity of the second part should automatically satisfy. The second part of Eq. (15.15) contains only the diagonal terms. Hence, λ is an eigen velocity-dependent parameter but satisfies the first eigen equation. It can be found that there are few unique value of λ for which all the eigen velocities are automatically satisfied.

With a different view point, it can be said that Eq. (15.15) has four roots. Only positive roots are considered. The parameter λ was selected such a way that $\lambda<\tau^{2.5}$ {Lazar, 2006 #27}. The iteration of λ is performed for the solution of nonlinear

equation. In this chapter, however, we assumed three different values of λ for three nonlocal eigen velocities (quasi longitudinal, quasi shear 1, and quasi shear 2) at a desired central frequency discussed later. Values of $\lambda = \nu_0\ \ell$ may contribute to the picosecond fluctuation of time of flight (TOF) of wave packets. However, it is extremely hard to detect using current hardware. The experimental determination of wave velocities and dispersion relations are discussed in the next section. It was found that the dispersion relation at macroscale has no influence from the perturbation parameter λ. It was found that λ is least sensitive and is assumed constant. The estimated value of ν_0 is calculated (using the material properties listed in the later sections) close to $\sim$0.0012 for the $\tau_0 = 0$. If the picosecond measurement technique is evolved in the future and the fluctuation of TOF can be measured accurately, the λ and the other nonlocal parameters can be measured. It can then be inferred that these parameters actually play critical roles.

15.3 Damage State Quantification Process

A brief discussion of the mathematical derivation in Sect. 15.2 leads us to realize that the newly formulated QUIC method requires a suitable nonlocal kernel function as written in Eq. (15.7), satisfying Eq. (15.3) with a known nonlocal operator L in Eq. (15.2) or vice versa. If the kernel function is calculated from *an* ab initio dynamics study, the function would not be the same as written in Eq. (15.7). Then, it is required to find a suitable operator L with respective nonlocal parameters. For most materials, it is too time consuming to calculate a suitable kernel function or a suitable operator for each study. Hence, using the QUIC process, the following arguments are presented to take an alternative approach for the multiscale quantification of precursor damage. The proposed approach may not be suitable for multiscale material modeling but will certainly be suitable for material state assessment or precursor damage quantification. Precursor damage quantification is essentially the quantification of the incremental change in the material state.

15.3.1 Incremental Damage State and Its Relation with Nonlocal Parameters

Please note that it is not easy to calculate the exact nonlocal kernel function which may manifest an anisotropic nonlocal behavior. As the absolute material state is unknown and precursor damage state is an incremental measure of differences in different states, we are only interested in incremental change in nonlocal parameters. Hence, hypothetically there is no restriction in assuming different sets of isotropic nonlocal kernel functions by changing its nonlocal parameters τ and ν being their

shape parameters. The unknown kernel function can be presented as a superposition of multiple isotropic kernel function with their respective contribution factors. It is hypothesized that when a material is approaching towards the damage, the precursor damage prevails and the long-range nonlocal effect must be modified. The modified nonlocal effect can be simulated by changing the shape parameters of the kernel functions and their contribution factors. If there is any possibility to obtain the shape parameters correlated with any other observable physical parameter (e.g., slowness of the ultrasonic wave velocities at high frequencies), it is possible to quantify the incremental change in the material state. Thus, it is not necessary to know any exact expression of a nonlocal kernel function. Hence, we need two approaches, a theoretical approach discussed in Sect. 15.2, where eigen wave velocities can be parameterized using nonlocal kernels and an experimental approach, where slowness of wave velocities can be determined experimentally at multiple high frequencies ($\geq$25 MHz).

First, it is recognized that there are some difficulties in obtaining the right dispersion curves for a specific composite material. Primary reason is that the solution of dispersion curve requires physical values of the material properties which are sometime wrong or not explicitly known. Say, the given material properties by the vendor are not accurate or incorrect. Then, the dispersion curves using the given material properties may not be accurate. Now from experiments, it is possible to find the pristine state wave velocity which may not match with the velocities obtained from theoretically calculated dispersion curves. Hence, it is proposed to account for the discrepancy and compensate the effect through a separate nonlocal parameter. The proposed process will depend on the ultrasonic NDE testing methods (e.g., scanning acoustic microscope (SAM)) or the NDE technique using embedded sensors discussed in Sect. 15.5.4. In the following Sect. 15.3.2, the off-line NDE using SAM is described.

15.3.2 Understanding Material Signature Using Scanning Acoustic Microscope

A schematic of SAM is shown in Fig. 15.4. A piezoelectric element is activated with a pulser using a controller which generated ultrasonic stress waves in the lens rod. The plane waves propagate through the lens rod to the concave lens surface. Then, the waves are refracted by the concave spherical lens and form a spherical wave front that focuses the wave at the focal point of the lens. In pulse-echo mode after pulsing or actuating the piezoelectric element, the circuit switches to the signal receiver mode. The wave propagating in the forward direction interacts with the specimen and reflected ultrasonic wave comes back to the lens and are then sensed by the same piezoelectric element. The ultrasonic signature (US) was then obtained as A-scan by plotting the voltage fluctuation at the sensing terminal over time. This A-scan signature is the response from a specific location on the material, we call

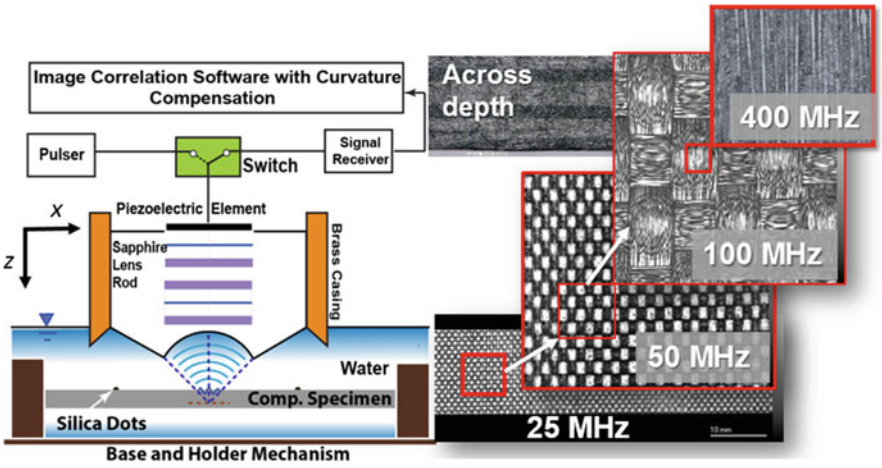

Fig. 15.4 Schematics of scanning acoustic microscopy (SAM) and respective C-scans from a woven composite specimen with different transducers with different central frequencies

a pixel point, where the lens in focused. The total energy of the reflected transient signal can be plotted over an entire scanning area as C-scan. Figure 15.4 shows the C-scan images of a woven composite specimen using ~25, ~50, ~100, and ~400 MHz transducers with increasing level of details across scales. Similar scans can be obtained at different depths when the transducer is defocused at each step of the defocusing distance across the depth along z axis (Fig. 15.4).

An A-scan signal obtained from a SAM experiment is shown for an example (Fig. 15.5a). Similar A-scan signals can be obtained at every incremental depth when the transducer is moved towards the specimen, which is called defocus distance. At every Δz distance, the fluctuation of voltage in the A-scan signal is summed over time to calculate the total signal energy. The plot of this total signal energy or the signal voltage across the depth is called V(z) curve [94, 98] (Fig. 15.5b). As shown in Fig. 15.5a, a typical A-scan signal can be found with a strong first arrival of the wave packet from the surface of the specimen and a weak reflected signal from the back of the specimen. The time difference between these two arrivals of the wave packets can be marked as TOF. If the thickness of the specimen (Fig. 15.5c) is known, dividing the thickness of the specimen by the TOF, one could calculate the wave velocity along the z direction in the specimen. Figure 15.5d shows a typical quasi-longitudinal wave velocity profile over a sample scanned area.

The ultrasonic signals were summed over time and the values obtained across the depth z were named V (z). The mathematical expression of V(z) for a point-focused acoustic beam interacting with composite material is given by [94, 97, 98, 112]:

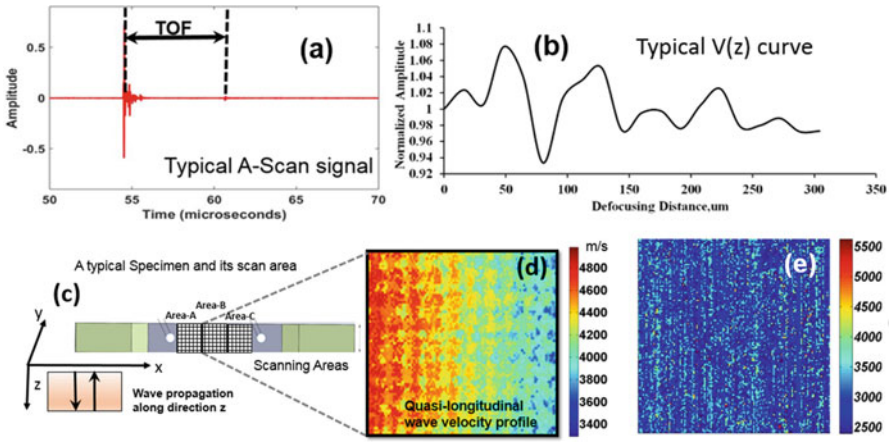

Fig. 15.5 (**a**) A typical A-scan signal from SAM at a pixel point on the material, (**b**) a computed typical V(z) curve at a pixel point when the A-scan signals are taken at different depths along z (Fig. 15.4) by defocusing or moving the transducer towards the specimen, (**c**) a typical scan area where SAM was performed on a composite specimen, (**d**) a typical quasi-longitudinal wave velocity profile calculated using the TOF assuming constant thickness of the specimen, and (**e**) a typical SAW wave velocity profile of a unidirectional composite specimen obtained from V(z) curves

$$V(z) = \int_0^{\theta_m} P(\theta)\, \overline{R(\theta)} \exp(-2ik\cos\theta)\, d\theta \tag{15.16}$$

where $P(\theta)$ is the pupil function. For a point-focused transducer, the reflection coefficient, $R(\theta, \varphi)$, depends on the polar angle θ and the sagittal plane of orientation averaged over azimuth angle φ,

$$\overline{R(\theta)} = \frac{1}{2\pi} \int_0^{2\pi} R(\theta, \varphi)\, d\varphi \tag{15.17}$$

$k = \frac{2\pi f}{C_f}$ is wave number, C_f the wave velocity in the coupling medium; excitation frequency is f and fz is the distance between the lens and sample surface.

Constructive and destructive interference of reflected ultrasonic wave and the surface acoustic waves creates peaks and dips in the V(z) signal as shown in a Typical V(z) curve (Fig. 15.5b). Surface acoustic wave velocity is calculated by using the difference between two consecutive peaks in the V(z) curve. The mathematical expression for the surface wave velocity is written as [113].

$$C_{SAW} = \frac{C_f}{\sqrt{\frac{C_f}{2\Delta z_{SAW} f} - \left(\frac{C_f}{4\Delta z_{SAW} f}\right)^2}} \tag{15.18}$$

Upon rearrangement of Eq. (15.18), distance between two successive peaks corresponding to SAW can be obtained by

$$\Delta z_{SAW} = \frac{1}{2f\left[\frac{1}{C_f} - \left(\frac{1}{C_f^2} - \frac{1}{C_{SAW}^2}\right)^{1/2}\right]} \tag{15.19}$$

As this chapter is not dedicated to SAM, detailed discussion on acoustic microscopy and its application for wave velocity measurement can be found in reference [113].

15.3.3 Identification of Nonlocal Parameter from Scanning Acoustic Microscope Data

A typical nonlocal dispersion curve is shown in Fig. 15.6. When the nonlocal parameter $\tau = 0$, the nonlocal Christoffel solution returns the nondispersive (i.e., independent of frequency) bulk wave velocities in the composite material if the respective material properties are provided in Eq. (15.15). However, for all possible nonzero values of nonlocal parameter τ, the nonlocal Christoffel solution returns three dispersive wave velocities, when the actuation frequencies are provided. Figure 15.6 shows the dispersive quasi-longitudinal wave velocity in a carbon fiber composite material with material properties (obtained from vendor) written in Table 15.1.

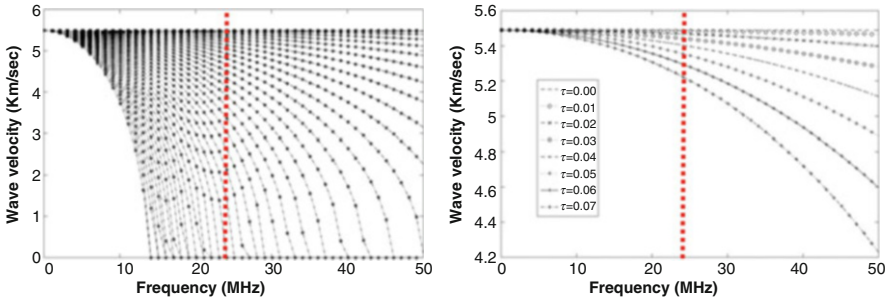

Fig. 15.6 Nonlinear dispersion of quasi-longitudinal wave mode in carbon-fiber composite specimen

Table 15.1 Material properties [114]

E_{11}	E_{22}	E_{33}	G_{12}	G_{13}	G_{23}	ν_{12}	ν_{13}	ν_{23}	Density
65 GPa	67 GPa	8.6 GPa	5 GPa	5 GPa	5 GPa	0.09	0.09	0.3	1605 kg/mm^3

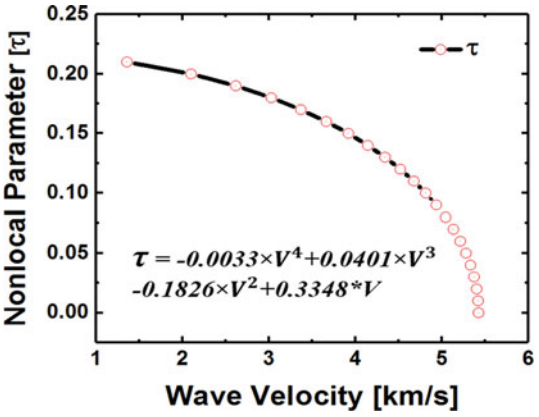

Fig. 15.7 Nonlinear variation of the nonlocal parameter with dispersive quasi-longitudinal wave velocity at ~25 MHz frequency

The dispersion of wave velocities obtained from the nonlocal Christoffel equation is the function of frequency and the nonlocal parameter. Now say, for example, a ~25-MHz SAM lens was chosen for the precursor damage investigation. The red line in Fig. 15.6a, b indicates the ~25-MHz frequency and the curves that are relevant at that frequency of interest. Figure 15.6b shows a zoomed in version of the same curve with selected number of dispersion curves from Fig. 15.6a. Next one would need the nonlocal dispersion curve at a fixed frequency, a curve that demonstrates the relation between the change in wave velocities with respect to the nonlocal parameter at a fixed frequency (here, ~25 MHz). A typical nonlocal wave velocity plot is presented in Fig. 15.7. Through linear regression, one could obtain a mathematical equation for the relation between the nonlocal parameter and the quasi-longitudinal wave velocity in the composite material. Further to calculate the nonlocal parameter from the equation, it is necessary to experimentally measure the wave velocities (please refer Fig. 15.5) from the SAM data. As described in Sect. 15.3.2, the wave velocity can be obtained from TOF calculation and using the library function suitable nonlocal parameter can be obtained. Further, how this nonlocal parameter will result the nonlocal damage entropy (NLDE) is discussed in the following section.

15.3.4 *Nonlocal Damage Entropy: Precursor Quantification Process Using Scanning Acoustic Microscope and Quantitative Ultrasonic Image Correlation*

Precursor damage is a slow growing process in a distributed fashion. No static test on composite materials can manifest the slow growth of the distributed damages. Hence, it is mandatory to perform a detailed fatigue test on the composite specimens to understand the process and quantify the damage state sequentially over time represented by the fatigue cycles. A step-by-step damage quantification process using QUIC is described below. Figure 15.8 shows the quantification process using a flowchart.

Step 1: A composite material in hand with unknown material properties will first need an intelligent guess of the material properties or material properties to be obtained from the vendor. The material properties can be experimentally derived using ultrasonic immersion testing followed by optimization [115]. In the very heart of QUIC method, it is assumed that the material properties provided by the vendor to compute dispersion curve were incorrect, which is not considered in any

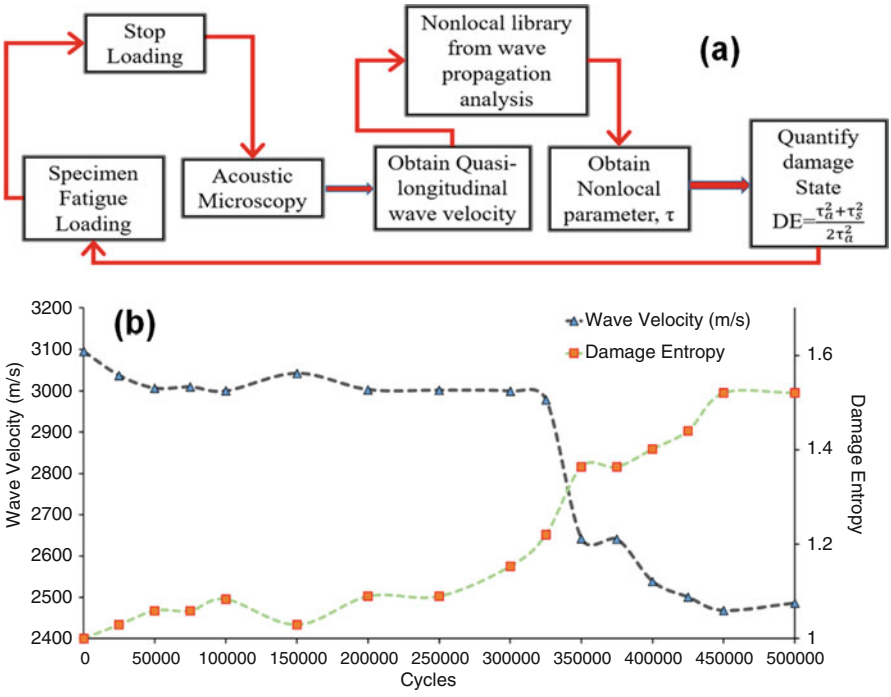

Fig. 15.8 (**a**) A flow chart showing the process to quantify the Precursor Damage in composites using nonlocal damage entropy (NLDE), (**b**) A typical DE curve obtained from an ASTM standard carbon fiber four layers woven composite specimen fatigued till 500,000 cycles

other methods. Hence, it is proposed that the estimated nonlocal parameters should be corrected that will compute the damage entropy. It is obvious that the error in approximated material properties will affect the interpretation of the precursor damage state and has been proposed to alleviate the shortcoming by introducing the nonlocal parameter called material property adjuster.

It is assumed that the wave signals are the true response of the material state.

Step 2: Using the material properties, a library of nonlocal wave velocity curves is constructed by solving the eigenvalue problem in Eq. (15.15). A library function is created which takes two inputs (the experimental wave velocity and the center frequency of scanning using SAM) and returns an output (the nonlocal parameter τ).

Step 3: Next, the composite specimen is scanned using broadband ∼25, or ∼50, or ∼100 MHz transducers based on required influential scale. The transducers are broad band, for example, a 50-MHz transducer actuates frequencies from ∼5 to ∼75 MHz with maximum amplitude close to ∼50 MHz. Hence, for analysis, multiple frequencies could be used in the library function at the same time to retrieve the frequency-dependent nonlocal parameters. The pulse-echo signal from each pixel point (as discussed in Sect. 15.3.2) on the specimen was recorded for further analysis.

Step 4: At each pixel point, an A-scan signal is generated and C-scan data is generated. By moving the transducer towards the material at different depths, Z-scan data were generated with different defocus distance across the material depth.

Step 5: TOF was measured at every pixel points. Reason for using backside reflection is that the wave traveled twice through the thickness and is more affected by the material degradation. Please refer to Figs. 15.4 and 15.5.

Step 6: In this step, the thickness of the specimen was assumed constant during the QUIC experiments. Next at each pixel, the TOF measured was used to calculate quasi-longitudinal wave velocity in the composite specimen. This step provides a matrix composed of wave velocities on a material grid.

Step 7: Next, the nonlocal parameter at each pixel was obtained. The value of the nonlocal parameter τ was using the library function obtained and discussed in Sects.15.3.1 and 15.3.2. The wave velocity at each pixel point and the central frequency of the transducer are the inputs to the function. If one needs to analyze the data using broadband transducer, multiple frequency could be used as input. This function constructs multiple two-dimensional (2D) frequency-dependent map of τ on the specimen or only one 2D map, if only the central frequency is used. Very unlikely, this map will have all zero values. Some pixel point may not have any contributions. A surface plot of τ with nonzero values can be achieved and the mean and standard deviation values of τ can be returned at the pristine state.

Step 8: In the beginning, the specimen is at the pristine state and assumed to be undamaged and thus it can be assumed that the mean τ is emerging due to approximated or incorrect material properties. The nonlocal parameter associated with this error is essential for precursor damage quantification and hence, the material property adjuster was not ignored.

Step 9: This is named as "intrinsic material property adjuster" or τ_a.

Step 10: Then, the specimens are subjected to the fatigue loading and the process is repeated. At every interval when the experiments are stopped, SAM scans are performed and τ are calculated. The parameter is defined as "intrinsic damage state quantifier" or τ_s.

Step 11: Next at the end of every fatigue interval, the "nonlocal damage entropy (NLDE)" is calculated. Mathematical expression for the "nonlocal damage entropy" (NLDE) can be written as

$$NLDE = \frac{{\tau_a}^2 + {\tau_s}^2}{2\left({\tau_a}^2\right)} \tag{15.20}$$

Please note that the mean values of the "intrinsic material property adjuster" and the "intrinsic damage state quantifier" are used to calculate the NLDE.

Step 12: Plot the NLDE over the number of fatigue cycles and analyze the trend. A typical wave velocity reduction and NLDE curves are presented in Fig. 15.8b.

Please note that the abovementioned process is described for NLDE calculation using quasi-longitudinal wave velocities. Similar NLDE could be also calculated using the SAW wave velocity using Eq. (15.18). Here, in this chapter, we will keep our discussion restricted to the quasi-longitudinal wave velocity only.

15.3.5 Damage State Quantification from Evaluation of Stiffness Degradation

Another alternative derivative approach from the above data is to calculate material stiffness along the thickness direction (along direction-3) at every pixel, distributed over the scanning areas. The stiffness can be obtained at the regular fatigue interval from the measured quasi-longitudinal wave velocity profile discussed above in Sect. 15.3.4. Damage tenor can be calculated using stiffness-degradation method described below [116]:

$$\begin{aligned} D_{ii} &= 1 - \frac{C_{ii}}{C_{ii}^0} \\ i &= 1, 2, \ldots, 6 \end{aligned} \tag{15.21}$$

$$\begin{aligned} D_{ij} &= \frac{C_{ii}^0 - C_{ij}}{C_{ij}^0 + \text{sign}\left(C_{ii}^0 - C_{ij}\right).\sqrt{C_{ii}C_{ij}}} i \neq j \\ i &= 1, 2, \ldots, 6 \\ j &= 1, 2, \ldots, 6 \end{aligned} \tag{15.22}$$

where C_{ij} is the stiffness tensor. To calculate damage across the thickness of the specimen, stiffness component (C_{33}) in Eq. (15.22) can be replaced by the quasi-longitudinal velocity as follows:

$$D_{33}^{N} = 1 - \frac{qL_{33}^{N}}{qL_{33}^{0}} \tag{15.23}$$

where qL_{33}^{0} is the quasi-longitudinal wave velocity at the pristine state of the composite specimen along the direction 3, and qL_{33}^{N} is the wave velocity after N-th fatigue cycle in the same specimen. Then, the cumulative damage growth can be calculated as:

$$CDI = \sum_{k=1}^{N} D_{33}^{k} \tag{15.24}$$

15.4 Coda Wave Interferometry: Low-Frequency Method

It is our objective to quantify the precursor damage using multiscale approach for both online and off-line applications. To extract the information from microscale, we adopted the off-line SAM-based high-frequency QUIC approach to quantify the damage state in composite materials. On the other hand, we also intent to implement an online NDE process at lower frequencies (≤500 KHz) using Guided wave approach that can detect, quantify, and monitor the precursor damage state in composites in real time, without altering the component materials that constitute the composites. It was found that the "Coda wave" in the Guided wave signals, that comes later followed by the symmetric and antisymmetric wave modes, often ignored in damage detection, carries significant information on the damage precursor state. The later part of the signal which is called "'Coda wave" are highly sensitive to weak changes in the material due to multiple scattering and long travel path [117–122].

15.4.1 Background

Coda wave interferometry (CWI) technique is a promising nondestructive technique which was first used by the seismologist to detect slight changes in coda wave velocity in the earth crust due to earthquakes [117, 122–128]. Later, this technique was successfully extended to measure relative velocity change in concrete due to the development of the small-scale (∼mm) damages [119, 121, 129, 130]. To understand the correlations between ultrasonic amplitude decay and the frequency-dependent shift in the coda wave velocity, ultrasonic measurements were carried out between the range ∼150 kHz to ∼1 MHz [121]. Wave velocity change due to thermal effect was also estimated in Ref. [131]. Larose et al. [119] estimated relative change in coda wave velocity in concrete in the order of $\frac{\nabla V}{V} = 10^{-4}$. With precise measurement of wave velocities, it was found that the CWI was

always more accurate compared to the conventional TOF measurement from direct wave at lower frequencies. Commonly, the CWI analysis was performed using two techniques: (a) doublet [118, 132, 133], and (b) stretching [119, 120, 129, 131, 134]. In the doublet method, several time windows in the coda parts of the signal were selected and time shift in each window were calculated by cross-correlation technique. By averaging the time shifts obtained from different time windows, time shift of the coda wave is obtained and correlated with the relative wave velocity change. Stretching technique is commonly used in nondestructive testing, time axis of the perturbed signal is either compressed or stretched, and then cross-correlation is performed. Stretch parameter that maximizes the cross-correlation is reported to correlate the relative wave velocity change in the material. Shukui Liu et al. [135] recently proposed Taylor series expansion technique to calculate the stretch parameters because the cross-correlation technique is computationally expensive and power consuming. Although CWI is very promising to detect damages at the small scales, no attempt has been made so far to extend the technique to detect micro-cracks in the carbon-fiber composite materials. Composite is a heterogeneous medium designed to develop damage precursors in a distributed form, which interact with one another and form a fracture path to fail if further load is applied. Coda wave is sensitive to these weak changes when interacts with the distributed damages many times while traveling through the composite specimen. Hence, we identified that the coda wave has the potential to be a promising online tool for precursor damage detection if conventional CWI is redefined for composites.

15.4.2 Mathematical Treatment of Coda Wave for Damage Quantification

Due to heterogeneity in the composite material, coda wave scattered multiple times in the material medium and made it extremely sensitive to small-scale changes in the medium. A typical Guided wave signal with its respective coda part is shown in Fig. 15.9.

15.4.2.1 Stretching Technique with Cross-Correlation

Say, for example, sensor signals are recorded at two different states of material and two such sample signals are presented in Fig. 15.9. Pristine state and damaged state signals are designated as $h_1(t)$ and $h_k\ (t)$, respectively. Sometimes, the phase shifts in the Guided wave signals due to the precursor damages are insignificant or undetectable. However, the phase shifts in the coda wave signals are not ignorable in composites. Although not ignorable, the phase shifts are not divergent. Hence, the damage state signal can be equivalent to the time stretch version of the pristine state signal plus distortion [135].

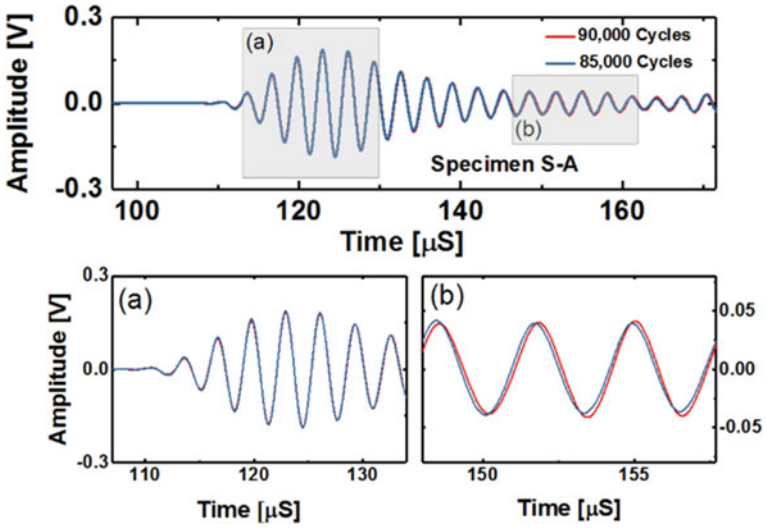

Fig. 15.9 Guided wave sensor signals at two consecutive states of material between which a perturbation of signal stretch is evident in the coda part [136, 137]

$$h_k(t) = h_1\left(t\left(1+\alpha\right)\right) + n(t) \tag{15.25}$$

where α is relative stretch parameter and $n(t)$ is the distortion. Distortion can be neglected if α is very small. In the stretching method, the time scale of the perturbed state signal was stretched (+ sign) or compressed (− sign) by a suitable stretch parameter value, α as $t_k = t(1\text{-}\alpha)$. A range of α can be selected [−value $\leq \alpha \leq$ value] and cross-correlation can be performed between $h_k[t(1\text{-}\alpha]$ and $h_1(t)$. α that maximizes the normalized cross-correlation should be considered the critical stretch parameter (α_k) and should be used to measure the relative average velocity change in the medium [121].

$$CrCr_k\left(\alpha\right) = \frac{\int_{t-T/2}^{t+T/2} h_k\left[t\left(1-\alpha\right)\right] h_1(t)dt}{\int_{t-T/2}^{t+T/2} h_k^2\left[t\left(1-\alpha\right)\right] dt \int_{t-T/2}^{t+T/2} h_1^2(t)dt} \tag{15.26}$$

$$\alpha_k = \max_{\alpha\in\Omega}\left(CrCr_k\left(\alpha\right)\right) \tag{15.27}$$

$$\alpha_k = \left(V_k - V_1\right)/V_1 \tag{15.28}$$

where T is the time window selected for computation. V_1 is velocity at pristine state, while V_k is the velocity at the perturbed state.

15.4.2.2 Taylor Series Expansion Theory

By implementing the Taylor series expansion technique, the stretch parameters can be calculated using Eq. (15.29) [42]. This technique is computationally less expensive than the cross-correlation technique and useful to calculate the stretch parameter for long-range signals [135].

$$\alpha_k \approx \frac{1}{n}\sum_{i=2}^{n+1} \frac{2\left[h_k\left(t_i\right) - h_1\left(t_i\right)\right]}{f_s t_i \left[h_1\left(t_{i+1}\right) - h_1\left(t_{i-1}\right)\right]} \tag{15.29}$$

where n is the total number of data points used in the calculation, t_i is the timestamp, and f_s is the sampling frequency.

15.4.2.3 Application of Coda Wave Interferometry for Precursor Quantification in Composites

It was found that for composites, due to unique oscillating pattern of coda wave velocities, the stretch parameter is incremental in both positive and negative direction in time, which particularly holds the key for precursor damage identification in composite using coda waves. Hence, instead of calculating the stretch parameter by comparing pristine and damaged state signal for total length of the signal, an incremental stretch parameter between two consecutive recorded signals is considered and can be written as follows:

$$CrCr_k\left(\alpha_k\right) = \frac{\int_{t-T/2}^{t+T/2} h_k\left[t\left(1-\alpha\right)\right] h_{k-1}(t)dt}{\int_{t-T/2}^{t+T/2} h_k^2\left[t\left(1-\alpha\right)\right] dt \int_{t-T/2}^{t+T/2} h_{k-1}^2(t)dt} \tag{15.30}$$

$$\alpha_k \approx \frac{1}{n}\sum_{i=2}^{n+1} \frac{2\left[h_k\left(t_i\right) - h_{k-1}\left(t_i\right)\right]}{f_s t_i \left[h_{k-1}\left(t_{i+1}\right) - h_{k-1}\left(t_{i-1}\right)\right]} \tag{15.31}$$

Overall, the damage growth can be visualized and quantified by presenting the cumulative sum of the stretch parameter over the fatigue life of the specimen as follows [136, 137]:

$$DG_N = \sum_{k=1}^{N} \alpha_k \tag{15.32}$$

Further, the normalized precursor damage growth can be calculated as:

$$DGNorm_N = \frac{\sum_{k=1}^{N} \alpha_k}{\max\limits_{k \in N}\left(DG_k\right)} \tag{15.33}$$

where N is the number of fatigue loading cycle.

15.5 Experimental Design

To demonstrate the multiscale precursor damage quantification process using a practical example, a detailed experimental design is presented in this section.

15.5.1 Materials and Specimen Preparation [136, 137]

In this study, woven carbon-fiber composite material was used with four layers. Thickness of each lamina was 280 μm. Figure 15.10 shows the schematic of the specimen, optical image, and a SAM B-scan. Dimensions of the specimen were according to American Standard for Testing and Material standard, ASTM D 3039 [138]. For manufacturing the tabs, glass-fiber composite was used. Length and width of the tabs were selected properly based on the experimental requirements. Chamfer angle at the end of the tab was provided to avoid stress concentration at the grip. Once the specimens were prepared, next piezoelectric wafer active sensors (PWAS) from Steminc Steiner & Martins, Inc. were mounted on the specimen using Hysol 9394. Totally, eleven (11) specimens were prepared. Three (3) specimens (T1-T3) were tested under pure tensile load to estimate the maximum tensile strength of the composite, and one (1) specimen (F-L) was tested under fatigue loading

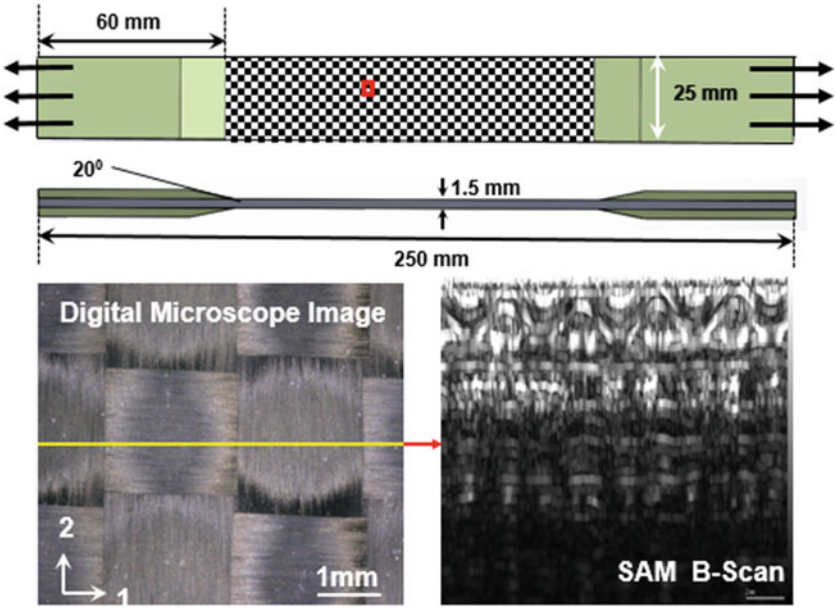

Fig. 15.10 Schematic of specimen geometry and material used for precursor damage experiments [136, 137]

with maximum load being the ∼50% of the ultimate strength of the specimen to estimate the maximum fatigue life. In this precursor study, the fatigue life was intentionally marked when the first delamination in the specimen was detected and which was approximately ∼one million cycles. However, the fatigue test on F-L was continued till the end of two million cycles. The specimen F-L did not fracture at the end of the test but was significantly damaged as discussed in the following section. From the remaining seven (7) specimens, each was tested under tensile–tensile fatigue up to ∼30% of the fatigue life, i.e., up to ∼300,000 cycles. The avg. length, width, and thickness of the specimens were ∼249.733, ∼24.72, and ∼1.5023 mm. The nomenclature of the specimens are SA, S-B, S-C, S-D, S-E, S-F, and S-G which were tested under fatigue loading. Please note that S-A, S-B, S-C, and S-D were used for CWI-based precursor damage quantification but S-E, S-F, and S-G were used for QUIC-based precursor damage quantification, of which S-A was decommissioned to perform SEM after 300,000 cycles to prove the existence of precursor damage in the specimen. Specimen S-E was used for both CWI and QUIC precursor damage quantification for comparison.

15.5.2 Tensile Test

On two specimens T1 and T3, the tensile tests were performed in order to obtain the ultimate tensile strength of the composite. For the tensile test, a 5-mm Wire Lead Strain Gauge with size 9.5 × 3.5 mm was mounted on each tensile specimen Tensile loading was applied under displacement control mode at the rate of 0.03 cm/min until the total fracture of the specimen. The average strain rate was $3.25 \times 10^{-5}\ s^{-1}$. Figure 15.11 shows the stress–strain plot from the experiments and optical images of the fractured specimens.

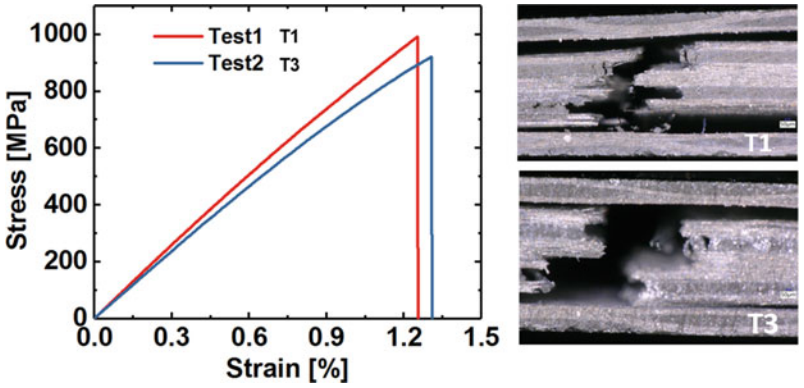

Fig. 15.11 Stress–strain curve of the material and failure images from T1 and T3 specimens [136, 137]

15.5.3 *Fatigue Testing*

In order to develop progressive damage over time in the composite specimens (Figure 15.12a), fatigue loading was performed under MTS 810 machine (Figure 15.12b). The experimental means for CWI and QUIC are shown in Figure 15.12c–f. First to estimate the fatigue life of the material, one specimen (F-L) was subjected to fatigue loading until two million cycles. The F-L specimen was subjected to tensile–tensile fatigue loading ($f = 10$ Hz) with load ratio $R = 0.01$ ($R = F_{\min}/F_{\max}$). Approximately, 50% of the tensile strength (~4100 lbf or ~17.6 KN) was used as the maximum load in the fatigue loading to study the precursor. Although significant damages were observed by the Micro-Optical Microcopy and SAM (Fig. 15.13), the specimen was not failed. Delamination was first observed close to ~one million cycles and we marked the fatigue life. Next, the remaining eight (8) specimens (S-A, S-B, S-C, S-D, S-E, S-F, and S-G) were subjected to the similar fatigue loading up to ~30% of the fatigue life to ~300,000 cycles, except one, which is S-E for which fatigue was continued till 500,000 cycle to extract additional information. The tests were stopped every 5000 cycles for precursor damage investigation using

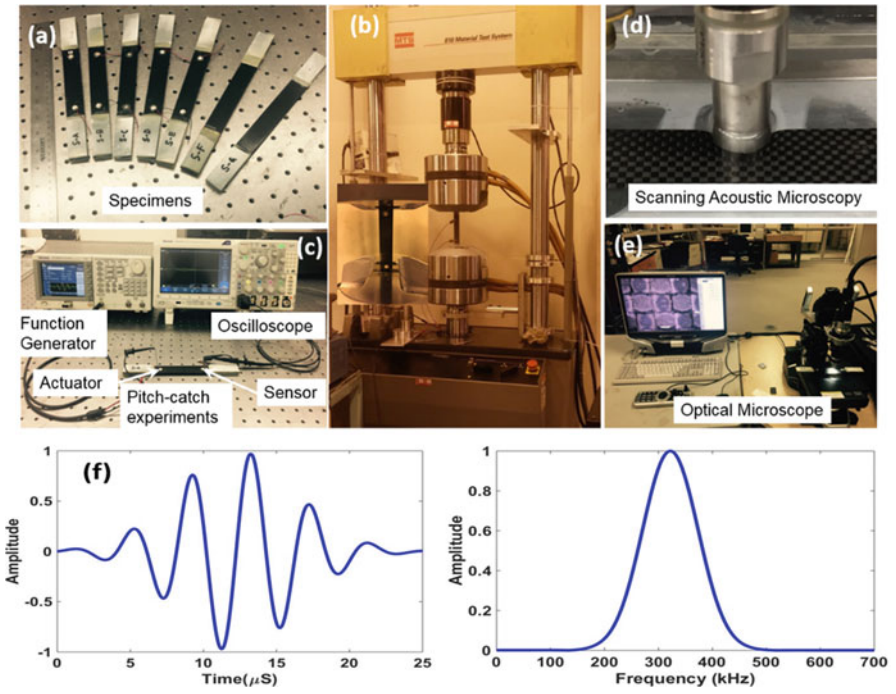

Fig. 15.12 (**a**) Composite specimens used for fatigue testing, (**b**) experimental setup for fatigue testing, (**c**) pitch-catch experiments setup, (**d**) SAM for ultrasonic inspection of the specimen, (**e**) digital microcopy for damage inspection, and (**f**) Gaussian wave signal (tone burst) used for pitch-catch experiments and its frequency transformation [136, 137]

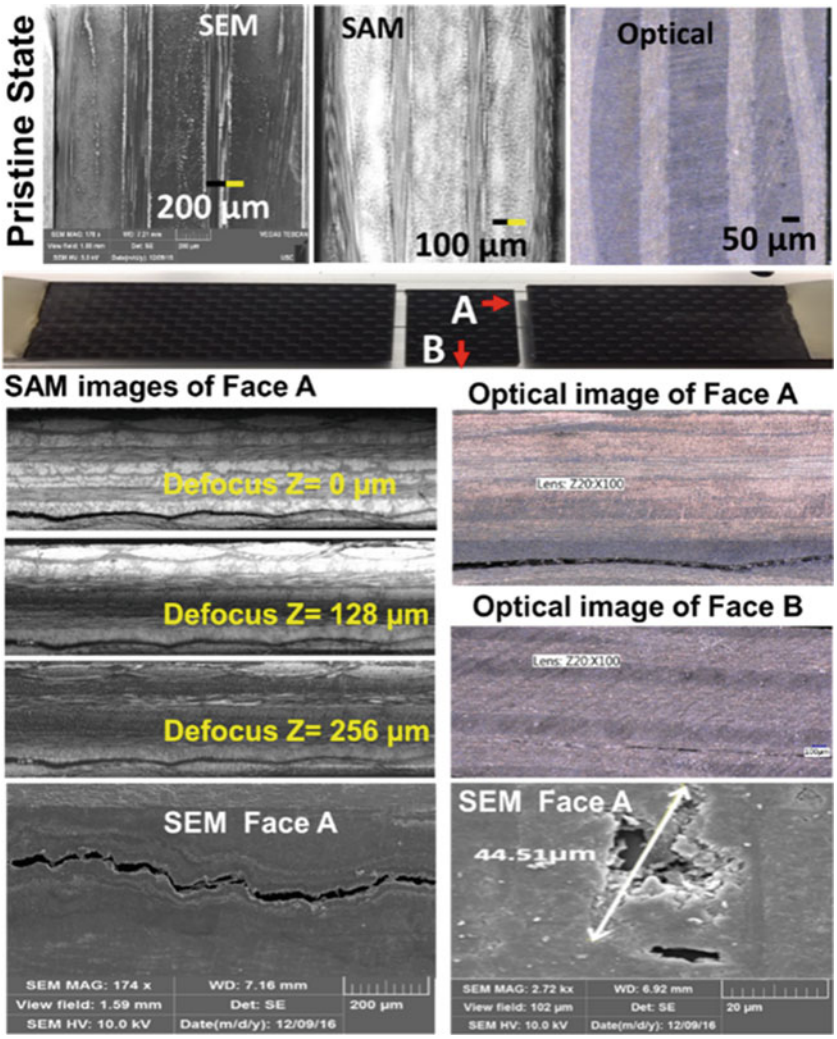

Fig. 15.13 Damages in woven composite specimen observed after two million cycles, delamination started after one million cycles [136, 137]

CWI and QUIC. At every 5000-cycle interval, pitch-catch Guided wave experiments were performed using PWAS mounted on the specimens. To monitor the material degradation or to investigate the development of the precursor damage inside the specimen, QUIC using SAM (as discussed in Sect. 15.3.4 and Fig. 15.8) was performed at every 5000-cycle interval on the S-E, S-F, and S-G specimens.

15.5.4 Pitch-Catch Ultrasonic Lamb Wave Experiment

Two high-frequency PWAS were attached to each specimen. A five-count tone burst signal with central frequency, $f_c = 324$ kHz, was used for actuation of Guided wave (Fig. 15.12f). The central frequency 324 KHz was selected from wave tuning experiment on the specimen S-A. Tektronix AFG3021C (25 MHz, 1-Ch Arbitrary Function Generator) was used to generate the tone burst actuation at the interval of 1 ms. For actuation, peak-to-peak amplitude of the burst signal was set to 20 V. Lamb wave generated by the actuator propagated through the specimen and interacted with the damages which were then sensed by the sensors. Tektronix MDO3024 (200 MHz, 4-Ch Mixed Domain Oscilloscope) was used to record the sensor signals. Sensor signals were collected at 50.0 MS/s sampling rate with 10,000 data points. Signals were saved for further CWI analysis after averaging 512 actuations for noise cancellation at both pristine state and at different loading cycles.

15.6 Results and Discussion

15.6.1 Probability Distribution of Quasi-Longitudinal Wave Velocity

First to investigate the effect of damage development on the wave velocity distribution in a probabilistic sense, quasi-longitudinal wave velocity profile was obtained from the pristine state specimens from three different locations by following the process described in sections above. Next, at the end of each fatigue interval, a probability density function that best explains the distribution of the wave velocities over the areas Area-A, Area-B, and Area-C was calculated. Although quite small, the degradation of the mean stiffness in three scan areas, between the pristine state and the state at the end of the 110,000 cycles of fatigue, was evident (Fig. 15.14). Possibly, this is the cause of the reduction of the quasi-longitudinal wave velocities due to the precursor damage developed in the specimen in a distributed sense. This signifies that the material properties started to compromise at as early as 10% of the fatigue life of the composite specimens where QUIC and Optical Microscopy indicated early initiation of damage. Surprisingly, low-frequency CWI-based quantification method also indicated anomalous behavior just before 100,000 cycles in all the five specimens (S-A, S-B, S-C, S-D, and S-E). It can be argued that this evidence is not coincidental but indicative of precursor damage in the specimens.

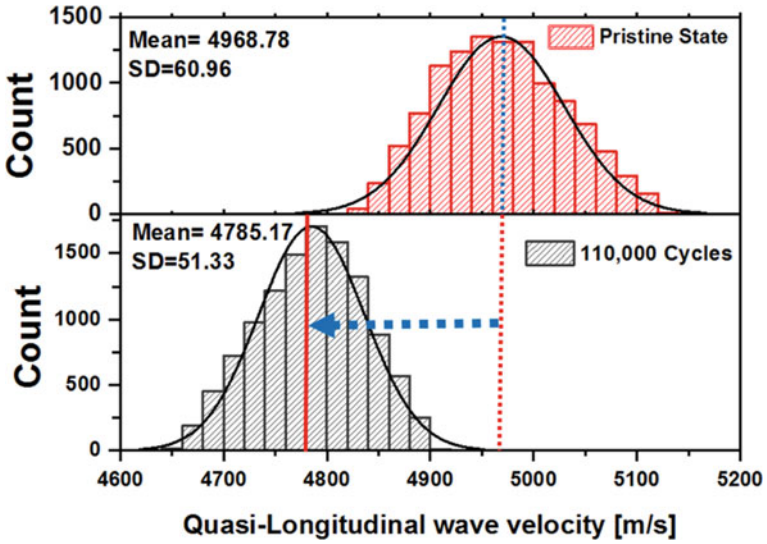

Fig. 15.14 Probability density distribution of wave velocities, (**a**) pristine state, and (**b**) 110,000 cycles [136, 137]

15.6.2 Precursor Damage Quantification Using Coda Wave Interferometry

Precursor damage growth in four composite specimens S-A, S-B, S-C, and S-D were first quantified using the coda wave method at lower frequencies. Using conventional low-frequency SHM method, it is difficult to get indication of precursor damage. However, CWI method has potential towards identifying and quantifying precursor damage. The precursor damage index obtained from CWI analysis was calculated employing both the cross-correlation and Taylor series expansion technique as shown in Fig. 15.15. Indication of damage growth obtained from both the techniques was qualitatively in good agreement. Many peaks and dips were observed in the damage index from both the methods at certain intervals. It is argued that these fluctuations are not arbitrary but hold the key to understand the material behavior. Life span of the specimens under operation simulated by the number of fatigue cycles associated with these fluctuations is consistent between two methods of CWI (cross-correlation and Taylor series expansion technique). These fluctuations are even consistent among all the specimens. It is evident that CWI analysis has indicated a physical phenomenon which is hypothesized to be the precursor damage in the specimen. Peaks in the PDI are corresponding to the decrease in the wave velocity in the coda signal, whereas dips are corresponding to the increase in the wave velocity in the coda signals. This representation of our findings helps to state further that the decrease in the wave velocity in the coda corresponds to local microscale damage that leads to material degradation and local

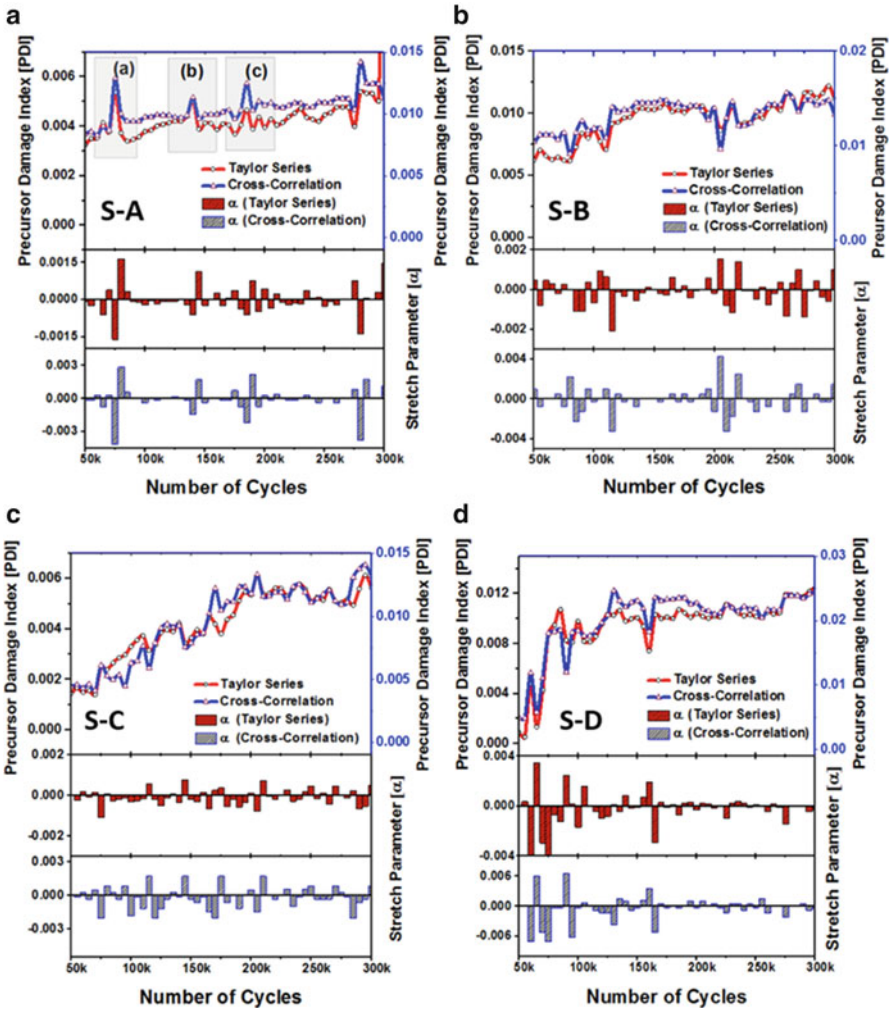

Fig. 15.15 Damage growth quantified by coda wave interferometry (CWI) for specimens, (**a**) S-A, (**b**) S-B, (**c**) S-C, and (**d**) S-D [136, 137]

stress concentration, whereas decrease in PDI immediately followed by the increase can be explained by the microstructure reorientation and relaxation of local stress concentration, which are periodically taking place inside the composite specimens during the fatigue experiment. To investigate this phenomenon in a great detail, the peaks from Fig. 15.15 S-A were selected at 75000, 140,000, and 185,000 cycles, respectively, with their neighboring points. Slopes between the points (1, 2, and 3) at 70,000, 75,000, and 80,000 cycles, respectively, are shown in Fig. 15.16. Based on representation in Fig. 15.16, it can be said that the slope of the connecting lines in the precursor damage index curve between two fatigue intervals could decrease

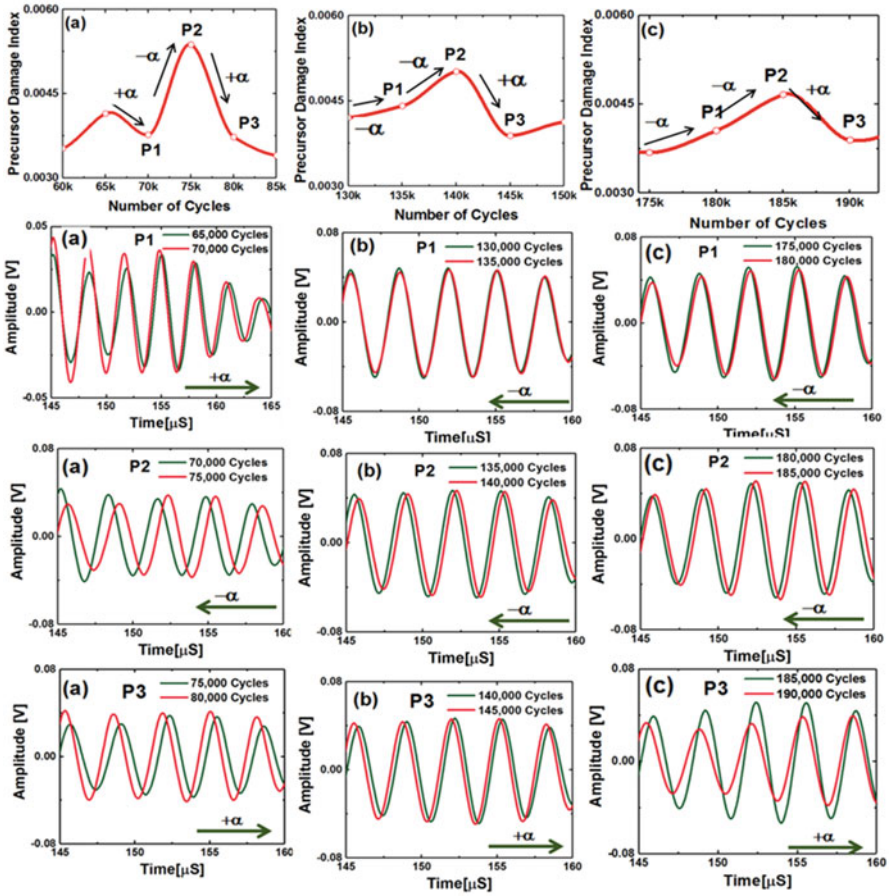

Fig. 15.16 Phase shift of the coda wave at the peaks (**a**–**c**) for specimen S-A [136, 137]

and/or increase with fatigue cycles. While analyzing the precursor damage index peak designated as (a) in Fig. 15.16a, it can be found that the slope towards the P1 is negative, P1-P2 is positive, and P2-P3 is negative. Now, to calculate the stretch parameter at P1, the coda part of the two consecutive signal after 65,000 and 70,000 cycles are compared as shown in Fig. 15.16 left column. It is observed from the figure that the phase of the coda part of the signal at the end of 65,000 fatigue cycles leads the phase of the signal at the end of 70,000 fatigue cycles. This is due to the fact that relative wave velocity was increased towards P1. At P2, stretch parameter is calculated for the signal at 75000. Phase of the coda wave after 75,000 cycles leads the phase in the signal after 70,000 cycles; that means that the average relative velocity of the material is decreased due to new precursor damage initiation. At P3 (80,000 cycles), relative wave velocity again increased, because the phase shift is positive between the signals after 75,000 cycles and

Table 15.2 Percent change in relative coda wave velocity

	Location-1	Location-2	Location-3
Fig 15.15a	0.03%	−0.42%	0.29%
Fig 15.15b	−0.02%	−0.15%	0.17%
Fig 15.15c	−0.072%	−0.217%	0.219%

80,000 cycles. The stretch parameter at locations P1, P2, and P3 are calculated as 0.00029, −0.0042, and 0.0029, respectively, which corresponds to 0.029%, −0.42%, and 0.09% change in average wave velocity between two successive cycles in the medium. It is also interesting to note that phase difference at P2 is higher compared to P1 and P3, as evident in Fig. 15.16 left column and which is in agreement with the calculated stretch parameter. Using the similar process, percent change in relative wave velocity between two successive fatigue cycles was calculated at locations (a), (b), and (c) and is listed in the Table 15.2.

It is identified that whenever there has been a change in the sign of the stretch parameters from positive to negative or from negative to positive followed by immediate positive stretch or negative stretch, respectively, is the indication of the precursor damage in the specimen. This statement is next validated and proved by the results obtained from NLDE using the nonlocal method and presented in the following section. This unique and consistent phenomena will help devise new damage detection algorithm for online precursor damage detection and quantification.

15.6.3 Precursor Damage Quantification Using Nonlocal-Continuum Physics

As described in Sect. 15.5, damage development stages in three composite specimens S-E, S-F, and S-G were studied using QUIC employing SAM. Damage growth was quantified using high-frequency nonlocal ultrasonic technique with ∼25 MHz, ∼50 MHz, and ∼100 MHz confocal transducers for increased resolution. Experimentally, it was observed that matrix-microcracking under dynamic loading developed across the cross-section and may act as energy barriers. Quasi-longitudinal wave velocities along the thickness directions were calculated at the scanning areas Area-A, Area-B, and Area-C, respectively, as shown in Fig. 15.5. Each scanning area was discretized into 125 × 125 pixel points and wave velocities were calculated at each pixel point. At the pristine state, the average quasi-longitudinal wave velocities obtained from specimens S-E, S-F, and S-G were 5056.91 m/s, 5171.39 m/s, and 4959.014 m/s, respectively. However, the quasi-longitudinal wave velocity calculated after 300,000 cycles were 4950.1 m/s, 4754.06 m/s, and 4795.641 m/s in those specimens, respectively. Damage growth in the specimens was estimated by plotting the cumulative DE described in Sect. 15.3.4 with the fatigue cycles. Figure 15.17 shows the results obtained from QUIC. The DE is designated as NLDE in Fig. 15.17. Although the increasing trend of the

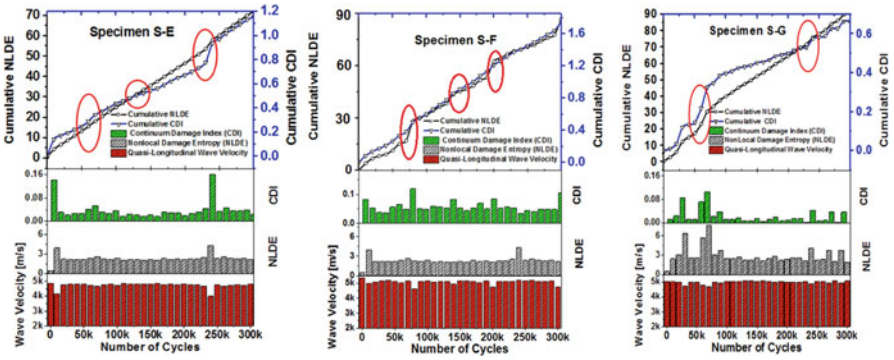

Fig. 15.17 NLDE and cumulative damage index (CDI, Eq. (15.24)) quantified by QUIC using SAM [136, 137]

DE growth pattern is promising, we focus more on the incremental change in the DE which was observed consistently in all three specimens near similar fatigue interval. In fact, the sudden jumps in DE were evident from 10,000 to 15,000 earlier than the sign fluctuation in the stretch parameter observed in precursor damage index obtained from the CWI analyses. This is because the DE employs high-frequency QUIC method which should be more sensitive than the pitch-catch online sensor signals.

15.6.4 Precursor Damage Indication from SAW Velocity Profiles

S-E was the only specimen that was continued till 500,000 cycles of fatigue. Figure 15.18a shows the mean and standard deviation of the SAW velocity obtained from the SAW profile over the gauge area Area-B from the specimen S-E. As discussed in Sect. 15.3.2, the SAW velocity calculation requires Z-scans across the depth of a specimen with different defocus distance of the confocal lens and hence, it is time consuming. Thus, the SAW velocity profiles were calculated at every 50,000-cycle interval. It can be seen from the curves that due to the precursor damage initiation, degradation of material properties caused the overall decrease in mean SAW velocity, which is also evident from Fig. 15.14. However, the standard deviation of SAW velocity profiles had unprecedented fluctuations between 100,000–300,000 cycles, which can be viewed as material settlement or microstructure reorientation, but overall the standard deviation increased after 500,000 cycle of loading. Figure 15.18b shows the SAW velocity profile at the pristine state, after 350,000 cycles and 500,000 cycles of fatigue loading on the specimen S-E.

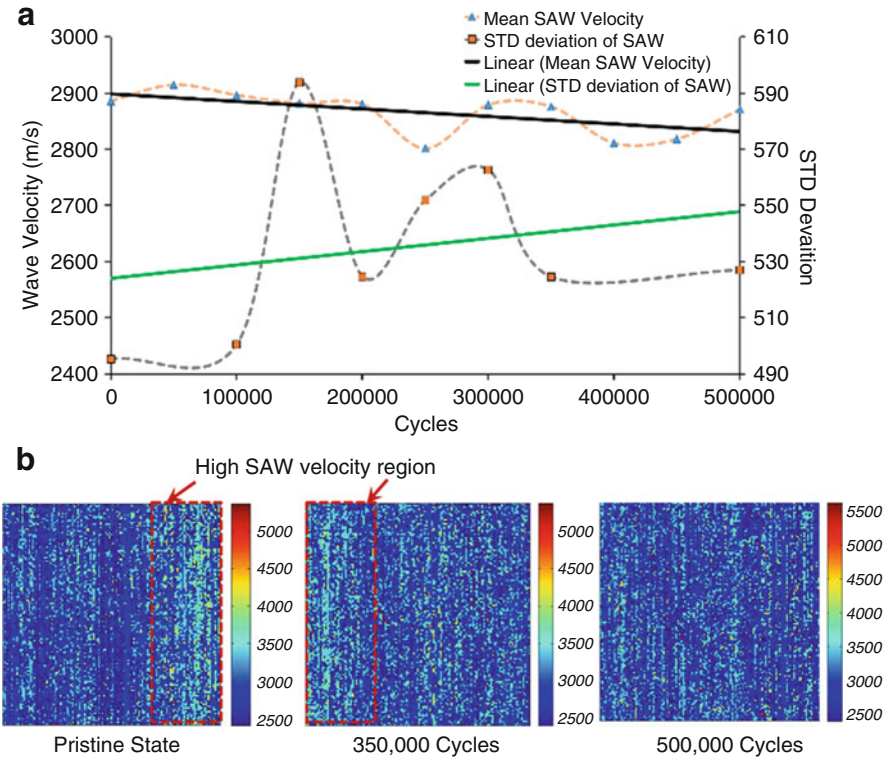

Fig. 15.18 (**a**) Statistical analyses of the SAW velocity profile and variation of Mean and Standard deviation of SAW with cycles. (**b**) SAW velocity profile on Area-B at pristine state, after 350,000 cycles and 500,000 cycles

15.6.5 Damage Characterization Using Optical Microcopy: Verification

Optical microscopy imaging was performed on the composite specimens to examine the development of micro-cracks inside the specimens as it was hypothesized many times throughout this chapter. At the pristine state, very few damages were present in the form of local voids as manufacturing defects in the specimens (max. Size $\sim \pm 5$ μm). However, it is evident from the microscopy images that the density of microstructural damages increased due to the fatigue loading. Matrix cracking, fiber breakage, and localized interlaminar delamination are observed at the end of ~160,000 and ~300,000 cycles. Average size of the matrix-cracks was observed close to ~224 μm. Large-scale damages such as edge delamination were not observed in the specimens. To investigate the development of precursor damages across the width, at the end of 300,000 cycles specimen S-A was decommissioned and was cut at three locations (Fig. 15.19), carefully using waterjet machine. Face A,

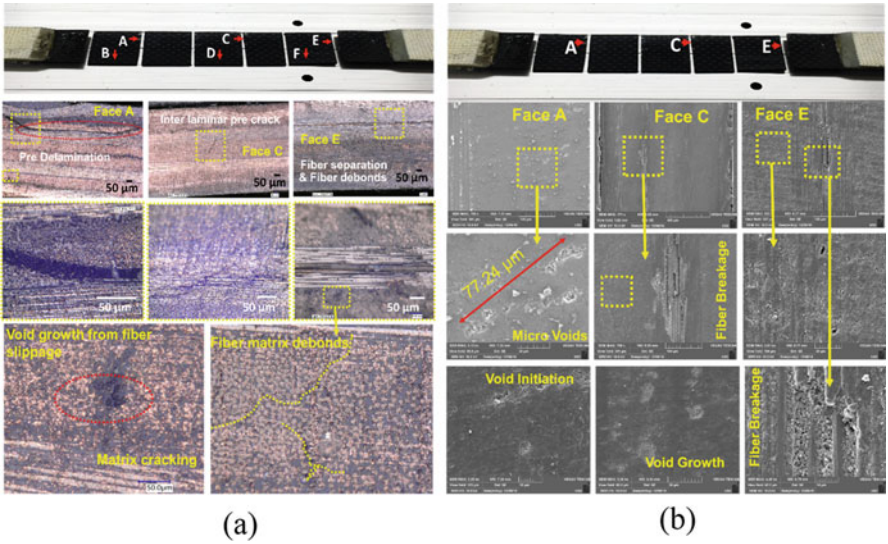

Fig. 15.19 (**a**) Optical microscopy images of the decommissioned specimen S-A at the end of 300,000 cycles; (**b**) scanning electron microscopy (SEM) images from the decommissioned specimen S-A after 300, 000 cycles of fatigue loading [136, 137]

B, and C, then were grinded up to 3 mm by using P1200 sand paper. Afterwards, all faces were polished with P2400 sandpaper to get a smooth surface. Predelamination, fiber separation and fiber debond, void growth from fiber slippage, and interlaminar delamination crack joining two adjacent matrix cracks are evident in specimen S-A (Fig. 15.19).

15.6.6 Damage Characterization Using Scanning Electron Microscope (SEM)

Face A, C, and E were further investigated using SEM VEGA3 TESCAN and a summary of our findings is presented in Fig. 15.19. Multiple sites of void initiation, fiber breakage, and void growth were identified and they confirm the findings from the benchmark studies.

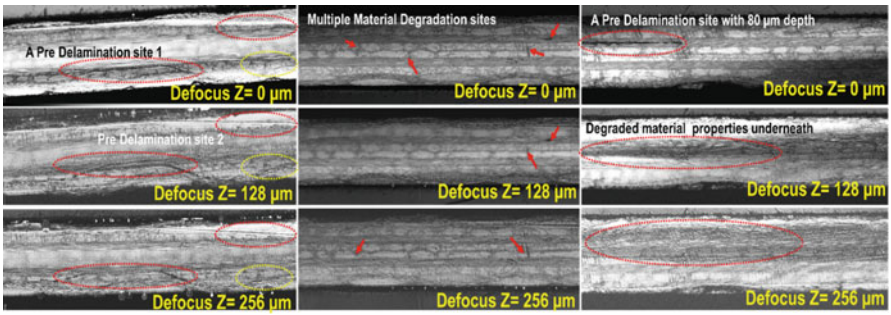

Fig. 15.20 SAM images from the decommissioned specimen S-A after 300,000 cycles of fatigue loading [136, 137]

15.6.7 Damage Characterization from Scanning Acoustic Microscopy

Scanning acoustic microscopy (SAM) imaging was performed on the specimen to investigate the damage developments on the surface as well as inside the specimens which were not accessible by the optical microscopy. SAM C-scans were performed using high-resolution ∼100-MHz ultrasonic transducer at three defocused distances (Fig. 15.20) at three locations identified as Face A, C, and E. Matrix cracking was clearly visible on the surface of the specimens. Couple of predelamination sites were observed. Additionally, degraded material properties were observed beneath the predelamination site. Multiple immature interlaminar delamination track was observed joining two matrix cracks or matrix fiber debond tracks.

15.7 Conclusions

Objective of this chapter was to present the applicability of a new precursor damage detection method using both high- and low-frequency ultrasonic methods, which makes the process multiscale. In high-frequency ($\sim > 25$ MHz) range, QUIC is presented using SAM while hybrid with nonlocal mechanics of materials. A detailed mathematical description and an experimental process is described. To demonstrate the applicability of the process, SAM was used to measure quasi-longitudinal (QL) wave velocity on the gage sections of the specimen and nonlocal parameters were calculated from the dispersion curve obtained from nonlocal Christoffel equation. Damage growth was quantified by a suitable parameter called NLDE. Continuum damage index (CDI) across the thickness of the specimen was also quantified by stiffness-degradation method. Cumulative damage growth was plotted with the number of fatigue cycle. Quasi-longitudinal wave velocities are measured on the surface of the specimen at the interval of 10,000 cycles until

300,000 cycles. Probability distribution of the wave velocities over the specimen was plotted at pristine state and at the end of ∼110,000 cycles. Significant changes in the distribution with shift in mean and standard deviation were observed due to the precursor damage development. In the low-frequency ($\leq$1 MHz) range, Guided CWI is presented to demonstrate the possibility of detecting precursor damage. The proposed modified CWI created an opportunity to reliably detect precursor damage state in the materials, which was validated via multiple other benchmark studies which shows practical state of the materials through images and quantified material state data. A detailed study with seven woven fiber composite specimens that are tested under high-cycle low-load (HCLL) fatigue loading is presented to study the progressive precursor damage inside the specimen within their 30% of life calculated to be ∼300,000 cycles. The modified CWI technique based on stretching method was used for the first time for damage detection and quantification in composite material under fatigue loading. Damage growth from both CWI- and SAM-based techniques is correlated further. It was identified that whenever there has been a change in the sign of the stretch parameters (in the coda wave) from positive to negative or from negative to positive followed by immediate positive stretch or negative stretch, respectively, is the indication of the precursor damage in the specimen. This statement is thoroughly validated and proved by the results obtained from our other studies like QUIC, and benchmark studies on optical microscopy and SEM. This unique blend of methods at multiple length scales and the consistent phenomena that was observed will help devise new damage detection algorithm for online precursor damage detection and quantification.

Acknowledgments The research was partially funded by NASA, Contract No. NNL15AA16C and ASPIRE-I grant supported by Office of Vice President of Research at the University of South Carolina, grant no. 15540-E422. Author thanks the PVATepla, Germany for providing valuable inputs and know how on the SAM scanning procedures.

References

1. J.-B. Donnet, R.C. Bansal, *Carbon Fibers* (CRC Press, Boca Raton, 1998)
2. A. Miller, The Boeing 787 Dreamliner, in *Keynote Address, 22nd American Society for Composites Technical Conference* (2007)
3. W.G. Roeseler, et al., Composite structures: The first 100 years. in *16th International Conference on Composite Materials* (2007)
4. J. Bell, *Condition Based Maintenance Plus DoD Guidebook* (DoD, Washington, DC, 2008)
5. A.K. Jardine, D. Lin, D. Banjevic, A review on machinery diagnostics and prognostics implementing condition-based maintenance. Mech. Syst. Signal Process. **20**(7), 1483–1510 (2006)
6. A. Hall, I.V. Brennan, A. Ghoshal, et al., in *Report for the US Army Research Laboratory*. Damage precursor investigation of fiber-reinforced composite materials under fatigue loads (US Army Research Laboratory, Aberdeen, 2013)
7. Reifsnider, K.L. and S.W. Case, Damage tolerance and durability of material systems. Damage Tolerance and Durability of Material Systems, by Kenneth L. Reifsnider, Scott W. Case, pp. 435. ISBN 0-471-15299-4. Wiley-VCH, Hoboken, 2002

8. S. Banerjee, X.P. Qing, S. Beard, F.K. Chang, Statistical damage estimation at hot spots using gaussian mixture model. *IWSHM* (2009)
9. S. Banerjee, Estimation of damage sate in materials using nonlocal perturbation: Application to active health monitoring. J. Intell. Mater. Syst. Struct. **20**(10), 1221–1232 (2009)
10. B. Piascik, J. Vickers, D. Lowry, S. Scotti, J. Stewart, A. Calomino, *DRAFT Materials, Structures, Mechanical Systems, and Manufacturing Roadmap, Technology Area 12*, ed. by N.A.a.S.A. (NASA) (2010)
11. D. Stargel, E. Tueget, Condition based maintenance plus structural integrity, in *AFOSR Structural Health Monitoring Workshop* (Covington, KY, 2008)
12. S.W. Tsai, E.M. Wu, A general theory of strength for anisotropic materials. J. Compos. Mater. **5**(1), 58–80 (1971)
13. H.T. Hahn, Nonlinear behavior of laminated composites. J. Compos. Mater. **7**(2), 257–271 (1973)
14. H.T. Hahn, S.W. Tsai, Nonlinear elastic behavior of unidirectional composite laminae. J. Compos. Mater. **7**(1), 102–118 (1973)
15. Z. Hashin, Failure criteria for unidirectional Fiber composites. J. Appl. Mech. **47**(2), 329–334 (1980)
16. J.D. Lee, Three dimensional finite element analysis of layered fiber-reinforced composite materials. Comput. Struct. **12**(3), 319–339 (1980)
17. K.N. Shivakumar, W. Elber, W. Illg, Prediction of low-velocity impact damage in thin circular laminates. AIAA J. **23**(3), 442–449 (1985)
18. F.-K. Chang, K.-Y. Chang, Post-failure analysis of bolted composite joints in tension or shear-out mode failure. J. Compos. Mater. **21**(9), 809–833 (1987)
19. F.-K. Chang, K.-Y. Chang, A progressive damage model for laminated composites containing stress concentrations. J. Compos. Mater. **21**(9), 834–855 (1987)
20. J. Engblom, J.J. Havelka, Transient response predictions for transversely loaded laminated composite plates. *30th Structures, Structural Dynamics and Materials Conference* (American Institute of Aeronautics and Astronautics, Reston, 1989)
21. H.Y. Choi, H.-Y.T. Wu, F.-K. Chang, A new approach toward understanding damage mechanisms and mechanics of laminated composites due to low-velocity impact: Part II—Analysis. J. Compos. Mater. **25**(8), 1012–1038 (1991)
22. M.-H.R. Jen, Y.S. Kau, J.M. Hsu, Initiation and propagation of delamination in a centrally notched composite laminate. J. Compos. Mater. **27**(3), 272–302 (1993)
23. S. Liu, Z. Kutlu, F.-K. Chang, Matrix cracking-induced delamination propagation in graphite/epoxy laminated composites due to a transverse concentrated load. *in Comp Materials: Fatigue and Fracture, Fourth Volume,* ed. by W.W. Stinchcomb, N.E. Ashbaugh, vol. 1156 of ASTM STP: pp. 86–101 (American Society for Testing and Materials, Philadelphia, 1993)
24. G.A.O. Davies, X. Zhang, Impact damage prediction in carbon composite structures. Int. J. Impact Eng. **16**(1), 149–170 (1995)
25. R.M. Jones, *Mechanics of Composite Materials* (CRC Press, Boca Raton, 1999)
26. J.P. Hou, N. Petrinic, C. Ruiz, A delamination criterion for laminated composites under low-velocity impact. Compos. Sci. Technol. **61**(14), 2069–2074 (2001)
27. L. Iannucci, Progressive failure modelling of woven carbon composite under impact. Int. J. Impact Eng. **32**(6), 1013–1043 (2006)
28. Y. Mi, M.A. Crisfield, G.A.O. Davies, H.B. Hellweg, Progressive delamination using interface elements. J. Compos. Mater. **32**(14), 1246–1272 (1998)
29. M. Chen, A.J. Crisfield, E.P. Kinloch, F.L. Busso, Y. Matthews, J. Qiu, Predicting progressive delamination of composite material specimens via interface elements. Mech. Compos. Mater. Struct. **6**(4), 301–317 (1999)
30. R. Wisnom, R. Michael, F.-K. Chang, Modelling of splitting and delamination in notched cross-ply laminates. Compos. Sci. Technol. **60**(15), 2849–2856 (2000)
31. C. Soutis, P.T. Curtis, A method for predicting the fracture toughness of CFRP laminates failing by fibre microbuckling. Compos. A: Appl. Sci. Manuf. **31**(7), 733–740 (2000)

32. C. Soutis, F.C. Smith, F.L. Matthews, Predicting the compressive engineering performance of carbon fibre-reinforced plastics. Compos. A: Appl. Sci. Manuf. **31**(6), 531–536 (2000)
33. V.J. Hawyes, P.T. Curtis, C. Soutis, Effect of impact damage on the compressive response of composite laminates. Compos. A: Appl. Sci. Manuf. **32**(9), 1263–1270 (2001)
34. Y. Zhuk, I. Guz, C. Soutis, Compressive behaviour of thin-skin stiffened composite panels with a stress raiser. Compos. Part B **32**, 696–709 (2001)
35. P.P. Camanho, C.G. Davila, *Mixed-Mode Decohesion Finite Elements for the Simulation of Delamination in Composite Materials*. NASA/TM-2002-211737 (2002)
36. L.M. Kachanov, Time of the rupture process under creep conditions. Izv. Akad. Nauk. SSR Otd. Tech. Nauk **8**, 26–31 (1958)
37. Y. Rabotnov, Creep rupture. *Proceedings of the12th International Congress of Applied Mechanics* (1968)
38. R. Vaziri, M. Olson, D. Anderson, Damage in composites: A plasticity approach. Comput. Struct. **44**, 103–116 (1992)
39. O. Allix, P. Ladevèze, Interlaminar interface modelling for the prediction of delamination. Compos. Struct. **22**(4), 235–242 (1992)
40. P. Ladeveze, E. LeDantec, Damage modelling of the elementary ply for laminated composites. Compos. Sci. Technol. **43**(3), 257–267 (1992)
41. A. Matzenmiller, J. Lubliner, R.L. Taylor, A constitutive model for anisotropic damage in fiber-composites. Mech. Mater. **20**(2), 125–152 (1995)
42. A.F. Johnson, Modelling fabric reinforced composites under impact loads. Compos. A: Appl. Sci. Manuf. **32**(9), 1197–1206 (2001)
43. A.F. Johnson, A.K. Pickett, P. Rozycki, Computational methods for predicting impact damage in composite structures. Compos. Sci. Technol. **61**(15), 2183–2192 (2001)
44. K.V. Williams, R. Vaziri, Application of a damage mechanics model for predicting the impact response of composite materials. Comput. Struct. **79**(10), 997–1011 (2001)
45. P.P. Camanho, C.G. Davila, *Physically Based Failure Criteria for FRP Laminates in Plane Stress.* NASA-TM (2003)
46. P. Ladevèze, G. Lubineau, On a damage mesomodel for laminates: Micromechanics basis and improvement. Mech. Mater. **35**(8), 763–775 (2003)
47. P. Ladevèze, G. Lubineau, in *Science and Technology of the Fatigue Response of Fibre-Reinforced Plastics. Section a Computational Meso-Damage Model for Life Prediction for Laminates*, ed. by B. Harris. Fatigue in composites (Woodhead Publishing/CRC Press, Sawston\Boca Raton, 2003)
48. K.V. Williams, R. Vaziri, A. Poursartip, A physically based continuum damage mechanics model for thin laminated composite structures. Int. J. Solids Struct. **40**(9), 2267–2300 (2003)
49. J. Lemaitre, R. Desmorat, *Engineering Damage Mechanics, Ductile, Creep, Fatigue and Brittle Failures* (Springer, The Netherlands, 2005)
50. S.T. Pinho, L. Iannucci, P. Robinson, Physically-based failure models and criteria for laminated fibre-reinforced composites with emphasis on fibre kinking: Part I: Development. Compos. A: Appl. Sci. Manuf. **37**(1), 63–73 (2006)
51. S.T. Pinho, L. Iannucci, P. Robinson, Physically based failure models and criteria for laminated fibre-reinforced composites with emphasis on fibre kinking. Part II: FE implementation. Compos. A: Appl. Sci. Manuf. **37**(5), 766–777 (2006)
52. M.V. Donadon, L. Iannucci, B.G. Falzon, J.M. Hodgkinson, S.F.M. de Almeida, A progressive failure model for composite laminates subjected to low velocity impact damage. Comput. Struct. **86**(11–12), 1232–1252 (2008)
53. M.V. Donadon, S.F.M. De Almeida, M.A. Arbelo, A.R. de Faria, *A Three-dimensional ply failure model for composite structures*. Int. J. Aerosp. Eng. **2009**, 22 (2009)
54. P. Ladevèze, G. Lubineau, On a damage mesomodel for laminates: Micro–meso relationships, possibilities and limits. Compos. Sci. Technol. **61**(15), 2149–2158 (2001)
55. P. Ladevèze, A. Nouy, On a multiscale computational strategy with time and space homogenization for structural mechanics. Comput. Methods Appl. Mech. Eng. **192**(28–30), 3061–3087 (2003)

56. D.H. Allen, Damage Evolution in Laminates. ed. By R. Talreja. *Damage Mechanics of Composite Materials* (Elsevier: Amsterdam, 1994), pp. 79–114
57. M.L. Phillips, C. Yoon, D.H. Allen, A computational model for predicting damage evolution in laminated composite plates. J. Eng. Mater. Technol. **21**, 436–444 (1999)
58. K.L. Reifsnider, W. Scott, *Damage Tolerence and Durability in Material Systems* (Wiley-Interscience, New York, 2002)
59. R.M. Haj-Ali, A.H. Muliana, A multiscale constitutive framework for the nonlinear analysis of laminated composite materials and structures. Int. J. Solids Struct. **41**(3), 3461–3490 (2004)
60. L.N. McCartney, G.A. Schoeppner, in *Multiscale Modelling of Composite Material Systems: The Art of Predictive Damage Modelling*, ed. by C. Soutis, P. W. R. Beaumont. Multiscale predictive modelling of cracking in laminated composites (Woodhead Publishing, Cambridge, 2005), pp. 65–98
61. C. Soutis, P. W. R. Beaumont (eds.), *Multiscale Modelling of Composite Material Systems: The Art of Predictive Damage Modelling* (Woodhead Publishing, Cambridge, 2005)
62. P.C. Andia, F. Costanzo, G.L. Gray, A classical mechanics approach to the determination of the stress-strain response of particle systems. Model. Simul. Mater. Sci. Eng. **14**, 741–757 (2006)
63. R. Talreja, Damage analysis for structural integrity and durability of composite materials. Fatigue Fract. Eng. Mater. Struct. **29**, 481–506 (2006)
64. S. Ghosh, in Aduptive concurrent multi-level model for multiscale analysis of composite materials including damage, eds. By Y.W. Kwon, D.H. Allen, R. Talreja. Multiscale Modeing and Simulation of Composite Materials and Structures (Springer, New York, 2008)
65. Y. W. Kwon, D. H. Allen, R. Talreja (eds.), *Multiscale Modeling and Simulation of Composite Materials and Structures* (Springer, New York, 2008)
66. D.J. Bernard, G. Dace, O. Buck, Acoustic harmonic generation due to thermal Embrittlement of Inconel 718. J. Nondestruct. Eval. **16**, 67–75 (1997)
67. J.L. Blackshire et al., in Nonlinear Laser Ultrasonic Measurements of Localized Fatigue Damage, eds. By D.O. Thompson, D.E. Chimenti. *Review of Progress in QNDE* (*Quantitative Nondestructive Evaluation*) (Springer, New York, 1998). pp. 1479–1488
68. G.E. Dieter, *Mechanical Metallurgy* (McGraw Hill, London, 1998)
69. P.B. Nagy, Fatigue damage assessment by nonlinear ultrasonic materials characterization. Ultrasonics **36**(1–5), 375–381 (1998)
70. B. Otto, in Fatigue Damage and its Nondestructive Evaluation: An Overview, eds. By D.O. Thompson, D.E. Chimenti. *Review of Progress in Quantitative Nondestructive Evaluation* (Springer, New York, 1998). p. 1
71. Q.Y. Wang et al., Fatigue Fract. Eng. Mater. Struct. **22**, 673 (1999)
72. Y. Zeng, R.G. Maev, I.Y. Solodov, Nonlinear acoustic applications for material characterization: A review. Can. J. Phys. **77**, 927–967 (1999)
73. J. Herrmann et al., Assessment of material damage in a Nickel-Base superalloy using nonlinear Rayleigh surface waves. J. Appl. Phys. **99**(12), 124913–124920 (2006)
74. S. Hirsekorn, U. Rabe, W. Arnold, Characterization and evaluation of composite laminates by nonlinear ultrasonic transmission measurements, in *European Conference on Non-destructive Testing*, France, 2006
75. M. Deng, J. Pei, Assessment of accumulated fatigue damage in solid plates using nonlinear lamb wave approach. Appl. Phys. Lett. **90**, 121902 (2007)
76. H.A. Bruck, S.R. McNeill, M.A. Sutton, W.H. Peters III, Digital image correlation using Newton-Raphson method of partial differential correction. Exp. Mech. **29**(3), 261–267 (1989)
77. T.C. Chu, W.F. Ranson, M.A. Sutton, Applications of digital-image-correlation techniques to experimental mechanics. Exp. Mech. **25**(3), 232–244 (1985)
78. N. McCormick, J. Lord, Digital image correlation. Mater. Today **13**(12), 52–54 (2010)
79. S.A. Adelman, J.D. Doll, Generalized Langevin equation approach for atom/solid-surface scattering: General formulation for classical scattering off harmonic solids. J. Chem. Phys. **64**, 2375–2388 (1976)

80. F.F. Abraham et al., Spanning the continuum to quantum length scales in a dynamic simulation of brittle fracture. Europhys. Lett. **44**(6), 783–787 (1998)
81. F.F. Abraham, H. Gao, How fast can cracks propagate? Phys. Rev. Lett. **84**(14), 3113–3116 (2000)
82. T. Belytsckko, S.P. Xiao, Coupling methods for continuum model with molecular model. Int. J. Multiscale Com. Eng. **1**, 115–126 (2003)
83. R.B. Lechoucq, S.A. Silling, Peridynamic theory for solid mechanics. Adv. Appl. Mech. **44**, 73–168 (2010)
84. A.C. Egingen, D.G.B. Edelen, On nonlocal elasticity. Int. J. Eng. Sci. **10**, 233–248 (1972)
85. A.C. Eringen, *Developments of Mechanics*, vol 3 (Wiley, New York, 1965)
86. A.C. Eringen, *Mechanics of Continua* (Wiley, Hoboken, 1967)
87. A.C. Eringen, Continuum mechanics at the atomic scale. Crystal Lattice Defects **7**, 109–130 (1977)
88. A.C. Eringen, On differential equations of nonlocal elasticity and solution of skew dislocation and surface waves. J. Appl. Phys. **54**(9), 4703–4710 (1983)
89. A.C. Eringen, *Nonlocal Continuum Field Theories* (Springer, New York, 2002)
90. R.O. Mindlin, Micro-structure in linear elasticity. Arch. Ration. Mech. Anal. **16**, 51 (1964)
91. R.A. Toupin, Elastic materials with couple-stresses. Arch. Ration. Mech. Anal. **11**, 385 (1962)
92. E. Cosserat, F. Cosserat, *Theories des Corps Deformables* (Hermann, Paris, 1909)
93. S. Banerjee, R. Ahmed, Precursor/incubation of damage state quantification using hybrid microcontinuum approach and high frequency ultrasonic. IEEE Trans. Ultrason. Ferroelectr. Freq. Control **60**(6), 1141–1151 (2013)
94. G.A.D. Briggs, O.V. Kolosov, *Acoustic Microscopy*, 2nd edn. (Oxford University Press, New York, 2010)
95. E. Drescher-Krasicka, J.R. Wilis, Mapping stress with ultrasound. Nature **384**, 52–55 (1996)
96. T. Kundu, Inversion of acoustic material signature of layered solids. J. Acoustic. Soc. Am. **91**(2), 591–600 (1992)
97. M. Nishida, T. Endo, T. Adachi, H. Matsumoto, Measurement of local elastic moduli by magnitude and phase acoustic microscope. NDT&E Int. **30**(5), 271–277 (1997)
98. P. Zinin, W. Weise, in Theory and Applications of Acoustic Microscopy, ed. By T. Kundu. *Ultrasonic Nondestructive Evaluation, Engineering and Biological Material Characterization* (CRC Press, Boca Raton, 2004)
99. S. Banerjee, R. Ahmed, Precursor/incubation of multi-scale damage state quantification in composite materials: Using hybrid microcontinuum field theory and high-frequency ultrasonics. IEEE Trans. Ultrason. Ferroelectr. Freq. Control **60**(6), 1141–1151 (2013)
100. S. Yadav, S. Banerjee, T. Kundu, On sequencing the feature extraction techniques for online damage characterization. J. Intell. Mater. Syst. Struct. **24**, 473–483 (2013)
101. A.C. Eringen, On differential equations of nonlocal elasticity and solutions of screw dislocation and surface waves. J. Appl. Phys. **54**(9), 4703–4710 (1983)
102. A. Shelke et al., Multi-scale damage state estimation in composites using nonlocal elastic kernel: An experimental validation. Int. J. Solids Struct. **48**(7–8), 1219–1228 (2011)
103. S.A. Silling, Reformulation of elasticity theory for discontinuities and long-range forces. J. Mech. Phys. Solids **48**(1), 175–209 (2000)
104. Z.P. Bazant, M. Jirásek, Nonlocal integral formulations of plasticity and damage: Survey of progress. J. Eng. Mech. **128**(11), 1119–1149 (2002)
105. F. Bobaru, S.A. Silling, Peridynamic 3D models of nanofiber networks and carbon nanotube-reinforced composites. in *Materials Processing and Design: Modeling, Simulation and Applications-NUMIFORM 2004-Proceedings of the 8th International Conference on Numerical Methods in Industrial Forming Processes* (AIP Publishing, Melville, 2004)
106. B. Kilic, A. Agwai, E. Madenci, Peridynamic theory for progressive damage prediction in center-cracked composite laminates. Compos. Struct. **90**(2), 141–151 (2009)
107. B. Kilic, E. Madenci, Structural stability and failure analysis using peridynamic theory. Int. J. Nonlin. Mech. **44**(8), 845–854 (2009)

108. M. Lazar, G.A. Maugin, E.C. Aifantis, On a theory of nonlocal elasticity of bi-Helmholtz type and some applications. Int. J. Solids Struct. **43**(6), 1404–1421 (2006)
109. L. Brillouin, *Wave Propagation in Periodic Structures* (Dover Publications, USA, 1953)
110. A. Chakraborty, Wave propagation in anisotropic media with non-local elasticity. Int. J. Solids Struct. **44**(17), 5723–5741 (2007)
111. R.C. Picu, On the functional form of non-local elasticity kernels. J. Mech. Phys. Solids **50**(9), 1923–1939 (2002)
112. W. Weise, P. Zinin, A. Briggs, T. Wilson, S. Boseck, Examination of the two dimensional pupil function in coherent scanning microscopes using spherical particles. J. Acoustic. Soc. Am. **104**, 181–191 (1998)
113. T. Kundu, J. Bereiter-Hahn, I. Karl, Cell property determination from the acoustic microscope generated voltage versus frequency curves. Biophys. J. **78**, 2270–2279 (2000)
114. M. Gresil, V. Giurgiutiu, Prediction of attenuated guided waves propagation in carbon fiber composites using Rayleigh damping model. J. Intell. Mater. Syst. Struct. **26**(16), 2151–2169 (2015)
115. B. Hosten, M. Castaings, T. Kundu, in Identification of Viscoelastic Moduli of Composite Materials from the Plate Transmission Coefficients Review of Progress, eds. By D.E. Chimenti, D.E. Thompson. *Quantitative Nondestructive Evaluation*, Vol. 17. (Plenum Press, New York, 1998)
116. P. Marguères, F. Meraghni, Damage induced anisotropy and stiffness reduction evaluation in composite materials using ultrasonic wave transmission. Compos. A: Appl. Sci. Manuf. **45**(0), 134–144 (2013)
117. R. Snieder, H. Douma, in Coda Wave Interferometry. *2004 McGraw-Hill Yearbook of Science and Technology*, Vol. 54 (McGraw-Hill, New York, 2004)
118. R. Snieder, The theory of coda wave interferometry. Pure Appl. Geophys. **163**(2-3), 455–473 (2006)
119. E. Larose, S. Hall, Monitoring stress related velocity variation in concrete with a $2\times 10-5$ relative resolution using diffuse ultrasound. J. Acoust. Soc. Am. **125**(4), 1853–1856 (2009)
120. D.P. Schurr et al., Damage detection in concrete using coda wave interferometry. NDT&E Int. **44**(8), 728–735 (2011)
121. T. Planès, E. Larose, A review of ultrasonic coda wave interferometry in concrete. Cem. Concr. Res. **53**, 248–255 (2013)
122. R. Snieder et al., Coda wave interferometry for estimating nonlinear behavior in seismic velocity. Science **295**(5563), 2253–2255 (2002)
123. M. Fehler, P. Roberts, T. Fairbanks, A temporal change in coda wave attenuation observed during an eruption of Mount St. Helens. J. Geophys. Res. Solid Earth **93**(B5), 4367–4373 (1988)
124. A. Grêt, R. Snieder, U. Özbay, Monitoring in situ stress changes in a mining environment with coda wave interferometry. Geophys. J. Int. **167**(2), 504–508 (2006)
125. D. Pandolfi, C. Bean, G. Saccorotti, Coda wave interferometric detection of seismic velocity changes associated with the 1999 M= 3.6 event at Mt. Vesuvius. Geophys. Res. Lett. **33**(6), L06306 (2006)
126. C. Sens-Schönfelder, U. Wegler, Passive image interferometry and seasonal variations of seismic velocities at Merapi volcano, Indonesia. Geophys. Res. Lett. **33**(21), L21302 (2006)
127. M.M. Haney et al., Observation and modeling of source effects in coda wave interferometry at Pavlof volcano. Lead. Edge **28**(5), 554–560 (2009)
128. F. Martini et al., Seasonal cycles of seismic velocity variations detected using coda wave interferometry at Fogo volcano, São Miguel, Azores, during 2003–2004. J. Volcanol. Geotherm. Res. **181**(3), 231–246 (2009)
129. O. Abraham, et al., Monitoring of a large cracked concrete sample with non-linear mixing of ultrasonic coda waves. in *EWSHM-7th European Workshop on Structural Health Monitoring* (2014)
130. E. Niederleithinger, et al., Coda Wave Interferometry used to localize compressional load effects in a concrete specimen. in *EWSHM-7th European Workshop on Structural Health Monitoring* (2014)

131. Y. Zhang et al., Study of stress-induced velocity variation in concrete under direct tensile force and monitoring of the damage level by using thermally-compensated coda wave interferometry. Ultrasonics **52**(8), 1038–1045 (2012)
132. G. Poupinet, W. Ellsworth, J. Frechet, Monitoring velocity variations in the crust using earthquake doublets: An application to the Calaveras Fault, California. J. Geophys. Res. Solid Earth **89**(B7), 5719–5731 (1984)
133. C. Payan et al., Determination of third order elastic constants in a complex solid applying coda wave interferometry. Appl. Phys. Lett. **94**(1), 011904 (2009)
134. Y. Zhang et al., Diffuse ultrasound monitoring of stress and damage development on a 15-ton concrete beam. J. Acoust. Soc. Am. **139**(4), 1691–1701 (2016)
135. S. Liu et al., A novel coda wave interferometry calculation approach using Taylor series expansion, in *International Workshop on Structural Health Monitoring* (Stanford, Palo Alto, CA 2015)
136. S. Patra, S. Banerjee, Material State Awareness for Composite Part II: Precursor Damage Analysis and Quantification of Degraded Material Properties Using Quantitative Ultrasonic Image Correlation (QUIC), Material, Vol. 10(12), pp. 1444 (2017)
137. S. Patra, S. Banerjee, Material State Awareness for Composite Part I: Precursor Damage Analysis Using Ultrasonic Guided Coda Wave Interferometry (CWI), Material, Vol. 10(12), pp. 1436 (2017)
138. D. Astm, *3039/D 3039M. Standard Test Method for Tensile Properties of Polymer Matrix Composite Materials* (2000)

Chapter 16
Anharmonic Interactions of Probing Ultrasonic Waves with Applied Loads Including Applications Suitable for Structural Health Monitoring

Julian Grill and Wolfgang Grill

16.1 Introduction

As illustrated by the articles of this book, a substantial fraction of ultrasonic techniques for NDE or NDT involves the observation of anharmonic effects. Early developments can already be identified in 1965 [1]. Currently ultrasound at sufficiently high power levels is usually employed such that frequency doubling or additive and subtractive wave mixing and in some cases even higher order effects can be observed and employed [2]. In Table 16.1 this well-established scenario is demonstrated in a simplified scheme.

Heterodyning of monitored signals at sum and difference frequencies with f_1 (Table 16.1, generalized case) can be employed to convert the respective frequencies to f_2. For sufficiently small f_2 the obtained frequencies can be near zero. This case is usually addressed as homodyning where the center frequency for excitation f_1 is used as reference. It is a well-established technique for phase detection including also quadrature detection that delivers the observed signal near f_1 in the complex plane (for quadrature detection in the GHz-regime with high resolution, see [3, 4]). The observed phase shifts relate to rather small frequency shifts.

In anharmonic monitoring and more general in four-wave mixing (FWM) it is often sufficient to use two different input signals. In this case just one of the input signals needs to have sufficiently high magnitude leading to respective power density levels needed to obtain the desired mixing at signal levels that can be securely monitored. The generalized case of FWM is extensively treated for electromagnetic waves (for novel applications, see [5]). It is fortunately also employed for acoustics [6].

J. Grill · W. Grill (✉)
ASI Analog Speed Instruments GmbH, Koenigstein im Taunus, Burgweg 8, Germany
e-mail: jg@analogspeed.de; wg@analogspeed.de

T. Kundu (ed.), *Nonlinear Ultrasonic and Vibro-Acoustical Techniques for Nondestructive Evaluation*, https://doi.org/10.1007/978-3-319-94476-0_16

Table 16.1 Schematic for monitoring of nonlinear interaction of ultrasonic waves

Nonlinear monitoring
Due to nonlinear response the output signal does not vary in direct proportion to the input signal
Special (simple) case of nonlinear monitoring
1 frequency for excitation (monochromatic case)
Let be:
Response to signal A at frequency f_1 = response (A)
Response to signal B at frequency f_1 = response (B)
Observe that:
response (A + B) $\neq$ response (A) + response (B)
2nd order responses appear at frequencies:
$f_1 + f_1 = 2f_1$
and $f_1 - f_1$ = DC (frequency is zero)
(and possible higher order effects)
More general nonlinear monitoring (Four-Wave Mixing, FWM)
2 frequencies for excitation
Let be:
Response to signal A at frequency f_1 = response (A)
Response to signal B at frequency f_2 = response (B)
Observe that:
response (A + B) $\neq$ response (A) + response (B)
2nd order responses appear at frequencies:
$f_1 + f_2$
and $f_1 - f_2$
resulting in two different frequencies (as input frequencies) following nonlinear interaction (and possible higher order effects)

The monitoring schemes presented here allow ultrasonic monitoring with relatively low power levels of the incoming acoustic waves. This constitutes a general advantage for many applications involving sensitive specimen like certain aircraft components that might be damaged by high power ultrasound.

For insight to the scenario of modulation by nonlinear interaction as exemplified here it might be helpful to realize that some similarities between amplitude, frequency, and phase modulation become more pronounced for rather small modulations. All three types of modulations lead to sidebands. This has been nicely pointed out by developers of novel instrumentation for wideband vector detection (note by a member of Zurich Instruments as listed in [7]). The (quote:) "amplitude and (narrow band) frequency modulations have equal Fourier power spectral densities: in fact their Fourier transforms differ by the sign of the sidebands but this disappears when squaring to obtain the power density."

Historically phase monitoring of ultrasonic signals was originally used for the determination of time of flight (TOF) variations with high resolution (for high resolution monitoring avoiding even resonances of the transducers, see [8]). Phase

shifts can be caused by velocity changes or distance variations if the frequency (or in the case of pulsed excitation the spectrum) remains constant. Otherwise similar phase shifts can also be caused by alteration of the frequency (or center frequency for pulsed excitation). In all these three cases the detected signal undergoes a frequency variation, which is necessary to cause any observable phase shift. This can most easily be realized with continuous narrow band excitation when no considerable interferences occur along the path from generation to detection of the propagating acoustic waves including the transducers and the electric transmission of the signals.

It is important to realize the fundamental similarity of the effects of velocity changes, path length variations, and frequency alterations on the observable phase shifts in detected signals. All three types of variations produce frequency shifts as demonstrated in Table 16.1 for anharmonic effects of interacting acoustic waves by FWM including the interaction of mechanical excitations involving acoustic waves. This is especially important for quasi-static modulations with intrinsically small modulation frequencies as present in some of the applications discussed here.

To extend the scenario of acoustic waves to the quasi-static regime one should keep in mind that acoustic waves involve time and space dependent variations of the stress and strain. Also involved are particle velocities, which at fixed magnitudes of the acoustic waves will diminish when approaching the static scenario. The interaction of the monitoring acoustic waves and their accompanying stress and strain variations with quasi-static stress and strain is nevertheless covered by FWM. The necessity to conserve momentum in FWM is in so far simplified, as the quasi-static case relates to intrinsically small momenta of the acoustic waves providing the involved stress and strain. The interaction with the probing ultrasonic waves will therefore only lead to negligible changes in directionality.

Historically the interactions of stress and strain with propagating acoustic waves have been addressed as acoustoelastic effect [9]. Early applications involve the monitoring of tension in bolts as outlined in 1964 by a respective first patent [10]. The underlying principle of stress detection via acoustic oscillations has been realized even earlier as demonstrated by a patent submitted already in 1924 [11]. These early patents have been followed by rapidly progressing developments leading to at least five companies, which currently supply equipment for similar purposes as mentioned in the first patent for monitoring of stress in bolts.

It needs to be mentioned that the observed effects including the acoustoelastic effect have so far been either contributed to tension respectively stress, to deformation respectively strain, or even more general simply to load. Within the linear elastic regime of a materials stress–strain relation may the origin of the observed effects be practically and interchangeably attributed to either of the linear related parameters. This is often the case without further consideration. Only recently has a detailed analysis regarding the individual influences of stress and strain on the propagation of acoustic waves been started [12]. This is of special interest for the nonlinear regime of plastic deformation where stress and strain are not simply linear related and irreversible deformations occur.

Relations between stress and strain represent one of the most elementary forms of materials characterization. They are of essential interest to engineers when evaluating the performance of parts and components under load and during operation. Materials stress–strain relations are commonly determined with standardized samples on universal test machines. Using ultrasonic waves to monitor stress–strain relations of components of machines, cars, aircraft, or other assembled units on the other hand allows the determination of the actual mechanical status and integrity of the monitored part while in use. Besides of the general interest in a better understanding of the underlying physical coupling mechanisms this special goal of interest to mechanical or civil engineers has been a main driving force behind the developments reported here.

Concerning the extension of FWM principles to low frequencies it should be kept in mind that well-established ultrasonic monitoring techniques employed for monitoring of slowly varying transport properties of ultrasound as caused by temperature variations are often based on pulsed excitation and detection with single-ended or double-ended operation of the involved ultrasound transducers. These techniques have already been extended to rather high repetition rates as demonstrated by the monitoring of the modulation of high frequency ultrasound in scanning acoustic microscopy [3, 13]. There the ultrasound is generated with piezoelectric transducers by switched sinusoidal electric fields generated by a monochromatic source. The frequency range is around 1 GHz (0.8–1.2 GHz). Monitoring is conducted with repetition rates of typically 2 MHz allowing a bandwidth for shifts in frequency, in phase, and in magnitude from static to 1 MHz. This is performed by vector detection based on the correlation with sinusoidal functions referenced to the source by analog electronic signal processing. It demonstrates that at least since 1994 the techniques historically involved in quasi-static monitoring have already been extended to bandwidths in the regime of ultrasonic frequencies. Such correlation techniques suitable for high resolution monitoring can therefore be employed to study nonlinear effects by FWM from static to the range of ultrasonic frequencies up to at least 1 MHz.

At sufficiently low frequencies the involved interactions can be separated into contributions originating from stress or strain. Therefore, a theoretical section starting with a description of quasi-static coupling follows the introduction. This is ensued by the presentation of monitoring techniques and by the demonstration of respective experimental results. Finally some more general applications are presented to inform about the range of applications for the developed monitoring schemes.

16.2 Basic Theoretical Background and Modeling

The origin of the influence of stress on the propagation of acoustic waves can most easily be demonstrated by modeling of a one-dimensional atomic chain. This has been well established by lattice dynamics (for a novel textbook article, see, for

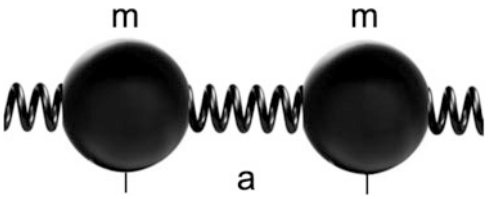

Fig. 16.1 Two elements of a strictly periodic linear chain of mass points, symbolized by spheres, with mass m, positioned at a distance a, and connected by mass free springs with spring constant C or an assumed potential that can also contain higher order terms relating to nonlinear springs

example, [14]). On the other hand, the atomic chain model may also be deemed as a form of finite element modeling, widely used by engineers.

With regard to the discussed patents and applications, and for the sake of simplicity and an easier understanding of the underlying physical effects and coupling mechanism, presentations in this chapter will be strictly confined to the idealized basic conditions of a homogeneous isotropic material experiencing only uniaxial and homogeneously distributed stress and strain, both coaligned with the propagation direction of the probing ultrasound waves.

Treated is a strictly periodic linear chain of mass points connected by mass free springs (Fig. 16.1), which are characterized by their potentials. The potentials can be parabolic to model springs following Hooke's law or they can contain higher order terms relating to nonlinear springs. Historically relevant potentials describing the nonlinear interatomic forces are the Lennard-Jones potential [15] and the Morse-Feshbach potential [16].

The basic features employed in the early patents for the detection of loads in bolts are based on the propagation characteristics of longitudinal acoustic bulk waves [10]. Their transport properties under stress or strain can be modeled by extensional acoustic waves traveling on a chain of point masses also addressed as atomic chain. Similar basic features of flexural acoustic waves traveling on strings, relating to transverse polarized bulk waves as also employed for monitoring of loads in bolts have, for example, been treated by Caamaño-Withall and Krysl [17].

For extensional acoustic waves traveling on a string of point masses with forces between adjoining masses described by a perfect harmonic potential, which can be covered by a mass free spring following Hooke's law with a spring constant C, the velocity of the acoustic waves can easily be equated (see, for example, [18]). In the limit of long wavelengths with respect to the distances between mass points the phase and group velocities are identical. The velocity of extensional acoustic waves v_E is then given by:

$$v_E = a\,(C/m)^{1/2}$$

where a is the distance between mass points with mass m and C the spring constant of the idealized mass free springs following Hooke's law. From this relation follows

that for the time t_a needed under these conditions for an extensional acoustic wave to pass from one point mass to the next:

$$t_a = (m/C)^{1/2}$$

When presuming a harmonic potential C remains constant under extension or compression. Together with the conservation of mass it follows that t_a remains constant and independent of the length of a. The same holds for the time needed to pass over any selected fixed number of adjoining unit cells of the chain.

There are many alternating descriptions in early patents covering the coupling of stress and strain or simply load to propagating longitudinal polarized acoustic waves employed for monitoring. In view of these patents it is important to realize that for assumed harmonic interaction between neighboring mass points or atoms in the material the lengthening of a bolt or screw caused by external forces due to tightening would not affect the time of flight of longitudinal polarized ultrasound used for monitoring. Under the normally given experimental conditions with single- or double-ended monitoring with acoustic waves and glued or otherwise fixated transducers the velocity of extensional acoustic waves v_E will vary under extensional strain, but this effect is fully compensated for the observed TOF by lengthening of the path traveled by the waves.

The model of a chain of mass points respectively atoms as presented above neglects relativistic features. Therefore under elongation or compression the TOF for transport over a fixed number of unit cells via strictly harmonic interactions would only vary according to the speed of light. This relativistic effect is nevertheless way too small to explain the observed coupling coefficients caused by what is historically addressed as acoustomechanical coupling (for an example, see [9]).

As well and long known from thermal expansion, it is the influence of anharmonic forces between adjoining mass points that leads to nonlinear effects as exemplified by the Lennard-Jones potential (Fig. 16.2).

Regarding the coupling effects it now becomes clear that strain affecting the forces between two idealized point masses or atoms in the model via anharmonic potentials must be what induces a variation of TOF. It is the weakening of these interatomic forces under elongation, as described by the Lennard-Jones potential that leads to measurable variations of TOF for longitudinally polarized ultrasonic waves. This is what allows monitoring of loads on bolts either with double-ended operation of ultrasonic transducers fixed to both ends or with single-ended operation of only one transducer observing reflections from the other end.

Besides of the discussed anharmonic potentials affecting the transport properties of transversely polarized acoustic waves leading to an increased TOF under elongation there is also a counteracting effect. It is caused by stress induced flexural rigidity influencing modes with transverse components. This effect is well known from string instruments, where transverse oscillations relating to standing flexural guided acoustic waves will increase in frequency under increasing tensional stress, which is widely used for tuning of musical instruments.

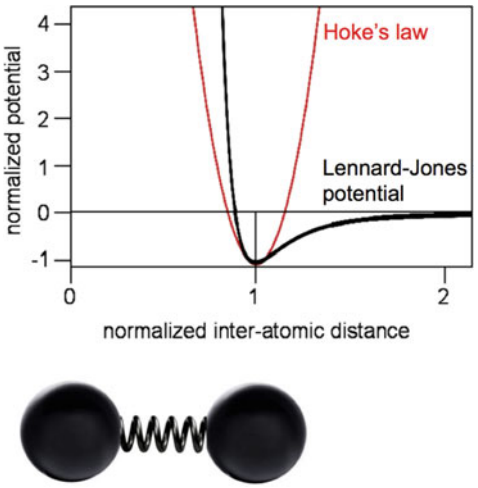

Fig. 16.2 Lennard-Jones potential in comparison to a harmonic potential relating to Hooke's law for interatomic forces with distance normalized to equilibrium conditions and potential normalized to maximum attraction

An idealized string with zero flexural rigidity under complete absence of tensional stress and infinite extensional rigidity even under large stress with a mass density of ρ has a phase velocity of flexural guided acoustic waves v_F under an axial stress of σ of [19]:

$$v_F = (\sigma/\rho)^{1/2}$$

An example of this velocity dependence on stress and density is illustrated in Fig. 16.3 for a string with diminishing flexural stiffness. For the material copper the yield strength is near 345 MPa but depends on thermal treatment.

The discussed different coupling mechanisms allow simultaneous monitoring of both stress and strain by observation of the transport properties of acoustic waves. The influence of strain will predominately affect the propagation of longitudinal polarized acoustic waves including extensional guided waves. The influence of stress will predominantly affect the propagation of flexural guided waves for sufficiently long wavelengths where the influence of rigidity to bending diminishes. Especially suitable modes for monitoring of stress and strain with guided acoustic waves are illustrated in Figs. 16.4 and 16.5.

As calculated with the software DISPERSE provided by the Imperial College, London, the useful range for monitoring of stress and strain is indicated in Fig. 16.5 for the example of a brass rod of 1 mm diameter.

Concerning guided acoustic waves traveling on plates, addressed as Lamb waves, the scenario is not much different as it is for rods fabricated from the same material with identical lateral dimensions. This can be compared in Figs. 16.5 and 16.6.

In Fig. 16.6 v_L represents the dispersion relation of longitudinal polarized bulk waves. v_{2D} relates to the velocity of extensional waves determined by a two-dimensional version of Young's modulus given by the elastic properties for a sideways infinitely extended sheet under otherwise similar conditions. v_T represents

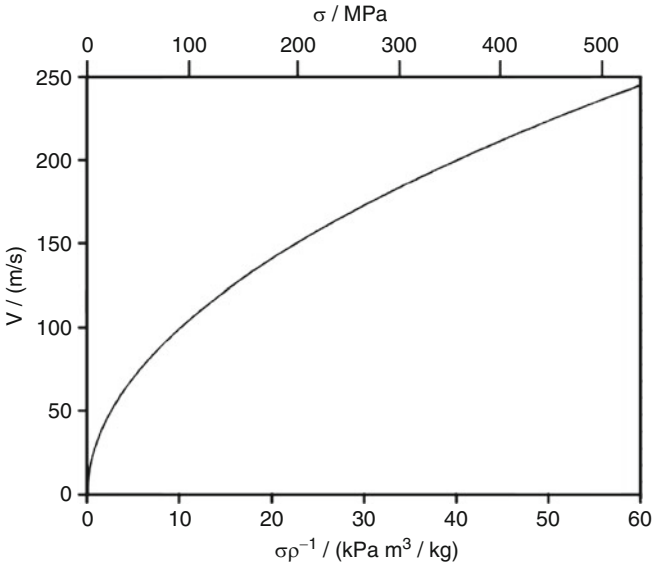

Fig. 16.3 Dependence of the velocity v on σ/ρ of flexural guided acoustic waves traveling on a string with density ρ under tension σ with the upper scale relating to the density of copper

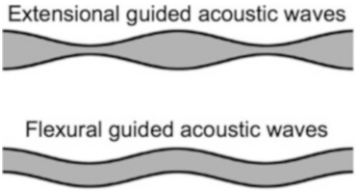

Fig. 16.4 Cross-sectional view of extensional and flexural guided waves traveling on strings or sheets with amplitudes exaggerated for demonstration

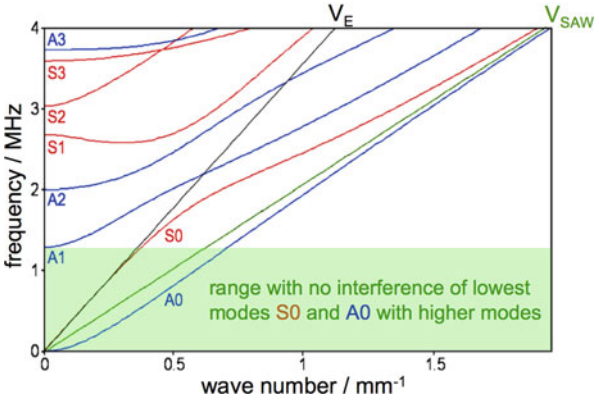

Fig. 16.5 Dispersion relation of guided waves traveling on a 1 mm diameter brass rod for symmetric modes S_i and antisymmetric modes A_i with velocities of surface acoustic waves (SAW; v_{SAW}) and as given by Young's modulus E (v_E), both indicated with lines, representing the asymptotic properties of the guided waves of the lowest branches ($i = 0$) of the symmetric and antisymmetric modes

the dispersion relation of transversely polarized bulk waves and v_{SAW} relates to surface acoustic waves. All these extra displayed dispersion relations are linear within the range displayed in the graph.

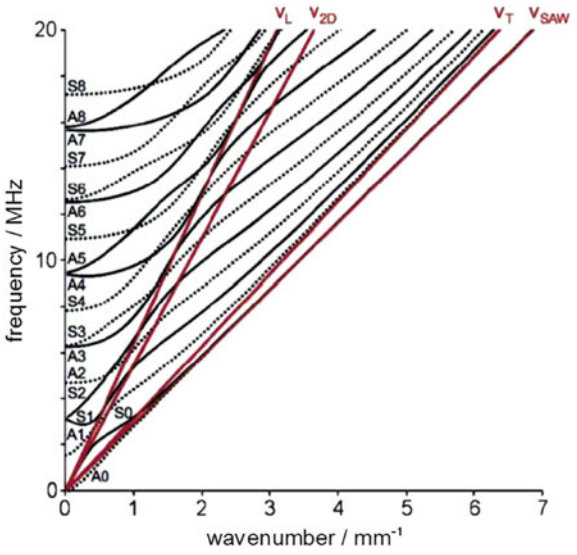

Fig. 16.6 Dispersion relation of guided waves traveling on a 1 mm sheet of brass with lines representing the asymptotic properties of the guided modes of the lowest branches

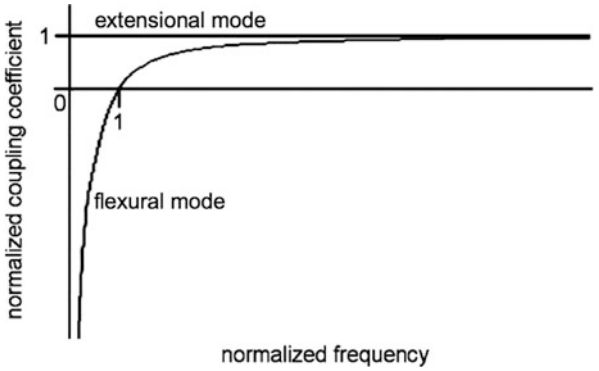

Fig. 16.7 Sketch of the dependence of the acoustoelastic coupling coefficients for extensional and flexural guided acoustic modes. The high frequency asymptotic value and the frequency for the zero crossing of the coefficient for the flexural mode are normalized to 1. The negative vertical axis is also the asymptote of the flexural mode for diminishing frequencies

The expected variations of the coupling coefficients for the lowest modes of guided waves traveling on sheets (Lamb waves) or on rods are sketched in Fig. 16.7.

The zero crossing of the coupling coefficient for the lowest guided antisymmetric mode is to be expected in the frequency regime where this mode changes from the dispersion relation similar to SAW to a parabolic dispersion relation when approaching low frequencies. For the example of a 1 mm diameter brass rod shown in Fig. 16.5 this happens near a wave number of 0.5 mm^{-1}. The actual value

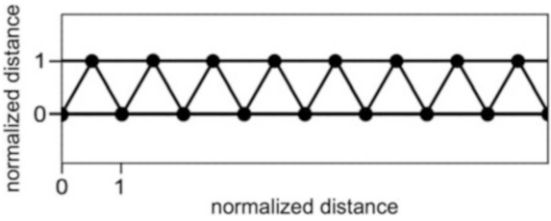

Fig. 16.8 Two-dimensional mesh of mass points illustrated by dots connected with idealized mass free elastic rods only providing axial stiffness

should be determined experimentally since sufficient analytical modeling is not yet available.

To demonstrate that the expected behavior can at least be verified via numeric modeling, a two-dimensional model with a most simple arrangement of mass points connected by idealized mass free elastic rods, which only provide axial stiffness as given by Young's modulus, is represented in Fig. 16.8. This model was employed for modeling of the transport properties of flexural waves with particle velocities in the plane of the image. A chain of mass points as used for demonstration of the influence of stress or strain on extensional waves cannot provide the flexural stiffness required for flexural acoustic waves to be able to propagate in the absence of tensional stress.

The dispersion relations obtained by model calculations for a stress free state and with axial extensional strain, horizontally oriented in Fig. 16.8, are demonstrated in Fig. 16.9. In the stress free state the tangent for diminishing frequency is horizontal indicating a vanishing group velocity. But for long wavelength and propagation under extensional stress the guided flexural waves still propagate with a finite group velocity. This is pointed out by the lines in Fig. 16.9. The grey lines indicate the finite slope in the limit of diminishing frequencies under load in comparison to the maximum group velocity obtained for higher frequencies, which is represented by a dotted line.

Besides of evaluating dispersion relations the modeling also delivers the time dependent distribution of amplitudes for propagating flexural acoustic waves (Fig. 16.10). As it can be deduced from the graphs (Figs. 16.9 and 16.10), extensional stress accompanied by strain affects the dispersion relation and leads to a remarkably increased group velocity of low frequency guided waves traveling on the mesh of point masses. The general scenario obtained by modeling resembles the predictions based on elementary properties as discussed first in this section by rather basic analytic reasoning.

This finalizes the presentation of basic features and modeling for the dependence of the transport properties of acoustic waves on stress or strain under approximate steady-state conditions, relating to the low frequency limit of FWM. The obtained predictions are to be verified by experimental procedures presented next, starting with the experimental set-ups and followed by the evaluation and discussion of the results of monitoring.

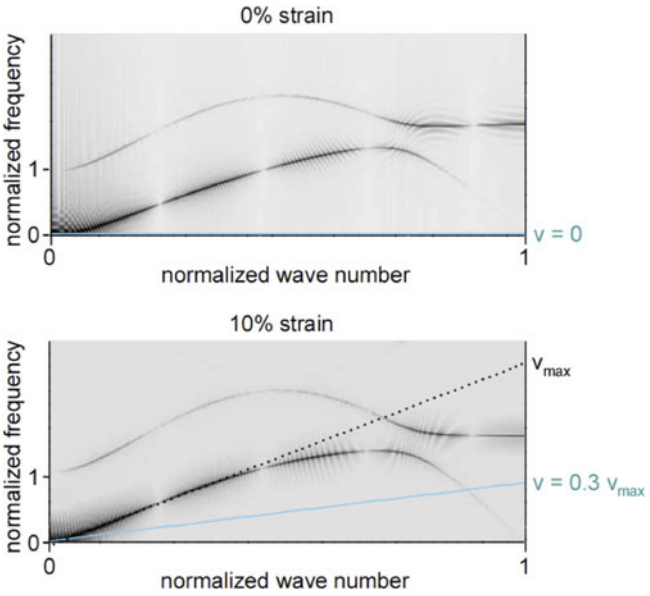

Fig. 16.9 Dispersion relation of flexural waves traveling on a two-dimensional mesh of mass points (Fig. 16.8) in a stress free state (top) and with 10% axial strain (bottom) created by a suitable axial stress

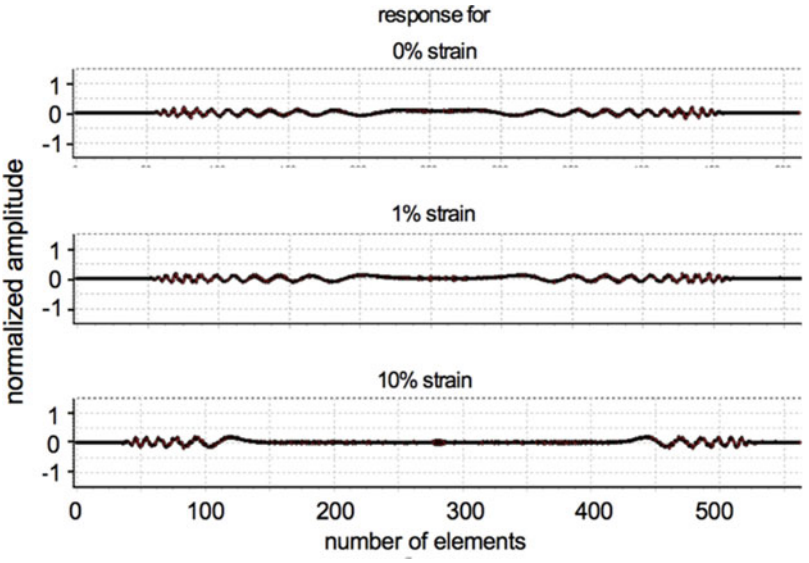

Fig. 16.10 Amplitude distribution at a fixed time following excitation by a sharp flexural pulse in the center of the sample

16.3 Experimental Set-Up and Monitoring Schemes

To demonstrate the possibility to synchronously determine stress and strain solely by monitoring with acoustic waves, experiments combining acoustic monitoring with conventional monitoring for the dependence of stress and strain are conducted. Two methods were realized: Standard samples well introduced for the monitoring of stress and strain with conventional test equipment were fitted with ultrasonic transducers (Fig. 16.11). This allows simultaneous monitoring of stress and strain with acoustic waves while performing standard tensile testing with commercially available equipment. For the application demonstrated here the dynamic testing system Zmart.Pro from Zwick GmbH & Co. KG, Ulm, Germany, was kindly provided by the Institute for Materials Applications in Mechanical Engineering (IWM) of the RWTH-Aachen. A suitable set-up for the simultaneous comparative observation of the stress–strain relation in thin wires was also constructed (Fig. 16.12). Both of these set-ups employed dedicated mode selective transducers for symmetric and antisymmetric waves (Figs. 16.11 and 16.13) as developed earlier for Lamb waves [20].

The functional principle of the electronic set-up employed for generation and detection including data storage is presented in Fig. 16.14. The selection of suitable signals for generation including arbitrary signals, pulsed excitation, and switched sinusoidal or chirped excitation is supported by dedicated software. The developed program also provides numerical correlation procedures for real-time processing and evaluation of stored data. This allows to determine variations of TOF for selected portions of the recorded signals (for details, see [21]). In Fig. 16.15 the interface used for operation and data analysis is demonstrated as it was applied in monitoring of guided acoustic waves under variable load.

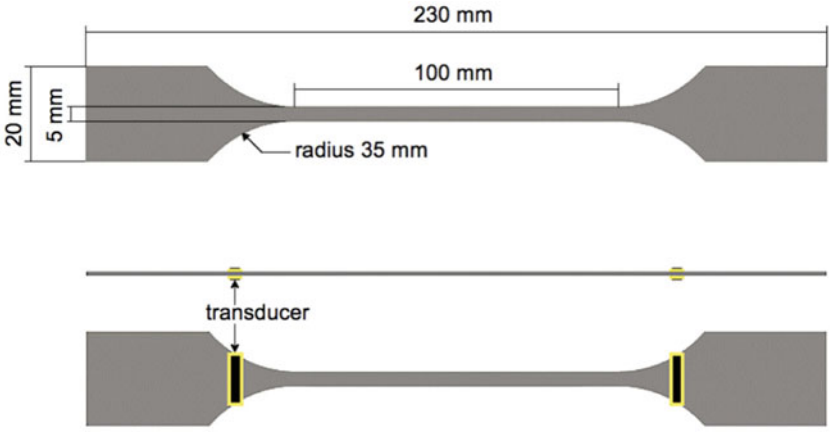

Fig. 16.11 Standardized aluminum sheet metal sample (0.8 mm) for stress–strain testing with mode selective wideband transducers in double-ended arrangement

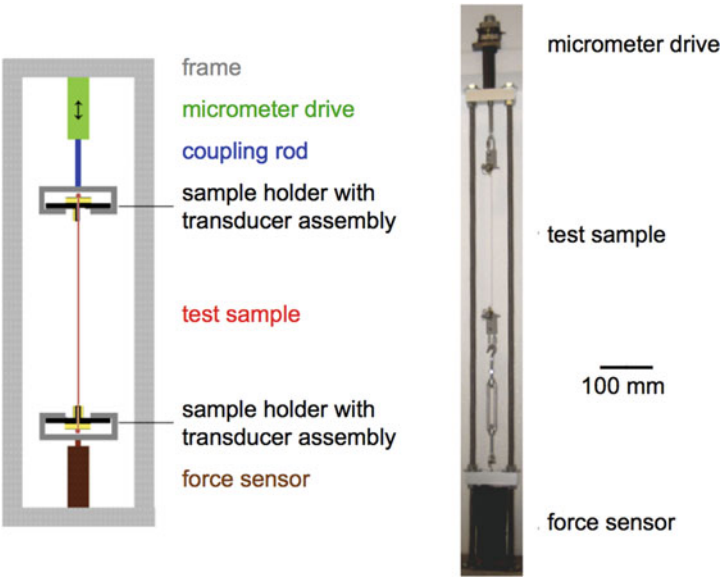

Fig. 16.12 Set-up (left: functional sketch; right: actual device) for conventional testing of the stress–strain relation of wires in combination with monitoring by guided acoustic waves

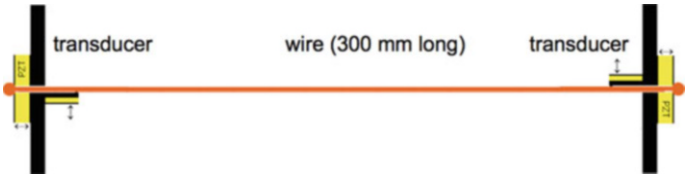

Fig. 16.13 Transducers, wire sample, and sample holders (black) for mode selective excitation of guided acoustic waves traveling on wires suitable for synchronous stress–strain testing in combination with a conventional test device (Fig. 16.12)

Monitoring with chirped wideband signals is well established in radar technology but unfortunately only rarely used in ultrasonics. In early applications involving chirped electromagnetic signals dispersive analog devices were used to compress the chirped signals such that short pulses become visible. This method has some advantages, which are still of interest even under the impact of quite impressive modern developments of electronic equipment.

On one hand, a short pulse, mathematically idealized a Dirac pulse also addressed as δ-function, appears well suited to determine any time of flight (TOF). On the other hand, it has the disadvantage that the signal power accumulates over a very short interval (theoretically idealized even infinitely short). As a result the maximum integrated pulse energy at the output of electronic amplifiers with limited output voltage is therefore rather limited. Nevertheless the Greens function formalism for the impulse response is based on δ-functions. For any practical applications

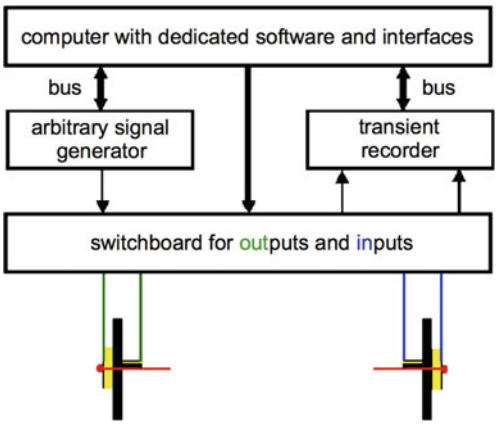

Fig. 16.14 Functional sketch of the electronic devices used for signal generation and detection

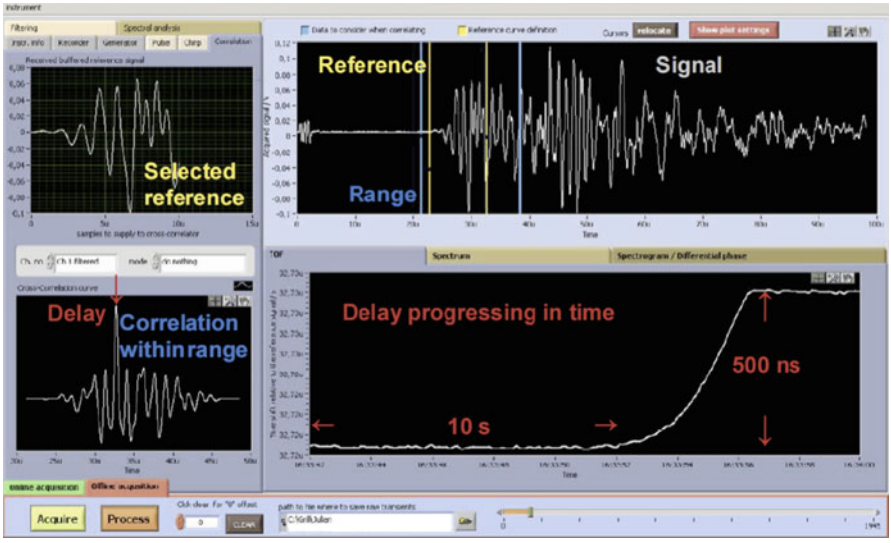

Fig. 16.15 Example for the displayed interface used for the selection of excitation signals, data storage, signal and data analysis, and general operation of the electronic equipment with explanatory inserts

such idealized functions need to be approximated by short pulses. By Fourier transformation it becomes evident that a δ-function is represented by a white spectrum with frequency independent intensity and a phase condition identical to that of cosine functions if the pulse is positioned at zero on the temporal axis.

But a broad spectrum can also be obtained by a chirped signal. Historically this has first been realized by an approximately linear chirp in frequency over time. With the aid of a frequency dependent phase shift and corrections for the actual frequency dependent magnitudes such a signal can be compressed to an approximate Dirac pulse (for a demonstration, see [22]). In practical applications signals are bandwidth limited and the compressed pulses will have a finite width determined by the available bandwidth.

It should be of interest to realize that the underlying principles, the Greens function formalism and Fourier transformation, were both originally introduced to solve differential equations. They also serve surprisingly well in practical applications as discussed here.

With an analysis based on FFT (fast Fourier transformation) and numerical data evaluation the pulse compression can be replaced by a correlation to observe temporal shifts relating to variations of TOF in the applications presented here. Both principles lead to similar resolutions for TOF variations. In respective patents [23] pulse compression is employed and even additionally used to correct for the disturbing influence of coaxial wires with different length involved in the signal transport [24]. Different to this commercial solution the analysis involved in data processing presented here is based on correlations.

Many published schemes perform such correlations with idealized programmed chirp signals which are used as input for conversion to an electrical signal by an arbitrary function generator driving the transducer generating the ultrasonic waves. Using a received signal as reference instead has the advantage that the alterations of the electrical input signal with respect to the received output signal cannot disturb the correlation procedures. Such alterations can be caused by the resonances in the transducers [25] and by band gaps possibly present in the transport medium for the guided acoustic waves. This leads to an improved resolution in the applications presented here. Depending on the application the reference signal is usually selected either in the absence of any load or at a given time after which variations of the load should be observable with high resolution. For recorded data a reference can also be taken for conditions under which a favorable reference signal has been observed.

For wideband excitation in the regime of dispersion corrections will be needed prior to correlation procedures. Guided waves traveling on wires or plates (Lamb waves) can be readily modeled and respective corrections are therefore in these cases available. On the other hand, the dispersion can be determined from experimental results and can subsequently be employed for corrections whenever needed. In Fig. 16.16 an example for the determination of the dispersion relations on the basis of measurements performed with the developed hard and software is presented to exemplify this possibility. The measurements were conducted with guided acoustic waves (Lamb waves) propagating on an aluminum sheet metal. Generation and detection was performed with mode sensitive transducers and respective signal processing. The tilted axis at the bottom of each graph indicates the temporal shift caused by the time dependent linear chirp employed for excitation, which had to be corrected prior to comparison to the modeled dispersion relations.

Compared to the application of chirped signals in radar technology with frequencies even in the GHz-regime, the application of this principle to ultrasonic waves in the upper kHz- and lower MHz-regime has the advantage that analog signals employed for generation and the received signals can both be converted from and to digital data by DA- and AD-conversion. For this frequency regime even 16-bit converters are readily available. When repetitive pulsed generation is involved these conversions are performed by arbitrary signal generators and transient recorders as presented in Fig. 16.14.

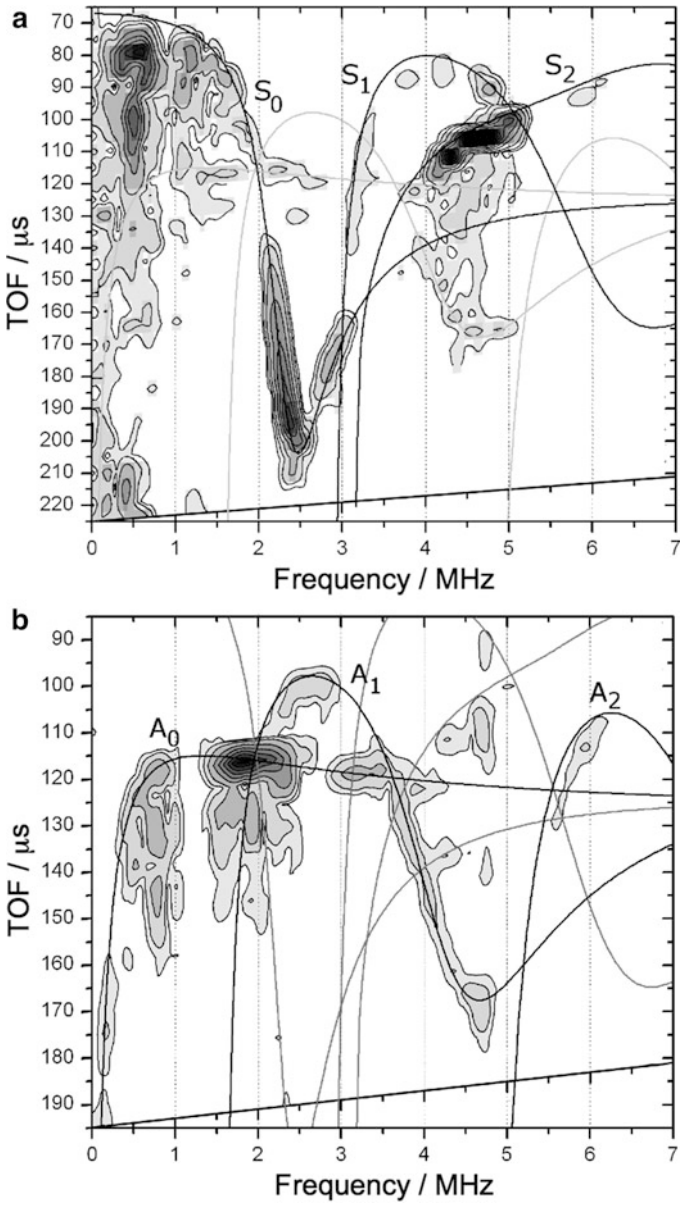

Fig. 16.16 Dispersion relations for symmetric (top) and antisymmetric (bottom) modes as determined by Fourier analysis of the data obtained by mode selective monitoring with chirped wideband signals of Lamb waves traveling on aluminum sheet metal (grey scale with white representing zero magnitude) with modeled dispersion relations indicated as solid lines

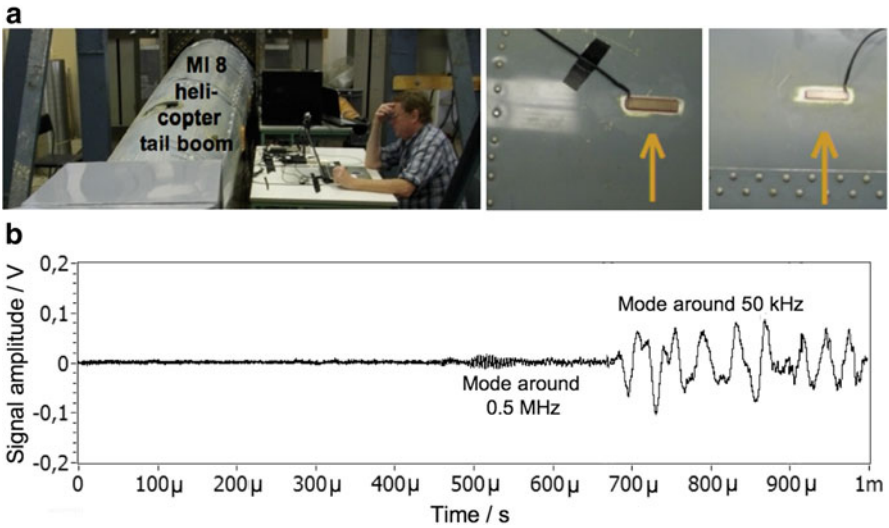

Fig. 16.17 Tail boom of an MI 8 helicopter (top, left) mounted in a vibration test apparatus with electronic components and the operating experimentalist, accompanied by detailed images of the mounted transducers (top, center, and right) and the received signals (bottom)

In early radar applications with chirped excitation the received signals were enhanced in magnitude by pulse compression prior to monitoring. By this they were raised above noise level prior to monitoring by visual observation on the radar screen—a cathode ray tube operated in angular coordinates. Different to this situation, received signals for ultrasonic applications as discussed and presented here are usually well above noise level. This is demonstrated in Fig. 16.17 for the transport of guided acoustic waves (Lamb waves) traveling over about 2 m of the hull of an MI 8 helicopter, manufactured from aluminum sheet metal (for details and additional results, see [26]). A wideband linear chirp starting at zero time and ranging from 20 kHz to 1 MHz with peak voltages of 6 V is used for excitation by a PZT transducer. The signal is delivered by a source with an impedance of 50 Ω. Under this condition the available electrical peak power for excitation is only 0.72 W. Such low power levels are especially of interest in monitoring of aircraft to avoid any possible distortion of sensitive components. Detection of the excited guided acoustic waves is performed under double-ended configuration via a second PZT transducer.

Under such conditions the received electrical signals can first be digitized and then compressed or correlated by digital data processing. An already well-established monitoring scheme also based on digital signal generation and detection is the application of time reversal techniques for ultrasonics by digital signal processing [27]. This scenario is quite different to earlier developed high frequency acoustic echo techniques where direct recording of the time dependent amplitude is impossible [28]. Therefore, nonlinear transport media were employed, providing analog signal processing in the path of the acoustic waves, delivering the observed phonon echoes by FWM.

The detailed discussion of the conditions favorable for digital signal processing serves the purpose of clarification under which conditions digital processing can be used to replace analog signal processing. The reader might nevertheless want to keep in mind that analog signal processing of electrical signals can often be performed much faster than digital processing. This is especially valuable for real-time processing at high repetition rates and for high signal frequencies. In this case the required amount of real-time signal and data processing may easily exceed the limitations of the available digital hardware.

If processing is restricted to correlations with monochromatic signals, the earlier discussed quadrature detection is a well-established alternative method for analog signal processing, which is still widely in use. In these cases the necessary multiplications for signal correlations are performed by mixers. In experiments with repetitively pulsed excitation integration is performed by gated signal averagers whereas in continuous wave (CW) applications this task is performed by low pass filters. In applications with sufficiently narrow bandwidth vector detection of the real and imaginary part of the representation in the complex plain by analog signal processing can even be used to deliver a Hilbert transformation of the received signal.

Mixing involved in quadrature detection converts the frequency range used for excitation to a band around zero frequency. For the relatively low frequencies of the output signal digital processing is usually readily available and can replace hardware filters and other wired signal processing units as involved traditionally in analog multiplication or rectification of electrical signals.

16.4 Monitoring of Stress and Strain with Acoustic Waves

The developed monitoring scheme is first demonstrated for a brass wire, followed by a copper wire as an example for a rather supple metal. Finally it is applied to a test sample from aluminum sheet metal as used for airplanes serving as an example for testing of a material widely used for the construction of aircraft components, where structural health monitoring is of growing interest.

Figure 16.18 demonstrates the dependence of the directly monitored signals on the time during forced linear elongation of the 0.8 mm brass wire sample with a speed of about 0.205 mm/s. The measured force shows a behavior well known from conventional monitoring and partly reflects the stress over strain dependencies since the strain forced on the sample rises linear in time for the conducted experiment.

The upper graph in Fig. 16.18 shows the results of conventional monitoring. The two lower ones demonstrate the observed variations of TOF as observed under externally forced elongation. Prior to the onset of disintegration at 13.75 s the extensional guided acoustic mode shows a steady nonlinear rise of the observed variation of TOF. The flexural mode shows a variation of TOF at the beginning that is obviously dominated by the tensional stiffening caused by increasing stress due to the externally forced strain. It shows the reduction in TOF as to be expected

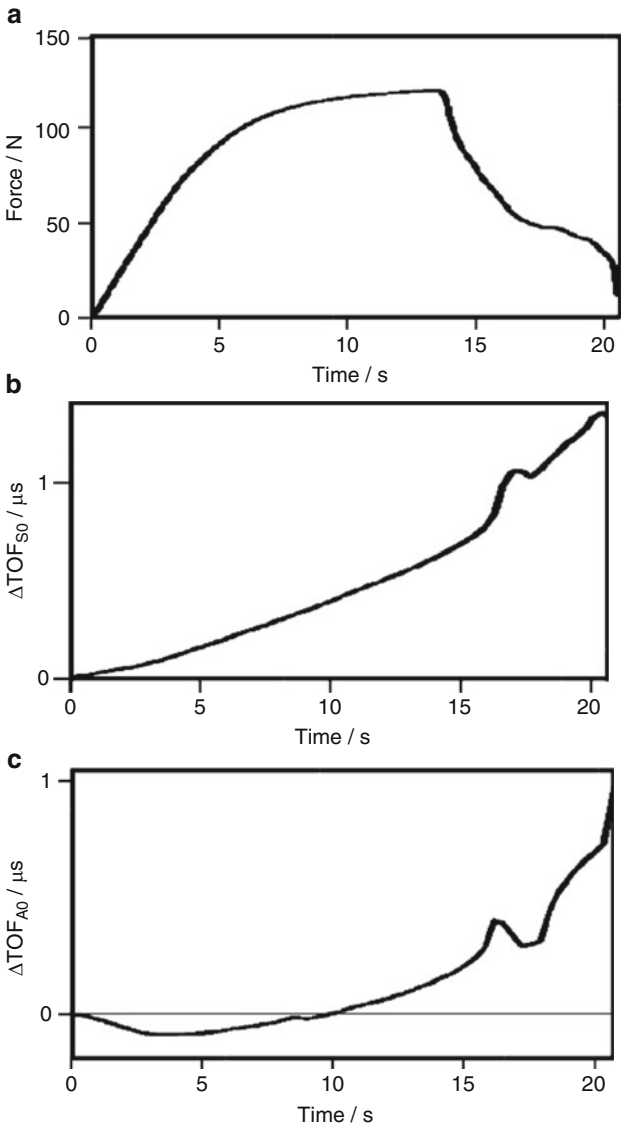

Fig. 16.18 Presentation of the direct results from monitoring of a 0.8 mm diameter brass rod for the elongation over time as enforced by the motor drive and the detected resulting force (top) in comparison to the variation of TOF as determined by the lowest extensional mode of guided acoustic waves (center) and as determined by the lowest flexural guided acoustic mode (bottom)

for soft enough strings according to the presented models. Finally in the regime of irreversible plastic deformation the rise of TOF due to lengthening of the specimen overcomes the influence of tensile stiffening.

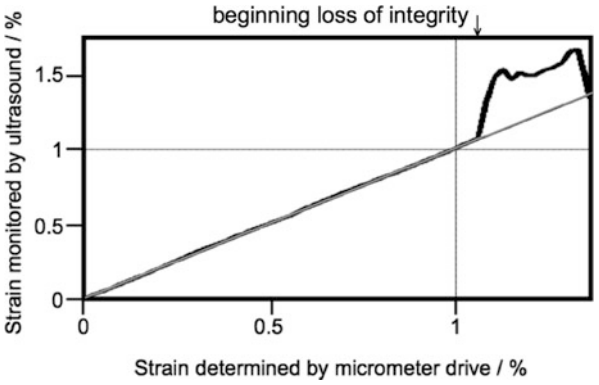

Fig. 16.19 Comparison of conventionally determined strain to the strain derived from monitoring with guided ultrasonic waves (black) and the idealized linear dependence (tilted grey line)

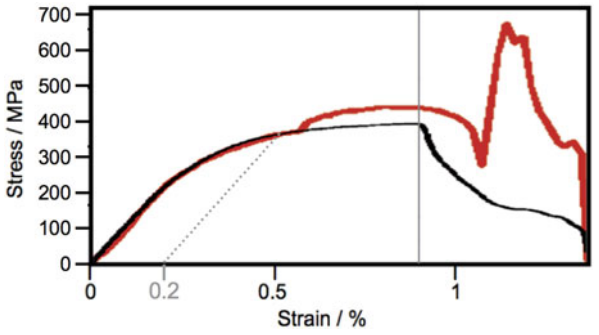

Fig. 16.20 The stress–strain relation as determined conventionally (black) and by ultrasonic monitoring with guided acoustic waves (red) with a vertical grey line indicating the onset of disintegration and a dotted grey line indicating the offset yield strength

The determination of the stress–strain relation just from acoustic monitoring clearly requires some processing of the raw data presented in Fig. 16.18. This was achieved by fitting linear combinations of the lowest possible orders of the observed ΔTOF. The results are demonstrated in Figs. 16.19 and 16.20. In all graphs the derived strain relates to the engineering normal strain, also addressed as engineering strain or nominal strain.

The result presented in Fig. 16.19 fits the ideal relation within a maximum error of $\pm 0.016\%$ strain prior to the onset of disintegration. It was obtained by a fitting routine for the ultrasonically determined strain ε_a by observation of the lowest guided symmetric and antisymmetric acoustic modes of:

$$\varepsilon_a = S\,(\Delta\mathrm{TOF}_{S0} - 1.6\Delta\mathrm{TOF}_{A0})$$

with the parameter S adjusted to fit with the slope of the conventional determined strain in the linear elastic regime. $\Delta\mathrm{TOF}_{\mathrm{ii}}$ denotes the observed variations of the TOF of the respective modes (ii) with respect to the strain and stress free state.

The strain determined by ultrasonic monitoring with the aid of the fitting parameters serving as calibration for the developed monitoring scheme can now be used to determine the stress–strain relation solely by monitoring with guided acoustic waves. The result is presented in Fig. 16.20.

The acoustically determined stress was fitted by a linear admixture of the results from the two lowest modes of the guided acoustic waves. Up to slightly above the yield strength it remains within a maximum error range of +2 MPa to –10 MPa. The maximum error at a strain of about 0.1% is obviously due to some higher order terms not embodied by the fitting procedure. At a strain of about 0.6% the acoustically determined stress markedly deviates from the conventionally observed one. This is most likely due to a premature mechanical failure of the bond between acoustic transducer and test specimen and indicates that the chosen transducer design may require future refinements.

The test of the developed monitoring scheme on brass nonetheless demonstrates that the relation between stress and strain can be monitored up to about 110% of the yield strength. In the regime of plastic deformation above that value the results of acoustic monitoring differ significantly from those of the conventional monitoring. This may possibly be improved with refined transducer designs. But, on the other hand, it should also not be too surprising, since guided waves on rods and plates have a dispersion relation depending on the lateral extension, which begins to vary significantly in the regime of substantial plastic deformation. In this regime the guided waves selected for monitoring may even be influenced by band gaps (see, for example, dispersion relations in Figs. 16.4 and 16.6) or may suffer from substantial variations of the transport velocities near these gaps.

For structural health monitoring of parts essential for the mechanical stability of sensitive components, as, for example, sections of the body, wings, or fuselage of aircraft, the actual goal for the development of the presented monitoring scheme, the range of reliable monitoring with an upper limit slightly above the yield strength is sufficient to determine if monitored parts have already suffered from plastic deformation.

Before proceeding to the test of aluminum sheet metal, as widely used in aircraft, the test of a copper wire is presented as an example for a rather supple material. Copper is soft with respect to bending and with respect to axial tension. It is therefore of interest to study, if acoustic monitoring of the stress–strain relation can be feasible even under these circumstances.

The wire from high purity DSA (dead soft annealed) copper with 0.8 mm diameter and a length of 300 mm did not transport guided acoustic waves of the lowest symmetric mode with a quality sufficient enough to allow monitoring with the necessary resolution. Similarly antisymmetric guided waves with a center frequency of 5 kHz were not transported well in the absence of stress either. Figure 16.21 presents the direct results of synchronous monitoring with conventional equipment and by guided acoustic waves. It shows that guided waves with frequencies in the audible range near 5 kHz can be monitored under stress above 5 MPa and provide reliable data at and above 40 MPa. Since the strain could not be monitored with guided acoustic waves of the lowest symmetric mode as originally planned, the strain in the presented graphs for copper is determined by conventional monitoring and relates to the chosen speed of the motor drive (0.079 mm/s) forcing extensional strain on the tested sample.

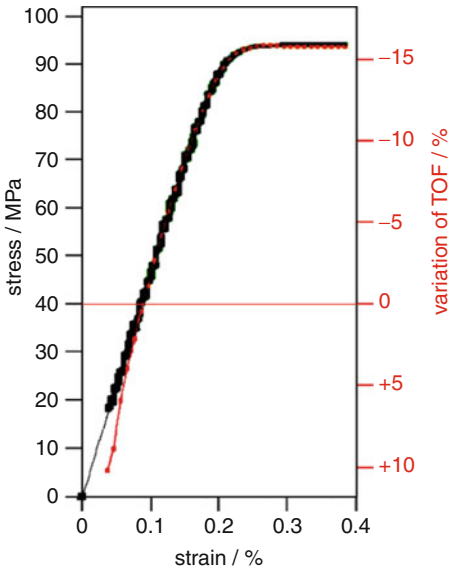

Fig. 16.21 Stress–strain relations determined by conventional monitoring (black data points with connecting lines) and by observed variation of TOF for monitoring with guided acoustic waves of the lowest antisymmetric modes with a center frequency of 5.5 kHz (red data points with connecting red line) with the scale for variations of TOF adjusted to demonstrate similarities in the observed dependencies

Figure 16.21 demonstrates that the observed variation of TOF can be referenced to stress of over 40 MPa with proper scaling factors. Above this stress the results fit well with the conventionally monitored stress. This demonstrates the applicability of the expected effects for the acoustic monitoring of stress by antisymmetric guided waves even for a rather supple metal. Well covered is the upper half of the linear range and the entire adjacent regime from the beginning of plastic deformation to the extension under constant stress. The covered regime is especially valuable for structural health monitoring. The termination of the measurement at a strain close to 0.4% was performed to allow additional runs with the same sample. Due to the resulting pre-stressing the following graphs for experiments on copper therefore show slight deviations of the conventionally determined stress–strain relation.

In Fig. 16.22 results for monitoring with antisymmetric guided acoustic waves at a higher frequency are demonstrated. Here quadratic dependencies for a stress up to 90 MPa are evident. This allows a determination of the stress by respective correction of the acoustic data in the regime of low stress not well covered by monitoring at 5 kHz (Fig. 16.21). At higher stress additionally the dependence on lengthening of the sample becomes progressively evident. This becomes even clearer for monitoring at higher frequencies. Therefore, the results for monitoring at a center frequency of 3 MHz are displayed in Fig. 16.23.

Besides of an initial irregular response at very low stress, the monitoring of variations of TOF at a center frequency of 3 MHz starts out as expected from the soft string model at low stress with a reduction of TOF. Near a stress of about 40 MPa this changes and is finally dominated by effects caused by lengthening. In the regime of plastic deformation under nearly constant stress the strain can therefore be monitored as demonstrated by the fitted red line in Fig. 16.23. The

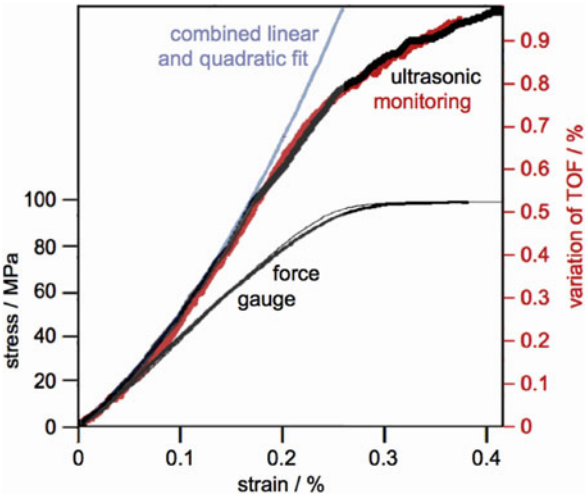

Fig. 16.22 Conventionally determined stress and strain and observed variation of TOF for the lowest antisymmetric mode around 300 kHz for a soft copper wire (diameter 0.8 mm, length 300 mm) with two measurements displayed for demonstration of repeatability

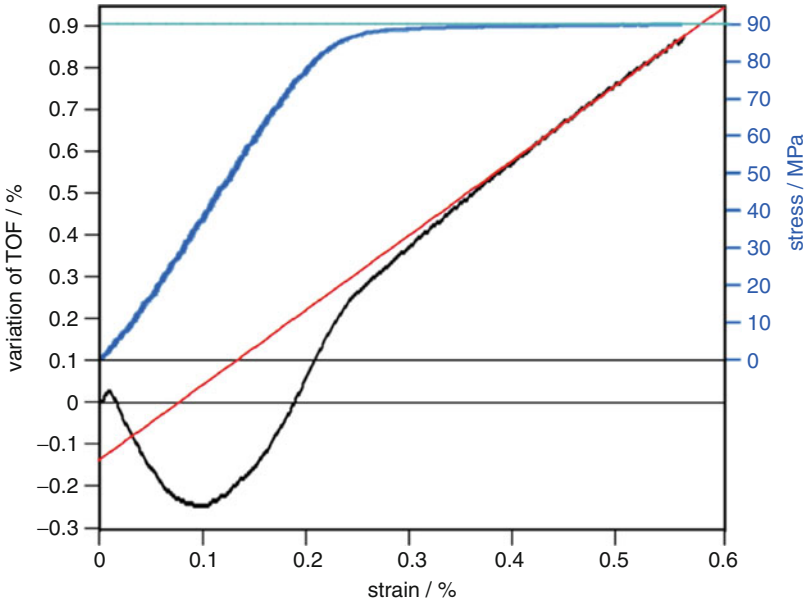

Fig. 16.23 Conventionally determined stress and strain (blue) and observed variation of TOF for the lowest antisymmetric mode around 3 MHz for a soft copper wire (diameter 0.8 mm, length 300 mm) with lines fitted to the asymptotic behavior

deviation from the red line is displayed in Fig. 16.24. It relates to the conventionally determined stress in good approximation for values above 80 MPa if properly scaled by a factor and adjusted by an offset.

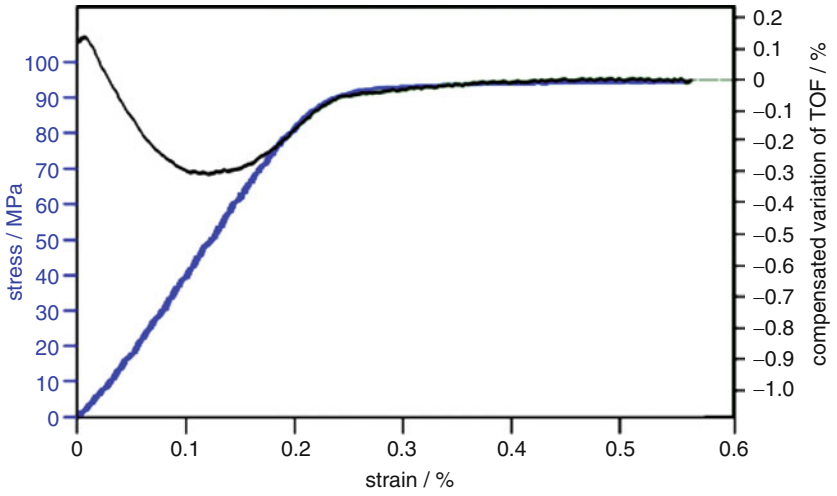

Fig. 16.24 Similar to Fig. 16.23 but with the result of the acoustic monitoring (black) corrected by subtraction of a linear function as displayed in red in Fig. 16.23 and scales for the resulting compensated variation of TOF adjusted to fit the results of the conventional stress–strain relation above a strain of about 1.8%

This demonstrates that even for DSA copper and in the absence of sufficiently sizable signals obtainable with the lowest symmetric mode, the linear elastic regime of the stress–strain relation can still be covered with monitoring of the stress. For this regime the strain can be derived from the monitored stress because they are linear related. In the regime of beginning plastic deformation to excessive plastic deformation under approximately constant stress, strain and stress can both be monitored independently. This can be done with the use of low (even audible 5 kHz) and higher frequency (around 3 MHz) guided antisymmetric acoustic waves. Further details like actually determined parameters for the fitting are omitted here, since this is demonstrated in detail for the following final and more practical choice of aluminum sheet metal for a standard test sample as employed traditionally for conventional monitoring of the stress–strain relation of metals.

The results of the measurement on the aluminum test sample are displayed in Fig. 16.25.

The elongation relating to the externally applied strain of the sample with a length of the probed part of about 100 mm rises linear in the experiment. The best fit of an acoustically determined elongation E_a to the one applied externally by the dynamic testing system was obtained with the following summation:

$$E_a = 49.95\ T_{\mathrm{rA0f}}\ \mathrm{mm} + 24.98\ T_{\mathrm{rA0s}}\ \mathrm{mm} + 27.97\ T_{\mathrm{rS0}}\ \mathrm{mm}$$

with T_r representing the relative variation of the monitored TOF:

$$\Delta\mathrm{TOF}/\mathrm{TOF}$$

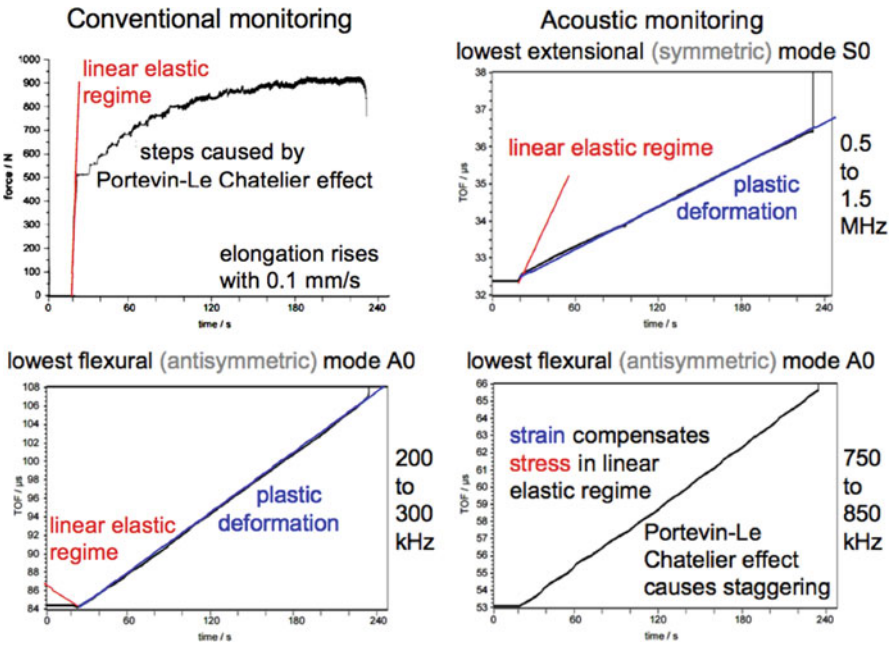

Fig. 16.25 Results of synchronous measurement by conventional monitoring and by acoustic monitoring with lowest symmetric and antisymmetric mode of guided acoustic waves

The additional indices indicate the selected mode. A0s relates to the antisymmetric mode with a center frequency of 250 kHz, A0f to the same mode but with a center frequency of 800 kHz, and S0 to the monitored symmetric mode with a center frequency of 1 MHz.

The results presented in Fig. 16.26 are obtained by conversion to strain based on the length of the active part of the sample. The absolute deviation of the acoustically determined strain with respect to ideal monitoring (red line in Fig. 16.26) is always within $\pm 0.3\%$.

For many applications monitoring of the strain alone, as demonstrated in Fig. 16.26, may already be sufficient. This could, for example, be used to monitor plastic deformations resulting from mechanical overloads during operations. In aerospace applications it should be well suitable for testing critical parts and components of aircraft during checkups and maintenance procedures on ground.

But the developed acoustic monitoring scheme additionally also allows the simultaneous determination of actual stresses and with that even allows recording and analyzing actual load collectives and load spectra during operation. This opens a wide range of potential applications in the fields of structural health monitoring, smart structures, reliability and durability analysis, and life-cycle optimization.

The result of a respective fitting procedure based on the observed variations of TOF for all three monitored guided modes is demonstrated in Fig. 16.27.

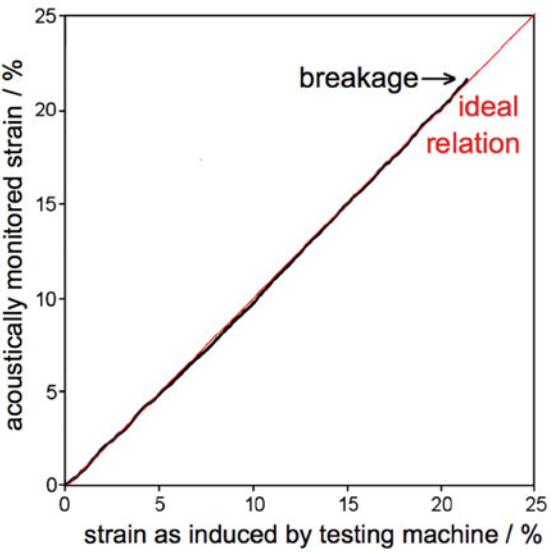

Fig. 16.26 Comparison of conventionally determined strain with the strain determined by monitoring with guided acoustic waves for the tested aluminum sample

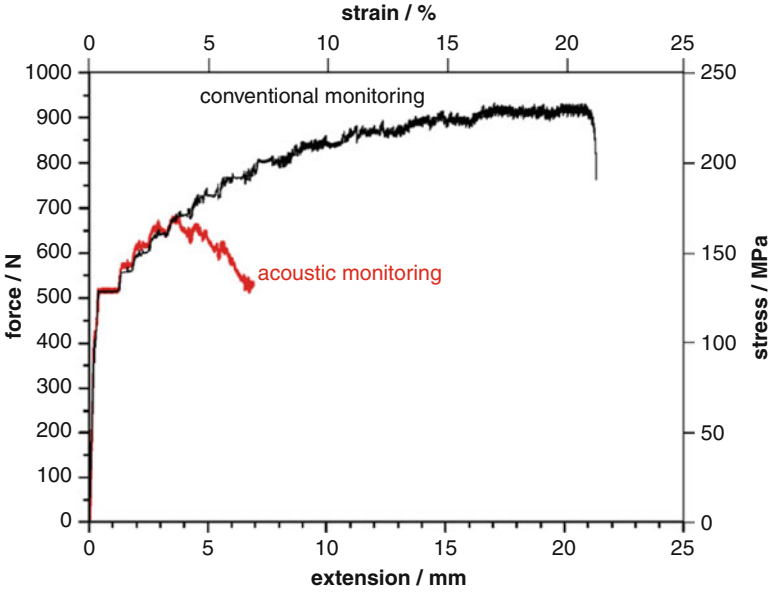

Fig. 16.27 Conventionally determined stress–strain relation of the monitored aluminum sample in comparison to acoustic monitoring based on a linear superposition of the relative variations of the observed TOF for the selected modes

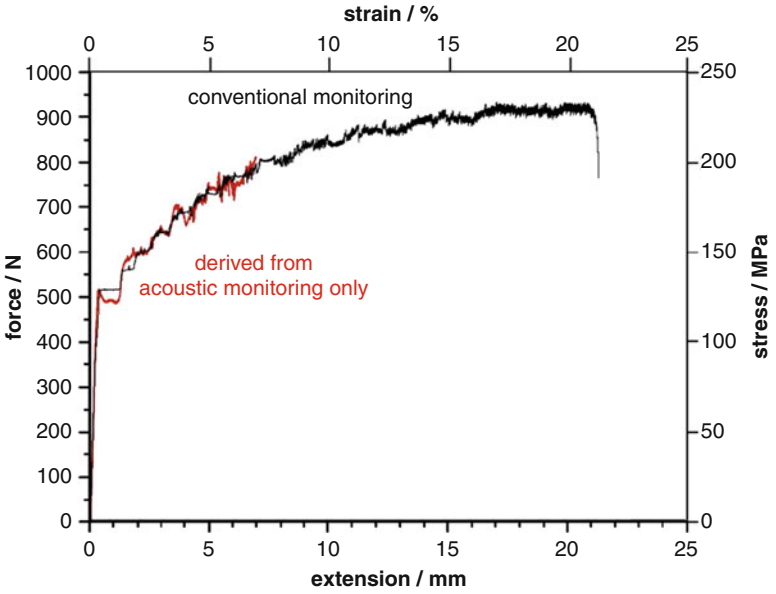

Fig. 16.28 The stress–strain relation of the monitored aluminum sample as determined conventionally in comparison to acoustic monitoring based on a superposition of TOF of the monitored modes including quadratic terms

To determine the stress ε from the monitoring with guided acoustic waves, the following equation with an additional fitted proportionality factor was employed:

$$\varepsilon \approx \frac{1}{2} T_{\mathrm{rA0f}} + \frac{1}{4} T_{\mathrm{rA0s}} + \frac{1}{4} T_{\mathrm{rS0}}$$

The admixture with prefactors of ½ and ¼ leads to the best fit based on an approximation by linear superposition of the results of acoustic monitoring (Fig. 16.27).

Up to a strain of almost 4% the fit by linear superposition represents the conventionally determined stress–strain relation within a maximum error of the stress of 0.35%. But above a strain of 4% a substantial and increasing deviation is obvious. In part this can be overcome by a higher order superposition as demonstrated in Fig. 16.28.

Whereas higher order corrections can extend the fitting to values of a strain of about 7%, at the onset of plastic deformation the agreement with conventional monitoring is substantially reduced with respect to the linear fitting procedure (Fig. 16.27). With the performed higher order fitting the error regarding stress rises to 10% and a bad representation of the steps caused by the Portevin-Le Chatelier effect [29] is obtained. This effect observed for higher order fitting is based on a process of local deformations in shear bands and still requires further scientific investigation.

Even though an almost surprisingly close fit could be obtained for the strain solely based on acoustic monitoring up the point of disintegration (Fig. 16.26) this is not possible for the stress derived from acoustic monitoring. Above a strain of 7% fitting procedures become obsolete and a reasonably good fitting is only achieved for linear interpolation up to a strain of almost 4%. This is most likely due to anisotropies resulting from excessive irreversible deformation in the plastic regime as caused by the Portevin-Le Chatelier effect and possibly also by a substantial variation of the dispersion relations and transport properties of the guided acoustic waves.

Nevertheless are the demonstrated resolution and the achievable range of up to 8-times of the elastic limit both well suited for applications involving structural health monitoring. Following an initial calibration procedure including the determination of fitting parameters the developed monitoring scheme for the determination of the stress–strain relation can even be operated in real time solely based on monitoring of acoustic waves. The procedures needed for evaluation only require a parameterized addition of the variation of the different times-of-flight observed in monitoring with the lowest symmetric and antisymmetric guided acoustic modes. The scheme is especially well suited for sheet materials and rods, where the propagation of guided waves is rather well defined. Generally any set of modes including bulk modes with different fractions of transversely and longitudinally polarized components, including pure transverse or longitudinal polarized modes, will exhibit the basic features employed here for the demonstrated feasibility of the developed monitoring scheme.

Since practical applications involving guided acoustic waves will always be influenced by thermal effects the following applications for the developed monitoring scheme include a demonstration on how an average temperature along the path of propagation of guided acoustic waves can be determined. The presented applications include also a demonstration of the alteration of the transport properties of acoustic waves under strong shaking, as they occur in aircraft during flight.

16.5 Related Applications of the Developed Monitoring Scheme

A tail boom of an MI 8 helicopter mounted on a shaker (as demonstrated in Fig. 16.17) has been monitored with different modes of guided ultrasonic waves for several hours over which the temperature in the room varied. The results are demonstrated in Fig. 16.29.

The temperature dependence observed for a center frequency of 50 kHz for the lowest branch of the antisymmetric Lamb waves is (13.8 ± 0.2) ns/K. For a center frequency of 0.5 MHz the respective value for the lowest branch of symmetric Lamb waves is (10.7 ± 0.2) ns/K. The temperature resolution achievable for monitoring with guided acoustic waves is about 0.05 K [26]. In the absence of anomalies as

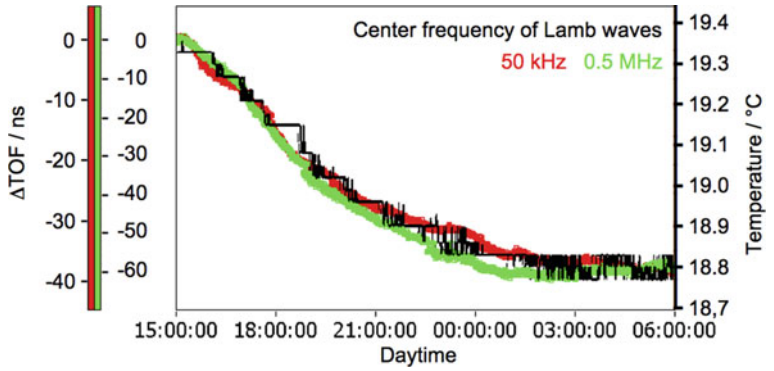

Fig. 16.29 Temperature dependence of TOF as difference to the initially observed TOF over daytime (3 pm to 6 am) in comparison to the temperature of the helicopter tail boom with adjusted scales to demonstrate the proportionality

caused by phase transitions and if variations are not too large the temperature relates to a linear average over the traveled path of the acoustic waves. This coincides with similar experiences in measurements conducted to determine stress and strain with the presented monitoring scheme. Since the temperature affects TOF due to thermal expansion, the influence has the same sign for all modes. And because the effects of stress and strain involve different signs and different sensitivities, the temperature, stress, and strain can all three be determined with guided acoustic waves. To do this of course at least 3 or even more suitable modes need to be observed.

For the same set-up the signals have been monitored prior, during and following the shaking procedures of the helicopter tail boom. An example of the obtained results is displayed in Fig. 16.30 (for further details, see [26]). During shaking an increase in TOF is observed, which exponentially returns to a lower value with a time constant of about 1 min. The identification of the origin of this relaxation requires further studies since it is close to the expected thermal time constants, but may also indicate a recovery of the riveted joints from slippage due to shaking. Following this relaxation a permanent offset of about +5 ns with respect to the initial value of TOF is observed. This indicates a small loss of mechanical stability of the riveted helicopter tail boom due to shaking.

The preceding application demonstrates that even very small variations of the conditions influencing the transport of guided acoustic waves can be monitored reliably by integral monitoring with the developed monitoring schemes. This is further demonstrated with an application involving the tail boom of a Eurocopter (for further details, see [30]). The wall of the tail boom is a sandwich structure consisting of two fiber-enforced layers with a low-density spacer. The test was performed to demonstrate the capabilities of integral monitoring of ablation with suitable guided ultrasonic waves. A half pipe of a Eurocopter tail boom that was available for the research was not allowed to be damaged by delamination. Because of this the experiments had to be restricted to studying effects of ablation by

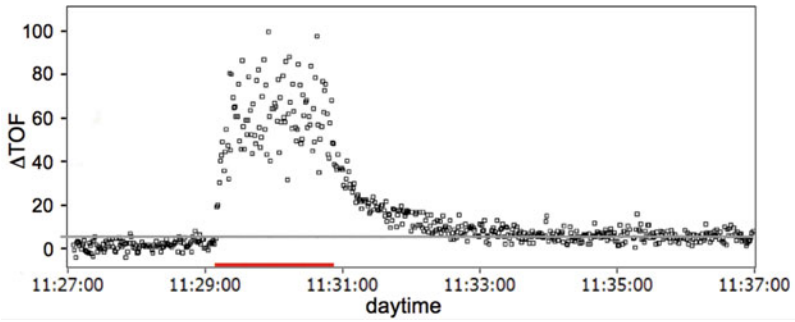

Fig. 16.30 Variation of TOF observed for the tail boom of a MI 8 helicopter for Lamb waves with shaker on for the indicated time (marked red) with 10% of the maximum nominal amplitude and for single shot monitoring (no averaging)

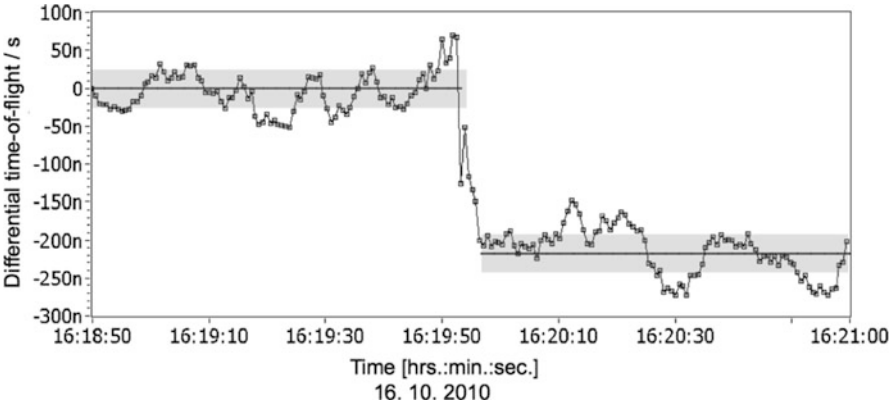

Fig. 16.31 Variation of TOF for selected Lamb wave mode over daytime with removal of tape at 16:19:50 to test the sensitivity for ablation

attaching and removing a suitable test object from the surface of the tail boom. For this purpose a sticky tape (3M™ Hazard Marking Vinyl Tape 766 black and yellow; thickness 5.0 mil = 0.125 mm; vinyl backing with a rubber adhesive; 50 mm wide; with an aerial density of about 1 mg/cm^2) was attached to the surface. In Fig. 16.31 the effect of removal of the tape is demonstrated.

The noise equivalent resolution indicated by grey bars in Fig. 16.31 relates to the removal of about 1 mg material from the surface of the monitored Eurocopter tail boom. This test demonstrates the high resolution obtainable with the developed monitoring schemes. But it is also clear that temperature effects have to be compensated to reach the demonstrated resolution in practical applications. The preceding application demonstrates this possibility. The ablation test furthermore demonstrates that for applications where stress–strain relations should be monitored effects like ablation or delamination may interfere with such monitoring. Similar distortions were already observed previously during stress–strain monitoring experiments with

aluminum when the Portevin-Le Chatelier effect occurred. Some care has been taken to demonstrate that such uncertainties can possibly be overcome with an observation of a sufficient number of modes, each with different sensitivity to parameters like stress, strain, or temperature.

Nevertheless, the primary goal of the presented developments is integral testing by guided ultrasonic waves. "Integral" hereby indicates that neither the exact location or type of a possible flaw nor the exact type of derangement of the monitored part needs to be determined. For the selected scenario it is sufficient to reliably determine if excessive loads causing unacceptable plastic deformation or if other kinds of deterioration have occurred. If this is the case an instant warning can be triggered. Depending on predetermined limits this may even include a demand for a replacement of the monitored part or the requirement of a traditional NDT inspection to determine what repairs are necessary.

The first demonstrated monitoring of stress and strain relates to a basic relation traditionally used to determine the stability and influence of overload conditions in engineering. The few selected additional applications were presented to give some insight to the possibilities for monitoring of additional parameters but also to demonstrate the necessity to reliably monitor effective temperatures in applications involving monitoring by acoustic waves whenever they are (at least partially) based on anharmonic effects. Since anharmonic effects also cause thermal expansion, it is a usual observation that with an increasing sensitivity for anharmonic monitoring the sensitivity to temperature influences also rises. As observed in the applications under practical conditions the influences on the measured TOF are often on similar scales.

The presented monitoring schemes demonstrate that the influence of temperature can also be determined with the guided acoustic waves involved in monitoring of stress and strain. This offers the opportunity to correct for disturbing thermal effects, which is especially important for monitoring of parts while in use, like applications for in-flight monitoring of structural aircraft components, for continuous structural health and load monitoring of civil structures like bridges and towers, and for applications in the field of reliability and life-cycle optimization of machinery.

References

1. H.O. Berktay, Possible exploitation of nonlinear acoustics in underwater transmitting applications. J. Sound Vib. **2**(4), 435–461 (1965). https://doi.org/10.1016/0022-460X(65)90122-7
2. M.F. Hamilton, D.T. Blackstock, *Nonlinear Acoustics* (Acoustical Society of America, Melville, 2008). ISBN 0-12-321860-8
3. W. Grill, K. Hillmann, K.U. Würz, Joachim Wesner, in Scanning Acoustic Microscopy with Phase Contrast. eds. By A. Briggs, W. Arnold. *Advances in Acoustic Microscopy*, vol. 2 (Plenum Press, New York. 1996). p. 167
4. K.-U. Würz, J. Wesner, K. Hillmann, W. Grill, Determination of elastic constants using a scanning acoustic microscope. Z. Phys. B Condens. Matter **97**(4), 487–492 (1995). https://doi.org/10.1007/BF01322428

5. T. Schneider, Nonlinear Optics in Telecommunications, in *Advanced Texts in Physics. Four-Wave-Mixing (FWM)*, (Springer, Berlin, 2004), pp. 167–200
6. H.J. Simpson, P.L. Marston, in Parametric Layers, Four-Wave Mixing, and Wave-Front Reversal. eds. By M.F. Hamilton, D.T. Blackstock. *Nonlinear Acoustics*. (ASA, Austin, 2008); originally published in 1998
7. Michele Zaffalon, http://www.zhinst.com/blogs/michele/files/downloads/2012/12/AMFM.pdf, March 2017; contact via: michele.zaffalon@zhinst.com
8. T.J. Kim, W. Grill, Determination of the velocity of ultrasound by short pulse switched sinusoidal excitation and phase-sensitive detection by a computer-controlled pulse-echo system. Ultrasonics **36**(1–5), 233–238 (1998)
9. R. Ellwood, T. Stratoudaki, S.D. Sharples, M. Clark, M.G. Somekh, Determination of the acoustoelastic coefficient for surface acoustic waves using dynamic acoustoelastography: an alternative to static strain. J. Acoust. Soc. Am. **135**(3), 1064–1070 (2014). https://doi.org/10.1121/1.4864308
10. W.H. Klever, J.W. Wilhelm, Ultrasonic bolt tension tester, U.S. Patent 3,306,100. Submitted: 25 Feb 1964
11. A.M. Nicolson, Piezo-stress-sensor, US. Patent 2137852. Submitted: 8 Jan 1924
12. K.S. Tarar, M. Pluta, U. Amjad, W. Grill, Lattice dynamics approach to determine the dependence of the time-of-flight of transversal polarized acoustic waves on external stress. Proc. SPIE **7984**, 79842R (2011)
13. K. Hillmann, W. Grill, J. Bereiter-Hahn, Determination of ultrasonic attenuation in small samples of solid material by scanning acoustic microscopy with phase contrast. J. Alloys Compd. **211/212**, 625–627 (1994)
14. D.K. Ferry, in Lattice Dynamics. *Semiconductors Bonds and Bands* (IOP Publishing Ltd, Bristol, 2013). pp. 3-1–3-32
15. J.E. Lennard-Jones, On the determination of molecular fields. Proc. R. Soc. Lond. A **106**(738), 463–477 (1924). https://doi.org/10.1098/rspa.1924.0082
16. P. Morse, H. Feshbach, Methods of Theoretical Physics, vol. 1, in *International Series in Pure and Applied Physics*, (McGraw-Hill, Boston, 1953)
17. Z. Caamaño-Withall, P. Krysl, Taut string model: getting the right energy versus getting the energy the right way. World J. Mech. **6**(2), 24–33 (2016)
18. K.S. Tarar, R. Meier, U. Amjad, W. Grill, Stress detection with guided acoustic ultrasonic waves by non-linear elastic and geometric effects. Proc. SPIE **2009**, 729518 (2009)
19. T.C.A. Molteno, N.B. Tufillaro, An experimental investigation into the dynamics of a string. Am. J. Phys. **72**(9), 1157–1169 (2004)
20. A. Abdelrahman, U. Amjad, D. Jha, K.S. Tarar, W. Grill, Zero order mode selective excitation and highly resolved observations of Lamb waves. Proc. SPIE **7984**, 798413 (2011). https://doi.org/10.1117/12.880602
21. J.Y. Grill, Ultrasonic detection of stress and strain in materials under load. Diploma Thesis, RWTH-Aachen, 2014
22. K.S. Tarar, R. Meier, E. Twerdowski, R. Wannemacher, W. Grill, A differential method for the determination of the time-of-flight for ultrasound under pulsed wide band excitation including chirped signals. Proc. SPIE **2008**, 6935 (2008). https://doi.org/10.1117/12.776158
23. G. Adlhoch, W. Grill, R. Kociorski. A method for determining the clamping force of linking units by means of ultrasonic agitation. Patent DE102004038638B3, 9 Aug 2004
24. W. Grill, R. Kociorski, Method for correcting the influence of signal transmission lines on changes of signal transit times when conducting ultrasonic measurements. Patent WO2005121773A1 (CA2569839A1, DE102004027919B3, EP1754051A1, EP1754051B1), 9 June 2004
25. M. Niksch, W. Grill, Numerical calculations of ultrasonic echo patterns and implications on the determination of the velocity of sound. Acoustica **64**, 26 (1987)
26. G. Birkelbach, W. Grill, S. Kuznetsov, V. Pavelko, Integral structural health and load monitoring of a helicopter tail boom manufactured from aluminum sheet metal with support from frames and stringers by guided ultrasonic waves. Proc. SPIE **2012**, 8348 (2012)

27. M. Fink, Time reversed acoustics. Phys. Today **50**, 64–40 (1997)
28. K. Fossheim, in Nonequilibrium Phonon Dynamics, ed. By W.E. Bron. *Phonon Echoes, Polarization Echoes, and Acoustic Phase Conjugation in Solids*, vol. 124. NATO ASI Series (Springer, Boston, 1985). pp. 277–312
29. V. Jeanclaude, C. Fressengeas, Le Chatelier effect. Propagating pattern selection in the Portevin. Scr. Metall. Mater. **29**, 9 (1993)
30. G. Birkelbach, I.J. Aldave, I. López, W. Grill, Integral ultrasonic structural health and load monitoring on a fiber reinforced polymer-based composite helicopter tail boom. Proc. SPIE **2012**, 8348 (2012). https://doi.org/10.1117/12.914968

Chapter 17
Noncontact Nonlinear Ultrasonic Wave Modulation for Fatigue Crack and Delamination Detection

Hoon Sohn, Peipei Liu, Hyung Jin Lim, and Byeongjin Park

17.1 Introduction

Fatigue crack is a progressive and localized structural damage that occurs when a structure is subjected to cyclic loading. It is a critical concern for in-service metallic structural components for the failures caused by fatigue crack, which constitute nearly 90% of the total failures in metallic structures. Additionally, a fatigue crack only becomes conspicuous after the crack approaches approximately 80% of the structural fatigue life. For laminated composite structural components, delamination is a critical failure mechanism in the form of separated layers caused by cyclic loading or impact because the composite laminates do not provide reinforcement through the thickness. Damages like fatigue crack and delamination are often invisible or barely visible but may compromise the integrity of structural components and cause catastrophic failures.

To detect fatigue crack and delamination, various nondestructive evaluation (NDE) techniques have been developed such as ultrasonic, acoustic emission, thermography, eddy current, magnetic particle inspection, and X-ray. Among these developed NDE techniques, the ultrasonic technique has proven its effectiveness in achieving a reasonable compromise between the damage sensitivity and the sensing range. The advantages of ultrasonic-based damage detection include: (1)

H. Sohn (✉) · P. Liu · H. J. Lim
Department of Civil and Environmental Engineering, KAIST, Daejeon, Republic of Korea
e-mail: hoonsohn@kaist.ac.kr

B. Park
Korea Institute of Materials Science, Changwon, Gyeongsangnam-do, Republic of Korea

T. Kundu (ed.), *Nonlinear Ultrasonic and Vibro-Acoustical Techniques for Nondestructive Evaluation*, https://doi.org/10.1007/978-3-319-94476-0_17

It is sensitive to both surface and subsurface damages; (2) Often only one surface needs to be accessible; (3) It owns high accuracy in determining damage position and estimating its size and shape; and (4) It can be made portable and highly automated operation.

The ultrasonic techniques can be divided into linear and nonlinear ultrasonic techniques. Linear ultrasonic techniques use linear features of ultrasonic waves, such as variations of the amplitude, phase, and mode conversion of the transmitted or reflected ultrasonic waves at structural damage. These linear features have been widely studied and showed a great potential for various gross structural damage detection. However, these linear features may lose their sensitivity to early-stage damages whose dimensions are much smaller than the ultrasonic wavelength. Furthermore, the interpretation of linear features becomes complex in plate-like structures due to dispersion and multimode characteristics, and even more challenging in inhomogeneous materials like composites. On the other hand, nonlinear ultrasonic techniques mainly focus on nonlinearity induced by structural damage and investigate the frequency variations of the acquired ultrasonic waves. More specifically, damage-induced nonlinearity can result in creation of accompanying harmonics (sub-harmonics), modulations between different frequencies, and change of resonance frequencies due to amplitude variation of the driving input. These nonlinear features are observed in the course of structural degradation processes much sooner than any changes of linear features can be detected, making the nonlinear ultrasonic features more attractive for early-stage damage detection.

For brief introduction, different nonlinear ultrasonic phenomena are summarized as follows (Fig. 17.1): (1) Harmonic: When the waveform of the incident wave at frequency f_a is distorted by a nonlinear source, higher harmonic waves are generated with frequencies at $2f_a$, $3f_a$, etc.; (2) Sub-harmonic: Sub-harmonic is a nonlinear wave distortion resulting in the doubling of the period and frequency of $f_a/2$; (3) Nonlinear ultrasonic modulation: When two input waves at distinctive frequencies f_a and f_b ($f_a > f_b$) encounter a nonlinear source, modulated components are generated at frequencies $f_a \pm f_b$, $f_a \pm 2f_b$, $2f_a \pm f_b$, etc. Here, when f_a is equal to f_b, the corresponding modulation components become harmonics (self-modulation); and (4) Resonance frequency shift: The presence of a nonlinear source is manifested by a shift in the resonance frequency, as the amplitude of the driving input changes.

Though all these different nonlinear ultrasonic techniques are able to detect structural damage at its early stage, the nonlinear ultrasonic modulation technique offers the following advantages: (1) The nonlinear modulation technique is less influenced by unwanted nonlinear sources such as transducers, data acquisition systems, and even the bonding conditions (couplant) of the transducers; (2) Since the nonlinear components are generated only when some necessary conditions are satisfied for a damaged structure, it is relatively easier to satisfy the conditions for modulation generation with two distinct input frequencies at our disposal; and (3) It is easier to avoid interference with other noise sources.

Besides the nonlinear ultrasonic techniques, another trend in NDE is to adopt noncontact ultrasonic techniques so that structural components can be inspected without any contact transducer nor couplants. Moreover, structural damage can

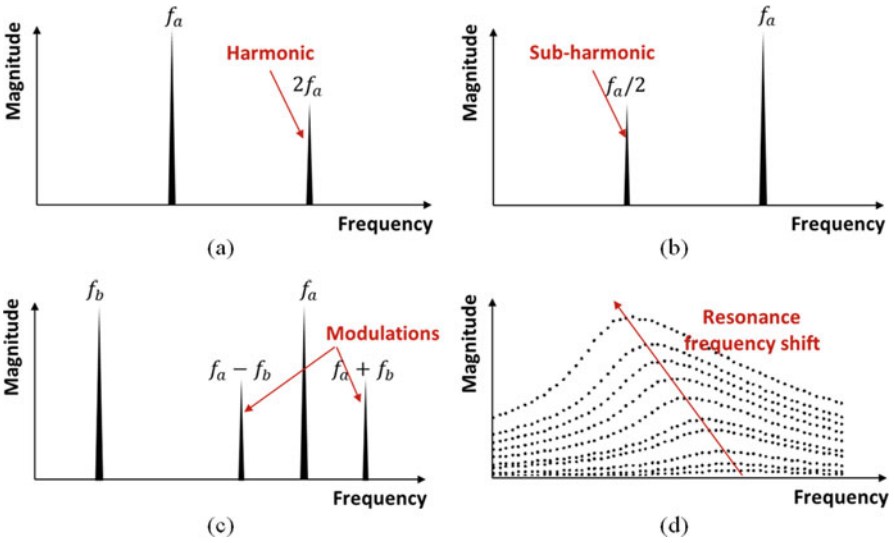

Fig. 17.1 Illustration of multiple nonlinear ultrasonic phenomena: (**a**) harmonic, (**b**) sub-harmonic, (**c**) nonlinear ultrasonic modulation, and (**d**) resonance frequency shift

be located and even visualized through noncontact scanning. Also, noncontact ultrasonics can facilitate the monitoring of structures or components that roll continuously on a production line, in extreme environmental conditions, coated, oxidized, or just difficult to physically access.

This chapter introduces noncontact nonlinear ultrasonic modulation techniques for fatigue crack and delamination detection. First, overviews of noncontact ultrasonic measurement systems using EMAT, ACT, and laser are provided specifically for generation and sensing of modulation components. Second, the principle of nonlinear ultrasonic modulation and the necessary conditions for nonlinear modulation generation are also reviewed. Third, representative damage detection algorithms based on ultrasonic modulation components are introduced. Last, examples of noncontact nonlinear ultrasonic modulation techniques applied to fatigue crack and delamination detection are showcased at the end of this chapter.

17.2 Noncontact Ultrasonic Generation and Measurement

For generation and sensing of ultrasonic waves, contact transducers are typically surface mounted on target structures. The most commonly used contact transducers are wedge transducer, piezoelectric transducer (PZT), fiber optic sensor, acoustic emission sensor, etc. These contact transducers have the following limitations: (1) The couplant layer can be a source of considerable variability in sensitivity and also in bandwidth (it can also be a source of nonlinearity); (2) High spatial resolution

is hard to achieve using contact transducers; (3) Transducer installation and cabling are costly and labor-intensive; and (4) For certain applications, there is no access to attach transducers on the target structure.

In recent years, there has been a growing interest in using noncontact transducers for field inspection of large scale or moving parts. The noncontact transducers generate or receive ultrasonic signals to or from the target structure without making direct or indirect contact. Using noncontact ultrasonic transducers, structures can be inspected without the fear of contamination from couplants. For noncontact ultrasonics, various transducers such as air-coupled transducer (ACT), electromagnetic acoustic transducer (EMAT), electronic speckle pattern interferometry (ESPI), and laser are used. Here, explanations will be given for these noncontact ultrasonic transducers.

17.2.1 Electromagnetic Acoustic Transducer (EMAT)

Electromagnetic acoustic transducer (EMAT) generates and measures ultrasonic waves using electromagnetic mechanisms. EMAT normally consists of a magnet and an electric coil as shown in Fig. 17.2. The electric coil driven by an alternating current (AC) electric signal generates an AC magnetic field, and the magnet in EMAT produces a bias magnetic field. Through the interaction of these two magnetic fields, ultrasonic waves can be generated in the test material (e.g., conductive and ferromagnetic materials) when the material is placed close to an EMAT. The biggest advantage of EMAT is its ability to generate a specific ultrasonic wave mode for structural damage detection, such as shear horizontal (SH) bulk waves, surface waves, and Lamb waves [1–4]. However, when it comes to real applications, it becomes challenging to control and maintain the spacing between the transducer and the structure. Its application is limited to metallic or magnetic materials, and, to the best of the authors' knowledge, EMAT has not yet been used for nonlinear ultrasonic modulation.

17.2.2 Air-Coupled Transducer (ACT)

Air-coupled transducer (ACT) transfers ultrasonic waves to the target structure through air. However, only small fraction of the sound energy at the source can be transmitted to the target structure due to large acoustic impedance mismatch between air and the target material [5]. Methods for minimizing the acoustic impedance mismatch have been intensively investigated in the past. Electrostatic air-coupled and piezoelectric air-coupled transducers have constituted the most popular design, and have been used for many damage detection applications [6, 7].

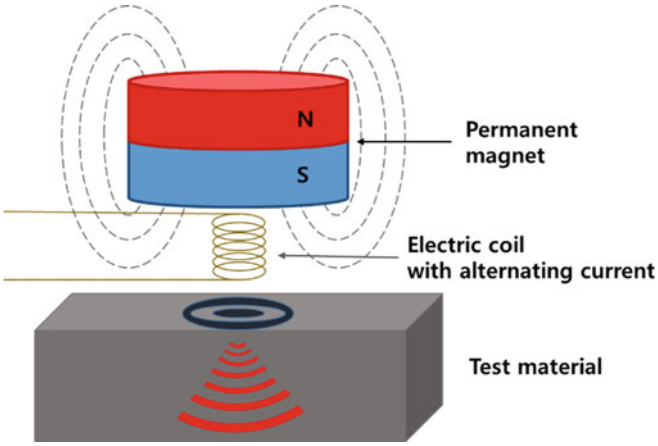

Fig. 17.2 Schematic of an electromagnetic acoustic transducer (EMAT)

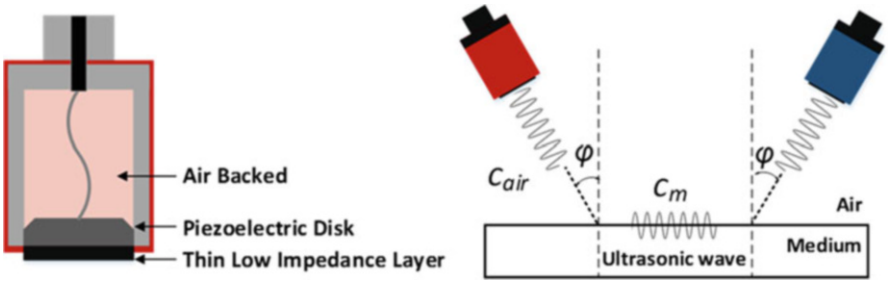

Fig. 17.3 Piezoelectric ACT composition (left) and the alignment for effective ultrasonic generation and measurement (right)

As one of the most popularly used ACTs, the piezoelectric ACT is mainly composed of a piezoelectric disk attached with a thin low impedance layer (Fig. 17.3). The piezoelectric disk converts a given electrical voltage signal into mechanical deformation. The thin low impedance layer enhances the efficiency in deformation transmission from the piezoelectric disk into air, by matching the acoustic impedance between the piezoelectric disk and the air. In this way, ultrasonic waves can be efficiently generated in the target structure. For ultrasonic measurement, ultrasonic waves propagating in the target structure successively deform the air, the thin low impedance layer, and the piezoelectric disk. The deformation in the piezoelectric disk can be converted back into measurable electrical voltage. The thin low impedance layer also improves the measurement efficiency.

For effective generation and measurement of ultrasonic waves in the target structure, proper ACT alignment is always required [5]. Based on Snell's law, when waves go through two different media, the relationship between the incidence angle and the refraction angle can be described as:

$$\frac{\sin\varphi}{\sin\theta} = \frac{c_{\text{air}}}{c_m} \tag{17.1}$$

where φ and θ indicate angles of incidence and refraction, and c_{air} and c_m imply the velocity of the waves in air and the target structure, respectively. When ultrasonic waves propagate along the surface, $\theta = 90^{\circ}$ as shown in Fig. 17.3, Eq. (17.1) can be presented as:

$$\sin\varphi = \frac{c_{\text{air}}}{c_m}, \quad \varphi = \sin^{-1}\frac{c_{\text{air}}}{c_m} \tag{17.2}$$

17.2.3 Laser-Based Ultrasonic Generation

For ultrasonic generation, the laser is a device which amplifies the light intensity through a quantum process known as stimulated emission. The amplified laser beam is emitted in a form of a short pulse (from tens of nanoseconds to femtoseconds) with high peak power. Common lasers used for ultrasonic generation are solid state Q-switched Nd:YAG lasers and gas lasers (CO_2 or Excimers), and they are used as a transient source of high-power localized heat. A number of different physical processes take place when a solid surface is illuminated by a laser [8]; however in this chapter, the discussion is focused on laser power regimes that are suitable for ultrasonic wave generation. As shown in Fig. 17.4, the surface region of a sample absorbs the electromagnetic radiation from a laser, causing heating. The received thermal energy then propagates into the sample in the form of thermal waves. For typical Q-switched laser pulse duration, the thermal wave field only extends a few micrometers even in good conductors. The heated region undergoes thermal expansion, and thermoelastic stresses generate elastic (ultrasonic) waves which propagate deep within the sample. All types of elastic waves can be generated, including bulk waves (compression and shear), surface waves (including Rayleigh), and guided waves (e.g., Lamb waves in plates, extensional and flexural waves in rods). Note that the thermal expansion level is proportional to the gradient of the thermal energy, thus, it indicates that a high-power short-pulse laser is suitable for ultrasonic generation with a high efficiency.

17.2.4 Laser-Based Ultrasonic Measurement

For laser ultrasonic measurement, there are various means such as two-beam homodyne, two-beam heterodyne, Fabry-Perot, time-delay, multi-beam, dynamic holographic, fiber interferometry, optical beam deflection, and knife edge detection [8]. Among them, laser Doppler vibrometer (LDV), one type of the two-beam heterodyne interferometers, is one of the most widely used by taking advantage of the Doppler effect.

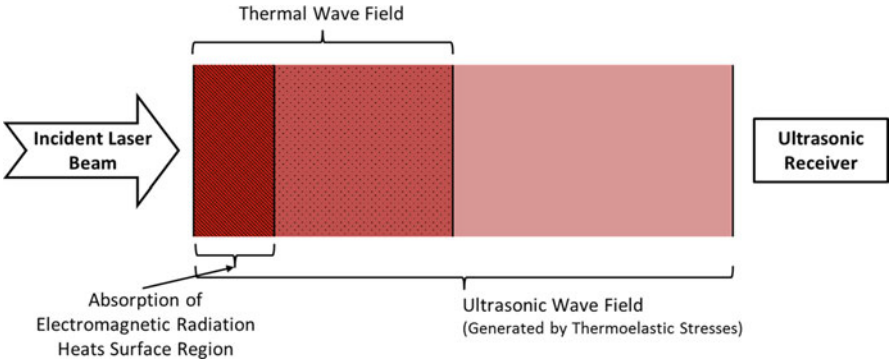

Fig. 17.4 Ultrasonic generation by a pulse laser

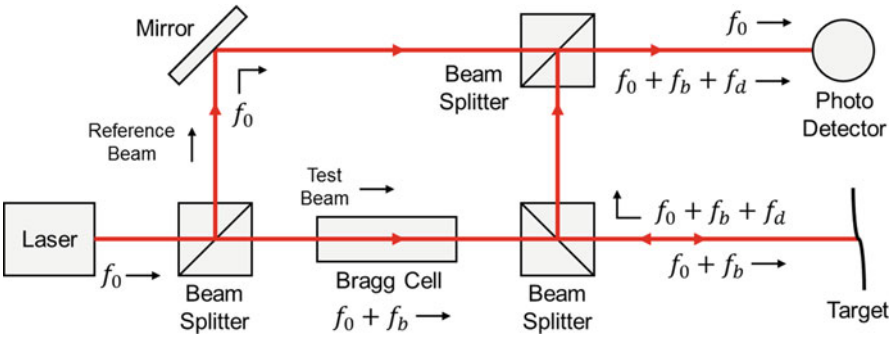

Fig. 17.5 Schematic of a typical laser Doppler vibrometer based on two-beam heterodyne method

If a laser beam is reflected by a moving object and detected by a measurement system, the measured Doppler frequency shift f_d can be interpreted as [9]:

$$f_d = 2 \cdot v/\lambda \tag{17.3}$$

where v is the velocity of the object and λ is the wavelength of the laser beam. To determine the object's velocity, the Doppler frequency shift needs to be measured with a known laser wavelength. This can be realized by using a LDV. LDV is a two beam laser interferometer that measures the frequency difference between an internal reference laser beam and a test laser beam. Though there are various types of laser can be used in LDV (e.g., laser diode, fiber laser, and Nd:YAG laser), the most commonly used is the helium-neon laser. Commercial LDVs mostly work in a heterodyne regime with a known frequency shift (typically 30–40 MHz) added to one of the two laser beams (Fig. 17.5).

The frequency shift should be selected greater than the maximum Doppler frequency shift, so that the frequency at the detector never falls to zero and thus sign ambiguity does not arise. A Bragg cell or an acousto-optic modulator is usually used to produce this frequency shift.

17.2.5 Laser Ultrasonic Scanning System

A complete noncontact laser ultrasonic scanning system is introduced in this section [10]. This system consists of an excitation unit, a sensing unit, and a control unit, as illustrated in Fig. 17.6. The excitation unit is comprised of a Q-switched Nd:YAG pulse laser, a galvanometer, and a focal lens. The laser source in the excitation unit has a wavelength of 532 nm and a maximum peak power of 3.7 MW. The Nd:YAG pulse laser can generate a pulse with 8 ns duration with a 20 Hz repetition rate. The galvanometer has a maximum rotating speed of 5730°/s, angular resolution of 6.6×10^{-4} °, and an allowable scan angle of ±21.8°. Through the galvanometer, the pulse laser can be shot at the desired excitation points. The focal lens installed in front of the galvanometer adjusts the laser beam size to less than 0.5 mm at the optical focal length of 2 m for achieving high spatial resolution. For the sensing unit, a commercial scanning LDV is used. The laser source in the sensing unit is a helium-neon (He-Ne) laser with a wavelength of 633 nm. The commercial scanning LDV has a maximum angular scan range of ±20° with a scanning speed of 2000°/s. Out-of-plane velocity with a range from 0.01 μm/s to 10 m/s can be measured using this one-dimensional LDV. Here, the system can be extended to conduct 3D measurement by using properly aligned and synchronized 3 LDVs. The control unit is composed of a personal computer (PC), controller, velocity decoder, and a 14-bit digitizer with a maximum sampling frequency of 2.56 MHz. The controller simultaneously launches the excitation laser beam and starts the data collection. It is also in control of aiming the excitation and sensing laser beams to desired target positions.

17.2.6 Different Scanning Strategies

Four different scanning strategies are given and compared [10]. Using this laser ultrasonic scanning system, two scanning strategies can be realized, that is, fixed laser excitation and scanning laser sensing (Fig. 17.7a), and scanning laser excitation and fixed laser sensing (Fig. 17.7b). When the laser ultrasonic scanning system is used together with a surface mounted PZT or a noncontact ACT, we can achieve two more scanning strategies, namely fixed PZT/ACT excitation and scanning laser sensing (Fig. 17.7c), and scanning laser excitation and fixed PZT/ACT sensing (Fig. 17.7d). The four scanning strategies have their own advantages and disadvantages, and suit for different applications. A brief comparison and discussion is given below.

Theoretically, based on the linear reciprocity of ultrasonic waves, the scanning strategies shown in Fig. 17.6a, b offer the identical scanning results. However, in practice, the excitation laser is more effective in scanning than the sensing laser. This is because the target surface irregularity and the incident angle of the laser beam have little effect on the ultrasonic generation by a Nd:YAG laser, while the sensitivity of LDV heavily depends on the surface condition of the sensing points

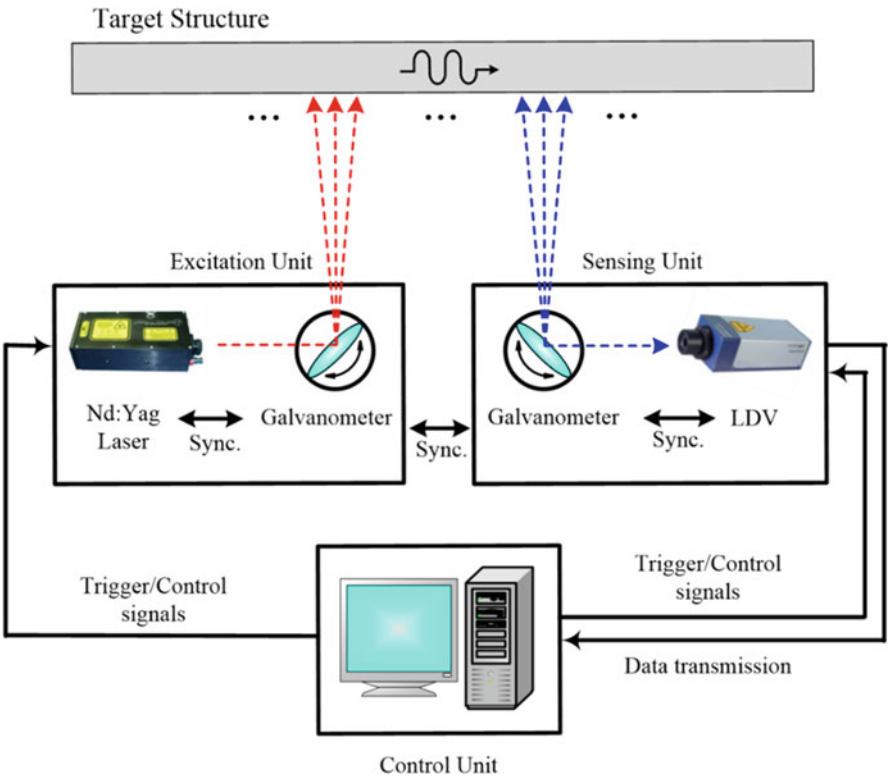

Fig. 17.6 Schematic diagram of a noncontact laser ultrasonic scanning system [10]

and the incident angle of the sensing laser beam. Often, a retro-reflective tape or special coating is applied to the sensing surface to improve the LDV sensitivity by increasing the light intensity of the backscattered laser beam along the incident angle. Typically, the allowable incident angle for an excitation laser is up to $\pm 70^\circ$ while $\pm 20^\circ$ for a sensing laser [8].

For the scanning strategy shown in Fig. 17.7c, when a fixed PZT or ACT is used for ultrasonic generation, any arbitrary waveform such as a narrowband tone-burst signal can be exerted to an excitation point with high energy level. The desired narrowband excitation and high excitation energy makes the following signal processing clearer and easier. Also, the high excitation energy may augment inspection speed by reducing the time averaging for ultrasonic measurement with LDV. Note that, though the input waveform of a laser excitation is limited to a wideband pulse in this discussion, there still exist some special techniques to generate narrowband inputs with laser [11, 12].

A similar wavefield image can be created by the scanning strategy shown in Fig. 17.7d unless the excitation is limited to a pulse input. However, for some specific applications such as curved surfaces or large scanning areas, the scanning strategy

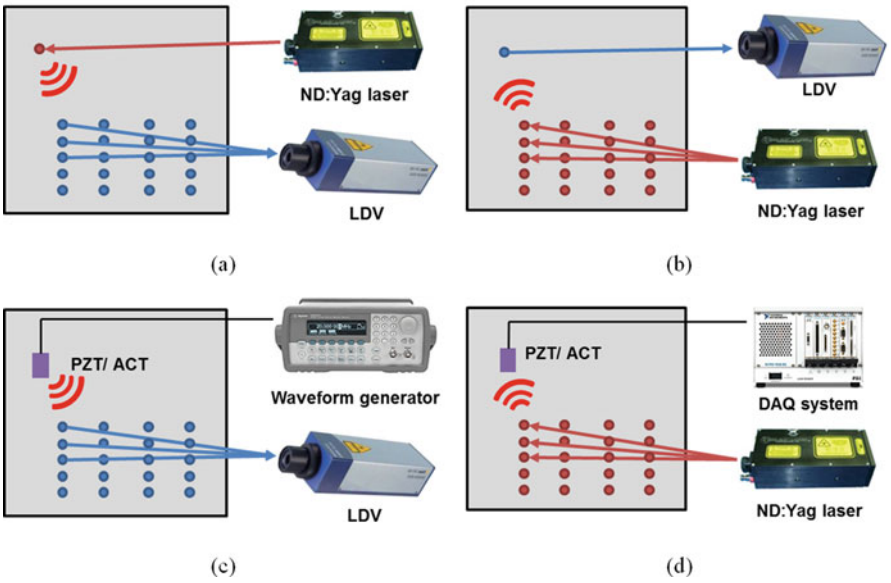

Fig. 17.7 Four different scanning strategies: (**a**) fixed laser excitation and scanning laser sensing, (**b**) scanning laser excitation and fixed laser sensing, (**c**) fixed PZT/ACT excitation and scanning laser sensing, and (**d**) scanning laser excitation and fixed PZT/ACT sensing

shown in Fig. 17.7d is more effective than the strategy shown in Fig. 17.7c, because the surface irregularity and the incident angle of the laser beam have less effect on the ultrasonic generation by the Nd:YAG laser, comparing with the ultrasonic sensing by LDV.

17.3 Basic Principle of Nonlinear Ultrasonic Modulation

17.3.1 Nonlinear Ultrasonic Modulation

When two waves a and b at a high frequency (HF) f_a and a low frequency (LF) f_b ($f_a > f_b$) propagate in the x-direction of a plate-like structure without any nonlinear source, the induced displacement can be presented as:

$$u_0 = \mathrm{A}_0 \exp\left(i\left(\kappa_a x - 2\pi f_a t\right)\right) + \mathrm{B}_0 \exp\left(i\left(\kappa_b x - 2\pi f_b t\right)\right) \tag{17.4}$$

where A_0, B_0 and κ_a, κ_b are the amplitudes and wavenumbers for the waves a and b, respectively.

However, when the waves propagate in a structure with either a localized or distributed nonlinear source, due to the interaction of the propagating waves with the

nonlinear source, the induced displacement u_1 can be expressed as the summation of the linear, u_1^L, harmonics, u_1^H, and modulation, u_1^M, components [13, 14]:

$$u_1 = u_1^L + u_1^H + u_1^M \tag{17.5}$$

where

$$u_1^L = \mathrm{A}_1^L \exp\left(i\left(\kappa_a x - 2\pi f_a t\right)\right) + \mathrm{B}_1^L \exp\left(i\left(\kappa_b x - 2\pi f_b t\right)\right) \tag{17.6}$$

$$u_1^H = \mathrm{A}_1^H \exp\left(2i\left(\kappa_a x - 2\pi f_a t\right)\right) + \mathrm{B}_1^H \exp\left(2i\left(\kappa_b x - 2\pi f_b t\right)\right) \tag{17.7}$$

and

$$u_1^M = \mathrm{A}_1^M \exp\left(i\left[\left(\kappa_b \pm \kappa_a\right) x - 2\pi\left(f_a \pm f_b\right) t\right]\right) \tag{17.8}$$

where A_1^L and B_1^L are the amplitudes of the linear components at f_a and f_b, A_1^H and B_1^H are the amplitudes of the second harmonics at $2f_a$ and $2f_b$ induced by the nonlinear source, respectively. A_1^M is the amplitude of the first modulations (sidebands) at $f_a \pm f_b$ induced by the mutual interaction between the input waves at the nonlinear source. For simplicity, higher-order nonlinear components are omitted. This phenomenon is called nonlinear ultrasonic modulation or nonlinear wave modulation. Because this phenomenon occurs only if there are nonlinear sources, it can be considered a signature of the presence of nonlinearity, and thus the existence of nonlinear damage, assuming that the inherent material nonlinearity is weak. Indeed, most structural damage evolves in a nonlinear manner, causing an intact structure with predominantly linear properties to exhibit nonlinear properties [15–22].

17.3.2 Necessary Conditions for Nonlinear Ultrasonic Modulation

Actually, nonlinear wave modulation can be produced by either the distributed material nonlinearity or a localized damage. Relevant findings are summarized as follows [23]:

(1) Distributed material nonlinearity: The source of material nonlinearity can be the crystallographic defect or irregularity within a material, including distributed dislocation and interatomic potential in the material. Besides, initial micro-cracks/voids distributed over the entire material can also contribute to the material nonlinearity. Comparing with the localized nonlinearity caused by damage such as a fatigue crack, the distributed material nonlinearity is not

localized (global characteristic) and usually shown to be weak [24, 25]. However, the distributed material nonlinearity can occasionally give non-negligible contribution to the measured nonlinear components [14].

(2) Localized damage nonlinearity: Take the crack damage as an example. The crack surface will alternate between open and closed (contact) conditions when ultrasonic waves or vibrations are applied to the cracked structure. This is known as "breathing crack" or "contact acoustic nonlinearity (CAN)" [14, 18, 26, 27]. For cracks with rough surfaces, even when they are not completely open or closed ("micro-contact"), they are still able to produce localized nonlinearity [28]. Additionally, it is demonstrated that dissipative mechanisms (friction) between the crack surfaces can also cause nonlinearity. This localized nonlinearity caused by crack opening/closing or friction has been shown to be much stronger compared to the distributed material nonlinearity [24] (Klepka et al. 2002).

However, there are some conditions need to be satisfied to observe the modulations with both distributed material nonlinearity and a localized damage. The necessary conditions for the distributed material nonlinearity in a plate-like structure can be summarized as below:

(1) Synchronism condition: In the propagating waves, the phase velocities of HF and LF inputs, f_a and f_b, should be identical to the phase velocity at $f_a \pm f_b$ [13, 29]. From the viewpoint of vibration, the mode shape of vibration at $f_a \pm f_b$ should be resulted from the point-wise multiplication of the vibration mode shapes caused by the HF and LF inputs [30].

(2) Non-zero power flux condition: From the viewpoint of wave propagation, in order to transmit the energy from the input waves to the nonlinear modulation waves, the mode types of both the input waves and the modulation waves should be matched [13, 29]. For a plate-like structure, only the S Lamb wave modes can produce nonlinear harmonic waves at even order harmonics [31]. Similarly, when the HF and LF inputs are both A Lamb wave modes, they will not be able to generate the first nonlinear modulation components ($f_a \pm f_b$). For vibrations, in addition to the thickness direction, the mode types (longitudinal or flexural) should also be matched in the longitudinal direction.

Also, the necessary conditions for localized nonlinearity such as a fatigue crack in a plate-like structure can be summarized as follows [23]:

(1) Crack perturbation condition: Both the input waves should oscillate the strain at the crack. In stationary vibrations, the node is defined as a point where the vibration shows the minimum amplitude (zero strain), whereas the anti-nodes refer to the maximum amplitude (maximum strain). Thus, the nonlinear modulation will not be generated when the crack happens to be located at one of the vibration nodes induced by the inputs. For transient wave propagation, this condition is unconditionally satisfied since the strain at the crack must be perturbed during the wave propagation.

(2) Mode matching condition: One of the input waves should be modulated at the crack location by the crack motion induced by the other wave. For example, a HF longitudinal wave and a LF shear horizontal wave are propagating in the x-direction through a crack. Here, the crack orientation (z-direction) is perpendicular to the wave propagation direction. Crack motion caused by the LF shear horizontal wave (crack oscillation/ friction in the y-direction) will not modulate the HF longitudinal wave because their motions are orthogonal to each other. Thus, nonlinear modulation will not be produced in this example. A previous study also demonstrates that large amplitude of nonlinear modulation can be observed if the ultrasonic signal is modulated by the crack motion (Klepka et al. 2002).

17.3.3 Controlling of the Inputs for Nonlinear Ultrasonic Modulation

There are two practical solutions to ensure that the modulation can be generated and detected from a damaged structure:

(1) The first method is to sweep the input frequencies. That is, a fixed LF and a sweeping HF signals are used as input or the other way around. Didenkulov et al. found that cracks in concrete beams generated significant modulation components when a sweeping LF signal was used [32]. The sweeping of HF input for the modulation generation was studied by Duffour et al. [27]. This HF dependence was also noted by Courtney et al. [33]. A fixed LF and a sweeping HF were used to find an optimal combination that can amplify the modulation level caused by a crack [30].

Moreover, both the HF and LF inputs can be swept to increase the possibility to satisfy the necessary conditions for modulation generation. For example, a first sideband spectrogram is created by sweeping both the LF and HF inputs over specified frequency ranges to study the effect of input frequency combination on the modulation amplitude [34]. This experiment was conducted on aluminum plate specimens with a fatigue crack, and Fig. 17.8 gives an example of the first sideband spectrogram by sweeping the LF inputs from 10 to 20 kHz and the HF inputs from 80 to 110 kHz. It can be seen that only for certain HF and LF combinations, the nonlinear modulation components have higher amplitudes in the presence of a fatigue crack. Though sweeping of the input frequencies can increase the possibility of modulation generation for structural damage detection, sweeping over a wide frequency range takes a long data collection time and can be impractical for field applications.

(2) The second method is to use a wideband signal as an input. That is, rather than using two distinctive input frequencies, a single wideband excitation is used instead [35–37]. When a wideband excitation signal (e.g., a pulse laser)

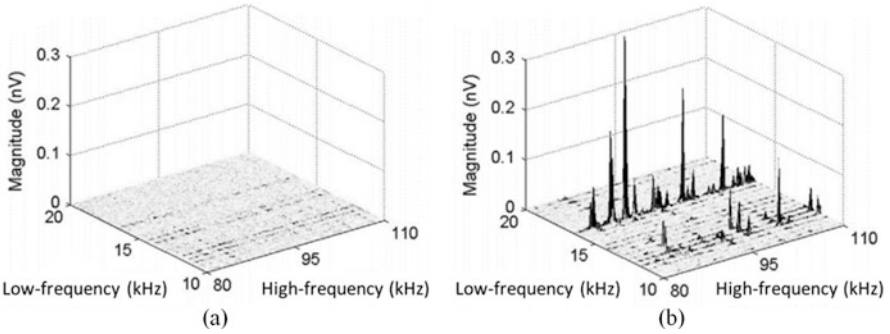

Fig. 17.8 The first sideband spectrogram obtained from aluminum specimens by sweeping the HF inputs from 10 to 20 kHz and the LF inputs from 80 to 110 kHz: (**a**) intact case, (**b**) damage case [34]

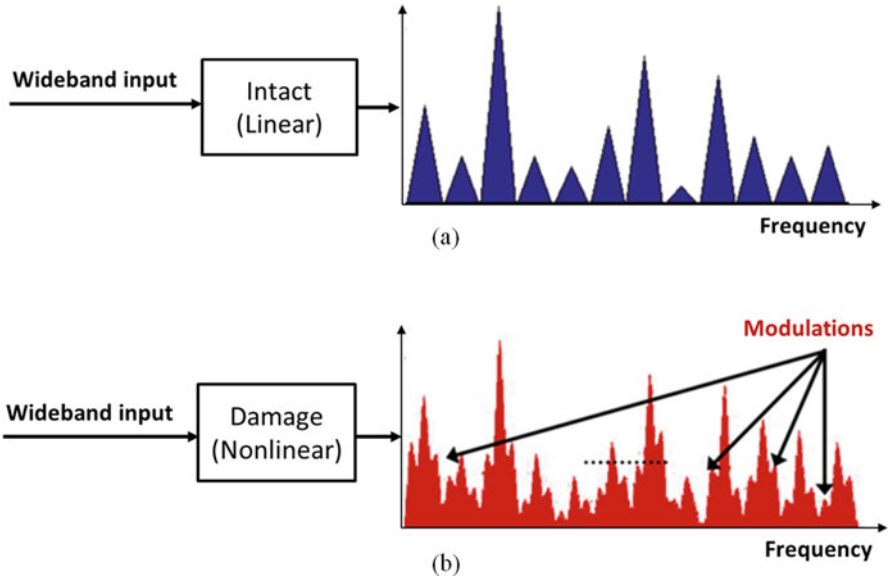

Fig. 17.9 Illustration of nonlinear ultrasonic modulation using a wideband input: (**a**) intact case, (**b**) damage case [35–37]

is applied to a structure, different frequency peaks will be generated in the frequency domain due to different wave modes, such as guided waves (Lamb waves) propagating in a plate and standing waves of a structure. Nonlinear ultrasonic modulation can take place among these different frequency peaks if there is damage in the structure, as shown in Fig. 17.9. In this way, the wideband input guarantees that the necessary conditions can be satisfied among at least certain frequency combinations in the generated frequency band. Here, the test data collection time can be significantly reduced compared with the

time using frequency sweeping. Because the nonlinear modulation components and the linear response components may overlap in the frequency domain using a wideband input, it requires additional damage detection techniques to investigate the generation of nonlinear modulation components under a damage condition.

One issue to be concerned is that the energy level for each frequency component under a wideband input might be much lower than the energy level achieved with two single distinctive input frequencies. However, the feasibility of nonlinear wave modulation with a wideband input has been indirectly proven in several studies. de Lima et al. showed that nonlinear modulation can be produced even at a very low strain level by the crack-induced dislocation, friction, stress concentration, or temperature gradient [29]. Van Den Abeele et al. investigated the effect of the strength of the LF input signal on the modulation energy, and showed that the nonlinear modulation in a structure with nonlinearity remains significant and measurable even when the strength of the LF signal is almost zero [28]. Therefore, even when the energy level at each frequency component caused by a wideband excitation is relatively low, the nonlinear behavior of a damaged structure can still be detected using the wideband input. In addition, because multiple frequency peaks can be generated by a wideband excitation, higher-order nonlinear modulations (cascade cross modulations) can be generated as well in the presence of damage.

17.4 Damage Detection Techniques Using Noncontact Nonlinear Ultrasonic Modulation

The majority of existing nonlinear ultrasonic modulation-based damage detection techniques use two distinct frequencies as inputs. Structural damage is detected by comparing the nonlinear features (e.g., the nonlinear modulation amplitude or the nonlinear coefficient) obtained from the current state of structure with the baseline data obtained from the intact condition. However, there are two major issues need to be considered: (1) The amplitude of the damage-induced modulation components is at least one or two orders of magnitude smaller than that of the linear response components. Test noises, varying with environmental and operational conditions, can deteriorate the performance of these damage detection techniques; and (2) The input frequencies need to be carefully selected, because the generation of nonlinear modulation also depends on the choice of the input frequencies and can also be easily affected by the configuration of the damage as well as by variations in the environmental and operational conditions (e.g., temperature and loading) of the target structure.

This section lists some representative damage detection techniques using noncontact nonlinear ultrasonic modulation, which can tackle the above-mentioned issues to a certain extent.

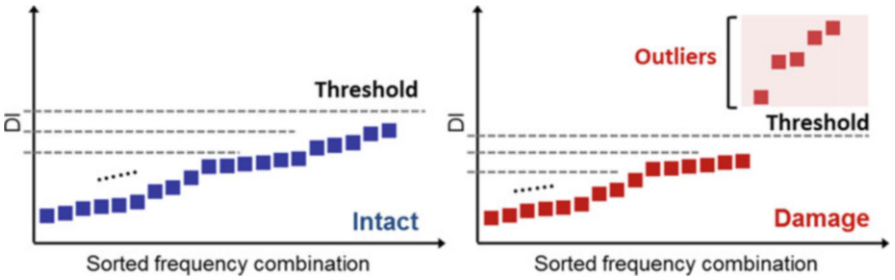

Fig. 17.10 Illustration of sequential outlier analysis with multiple LF and HF inputs

17.4.1 Sequential Outlier Analysis Technique

The first structural damage detection technique is based on sequential outlier analysis [38]. As previously discussed, the nonlinear modulation components can be generated only at some specific input frequency combinations even at the presence of nonlinear sources, and the optimal input frequency combinations will change over time for field applications due to operational and environmental variations. Here, the principle idea is to sweep the input LF and HF signals over a specified frequency range. A damage index (DI), indicating the nonlinear modulation in the measured response, is calculated for each LF and HF combination. Since nonlinear ultrasonic modulation doesn't occur for all the LF and HF combinations, damage can be detected without relying on any baseline data through a simple sequential outlier analysis of all the DIs. The procedure of the sequential outlier analysis can be summarized as follows (Fig. 17.10) [39]:

(1) All DI values are rearranged in an ascending order.
(2) For the n-1 smallest DI values, a parametric distribution is fitted assuming that there are no outliers among these n-1 DI values. A threshold is then computed from this fitted distribution with a user specified confidence level.
(3) If the nth smallest DI value is over the threshold, it indicates the existence of damage and all the DI values larger than the nth DI value are determined as outliers, as illustrated in Fig. 17.9. If not, repeat steps (2) and (3) for the next smallest value $n + 1$ until the largest DI value is tested.

17.4.2 Spatial Comparison Technique

The second structural damage detection technique is based on spatial comparison [40]. By taking advantages of a laser ultrasonic scanning system, ultrasonic response obtained from a specific spatial point can be compared with other responses obtained from its spatially adjacent points. The basic premise is that, unless there exists

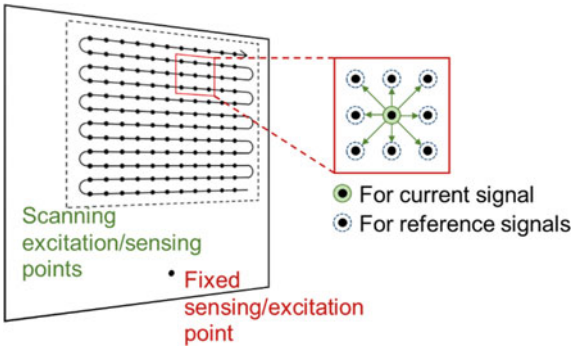

Fig. 17.11 Illustration of spatial comparison technique through laser scanning

anomaly (e.g., damage) among spatially adjacent points, ultrasonic waves from these points should be similar. Thus, without the baseline data from the intact condition, damage can still be detected or even visualized by spatial comparison. The basic procedure can be summarized as follows:

(1) When the sensing/excitation point is fixed on the target structure, the responses are measured for all the scanning excitation/sensing points within a specified inspection area as illustrated in Fig. 17.11.
(2) For each spatial point in the inspection area, the response signals obtained from its adjacent points are used as references. The current response from each spatial point can be compared with the adjacent references signals, and DI can be acquired for each spatial point.
(3) All DI values can be visualized for the entire inspection area, and spatial points with high DI values indicate the existence and the location of the damage.

17.4.3 Sideband Peak Count Technique

This sideband peak count (SPC) technique is for damage detection using nonlinear ultrasonic modulation with a wideband input. This SPC technique keeps track of the relatively weak spectral peaks, rather than the dominant peaks, generated due to the damage-induced nonlinear modulation [35–37, 41]. The procedure for SPC technique can be summarized as follows [35–37]:

(1) Spectral density distribution $P_x(f)$ of the wideband ultrasonic response signal $x(t)$ is calculated in the frequency domain:

$$P_x(f) = E\left[X(f)X^*(f)\right] \tag{17.9}$$

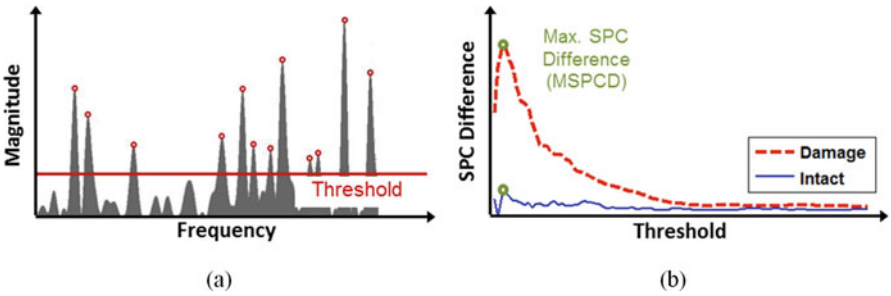

Fig. 17.12 Illustration of sideband peak count (SPC) technique: (**a**) a moving threshold is set to count the ratio of the spectral peak number over the threshold to the total peak number, (**b**) SPC difference increases in the damage case especially when the threshold is low [35–37]

where $X(f)$ is the Fourier transform of $x(t)$ and "asterisk" denotes the complex conjugate. $P_x(f)$ within a specified frequency range is selected and normalized to fit its values within unity.

(2) The SPC is defined as the ratio of the spectral peak number (N_p) over a moving threshold (T) to the total peak number (N_t) within the specified frequency range, as shown in Fig. 17.12a. When T moves from 0 to 1, the SPC value varies with T, and a SPC plot can be achieved:

$$\mathrm{SPC}(T) = \frac{N_p(T)}{N_t} \tag{17.10}$$

(3) A SPC difference is calculated between the SPC plots obtained from the current and reference conditions. As the level of nonlinearity increases, more sideband peaks show up in the spectrum or the sideband energy grows as a consequence. Therefore, the SPC plot will show larger values for the damage case than for the intact case, and the SPC difference becomes positive for the damage case. The maximum SPC difference (MSPCD) is selected as a nonlinear damage feature for damage detection:

$$\mathrm{MSPCD} = \max(\mathrm{SPC}_c - \mathrm{SPC}_r) \tag{17.11}$$

where SPC_c and SPC_r are the SPC plots obtained from the current and reference conditions, respectively. Figure 17.12b shows a representative plot of SPC difference obtained from an experiment.

Here, in conjunction with the spatial comparison technique in Sect. 17.4.2, the SPC can becalculated for all spatial points within the scanning area. For each spatial

point, the MSPCD is then achieved by comparing its SPC plot with other reference SPC plots obtained from its adjacent points. Slightly different from Eq. (17.3), the MSPCD here is redefined as:

$$\mathrm{MSPCD}_n = \max\left(\left|\mathrm{SPC}_c - \mathrm{SPC}_{r,n}\right|\right)$$
$$\mathrm{MSPCD} = \frac{1}{N}\sum\nolimits_{n=1}^{N}\mathrm{MSPCD}_n \tag{17.12}$$

where $\mathrm{SPC}_{r,n}$ is the reference SPC plot from each adjacent point, and N is the total number of the adjacent points. In this way, damage can be detected and even visualized by spatial comparison, which frees the SPC technique from the adverse influence caused by varying operational and environmental conditions of the target structure.

To further improve the SPC technique, ultrasonic response signals are transformed into a new spectral correlation domain instead of the spectral frequency domain [42]:

$$S_x(f_a, f_b) = E\left[X(f_a)\,X^*(f_b)\right] \tag{17.13}$$

when $f_a = f_b = f$, $S_x(f,f)$ equals to its spectral density function $S_x(f,f) = P_x(f) = E[X(f)X^*(f)]$. Here, if the specified range of f varies from f_1 to f_2, the new SPC operation is conducted in the corresponding spectral correlation region $S_x(f_a,f_b)$ $(f_a > f_b)$, as shown in Fig. 17.13. The SPC in Eq. (17.10) is redefined as the ratio of the number of the spectral correlation peaks over a moving threshold plane to the total peak number within a specified spectral correlation region. Then, we can calculate the SPC difference and obtain the MSPCD value as defined in Eq. (17.11) or (17.12). Because of some properties of spectral correlation, compared with the SPC technique in the spectral frequency domain, this new SPC technique owns the following advantages: (1) It is more robust against noise interferences; and (2) It owns a higher sensitivity to damage.

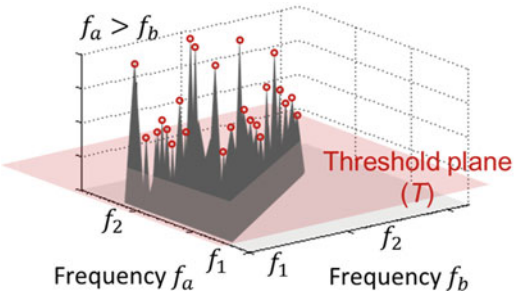

Fig. 17.13 Illustration of SPC technique in the spectral correlation domain

17.4.4 State Space Attractor Technique

The state space attractor technique is another technique to estimate the nonlinearity within the response to a wideband excitation. Recently, the sensitivity of data-driven dynamic state space attractors to nonlinear damage has been shown by checking the geometric variations of the attractors obtained under either deterministic or stochastic excitations [35–37, 43–45].

Considering the target structure as a dynamical system, and let us assume the dynamical system can be described by a first-order differential equation:

$$\dot{\boldsymbol{x}} = f(\boldsymbol{x}, t) \tag{17.14}$$

With an initial value $\boldsymbol{x}(0)$ in a state space defined by the system variables $\boldsymbol{x}$, the solution to this equation will trace out a trajectory, and this trajectory will approach a state space attractor of the dynamical system as the transients die out. This state space attractor is defined as a geometric object to which all trajectories belong in the state space [44]. In practice, lag copies of a single time series $x(n)$ of the system response data can be concatenated to qualitatively reconstruct the attractor according to the mathematical embedding theory proposed by Takens [46]. Here n ($n = 1, 2, \ldots, N$) is the discrete time index. The reconstructed attractor $\boldsymbol{X}$ at each discrete time instance can be expressed as:

$$\begin{aligned} \boldsymbol{X}(n) &= \left[x(n), x\left(n + T_{\text{lag}}\right), \ldots, x\left(n + (m-1)\,T_{\text{lag}}\right)\right] \\ & n = 1, 2, \ldots, N - (m-1)\,T_{\text{lag}} \end{aligned} \tag{17.15}$$

where T_{lag} is the time lag and m is the embedding dimension (Fig. 17.14). Only with proper selection of T_{lag} and m, the reconstructed state space attractor can truly preserve the underlying system dynamics. The autocorrelation method and the average mutual information (AMI) function are commonly used for selection of T_{lag}. As for selection of m, two common techniques are the false nearest neighbors (FNNs) method and the singular system analysis. Readers can find details about these aforementioned methods in Overbey et al. [45].

In order to quantitatively indicate the geometric variation of the state space attractors, a statistical distance called Bhattacharyya distance (BD) is introduced as the nonlinear damage feature [40, 44, 45]. Here, two time series are needed, one from the current condition of the target structure and the other from a reference condition. Thus, two attractors can be reconstructed, namely current attractor $\boldsymbol{X}$ and reference attractor $\boldsymbol{Y}$, respectively. The procedure for BD extraction can be summarized as follows (Fig. 17.15):

(1) Q fiducial points $\boldsymbol{Y}(i)$ ($1 \le i \le N - (m-1)T_{\text{lag}}$) are randomly selected from $\boldsymbol{Y}$. To make sure the extracted BD feature is not affected by the addition of successive fiducial points, a convenient rule is to choose the number $Q = N/100$ [47].

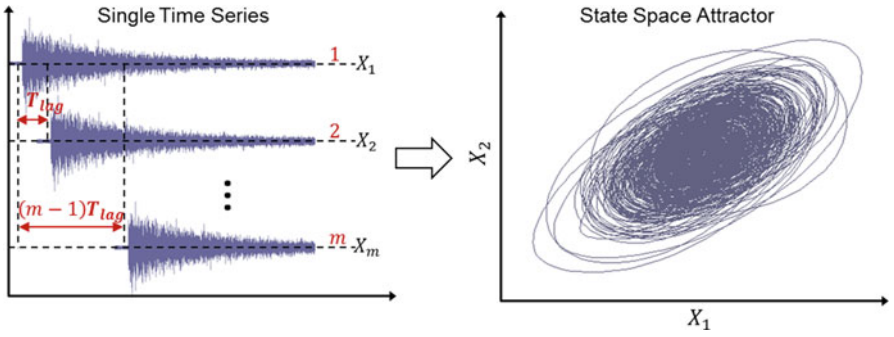

Fig. 17.14 Illustration of state space attractor reconstruction from a single time series

(2) For each fiducial point $\boldsymbol{Y}(i)$, P nearest neighbors $\boldsymbol{X}_{ci}(j)$ $(1 \le j \le N-(m-1)T_{\text{lag}})$ are selected from $\boldsymbol{X}$. An optimal choice is $P = N/1000$ [48]. The fiducial point and its neighbors are then time-evolved with a time step L (in most cases, $L = 1$), and the mass centroid is computed for the time-evolved neighborhood:

$$\widehat{\boldsymbol{Y}}_c\,(i+L) = \frac{1}{P} \sum_{1 \le j \le N-(m-1)T_{\text{lag}}} \boldsymbol{X}_{ci}\,(j+L) \tag{17.16}$$

And the error between the mass centroid and the time-evolved fiducial point:

$$e_{ci} = \left\| \widehat{\boldsymbol{Y}}_c\,(i+L) - \boldsymbol{Y}\,(i+L) \right\| \tag{17.17}$$

where $\|\cdot\|$ presents the Euclidean norm. Next, for each fiducial point, P nearest neighbors $\boldsymbol{X}_{ri}(j)$ are also selected from the reference attractor itself. Another error e_{ri} can be calculated for each fiducial point using Eqs. (17.16) and (17.17). The total number of e_{ci} or e_{ri} is Q.

(3) BD is computed to statistically estimate the difference between e_{ri} and e_{ci} obtained from the reference and current attractors:

$$\text{BD} = \frac{1}{4}\frac{(\mu_c - \mu_r)^2}{{\sigma_c}^2 + {\sigma_r}^2} + \frac{1}{2}\ln\left[\frac{{\sigma_c}^2 + {\sigma_r}^2}{2\sigma_c\sigma_r}\right] \tag{17.18}$$

where μ_r, σ_r and μ_c, σ_c denote the mean and standard deviation of e_{ri} and e_{ci}, respectively. If the current condition of the target structure differs from its reference condition, there will be a big geometrical variation between the reconstructed current attractor and the reference attractor, resulting in a large BD value.

Also, in conjunction with the spatial comparison technique in Sect. 17.4.2, the state space attractor can be reconstructed for all spatial points within the scanning area, and the BD value can be computed by spatial comparison. For each spatial

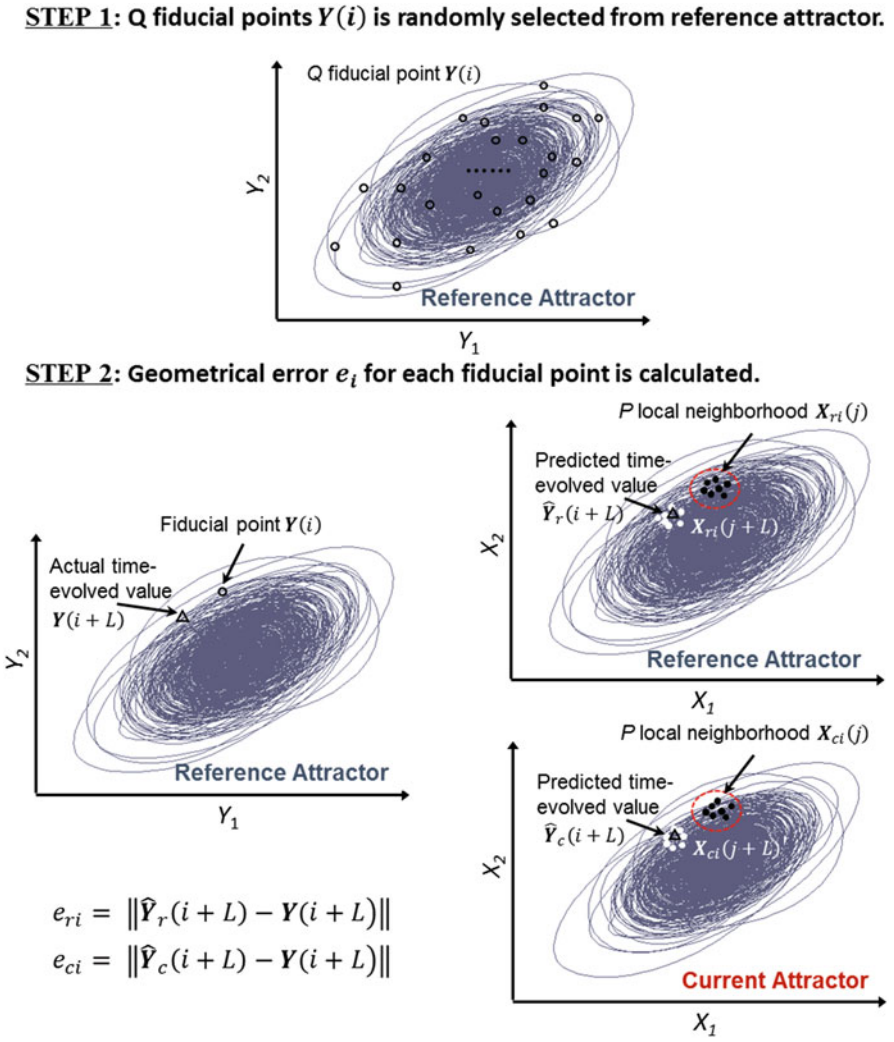

Fig. 17.15 Overview of the BD computation between the current and reference state space attractors [40]

point, the attractors reconstructed from its adjacent points can be treated as its reference attractors. In this way, even without the baseline data obtained from the intact condition, damage can also be detected or visualized.

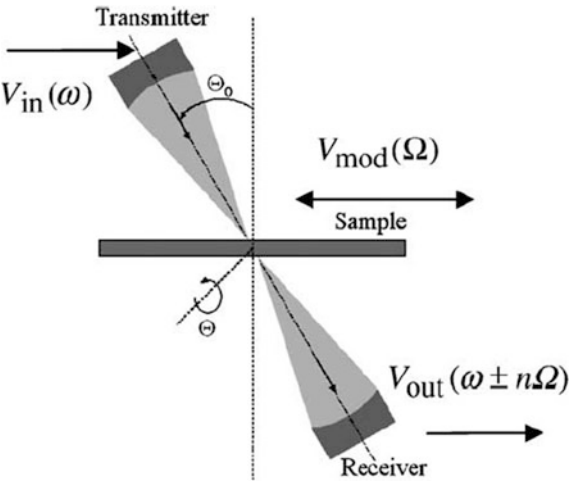

Fig. 17.16 Experimental configuration for nonlinear ultrasonic modulation using ACTs [6]

17.5 Applications Using ACT-Based Measurement Systems

17.5.1 Fatigue Crack Detection in Plates

As shown in Fig. 17.16, a pair of focused ACTs was used to generate and receive high frequency (HF, $\omega \approx 450$ kHz) longitudinal or flexural waves in plate-like samples. Low frequency (LF, $\Omega \sim 1$–20 kHz) vibrations were excited with a shaker or a loudspeaker [6]. Here, 2D scanning of the co-axial ACTs over the plate-like samples was implemented by a stepping motor controlled scanning assembly. In this experiment, two different acoustic modes of operation were used, namely normal transmission mode (NTM) and slanted transmission mode (STM). In NTM, longitudinal waves were generated and transmitted through the sample by aligning the ACTs normal to the sample surface ($\theta_0 = 0$ in Fig. 17.16). In STM, A0 Lamb wave mode was generated along the sample by adjusting the incidence angle θ_0 according to the Snell's law.

The plate used in experiment was a thin plate of polystyrene with a thickness of 1.15 mm. A realistic cutting crack was made by an impacting hammering in the plate. Figure 17.17 shows the NTM linear and sideband (modulation) B-scans of the impact crack in plate. Both the linear and sideband images clearly discern the crack by a local increase in a linear transmission or sideband generation. However, the contrast of the images was measured to be different: $\Delta V/V \approx 5$ for the linear image, which is much lower than $\Delta V/V \approx 80$ at the modulation components. Here, V is the average value of the intact area, and ΔV is the difference between the measured value from the crack and V. Figure 17.18 gives the STM mode results for the impact crack. Firstly, the image at the fundamental frequency drops down at the crack location because of flexural wave scattering while the sideband images rise at the crack location due to local nonlinear generation, giving an inverse contrast of

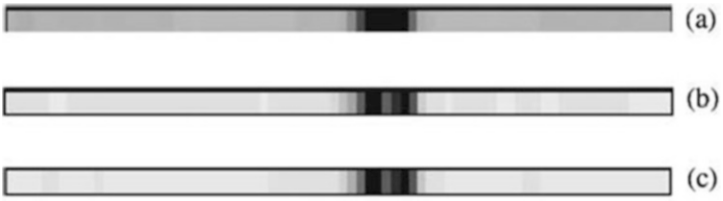

Fig. 17.17 Crack imaging in NTM: (**a**) linear image (at fundamental frequency 451.4 kHz), (**b**) sideband image (at first difference frequency 449.7 kHz), and (**c**) sideband image (at first sum frequency 453.1 kHz) [6]

Fig. 17.18 Crack imaging in STM: (**a**) linear image (at fundamental frequency 452.7 kHz), (**b**) sideband image (at first sum frequency 454.4 kHz), and (**c**) sideband image (at second sum frequency 456.1 kHz) [6]

images in Fig. 17.18. Secondly, the contrast of the images also reveals an evident priority for the sideband images: $\Delta V/V \approx -0.5$ for the linear image, which is much lower than $\Delta V/V \approx 10$ at the modulation components.

Another experiment was conducted on aluminum plates with fatigue cracks [19]. Two distinctive frequency input signals were created by two ACTs and the corresponding ultrasonic responses were scanned using a 3D LDV, as shown in Fig. 17.19. For each scanning point, the damage index (DI) was defined as the first sideband components normalized with respect to the multiplication of amplitudes of LF and HF inputs. After visualizing all the DI values, fatigue crack can be detected and located, as explained in Sect. 17.4.2. Two aluminum plates were fabricated and micro-cracks and a macro-crack were introduced to specimen I and II, respectively, after different cycles of tensile loading. The lengths and widths of micro-cracks near the center hole of specimen I were less than 60 μm and 1 μm, respectively. For the macro-crack in specimen II, micro-cracks at the indented point and the crack tip were also observed.

Considering the conditions for modulation generation, 45 and 160 kHz were selected for specimen I, and 46 and 156 kHz for specimen II. Figure 17.20 shows the visualization results for specimens I and II using all the DI values extracted from the measured in-plane response components. For specimen I, because of the formation of micro-cracks, high DI values exist near the center hole (Fig. 17.20a). For specimen II, it is noted that the highest DI values are observed near the indented point and the crack tip (Fig. 17.20b). This experiment shows that the largest nonlinear ultrasonic modulation occurred where the crack width is less than 1 μm.

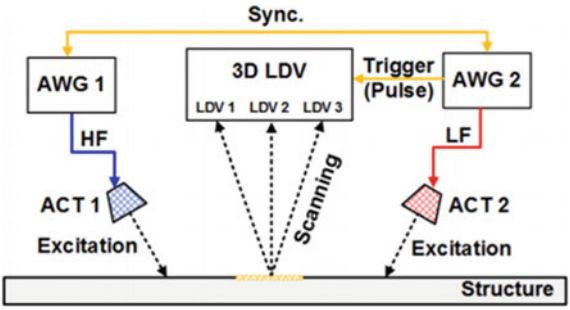

Fig. 17.19 Experimental configuration for noncontact fatigue crack visualization using ACTs for ultrasonic generation and LDV for ultrasonic response scanning [19]

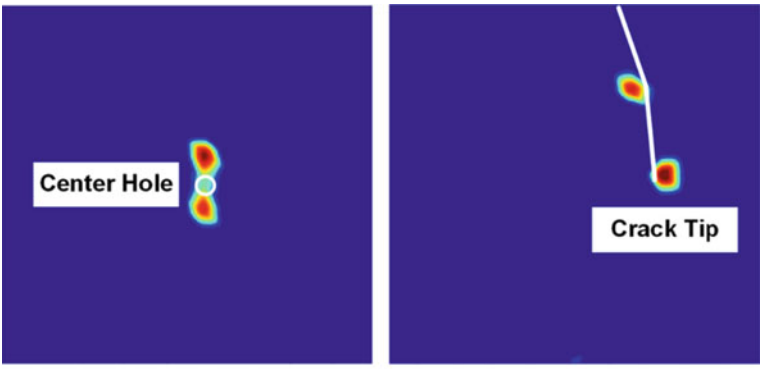

Fig. 17.20 Visualization results for (**a**) the micro-crack (specimen I) and (**b**) macro-crack (specimen II) [19]

17.5.2 Fatigue Crack Detection in Rotating Shafts

Shafts in drop lifts are very susceptible to fatigue cracks as they are often under high speed rotation with a repetitive heavy loading. However, it is difficult to use conventional contact transducers to monitor these shafts because they are continuously under rotation and hard to access physically.

In the experiment, noncontact ACTs were used for fatigue crack detection in a scaled steel shaft specimen [49]. As shown in Fig. 17.21a, the scaled shafts are composed of three parts with different diameters. Through cyclic torsional loading of 5 kN · m, a fatigue crack was introduced after 15,000 cycles at the connection area between the leftmost and the center parts. The fatigue crack was then visualized in a penetrant testing (Fig. 17.21b). Figure 17.22 represents the overall setup for this experiment. For various input frequency combinations, the LF input was varied from 90 to 135 kHz with 5 kHz increment, and the HF input from 150 to 170 kHz with 10 kHz increment, respectively.

The overview of the experimental procedure is provided here. First, LF and HF inputs are simultaneously applied through two ACTs, respectively, to the shaft for

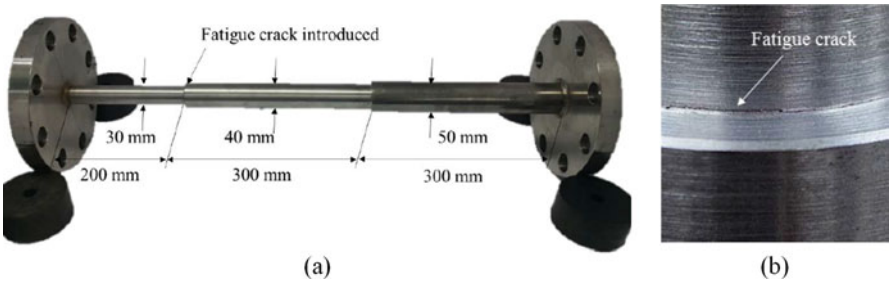

Fig. 17.21 (**a**) Steel shaft specimen with a fatigue crack and (**b**) close-up image of the fatigue crack through a penetrant testing [49]

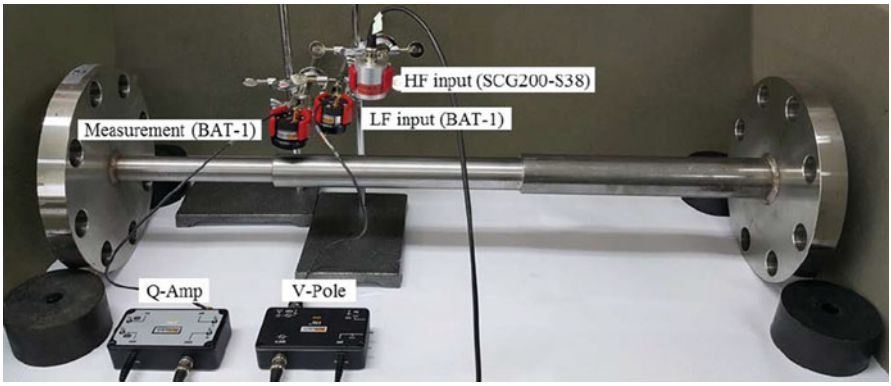

Fig. 17.22 Experimental setup for noncontact fatigue crack detection in a shaft [49]

generating nonlinear ultrasonic modulation. LF and HF inputs are also individually applied to the shaft for removing the noise effect at the modulation frequencies. Then, a damage index (DI) is defined as the energy of the first nonlinear modulation components. Finally, the previous operations are repeated with different HF and LF input combinations. Fatigue crack is then detected via an outlier analysis of all the DI values, assuming not all the input frequency combinations satisfy the necessary conditions for nonlinear ultrasonic modulation, as explained in Sect. 17.4.1.

Figure 17.23 presents the sorted DI values and the threshold values calculated using the above-mentioned sequential outlier analysis for both intact and damaged shafts. For the intact shaft (Fig. 17.23a), the DI values from all the input frequency combinations do not exceed the outlier threshold. But for the damaged shaft (Fig. 17.23b), there are four DI values higher than the outlier threshold, implying the existence of crack in the shaft. Note that the outlier threshold is automatically determined for each shaft, without any comparison with reference or baseline data.

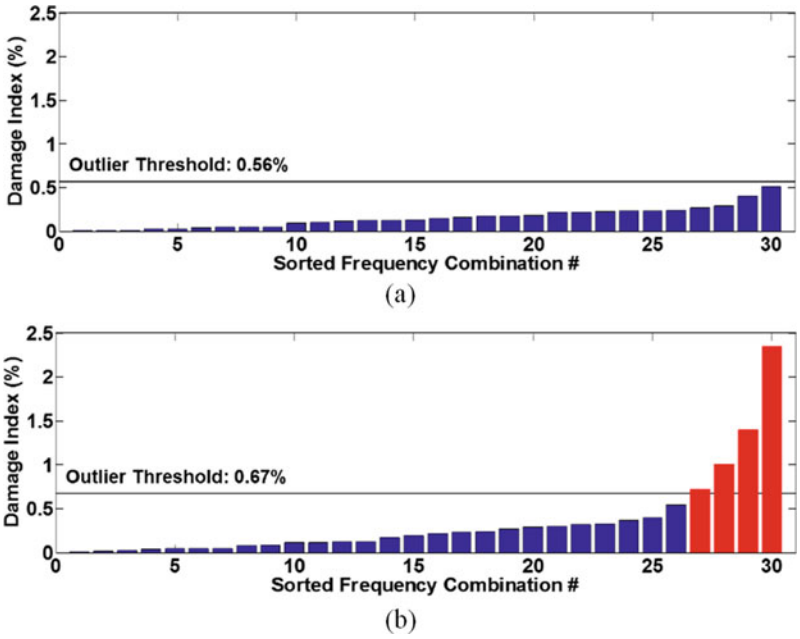

Fig. 17.23 Sorted DI values and the corresponding threshold calculated using a sequential outlier analysis for (**a**) an intact shaft and (**b**) a damaged shaft [49]

17.6 Applications Using Laser-Based Measurement Systems

17.6.1 Fatigue Crack Detection on Plates

The first example used a laser-based monitoring system for crack detection in a plate of colored glass, as shown in Fig. 17.24. Different from the laser measurement system introduced in the previous section, this laser system tried to generate LF and HF input signals by periodically modulating the intensity of continuous wave lasers [50]. Here, the LF was set as 1 Hz, and the HF as 16 kHz. The HF was chosen to maximize the amplitude of the detected signal.

This experiment first studied the use of laser-induced heating to tune the crack locally to its most nonlinear state. As shown in Fig. 17.25a, when LF was set to 0 Hz, the dependence of the acoustic signal on the power of the laser at HF = 16 kHz was determined. When the laser power increases from 40 to 120 mW, the strongest dependence of the optoacoustic conversion efficiency on the laser power is found at approximately 80 mW. This observation can be attributed to heating-induced transition of the crack from an open to a closed state. Thus, when the laser power is around 80 mW, the crack will show the most nonlinearity. This was confirmed by the test results of nonlinear ultrasonic modulation shown in Fig. 17.25b, c. In Fig. 17.25b, c, the LF was modulated at LF = 1 Hz, and the signals at HF,

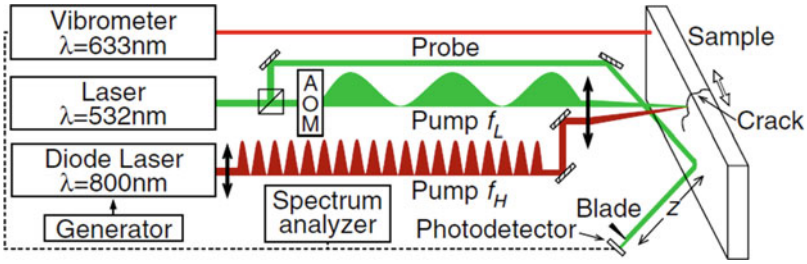

Fig. 17.24 Experimental setup for crack detection in a plate of colored glass [50]

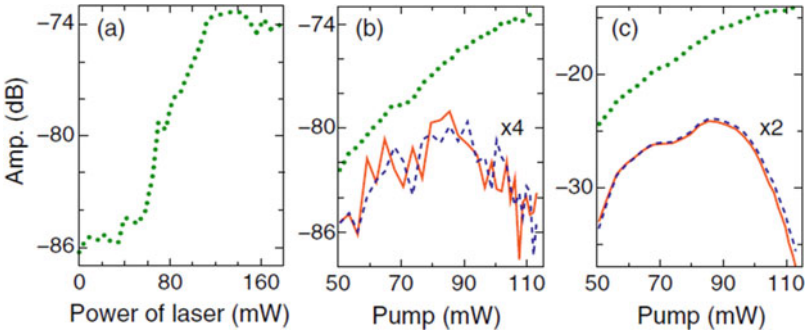

Fig. 17.25 Dependence of the photoacoustic signal amplitude on the heating laser power at frequencies HF (dotted line), HF+LF (dot-dashed line), and HF-LF (solid line). (**a**) Unmodulated laser heating, (**b**) modulated laser heating, detected by a laser vibrometer, and (**c**) modulated laser heating, detected by an in-contact accelerometer. Amplitudes at frequencies HF+LF (dot-dashed line) and HF-LF (solid line) are multiplied by 4 and 2, respectively, in (**b**, **c**) [50]

HF+LF, and HF-LF were detected by a laser vibrometer and by an accelerometer for comparison, respectively. Here, the maximum signals at the modulation frequencies were detected at approximately 80 mW average power of the laser.

Figure 17.26 presents the result of one-dimensional scanning image of a crack. For this result, the test was conducted on a somewhat different sample, and the lasers were modulated with LF = 2 Hz and HF = 18 kHz. The modulation at HF ± 2LF was measured. The relative position between the excitation laser beams and the crack was adjusted progressively by moving the sample in a direction perpendicular to the crack, with a moving step of 50 μm. From Fig. 17.26, it shows that only the modulation components provide sufficient contrast for reliable determination of the position of the crack.

Another experiment was conducted on aluminum plates with fatigue cracks using the laser measurement system introduced in Sect. 17.2.5 [35–37]. Two identical aluminum plates were prepared, and a notch was introduced in the middle of one side of the specimen as shown in Fig. 17.27. Fifteen millimeter long fatigue cracks were introduced to each specimen through fatigue tests. The crack widths are generally less than 10 μm and even less than 5 μm around the crack tips.

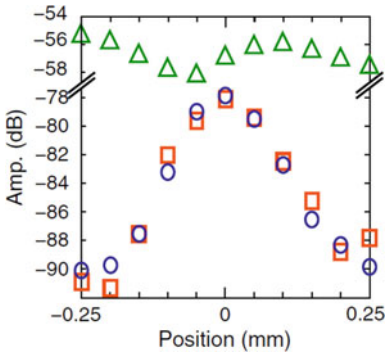

Fig. 17.26 Dependence of the amplitude of the photoacoustic signal on the relative position between the common focus spot of the laser beams and the crack at frequencies HF (open triangle), HF+2LF (squares), and HF-2LF (circles) [50]

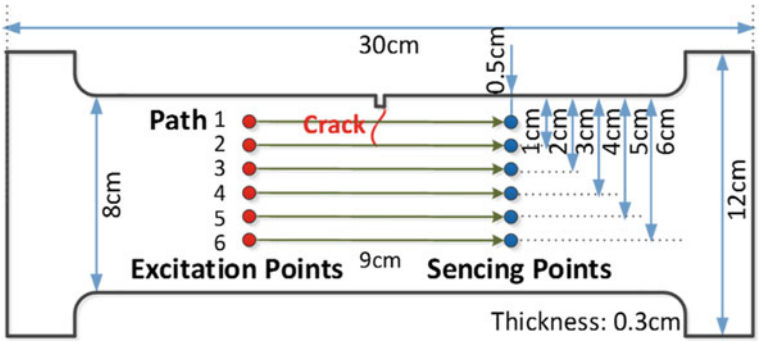

Fig. 17.27 Specimen dimensions, crack location, and laser excitation and sensing arrangement [35–37]

Figure 17.27 also defines six pairs of excitation and sensing laser beam points for examining the capability of damage localization based on the nonlinear ultrasonic modulation technique. For each specimen, ultrasonic responses were measured three times from every path in the intact condition. Among the three measured responses, one was treated as the reference signal and the other two as the signals collected for the intact case. After the fatigue test, ultrasonic responses were recorded once again for the damage case.

In this experiment, since the input signal is a pulse laser, the sideband peak count (SPC) technique, which is introduced in Sect. 17.4.3, was adopted to statistically estimate the crack-induced nonlinear modulation. Figure 17.28 shows the SPC value and its difference from the reference case obtained for the intact and damage cases of specimen I. As path 2 passing through the crack tip, difference can be clearly observed between the intact and damage cases, as shown in Fig. 17.28a. Especially when the threshold is relatively low, the maximum SPC difference (MSPCD) can be achieved over 0.15 for the damage case. As for path 3 not passing through the crack, the corresponding SPC and its difference are plotted in Fig. 17.28b. By comparison, it can be seen that, when the generated ultrasonic waves propagate directly through the crack tip, a higher MSPCD value can be obtained in the damage case than in the intact case.

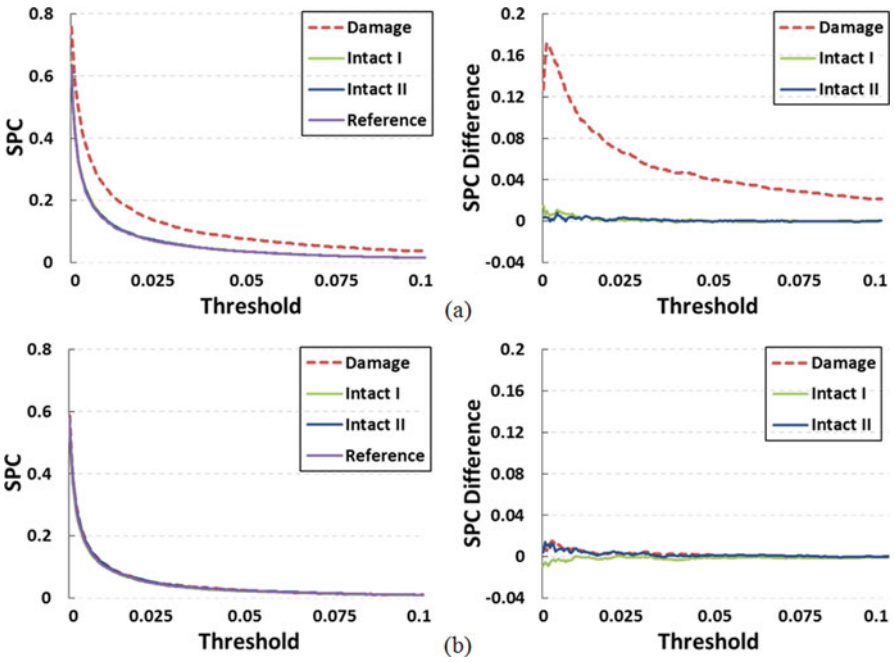

Fig. 17.28 SPC and its difference plots obtained from different paths in specimen I: (**a**) path 2, (**b**) path 3 [35–37]

The MSPCD values corresponding to all the six paths in the two specimens are calculated and summarized in Fig. 17.29. It shows that the MSPCD value is much higher for the path passing through the crack, especially through the crack tip. Note, the power level was kept below 0.2 MW for the excitation laser beam in this experiment, to make sure that it can cause crack opening and closing only as the generated ultrasonic waves pass directly through the crack. Figure 17.29 also implies that the crack tip shows the highest nonlinearity as the crack width is minimum and the crack opening and closing is most prominent at the crack tip.

17.6.2 Delamination/Debonding Detection on Wind Turbine Blades

An actual 10 kW wind turbine blade (Fig. 17.30) was fabricated for additional validation of the noncontact nonlinear ultrasonic modulation technique. The wind turbine blade is made of glass fiber reinforced polymer (GFRP) material, consisting of 6 piles with a layup of [0/±45]s. For the GFRP material, its elastic modulus E_1, shear modulus G_{12}, and poisson ratio ν_{12} are 24.65 GPa, 8.532 GPa, and 0.476, respectively [40].

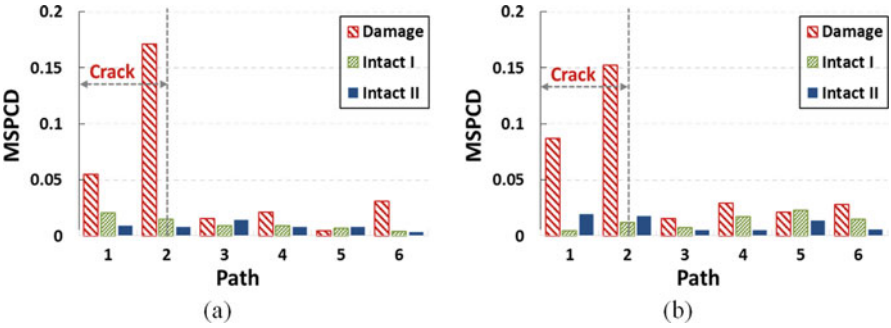

Fig. 17.29 MSPCD obtained under laser pulse excitation with 0.2 MW peak power: (**a**) specimen I, (**b**) specimen II [35–37]

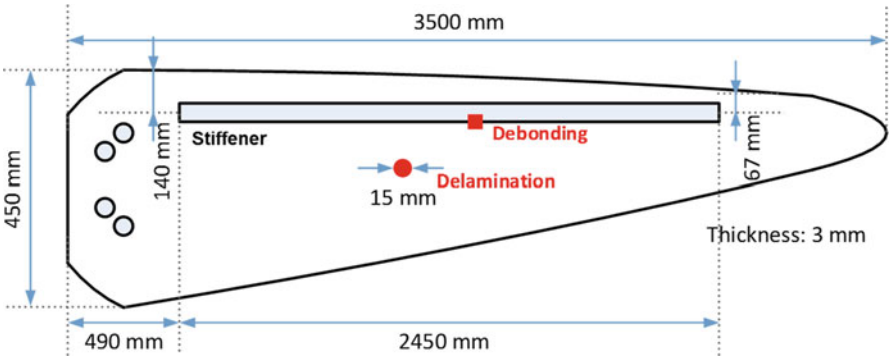

Fig. 17.30 Dimensions of a full scale wind turbine blade with simulated delamination and debonding [40]

As shown in Figs. 17.30 and 17.31, two types of typical damages for composite structures, namely delamination and debonding, were intentionally produced during the fabrication of the wind turbine blade. To simulate the delamination damage, a circular Teflon tape with a diameter of 15 mm was inserted between 3rd and 4th ply during the blade fabrication. As for the debonding damage, a small localized gap was introduced by removing some glue between the blade skin and a stiffener adhering to the skin.

This experiment used the laser measurement system introduced in Sect. 17.2.5 and the scanning laser excitation and fixed laser sensing strategy was adopted for damage detection. As shown in Fig. 17.31, the scanning area was defined as a 50 × 50 mm square area containing the delamination or debonding damage. For excitation scanning, 400 (20 × 20) excitation points were defined within the scanning area with a spatial resolution of 2.5 mm. The distance from the fixed laser sensing point to the closest excitation point was 20 mm. For each excitation point, the ultrasonic response was measured for 0.4 ms long with a sampling rate of 2.56 MHz and 100 time averaging to improve its signal to noise ratio.

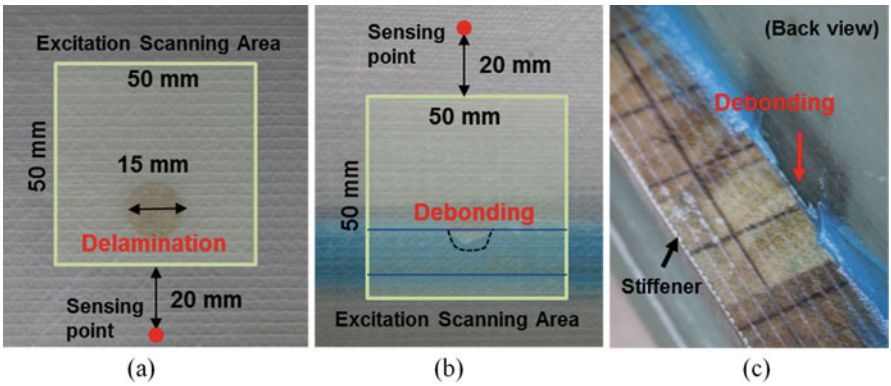

Fig. 17.31 Close-up images of the simulated damages and the defined laser scanning region: (**a**) delamination, (**b**) debonding (front view), and (**c**) debonding (back view) [40]

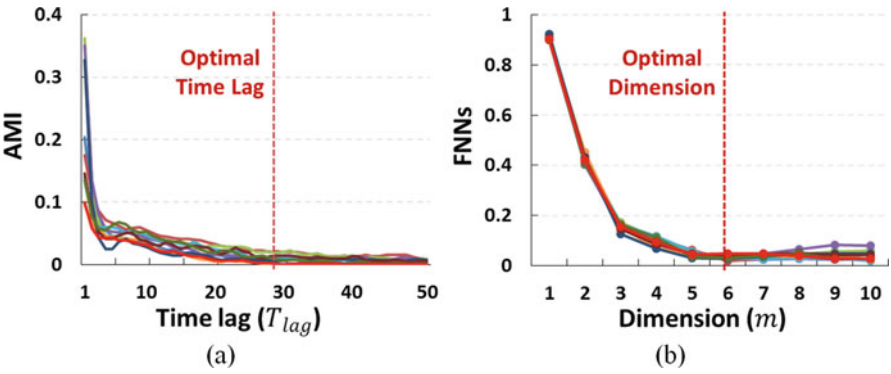

Fig. 17.32 Parameter selection results using average mutual information (AMI) and false nearest neighbors (FNNs) functions: (**a**) time lag T_{lag} and (**b**) dimension m [40]

The state space attractor technique, which is introduced in Sect. 17.4.4, was adopted to detect the damage-induced nonlinear modulation. For proper reconstructing the state space attractor, relevant parameters need to be first selected, including the optimal time lag T_{lag} and the embedding dimension m. Figure 17.32 presents the selection results for T_{lag} and m by using the average mutual information (AMI) and false nearest neighbors (FNNs) functions, respectively. Here, ten randomly selected ultrasonic responses from the two scanning areas were used as input to the AMI and FNNs functions. The proper parameters are selected when AMI or FNNs values decline to almost zero. In this experiment, $T_{\text{lag}} = 30$ and $m = 6$ was selected for attractor reconstruction.

After the attractors were reconstructed using the selected parameters, BD values were then calculated for all the scanning points and visualized for damage detection from the two scanning areas, as shown in Fig. 17.33. It can be seen that the BD values significantly increase at the edge of the damaged area. This is because the

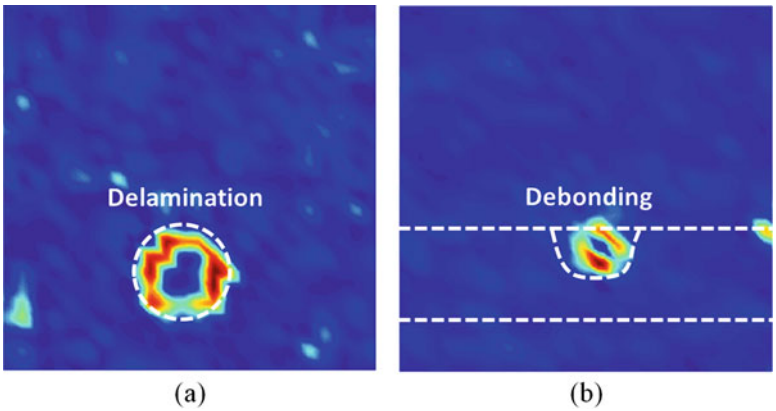

Fig. 17.33 Damage detection results based on the state space attractor technique: (**a**) delamination and (**b**) debonding [40]

edge of damage in this experiment shows the highest acoustic nonlinearity. As for the scanning points in the middle of the damaged area, the corresponding BD values remain low because the scanning points within the damaged area are all affected by the damage.

17.7 Discussions

ACT and laser, as fully noncontact transducers, can be rapidly deployed and require less maintenance since no sensors are needed to place on the target structure. However, both the ACT and laser also have some limitations which need our attention for future improvement. For ACT, its limitations mainly include: (1) High transmission power is in requirement due to acoustic impedance mismatch; (2) Proper ACT alignment demands the pre-knowledge of wave speed in the target structure; and (3) High spatial resolution is hard to achieve during ACT scanning. For laser, its limitations include: (1) The laser excitation is limited to pulse form for effective thermal/ultrasonic wave generation; (2) High spatial resolution for laser scanning requires long date collection time; (3) The laser test can be affected by the surface condition of the target structure; and (4) Retinal or skin damage might be caused when the high-power laser beam is directly or indirectly exposed to eye or skin.

To tackle these limitations, besides further optimization of the ACT and laser transducers (allowing a portable instrument of uncompromised performance), there are some researchers working on the experimental approaches with these noncontact transducers. For example, to accelerate the scanning procedure, several techniques have been developed via two-stage scanning [51], or compressed sensing with binary search [52]. Moreover, multi-channel systems with ACT or laser have

been developed also allowing rapid inspection of the target structure with high spatial resolution. However, these improved techniques still need to be explored for nonlinear ultrasonic modulation-based structural damage detection.

For fatigue crack and delamination detection, the noncontact nonlinear ultrasonic modulation technique has shown its capability to detect and locate fatigue crack and delamination at the early stage. Still, there is more work need to be explored, such as damage quantification using nonlinear features. Moreover, for fatigue crack, a big challenge is to predict the crack growth based on the noncontact nonlinear ultrasonic modulation technique. Considering the nonlinear techniques are much more sensitive to micro-crack than the macro one, a promising approach for crack prognosis is to fuse the nonlinear features with the linear ones. Another challenge for fatigue crack detection is to detect the closed cracks, which may suppress the modulation effect to an unmeasurable level. For delamination detection, besides its location, the depth of the delamination is also very crucial in some applications. On the other hand, the applications of noncontact nonlinear ultrasonic modulation technique can be expanded to defect detection on micro structures such as semiconductor chips and printed circuit boards, where there is no access to attach transducers.

17.8 Conclusions

This chapter explores the applications of the nonlinear ultrasonic modulation techniques in a noncontact manner, which can be realized using air-coupled transducers, laser, and so forth. The noncontact nonlinear ultrasonic modulation techniques can provide the following advantages: (1) Spatial resolution much higher than most conventional discrete sensors can achieve can be easily realized; (2) Small incipient damages in the range of micro-cracks and millimeter delamination can be detected; (3) The proposed techniques can be applied to moving targets, micro systems, and under harsh environmental conditions due to their noncontact nature; and (4) Damage can be detected or visualized without the baseline data acquired from the intact condition of the target structure. This chapter explains the basic principle of nonlinear ultrasonic modulation and lists some corresponding damage detection techniques. Moreover, several applications using the noncontact nonlinear ultrasonic modulation techniques are provided for crack detection in plate and rotating shaft specimens, and delamination and debonding detection on wind turbine blade made of glass fiber reinforced polymer (GFRP) material.

References

1. M. Hirao, H. Ogi, An SH-wave EMAT technique for gas pipeline inspection. NDT & E Int. **32**(3), 127–132 (1999)

2. R. Murayama, K. Ayaka, Evaluation of fatigue specimens using EMATs for nonlinear ultrasonic wave detection. J. Nondestruct. Eval. **26**, 115–122 (2007)
3. R.B. Thompsonin, *Physical Principles of Measurements with EMAT Transducers*, eds. By R.N. Thurston, A.D. Pierce. Ultrasonic Measurement Methods, Physical Acoustics, vol. XIX (Academic, San Diego, 1990)
4. M. Vasiljevic, T. Kundu, W. Grill, E. Twerdowski, Pipe wall damage detection by electromagnetic acoustic transducer generated guided waves in absence of defect signals. J. Acoust. Soc. Am. **123**(5), 2591–2597 (2008)
5. M. Castaings, P. Cawley, The generation, propagation, and detection of Lamb waves in plates using air-coupled ultrasonic transducers. J. Acoust. Soc. Am. **100**, 3070–3077 (1996)
6. E.M. Ballad, S.Y. Vezirov, K. Pfleiderer, I. Solodov, G. Busse, Nonlinear modulation technique for NDE with air-coupled ultrasound. Ultrasonics **42**, 1031–1036 (2004)
7. R. Kažys, A. Demčenko, E. Žukauskas, L. Mažeika, Air-coupled ultrasonic investigation of multi-layered composite materials. Ultrasonics **44**, 819–822 (2006)
8. Scruby C.B. and Drain L.E. (1990), Laser Ultrasonics: Techniques and Applications, Taylor & Francis, London.
9. L.E. Drain, *The Laser Doppler Technique* (Wiley, New York, 1980)
10. Y.K. An, B. Park, H. Sohn, Complete noncontact laser ultrasonic imaging for automated crack visualization in a plate. Smart Mater. Struct. **22**, 025022 (2013)
11. J. Huang, S. Krishnaswamy, J.D. Achenbach, Laser-generation of narrow-band surface waves. J. Acoust. Soc. Am. **92**, 2527–2531 (1992)
12. H. Kim, K. Jhang, M. Shin, J. Kim, A noncontact NDE method using a laser generated focused-Lamb wave with enhanced defect-detection ability and spatial resolution. NDT & E Int. **39**, 312–319 (2006)
13. W.J.N. de Lima, M.F. Hamilton, Finite-amplitude waves in isotropic elastic waveguides with arbitrary constant cross-sectional area. Wave Motion **41**, 1–11 (2005)
14. V.Y. Zaitsev, L.A. Matveev, A.L. Matveyev, On the ultimate sensitivity of nonlinear-modulation method of crack detection. NDT & E Int. **42**, 622–629 (2009)
15. F. Aymerich, W.J. Staszewski, Experimental study of impact-damage detection in composite laminates using a cross-modulation vibro-acoustic technique. Struct. Health Monit. **9**(6), 541–553 (2010)
16. X.J. Chen, J.Y. Kim, K.E. Kurtis, J. Qu, C.W. Shen, L.J. Jacobs, Characterization of progressive microcracking in Portland cement mortar using nonlinear ultrasonics. NDT & E Int. **41**, 112–118 (2008)
17. A.J. Croxford, P.D. Wilcox, B.W. Drinkwater, P.B. Nagy, The use of non-collinear mixing for nonlinear ultrasonic detection of plasticity and fatigue. J. Acoust. Soc. Am. **126**(5), EL117–EL122 (2009)
18. A. Klepka, L. Pieczonka, W.J. Staszewski, F. Aymerich, Impact damage detection in laminated composites by non-linear vibro-acoustic wave modulations. Composites **65**, 99–108 (2014)
19. H.J. Lim, B. Song, B. Park, H. Sohn, Noncontact fatigue crack visualization using nonlinear ultrasonic modulation. NDT & E Int. **73**, 8–14 (2015)
20. M. Meo, U. Polimeno, G. Zumpano, Detecting damage in composite material using nonlinear elastic waves spectroscopy method. Appl. Compos. Mater. **15**(3), 115–126 (2008)
21. Z. Parsons, W.J. Staszewski, Nonlinear acoustics with low-profile piezoceramic excitation for crack detection in metallic structures. Smart Mater. Struct. **15**, 1110–1118 (2006)
22. K. Warnemuende, H.C. Wu, Actively modulated acoustic nondestructive evaluation of concrete. Cem. Concr. Res. **34**, 563–570 (2004)
23. H.J. Lim, H. Sohn, Necessary conditions for nonlinear ultrasonic modulation generation given a localized fatigue crack in a plate-like structure. Materials **10**, 248 (2017)
24. M. Hong, Z. Su, Q. Wang, L. Cheng, X. Qing, Modeling nonlinearities of ultrasonic waves for fatigue damage characterization: theory, simulation, and experimental validation. Ultrasonics **54**, 770–778 (2014)
25. V.E. Nazarov, L.A. Ostrovsky, I.A. Soustova, A.M. Sutin, Nonlinear acoustics of micro-inhomogeneous media. Phys. Earth Planet. Inter. **50**, 65–73 (1988)

26. D. Donskoy, A. Sutin, A. Ekimov, Nonlinear acoustic interaction on contact interfaces and its use for nondestructive testing. NDT & E Int. **34**, 231–238 (2001)
27. P. Duffour, M. Morbidini, P. Cawley, A study of the vibro-acoustic modulation technique for the detection of cracks in metals. J. Acoust. Soc. Am. **119**(3), 1463–1475 (2006)
28. K. Van Den Abeele, P.A. Johnson, A. Sutin, Nonlinear elastic wave spectroscopy (NEWS) techniques to discern material damage, part I: nonlinear wave modulation spectroscopy (NWMS). Res. Nondestruct. Eval. **12**(1), 17–30 (2000)
29. W.J.N. de Lima, M.F. Hamilton, Finite-amplitude waves in isotropic elastic plates. J. Sound Vib. **265**, 819–839 (2003)
30. N.C. Yoder, D.E. Adams, Vibro-acoustic modulation using a swept probing signal for robust crack detection. Struct. Health Monit. **9**(3), 257–267 (2010)
31. A. Srivastave, F.L. di Scalea, On the existence of antisymmetric or symmetric Lamb waves at nonlinear higher harmonics. J. Sound Vib. **323**, 932–943 (2009)
32. I.N. Didenkulov, A.M. Sutin, A.E. Ekmov, V.V. Kazakov, Interaction of sound and vibrations in concrete with cracks. Proc. AIP Conf. **524**, 279–282 (1999)
33. C.R.P. Courtney, B.W. Drinkwater, S.A. Neild, P.D. Wilcox, Factors affecting the ultrasonic intermodulation crack detection technique using bispectral analysis. NDT & E Int. **41**, 223–234 (2008)
34. H. Sohn, H.J. Lim, M.P. DeSimio, K. Brown, M. Derisso, Nonlinear ultrasonic wave modulation for fatigue crack detection. J. Sound Vib. **333**(5), 1473–1484 (2013)
35. G. Liu, Z. Mao, M.D. Todd, Z. Huang, Localization of nonlinear damage using state-space-based predictions under stochastic excitation. Smart Mater. Struct. **23**(2), 025036 (2014)
36. P. Liu, H. Sohn, T. Kundu, S. Yang, Noncontact detection of fatigue cracks by laser nonlinear wave modulation spectroscopy (LNWMS). NDT & E Int. **66**, 106–116 (2014)
37. P. Liu, H. Sohn, T. Kundu, Fatigue crack localization using laser nonlinear wave modulation spectroscopy (LNWMS). J. Korean Soc. Nondestr. Test. **34**(6), 419–427 (2014)
38. H.J. Lim, H. Sohn, M.P. DeSimio, K. Brown, Reference-free fatigue crack detection using nonlinear ultrasonic modulation under various temperature and loading conditions. Mech. Syst. Signal Process. **45**, 468–478 (2014)
39. H. Sohn, H.W. Park, K.H. Law, C.R. Farrar, Combination of a time reversal process and a consecutive outlier analysis for baseline-free damage diagnosis. J. Intell. Mater. Syst. Struct. **18**, 335–346 (2007)
40. P. Liu, H. Sohn, B. Park, Baseline-free damage visualization using noncontact laser nonlinear ultrasonics and state space geometrical changes. Smart Mater. Struct. **24**(6), 065036 (2015)
41. J.N. Eiras, T. Kundu, M. Bonilla, J. Payá, Nondestructive monitoring of ageing of alkali resistant glass fiber reinforced cement (GRC). J. Nondestruct. Eval. **32**, 300–314 (2013)
42. P. Liu, H. Sohn, S. Yang, H.J. Lim, Baseline-free fatigue crack detection based on spectral correlation and nonlinear wave modulation. Smart Mater. Struct. **25**, 125034 (2016)
43. L. Moniz, J.M. Nichols, C.J. Nichols, M. Seaver, S.T. Trickey, M.D. Todd, L.M. Pecora, L.N. Virgin, A multivariate, attractor-based approach to structural health monitoring. J. Sound Vib. **283**, 295–310 (2005)
44. J.M. Nichols, Structural health monitoring of offshore structures using ambient excitation. Appl. Ocean Res. **25**(3), 101–114 (2003)
45. L.A. Overbey, C.C. Olson, M.D. Todd, A parametric investigation of state-space-based prediction error methods with stochastic excitation for structural health monitoring. Smart Mater. Struct. **16**, 1621–1638 (2007)
46. F. Takens, in *Dynamical Systems and Turbulence*. Detecting Strange Attractors in Turbulence (Springer, Warwick, 1981)
47. L.M. Pecora, T.L. Carroll, Discontinuous and nondifferentiable functions and dimension increase induced by filtering chaotic data. Chaos **6**(3), 432–439 (1996)
48. L.A. Overbey, M.D. Todd, Damage assessment using generalized state-space correlation features. Struct. Health Monit. **7**, 347–363 (2008)
49. B. Song, B. Park, H. Sohn, C.W. Lim, J.R. Park, Detection of fatigue crack on a rotating steel shaft using air-coupled nonlinear ultrasonic modulation. Proc. SPIE **9435**, 943513 (2015)

50. S. Mezil, N. Chigarev, V. Tournat, V. Gusev, All-optical probing of the nonlinear acoustics of a crack. Opt. Lett. **36**, 3449–3451 (2011)
51. B. Park, H. Sohn, Instantaneous damage identification and localization through sparse laser ultrasonic scanning, in *EWSHM-7th European Workshop on Structural Health Monitoring* (2014), pp. 647–654
52. B. Park, H. Sohn, P. Liu, Accelerated noncontact laser ultrasonic scanning for damage detection using combined binary search and compressed sensing. Mech. Syst. Signal Process. **92**, 315–333 (2017)

Chapter 18
Characterizing Fatigue Cracks Using Active Sensor Networks

Ming Hong and Zhongqing Su

18.1 Introduction

Engineering structures and systems, such as aircraft, trains, pressure vessels, wind turbines, and other civil infrastructure, are often operated in adverse working conditions and are prone to various types of damage that may put their normal operations at high risk. For metallic structures, which are ubiquitous in engineering applications, one of the most representative damage types is fatigue accumulation, which is caused by cyclic loading experienced throughout the entire life of many structures. Without proactively evaluating or monitoring the health conditions of these structures when they are in public service, fatigue damage may lead to catastrophic consequences. For instance, the Eschede train disaster in 1998, which is the deadliest high-speed train accident hitherto, was due to a single fatigue crack in the wheel rim caused by repetitive loads [1]. In another instance, the disintegration and crash of China Airlines Flight 611 in 2002, incurred from a tiny fatigue crack in the doubler plate that grew substantially amid the harsh flight environment, serves as another sad example in which all 225 people on board were killed.

In this backdrop, significant research and development efforts have been cast in the field of nondestructive evaluation (NDE). NDE methods, usually carried out on a routine schedule, attempt to identify any damage in an engineering structure in order to prevent critical or catastrophic structural or system failure. Over the years, a wide range of NDE techniques have been developed, exemplified by visual inspection, ultrasonic scanning, radioscopy, dye penetrant testing, shearography, magnetic resonance imagery, acoustical holography, eddy-current, infrared thermography, laser interferometry, and so on [2–7]. These NDE tools have matured over the years

M. Hong · Z. Su (✉)
Department of Mechanical Engineering, The Hong Kong Polytechnic University, Kowloon, Hong Kong SAR
e-mail: ming.hong@connect.polyu.hk; zhongqing.su@polyu.edu.hk

T. Kundu (ed.), *Nonlinear Ultrasonic and Vibro-Acoustical Techniques for Nondestructive Evaluation*, https://doi.org/10.1007/978-3-319-94476-0_18

and have been implemented successfully to enhance the integrity and reliability of engineering structures. Generally speaking, it is understood that damage may alter either local or global material properties of a structure, including its local effective stiffness, density, thermal properties, electric/magnetic conductivity, strain energy, and/or electro-mechanical impedance [8]. Using a variety of transducers, NDE methods try to capture responses acquired from the structure, compare signals retrieved at different times, and establish certain link between the differences in signals to dominant features that may possibly identify and characterize damage.

In the context of fatigue damage identification, however, most existing NDE techniques are inefficient and impractical. As mentioned before, traditional NDE-based inspections are conducted periodically, disregarding any working condition change or progressive deterioration of the structure. These intermittent inspections are usually not robust enough to prevent structural failure that may occur without any prior warning, such as small-scale fatigue cracks that may be formed and developed very quickly during the operation of the structure. For example, the fall of the vertical stabilizer off Flight TS 961 (Airbus A310) in 2005 occurred only five days after its routine A-check, while the next major C-check was scheduled for one year later [9]. Meanwhile, many NDE techniques consume a considerable amount of time, require downtime of inspected structures, and thus incur high cost in terms of labor and operational disruption. Confronted by these two inherent bottlenecks, traditional NDE techniques are not well suited for automatic and real-time evaluation of service conditions of materials and structures that experience continuous cyclic loading, owing to the point-by-point inspection philosophy and bulky devices adopted, which are developed to best accommodate offline periodical maintenance.

Enabled by recent technological advances and breakthroughs in sensor technology, signal processing, informatics, applied mechanics, and material sciences, some conventional NDE techniques have evolved to become the building blocks of what is now known as structural health monitoring (SHM), which aims to achieve continuous (or real-time), condition-based, and automated surveillance of the overall integrity of structures during their normal operation. The idea of using integrated sensor networks, pre-developed theoretical models, and advanced signal processing and data management techniques has become particularly relevant and promising for the characterization of early-stage fatigue damage, which have been a major threat to many engineering structures as discussed earlier.

Among the existing techniques for fatigue damage identification, ultrasonic guided wave testing (GWT) has emerged as one of the most effective tools, particularly for plate-like structures where propagating elastic waves are confined by boundaries and guided by the structure. This active, wave-based approach, often used in conjunction with active sensor networks, canvasses damage-induced local abnormalities in captured waves that propagate through the inspection area. Compared with other techniques that examine diffuse defects and variations in mechanical properties of materials, GWT-based methods show a prominent capability of assessing subtle flaws associated with strength variations. Central to the increasing awareness of the use of GWT are the appealing merits of ultrasonic

waves, including high sensitivity to structural damage, omnidirectional dissemination, fast propagation, and strong penetration through thickness, while maintaining relatively high noise tolerance due to its active nature [10]. It can be implemented with only a few miniaturized transducers with low energy consumption to scan a substantial area promptly, with the prospect of being implemented for in situ damage characterization. Hence, in this chapter, focus is placed exclusively on the modeling of guided waves and its use in damage identification. In particular, nonlinear guided wave features, to be introduced in Sect. 18.2, will be modeled theoretically and numerically, and applied to the characterization of fatigue damage in conjunction with the use of active sensor networks.

18.2 Guided Waves in Plate-like Structures

To understand how guided waves can be used to identify fatigue damage, particularly early-stage fatigue cracks that are small in scale, it is necessary to first review some fundamental properties of guided waves, as well as the feature types that can be extracted from guided wave signals.

Guided waves are elastic waves that propagate in a waveguide such as a plate or a shell, concentrate their energy near a single boundary or between two boundaries. One type of guided waves of particular interest, called Lamb waves, is confined within thin plate- or shell-like structures whose planar dimensions are far greater than their thickness, which is on the same order of magnitude of the probing wavelength. Since applications of plate-like structures are ubiquitous in engineering structures (e.g., airplane wings, control surfaces, solar panels of satellites), using Lamb waves for damage detection is highly representative of a diversity of guided-wave-based NDE/SHM techniques. Therefore, in this chapter, discussions of guided ultrasonic waves are primarily focused on the characteristics and usage of Lamb waves, in the context of fatigue damage evaluation for thin plate structures.

18.2.1 Fundamentals of Lamb Waves

Since the 1990s, Lamb waves have become increasingly popular in the practices of NDE and SHM, as people's understandings in them advance with rapidly increasing computational capabilities. As briefly mentioned earlier, Lamb waves feature a range of superb characteristics, including:

- The ability to inspect a large area in a short amount of time, due to their fast wave propagation and generally low attenuation;
- The capability of evaluating hidden or inaccessible structural components, thanks to their omnidirectional propagation in the inspected structure;

- Strong penetration through thickness, hence no need to remove any protective layer of the structure;
- The superior sensitivity to various types of damage by making use of different wave modes and diverse signal features;
- Low energy consumption; and
- Great potential for online SHM with cost-effective implementation using sparse sensor networks.

It is not the authors' intention to fully recapitulate the theoretical aspects of Lamb waves, which have been addressed in the literature substantially [5, 8, 11, 12]. Nevertheless, for the application of active Lamb waves in damage characterization, it is necessary to comprehend its key properties as discussed below.

Consider a thin, isotropic and homogeneous plate, the equation for elastic waves propagating in such a medium can be described as [11]:

$$\mu \cdot u_{i,jj} + (\lambda_L + \mu) \cdot u_{j,ji} + \rho \cdot f_i = \rho \cdot \ddot{u}_i \quad (i, j = 1, 2, 3)\,. \tag{18.1}$$

In the above, f_i signifies the body force, u_i the displacement in the x_i direction, ρ the density, and μ the shear modulus of the plate. $\lambda = 2\mu\nu/(1-2\nu)\nu$ is the Lamé's first parameter (ν is the Poisson's ratio).

An efficient means to solve Eq. (18.1) resides on displacement potentials, which employs Helmholtz decomposition [11, 12] to split displacement into scalar and vector potentials. Under the plane strain condition and in the absence of body force, the above equation can be decomposed into two uncoupled parts, as:

$$\frac{\partial^2 \phi}{\partial x_1^2} + \frac{\partial^2 \phi}{\partial x_3^2} = \frac{1}{c_L^2}\frac{\partial^2 \phi}{\partial t^2} \tag{18.2a}$$

$$\frac{\partial^2 \psi}{\partial x_1^2} + \frac{\partial^2 \psi}{\partial x_3^2} = \frac{1}{c_T^2}\frac{\partial^2 \psi}{\partial t^2}, \tag{18.2b}$$

where Eq. (18.2a) governs the longitudinal wave mode, while Eq. (18.2b) governs the transverse mode. Here, ϕ and ψ are the scalar and vector potentials, respectively, and $c_L = \sqrt{\frac{\lambda+2\mu}{\rho}}$ is the velocity of the longitudinal mode, and $c_T = \sqrt{\frac{\mu}{\rho}}$ is the transverse mode velocity.

Solving Eqs. (18.2a) and (18.2b) with traction-free boundary conditions at both surfaces, the general description of Lamb waves can be obtained as:

$$\frac{\tan(qh)}{\tan(ph)} = -\frac{4k^2 qp}{\left(k^2 - q^2\right)^2} \quad \text{(symmetric modes)}\,, \tag{18.3a}$$

$$\frac{\tan(qh)}{\tan(ph)} = -\frac{\left(k^2 - q^2\right)^2}{4k^2 qp} \quad \text{(antisymmetric modes)}\,, \tag{18.3b}$$

where $p^2 = \frac{\omega^2}{c_L^2} - k^2$, $q^2 = \frac{\omega^2}{c_T^2} - k^2$, and $k = \frac{2\pi}{\lambda_w}$. Here, h is the half thickness of the plate. c_L and c_T are the longitudinal and transverse wave velocities in the plate, respectively. k, ω, and λ_w are the wavenumber, circular frequency, and wavelength of the wave, respectively. As can be seen from Eqs. (18.3a) and (18.3b), Lamb waves can be decomposed into two types of modes in terms of particle motion patterns: symmetric modes and antisymmetric modes. Meanwhile, each type of modes comprises a fundamental mode and higher-order modes. By convention, S_i and A_i ($i = 0, 1, 2, 3\ldots$) are used to denote the symmetric and antisymmetric modes, respectively, with the subscript i being the order of the mode. Predominantly, symmetric modes have radial in-plane particle displacement, while antisymmetric feature mostly out-of-place displacement. The distinct particle motion patterns of the two modes create possibilities of using a specific mode to detect a particular type of damage in NDE and SHM applications [8].

Equation (3), though formulated rather simply, may only be solved using numerical methods. At a given angular frequency ω, the wavenumber k can be determined iteratively, which in turn specifies the wave's phase and group velocities. Generically, phase velocity is the propagation velocity of the wave phase at a specific frequency, while group velocity is the rate at which the wave's overall shape/energy/information is propagated. Both of them depend on k (hence on wavelength λ_w and frequency ω); for phase velocity, $c_{ph} = \frac{\omega}{k}$, and for group velocity, $c_g = \frac{\partial \omega}{\partial k}$. To illustrate this dependency, the phase velocities and group velocities of Lamb waves in an A606 steel plate are displayed in Fig. 18.1 as functions of the frequency-thickness product. It can be observed that both phase and group velocities of all the wave modes vary with the product of the wave's frequency and the thickness of the plate. This nature of Lamb waves (and guided waves in general) is termed dispersion, and the velocity curves in Fig. 18.1 are referred to as dispersion curves.

It can also be seen in Fig. 18.1 that, at any frequency-thickness combination, there are at least two wave modes that coexist and propagate simultaneously. As the frequency-thickness product increases, more modes are introduced to the structure gradually. This phenomenon is known as the multimodality of Lamb waves, which may create significant challenges in interpreting acquired signals in damage identification problems.

18.2.2 Linear Features of Lamb Waves for Identification of Gross Damage

In SHM practices, the Lamb-wave-based monitoring principle has been deployed in a diversity of fashions, striking the balance among resolution, detectability, practicality, and cost. In the last two decades, the majority of such techniques have been aimed at exploring changes in damage-scattered waves, which are documented in the time histories in the form of amplitude alteration and/or phase deviation (in

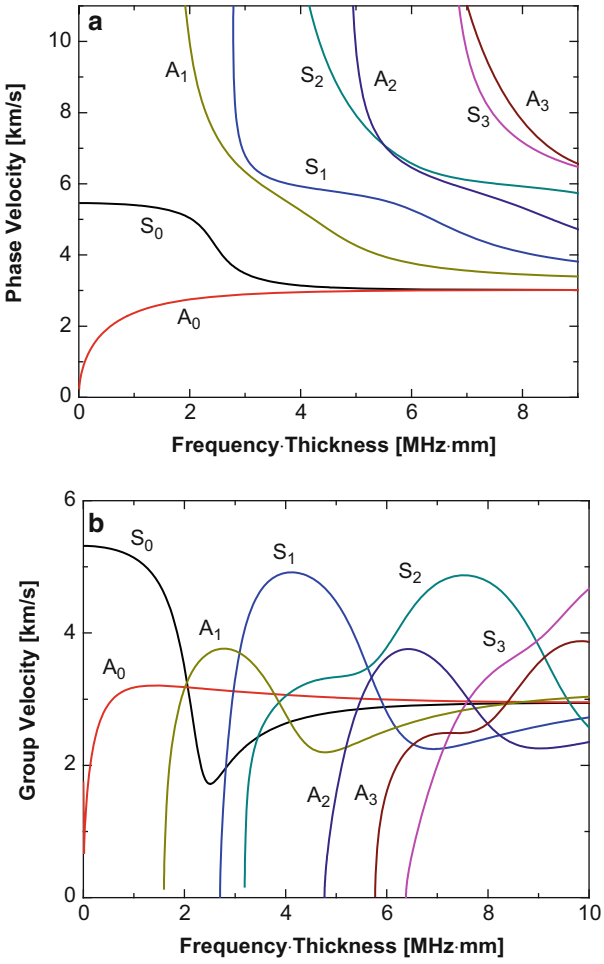

Fig. 18.1 Dispersion curves of phase velocities (**a**) and group velocities (**b**) in A606 steel

comparison with baseline signals) in most studies. These features are typified by the delay in the time of flight (ToF) [13–17], wave reflection/transmission [18–21], energy dissipation [22], as well as mode conversion [23, 24], which usually present, to some extent, linear relations with damage parameters such as location, and are therefore colloquially referred to as *linear Lamb wave features*.

For example, ToF—one widely used and most straightforward linear Lamb wave feature—refers to the time spent for a particular wave packet to travel a certain distance. In particular, if the ToF of the damage-scattered wave packet can be found by comparing the current (damaged) signal with its baseline (healthy) signal, it is then possible to find the distance of the damage from the sensor provided that the wave velocity is known beforehand. If there are multiple sensing paths available in a sensor network, then the damage can be triangulated using ToF information from signals acquired from different paths.

Another popular linear Lamb wave feature is the signal energy in the time domain as manifested by the signal magnitude. Since damage may have different shapes, severities, orientations, and distances to individual sensors in the sensor network, these variations may result in distinct magnitudes featured by damage-scattered waves. Especially when the damage takes a formality of crack with a dominant dimension in a particular dimension, the intensity of the energy of damage-scattered waves can be exploited to depict the orientation of the damage [25]. Thus, when used in conjunction with the ToF feature, wave energy intensity can offer further insight on the orientation and even shape of the damage, in addition to its location information determined by ToFs.

Generally speaking, linear Lamb wave features can be employed to evaluate gross damage with a characteristic size of the same order of magnitude of the probing wavelength, such as open cracks, voids, delamination, and through-holes [26, 27]. Thus, the sensitivity of linear Lamb wave features is substantially wavelength-dependent. When used to characterize undersized damage such as barely visible fatigue cracks, linear feature-based detection may become problematic, because the small damage whose dimension is smaller than the wavelength of the probing wave may not induce sufficiently phenomenal wave scattering, failing to change linear wave features. One can increase excitation frequency of probing waves, however, it is at the cost of introducing complexity to signal appearance, because waves feature multiple modes and dispersive properties at higher frequencies.

18.2.3 Nonlinear Features of Lamb Waves for Characterization of Undersized Damage

Yet, damage in real-world engineering structures often initiates from defects or degradation at imperceptible levels, which may nevertheless develop to a considerable scale and result in material failure rather quickly, without sufficient warning in advance. Thus, selecting appropriate Lamb wave features that are sensitive to small-scale damage is crucial in preventing structural failure. While linear features usually fail to do so as explained earlier, it has been found that small-scale damage usually affects the nonlinear material properties significantly, which can be accordingly documented by some nonlinear features of Lamb waves. Motivated by this, there have been increasing endeavors in exploiting nonlinear signal features extracted from Lamb waves to characterize small-scale damage [28–36]. More specifically, this group of techniques is based on the premise that Lamb waves, when propagating in an elastic medium, can be distorted by the inherent nonlinearity of the medium, resulting in an energy shift from the excitation frequency to other frequency bands and generating nonlinear features discernible in the frequency domain. When damage emerges in the medium, additional, local nonlinearities may appear and reinforce the nonlinear features in acquired Lamb wave signals traversing the damaged region. These localized nonlinearities may come from, but

are not limited to, damage-driven plasticity, geometric effects, hysteresis, frictional, and thermal effects. In addition, when Lamb waves traverse crack-like damage, the "breathing" behavior of the crack interface, under cyclic loads, creates localized nonlinear behaviors and introduces the so-called contacting acoustic nonlinearity (CAN) [28]. Nonlinear Lamb wave features that are often exploited in this category include second [29–31] or sub-harmonics [32], mixed frequency responses [33] (e.g., nonlinear wave modulation spectroscopy), shift of resonance frequency [34] (e.g., nonlinear resonant ultrasound spectroscopy), dual frequency mixing [35], to name a few, as reviewed comprehensively elsewhere [28].

The discussion of using nonlinear features of Lamb waves for fatigue damage characterization in this chapter will be focused on second harmonics, as this feature has gained prominence in characterizing undersized damage such as early-stage fatigue cracks [30, 31]. To exploit second harmonics, the probing Lamb waves are often excited at a monochromatic frequency (denoted by f_E). Since undersized damage will introduce local nonlinearities to the material, extra components would appear in signal spectra at twice the excitation frequency, i.e., $2f_E$. These components are the second harmonics of the probing waves. The detection making use of nonlinear features is, in principle, less restricted by the probing wavelength. In other words, the effectiveness of using nonlinear Lamb wave features in detecting undersized damage originates from its sensitivity to locally enhanced medium nonlinearities caused by damage.

18.3 Modeling of Nonlinear Attributes of Lamb Waves

There has been a rich body of literature on the use of nonlinear features of Lamb waves for damage identification. However, most of the existing research strengths have been in the nature of experimental observation. There are rather limited studies devoted to the analytical investigation or numerical simulation of nonlinear Lamb waves propagating in structures with small-scale damage. Among representative numerical methods for simulating nonlinearities of the medium and/or damage are Local Interaction Simulation Approach [37], or LISA, finite element methods (FEMs) [38, 39], Galerkin FEM [40], etc.

In general, the paramount challenge in analytically or numerically modeling nonlinear features of guided waves is to include all possible sources of nonlinearities. The possible sources particularly include material nonlinearity of the medium, the damage, and the modulation of damage on the probing waves. To this end, this section focuses on the establishment of a dedicated modeling approach capable of interpreting nonlinearities embodied in captured Lamb wave signals. Rather using bulky transducers, the approach employs miniaturized piezoelectric sensors (e.g., PZT wafers) that can be networked and permanently integrated with a structure under inspection, benefiting the extension of the approach to embeddable NDE/SHM.

18.3.1 Modeling Nonlinearities in an Elastic Medium

Consider an isotropic homogeneous solid. Nonlinearities from the medium that can distort guided ultrasonic waves may originate from various sources, such as the material, plasticity in damaged area, crack surfaces, surface roughness, hysteresis, and thermal friction, to name a few. The modeling of nonlinearities in this section is split into two scenarios: the intact state and fatigue damaged state.

18.3.1.1 Intact Medium

Assume that the discussed medium is free of fatigue damage, and there will be of two major sources of nonlinearity: the inherent nonlinearity from material and convective nonlinearity, which can be referred to collectively as the mesoscopic nonlinearities of the material [41]. Specifically, the material nonlinearity comes from the intrinsic nonlinear elasticity (i.e., the elasticity of lattices). These nonlinearity effects, though trivial, can be manifested by ultrasonic waves propagated in such a medium.

With a second-order approximation, the three-dimensional (3-D) stress–strain correlation of the medium can be defined as [42]

$$\sigma_{ij} = \left(C_{ijkl} + 1/2 M_{ijklmn}\varepsilon_{mn}\right)\varepsilon_{kl}. \tag{18.4}$$

In the above, σ_{ij} denotes the stress tensor; ε_{mn} and ε_{kl} are the strain tensors. C_{ijkl} (as well as those in its form) is the second-order elastic (SOE) tensor, to be defined with Lamé's parameters λ and μ. M_{ijklmn} is a tensor to be correlated with the material and convective nonlinearities. The notion of convective nonlinearity is closely related to the material nonlinearity. Provided the second term in the parenthesis (i.e., $1/2M_{ijklmn}$) neglected, Eq. (18.4) retreats to the 3-D Hooke's Law of linear elasticity. Generally, wave equations are expressed in Eulerian coordinates, while nonlinear elasticity in Lagrangian coordinates. Once material nonlinearity is taken into account, a descriptive difference would take place from the second-order term of any physical quantity [43]. This means that the convective nonlinearity is induced mainly due to the mathematic transformation between the two coordinate systems. M_{ijklmn} addresses both the material and convective nonlinearities, defined as [44]

$$M_{ijklmn} = C_{ijklmn} + C_{ijln}\delta_{km} + C_{jnkl}\delta_{im} + C_{jlmn}\delta_{ik}, \tag{18.5}$$

where

$$\begin{aligned} C_{ijklmn} = {} & \tfrac{1}{2}\mathcal{A}\left(\delta_{ik}I_{jlmn} + \delta_{il}I_{jkmn} + \delta_{jk}I_{ilmn} + \delta_{jl}I_{ikmn}\right) \\ & + 2\mathcal{B}\left(\delta_{ij}I_{klmn} + \delta_{kl}I_{mnij} + \delta_{mn}I_{ijkl}\right) + 2\mathcal{C}\delta_{ij}\delta_{kl}\delta_{mn}. \end{aligned} \tag{18.6}$$

In Eqs. (18.5) and (18.6), δ_{km} and the like with different index orders are the Kronecker deltas; I_{jlmn} (as well as those in its form) is the fourth-order identity tensor, and C_{ijklmn} the third-order elastic (TOE) tensor associated with material nonlinearity. The last three terms in Eq. (18.5) address the convective nonlinearity. C_{ijklmn} can be calculated using three TOE constants $\mathcal{A}$, $\mathcal{B}$, and $\mathcal{C}$ (due to inherent properties of the material) that are to be acquired using experimental means [45, 46]. With Voigt notation, C_{ijklmn} reads

$$\begin{cases} c_{111} = 2\mathcal{A} + 6\mathcal{B} + 2\mathcal{C} \\ c_{112} = 2\mathcal{B} + 2\mathcal{C} \\ c_{123} = 2\mathcal{C} \\ c_{144} = 1/2\mathcal{A} + \mathcal{B} \\ c_{155} = \mathcal{B} \\ c_{456} = 1/4\mathcal{A}, \end{cases} \tag{18.7}$$

where $c_{IJK} = C_{ijklmn}$ ($I, J, K \in \{1, 2, \ldots, 6\}$).

First consider a 1-D medium (e.g., a rod) governed by the 1-D nonlinear stress–strain equation as

$$\sigma = \left(E + \frac{1}{2}E_2\varepsilon\right)\varepsilon, \tag{18.8}$$

where σ and ε are the stress and strain of the medium, respectively. E and E_2 are the first- and second-order Young's moduli, respectively, with the former reflecting the linear properties while the latter introducing nonlinear effects [47] to the medium. Solving Eqs. (18.4), (18.5), and (18.6) yields

$$E_2 = 3(\lambda + 2\mu) + 2\mathcal{A} + 6\mathcal{B} + 2\mathcal{C}. \tag{18.9}$$

Further, taking the ratio of the two Young's moduli leads to

$$\beta_g = \frac{E_2}{E} = 3 + \frac{2\mathcal{A} + 6\mathcal{B} + 2\mathcal{C}}{\lambda + 2\mu}. \tag{18.10}$$

In this study, β_g defined by Eq. (18.10) is referred to as the *global nonlinearity parameter* of the medium in its intact state. It is obvious that β_g is dominated by material properties (e.g., Young's modulus and TOE constants) in the case that the medium is free of fatigue damage.

18.3.1.2 Fatigued Medium

Now, extend the preceding discussion to the case of the same medium with fatigue damage. There are now additional sources of nonlinearities besides β_g. In low-cycle

fatigue (LCF), the loading stress is larger than the yield strength of the medium, and thus, bulk plastic deformation takes place [48]; in high-cycle fatigue (HCF), localized micro-plastic deformation exists in the region of crack initiation. In both LCF and HCF, localized plasticity exists near fatigue cracks that distorts guided waves and induces nonlinear properties in the signals.

To reflect the localized plasticity, a *local nonlinearity parameter* β_l is developed, on top of β_g, to account for local nonlinearities incurred by fatigue damage. One way to express β_l (for the dislocation dipole setting [49]) is

$$\beta_l = \frac{16\pi\Omega R_{L-S}^2 \Lambda {h_d}^3 (1-\nu)^2 (\lambda + 2\mu)^2}{\mu^2 b}. \tag{18.11}$$

In the above, Ω is a factor of convention from dislocation to longitudinal displacements, and $R_{L\text{–}S}$ is another factor of conversion from longitudinal to shear displacements. Λ is the dipole dislocation density reflecting the plastic strain in the medium. h_d, ν, and b are the dipole height, Poisson's ratio, and Burgers vector, respectively. As recognized [50], the plastic deformation-induced nonlinearity is more significant, compared with intrinsic material nonlinearity, to distort probing waves.

With both global and local nonlinearity, a hybrid *acoustic nonlinearity parameter* β is defined as

$$\beta = \begin{cases} \beta_g, & \text{Intact state} \\ \beta_g + \beta_l. & \text{Damaged state due to local plasticity} \end{cases} \tag{18.12}$$

Provided localized plasticity is generated in the medium, β is supposed to increase—that is the cornerstone of characterizing fatigue damage using β.

18.3.1.3 Contact Acoustic Nonlinearity (CAN)

On top of the above β, *contact acoustic nonlinearity* (CAN) is also expected to be generated when probing waves are traversing a fatigue crack. To this end, a "breathing crack model" is [51] developed. In brief, when ultrasonic waves interact with the two interfaces of a fatigue crack, the "breathing" motion pattern under cyclic loading closes the gap between two interfaces during wave compression; when tension opens the crack, propagation of tensile stress is blocked. This jointly imposes additional localized nonlinearity, CAN, to wave signals [28].

18.3.2 Modeling Nonlinear Lamb Waves

Using the 1-D medium discussed in the above, now focus on the longitudinal waves in the medium. Without considering dispersion and attenuation, the equation for ultrasonic waves in the Lagrangian coordinates is formulated as

$$\rho \frac{\partial^2 u\,(x,t)}{\partial t^2} = \frac{\partial \sigma}{\partial x}. \tag{18.13}$$

In the above, ρ and $u\,(x, t)$ signify the density of the medium and the particle displacement at instant t (abbreviated as u), respectively. Expanding the modeling earlier, one can depict wave propagation by solving Eqs. (18.8) and (18.13) using a perturbation method [47]. Specifically, substituting $\sigma = \left(E + \frac{1}{2}\beta E\varepsilon\right)\varepsilon$ into Eq. (18.13) yields

$$\rho \frac{\partial^2 u}{\partial t^2} = E\frac{\partial^2 u}{\partial x^2} + \beta E \frac{\partial u}{\partial x}\frac{\partial^2 u}{\partial x^2}. \tag{18.14}$$

Using the perturbation method, u can be defined in the form of

$$u = u_0 + u_1, \tag{18.15}$$

where u_0 is the incident wave, and u_1 is the first-order perturbation reflecting the nonlinear component of u, which is assumed to be much smaller than u_0. Substituting Eq. (18.15) into Eq. (18.14) gives rise to

$$\rho \frac{\partial^2 u_0}{\partial t^2} - E\frac{\partial^2 u_0}{\partial x^2} + \rho \frac{\partial^2 u_1}{\partial t^2} - E\frac{\partial^2 u_1}{\partial x^2} - \beta E \frac{\partial\,(u_0+u_1)}{\partial x}\frac{\partial^2\,(u_0+u_1)}{\partial x^2} = 0. \tag{18.16}$$

Here, because the nonlinear terms involving the perturbed displacement u_1, i.e., $\rho\frac{\partial^2 u_1}{\partial t^2} - E\frac{\partial^2 u_1}{\partial x^2} - \beta E\frac{\partial(u_0+u_1)}{\partial x}\frac{\partial^2(u_0+u_1)}{\partial x^2}$, are sufficiently small when compared to the linear term, $\rho\frac{\partial^2 u_0}{\partial t^2} - E\frac{\partial^2 u_0}{\partial x^2}$, one has

$$\rho \frac{\partial^2 u_0}{\partial t^2} = E\frac{\partial^2 u_0}{\partial x^2} \tag{18.17a}$$

$$\rho \frac{\partial^2 u_1}{\partial t^2} = E\frac{\partial^2 u_1}{\partial x^2} + \beta E \frac{\partial\,(u_0+u_1)}{\partial x}\frac{\partial^2\,(u_0+u_1)}{\partial x^2}. \tag{18.17b}$$

Again, neglecting u_1 in the terms where u_0 is present, Eq. (18.17b) retreats to

$$\frac{\partial^2 u_1}{\partial t^2} = \frac{E}{\rho}\frac{\partial^2 u_1}{\partial x^2} + \beta\frac{E}{\rho}\frac{\partial u_0}{\partial x}\frac{\partial^2 u_0}{\partial x^2}, \tag{18.18}$$

where $\frac{E}{\rho} = c$ is wave velocity.

Assume u_0 to be a harmonic wave that follows

$$u_0 = A_1 \sin(\omega t - kx). \tag{18.19}$$

Recall that ω and k are the angular frequency and wavenumber, respectively, and here A_1 represents the magnitude of the fundamental mode. Substituting Eq. (18.19) into Eq. (18.18) leads to

$$\frac{\partial^2 u_1}{\partial t^2} - c^2 \frac{\partial^2 u_1}{\partial x^2} = \frac{\beta c^2 k^3 A_1^2}{2} \sin(2\omega t - 2kx). \tag{18.20}$$

Equation (18.20) is an inhomogeneous second-order partial differential equation, whose typical solution to the perturbation is in the form of [52]

$$u_1 = A_2 x \cos(2\omega t - 2kx), \tag{18.21}$$

where A_2 is the amplitude of the perturbed wave component (the second harmonics) to be determined. Plugging Eq. (18.21) into Eq. (18.20), it can be found that

$$A_2 = -\frac{\beta}{8} A_1^2 k^2 x. \tag{18.22}$$

The final solution to the particle displacement u hence becomes

$$u = A_1 \sin(\omega t - kx) + A_2 \cos(2\omega t - 2kx). \tag{18.23}$$

Rearranging Eq. (18.21), β can be obtained as

$$\beta = -\frac{8}{k^2 x} \frac{A_2}{A_1^2}. \tag{18.24}$$

At this point, β can be redefined, from the perspective of ultrasonics, as the acoustic nonlinearity parameter (ANP) associated with the acquired wave, and will be referred to as such hereafter. In principle, if one has acquired positive values for A_1 and A_2, the obtained value of ANP should be negative, which is consistent with a negative E_2 in Eq. (18.10), because a material's nonlinear stress–strain curve is generally concave in nature. However, since amplitudes retrieved in practice (such as from the spectrum) are always positive, ANP is usually defined without the negative sign, as

$$\widehat{ANP} = \frac{8}{k^2 x} \frac{A_2}{A_1^2}. \tag{18.25}$$

It is noteworthy that the observed value, $\widehat{ANP}$, is not always equal to the magnitude of modeled β defined by Eq. (18.12), in particular when the medium

features fatigue damage, because some sorts of nonlinearity sources (e.g., CAN) are not reflected in the model as discussed in Sect. 18.3.1, which, however, also induce higher-order harmonics and can be calibrated by $\widehat{ANP}$. The actual change in $\widehat{ANP}$ as a result of local plasticity and microcracks should be larger than the value of β_l as analytically obtained from Eq. (18.11). For evaluating fatigue damage, it might not be necessary to exactly match the measured value ($\widehat{ANP}$) to the modeled one (β). Previous studies [50, 53] have demonstrated that the increase in the nonlinearities of the material due to plasticity-driven fatigue damage can be timely signaled by the increase in the measured value.

As implied by Eq. (18.25), the degree of nonlinearities associated with the material and fatigue damage is linked to magnitudes of both the fundamental and second harmonic modes. For detection purpose, the change in $\widehat{ANP}$, instead of its value, is more significant, in which $\widehat{ANP}$ can be normalized with regarding to its initial value in the intact state of the medium, namely a *relative acoustic nonlinearity parameter* (RANP), as

$$RANP = \frac{A_2}{A_1^2}. \tag{18.26}$$

This relatively defined nonlinearity parameter is proportional to $\widehat{ANP}$ and associated with nonlinear properties of waves, conducive to quantitative evaluation of fatigue damage.

As reviewed in Sect. 18.2, Lamb waves feature dispersive and multimodal properties. The dispersive natures make extraction of wave nonlinearity a daunting task. However, there exist certain wave modes excited at prudentially selected frequencies that can be exploited to generate prominent, cumulative second harmonics with a reasonable signal-to-noise ratio (SNR). A rich body of research has gone into this issue and provided criteria for the selection of wave mode and excitation frequency [31, 54, 55] for metallic plate structures. Finally, it is important to also realize that damage-induced nonlinearities, such as plasticity and CAN, are very local phenomena. Thus, the cumulative effect of second harmonics due to these local nonlinearities is limited.

For illustration, Fig. 18.2 displays the dispersion curves calculated using DISPERSE® for Lamb waves in an aluminum (6061-T6) plate from 0 to 10 MHz mm. Mode pair (S_1, S_2) is an option that meets the internal resonance requirement, hence called a *synchronized mode pair* hereinafter. In this mode pair, S_1 is the first-order symmetric mode at 3.59 MHz mm, and S_2 the second-order symmetric mode at 7.18 MHz mm, both of which have the same phase and group velocities, respectively. Once S_1 is generated and guided by the medium under inspection, S_2 will be produced at twice the excitation frequency as the corresponding second harmonic of S_1. With the same phase velocities, S_2 is cumulative along wave propagation.

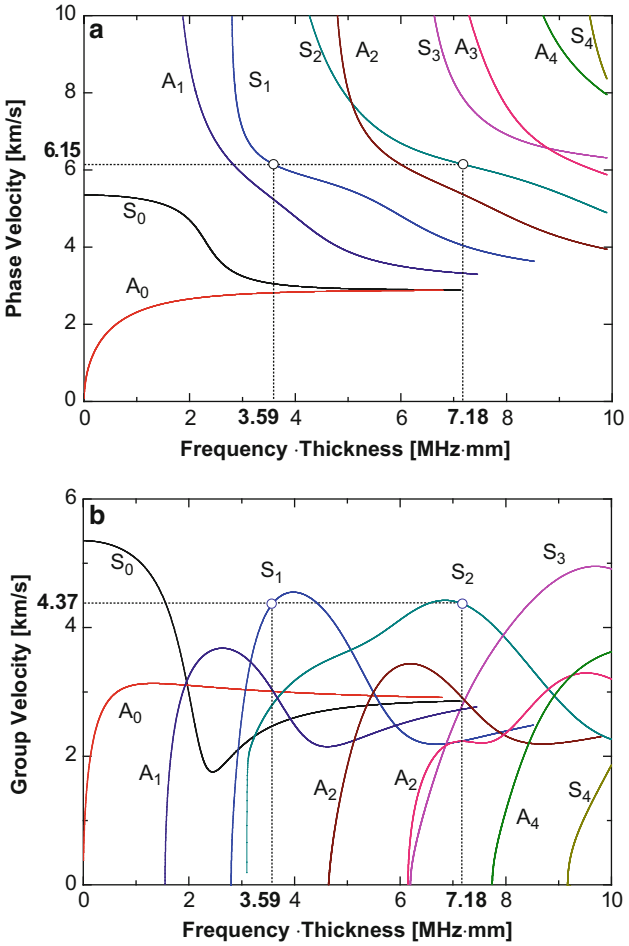

Fig. 18.2 Dispersion curves of phase velocities (**a**) and group velocities (**b**) in a 6061-T6 aluminum plate. (S1, S2) is shown as a synchronized mode pair meeting the internal resonance criterion

Expanding the above modeling from a 1-D rod to a plate-like medium, ANP for Lamb waves can be defined by multiplying Eq. (18.25) with a scaling factor γ [36], as

$$\widehat{ANP}_L = \frac{8}{k^2 x}\frac{A_2}{A_1^2}\gamma. \tag{18.27}$$

$\widehat{ANP}_L$ signifies the measured ANP for Lamb waves. Because γ remains unchanged regardless of the presence of fatigue damage, it can be eliminated upon the normalization process of $\widehat{ANP}$. Therefore, the RANP, defined by Eq. (18.26), is able to evaluate fatigue damage in the plate as well.

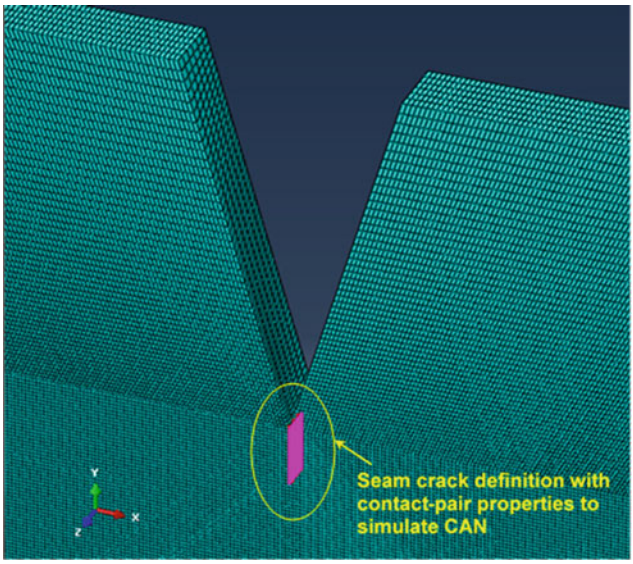

Fig. 18.3 Fatigue crack model in FEM (highlighted region is the crack interface with seam crack definition and contact-pair properties)

18.3.3 Realization in Finite Element Method

Residing on the above analysis, a dedicated modeling approach is realized and implemented in conjunction with the use of commercial FEM software Abaqus®/Explicit, including the major sources of nonlinearities as discussed in the above. A modified nonlinear stress–strain relation is introduced to Abaqus®/Explicit via a user subroutine VUMAT, to model material, convective, and plasticity-driven nonlinearities. In particular, to model the plasticity-driven nonlinearity, an additional local nonlinearity parameter is added to the global nonlinearity parameter.

To model a fatigue crack in the medium and depict the "breathing crack model" when Lamb waves traverse the crack, a seam crack definition is used which imposes on each surface of the crack, as shown schematically in Fig. 18.3. A contact-pair interaction is defined on the interface of the crack, to induce CAN when waves passing the crack. This modeling is illustrated in Fig. 18.4a–d, from which it can be observed that the stress field induced by traversing waves is continuously transmitted through the crack when the crack is closed (Fig. 18.4b, c), while on the contrary an open crack interrupts the transmission process (Fig. 18.4d).

Using the above modeling technique, case studies are performed and analyzed (to be detailed in Sect. 18.3.4). To briefly illustrate the signal processing technique, a typical Lamb wave signal captured is shown in Fig. 18.5. For constructing RANP, a short-time Fourier transform (STFT) analysis is applied on the signal, and the accordingly obtained spectrogram is displayed in Fig. 18.6. In the spectrogram,

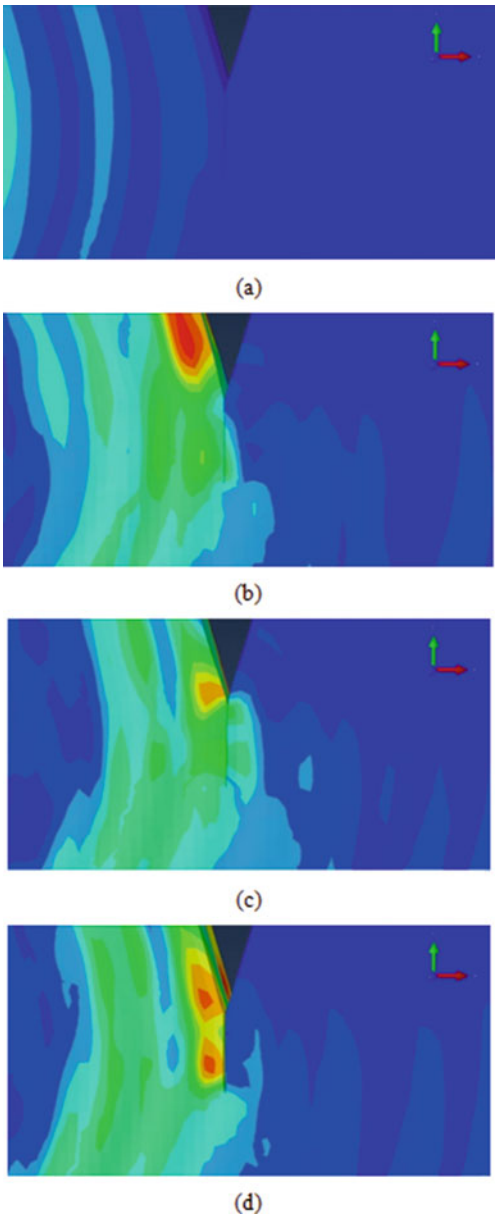

Fig. 18.4 Generated wavefields at representative moments when waves are traversing breathing crack with CAN in modeling: (**a**) waves approaching the crack; (**b**) stress traversing the crack when the crack is closed; (**c**) stress transmitting through the closed crack; and (**d**) stress blocked when the crack is open

the amplitude profiles can be extracted at the fundamental and second harmonic frequencies as functions of time. For the model pair (S_1 and S_2) that is selected according to the selection criteria, both modes will first be captured by the sensor, owing to their greatest velocity among all possible modes at these two frequencies. The first peak value of the amplitude profile at the excitation frequency is denoted as

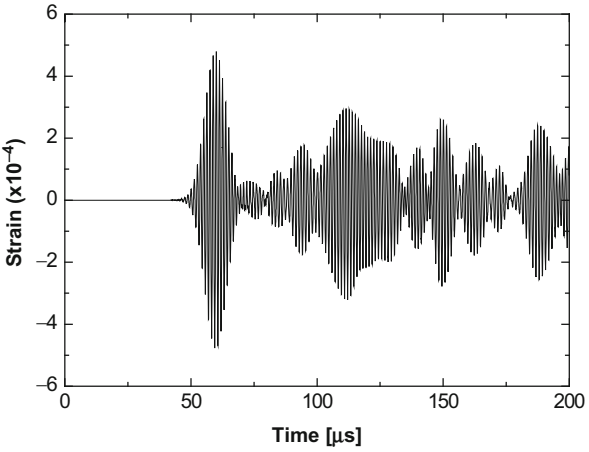

Fig. 18.5 A typical Lamb wave signal from simulation

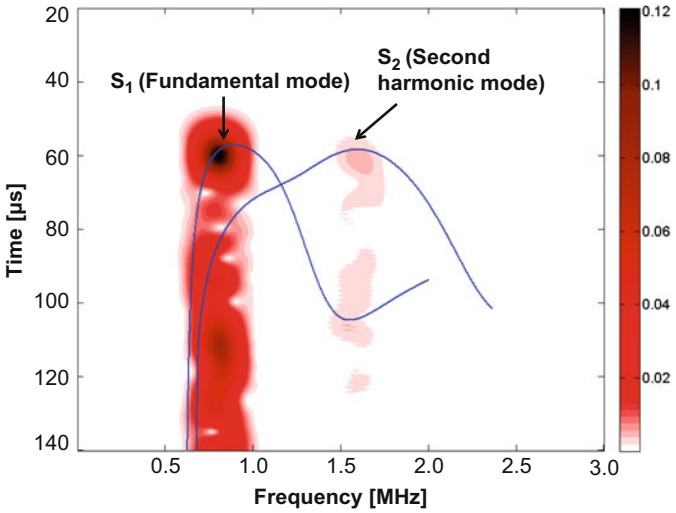

Fig. 18.6 Time–frequency deployment of the signal in Fig. 18.5 obtained via STFT (integrated with dispersion curves)

A_1 (for S_1), and the first peak value of the profile at the double excitation frequency as A_2 (for S_2), Fig. 18.7. Based on ascertained A_1 and A_2, the RANP associated with this particular signal can be calculated using Eq. (18.26).

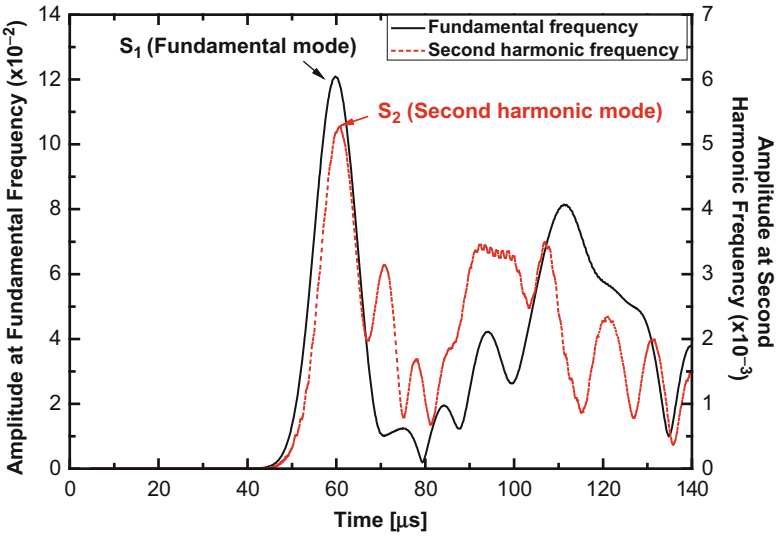

Fig. 18.7 Amplitude profiles of the signal energy at the fundamental frequency and at the double frequency

18.3.4 Simulation Results and Experimental Validation

The proposed modeling technique is verified by case studies, followed by experimental validation.

18.3.4.1 RANP vs. Wave Propagation

Based on the above analysis and modeling, it is speculated that, with a selected mode pair, the constructed RANP is proportional to wave propagation distance if the medium remains intact. To demonstrate this, a 6061-T6 aluminum plate ($400 \times 380 \times 4.5$ mm^3), shown schematically in Fig. 18.8a, is modeled, using the developed modeling approach. The 3-D nonlinear elastic stress–strain relation described by Eq. (18.4) is recalled to define material properties through VUMAT, introducing both the mesoscopic nonlinearities. The SOE constants (Lamé's parameters λ and μ) can be calculated in terms of the material's Young's modulus (68.9 GPa in this case) and Poisson's ratio (0.33). The TOE constants of the aluminum are: $\mathcal{A} = -320$ GPa, $\mathcal{B} = -200$ GPa and $\mathcal{C} = -190$ GPa [45]. 3-D eight-node brick elements in Abaqus® are used to mesh the medium. In the mesh, 20 elements are allocated per wavelength of the fundamental wave mode, while nine elements are assigned along the plate's thickness, in order to warrant simulation precision.

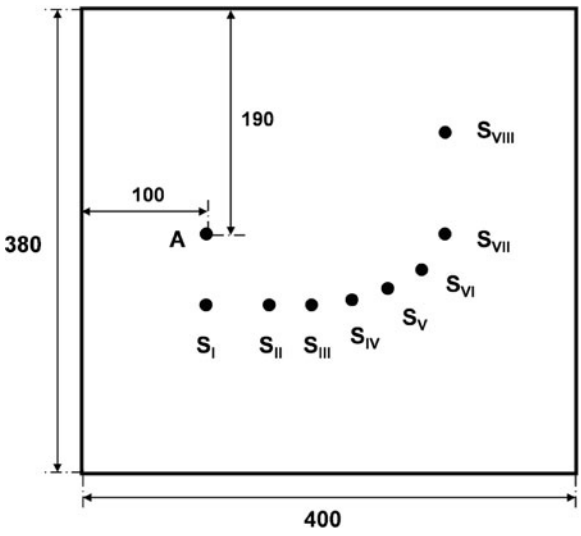

(a)

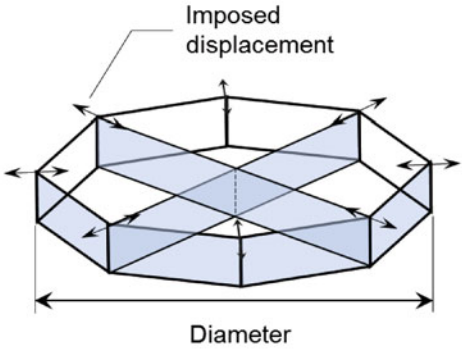

(b)

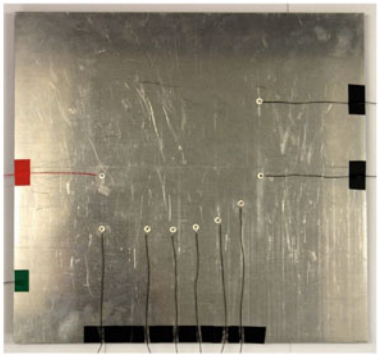

(c)

Fig. 18.8 An aluminum plate with eight sensing paths **A** – $\mathbf{S}_i$ ($i = \mathrm{I}, \mathrm{II} \ldots \mathrm{VIII}$): (**a**) schematic diagram (dimensions displayed in mm); (**b**) PZT model for actuators; and (**c**) specimen in the experiment

Nine circular PZT wafers (Φ 8 mm; thickness: 0.5 mm each) are collocated on a side of the aluminum plate. These PZT wafers function, respectively, as a wave actuator (**A**) and sensors ($\mathbf{S_I} - \mathbf{S_{VIII}}$), leading to eight sensing paths. These eight sensing paths are deliberately configured, to deliver a distance d_i (i = I, II ... VIII) between **A** and $\mathbf{S}_i$ ranging from 60 to 200 mm with an increment of 20 mm, illustrated in Fig. 18.8a. Each PZT wafer is modeled by meshing it using four elements. By imposing uniform in-plane radial displacements on the nodes along periphery of the PZT wafer, Fig. 18.8b, five-cycle Hann-windowed sinusoidal tone bursts are excited at 800 kHz. The excitation frequency of 800 kHz enables the generation of the S_1 mode as the fundamental wave mode in accordance with Fig. 18.2 (plate thickness: 4.5 mm). Wave signals (in-plane elemental strains) are acquired at locations of eight sensors.

In experimental, the measurement configuration that is the same as that in simulation is adopted. Nine PZT wafers are surface-mounted on a 6061 aluminum plate (free of damage), as shown in Fig. 18.8c. These wafers are connected to a signal generation and acquisition system developed on a VXI platform [25]. The same excitation signal as in the simulation is remained, and probing waves are generated by an Agilent® E1441 arbitrary waveform generator, amplified by a Ciprian© US-TXP-3 linear power amplifier to 100 $V_{p\text{-}p}$, and then applied on the PZT actuator. Signals are acquired with Agilent® E1438 signal digitizer at a sampling rate of 100 MHz.

STFT-based signal processing is applied on all captured signals, to extract signal features for constructing RANP via each sensing path using Eq. (18.26). The relationships of RANP versus wave propagation distance obtained from the simulation and the experiment are displayed in Fig. 18.9a, b, respectively. It is obvious that both highlight a quasi-linear cumulative increase of RANP over wave propagation. This has demonstrated that the nonlinearity embodied in captured wave signals is from the intrinsic nonlinearity of the medium. Good matching between the two relationships in Fig. 18.9 has validated the developed modeling technique.

18.3.4.2 RANP vs. Sensing Path Offset

Next, Lamb wave propagation in an aluminum plate bearing a fatigue crack is evaluated using the developed modeling approach and experimental validation, with an aim to develop a quantitative correlation between RANP of each sensing path and the offset distance from that sensing path to the fatigue crack site. With the presence of a fatigue crack, the plasticity-driven nonlinearity and CAN are introduced in the modeling.

The same aluminum plate (400 × 240 × 4.5 mm^3) is modeled, as shown schematically in Fig. 18.10a. To initiate a fatigue crack, a triangular notch of 15 × 25 mm is presumed at the center of the upper edge, consistent with the subsequent experiment configuration. A surface crack (approximately 4 mm long and 2.25 mm deep), running in parallel with the plate width, is modeled. The crack features a uniform initial clearance of zero between the two crack surfaces. Ten

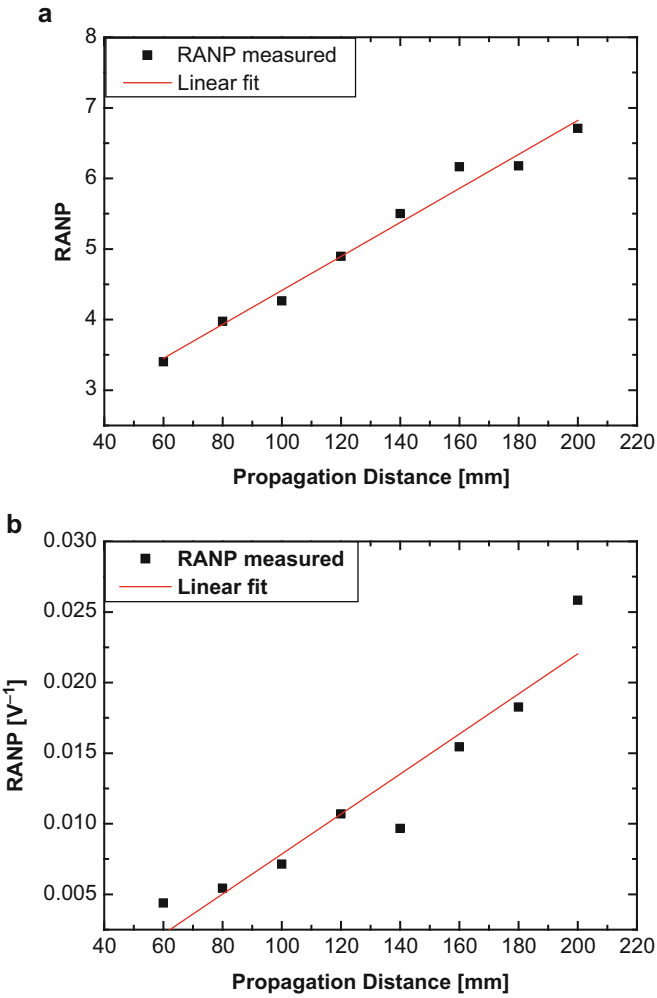

Fig. 18.9 RANP versus wave propagation distance from simulation (**a**) and from the experiment (**b**), respectively

circular PZT wafers (Φ 5 mm; thickness: 0.5 mm each) are allocated on the plate. The positions of these PZT wafers result in five sensing paths $\mathbf{A_i} - \mathbf{S_i}$ (i = I, II . . . V) with each of them being 200 mm long, all perpendicular to the crack. The offset distance d_o (defined in Fig. 18.10b) from the middle point of the fatigue crack to each sensing path is 0, 10, 20, 30, and 40 mm, respectively.

The same simulation procedures, from meshing, material definition, wave excitation, signal acquisition, and dynamic calculation, are recalled. The following parameters are adopted [56] for estimating the local nonlinearity parameter using Eq. (18.11): $\Omega = R_{L-S} = 0.33$, $b = 0.286$ nm, $\Lambda = 1 \times 10^{15}$ m^{-2}, and $h_d = 5.4$ nm.

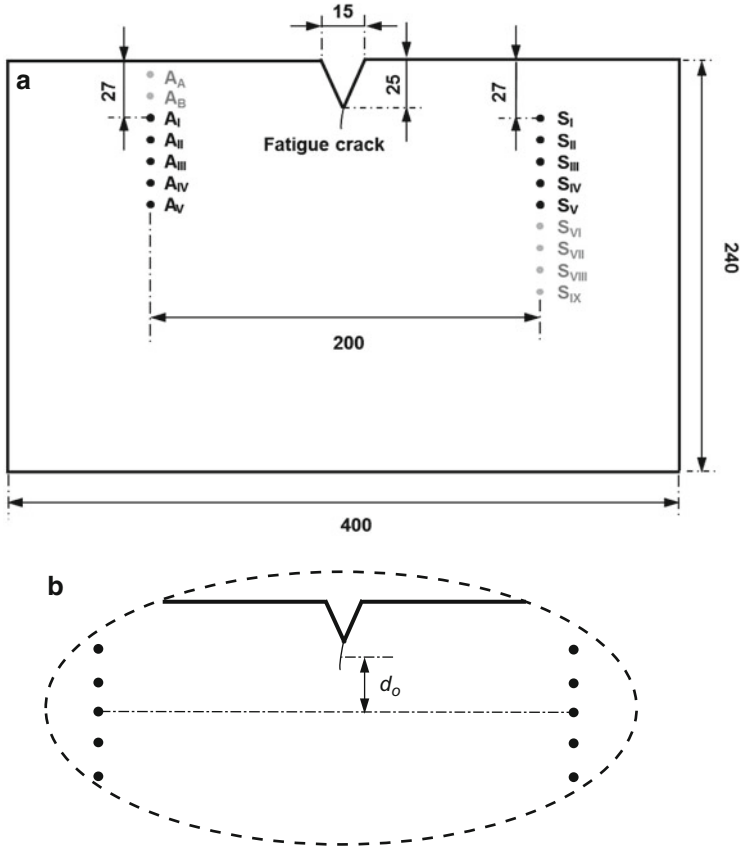

Fig. 18.10 (**a**) An aluminum plate bearing a fatigue crack initiator (unit: mm): $\mathbf{A}_i - \mathbf{S}_i$ ($i = \mathrm{I}, \mathrm{II} \ldots \mathrm{V}$) for initial testing, and additional wafers $\mathbf{A}_\mathbf{A}$, $\mathbf{A}_\mathbf{B}$, and $\mathbf{S}_j$ ($j = \mathrm{VI}, \mathrm{VII}, \mathrm{VIII}, \mathrm{IX}$) for testing in Sect. 18.3.4.3; and (**b**) definition of d_o (crack length exaggerated)

CAN is taken into account in the model. The tone bursts, modulated by a 16-cycle Hann window, are excited at 800 kHz. Compared with the five-cycle signal used earlier, the adoption of the 16-cycle tone bursts is to strike a balance between easy isolation of different wave packets and explicit recognition of second harmonics.

In experiment, an aluminum plate (6061-T6) of the same dimensions and the same PZT configuration as in simulation is used. The specimen has undergone a HCF before signal measurement. After approximately 200,000 cycles (at 5 Hz and with a magnitude of 10 kN), a barely visible fatigue crack is generated, roughly 4 mm long and half of the plate thickness deep. Ten PZT wafers of 5 mm in diameter for each are attached to the plate in line with Fig. 18.10a, only after completing the fatigue testing, in order to avoid possible degradation in adhesive layers during the fatigue processing. The test is carried out in accordance with the experiment procedure described in the previous case study (Sect. 18.3.4.1).

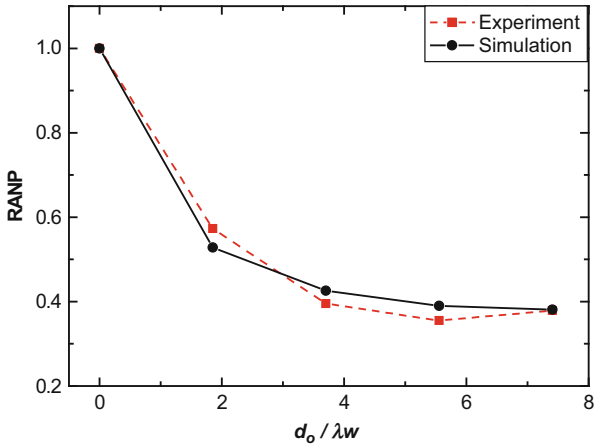

Fig. 18.11 Normalized RANP versus d_o/λ_w (normalized offset distance with regard to probing wavelength λ_w) from the simulation and experiment

Applied with STFT-based signal processing, RANP is calculated for each sensing path and then normalized with regarding to that ascertained via $\mathbf{A_I} - \mathbf{S_I}$, as exhibited in Fig. 18.11, against the offset distance. Note that d_o is normalized in the figure with respect to the probing wavelength λ_w, so that the correlation obtained can be extended to general cases of arbitrary frequency-thickness products. The two curves in Fig. 18.11 agree with one another quantitatively, with the greatest error less than 9%, corroborating the effectiveness of the modeling approach.

The relationship of RANP versus d_o/λ_w implies that RANP reaches its peak value when the sensing path right traverses the fatigue crack (i.e., $\mathbf{A_I} - \mathbf{S_I}$). Then, RANP decreases quickly, as d_o/λ_w increases to 1.8 (corresponding to $d_o = 10$ mm), and then the decrease slows down as d_o/λ_w reaches 3.6 (corresponding to $d_o = 20$ mm). Beyond this point, RANP decreases gradually to approximately 40% of its largest magnitude and no considerable change can be observed after d_o/λ_w reaches 5.5 ($d_o = 30$ mm).

18.3.4.3 Dependence on Angle of Incidence and Wave Propagation Distance

Note that the relationship of RANP versus d_o/λ_w presented in Fig. 18.11 is ascertained when all the sensing paths are 200 mm in length, and perpendicular to the crack. To take a step further, RANP is also obtained, using FEM simulation, when the length of sensing path and angle of incidence of the probing waves vary. With additional PZT wafers (actuators $\mathbf{A_A}$, $\mathbf{A_B}$, and sensors $\mathbf{S_{VI}}$, $\mathbf{S_{VII}}$, $\mathbf{S_{VIII}}$, $\mathbf{S_{IX}}$ in Fig. 18.10a), a series of sensing paths of different lengths and different angles of incidence is formed. The path length varies from 100 to 400 mm in an increment of

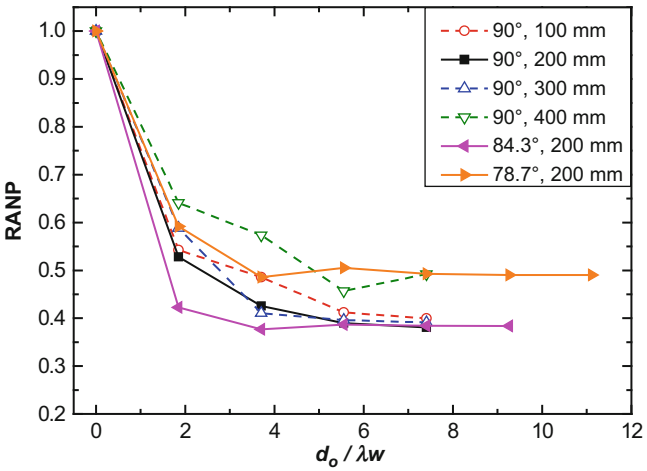

Fig. 18.12 RANP *versus* d_o/λ_w, subjected to angle of incidence (solid lines) and wave propagation distance (dashed lines)

100 mm, and the angle of incidence from 90° ($\mathbf{A_I} - \mathbf{S_I}$) through 84.3° ($\mathbf{A_B} - \mathbf{S_{II}}$) to 78.7° ($\mathbf{A_A} - \mathbf{S_{III}}$). Figure 18.12 shows the obtained correlation between *RANP* and d_o/λ_w, to observe no significant difference in terms of the trend of the curves when the incident angles are different. All curves indicate a 40–60% drop in RANP in the region near the crack; the change in RANP is minute when $d_o/\lambda_w > 3.6$. This observation has corroborated the statement made earlier that the local nonlinearity due to fatigue damage (β_l) is more significant compared with that due to material (β_g).

Both Figs. 18.11 and 18.12 have demonstrated a reliable relationship between RANP and the offset distance of sensing paths in a sensor network. With an up to approximately ±10° change from orthogonality in the incidence angle and different wave propagation distance, RANP is observed to be more dependent on the offset distance. This observation would be of importance when a dense sensor network is used to localize fatigue damage.

18.4 System Development for Implementation

The preceding sections have been focused on the theoretical development of a Lamb-wave-based NDE/SHM approach using nonlinear signal features. From a practical point of view, the implementation of any NDE/SHM strategy in the real world requires dedicated hardware and software systems, whose performances are critical to the success of the developed strategy. Both functionality and practicality need to be carefully addressed when designing, selecting, and integrating algo-

rithms, devices, modules, and tools. In prevailing experimental studies, isolated or incoherent sensing and measurement devices, such as ultrasonic wedge transducers, function generators, and oscilloscopes, are usually employed for guided wave generation and acquisition. Applicability of these devices and techniques is often limited to simple structures examined in well-controlled laboratorial environment. To develop a robust guided wave SHM strategy for real-world applications, a modularized system is configured in this study, by virtue of a virtual instrument technique. This section discusses the sensing technique employed in this system and the modularized hardware components for in situ deployment.

18.4.1 Decentralized Standard Sensing

A PZT wafer provides substantial weight saving over conventional ultrasonic transducer, with merits like low-power consumption, negligible footprints, ease of integration into host structures, high operating frequency, dual roles as an actuator and a sensor, as well as reasonably low cost. However, a single PZT wafer performs local acquisition of guided waves, and generally tends to supply inadequate information for SHM of engineering structures which often serve in harsh working conditions. This erodes the confidence in the obtained result for damage detection purposes. Spatially distributed PZT wafers are thus linked to configure a sensor network. By "communicating" with each other, individual sensors act cooperatively to allow desirable redundancy and to enhance reliability of guided wave signal acquisition.

However, for many structures such as high-speed vehicles or satellites, it is often uneconomic and sometimes infeasible to prudentially allocate every single sensor in a sensor network towards a cost-effective configuration, due to the complex and diverse geometries involved. For most field applications, unlike laboratorial experiments, optimization of sensor placement on a case-by-case basis cannot be achieved until the actual test has been done. This would require additional access to the structures in operation in order to modify the current sensor network configuration, which is most likely impossible. Moreover, to manually affix individual wafers to inspected structures with adhesives, and solder insulated wires on each of them can unavoidably introduce performance inconsistency from one wafer to one another, leading to discrepancy and monitoring instability. With such inefficiency recognized, a sensor networking approach based on the concept of "decentralized standard sensing" is developed in this study, aimed at an effortless and universal solution to guided wave excitation and generation in various structures with high flexibility yet a reduced cost.

Conceptually, "standard sensing" refers to a standardized sensing unit, made up of a PZT wafer and a self-developed printed circuit board (both embedded in a polyimide film), as shown in Fig. 18.13. The film not only covers the wafer and the circuit for protection purposes, but also provides a convenient surface for installation of the unit on the inspected structure. Thin and flexible, the polyimide film can

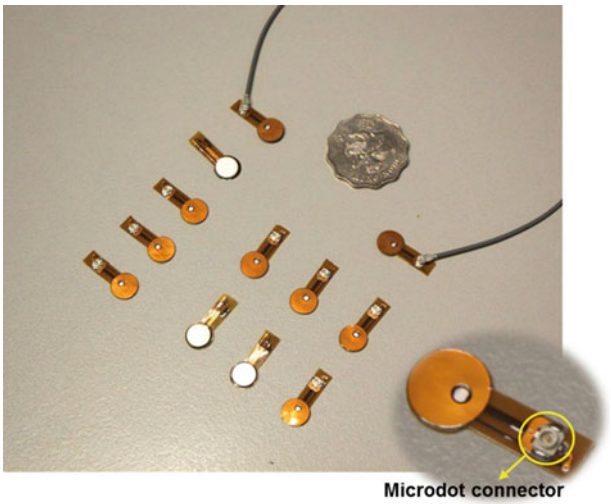

Fig. 18.13 Standard PZT sensing units with a close-up view

deform to adapt to curved surfaces of aerospace structures. Inside the film, the circuit is connected to the electrodes of a PZT wafer via soldering and/or conductive adhesives, and a standard microdot connector (see the insert of Fig. 18.13) in the circuit enables a quick, standardized connection to the controlling hardware through a shielded cable. Each sensing unit features a thickness of less than 0.2 mm and a weight less than 3 g, contributing negligible weight and volume penalty to the host structure. With reversible piezoelectricity, each unit can alternate its role between an active actuator and a passive sensor through a switch array controller. A multitude of such units can be flexibly networked to configure a sensor network, which can be permanently integrated into host structures to accommodate their diverse geometrical identities and boundary conditions. Notably, the use of the standardized units can avoid deliberate consideration on positioning of individual sensors, saving significant efforts when large-scale sensor networks are concerned. To ensure its functionality in rugged working conditions, each unit is managed to be insulated from the environment through an epoxy layer once attached to the structure.

In parallel, "decentralization" in the concept signifies the self-contained functionality of individual units in a configured sensor network. Being a standalone functional unit, a standardized sensing unit can be independently prefabricated, stored, and integrated into a sensor network. During signal processing, a sensing unit is independent of other units in the network—an important feature when the measurement is conducted in harsh conditions. Warranted by high redundancy, such decentralization effectively de-emphasizes the contribution from individual units, thus enhancing error-tolerance and resistance to malfunctions of individual sensors in a large-scale network. This trait can be particularly important for SHM, without which the erroneous or incomplete perceptions from a few sensors (due to various factors such as measurement uncertainty) may interfere with useful information perceived by others in the network, delivering inaccurate monitoring results.

18.4.2 Development of a Modularized In Situ Diagnostic System

As mentioned earlier, in conventional laboratorial tests, guided wave generation and acquisition can be easily achieved with separate measurement devices; for real-world SHM applications, nevertheless, it is desirable that all the functional units are well integrated with mutual communication to fulfill the designated SHM task. To deploy the proposed SHM method, a compact, integrated online diagnosis system is developed on a PCI eXtensions for Instrumentation (PXI) platform with the virtual instrument technique. In conjunction with the use of active sensor networks as discussed in the previous section, the developed system embraces some commercial technologies, including a sensor network control module, an arbitrary waveform generation (AWG) module (with amplification), a multi-channel data acquisition (DAQ) module, and a central control and data processing (CCDP) module. The schematic diagram of the diagnostic system (with the five pivotal modules) is shown in Fig. 18.14a, and the actual system is photographed in Fig. 18.14b.

More specifically, the CCDP commands all other functional modules. This module integrates all the necessary digital signal processing tools including correlation calculation, Hilbert transform, and STFT-based analysis. These preprogrammed algorithms enable the system to analyze and interpret acquired signals in multiple dimensions (e.g., time domain, frequency domain, and time–frequency domain), in order to enhance the effectiveness of identification of different types of damage under a wide range of working conditions. They can also minimize the interference from measurement noise and uncertainties, enhance the SNR, extract desired signal features, and consolidate all the information provided by the entire sensor network. Upon signal processing, damage in the medium, if any, will be presented in diagnostic images using appropriate imaging algorithms. The software features a three-layer architecture, as shown in Fig. 18.15. All the modules are integrated on a PXI bus platform to configure a compact diagnosis system.

18.5 Characterization of Multiple Fatigue Cracks in Aluminum Plates

While simulation and preliminary experiments have been performed in the previous sections to study the feasibility of using nonlinear Lamb wave attributes for fatigue damage identification, the techniques have not been implemented with sensor networks, which is one of the most crucial concepts for real-time SHM. In this section, a case study is presented, where nonlinear Lamb wave features extracted from active sensor networks are employed for locating fatigue damage in plate structures. More specifically, a RANP estimate is calculated for each sensing path in the sensor network, and a corresponding damage index is produced through a frequency domain analysis for damage diagnostic imaging.

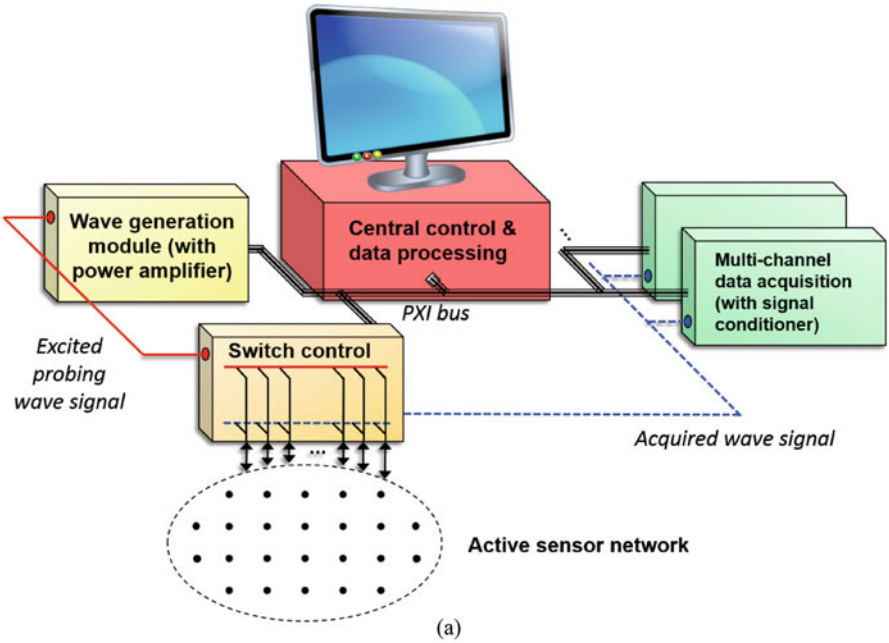

(a)

(b)

Fig. 18.14 (**a**) Schematic diagram of the framework of the configured system with five pivotal modules; and (**b**) the integrated SHM system

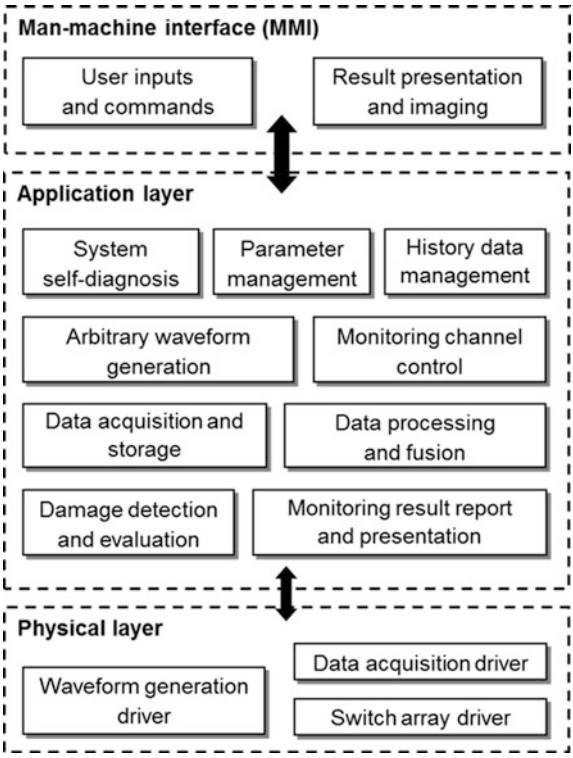

Fig. 18.15 The three-layer software architecture of the configured SHM system

18.5.1 Experimental Investigation

As schematically shown in Fig. 18.16a, the aluminum panel under inspection measures 380 × 400 × 4.5 mm^3 with four through-thickness rivet holes for bond connections (10 mm in diameter each) in an engineering context. The sample undergoes a fatigue testing procedure on a digitally controlled MTS® testing platform (858 Mini Bionix), subject to a sinusoidal tensile load of 5 Hz, as photographed in Fig. 18.16b. A tiny notch with a sharp tip is inscribed at the edge of each of two randomly chosen rivet holes (Holes 1 and 2), to expediate initiation and growth of fatigue cracks. After circa 500,000 cycles, two barely visible fatigue cracks are produced: Crack 1 is about 5 mm long, initiated from Hole 1 as displayed in Fig. 18.16c, and Crack 2 is about 3 mm long at Hole 2. Eight PZT wafers (diameter: 5 mm, thickness: 0.5 mm each), denoted by $\mathbf{T}_i$ ($i = 1, 2 \ldots 8$) with respective coordinates shown in Fig. 18.16a, are surface-mounted on the fatigued plate to form an active sensor network. This sensor network offers 56 sensing paths, which are instrumented with the SHM system introduced in Sect. 18.4. In conjunction with the system, a Ciprian© US-TXP-3 power amplifier is specifically chosen to provide a large enough excitation voltage (80 $V_{p\text{-}p}$) on PZT actuators for second harmonic observation. 16-cycle Hann-windowed sinusoidal tone bursts at

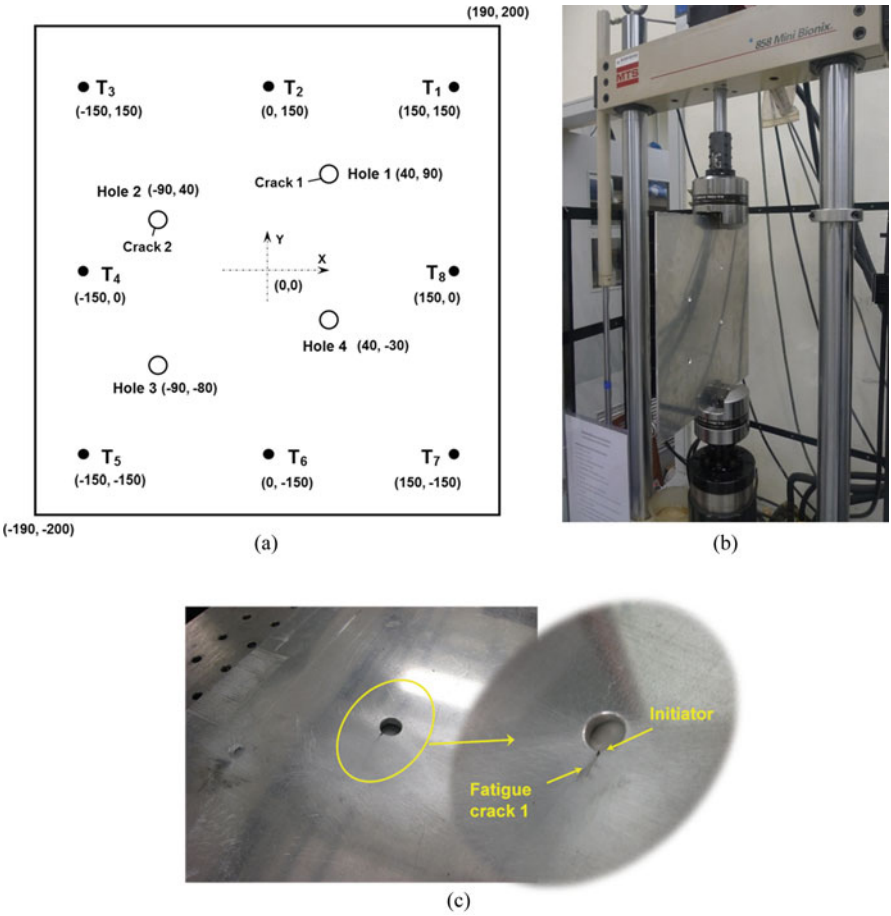

Fig. 18.16 (**a**) Schematic diagram of the aluminum panel with four rivet holes, attached with an active PZT sensor network consisting of eight sensors (all dimensions and coordinates shown in mm); (**b**) the specimen undergoing fatigue testing; and (**c**) a close-up of Crack 1 after fatigue testing

800 kHz, conforming to the mode selection criterion described in Sect. 18.3.2 and the dispersion curves in Fig. 18.2 is generated, making S_1 the probing fundamental mode and S_2 the cumulatively generated second harmonics once nonlinearities in the structure are encountered. Response wave signals are then captured by the system and stored and processed by the CCDP module of the SHM system. Notice that in this method no baseline (healthy condition) information is acquired.

18.5.2 Signal Processing and Imaging

The procedure of diagnostic damage imaging is established based on the correlation between the offset distance (d_o) from the fatigue damage to a particular sensing path in the sensor network and the value of RANP extracted from the Lamb wave signals acquired via that sensing path. It has been shown in Sect. 18.3.4 that the smaller d_o is, the higher RANP is, presenting approximately monotonous variation. In addition, such a correlation is observed to be insensitive to the difference in the length of a sensing path, which can be attributable to the fact that the local nonlinearity due to fatigue damage (β_l) is more dominant in the signal compared with that due to material (β_g). It is also relevant to note that RANP captured via a sensing path possesses high inertness to distant damage away from that path, implying a sensing path perceives the damage near it only. Such a trait makes it possible to identify multi-fatigue damage using such a nonlinear parameter.

Residing on RANP, a damage index (DI) for the inspected region is constructed using a probability imaging algorithm (PIA) [57]. The PIA differentiates itself from traditional damage imaging techniques such as tomography by taking advantage of its unique traits, such as the use of sparse sensor networks and the adoption of a fast imaging algorithm. With PIA, the plane structure of the structure under inspection is virtually meshed into an image. The probability of damage presence at each spatial point is represented by the value borne by its corresponding pixel in the image (called *field value*), which is adjusted by a weight function that determines the influence of each sensing path in the sensor network. For a RANP-based DI, its field value at pixel (x, y) is defined as:

$$DI_{i,j}(x, y) = RANP_{i,j}\left[\frac{\varsigma - R_{i,j}(x, y)}{\varsigma - 1}\right]. \tag{18.28}$$

The subscript i, j stresses that the index is defined for a single sensing path from transducer $\mathbf{T_i}$ to $\mathbf{T_j}$. In addition, ς is a scaling parameter. $R_{ij}(x, y)$ is a weight parameter [57, 58] which reads

$$R_{i,j}(x, y) = \begin{cases} \dfrac{\sqrt{(x_m - x_i)^2 + (y_n - y_i)^2} + \sqrt{(x_m - x_j)^2 + (y_n - y_j)^2}}{\sqrt{(x_i - x_j)^2 + (y_i - y_j)^2}} & \text{when} \quad R_{i,j}(x, y) < \varsigma \\ \varsigma. & \text{when} \quad R_{i,j}(x, y) \geq \varsigma \end{cases} \tag{18.29}$$

With Eq. (18.28), each sensing path in the sensor network contributes a probabilistic image. Ideally, all the field values are low provided the inspected area is free of fatigue damage (practically it is not zero due to noise interference), while they are elevated pronouncedly at those pixels contained in the fatigue damage zone, subject to the corresponding d_o.

As an example, the time domain signal captured via sensing path $\mathbf{T_2} - \mathbf{T_7}$ is displayed in Fig. 18.17a. To facilitate the extraction of the amplitudes of the second

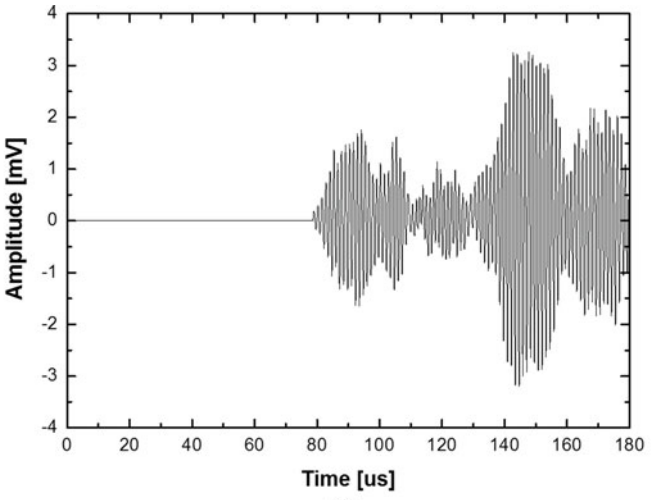

(a)

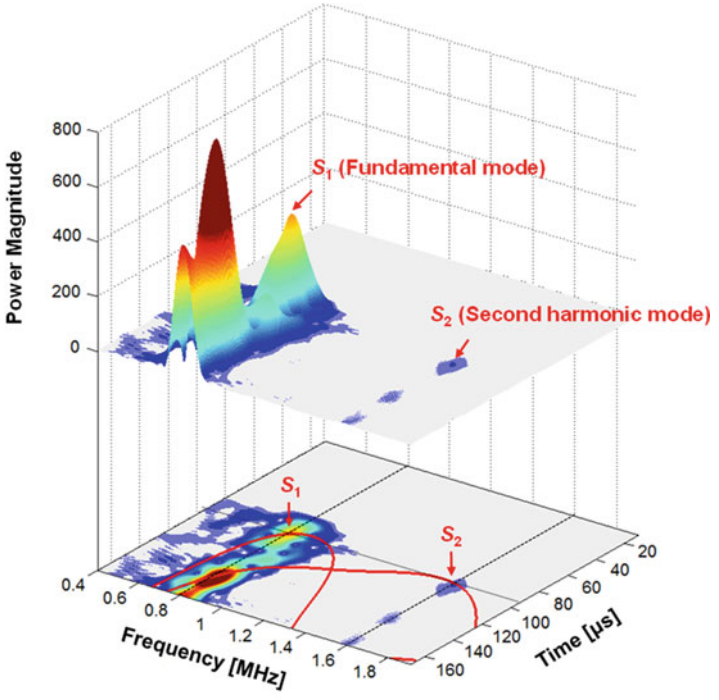

(b)

Fig. 18.17 (**a**) Time domain signal acquired via sensing path $\mathbf{T_2 - T_7}$; (**b**) time–frequency spectrogram of the signal in (**a**) obtained using STFT, with 3-D and planar representations integrated with dispersion curves of S_1 and S_2; and (**c**) amplitude profiles extracted from (**b**) at the fundamental frequency (800 kHz) and at the second harmonic frequency (1.6 MHz), respectively

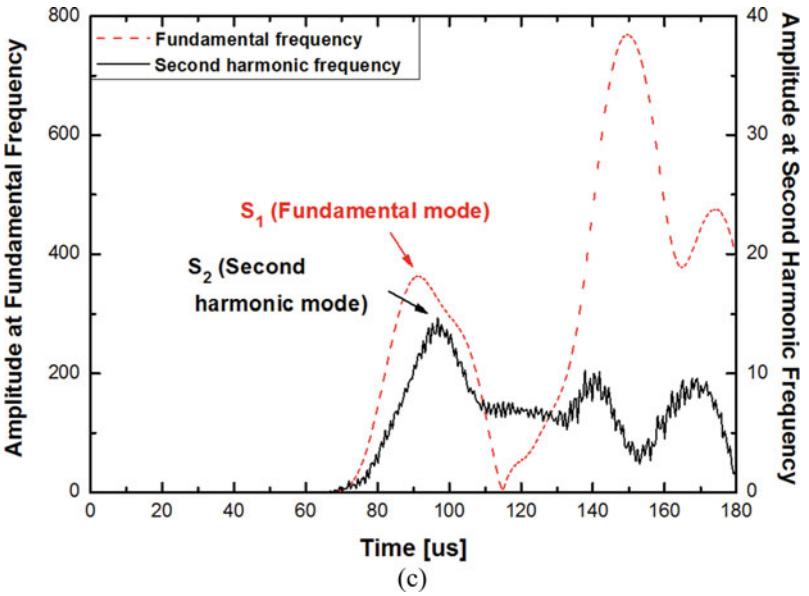

Fig. 18.17 (continued)

harmonic mode (S_2) and of the fundamental mode (S_1), STFT is performed to deploy the signal over a time–frequency domain, as shown in Fig. 18.17b. The fundamental and second harmonic modes are then extracted at 800 kHz and at 1.6 MHz, respectively, and their amplitude profiles are plotted against time, as shown in Fig. 18.17c, where A_1 and A_2 can be respectively determined. Now, the RANP for this sensing path can be calculated using Eq. (18.26), and the DI is subsequently computed through Eqs. (18.28) and (18.29) by which a source image can be created, as exemplified by Fig. 18. This source image reflects the probability of damage occurrence at each pixel perceived by a particular sensing path, calibrated in gray scale. The scaling parameter ς in Eqs. (18.28) and (18.29) is empirically adjusted to control the effective area regulated by each sensing path, which can be estimated by referring to the conclusions from Sect. 18.3.4 and Fig. 18.11.

Repeating this process for the other 55 sensing paths, 56 source images are then obtained, which then can be fused into a final diagnostic image as shown in Fig. 18.19 by taking the arithmetic average of 56 field values at each pixel. As can been seen, two regions with larger grayscale values (i.e., higher field values) can be observed, covering Holes 1 and 2 as well as their vicinities. These darker areas imply higher probabilities of fatigue cracks occurring, although artifacts due to measurement noise can also be seen in the image.

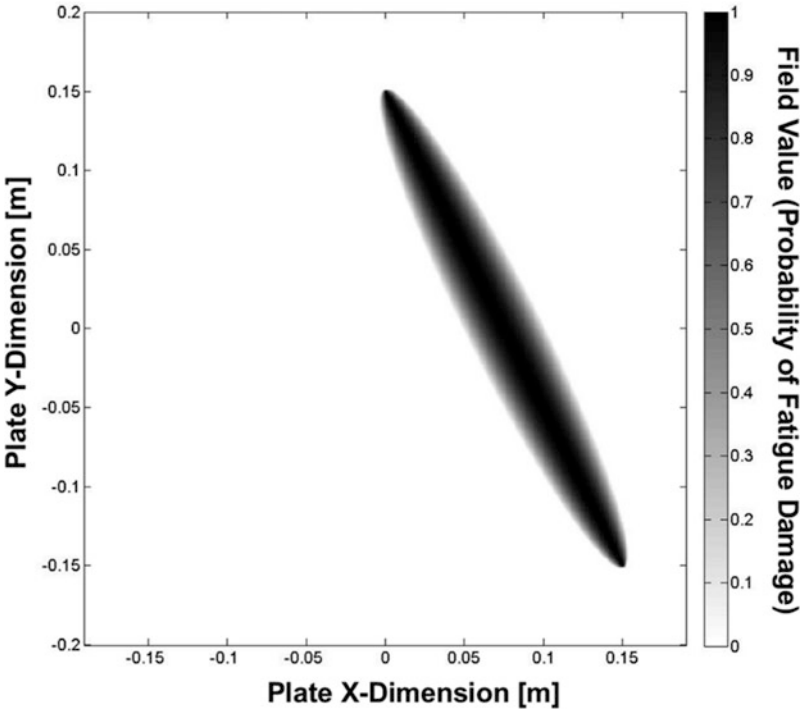

Fig. 18.18 A source image obtained using RANP-based DI showing the probability of damage occurrence over the entire plate area, as perceived by a single sensing path

18.5.3 Results and Discussions

Once the diagnostic image is constructed, a threshold κ can be further applied to the field values of the DI in order to enhance the identification result by masking measurement noise. More specifically, κ is a preset percentage of the maximum field value of the image, and any field value less than κ is forced to approach zero. As some representative results, Fig. 18.20 displays the diagnostic images. When $\kappa = 0.8$, two fatigue damage zones are clearly pictured in Fig. 18.20d. It is noteworthy that these two highlighted regions have nothing to do with the rivet holes themselves or the fatigue crack initiators at the hole edges. In fact, the two highlighted zones not only capture the fatigue cracks, but also describe any plastic regions around them, as plasticity-induced nonlinearities in the vicinities of the cracks would also contribute to the increase in RANP.

It is important to point out that this approach would explore any abnormal, local increase in RANP due to damage-induced nonlinearities; thus, it may be independent of any baseline condition in which the connatural material nonlinearity, geometric nonlinearity, and gross damage (e.g., the rivet holes in this study) in the structure would not increase RANP locally.

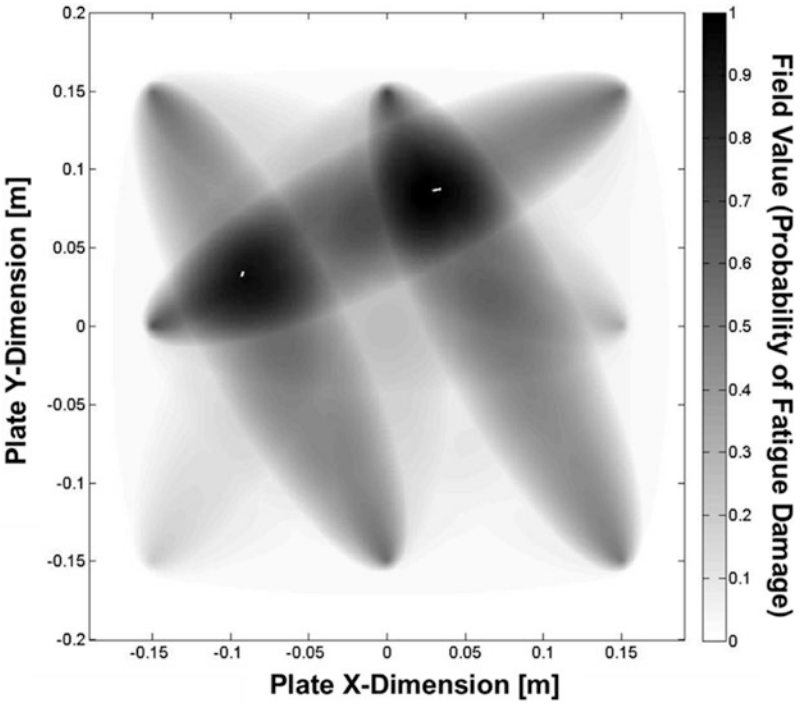

Fig. 18.19 Final diagnostic image after fusing source images, with two areas with particularly high (dark) field values, indicating higher probabilities of damage occurring at these two places

18.6 Conclusions

In this chapter, a damage identification method based on Lamb waves is investigated, through the modeling of nonlinear Lamb wave features and its application in characterizing multiple fatigue cracks in aluminum plates in conjunction with the use of an active sensor network. In doing so, propagation characteristics of Lamb waves in thin plate structures are first reviewed, and linear and nonlinear features of Lamb wave signals are briefly discussed. A dedicated modeling technique is then established to understand the nonlinearity related to the material and fatigue damage. A nonlinear feature, RANP, is engineered to measure nonlinearity introduced into ultrasonic signals. Results from the simulation and experiment show good consistency, both revealing that the parameter RANP grows cumulatively with wave propagation due to the material, and RANP changes subjected to the offset distance from a sensing path to the damage site.

In the meantime, an in situ health diagnosis system, largely oriented at real-world SHM for in-service engineering structures, is developed by exploring local propagation characteristics of actively generated guided waves in a sensor network. Using such a system, a proof-of-concept case study is presented, in which fatigue

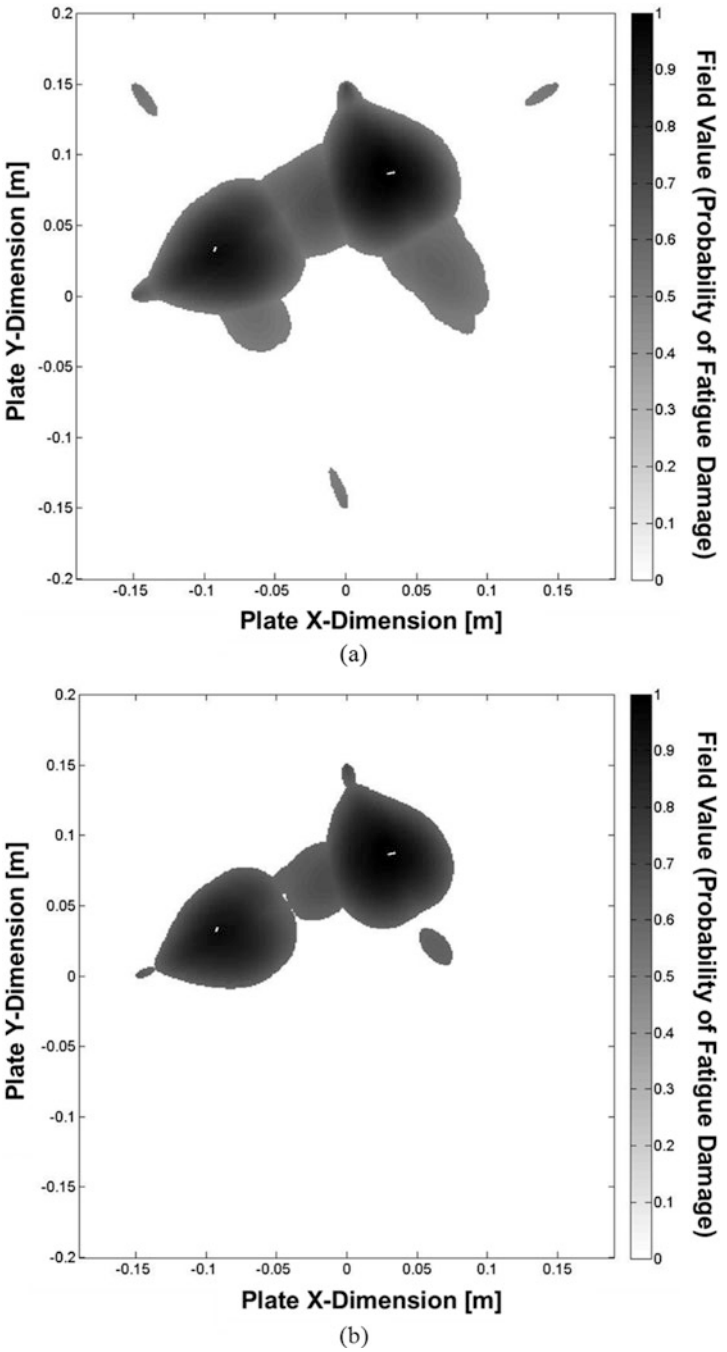

Fig. 18.20 Diagnostic images applied with different threshold: (**a**) $\kappa = 0.5$; (**b**) $\kappa = 0.6$; (**c**) $\kappa = 0.7$; and (**d**) $\kappa = 0.8$

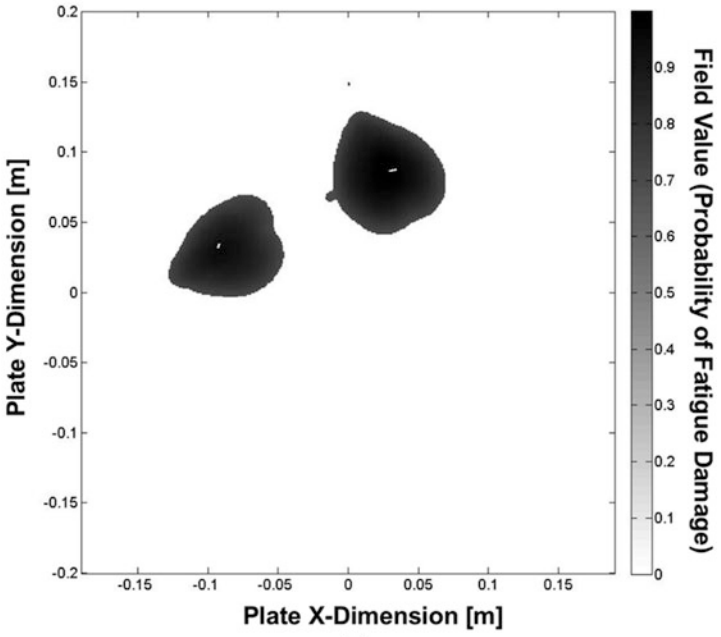

(c)

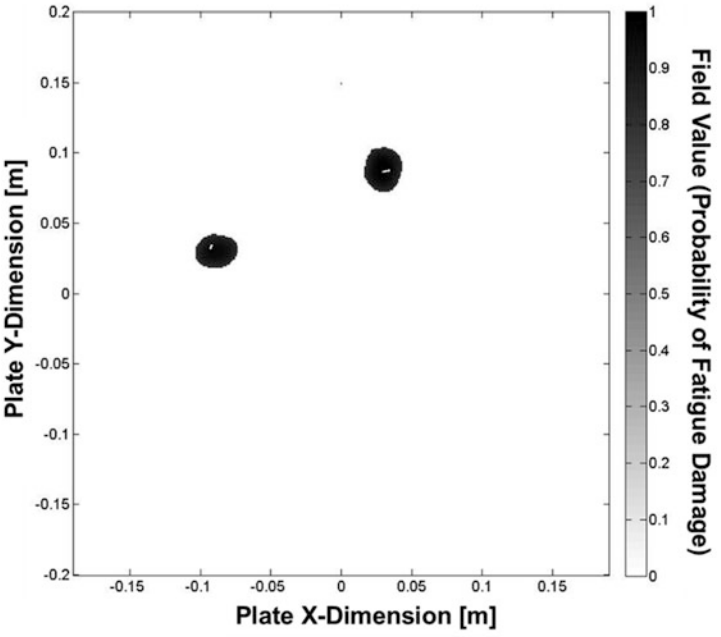

(d)

Fig. 18.20 (continued)

cracks in an aluminum panel are evaluated experimentally using the developed RANP feature. A damage imaging algorithm based on RANP is then developed, which is found to be highly sensitive to damage-induced nonlinearities and is successfully employed to locate multiple small-scale fatigue cracks simultaneously, using the spatial information provided by the arrangement of the sensor network. As illustrated in the case study, accurate characterization results have demonstrated the feasibility of the proposed modeling approach in quantitatively characterizing real-world fatigue damage.

References

1. National Aeronautics and Space Administration (NASA). Derailed, System Failure Case Studies 1 (2007). https://nsc.nasa.gov/SFCS/SystemFailure-CaseStudyFile/Download/409, retrieved 2 Dec 2016
2. J.D. Achenbach, Quantitative nondestructive evaluation. Int. J. Solids Struct. **37**, 13–27 (2000)
3. C. Boller, Ways and options for aircraft structural health management. Smart Mater. Struct. **10**, 432–440 (2001)
4. J. Gray, G.-R. Tillack, in X-ray Imaging Methods Over the Last 25 Years – New Advances and Capabilities, eds. By D.O. Thompson, D.E. Chimenti. *Review of Progress in Quantitative Nondestructive Evaluation*, vol. 20 (American Institute of Physics, New York, 2001), pp. 16–32
5. J.D.N. Cheeke, *Fundamentals and Applications of Ultrasonic Waves* (CPC Press, Boca Raton, 2002)
6. D.L. Balageas, Structural health monitoring R&D at the European Research Establishments in Aeronautics (EREA). Aerosp. Sci. Technol. **6**, 159–170 (2002)
7. H. Sohn, C.R. Farrar, F.M. Hemez, D.D. Shunk, D.W. Stinemates, B. R. Nadler, A review of structural health monitoring literature: 1996-2001. Los Alamos National Laboratory Report LA-13976-MS (2003)
8. Z. Su, L. Ye, *Identification of Damage Using Lamb Waves: From Fundamentals to Applications* (Springer, Berlin, 2009)
9. D. Pascoe, Composite troubles in aircraft (2005). http://www.yachtsurvey.co-m/composite_troubles_in_aircraft.htm, retrieved 3 Dec 2016
10. A. Raghavan, C.E.S. Cesnik, Review of guided-wave structural health monitoring. Shock Vib. Digest **39**, 91–114 (2007)
11. J.L. Rose, *Ultrasonic Waves in Solid Media* (Cambridge University Press, New York, 1999)
12. J.D. Achenbach, *Wave Propagation in Elastic Solids* (North Holland/Elsevier Science Publishers, Amsterdam, 1973)
13. L. Yu, V. Giurgiutiu, Multi-mode damage detection methods with piezoelectric wafer active sensors. J. Intell. Mater. Syst. Struct. **20**, 1329–1341 (2009)
14. P. Kudela, W. Ostachowicz, A. Zak, Damage detection in composite plates with embedded PZT transducers. Mech. Syst. Signal Process. **22**, 1327–1335 (2008)
15. T. Wandowski, P. Malinowski, W. Ostachowicz, Damage detection with concentrated configurations of piezoelectric transducers. Smart Mater. Struct. **20**, 025002 (2011)
16. T. Clarke, P. Cawley, P.D. Wilcox, A.J. Croxford, Evaluation of the damage detection capability of a sparse-array guided-wave SHM system applied to a complex structure under varying thermal conditions. IEEE Trans. Ultrason. Ferroelectr. Freq. Control **56**, 2666–2678 (2009)
17. J. Moll, R.T. Schulte, B. Hartmann, C.-P. Fritzen, O. Nelles, Multi-site damage localization in anisotropic plate-like structures using an active guided wave structural health monitoring system. Smart Mater. Struct. **19**, 045022 (2010)

18. W. Ostachowicz, P. Kudela, P. Malinowski, T. Wandowski, Damage localisation in plate-like structures based on PZT sensors. Mech. Syst. Signal Process. **23**, 1805–1829 (2009)
19. Michaels, J. E., Croxford, A. J., Wilcox P. D. Imaging algorithms for locating damage via in situ ultrasonic sensors. 2008 IEEE Sensors Applications Symposium, Atlanta, GA, 2008, pp. 63–67
20. Y.L. Koh, W.K. Chiu, N. Rajic, Effects of local stiffness changes and delamination on Lamb wave transmission using surface-mounted piezoelectric transducers. Compos. Struct. **57**, 437–443 (2002)
21. D.C. Betz, G. Thursby, B. Culshaw, W.J. Staszewski, Identification of structural damage using multifunctional Bragg grating sensors: I. Theory and implementation. Smart Mater. Struct. **15**, 1305–1312 (2006)
22. Z. Wu, X.P. Qing, F.-K. Chang, Damage detection for composite laminate plates with a distributed hybrid PZT/FBG sensor network. J. Intell. Mater. Syst. Struct. **20**, 1069–1077 (2009)
23. J. Zhang, B.W. Drinkwater, P.D. Wilcox, A.J. Hunter, Defect detection using ultrasonic arrays: the multi-mode total focusing method. NDT & E Int. **43**, 123–133 (2010)
24. C. Ramadas, K. Balasubramaniam, M. Joshi, C.V. Krishnamurthy, Interaction of guided Lamb waves with an asymmetrically located delamination in a laminated composite plate. Smart Mater. Struct. **19**, 065009 (2010)
25. C. Zhou, Z. Su, L. Cheng, Quantitative evaluation of orientation-specific damage using elastic waves and probability-based diagnostic imaging. Mech. Syst. Signal Process. **25**, 2135–2156 (2011)
26. Z. Su, L. Cheng, X. Wang, L. Yu, C. Zhou, Predicting delamination of composite laminates using an imaging approach. Smart Mater. Struct. **18**, 074002 (2009)
27. Y. Lu, L. Ye, Z. Su, L.-M. Zhou, L. Cheng, Artificial neural network (ANN)-based crack identification in aluminum plates with Lamb wave signals. J. Intell. Mater. Syst. Struct. **20**, 39–49 (2009)
28. K.Y. Jhang, Nonlinear ultrasonic techniques for nondestructive assessment of micro damage in material: a review. Int. J. Precis. Eng. Manuf. **1**, 123–135 (2009)
29. C. Bermes, J.-Y. Kim, J. Qu, L.J. Jacobs, Nonlinear Lamb waves for the detection of material nonlinearity. Mech. Syst. Signal Process. **22**, 638–646 (2008)
30. J.H. Cantrell, W.T. Yost, Nonlinear ultrasonic characterization of fatigue microstructures. Int. J. Fatigue **23**, 487–490 (2001)
31. M. Deng, J. Pei, Assessment of accumulated fatigue damage in solid plates using nonlinear Lamb wave approach. Appl. Phys. Lett. **90**, 121902 (2007)
32. I. Solodov, J. Wackerl, K. Pfleiderer, G. Busse, Nonlinear self-modulation and subharmonic acoustic spectroscopy for damage detection and location. Appl. Phys. Lett. **84**, 5386–5388 (2004)
33. F. Aymerich, W. Staszewski, J. Experimental study of impact-damage detection in composite laminates using a cross-modulation vibro-acoustic technique. Struct. Health Monit. **9**, 541–553 (2010)
34. M. Muller, A. Sutin, R. Guyer, M. Talmant, P. Laugier, P.A. Johnson, Nonlinear resonant ultrasound spectroscopy (NRUS) applied to damage assessment in bone. J. Acoust. Soc. Am. **118**, 3946–3952 (2005)
35. T. Stratoudaki, R. Ellwood, S. Sharples, M. Clark, M.G. Somekh, I.J. Collison, Measurement of material nonlinearity using surface acoustic wave parametric interaction and laser ultrasonics. J. Acoust. Soc. Am. **129**, 1721–1728 (2011)
36. Y. Xiang, D. Deng, F.Z. Xuan, C.J. Liu, Experimental study of thermal degradation in ferritic Cr-Ni alloy steel plates using nonlinear Lamb waves. NDT & E Int. **44**, 768–774 (2011)
37. B.C. Lee, W.J. Staszewski, Lamb wave propagation modelling for damage detection: I. Two-dimensional analysis. Smart Mater. Struct. **16**, 249–259 (2007)
38. G. Zumpano, M. Meo, A new nonlinear elastic time reversal acoustic method for the identification and localisation of stress corrosion cracking in welded plate-like structures – A simulation study. Int. J. Solids Struct. **44**, 3666–3684 (2007)

39. G.P. Malfense Fierro, F. Ciampa, D. Ginzburg, E. Onder, M. Meo, Nonlinear ultrasound modelling and validation of fatigue damage. J. Sound Vib. **343**, 121–130 (2015)
40. O. Bou Matar, P. Guerder, Y. Li, B. Vandewoestyne, K. Van Den Abeele, A nodal discontinuous Galerkin finite element method for nonlinear elastic wave propagation. J. Acoust. Soc. Am. **131**, 3650–3663 (2012)
41. Y. Shen, V. Giurgiutiu, Predictive modeling of nonlinear wave propagation for structural health monitoring with piezoelectric wafer active sensors. J. Intell. Mater. Syst. Struct. **25**, 506–520 (2014)
42. A.N. Norris, in Finite-Amplitude Waves in Solids, eds. By M.F. Hamilton, D.T. Blackstock. *Nonlinear Acoustics* (Academic, San Diego, 1998), pp. 263–277
43. Z. Qian, *Nonlinear Acoustics*, 2nd edn. (Science Press, Beijing, 2009)
44. L.D. Landau, E.M. Lifshitz, *Theory of Elasticity*, 3rd edn. (Pergamon Press, Oxford, 1986)
45. W.J.N. de Lima, M.F. Hamilton, Finite-amplitude waves in isotropic elastic plates. J. Sound Vib. **265**, 819–839 (2003)
46. R.T. Smith, R. Stern, R.W.B. Stephens, Third-order elastic moduli of polycrystalline metals from ultrasonic velocity measurements. J. Acoust. Soc. Am. **40**, 1002–1008 (1966)
47. S.M. Liu, S. Best, S.A. Neild, A.J. Croxford, Z. Zhou, Measuring bulk material nonlinearity using harmonic generation. NDT & E Int. **48**, 46–53 (2012)
48. A. Manonukul, F.P.E. Dunne, High- and low-cycle fatigue crack initiation using polycrystal plasticity. Proc. R. Soc. London Ser. A **460**, 1881–1903 (2004)
49. C. Bermes, Generation and detection of nonlinear Lamb waves for the characterization of material nonlinearities, MS Thesis, Georgia Institute of Technology, 2006
50. C. Pruell, J.-Y. Kim, J. Qu, L.J. Jacobs, Evaluation of fatigue damage using nonlinear guided waves. Smart Mater. Struct. **18**, 035003 (2009)
51. K. Kawashima, R. Omote, T. Ito, H. Fujita, T. Shima, Nonlinear acoustic response through minute surface cracks: FEM simulation and experimentation. Ultrasonics **40**, 611–615 (2002)
52. R. Truell, C. Elbaum, B.B. Chick, *Ultrasonic Methods in Solid State Physics* (Academic, New York, 1969)
53. J.-Y. Kim, L.J. Jacobs, J. Qu, Experimental characterization of fatigue damage in a nickel-base super alloy using nonlinear ultrasonic waves. J. Acoust. Soc. Am. **120**, 1266–1273 (2006)
54. M. Deng, Cumulative second-harmonic generation of generalized Lamb-wave propagation in a solid waveguide. J. Phys. D. Appl. Phys. **33**, 207–215 (2000)
55. J.L. Rose, *Ultrasonic Guided Waves in Solid Media* (Cambridge University Press, New York, 2014)
56. J.H. Cantrell, Substructural organization, dislocation plasticity and harmonic generation in cyclically stressed wavy slip metals. Proc. R. Soc. London, Ser. A **460**, 757–780 (2004)
57. X. Zhao, H. Gao, G. Zhang, B. Ayhan, F. Yan, C. Kwan, J.L. Rose, Active health monitoring of an aircraft wing with embedded piezoelectric sensor/actuator network: I. Defect detection, localization and growth monitoring. Smart Mater. Struct. **16**, 1208–1217 (2007)
58. C. Zhou, Z. Su, L. Cheng, Probability-based diagnostic imaging using hybrid features extracted from ultrasonic Lamb wave signals. Smart Mater. Struct. **20**, 125005 (2011)

Index

T. Kundu (ed.), *Nonlinear Ultrasonic and Vibro-Acoustical Techniques for Nondestructive Evaluation*, https://doi.org/10.1007/978-3-319-94476-0